

1st International Symposium of the International Gravity Field Service

“GRAVITY FIELD OF THE EARTH”

**28 August – 1 September, 2006
Istanbul, TURKEY**

It was a great pleasure to welcome you to the First International Symposium of The International Gravity Field Service (IGFS), to be held August 28 - September 1, 2006 in Istanbul / Turkey.

This was the first symposium of the International Gravity Field Service (IGFS) of the International Association of Geodesy (IAG), and it continues the series of symposia of the former International Gravity and Geoid Commission.

IGFS is a new unified "umbrella" IAG service, which will coordinate collection, validation, archiving and dissemination of gravity field related data, exchange of software of relevance for gravity field activities, and courses, information materials and general public outreach relating to the earth's gravity field.

The overall goal of IGFS is to coordinate the servicing of the geodetic and geophysical community with gravity field-related data, software and information. The combined data of the IGFS entities data will include both satellite-derived global models, terrestrial, airborne, satellite and marine gravity observations, earth tide data, GPS leveling data, digital models of terrain and bathymetry, as well as ocean gravity field and geoid from satellite altimetry. Both the static and the temporal variations of the gravity field will be covered by the IGFS.

IGFS is not handling gravity field data distribution directly - IGFS will function as a unifying service for the following gravity-field related IAG services - "IGFS Centres":

BGI (International Gravity Bureau - collection, archiving and distribution of gravity data), IGeS (International Geoid Service - collection and distribution of geoid models, geoid schools, ICET (International Center for Earth Tides - collection and archiving of global earth tide data), ICGEM (International Centre for Global Earth Models - distribution of satellite and surface spherical harmonic models), IDEMS (International DEM Service - Global Digital Terrain Models).

The symposium mainly aimed to bring together geoscientists working in general areas of modeling the Earth's gravity field. Major scientific themes considered for the 1st International Symposium of the IGFS include;

- Gravity field modeling from combinations of local and satellite data
- Regional geoid projects
- Vertical datum and height systems
- New Earth Geopotential Models (EGM05)

- Satellite Gravity Missions
- Satellite Altimetry
- Airborne Gravity
- Global terrain models for physical geodesy
- Absolute Gravity and gravimetric networks
- Geodynamics and gravity change

We decided to publish the papers presented in the symposium, and selected a Turkish Journal that is dedicated to geodesy and photogrammetry.

A total of 78 papers have been submitted to appear in this symposium proceedings. All of the papers were peer reviewed by conveners and selected referees.

Such scientific assemblies are held every two years, but in separate locations. Hence this symposium of the IGFS offered opportunities to present and discuss earth's gravity field related research and applications.

First International Symposium of The International Gravity Field Service (IGFS) took place in Istanbul. Although thousands of years have passed, Istanbul still maintains its geographical importance. Today Istanbul is a huge metropolis connecting continents, cultures, religions, and being home to eleven million people and one of the greatest business and cultural center of the region.

The venue for the Scientific Assembly was The Cultural Center of Military Museum, Harbiye, Istanbul. The Cultural Center within the constitution of the Military Museum is fully equipped to serve as a venue for cultural, scientific and arts activities. All sort of activities such as scientific sessions, special meetings of work groups, exhibitions and so on were held within the Cultural Center's meeting rooms and exhibition halls during IGFS 2006.

We would like to thank Turkish National Union of Geodesy and Geophysics (TNUGG), International National Union of Geodesy and Geophysics (IUGG), International Association of Geodesy (IAG), Turkish National Research Council (TUBITAK) and International Gravity Field Service (IGFS) for their valuable efforts and contributions for this symposium.

We also would like to thank, in particular, Maj.Gen.Necdet Soyer (President of TNUGG), Michael Sideris (Vice-President of IAG), Rene Forsberg (President of IGFS), Local Organizing Committee (Ali Kılıçoğlu, Ugur Şanlı, Orhan Fırat, Bihter Erol, Onur Yılmaz, Tevfik Özlüdemir), Conveners (Carl-Heinz Ilk, Urs Marti, Ali Kılıçoğlu, Jaako Makinen, Nikolaos K. Pavlis, Steve Kenyon, Nico Sneeuw, Mahmut O.Karslıoğlu Wolfgang Bosch, Ugur Şanlı, Christopher Jekeli, Michael Kuhn, Olivier Francis, Herbert Wilmes, Martin Vermeer) and Mehmet Emin Ayhan (Chief Editor of Harita Dergisi (Journal of Mapping)).

Assoc.Prof.Dr.Ali KILIÇOĞLU

Prof.Dr.Rene FORSBERG

Combination of Ground Gravimetry and GOCE Data for Local Geoid Determination: a Simulation Study

A. Maggi⁽¹⁾, F. Migliaccio⁽¹⁾, M. Reguzzoni⁽²⁾, N. Tselfes⁽³⁾

⁽¹⁾ DIIAR - Politecnico di Milano - Piazza Leonardo da Vinci, 32 - 20133 Milano - Italy

⁽²⁾ Geophysics of the Lithosphere Dept. - Italian National Institute of Oceanography and Applied Geophysics (OGS) c/o Politecnico di Milano, Polo Regionale di Como - Via Valleggio, 11 - 22100 Como - Italy

⁽³⁾ DIIAR - Politecnico di Milano, Polo Regionale di Como - Via Valleggio, 11 - 22100 Como - Italy

Abstract. The satellite gravity field mission GOCE will deliver data and products such as orbit tracking data, observations of the second order derivatives of the gravitational potential and global gravity field models. The space-wise approach will produce filtered versions of these observations, as well as a gravity field model.

Local geoid determination is traditionally made using gravity anomaly data and a global gravity field model as reference, according to the remove-restore technique. Therefore the contribution of the GOCE mission to such a computation can be the global model that is expected to be of high quality. Apart from that, the filtered observations from the space-wise approach can be used as an additional data set.

These expected contributions are evaluated here via simulations. Geoid heights and gravity anomalies are simulated in the Piemonte area in north-western Italy and solutions by least squares collocation are obtained. It is found that using a GOCE reference model with very accurate low degree coefficients leads to better results with respect to older models of lower long wavelength accuracy. When filtered second radial derivatives of the potential coming from the space-wise approach are additionally included it is seen that results improve even more.

Keywords. GOCE mission, space-wise approach, collocation, local geoid.

1 Introduction

GOCE (Gravity field and steady-state Ocean Circulation Explorer) is a satellite mission (ESA, 1999) designed by ESA (European Space Agency), which will be launched in 2007. The goal of this mission is the determination of the stationary part of the gravity field to a high degree of accuracy and spatial resolution. The main instrument on board the satellite will be the “gradiometer” that is composed by six accelerometers and will measure the second

derivatives of the potential (the full tensor) along the satellite orbit (the so-called gradients). Additional information on the gravity field will be derived from the tracking of the satellite orbit by means of a GPS receiver, in combination with measurements of the non-gravitational forces by the accelerometers.

Three different approaches will be applied for the estimation of a global gravity field model (Rummel et al., 2004) from GOCE observations: the direct approach (Bruinsma et al., 2004), the time-wise approach (Pail et al., 2005) and the space-wise approach (Migliaccio et al., 2004) that is realized by the Politecnico di Milano and the University of Copenhagen.

According to the space-wise approach, at the first step, the gravitational potential is directly estimated along the orbit using the orbit tracking data, via the energy conservation method (Jekeli, 1999; Visser et al., 2003). These estimates together with the gradiometric observations are transformed to the frequency domain and filtered by a Wiener filter along the orbit (Albertella et al., 2004; Migliaccio et al., 2005). The filtered data, transformed back to the time domain, are interpolated on a spherical grid with radius equal to the mean satellite altitude by least squares collocation. Using these gridded values a spherical harmonic model of the gravitational potential is computed by integration (Migliaccio and Sansò, 1989). Iterations are made to recover any signal loss due to the initial filtering.

The purpose of this paper is to investigate the significance of the contribution of the GOCE mission and the space-wise approach to local geoid determination by least squares collocation. In particular, this study deals with three outputs of the space-wise approach: 1) the gravity field model, that, along with error covariances, represents the main product of GOCE, whether it comes from the space-wise approach or not, 2) the along track filtered gradients and 3) the gridded gradients. The investigation will be made with simulations. No topographic information will be used, even though

this is possible with real data (Arabelos and Tscherning 1990).

2 A GOCE simulation solution

In the framework of the EGG-C (European GOCE Gravity Consortium) (Balmino, 2001) activities for the preparation of the actual GOCE mission, full simulation solutions are computed (Migliaccio et al, 2005), so that method and software efficiency are tested and ultimately ensured. The latest simulated data set used by EGG-C includes: 60 days of observations at 1Hz sampling rate, gradients and orbit based on the EGM96 model (Lemoine et al, 1998), non-gravitational effects, satellite and instrument orientation parameters and realistic noise. In order to obtain the results presented in this paper, the space-wise approach has been applied to this GOCE data set.

The noise of the measured gradients is of several tens of Eötvös (table 1). After the Wiener filter along the orbit and three iterations the noise decreases to a few milli-Eötvös (table 2). Note that the gradients are measured in the gradiometer reference frame (x,y,z) but through the filtering the observations are transformed into the Local Orbital Reference Frame (ξ,η,r) (LORF), where ξ is almost along-track, η cross-track and r radial.

Table 1. The error standard deviation of the observed gradients along the orbit, in Eötvös (10^{-9}s^{-2}).

T_{xx}	T_{xy}	T_{xz}	T_{yy}	T_{yz}	T_{zz}
109	115	31	61	331	66

Table 2. The error standard deviation of the filtered gradients along the orbit, in milli-Eötvös (10^{-12}s^{-2}).

$T_{\xi\xi}$	$T_{\xi\eta}$	$T_{\xi r}$	$T_{\eta\eta}$	$T_{\eta r}$	T_{rr}
2.3	11.0	2.5	3.5	23.0	3.2

Using the four most accurate filtered gradients a global spherical grid of second order radial derivatives (T_{rr}) is predicted. The error standard deviation is below the milli-Eötvös level, apart from the polar caps that are not covered with observations because of the GOCE orbit inclination ($i = 96.5^\circ$).

The final gravity field model is produced from the combination of the above grid of radial derivatives

and a spherical grid of potential values. The coefficients are calculated by numerical integration. The quality of the model is very high, its error degree variances are smaller (up to degree 200) than the nominal error degree variances of EGM96 (Fig. 1). Such an accuracy is like the one expected from GOCE, regardless of the approach used for the data analysis. The error degree variances are smaller than the degree variances of the field generated as the difference between EGM96 and EIGEN_cg03c (Reigber et al., 2006). This does not imply a judgement by the authors about the quality of these models. However these large differences are similar to the nominal EGM96 errors and this is useful to perform simulations where models with significant long wavelength errors are used as reference.

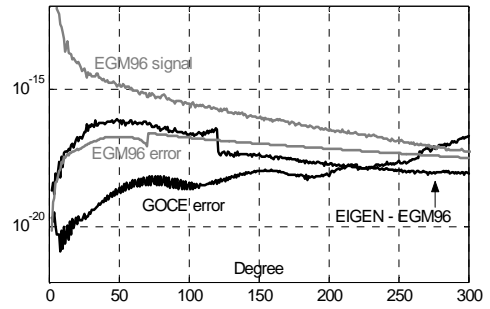


Fig. 1 Signal and error degree variances.

3 Local geoid determination

3.1 Collocation with ground gravity data

A local geoid determination is often made using the well-known method of least squares collocation (Moritz, 1980). The covariance and cross covariance functions of the gravity anomaly Δg and the potential T (that depend on the spherical distance ψ and radii of points) are required:

$$C_{\Delta g_P, \Delta g_Q} = \frac{\mu^2}{R^4} \sum_{\ell=\ell_{\min}}^{\ell_{\max}} \alpha_{\ell}^2 \tilde{\sigma}_{\ell}^2 \left(\frac{R^2}{r_P r_Q} \right)^{\ell+2} P_{\ell}(t), \quad (1)$$

$$C_{T_P, T_Q} = \frac{\mu^2}{R^2} \sum_{\ell=\ell_{\min}}^{\ell_{\max}} \tilde{\sigma}_{\ell}^2 \left(\frac{R^2}{r_P r_Q} \right)^{\ell+1} P_{\ell}(t), \quad (2)$$

$$C_{\Delta g_P, T_Q} = \frac{\mu^2}{R^3} \sum_{\ell=\ell_{\min}}^{\ell_{\max}} \alpha_{\ell} \tilde{\sigma}_{\ell}^2 \left(\frac{R}{r_P} \right)^{\ell+2} \left(\frac{R}{r_Q} \right)^{\ell+1} P_{\ell}(t), \quad (3)$$

where $t = \cos\psi$, $P_\ell(t)$ are Legendre polynomials of degree ℓ , R is the mean earth radius, r_P, r_Q are the radii of the points P and Q , μ is the gravitational constant times the earth mass, $\tilde{\sigma}_\ell^2$ are some adapted signal degree variances and $\alpha_\ell = (\ell - 1)$. A vector of predicted geoid undulation is made by:

$$\hat{\mathbf{N}} = \frac{1}{\bar{\gamma}} \mathbf{C}_{sT}^T (\mathbf{C}_{ss} + \mathbf{C}_{vv})^{-1} \mathbf{y}, \quad (4)$$

where \mathbf{y} is the vector of observed gravity anomalies, \mathbf{C}_{ss} is a matrix computed from the Δg covariances, \mathbf{C}_{sT} is a matrix computed from the Δg and T cross covariances and \mathbf{C}_{vv} describes the Δg noise. If white noise is considered, this matrix equals the identity matrix times the noise variance, i.e.:

$$\mathbf{C}_{ss} = \mathbf{C}_{\Delta g \Delta g}, \quad (5)$$

$$\mathbf{C}_{sT} = \mathbf{C}_{\Delta g T}, \quad (6)$$

$$\mathbf{C}_{vv} = \mathbf{C}_{v_{\Delta g}} = \sigma_{v_{\Delta g}}^2 \mathbf{I}. \quad (7)$$

The value $\bar{\gamma}$ is the mean normal gravity used throughout the simulations.

The prediction error covariance matrix is computed by the least squares collocation estimation error formula:

$$\mathbf{C}_e = \frac{1}{\bar{\gamma}^2} (\mathbf{C}_{TT} - \mathbf{C}_{sT}^T (\mathbf{C}_{ss} + \mathbf{C}_{vv})^{-1} \mathbf{C}_{sT}), \quad (8)$$

where the matrix \mathbf{C}_{TT} is computed from the potential covariance function.

In order to make comparisons with the actual prediction errors computed from simulations, the point-wise standard deviation is used:

$$\sigma_i = \sqrt{\mathbf{C}_e(i, i)}. \quad (9)$$

3.2 Utilization of GOCE data

To use the filtered or gridded second radial derivatives from the space-wise approach, the following functions are also needed: the covariance function of T_{rr} and their cross covariance functions with T and Δg .

$$\mathbf{C}_{T_{rr}, T_{rrQ}} = \frac{\mu^2}{R^6} \sum_{\ell=\ell_{\min}}^{\ell_{\max}} \beta_\ell^2 \tilde{\sigma}_\ell^2 \left(\frac{R^2}{r_P r_Q} \right)^{\ell+3} P_\ell(t), \quad (10)$$

$$\mathbf{C}_{T_{rr}, T_Q} = \frac{\mu^2}{R^4} \sum_{\ell=\ell_{\min}}^{\ell_{\max}} \beta_\ell \tilde{\sigma}_\ell^2 \left(\frac{R}{r_P} \right)^{\ell+3} \left(\frac{R}{r_Q} \right)^{\ell+1} P_\ell(t), \quad (11)$$

$$\mathbf{C}_{\Delta g_P, T_{rrQ}} = \frac{\mu^2}{R^5} \sum_{\ell=\ell_{\min}}^{\ell_{\max}} \delta_\ell \tilde{\sigma}_\ell^2 \left(\frac{R}{r_P} \right)^{\ell+2} \left(\frac{R}{r_Q} \right)^{\ell+3} P_\ell(t), \quad (12)$$

where $\beta_\ell = (\ell + 1)(\ell + 2)$ and $\delta_\ell = \alpha_\ell \beta_\ell$.

The covariance functions needed to combine the second radial derivatives are easy to compute and implement because the radial direction of LORF coincides with the up direction of a East-North-Up (ENU) frame. If other derivatives along directions not coinciding with ENU were to be used then all the covariance functions would have to be computed and linear combinations would have to be made, according to the rotations between the used directions and the ENU (Tscherning, 1993). This procedure is made inside the space-wise approach, because the other two directions of LORF differ from the East and North. However the filtered and gridded second radial derivatives produced from the space-wise approach are easy to handle in data combinations via collocation.

The matrices and vectors in the equations (4) and (8) change: the vector \mathbf{y} now includes, in addition to the gravity anomalies, the along track filtered or gridded radial derivatives. Besides, the signal and error matrices include the covariances of T_{rr} and their cross covariances with T and Δg , i.e.:

$$\mathbf{C}_{ss} = \begin{bmatrix} \mathbf{C}_{\Delta g \Delta g} & \mathbf{C}_{\Delta g T_{rr}} \\ \mathbf{C}_{\Delta g T_{rr}}^T & \mathbf{C}_{T_{rr} T_{rr}} \end{bmatrix}, \quad (13)$$

$$\mathbf{C}_{sT} = \begin{bmatrix} \mathbf{C}_{\Delta g T} \\ \mathbf{C}_{T_{rr} T} \end{bmatrix}, \quad (14)$$

$$\mathbf{C}_{vv} = \begin{bmatrix} \mathbf{C}_{v_{\Delta g}} & \mathbf{0} \\ \mathbf{0} & \mathbf{C}_{v_{T_{rr}}} \end{bmatrix}. \quad (15)$$

To compute the T_{rr} noise matrix elements an error function, predicted inside the space-wise procedure, is used. For the case of along track filtered data it is a function of time, while for the case of the gridded data it is a function of spherical distance.

3.3 A simulation of geoid prediction

The local geoid prediction is made over the Piemonte area in northern Italy. The data are simulated from EGM96 up to degree and order 360 and GPM98 (Wenzel, 1998) from degree 361 to 720 and order 0 to 720, so that high frequencies are added. 2400 observations of gravity anomaly are generated on a spherical grid with coordinates $43 < \varphi < 47$ degrees, $6 < \lambda < 10$ degrees and with 5 mGal of white noise. The geoid is predicted on a regular spherical grid with latitude $44 < \varphi < 46$ and longitude $7 < \lambda < 9$ with spacing of 0.1 degrees.

In the GOCE filtered gradients and gridded data GPM98 is added from harmonic degree 361 to 720. For the along track filtered gradients the orbit is prolonged to a time span of 6 months and the errors after filtering are reproduced spectrally. From these gradients 1939 values inside the area $41 < \varphi < 49$, $4 < \lambda < 12$ (4 times wider than the ground data area) are selected after an under-sampling of 1 to 5. This procedure has been applied because the spatial coverage is much better with 6 months of data and under-sampling than with 60 days and less or no under-sampling. The GOCE mission will deliver 1 year of data at least. For the same area 1600 gridded second order radial derivatives were selected.

The gravity anomaly covariance function is locally fitted to the gravity anomaly data. The degree variances σ_ℓ^2 that describe the true signal (after the removal of a reference model) are transformed into the values $\tilde{\sigma}_\ell^2$, so that the correlation length of the covariance function either increases (eq. 16) or decreases (eq. 17) and the variance is scaled to fit the empirical function:

$$\tilde{\sigma}_\ell^2 = \sigma_\ell^2 \sigma_0^2 [\ln(a(\ell - \ell_{\min}) + 1) + 1]^n, \quad (16)$$

$$\tilde{\sigma}_\ell^2 = \sigma_\ell^2 \sigma_0^2 (e^{-a(\ell - \ell_{\min})})^n. \quad (17)$$

The ‘‘sensitivity parameter’’ a is fixed to the value 0.1, and the parameter $n \in \mathbb{N}$ and the ‘‘scale factor’’ σ_0^2 are determined empirically. The limits $\ell_{\min} = 2$, and $\ell_{\max} = 720$ are used. The fitted function is propagated to the potential and the second radial derivatives and it is compared to the empirical ones (since this is a simulation an empirical function of the potential is computed from the known true values). The case when a GOCE model up to degree and order 200 has been used as reference is presented in figure 2. The propagation from the

covariance estimated from Δg to that of T is of good quality but the propagation to the covariance of T_{rr} is poor. This is found to hold also when different reference models are used, although the case presented is that of the poorest propagation to the covariance of T_{rr} . This is because, as further experiments have shown, the upward continued covariance is quite sensitive when the covariance function has been fitted to ground data by a simple model like (eq. 16) and (eq. 17). The same effect occurs if the degree variances are fitted to the T_{rr} , i.e. the propagation to the Δg and the T variance is of bad quality. The results show that it is better to use the degree variances of the Δg data, even when only the T_{rr} data are used for the geoid prediction. This may happen because the Δg data have a more local character and are closer (in altitude) to the points where the geoid is predicted and is also due to the well-known instability of the downward continuation operator. A possible solution could be to perform a simultaneous fit to T_{rr} and Δg (Knudsen 1987). Fortunately the collocation results are robust to some variations of the covariance function (Sansò et al, 1999).

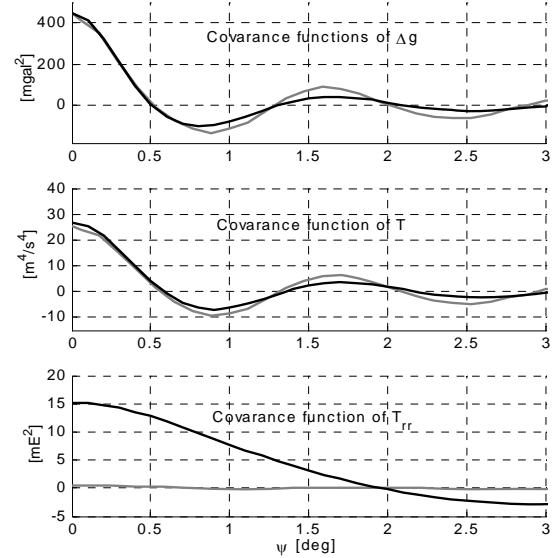


Fig. 2 Empirical (gray), fitted (dotted black) and propagated (black) covariance functions.

The EIGEN model up to degree and order 360 can be used too as reference model; its differences to EGM96 (Fig. 1) can be regarded, for the scope of this simulation, as long wavelength errors. The actual residual geoid heights when the GOCE model up to degree and order 200 is used as reference have

a much smaller mean value (table 3). This is due to the quality of the low degree coefficients that represent longer wavelengths of the signal. On the other hand the standard deviation is larger, i.e. more signal remains, due to the smaller maximum degree.

When a GOCE model is subtracted the residual signal may be correlated with the errors of the gridded data. This is ignored in the formulation of the prediction procedure for the sake of simplicity.

Table 3. Reference model with maximum degree, mean and standard deviation of the residual geoid heights (N) in cm.

model	max degree	mean N	std N
EIGEN	360	-103	34
GOCE	200	5	64

The residual geoid is now predicted with the gravity anomaly data only. It can be seen that the GOCE model leads to superior results (table 4, cases a and b). The local gravity data cannot compensate the long wavelength information that is missing from the “less accurate” reference model (case a).

If then the along track T_{rr} data are combined the results are even better. In fact, the case when the less accurate reference model is used (case c) is now closer to the other case (case d), i.e. the T_{rr} data can account for the long wavelength information that is missing from the less accurate model. Note that in the case a, edge effects are present. These effects vanish in all other cases, depicting in another way the significance of long wavelength information.

If the gridded T_{rr} are used then the solution improves more (case e). This was expected, since in this case the gridded T_{rr} data have better accuracy than the along track filtered data. Note also that the collocation with the gridded T_{rr} data only (case f) improves the solution, i.e. the standard deviation of the residual geoid goes down from 64 cm (table 3) to 14.3 cm (table 4). This shows that there is “GOCE information” beyond degree and order 200.

The good fit to the gravity anomaly covariance and the reasonable propagation to the potential covariance ensures a good error prediction to evaluate, in a true case, the significance of any data set used (e.g. GOCE T_{rr} data). Here the predicted error (table 4) is computed as the mean of all predicted point-wise standard deviations.

Even though a covariance function that is not in agreement with the empirical covariance function of T_{rr} is used, the prediction of the geoid with this data

set is quite good. The predicted error is also very close to the empirical one. This can be explained by considering that (see Fig. 2) the covariance of Δg propagated to T_{rr} at satellite altitude is mostly a scaled version of the empirical one, as if the signal T_{rr} itself were multiplied by a factor. Now if the collocation prediction and error equations are seen:

$$\hat{\mathbf{N}} = \frac{1}{\bar{\gamma}} \mathbf{C}_{T_{rr}T}^T \mathbf{C}_{T_{rr}T}^{-1} \mathbf{T}_{rr}, \quad (18)$$

$$\mathbf{C}_e = \frac{1}{\bar{\gamma}^2} (\mathbf{C}_{TT} - \mathbf{C}_{T_{rr}T}^T \mathbf{C}_{T_{rr}T}^{-1} \mathbf{C}_{T_{rr}T}), \quad (19)$$

we immediately see that such formulas are invariant under a multiplication of T_{rr} (but not of T) by a scale factor. This might be a mechanism through which part of the inconsistency is absorbed.

Table 4. The reference model, the data used, the empirical standard deviation with respect to the “true geoid” (emp.) and the predicted error (pred.) of every simulation case in cm.

case	model	data used	emp.	pred.
a	EIGEN	Δg	11.6	10.1
b	GOCE	Δg	2.7	2.9
c	EIGEN	$\Delta g + T_{rr}$	2.9	3.8
d	GOCE	$\Delta g + T_{rr}$	2.4	2.3
e	GOCE	$\Delta g + \text{grid } T_{rr}$	1.7	1.7
f	GOCE	grid T_{rr}	14.3	19.4

4 Conclusions

The GOCE gravity field model is expected to have high quality. The very good long wavelength information will be very useful for local gravity field modelling. The results presented in this paper show that the processed data coming from the space-wise approach will also be useful for local applications. Error propagation is essential to assess the significance of combining these data.

The along track filtered values of the potential and the gradients (apart from the second radial derivatives) coming from the space-wise approach have not been used. This may be done in the future. However this is not expected to improve the results significantly with respect to the results presented here; the information coming from the potential is probably fully included in the reference model of

degree and order 200 and the information from the gradients is included into the gridded data via the gridding procedure by collocation (Reguzzoni et al, 2006). This grid seems to have a higher frequency information content that can be used to improve local geoid computations beyond the remove restore procedure with a model up to degree 200.

Acknowledgement

This work was performed under ESA contract No. 18308/04/NL/NM (GOCE HPF).

References

- Albertella, A., F. Migliaccio, M. Reguzzoni and F. Sansò (2004). Wiener filters and collocation in satellite gradiometry. In: *International Association of Geodesy Symposia, '5th Hotine-Marussi Symposium on Mathematical Geodesy'*, F. Sansò (ed), vol. 127, Springer-Verlag, Berlin, pp. 32-38.
- Arabelos, D. and C. C. Tscherning (1990). Simulation of regional gravity field recovery from satellite gradiometer data using collocation and FFT. *Bulletin Geodesique*, 64, pp. 363-382.
- Balmino, G. (2001). The European GOCE Gravity Consortium (EGG-C). In: *Proc. of 1st International GOCE User Workshop*. ESA-ESTEC, Noordwijk, The Netherlands, April 23-24 2001.
- Bruinsma, S., J.C. Marty and G. Balmino (1997). Numerical simulation of the gravity field recovery from GOCE mission data. In: *Proc. of 2nd International GOCE User Workshop*. Frascati, Italy, March 8-10 2004.
- ESA (1999). Gravity Field and Steady-State Ocean Circulation Mission. ESA SP-1233 (1). ESA Publication Division, c/o ESTEC, Noordwijk, The Netherlands.
- Jekeli, C. (1999). The determination of gravitational potential differences from satellite-to-satellite tracking. *Celestial Mechanics and Dynamical Astronomy*, 75, pp. 85-101.
- Knudsen, P. (1987). Estimation and modelling of the local empirical covariance function using gravity and satellite altimeter data. *Bulletin Geodesique*, 61, pp. 145-160.
- Lemoine, F.G., S.C. Kenyon, J.K. Factor, R.G. Trimmer, N.K. Pavlis, D.S. Chinn, C.M. Cox, S.M. Klosko, S.B. Luthcke, M.H. Torrence, Y.M. Wang, R.G. Williamson, E.C. Pavlis, R.H. Rapp and T.R. Olson (1998). The development of the joint NASA GSFC and NIMA geopotential model EGM96. NASA/TP-1998-206861, Goddard Space Flight Center, Greenbelt, Maryland.
- Migliaccio, F., and F. Sansò (1989). Data processing for the Aristoteles mission. In: *Proc. of the Italian Workshop on the European Solid-Earth Mission Aristoteles*. Trevi, Italy, May 30-31 1989, pp. 91-123.
- Migliaccio, F., M. Reguzzoni, and F. Sansò (2004). Space-wise approach to satellite gravity field determination in the presence of coloured noise. *Journal of Geodesy*, 78, pp. 304-313.
- Migliaccio, F., M. Reguzzoni, and N. Tselfes (2005). GOCE: a full-gradient Solution in the Space-wise Approach. *Proc. Of the IAG2005 – Scientific Assembly*, 22-26 August 2005, Cairns, Australia. In print.
- Moritz, H. (1989) Advanced Physical Geodesy. Wichmann, Karlsruhe.
- Pail, R., W.D. Schuh and M. Wermuth (2005). GOCE Gravity Field Processing. In: *International Association of Geodesy Symposia, 'Gravity, Geoid and Space Missions'*, C. Jekeli, L. Bastos and J. Fernandes (eds), vol. 129, Springer-Verlag, Berlin, pp. 36-41.
- Reigber, C., P. Schwintzer, R. Stubenvoll, R. Schmidt, F. Flechtner, U. Meyer, R. König, H. Neumayer, Ch. Förste, F. Barthelmes, S. Y. Zhu, G. Balmino, R. Biancale, J. M. Lemoine, H. Meixner and J. C. Raimondo (2006). A High Resolution Global Gravity Field Model Combining CHAMP and GRACE Satellite Mission and Surface Data: EIGEN_cg01c. *Scientific Technical Report STR06/07*.
- Reguzzoni, M., N. Tselfes and G. Venuti (2006). Stepwise Solutions to Random Field Prediction Problems. Products and Processing Strategy. Presented at the, '*6th Hotine-Marussi Symposium on Mathematical Geodesy*', Wuhan, China, May 29 - June 2, 2006.
- Rummel, R., T. Gruber and R. Koop (2004). High Level Processing Facility for GOCE: Products and Processing Strategy. In: *Proc. of 2nd International GOCE User Workshop*. Frascati, Italy, March 8-10 2004.
- Sansò, F., G. Venuti and C. C. Tscherning (1999). A theorem of insensitivity of the collocation solution to variations of the metric of the interpolation space. In: *International Association of Geodesy Symposia*, vol. 121, K.P. Schwarz ed., Springer-Verlag, Berlin, pag. 233-240.
- Tscherning, C. C. (1993). Computation of Covariances of Derivatives of the Anomalous Gravity Potential in a Rotated Reference Frame. *Manuscripta geodaetica*, 18, pp. 115-123.
- Visser, P.N.A.M., N. Sneeuw and C. Gerlach (2003). Energy integral method for gravity field determination from satellite orbit coordinates. *Journal of Geodesy*, 77, pp. 207-216.
- Wenzel, G. (1998). Ultra high degree geopotential models GPM98A, B and C to degree 1800. *Proceedings Joint Meeting of the International Gravity Commission and International Geoid Commission*, September 7-12, Trieste 1998. Bollettino di Geofisica teorica ed applicata.

Determination of the Quasigeoid by Solving the Neumann Boundary Value Problem

Marcel Mojzeš, Juraj Janák, Juraj Papčo, Michal Šprlák, Miloš Vaľko
Slovak University of Technology, Radlinského 11, 81368 Bratislava, Slovak Republic

Abstract: GPS data, gravimetric data and digital elevation models have been used for the determination of quasigeoid by solving the second (Neumann) geodetic boundary value problem (GBVP). Measured point gravity values and mean Bouguer gravity anomalies have been transformed into gravity disturbances using the ellipsoidal heights obtained from digital elevation models DMR50 (local digital elevation model for Slovakia, 100 m x 100 m grid), GTOPO30 and SRTM3 (global digital elevation models) combined with EGG97 quasigeoidal heights. In this paper we present our computation process starting from input data compilation and transformation, then describing the numerical solution to the second GBVP and finally testing and discussing the obtained results.

Keywords: second boundary value problem, gravity disturbance, quasigeoid

1 Introduction

The solution to the third geodetic boundary value problem (GBVP) for quasigeoid determination formulated by Molodensky et al. (1962) is based on free-air gravity anomalies known on the Earth surface. In order to obtain the surface gravity anomaly, one needs to measure horizontal position (φ, λ) , the height above sea level H and gravity g . The second GBVP, based on gravity disturbances, enables to determine the quasigeoid using gravity, GPS observations data and terrain elevation with no need of levelling. Therefore, it is possible to expect higher accuracy in quasigeoid determination because of better consistency of the used reference systems.

Nowadays, there exist a lot of modifications of third GBVP solutions that are verified in many practical experiments (see, e.g., Sansó et al. 1994, Vaniček and Christou 1994, Mojzeš et al. 2006, Osada et al. 2005). The solution of the second GBVP is based on gravity disturbances, that are defined in the entire Euclidian space \mathbb{R}^3 formulas follows

$$\delta \bar{g}(P) = \bar{g}(P) - \bar{\gamma}(P), \quad (1)$$

where $\bar{g}(P)$ is the gravity vector and $\bar{\gamma}(P)$ is the normal gravity vector. Providing that the angle between those vectors is sufficiently small, one can rewrite eq. (1) in a scalar form

$$\delta g(P) = g(P) - \gamma(P). \quad (2)$$

The value $g(P)$ is obtained by gravimetric measurement and $\gamma(P)$ can be calculated. In order to get the gravity disturbance at point P we need to determine the value of g at P and position of P in terms of ellipsoidal coordinates.

The basic mathematical model of quasigeoid determined from gravity disturbances is known and it has been presented in many publications (see, e.g., Hotine 1969, Fei and Sideris 2000, Wellenhof and Moritz 2005).

The solution of the second GBVP is derived from the Molodensky concept (Molodensky et al. 1962). Let P be the point on the Earth surface S where we wish to determine the height anomaly ζ . According to Runge's theorem (Moritz 1980), there exists a spherical or ellipsoidal surface passing through point P on which there is a disturbing potential \bar{T} , which obeys the following conditions (Fei and Sideris 2000):

1. $\nabla \bar{T}(Q) = 0$ for Q outside S ,
2. $|T(Q) - \bar{T}(Q)| < \varepsilon$ for Q on S ,
3. $|\delta g(Q) - \delta \bar{g}(Q)| < \varepsilon'$ for Q on S ,

where $\delta \bar{g}$ is the gravity disturbance on the reference surface. The relation between the gravity disturbance and the disturbing potential for spherical approximation is as follows:

$$\left(\frac{\partial T}{\partial r}\right)_P = -\delta\bar{g}(P). \quad (4)$$

2 Mathematical model

The difference between the δg on the earth surface S and $\delta\bar{g}$ on the reference surface is defined as follows (Moritz, 1980):

$$\delta g_1(P) = \delta g(P) - \delta\bar{g}(P) = \frac{R^2(P)}{2\pi} \iint_{\sigma_Q} (h_Q - h_P) \cdot \frac{\delta g(Q)}{l_{P,Q}^3} d\sigma_Q, \quad (5)$$

where h stands for ellipsoidal height. From the first and second condition in eq. (3), it is possible to write the following formula for height anomaly:

$$\zeta(P) = \frac{R(P)}{4\pi\gamma(P)} \iint_{\sigma_Q} H(\psi_{P,Q}) \delta\bar{g}_Q d\sigma_Q \quad (6)$$

where $H(\psi_{P,Q})$ is the Hotine function defined by following formula:

$$H(\psi_{P,Q}) = \frac{1}{\sin(\psi_{P,Q}/2)} - \ln\left(1 + \frac{1}{\sin(\psi_{P,Q}/2)}\right), \quad (7)$$

where $\psi_{P,Q}$ is the spherical distance between the points P and Q . If in eq. (6) we replace the gravity disturbance on the reference surface by

$$\delta\bar{g}(Q) = \delta g(Q) + \delta g_1(Q), \quad (8)$$

then we can compute the height anomaly using

$$\zeta(P) = \zeta_{\delta g}(P) + \zeta_{\delta g_1}(P), \quad (9)$$

where

$$\zeta_{\delta g}(P) = \frac{R(P)}{4\pi\gamma(P)} \iint_{\sigma_Q} H(\psi_{P,Q}) \delta g(Q) d\sigma_Q, \quad (10)$$

$$\zeta_{\delta g_1}(P) = \frac{R(P)}{4\pi\gamma(P)} \iint_{\sigma_Q} H(\psi_{P,Q}) \delta g(Q) d\sigma_Q, \quad (11)$$

with δg_1 - the terrain correction of gravity disturbance and $\zeta_{\delta g_1}$ - the terrain correction of the Hotine formula.

Equations (10) and (11) serve for the computation of height anomaly on S including, approximately, the terrain effect.

3 Remove-restore technique

To solve (6) one needs to know the gravity disturbances all over the Earth with an optimal density. Nowadays there are some areas with sufficiently dense gravity data coverage while others are not. To overcome that difficulty we use a global geopotential model. The idea is based on the remove-restore technique. The first step of the remove-restore technique is to divide the gravity disturbance into three components:

$$\delta g(P) = \delta g_m(P) + \delta g_{res}(P) + \delta g_1(P), \quad (12)$$

where

$$\delta g_{res}(P) = \delta g(P) - \delta g_m(P) - \delta g_1(P), \quad (13)$$

where δg is determined by direct gravimetric and GPS measurements. The long wavelength (model) component in spherical approximation can be computed from the global geopotential model, by formula (see, e.g. Wenzell, 2005),

$$\delta g_m(P) = \frac{GM}{r_p^2} \sum_{n=2}^{n_{max}} (n+1) \left(\frac{a}{r_p}\right)^n \cdot \sum_{m=0}^n \left(\Delta\bar{C}_{n,m} \cos(m\lambda_p) + \Delta\bar{S}_{n,m} \sin(m\lambda_p) \right). \quad (14)$$

$$\bar{P}_{n,m}(\sin \bar{\varphi}_p),$$

where $r_p, \bar{\varphi}_p, \lambda_p$ are spherical coordinates of point P , GM is geocentric gravitational constant a is major semi axis of reference ellipsoid, and $\Delta\bar{C}_{n,m} = \bar{C}_{n,m} - \bar{C}_{n,m}^{ell}$ for $m=0$, $\Delta\bar{C}_{n,m} = \bar{C}_{n,m}$ and $\Delta\bar{S}_{n,m} = \bar{S}_{n,m}$ for $m \neq 0$ are fully normalized spherical harmonic coefficients, $\bar{P}_{n,m}$ are fully normalized associated Legendre functions of 1st kind, n is degree and m is order.

Knowing δg and δg_m , we can compute approximate residual gravity disturbances

$$\delta g'_{res}(P) = \delta g(P) - \delta g_m(P), \quad (15)$$

which we can then use for the computation of δg_1 :

$$\delta g_1(P) = \frac{R^2(P)}{2\pi} \iint_{\sigma_Q} (h_Q - h_P) \frac{\delta g'_{res}(Q)}{l_{P,Q}^3} d\sigma_Q. \quad (16)$$

The final height anomaly at point P can be computed from

$$\zeta(P) = \zeta_m(P) + \zeta_{res}(P) + \zeta_{\delta g_1}(P), \quad (17)$$

where

$$\zeta_m(P) = \frac{GM}{r_P \gamma_P} \sum_{n=2}^{n_{max}} \left(\frac{a}{r_P} \right)^n \sum_{m=0}^n \left(\Delta \bar{C}_{n,m} \cos(m\lambda_P) + \Delta \bar{S}_{n,m} \sin(m\lambda_P) \right). \quad (18)$$

$$\bar{P}_{n,m}(\sin \bar{\varphi}_P),$$

$$\zeta_{res}(P) = \frac{R_P}{4\pi\gamma_P} \iint_{\sigma_Q} H(\psi_{P,Q}) \delta g_{res}(Q) \cdot d\sigma_Q. \quad (19)$$

4 Input data

4.1 Compilation of the free-air gravity anomaly 20"×30" grid

The free-air gravity anomaly grid has been compiled using two different sources of data. The first source was the detailed gravity measurements of Slovakia – over 200 000 point gravity data (Kubeš *et al.*, 2001), in terms of refined Bouguer gravity anomalies, enriched by approximately 600 point gravity data from Poland and about 150 new gravity measurements from extremely rough terrain in High Tatra Mountains. The second source was the mean Bouguer gravity anomalies on a 5'×7.5' geographic grid - more than 20 000 mean gravity data within the area bounded by $44^\circ < \varphi < 55^\circ$ and $12^\circ < \lambda < 30^\circ$. All gravity data have been computed in, or transferred to, the gravimetric

reference system GrS-95, which is based on 16 absolute gravity points (Klobušíak and Pecár, 2004) and the GRS-80 normal gravity field (Moritz, 1992). The refined Bouguer gravity anomalies originated from the first source have been compiled using the following equation (Kubeš *et al.*, 2001):

$$\Delta g_B = g - \gamma_0 + \delta g_{FA} - \delta g_{BS} + \delta g_t + \delta g_a, \quad (20)$$

where g is measured gravity, γ_0 is normal gravity at the GRS-80 ellipsoid computed according to Somigliana (1929) with the use of the formula

$$\gamma_0 = \frac{a\gamma_a \cos^2 \varphi + b\gamma_b \sin^2 \varphi}{\sqrt{a^2 \cos^2 \varphi + b^2 \sin^2 \varphi}}, \quad (21)$$

δg_{BS} is the gravity effect of the radius of 166.7 km, computed according to the formula of Cassinis *et al.* (1937). The last two terms in (20) are the terrain correction computed up to 166.7 km using DMR50 digital terrain model (see Kubeš *et al.*, 2001; Grand *et al.*, 2004) and the δg_a is the atmospheric reduction computed according to formula (Torge, 1989)

$$\delta g_a = 0.874 - 9.9 \cdot 10^{-5} H + 3.56 \cdot 10^{-9} H^2. \quad (22)$$

In the Somigliana's formula, a and b are the major and minor semi-axis of the reference ellipsoid, γ_a and γ_b are the normal gravity at the equator and the pole, and φ is ellipsoidal latitude. The second term in equation (20) δg_{FA} is the free-air reduction of normal gravity computed from (Torge, 1989)

$$\delta g_{FA} = - \left(\frac{\partial \gamma_0}{\partial H} H + \frac{1}{2} \frac{\partial^2 \gamma_0}{\partial H^2} H^2 \right), \quad (23)$$

where H is the Molodensky normal height obtained by levelling and gravimetry.

Unfortunately, the mathematical procedure used to produce the mean Bouguer gravity anomalies in the second source is not exactly known. The refined Bouguer gravity anomalies coming from both mentioned sources have been merged into one file in such a way that the mean data do not overlap with point data, and were subsequently interpolated into a 20"×30" geographic grid. The method used for interpolation was Kriging with the linear variogram assuming anisotropy coming from the

convergence of meridians. Finally, the grid of refined Bouguer gravity anomalies $\Delta g_{B,GRID}$ has been converted into free-air gravity anomalies grid of the same spacing according to the following formula:

$$\Delta g_{FA,GRID} = \Delta g_{B,GRID} + \delta g_{BS,GRID} - \delta g_{t,GRID} \cdot (24)$$

Heights necessary for computation of $\delta g_{BS,GRID}$ were obtained from the GTOPO30 digital elevation model (edcdaac.usgs.gov/gtopo30/gtopo30.html).

There are several approaches for computation of $\delta g_{t,GRID}$ in eq. (24), i.e., the terrain correction in the geographic grid. It is important that terrain corrections in eq. (20) and (24) are compatible. In our solution this term was computed using an approach developed at the University of New Brunswick and improved at the Slovak University of Technology (see Janák et al., 2006). Heights necessary for computation of $\delta g_{t,GRID}$ have been obtained from the STRM3 digital elevation model.

4.2 Transformation of gravity anomaly to gravity disturbance

The free-air gravity anomalies have been transformed into gravity disturbances according to the relation

$$\delta g(P) = \Delta g_{FA}(P) - \frac{\partial \gamma}{\partial h} \zeta_{EGG97}, \quad (25)$$

where $\partial \gamma / \partial h = -0.3086 \text{ mGal/m}$ and ζ_{EGG97} have been interpolated from the quasigeoid model EGG97 (Denker et al., 1997).

5 Practical solution

The EGM96 global geopotential model to degree and order 360 (Lemoine et al., 1996) and the GRS-80 normal gravity field (Moritz, 1988) were chosen for the computation. The model component of the quasigeoid computed according to eq. (18) is plotted in Fig. 1. The residual component of the quasigeoid has been computed according to eq. (19) in the area $47.5^\circ \leq \varphi \leq 50.0^\circ$ and $16.7^\circ \leq \lambda \leq 23.0^\circ$ by using the 1D-FFT method (Fig. 2). The terrain correction of the Hotine formula has been computed according to eq. (11) in the same area (Fig. 3). The residual

components ζ_{res} and $\zeta_{\delta g_1}$ have been integrated up to radius of one degree. The final quasigeoid computed with eq. (17) is plotted in Fig. 4.

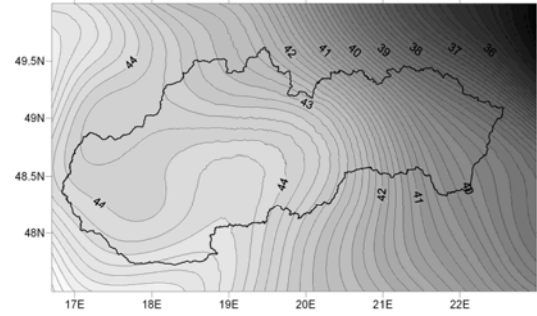


Fig.1. Model component of the quasigeoid (m)

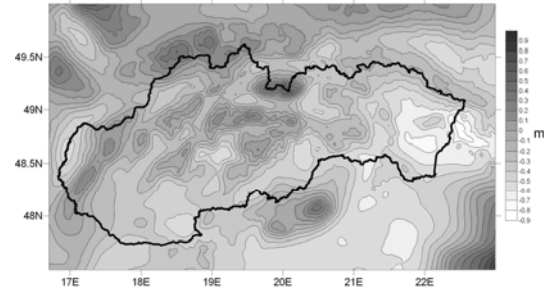


Fig.2. Residual component of the quasigeoid (m)

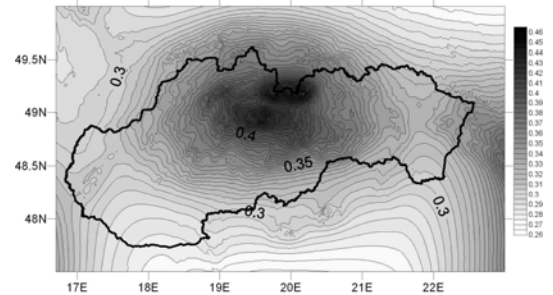


Fig. 3. Terrain correction (m)

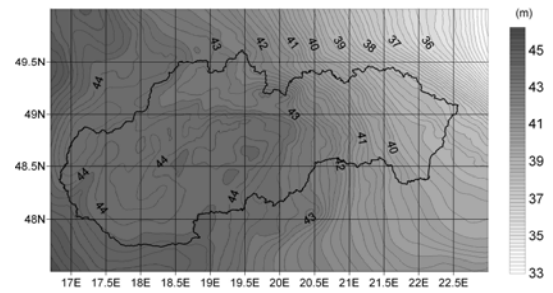


Fig. 4. Final quasigeoid (m)

6 Testing of final gravimetric quasigeoid

The final gravimetric quasigeoid, determined by the second GBVP solution was tested by use of 61 discrete GPS points linked by precise levelling with, which were connected on the Reference Levelling Network 1957 of Slovak Republic using precise spirit levelling. The statistics of the differences between gravimetric and GPS/levelling quasigeoid are shown in Table 1.

Table 1. Statistics of comparison to GPS/levelling

Parameter	Value (m)
Mean value of differences	0.534
Difference between min and max	0.366
Standard deviation	0.070

Differences between the gravimetric and GPS/levelling quasigeoid are depicted in Fig. 5.

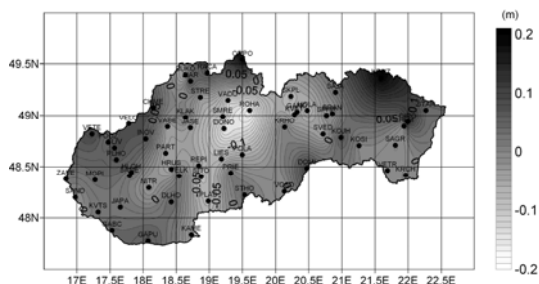


Fig. 5. Differences between gravimetric and GPS/levelling quasigeoid

7 Conclusion

The use of gravity disturbance in computing a gravimetric quasigeoid has been investigated in this paper. The gravimetric quasigeoid has been computed solving the second geodetic boundary value problem. The computations were based on the available gravity data in Slovakia. The computed quasigeoid has been compared with GPS/levelling data. The standard deviation of the differences is 0.070 m.

Finally, it should be noted that the distribution of the GPS stations in Slovakia is different in western, central and eastern parts. For better testing of the gravimetric quasigeoid we need a uniform distribution of GPS stations.

The use of gravity disturbances for determining the gravimetric quasigeoid has the following advantages:

- the gravity disturbances are determined from GPS and gravimetric measurements are computed by a simple formula;
- the source of systematic errors, caused by inconsistency of vertical reference systems is eliminated;
- for the computation of the topographic correction of the gravity disturbance the ellipsoidal heights are used; and
- zero-tide model is applied only for gravity and GPS measurements.

For achieving higher accuracy in the future, we need:

- to homogenize the reduction of gravimetric and GPS measurements in the zero-tide reference system in agreement with the IAG Resolution Nr. 16 from 1983;
- to study the influence of the topographic effects on the quasigeoid determination;
- to use new models from satellite gravity gradiometry (e.g. GOCE) for the determination of the quasigeoid;
- to perform densification of the gravimetric and GPS measurements in high mountains.

Acknowledgement. This investigation was supported by the Grant Agency VEGA of Slovak Republic, Project No. 1/1433/04.

References

- Cassinis G, Dore P, Ballarin S (1937) Tavole fondamentali per la riduzione dei valori osservati della gravità. Tipografia legatoria Mario Ponzio, Pavia.
- Denker H, Torge W (1998) The European gravimetric quasigeoid EGG97, IAG Symposia 119:249-254, Springer Verlag.
- Fei, ZL, Sideris, MG (2000) GPS Levelling and the Second Geodetic Boundary Value Problem. IAG Symposia Proceed. of Gravity, Geoid and Geodynamics 2000, pp 341-346, Springer 2001, vol 123, Banff, Alberta, Canada.
- Grand T, Pašteka R, Šefara J, (2004) New version of terrain corrections in the Slovak regional gravity database. Contributions to Geophysics and Geodesy, 34/4, pp. 315-337.
- Hotine M (1969) Mathematical geodesy. ESSA Monograph 2, Washington D.C.
- Janák J, Pašteka R, Zahorec P, Loviška Z (2006) Terrain correction in extremely disturbed terrain. Contributions to Geophysics and Geodesy, 36, pp. 41-52.
- Klobušiak M, Pecár J (2004) Model and algorithm of effective processing of gravity measurements realized with a group of both of absolute and relative gravimeters.

- Geodetic and Cartographic Horizon, 50/92, pp. 99-110. (in Slovak).
- Kubeš P, Grand T, Šefara J, Pašteka R, Bielik M, Daniel S, (2001) Atlas of geophysical maps and profiles. Final report of geological project 0801840301/180. Ministerstvo životného prostredia SR a Štátny geologický ústav Dionýza Štúra, Bratislava. (in Slovak).
- Lemoine FG et al. (1998) The Development of the joint NASA GSFC and the National Imagery and Mapping Agency (NIMA) geopotential model EGM96 NASA/TP – 1998 – 206861, Maryland.
- Mojzeš M, Janák J, Papčo J (2006) Improvement of the gravimetric model of quasigeoid in Slovakia. Newton's Bulletin N. 3. Politecnico di Milano. (Available online)
- Molodensky MS, Yeremeev VF, Yurkina MI (1962) Methods for study of external gravitational field and figure of the earth. Jerusalem. Israel Programme for Scientific Translation, 1962.
- Moritz H (1980) Advanced Physical Geodesy. Herbert Wichmann Verlag, Karlsruhe.
- Moritz H (1992) Geodetic Reference System 1980. Bulletin Géodésique, 66, pp. 187-192.
- Osada E, Krynski J, Owczarek M (2005) A robust method of quasigeoid modelling in Poland based on GPS/levelling data with support of gravity data. Geodesy and Cartography, Vol. 54, No 3, pp. 99-117.
- Somigliana C. (1929) Teoria generale del campo gravitazionale dell'ellissoide di rotazione. Mem. Della Soc. Astron. Ital., IV, Milano.
- Sansó F, Brovelli MA, Migliaccio F, Vajani C (1994) International School for the Determination and Use of the Geoid. Lecture Notes. International Geoid service. D.I.I.A.R.- Politecnico di Milano.
- Torge W (1989) Gravimetry. De Gruyter, Berlin.
- Vaniček P, Christou NT (1994) Geoid and its Geophysical Interpretations. CRC Press.
- Wellen Hof BH, Moritz H (2005) Physical Geodesy. Springer Verlag, Wien.
- Wenzel G (2005) Global Models of the Gravity Field of High and Ultra-high Resolution. Lecture Notes on Global Geopotential Models. International School for the Determination and use of the Geoid. International Geoid Service D.I.I.A.R. - Politecnico di Milano.

OCTAS with a focus on the importance of a high accuracy geoid

O. C. D. Omang, D. Solheim, A. Hunegnaw

Geodetic Division, NMA, Kartverksveien 21, N-3511 Hønefoss, Norway; e-mail:ove.omang@statkart.no

D.I. Lysaker

Department of Mathematical Sciences and Technology, UMB, POBox 5003, N-1432 Ås, Norway

K. Ghazavi, H. Nahavandchi

Department of Geomatics, NTNU, Høgskoleringen 7G, N-7491 Trondheim, Norway

Abstract. The OCTAS project is a multidisciplinary approach to determine the mean dynamic sea surface topography (MDT) in the Fram Strait and adjacent seas. This will serve as input to ocean circulation and transport studies in the polar region. Improved determination of MDT will allow assessment of its impact on circulation studies and associated climate modeling.

To achieve this objective high accuracy gravimetric geoid and mean sea surface models are required, and these will be derived as part of the project.

New airborne gravity data has been obtained. All gravity data has been error screened and quality assured by removing dubious data and adjusting marine gravity data when necessary, in order to derive a regional high accuracy gravimetric geoid. Mean sea surfaces from satellite altimetry and mean dynamic topography from climatology and hydrography are under development. A preliminary assessment of these data sets have been made and techniques are being developed to optimally estimate the different quantities in an integrated approach.

Keywords. OCTAS – MDT – MSSH – Adjusted Marine Gravity Data – New Airborne Gravity Data

1 Introduction

The Norwegian OCTAS Project running from 2003 to 2007 focuses on the ocean circulation in the Fram Strait and adjacent sea with the main objective to improve sea surface topography determination and to study the impact on ocean modelling, see Fig. 1. A central quantity for studying and understanding the ocean circulation is the Mean Dynamic Topography (MDT), which is the difference between the mean sea surface heights (MSSH) and the geoid. The MDT provides the absolute reference surface for the ocean circulation and is, in particular, expected to improve the determination of the mean ocean circula-

tion. This, in turn, will advance the understanding of the role of the ocean mass and heat transport in climate change.

Up to the expected launch of GOCE the gravimetric geoid is not known with sufficient accuracy to allow full use of the massive sea surface height information, which several satellite altimetry missions have regularly provided since the early 90-ies, in global analysis of the ocean circulation. However, in a few marine regions in the world sufficient in-situ information about the Earth's gravity field exists to compute a more accurate geoid. The region covering the Northern North Atlantic and the Nordic seas between Greenland, Iceland, Norway and the UK, including the Fram Strait is one of those regions. One goal of the OCTAS project is therefore to determine an accurate geoid in the Fram Strait and the adjacent seas.

New airborne gravity measurements have been carried out. The marine gravity data have been adjusted and error screened with the help of the new airborne gravity data. Both new airborne gravity data and the adjusted marine gravity data will improve the quality of the gravimetric geoid. The new geoid is used together with an accurate MSSH to determine the MDT.

2 Airborne Gravity Survey

In a joint cooperation between Geoid and Ocean Circulation in the North Atlantic (GOCINA) and Ocean Circulation and Transport Between North Atlantic and the Arctic Sea (OCTAS) new airborne gravity data was collected during summer 2003 in the Northern North Atlantic. In Fig. 2 the OCTAS part of the airborne measurement campaign is visible. For information about the airborne gravity data collected by GOCINA, see e.g. Forsberg *et al.* (2004).

The airborne survey was carried out with an aircraft equipped with GPS receivers, laser altimetry, Inertial Navigation Systems (INS), and a modern LaCoste & Romberg marine gravimeter. The measure-

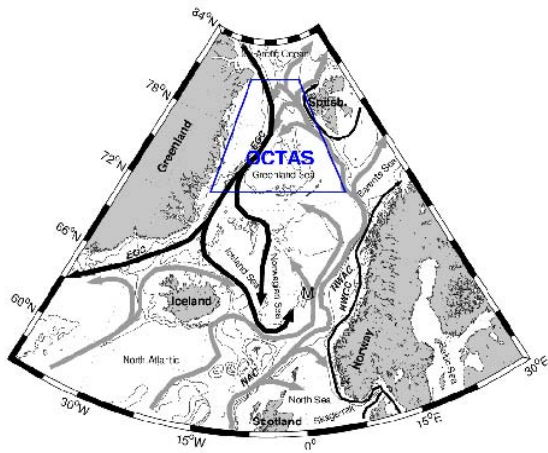


Fig. 1. OCTAS study area

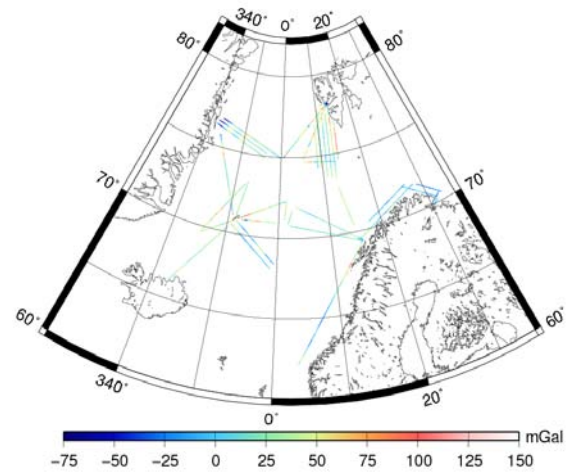


Fig. 2. New airborne gravity data measured by OCTAS during 2003

ment was done around Greenland, Svalbard, Jan Mayen and along the Norwegian coast. This additional survey (including the GOCINA measurement along a band of Greenland over Iceland and Faeroe-Shetland to Norway) were particularly important since it ties in as many possible different marine surveys; to check data and allow improvements by cross-over adjustment as well as filling in some major area data voids.

A total of 9222 measurements divided into 35 profiles of airborne gravity tracks have been processed. An internal cross over computation (airborne gravity data only) show an RMS of 1.6 mGal, while compared to the marine data give an RMS of 4.51 mGal, see Table 1.

	N	Mean	Min	Max	RMS
Internal	15	0.71	-2.87	3.79	1.58
Marine	548	0.44	-27.44	20.54	4.51

Table 1. Statistics of the cross over computations with marine gravity data and with itself. Values in mGal

3 Marine Gravity Data

The main marine gravity data set used in this study has been acquired from BGI, NGDC, Norwegian Mapping Agency (NMA), and from international and national oil companies. The data set was recently improved with a major airborne gravity survey campaign held in 2003 under the scope of the GOCINA and OCTAS project, see Sect. 2.

Marine gravity measurements are, in principle, very precise – military trials of a type of gravity sensor now commercially available achieved RMS cross-over errors of only ± 0.38 mGal (Bell and Watts, 1989) us-

ing BGM-3 sea gravimeter. For a variety of reasons, the accuracy of marine gravity anomalies does not match this precision. Some relate to measuring gravity on an imperfectly stabilised platform, with others due to systematic instrument errors, loosing reference to an absolute gravity datum and uncertainties in the navigation system, in terms of course, speed, and position errors, affect the Eötvös correction. Wessel and Watts (1988) review these problems in depth and see also Torge (1989).

Our strategy involves pre-processing the raw gravity data followed by network adjustment. Pre-processing aims to reduce the dynamical errors associated with courses changes, smooth out high-frequency noise, and remove spikes and gross blunders. Network adjustment aims to remove the systematic effects of datum offsets, different gravity reference systems and drift in the gravity meter zero.

The basic component of our pre-processing algorithm is the *line-segment*. A line-segment is a component of a survey where the ship's course is adequately straight. Point-to-point vectors are compared with chosen criteria for breaking surveys into line-segments: a break can be triggered by a large change in course azimuth or an excessive gap between points. For each line-segment, we represent the long-track free-air anomaly as well as the eastings and northings defining the ship's position, by a continuous function. Chebyshev polynomials represent our best estimate for the true shape of the gravity anomaly profile and smooth out point-to-point noise. Statistics derived from the residuals between the fitted curve and the point data are used to estimate the stationary random component of the data errors. The subsequent

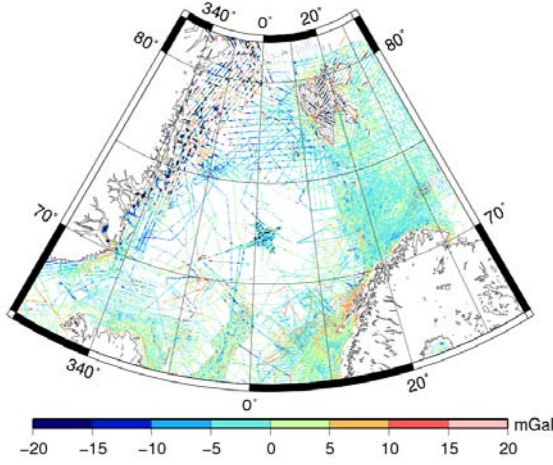


Fig. 3. KMS02 free-air anomalies minus marine gravity data

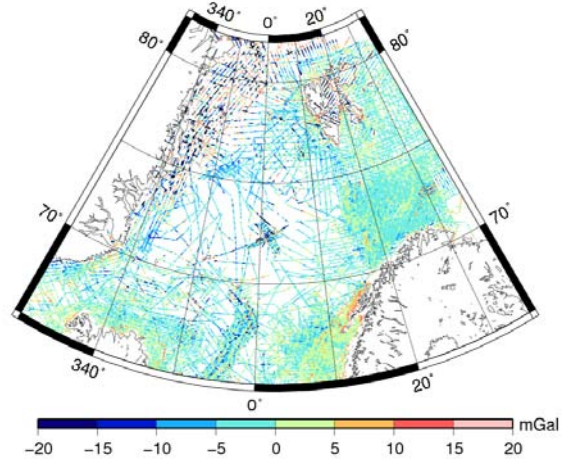


Fig. 4. KMS02 free-air anomalies minus adjusted marine gravity data

network adjustment is to suppress the remaining systematic errors.

The network adjustment model fit an independent datum shift parameter to each survey or survey leg. For any survey with sufficient number of crossing points to remain stable with a second free parameter, the model will include drift rate. The adjustment estimated these model parameters by minimizing the cross over errors, weighting the observed free air anomaly at the crossing according to the standard deviation of the polynomial curve fit for that line-segment in the least square sense.

For the approximately 45000 cross-over points in the northern Atlantic Ocean, network adjustment reduces the standard deviation of the cross-over errors from 4.13 mGal to 1.64 mGal. Similarly the difference between KMS02 altimetry anomalies and shipborne and airborne data improved, with the adjustment reducing the standard deviation of the differences from 8.15 to 6.07 mGal. The difference between KMS02 based free-air anomalies and marine free-air anomalies before and after adjustment are shown in Fig. 3 and Fig. 4 respectively. The difference shows that the network adjustment has contributed in the adjustment of a number of surveys that have a datum shift due to a bad harbour ties.

4 Computational Methods

In OCTAS we have looked into different ways of computing the MDT. One method is to compute the gravimetric geoid, and by combining this geoid with a MSSH yields a MDT.

$$MDT = MSSH - Geoid \quad (1)$$

Secondly, the MDT may be computed directly from different types of observation data using estimations techniques such as least squares collocation (LSC).

4.1 Geoid determination

Gravity data used in the geoid computation are a combination of adjusted marine data, new and old airborne measurements, land data in Scandinavia and data from the Arctic Gravity Project (ArcGP). Voids in the data distribution were patched with satellite altimetry gravity data (KMS02).

The combined gravity data set is build up of Bouguer anomalies on land and free-air anomalies at sea. We are using the remove-restore technique in combination with the residual terrain model (RTM) method Forsberg (1984).

The reduced anomalies are obtained using a Bouguer plate approximation

$$\Delta g_{red} = \Delta g + 2\pi G\rho h_{ref} - \Delta g_{ggm}, \quad (2)$$

where h_{ref} is a smooth reference surface of resolution approx. 50 km and Δg_{ggm} is the global geopotential model. The reduced gravity data Δg_{red} is gridded and Faye anomalies, Δg_{faye} , are obtained after restoring the RTM terrain effect $2\pi G\rho(h - h_{ref})$. The residual quasigeoid is estimated using multi-band spherical 2D-FFT (Forsberg and Sideris, 1993)

$$\zeta_{res} = F^{-1}[F(\Delta g_{faye})F(S^\tau(\psi))] \quad (3)$$

where F and F^{-1} are the Fourier and the inverse Fourier transform, respectively.

$S^\tau(\psi)$ is the Wong-Gore modified Stokes' function with truncation degree τ given as (Wong and

Gore, 1969)

$$S^\tau(\psi) = \sum_{n=\tau}^{\infty} \frac{2n+1}{n-1} P_n(\cos \psi) \quad (4)$$

where P_n is Legendre polynomials. As Eq. (4) indicates the Wong-Gore modification gives a kernel function taking summation only from τ to infinity. The long wavelength part of the signal is thereby removed, and the changing of τ compares to some degree to the selection of different capsizes.

Restoring the global geopotential model (GGM) gives the quasigeoid,

$$\zeta = \zeta_{\text{res}} + \zeta_{\text{ggm}} \quad (5)$$

Over sea, or where height equals zero, the quasigeoid ζ equals the geoid, N .

5 LSC

Considering only geodetic measurements, MDT is simply given by subtracting MSSH and the geoid.

$$MDT = MSSH - N + \epsilon \quad (6)$$

where ϵ is noise. The data coverage however, especially gravity data, is not complete, so more advanced combination methods may be needed.

LSC is a well known technique to combine different geodetic measurements, e.g. gravity anomalies, the geoid and altimetry sea surface heights. The measurements are associated with the anomalous gravity potential T of the Earth through linear functionals.

$$\Delta g = L_{\Delta g}(T) = \frac{\partial T}{\partial r} - 2\frac{T}{r} \quad (7)$$

$$N = L_N(T) = \frac{T}{\gamma} \quad (8)$$

The signal x (e.g. the geoid) is given by the formula

$$x = C_x^T (C + D)^{-1} y \quad (9)$$

where C_x is the covariance function between the observations and the signal, C is the covariance function between the observations and D is the covariance function for the measurement noise. The a posteriori error covariance between two estimated quantities is given by

$$c_{xx'} = c_{xx'} - C_x^T (C + D)^{-1} C_x \quad (10)$$

5.1 Covariance functions

The covariances are obtained using kernel functions. The kernel associated with the gravity field is derived using the spherical harmonic expansion of T (the anomalous gravity field) and some a priori variances. The covariance between T in the points P and Q depend only on the spherical distance between them, and are thus independent of location and azimuth (i.e. a homogeneous and isotropic kernel). More details in Moritz (1980). Applying the linear functionals yield the expressions of the covariances

$$C_{NN} = \sum_{i=2}^{\infty} \left(\frac{1}{\gamma}\right)^2 \sigma_i^{TT} P_i(\cos \Psi) \quad (11)$$

$$C_{\Delta g \Delta g} = \sum_{i=2}^{\infty} \left(\frac{i-1}{R}\right)^2 \sigma_i^{TT} P_i(\cos \Psi) \quad (12)$$

$$C_{N \Delta g} = \sum_{i=2}^{\infty} \left(\frac{i-1}{R\gamma}\right) \sigma_i^{TT} P_i(\cos \Psi) \quad (13)$$

The covariance function of the MDT is expressed, similar to the gravity field, as

$$C_{\zeta \zeta} = \sum_{i=1}^{\infty} \sigma_i^{\zeta \zeta} P_i(\cos \Psi) \quad (14)$$

5.2 Covariance function modelling

In LSC it is very important to take the full signal/error content into account. This means that the covariance function models should agree with the empirically determined characteristics in the local area, such as the variance and the correlation length.

The covariance functions for gravity anomalies and geoid heights are modelled using a Tscherning/Rapp degree variance model (Tscherning and Rapp, 1974)

$$\sigma_i^{TT} = \begin{cases} \epsilon_i^{GRACE} & i=2, \dots, 90 \\ \epsilon_i^{EGM96} & i=90, \dots, 360 \\ \frac{A}{(i-1)(i-2)(i+4)} \left(\frac{R_B^2}{R^2}\right)^{i+1} & i=360, \dots \end{cases} \quad (15)$$

The model is fitted to local empirical covariance values calculated from reduced marine, land and airborne gravity data in a least squares iterative inversion technique (Knudsen, 1987). More details in e.g. Knudsen and Vest (2005).

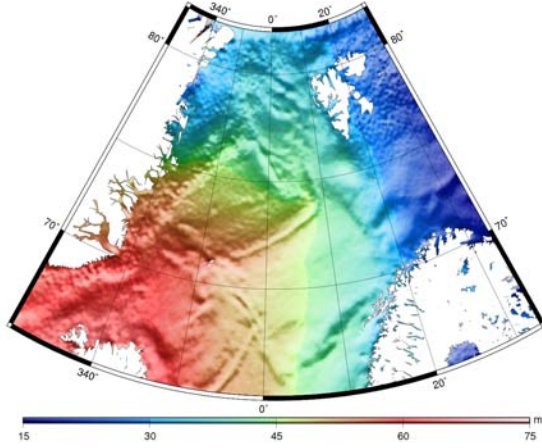


Fig. 5. The OCTAS06.v1 mean sea surface model

The covariance functions for MDT are modelled with Knudsen degree variance model (Knudsen and Vest, 2005)

$$\sigma_i^{\zeta\zeta} = b \left(\frac{k_2^3}{k_2^3 + i^3} - \frac{k_1^3}{k_1^3 + i^3} \right) s^{i+1} \quad (16)$$

The spectrum of the MDT is assumed to have a decay similar to the geoid. The model is fitted to empirical covariance values determined from synthetic data (MSSH - Geoid).

By assuming no correlations between the components in Eq. (6) the covariance function for MSSH is given by

$$C_{MSSH} = C_N + C_{MDT} \quad (17)$$

$$D_\epsilon = \sum_i D_i \quad (18)$$

where D_i are the covariance values associated with the different error components in ϵ . The assumption of no correlation between the gravity field and sea surface heights may not be correct (Knudsen, 1991).

6 OCTAS MSSH

In deriving the first version of the MSSH model for the OCTAS study area, ENVISAT (cycles 11-35) and ERS-2 (cycles 1-85) data are used. These data have been extracted from altimetry data base (Stack File) at the Ohio State University. The ENVISAT and ERS-2 satellite should give slightly different sea surface height signal, therefore, a bias of approximately 36 cm to the ENVISAT data is adjusted for. This model, OCTAS06.v1, is illustrated in Figure 5. The resolution of OCTAS06.v1 model is 3 minutes in latitude and 6 minutes in longitudes.

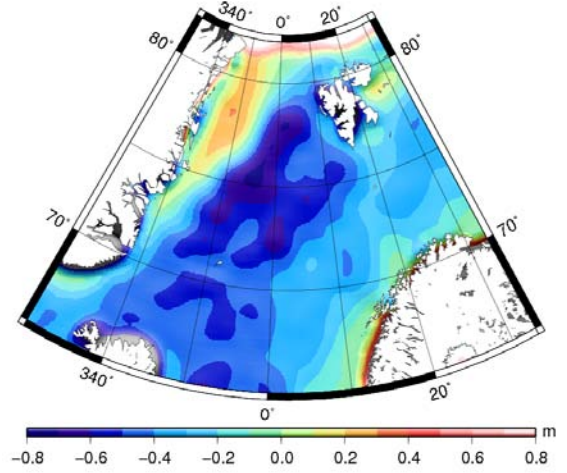


Fig. 6. An MDT derived from OCTAS06.v1 MSSH and a geoid model based on adjusted marine gravity data. MDT is low-pass filtered

7 Results

In Fig. 6 a synthetic MDT, derived from a geoid and the OCTAS06.v1 MSSH model, is illustrated. The gravimetric geoid was estimated following Sect. 4.1, using, as input data, the adjusted marine gravity measurements, land data, and KMS02 satellite altimetry data (fill gaps in the marine gravity data set). The geoid and MSSH model was combined [Eq. (1)] and then low-pass filtered.

The MDT may be estimated directly using LSC, see Sect. 5. The LSC method is quite computer demanding due to matrix inversion, so a smaller area with fewer measurement was selected. The computed MDT, in Fig. 7, is derived from marine, airborne, land gravity data and KMS04 MSSH.

The two estimated MDTs, Figs. 6 and 7, show similar major oceanographic features as the OCCAM MDT in Fig. 8. Excluding the areas around the Greenland coast and north of Svalbard, a comparison to OCCAM MDT gives a standard deviation of approximately 10 cm and 15 cm for synthetic MDT and LSC based MDT, respectively.

8 Conclusions

The marine gravity data in the Northern North Atlantic has been error screened and adjusted using new airborne gravity data. The standard deviation of the cross-over errors for the marine gravity data was reduced from 4.1 mGal to 1.6 mGal.

Based on adjusted gravity data new geoid model was computed and combined with the first OCTAS

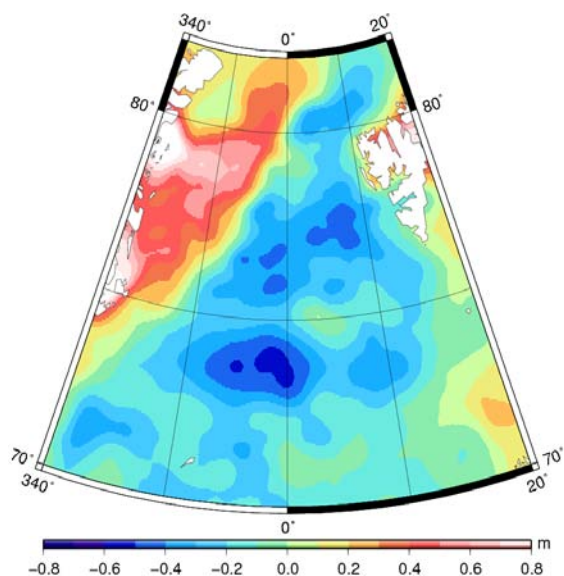


Fig. 7. MDT derived from a combination of gravity and MSSH data using least square collocation. MDT is low-pass filtered

MSSH model a synthetic MDT was computed. Both the synthetic and the LSC based MDTs give an overall good representation of the major oceanographic features in the Northern North Atlantic, when compared to the OCCAM MDT.

Acknowledgements. The OCTAS project is supported by the Norwegian Research Council.

References

- Bell, E. and Watts, A. (1989). Evaluation of BGM-3 sea gravity meter system onboard R/V Conrad. *J. Geophysics*, **51**(7), 1480–1493.
- Forsberg, R. (1984). A study of terrain reductions, density anomalies and geophysical inversion methods in gravity field modelling. Technical Report 355, Dept of Geodetic Science and Surveying, Ohio State University, Columbus.
- Forsberg, R. and Sideris, M. (1993). Geoid computations by the multi-band spherical FFT approach. *Manuscripta Geodaetica*, **18**, pp 82–90.
- Forsberg, R., Olesen, A., Vest, A., Solheim, D., Hipkin, R., Omang, O., and Knudsen, P. (2004). Gravity field improvements in the north atlantic region. In *2nd International GOCE User Workshop*. ESA.
- Knudsen, P. (1987). Estimation and Modelling of the Local Empirical Covariance Function using grav-

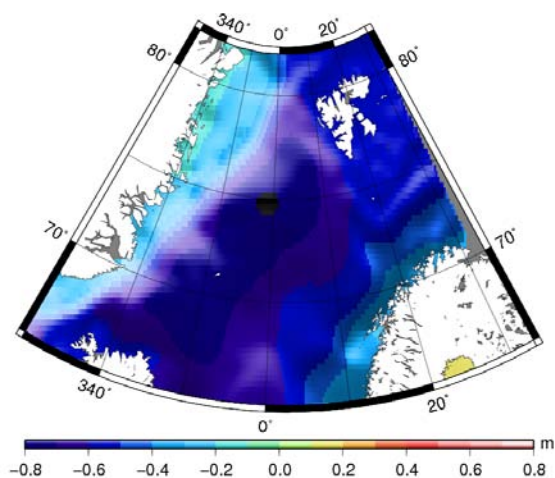


Fig. 8. OCCAM MDT

ity and satellite altimeter data. *Bulletin Geodésique*, **61**, 145–160.

Knudsen, P. (1991). Simultaneous estimation of the gravity field and sea surface topography from satellite altimeter data by least-squares collocation. *Geophysical Journal International*, **104**(2), 307–317.

Knudsen, P. and Vest, A. (2005). Integrating gravimetry and altimetry by collocation. In *Cahiers du Centre Europeen de Geodynamique et de Seismologie*, volume 25. Proceedings of the Workshop: GOCINA: Improving modelling of ocean transport and climate prediction in the North Atlantic region using GOCE gravimetry.

Moritz, H. (1980). *Advanced Physical Geodesy*. Abacus, Turnbridge Wells Kent, Kent, England.

Torge, W. (1989). *Gravimetry*. De Gruyter, Berlin, New York.

Tscherning, C. and Rapp, R. (1974). Closed Covariance Expressions for Gravity Anomalies, Geoid Undulations and Deflections of the Vertical Implied by Anomaly Degree Variances. Reports of Dep. of Geodetic Science and Surveying 208, The Ohio State University, Columbus.

Wessel, P. and Watts, A. (1988). On the accuracy of marine gravity measurements. *J Geophysical Research*, **93**(B1), 393–413.

Wong, L. and Gore, R. (1969). Accuracy of geoid heights from modified Stokes kernels. *Geophys. J. R. astr. Soc.*, **18**, 81–91.

Error Evaluation for Regional Geoid Computation Using Varying Integration Cap Sizes in a Synthetic Environment

K.I. Wolf¹ and B. Kieler²

¹Institut für Erdmessung, Leibniz University of Hannover, Schneiderberg 50, D-30167 Hannover, Germany
Email: wolf@ife.uni-hannover.de

²Institut für Kartographie und Geoinformatik, Leibniz University of Hannover, Appelstrasse 9a, D-30167 Hannover, Germany

Abstract. A modified Stokes' function with different maximum integration radii is applied to synthetic gravity data for quasigeoid solutions. The spectral combination method is used. The synthetic environment comprises a geopotential model and regional terrestrial gravity data, both including (uncorrelated and correlated) noise, and permits a closed-loop validation in all points. Due to the enhanced synthetic data set including noise, the computation results are closer to reality than simulations neglecting noise. The closed-loop differences meet the error estimates from error assessment based on degree variances. Main objective of the investigations is the study of the effect of varying integration cap sizes on the quasigeoid heights. Based on the same modified kernel function, the 1st and 2nd zero-crossing are chosen as constant cut-off distance, moreover a Meissl modified kernel is used based on a cut-off at the 1st minimum of the kernel and finally a fixed integration area with varying cut-off radii is used. The cut-off at the 2nd zero-crossing and the integration using a fixed input area show the best results. In the synthetic environment a quasigeoid can be derived with an accuracy of 1 cm and 13 cm (resolution about 15 km) based on regional gravity data with 1 mgal uncorrelated and 5 mgal correlated noise, respectively, and a high-resolution GPM (GRACE model, EGM96).

Keywords. geoid computation, spectral combination, synthetic data

1 Introduction

For an optimal geoid computation, data from a geopotential model (GPM) and terrestrial gravity data (as well as terrain data) are combined. A spectral combination of the source data can be achieved using integral formulas with modified kernel functions. In

regional computations, the results of integral methods are affected by a more or less favourable cut-off point of the kernel function. The minimization of the resulting omission error is therefore often one aim of kernel modifications (Meissl, 1971; Molodenskii et al., 1962; Vaníček and Kleusberg, 1987; Vaníček and Featherstone, 1998). In this paper the effect of the kernel cut-off is investigated using synthetic data in a closed-loop procedure. Synthetic data are advantageous for evaluating a computation method as the results can be validated with exact reference values, see also (Ågren, 2004). Furthermore, the closed-loop differences are compared with results from error assessment based on signal and error degree variances.

2 Computation Method

Molodenskii's formula as basic formula for quasigeoid computation by integration of terrestrial gravity anomalies Δg^T reads neglecting the Molodenskii correction (Heiskanen and Moritz, 1967)

$$\zeta(\theta_P, \lambda_P, r_P) = \frac{R}{4\pi\gamma_P} \iint_{\sigma} S(\psi, r_P, R) \Delta g_Q^T d\sigma \quad (1)$$

with the coordinates $(\theta_P, \lambda_P, r_P)$ of the computation point P . The spherical distance ψ between point P and the source points Q is used as well as the extended (Pizetti-) Stokes' function $S(\psi, r_P, R)$ and the normal gravity γ_P in point P . The integration surface σ is the unit sphere. The formula, as used here, is based on spherical approximations: 1) The relation between the disturbing potential T and the gravity anomaly is simply approximated by

$$\Delta g = - \left(\frac{\partial T}{\partial r} \right) - \frac{2}{r} T. \quad (2)$$

2) The telluroid, on which (2) holds, is approximated by a sphere, neglecting the Molodenskii correction. All gravity anomalies are assumed to be located on a sphere with radius R .

The first approximation causes an error in the order of the flattening of the ellipsoid (approx. 0.3%). This error can be accepted if the gravity anomalies Δg^T are referenced to a high resolution GPM. Applying the remove-restore procedure the residual gravity anomaly

$$\Delta g' = \Delta g^T - \Delta g^M \quad (3)$$

is used in (1), which results in the residual height anomaly ζ' ; ζ has to be restored by

$$\zeta = \zeta' + \zeta^M. \quad (4)$$

The functionals Δg^M and ζ^M are based on the GPM, Δg^M is computed using ellipsoidal approximations given in (Wenzel, 1985). The error induced by the second approximation can be reduced to 1 cm by a residual terrain model reduction of $\Delta g'$ (Denker and Tziavos, 1999). As the synthetic data are generated on the ellipsoid, this is neglected in the present study.

Due to the limited terrestrial gravity data, the integration (1) can only be evaluated regionally. Cutting-off the kernel function S at a distance $\psi_c < \pi$ results in an omission error (e.g. Heiskanen and Moritz, 1967). The omission error can be reduced by modifying the integral kernel S .

Starting from a constant cut-off distance ψ_c (Meissl, 1971) proposed the modification

$$S^M(\psi, r_P, R) = S(\psi, r_P, R) - S(\psi_c, r_P, R) \quad (5)$$

to force a zero-crossing of the kernel function at ψ_c . (Sjöberg, 1981) and (Wenzel, 1982) suggested an optimal combination of terrestrial and GPM data by introducing the spectral weights

$$w_\ell = \frac{\sigma_\ell^2(\epsilon_{\Delta g^M})}{\sigma_\ell^2(\epsilon_{\Delta g^M}) + \sigma_\ell^2(\epsilon_{\Delta g^T})} \quad (6)$$

for $\ell > 1$ with the error degree variances $\sigma_\ell^2(\epsilon_{\Delta g^M})$ of the GPM and the error degree variances $\sigma_\ell^2(\epsilon_{\Delta g^T})$ of the terrestrial gravity data. The modified kernel reads

$$S^W(\psi, r_P, R) = \sum_{\ell=2}^{\infty} \frac{2\ell+1}{\ell-1} \left(\frac{R}{r_P}\right)^{\ell+1} w_\ell P_\ell(\cos \psi) \quad (7)$$

with the Legendre polynomials P_ℓ . Due to larger long wavelength errors in Δg^T than in Δg^M , the weights w_ℓ of the terrestrial gravity data are close to zero for small degrees ℓ . Missing the long wavelength part, the modified kernel S^W has a steeper descent to zero than the unmodified kernel S . Thus, the omission error is implicitly reduced by this modification. In the numerical experiment the modified kernel (7) is used. Furthermore - motivated by a proposal of (Heck and Grüniger, 1987) based on Meissl's modification and a modification of (Wong and Gore, 1969) - Meissl's method (5) is applied

on the modified kernel (7) when cutting-off the kernel at its 1st local minimum. Meissl's modification can also be formulated using spectral weights (Heck and Grüniger, 1987), the weights for the combined modification read therewith:

$$w_\ell^M = \begin{cases} \frac{r_P}{R} S^W(\psi_c, r_P, R) & \ell = 0 \\ 0 & \ell = 1 \\ w_\ell & \ell > 1. \end{cases} \quad (8)$$

The zero degree term has then to be added in (7).

3 Error Assessment

The closed-loop results are validated by a comparison with results from an error assessment based on signal and error degree variances of the gravity anomalies. The formulas for the error estimation are presented very briefly, a report in more detail will follow in near future. The formulas can also be derived from (Heck and Grüniger, 1987). The variance $m_{\delta\zeta}^2$ of the quasigeoid can be estimated by

$$m_{\delta\zeta}^2 = \frac{R^2}{4\gamma^2} \left[\sum_{n=2}^{n_{\max}} (\bar{Q}_n^{1-w_\ell} + Q_n^1)^2 \sigma_n^2(\epsilon_{\Delta g^M}) + \sum_{n=2}^{\infty} (\bar{Q}_n^{w_\ell})^2 \sigma_n^2(\epsilon_{\Delta g^T}) + \sum_{n=n_{\max}+1}^{\infty} (Q_n^{w_\ell})^2 \sigma_n^2(\Delta g) \right]. \quad (9)$$

The Molodenskii coefficients Q_n , cf. (Molodenskii et al., 1962), applied to the kernel $S^W(\psi, r_P, R)$ read

$$Q_n^{w_\ell}(\psi_c) = \int_{\psi=\psi_c}^{\pi} S^W(\psi, r_P, R) P_n(\cos \psi) \sin \psi d\psi. \quad (10)$$

Equation (10) is evaluated numerically by the aid of recursion formulas (Paul, 1973). The spectral weights w_ℓ enter the computation of $S^W(\psi, r_P, R)$, see (7). For Q_n^1 , used in (9), the weights w_ℓ are set to 1.0 for all ℓ . In addition the relation

$$\begin{aligned} \bar{Q}_n^{w_\ell}(\psi_c) &= \int_{\psi=0}^{\psi_c} S^W(\psi, r_P, R) P_n(\cos \psi) \sin \psi d\psi \\ &= \frac{2}{n-1} \left(\frac{R}{r_P}\right)^{n+1} w_n - Q_n^{w_\ell}(\psi_c) \end{aligned} \quad (11)$$

holds, correspondingly for $\bar{Q}_n^{1-w_\ell}$ by replacing w_ℓ with $1 - w_\ell$ and w_n with $1 - w_n$, respectively.

The error degree variances $\sigma_\ell^2(\epsilon_{\Delta g^M})$, used in (6) and (9), are derived from the standard deviations of the spherical harmonic coefficients ($\sigma_{C_{\ell m}}^2$, $\sigma_{S_{\ell m}}^2$) of the GPM:

$$\sigma_\ell^2(\epsilon_{\Delta g^M}) = \left(\frac{GM}{R}\right)^2 \left(\frac{a}{R}\right)^{2\ell} \left(\frac{\ell-1}{R}\right)^2 \sum_{m=0}^{\ell} (\sigma_{C_{\ell m}}^2 + \sigma_{S_{\ell m}}^2). \quad (12)$$

The signal degree variances $\sigma_\ell^2(\Delta g)$ are based on the signal degree variance model by (Tscherning and Rapp, 1974) with global parameters.

The error degree variances $\sigma_\ell^2(\epsilon_{\Delta g^T})$ related to the terrestrial gravity anomalies are derived from the data noise, i. e., for uncorrelated or correlated noise.

Uncorrelated Noise. Error degree variances are derived as band-limited white noise by distributing the noise $\epsilon_{\Delta g}$ equally over a spectral range ℓ_{range} , which is chosen depending on the resolution of the terrestrial input data:

$$\sigma_\ell^2(\epsilon_{\Delta g^T}^{UC}) = \frac{\epsilon_{\Delta g}^2}{\ell_{range}}. \quad (13)$$

Strictly uncorrelated noise may not be realistic but is often assumed in practice due to the lack of information about the true correlation behaviour.

Correlated Noise. Error degree variances are derived by a Legendre transformation of the error covariance function, cf. (Wenzel and Arabelos, 1981):

$$\sigma_\ell^2(\epsilon_{\Delta g^T}^C) = \frac{2\ell + 1}{2} \int_0^\pi E_{\Delta g}(\psi) P_\ell(\cos \psi) \sin \psi d\psi. \quad (14)$$

For the error covariances $E_{\Delta g}$, the following model, based on (Weber and Wenzel, 1983), is chosen:

$$E_{\Delta g}(\psi) = \epsilon_{\Delta g}^2 e^{-4.0 \cdot \psi [^\circ]}. \quad (15)$$

Correlated noise is considered only in a few other error studies, e. g. (Ågren, 2004).

4 Synthetic Data

Synthetic data sets are produced for a closed-loop computation. For this purpose, a blended geopotential model (GPM1300S) is created by combining the coefficients from an actual GRACE(01S) GPM ($\ell = 0 \dots 89$, GFZ, 2003), EGM96 ($\ell = 90 \dots 360$, Lemoine et al., 1998), and GPM98C ($\ell = 361 \dots 1300$, Wenzel, 1999), cf. (Wolf and Denker, 2005). From this ground-truth model, the following input data sets are derived:

- A. Two GPM to degree $\ell_{max} = 360$, serving as reference models in the remove-restore procedure, are derived from GPM1300S. The first model, GPM360S (without noise), simply consists of the GPM1300S coefficients up to degree $\ell_{max} = 360$, while for the second (clone) model, GPM360I, noise is added according to the standard deviations of the coefficients.
- B. Three sets of gravity anomalies on the ellipsoid are derived: The first data set Δg^{1300S} (without noise) is based on the GPM1300S up to degree $\ell_{max} = 1300$. The second data set Δg^T (with noise) is created from Δg^{1300S} by adding noise $\epsilon_{\Delta g}$. Finally, the third data set Δg^M is computed from GPM360I.

Table 1. Statistics of the synthetic gravity anomalies and quasigeoid heights in mgal and m, respectively.

Data set	Mean	Std	Min	Max
Δg^{1300S}	10.283	34.097	-174.228	271.359
Δg^M	10.298	32.465	-145.932	145.334
$\Delta g^{1300S-M}$	-0.006	12.492	-46.461	53.394
ζ^{1300S}	43.316	8.226	15.841	59.502
ζ^M	43.317	8.237	16.499	59.440
$\zeta^{1300S-M}$	-0.001	0.429	-1.549	2.108

- C. Quasigeoid heights ζ^{1300S} are computed from GPM1300S on the ellipsoid, serving as ground-truth data. For the restore step ζ^M based on GPM360I are generated.

The synthetic Δg^T simulate gravity anomalies which are reduced by residual terrain effects. Therefore, the limit $\ell_{max} = 1300$ of the signal spectrum was considered as sufficient.

The data sets are computed on a 0.1° geographical grid within a test area, limited by $36.5^\circ \leq \varphi \leq 58.5^\circ$ and $-7.0^\circ \leq \lambda \leq 27.0^\circ$. The statistics of the data sets are listed in Table 1. The residual gravity anomalies $\Delta g'$ are computed according to (3) using Δg^T and Δg^M as described above.

The noise $\epsilon_{\Delta g}$ for the terrestrial gravity data is simulated as uncorrelated (UC) and correlated (C) version with two noise levels (1 mgal and 5 mgal) resulting in four different scenarios labelled with 1UC, 1C, 5UC and 5C. The uncorrelated noise is generated based on independent normal distributed random numbers, the correlated noise with a space domain approach by multiplying a vector of uncorrelated values with the Cholesky factor of the error covariance matrix, cf. (Wolf, 2006). A frequency domain approach can be found in (Ågren, 2004).

5 Numerical Experiments

Closed-loop computations are performed based on the four scenarios 1UC, 1C, 5UC and 5C. The spectral weights w_ℓ are derived according to (6) using the error degree variances (12) for Δg^M together with (13) and (14) for uncorrelated and correlated noise, respectively. The resulting spectral weights are shown in Fig. 1, the modified kernel functions (7) for the different scenarios are given in Fig. 2. Based on these kernels five scenarios with different maximum integration radii are selected: First and 2nd zero-crossing, as well as the 1st local minimum of the kernel function are chosen as constant cut-off distance, see Table 2. The integration area is a moving spherical cap. Meissl's modification (8) is applied with a cut-off at the 1st local minimum. Finally, the

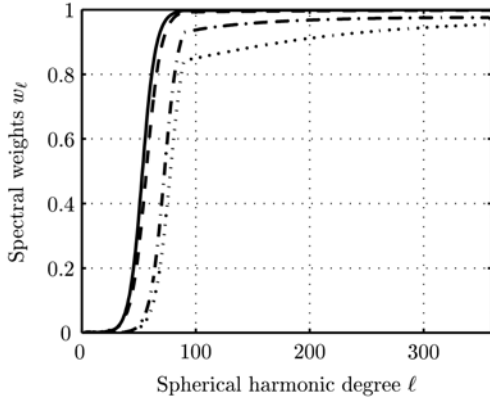


Fig. 1. Spectral weights w_ℓ according to (6) for the four scenarios 1UC (—), 1C (---), 5UC (-.-), 5C(⋯).

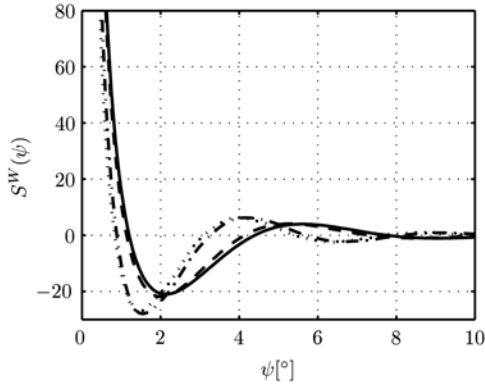


Fig. 2. Kernel functions modified with spectral weights (6) for the scenarios 1UC (—), 1C (---), 5UC (-.-), 5C(⋯).

whole test area is used for all computation points, the cut-off radii vary.

Residual quasigeoid heights ζ' are computed by evaluating (1), applying the 1D FFT approach of (Haagmans et al., 1993). The modified kernel S^W and the residual gravity anomalies $\Delta g'$ are used. The final quasigeoid heights ζ are restored by (4).

The synthetic data is then exploited by computing closed-loop differences for all data points using ζ^{1300S} as exact reference. Keeping always a constant cut-off distance ψ_c in the integration, quasigeoid heights can only be computed in a smaller inner area of the test area. For a fair comparison

Table 2. Cut-off distances ψ_c in the different noise scenarios, units degree.

	ψ_c	1UC	1C	5UC	5C
1 st zero-crossing (1ZC)		1.2	1.1	0.9	0.8
1 st local minimum (1MIN)		2.1	2.0	1.5	1.4
2 nd zero-crossing (2ZC)		4.4	4.1	3.3	3.1

Table 3. Statistics of the closed-loop results $\zeta^{1300S} - \zeta$ for the different scenarios (Sc.), units cm. The abbreviations mean different cut-off distances of the kernel: 1/2ZC:= 1st/2nd zero-crossing, 1MIN:= 1st local minimum, Meissl:= Meissl's modification based on 1MIN, Area...:= fixed integration area with varying cut-off distances (statistics refer to the same computation results but to different evaluation areas depending on the border size for comparison with the 1ZC, 1MIN and 2ZC scenario, see Fig. 3).

Sc.	ψ_c	Mean	Std	Min	Max	
1UC	1ZC	-0.07	3.75	-13.61	14.09	
	1MIN	-0.21	4.21	-17.61	22.30	
	2ZC	-0.16	1.54	-5.73	6.54	
	Meissl	-0.13	1.75	-7.30	7.15	
	Area1ZC	-0.09	1.70	-7.25	7.57	
	Area1MIN	-0.14	1.36	-5.70	6.01	
	Area2ZC	-0.19	1.21	-5.70	4.91	
	1C	1ZC	0.07	4.94	-19.72	18.54
		1MIN	-0.22	5.28	-23.33	24.20
2ZC		0.02	3.39	-9.19	14.17	
Meissl		-0.07	3.50	-13.72	11.49	
Area1ZC		-0.08	3.46	-12.03	14.10	
Area1MIN		-0.23	3.27	-12.03	11.99	
Area2ZC		-0.02	3.24	-9.29	11.99	
5UC		1ZC	-0.12	8.19	-29.48	32.69
		1MIN	-0.28	8.44	-31.18	37.81
	2ZC	-0.08	4.81	-19.59	18.90	
	Meissl	-0.35	5.54	-22.91	23.19	
	Area1ZC	-0.03	4.68	-19.66	21.67	
	Area1MIN	-0.13	4.55	-19.66	17.63	
	Area2ZC	-0.23	4.41	-17.50	17.07	
	5C	1ZC	0.49	14.13	-51.71	50.59
		1MIN	0.09	14.11	-53.85	50.98
2ZC		-0.28	13.00	-44.29	47.60	
Meissl		0.40	13.55	-46.26	48.64	
Area1ZC		0.06	12.78	-49.28	41.74	
Area1MIN		-0.11	12.86	-49.28	41.74	
Area2ZC		-0.39	12.79	-44.69	41.46	

the same border size is left out for the results based on a fixed integration area with varying cut-off radii. Close to the border, edge effects causes strong errors which are excluded in this way. For each ψ_c (1st and 2nd zero-crossing, 1st local minimum, cf. Table 2) an appropriate border size is chosen (Fig. 3), considering the meridian convergence for the borders in east-west direction. Thus, the statistics of the closed-loop differences based on the fixed integration area with varying cut-off radii - named with "Area..." in Table 3 - refer to the same computation results but to different evaluation areas.

The standard deviations based on the closed-loop differences in Table 3 range from 1.2 cm (1UC) to 14.1 cm (5C). The results of the cut-off at the 1st zero-crossing are not promising. Although the kernel

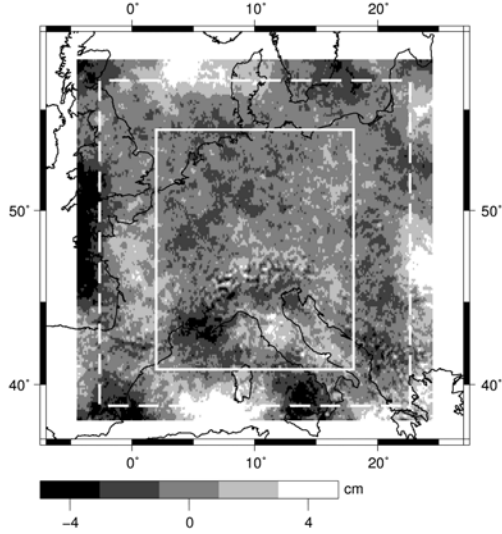


Fig. 3. Closed-loop differences for scenario 1UC using the whole area as fixed input for integration. A border is left out in the size of ψ_c of 1ZC, cf. Table 2. Borderlines 1MIN (dashed) and 2ZC (solid) are indicated.

function is zero at the cut-off, it is too abrupt and produces an inhomogeneous error behaviour. Cutting-off the kernel function at the 1st local minimum gives the worst results, the jump from the kernel's minimum to zero is very unfavourable. Meissl's modification can improve the results by a factor of 1.5 . . . 2 for the scenarios 1UC, 1C and 5UC. Cutting-off the kernel at the 2nd zero-crossing leads to similar results as if using always the whole area for integration. In the latter case the best results are achieved in all noise scenarios. The closed-loop differences for the scenario 1UC are shown in Fig. 3. One can see that the differences increase near the borders, a distance from the edges of the input area according to the 2nd zero-crossing of S^W yields better results.

An improvement for too short or unfavourable constant cut-off distances may be achieved by applying the kernel modification proposed by (Sjöberg, 1991) which optimizes not only in view of the errors of the GPM and the terrestrial gravity data (as in (6)) but also minimizes the omission error, see (Ågren, 2004). But the determination of the spectral weights is then more complex and can lead to a numerical instable equation system, why it is not used in the present study.

Concerning the computation time of the actual MATLAB implementation, the integration over the whole data area is about ten times more time consuming than the integration over the limited moving

Table 4. Statistics of the statistical error assessment, units cm. The abbreviations indicate the different summation parts in formula (9) coming from $M := \sigma_n^2(\epsilon_{\Delta g^M})$, $T := \sigma_n^2(\epsilon_{\Delta g^T})$ and $O := \sigma_n^2(\Delta g)$.

Sc.	ψ_c	M	T	O	$m_{\delta\zeta}$
1UC	1ZC	3.83	2.06	0.30	4.36
	1MIN	4.09	1.96	1.17	4.69
	2ZC	1.25	2.00	0.07	2.36
	Meissl	1.62	2.37	0.02	2.87
	180°	0.79	1.99	0.00	2.14
1C	1ZC	4.41	2.78	0.37	5.23
	1MIN	4.55	2.79	1.10	5.45
	2ZC	1.45	2.90	0.07	3.24
	Meissl	2.04	3.08	0.02	3.69
	180°	1.00	2.92	0.00	3.08
5UC	1ZC	7.75	8.52	0.42	11.53
	1MIN	8.02	8.11	1.23	11.47
	2ZC	4.08	8.33	0.11	9.27
	Meissl	4.65	9.81	0.10	10.86
	180°	3.08	8.31	0.00	8.86
5C	1ZC	9.73	10.93	0.34	14.64
	1MIN	9.74	10.90	1.26	14.67
	2ZC	6.24	11.49	0.08	13.08
	Meissl	6.75	12.35	0.20	14.08
	180°	5.26	11.62	0.00	12.75

spherical caps. But as the absolute computation time amounts only to some minutes on a standard pc this is not regarded as an essential disadvantage.

Results of the statistical error estimation based on signal and error degree variances are shown in Table 4. The three different summation parts of the total variance $m_{\delta\zeta}^2$ according to (9) are listed. For the scenarios based on input data with correlated noise, the error predictions fit very well with the closed-loop differences within 6 mm comparing the standard deviations. For the uncorrelated scenarios, the error assessment looks much more pessimistic (up to a factor of 2). This is caused by the modelling technique of the error degree variances $\sigma_{\ell}^2(\epsilon_{\Delta g^T}^{\text{UC}})$, where correlation remains, as noted earlier (Wolf, 2006). The error assessment based on Meissl's modification confirms the closed-loop results. The omission error is reduced by a factor up to 50 using Meissl's modification for the cut-off at the 1st local minimum. The closed-loop differences of the scenario using the whole input data area are comparable with results of the error assessment without cutting-off the kernel. The error estimates agree with the closed-loop results within 2 mm for the correlated scenarios and within 1 cm and 4.5 cm for the 1UC and the 5UC scenario, respectively.

6 Conclusions

Errors for regional quasigeoid computation were studied. Regional gravity anomaly data were spectrally combined with data from actual GPM. The effect of cutting-off the integration kernel was investigated. Closed-loop differences were computed using synthetic data sets including correlated and uncorrelated noise for the terrestrial data as well as noise for the GPM. Therefore, the closed-loop differences reflect the final quasigeoid errors better than using noise-free simulation data. Of course, real data sets differ from the used synthetic data concerning, e. g., maximum frequencies of the signal and uncertain or inhomogeneous quality. The closed-loop differences in this study were confirmed by statistical error estimation. The best and most homogeneous results were achieved integrating for all points over a fixed area with varying cut-off radii. When using a constant cut-off distance, the 2nd zero-crossing or the 1st local minimum including the modification of Meissl should be chosen.

A spectrally combined quasigeoid was derived with an accuracy of 1.2 cm and 12.8 cm (resolution about 15 km) based on (synthetic) regional gravity data with 1 mgal uncorrelated and 5 mgal correlated noise, respectively, and a high-resolution GPM (GRACE models augmented by EGM96).

Acknowledgments. We like to thank L. E. Sjöberg and an anonymous reviewer for their constructive remarks and careful corrections of the paper.

References

- Ågren, J. (2004). Regional Geoid Determination Methods for the Era of Satellite Gravimetry - Numerical Investigations Using Synthetic Earth Gravity Models. PhD thesis, Royal Institute of Technology, Stockholm.
- Denker, H. and Tziavos, I. N. (1999). Investigation of the Molodenskii Series Terms for Terrain Reduced Gravity Field Data. *Boll Geofisica Teor ed Appl*, 40:195–203.
- GFZ (2003). First GFZ GRACE Gravity Field Model EIGEN-GRACE01S. <http://www.gfz-potsdam.de/pbl/op/grace/results/>.
- Haagmans, R., de Min, E., and van Gelderen, M. (1993). Fast Evaluation of Convolution Integrals on the Sphere Using 1D FFT, and a Comparison with Existing Methods for Stokes' Integral. *Man Geod*, 18:227–241.
- Heck, B. and Grüniger, W. (1987). Modification of Stokes' Integral Formula by Combining two Classical Approaches. In *Advances in Gravity Field Modelling, Proc XIX General Assembly, IAG Symposia, Vancouver, Canada, August 10-22, 1987*, pp. 319–337.
- Heiskanen, W. A. and Moritz, H. (1967). *Physical Geodesy*. San Francisco. W. H. Freeman and Company.
- Lemoine, F. G. et al. (1998). The Development of the Joint NASA GSFC and NIMA Geopotential Model EGM96, NASA/TP-1998-206861. Tech report, NASA.
- Meissl, P. (1971). Preparations for the Numerical Evaluation of Second Order Molodenskii-type Formulas. OSU Rep 163, Ohio State University, Columbus, USA.
- Molodenskii, M. S., Eremeev, V. F., and Yurkina, M. I. (1962). *Methods for Study of the External Gravitational Field and Figure of the Earth*. Israel Program for Scientific Translations, Jerusalem.
- Paul, M. K. (1973). A Method of Evaluating the Truncation Error Coefficients for Geoidal Height. *Bull Géod*, 110:413–425.
- Sjöberg, L. E. (1981). Least-Squares Combination of Satellite and Terrestrial Data in Physical Geodesy. *Ann. Géophys.*, 1:25–30.
- Sjöberg, L. E. (1991). Refined Least Squares Modification of Stokes' Formula. *Man Geod*, 16:367–375.
- Tscherning, C. C. and Rapp, R. H. (1974). Closed Covariance Expressions for Gravity Anomalies, Geoid Undulations, and Deflections of the Vertical Implied by Anomaly Degree Variance Models. OSU Rep 208, Ohio State University, Columbus, USA.
- Vaniček, P. and Featherstone, W. E. (1998). Performance of Three Types of Stokes' Kernel in the Combined Solution for the Geoid. *J Geod*, 72:684–697.
- Vaniček, P. and Kleusberg, A. (1987). The Canadian Geoid - Stokesian Approach. *Man Geod*, 12:86–98.
- Weber, G. and Wenzel, H.-G. (1983). Error Covariance Functions of Sea Gravity Data and Implications for Geoid Determination. *Mar Geodesy*, 75(1-4):199–226.
- Wenzel, H.-G. (1982). Geoid Computation by Least-Squares Spectral Combination Using Integral Kernels. In *Proc General Meeting of the IAG, Tokyo, May 7-15, 1982*, pp. 438–453, Berlin. Springer.
- Wenzel, H.-G. (1985). Hochauflösende Kugelfunktionsmodelle für das Gravitationspotential der Erde. Number 137 in *Wiss Arb Uni Hannover. Institut für Erdmessung*.
- Wenzel, H.-G. (1999). Schwerefeldmodellierung durch ultra hochauflösende Kugelfunktionsmodelle. *ZfV*, 124(5):144–154.
- Wenzel, H.-G. and Arabelos, D. (1981). Zur Schätzung von Anomalie-Gradvarianzen aus lokalen Kovarianzfunktionen. *ZfV*, 106(5):234–243.
- Wolf, K. I. (2006). Considering Coloured Noise of Ground Data in an Error Study for External GOCE Calibration / Validation. In Knudsen, P., Johannessen, J., Gruber, T., Stammer, S., and van Dam, T., (eds.), *Proc GOCINA Workshop, April, 13-15, 2005*, vol 25 of *Cahiers du Centre Européen de Géodynamique et de Séismologie*, pp. 85–92. Luxembourg.
- Wolf, K. I. and Denker, H. (2005). Upward Continuation of Ground Data for GOCE Calibration / Validation Purposes. In Jekeli, C., Bastos, L., and Fernandes, J., (eds.), *Proc IAG Int Symp, Porto, Portugal, Aug. 30 - Sept. 3, 2004*, IAG Symposia 129, pp. 60–65. Berlin. Springer.
- Wong, L. and Gore, R. (1969). Accuracy of Geoid Heights from Modified Stokes Kernels. *Geophysical Journal of the Royal Astronomical Society*, 18(1):81–91.

Optimized Solution and a Numerical Treatment of Two-boundary Problems in Combining Terrestrial and Satellite Data

P. Holota¹ and O. Nesvadba²

¹ Research Institute of Geodesy, Topography and Cartography, 250 66 Zdíby 98, Praha-východ, Czech Republic, e-mail: holota@pecny.asu.cas.cz, Tel.: +420 323649235, Fax: +420 284890056

² Land Survey Office, Pod Sídlištěm 9, 182 11 Praha 8, Czech Republic, e-mail: nesvadba@bonbox.cz, Tel.: +420 286840435

Abstract. Gravity field studies today develop under an unprecedented progress in measuring techniques. These advances open problems of theoretical and practical nature. The purpose of this paper is to show a spectral and a space domain interpretation of an optimization concept in combining terrestrial and satellite gravity field data and especially to study the numerical treatment of this concept. Because the problems under study are overdetermined by nature, methods typical for the solution of boundary-value problems are applied together with an optimization approach. In addition to the results reached in the spectral domain the use of series summation techniques is investigated in order to find their interpretation in terms of Green's functions related to the particular combination scheme. This makes it also possible to show the tie between the global and the local modelling of the gravity field.

Keywords. Modelling of the Earth's gravity field, geodetic boundary-value problems, overdetermined problems, terrestrial and satellite data, optimization

1 Introduction

One of the challenges in gravity field modelling today is the combination of heterogeneous gravity data. Because excess data appear in a number of typical cases, overdetermined problems have to be solved. Two cases are discussed in this paper, i.e. the combination of terrestrial gravity measurements with satellite-only models of the Earth's gravity field and with data coming from satellite missions like e.g. GOCE [treated within the so-called space-wise approach, see e.g. Migliaccio et al. (2004)]. Still other mixed problems are considered in Holota (1995, 2007) and Holota and Kern (2005).

In the sequel Ω means a domain bounded by two surfaces. With some simplification we can even

suppose that Ω is bounded by two spheres of radius R_i and R_e , respectively, assuming $R_i < R_e$.

2 Gravimetry and a satellite-only model

In this case we will consider the following problem

$$\Delta T = 0 \quad \text{in } \Omega \quad (1)$$

$$\frac{\partial T}{\partial r} + \frac{2}{R_i} T = -\Delta g \quad \text{for } r = R_i \quad (2)$$

$$T = t \quad \text{for } r = R_e \quad (3)$$

Here Δ is Laplace's operator, Δg the usual gravity anomaly and t means the input obtained from an available satellite-only gravity field model.

The domain Ω is bounded. Therefore, when using the apparatus of spherical harmonics, we look for the solution $T = T(r, \varphi, \lambda)$ in the form

$$T = \sum_{n=0}^{\infty} \left(\frac{R_i}{r} \right)^{n+1} T_n^{(i)}(\varphi, \lambda) + \sum_{n=0}^{\infty} \left(\frac{r}{R_e} \right)^n T_n^{(e)}(\varphi, \lambda) \quad (4)$$

where $T_n^{(i)}$ and $T_n^{(e)}$ are the respective Laplace surface spherical harmonics, cf. Grafarend and Sansò (1984). Inserting then into Eqs. (2) and (3), we obtain for any individual n the following system

$$(n-1)T_n^{(i)} - (n+2)q^n T_n^{(e)} = R_i \Delta g_n \quad (5)$$

$$q^{n+1} T_n^{(i)} + T_n^{(e)} = t_n \quad (6)$$

where $q = R_i/R_e$, while Δg_n and t_n are Laplace's surface spherical harmonics in the expansions of Δg and t , respectively, i.e. in

$$\Delta g(\varphi, \lambda) = \sum_{n=0}^{\infty} \Delta g_n(\varphi, \lambda) \quad (7)$$

and

$$t(\varphi, \lambda) = \sum_{n=0}^{\infty} t_n(\varphi, \lambda) \quad (8)$$

The regularity of the system has to be discussed first. The determinant is $D_n = (n+2)(1+q^{2n+1}) - 3$. Thus we have to examine the equation $D_n = 0$. It defines q as a function of n . Confining ourselves

to real functions, we obtain

$$q_n = q(n) = -[1 - 3/(n+2)]^{1/(2n+1)} \quad (9)$$

which yields $q_0 = 0.5$, $q_1 = 0$, $q_2 \doteq -0.758$, $q_3 \doteq -0.877$, \dots , $q_{10} \doteq -0.986$ and, obviously, $\lim_{n \rightarrow \infty} q_n = -1$. Recalling in addition that in our applications $q = R_i/R_e$ is positive and definitely greater than 0.5, we can conclude that the system given by Eqs. (5) and (6) is regular in our studies. Hence for the individual n we have

$$T_n^{(i)} = [R_i \Delta g_n + (n+2)q^n t_n] / D_n \quad (10)$$

and

$$T_n^{(e)} = -[R_i q^{n+1} \Delta g_n - (n-1)t_n] / D_n \quad (11)$$

Remark 1. It is also clear that the use of a satellite-only model (within the concept as above) results in a modification of the Stokes like problem and has a beneficial effect on the uniqueness of the solution.

3 Gravimetry and gradiometry

The solvability problems seem to be less complicated when combining satellite gravity gradiometry and terrestrial gravimetry data. Confining ourselves to radial gravity gradients only, we can consider the following problem

$$\Delta T = 0 \quad \text{in } \Omega \quad (12)$$

$$\frac{\partial T}{\partial r} + \frac{2}{R_i} T = -\Delta g \quad \text{for } r = R_i \quad (13)$$

$$\frac{\partial^2 T}{\partial r^2} = G \quad \text{for } r = R_e \quad (14)$$

The input from satellite gradiometry is symbolized by

$$G(\varphi, \lambda) = \sum_{n=0}^{\infty} G_n(\varphi, \lambda) \quad (15)$$

where again G_n are the respective surface spherical harmonics. Hence, for T as in Eq. (4) the following system can be deduced for any individual n

$$(n-1)T_n^{(i)} - (n+2)q^n T_n^{(e)} = R_i \Delta g_n \quad (16)$$

$$(n+1)(n+2)q^{n+1} T_n^{(i)} + n(n-1)T_n^{(e)} = R_e^2 G_n \quad (17)$$

in view of the orthogonality of spherical harmonics. Clearly, $D_n^g = n(n-1)^2 + (n+1)(n+2)^2 q^{2n+1}$ is the determinant of the system and it always differs from zero, when $q > 0$ (which is our case). Thus

$$T_n^{(i)} = [R_i n(n-1) \Delta g_n + R_e^2 (n+2) q^n G_n] / D_n^g \quad (18)$$

and

$$T_n^{(e)} = -[R_i (n+1)(n+2) q^{n+1} \Delta g_n - R_e^2 (n-1) G_n] / D_n^g \quad (19)$$

A note analogous to Remark 1 may be added also here, but with the difference that another kind of input data is used for $r = R_e$.

4 Optimization

In both the cases we found a solution T which is harmonic in the bounded domain Ω . The problem, however, is that in general the continuation of T for $r > R_e$ need not be regular at infinity, i.e., it is not guaranteed that for $r \rightarrow \infty$ the continuation decreases as c/r (c is a constant) or faster. This can be considered a consequence of a contamination of the input data by measurement errors. Clearly, the data given for $r = R_i$ are enough to determine a harmonic function in $\Omega_{ext} \equiv \{\mathbf{x} \in \mathbf{R}^3; r > R_i\}$ and thus in $\Omega \subset \Omega_{ext}$. The data for $r = R_e$ have the nature of excess data and give rise to ("internal") terms $(r/R_e)^n T_n^{(e)}$ that are not regular at infinity. The problem has been treated in literature as an overdetermined problem, see e.g. Sacerdote and Sansò (1985) and Rummel et al. (1989). Here we approach it through an analytical regularization.

In solving this overdetermined problem, we will look for a harmonic function f which is regular at infinity and minimizes the following functional

$$\Phi(f) = \int_{\Omega} (f - T)^2 dx \quad (20)$$

In particular, we will suppose that $f \in H_2(\Omega_{ext})$, where $H_2(\Omega_{ext})$ is the space of harmonic functions endowed with inner product

$$(f, g) = \int_{\Omega_{ext}} (fg/r^2) dx \quad (21)$$

The functional Φ is coercive and attains its minimum in $H_2(\Omega_{ext})$, see Holota and Kern (2005), Holota (2007) and also Nečas and Hlaváček (1981). Hence, assuming that at a point $f \in H_2(\Omega_{ext})$ the functional Φ has its local minimum, we know that its Gateaux's differential equals zero at the point f . This immediately yields

$$\int_{\Omega} f v dx = \int_{\Omega} T v dx \quad (22)$$

for all $v \in H_2(\Omega_{ext})$. Note that Eq. (22) represents Euler's necessary condition for Φ to have a minimum at the point f .

The integral identity given by Eq. (22) is a natural starting point for a numerical solution. First, however, we put for the indices $n = 0, 1, 2, \dots$ and $m = -n, -n+1, \dots, -1, 0, 1, \dots, n-1, n$

$$Y_{nm}(\varphi, \lambda) = P_{n|m|}(\sin \varphi) \begin{cases} \cos m\lambda & \text{for } m \geq 0 \\ \sin |m|\lambda & \text{for } m < 0 \end{cases} \quad (23)$$

where $P_{n|m}$ is the usual (associated) Legendre function. Then $v_{nm} = (R_i/r)^{n+1} Y_{nm}(\varphi, \lambda)$ are the solid spherical harmonics and in general

$$f = \sum_{n=0}^{\infty} \sum_{m=-n}^{m=n} f_{nm} v_{nm} \quad (24)$$

where f_{nm} are scalar coefficients. In consequence, using the orthogonality of spherical harmonics, Eq. (22) transforms into the following system for the coefficients f_{nm}

$$f_{nm} \int_{\Omega} v_{nm}^2 dx = \int_{\Omega} T v_{nm} dx \quad (25)$$

Here

$$\int_{\Omega} v_{nm}^2 dx = \frac{R_i^3 (1-q^{2n-1})}{2n-1} \int_{\sigma} Y_{nm}^2(\varphi, \lambda) d\sigma \quad (26)$$

where $d\sigma$ is the surface element of the unit sphere σ . As to the integral on the right hand side of Eq. (25), we recall that in general

$$T_n^{(i)} = T_n^{(i)}(\varphi, \lambda) = \sum_{m=-n}^{m=n} a_{nm}^{(i)} Y_{nm}(\varphi, \lambda) \quad (27)$$

and

$$T_n^{(e)} = T_n^{(e)}(\varphi, \lambda) = \sum_{m=-n}^{m=n} a_{nm}^{(e)} Y_{nm}(\varphi, \lambda) \quad (28)$$

where $a_{nm}^{(i)}$ and $a_{nm}^{(e)}$ are scalar coefficients. Thus, after some algebra, $f_{nm} = a_{nm}^{(i)} + \alpha_n a_{nm}^{(e)}$, where

$$\alpha_n = \frac{(2n-1)(1-q^2)}{2(1-q^{2n-1})} q^{n-2} \quad (29)$$

Hence, inserting into Eq. (24), we get

$$f = \sum_{n=0}^{\infty} \left(\frac{R_i}{r} \right)^{n+1} [T_n^{(i)} + \alpha_n T_n^{(e)}] \quad (30)$$

In particular, $\alpha_0 = (1+q)/2q$ and $\lim_{n \rightarrow \infty} \alpha_n = 0$ as $n \rightarrow \infty$. Other values of α_n are in Fig. 1.

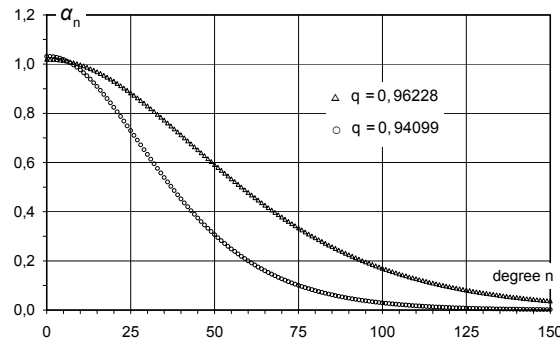


Figure 1. Values of α_n for $R_i = 6378 \text{ km}$ and two cases of R_e : $R_e = R_i + 250 \text{ km}$ and $R_e = R_i + 400 \text{ km}$, i.e., for $q = 0.96228$ and $q = 0.94099$, respectively.

5 Optimized solution

In order to apply our optimization to the problems in Sections 2 and 3 we still have to return to surface spherical harmonics $T_n^{(i)}$ and $T_n^{(e)}$, as they were

derived in these particular cases.

For the problem in Section 2 $T_n^{(i)}$ and $T_n^{(e)}$ are given by Eqs. (10) and (11). Thus, in view of Eq. (30), the optimization leads to

$$f = \sum_{n=0}^{\infty} \left(\frac{R_i}{r} \right)^{n+1} \left[A_n^{(i)} \frac{R_i}{n-1} \Delta g_n + A_n^{(e)} t_n \right] \quad (31)$$

with

$$A_n^{(i)} = (n-1)(1-\alpha_n q^{n+1})/D_n \quad (32)$$

$$A_n^{(e)} = [(n+2)q^n + \alpha_n(n-1)]/D_n \quad (33)$$

Note that for $n=1$

$$\frac{A_n^{(i)}}{n-1} = \frac{1-\alpha_1}{3q^3} = \frac{2-(1+q)q}{6q^3} \quad (34)$$

which is close to zero. The values of the coefficients $A_n^{(i)}$ and $A_n^{(e)}$ can be seen from Fig. 2.

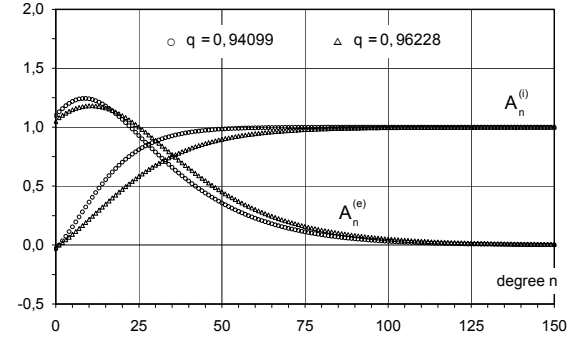


Figure 2. The coefficients $A_n^{(i)}$ and $A_n^{(e)}$ for $q = 0.96228$ and $q = 0.94099$ ($R_e = R_i + 250 \text{ km}$ and $R_e = R_i + 400 \text{ km}$) in case of gravimetry and a satellite-only model.

Similarly, in case of the problem in Section 3 the optimization leads to

$$f = \sum_{n=0}^{\infty} \left(\frac{R_i}{r} \right)^{n+1} \left[A_n^{(i)} \frac{R_i}{n-1} \Delta g_n + A_n^{(e)} \frac{R_e^2}{(n+1)(n+2)} G_n \right] \quad (35)$$

with

$$A_n^{(i)} = \frac{n-1}{D_n^g} [n(n-1) - \alpha_n(n+1)(n+2)q^{n+1}] \quad (36)$$

$$A_n^{(e)} = \frac{(n+1)(n+2)}{D_n^g} [(n+2)q^n + \alpha_n(n-1)] \quad (37)$$

Note as above that for $n=1$ we have

$$\frac{A_n^{(i)}}{n-1} = -\frac{\alpha_1}{3q} = -\frac{1+q}{6q^2} \doteq -0.33. \quad (38)$$

The values of the coefficients $A_n^{(i)}$ and $A_n^{(e)}$ are then illustrated in Fig. 3.

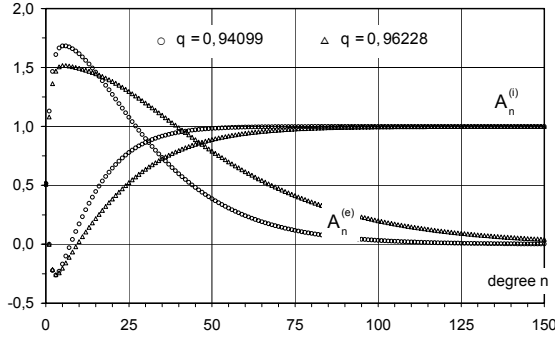


Figure 3. The coefficients $A_n^{(i)}$ and $A_n^{(e)}$ for $q = 0.96228$ and $q = 0.94099$ ($R_e = R_i + 250\text{km}$ and $R_e = R_i + 400\text{km}$) in case of gravimetry and gradiometry.

From Figs. 2 and 3 one can see how the input data are combined in the spectral domain. Both the figures show that the optimization applied offers a natural concept for weighting the input data. In addition in Fig. 3 one can see a relatively slow decay of $A_n^{(e)}$ with degree n for a low altitude (250km), compared to $A_n^{(e)}$ related to the contribution of the satellite-only model, cf. Fig. 2. This also shows advantages of satellite gradiometry at low altitudes.

6 Spectrum and the integral kernel

Our aim is now to make an attempt to sum the terrestrial term

$$f_{terr} = \sum_{n=0}^{\infty} \left(\frac{R_i}{r} \right)^{n+1} A_n^{(i)} \frac{R_i}{n-1} \Delta g_n \quad (39)$$

in our two cases, i.e. in Eq. (31) and Eq. (35). In the first case $A_n^{(i)}$ is given by Eq. (32), so that after some manipulation we have

$$f_{terr} = -\frac{R_i^2}{r} \cdot \frac{1-q}{2(2q-1)} \Delta g_0 + \frac{R_i^3}{r^2} \cdot \frac{2-(1+q)q}{6q^2} \Delta g_1 + \frac{R_i}{4\pi} \int_{\sigma} S^*(r, \psi) \Delta g d\sigma \quad (40)$$

where

$$S^*(r, \psi) = \sum_{n=2}^{\infty} A_n^{(i)} \frac{2n+1}{n-1} \left(\frac{R_i}{r} \right)^{n+1} P_n(\cos \psi) \quad (41)$$

Similarly, in the second case $A_n^{(i)}$ is given by Eq. (36) and we have

$$f_{terr} = \frac{R_i^2}{r} \cdot \frac{1+q}{4q} \Delta g_0 - \frac{R_i^3}{r^2} \cdot \frac{1+q}{6q^2} \Delta g_1 + \frac{R_i}{4\pi} \int_{\sigma} S^*(r, \psi) \Delta g d\sigma \quad (42)$$

where the kernel function $S^*(r, \psi)$ appears again, but stress that now with $A_n^{(i)}$ given by Eq. (36).

It is thus clear that for a space domain interpretation of the contribution of terrestrial data the key problem is to find explicitly how the function $S^*(r, \psi)$ depends on the angle ψ in our two cases.

For $r = R_i$ an immediate summation of about 300 or 450 first terms, in dependence of the two values of q considered (and the relative accuracy 10^{-16} , the so-called “machine ε ” in the IEEE754 floating-point arithmetic), yields the following Figs. 4 and 5, where also the classical Stokes function $S(R_i, \psi) = S(\psi)$ has been drawn for comparison.

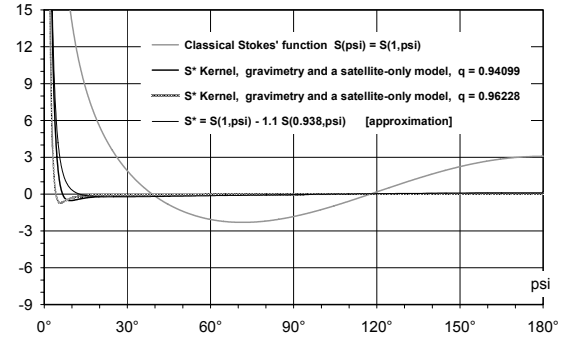


Figure 4. Problem in Sect. 2: the kernel function $S^*(R_i, \psi)$ for $q = 0.96228$ and $q = 0.94099$. Approximate values of the kernel function $S^*(R_i, \psi)$ for $q = 0.94099$.

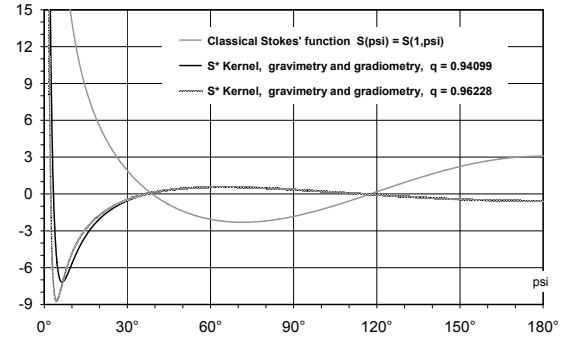


Figure 5. Problem in Sect. 3: the kernel function $S^*(R_i, \psi)$ for $q = 0.96228$ and $q = 0.94099$.

From the figures it is also clear that in f_{terr} given by Eq. (40) or (42) the influence of distant zones is considerably suppressed. This is an important feature which gives a possibility to reduce the need for a global coverage with gravity data and also to put the concepts outlined in this paper in the right context.

Remark 2. We also tried to sum the series giving $S^*(r, \psi)$ analytically. Various functions have been used to approximate the coefficient $A_n^{(i)}$. First a fit by means of rational functions has been tested. Especially those rational functions have been used, which allow a decomposed into partial fractions related to simple real roots, since this gives more

chance to manage the summation. Nevertheless, the summation was rather complex anyhow and we, therefore, looked for another solution. In particular for the problem in Section 2 we found that a good approximation of $A_n^{(i)}$ can be achieved by means of $A(n) = 1 - ak^{n+1}$ where a and k are suitably chosen parameters such that $a > 0$ and $0 < k < 1$. We can then put with some approximation $A_n^{(i)} \approx A(n)$. Hence, substituting into Eq. (41), we have $S^*(r, \psi) \approx S(x, \psi) - aS(kx, \psi)$, where $x = (R_i/r)$ and $S(x, \psi)$ is the famous (extended) Stokes function. Its closed form may be found, e.g., in Heiskanen and Moritz (1967) or Pick et al. (1973). In numerical experiments done for the problem in Section 2 and $q = 0.94099$ a good fit has been reached for $a = 1.1$ and $k = 0.938$. For $x = 1$, i.e., $r = R_i$, the approximate values of $S^*(R_i, \psi)$ given by $S(1, \psi) - 1.1S(0.938, \psi)$ can be seen from Fig. 4, but were not used in the computations.

7 Numerical test of the procedure and final comments

In order to check the efficiency of the procedure discussed in this paper, we tested the whole approach numerically by means of simulated input data. For this purpose we used the potential W of the gravity field model EGM96 and the potential U of the Somigliana-Pizzetti normal gravity field with parameters given in GRS1980, see Lemoine et al., (1998) and Moritz (1980).

The anomaly Δg was simulated in a “regular” grid on the sphere of radius $R_i = 6378 \text{ km}$. The grid is given by the 10th level of the refinement of an initial icosahedron, which implies more than 10 000 000 data points. The hierarchically created grids were also efficiently exploited for Romberg’s integration method in calculating the surface integral in Eqs. (40) and (42), cf. Nesvadba et al. (2007). [Note that the method was used in a somewhat generalized form compared to a one-dimensional case discussed, e.g., in Press et al. (1992).] In contrast, t and G were simulated by means of the harmonic coefficients in t_n and G_n , respectively, taken from the expansions of the disturbing potential $T = W - U$ and its second radial derivatives restricted to the sphere of radius $R_e = R_i + 250 \text{ km}$.

In the sequel the problem in Section 2, i.e. the combination of gravimetry and a satellite-only model, is treated first: f_{terr} given by Eq. (40) and

$$f_{sat} = \sum_{n=0}^{\infty} \left(\frac{R_i}{r} \right)^{n+1} A_n^{(e)} t_n \quad (43)$$

with $A_n^{(e)}$ given by Eq. (33) were computed for $r = R_i$ and $q = 0.96228$, i.e., $R_e = R_i + 250 \text{ km}$. The composition $f = f_{terr} + f_{sat}$ shown in Fig. 6 then yields the optimized solution.

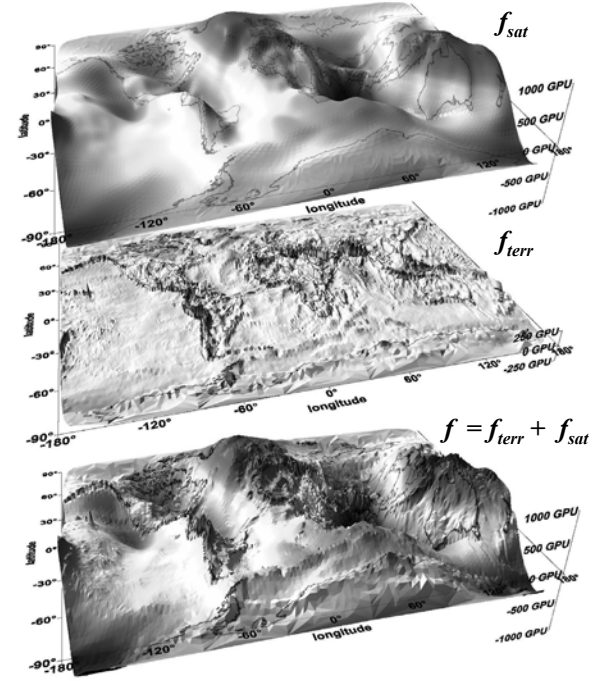


Figure 6. The composition $f = f_{terr} + f_{sat}$ for $r = R_i$ in case of the problem in Sect. 2, i.e. the combination of gravimetry and a satellite-only model ($R_i = 6378 \text{ km}$ and $R_e = R_i + 250 \text{ km}$, i.e. $q = 0.96228$).

A similar illustration is in Fig. 7. It concerns the problem considered in Section 3, i.e. the combination of gravimetry and gradiometry. The terrestrial part f_{terr} given by Eq. (42) and

$$f_{sat} = \sum_{n=0}^{\infty} \left(\frac{R_i}{r} \right)^{n+1} A_n^{(e)} \frac{R_e^2}{(n+1)(n+2)} G_n \quad (44)$$

with the coefficients $A_n^{(e)}$ given by Eq. (37) were computed for $r = R_i$ and $q = 0.96228$, i.e., $R_e = R_i + 250 \text{ km}$, similarly as above.

In both the cases the compositions f shown in Figs. 6 and 7 were compared with T restricted to $r = R_i$, as obtain directly from W and U , see Fig. 8. The results of the comparison are nearly the same in both the cases considered. Globally the RMS of the differences expressed in GeoPotential Units ($1 \text{ GPU} \equiv 1 \text{ m}^2 \text{ s}^{-2}$) does not exceed 0.06 GPU (max. difference smaller than 0.9 GPU) and is well within an apriori estimate of the error, as derived from Romberg’s integration method. This supports our conviction that the method discussed in this contribution is capable to provide useful results. It will be further developed a next paper on this topic.

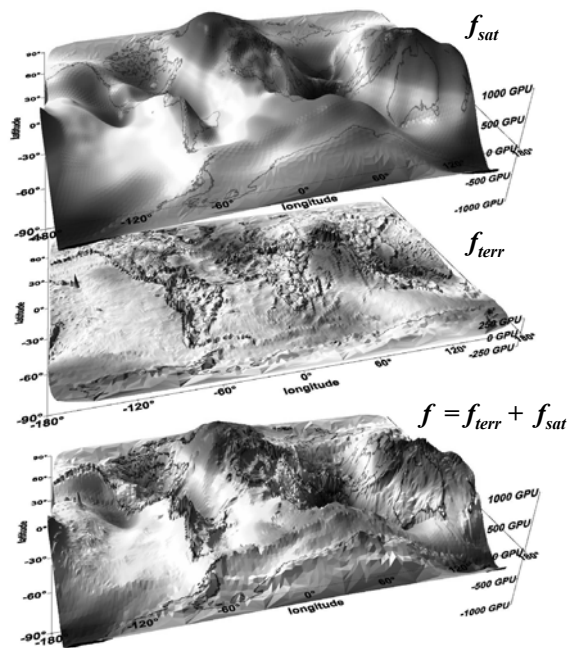


Figure 7. The composition $f = f_{terr} + f_{sat}$ for $r = R_i$ in case of the problem in Sect. 3, i.e. the combination of gravimetry and satellite gradiometry ($R_i = 6378 \text{ km}$ and $R_e = R_i + 250 \text{ km}$, i.e. $q = 0.96228$).

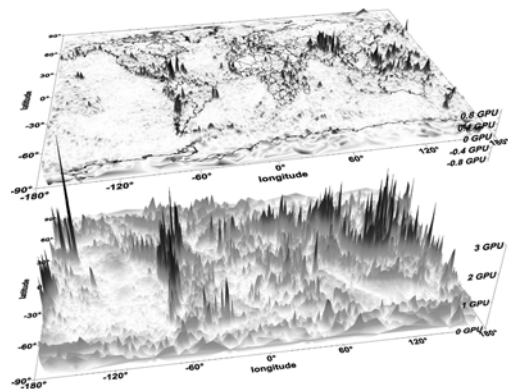


Figure 8. (Above) Error of the result, i.e., $f - T = f - (W - U)$. (Below) An a priori estimate of the error as obtained from Romberg's integration method.

Note finally that the stochastic nature of the terrestrial and the satellite input data give rise to a stochastic process in the 3-dimensional domain Ω . The process is not specially discussed in this paper and it is also not explicitly reflected in the structure of the functional Φ , see Eq. (20). Nevertheless, preparatory steps for the respective studies and the use of noisy data were made in Holota (2007), where together with Φ also functionals of different structure have been discussed.

Acknowledgements. The work on this paper was supported by the Grant Agency of the Czech Republic through Grant

No. 205/06/1330. The presentation of the paper at the 1st International symposium of the International Gravity Field Service, Istanbul, Aug 28 - Sept 1, 2006, was sponsored by the Ministry of Education, Youth and Sports of the Czech Republic through Projects No. LC506. Computing facilities (SGI Altix system) were kindly provided by the Supercomputing Centre of the Czech Technical University, Prague. All this support is gratefully acknowledged. Thanks go also to two anonymous reviewers for their valuable comments.

References

- Grafarend E and Sansò F (1984) The multibody space-time geodetic boundary value problem and the Honkasalo term. *Geophys. J.R. astr. Soc.* 255-275
- Heiskanen WA and Moritz H (1967) *Physical geodesy*. W.H. Freeman and Company, San Francisco and London
- Holota P (1995) Boundary and initial value problems in airborne gravimetry. In: *Proc. IAG Symp. on Airborne Gravity Field Determination, IUGG XXI Gen. Assembly, Boulder, Colorado, USA, July 2-14, 1995*, Special report No. 60010 of the Dept. of Geomatics Engineering at The University of Calgary, Calgary, 67-71
- Holota P and Kern M (2005) A study on two-boundary problems in airborne gravimetry and satellite gradiometry. In: Jekeli C, Bastos L and Fernandes J (Eds.) *Gravity, Geoid and Space Missions. GGSM 2004, IAG Intl. Symp., Porto, Portugal, Aug 30 - Sept 3, 2004*. IAG Symposia, Vol. 129, Springer, Berlin etc., 173-178
- Holota P (2007) On the combination of terrestrial gravity data with satellite gradiometry and airborne gravimetry treated in terms of boundary-value problems. In: Tregoning P and Rizos C (Eds.) *Dynamic Planet. IAG Symp., Cairns, Australia, 22-26 Aug 2005*. IAG Symposia, Vol. 130, Springer, Berlin etc., Chap. 53, 362-369
- Lemoine FG et al. (1998) The development of the Joint NASA GSFC and National Imagery and Mapping Agency (NIMA) Geopotential Model EGM96. NASA/TP-1998-206861, NASA, GSFC, Greenbelt, Maryland
- Migliaccio F, Raguzzoni M and Sansò F (2004) Space-wise approach to satellite gravity field determination in the presence of coloured noise. *J. of Geod.*, Vol. 78, 304-313
- Moritz H (1980) Geodetic reference system 1980. *Bull. Géod.*, Vol. 54, No. 3 (Geodesist's Handbook), 395-405
- Nečas J and Hlaváček I (1981) *Mathematical theory of elastic and elasto-plastic bodies: An introduction*. Elsevier Sci. Publ. Company, Amsterdam-Oxford-New York
- Nesvadba O, Holota P and Klees R (2007) A direct method and its numerical interpretation in the determination of the Earth's gravity field from terrestrial data. In: Tregoning P and Rizos C (Eds.) *Dynamic Planet. IAG Symp., Cairns, Australia, 22-26 Aug 2005*. IAG Symposia, Vol. 130, Springer, Berlin etc., Chap. 54, 370-376
- Pick M, Pícha J and Vyskočil V (1973) *Theory of the Earth's Gravity Field*. Elsevier, Amsterdam
- Press WH, Teukolsky SA and Vetterling WT (1992) *Numerical recipes in C: The art of scientific computing*. Cambridge University Press, New York
- Rummel R, Teunissen P and Van Gelderen M (1989) Uniquely and over-determined geodetic boundary value problem by least squares. *Bull. Géod.*, Vol. 63, 1-33
- Sacerdote F and Sansò F (1985) Overdetermined boundary value problems in physical geodesy. *Manuscripta Geodetica*, Vol. 10, No. 3, 195-207

Ground-Vehicle INS/GPS Vector Gravimetry Assessment Using Repeated Traverses in Montana

X. Li, C. Jekeli

Division of Geodesy and Geospatial Science, School of Earth Sciences

The Ohio State University, 125 South Oval Mall, Columbus, OH 43210-1398

Abstract

We explore methods to assess the precision of gravity vector components estimated from a ground vehicle INS/GPS system. Tests of the system were conducted in western Montana with repeated traverses along several highways. The gravity estimates were obtained through a series of processing steps that included B-spline smoothing, a Kalman filter, wavelet de-noising, wave-number correlation filtering, and correction for bias and scale factor errors. The results showed significant repeatability in the vertical and horizontal gravity components estimated independently from duplicated traverses. While the estimated vertical components also agree well with existing control data (2mgal; s.d.) and in some cases had internal consistency better than 1 mgal (s.d.), the estimated horizontal components are much less coherent between repeated tracks. However, after removing a scale factor error they exhibit clear correlation at all frequencies with repeatability of 1 mgal to 6 mgal (s.d.), depending on the test traverse and the horizontal component. Comparison to DEFLEC99 control data (whose validity remains in question) indicates differences up to 9 mgal (s.d.), or more.

Keywords. Vector Gravimetry, Wavelet de-noising, Wave-Number Correlation, Inertial Navigation System (INS), GPS.

1 Introduction

For an airborne INS/GPS vector gravimetric system, Kwon and Jekeli (2001) developed a unique Kalman filter and obtained gravity disturbance estimates with precision better than ± 3 mGal in the down component, and ± 6 to ± 8 mGal in the horizontal components. These estimates formally are derived directly from the Kalman filter residuals by assuming no particular gravity disturbance model in the state space. Although a lack of theoretical completeness with this approach has been argued by Schaffrin et al. (2002), who advocate modeling the gravity disturbance as a state either deterministically or stochastically, we have

found similarly good results using the same Kalman filter for a ground-vehicle based INS/GPS vector gravimetric system (see below). Furthermore, we applied additional data processing techniques, such as wavelet de-noising, to better isolate the gravity anomalies from the adjusted system noise in the observation residuals.

This paper briefly describes these techniques and the results of gravity disturbance vector estimation from such a system operated in western Montana in April and June 2005. The INS was a Honeywell H764 model and the vehicle carried a number of GPS receivers (Trimble 5700 and Novatel, among others). Several highways were traversed at least twice, including interstate I90 between Butte and Missoula and state route 43 eastward from Chief Joseph Pass. More details of the data collection is given by Jekeli and Li (2006). Section 2 introduces the wavelet de-noising approach. Wave-correlation techniques, described in Section 3, were also applied to take advantage of the repeated traverses. The final estimates of the horizontal components were corrected for a bias and scale factor error. They were analyzed in the frequency domain (Section 4) in order to discern their most accurate spectral window. Finally, Section 5 summarizes the analysis of the ground-vehicle based vector gravimetric system.

2 Wavelet De-Noising

Based on previous studies by Jekeli (2000) and Kwon and Jekeli (2001), a preliminary gravity disturbance estimate, $\Delta \vec{Z}$, is given by the following equation for the Kalman filter residual at time or space point, k :

$$D\vec{Z}_k = d\vec{g}_k^i + d\vec{x}_k^i - C_b^i \vec{e}_a \quad (1)$$

where $d\vec{x}^i$ is the GPS acceleration error and \vec{e}_a is the accelerometer processing error. Equation (1) clearly shows that the gravity disturbances are comingled with the GPS acceleration errors and the accelerometer processing errors. To identify better the gravity signal, $d\vec{g}$, within the observation

residual, $\Delta\bar{Z}$, at any frequency and at any time, the wavelet de-noising method is used due to its property of no spectral leakage (Li et al. (2004)), among other advantages (Donoho and Johnstone, 1994, 1995).

From the wavelet domain point of view, each component of $\Delta\bar{Z}$ in equation (1) can be written as follows:

$$\Delta Z(k) = \mathbf{d}g(k) + N(k) \quad (2)$$

where $N(k)$ is the combination of GPS acceleration error and accelerometer processing error at point, k . We expect N to be approximately white noise if the INS/GPS error dynamics model was correct and the Kalman filter was successful in estimating the systematic errors. To recover the gravity disturbances, first, ΔZ is transformed from the time or space domain into the wavelet domain by a linear forward wavelet transform as follows:

$$Y = w(\Delta Z) \quad (3)$$

where Y is the wavelet coefficient and $w(\bullet)$ denotes the forward wavelet transform operator. Then the wavelet coefficients are processed by the following equations:

$$Y' = D(Y, I) = \begin{cases} \text{sgn}(Y) * (|Y| - I) & \text{if } |Y| \geq I \\ 0 & \text{if } |Y| < I \end{cases} \quad (4)$$

$$I = d(Y) \quad (5)$$

where $D(\bullet, I)$ denotes the de-noising operator with soft threshold I , and $d(Y)$ is a data-adaptive threshold (Hybrid SureShrink criterion; see Donoho and Johnstone, 1994, 1995) that depends on the level of decomposition and on the wavelet coefficient Y (Taswell, 2000). Finally, the estimation of the gravity disturbance is obtained by transforming the processed wavelet coefficients back into the original domain with the same wavelet bases as used in equation (3):

$$\widehat{\mathbf{d}g}(k) = w^{-1}(Y') \quad (6)$$

where $w^{-1}(\bullet)$ denotes the inverse wavelet transform operator.

3 Wave-Number Correlation

If the INS/GPS system has been operated repeatedly along the same traverse, the wave-number correlation method (Kwon, 2000) can be used to isolate the correlations of the duplicated estimates

of the gravity vectors. These correlations are expected to indicate the gravitational signal, but would also include existing repeated system errors.

Suppose there are two traverses along the same road. After wavelet de-noising we obtain two gravity disturbance estimates, $\widehat{\mathbf{d}g}^1$ and $\widehat{\mathbf{d}g}^2$, respectively. From their Fourier transforms, $G_n^1 = F(\widehat{\mathbf{d}g}^1)$ and $G_n^2 = F(\widehat{\mathbf{d}g}^2)$, where n is the wave number, the correlation coefficient is given by

$$\mathbf{s}_n = \frac{\text{Re}\{G_n^1\} \text{Re}\{G_n^2\} + \text{Im}\{G_n^1\} \text{Im}\{G_n^2\}}{|G_n^1| |G_n^2|} \quad (7)$$

Then, the signal is filtered in the frequency domain according to the following equation:

$$\bar{G}_n^{1,2} = \begin{cases} G_n^{1,2} & \text{if } \mathbf{s}_k \geq \text{tol} \\ 0 & \text{if } \mathbf{s}_k < \text{tol} \end{cases} \quad (8)$$

where tol is a specified tolerance, e.g., 0.5. Finally, the new estimates in the space domain are:

$$\widehat{\mathbf{d}g} = \frac{1}{2} F^{-1} \{ \bar{G}_n^1 + \bar{G}_n^2 \} \quad (9)$$

4 Data Processing and Results

The preliminary estimates of the gravity disturbances were reported by Jekeli and Li (2006). They resulted from an initial B-spline smoothing with a 180-second averaging window and a Kalman filter that estimated bias and scale factor errors in the inertial measurement units. Interpolated gravity disturbances from an NGA data base and deflections of the vertical from DEFLEC99 (NGS) served as a ‘‘control’’ for comparison purposes.

The down component estimates are generally better than the horizontal estimates both in system repeatability and in system accuracy compared to the control data. Table 1 lists the mean and standard deviations of estimate differences along the first 60 km on SR43 eastward from Chief Joseph Pass. Table 2 shows the same statistics for differences between points 45 km and 95 km eastward from Missoula on I90. Both tables show that the stand-alone Kalman filter works well at least for this component.

Table1: SR43 down gravity difference statistics.

SR43 Down (mGal)	Mean	STD
Traverse 1 – Traverse 2	-3.58	2.05
Traverse 1 – Control	32.94	2.23
Traverse 2 – Control	36.52	2.71

Table 2: I90 down gravity difference statistics.

I90 Down (mGal)	Mean	STD
Traverse 2 – Traverse 3	3.31	2.05
Traverse 2 – Traverse 4	-5.28	0.72
Traverse 3 – Traverse 4	-8.59	2.49
Traverse 2 – Control	50.22	3.19
Traverse 3 – Control	46.91	2.86
Traverse 4 – Control	55.50	3.33

Wavelet de-noising and wave-number correlation filter (WCF) methods were used to remove any remaining filter errors, \tilde{d}_k^i and $C_b^i e_a$, in equation (1), from the gravity disturbance components. Figures 1-6 show the final gravity disturbances estimates on SR43 and I90 after applying these two filters. The de-noised results are not substantially different than the unprocessed Kalman filter residuals, but some very high-frequency variations have been smoothed out, as expected.

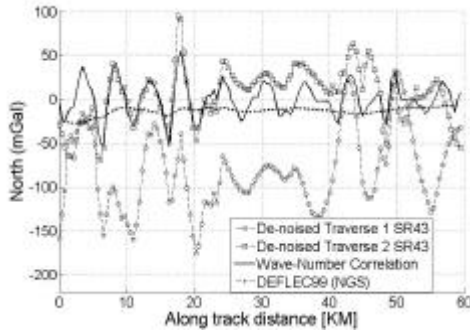


Figure 1: SR43 north gravity disturbance estimates after applying de-noising and wave-number correlation filters.

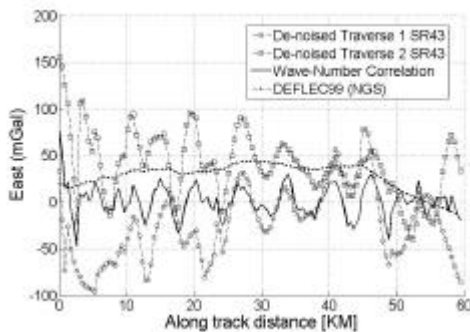


Figure 2: SR43 east gravity disturbance estimates after applying de-noising and wave-number correlation filters.

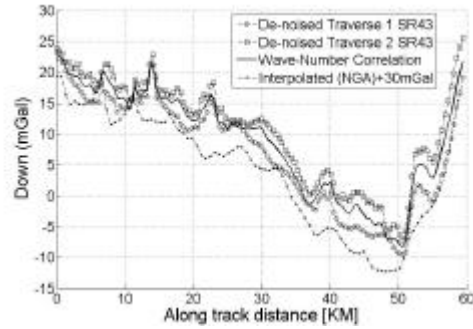


Figure 3: SR43 down gravity disturbance estimates after applying de-noising and wave-number correlation filters.

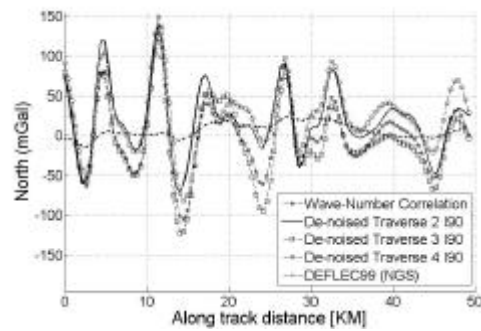


Figure 4: I90 north gravity disturbance estimates after applying de-noising and wave-number correlation filters.

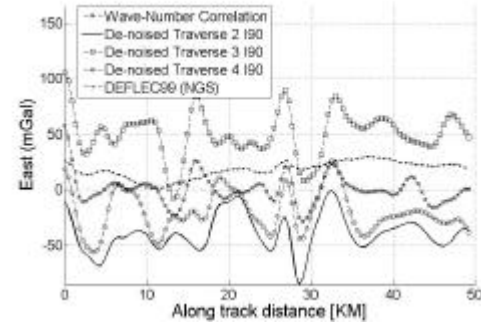


Figure 5: I90 east gravity disturbance estimates after applying de-noising and wave-number correlation filters.

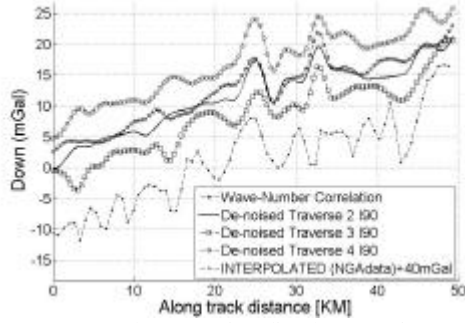


Figure 6: I90 down gravity disturbance estimates after applying de-noising and wave-number correlation filters.

The corresponding statistics for the down component estimates on these two road segments are shown in Tables 3 and 4, respectively. Table 3 indicates a slight improvement (5.4%) in the standard deviation of system repeatability on SR43 after wavelet de-noising (first line in the table) and a total improvement (in standard deviation) relative to NGA control of about 3% - 20% after further applying the wave-number correlation filter (last line in the table). On I90, somewhat greater improvement was obtained in system repeatability (11%) after de-noising, but the WCF yielded the same improvement in standard deviation relative to NGA control (5% - 15%).

Table3: SR43 down gravity component statistics for Figure 3.

SR43 Down (mGal)	Mean	STD
Traverse 1 – Traverse 2	-3.58	1.94
Traverse 1 – Control	32.94	2.19
Traverse 2 – Control	36.52	2.57
WCF – Control	34.73	2.16

Table 4: I90 down gravity component statistics for Figure 6.

I90 Down (mGal)	Mean	STD
Traverse 2 – Traverse 3	3.31	1.67
Traverse 2 – Traverse 4	-5.28	0.64
Traverse 3 – Traverse 4	-8.59	2.11
Traverse 2 – Control	50.22	3.08
Traverse 3 – Control	46.91	2.60
Traverse 4 – Control	55.50	3.22
WCF(2,3) – Control	48.57	2.72

Both the wavelet de-noising and the wave-number correlation could not remove satisfactorily the system errors in the horizontal estimates. However, there are clear correlations in the repeated traverses as shown in Figures 1, 2, 4, and 5. The repeatability can be analyzed in the frequency domain by using Parseval's Theorem. Accordingly, the standard deviation (*STD*) of the differences of the duplicated gravity disturbance estimates is given by

$$STD = \sqrt{\frac{1}{T} * \frac{\Delta t}{2N} \sum_1^{2N} (G_t)_n (G_t^*)_n}, \quad (10)$$

where T is the total length of the traverse, Δt is the sampling interval, $2N$ is the total number of the sampling points, and

$$G_t = F(\mathbf{d}\hat{g}^1 - \mathbf{d}\hat{g}^2 - \text{mean}(\mathbf{d}\hat{g}^1 - \mathbf{d}\hat{g}^2)) \quad (11)$$

is the bias-free Fourier transform of the estimate difference. Then the *STD* in the frequency band [$F1, F2$] is given by:

$$STD_{F1}^{F2} = \sqrt{\frac{1}{T} * \frac{\Delta t}{2N} \left\{ \sum_{m1}^{m2} (G_t)_n (G_t^*)_n + \sum_{2N-m2+1}^{2N-m1+1} (G_t)_n (G_t^*)_n \right\}} \quad (12)$$

where $m1 = F1 * 2N\Delta t$ and $m2 = F2 * 2N\Delta t$. These spectral analyses of the gravity disturbance estimates on SR 43 and I90 are given in Tables 5 and 6, respectively. The Nyquist frequency, f_N , corresponds to the 1 Hz GPS sampling interval (vehicle velocity of about 22 m/s). We note a clear band of higher correlation (3-6 km wavelengths) in the repeated traverses on SR43. On I90, the correlations (or lack thereof) are fairly evenly distributed over all frequency bands.

With respect to the control data there is a severe (and repeated) scale factor discrepancy in the horizontal gravity estimates. Although the scale error in the control data is not yet known (the DEFLEC99 data are scheduled to be independently validated by astrogeodetic measurements), it is more likely that the INS has a systematic scale error that repeats even after separate initializations. To determine the scale error, as well as a possible bias, we fitted the horizontal estimates to the DEFLEC99 data using the following model:

$$DEFLEC99_{n,e} = B_{n,e} + \mathbf{r}_{n,e} * \mathbf{d}\hat{g}_{n,e} \quad (13)$$

The bias, B , and the scale factor, \mathbf{r} , were solved by simple least squares for each horizontal component and for each traverse. Applying the estimated bias and scale factor, the modified horizontal estimates are shown in Figure 7-10.

Table 5: Gravity estimation repeatability per spectral band on SR43.

Lower bound (Cycle/km)	Upper bound (Cycle/km)	North (mGal)	East (mGal)	Down (mGal)
0.00	0.017	0.00	0.00	0.00
0.017	0.02	20.36	24.52	0.67
0.02	0.04	21.12	26.79	0.72
0.04	0.06	7.14	11.76	0.39
0.06	0.08	13.39	10.93	0.35
0.08	0.10	19.06	15.02	0.83
0.10	0.12	26.16	17.75	0.85
0.12	0.14	17.25	12.15	0.21
0.14	0.16	12.53	10.46	0.27
0.16	0.18	4.78	2.34	0.32
0.18	0.20	4.66	6.51	0.29
0.20	0.22	6.36	9.42	0.44
0.22	0.24	2.60	5.48	0.21
0.24	0.26	3.36	4.98	0.13
0.26	0.28	3.80	2.66	0.13
0.28	0.30	4.82	5.18	0.10
0.30	f_N	12.66	15.03	0.73
0	f_N	53.79	53.15	1.94

Table 6: Gravity estimation repeatability per spectral band (Traverses 2 & 4) on I90.

Lower bound (Cycle/km)	Upper bound (Cycle/km)	North (mGal)	East (mGal)	Down (mGal)
0.00	0.02	0.00	0.00	0.00
0.02	0.04	4.33	1.55	0.04
0.04	0.06	5.11	3.72	0.08
0.06	0.08	3.77	3.60	0.26
0.08	0.10	6.34	4.22	0.29
0.10	0.12	7.03	5.58	0.34
0.12	0.14	6.91	3.98	0.31
0.14	0.16	5.71	1.46	0.07
0.16	0.18	2.69	1.96	0.07
0.18	0.20	4.13	2.74	0.05
0.20	0.22	3.88	2.22	0.05
0.22	0.24	2.25	1.55	0.03
0.24	0.26	1.89	1.50	0.05
0.26	0.28	2.57	1.44	0.06
0.28	0.30	2.56	1.65	0.03
0.30	f_N	2.99	2.76	0.08
0	f_N	17.29	11.38	0.64

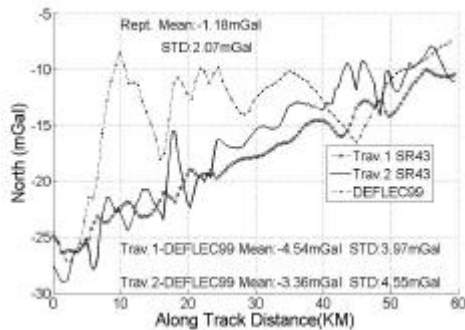


Figure 7: SR43 North gravity disturbance estimates after applying de-noising and bias and scale factor corrections.

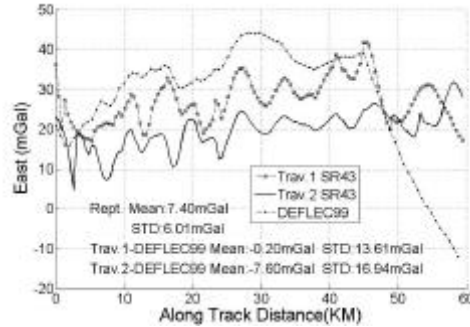


Figure 8: SR43 East gravity disturbance estimates after applying de-noising and bias and scale factor corrections.

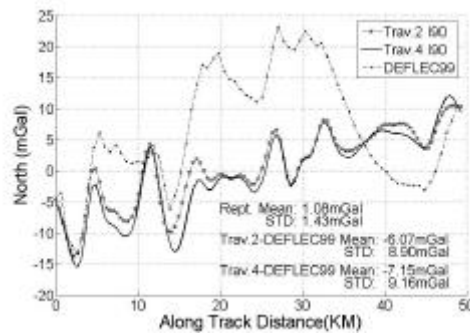


Figure 9: I90 North gravity disturbance estimates after applying de-noising and bias and scale factor corrections.

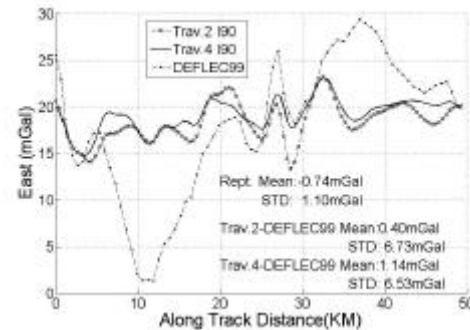


Figure 10: I90 East gravity disturbance estimates after applying de-noising and bias and scale factor corrections.

Frequency-domain analyses of the differences (Tables 7 and 8) now show that in all cases the correlations are well distributed across all bands. But, more important the overall repeatability is at the level of 1-1.5 mgal on the I90 segment and 2-6 mgal on the SR43 segment.

Table 7: Gravity estimation repeatability per spectral band on SR43.

Lower bound (Cycle/km)	Upper bound (Cycle/km)	North (mGal)	East (mGal)
0.00	0.017	0.00	0.00
0.017	0.02	0.82	1.52
0.02	0.04	0.89	2.17
0.04	0.06	0.41	1.67
0.06	0.08	0.33	0.84
0.08	0.10	0.35	1.61
0.10	0.12	0.60	2.58
0.12	0.14	0.29	2.13
0.14	0.16	0.37	1.79
0.16	0.18	0.41	0.62
0.18	0.20	0.41	1.12
0.20	0.22	0.71	1.65
0.22	0.24	0.48	0.45
0.24	0.26	0.34	0.41
0.26	0.28	0.13	0.16
0.28	0.30	0.34	0.32
0.30	f_N	0.73	1.94
0	f_N	2.07	6.01

Table 8: Gravity estimation repeatability per spectral band (Traverses 2 & 4) on I90.

Lower bound (Cycle/km)	Upper bound (Cycle/km)	North (mGal)	East (mGal)
0.00	0.02	0.00	0.00
0.02	0.04	0.46	0.12
0.04	0.06	0.51	0.26
0.06	0.08	0.31	0.36
0.08	0.10	0.54	0.39
0.10	0.12	0.59	0.59
0.12	0.14	0.53	0.52
0.14	0.16	0.46	0.11
0.16	0.18	0.24	0.14
0.18	0.20	0.25	0.24
0.20	0.22	0.27	0.22
0.22	0.24	0.19	0.12
0.24	0.26	0.13	0.14
0.26	0.28	0.18	0.14
0.28	0.30	0.17	0.11
0.30	f_N	0.20	0.13
0	f_N	1.43	1.10

5 Summary and Conclusions

To assess the precision of the ground-vehicle INS/GPS vector gravimetric system, several repeated traverses were carried out in western Montana on different dates. The estimates were obtained through a series of processing steps that included B-spline smoothing, a Kalman filter, wavelet de-noising, wave-number correlation filtering, and correction for bias and scale factor errors. The analyses led to the following conclusions:

1. The gravity disturbance estimates show significant repeatability in the vertical and horizontal components from independently repeated traverses.
2. The estimates of the down component agree well (2-3mgal *STD*) with the interpolated ground control data. Repeatability was as good as 1mgal (*STD*).
3. The Kalman filter estimates of the repeated horizontal components show clear correlation but also large scale factor errors with respect to the control data. Removing this error (and a bias) yields repeatability of better than 2 mgal (*STD*) on one traverse and 2-6 mgal (*STD*) on another.
4. Further enhancement of horizontal gravity data processing is indicated to estimate the scale factor error, which appears to reside in the INS.
5. There remain significant differences between the final horizontal estimates and the DEFLEC99 control data (up to 9 mgal (s.d.), or more). Final assessment of these estimates awaits an independent determination of control using astrogeodetic observations along the surveyed roads.

Acknowledgments

This work was supported under a research grant from the National Geospatial-Intelligence Agency.

References

- Donoho DL, Johnstone IM (1994): Ideal Spatial Adaptation via Wavelet Shrinkage. *Biometrika*, **81**, 425-455
- Donoho DL, Johnstone IM (1995): Adapt to unknown smoothness via wavelet shrinkage. *J. Amer. Statist. Assoc.* **90**, 1200-1224
- Jekeli C (2000): *Inertial Navigation Systems with Geodetic Applications*. Walter de Gruyter, Berlin
- Jekeli C, Li X (2006): INS/GPS Vector Gravimetry Along Roads in Western Montana. Report 477, Geodetic Science, Ohio State University (http://www.ccegs.ohio-state.edu/greports/reports/report_477.pdf)
- Kwon JH (2000): Airborne Vector Gravimetry Using GPS/INS, PhD dissertation. Report 453, Geodetic Science, Ohio State University (http://www.ccegs.ohio-state.edu/greports/reports/report_453.pdf)
- Kwon JH, Jekeli C (2001): A new approach for airborne vector gravimetry using GPS/INS. *Journal of Geodesy*, **74**(10), 690-700
- Li X, Jekeli C (2004): Improving Resolution of Airborne Gravimetric System by Use of Wavelet Shrinkage Denoising. In: Proceedings of ION 60th Annual Meeting.
- Schaffrin B, Kwon JH (2002): A Bayes filter in Friedland form for INS/GPS vector gravimetry. *Geophys. J. Int.*, **149**(1), 64-75.
- Taswell C (2000): The what, how, and why of wavelet shrinkage denoising. *IEEE Computing in Science & Engineering*, **2**(3), 12-19.

Centimetre quasigeoid modelling in Poland using heterogeneous data

Jan Krynski

Institute of Geodesy and Cartography, 27 Modzelewskiego St., PL 02-679 Warsaw, Poland

Fax: +48 22 3291950, Tel.: +48 22 3291904, E-mail: krynski@igik.edu.pl

Adam Lyszkowicz

University of Warmia and Mazury, 12 Heweliusza St., PL 10-724 Olsztyn, Poland

Fax: +48 89 5234878, Tel.: +48 89 5234579, E-mail: adam@moskit.uwm.edu.pl

Space Research Centre, Polish Academy of Sciences, 18A Bartycka St, PL 00-710 Warsaw, Poland

Fax: +48 22 8403131, Tel.: +48 22 8403766, e-mail: adam@cbk.waw.pl

Abstract. Geodetic, gravimetric, astronomical, geological and satellite data acquired within the cooperation of national and foreign research centres have been qualitatively analysed in 2002-2005. They have been transformed to unified reference systems in accordance with recent standards, and archived in the databases. The analysis of the existing data have been supported with control surveys. Precisely determined heights of 868 km GPS/levelling traverse consisting of 190 stations provided quality control of astro-geodetic, gravimetric, GPS/levelling, integrated as well as best fitted to the POLREF sites quasigeoid models developed. Major research concerned analysis of digital terrain models, technology of the terrain correction computation, methodology of mean gravity anomaly determination, and the choice of global geopotential model best suited for quasigeoid modelling in Poland. Quasigeoid models in Poland developed exhibit very high quality. Model of quasigeoid best fitted to the POLREF sites, of accuracy of 2 cm, should replace the quasigeoid model recently used in surveying practice in Poland. Quality of heights of the sites of the POLREF network, that results from surveying strategy and technology used was found insufficient as the basis for best fitted quasigeoid model for levelling with GPS in Poland.

Keywords. Quasigeoid modelling, geopotential models, gravity data, GPS/levelling data, digital terrain models, terrain corrections, mean gravity anomalies

1. Introduction

An increase of coverage land areas with deflections of the vertical and with gravity data in the first decades of 20th century resulted in developing

regional geoid models (e.g. Hirvonen, 1934; Tanni, 1948). The first gravimetric geoid model for the region of Central Europe, including Poland, was computed by Tanni (1949). Its accuracy can be estimated as about 3 m.

The first regional astro-gravimetric geoid model for Poland of accuracy of ~60 cm was developed at the Institute of Geodesy and Cartography, Warsaw, in 1961 (Bokun, 1961) from about a hundred of astro-geodetic deflections of the vertical and gravity obtained from the gravity maps. That model was refined in 1970 with the use of more data and more detail gravity maps. Its accuracy is about 30 cm.

Precise modelling of regional geoid became one of the major tasks of numerous research groups and surveying and mapping agencies in the last decades. The release of gravity data in Poland in early 1990s resulted in further advance in geoid modelling in Poland. The first gravimetric quasigeoid model for Poland of accuracy of ~10 cm was calculated at the Space Research Centre of the Polish Academy of Sciences, Warsaw, in 1993, using the LS collocation combined with the integral method (Łyszkowicz, 1993). It was followed by the quasi-97b gravimetric quasigeoid model of 5 cm accuracy, developed with the FFT technique using substantially extended gravity data coverage (Łyszkowicz, 1998).

Access to raw gravity data, development of high-resolution digital terrain models and densification of precise GPS/levelling heights stimulated towards undertaking an extensive research on modelling a precise quasigeoid in Poland. The team of researchers of different disciplines of Earth sciences, under the leadership of the Institute of Geodesy and Cartography, Warsaw, has conducted in 2002-2005 an advanced research on modelling a centimetre quasigeoid in Poland with the use of geodetic, gravimetric, astronomic, geological and satellite data (Krynski, 2005).

2. Data used

Gravity data available at the area of interest is not uniform both in terms of quality and coverage.

Terrestrial gravity data acquired within last 50 years consists of 1 089 062 point gravity data ($\sigma = 0.075$ mGal) almost uniformly distributed over Poland, as well as point and mean gravity anomalies ($\sigma = 1.0$ mGal) of different spatial resolution from neighbouring countries. Marine gravity data from four geophysical marine missions from 1971 to 2000 cover Southern Baltic Sea ($\sigma = 0.5$ -2.6 mGal). Airborne gravity data ($\sigma = 1.5$ mGal) from the Baltic Sea acquired in 1999 by KMS, Copenhagen. Also $2' \times 2'$ mean gravity anomalies ($\sigma = 4.0$ mGal) derived at the KMS from the Geosat and ERS-1 altimetry data were used. All gravity data have been transformed to ETRS89 and to POGK-99 gravity system (an official gravity system in Poland) (Krynski, 2006; Krynski and Lyszkowicz, 2006b).

GPS/levelling data used consisted of heights of over 900 POLREF ($\sigma = 2$ cm), EUVN ($\sigma = 2$ cm) and WSSG (Military Satellite Geodetic Network) ($\sigma = 3.5$ cm) sites (Krynski, 2006).

The set of deflections of the vertical consists of 165 astro-geodetic deflections from 1952-1975 ($\sigma = 0.5''$) and 370 astro-gravimetric deflections of the vertical determined in 1960s ($\sigma = 0.7''$) (Rogowski et al., 2005). Additional astronomical observations at 29 points were performed with circumzenithal in 2003-2004 with standard error $\sigma = 0.3''$ -0.5''.

Three digital terrain models: DTED2, SRTM3 and SRTM30 were used. Vertical accuracy of the DTED2 of resolution $1'' \times 1''$ (49°-50°N) and $1'' \times 2''$ (50°-55°N) varies from 2 m to 7 m, while its

horizontal accuracy equals to 15 m (Krynski et al., 2005). The SRTM3 and SRTM30 are based on Shuttle Radar Topography Mission data. Absolute vertical and horizontal accuracy of the SRTM3 of $3'' \times 3''$ resolution, is specified as 16 m and 20 m, respectively (JPL, 2004). The SRTM30 of $30'' \times 30''$ resolution is a generalization of the SRTM3.

3 Search for most suitable GGM

Six different GGMs were considered. Two kinds of numerical tests with the use of terrestrial gravity data and GPS/levelling height anomalies were conducted. Firstly, height anomalies at GPS/levelling POLREF and EUVN sites were compared with the corresponding ones computed from various GGMs. Secondly, the terrestrial gravity anomalies were compared with corresponding gravity anomalies computed from GGMs. Statistics for both tests are presented in Table 1 (Krynski and Lyszkowicz, 2005, 2006a).

The quasigeoid models obtained with the use of different GGMs were verified against corresponding height anomalies at GPS/levelling sites. High-resolution GGM02S/EGM96, derived as a combination of GRACE-based data with the EGM96 model (the coefficients up to degree and order 90 of GGM02S/EGM96 correspond to those of GGM02S including the C_{20} , and from degree and order 100 to the ones of EGM96; the transition coefficients – of degree 90 to 100 – were obtained using linear blending), fits best to height anomalies at POLREF and EUVN sites and also to terrestrial gravity data (Krynski and Lyszkowicz, 2005).

Table 1. Statistics of residuals in height anomaly and gravity anomaly obtained for different GGMs

Model	Degree	Residuals in height anomaly [m]				Residuals in gravity anomaly [mGal]			
		Mean	Std dev.	Min	Max	Mean	Std dev.	Min	Max
EGM96	360	-0.53	0.19	-1.03	0.08	-0.18	9.39	-112.01	137.34
EIGEN-CH03S	140	-0.33	0.76	-2.22	1.06	0.00	17.30	-111.42	182.54
GGM01S	120	-0.36	0.46	-1.70	1.05	0.26	15.37	-109.94	166.07
GGM02S (140)	160	-0.34	0.47	-1.53	1.23	-0.14	14.81	-111.89	157.57
GGM02C	200	-0.35	0.26	-1.09	0.49	-0.20	12.44	-115.57	153.86
GGM02S/EGM96	360	-0.37	0.13	-0.79	0.05	-0.30	9.31	-115.56	135.44

4 Terrain corrections

The prism method was used for the determination of terrain corrections. The size of the area covered by height data used for computing the terrain corrections, i.e. the radius d of integration of prisms, depends on required accuracy. Numerical experiments with computing the terrain corrections

with the use of high resolution DTMs enabled to precisely determine the optimum maximum radius d of integration of prisms for a required accuracy of the solution (Table 2). Practical method for determining d considering roughness of topography Δh and required accuracy of terrain corrections was developed (Grzyb et al., 2006).

The “2005” terrain correction set has been calculated for 1 078 046 gravity stations with the use of DTED2, SRTM3 and SRTM30 data and with $d = 200$ km. Maximum terrain correction in Poland – excluding the region of Tatra Mountains with no gravity stations – reaches 22.3 mGal. Only 10% of all calculated terrain corrections exceed 0.5 mGal, and 3% are larger than 1 mGal.

Table 2. The optimum maximum d [km] for different distortions Δh of the terrain elevation

Accuracy of the terrain correction [mGal]	Distortion Δh of terrain elevation relative to a gravity station		
	$\Delta h = 15$ m (flat)	$\Delta h = 50$ m (hilly)	$\Delta h = 300$ m (mountainous)
0.1	14.9	205	280
0.2	0.22	118	265
0.3	0.06	33	249

Height data available in Poland seem sufficient in terms of resolution for computing the terrain corrections in most areas (over 80%) with an accuracy required for a centimetre quasigeoid modelling. For flat terrain, a DTM of resolution 100 m \times 100 m seems quite sufficient to ensure accuracy better than 0.1 mGal while in hilly regions the DTED2 model is needed. To reach, however such accuracy in mountainous regions a DTM of higher resolution is required (Grzyb et al., 2006).

5 Mean gravity anomalies

1' \times 1' mean Faye anomalies for Poland were generated using Bouguer anomalies (Kryński et al., 2005b). They were calculated starting from point gravity data (1-6 gravity data per km² in Poland) according to the following algorithm. Point Faye anomalies calculated with the use of surveyed heights of gravity stations and terrain corrections were transformed into point Bouguer anomalies using density of 2.67 g/cm³ that were further interpolated together with heights from DTED2 and computed on a dense grid used as basis for generating mean Bouguer anomalies and mean heights in 1' \times 1' blocks. Mean Bouguer anomalies and mean heights were finally used for calculating 1' \times 1' mean Faye anomalies (Krynski, 2006).

6 GPS/levelling control traverse

For verification of quasigeoid models as well as for estimation of their accuracy and evaluation of interpolation algorithms for GPS/levelling quasigeoid, a GPS/levelling control traverse has

been established across Poland (Krynski, 2006). The traverse of 868 km surveyed in 2003-2004 consists of 190 stations (1/4.6 km) of precisely determined ellipsoidal and normal heights.

Observation strategy developed and processing methodology applied ensure accuracy of quasigeoid heights at traverse points at a centimetre level. 49 stations of the traverse considered as the 1st order control were surveyed in one or two 24h sessions. The remaining 141 stations were surveyed in 4h sessions. The coordinates of 1st order control were determined using the EUREF Permanent GPS Network (EPN) strategy with the Bernese v.4.2. Accuracy of the coordinates determined is at the level of single millimetres. The coordinates of 141 points were calculated using the Pinnacle program with the 1st order control as reference (Cisak and Figurski, 2005). Deviation of height anomalies of the GPS/levelling control traverse from those computed from the GUGiK 2001 quasigeoid model (recently official in Poland gravimetric quasigeoid fitted to the POLREF sites) are shown in Figure 1.

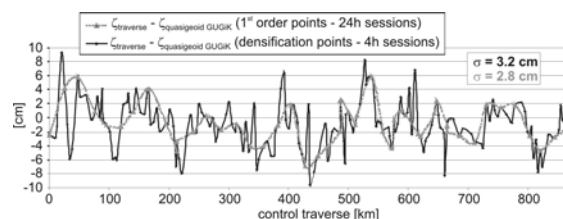


Fig. 1. Fit of heights of GPS/levelling control traverse to the GUGiK 2001 quasigeoid

7 Quasigeoid models developed

The astro-gravimetric quasigeoid model was calculated using the principle of astronomical levelling. The network of 384 astro-gravimetric deflections of the vertical was fitted to the network spanned on 197 astro-geodetic deflections. Standard deviation of adjusted quasigeoid heights does not exceed 0.225 m while average standard deviation equals to 0.065 m.

Gravimetric quasigeoid models were calculated using the remove-restore strategy. Height anomaly ζ is expressed as a sum of three components that represent global, regional and local effects, respectively. The first component is calculated directly from the GGM, the second one – using mean Faye anomalies, and the third one – using topography (Forsberg, 2005). The integral representing the second component was evaluated in the frequency domain by the multi-band fast Fourier Transform (Krynski and Lyszkowicz,

2006a). The consecutive models of gravimetric quasigeoid (Table 3) were calculated with the use of different GGMs and six gravity data sets being improved in the process of conducting the project (Krynski and Lyszkowicz, 2006b).

Table 3. Gravimetric quasigeoid models computed

Quasigeoid model	Data set	GGM
quasi97b	1	EGM96
quasi04a	2	EGM96
quasi04b	2	GGM02S
quasi04c	2	GGM02S/EGM96
quasi04d	3	GGM02C
quasi05a	4	EGM96
quasi05b	5	EGM96
quasi05c	5	GGM02S/EGM96
quasi06a	6	GGM02S/EGM96

Height anomalies of the POLREF sites were used for estimating the external accuracy of computed gravimetric quasigeoid models. On the other hand gravimetric quasigeoid models were used for evaluating quality of height anomalies at the POLREF sites (Table 4) (Krynski and Lyszkowicz, 2006b).

Table 4. Statistics of differences between the heights of quasigeoid models and the POLREF sites (Min and Max after removing the bias, i.e. with the mean = 0) [cm]

Model	Bias	Std dev.	Min	Max
quasi97b	-30.0	3.4	-9.2	12.4
quasi04a	-30.4	3.2	-8.4	10.1
quasi04b	-29.6	4.1	-12.0	10.8
quasi04c	-31.3	3.9	-10.2	11.4
quasi04d	-32.4	3.6	-10.5	10.9
quasi05a	-12.5	3.6	-9.2	9.0
quasi05b	-13.0	3.6	-9.2	9.0
quasi05c	-13.2	3.7	-10.1	9.7
quasi06a	-12.7	3.8	-10.3	10.1

For all quasigeoid models developed, standard deviation of their fit to the POLREF data remains at the same level; it slightly varies within the range 3.2-4.1 cm, and does not indicate any improvement due to refining gravity data. The bias, however, gets significantly reduced from -30 cm to -13 cm after using refined gravity data. The results obtained indicate that the quality of heights of the POLREF sites is not any longer sufficient to evaluate quality of high precision gravimetric quasigeoid models for Poland (Krynski and Figurski, 2006).

A pure numerical GPS/levelling quasigeoid model spanned on quasigeoid heights of the POLREF sites were developed (Krynski et al, 2005d). It applies the “kriging” model that is based on LS collocation with 4-order polynomial trend and a signal. Statistics of the fit of that model to the EUVN and WSSG sites are given in Table 5.

Table 5. Statistics of the fit of GPS/levelling quasigeoid model („kriging”) to the EUVN and WSSG sites [cm]

	Mean	Std dev.	Min	Max
$\zeta_{\text{model}} - \zeta_{\text{EUVN}}$	-3.4	4.8	-21.3	10.3
$\zeta_{\text{model}} - \zeta_{\text{WSSG}}$	-3.1	5.4	-16.7	21.6

Another GPS/levelling quasigeoid model spanned on quasigeoid heights at the POLREF sites was developed with support of mean 1' × 1' gravity anomalies (Krynski et al, 2005d). Statistics of its fit to the EUVN and WSSG sites are given in Table 6.

Table 6. Statistics of the fit of GPS/levelling gravity quasigeoid model with support of gravity data to the EUVN and WSSG sites [cm]

	Mean	Std dev.	Min	Max
$\zeta_{\text{model}} - \zeta_{\text{EUVN}}$	-3.1	2.9	-12.4	2.1
$\zeta_{\text{model}} - \zeta_{\text{WSSG}}$	-3.2	5.5	-25.9	43.8

GPS/levelling quasigeoid models spanned on quasigeoid heights at the POLREF sites exhibit almost the same bias of 3 cm. Adding gravity data substantially improves GPS/levelling quasigeoid model with respect to the heights of the EUVN sites. Evaluation of the effect of adding gravity data on GPS/levelling quasigeoid model, with respect to the heights of the WSSG sites is not representative due to varying outliers eliminated.

An integrated GPS/levelling/gravity/topography model of quasigeoid was developed (Osada et al., 2005). It uses the LS collocation for fitting the quasigeoid model to height anomalies at GPS/levelling sites with simultaneous determination of model parameters. The model was evaluated at the POLREF, EUVN and WSSG sites (Table 7).

Table 7. Statistics of the fit of the integrated GPS/levelling/gravity/topography quasigeoid model to the POLREF EUVN and WSSG sites [cm]

	Mean	Std dev.	Min	Max
$\zeta_{\text{model}} - \zeta_{\text{POLREF}}$	0.5	0.7	-1.3	3.0
$\zeta_{\text{model}} - \zeta_{\text{EUVN}}$	-0.5	0.6	-2.3	1.2
$\zeta_{\text{model}} - \zeta_{\text{WSSG}}$	-1.5	4.0	-24.3	38.9

The fit of the integrated quasigeoid model to the POLREF EUVN and WSSG sites corresponds to a

priori variances used for height anomalies at those sites.

Gravimetric quasigeoid model best fitted to GPS/levelling at the POLREF sites was developed (Krynski and Lyszkowicz, 2006a). The difference between the GPS/levelling height anomaly and gravimetric quasigeoid height is expressed in terms of trend modelled by 3-parameter datum shift. After computing the trend parameters, an empirical covariance function of the de-trended residuals was calculated and modelled by a simple mathematical function (Krynski and Lyszkowicz, 2006a; 2006b). Based upon the computed set of 330 height anomaly differences, datum shift components $\Delta X = -30.1$ cm, $\Delta Y = -27.5$ cm, and $\Delta Z = 12.8$ cm were determined by using the LS method, and the mean measure of the fit equals to 1 cm.

8 Quality of quasigeoid models developed

The integrated, best-fitted and gravimetric quasigeoid models developed were mutually compared and the residual height anomalies were

analysed (Krynski, 2006). The accuracy of the models was also evaluated with the use of height anomalies of the POLREF sites as well as in some cases of the EUVN and WSSG sites. Independent assessment of the accuracy of quasigeoid models was done with use of height anomalies at the sites of a precise GPS/levelling control traverse (Fig. 2, Table 8).

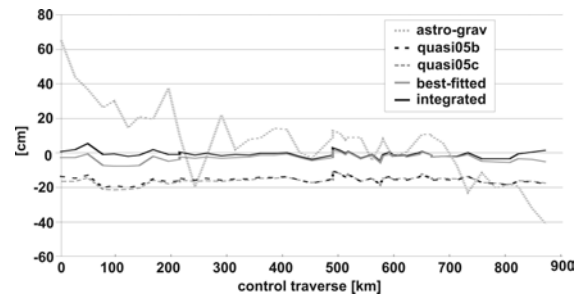


Fig. 2. The fit of quasigeoid models to the sites of GPS/levelling control traverse [cm]

Table 8. Statistics of the fit of representative quasigeoid models to the sites of the GPS/levelling control traverse and the inclination of the models with respect to the control traverse in N-E direction [cm]

Quasigeoid model	Mean	Std dev.	Min	Max	N-E incl.
astro-gravimetric	8	21	-40	65	-0.15"
gravimetric (quasi05b)	-15	2.1	-20	-11	~0
gravimetric (quasi05c)	-16	2.3	-21	-11	~0
gravimetric-best-fitted	-2.7	2.0	-7.4	2.0	0.004"
integrated („2005")	-0.7	1.8	-4.7	5.4	-0.004"

Quality of astro-gravimetric quasigeoid is substantially lower than the quality of remaining quasigeoid models developed. It might be improved by some densification of astronomic deflections of the vertical and generating a high resolution new set of gravimetric deflections of the vertical using the available unified gravity data.

Heights of the GPS/levelling control traverse sites, as much more precisely determined than the ones of the POLREF network, are more suitable for evaluation of accuracy of gravimetric quasigeoid models. Standard deviations of fitting quasigeoid models to the control traverse sites are at the level of 2 cm, while when fitting to the POLREF sites they are hardly below 4 cm (see Table 4).

Quality of best-fitted gravimetric quasigeoid as well as the integrated quasigeoid in Poland seems at

the moment mainly limited by the quality of the GPS/levelling heights.

Summary and conclusions

All available data has been gathered, extensively qualitatively and quantitatively analysed, verified, and unified. Particularly, the extensive research was done on over a million of gravity data, acquired within last 50 years, that have become for the first time available for gravity field modelling.

Precise terrain corrections were calculated for all gravity data within the radius of 200 km using high-resolution digital terrain model DTED2. A new set of $1' \times 1'$ mean Faye anomalies for Poland was generated.

A GPS/levelling control traverse established across Poland proved to be a powerful tool for

quality control of precise quasigeoid models in Poland.

Quality of heights of the POLREF sites does not correspond to the accuracy of below 2 cm claimed in the documentation. It is not sufficient for quality control of precise quasigeoid models in Poland.

New models of astro-gravimetric, gravimetric as well as best fitted quasigeoid model and integrated quasigeoid model based on gravity, GPS/levelling and topographic data were developed. Accuracy of the developed quasigeoid models has been evaluated by comparing quasigeoid heights with the respective ones on the sites of the GPS/levelling control traverse: 21 cm for the astro-gravimetric quasigeoid, 2.2 cm for the gravimetric quasigeoid, 2.0 cm for the gravimetric best-fitted quasigeoid, and 1.8 cm for the integrated quasigeoid.

Developed methods and computing strategies as well as experience gained reflect high potentiality for further research on developing precise quasigeoid models in Poland.

Acknowledgements

The research was supported by the Polish State Committee for Scientific Research (grant PBZ-KBN-081/T12/2002). The authors express their sincere thanks to the Military Geography Board of the General Staff of the Polish Military for providing the DTED model, to the Danish National Space Center, Copenhagen for providing airborne and some marine gravity data, and to Dr. H. Denker from the Institut für Erdmessung, Universität Hannover, for making available a Middle-European part of the SRTM3 model.

References

- Bokun J., (1961): The problem of determination of geoid undulations from Krasovsky ellipsoid considering available astro-geodetic and gravimetric data (in Polish), *Proceedings of the Institute of Geodesy and Cartography*, Warsaw, Vol. VIII, No 1(17), pp. 113–140.
- Cisak J., Figurski M., (2005): Control GPS/levelling traverse, *II Workshop on Summary of the project on a cm geoid in Poland*, 16-17 November 2005, Warsaw (CD).
- Forsberg R., (2005): Terrain Effects in Geoid Computations, *International School for the Determination and Use of the Geoid*, Budapest, pp. V1-V38.
- Grzyb M., Krynski J., Mank M., (2006): The effect of topography and quality of a digital terrain model on the accuracy of terrain corrections for centimetre quasigeoid modelling, *Geodesy and Cartography*, Vol. 55, No 1, pp. 23-46.
- Hirvonen R.A., (1934): The Undulations of the Geoid, *Veöff. Finnish Geodetic Institute*, No 19, Helsinki.
- JPL, (2004): SRTM – The Mission to Map the World, Jet Propulsion Laboratory, *California Institute of Technology*, <http://www2.jpl.nasa.gov/srtm/index.html>.
- Krynski J., (2005): Summary of the results of the project on a cm geoid in Poland, *II Workshop on Summary of the project on a cm geoid in Poland*, 16-17 November 2005, Warsaw (CD).
- Krynski J., (2006): Final substantial report on the results of the project PBZ-KBN-081/T12/2002 on “Modelling a centimetre quasigeoid in Poland with the use of geodetic, gravimetric, astronomic, geological and satellite data” (in Polish), Institute of Geodesy and Cartography, *Report for the Ministry of Education*, Warsaw (132 pp).
- Krynski J., Figurski M., (2006): *Results of re-processing of GPS data from EUREF-POL, POLREF and EUVN campaigns using EPN standards*, Symposium of the IAG Subcommission for Europe (EUREF) held in Riga, Latvia, 14–17 June 2006, EUREF Publication No 16, *Mitteilungen des Bundesamtes für Kartographie und Geodäsie*, Frankfurt am Main (in print).
- Krynski J., Lyszkowicz A., (2005): Study on choice of global geopotential model for quasigeoid determination in Poland, *Geodesy and Cartography*, Vol. 54, No 1, pp. 17–36.
- Krynski J., Lyszkowicz A., (2006a): Regional quasigeoid determination in the area of Poland, *5th FIG regional Conference for Africa*, Accra, Ghana, 8-11 March 2006.
- Krynski J., Lyszkowicz A., (2006b): The overview of precise quasigeoid modelling in Poland. 2nd Workshop on International Gravity Field Research 2006, 8-9 May 2006, Smolenice, Slovakia, *Contributions to Geophysics and Geodesy*, Geoph. Inst. of Slov. Acad. of Sc. (in print).
- Krynski J., Mank M., Grzyb M., (2005): Evaluation of digital terrain models in Poland in view of a cm geoid modelling, *Geodesy and Cartography*, Vol. 54, No 4, pp. 155-175.
- Lyszkowicz A., (1993): The Geoid for the Area of Poland, *Artificial Satellites*, Vol. 28, No 2, *Planetary Geodesy*, No 19, pp. 75-150.
- Lyszkowicz A., (1998): The Polish gravimetric quasi-geoid QUASI97b versus vertical reference system Kronstadt86, *Reports of the Finnish Geodetic Inst.*, 98:4, pp. 271-276.
- Osada E., Karsznia K., Owczarek M., 2003: Qualitative and quantitative analysis of the POLREF, EUVN and WSSG GPS data. A model of GPS/levelling/gravity geoid (in Polish), Wroclaw University of Technology, *Report for the Inst. of Geodesy and Cartogr.*, Warsaw, (178 pp).
- Osada E., Krynski J., Owczarek M., (2005): A robust method of quasigeoid modelling in Poland based on GPS/levelling data with support of gravity data, *Geodesy and Cartography*, Vol. 54, No 3, pp. 99–117.
- Rogowski J.B., Bogusz J., Kujawa L., Klek M., Barlik M., (2005): New astro-geodetic geoid in Poland, *Workshop II “Summary of the project on a cm geoid in Poland”*, Inst. of Geodesy and Cartography, 16-17 November (CD).
- Tanni L., (1948): On the continental undulations of the geoid, as determined from the present gravity material, *Publ. Intern. Isost. Inst.*, No 18, Helsinki; *Annales Academiae Scientiarum Fennicae*, Series A, III, *Geologica-Geographica*, 16.
- Tanni L., (1949): The regional rise of the geoid in Central Europe, *Annales Academiae Scientiarum Fennicae*, Series A, Helsinki; *Annales Academiae Scientiarum Fennicae*, Series A, III, *Geologica-Geographica*, 20.

Wavelet Evaluation of the Terrain Correction Integral

M. El-Habiby, M. G. Sideris

Department of Geomatics Engineering,

The University of Calgary, 2500 University Drive N.W., Calgary, Alberta, Canada, T2N 1N4

Abstract. A computational scheme using the wavelet transform is employed to evaluate the terrain correction integral. The efficiency of the wavelet multiresolution analysis as an alternative approach to the well-established Fast Fourier Transform (FFT) is studied. The integral is approximated in finite multiresolution analysis subspaces, using a two-dimensional wavelet algorithm. An orthogonal wavelet base function is used to build the wavelet algorithm. The characteristics of the base function and its effect on the results are investigated. This algorithm solves the problem in a point-wise procedure. The role of the kernel singularity in the wavelet multiresolution analysis is studied. Wavelet thresholding is used for the compression of the kernel, and hard and soft thresholding are tested. Global thresholding is compared to level direction-wise thresholding. Because of the fast decreasing kernel, high compression levels are achieved without loss of accuracy. A numerical example is given to clarify the use of this procedure in the numerical evaluation of the terrain correction integral. Conclusions and recommendations are given with respect to the suitability, accuracy, and efficiency of this method.

Keywords. Wavelet multiresolution analysis, hard thresholding, level direction-wise thresholding, terrain corrections.

1 Introduction

Wavelet analysis is a comparatively young branch in signal processing. Wavelet expansions allow better local description and decomposition of signal characteristics [Burrus et al., 1998]. For many years, the evaluation of geodetic integrals in physical geodesy has been governed by the theory of Fourier transformation. This classical approach is based on the Fast Fourier Transform (FFT) [Sideris

and Li, 1993]. This approach is well established and is now a standard geodetic tool.

Sideris (1984) first evaluated the terrain correction integral using Fast Fourier Transform (FFT) for dense grids. Sideris and Li (1993) introduced zero padding to the solution of gravity field convolutions without windowing, using FFT. Li et al. (2000) developed a unified set of formulas for the computations of the topographic effects in terrestrial and airborne gravimetry.

Wavelet transformation has proved to be an efficient tool for many problems related to the analysis and processing of signals with complex structures. Its efficiency comes from its localization properties, data compression, and ability to deal with stationary and non-stationary noise in the wavelet domain [El-Habiby and Sideris, 2006].

It is therefore a very powerful tool for evaluating geodetic integrals because of its localization power in the space and frequency domain. The wavelet transform of singular kernels leads to a significant number of small value coefficients, thus achieving high compression levels of the kernels. In this paper, the terrain correction integral is evaluated by treating it as a direct convolution problem.

The main objective of this study is the verification of the efficiency of the wavelet transform approach as an alternative to the FFT to evaluate the terrain correction integral.

2 Wavelets as a Filtering Tool

The discrete wavelet transform (DWT) coefficients $\omega_{j,k}$ of a signal or a function $f(t)$ are computed by the following inner product:

$$\omega_{j,k} = \langle f(t), \psi_{j,k} \rangle \quad (1)$$

where $\psi_{j,k}$ are the wavelet base functions, and j and k are integer indices for the scale and translation of the wavelet function, respectively. The inverse wavelet transform is used for the

reconstruction of the signal from the wavelet coefficients $\omega_{j,k}$ by

$$f(t) = \sum_j \sum_k \omega_{j,k} \psi_{j,k}(t) \quad (2)$$

Equations (1) and (2) are called ‘‘analysis’’ and ‘‘synthesis,’’ respectively. The dyadic wavelet algorithm developed by Daubechies is used here [Daubechies, 1992]. $\psi_{j,k}$ is a shifted version of the scaling function $\varphi_{j,k}$ into other V (approximation) and W (detail) spaces. These subspaces are based on the concept of multiresolution analysis (MRA).

The multiresolution analysis (MRA) is used for the fast decomposition of a signal into independent frequency bands through a nested sequence.

A number of scaling coefficients $h_k \in L_2(\mathfrak{R})$ represent the scaling function, which is the base of space V_0 :

$$\varphi(x) = \sqrt{2} \sum_{k \in \mathbb{Z}} h_k \varphi(2x - k) \quad (3)$$

The base of W_0 is represented by the detailing function $\psi_{j,k}$

where

$$\psi(x) = \sqrt{2} \sum_{k \in \mathbb{Z}} g_k \varphi(2x - k) \quad (4)$$

ψ is the wavelet function that is generated from the original mother wavelet function and g_k are the detail coefficients.

The relation between the scaling coefficients and the detail coefficients is

$$g_k = (-1)^k h_{1-k} \quad (5)$$

For the 2-D wavelet transform, the Mallat algorithms utilize a tensor product of two different directional one-dimensional wavelet transforms [Chui et al., 1994; Mallat, 1997]:

$$\varphi^{app.}(x, y) = \varphi(x) \cdot \varphi(y) \quad (6)$$

$$\psi^{Horiz.}(x, y) = \psi(x) \cdot \varphi(y) \quad (7)$$

$$\psi^{Vert.}(x, y) = \varphi(x) \cdot \psi(y) \quad (8)$$

$$\psi^{Diag.}(x, y) = \psi(x) \cdot \psi(y) \quad (9)$$

where equations (6) to (9) are the two dimensional wavelet decompositions representing the approximation, horizontal, vertical, and diagonal sets of wavelet coefficients, respectively. Daubechies (db) wavelets with four vanishing moments are used in this case study (Figure 1). Daubechies wavelets have energy concentrated in timed, continuous, null moments, and decrease quickly towards zero as the input tends to infinity. Daubechies wavelets have no explicit expression except for db1 (Haar wavelet) [Keller, 2004].

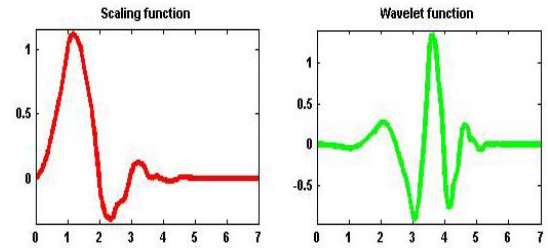


Fig. 1 Daubechies with four vanishing moments: scaling function to the left and wavelet function to the right

2.1 Wavelet thresholding

Wavelet thresholding is a technique used to compress the wavelet coefficients matrix representing the geodetic integral kernel. Wavelet coefficients (absolute) larger than the certain specified threshold δ are the ones that should be included in the reconstruction. The reconstructed function is as follows [Ogden, 1997]:

$$\hat{f}(t) = \sum_j \sum_k I_{\{|\omega_{j,k}| > \delta\}} \omega_{j,k} \psi_{j,k}(t) \quad (10)$$

where $I_{\{|\omega_{j,k}| > \delta\}}$ is the indicator function of this set.

The problem is always in making the decision about the thresholding value. The thresholding value can be obtained as follows:

$$\delta = \text{median}(|\text{detail wav. coef. at level 1}|) \quad (11)$$

If it is equal to zero, then an alternative choice is

$$\delta = 0.05 \times \max(|\text{detail wav. coef. at level 1}|) \quad (12).$$

For more detail, see Donoho and Johnstone, (1994). Soft thresholding and hard thresholding were tested. Both gave similar results, although soft thresholding scales the wavelet coefficients, while hard thresholding just cuts the coefficients below a certain value without any distortions. Consequently, hard thresholding is preferred in this paper, as defined by the following expression:

$$\hat{\omega}_{j,k} = \begin{cases} \omega_{j,k}, & \text{if } |\omega_{j,k}| \geq \delta \\ 0, & \text{otherwise} \end{cases} \quad (13)$$

2.2 Terrain correction integral in the wavelet frame

The terrain correction integral was evaluated using the wavelet technique. The equation for the terrain correction integral in planar approximation is used in this study, as follows:

$$c(x_2, y_2) = \frac{G\rho}{2} \iint [H(x_1, y_1) - H(x_2, y_2)]^2 K_c dx_1 dy_1 \quad (14)$$

$$\text{where } K_c = \frac{l}{l^3(x_1, y_1, x_2, y_2)} \quad (15)$$

c is the terrain correction at the computational point,
 G is the gravitational constant, $6.67 \times 10^{-8} \text{ cm}^3 \text{g}^{-1} \text{s}^{-2}$,
 ρ is the mean density of the topographic masses, 2.67 g cm^{-3} ,
 l is the distance between the data points (x_1, y_1) and the computation point (x_2, y_2) ,
and

H are the heights of the points

The terrain correction kernel produces the matrices used for determining the wavelet coefficients. These coefficients are used to build up the design matrix during the evaluation of the terrain correction formula. For gridded data with equal spacing, which is the case in this study, the elements of the matrix in the spatial domain are as follows:

$$[(x_2 - x_1)^2 + (y_2 - y_1)^2]^{-3/2} \quad (16)$$

for $x_2 \neq x_1$ or $y_2 \neq y_1$ and zero for $x_2 = x_1$ and $y_2 = y_1$. The zero value compensates for the singularity at the computational point [Li, 1993]. Equation (14) is divided into three parts and each part is a discrete convolution:

$$c(x_2, y_2) = \frac{G\rho}{2} [E_1 + E_2 + E_3] \quad (18)$$

where

$$E_1 = \iint H^2(x_1, y_1) K_c dx_1 dy_1 \quad (19)$$

$$E_2 = -2H(x_2, y_2) \iint H(x_1, y_1) K_c dx_1 dy_1 \quad (20)$$

$$E_3 = H^2(x_2, y_2) \iint K_c dx_1 dy_1 \quad (21)$$

Equations (19), (20) and (21) are evaluated as convolutions. The convolution in the last equation is done between a unit grid (has a value of 1 for all the grid points) and the kernel. The procedure for the implementation of these integrals in the wavelet frame is described in the following, using E , as an example:

The two-dimensional wavelet transform representation of H^2 is done as follows:

$$\begin{aligned} \alpha^{app.} &= \iint H^2 \varphi(x) \varphi(y) dx dy \\ \alpha^{Horiz.} &= \iint H^2 \varphi(x) \psi(y) dx dy \\ \alpha^{Vert.} &= \iint H^2 \psi(x) \varphi(y) dx dy \\ \alpha^{Diag.} &= \iint H^2 \psi(x) \psi(y) dx dy \end{aligned} \quad (22)$$

Then the kernel is represented in the wavelet frame by the following two dimensional transformations:

$$\begin{aligned} \beta^{app.} &= \iint K_c \varphi(x) \varphi(y) dx dy \\ \beta^{Horiz.} &= \iint K_c \varphi(x) \psi(y) dx dy \\ \beta^{Vert.} &= \iint K_c \psi(x) \varphi(y) dx dy \\ \beta^{Diag.} &= \iint K_c \psi(x) \psi(y) dx dy \end{aligned} \quad (23)$$

Using Belykin's [1993] algorithm, K_c and H^2 , are represented on a wavelet basis using the wavelet decomposition coefficients. That is, h stands for the approximation decomposition (low pass filter) and g for the detailing coefficients (high pass filter), as follows:

$$\begin{aligned} K_c &= \sum_q \sum_s \beta^{app.} h_q(x) h_s(x) + \sum_q \sum_s \beta^{Horiz.} h_q(x) g_s(x) \\ &+ \sum_q \sum_s \beta^{Vert.} g_q(x) h_s(x) + \sum_q \sum_s \beta^{Diag.} g_q(x) g_s(x) \end{aligned} \quad (24)$$

The summation is over dyadic intervals to avoid redundancy and decrease the computational effort. This kernel formula (24) is substituted in the E_1 to yield the following equation:

$$\begin{aligned}
E_1(x_2, y_2) = & \iint [\sum_q \sum_s \beta^{app} \cdot h_q(x)h_s(x) \\
& + \sum_q \sum_s \beta^{Horiz} h_q(x)g_s(x) + \sum_q \sum_s \beta^{Vert} g_q(x)h_s(x) \\
& + \sum_q \sum_s \beta^{Diag} g_q(x)g_s(x)] H^2 dx_1 dy_1
\end{aligned} \tag{25}$$

The wavelet transform of the H^2 is implemented in equation (25) and by interchanging the order of integration and summation and subsequently integrating, the solution takes the form:

$$\begin{aligned}
E_1(x_2, y_2) = & \sum \sum \alpha^{app} \beta^{app} + \sum \sum \alpha^{Horiz} \beta^{Horiz} \\
& + \sum \sum \alpha^{Vert} \beta^{Vert} + \sum \sum \alpha^{Diag} \beta^{Diag}
\end{aligned} \tag{26}$$

This solution can be summarized as the element-by-element multiplication of wavelet transform coefficients of the kernel and the signal. Then, the product output matrix is summed up to have the solution directly at the computational point. It is worth mentioning that the step of inverse wavelet transform is done implicitly. Consequently, using this algorithm decreases the computational effort needed for to standard algorithms.

The procedure used in solving the terrain correction integral is a combination of the Beylkin (1993) non-standard algorithm for fast wavelet computations of linear operators, hard thresholding, and the Mallat algorithm.

3 Results

3.1 Data used and testing procedure

The data used is a set of point heights (Figure 2). These are on a 36×56 grid with $1 \text{ km} \times 1 \text{ km}$ spacing. The area is of very rough terrain; the statistics of the data heights are shown in Table 1.

Table 1 Height statistics

Max. (m)	Min. (m)	Mean (m)	RMS (m)
3395	1204	2115.08	2143.91

Numerical integration, FFT, and wavelet solutions are compared in this study. The wavelet solution is repeated with different kernel compression levels. The singularity of the kernel and the vanishing moments of the used wavelet family (Daubechies with four vanishing moments) are the main factors for having high compression levels. The combined approach of global and level-wise thresholding is

tested. The numerical integration solution is the reference for all other solutions.

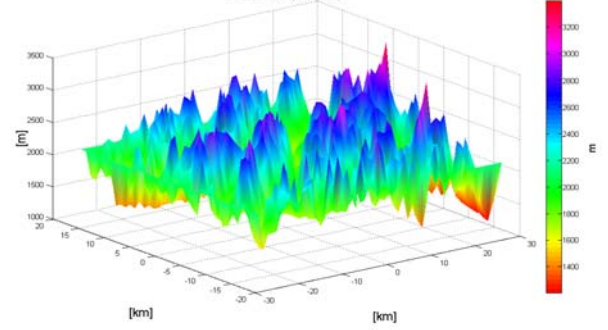


Fig. 2 Grid of point heights.

3.2 Full matrix wavelet solution

All three solutions are practically identical. Figure 3 shows the wavelet solution without compression. The difference between the wavelet solution and the numerical integration solution is shown in Figure 4; it has RMSE value of 0.000 mGal.

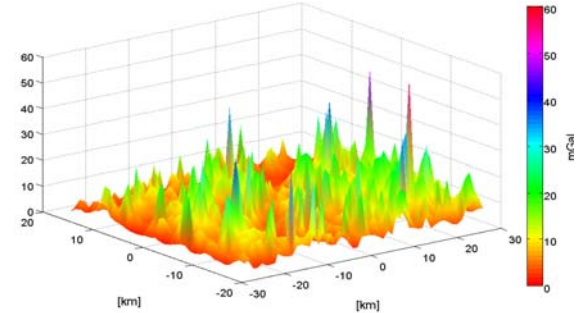


Fig. 3 Full matrix wavelet solution

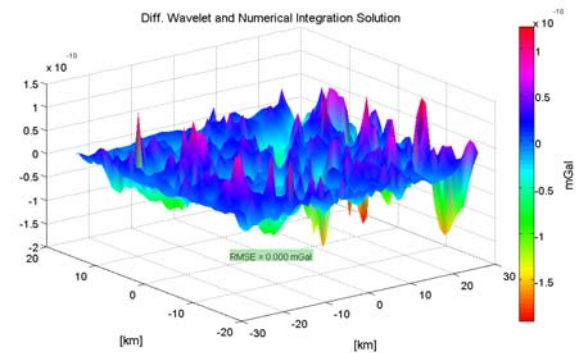


Fig. 4 Difference between wavelet solution and numerical integration solution.

Although both the wavelet and the FFT are at the same level of accuracy, the wavelet algorithm

requires large memory (50.8 MB) to allocate the wavelet coefficient matrix of the kernel. In the case of FFT solution, 0.2 MB is required for allocating the FFT transformed kernel with zero-padding. This is the main drawback of the wavelet algorithm. A compression technique can be used, as mentioned before, for decreasing the memory required for allocating the wavelet coefficients matrix of the kernel and also to speed up the computations.

3.3 Global thresholding wavelet solutions

The wavelet evaluation of the Terrain correction integral is repeated again with different kernel compression levels. First, a global thresholding is applied using equations 10, 11, 12, and 13. A threshold value of 5.7×10^{-7} is used.

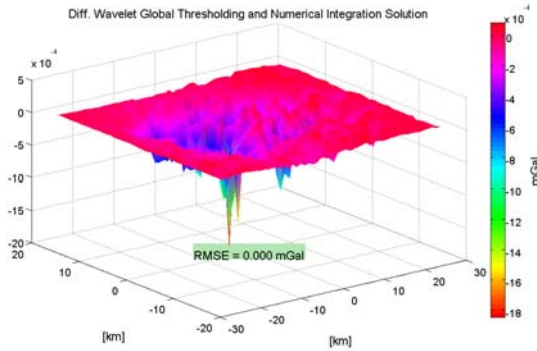


Fig. 5 Difference between wavelet global thresholding (70% compression) and numerical integration

The compression level (70%) corresponding to this thresholding value gives almost identical in comparison to the numerical integration solution, as shown in Figure 5. The RMSE of the differences is 0.000 mGal. Larger thresholding values are used for the evaluation of the terrain correction integral using the wavelet global thresholding technique. At 5.7×10^{-3} thresholding value, 93% compression level is achieved with 5.6 MB storage space. The RMSE accuracy (0.12 mGal) achieved at this compression level is acceptable for this application. The acceptable accuracy obtained at this high compression level is mostly the result of the fact that the kernel drops very fast with distance (with power of -3), in addition to the wavelets (Daubechies) four vanishing moments. Table 2 shows the comparison between different solutions with different thresholding values in comparison to the wavelet solution without compression and the FFT solution. It is clear that the a significant improvement in the time and memory required for

the evaluation of the terrain correction integral using wavelet transform; 93% compression level (0.12 mGal) with RMSE accuracy equal to 012 mGal is achieved.

Table 2 Wavelet global thresholding solutions

Value	FFT	Full	5^{-3}	5^{-2}	5^{-1}
RMSE (mGal)	0.00	0.00	0.12	1.21	8.27
Comp. %	-	-	93%	96%	98%
Storage (MB)	0.2	50.8	5.6	3.2	1.3
Time (second)	0.05	0.5	0.15	0.15	0.15

3.4 Level-direction wise thresholding wavelet solutions

In the previous subsection, four levels of decomposition are done for the kernel; each one of these decompositions consists of three wavelet coefficients sets in three directions (horizontal, vertical, and diagonal). One global thresholding value is applied to all these levels and in all directions per level.

In the level-direction wise approach, the global fixed value thresholding solution is combined with level direction-wise change in the threshold's value. The threshold value that is computed from equation 11 or 12 is taken as the minimum reference value. Larger different thresholding values are introduced for the diagonal, horizontal, or vertical coefficients at each level of decomposition. For example, different thresholding values are applied instead of the global thresholding value (5.7×10^{-1}) corresponding to 98% compression level, as shown in table 3:

Table 3 Level direction-wise thresholding (98% to 97%)

	Horizontal	Diagonal	Vertical
Level 1	5.7×10^{-1}	5.7×10^{-1}	5.7×10^{-1}
Level 2	5.7×10^{-1}	5.7×10^{-1}	5.7×10^{-1}
Level 3	5.7×10^{-2}	5.7×10^{-2}	5.7×10^{-2}
Level 4	5.7×10^{-3}	5.7×10^{-2}	5.7×10^{-3}
RMSE	2.5		
Comp. %	97%		
Storage (MB)	1.8		
Time (second)	0.15		

At levels 1 and 2 a high thresholding value is used (5.7×10^{-1}), and a different value (5.7×10^{-2}) was used for level 3 in all directions and at level 4 in the diagonal direction only. For level 4 in the horizontal and vertical directions a thresholding value equal to

(5.7×10^{-3}) was used. If this approach is compared to the global thresholding case with one fixed value (5.7×10^{-1}), it is seen that a 70% gain in accuracy is achieved with 1% loss in the compression level. For the 96% compression level in table 2, another combination of thresholding values is tested, where a thresholding value equal to (5.7×10^{-2}) is used for the first level of decomposition and (5.7×10^{-3}) is used for the other 3 decomposition levels. The accuracy improved from 1.21 mGal to 0.18 mGal (85% improvement), with 1.8% loss in the compression level (96% to 94.2%), as shown in Figure 6. The main benefit from this combination is to increase the compression levels for the wavelet coefficients matrices without loss of accuracy. Figure 6 shows the results from this algorithm at different compression levels. It is seen that this algorithm is more effective at high compression levels.

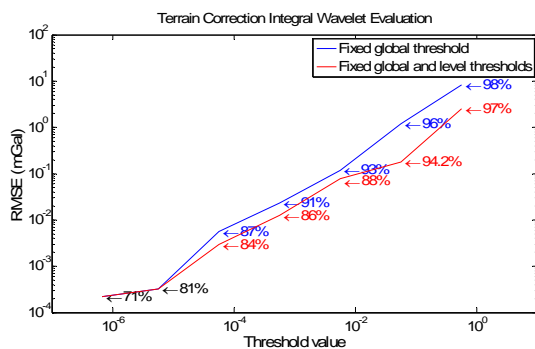


Fig. 6 Wavelet global thresholding solutions versus wavelet global and level direction-wise thresholding solutions

4 Conclusions

Wavelet evaluation of geodetic integrals can be done efficiently. The global thresholding and the combined approaches introduced in this paper are very effective for evaluating the terrain correction integral, especially with rough areas. Orthogonal wavelets are essential for using this algorithm. The number of multiplications and the required matrix storage can be reduced by compression through the wavelet hard thresholding technique. In comparison to the numerical integration and FFT approaches, it gives practically identical results using full matrices without any thresholding. The main drawback is the space required for allocating the wavelet coefficients matrix in the memory. This problem is solved using the global and level direction-wise thresholding techniques. In the evaluation of the terrain correction integral, compression levels of

91% are achieved with no loss of accuracy. A compression level of 93% is achieved with an RMSE of 0.12 mGal. 97% compression level is achieved using the level-direction wise thresholding with 2.5 mGal accuracy. The fast decrease of the kernel is the main reason for these high compression levels. The wavelet global thresholding and the wavelet level direction-wise approaches are efficient techniques for the evaluation of geodetic integrals.

References

- Beylkin G. (1993), Wavelets and Fast Numerical Algorithms, Lecture Notes for short course, AMS-93, Proceedings of Symposia in Applied Mathematics, v.47, pp. 89-117, 1993.
- Burrus, C. S., R. A. Gopinath, and H. Guo (1998). Introduction to Wavelets and Wavelet Transforms: A Primer. Prentice Hall, Upper Saddle River, New Jersey, USA.
- Chui, C. K., L. Monefusco, and L. Puccio (1994). Wavelets: theory, algorithms, and applications. Wavelet analysis and its applications, Vol. 5, Academic Press, INC.
- Daubechies, I. (1992). Ten lectures on wavelets. Society for Industrial and Applied Mathematics.
- Donoho, D. L., and I. M. Johnstone (1994). Ideal Spatial Adaptation via Wavelet Shrinkage. Biometrika 81: pp. 425-455.
- El Habiby M.; and M.G. Sideris (2006). On the Potential of Wavelets for Filtering and Thresholding Airborne Gravity Data. Newton's Bulletin of the International Gravity Field Service, No.3, section 1.
- Keller, W. (2004). Wavelets in Geodesy and Geodynamics. Walter de Gruyter.
- Li Y.; M. G. Sideris; and K. P. Schwarz (2000). Unified terrain correction formulas for vector gravity measurements. PINSA, 66, A, No. 5, pp. 521-535
- Mallat, S. G. (1997). A wavelet tour of signal processing, Academic Press, San Diego.
- Ogden, R. T. (1997). Essential Wavelets for Statistical Applications and Data Analysis. Birkhäuser, Boston, USA.
- Sideris, M. G. and Y., Li (1993). Gravity field convolutions without windowing and edge effects, Bulletin Geodesiqu, Vol. 67, pp. 107-118.
- Sideris, M. G. (1984). Computation of gravimetric terrain corrections using Fast Fourier transform techniques. UCSE Reports, No. 20007, Master Thesis, University of Calgary, Calgary, Alberta, Canada.

Local Geoid Surface Approximation by Fuzzy Inference Systems: Case Studies in Turkey

Mustafa Acar, M. Tevfik Özlüdemir, Rahmi Nurhan Çelik, Tevfik Ayan
Istanbul Technical University, Division of Geodesy, 34469 Maslak, Istanbul, Turkey
e-mail: acarmusta@itu.edu.tr

Abstract. As one of the actual topics in the field of geodesy, geoid determination has never lost its priority. Wide-use of advanced space techniques in geodetic applications has even made geoid determination a more important research field. For example, ellipsoidal heights used for geoid height determination can be obtained much more precisely and reliably with space-based positioning techniques. Being parallel to the developments in space-based techniques, enormous advances in computer technology have enabled geodesists to easily apply some analysis and algorithms that had seemed to be much more complicated till 1980s. Through these developments new analysis techniques have also been developed. Fuzzy logic method that is widely employed in particular in case of low precision, uncertainty and the lack of information is one of these methods. In recent years, fuzzy logic algorithms have been widely applied in such geodetic studies as deformation analysis, ambiguity resolution in GPS, remote sensing, prediction of earth orientation parameters, GIS applications, immovable property valuation and etc. In this study, application of fuzzy logic approach in geoid surface approximation is discussed. The data belong to two different regions located in Istanbul and Sakarya, a town about 150 km east of Istanbul. The topographic structures of these regions have different characteristics. For these two regions, geoid heights have been determined through fuzzy logic approach and the obtained results are interpreted.

Keywords. Geoidal Height (undulation), Geoid Surface Approximation, Fuzzy Inference Systems, Soft Computing, ANFIS

1 Introduction

Today space based positioning techniques are widely used in geodetic and geodynamic applications. In former conventional techniques, positions were determined in two steps. In the first

step latitude and longitude (φ, λ) were determined by triangulation and astronomic observations. The second step comprises of the determination of heights (H) by levelling and gravimetric measurements. Modern space based GPS technique has the capability of determining three dimensional coordinates in a very short time comparing to the conventional techniques and provide latitude, longitude and height of a point with respect to its reference ellipsoid, the geocentric WGS84 (World Geodetic System 1984).

In geoid determination space based positioning techniques are also employed widely. As aforementioned, GPS technique provides ellipsoidal heights that are reckoned from ellipsoid. However, most users desire heights in a natural system rather than purely geometric ellipsoidal heights. Most surveying measurements are made in relation to the geoid, which is the equipotential surface of the Earth's gravity field, not ellipsoid because the surveying equipment is aligned with the local gravity vector, which is perpendicular to the local equipotential surface passing through an observation point, usually through the use of a spirit bubble (Featherstone 2001).

The most common natural height is the orthometric height above the geoid that has a physical meaning and depends on the gravity field of the world. The relation between ellipsoidal heights and orthometric heights can be set up by geoid determination.

Gravimetric method is the most commonly applied method for precise geoid determination. However, the application of this technique is mainly dependent on the availability of high-resolution gravity data. In case of the lack of proper gravity data, the geoid could be modelled with different geometric methods such as astro-geodetic method or geoid height from GPS in conjunction with spirit levelling (Kuhar et al. 2001). Geoid height that is the difference between ellipsoidal height and orthometric height could be efficiently used for computing orthometric heights using coordinates

obtained from satellite measurements through fitting.

In this study, fuzzy logic approach in geoid surface approximation has been applied on some GPS/Levelling data collected in Istanbul and Sakarya towns which have different topographic structures.

2 Geoid Height Determination by GPS/Levelling

One of the main objectives of the development and improvement of geoid models has become to meet the requirements of the GPS users who want to have their GPS ellipsoidal heights converted into the local vertical datum (Engelis et al. 1985, Akyilmaz et al. 2003). In order to convert ellipsoidal heights derived from GPS measurements into conventional orthometric heights, the relationship between the geoid and the ellipsoid must be known (Kotsakis and Sideris 1999). The situation is illustrated in Fig. 1.

The relation between ellipsoid and orthometric heights can be written as follows:

$$h \approx H + N \quad (1)$$

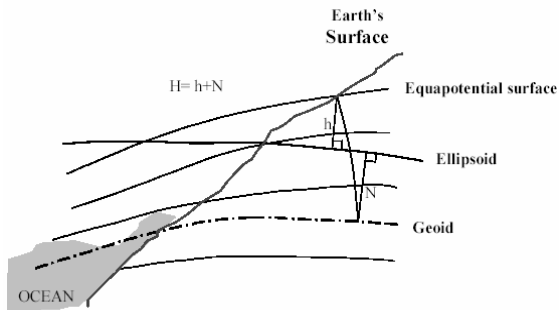


Fig. 1 Relation between ellipsoidal and orthometric heights (Akyilmaz et al. 2003)

As given in Eq. 1 mathematical relationship between geoid, ellipsoidal, and orthometric heights is very simple. In this case the deflection of the vertical and the curvature of the plumb line are neglected.

In practice, this expression reflects the possibility of GPS levelling, because it states that if the geoid height N is known, the orthometric height H (or normal height, depending on the definition of the quasi-geoid, but hereafter referred to as orthometric height) can be obtained from ellipsoidal height h determined by GPS. Obtaining orthometric heights this way, could in certain circumstances, depending

on the required accuracy, replace conventional spirit levelling and thus make the levelling procedure cheaper and faster (Mårtensson 2002, Yılmaz and Arslan 2005)

GPS/Levelling involves relative geoid heights and is independent of any reference system, as it involves determining the separation of two physical surfaces: the topographic surface and the geoid. Requires geoid heights on a reference ellipsoid to which the GPS heights are also referred (either a local ellipsoid if GPS heighting process applied after GPS transformation to local datum, or a global ellipsoid if GPS results are not first transformed).

The determination of the geoid is in fact based on geoid heights. A geoid model is created through the interpolation of the known geoid heights at the control points that are located and distributed properly on the ground. The accuracy of the geoid depends on the accuracy of the input data, i.e. the accuracy and the density of the known geoid heights rather than the method used for interpolation. For geoid modelling different methods can be employed such as least squares collocation, multi-parameter polynomial fitting, multi-quadratic or weighted linear interpolations etc. All these methods have been evaluated only from the mathematical point of view and have often neglected the physical aspects of the geoid. In other words, the mentioned approaches use only latitude and longitude as input values. Inclusion of ellipsoidal heights as input values would make the approximation more realistic taking into account the physical characteristics of the geoid. Soft computing techniques enable us to apply such an approximation. This study focuses on the application of one of such soft computing techniques, namely fuzzy inference systems for geoid approximation.

3 Adaptive Neuro-Fuzzy Inference Systems

The acronym ANFIS derives its name from Adaptive Neuro-Fuzzy Inference Systems, feed-forward adaptive networks, which are functionally equivalent to fuzzy inference systems. The basic idea of ANFIS can be described as follows: A fuzzy inference system is typically designed by defining linguistic input and output variables as well as an inference rule base. However, the resulting system is just an initial guess for an adequate model. Hence, its premise and consequent parameters have to be tuned based on the given data in order to optimize the system performance. In ANFIS this

step is based on a supervised learning algorithm (Akyilmaz et al. 2003, Akyilmaz 2005, Jang 1993, Yilmaz and Arslan 2006).

For simplicity, assume that the fuzzy inference system under consideration has two inputs x and y and one output f . Additionally, suppose that the rule base contains two fuzzy *if-then* rules of the Takagi and Sugeno's type (Takagi and Sugeno 1983) as

- Rule 1: If x is L_1 and y is B_1 ; then $f_1 = p_1x + q_1y + r_1$
 Rule 2: If x is L_2 and y is B_2 ; then $f_2 = p_2x + q_2y + r_2$

The associated fuzzy reasoning and ANFIS structure are shown by Fig. 2(a), Fig. 2(b) respectively.

Note that the node functions in the same layer are of the same function family (all circles without parameters or square nodes with parameters) (Akyilmaz et al. 2003, Jang 1991, Yilmaz and Arslan 2005)

The functions of each layer can be described as follows:

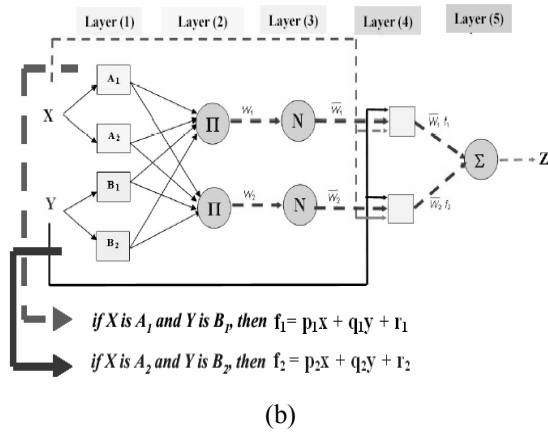
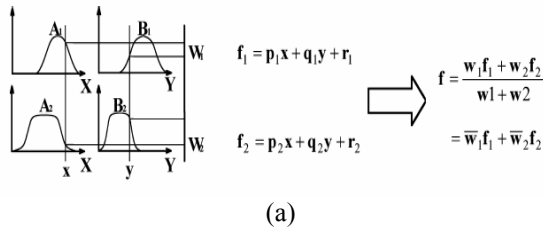


Fig. 2 (a), (b): (a) Type-3 fuzzy reasoning, (b) equivalent ANFIS (Yilmaz and Arslan 2006)

Layer 1: Every node i in this layer is a square node with a node function

$$\begin{aligned} O_{1,i} &= \mu_{A_i}(x) & i=1,2 \\ O_{1,i} &= \mu_{B_{i-2}}(y) & i=3,4 \end{aligned} \quad (2)$$

where x and y are the input to node i , and A_i is the linguistic label (small, medium, large, etc.) associated with this node function. In other words, $O_{1,i}$ is the membership function of A_i and it specifies the degree to which the given x satisfies the quantifier A_i . Usually, the membership function $\mu_{A_i}(x)$ is chosen to be bell-shaped with the maximum value equal to 1 and the minimum value equal to 0 such as, e.g., the generalized bell function (see Fig. 3)

$$\mu_{A_i}(x) = \frac{1}{1 + \left[\left(\frac{x - c_i}{a_i} \right)^2 \right]^{b_i}} \quad i=1,2 \quad (3)$$

where, $\{a_i, b_i, c_i\}$ is the parameter set. As the values of these parameters change, the bell-shaped functions vary accordingly. Thus various membership functions on linguistic label A_i are defined. In fact, any continuous and piecewise differentiable functions, such as commonly used trapezoidal or triangular-shaped membership functions can also be considered as qualified candidates for node functions in this layer. Parameters in this layer are called "premise parameters" (Jang 1993).

Layer 2: Every node in this layer is a circle node, which performs a fuzzy intersection operation on the incoming signals from the first layer and sends the result to the next layer.

For instance,

$$O_{2,i} = w_i = \mu_{A_i}(x) \mu_{B_i}(y) \quad i=1,2 \quad (4)$$

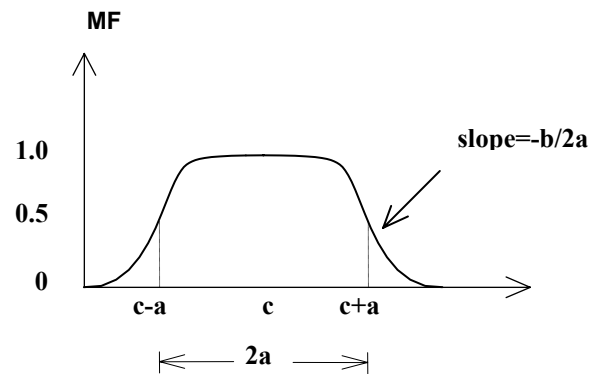


Fig. 3 Meanings of the parameters in the generalized bell membership function

The left equation shows fuzzy intersection by the algebraic product, the second one the minimum intersection as they are called. Both variants are consistent extensions of intersection in classical set theory. Please note that each node output represents the firing strength of a rule.

Layer 3: Every node in this layer is a circle node such that the i -th node calculates the ratio of the i -th rule's firing strength to the sum of all rules' firing strengths as

$$O_{3,i} = \bar{w}_i = \frac{w_i}{w_1 + w_2} \quad i=1,2 \quad (5)$$

Outputs of this layer can be called normalized firing strengths.

Layer 4: Every node in this layer is a square node with a node function that calculates the output for corresponding rules weighted by its normalized firing strength such that

$$O_{4,i} = \bar{w}_i f_i = \bar{w}_i (p_i x + q_i y + r_i) \quad i=1,2 \quad (6)$$

where \bar{w}_i is the output of the previous layer, and $\{p_i, q_i, r_i\}$ is the set of parameters which are called "consequent parameters" (Jang1995, Yilmaz and Arslan 2006).

Layer 5: The single node in this layer is a circle node that computes the overall output by using the weighted average defuzzification method as

$$O_{5,i} = f = \frac{\sum_i w_i f_i}{\sum_i w_i} \quad i=1,2 \quad (7)$$

ANFIS is the major training routine for Sugeno-type fuzzy inference systems. ANFIS uses a hybrid learning algorithm (see Fig. 4) to identify parameters of Sugeno-type fuzzy inference systems (URL1 2006). ANFIS applies a combination of the least-squares method and the back-propagation gradient descent method for training FIS membership function parameters to emulate a given training data set (URL1 2006, URL2 2006). This approach is thus called hybrid learning method since it combines gradient descent and the least-squares method.

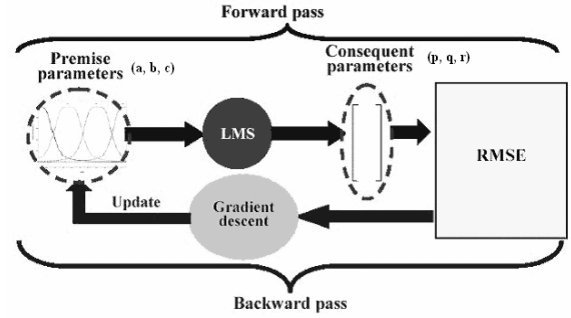


Fig. 4 ANFIS learning using hybrid technique (Walid 2005, Yilmaz and Arslan 2006)

4 Numerical Example

Geoid determination through fuzzy inference method of which details are given in the previous section has been applied on two data sets. These data sets belong to Istanbul and Sakarya which have different topographic characteristics. Figure 5 and 6 show these selected test areas. Such information as the number of points, size of the areas, density of the GPS/Levelling points regarding the test areas are given in Table 1.

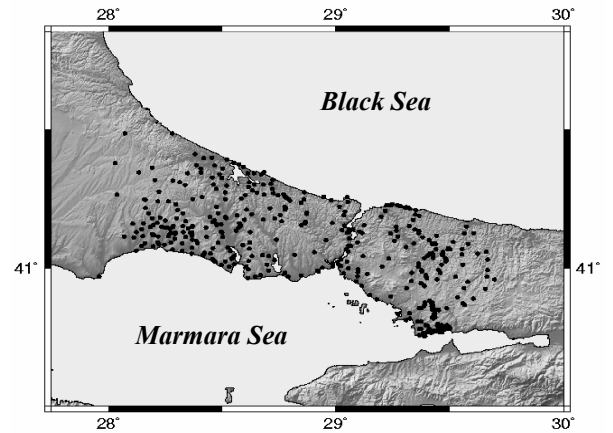


Fig. 5 Point distribution of the study area in Istanbul

The data collected in Istanbul belongs to a geodetic network densification project covering administrative area of the city. As seen in Fig. 5, the point distribution and the density of GPS/Levelling points in this project are optimal. However, both the point distribution and density are rather poor in Sakarya of which data belongs to a cadastral project (see Fig. 6). Orthometric heights in Istanbul vary between 1-480 m while they are in the range between 2-1599 m in Sakarya.

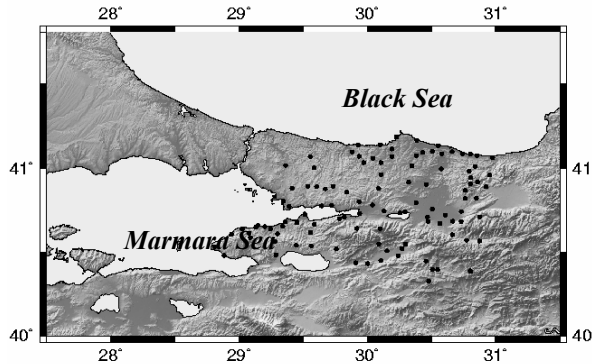


Fig. 6 Point distribution of the study area in Sakarya

Table 1. Information about the test areas

Test Area	Number of Points	Area (km ²)	Point/km ²	Point distribution
Istanbul	409	10400	1/25	Good
Sakarya	109	18000	1/165	Poor

In some studies (Ayan et al. 1999, Ayan et al. 2001, Erol and Çelik 2005) polynomial fitting procedures have been applied on the same data set for geoid modelling. In these polynomial fitting applications, uniformly distributed and randomly selected 350 points out of 409 and 19 points out of 109 have been used for geoid modelling in Istanbul and Sakarya, respectively. The remaining points have been used for testing the model. The degrees of polynomial fitting employed for GPS/Levelling geoid modelling and the accuracies obtained by these models are listed in Table 2 (Erol and Çelik 2005).

Table 2. Results of the polynomial fitting

Test Area	GPS/Levelling Data		GPS/Levelling Geoid	
	Measur. Type	Accuracy (cm)	Poly. degr.	RMS (cm)
Istanbul	GPS	±1.3	5	±4
	Geometric Levelling	±2.0		
Sakarya	GPS	±1.8	4	±20
	Precise Levelling	±0.2		

As part of this study, the same data set has been evaluated by fuzzy logic approach. Table 3 shows

the results of this approach. As seen from the results, in Istanbul region the model yields quite better results than polynomial fitting. The results in Sakarya region are also better.

Table 3. Results of the Fuzzy logic approach

Study Area	Model Data			Test Data		
	Min (cm)	Max (cm)	RMS (cm)	Min (cm)	Max (cm)	RMS (cm)
Istanbul	-7.7	9.5	2.5	-10.2	10.3	3.4
Sakarya	-26.5	34.3	8.1	-36.8	39.7	18.3

5 Conclusions

The main objective of this study is the application of a fuzzy inference system, an approach that has become widely used in geodesy in recent years, on geoid determination. This study only focuses on the application of fuzzy logic approach out of several soft computing techniques. The data belongs to two different regions having different topographies. The outputs obtained through the application of different methodologies in these regions have been compared. In Istanbul, where point distribution is quite good and orthometric heights vary from 4 to 400 m, the results obtained from either model or test data are quite satisfactory yielding proper accuracy required in the practical engineering applications that is defined as ± 5 cm in the Regulations for Large Scale Mapping and Geospatial Data Production that are the official regulations in Turkey. Fuzzy logic approach also yields considerable better results than the conventional polynomial fitting. Comparing to Istanbul, Sakarya is rather mountainous and its point distribution is quite poor. Therefore, the results obtained are not satisfactory in terms of the required accuracy. However, fuzzy logic approach employed for geoid modelling this region is also better than polynomial fitting in terms of its accuracy. In order to improve the model approximation in Sakarya region SRTM data will also be used in modelling.

References

- Akyılmaz, O., T. Ayan and M.T. Özlüdemir (2003). Geoid Surface Approximation by Using Adaptive Network Based Fuzzy Inference Systems. *Allgemeine Vermessungs-Nachrichten*, 8-9, pp. 308-315.

- Akyılmaz, O. (2005). Applications of Soft Computing Methods in Geodesy. Ph.D. Thesis, *Institute of Science and Technology*, Istanbul Technical University, Turkey (in Turkish).
- Ayan, T., A. Aksoy, R. Deniz, E. Arslan, R.N. Çelik, C. Özşamlı, H.H. Denli, S. Erol and B. Özöner (1999). Istanbul GPS network (IGNA). *Technical Report*, ITU Civil Engineering Faculty, Division of Geodesy, Istanbul (in Turkish).
- Ayan, T., R. Deniz, R.N. Çelik, H.H. Denli, M.T. Özlüdemir, S. Erol, B. Özöner, O. Akyılmaz, and C. Güney, (2001). İzmir Geodetic Reference System–2001, (IzJRS-2001). *Technical Report*, ITU Civil Engineering Faculty, Division of Geodesy, Istanbul (in Turkish).
- Engelis, T., R.H. Rapp and Y. Bock (1985). Measuring Orthometric Height Differences with GPS and Gravity Data. *Manuscripta Geodaetica*, 10 (3), pp. 187-194.
- Erol, B. and R.N. Çelik (2005). Precise Local Geoid Models in Engineering Measurements and Their Practical Applications in Turkey. In: *Proc. of 2th symposium on Engineering Measurements*, Istanbul, Turkey, November 23–25.
- Featherstone, W.E. (2001). Absolute and Relative Testing of Gravimetric Geoid Models Using Global Positioning System and Orthometric Height Data. *Computers&Geosciences*, 27, pp. 807-814.
- Jang, J.-S.R. (1991). Fuzzy Modelling Using Generalized Neural Networks and Kalman Filter Algorithm. In: *Proc. of the Ninth National Conference on Artificial Intelligence (AAAI-91)*, Anaheim, California, USA, July 15-19, pp. 762-767.
- Jang, J.-S.R. (1993). ANFIS: Adaptive Network Based Fuzzy Inference System. *IEEE Transactions on systems, Man, and Cybernetics*, 23 (3), pp. 665-685.
- Jang, J.-S.R. (1995). Neuro-Fuzzy Modelling and Control. *Proceedings of the IEEE*, 83 (3), pp. 378-406.
- Kotsakis, C. and M.G. Sideris (1999). On the Adjustment of Combined GPS/Levelling/Geoid Networks. *Journal of Geodesy*, 73, pp. 412–421.
- Kuhar, M., B. Stopar, G. Turk and T. Ambrožič (2001). The Use of Artificial Neural Network in Geoid Surface Approximation. *Allgemeine Vermessungs-Nachrichten*, 1, pp. 22-27.
- Mårtensson, S.G. (2002). Height Determination by GPS-Accuracy with Respect to Different Geoid Models in Sweden. In: *Proc of FIG XXII International Congress*, Washington D.C., USA, April 19-26.
- Takagi, T. and M. Sugeno (1983). Derivation of Fuzzy Control Rules from Human Operator's Control Actions. In: *Proc. of the IFAC Symp. on Fuzzy Information, Knowledge Representation and Decision Analysis*, Marseilles, France, July, pp. 55-60.
- Takagi, T. and M. Sugeno (1985). Fuzzy identification of systems and its application to modelling and control. *IEEE Trans. on Systems, Man and Cybernetics*, 15, pp. 116-132.
- URL1 (2006). Webpage of Mathworks Inc.. <http://www.mathworks.com/access/helpdesk/help/toolbox/fuzzy/anfis.html> (22/06/2006).
- URL2 (2006). Jyh-Shing Roger Jang's Homepage. <http://www.cs.nthu.edu.tw/~jang> (20/08/2006).
- Walid, A.H. (2005). Accuracy Enhancement of Integrated MEMS-IMU/GPS Systems for Land Vehicular Navigation Applications”, Ph.D. Thesis, *University of Calgary*, Calgary, Alberta, Canada.
- Yılmaz, M. and E. Arslan (2005). Fuzzy Applications in Geoid Height Determination. In: *Proc. of International Symposium on “Modern Technologies, Education and Professional Practice in Geodesy and Related Fields”*, Sofia, Bulgaria, November 3-4.
- Yılmaz, M. and E. Arslan (2006). Effect of The Type of Membership Function on Geoid Height Modelling with Fuzzy Logic. *Survey Review* (to be published).

Different Gravimetric Geoid Models over Iran with and without Terrestrial Gravity Data

H. Nahavandchi, A. Soltanpour

Norwegian University of Science and Technology, Department of Geomatics, 7491 Trondheim, Norway

Abstract. The quantity and quality of the terrestrial gravity plays a major role in the accuracy of local geoids. In countries, like Iran, where the gravity database is sparse and the quality is variable, the right selection of the computational technique is a key issue. Taken all limitations into account this study discusses the computation of the Iranian geoid. The collected gravimetric database consists of 16806 gravity points corresponding to 98 points per square km on average. This gravity database involves both old (low accuracy) and new, higher accuracy gravity. In this study the authors investigated two different procedures, one uses only geopotential models, corrected for the topographic and atmospheric effects and in the second group they also applied the different modification techniques of the classical Stokes's formula to integrate the terrestrial gravity data. The different gravimetric geoid solutions have been compared to GPS/levelling derived geoidal heights at some 200 points. The best gravimetric geoid solution has shown -117 cm mean bias and ± 67 cm standard deviation with respect to the GPS-levelling geoid. The same GPS-levelling comparison has resulted -25 cm mean offset and ± 114 cm standard deviation for the existing official Iranian geoid. After applying a (linear) fit to the residuals the standard deviation decreased to ± 36 cm. As expected the solution without terrestrial data has shown much worse statistics, so it has no practical advantage.

Keywords. geoid, global gravity model, topography

1 Introduction

The geoid, the equipotential surface of the Earth's gravity field, is more or less coincides with the mean sea level and it is used as the vertical datum for levelling networks. Geodesists use it as the reference surface for levelling while oceanographers need it for studies of ocean circulation, currents and tides. The geoid is also valuable for geophysicists as a tool for geodynamic studies, geophysical interpretation and prospecting. These applications require the knowledge of the geoid with a precision of better than 10 cm. An accurate solution of the boundary-value problem in physical geodesy is the well-known Stokes's formula:

$$N(R, \varphi, \lambda) = \frac{R}{4\pi\gamma} \iint_{\sigma} S(\psi) \Delta g(R, \varphi, \lambda) d\sigma \quad (1)$$

where N is the geoidal height computed at a point on the geoid with latitude φ , longitude λ and mean radius R , ψ is the spherical distance between computation and running points, Δg is the gravity anomaly on the geoid, γ is normal gravity on the ellipsoid, σ is the unit sphere and $S(\psi)$ is the original Stokes's formula.

The Stokes's formula requires that there are no masses (topography plus atmosphere) outside the geoid. This is achieved by mathematically removing the external masses or shifting them inside the geoid. The effect of the masses is then restored on the geoid after applying Stokes's integral. The topographic effects in precise geoid determination have been discussed in many papers (e.g. Sideris 1990; Tziavos et al. 1992; Forsberg 1994; Martinec and Vaníček 1994a, b; Nahavandchi and Sjöberg 1998; Sjöberg and Nahavandchi 1999; Nahavandchi 2000).

The incomplete global availability of reliable gravity measurements has precluded the accurate determination of the geoid using Stokes's formula. In practice, an approximate solution is used, where gravity data only in and close to the computation area is used. This truncation error can be reduced by the modification of the Stokes's kernel; in essence, the long-wavelength geoid contribution is determined from a geopotential model and the short-wavelength information is derived from terrestrial gravity and topographic data. The modification of the Stokes's formula, originating from Molodensky, aimed at reducing the truncation error committed by limiting the integration to a spherical cap around the computation point (Molodensky et al. 1962).

The potential use of GPS for precise height determination made the geoid a practically relevant product of physical geodesy. Earlier, GPS and levelling data have been used to empirically verify gravimetric geoid solutions (e.g. Sideris et al. 1992; Smith and Small 1999; Nahavandchi and Sjöberg 2001). Many studies have also been carried out to combine a gravimetric geoid and GPS-levelling data (e.g. Jiang and Duquenne 1996; Featherstone 2001). In this paper our objective is to determine different gravimetric geoid models over Iran. The study region, where the geoid is calculated, is still a 'white spot', where it is believed that all updates are welcome. Recently, different research groups used various procedures in their geoidal height computations over Iran. Ardalan and Grafarend (2004) computed a high-resolution geoid model without applying Stokes's

formula over Iran. The standard deviation of the differences of this geoid solution with the national geoid model of Iran was ± 91 cm. Safari et al. (2005) computed another geoid model based on an ellipsoidal gravimetric, altimetric and astronomic boundary value problem. The standard deviation of the differences between this geoid solution and 51 first-order GPS-levelling stations was ± 106.8 cm. Kiamehr (2006) used the classical Stokes approach and the least-squares modification of Stokes's formula to determine a newer geoid model for Iran. The geoid was based on GGM02s global gravity model (Tapley et al. 2005). The RMS of the differences between this geoid solution and 260 GPS-levelling stations is ± 58 cm. This paper investigates different geoid solutions with and without terrestrial gravity data, as well as different modification procedures. A comparison with the GPS-levelling geoid is also made.

2 Gravimetric Geoid Determination with Terrestrial Gravity Data

In practice, geoidal height can be computed by the following formula (see e.g. Heiskanen and Moritz 1967; Nahavandchi 2004):

$$N(R, \varphi, \lambda) = N_1(R, \varphi, \lambda) + N_2(R, \varphi, \lambda) + \delta N_{\text{Corr}} \quad (2)$$

where

$$\delta N_{\text{Corr}} = \delta N_{\text{tot}}^{\text{atm}}(R, \varphi, \lambda) + \delta N_{\text{ind}}^{\text{topo}}(R, \varphi, \lambda) + \delta N_{\text{dir}}^{\text{topo}}(R, \varphi, \lambda) \quad (3)$$

N is the final geoidal height computed at a point on the geoid, $\delta N_{\text{tot}}^{\text{atm}}(R, \varphi, \lambda)$ is the total effect (direct plus indirect) of atmospheric masses, $\delta N_{\text{ind}}^{\text{topo}}(R, \varphi, \lambda)$ is the primary indirect effect on geoid due to topography, $\delta N_{\text{dir}}^{\text{topo}}(R, \varphi, \lambda)$ is the direct effect of topography on the long-wavelength part of the computed geoid, $N_1(R, \varphi, \lambda)$ is the short-wavelength contribution to the geoid computed from Stokes's integral and $N_2(R, \varphi, \lambda)$ is the long-wavelength contribution to the final geoid determined from a global geopotential model. The short-wavelength part of the geoid can be determined from

$$N_1(R, \varphi, \lambda) = \frac{R}{4\pi\gamma} \iint_{\sigma_0} S^{\text{Mod}}(\psi) \left[\Delta g_{\text{corr}}^{\text{H}^*}(R, \varphi, \lambda) \right] d\sigma \quad (4)$$

where

$$\Delta g_{\text{corr}}^{\text{H}^*}(R, \varphi, \lambda) = \Delta g^{\text{H}^*}(R, \varphi, \lambda) + \delta \Delta g_{\text{ellip}} + \delta \Delta g_{\text{sec ind}}^{\text{topo}}(R, \varphi, \lambda) \quad (5)$$

where $\Delta g^{\text{H}^*}(R, \varphi, \lambda)$ is the Helmert anomaly on the geoid, $\delta \Delta g_{\text{ellip}}$ is the ellipsoidal correction, $\delta \Delta g_{\text{sec ind}}^{\text{topo}}(R, \varphi, \lambda)$ is the secondary indirect effect on gravity anomaly due to topography, σ_0 defines truncation cap and $S^{\text{Mod}}(\psi)$ is a modification to the original Stokes's formula $S(\psi)$. In this study we use Helmert's second condensation method (Heiskanen and Moritz 1967, p.145) to reduce the topography, implying that the topography is condensed to a surface layer at sea level, the condensation that preserves the mass, for which the Helmert-model Earth has the same mass as the real Earth. $\Delta g^{\text{H}}(r, \varphi, \lambda)$ is the Helmert gravity anomaly on topography which can be obtained from the sum of the original free-air gravity anomaly and the direct topographic effect referred to the Earth's surface. Helmert gravity anomaly on the topography can be determined from the following formula:

$$\Delta g^{\text{H}}(r, \varphi, \lambda) = \Delta g_{\text{free-air}}(r, \varphi, \lambda) + \delta \Delta g_{\text{dir}}^{\text{topo}}(r, \varphi, \lambda) \quad (6)$$

where $\Delta g_{\text{free-air}}$ is computed from the observed surface gravity (g) corrected for the free-air correction ($0.3086H$) and normal gravity (γ) ($\Delta g_{\text{free-air}} = g - \gamma + 0.3086H_p$, where H_p is the orthometric heights in meters and the gravity units are in mGal), $\delta \Delta g_{\text{dir}}^{\text{topo}}(r, \varphi, \lambda)$ is the direct topographical correction to the observed gravity anomalies. Here $r = R + H_p$. The notation $\Delta g^{\text{H}^*}(R, \varphi, \lambda)$ is used for $\Delta g^{\text{H}}(r, \varphi, \lambda)$ analytically downward continued from the surface to sea level ($\Delta g^{\text{H}^*}(R, \varphi, \lambda) = \Delta g^{\text{H}}(r, \varphi, \lambda) + \delta \Delta g_{\text{dwc}}^{\text{H}}$). Here $\delta \Delta g_{\text{dwc}}^{\text{H}}$ is the effect of downward continuation of $\Delta g^{\text{H}}(r, \varphi, \lambda)$ from the Earth's surface to sea level. Martinec and Vaníček (1994a, b) formulas are used to correct for the direct, primary and the secondary indirect topographical effect in this study. The downward continuation correction is computed based on a discrete formula developed in Martinec (1996, 1998). The total atmospheric effect is computed using the formula derived in Sjöberg and Nahavandchi (2000). The ellipsoidal correction is derived by the formula given in Moritz (1980). Interested readers are also referred to Sjöberg and Nahavandchi (1999), Nahavandchi (2000) and Nahavandchi and Sjöberg (2001) for detailed treatment of correction terms.

The long-wavelength part of the geoid can be determined from

$$N_2(R, \varphi, \lambda) = \frac{R}{2\gamma} \sum_{n=2}^M s'_n \Delta g_n \quad (7)$$

where s'_n are modification parameters.

Different modification methods of Stokes's formula were applied in this study: modified Wong-Gore (1969), Vaniček-Kleusberg (1987), Molodensky (1962) and the least-squares (Sjöberg 1984) models. Interested readers are referred to Nahavandchi and Sjöberg (2001) for definition of modification parameters and related kernel modifications in the different models.

3 Gravimetric Geoid Determination without Terrestrial Gravity Data

Unfortunately, the gravity data in Iran is sparse and the available gravity data have been collected over a long time span, using different methods, equipment and reference frames. The inconsistency and limitation in the gravity data is why this section introduces geoid models determined without the use of terrestrial gravity data. Nahavandchi (2002) presented two models:

3.1 Model A

This model employs the geopotential coefficients with the assumption that the external harmonic series expansion is convergent on the Brillouin sphere. However, a bias is expected for the external harmonic series when applied at the geoid within the topographic masses. This bias can be estimated by removing the topographic (δN_{tot}^M) and atmospheric (δN_{tot}^a) masses (such that we can now continue the external harmonic series of the geopotential downwards to the geoid - they are now harmonic between the geoid and the topography). The realization is shown by the following formula (Heiskanen and Moritz 1967; see also Nahavandchi 2002):

$$N(R, \phi, \lambda) = \frac{GM_3}{R\gamma} \sum_{n=0}^M \left(\frac{a_1}{R}\right)^n \sum_{m=0}^n \left[\frac{GM_1}{GM_3} C_{nm} - \frac{GM_2}{GM_3} \left(\frac{a_2}{a_1}\right)^n C'_{nm} \right] \times \cos m\lambda + \frac{GM_1}{GM_3} S_{nm} \sin m\lambda \left[P_{nm}(\sin\phi) - \frac{1}{\gamma} (W_0 - U_0) + \delta N_{\text{tot}}^M + \delta N_{\text{tot}}^a \right] \quad (8)$$

where

$$\delta N_{\text{tot}}^M = -\frac{2\pi\mu}{\gamma} \sum_{n,m} (H^2)_{nm} Y_{nm}(P) - \frac{4\pi\mu}{3R\gamma} \sum_{n,m} (H^3)_{nm} Y_{nm}(P) \quad (9)$$

and

$$\delta N_{\text{tot}}^a = -\frac{4\pi\rho_0 R}{\gamma} \sum_{n,m} \frac{1}{n-1} H_{nm} Y_{nm}(P) \quad (10)$$

where

$$(H^v)_{nm} = \frac{1}{4\pi} \iint_{\sigma} H_P^v Y_{nm} d\sigma, \quad v = 1, 2, 3 \quad (11)$$

and Y_{nm} are fully normalized spherical harmonics. Also ρ_0 is the density at the radius of sea level (ρ^0) multiplied by the gravitational constant (G), a_1 is the equipotential scale factor for a global geopotential model (for EGM96=6378.1363 km), a_2 is the equipotential radius of GRS-80 (6378.137 km), GM_1 is the gravity-mass constant for a global geopotential model (for EGM96= $3.986004415 \times 10^{14} \text{ m}^3\text{s}^{-2}$), GM_2 is the gravity-mass constant of GRS-80 ($3.986005000 \times 10^{14} \text{ m}^3\text{s}^{-2}$), GM_3 is the best estimate of gravity-mass constant for the Earth ($3.986004418 \times 10^{14} \text{ m}^3\text{s}^{-2}$), W_0 is the adopted gravity potential on the geoid ($62636856.88 \text{ m}^2\text{s}^{-2}$), U_0 is defined as the normal gravity potential on the ellipsoid ($62636860.8 \text{ m}^2\text{s}^{-2}$), C_{nm} , S_{nm} are fully normalized geopotential coefficients of a global geopotential model in a non-tidal system, C'_{nm} are fully normalized normal potential coefficients of GRS-80 in a non-tidal system and $S'_{nm}=0$.

3.2 Model B

The second model is based on the fact that the geoid can be computed through height anomaly ζ_0 and the height anomaly can be computed by the geopotential coefficients at the topography not onto the geoid. Therefore, one can ignore the bias due to the non-harmonicities in the previous formula. This procedure is realized as (see Heiskanen and Moritz 1967; Rapp 1997; Nahavandchi 2002):

$$N(R, \phi, \lambda) = \zeta_0(r, \phi, \lambda) + \text{correction terms} = \zeta_0(r, \phi, \lambda) + \frac{\partial \zeta}{\partial r} H + \frac{\partial \zeta}{\partial \gamma} \frac{\partial \gamma}{\partial H} H + \frac{(\Delta g_{\text{Bouguer}})}{\bar{\gamma}} H + \frac{H_P^2}{2\bar{\gamma}} \left(\frac{\partial \Delta g_{\text{Free-air}}}{\partial H} \right) \quad (12)$$

where all terms in Equation (12) are defined in Nahavandchi (2002). $\zeta_0(r, \phi, \lambda)$ and the first three correction terms in Equation (12) is computed from a spherical harmonic representation of geopotential. The last correction term is computed from an integral formula (see Nahavandchi 2002).

4 Numerical Investigations

4.1 Data Sources

This study focuses on the determination of different gravimetric geoid models for Iran. The distribution of the terrestrial gravity data used is shown in Figure 1. The gravity data was provided by the Iranian Mapping Authority (National Cartographic Center of Iran, NCC). The topographic information in the form of a 1 km Digital Elevation Model (DEM) was provided by the National Geophysical Data Center (NGDC) (<http://www.ngdc.noaa.gov/mgg/topo/globe.html>)

and it was used for the computation of the topographic corrections.

The height coefficients H_{nm} , $(H^2)_{nm}$ and $(H^3)_{nm}$ were determined using Equation (11). For this, a $30' \times 30'$ DEM was generated using the GETECH $5' \times 5'$ DEM (1995) and averaged using area weighting. The spherical harmonic coefficients of the topography were computed to degree and order 360. This degree and order (360) was used in all topographical corrections in this study. The parametric definitions are: $\mu = G\rho_0$ where $G = 6.673 \times 10^{-11} \text{ m}^3 \text{ kg}^{-1} \text{ s}^{-2}$ and $\rho_0 = 2670 \text{ kgm}^{-3}$, $\rho^0 = 1.23 \text{ kgm}^{-3}$, $R = 6371 \text{ km}$, and $\gamma = 981 \text{ Gal}$. The gravity anomalies were interpolated to a grid with $10' \times 10'$ resolution. The global geopotential model of GGM02s (Tapley et al. 2005) to degree and order 120 is used throughout this study.

4.2 Computations

Prior to the geoid computations, the correction terms are computed. The direct topographic effect reaches a maximum value of 242.32 mGal, the primary indirect effect has a minimum value of -149.7 cm (largest value in an absolute sense), and the total atmospheric effect ranges from -10.4 to -25.2 cm. Thereafter, different geoid models were computed based on the mentioned modification procedures. 200 GPS-levelling points distributed over Iran, were used to test the different gravimetric geoid versions. The rough accuracy estimate of the levelled heights in Iran is around 70 cm in the absolute sense (Hamesh 1991). The height system used is rather ambiguous, but it is assumed to be an orthometric system (ibid.). The GPS ellipsoidal heights in Iran are referred to the WGS84 datum. The accuracy of the ellipsoidal height computed from GPS is estimated about 25 cm (Nilforoushan 1995). In Table 1 the statistics of the geometric (GPS-levelling) and gravimetric geoid differences are presented. The final Iranian Gravimetric Geoid (IRGG05, see in Fig.2) is computed using the Vaniček-Kleusberg solution as it has the best fit to the geometric geoid. At the IRGG05 geoid solution the GGM02s geopotential model and the gravity data, integrated with 3 degrees truncation cap is used. IRGG05 refers to the Geodetic Reference System 1980 (GRS80) (Moritz 1980).

The gravimetric geoid model of Iran is then fitted to 200 GPS-levelling geoid heights using the least-squares collocation method. A linear model was used to remove the trend from the data. Table 2 shows the statistics of the differences between the gravimetric geoid solutions and the GPS-levelling geoid. The official geoid model of Iran (Hamesh and Zomorrodian 1992) is also included in the comparisons. The results show that the gravimetric geoid model, computed in this study provides the smallest residuals.

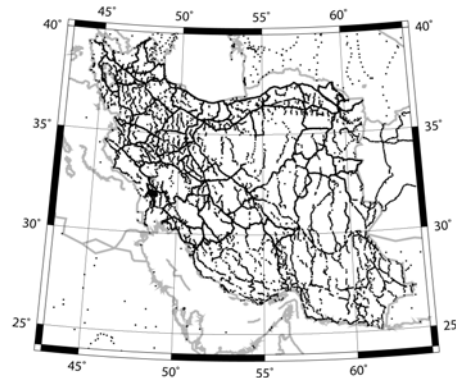


Fig. 1 Gravity data distribution in Iran.

Table 1. The statistics of the differences between the geometric geoid, and the gravimetric geoid computed by different modification procedures.

	Molodensky	Least-squares	Wong-Gore	Vaniček-Kleusberg
Max	1.406	2.158	1.897	1.068
Min	-2.615	-2.559	-2.987	-2.682
Mean	-0.917	-0.572	-0.885	-1.173
Std	0.702	0.738	0.894	0.672

Table 2. The statistics that show the differences between the geometric and gravimetric geoidal heights with different solutions 1) New geoid model of Iran computed by the Vaniček-Kleusberg solution (GGM02s is used as the long-wavelength geoid, M=120) before fitting; 2) after de-trending with linear model; 3) after fitting using Least-squares collocation; 4) official geoid of Iran (Hamesh and Zomorrodian 1992) before fitting; 5) official geoid of Iran (Hamesh and Zomorrodian 1992) after de-trending with linear model and fitting using Least-squares collocation.

	Solution 1	Solution 2	Solution 3	Solution 4	Solution 5
Max	1.068	2.094	1.278	2.829	3.109
Min	-2.682	-1.411	-1.398	-4.341	-2.621
Mean	-1.173	0.000	0.000	-0.259	0.000
Std	0.672	0.659	0.363	1.140	0.580

In the next step, the geoid models A and B, which do not use terrestrial gravity data (described in Section 3), were computed. They were created to test the capability of the geoid computations, where no terrestrial gravity data is available. The accuracy of these two geoid models was estimated with the earlier used 200 GPS-levelling points. Figure 3 shows the total topographic correction applied in model A. Thereafter, the geoid was computed using Equations (8)-(10) as shown in Figure 4. This geoid model is also referred to the GRS80 reference ellipsoid and is comparable with the geoid derived from terrestrial gravity data. Note that the computation area is slightly

different from the geoid derived using terrestrial gravity data.

Thereafter, model B (not using terrestrial gravity data) was employed. Prior to the geoid determination all correction terms were computed [see Equation (12)]. The sum of all correction term is plotted in Figure 5.

Table 3 shows the comparisons of these two geoid models at the same 200 GPS-levelling stations. Both models provide agreement about 1 m with GPS-levelling data. This accuracy is acceptable considering the fact that no terrestrial gravity data were applied in these two models.

Table 3. Statistics showing the differences between GPS-levelling geoidal heights and the two other geoid models without terrestrial gravity data in metres

	Mean	Max	Min	SD
Model A	-1.617	1.553	-3.322	0.968
Model B	-1.464	2.208	-3.211	1.013

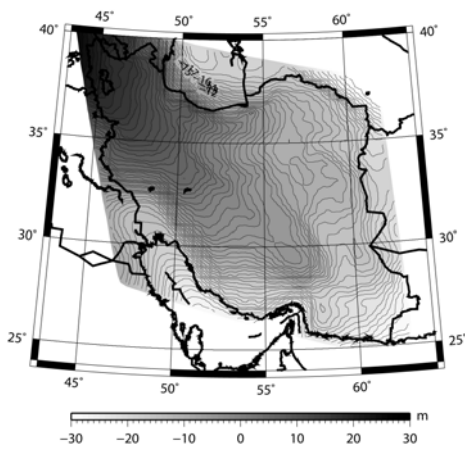


Fig. 2 The gravimetric geoid model of Iran (IRGG05).

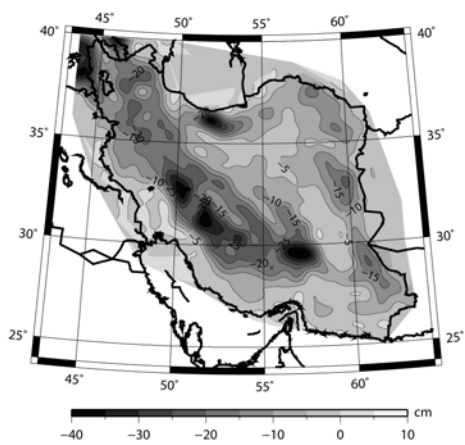


Fig. 3 The total topographic correction computed for the geoid model A without terrestrial gravity data.

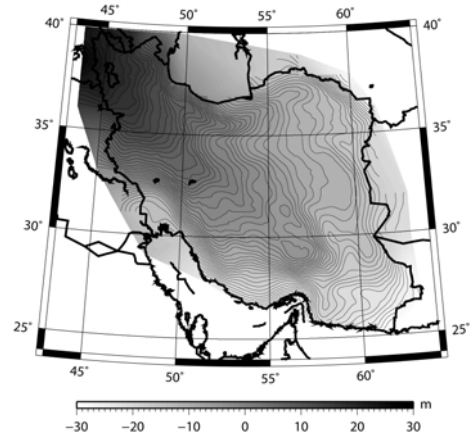


Fig. 4 The geoid model of Iran computed using model A without terrestrial gravity data

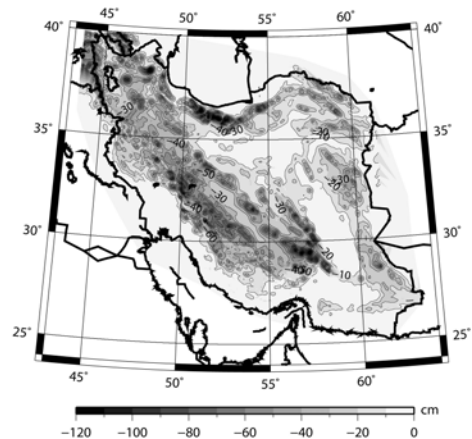


Fig. 5 The total correction terms computed for the geoid model B without terrestrial gravity data

6 Discussions

This study targeted at the determination of a new geoid model over Iran, (IRGG05) based on different modification methods of Stokes's formula. Sparse terrestrial gravity data with 3 degrees of integration cap and the GGM02s geopotential model was used. 200 GPS-levelling points were used to select the best fitting gravimetric solution. According to this test the solution based on the Vaniček-Kleusberg modification method was selected as the final gravimetric geoid model of Iran (IRGG05).

The overall comparison among different geoid models (over Iran) shows that the IRGG05 solution obtains one of the best results. However, further investigations are needed for the actual performance of IRGG05 among all geoid solutions over Iran. Denser and more precise GPS-levelling data are needed.

The treatment of the gravity data, collected with the different methods and equipment, during several

decades by different specifications, requires careful investigation before it is used for geoid computation. The gravity data are affected by various systematic errors, and they are referred to different reference frames. Also, the lack of accurate heights is usually an important error source. It was for these reasons, the geoid models without terrestrial gravity data were also created. The accuracy of those models however does not fit for the practical needs.

Finally, it should be noted that in computation of the topographic corrections by integral formulas, the resolution of the DEM models plays an important role. A global model is used in this study while the DEMs with higher resolution, for example, the data provided by the Shuttle Radar Topography Mission (SRTM) will provide slightly different results.

Acknowledgement: This work is a part of a project funded by the Department of Research and Development of National Cartographic Center (NCC) of Iran. We thank Dr. Ambrus Kenyeres and an anonymous reviewer and Dr. Urs Marti for their time and constructive criticism.

References

- Ardalan AA, Grafarend EW (2004) High-resolution geoid computation without applying Stokes' formula case study: high-resolution geoid of Iran. *Journal of Geodesy* 78: 138-156
- Featherstone WE (2001) Absolute and relative testing of gravimetric geoid models using Global Positioning System and orthometric height data. *Computers and Geosciences* 27: 807-814
- Forsberg R (1994) Terrian effects in geoid computations. In: Lecture Notes, International School for the determination and use of the geoid, IGeS: 101-134
- GETECH (1995) Global DTM5. Geophysical Exploration Technology (GETECH), University of Leeds, Leeds
- Hamesh M (1991) Technical Report about adjustment of Iranian first order levelling network. *NCC Journal of Surveying* 1: 9-20
- Hamesh M, Zomorrodian H (1992) Iranian gravimetric geoid determination- Second step. *NCC Journal of Surveying* 6: 17-24, 52-63
- Heiskanen WA, Moritz H (1967) Physical Geodesy. W H Freeman and Company, San Francisco
- Jiang Z, Duquenne H (1996) On the combined adjustment of a gravimetrically determined geoid and GPS levelling stations, *Journal of Geodesy* 70: 505-514
- Kiamehr R (2006) A strategy for determining the regional geoid in developing countries by combining limited ground data with satellite-based global geopotential and topographical models: a case study of Iran. *Journal of Geodesy* 79: 602-612.
- Martinec Z (1996) Stability investigations of a discrete downward continuation problem for geoid determination. *Journal of Geodesy* 70: 805-823
- Martinec Z (1998) Boundary-value problems for gravimetric determination of a precise geoid. Springer-Verlag, Berlin Heidelberg, Germany
- Martinec Z, Vaniček P (1994a) Direct topographical effect of Helmert's condensation for a spherical approximation of the geoid. *Manuscripta Geodaetica* 19: 257-268
- Martinec Z, Vaniček P (1994b) The indirect effect of topography in the Stokes- Helmert technique for a spherical approximation of the geoid. *Manuscripta Geodaetica* 19: 213-219
- Molodensky MS, Eremeev VF, Yurkina MI (1962) Methods for study of the external gravitational field and figure of the Earth. Office of Technical Services, Department of Commerce, Washington DC
- Moritz H (1980) Advanced physical geodesy. Herbert Wichman Verlag, Karlsruhe
- Nahavandchi H (2000) The direct topographical correction in gravimetric geoid determination by the Stokes-Helmert method. *Journal of Geodesy* 74: 488-496
- Nahavandchi H. (2002) Two different methods of geoidal height determinations using a spherical harmonic representation of the geopotential, topographic corrections and the height anomaly-geoidal height difference. *Journal of Geodesy* 76: 345-352
- Nahavandchi H (2004) The quest for a precise geoidal height model. *Kart og Plan* 1: 46-56
- Nahavandchi H, Sjöberg LE (1998) Terrain correction to power H^2 in gravimetric geoid determination. *Journal of Geodesy* 72: 124-135
- Nahavandchi H, Sjöberg LE (2001) Precise geoid determination over Sweden using the Stokes-Helmert method and improved topographic corrections. *Journal of Geodesy* 75: 74-88
- Nilforoushan F (1995) Adjustment of Iranian GPS network. MSc Thesis, Faculty of Civil Engineering, K.N. Toosi University of Technology, Tehran
- Rapp RH (1997) Use of potential coefficient models for geoid undulation determinations using a spherical harmonic representation of the height anomaly/geoid undulation difference. *Journal of Geodesy* 71: 282-289
- Safari A., Ardalan AA, Grafarend EW (2005) A new ellipsoidal gravimetric, satellite altimetry and astronomic boundary value problem, a case study: the geoid of Iran. *Journal of Geodynamics* 39: 545-568.
- Sideris MG (1990) Rigorous gravimetric terrain modeling using Molodensky's operator. *Manuscripta Geodaetica* 15: 97-106
- Sideris MG, Mainville A, Forsberg R (1992) Geoid testing using GPS and levelling. *Australian Journal of Geodesy, Photogrammetry and Surveying* 57: 62-77
- Sjöberg LE (1984) Least squares modification of Stokes' and Vening Meinez's formulas by accounting for errors of truncation, potential coefficients and gravity data, Report No. 27, Department of Geodesy, University of Uppsala, Uppsala, Sweden
- Sjöberg LE, Nahavandchi H (1999) On the indirect effect in the Stokes-Helmert method of geoid determination. *Journal of Geodesy* 73: 87-93
- Sjöberg LE, Nahavandchi H (2000) The atmospheric geoid effects in Stokes formula. *Geophysical Journal International* 140: 95-100
- Smith DA, Small HJ (1999) The CARIB97 high-resolution geoid height model for the Caribbean Sea. *Journal of Geodesy* 73: 1-9
- Tapley B, Ries J, Bettadpur S, Chambers D, Cheng M, Condi F, Gunter B, Kang Z, Nagel P, Pastor R, Pekker T, Poole S, Wang F (2005) GGM02 - An improved Earth gravity field model from GRACE. *Journal of Geodesy* 79: 467-478
- Tziavos IN, Sideris MG, Schwarz KP (1992) A study of the contribution of various gravimetric data types on the estimation of gravity field parameters in the mountains. *Journal of Geophysical Research* 97: 8843-8852
- Vanicek P, Kleusberg A (1987) The Canadian geoid-Stokesian approach, *Manuscripta Geodaetica* 12: 86-98.
- Wong L, Gore R (1969) Accuracy of geoid heights from the modified Stokes's kernels. *Geophysical Journal Research Astronomical Society* 18: 81-91

A data set to test geoid computation methods

H. Duquenne

Laboratoire de Recherche en Géodésie, Institut Géographique National, 6-8 avenue Blaise Pascal, F-77455 Marne la Vallée CEDEX, France

Abstract. Upon the request of the steering committee of the European Gravity and Geoid Project, the Institut Géographique National has prepared a data set to test geoid computation methods and programs. The set consists of digital terrain models, gravity data and levelled GPS points prepared in such a way that the computation of a $3^\circ \times 2^\circ$ geoid is feasible. The first section describes the motivations for the preparation of this data set and the specifications. In the next two sections, the area characteristics and the data are presented. The fourth section gives an evaluation of the quality of the data set through a first solution for the quasigeoid. Finally a practical way to retrieve the data and future perspectives are outlined.

Keywords. Geoid modelling, quality control.

1 Motivations and objectives

At the IAG international symposium GGSM 2004 in Porto, the steering committee of the European Gravity and Geoid Project (EGGP) asked the Institut Géographique National (IGN) to provide interested institutions and researchers with a data set to test methods and software to compute geoid models. As other mapping agencies, the IGN is specially involved in the evaluation of geoid models and could only reply positively to this request.

A suitable test data set should satisfy the following requirements:

- The size of the test area should be large enough to allow the evaluation of geoid models at least at short and medium wavelengths.
- Diverse kinds of field-related data should be available so that all computation methods can be used or tested.
- The data coverage should be dense and homogeneous.
- The topographic and geological features of the area should vary so that the influence of terrain density changes can be studied.
- The data accuracy should be sufficient to avoid problems in separating errors in the data from errors in the models or software.
- The data should refer to known reference sys-

tems to avoid inconsistencies in the geoid computation.

- The data set should be easily accessible.

The data set presented below corresponds to these specifications more or less accurately.

2 Presentation of the area

The target area for the geoid, which can be computed, is plotted in the Figure 1. The area is located in the centre of France. It covers the northern part of the Massif Central and the southern part of the Paris Basin. Its size is about 200×200 km. It contains various types of terrains and geological structures:

- The Limousin plateau of the Hercynian era,
- Medium sized mountains of the tertiary era, cut by gaps where the Loire and Allier rivers flow through narrow valleys,
- About 60 old volcanoes of the so called “Chaîne des Puys” from the Puy de Dôme to the Plomb du Cantal, in Alvernia. Some of the volcanoes are visible on the map.
- In the north the large and flat Paris Basin begins.

Heights vary from less than 150 metres (near the north-western corner of the area) to 1886 metres at the Puy de Sancy.

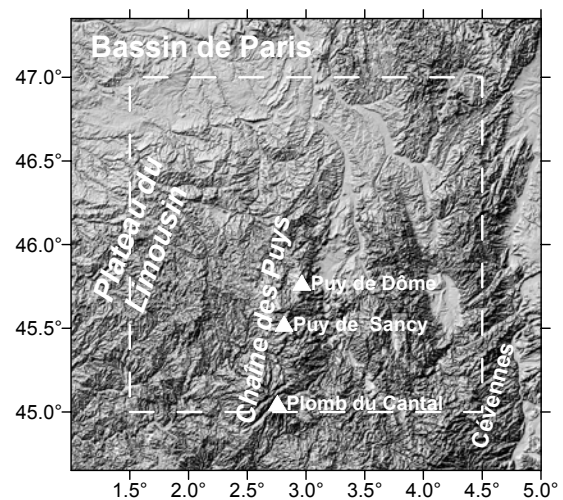


Fig. 1. Area for geoid computation. The geoid area is delimited by the broken white line.

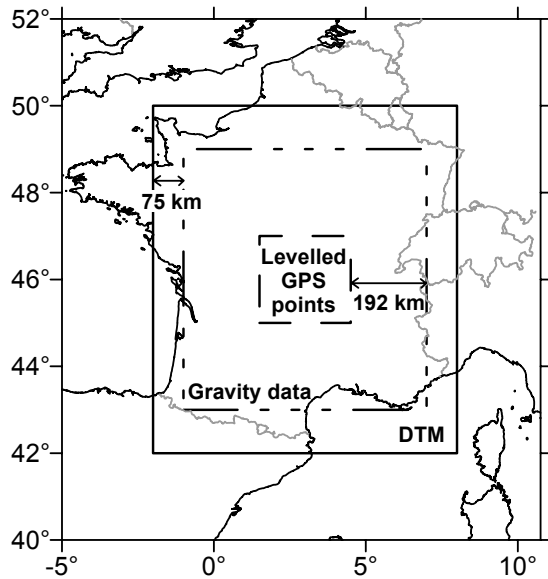


Fig. 2. Limits for the respective areas covered with levelled GPS points, gravity data and DTM's.

3 Data description

Figure 2 shows the respective regions covered by three types of data:

- Levelled GPS points are provided within the inner square delimited by the broken line; this area is the same as the geoid target area.
- Gravity data cover the square delimited by a “dash dot” line, which extends beyond the geoid area with a margin of 192 km.
- The digital terrain models are delimited by the continuous line. The margin allows terrain corrections within a radius of 75 km.

3.1 Levelled GPS points

75 levelled GPS points are available (Figure 3). They originate from the “French Basic Network” (SGN, 1996), which is the French first order GPS network, and from the so called “NIVAG” data set (Bouron, 2004), which has been established to maintain the national levelling network by combining precise levelling and GPS measurements. The geodetic coordinates refer to the RGF93 reference frame, which is fully compatible with ETRS89. The standard deviation of the ellipsoidal heights is about 2~3 cm for the RBF points, and slightly better for the NIVAG points. All the points are linked to the national levelling network (NGF-IGN69) by precise levelling with redundant observations. The total

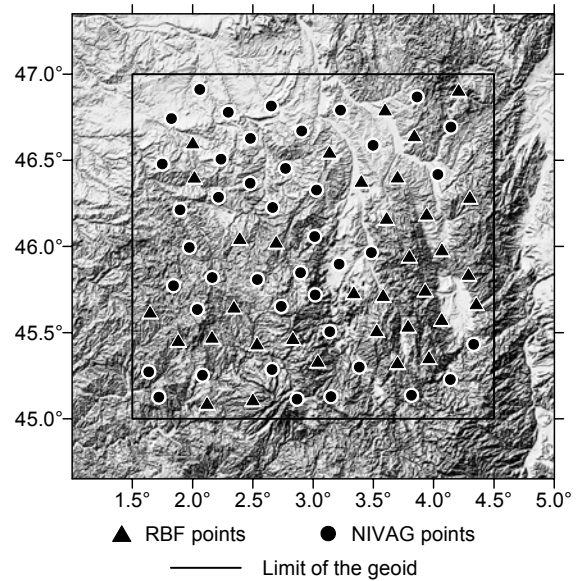


Fig. 3. Distribution of the levelled GPS points.

standard deviation of the difference in heights between neighbouring points is better than 2 cm, including the uncertainties of the basic network and of the local ties.

3.2 Gravity data

Gravity data have been extracted from the data base of the Bureau Gravimétrique International, which was supplied by the Bureau de Recherches Géologiques et Minières for the French territory. The number of points is about 240000, within the

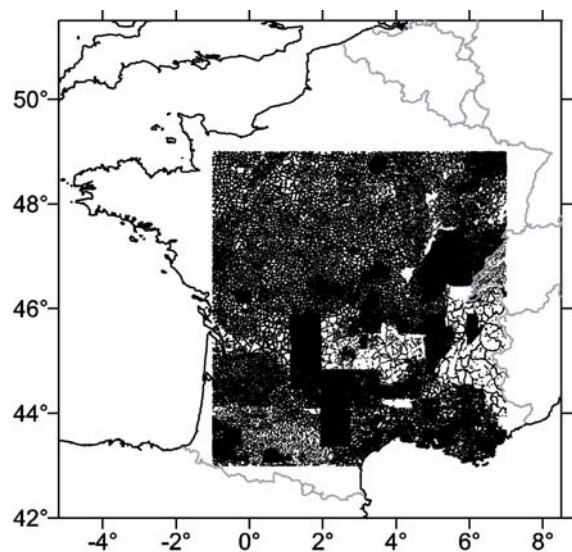


Fig. 4. Gravity data.

limits $43^\circ \leq \varphi \leq 49^\circ$, $-1^\circ \leq \lambda \leq 7^\circ$ (Figure 4). The mean density is 0.59 points per square kilometer with significant variations. Data are sparse in some mountainous areas, especially in the southern part of the geoid computation area. Although mainly measured before 1971, the gravity values have been converted to the IGSN71 system. They have been checked at BGI with the DIVA software, which uses a re-interpolation by collocation (Toustou, 1991). The accuracy of gravity values has been evaluated as 0.25~0.75 mGal. These figures may worsen up to 1 or 2 mGal when computing Bouguer or residual anomalies due to errors in position or inconsistencies with the digital terrain model.

3.3 Digital terrain models

Two digital terrain models are provided in the limits $42^\circ \leq \varphi \leq 50^\circ$, $-2^\circ \leq \lambda \leq 8^\circ$. One of them expresses normal heights referred to the NGF-IGN69 system; the other gives heights above the GRS80 ellipsoid in the RGF93/ETRS89 system. The former has been obtained in 1992 from the IGN's height data base which has been built up from regular topographic maps or aerial surveys (Duquenne, 1992). The latter DTM has been derived from the former using the RAF98 conversion grid (Duquenne, 1998). Given values in both models correspond to the average height of each pixel. The resolution of both models is 4.5" in latitude and 6" in longitude (about 140 m). The accuracy of the DTM's has been evaluated by a comparison with 753 geodetic benchmarks known to be at the terrain level. A standard deviation of 5 metres has been found in flat (open or wooded) terrain, up to 15 m in very rough topography.

4 A preliminary solution for the geoid

In order to test the data set, a model of the quasigeoid has been computed, using the residual terrain approach and the GRAVSOFIT package (Forsberg, 1994; Tscherning et al., 1992). The long wavelength contribution of the gravity field has been modelled by an Earth gravitational model obtained from a combination of GGM02S (Tapley et al., 2005) from degree 0 to 110 and EGM96 (Lemoine et al., 1998) from degree 110 to 360. Owing to the roughness of the topography in some areas, terrain effects have been computed by numerical integration. All available gravity data were used to compute a grid of the quasigeoid. Tests with fixed radius for Stokes's integration (100 km, 150 km) gave less accurate results. In this preliminary solu-

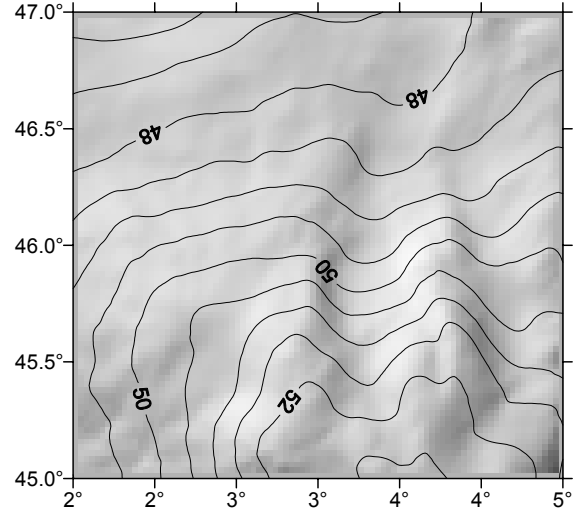


Fig. 5. The quasigeoid. Units are metres.

tion, neither the atmospheric correction (Sjöberg, 1998) nor the ellipsoidal correction (Sjöberg, 2002) were applied. Figure 5 shows the quasigeoid. Tables 1 and 2 summarize the statistics of gravity anomalies (Δg : free-air, Δg_{GGM} : from the global model, Δg_{res} : residual) and height anomalies (ζ_{res} : residual, ζ_{GGM} : from the global model, ζ : total), respectively.

Table 1. Statistics of gravity data. Units are mGal.

	Mean	Std. dev.	Min	Max
Δg	3.06	20.70	-127.47	177.82
Δg_{GGM}	8.76	17.95	-34.92	122.65
Δg_{res} (points)	-1.03	8.89	-59.11	61.44
Δg_{res} (grid)	0.25	8.74	-35.12	60.05

Table 2. Statistics of height anomalies. Units are metres.

	Mean	Std. dev.	Min	Max
ζ_{res}	0.10	0.11	-0.28	0.44
ζ_{GGM}	49.46	1.46	46.70	52.62
ζ	49.59	1.52	46.64	52.70

Table 3. Comparison between the gravimetric quasigeoid and 75 GPS-levelling control points. Units are metres.

Trend removed	Mean diff.	Std. dev.	Min diff.	Max. diff.
None	-0.184	0.038	-0.292	-0.117
Constant	0	0.038	-0.108	0.067
Linear trend	0	0.037	-0.069	0.093

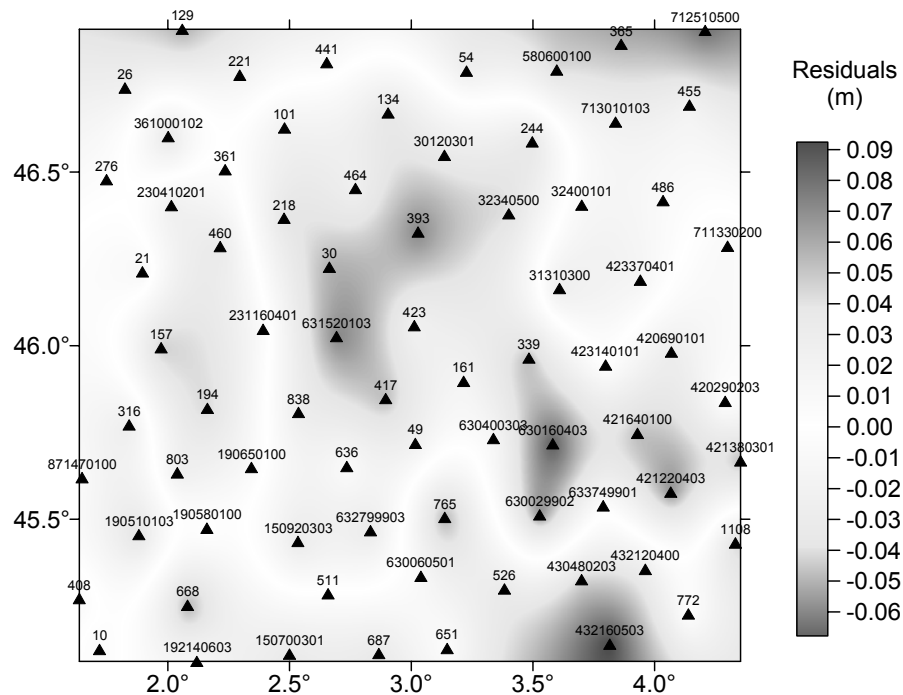


Fig. 6. Residuals of the differences between the gravimetric quasigeoid and the levelling-GPS data after a 3-parameter regression.

A comparison of the quasigeoid with GPS-leveling data can be used to estimate the total accuracy of the data and the computation method; in addition, a check for outliers can be performed. Table 3 gives the statistics of the differences between the gravimetric quasigeoid and the geometric quasigeoid computed from the 75 GPS and levelling points. A trend has been removed as denoted in the first column. The average difference (-0.184 m) is due to inconsistencies between the datums: the French height reference system NGF-IGN69 is known to be affected by a systematic error consisting of a constant and a NS-slope. The accuracy (0.038 m) is similar to those related in other works.

Figure 6 depicts the residuals of the 3-parameter regression. The maximum value (0.093 m) occurs in an area where the gravity data are very sparse.

5 Practical considerations

The data described above consists of 3 subsets: GPS and levelling points, gravity data and DTM's. The first two are in the public domain and can be used without any authorisation. On the contrary the DTM's are considered to be commercial products. Their use is presently limited to research on geoid modelling in the scope of the European Geoid and Gravity Project and require signing an agreement. A

new DTM derived from the SRTM data is in preparation: it will be usable with fewer formalities. Moreover the complete data set will be made available through the website of the International Geoid Service: <http://www.iges.polimi.it/>. For the moment, geodesists interested in getting the data should send an e-mail to Henri.Duquenne@ign.fr.

6 Conclusions and future developments

A data set to evaluate geoid computation methods and software has been prepared. It could also be useful for training purposes. Comparison of a first solution for the geoid with levelled GPS points yields an estimate for the precision of 3.8 cm, including errors in the data and method. Nevertheless this data set may not completely fulfill the requirements listed in the section 1 above. The size of the computation area could be increased, but this requires international cooperation. The density and quality of the gravity data could be improved, mainly in the south-western part of the area of computation. New kinds of data could be measured and included (deflections of the vertical, gravity gradients). Finally, the main problem for the evaluation of the geoid modelling is still pending: how to separate errors in the data from errors due to the meth-

odology or approximations. The solution could be to build a set of synthetic data on the basis of the real data. The former could be fully coherent and errorless while being as realistic as possible.

Acknowledgements

The author would like to thank the referees, Dr. B. Bürki and Dr. H. Denker, for their encouraging comments and their constructive recommendations. Mrs Susan Ash helped to improve the English version of the manuscript.

References

- Bouron, P. (2004). Entretien du NGF avec assistance GPS (NIVAG) – Spécifications de produit. Technical report nr. IT 244, Service de Géodésie et Nivellement, Institut Géographique National (in French).
- Duquenne, H. (1992). The new digital terrain model of France. In: proc. of the First Continental Workshop on the Geoid in Europe, pp 58-71. Research Institute of Geodesy, Topography and Cartography, Prague.
- Duquenne, H. (1998). QGF98, a new solution for the quasigeoid in France. In: proc. of the Second Continental Workshop on the Geoid in Europe. Reports of the Finnish Geodetic Institute 98:4, pp 251-255.
- Forsberg, R. (1994). Terrain effects in Geoid Computations. Lectures Notes. In: International School for the Determination and Use of the Geoid. International Geoid Service. DIIAR, Milan, Italy.
- Lemoine, F.G., Kenyon, S.C., Factor, J.K., Trimmer, R.G., Pavlis, N.K., Chinn, D.S., Cox, C.M., Klosko, S.M., Luthcke, S.B., Torrence, S.B., Wang, Y.M., Williamson, R.G., Pavlis, E.C., Rapp, R.H. and Olson T.R. (1998). The Development of the Joint NASA GSFC and the National Imagery and Mapping Agency (NIMA) Geopotential Model EGM96. Technical report, NASA/GSFC.
- SGN (1996). Spécifications du Réseau de Base Français. Version 2.2. Technical report nr. IT 152, Service de Géodésie et Nivellement, Institut Géographique National (in French).
- Sjöberg, L.E. (1998). The atmospheric geoid and gravity corrections. In: proc. of the 2nd Continental Workshop on the Geoid in Europe. Reports of the Finnish Geodetic Institute 98:4.
- Sjöberg, L.E. (2002). The ellipsoidal correction to Stokes's formula. In: "Gravity and Geoid 2002", proc. of the 3rd Meeting of the ICGC, Ziti editions.
- Tapley, B., Ries, J., Bettadpur, S., Chambers, D., Cheng, M., Condi, F., Gunter, B., Kang, Z., Nagel, P., Pastor, R., Pekker, T., Poole, S. and Wang, F. (2005). GGM02. An improved Earth gravity field model from GRACE. *J. Geod.*, 79, 467–478.
- Toustou D. (1991). Chaîne de validation interactive de données gravimétriques: DIVA. - Note technique n° 10, Bureau Gravimétrique International (in French).
- Tscherning C.C., Forsberg R. and Knudsen P. (1992). The GRAVSOFTE package. In: proc of the First Continental Workshop on the Geoid in Europe. Research Institute of Geodesy, Topography and Cartography, Prague, Czech Republic.

Application of Fuzzy Logic Theory to Geoid Height Determination

M. Yilmaz

Geodesy and Photogrammetry Engineering, Geodesy Division,
Harran University, Engineering Faculty, Osmanbey Campus, 63100, Sanliurfa, Turkey

E. Arslan

Geodesy and Photogrammetry Engineering, Geodesy Division,
Istanbul Technical University, Civil Engineering Faculty, 34469, Istanbul, Turkey

Abstract. Today, because satellite based positioning techniques such as GPS and GLONASS has a wide range use in practical geodetic applications, precise geoid determination became a major issue of geodesy. The reason for this, heights obtained with satellite measurements and conventional way are determined according to different referents surfaces. Ellipsoidal height can be determined with satellite measurements easily. However, in many geodetic applications instead of ellipsoidal heights, orthometric heights, reckoned from geoid, are required. Because orthometric and ellipsoidal heights are determined according to different surfaces, these two height systems are not collided each other and the difference between the systems are called geoid height or geoid undulation and geoid height is a transformation parameter used between the two systems. If geoid height could be determined precisely, orthometric heights can be obtained from ellipsoidal heights easily. Therefore, instead of conventional way of leveling, heights can be obtained with GPS measurements by saving time and money. In this study, geoid heights were determined by polynomial coefficients and Fuzzy logic (both Mamdani and Sugeno Fuzzy model) using data in Istanbul and effect of calculation methods of geoid height were examined.

Keywords. Geoid height, GPS, orthometric height, ellipsoidal height, Fuzzy logic, polynomial coefficients.

1 Introduction

The geoid is an equipotential (level) surface of the earth's gravity field which coincides with mean sea level (MSL) in the open oceans. As such, the geoid provides a meaningful reference frame for defining height. The importance of accurately modeling the geoid has increased in recent years with the advent

of satellite positioning systems such as the Global Positioning System (GPS). GPS provides height information relative to a best-fitting earth ellipsoid rather than the geoid (Seager (1999)). To convert ellipsoidal heights derived from GPS to conventional (and meaningful) orthometric heights, the relationship between the geoid and the ellipsoid must be known (Kotsakis and Sideris (1999)). The relation between ellipsoid, geoid and geoid height can be written following simple equation

$$H = h - N + \epsilon \quad (1)$$

where h are ellipsoidal heights obtained from GPS observations, H are orthometric heights derived from spirit leveling and gravimetry, N are geoid heights and ϵ are small quantities due to the deflection of the vertical and the curvature of the plumb line (Torge (1980)).

In this study, how to calculate geoid height by Fuzzy logic and polynomial coefficients are explained and a case study is performed. In the case study, Fuzzy models (Sugeno and Mamdani) and polynomial coefficients are used to determine geoid height. 200 points distributed in Istanbul (Turkey) are used to construct fuzzy models and to determine polynomial coefficients; on the other hand, 50 points are used to test of calculations. Calculations are interpreted, discussed and conclusion is drawn.

2 Gps/levelling Geoid Height Determination

The satellite based global positioning system Navstar-GPS (from now on referred to as GPS only) have had a tremendous impact on geodesy and surveying since its introduction some 20 years ago. The most widespread use of GPS in geodesy has, however, been on obtaining two dimensional positions, leaving the third dimension (height) out mainly because of the problems associated with

different reference systems. Heights obtained by GPS are above an ellipsoid and are fundamentally different from traditionally obtained heights which are given with respect to the geoid. Mathematically, there is a simple relation between the two reference systems (where we have neglected the deflection of the vertical and the curvature of the plumb line) and this simple relation was stated in equation 1.

In practice, the expression reflects the possibility of GPS leveling, because it states that if the geoid height N is known, the orthometric height H (or normal height, depending on the definition of the geoid, but hereafter referred to as orthometric height) can be obtained from ellipsoidal height h determined by GPS. Obtaining orthometric heights this way, could in certain circumstances, depending on the required accuracy, replace conventional spirit leveling and thus make the leveling procedure cheaper and faster (Mårtensson (2002)).

3 Determination of Geoid Height According to Polynomial Coefficients

Polynomial surface fitting is one of the most common methods used in surface fitting. The goal of this method is that study area is expressed only one function. Put it another way, with points which characterize the region and arguments (X, Y, N , or μ, λ, N) that required to solve problem, it is a determination of polynomial coefficients using model points to find geoid height at a point whose horizontal coordinates known in the region. Furthermore, polynomial coefficient is widely used as a trend surfaces in the study area in some methods such as Kriging and Collocation. Degree of polynomial is determined by highest degree term in a polynomial.

Surface is generally expressed with a two parameter high degree polynomial as equation (2) which is general expression of orthogonal polynomial

$$N(X, Y) = \sum_{k=0}^n \sum_{j=0}^k a_{ij} x^i y^j \quad (2)$$

where,

a_{ij} : unknown polynomial coefficients,

n : degree of polynomial,

x, y : horizontal or geographical coordinates of points.

If number of model points will be greater than number of polynomial coefficients to be determined, polynomial coefficients are determined

according to Least Square Method (LSM). More details can be found Yilmaz and Arslan (2005) and Ayan et al. (1999).

4 Fuzzy Logic

Fuzzy sets and fuzzy logic were developed to represent, manipulate, and utilize uncertain information and to develop a framework for handling uncertainty and imprecision in real-world applications (Lin et al. (2003)). Fuzzy logic systems provide an effective and accurate method for describing human perceptions.

Fuzzy logic provides an inference structure that enables approximate human reasoning capabilities to be applied to knowledge-based systems. The theory of fuzzy logic provides a mathematical strength to capture the uncertainties associated with human cognitive processes, such as thinking and reasoning. The conventional approaches to knowledge representation lack the means for representing the meaning of fuzzy concepts (Walid, 2005).

Some of the essential characteristics of fuzzy logic relate to the following (Zadeh (1984)):

- Exact reasoning is viewed as a limiting case of approximate reasoning.
- Everything is a matter of degree.
- Knowledge is interpreted a collection of elastic or, equivalently, fuzzy constraint on a collection of variables.
- Inference is viewed as a process of propagation of elastic constraints.
- Any logical system can be fuzzified.

In addition, there are also two main characteristics of fuzzy systems that give them better performance for specific applications:

- Fuzzy systems are suitable for uncertain or approximate reasoning, especially for the system with a mathematical model that is difficult to derive.
- Fuzzy logic allows decision making with estimated values under incomplete or uncertain information.

There are two fuzzy models used in practice. These are Mamdani fuzzy model and Sugeno fuzzy model.

4.1 Mamdani Fuzzy Model

The Mamdani Fuzzy model was proposed as the very first attempt to control a steam engine and boiler combination by a set of linguistic control rules obtained from experienced human operators. Mamdani fuzzy logic use the linguistic variables to

describe the process states and use these variables as input to control rules. Input variables are the basic of system. The terms of the linguistic variables are fuzzy sets with certain shape. It usually uses the trapezoidal or triangular fuzzy set but other shapes are possible.

Mamdani Fuzzy model can be formed in five steps and these are (www1 (2005));

- Fuzzify input: decide all fuzzy statements in the antecedent and get a degree of membership between 0 and 1.
- Apply fuzzy operator to multiple part antecedents: use the fuzzy logic operators and resolve the antecedent to a single number between 0 and 1. It is the degree of support for the rule.
- Apply implication method: use the degree of support for the rule to shape the output fuzzy set.
- Aggregate all Outputs: combine all the fuzzy sets that represent the outputs of each rule.
- Defuzzify: defuzzify the aggregate output fuzzy set into a single number.

Advantages and disadvantages of Mamdani Fuzzy model can be summarized as follow;

Advantages of the Mamdani Fuzzy method:

- It is simple to build.
- It is the basic of the other fuzzy method.
- It is suited to human feeling.

Disadvantages of the Mamdani Fuzzy method:

- It is too simple to control the process quickly and only suited to the long delay system, such as the temperature control system.
- When it controls the high frequent input system, it needs additional device to improve the efficiency.

4.2 Sugeno Fuzzy Model

The Sugeno fuzzy model (also known as the TSK Fuzzy model) was proposed by Takagi, Sugeno, and Kang (Sugeno and Kang (1988)), (Takagi and Sugeno (1985)) in an effort to develop a systematic approach to generating Fuzzy rules from a given input output data set. A typical Fuzzy rule in a Sugeno Fuzzy model has the form

If x is A and y is B then $z = f(x,y)$

Where A and B are Fuzzy sets in the antecedent, while $z = f(x,y)$ is a crisp function in the consequent. Usually $f(x,y)$ is a polynomial in the input variables x and y , but it can be any function as long as it can appropriately describe the output of the system within the Fuzzy region specified by the antecedent of the rule. When $f(x,y)$ is a first-order polynomial, the resulting Fuzzy inference system is called a first

order Sugeno Fuzzy model, which was originally proposed in Sugeno and Kang (1988), Takagi and Sugeno (1985). When f is a constant, we then have a zero order Sugeno Fuzzy model, which can be viewed either as a special case of the Mamdani Fuzzy inference system, in which each rule's consequent is specified by a Fuzzy singleton (or a prediffuzzified consequent).

Advantages of the Sugeno Fuzzy method (www1 (2005)); (www2 (2005));

- It is very suitable to compute
- It can use linear techniques to control the non-linear system.
- It can optimize the parameters of the output to improve the efficiency.
- It has the continuous output surface.
- It can be analyzed by mathematics.

Disadvantages of the Sugeno Fuzzy method (www2 (2005));

- It is not intuitive.
- When using the higher order Sugeno method, it is complex.

4.2.1 Adaptive Network Based Fuzzy Inference Systems

Adaptive Network based Fuzzy Inference Systems (ANFIS) are feed-forward adaptive networks which are functionally equivalent to fuzzy inference systems. The basic idea of ANFIS can be described as follows: A fuzzy inference system is typically designed by defining linguistic input and output variables as well as an inference rule base. However, the resulting system is just an initial guess for an adequate model. Hence, its premise and consequent parameters have to be tuned based on the given data in order to optimize the system performance. In ANFIS this step is based on a supervised learning algorithm (Jyh- Shing (1993)).

All types of fuzzy inference systems can be subjected to such a procedure. However, the complexity of the problem depends on the type of reasoning in the consequent part even if the results of all three types would not change significantly for the same data set. Therefore, in this section, Type-3 ANFIS is explained which is least complex and hence used for the prediction of the geoid heights. For simplicity, assume that the fuzzy inference system under consideration has two inputs x and y and one output f . Additionally, suppose that the rule base contains two fuzzy *if-then* rules of Takagi and Sugeno's type (Takagi and Sugeno (1983) as

Rule 1: If x is A_1 and y is B_1 ; then $f_1 = p_1x + q_1y + r_1$.
Rule 2: If x is A_2 and y is B_2 ; then $f_2 = p_2x + q_2y + r_2$.

Note that the node functions in the same layer are of the same function family (all circles without parameters or square nodes with parameters) (Akyilmaz et al. (2003)).

The functions of each layer can be described as below

Layer 1: Every node i in this layer is a square node with a node function

$$\begin{aligned} O_{1,i} &= \mu_{A_i}(x) \quad i=1,2 \\ O_{1,i} &= \mu_{B_{i-2}}(x) \quad i=3,4 \end{aligned} \quad (3)$$

where, x and y are the input to node i , and A_i is the linguistic label (small, medium, large, etc.) associated with this node function. In other words, $O_{1,i}$ is the membership function of A_i and it specifies the degree to which the given x satisfies the quantifier A_i . Usually, the membership function $\mu_{A_i}(x)$ is chosen to be bell-shaped with the maximum value equal to 1 and the minimum value equal to 0 such as, e.g., the generalized bell function

$$\mu_{A_i}(x) = \frac{1}{1 + \left[\left(\frac{x - c_i}{a_i} \right)^2 \right]^{b_i}} \quad i=1,2 \quad (4)$$

where, $\{a_i, b_i, c_i\}$ is the parameter set. As the values of these parameters change, the bell-shaped functions vary accordingly. Thus various membership functions on linguistic label A_i are defined. In fact, any continuous and piecewise differentiable functions, such as commonly used trapezoidal or triangular-shaped membership functions can also be considered as qualified candidates for node functions in this layer. Parameters in this layer are called “premise parameters” (Hines (1997)).

Layer 2: Every node in this layer is a circle node, which performs a fuzzy intersection operation on the incoming signals from the first layer and sends the result to the next layer.

For instance,

$$O_{2,i} = w_i = \mu_{A_i}(x) \cdot \mu_{B_i}(y) \quad i=1,2 \quad (5)$$

Layer 3: Every node in this layer is a circle node such that the i -th node calculates the ratio of the i -th

rule’s firing strength to the sum of all rules’ firing strengths as

$$O_{3,i} = \bar{w}_i = \frac{w_i}{w_1 + w_2} \quad i=1,2 \quad (6)$$

Outputs of this layer can be called normalized firing strengths.

Layer 4: Every node in this layer is a square node with a node function that calculates the output for corresponding rules weighted by its normalized firing strength such that

$$O_{4,i} = \bar{w}_i f_i = \bar{w}_i (p_i x + q_i y + r_i) \quad i=1,2 \quad (7)$$

where, \bar{w}_i is the output of the previous layer (layer 3), and $\{p_i, q_i, r_i\}$ is the set of parameters which are called “consequent parameters” (Jyh-Shing (1995)).

Layer 5: The single node in this layer is a circle node that computes the overall output by using the weighted average defuzzification method as

$$O_{5,i} = f = \frac{\sum_i \bar{w}_i f_i}{\sum_i \bar{w}_i} \quad i=1,2 \quad (8)$$

5 Used Data

In this study 200 points whose latitude, longitude, ellipsoidal and orthometric heights known in Istanbul (Turkey) region are used to construct fuzzy models and to determine polynomial coefficients for the region. The points are homogenously distributed in Istanbul and point density is nearly one point in 25 km². Data covers the region between 41°29′ 11″.07 > φ > 40° 45′ 11″.46 and 29° 41′ 50″.69 > λ > 27° 57′ 36″.02. RMSE value of ellipsoidal height precision of data is nearly ± 3.5 cm (Ayan et al. (1999)). To check for the calculations 50 points which had not been included in fuzzy models are used.

6 Results

Using 200 model points two different fuzzy models were constructed. The first Fuzzy model was constructed according to Sugeno type and the second one was according to Mamdani type. Both

Fuzzy models were two inputs (Latitude and longitude) and one output (geoid heights). Inputs were divided five subsets and triangular membership function was used in the two Fuzzy models. Both fuzzy model calculations were performed using fuzzy toolbox in Matlab. 200 model points were also used to determine significant polynomial coefficients for region. A fifth degree polynomial coefficient was determined for the region. Three coefficients were eliminated after significance test.

Results of the two fuzzy models and fifth degree polynomial coefficients in both model and test data can be seen in Table 1.

Table 1. Results of geoid height calculated by Sugeno, Mamdani and polynomial coefficient in both model and test points.

Model Data			
Method	Min (cm)	Max (cm)	RMSE (cm)
Sugeno	-0.0907	0.0831	0.0304
Mamdani	-0.4384	0.4480	0.1368
Polynomial	-0.0992	0.0907	0.0396
Test Data			
Sugeno	-0.0968	0.0928	0.0385
Mamdani	-0.2709	0.2218	0.1103
Polynomial	-0.0960	0.1040	0.0404

When the results in table 1 were examined, it can be seen that Mamdani type of Fuzzy model gave the worst RMSE which were ± 0.1368 and ± 0.1103 cm in both model and test data respectively. Although Sugeno type of Fuzzy model results were the best of all, fifth degree polynomial coefficients results were also fairly good results especially the used data quality and data density. Fuzzy model was trained with model data according to hybrid method (least square adjustment was used to determine premise parameters and neural network was used to find error distribution and consequent parameters) in Sugeno type of Fuzzy model. On the other hand, the model was not trained with model data in Mamdani type of Fuzzy model. Mamdani type of Fuzzy model took more time to build than Sugeno type because the span of each subset of every input had to be determined by user and rules were formed by user in Mamdani type. However, determination of span of subsets of inputs and rules were formed automatically in Sugeno type. Geoid height errors in test data for the three calculation methods can be seen in Fig. 1 and Fig. 2.

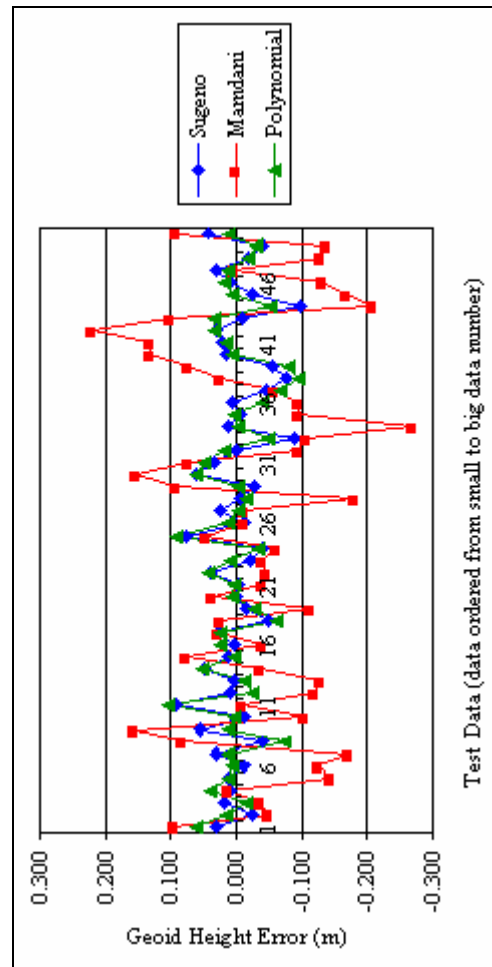


Fig. 1 Graphical representation of geoid height errors in test data for three calculation methods.

7 Conclusion and Recommendation

Geoid height is a transformation between orthometric (traditional way of leveling) and ellipsoidal (obtained from satellite measurements) height. Therefore geoid determination became a major problem of geodesy recently. In this study, geoid heights were determined using three different methods. These methods were Mamdani and Sugeno type of fuzzy models and a fifth degree polynomial coefficient method. Sugeno type of fuzzy modeling gave the best results because it was possible to form trained fuzzy model. It was also easy to construct. However, Mamdani type of fuzzy model took too much time to form and gave the worst results of all. Polynomial coefficient method gave very good results according to data quality. Geoid determination method, data density and data

quality were the factors effecting geoid height precision.

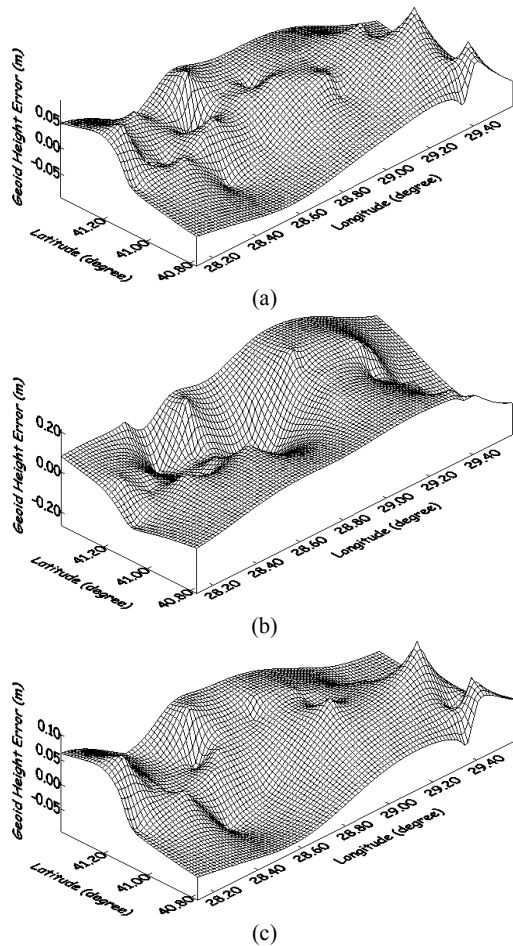


Fig. 2: Geoid height error at test points determined by (a) Sugeno Fuzzy (b) Mamdani Fuzzy and (c) 5th degree polynomial coefficients

References

- Akyılmaz, O., Ayan, T., and Özlüdemir, T. (2003). Geoid surface approximation by using Adaptive Network Based Fuzzy Inference Systems, AVN p. 308 – 315.
- Ayan, T., Aksoy, A., Deniz, R., Arslan, E., Çelik, R.N., Özşamli, C., Denli, H., Erol, S., Özöner, B. (1999). Istanbul GPS network technical report, ITU Civil Engineering Faculty, Department of Geodesy and Photogrammetry Engineering, Istanbul.
- Hines, J.W. (1997). MATLAB supplement to Fuzzy and neural approaches in engineering, John Wiley & Sons Inc, New York.
- Jyh- Shing, R. J. (1993). ANFIS: adaptive – network based fuzzy inference system, IEEE Transactions on systems, man, and Cybernetics, 23, No:3, 665-685.
- Jyh- Shing, R. J. (1995). Neuro–fuzzy modelling and control, Proceedings of the IEEE, 83, No:3, 378-406.
- Kotsakis, C., Sideris, M.G. (1999). On the adjustment of combined GPS/levelling/ geoid networks. J Geod 73:412–421.
- Lin, J. W.; Hwang, M. I.; and Becker, J. D. (2003). “A fuzzy neural network for assessing the risk of fraudulent financial reporting”, Managerial Auditing Journal 18/8 pp 657-665.
- Mårtensson, S.G. (2002). Height Determination by GPS – Accuracy with Respect to Different Geoid Models in Sweden, FIG XXII International Congress Washington, D.C. USA, April 19-26.
- Seager, J., Collier, P., and Kirby, J. (1999). Modelling geoid undulations with an artificial neural network. IIEEE, International Joint Conference on Volume 5, 10-16 July Page(s):3332 – 3335.
- Sugeno, M., and Kang, G.T. (1988). Structure identification of Fuzzy model, Fuzzy Sets and Systems, Vol. 28, pp. 15-33.
- Takagi, T., and Sugeno, M. (1983). Derivation of fuzzy control rules from human operator’s control actions. Proc. Of the IFAC Symp. on Fuzzy Information, Knowledge Representation and Decision Analysis, 55-60.
- Takagi, T. and Sugeno, M. (1985). Fuzzy identification of systems and its applications to modeling and control, IEEE Trans. Systems, Man, and Cybernetics, Vol. 15, pp. 116-132.
- Torge, W. (1980). Geodesy. Walter de Gruyter, Berlin.
- Walid, A. H. (2005). “Accuracy Enhancement of Integrated MEMS-IMU/GPS Systems for Land Vehicular Navigation Applications”, *Ph. D. Thesis*, Department of Geomatics Engineering, University of Calgary, Calgary, Alberta, Canada.
- Yılmaz, M., and Arslan, E. (2005). Effect of point density on geoid height determination, 10th Turkish Mapping Scientific and Technical Congress, Ankara.
- Zadeh, L. (1984). “Making Computers Think Like People”, IEEE Spectrum, Vol.(7), pp 26-32.
- www1: <http://www.cems.uwe.ac.uk/~xzhang/PDF/MSc/Fuzzy%20Logic.pdf>. (08/09/2005).
- [www2: <http://www.mathworks.com/access/helpdesk/help/toolbox/fuzzy/> (11/10/2005).

A new Taiwanese geoid model based upon airborne, satellite and terrestrial gravimetric data

A. Ellmann

Department of Geodesy and Geomatics Engineering, University of New Brunswick, Fredericton, Canada
Department of Civil Engineering, Tallinn University of Technology, Ehitajate tee 5, Tallinn, Estonia

C. Hwang, Y-S. Hsiao

Department of Civil Engineering, National Chiao Tung University, 1001 Ta Hsueh Road, Hsinchu, Taiwan

Abstract. A new airborne gravity survey was conducted over Taiwan in 2004-2005. The survey results in conjunction with existing terrestrial, marine and satellite altimetry data are used for creating a consistent $2' \times 2'$ grid of gravity anomalies referred to the Earth's surface. For this, the gravity anomalies observed at the flight level are downward continued to the topographic surface. After the gridding, to solve the boundary value problem (BVP) by Stokes's formula, the surface gravity anomalies are continued further to the sea level. The inverse of Poisson's integral formula is used at these steps. The effects of topographic masses are estimated by applying Helmert's second condensation method. A modified Stokes's formula is used for evaluating the short wavelength geoid contribution, whereas the long wavelength geoid information stems from a recent GRACE-based geopotential model. The effect (in terms of geoidal heights) of inclusion the airborne data exceeds one metre over the mountainous part of Taiwan.

Keywords: airborne gravimetry, BVP, downward continuation, Helmert condensation,

1 Introduction

Over the past years several geoid models have been computed over Taiwan, see Hwang (1997) and references therein. Recent geoid computations employed the so-called 'remove-compute-restore' (r-c-r) principles and have been carried out by the GRAVSOF (Tscherning et al., 1992) software. According to this method the residual terrain model (RTM) gravity effect and the long wavelength gravity field from the EGM96 (Lemoine et al., 1998) model are removed from the surface-related free-air anomalies. The Fourier transform and least-squares collocation were used to transform these residual gravity anomalies into the residual geoid. After adding to it the RTM contribution and the EGM96 based reference spheroid one arrives at the quasi-geoid model, which is then converted into geoidal heights. Note that in these computations the integration is preceded by the unmodified Stokes

function and the full expansion (i.e. up to degree 360) of the EGM96 is used. The estimation of the residual topographical effects is based on the planar approximation of the topography.

This contribution aims at summarizing the application of the Stokes-Helmert approach for computing a new geoid model for Taiwan. It should be noted that the Stokes-Helmert principles deviate quite a lot from those applied in earlier studies. Due to space limitations, however, their comparison with the r-c-r scheme is considered to be outside the scope of this study. Instead, the focus here is on incorporating the airborne data into the geoid determination procedure. Second, the recent improvements of the gravity data in the global scale have significant computational implications for regional geoid modelling as well. In this context a typical computational set-up with employing up-to-date (e.g., GRACE-based) geopotential models (GGM) for regional modelling is revisited.

We continue with a general summary of the Stokes-Helmert geoid modelling principles. A brief description of the characteristics of the target area and available data is given in Section 3. As is well known these factors may impose important constraints to geoid modelling. Computation of the Helmert anomalies and their downward continuation is tackled in Section 4. Some aspects of the anomaly gridding and solving Stokes's BVP are described in Sections 5 and 6, respectively. The effect of inclusion the airborne data is shown in Section 7. A brief summary concludes the paper.

2 Stokes-Helmert's geoid modelling principles

The solution of the BVP by Stokes's method requires gravity observations that refer to the geoid. The gravity measurements are taken at the topographic surface or even above it. Thus, to satisfy the boundary condition the gravity anomalies need to be downward continued (DWC) to the geoid level. To ensure harmonicity of the quantities to be downward continued a number of different corrections related to the existence of topography and atmosphere need be introduced. As is well

known the evaluation of the topographical effects is one of the most serious limits in precise geoid modelling nowadays.

One way of estimating the effect of topographical masses is to use Helmert's second condensation model. According to this model a condensation layer located on the geoid replaces the Earth's topographical masses. So "Helmertized" gravity field can be downward continued to the geoid level, where it will be decomposed into low- and high-frequency parts. The long wavelength geoid information comes from the adopted GGM, whereas the short-wavelength part is obtained from the Stokesian integration over a limited domain. The truncation bias that occurs due to neglecting the remote zone is mitigated by modifying Stokes's formula. For more details on Stokes-Helmert scheme, see e.g., Vaniček and Martinec (1994), Martinec (1998), Vaniček et al. (1999) and references therein. A recent review can also be found in Ellmann and Vaniček (in press).

3 Target area and gravity data

The geographical limits of the target area are 21.5° and 25.5° northern latitudes, and 119.5° and 122.5° eastern longitudes (i.e. an area of 440 x 300 km²), see Fig. 1. The new geoid model comprises the whole of Taiwan together with a large portion of surrounding waters. Taiwan's terrain is complex and mostly inaccessible for conventional gravity survey. Over 75% of Taiwan's terrain is covered with hills and high mountains, with the highest point being nearly 4000 m. Here the existing gravity data are sparsely distributed and there have been uncertainties in the gravity datum and the coordinate system associated with point gravity data (Hwang et al., in press). Obviously, the shortages of the data in the (mountainous) centre of the target area affect negatively the reliability of the overall geoid determination results.

In order to enhance the spatial resolution of gravity data both on land and sea, an airborne gravity survey campaign was carried out in 2004-2005 over Taiwan using a LaCoste & Romberg air-sea gravimeter. The average flight altitude was 5156 m, the survey area (~75,000 km²) covers the major part of the target area (for an illustration see e.g., Hwang et al., in press, Fig. 1). The overall airborne gravity accuracy is estimated to be 2 mGal at a spatial (half wavelength) resolution of 6 km. A more detailed report of the survey particulars and quality assurance can be found in Hwang et al. (in press).

Recall, that the main objective of this study is to investigate the geoid improvements due to inclusion of the new airborne gravity data. For the sake of comparison two new geoid models are computed. The first model will be based on the existing

terrestrial, marine and satellite altimetry gravity data, hence to be referred to as *NoAirborne* geoid model. The second model combines exactly the same data-sets plus airborne gravity data. This model is referred to as *Airborne* geoid model.

The computational scheme of the *Airborne* geoid model is as follows: (i) DWC the airborne data to the earth's surface; (ii) construct the existing and airborne data into a uniform grid at the earth's surface; (iii) DWC the anomaly grid to the geoid level; (iv) Stokesian integration on the geoid level. The computational scheme for the *NoAirborne* model begins from step (ii). Since both models employ the Stokes-Helmert principles then their discrepancies indicate the geoid improvements due to the inclusion of the new airborne gravity data.

4 Downward continuation of Helmert's anomaly

4.1 Helmert's anomaly

Application of the Helmert reduction yields a new gravity field, which becomes slightly different from the actual gravity field. As a result, the corresponding Helmert anomalies, $\Delta g^h(r, \Omega)$, differ from the commonly used free-air anomalies, $\Delta g(r, \Omega)$. The relation between the two anomaly types can be expressed as (cf. Vaniček et al., 1999):



Fig. 1. Distribution of the terrestrial and marine gravity data-points in the target area (enclosed by the rectangle). The white polyhedral bounds the mountainous area (average $H > 1200$ m), where the airborne data will be used for the gridding.

$$\Delta g^h(r_f, \Omega) = \Delta g(r_f, \Omega) + \frac{\partial [V^t(r_f, \Omega) - V^{ct}(r_f, \Omega)]}{\partial r} + \frac{2}{r_f(\Omega)} [V^t(r_f, \Omega) - V^{ct}(r_f, \Omega)] + e_{ellips}(r_f, \Omega) \quad (1)$$

where $V^t(r, \Omega)$ and $V^{ct}(r, \Omega)$ are the potentials of topographic masses and condensation layer, respectively. The geocentric position (r, Ω) is represented by the geocentric radius $r(\Omega)$ and a pair of geocentric coordinates $\Omega = (\varphi, \lambda)$, where φ and λ are the geocentric spherical coordinates. All the quantities in Eq. (1) are referred to the flight level, $r_f(\Omega) = r_g(\Omega) + 5156$ m, where $r_g(\Omega)$ is the geocentric radius of the geoid surface. The term $e_{ellips}(r_f, \Omega)$ represents the ellipsoidal correction, which accounts for the deviation of the actual shape of the Earth from the spherical approximation of the fundamental gravimetric equation (for more details see, Vaniček et al., 1999). The formulation of the topographic terms in Eq. (1) employs the spherical approximation (Martinec, 1998). They can be evaluated by using the topographic elevation/density models in some numerical quadrature method (see e.g., Martinec, 1998). More specifically, the integration domain is usually divided among different element sizes, with small as possible elements close to the computation point. The topographic effects are estimated by using a new 3"x3" Taiwanese digital elevation model, it serves also as a basis for generating the sets of 30"x30" and 2'x2' mean heights, which are used for more distant masses with respect to the computation points.

Note that the atmospheric effects are neglected in Eq. (1). This due to the fact that the IAG atmospheric correction (Moritz, 1992) is already considered in the Taiwanese gravity data.

The gravity field over Taiwan is fairly complicated due to various regional geophysical phenomena. Recall also that the free-air anomalies are strongly correlated with the topography. Therefore, even at the flight altitude, the free-air anomalies are rather powerful, ranging from +257 to -173 mGal. It should be noted, however, that the corresponding Helmert anomaly field (obtained by Eq. (1)) is somewhat smoother than the initial free-air anomalies.

4.2 Downward continuation

Since the Helmert condensation has (numerically) removed the masses above the geoid then the Helmert anomaly can be continued all the way down to the geoid level (conversely, this is not the case for the free-air anomaly!). However, here we want to halt at the earth's surface. Recall that step (ii) aims

at combining the downward continued data points with the existing terrestrial data-points to form a uniform data grid at the earth's surface. Note, however, that the terrestrial data is of good quality and sufficiently dense in lowland (coastal) regions. Therefore the downward continued data will be used only in the regions above 1200 m.

In this study the downward continuation is solved by using the Poisson equation (Heiskanen and Moritz, 1967, p. 317). This integral formula had been originally designed as a formula for the upward continuation of harmonic quantities. In practice the integration is replaced by a summation over a regularly spaced grid of geographical coordinates. The resolution of the air-borne survey allows forming a 2'x2' anomaly grid, which thereafter will be used for downward continuation.

Importantly, the gridding helps to overcome the following shortage. Namely, the Poisson downward continuation is known to be an unstable problem. Due to the instability, existing errors in $\Delta g^h(r_f, \Omega)$, may appear magnified in the solution. However, when mean values (obtained from gridding) are used instead of point values, this problem is somewhat alleviated, as the mean values do not exhibit the highest frequencies (Sun and Vaniček, 1998). For solving Poisson's formula it is expressed as a system of linear equations (cf. Martinec, 1996):

$$\Delta \mathbf{g}^h(r_f, \Omega) = \mathbf{K}[r_f, \mathcal{Y}(\Omega, \Omega'), r_i] \Delta \mathbf{g}^h(r_i, \Omega') \quad (2)$$

where $\Delta \mathbf{g}^h(r_f, \Omega')$ is the vector of Helmert's anomaly at the flight altitude (5156 m), $\Delta \mathbf{g}^h(r_i, \Omega')$, is the vector of the gravity anomalies referred to an i -th layer with a geocentric radius r_i , $\mathbf{K}[r_f, \mathcal{Y}(\Omega, \Omega'), r_i]$ is the matrix of the values of the Poisson integral kernel multiplied by the area of integration element, $\psi(\Omega, \Omega')$ is the geocentric angle between the computation and integration points. Downward continuation is an inverse problem to the original Poisson integral. The matrix-vector form of Poisson's equation can then be used for solving the inverse problem, i.e. computing the unknown elements of the vector $\Delta \mathbf{g}^h(r_i, \Omega)$.

It is assumed that r_i in Eq. (2) represents the geocentric radius of a horizontal layer, which is also parallel to the geoid surface. Recall, that the product of the Helmert anomaly and geocentric radius, $\Delta g^h \cdot r$, is harmonic (Vaniček et al., 1996), and therefore such a field can be downward continued to any elevation within the interval of $r_g < r_g + H < r_f$.

Layer-wise DWC will be used to form a number of horizontal (2D) anomaly grids at different altitudes (the separation between the adjacent layers is set to 200 m) as follows. Since the mean 2'x2'

heights over Taiwan do not exceed 3400 m then the uppermost grid of downward continued gravity anomalies is formed at $H = 3400$ m. The next grid of gravity anomalies is formed at 3200 m. Further on, similar 2D grids are formed at the altitudes 3000 m, 2800 m, etc. all the way down to 1200 m. Remember, for each layer the Helmert anomalies at the flight level serve as initial values. In other words a 3D structure, a mesh, consisting of 14 horizontal layers is formed. The anomaly values at topographic surface points ($1200 < H < 3400$ m) are predicted by a simple “sandwich”-grid 3D interpolation. The resulting Helmert anomalies are referred to the surface of the Earth, $r_i(\Omega) = r_g(\Omega) + H(\Omega)$.

It should be noted that other strategies of combining different data-sets are still being tested and the results will be reported on in proper time. For instance, an alternative scheme is considered: (i) separate DWC of the airborne and terrestrial data-points to the geoid level; (ii) forming a uniform grid of gravity anomalies at the geoid level; (iii) using this grid for solving the BVP.

5 Gridding of anomalies

Many numerical procedures at geoid modelling require gravity/topographic data on regularly spaced grid of geographical coordinates. Within the target area the total number of the terrestrial, marine and satellite altimetry (KMS02 was used, see Anderson and Knudsen, 1998) gravity points exceeds 10000. The average number of gravity points per one degree square is about 1000 (1 point per 10 km²), which suggests that a 2'x2' grid resolution is a reasonable choice. The gridding is proceeded by a NCTU collocation program, whereas different weights are assigned for different data types.

Gridding is a critical issue, because any error committed at this stage will directly propagate into the geoid solution. Within the frame of an experiment, not described here, the gridding for the *NoAirborne* model was proceeded with the free-air anomalies. Better interpolation results, however, are usually achieved by using the smoother Bouguer anomalies. Therefore the *Airborne* model utilises the complete spherical Bouguer anomalies (Vaniček et al., 2004) for gridding. This anomaly is also called as *NoTopography* (NT) anomaly, since the attraction of the global topography has been completely subtracted from the “full” gravity. The complete spherical Bouguer anomaly is hence a smoother quantity than the simple or refined (planar) Bouguer anomalies. A more detailed discussion on the used gridding approach is spared for a forthcoming paper. The resulting grids of the NT-anomalies (*Airborne* scheme) and free-air anomalies (*NoAirborne*

scheme) are converted into surface-related Helmert anomalies, see Eq. (1). $\Delta g^h(r, \Omega)$ are thereafter downward continued to the geoid level. The same approach is used as described in Section 4.2, whereas the symbols r_f and r_i in Eq. (2) need to be replaced by r_t and r_g , respectively.

6 Solution to Stokes's boundary value problem

The Helmert gravity anomalies on the geoid level serve as an input when solving the Stokes boundary value problem. Strictly speaking, the original Stokes formula requires gravity anomalies over the entire Earth (Ω_0). In practice, however, the area of availability of anomalies is limited to some spatial domain (Ω_{ψ_0}) around the computation point. The truncation bias (that occurs when the remote zone, $\Omega_0 - \Omega_{\psi_0}$, is neglected in the integration) can be reduced by modifying Stokes's formula (Molodensky et al., 1960). This study employs the generalized Stokes scheme (cf. Vaniček and Sjöberg, 1991), which uses the long wavelength part of a GGM as follows:

$$N(\Omega) = \frac{V^t(r_g, \Omega) - V^c(r_g, \Omega)}{g_0(f)} + \frac{R}{2g_0(f)} \sum_{n=2}^M \frac{2}{n-1} \Delta g_n^h + \frac{R}{4pg_0(f)} \iint_{\Omega_{\psi_0}} S^M(y_0, y, (\Omega, \Omega')) \left(\Delta g^h - \sum_{n=2}^M \Delta g_n^h \right) d\Omega', \quad (3)$$

where R is the mean radius of the Earth; the modified Stokes function $S^M(y_0, y, (\Omega, \Omega'))$, can be computed according to Vaniček and Kleusberg (1987); $g_0(f)$ is the normal gravity (a function of latitude) at the reference ellipsoid, $d\Omega'$ is the area of the integration element. Note also that the used geopotential coefficients need first to be Helmertised to compute the harmonics $\Delta g_n^h(r_g, \Omega)$. For more details see Vaniček et al. (1995).

The Stokesian integration with Helmert's residual anomalies (i.e. the last term on the right hand side of Eq. (3)) results in the Helmert residual co-geoid. Since the low-degree reference gravity field is removed from the anomalies before the Stokes integration, then the long-wavelength geoid information, i.e. the reference spheroid of degree M (see Heiskanen and Moritz, 1967, p. 97), is added to the residual geoid.

As already noted, the condensation of the topographic masses causes the Helmert potential to become slightly different from the actual potential. Consequently, also the Helmert co-geoid does not

exactly coincide with the real geoid. The effect causing this change is called primary indirect topographic effect. Thus, the first term in the right hand side of Eq. (3) transfers the Helmert co-geoid into the actual geoidal heights.

The selection of the upper limit, M , which is used for defining the reference spheroid/anomaly and the modified Stokes function, $S^M(y_0, y, (\Omega, \Omega'))$, is important in geoid modelling. The following criteria were considered at the selection of the suitable limit (M) and corresponding integration radius ψ_0 . Obviously, the regional geoid models are also dependent, among other factors, on the quality of the used GGM. Recall that the high-degree GGM-s are determined from a combination of satellite data and terrestrial gravity data. This combination implies that the reference GGM and $Dg^h(r, \Omega)$ in Eq. (3) could be correlated with each other. One may want to avoid this undesirable feature. Therefore it is recommendable to use the “satellite-only” harmonics for computing the reference quantities in Eq. (3).

A new combination model EIGEN-CG03C (Förste et al., 2005) is based on the CHAMP mission and the global surface data, but takes also into account 376 days of the GRACE twin-satellites tracking data. The EIGEN-CG03C spherical harmonics are developed up to degree/order 360/360, which corresponds to a spatial resolution of 110 km. The EIGEN-CG03C “satellite-only” field is developed up to degree/order 150/150. However, the user of a GGM should not consider the “satellite-only” harmonics as an errorless dataset, especially at the higher degrees. Therefore one cannot increase the modification limit in Eq. (3) all the way up to maximum available spherical harmonic degree. For instance, the EIGEN-CG03C developers estimate an 1 cm accuracy in geoid modelling with a spectral resolution up to degree/order 75/75. For more details see the original publication.

Various aspects need to be considered when selecting the integration radius. Generally, a compromise is needed to balance between the shortages of the low- and high-degree parts of the gravity data. Fig. 1 demonstrates that the limited extension (especially to the west from the target area) of the gravity data is the most serious constraint for the present study.

The choice of $y_0 = 1.5^\circ$ is the basis for determining the upper modification limit M . According to an approach in Featherstone et al. (1998) we want the modified Stokes function $S^M(y_0, y, (\Omega, \Omega'))$ to become zero at the edge of the integration cap. The kernel is enforced to zero at $y_0 = 1.5^\circ$ with $M = 90$. This is satisfactory to us, since at the degree 90 the correlation between the EIGEN-CG03C-derived and terrestrial datasets is completely prevented. Even though this limit exceeds somewhat the sub-cm accuracy expectation, it is tolerable due

to limited availability of the regional gravity data. To eliminate the edge effect the gravity anomalies outside of the target area (where available) were also included into Stokes’s integration.

It should be noted, however, that in the case of sufficient data coverage a larger integration radius in conjunction with a smaller modification limit could provide more reliable results.

7 Discrepancies between the *Airborne* and *NoAirborne* geoid models

The resulting discrepancies between the *Airborne* and *NoAirborne* geoid models range between -1.1 and $+2.3$ m. Naturally, the largest discrepancies occur over the mountains, more specifically, inside the loops of the terrestrial gravity survey. Obviously, the new airborne gravity data has affected significantly the resulting geoid model. Note also that at the closest vicinity of the terrestrial survey loops the discrepancies remain relatively small.

Recall, also that different types of gravity anomalies were used for gridding of the *Airborne* and *NoAirborne* models. Therefore, the discrepancies between the *NoAirborne* and *Airborne* geoid models are not only due to inclusion of the airborne data, but also due to adoption of different anomaly types for gridding. This is in agreement with a recent study by Janák and Vaníček (2005), who demonstrate that different gridding strategies may have a significant effect (up to 1-2 metres) on the geoidal heights.

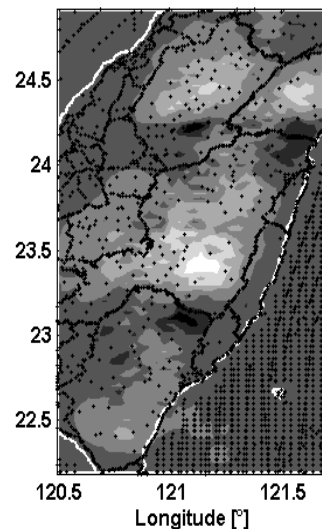


Fig. 2. Discrepancies between the two geoid models (“*NoAirborne*” minus “*Airborne*”) over the central part of Taiwan. The discrepancies range from -1.1 m (the darkest region) to $+2.3$ m (the brightest region). Black dots denote the locations of the point gravity data (downward continued airborne gravity points are not shown).

8 Summary and further studies

This contribution presents results for the effect of inclusion the airborne data on anomaly gridding over the mountainous parts of Taiwan, and the corresponding effects on geoid heights. Stokes-Helmert's geoid determination principles were applied for computing two new geoid models over Taiwan. The emphasis was given to the downward continuation of the harmonic Helmert anomaly and solving Stokes's BVP by using up-to-date GRACE-based reference models. We conclude, that the downward continued airborne gravity data in conjunction with surrounding terrestrial measurements are useful for geoid improvements over the areas with insufficient coverage of terrestrial data.

Evidently, the region of interest, due to its very complicated geophysical conditions, appears to be very challenging in the context of the geoid modelling. Geoid modelling in Taiwan is a continuous effort and the goal is to achieve a cm-level accuracy everywhere in Taiwan. Hence, the results here are only a part of the on-going work. Future studies include: (i) validation of the geoid models by using high-precision GPS-levelling data; (ii) comparisons with earlier geoid models in order to detected the most suitable geoid approach (e.g., r-c-r vs. Stokes-Helmert) (iii) usage of different reference models (e.g., EGM96 vs. GRACE-based models) and modification limits; (iv) application of different gridding approaches. Furthermore, another airborne gravity survey campaign (the flight altitude ~1500 m) was carried out over the Kuroshio Current east of Taiwan in 2006. It is of interest to utilise the new results in the Taiwanese geoid determination as well. The results of the aforementioned studies will be reported in forthcoming papers.

Acknowledgements This study is funded by the Ministry of Interior, Taiwan, under the project "Airborne gravity survey in Taiwan". The prime author is supported by the European Union Structural Funds, Project # 1.0101-0335.

References

- Andersen OB, Knudsen P (1998) Global Marine Gravity Field from the ERS-1 and GEOSAT Geodetic Mission Altimetry, *Journal of Geophysical Research*, **103(C4)**, 8129-8137.
- Heiskanen WH, Moritz H (1967) *Physical geodesy*. Freeman and Co, San Francisco.
- Ellmann A, Vaniček (in press) UNB application of Stokes-Helmert's approach to geoid computation. Accepted by: *Journal of Geodynamics*.
- Featherstone WF, Evans JD, Olliver JG (1998) A Meissl modified Vaniček and Kleusberg kernel to reduce the truncation error in gravimetric geoid determination. *Journal of Geodesy*, **72**, 154-160.
- Förste C, Flechtner F, Schmidt R, Meyer U, Stubenvoll R, Barthelmes F, König R, Neumayer KH, Rothacher M, Reigber C, Biancale R, Bruinsma S, Lemoine JM, Raimondo JC (2005) *A New High Resolution Global Gravity Field Model Derived From Combination of GRACE and CHAMP Mission and Altimetry/Gravimetry Surface Gravity Data*. A Poster presented at EGU General Assembly 2005, Vienna, Austria, 24-29, April.
- Hwang C (1997) Analysis of some systematic errors affecting altimeter-derived sea surface gradient with application to geoid determination over Taiwan. *Journal of Geodesy*, **71**, 113-130.
- Hwang C, Hsiao Y-S, Shih H-C, Yang M, Chen K-H, Forsberg R, Olesen AV (in press): Geodetic and geophysical results from a Taiwan airborne gravity survey: Data reduction and accuracy assessment. Accepted by: *Journal of Geophysical Research - Solid Earth*.
- Janák J, Vaniček P (2005) Mean free-air gravity anomalies in the mountains. *Studia Geophysica et Geodaetica*, **49**, 31-42.
- Lemoine FG, Kenyon SC, Factor JK, Trimmer RG, Pavlis NK, Chinn DS, Cox CM, Klosko SM, Luthcke SB, Torrence MH, Wang YM, Williamson RG, Pavlis EC, Rapp RH, Olson TR (1998) *The Development of Joint NASA GSFC and the National Imagery and Mapping Agency (NIMA) Geopotential Model EGM96*. NASA/TP-1998-206861, Greenbelt, MD.
- Martinec Z (1996) Stability investigations of a discrete downward continuation problem for geoid determination in the Canadian Rocky Mountains. *Journal of Geodesy*, **70**, 805-828.
- Martinec Z (1998) *Boundary value problems for gravimetric determination of a precise geoid*. Lecture notes in Earth sciences, Vol. 73, Springer, Berlin, Heidelberg, New York.
- Molodensky MS, Yeremeev VF, Yurkina MI (1960) *Methods for Study of the External Gravitational Field and Figure of the Earth*. TRUDY TsNIIGAIK, 131, Geodezizdat, Moscow. English transl.: Israel Program for Scientific Translation, Jerusalem 1962.
- Moritz H (1992) Geodetic Reference System 1980. *Bulletin Géodésique*, **66**, 187-192.
- Sun W, Vaniček P (1998) On some problems of the downward continuation of the 5' x 5' mean Helmert gravity disturbance. *Journal of Geodesy*, **72**, 411-420.
- Tscherning CC, Forsberg R, Knudsen P (1992) The GRAVSOFIT package for geoid determination. *Proceedings of the First Continental Workshop on the Geoid in Europe*, Prague, pp. 327-334, Springer-Verlag, New York.
- Vaniček P, Kleusberg A (1987) The Canadian geoid – Stokesian approach. Compilation of a precise regional geoid. *Manuscripta Geodaetica*, **12**, 86-98.
- Vaniček P, Sjöberg LE (1991) Reformulation of Stokes's Theory for Higher Than Second-Degree Reference Field and Modification of Integration Kernels. *Journal of Geophysical Research*, **96(B4)**, 6529-6339.
- Vaniček P, Martinec Z (1994) The Stokes-Helmert scheme for the evaluation of a precise geoid. *Manuscripta Geodaetica*, **19**, 119-128.
- Vaniček P, Najafi M, Martinec Z, Harrie L, Sjöberg LE (1995) Higher-degree reference field in the generalised Stokes-Helmert scheme for geoid computation. *Journal of Geodesy*, **70**, 176-182.
- Vaniček P, Sun W, Ong P, Martinec Z, Najafi M, Vajda P, Horst B (1996) Downward continuation of Helmert's gravity. *Journal of Geodesy*, **71**, 21-34.
- Vaniček P, Huang J, Novák P, Pagiatakis SD, Véronneau M, Martinec Z, Featherstone WE (1999) Determination of the boundary values for the Stokes-Helmert problem. *Journal of Geodesy*, **73**, 160-192.
- Vaniček P, Tenzer R, Sjöberg LE, Martinec Z, Featherstone WE (2004) New views of the spherical Bouguer gravity anomaly, *Geophysical Journal International*, **159**, 460-472.

Artificial Neural Network versus Surface Polynomials for Determination of Local Geoid

H. S. Kutoglu

Department of Geodesy and Photogrammetry,
Zonguldak Karaelmas University, 67100, Zonguldak, Turkey

ABSTRACT. National heights systems throughout the world are referenced to the geoid whereas heighting by GPS directly results in ellipsoidal heights. These GPS-defined ellipsoidal heights have to be transformed into the national height systems. In practice, the surface polynomials are the most practical method to perform the transformation. Because of advances in computer science, surveyors have had an alternative method, the artificial neural networks, to the surface polynomials. In this study, these two methods are compared to each other using the data from Istanbul, Turkey. The investigations carried out show that the neural network method provides comparable results in modeling general characteristics with the conventional polynomial, but better results in modeling local characteristics.

Keywords. Ellipsoidal height, orthometric height, geoid, surface polynomials, neural networks

1 Introduction

The GPS-defined ellipsoidal heights have to be transformed into the national height systems which are referenced to the geoid. A sufficiently accurate relationship between ellipsoidal (h) and geoid-referenced orthometric heights (H) is established by the following formula (Bomford, 1965; Vanicek and Krakiwsky, 1982; Torge, 1991):

$$h = H + N \quad (1)$$

where N is the ellipsoid-geoid separation which is also called geoid height or geoid undulation.

In this equation, the geoid heights at survey points need to be known to achieve the height transformation. For local applications, they can be interpolated successfully by low order surface polynomials using GPS/leveling control points (Illner and Jager, 1995; Collier and Croft, 1997). Apart from this, there are many other methods which have been frequently used and some of them

like trigonometric transformation (Heiskanen and Moritz, 1967) are rather old. Another method which has been widely used during the last few decades is Least-Squares Collocation. Recently developed methods are the Second-Generation wavelets and Artificial Neural Networks (see Duquenne et al., 2004; Iliffe et al., 2003; Kotsakis and Sideris, 1999; Soltanpour et al., 2006; Featherstone and Sproule, 2006; Kavzoglu and Saka, 2005).

In this study, we deal with Artificial Neural Network (ANN) method alternative to the surface polynomials for the interpolation of geoid heights. Although these two methods were compared by Kavzoglu and Saka (2005), they had been applied to the simplest training function of ANN. Today, more advanced methods and training functions are available for ANN. In addition, while the performances of the methods in their study were measured only by the root mean squared error (rmse) further analyses are employed in this study to compare both methods. Last but not least, the methods that they used unusually resulted in better approximations for the test points than the common points used for estimating the model parameters. The reason of that might be insufficient or over-controlled selection of the test points. For this investigation much more common point and much more test point are used. The data have been provided from a project carried out for renewing the geodetic infrastructure of Istanbul which is the most populated city in Turkey. With this project conducted by Istanbul Technical University, 650 points were positioned by GPS technique in ITRF94. To obtain orthometric heights in the Turkish national height system, leveling measurements were carried out for 453 of 650 points, and thus common points were produced for modeling the geoid in Istanbul locality called "local geoid" below (ITU, 2000). 100 points among them are randomly chosen as the check points to test the responses of both methods, used in this study, to the new points. Of course, the remaining 353 points are used for modeling the geoid (Fig. 1 and 2).

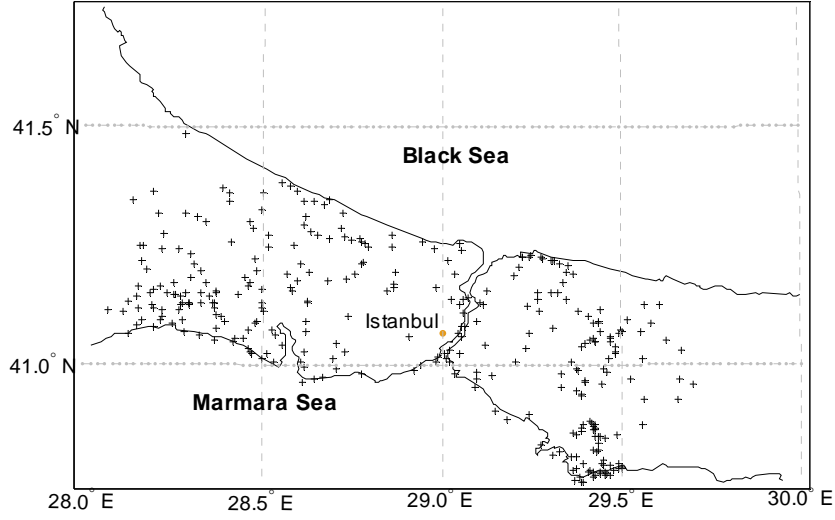


Fig. 1 Common points

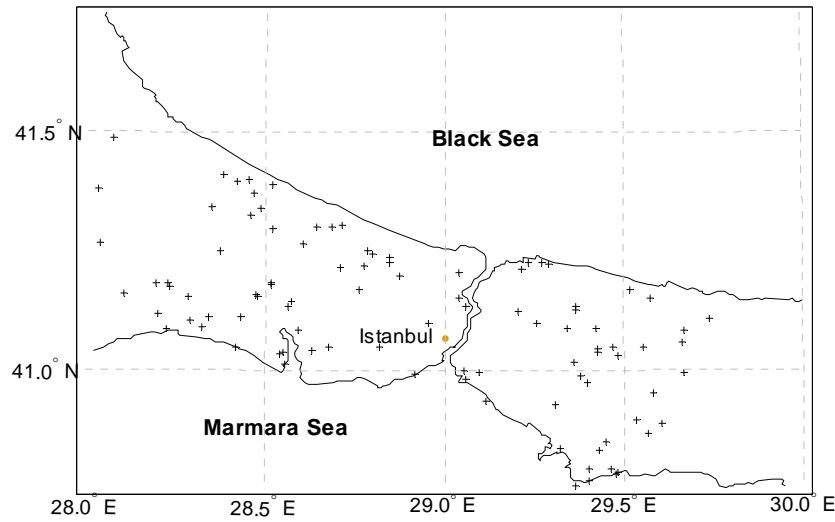


Fig. 2 Check points

2 Local Geoid by Surface Polynomials

For the interpolation of geoid heights, the equation of surface polynomials can be given by

$$N = \sum_{i=0}^k \sum_{j=0}^i a_{i-j,j} u^{i-j} v^j \quad (2)$$

where u and v represent position coordinates, a_{ij} symbolize the polynomial coefficients, and k is the

degree of polynomials. In this study, the position coordinates are obtained from the ellipsoidal geographical coordinates as follows

$$u = (\varphi - \varphi_0) / \sigma_\varphi, \quad v = (\lambda - \lambda_0) / \sigma_\lambda \quad (3)$$

where φ_0 and λ_0 are the arithmetic averages of latitude and longitude with the standard deviations σ_φ and σ_λ , respectively.

For the Istanbul data, the degree of the surface polynomials has been set 9 at first, but 9th order polynomials has been led to erratic results for the check points. Whereupon the degree of the polynomials has been decreased to 5 step by step which gives the most reasonable results. In Table 1, the statistically significant coefficients of the 5th order polynomial obtained from the common points are shown. Having applied these coefficients to the

common points the results obtained are plotted to give the contour map of local geoid in Fig. 3.

The comparison of the polynomial model values with the known heights are resulted in errors with the standard deviation of 4.2 cm which range from -10.81 cm to 11.26 cm. When the surface polynomials are applied to the check points the errors range from -146.92 cm to 35.84 cm. The standard deviation of the check point errors is 21.34 cm.

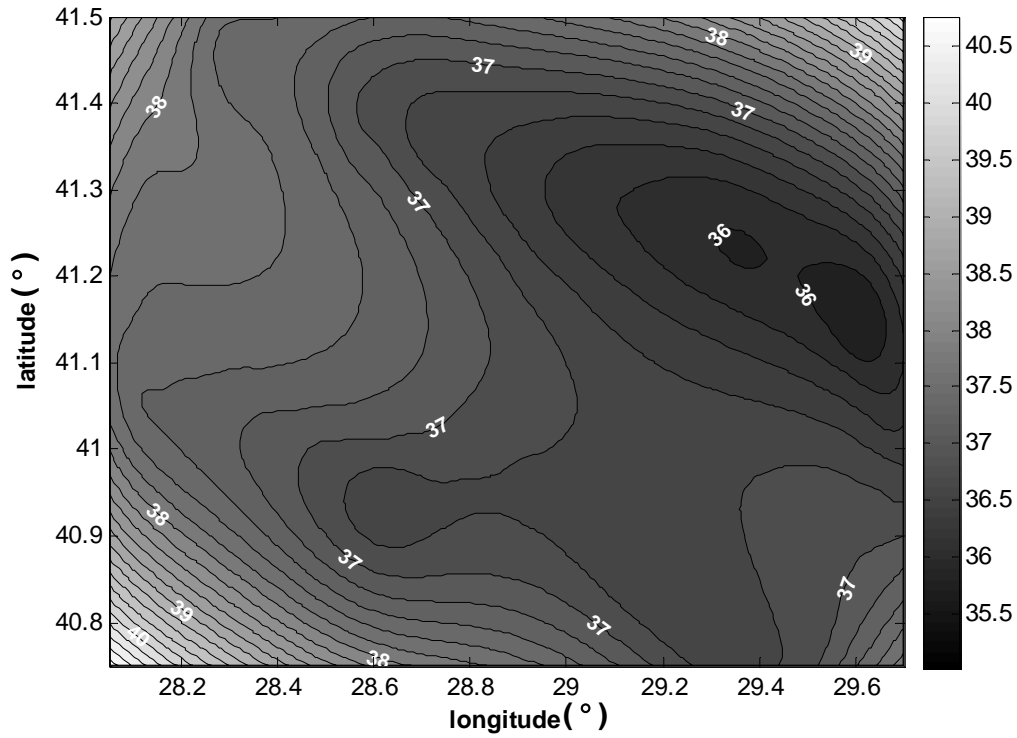


Fig. 3. Local geoid from 5th order surface polynomials

Table 1. Parameters of the surface polynomials obtained

Parameter	Value	Parameter	Value	Parameter	Value
a_{00}	36.911 ± 0.007	a_{30}	-0.012 ± 0.008	a_{04}	-0.059 ± 0.005
a_{10}	0.028 ± 0.011	a_{12}	-0.028 ± 0.021	a_{50}	0.016 ± 0.006
a_{01}	-0.545 ± 0.014	a_{03}	0.209 ± 0.018	a_{41}	0.108 ± 0.020
a_{20}	-0.292 ± 0.012	a_{40}	-0.009 ± 0.007	a_{32}	0.209 ± 0.025
a_{11}	-0.556 ± 0.012	a_{31}	-0.065 ± 0.019	a_{23}	0.090 ± 0.019
a_{02}	0.075 ± 0.012	a_{22}	-0.057 ± 0.016	a_{14}	-0.041 ± 0.013
				a_{05}	-0.065 ± 0.006

3 Local Geoid by Neural Networks

Neural Network method is an artificial intelligence technology which imitates human brain. This method is based on learning events using available samples and thus generating proper responses to new samples. The learning process is achieved by artificial neurons. General architecture of neural networks is composed of input, output and hidden layers. With respect to the problem, a neural network can be composed of many hidden layers which may contain a different number of neurons; however, in approximation problems one hidden layer usually suffices. Each neuron in a layer is connected to the neurons in the next layer through weights. The weighted sums of the neuron outputs in a layer are the inputs of the neurons for the next layer. In each neuron, the accepted input is added to the bias of the relevant neuron, and passed from a predefined activation function to produce the outputs. This process is continued as far as the output layer. The responses obtained in the output layer are then compared to the known sample values. Depending on the success in fitting of the responses to the sample values, all the weights of the network are altered through a predefined training function based on a specific learning rule. Using the new weights, the new responses are produced by the network. This procedure is carried on until the network produces responses that provide a predefined goal of a performance function, or reaches the maximum epoch number, or the number of maximum failure (Rumelhart et al., 1986; Hagan et al., 1996).

In this study, a neural network with one hidden layer is designated for modeling the local geoid surface of Istanbul. Its input layer contains two neurons to enter the position coordinates u and v into the network system. Of course, the output layer consists of one neuron to get the responses for the geoid heights. As for the hidden layer, the number of its neurons is determined as twenty four using the following equation offered in (Otto, 1995):

$$m = \frac{p}{5(n+s)} \quad (4)$$

where m is the number of neurons, p is the number of elements in the data set used in training, and n and s are the numbers of input and output neurons, respectively. The network which occurs after these settings up is displayed schematically in Fig. 4.

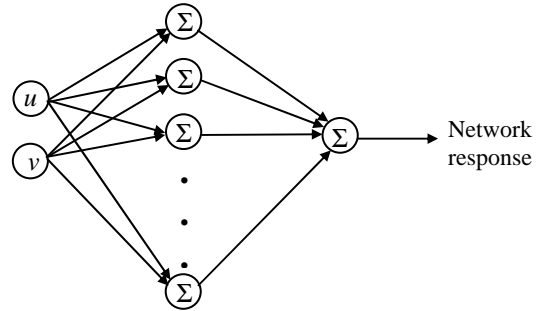


Fig. 4. Scheme of the neural network

This network is designed as a feedforward type of network which uses the backpropagation learning rule. For training function, the Levenberg-Morquardt function is applied. As usually applied in establishing networks for function approximation, the tangent sigmoid and linear activation functions are employed in the hidden and output layers, respectively.

The network is repeatedly trained by the common points until an optimum solution which is accomplished at the 35th iteration resulted in a mean square error (mse) of 1.2×10^{-3} . After the training process, the network is employed to compute the geoid heights of the common points. Fig. 5 displays the contour lines of local geoid using the geoid heights of the common points obtained from the network. According to the figure, the local geoid from the neural network is uneven in comparison to the one from the surface polynomials.

When the model values are compared with the known geoid heights the errors are found to range from -10.12 cm to 11.22 cm, and to deliver the standard deviation of 3.4 cm. As to the check points, applying the neural network is resulted in the errors with the standard deviation of 15.62 cm, which extend from -71.43 cm to 31.05 cm.

3 Discussion and Results

Based on the statistics given in Table 2, it can be said that both methods provides comparable solutions for the common points. The minimum and maximum values, ranges and absolute mean values of the errors obtained from each model are very close to each other. Their standard deviations are also in quite good agreement. In addition to these

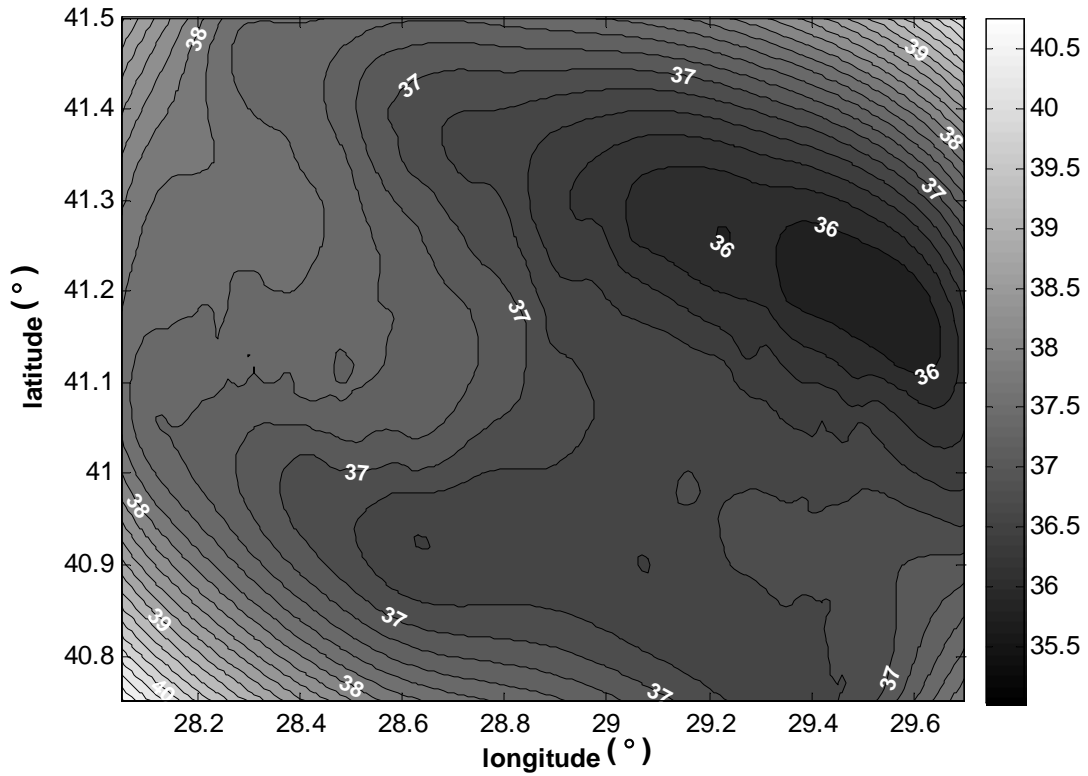


Fig. 5. Local geoid from neural network

statistics, the fitting index values, also known as coefficient of determination, take place in the table. Fitting index is an indicator from 0 to 1 (or presented as percentage) that reveals how closely the estimated values (\hat{y}_i) from an approximation model corresponds to the actual data (y_i), and obtained from

$$r^2 = \frac{\sum_i (\hat{y}_i - \bar{y})^2}{\sum_i (y_i - \bar{y})^2} \quad (5)$$

where \bar{y} is the mean value of the actual data (Chapra and Canale, 2002). As seen from the table the fitting index values for the common points confirm that the both methods have provided well approximations. However, if a comparison has to be made between the methods, the neural network is favored in terms of the whole statistics of the common points against the surface polynomials.

As for the check points, the error ranges of the polynomial and neural network models are about eight and five times larger than those obtained from the common points, respectively. Four times worse

absolute mean values are obtained from both methods. The errors of the check points from both models are resulted in about five times worse standard deviations. The fitting indexes are also lowered in comparison with the common points.

Table 2 Some statistics from the common and check points

	Polynomial		Neural Net	
	Common points	Check points	Common points	Check points
Min. (cm)	-10.81	-146.92	-10.12	-71.43
Max. (cm)	11.26	35.84	11.22	31.05
Range (cm)	22.07	182.76	21.34	102.48
Abs. mean (cm)	3.39	12.05	2.66	11.05
Std. dev. (cm)	4.21	21.34	3.40	15.62
Fitting ind. (%)	99.09	81.27	99.59	72.76

When comparing two methods, the surface polynomials is better only in fitting index although it is regarded as comparable to the neural network. This situation can be explained in that the general characteristics of the data has been approximated better by the surface polynomials while local characteristics by the neural network.

4 Conclusions

Based on these analyses above, comparable approximations for the common points are obtained from both of the methods. For the check points, the neural network gives better error range, absolute mean and standard deviation but the polynomial method provides relatively better fitting index. This means that the neural network is better in modeling local characteristics while the conventional method is better in modeling general ones.

At this point, practitioners must decide what they need: only a better fitting to general or a comparable fitting to general but also a better fitting to local. When making a decision flexibility in designing a neural network should be accounted for. For instance, hundreds of training using different methods of ANN, such as “radial basis networks” and “generalized regression networks”, and/or different number of neurons in the hidden layer have been carried out; however, only one which gives the best results has been brought into view in this study.

Finally, in the light of the findings above, it can be said that the neural network method is a practical alternative to the surface polynomials for local applications of geoid determination. Besides being an alternative, one may consider to combine both methods in a proper way, and to gather their strengths together.

Acknowledgement

The author would like to thank the Department of Geodesy and Photogrammetry at Istanbul Technical University for providing the data used in this study. Special thanks go to Prof. Dr. Tevfik Ayan.

References

- Bomford, B. G. (1965). *Geodesy*, Oxford University Press, Oxford.
- Chapra, S.C., Canale, R.P. (2002). *Numerical Methods for Engineers : with Software and Programming Applications*, The McGraw-Hill, New York.
- Collier, P.A., Croft, M.J. (1997). Height from GPS in an Engineering Environment. *Survey Review*, 34, 11-18.
- Duquenne H, Everaerts M, Lambot P (2004) Merging a gravimetric model of the geoid with GPS/levelling data: an example in Belgium, in: Jekeli C, Bastos L, Fernandes J (eds) *Gravity, Geoid and Space Missions*, Springer, Berlin Heidelberg New York, 131-136
- Featherstone WE, Sproule DM (2006) Fitting AUSGeoid98 to the Australian height datum using GPS data and Least squares collocation: application of a cross validation technique, *Survey Review*, Vol. 38 No. 301.
- Heiskanen W, Moritz H (1967). *Physical Geodesy*. Freeman, San Francisco
- Hagan, M. T., Demuth, H. B., Beal, M. H., (1996). *Neural Network Design*. PWS Publishing Company, Boston.
- Iliffe JC, Ziebart M, Cross PA, Forsberg R, Strykowski G, Tscherning CC (2003) OGS02: a new model for converting GPS-derived heights to local height datums in Great Britain and Ireland. *Survey Review* 37(290): 276-293
- Illner, M. R., Jäger, R. (1995). Integration von GPS-Höhen ins Landesnetz-Konzept und Realisierung im Programmsystem HEIDI. *Allg. Verm. Nachr.*, 102, 1-18.
- (ITU) Istanbul Technical University (2000). *Report on GPS Control Network Project of Istanbul Metropolitan Area*. Technical report, Istanbul.
- Kavzoglu T, Saka MH (2005) Modelling local GPS/levelling geoid undulations using artificial neural networks. *Journal of Geodesy* 78(9):520-527.
- Kotsakis J, Sideris MG (1999) On the adjustment of combined GPS/levelling/geoid networks. *Journal of Geodesy* 73:412-421.
- Otto, (1995). Identifikation Nichtlinearer Systeme mit Künstlichen Neuronalen Netzen, *Automatisierungstechnik*, 3(2), 62-68.
- Rumelhart, D. E., McClelland, and the PDP Research Group (1986). *Parallel Distributed Processing*, Vol. I, The M.I.T. Press, Cambridge.
- Soltanpour A, Nahavandchi H, Featherstone WE (2006) The use of second-generation wavelets to combine a gravimetric quasigeoid model with GPS-levelling data. *Journal of Geodesy* 80: 82-93
- Torge, W. (1991). *Geodesy*, Walter de Gruyter, New York.
- Vanicek, P., Krakiwsky, E. J. (1982). *Geodesy: The Concepts*, North-Holland Publishing Company, Oxford.

Astrogeodetic Validation of Gravimetric Quasigeoid Models in the German Alps - First Results

Christian Hirt, Institut für Erdmessung, Universität Hannover, Schneiderberg 50, 30167 Hannover, Germany
E-mail: hirt@mbox.ife.uni-hannover.de Fax: +49 511 762 4006

Heiner Denker, Institut für Erdmessung, Universität Hannover, Germany

Jakob Flury, Institut für Astronomische und Physikalische Geodäsie (IAPG), TU München, Germany

Andreas Lindau, Physikalisch-Technische Bundesanstalt, Braunschweig, Germany

Günter Seeber, Institut für Erdmessung, Universität Hannover, Germany

Abstract. In regions with a rough topography, e.g. the European Alps, the accuracy of geoid or quasigeoid models is often reduced. For the validation and accuracy assessment of gravimetric models, astronomical levelling is a well-suited independent method. In a test area, located in the German Alps, a new astrogeodetic data set was acquired using the Hannover Digital Zenith Camera System. Vertical deflections were determined at 100 new stations (spacing about 230 m) arranged in a profile of 23 km length. Repeated observations at 38 stations in different nights reveal an observational accuracy of about 0''08. In order to precisely interpolate the vertical deflection data between adjacent stations, topographic reductions of the observed deflections are carried out using a high-resolution digital terrain model. A least squares prediction approach is applied for the interpolation of a dense profile of deflection data. Eventually, the topography effect is restored. By computing the normal correction, the deflection data is reduced to the quasigeoid domain. The accuracy of the computed astrogeodetic quasigeoid profile is estimated to be at the millimeter-level. The available quasigeoid models, namely the German Combined Geoid GCG2005, the Digital Finite Height Reference Surface DFHRS and the quasigeoid by IAPG (TU Munich), are in agreement with the high-precision astrogeodetic quasigeoid profile by about 8 mm, 20 mm and 4 mm (RMS), respectively. A comparison of the astrogeodetic profile with GPS/levelling data yielded differences of 10 mm.

Keywords. Digital Zenith Camera System, vertical deflection, astrogeodetic quasigeoid profile, local quasigeoid evaluation

1 Introduction

During the recent years, considerable advances have been made in the astrogeodetic determination of the gravity field with Digital Zenith Camera Systems (Hirt 2004, Hirt and Bürki 2002). These new mea-

surement systems provide vertical deflection data accurate to 0''08-0''1 at a typical observation time of about 20 min per station. Besides regional applications, e.g. the combined gravity field determination in mountainous areas (e.g. Brockmann et al. 2004), vertical deflections may be used in the method of astronomical levelling in order to determine local geoid and quasigeoid (QG) profiles. Astrogeodetic vertical deflections represent independent observables which can be used for comparison with gravity field models based on gravimetric computation techniques. Provided that vertical deflection data is precisely observed at densely distributed stations and the interpolation between the observation sites is done with sufficient accuracy, astronomical levelling provides the shape of the local gravity field with an accuracy at the millimeter level over distances of about 10-20 km (section 4). As a consequence, astrogeodetic gravity field profiles may be used for the local validation and accuracy assessment of gravimetric gravity field models.

The aim of this work is the validation of different gravimetric QG models by a new set of astrogeodetic vertical deflections. The astrogeodetic data was determined in a test area, located in the German Alps, using the Hannover Digital Zenith Camera System TZK2-D (section 2). Due to the rough Alpine topography, the location is considered to represent a kind of area where gravity field models tend to show a reduced precision (e.g. Denker et al. 2003). The main focus of the paper is put on the thorough computation of the astrogeodetic QG profile. Different aspects are covered such as the role of Digital Terrain Model (DTM) data for topographic reductions, interpolation of the observed deflection data and the transition from the observations to the QG applying the normal correction (section 3). The computed astrogeodetic profile is suited for comparison with GPS/levelling data and gravimetric gravity field models (section 5). In order to avoid any dependencies of the results on density hypotheses, the comparison is restricted to the QG domain.

2 Astrogeodetic Observations

In autumn 2005, the Digital Zenith Camera System TZK2-D was used for extensive vertical deflection measurements at 103 new stations which are arranged in a profile. It is oriented in good approximation in North-South direction. Located in the Isar valley near the Ester mountains, the profile starts at the lake Walchensee, crosses Mittenwald and ends near the German-Austrian borderline. The profile length is about 23.3 km and the average station spacing is approximately 230 m.

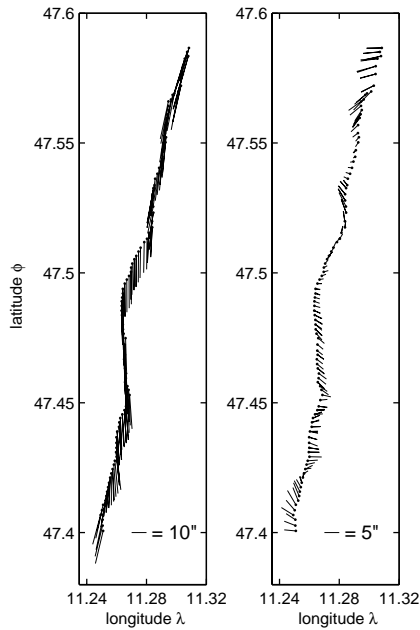


Figure 1. Observed vertical deflection data (left: original data, right: data centered to mean values)

The collection of the vertical deflection data was completed during a total observation period of 4 weeks. The observed data sets were processed using the Hannover astrogeodetic processing system AURIGA (Hirt 2004). The celestial reference was provided by the new high-precision UCAC and Tycho-2 star catalogues (for details see e.g. Zacharias et al. 2000). The campaign and processing statistics are given in Table 1.

Due to the good weather conditions during the campaign, about 38 stations were observed twice in different nights. The standard deviation obtained from the differences is found to be $0''.082$ both for ξ and η . These accuracy estimates agree well with values from other astrogeodetic measurement campaigns with the same instrument, cf. Hirt and Seiber (2005) or Hirt (2006). The distribution of TZK2-D stations and the acquired (ξ, η) -data is shown in

Station count	103
Double occupations (in different nights)	38
Station count per night	5-17
Single observations (total)	6700
Single observations (per station)	48
Processed UCAC stars (total)	589000
Processed UCAC stars (per station)	4180

Table 1. Statistics of the astrogeodetic measurement campaign 2005 in the German Alps

Fig. 1 in vector representation. The vertical deflection field (left part) is obviously dominated by a North-South trend showing the strong gravitational influence of the masses of the central Alps located South of the profile. The right part illustrates the structure of the observations after centering to their mean values. Thereby the largest portion of the attraction of the central Alps is removed and the gravitational attraction of the local topography becomes visible, illustrating the ability of the high-precision measurement system TZK2-D for observation of the fine structure of the gravity field.

3 Astrogeodetic QG Computation

The basic principle of astronomical levelling is to integrate vertical deflections (ξ, η) along a path from station 1 to station n (cf. Torge 2001):

$$\varepsilon = \xi \cos \alpha + \eta \sin \alpha \quad (1)$$

$$\Delta\zeta_{1n} = - \int_1^{n-1} \frac{\varepsilon_i + \varepsilon_{i+1}}{2} ds_{i,i+1} - E_{1n}^N \quad (2)$$

where ε is the deflection component given in the azimuth α of the section ds between adjacent stations. The term E_{1n}^N , referred to as normal correction or normal height reduction, reduces the vertical deflection data to the QG with the result that QG height differences $\Delta\zeta_{1n}$ are obtained. Evaluating the integral given in Eq. 2 presupposes a dense coverage of vertical deflection stations along the path so that the deflection data may be interpolated linearly – with sufficient accuracy – between adjacent stations (cf. Torge 2001). Such a dense coverage is particularly important in case of rough topography.

3.1 Interpolation of Deflection Data

The variation of observed vertical deflections $(\xi, \eta)_{obs}$ originates to a large extent from the gravitational forces of the local topographic masses (cf. Fig 1). DTM data may be used for the computation of topographic vertical deflections $(\xi, \eta)_{top}$, e.g. by applying the prism method (cf. Forsberg and Tscherning 1981, Denker 1988, Flury 2002). A topographically reduced set of vertical deflections shows

a much smoother behaviour than the observed surface data. It is suited for interpolation of deflection data $(\xi, \eta)_{prd}$ at intermediate stations, applying techniques such as least squares prediction.

For the topographic reduction of the observed deflection data $(\xi, \eta)_{obs}$ a local high-resolution DTM (spatial resolution of 50 m, area coverage of 50 km x 60 km) was provided by the surveying authority of the state Bavaria. It was used for the computation of a set of topographic vertical deflections $(\xi, \eta)_{top}$ at the TZK2-D stations and, in addition, at 9 intermediate points between each pair of observed stations, yielding an average station spacing of about 23 m. A comparison between the least squares interpolation and a simple linear interpolation of surface deflections (without using DTM data) yielded a QG difference of about 1 mm over a distance of 1 km at the beginning of the profile where the topography is extremely rugged. Therefore the simple linear interpolation approach does not meet the accuracy requirements of this work.

Fig. 2 (a) exemplarily shows the topographic deflection component ξ_{top} as well as the ξ_{obs} data derived from the TZK2-D observations for a part of the profile¹. Note that both data sets show a high-degree of correlation, reflecting the sensitivity of the astrogeodetic observations for the attraction of the local topographic masses. Fig. 2 (b) illustrates the very smooth behaviour of the topographically reduced deflection $\Delta\xi$ after removing the topographic effect from the observations. Figure 2 (c) shows the same quantity $\Delta\xi$, plotted however at a larger vertical scale. The topographically reduced deflection $\Delta\xi$ serves as input data set for the least squares prediction approach that decomposes the reduced deflection $\Delta\xi$ into a filtered component $\Delta\xi_{fil}$ and a residual noise vector ε_ξ . The residual noise vector (Fig. 2 (d)) contains random errors of the astrogeodetic observations and uncertainties attributable to the DTM data. The standard deviation computed from the noise vector is found to be $0''085$ for ξ and $0''082$ for η . It is considered to be a further confirmation of the high accuracy of the astrogeodetic observations presented in this paper.

For the set of intermediate points (about 900), the described interpolation approach provides predicted values $\Delta\xi_{prd}$. In the last step the topographic effect is restored. The obtained dense data set of predicted vertical deflections $(\xi, \eta)_{prd}$ shows a linear behaviour between each pair of adjacent stations (cf. Fig. 2 (e)). It is suited for integration along the path

¹Due to the restricted space, the prediction results for the component η are not depicted. They are found in Hirt and Flury (2006).

using the basic equation 2. For a detailed study on the combination of high-precision vertical deflection data and DTM data the reader is referred to Hirt and Flury (2006).

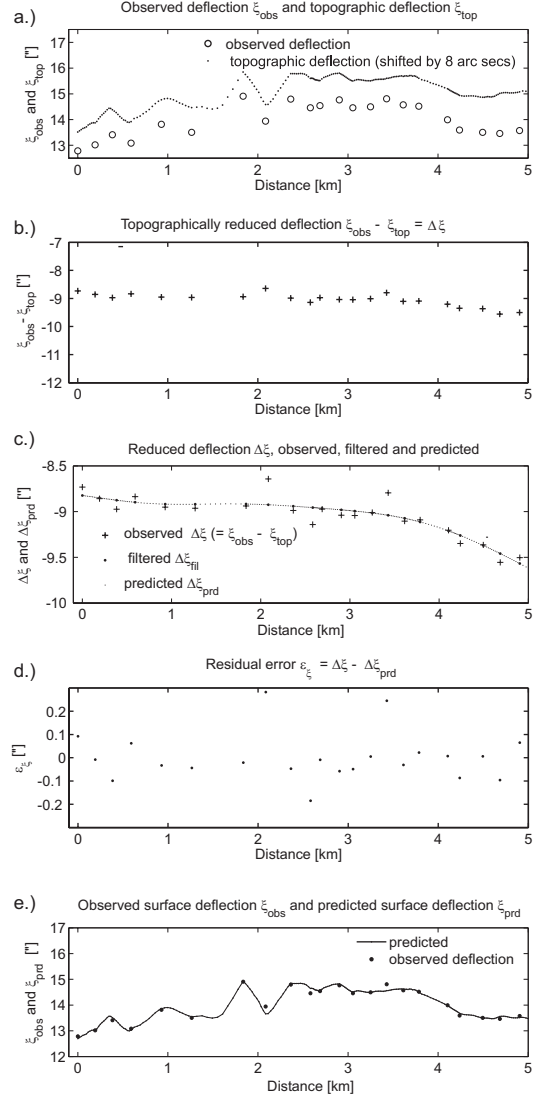


Figure 2. Least squares interpolation approach. (a): observed deflection ξ_{obs} and topographic deflection ξ_{top} . The latter is shifted by $8''$ for better visualization. (b): reduced deflection $\Delta\xi = \xi_{obs} - \xi_{top}$ (after removing the topographic influence from the observations). (c): reduced deflection ξ and predicted values at intermediate points. (d): noise vector ε_ξ . (e): result of the restitution: a dense profile of predicted surface deflection data $\xi_{prd} = \Delta\xi_{prd} + \xi_{top}$. Note that the peaks, e.g. apparent in (a) and (e) at distances 0.4 km, 1 km or 1.8 km, originate not from density anomalies but from azimuthal changes in the integration path. In astronomical levelling, peak-like structures are typical features when the stations are not exactly arranged in a straight line.

3.2 Normal Correction

The normal correction E_{1n}^N , which is also known from geometric levelling, is applied for the rigorous reduction of the vertical deflection data to the QG (cf. Torge 2001, p. 251):

$$E_{1n}^N = \int_1^n \frac{g - \gamma_0^{45}}{\gamma_0^{45}} dn + \frac{\bar{\gamma}_1 - \gamma_0^{45}}{\gamma_0^{45}} H_1 - \frac{\bar{\gamma}_n - \gamma_0^{45}}{\gamma_0^{45}} H_n. \quad (3)$$

The computation of the normal correction E_{1n}^N requires the knowledge of the surface gravity g along the profile, the height above mean sea level of the first station H_1 and last station H_n and the height differences dn between adjacent stations. The heights H_1, H_n and dn may be derived from DTM data. The mean normal gravity $\bar{\gamma}_1, \bar{\gamma}_n$ at the profile's first and last station as well as γ_0^{45} (arbitrary constant value) are computed using standard formulae of the normal gravity field (cf. Torge 2001, p. 106 and 112).

Today, the surface gravity g may be conveniently derived from gravity databases because the corresponding prediction accuracy of a few mgal meets already the requirements as shown below, and gravimetric measurements would imply additional expenses. Two different databases were used for providing the surface gravity g along the profile. The first one was created at the Physikalisch-Technische Bundesanstalt PTB (Braunschweig, Germany) and is mainly based upon digitized Bouguer anomaly contour maps. The second database is the one of the IAPG (TU Munich) which consists of a very dense set of gravity measurements (density of 2.5 points/km²) in the test area (cf. Flury 2002). A comparison between the predicted gravity values from both databases with ground truth gravity at 30 stations yielded accuracy estimates of about 2 mgal (PTB) and better than 0.5 mgal (IAPG). Fig. 3 shows the two normal correction profiles E_{1n}^N (PTB) and E_{1n}^N (IAPG), which were independently computed based on gravity predictions from both databases. The difference, depicted in the lower part of Fig. 3, shows that the normal correction is accurate to 0.1-0.15 mm. Hence the accuracy of the predicted gravity is completely sufficient for the QG computation.

3.3 Astrogeodetic QG Profile

Following Eqs. 1-2, the astrogeodetic QG profile is obtained. It is shown in Fig. 4.

4 Accuracy Assessment

Before doing the comparison with the gravity field models it is useful to assess the accuracy of the astrogeodetic QG profile. The observed astrogeodetic

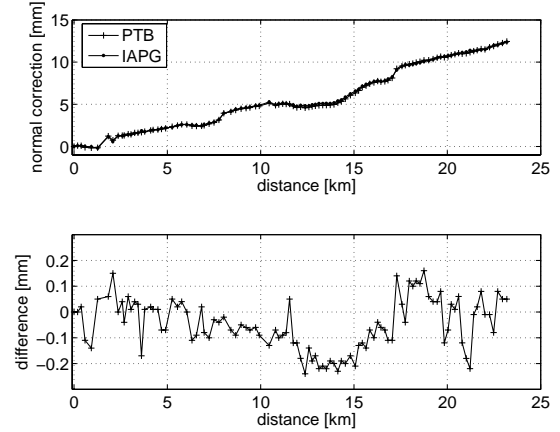


Figure 3. Normal correction of the astrogeodetic profile

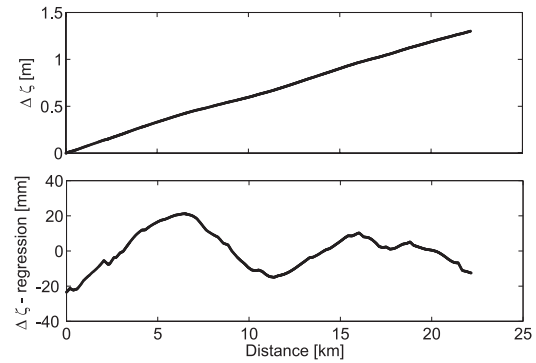


Figure 4. Astrogeodetic quasigeoid profile. The QG height changes by about 1.3 m over a distance of 23 km (upper part). The strong tilt of the QG in southern direction is due to the attraction of the central Alps. Detrending the QG profile makes the fine structure visible (lower part). The small peak-like features are due to azimuthal changes in the integration path.

data set may be divided into two disjunct subsets in a way that the first set consists of the odd station numbers and the second one of the even station numbers. Therewith the station spacing of the resulting profiles, each containing 51 stations, is 460 m. The subsets serve as input data for the computation of two independent astrogeodetic QG profiles. The differences give an empirical accuracy estimate of about 1-1.5 mm (cf. Fig. 5). Another assessment method is a formal error estimation based on the error sources affecting the computed QG undulations. Table 2 lists the known error sources as well as their total impact of about 2 mm on the computed QG. The impact of the (ξ, η) - random error on the QG was estimated applying the error propagation law of astronomical levelling, see Hirt and Seeber (2005). The systematic UCAC error is on the order of 0.01 due to Zacharias

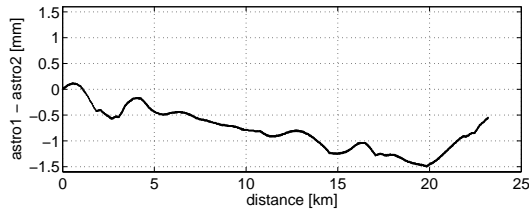


Figure 5. Differences between two quasigeoid profiles computed from two independent data sets of astrogeodetic observations.

et al. (2000). The computed deflection data is assumed to be affected by a systematic error of about $0''.005$ since the arithmetic mean from the UCAC and Tycho-2 processing results is used. The uncertainty of the normal correction is derived in section 3.2. It should be noted that another error source in astronomical levelling may be the influence of anomalous refraction on the observed deflection data (ξ, η) , see e.g. Hirt (2006). A small remaining refraction error cannot be excluded. However, it is assumed that the largest portion of refraction is cancelled out due to double observations on several stations and the changing weather conditions during the campaign.

The general conclusion is that the astrogeodetic QG computation is accurate to a few millimeters over a distance of 23 km. Therefore it is considered to provide the reference for a comparison with the gravity field models in the next section.

Source / Type	(ξ, η)	$\delta\Delta\zeta$
(ξ, η) random error	$0''.08 - 0''.09$	0.9-1.1 mm
systematic error from UCAC	$0''.005$	0.5 mm
normal correction		0.1-0.15 mm
Total:		≤ 2 mm

Table 2. Estimated error budget for the astrogeodetic QG. The symbol $\delta\Delta\zeta$ refers to the relative error of the QG height difference $\Delta\zeta$ over a profile distance of 23 km.

5 Comparisons

5.1 Astrogeodetic QG vs. GPS/levelling

A first comparison is carried out using a set of 5 GPS/levelling stations, covering the first half section of the astrogeodetic profile. The GPS/levelling data (Flury 2002) provides estimates for absolute QG heights ζ . The RMS computed from the differences between GPS/levelling and the astro-solution (Fig. 6) is 10 mm, and decreases to about 6 mm if the first GPS/levelling station (located eccentrically to the QG profile) is neglected. This very good agreement of the astrogeodetic and GPS/levelling data is

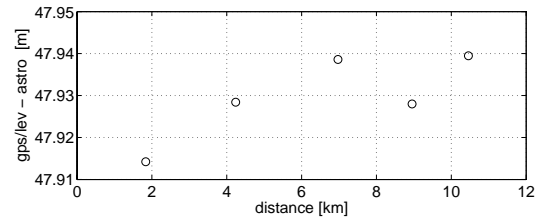


Figure 6. Comparison between GPS/levelling data and the astrogeodetic quasigeoid profile

at the centimeter accuracy level, normally associated with GPS height measurements.

5.2 Astrogeodetic QG vs. Gravimetric Gravity Field Models

In the working area, three gravimetric gravity field models are available: The German Combined Quasigeoid (GCG) 2005, computed as the average of two independent solutions from the German Federal Agency for Cartography and Geodesy (BKG) and the Institut für Erdmessung (Liebsch et al. 2006). The second model is the digital finite height reference surface DFHRS (Jäger 2006) which is designed as height surface at the 1-3 cm accuracy level. Moreover a gravimetric quasigeoid model for Bavaria, the IAPG QG developed by Gerlach (2003), is also used for a comparison.

The astrogeodetic QG solution does not provide any information on the (absolute) height of the profile. Therefore the comparison is done as bias-fit where the QG height differences at the first station are set to zero. The resulting difference profiles, the main result of this work, are shown in Fig. 7 and the corresponding statistics are listed in Tab. 3. Considering the location of the test area near the German-Austrian borderline and its overall mountainous character (e.g. inhomogeneous and incomplete gravity data), the agreement between the QG models and the astrogeodetic QG is surprisingly good. The GCG2005 agrees with the astrogeodetic QG better than 1 cm (RMS). The RMS difference for the DFHRS amounts to 2 cm, thus remains completely within the associated accuracy specification. An extremely good agreement is found between the IAPG QG and the astrogeodetic QG. Here, the RMS amounts to 4 mm as such reflecting the uncertainties of both data sets. One reason for this excellent result certainly is the much denser set of local input gravity data used in the IAPG QG-computation in comparison to the GCG2005 and DFHRS models.

6 Conclusions

For the astrogeodetic validation of gravity field models, a new high-precision vertical deflection data set

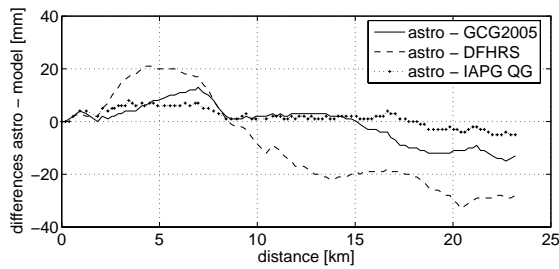


Figure 7. Comparison between the astrogeodetic quasigeoid profile and gravimetric gravity field models

	Astro quasigeoid vs ...		
	GCG [m]	DFHRS [m]	IAPG [m]
Min	-0.015	-0.033	0.005
Max	0.013	0.021	0.008
Mean	-0.001	-0.009	0.002
RMS	0.008	0.020	0.004

Table 3. Statistics of the comparison between the astrogeodetic quasigeoid profile and gravimetric gravity field models GCG, DFHRS and IAPG quasigeoid.

was acquired in the German Alps using the Digital Zenith Camera System TZK2-D. From repeated observations, the noise level of the vertical deflection data is estimated to be about $0''.08$. An independent confirmation, obtained by reducing the observations with DTM data, provides an accuracy estimation for the deflection data of about $0''.09$. The astrogeodetic quasigeoid profile used in the comparison was computed from a combination of the high-precision vertical deflection data, DTM data and predicted surface gravity data. A reasonable accuracy estimate for the astronomical quasigeoid profile is considered to be at the order of a few millimeters over a profile length of 23 km.

The comparison between the astrogeodetic QG and three different gravimetric gravity field models (GCG2005, DFHRS, IAPG QG) reveals a good agreement at the centimeter level. The agreement is considered to be completely satisfactory when taking the mountainous character of the test area into account. An extraordinary good agreement (RMS of 4 mm) is found between the IAPG QG and the astrogeodetic QG. As a general conclusion, this work practically proves the capability of astronomical levelling for the economic determination of quasigeoid profiles with millimeter-accuracy over 10-20 km. To the knowledge of the authors, this is the first time that a consistency at the millimeter level is obtained between an astrogeodetic and gravimetric gravity field model in a mountainous region.

7 Acknowledgements

The application of the Digital Zenith Camera System for gravity field determination is supported by the German National Research Foundation DFG. The authors are grateful to the students Ilka Rehr, Niels Hartmann, Eiko Münstedt and Rene Gudat for their restless and engaged support of the astrogeodetic measurements. The Bayerische Erdmessungskommission (BEK) and the Institute for Astronomical and Physical Geodesy IAPG (both Munich) are kindly acknowledged for supporting the field observations.

References

- Brockmann, E., Becker, M., Bürki, B., Gurtner, W., Haefele, P., Hirt, C., Marti, U., Müller, A., Richard, P., Schlatter, A., Schneider, D., and Wiget, A. (2004). *Realization of a Swiss Combined Geodetic Network (CH-CGN)*. EUREF'04 Symposium of the IAG Commission 1 - Reference Frames, Subcommittee 1-3a Europe (EUREF), Bratislava, Slovakia.
- Denker, H. (1988). *Hochauflösende regionale Schwerefeldbestimmung mit gravimetrischen und topographischen Daten*. Wissen. Arb. Fach. Vermessungswesen Univ. Hannover Nr. 156.
- Denker, H., Ihde, J., Müller, J., and Schirmer, U. (2003). *Development of a High Resolution Height Reference Surface for Germany using Gravity and GPS/Levelling Data*. IUGG Meeting 2003, Sapporo, Japan.
- Flury, J. (2002). *Schwerefeldfunktionale im Gebirge - Modellierungsgenauigkeit, Messpunktdichte und Darstellungsfehler am Beispiel des Testnetzes Estergebirge*. DGK C 557.
- Forsberg, R. and Tscherning, C. C. (1981). *The Use of Height Data in Gravity Field Approximation by Collocation*. JGR 86 No B9: 7843-7854.
- Gerlach, C. (2003). *Zur Höhensystemumstellung und Geoidberechnung in Bayern*. DGK C 571.
- Hirt, C. (2004). *Entwicklung und Erprobung eines digitalen Zenitkamerasystems für die hochpräzise Lotabweichungsbestimmung*. Wissen. Arb. Fach. Geodäsie und Geoinformatik Univ. Hannover Nr. 253.
- Hirt, C. (2006). *Monitoring and Analysis of Anomalous Refraction Using a Digital Zenith Camera System*. Astronomy and Astrophysics, accepted.
- Hirt, C. and Bürki, B. (2002). *The Digital Zenith Camera - A New High-Precision and Economic Astrogeodetic Observation System for Real-Time Measurement of Deflections of the Vertical*. Proceed. of the 3rd Meeting of the International Gravity and Geoid Commission of the International Association of Geodesy, Thessaloniki (ed. I. Tziavos): 161-166.
- Hirt, C. and Flury, J. (2006). *Astronomical-topographic levelling using high-precision astrogeodetic vertical deflections and DTM data*. Journal of Geodesy, in preparation.
- Hirt, C. and Seeber, G. (2005). *High-Resolution Local Gravity Field Determination at the Sub-Millimeter Level using a Digital Zenith Camera System*. Proceedings IAG Meeting "Dynamic Planet", Cairns 2005 (in press).
- Jäger, R. (2006). *Digitale Finite Elemente Höhenbezugsgläche*. URL: www.dfhb.de.
- Liesch, G., Schirmer, U., Ihde, J., Denker, H., Müller, J. (2006). *Quasigeoidbestimmung für Deutschland*. DVW-Schriftenreihe Nr 49: 127-146.
- Torge, W. (2001). *Geodesy, Third Edition*. W. de Gruyter, Berlin, New York.
- Zacharias, N., Zacharias, M. I., Urban, S. E., and Høg, E. (2000). *Comparing Tycho-2 astrometry with UCAC1*. The Astronomical Journal 120: 1148-1152.

Validation of marine geoid models in the North Aegean Sea using satellite altimetry, marine GPS data and astrogeodetic measurements

Müller, A., Bürki, B., Limpach, P., Kahle, H.-G. (Geodesy and Geodynamics Laboratory, ETH Zurich, Switzerland)

Grigoriadis, V. N., Vergos, G. S., Tziavos, I. N., (Department of Geodesy and Surveying, Aristotle University of Thessaloniki, Greece)

Abstract. A dedicated measuring campaign for geoid determination has been carried out in the North Aegean Sea, Greece, in May 2005. It was realized in the frame of a joint project between the Geodesy and Geodynamics Laboratory (GGL) of ETH Zurich, and the Department of Geodesy and Surveying of the Aristotle University of Thessaloniki. The measurement area is part of the North Aegean Trough (NAT), which forms a continuation of the seismically active North Anatolian Fault Zone. Different methods for geoid determination have been applied, including astro-geodetic observations with the new Zenith Camera DIADEM in order to determine highly-precise Deflections of the Vertical (DoV), as well as GPS boat and buoy measurements to provide Sea Surface Heights (SSH). The data gathered during the campaign were compared to existing local gravimetric and altimetric geoid models. They helped to detect long wavelength errors in the gravimetric geoid model, which are mainly due to existing data gaps in the marine area.

Keywords. Geoid determination, North Aegean Trough, Zenith Camera DIADEM, Deflections of the Vertical, Marine GPS, Sea Surface Heights **2**

1 Introduction

From the early seventies on, systematic attempts for precise geoid determination have been carried out in the Hellenic area. The recent gravimetric geoid solution HGFFT98 for the Hellenic area has been presented by Tziavos and Andritsanos (1999). In order to provide additional and independent data sets for an improved local geoid solution, a dedicated campaign was carried out in May 2005. The area under study is situated within $38^\circ < \varphi < 42^\circ$ N. and $22^\circ < \lambda < 27^\circ$ E. The measurement area forms part of the North Aegean Trough (NAT), which is considered to be a continuation of the seismically active North Anatolian Fault Zone. Highly-precise Deflections of the Vertical (DoV) have been observed with the di-

gital Zenith Camera DIADEM, developed at GGL. Additionally, offshore GPS boat and buoy measurements were carried out, thus scanning the sea surface with high resolution and accuracy. Some of the marine GPS measurements were conducted along the Jason satellite subtracks for validation purposes. The Sea Surface Heights (SSH) were corrected for tidal effects by using a permanent tide gauge installation. Geoid height differences calculated from DoV and compared with GPS based SSHs showed a very good agreement. The comparison of these data sets with the gravimetric geoid model HGFFT98 revealed significant disagreements. Apart from the gravimetric geoid model, a recent altimetric one based on SSHs from the Exact Repeat Missions (ERM) of ERS1, ERS2 and TOPEX/Poseidon has been employed for validation purposes (Tziavos et al. 2005). The comparison with the altimetric geoid model resulted in smaller differences, while it was also found that the altimetric, DoV and GPS models follow the same variations in the geoid height signal. Detailed validation tests of all existing data sources are presented and discussed in this paper.

2 Available data sets

2.1 Gravimetric model

The development of the gravimetric geoid solution HGFFT98 was based on an optimal combination of free-air gravity anomalies and GPS/Leveling geoid heights available for the Hellenic area. The marine gravity data were taken from the digitisation of Morelli's maps (Behrend et al 1996), so only few gravity observations were available for the area under study. The combined solution was determined using the Multiple Input – Multiple Output System Theory (MIMOST) presented by Andritsanos (2000), Andritsanos et. al. (2001). Due to the lack of specific information about the errors in both the gravimetric and GPS/Leveling input data, simulated noises were used as input error. Randomly distri-

buted fields were generated using a standard deviation of ± 5 mGal for the gravimetric data and ± 5 cm for the GPS/Leveling ones. In the case of repeat altimetric missions an estimation of the input error Power Spectral Density PSD function can be directly evaluated using this successive information. The final solutions and the error PSD function of the MIMOST method were calculated according to the following equations:

$$\hat{N}_o = \begin{bmatrix} H_{NN^{gr}} & H_{NN^{GPS}} \\ \left(\begin{bmatrix} P_{N_o^{gr}N_o^{gr}} & P_{N_o^{gr}N_o^{GPS}} \\ P_{N_o^{GPS}N_o^{gr}} & P_{N_o^{GPS}N_o^{GPS}} \end{bmatrix} - \begin{bmatrix} P_{m^{gr}m^{gr}} & 0 \\ 0 & P_{m^{GPS}m^{GPS}} \end{bmatrix} \right)^{-1} \begin{bmatrix} P_{N_o^{gr}N_o^{gr}} & P_{N_o^{gr}N_o^{GPS}} \\ P_{N_o^{GPS}N_o^{gr}} & P_{N_o^{GPS}N_o^{GPS}} \end{bmatrix} \begin{bmatrix} N_o^{gr} \\ N_o^{GPS} \end{bmatrix} \end{bmatrix} \quad (\text{eq.1})$$

$$P_{\hat{e}\hat{e}} = \left\{ \begin{bmatrix} H_{NN^{gr}} & H_{NN^{GPS}} \\ \left(\begin{bmatrix} P_{N_o^{gr}N_o^{gr}} & P_{N_o^{gr}N_o^{GPS}} \\ P_{N_o^{GPS}N_o^{gr}} & P_{N_o^{GPS}N_o^{GPS}} \end{bmatrix} - \begin{bmatrix} P_{m^{gr}m^{gr}} & 0 \\ 0 & P_{m^{GPS}m^{GPS}} \end{bmatrix} \right)^{-1} \begin{bmatrix} P_{N_o^{gr}N_o^{gr}} & P_{N_o^{gr}N_o^{GPS}} \\ P_{N_o^{GPS}N_o^{gr}} & P_{N_o^{GPS}N_o^{GPS}} \end{bmatrix} \begin{bmatrix} \hat{H}_{N_o^{gr}N_o^{gr}} & \hat{H}_{N_o^{gr}N_o^{GPS}} \\ \hat{H}_{N_o^{GPS}N_o^{gr}} & \hat{H}_{N_o^{GPS}N_o^{GPS}} \end{bmatrix} \begin{bmatrix} H_{NN^{gr}}^* \\ H_{NN^{GPS}}^* \end{bmatrix} - \begin{bmatrix} \hat{H}_{N_o^{gr}N_o^{gr}}^* & \hat{H}_{N_o^{gr}N_o^{GPS}}^* \\ \hat{H}_{N_o^{GPS}N_o^{gr}}^* & \hat{H}_{N_o^{GPS}N_o^{GPS}}^* \end{bmatrix} \begin{bmatrix} H_{NN^{gr}}^* \\ H_{NN^{GPS}}^* \end{bmatrix} \right\} \begin{bmatrix} P_{m^{gr}m^{gr}} & 0 \\ 0 & P_{m^{GPS}m^{GPS}} \end{bmatrix} \begin{bmatrix} H_{NN^{gr}}^* \\ H_{NN^{GPS}}^* \end{bmatrix} \quad (\text{eq.2})$$

where \hat{N}_o is the combined geoid estimation, N^{gr} and N^{GPS} are the pure gravimetric and GPS/Leveling signals respectively, N_o^{gr} and N_o^{GPS} are the gravimetric and GPS/Leveling observations, m^{gr} and m^{GPS} are the input noises, H_{xy} is the theoretical operator that connects the pure input and output signals, \hat{H}_{x_o, y_o} is the optimum frequency impulse response function, $P_{\hat{e}\hat{e}}$ is the error PSD function and e is the noise of the output signal.

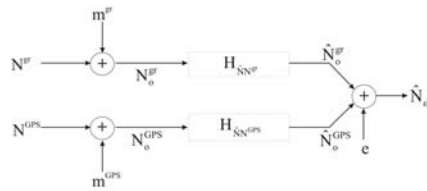


Fig. 1: A dual-input single output system for the prediction of geoid heights.

An Input-Output system of the kind described above and used for the development of the gravimetric model HGFFT98 is given in Fig. 1.

2.2 Altimetric model

The altimetric geoid model used as validation data set was computed from a combination of altimetric data from the ERM missions of ERS1/2 and TOPEX/Poseidon (T/P) (AVISO 1998). The ERS1 data (95576 point values) are taken from the 35-day ERM mission from April 14, 1992 to December 13, 1993 and March 21, 1995 to May 16, 1995 phases *c* and *g*, respectively. From ERS2, six years worth of data have been used (368617 point values) covering the period from 1995 to 2001. Finally, nine years of the T/P SSHs were employed (488634 point values) covering the period from 1992 to 2001.

The final altimetric model developed was a combination from all data sets employing least squares collocation (LSC) (Tziavos et al. 2005), by using a remove-compute-restore method. Hereby the global geopotential solution EGM96 and the effects of the bathymetry have been taken into account. In addition, the altimetric SSHs have been crossover adjusted and stacked. Thus, data over a much wider region than the area under study were used (Fig. 2).

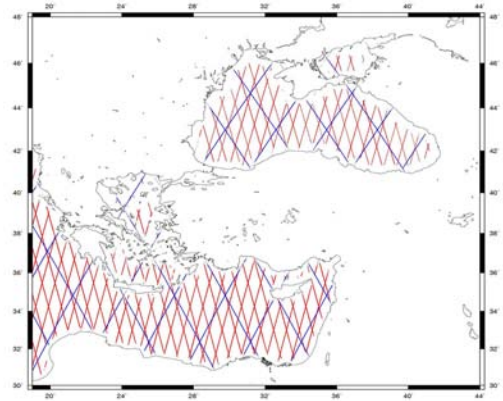


Fig. 2: Area under study for the development of the altimetric geoid and distribution of ERS1, ERS2 (gray) and T/P (black) tracks.

Moreover, the altimetric data have been reduced from the sea surface to the geoid using a local sea surface topography model developed by Rio (2004). The final altimetric geoid model for the North Aegean Sea is depicted in Fig. 3.

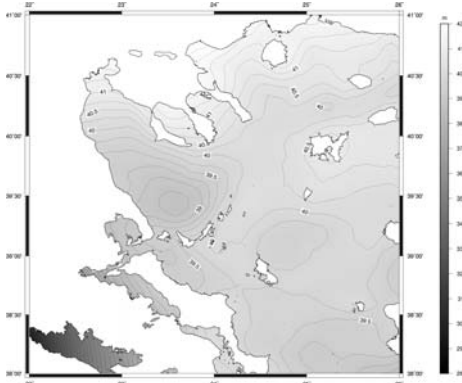


Fig. 3: The final LSC combined Mean Sea Surface model for North Aegean area.

3 Field measurements

3.1 DIADEM: Determination of Deflections of the Vertical

The digital Zenith Camera DIADEM (**D**igital **A**stronomical **D**eflection **M**easuring system) determines the physical plumb line (Φ, Λ) by directional measurements to the stars using a CCD camera (Fig. 4). The NS and WE components of the DoV (ξ, η) are determined using the following equations:

$$\xi = \Phi - \varphi \quad (\text{eq. 3})$$

$$\eta = (\Lambda - \lambda) \cos \varphi \quad (\text{eq. 4})$$

Differential GPS measurements have been carried out in order to provide geodetic coordinates with an adequate accuracy of better than 10 cm. The resulting DoV show an accuracy of about 0.15 arcsec. For detailed information about the instrumentation and method refer to Müller et al. (2004).

The distribution of Astro-stations was mainly motivated by the intention to cover the area around the North Aegean Trough (NAT), which is an important geological feature of the test area (Fig. 5). The NAT is a zone of deep water with maximum depths of up to 1500 m, trending from northeast to southwest across the North Aegean Sea. It forms the continuation of the seismically active North Anatolian Fault Zone. The NAT shows three distinctive depressions: the Sporades basin in southwest, the Mount Athos basin near Chalkidiki and the trough between the islands of Samothraki and Limnos (McNeill et al. 2004).



Fig. 4: DIADEM deployment. To determine the geodetic position the GPS antenna was put on the lens. For the astro-observations it was removed.



Fig. 5: Measuring area in the North Aegean Sea, Greece. The NAT as a zone of deep water is well recognizable.

The observations were carried out along the shore-line of the North Aegean Sea including the Sporades islands (Skiathos, Skopelos, Alonissos, Kira Panagia, Psathoura) and the islands of Thassos, Samothraki, Limnos and Agios Efstratios. Totally, 30 stations have been observed in 20 nights. In total 80 to 120 single solutions per station have been used for the determination of the direction of the local plumb line. The standard deviation of a single observation is better than 0.2 arcsec. The resulting DoV are shown in Fig. 6.

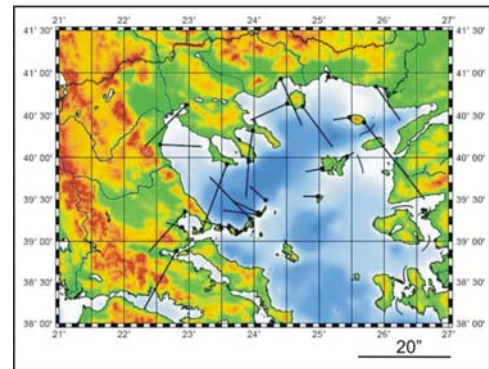


Fig. 6: DoV determined with DIADEM. The vectors shown indicate the DoV projected into the horizontal plane (components are equal to ξ and η).

The vectors on the three peninsulas of Chalkidiki, on the Sporades islands and on the islands of Thasos, Samothraki and Limnos clearly indicate the influence of the NAT representing a mass deficit with respect to the surrounding area. It is striking that on the island of Samothraki the DoV on the eastern station (Kipos) is about five times larger than on the western station (Kamariotissa) and nearly points to an opposite direction. This is mainly due to topographic and bathymetric features encountered there. The bathymetry at Kipos side shows a very steep gradient due to the trough between Limnos and Samothraki while at Kamariotissa the relief is much less inclined. The topography of the island is characterized by the Saos mountain, which reaches altitudes of up to 1600 m. This topographic mass excess causes larger gravity effects in the SE than in the NW of the island.

3.2 Marine GPS measurements: Determination of Sea Surface Heights

Enhanced ground-based methods have been developed for the precise determination of Sea Surface Heights (SSH), consisting in shipborne multi-antenna GPS measurements and GPS equipped buoys (Fig. 6). The SSH data provide local-scale information on the short-wave structure of the gravity field and can be used to improve local marine geoid solutions. They also contain information on the local dynamic ocean topography (DOT) and can be used for the validation and calibration of radar altimeter satellites. In addition, they can provide a link between offshore radar altimeter data and tide-gauge records.



Fig. 6: Left: GPS equipped buoy (diameter 35cm) containing receiver, antenna and battery. Right: sailing boat equipped with four GPS antennas (arrows).

Highly-precise GPS positioning of the buoys and the boat is achieved by simultaneously operating the buoy receivers, the receivers aboard the boat and several permanent terrestrial GPS reference stations, all operated at a sampling rate of 1 Hz. The coordi-

nates of the reference stations are first determined with respect to the ITRF reference frame. The kinematic positions of the buoys and the boat are then determined through differential GPS carrier phase processing with respect to the reference stations. In order to derive the Sea Surface Topography (SST) from the instantaneous SSHs, several corrections have to be applied, especially for tides and atmospheric effects (inverse barometer effect). The tide corrections have been kindly provided by E.C. Pavlis from JCET using the GOT00.2 tide model. The local tidal effects have been determined by using own tide gauges installed in the survey area. The inverse barometer corrections have been computed over the entire Mediterranean Sea using ECMWF atmospheric pressure data.

Two GPS surveys have been carried out in 2004/2005, totaling more than 1000 nautical miles of ship tracks (Fig. 7). For calibration and validation purposes of radar altimeter missions, the survey area has been chosen in the vicinity of Jason-1 ground-tracks. Dedicated buoy measurements have been performed along these Jason-1 tracks, including deployments with direct Jason-1 cross-overs, which provide precise ground-truth SSH information during the overflight.

The bathymetric low of the NAT is associated with a distinct depression of the SST, which reaches a minimum of 37.5 m above the WGS84 ellipsoid. The SST in the surrounding area is more than 39 m, reaching more than 40.5 m towards the north of the survey area (Fig. 7 and 8).

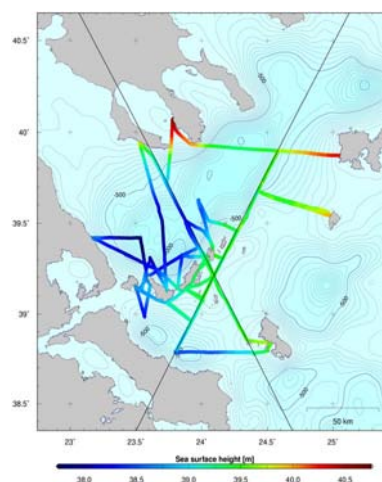


Fig. 7: Boat tracks with SSH profiles from combined shipborne/buoy GPS observations. Black lines: Jason-1 ground-tracks. Background: bathymetry.

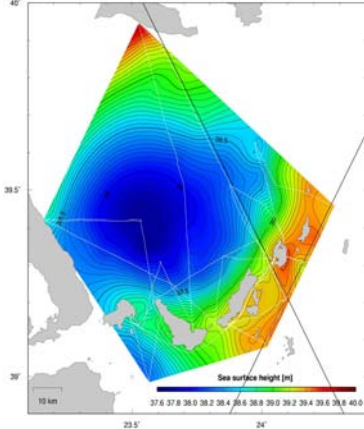


Fig. 8: Preliminary SST obtained by gridding the shipborne/buoy GPS data from the 2005 campaign (white lines). Iso-lines interval: 0.05 m. (Note that parts of the surface are extrapolated).

4 Results

4.1 Conversion of Deflections of the Vertical to geoid height differences

To compare DoV with SSH, they were transformed to geoid height differences ΔN using the principle of astronomical leveling. The average of the vertical deflections (ξ, η) between neighbouring stations P_i and P_{i+1} results in the component ε_i :

$$\varepsilon_i = \frac{\xi_i + \xi_{i+1}}{2} \cdot \cos \alpha_i + \frac{\eta_i + \eta_{i+1}}{2} \cdot \sin \alpha_i \quad (\text{eq. 5})$$

The vertical deflection ε describes the inclination of the equipotential surface in azimuth α . The equipotential profile ΔN is obtained by integrating single height increments $\varepsilon_i \cdot s_i$ from the first to the last station (n) of the profile:

$$\Delta N = - \sum_{i=1}^{n-1} \varepsilon_i \cdot s_i \quad (\text{eq. 6})$$

where s_i is the distance between the two stations.

4.2 Comparison of different data sets

The GPS based SSHs have been converted from the tide free to the mean tide system, and then corrected for the Mean Dynamic Sea Surface Topography (MDSST), yielding geoid heights in the mean tide system. These were re-converted to the tide free system, as the AUTH geoids are defined in this system. The overall corrections for the MDSST and the permanent tide effects were +5 cm and +1.4 cm, respectively, for the Northern Aegean Sea. By gridding the geoid heights, a preliminary shipborne geoid model (Limpach geoid) was obtained. For a

comparison, the Limpach geoid as well as the gravimetric and altimetric geoids were interpolated onto profiles through selected DIADEM stations. Fig. 9 shows a representative example for a profile between Skiathos, Glossa, Skopelos, Patitiri, Gerakas, Kira Panagia South, Kira Panagia North and Psathoura. It presents the geoid height differences obtained from DoV, SSH, altimetric and gravimetric geoid. For a local comparison, all heights have been referenced to the same level based on the gravimetric solution. Concerning the relative geoid undulations, the GPS, DIADEM and altimetric data show a very good agreement. In contrast, the gravimetric geoid model reveals a significant discrepancy in the end of the profile (Patitiri-Gerakas-Kira Panagia-Psathoura) as evidenced by the relatively small slope between 60 and 80 km distance of the profile.

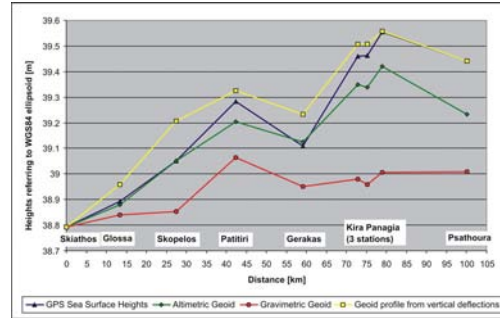


Fig. 9: Comparison between geoid height differences calculated from a) DoV b) SSH c) Altimetric geoid and d) Gravimetric geoid.

For a statistical approach, the gravimetric and the altimetric geoid models were interpolated onto the ship tracks. The heights obtained have been compared with the shipborne data. The mean difference between shipborne and gravimetric geoid heights is **70 cm** with a standard deviation of about **21 cm**.

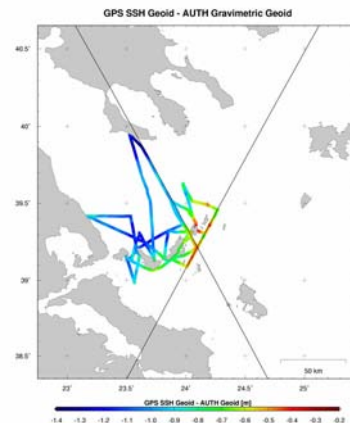


Fig. 10: Difference between Limpach geoid and gravimetric geoid model (HGFFT98) along boat tracks.

Fig. 10 illustrates the differences between the shipborne and the gravimetric geoid heights along the boat tracks. They range between -1.4 m and -0.2 m. The largest differences were found in the region of the NAT. This attributes to gravity data gaps in the marine area and the use of different reference surfaces where the available gravity data bases refer to. A comparison of shipborne and altimetric geoid heights showed a significant better agreement with a mean difference of about **4 cm** and a standard deviation of **14 cm**.

5 Conclusions

A dedicated astro-geodetic and marine GPS campaign in the North Aegean Sea has been conducted in order to validate and improve existing geoid models in this area. The marine GPS data yield instantaneous Sea Surface Heights of high spatial density that enables the determination of a Sea Surface Topography. The SST contains information on the local dynamic ocean topography and can be used to validate and calibrate satellite radar altimetric measurements. The highly-precise Deflections of the Vertical observed by the digital Zenith Camera DIADEM on several isles and at the coastline of the North Aegean Sea provide local geoid structures. They are helpful not only on islands but also in coastal areas, thus reinforcing the geoid determination in the crucial transition zone from the coast to the open sea. Geoid height differences, calculated from both data sets and compared along several profiles, showed a very good agreement within a few centimeters. The data helped to detect long wavelength errors in the gravimetric geoid model HGFFT98 from the Aristotle University of Thessaloniki. These errors are mainly due to a lack of marine gravity data in the area under study. Another reason may be the fact that the available gravity data bases refer to different reference surfaces. For the future it is planned to compute a new geoid solution by optimally combining all the available terrestrial and satellite data sources. In terms of the gravity data, a new high accuracy and resolution gravity data base for the entire Greece is under preparation.

References

- Andritsanos, V.D. (2000). *Optimum combination of terrestrial and satellite data with the use of spectral methods for applications in geodesy and oceanography*. PhD Dissertation, School of Rural and Surveying Engineering, Faculty of Engineering, The Aristotle University of Thessaloniki, Department of Geodesy and Surveying.
- Andritsanos, V.D., Sideris, M.G., Tziavos, I.N. (2001). *A survey of gravity field modeling applications of the Input-Output System Theory (IOST)*. IGeS Bulletin, Vol. 10, pp. 1-17.
- AVISO (1998). *AVISO User Handbook – Corrected Sea Surface Heights (CORSSHs)*. AVI-NT-011-311-CN, Ed 3.1.
- Behrend, D., Denker, H., Schmidt, K., (1996). *Digital gravity data sets for the mediterranean sea derived from available maps*. Bulletin d'information, No 78, pp. 31-39, BGI, 1996.
- McNeill, L.C., Mille, A., Minshull, T.A., Bull, J.M., Kenyon N.H., Ivanov, M. (2004). *Extension of the North Anatolian Fault into the North Aegean Trough: Evidence for transtension, strain partitioning, and analogues for Sea of Marmara basin models*. Tectonics, Vol. 23, TC2016, 2004.
- Müller, A., Bürki, B., Hirt, C., Marti, U. and Kahle, H.-G. (2004). *First Results from new High-precision Measurements of Deflections of the Vertical in Switzerland*. International Association of Geodesy Symposia, Vol. 129, Jekeli, C., Bastos, L., Fernandes, J. (eds.), Gravity Geoid and Space Missions 2004, Springer-Verlag Berlin Heidelberg, pp. 143-148.
- Rio, M.-H. (2004). *A Mean Dynamic Topography of the Mediterranean Sea Estimated from the Combined use of Altimetry, In-Situ Measurements and a General Circulation Model*. Geophysical Research Letter Vol. 6, 03626.
- Tziavos, I. N., Andritsanos, V. D. (1999). *Recent Geoid Computations for the Hellenic Area*. Phys. Chem. Earth (A), Vol- 24, No. 1, pp. 91-96.
- Tziavos, I. N., Vergos, G. S., Kotzev V., Pashova L. (2005). *Mean sea level and sea surface topography studies in the Black Sea and the Aegean*. International Association of Geodesy Symposia, Vol. 129, Jekeli, C., Bastos, L., Fernandes, J. (eds.), Gravity Geoid and Space Missions 2004, Springer-Verlag Berlin Heidelberg, pp. 254-259.

Fitting gravimetric quasigeoid model to GPS/levelling data in Poland

Jan Krynski

Institute of Geodesy and Cartography, 27 Modzelewskiego St., PL 02-679 Warsaw, Poland
Fax: +48 22 3291950, Tel.: +48 22 3291904, E-mail: krynski@igik.edu.pl

Adam Lyszkowicz

University of Warmia and Mazury, 12 Heweliusza St., PL 10-724 Olsztyn, Poland
Fax: +48 89 5234878, Tel.: +48 89 5234579, E-mail: adam@moskit.uwm.edu.pl
Space Research Centre, Polish Academy of Sciences, 18A Bartycka St, PL 00-710 Warsaw, Poland
Fax: +48 22 8403131, Tel.: +48 22 8403766, e-mail: adam@cbk.waw.pl

Abstract. Considerable investigations were conducted in Poland on the determination of precise gravimetric quasigeoid model using terrestrial and marine gravity data, geopotential models and height data. Quality of the model was evaluated using precise GPS/levelling data. Precise gravimetric quasigeoid model makes possible to transform ellipsoidal heights to normal heights, what is required for using GPS heighting in surveying practice. To determine transformation parameters, the gravimetric quasigeoid model needs to be fitted to GPS/levelling heights in the area of interest. In order to eliminate datum shift, residual long-wavelength gravity errors, as well as possible systematic errors in levelling, the residual height anomalies at GPS/levelling sites were modelled by a smooth function consisting of a trend function and a residual. The parameters of the model were determined using least-squares collocation. In practice, a trend was modelled by a plane function, and the residuals were modelled by Hirvonen's covariance function. For Poland the *a priori* error of 37 mm and the correlation length of 70 km were used. Obtained results show that the fit of gravimetric geoid to vertical datum, measured by the standard deviation of residuals at the GPS/levelling control traverse sites, is at the level of ± 1.5 cm.

Keywords. Quasigeoid, fit modelling, covariance models, corrector surface

1. Introduction

Observed elevation differences between points on the Earth's surface are traditionally obtained by spirit levelling, however, with the advent of satellite-based global positioning systems (GPS, GLONASS, and the forthcoming GALILEO) the

ability to obtain accurate heights at virtually any point on land or at sea has in fact been revolutionized.

The fundamental relationship that ties ellipsoidal heights obtained from global navigation satellite system (GNSS) measurements and heights with respect to a vertical datum established using spirit levelling and gravity data, is to the first approximation given by (Heiskanen and Moritz, 1967)

$$h - H - N = 0 \quad (1)$$

where h is the ellipsoidal height, H is the orthometric height, and N is the geoid undulation.

The implementation of (1) is in practice more complicated due to numerous factors that cause discrepancies when combining different heights. The main factors that cause those discrepancies are as follows:

- random errors in the derived heights h , H , and N ,
- datum inconsistencies inherent among the height types,
- systematic effects and distortions in the height data,
- assumptions and theoretical approximations made in processing of observed data,
- instability of reference station monuments over time.

The combined effects of these factors could be modelled by the use of a corrector surface. Thus the theoretical relationship between the three types of height data and the incorporation of an appropriate corrector surface model can be written as follows:

$$h - H - N = c \quad (2)$$

where c is the correction due to errors.

A variety of data that became available in Poland made possible to develop a number of different quasigeoid models such as astro-gravimetric,

gravimetric quasigeoid models, GPS/levelling quasigeoid models as well as the integrated (combined) quasigeoid model and the best-fitted quasigeoid model (Krynski and Lyszkowicz, 2006). Gravimetric quasigeoid model quasi05c computed in 2005 using upgraded gravity data from Poland and GGM02S/EGM96 global geopotential model seems presently the best pure gravimetric quasigeoid model for Poland. The experience with comparing of GPS/levelling heights and quasigeoid heights (Łyszkowicz, 2000) has shown long to medium wavelength discrepancies. It has been used to develop an empirical corrector surface which relates the quasi05c gravimetric quasigeoid model to the reference system of GPS/levelling heights. The advantage of such fitted quasigeoid model is that it will support direct conversion between the ellipsoidal reference system and vertical datum with normal heights, even if they are not defined on a common reference.

2. Corrector surface models

The choice of the parametric form of the corrector surface model is not a trivial task. In fact, the list of potential candidates for the “corrector” surface is extensive (Zhiheng and Duquenne, 1995). The selection process is arbitrary unless some physical reasoning can be applied to the residuals between the GPS-derived geoid heights ($h - H$) and the geoid heights from the gravimetric geoid model N , which fulfills

$$l_i = h_i - H_i - N_i \quad (3)$$

In the past, a simple tilted plane-fit model (3-parameter model) that in many cases satisfied accuracy requirements has frequently been used (Sideris, 1993; Milbert, 1995)

$$t_i = x_1 \cos \varphi_i \cos \lambda_i + x_2 \cos \varphi_i \sin \lambda_i + x_3 \sin \varphi_i \quad (4)$$

where the trend t represents the correction c in (2), and φ, λ are respectively the latitude and longitude of GPS/levelling point. However, as the achievable accuracy of GPS-derived as well as geoid heights improves, the use of such a simple model may not be sufficient, in particular in the region of larger size. The problem is further complicated because selecting the proper correction model type depends on data distribution, its density and quality, that vary for each case.

Another family of models is based on the general similarity datum shift transformation, with the simplified classic 4-parameter model (Heiskanen and Moritz, 1967) given by

$$t_i = x_1 + x_2 \cos \varphi_i \cos \lambda_i + x_3 \cos \varphi_i \sin \lambda_i + x_4 \sin \varphi_i \quad (5)$$

An extended version of the above model is given with adding a fifth parameter as follows (Kotsakis et al., 2001):

$$t_i = x_1 + x_2 \cos \varphi_i \cos \lambda_i + x_3 \cos \varphi_i \sin \lambda_i + x_4 \sin \varphi_i + x_5 \sin^2 \varphi_i \quad (6)$$

Many researchers have opted for applying anyone of the aforementioned trend surfaces and then modelling the remaining residuals using least-squares collocation (e.g. Milbert, 1998; Forsberg, 1998; Denker et al., 2000) as follows:

$$\hat{\mathbf{s}}_P = \mathbf{C}_P^T (\mathbf{C} + \mathbf{D})^{-1} (\mathbf{L} - \mathbf{t}) \quad (7)$$

where \mathbf{C}_P is the covariance matrix between the computed signal and observations, \mathbf{C} is the covariance matrix between observations, \mathbf{D} is the covariance matrix of observations errors, usually diagonal and constant: $\mathbf{D} = \sigma_0^2 \mathbf{I}$, and $(\mathbf{L} - \mathbf{t})$ is the vector of observations from which the trend was removed.

Equation (7) is usually implemented using one of Markov covariance models of the form

$$C(d) = C_0 e^{-d/\nu} \quad (8)$$

$$C(d) = C_0 \left(1 + \frac{d}{\nu}\right) e^{-d/\nu} \quad (9)$$

or Hirvonen's model

$$C(d) = C_0 / (1 + (d/\nu)^2) \quad (10)$$

where C_0 is the variance and ν is the correlation length, which are empirically determined from the actual data for each case, and d is the distance (Forsberg, 1998). The use of other types of covariance functions has also been investigated (e.g. Milbert, 1995).

3 Assessing the parametric model performance

The most common method used in practice to assess the performance of the selected parametric model is based on the statistics for the adjusted residuals after the least-squares fit. Those residuals \hat{v}_i are computed for each GPS/levelling site as follows:

$$\hat{v}_i = h_i - H_i - N_i - c_i \quad (11)$$

The model that results in the smallest residuals is considered the most appropriate one; it exhibits the best fit. A typical series of residuals reflecting differences between the original height misclosures l_i (3) and the adjusted residuals \hat{v}_i after the fit (11) is shown in Figure 1. Of note is the reduction in the average value to zero imposed by the least-squares adjustment. The values after fit give an assessment of the *precision* of the model as they indicate how well the data sets fit each other. Therefore, this method is valid for testing the precision of the model, but it should not be interpreted as the *accuracy* or the prediction capability of the model.

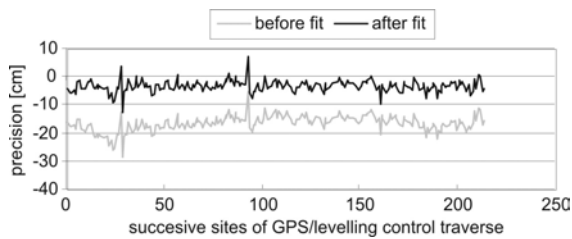


Fig. 1. Example of height misclosures before and after fitting parametric model

In order to estimate the accuracy of the predicted model, the model computed using the heights of the GPS/levelling POLREF sites will be checked at the sites of the GPS/levelling control traverse established for that purpose in Poland.

4 Results for the parametric model surface fits to the POLREF network

330 co-located GPS/levelling POLREF network points distributed throughout Poland (Zieliński et al., 1997) were used for the numerical tests. The distribution of height misclosures computed at each point using (3) is presented in Figure 2.

Statistics of those height misclosures are given in Table 1. The average misclosure equals -13.1 cm while an overall empirical standard deviation equals 3.7 cm.

Table 1. Statistics of the original height misclosures at the POLREF sites [cm]

Mean	Std dev.	Min	Max
-13.1	3.7	-23.3	-3.5

The POLREF network provides an excellent test field for different parametric models as the data

distribution is relatively consistent throughout the country with an average spacing of approximately 30 km between control points. In general, the dispersion of height misclosures at the POLREF sites is considerably smaller (ranges within 27 cm) than the respective one at other GPS/levelling networks investigated in the literature (e.g. Milbert, 1998).

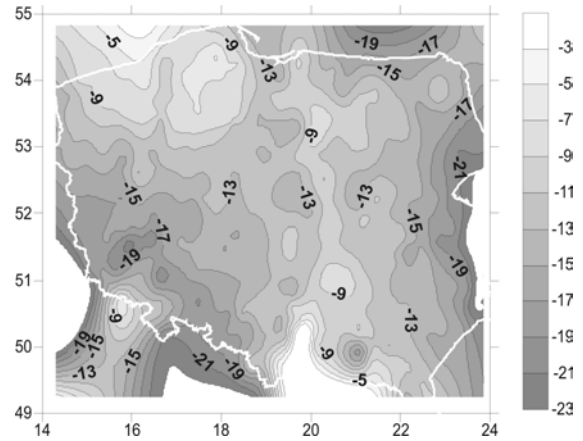


Fig. 2. Original height misclosures at the POLREF sites

Gravimetric quasigeoid model quasi05c was calculated using the remove-restore strategy as a sum of three components that represent global, regional and local effects, respectively. The first component was calculated using the coefficients of the GGM02S/EGM96 global geopotential model, the second one – using mean Faye anomalies Δg_F , and the third one – using topography (Krynski and Łyszkowicz, 2005).

The assessment procedure of the parametric model was tested using two pre-specified families of corrector surfaces, namely:

- tilted plane-fit model (4) and similarity-based transformation models (5) and (6),
- least-squares collocation model (7).

The trend t and de-trended residuals $(l - t)$ of height misclosures shown in Figure 2 have been modelled with the use of corrector surface models (3), (4) and (5). Their statistics are given in Table 2. Figure 3 shows the trend for the models considered.

What could be expected, the empirical standard deviation of residuals $(l - t)$ for the models investigated gets smaller with growing number of parameters in the model. Its value getting reduced from 3.56 cm for 3-parameter model to 2.75 cm for 5-parameter model indicates that the 5-parameter model approximates best de-trended residuals $(l - t)$ (Table 2). Thus, when fitting the gravimetric

quasigeoid to the POLREF sites with the use of modelling the trend only, the 5-parameter model is recommended to be applied.

Table 2. Statistics for trend and de-trended residuals of height misclosures [cm]

	3-parameter model		4-parameter model		5-parameter model	
	trend t	$(l-t)$	trend t	$(l-t)$	trend t	$(l-t)$
Mean	-13.20	0.00	-13.10	-0.05	-13.54	0.39
Std dev.	1.07	3.56	1.24	3.51	2.50	2.75
Min	-15.60	-9.19	-17.22	-8.86	-20.00	-7.11
Max	-11.20	11.81	-11.58	12.78	-6.52	9.37

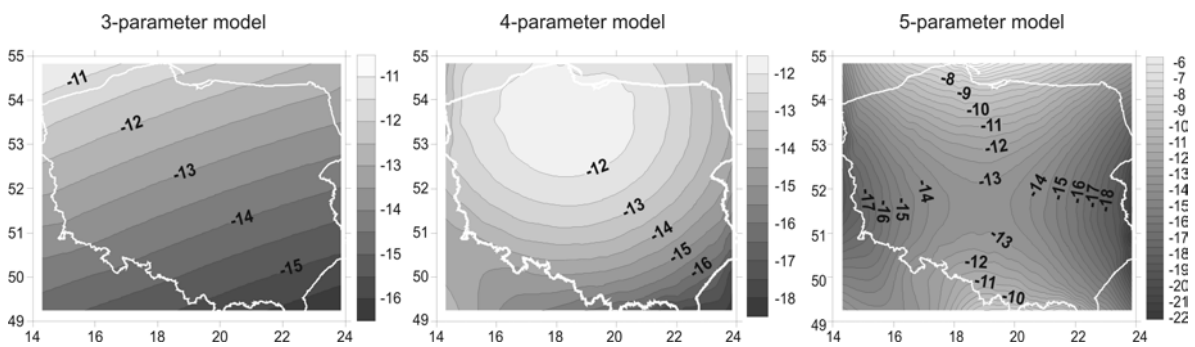


Fig. 3. The trend computed from the 3-, 4- and 5-parameter models

In the next step the least-squares collocation approach was investigated. After modelling the trend with the use of the 3-, 4- and 5-parameter models, the empirical covariance functions of de-trended residuals were computed. The variances C_0 and the correlation lengths ν computed for each case are given in Table 3.

Table 3. Empirical variance C_0 and the correlation length ν of de-trended residuals ($l-t$)

Model	C_0 [cm ²]	ν [degrees]
3-parameter	12.67	0.632
4-parameter	12.28	0.627
5-parameter	7.54	0.446

In the following step the empirical covariance function was compared with three analytical models of covariance function given by (8), (9) and (10). The results obtained show that Hirvonen's model suits best to empirical data. Figure 4 illustrates the covariance functions using the trend for the 3-parameter model.

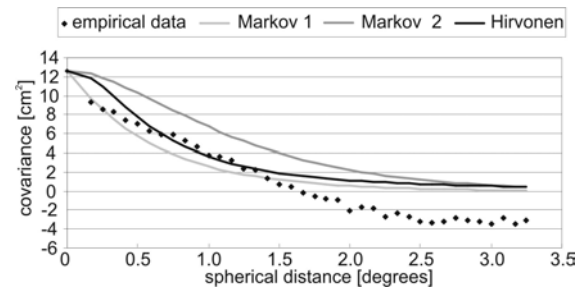


Fig. 4. Empirical covariance function of de-trended residuals ($l-t$) versus three analytical covariance functions

Based upon the set of de-trended residuals the least-squares collocation was used to predict the signal for the 3-, 4- and 5-parameter trend models with the use of empirical standard deviation σ_0 of observations equal to 3.7 cm (Table 1). The results of computations are summarized in Table 4. The fit is the same when the trend modelled by the 3- and 4-parameter surface and equals to 1.41 cm, while 5-parameter trend applied to signal prediction gives only slightly worse results.

The final corrector surface was thus computed using least-squares collocation. The trend was modelled by the plane (4) and the signal (Fig. 5) by

least-squares collocation with the accuracy of observations (GPS, levelling and geoid data) assumed as 3.7 cm. The *precision* of such fitted surface was estimated as ± 1.41 cm (Table 4).

Table 4. Statistics of residuals ($l - t - s$) for trend model by 3-, 4- and 5-parameter surface at the POLREF sites [cm]

	3-param.	4-param.	5-param.
Mean	-0.02	0.00	0.02
Std dev.	1.41	1.41	1.46
Min	-6.63	-6.63	-6.42
Max	6.82	7.01	7.29

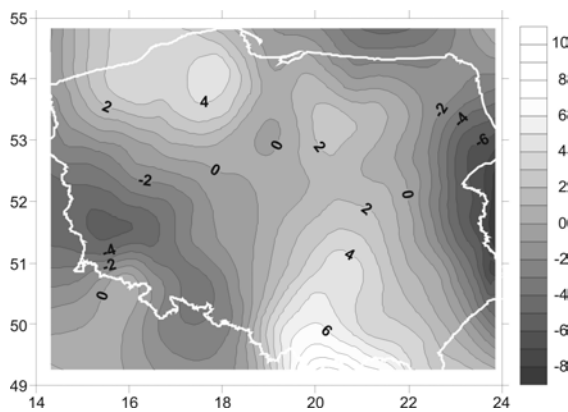


Fig. 5. Signal component (contour interval 1 cm)

5 Accuracy of corrector surface model

The accuracy of final corrector surface was checked on the GPS/levelling control traverse established in Poland in 2003–2004. The traverse contains 224 stations of precisely determined ellipsoidal and normal heights. The stations were located at the benchmarks of the 1st or 2nd order vertical control, or in their close vicinity. 77 stations of the traverse considered as the 1st order control were surveyed in one or two 24h sessions. The remaining 147 stations considered as densification points were surveyed in 4h sessions (Krynski et al., 2005). The coordinates of 77 1st order control stations were determined using the EPN strategy with the Bernese v.4.2 software. Accuracy of the coordinates determined is at the level of single millimetres for most of the stations. The coordinates of densification points were calculated using the Pinnacle program with the 1st order control stations as reference.

In recent test only 77 stations of superior accuracy were used to estimate the accuracy of the corrector surface model computed using least-

squares collocation with Hirvonen's covariance function and the trend obtained with the 3-parameter model. The statistics of the results at the sites of the control traverse are given in Table 5.

Table 5. Statistics of the trend t , the signal s , and residuals l and ($l - t - s$) for trend model by 3-parameter surface at the sites of the control traverse [cm]

	l	t	s	$l - t - s$
Mean	-15.9	-13.0	-0.3	-2.6
Std dev.	2.3	0.4	1.6	1.5
Min	-21.5	-13.5	-3.8	-6.9
Max	-11.1	-12.4	2.1	0.4

Table 5 shows that by applying the corrector surface, computed using least-squares collocation with Hirvonen's covariance function, the standard deviation of absolute normal height determined from GPS observations improves from 2.3 cm to 1.5 cm. Figure 6 shows that the accuracy, with respect to the heights of the control traverse sites of gravimetric quasigeoid model quasi05c, improved by the use of corrector surface.

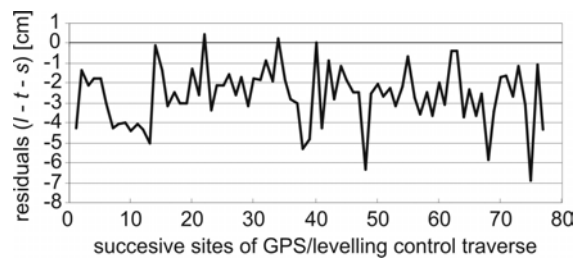


Fig. 6. Accuracy with respect to the heights of the control traverse sites of gravimetric quasigeoid model quasi05c improved by the use of corrector surface

Conclusions

Various methods of fitting the gravimetric quasigeoid model quasi05c to the vertical datum were investigated. The fit is based on the GPS/levelling POLREF network. It was assumed that the model which is characterized by the highest precision fits best to the vertical datum.

The quality of the fitting was studied with the use of different models, i.e. 3-, 4- and 5-parameter model and the least-squares collocation approach. The result of investigations shows that amongst parametric models the 5-parameter model gives the best fit of de-trended residuals to GPS/levelling sites with the lowest standard deviation of 2.75 cm.

In order to fit of quasi05c model by least-squares collocation, the empirical covariance function was computed with three analytical models: two Markov models and Hirvonen's model. It appeared that Hirvonen's model fits best to the empirical covariance function.

The final corrector surface was computed by least-squares collocation with Hirvonen's analytical covariance function where the trend was modelled by the plane (3-parameter model). The accuracy of observations derived from GPS/levelling data and geoid equal to 3.7 cm was used in the calculations, as the result of numerical tests. The precision of such computed corrector surface equals 1.25 cm, while its accuracy tested on the control traverse is estimated to be 1.5 cm.

Acknowledgements

The research was supported by the Polish State Committee for Scientific Research (grant PBZ-KBN-081/T12/2002). It was partially done in the framework of the statutory project "Problems of geodesy and geodynamics" of the Institute of Geodesy and Cartography, Warsaw.

References

- Denker H., Torge W., Wenzel G., Ihde J., Schirmer U., (2000). Investigation of different methods for the combination of gravity and GPS/levelling data, Springer, *International Association of Geodesy Symposia, Symposium 121: Geodesy Beyond 2000, The Challenges of the First Decade*, K.-P. Schwarz (ed.), IAG General Assembly, Birmingham, UK, July 19-30, 1999, pp. 137-142.
- Forsberg, R., (1998). Geoid Tayloring to GPS - with Example of a 1-cm Geoid of Denmark. Proceedings of the 2nd Continental Workshop on the Geoid in Europe, Budapest, Hungary, March 10-14, Vermeer M (Ed.). *Report of Finnish Geodetic Institute*, 98:4, pp. 191-198.
- Heiskanen, W.A., Moritz, H., (1967). *Physical geodesy*, W.H. Freeman and Company, San Francisco.
- Kotsakis C., Fotopoulos G., Sideris M.G., (2001). Optimal fitting of gravimetric geoid undulations to GPS/levelling data using an extended similarity transformation model. Presented at the 27th Annual meeting joint with the 58th Eastern snow conference of the Canadian Geophysical Union, Ottawa, Canada, May 14-17.
- Krynski J., Cisak J., Figurski M., Mank M., Bieniewska H., Moskwinski M., Sekowski M., Zanimonskiy Y., Zak L., (2005). GPS survey of control traverses and eventual link of the traverse sites to the vertical control with levelling as well as data processing (in Polish), Institute of Geodesy and Cartography, *Report for the Institute of Geodesy and Cartography*, Warsaw (27 pp).
- Krynski J., Lyszkowicz A., (2005). Study on choice of global geopotential model for quasigeoid determination in Poland. *Geodesy and Cartography*, Vol. 54, No 1, pp. 17-36.
- Krynski J., Lyszkowicz A., (2006). The overview of precise quasigeoid modelling in Poland. 2nd Workshop on International Gravity Field Research 2006, 8-9 May 2006, Smolenice, Slovakia, *Contributions to Geophysics and Geodesy*, Geophysical Institute of Slovak Academy of Sciences (in print).
- Łyszkowicz A., (2000). Improvement of the Quasigeoid model in Poland by GPS and levelling data. *Artificial Satellites*, Journal of Planetary Geodesy, Vol. 35, No 1, pp. 3-8.
- Milbert D.G., (1995). Improvement of a high resolution geoid height model in the United States by GPS height on NAVD88 benchmarks. *International Association of Geodesy Bulletin d'Information, New Geoids in the World*, G. Balmino, F. Sanso (Eds.), *IGeS Bulletin*, No 4, pp. 13-36.
- Millbert D.G., (1998). An accuracy assessment of the GEOID96 geoid height model for the State of Ohio. *Surveying and Land Information Systems*, Vol. 58, No 2.
- Sideris M.G., (1993). Test of a gravimetric geoid in GPS networks. *Surveying and Land Information Systems*, Vol. 53, No 2.
- Zhiheng Jiangl, Duquenne H., (1995). Optimal fitting of gravity geoid to GPS levelling points. Presented to XX General Assembly of European Geophysical Society, Hamburg, 3-7 April.
- Zieliński J.B., Łyszkowicz A., Jaworski L., Świątek A., Zdunek R., Gelo St., (1997). Polref-96 the New Geodetic Reference Frame for Poland, Springer, *International Association of Geodesy Symposia, Symposium 118: Advances in Positioning and Reference Frames*, F.K. Brunner (ed.), IAG Scientific Assembly, Rio de Janeiro, Brazil, September 3-9, 1997, pp. 161-166.

Modified Stokes' Kernel versus Window Technique: Comparison of Optimum Combination of Gravity Field Wavelengths in Geoid Computation

Hussein A. Abd-Elmotaal

Civil Engineering Department, Faculty of Engineering, Minia University, Minia 61111, Egypt

Norbert Kühtreiber

Institute of Navigation and Satellite Geodesy, TU Graz, Steyrergasse 30, A-8010 Graz, Austria

Abstract. Different approaches for combining the gravity field wavelengths in geoid computations have been investigated during the last two decades. The window technique has been suggested to get rid of the double consideration of the topographic-isostatic masses within the data window in the framework of the remove-restore technique. The modified Stokes' kernel has been suggested to possibly combine the local data signals with the global geopotential models. Both techniques have been used in computing a gravimetric geoid for Austria. A wide comparison between modified Stokes' kernel and window techniques has been carried out within this investigation in the framework of the geoid computation. The results proved that the reduced gravity anomalies using the window technique are the smoothest, un-biased and have the smallest range. The modified Stokes kernel technique gives the best fit to the GPS/levelling derived geoid. The window technique gives, however, fairly better results than the Stokes' un-modified kernel technique.

Keywords. Modified Stokes kernel, window technique, remove-restore technique, geoid determination.

1 Introduction

The optimum combination of gravity field wavelengths in the framework of geoid computation still remains a hot research topic. There are different approaches for such a combination of the wavelengths. The current investigation considers a comparison of three approaches, namely the traditional un-modified Stokes' kernel technique, the modified Stokes' kernel technique and the window technique

(Abd-Elmotaal and Kühtreiber, 2003).

The used data sets are described. The Stokes' technique of geoid determination, within the remove-restore scheme, with un-modified and modified Stokes' kernel, after Meissl (1971), is described. The window technique (Abd-Elmotaal and Kühtreiber, 2003) within the remove-restore scheme has been outlined. The harmonic analysis of the topographic-isostatic potential is then given. The reduced gravity using both techniques under investigations are then computed and compared. A gravimetric geoid for Austria has been computed by the three different approaches considered within the current investigation. A wide comparison among these approaches has been carried out in the framework of the geoid computation. The comparison is made on two different levels; the residual gravity anomalies after the remove step and the computed geoid signals.

It should be noted that many scholars have suggested different modifications of the Stokes' kernel and have studied the topic of the optimum combination of gravity field wavelengths. The reader may refer, e.g., to (Sjöberg and Hunegnaw, 2000; Novák et al., 2001; Sjöberg, 2003a; 2003b; 2004; Vaníček and Featherstone, 1998; Featherstone, 1999; 2003; Huang et al., 2000; Silva et al., 2002).

2 The Data

2.1 Gravity Data

The gravitational data set for this investigation is a set of free-air gravity anomalies at 5796 stations in Austria and neighbouring countries (Fig. 1). Figure 1 shows, more or less, a homogeneous data distribution within Austria. The gravity data outside Austria

have been included to correct the edge effect in the computed gravimetric geoid. The gravity data covers the window ($45.7^\circ \text{N} \leq \phi \leq 49.7^\circ \text{N}$ and $8.5^\circ \text{E} \leq \lambda \leq 18.2^\circ \text{E}$).

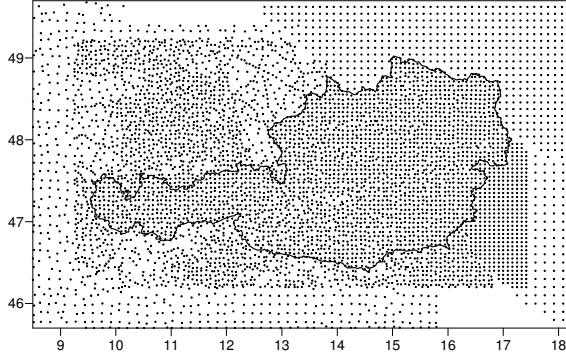


Figure 1. Distribution of the used gravity data set.

2.2 GPS Benchmarks

Figure 2 shows the distribution of the available GPS benchmarks (referred to ITRF96) with known orthometric heights (referred to UELN98) in Austria. It shows that most of the stations are located in the eastern part of Austria. Only few stations are located at the mountainous western part of Austria.

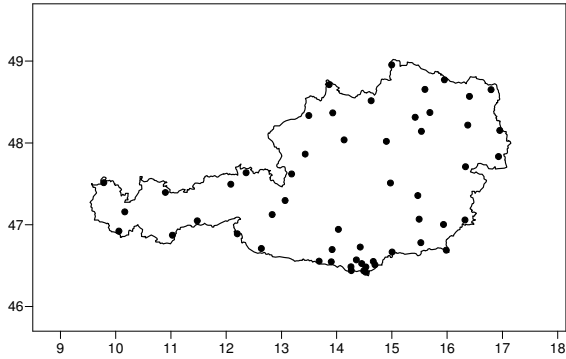


Figure 2. Used GPS benchmarks with known orthometric heights.

2.3 Digital Height Models

Two different Digital Height Models are available. A coarse model of $90'' \times 150''$ resolution in the latitude and the longitude directions, respectively, and a fine model of $11.25'' \times 18.75''$ resolution. The fine DHM covers the window $44.75^\circ \text{N} \leq \phi \leq 50.25^\circ \text{N}$; $7.75^\circ \text{E} \leq \lambda \leq 19.25^\circ \text{E}$. The coarse DHM covers the window $40^\circ \text{N} \leq \phi \leq 52^\circ \text{N}$; $5^\circ \text{E} \leq \lambda \leq 22^\circ \text{E}$.

The coarse DHM has been created by integrating

the Austrian fine DHM with GTOPO30 ($30'' \times 30''$) (Gesch and Larson, 1996) and global bathymetry model provided by the Naval Oceanographic Office ($1' \times 1'$). Figure 3 shows the coarse digital height model used for this investigation. It shows the high mountainous structure of the Alps.

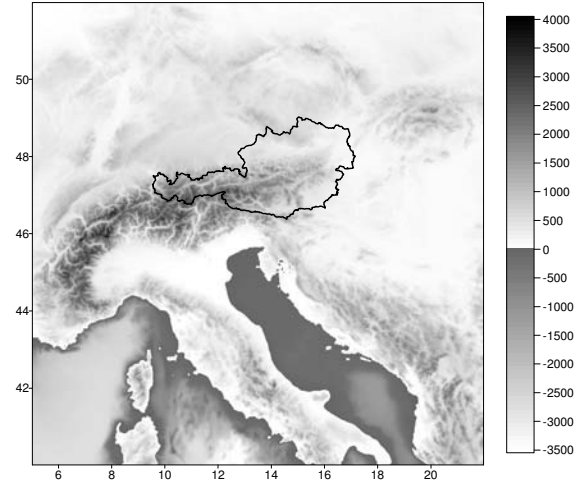


Figure 3. The coarse ($90'' \times 150''$) digital height model.

3 Traditional Remove-Restore Technique

Within the well-known remove-restore technique, the effect of the topographic-isostatic masses is removed from the source gravitational data and then restored to the resulting geoidal heights. For example, in the case of gravity data, the reduced gravity anomalies in the framework of the remove-restore technique are computed by

$$\Delta g_{red} = \Delta g_F - \Delta g_{GM} - \Delta g_h, \quad (1)$$

where Δg_F stands for the free-air anomalies, Δg_h is the effect of topography and its compensation on the gravity anomalies, and Δg_{GM} is the effect of the reference field on the gravity anomalies. Thus the final computed geoid N within the remove-restore technique can be expressed by:

$$N = N_{GM} + N_{\Delta g} + N_h, \quad (2)$$

where N_{GM} gives the contribution of the reference field, $N_{\Delta g}$ gives the contribution of the reduced gravity anomalies, and N_h gives the contribution of the topography and its compensation (the indirect effect).

4 Stokes' Integral with Stokes' Un-modified Kernel

The contribution of the reduced gravity anomalies $N_{\Delta g}$ can be given by Stokes' integral (Heiskanen and Moritz, 1967, p. 94)

$$N_{\Delta g} = \frac{R}{4\pi\gamma} \iint_{\sigma} \Delta g_{red} S(\psi) d\sigma, \quad (3)$$

where γ is the normal gravity, R is the mean earth's radius and $S(\psi)$ stands for the Stokes un-modified kernel given by (ibid., p. 94)

$$S(\psi) = \frac{1}{s} - 4 - 6s + 10s^2 - (3 - 6s^2) \ln(s + s^2) \quad (4)$$

with

$$s = \sin \frac{\psi}{2}, \quad (5)$$

and ψ is the spherical distance between the computational point P and the running point Q .

It is believed that using classical un-modified Stokes kernel in the remove-restore technique implies a wrong combination of gravity field wavelengths.

5 Stokes' Integral with Stokes' Modified Kernel

The contribution of the reduced gravity anomalies $N_{\Delta g}$ can be given by

$$N_{\Delta g} = \frac{R}{4\pi\gamma} \iint_{\sigma} \Delta g_{red} S^{ME}(\psi) d\sigma, \quad (6)$$

where $S^{ME}(\psi)$ is the modified Stokes' kernel after Meissl (1971) given by

$$S^{ME}(\psi) = S(\psi) - S(\psi_0) \quad \text{for } (0 < \psi \leq \psi_0), \quad (7)$$

where the optimal cap size ψ_0 is empirically determined through the comparison of the computed gravimetric geoid to the GPS/levelling geoid.

6 The Window Technique

The conventional way of removing the effect of the topographic-isostatic masses faces a theoretical problem. A part of the influence of the topographic-isostatic masses is removed twice as it is already included in the global reference field. This leads to some double consideration of that part of the topographic-isostatic masses. Figure 4 shows schematically the conventional gravity reduction for the

effect of the topographic-isostatic masses. The short-wavelength part depending on the topographic-isostatic masses is computed for a point P for the masses inside the circle. Removing the effect of the long-wavelength part by a global earth's gravitational potential reference field normally implies removing the influence of the global topographic-isostatic masses, shown as a rectangle in Fig. 4. The double consideration of the topographic-isostatic masses inside the circle (double hatched) is seen.

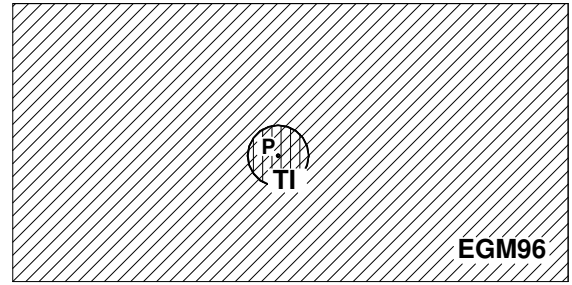


Figure 4. The traditional remove-restore technique.

A possible way to overcome this difficulty is to adapt the used reference field due to the effect of the topographic-isostatic masses for a fixed data window. Figure 5 shows the advantage of the window remove-restore technique schematically. Consider a measurement at point P , the short-wavelength part depending on the topographic-isostatic masses is now computed by using the masses of the whole data area (small rectangle). The adapted reference field is created by subtracting the effect of the topographic-isostatic masses of the data window, in terms of potential coefficients, from the reference field coefficients. Thus, removing the long-wavelength part by using this adapted reference field does not lead to a double consideration of a part of the topographic-isostatic masses (no double hatched area in Fig. 5).

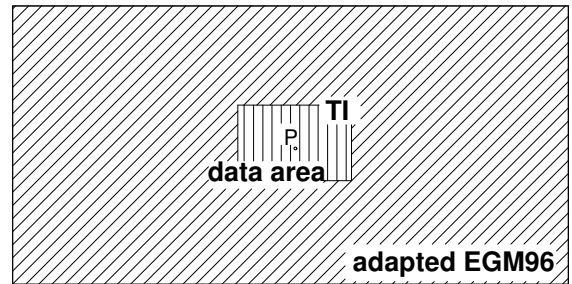


Figure 5. The window remove-restore technique.

The remove step of the window remove-restore

technique can then mathematically be written as

$$\Delta g_{red} = \Delta g_F - \Delta g_{GMAdapt} - \Delta g_h, \quad (8)$$

where $\Delta g_{GMAdapt}$ is the contribution of the adapted reference field. The restore step of the window remove-restore technique can be written as

$$N = N_{GMAdapt} + N_{\Delta g} + N_h, \quad (9)$$

where $N_{GMAdapt}$ gives the contribution of the adapted reference field. It should be noted that the contribution of the topography and its compensation (the indirect effect) N_h is computed using the Stokes' integral (3) using the un-modified Stokes' kernel given by (4).

7 Harmonic Analysis of the Topographic-Isostatic Potential

The harmonic coefficients of the topography and its isostatic compensation as well as the harmonic series expansion of the topographic-isostatic potential can be expressed by (Abd-Elmotaal and Kühtreiber, 2003, pp. 78–79; Hanafy, 1987, P. 80):

$$T_{TI}(P) = \frac{GM}{r_P} \sum_{n=0}^{\infty} \left(\frac{R}{r_P} \right)^n \sum_{m=-n}^n \bar{T}_{nm} \bar{R}_{nm}(P), \quad (10)$$

where

$$\begin{aligned} \bar{T}_{nm} = & \frac{R^3}{M(2n+1)(n+3)} \iint_{\sigma} \left\{ \rho_Q \left[\left(1 + \frac{H_Q}{R} \right)^{n+3} - 1 \right] \right. \\ & \left. + \delta \rho_Q \left(1 - \frac{T_o}{R} \right)^{n+3} \left[\left(1 - \frac{t_Q}{R-T_o} \right)^{n+3} - 1 \right] \right\} \\ & \times \bar{R}_{nm}(Q) d\sigma_Q, \end{aligned} \quad (11)$$

where T_o is the normal crustal thickness, H is the topographic height, t is the compensating root/antiroot and M denotes the mass of the earth, given by

$$M \doteq \frac{4\pi R^3}{3} \rho_M, \quad (12)$$

where ρ_M denotes the mean earth's density and ρ is given by

$$\begin{aligned} \rho &= \rho_o & \text{for } H \geq 0, \\ \rho &= \rho_o - \rho_w & \text{for } H < 0, \end{aligned} \quad (13)$$

where ρ_o denotes the density of the topography and ρ_w is the density of ocean's water. The density anomaly $\Delta \rho$ is given by

$$\Delta \rho = \rho_1 - \rho_o, \quad (14)$$

where ρ_1 is the density of the upper mantle.

Table 1. Statistics of the reduced gravity after each reduction step

reduced gravity	statistical parameters			
	min.	max.	average	st. dev.
	mgal	mgal	mgal	mgal
Δg_F	-154.16	187.15	9.70	42.16
$\Delta g_F - \Delta g_{GM}$	-210.72	132.27	-12.91	37.60
$\Delta g_F - \Delta g_{GM} - \Delta g_{TI}$	-123.66	81.97	-20.09	25.88
$\Delta g_F - \Delta g_{GMAdapt}$	-194.55	204.99	-1.46	44.43
$\Delta g_F - \Delta g_{GMAdapt} - \Delta g_{TIWin}$	-62.39	71.60	0.23	20.32

8 Gravity Reduction

The following parameter set has been used during the gravity reduction and the geoid determination as they empirically proved to fit the Austrian gravity field to a good extent (Kühtreiber and Abd-Elmotaal, 2001):

$$T_o = 30 \text{ km}, \quad (15)$$

$$\rho_o = 2.67 \text{ g/cm}^3, \quad (16)$$

$$\Delta \rho = 0.20 \text{ g/cm}^3. \quad (17)$$

The EGM96 geopotential model has been used for the traditional remove-restore technique. An adapted reference field has been created by subtracting the potential coefficients of the topographic-isostatic masses of the data window ($40^\circ \text{N} \leq \phi \leq 52^\circ \text{N}; 5^\circ \text{E} \leq \lambda \leq 22^\circ \text{E}$) computed by (11) from the EGM96 coefficients. This adapted reference field has been used for the window remove-restore technique.

Table 1 shows the statistics of the gravity reduction after each reduction step for the traditional and window remove-restore techniques. It should be noted that the reduced anomalies for Stokes' integral with modified Stokes' kernel are the same as those for the Stokes' kernel with un-modified Stokes' integral (the upper part of Table 1).

Table 1 shows that using the window technique gives the best reduced gravity anomalies. The range has dropped by its one-third and the standard deviation drops by about 20%. Also the reduced anomalies are perfectly centered (un-biased). This property makes the window-technique reduced anomalies suite best for interpolation and other geodetic purposes.

9 Geoid Computation

The contribution of the gravity anomalies on the geoid undulation $N_{\Delta g}$ has been computed by 1D-FFT technique using the FFTGEOID program by Sideris

Table 2. Statistics of the empirical tests for the cap size ψ_o for the Stokes/Meissl geoid

Cap size	Differences to GPS/levelling geoid			
	min.	max.	average	st. dev.
	m	m	m	m
$\psi_o = 0.5^\circ$	-4.58	-1.31	-2.57	0.81
$\psi_o = 1.0^\circ$	-2.73	-1.28	-1.90	0.40
$\psi_o = 1.5^\circ$	-1.69	-1.09	-1.30	0.14
$\psi_o = 1.7^\circ$	-1.37	-0.91	-1.08	0.10
$\psi_o = 2.0^\circ$	-1.10	-0.44	-0.78	0.14

and Li (1993). Three methods are used in the current investigation to compute a gravimetric geoid for Austria. They are:

- Stokes' integral using classical un-modified Stokes' kernel (classical Stokes geoid),
- Stokes' integral using Meissl's modified Stokes' kernel (Stokes/Meissl geoid),
- Stokes' integral using window technique (Window geoid).

All computed geoids are compared to the GPS/levelling geoid.

Figure 6 shows the absolute geoid differences between the classical Stokes geoid and the GPS/levelling geoid. Figure 6 shows a high-order polynomial structure of the differences. The range of the differences is quite large (about 2 m).

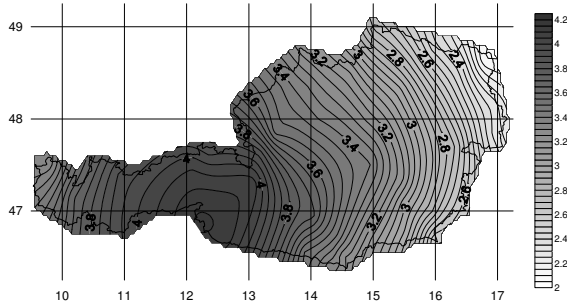


Figure 6. Absolute geoid differences between classical Stokes geoid and GPS/levelling geoid. Contour interval: 5 cm.

As mentioned earlier, the optimum cap size ψ_o can be empirically determined. This is achieved by comparing the computed Stokes/Meissl geoid to the GPS/levelling geoid. Table 2 shows the statistics of the empirical tests for the cap size ψ_o for the Stokes/Meissl geoid. It shows that $\psi_o = 1.7^\circ$ gives the optimum cap size in view of the standard deviation of the absolute differences to the GPS/levelling geoid.

Figure 7 shows the absolute geoid differences between the Stokes/Meissl geoid (cap size $\psi_o = 1.7^\circ$) and the GPS/levelling geoid. Figure 7 shows better polynomial structure of the differences than that in the case of Stokes geoid. The range of the differences drops to about 45 cm.

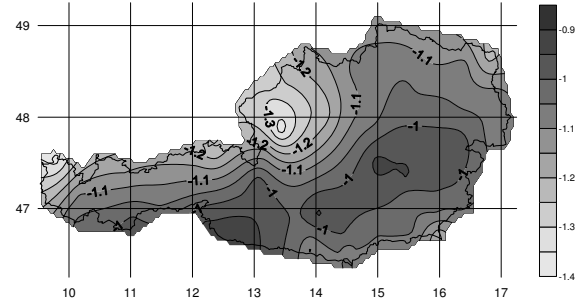


Figure 7. Absolute geoid differences between Stokes/Meissl geoid (cap size $\psi_o = 1.7^\circ$) and GPS/levelling geoid. Contour interval: 5 cm.

Figure 8 shows the absolute geoid differences between the window and the GPS/levelling geoids. Figure 8 shows better polynomial structure of the differences than that in the case of Stokes geoid. The range of the differences drops to about 1 m.

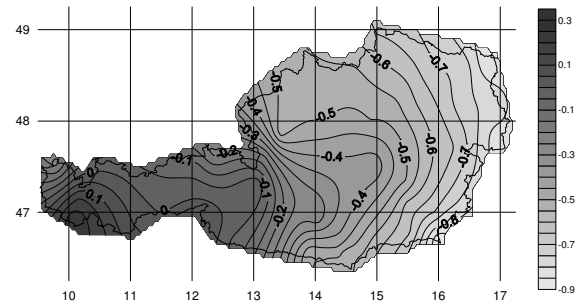


Figure 8. Absolute geoid differences between window geoid and GPS/levelling geoid. Contour interval: 5 cm.

Table 3 illustrates the statistics of the absolute geoid differences between the computed geoids within the current investigation and the GPS/levelling geoid. Table 3 shows that the Stokes geoid has the worst differences to the GPS/levelling. This confirms what has been stated earlier that using the classical un-modified Stokes kernel in the remove-restore technique implies a wrong combination of gravity field wavelengths. Table 3 shows also that either using the window technique or the modified Stokes kernel gives better differences to the GPS/levelling geoid (in terms of either the mean difference or the range/statndard deviation).

Table 3. Statistics of the absolute geoid differences between the computed geoids and the GPS/levelling geoid

geoid technique	statistical parameters			
	min.	max.	average	st. dev.
	m	m	m	m
Stokes	2.10	4.16	3.27	0.52
Stokes/Meissl	-1.37	-0.91	-1.08	0.10
Window	-0.89	0.24	-0.44	0.27

Table 4. Statistics of the geoid differences between the computed geoids and the GPS/levelling geoid after removing a trend function

geoid technique	statistical parameters			
	min.	max.	range	st. dev.
	cm	cm	cm	cm
Stokes	-22.1	16.7	38.8	7.3
Stokes/Meissl	-25.3	12.5	37.8	6.9
Window	-21.3	14.8	36.1	6.6

Table 4 illustrates the statistics of the geoid differences between the computed geoids within the current investigation and the GPS/levelling geoid after removing a third order surface polynomial trend function. Table 4 shows that the window technique gives the minimum range and standard deviation of the remaining differences.

10 Conclusions

Stokes technique, within the remove-restore scheme, with un-modified stokes kernel cannot correctly handle the combination of the geoid wavelengths. A modification of the kernel or a new technique should be introduced. Both the modified Stokes kernel and the window technique can handle the combination of the geoid wavelengths within the remove-restore scheme. The modified Stokes kernel technique gives the best fit to the GPS/levelling derived geoid. The reduced gravity anomalies using the window technique are the smoothest (20% less in the standard deviation), un-biased and have the smallest range (one-third less). This property makes the window-technique reduced anomalies suite best for interpolation and other geodetic purposes.

References

Abd-Elmotaal, H., and Kühtreiber, N. (2003) Geoid Determination Using Adapted Reference Field, Seismic Moho Depths

- and Variable Density Contrast, *Journal of Geodesy*, **77**, 77–85.
- Featherstone, W. (1999) A Comparison of Gravimetric Geoid Models over Western Australia, Computed using Modified Forms of StokesS Integral, *Journal of the Royal Society of Western Australia*, **82**, 137–145.
- Featherstone, W. (2003) Software for Computing Five Existing Types of Deterministically Modified Integration Kernel for Gravimetric Geoid Determination, *Computers & Geosciences*, **29**, 183–193.
- Gesch, D.B., and Larson, K.S. (1996) Techniques for Development of Global 1-Kilometer Digital Elevation Models, *In: Pecora Thirteen, Human Interactions with the Environment - Perspectives from Space, Sioux Falls, South Dakota, August 20–22, 1996*.
- Heiskanen, W.A., and Moritz, H. (1967) *Physical Geodesy*. Freeman, San Francisco.
- Huang, J., Vaníček, P., and Novák, P. (2000) An Alternative Algorithm to FFT for the Numerical Evaluation of Stokes’s Integral, *Studia geoph. et geod.*, **44**, 374–380.
- Kühtreiber, N., and Abd-Elmotaal, H. (2001) Gravimetric Geoid Computation for Austria Using Seismic Moho Data, *In Sideris, M., ed. (2001) Gravity, Geoid and Geodynamics 2000, International Association of Geodesy Symposia, Banff, Canada, July 31 – August 4, 2000*, **123**, 311–316.
- Meissl, P. (1971) A Study of Covariance Functions Related to the Earth’s Disturbing Potential, *Department of Geodetic Science, The Ohio State University, Columbus, Ohio*, **151**.
- Novák, P., Vaníček, P., Véronneau, M., Holmes, S., and Featherstone, W. (2001) On the Accuracy of the Modified Stokes’s Integration in High-Frequency Gravimetric Geoid Determination, *Journal of Geodesy*, **74**, 644–654.
- Sideris, M.G. and Li, Y.C. (1993) Gravity Field Convolutions Without Windowing and Edge-Effects, *Bulletin Geodesique*, **67**, 107–118.
- Silva, M.A., Blitzkow, D., and Lobianco, M.C.B. (2002) A Case Study of Different Modified Kernel Applications in Quasi-Geoid Determination, *Proceedings of the 3rd Meeting of the International Gravity and Geoid Commission, Thessaloniki, Greece, August 26–30, 2002*, 138–143.
- Sjöberg, L.E. (2003a) A Computational Scheme to Model the Geoid by the Modified Stokes Formula Without Gravity Reductions, *Journal of Geodesy*, **77**, 423–432.
- Sjöberg, L.E. (2003b) A General Model for Modifying Stokes Formula and its Least-Squares Solution, *Journal of Geodesy*, **77**, 459–464.
- Sjöberg, L.E. (2004) A Spherical Harmonic Representation of the Ellipsoidal Correction to the Modified Stokes Formula, *Journal of Geodesy*, **78**, 180–186.
- Sjöberg, L.E., and Hunegnaw, A. (2000) Some Modifications of Stokes’ Formula that Account for Truncation and Potential Coefficient Errors, *Journal of Geodesy*, **74**, 232–238.
- Vaníček, P., and Featherstone, W. (1998) Performance of Three Types of Stokes’s Kernel in the Combined Solution for the Geoid, *Journal of Geodesy*, **72**, 684–697.

Combination of Deflections of the Vertical and Gravity Anomalies in Difficult Geological Regions, A Case Study

B. Wiesenhofer, N. Kühtreiber
Institute of Navigation and Satellite Geodesy,
Graz University of Technology, Steyrergasse 30, A-8010 GRAZ, AUSTRIA

Abstract. The latest Austrian geoid has been computed by a combination of deflections of the vertical and gravity anomalies using least squares collocation. The computation results revealed regions with large discrepancies between the gravimetric and astro-geodetic geoid solution. One interesting region is the southeast of Austria. Investigations based on Least Squares Collocation have been conducted for this area. The solutions indicate potential reasons for these discrepancies and furthermore, define the criteria for the selection of additional measurement points of deflections of the vertical.

For these new measurements the software package ICARUS, developed by Beat Bürki, ETH Zürich, will be used.

This paper gives a first overview of the investigations up to summer 2006 which have been performed using a dataset of the southeast of Austria. The simulations clearly indicate erroneous measurements and regions with an insufficient distribution of measured points (deflections of the vertical).

Keywords. Local geoid, deflection of the vertical, Least Squares Collocation, ICARUS

1 Data

1.1 Input Data

Starting in 1978, astro-geodetic deflections of the vertical have been determined at 362 stations by the universities of Graz, Vienna and Innsbruck. At additional 202 stations astro-geodetic measurement campaigns to determine the deflections of the vertical have been conducted by the Federal Office of Metrology and Surveying (BEV). Austrian surveying points of first order in a distance of 10 to 15 kilometres have been used for those measurements. The deflections of the vertical have

been measured using the Zeiss Ni2 Astrolabium. Additionally Graz University of Technology used a zenith-camera in parallel sessions. The deflections of the vertical refer to the local Austrian datum of the Military Geographic Institute. Later on, the observations have been transformed to the geocentric system WGS84. The precision for the deflections of the vertical components ξ and η are given as ± 0.2 arcsec and ± 0.3 arcsec respectively.

The Institute for Meteorology and Geophysics (University of Vienna), the Institute of Geophysics (Mining University Leoben), the OMV, and also the BEV has provided gravity measurements within Austria. At the moment about 86000 gravity observations exist in the local Austrian datum. For the simulations the gravity measurements have been transformed to the geocentric system WGS84. The precision for the gravity anomalies is assumed to be ± 1.0 mgal. This value for the precision is defined based on measurement errors, errors due to the remove-restore procedure and based on the results of case studies in Kühtreiber (2003).

The height system used is the Austrian orthometric height system based on the tide gauge Trieste.

1.2 Reductions

To remove the long and short wavelength effect of the gravitational potential from the gravity anomalies and the deflections of the vertical a remove-restore procedure has been applied. To compute the long wavelength part in the remove-restore procedure the adapted EGM96 (Abd-Elmotaal and Kühtreiber, 2001) was used. For the short to medium wavelengths, a topographic isostatic reduction was performed using the adapted technique and a detailed height model with the resolution $11.25'' \times 18.75''$. For the isostatic model an Airy-Heiskanen approach with a standard constant density of 2.67 g/cm^3 , a normal thickness T of 30 km and a crust-mantle density contrast of 0.4 g/cm^3 were used (Kühtreiber, 2003).

1.3 Austrian Geoid Solutions

Based on the data sets described in section 1 an astro-geodetic and a gravimetric geoid solution were computed by Kühtreiber (2003).

The comparison of the astro-geodetic with the gravimetric geoid solution reveals regions with large discrepancies. The reasons for these discrepancies are manifold: the sparse distribution of the deflections of the vertical in combination with a complex geology in this region; furthermore erroneous measurements and unknown trend components might have resulted in these discrepancies as well.

Kühtreiber (2003) assumes that the sparse distribution of deflections of the vertical is mainly responsible for these differences.

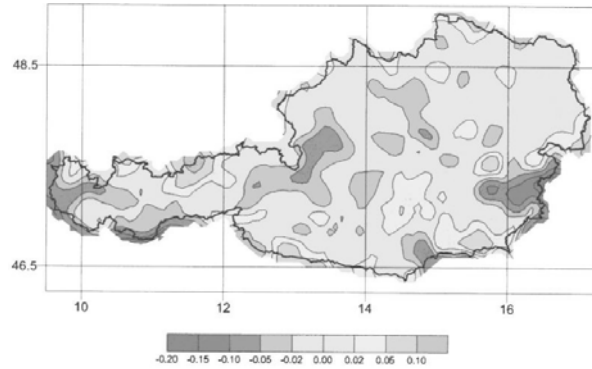


Fig. 1 Gravimetric minus astro-geodetic geoid solution given in cm

2 Simulations

The main objective of following simulations is to identify erroneous measurements and to highlight regions with an insufficient distribution of measured points.

2.1 Least Squares Collocation

The simulations have been done using the well-known Least Squares Collocation approach with:

$$\hat{s} = C_{sl}(C_{ll} + D)^{-1}l \quad (1)$$

where l is the vector of the observations, D is the error covariance matrix. The matrix C_{ll} is the covariance matrix of the observation and C_{sl} is the cross-covariance matrix of the observations and the estimated parameters s .

The basic covariance function of the disturbing potential is given by:

$$K_{(P,Q)} = \sum_{n=0}^{\infty} \sigma_n(T_P, T_Q) s^{n+1} P_n(\cos \psi) \quad (2)$$

with

$$s = \left(\frac{R^2}{r_P r_Q} \right) \quad (3)$$

where P and Q are the observation points, $\sigma_n(T_P, T_Q)$ denotes the degree variances of the disturbing potential, R is the radius of the Bjerhammar sphere, r_P, r_Q are the geocentric radii to the observations P and Q , which are separated by a spherical radius ψ .

The degree variances are obtained by an anomaly degree-variance model of Tscherning and Rapp (1974):

$$\sigma_n(\Delta g, \Delta g) = A \left(\frac{(n-1)}{(n-2)(n+B)} \right) \quad (4)$$

$$\sigma_n(T_P, T_Q) = \frac{R^2}{(n-1)^2} \sigma_n(\Delta g, \Delta g) \quad (5)$$

The covariance function of the gravity anomalies, the geoid undulation and the deflections of the vertical are derived by covariance propagation. These quantities are linear functionals of the anomalies potential T .

For the Austrian geoid computation the parameter B has been fixed to 24. The model parameters A and s are determined through an iterative adjustment procedure. By a recursive process the covariance model is fitted to the empirically determined covariance function of the gravity anomalies, which is given by its three essential parameters (the variance, the correlation length and the variance of the horizontal gradient). This fitting procedure was performed by Kühtreiber (2003) using 2489 gravity stations in Austria. The computation gave the following Tscherning-Rapp degree-variance model parameters: $A = 777.608$ mgal²; $B = 24$; $s = 0.997002$. In the following simulations the model is used as local covariance function. This means that all degree variances up to a certain degree N are equal to zero. The value of N results also from the above described estimation and is set to 79.

2.2 Implementation

The simulations were done using only selected data points in the southeast of Austria as shown in Figure 2. The used 192 measurements of deflections of the vertical are restricted to the Austrian territory, while the 1240 gravity data points are given in Austria and the neighbouring countries (Hungary and Slovenia).

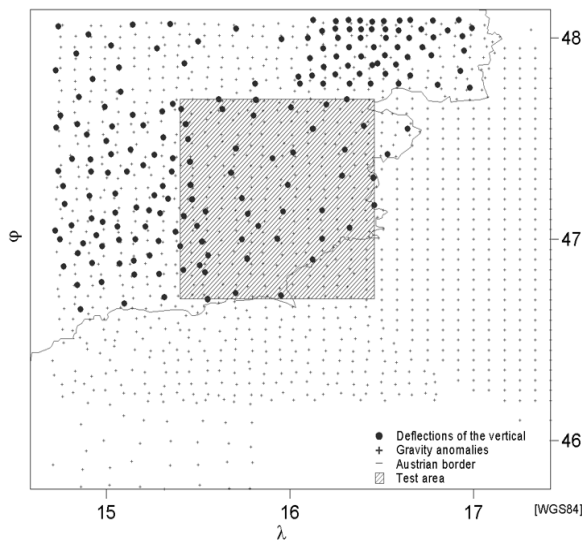


Fig. 2 Test area and input data

In the first investigation the quality of the measured deflections of the vertical is evaluated. Therefore deflections of the vertical have been predicted using least squares collocation. The prediction was done either by using deflections of the vertical only (without using the value at the prediction point), or by using gravity measurements only as observations. The differences between the measured and the predicted deflections of the vertical components ξ and η are shown in Figure 3 for the case of the prediction based on deflections of the vertical only and Figure 4 where for the prediction only gravity anomalies were used. As the scaling of the two figures is equal the comparison between the both allows identifying three main features.

First of all, big differences are visible in both figures, especially at the measurement points with the numbers 416, 421 and 698. The interpretation is that the measurements are erroneous. This result confirms the computation in Kühtreiber (2003) where the measurements at these points have been omitted. Secondly big discrepancies, which are obvious in the northeast in Figure 3, cannot be seen in Figure 4. That means while the prediction using

gravity anomalies only gives good results problems exist if only deflections of the vertical are used for the prediction. This leads to the following interpretation: It is assumed for the moment that the faulty measurements have already been detected (see above). Under the latter assumption it is very probable that the bad configuration is the reason for these discrepancies. Keep in mind that for the simulations using deflections of the vertical the input data are even less, as the measurement at the point of prediction is omitted. Last but not least there exist regions where both figures show good results. Of course this is the optimal case, which needs no further investigation.

Edge effects in the southeast of the test area need not to be discussed.

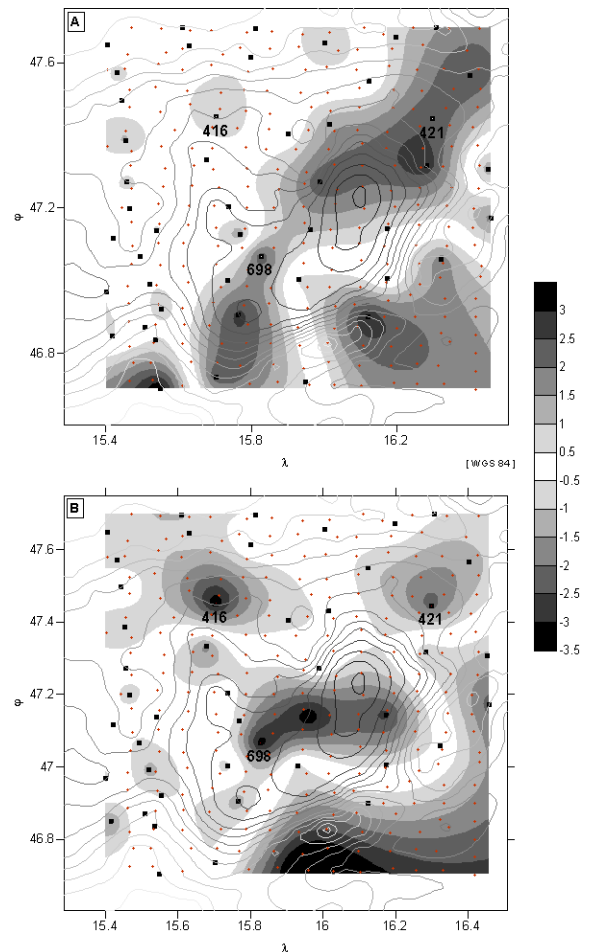


Fig. 3 Differences [arcsec] between the predicted and the measured values of the deflections of the vertical shown as colored filled contours. Prediction using existing measurements of deflections of the vertical only. The black contour lines represent the gravity anomaly field. 3A: Deflections of the vertical component ξ 3B: Deflections of the vertical component η

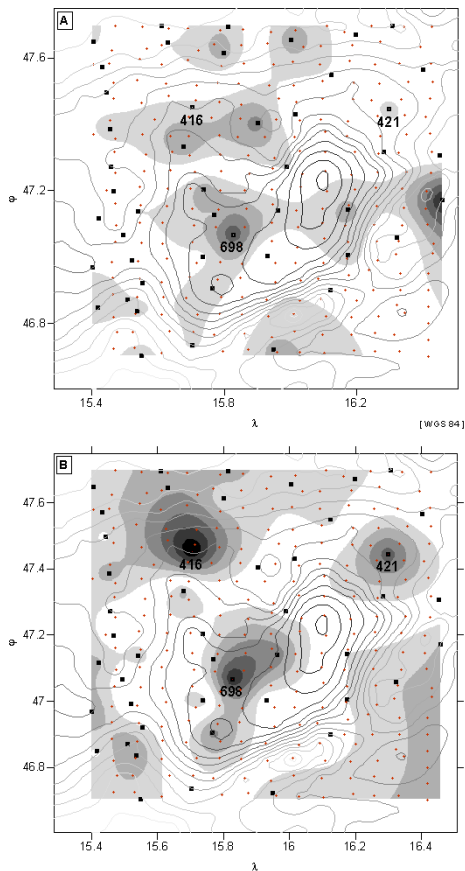


Fig. 4 Differences [arcsec] between the predicted and the measured value of the deflections of the vertical. Prediction using gravity anomalies only
 4A: Deflections of the vertical component ξ
 4B: Deflections of the vertical component η

Based on the above investigation it was decided to re-measure the deflections of the vertical at the points 416, 421 and 698. In addition, a densification of the deflections of the vertical is needed. Further simulations were done to identify the number and the position of points for additional measurements. The values ξ and η at these densification points (see triangles in Figure 5) are predicted by collocation using gravity anomalies only. The improvements we get by introducing these new stations are verified by repeating the above investigation. The difference between the predicted and the measured values of ξ and η are shown in Figure 5. If Figure 3 is compared to Figure 5 it is obvious that the big discrepancies in the northeast of the test area have vanished. The determination of the standard deviation of the Least Square Collocation is mainly influenced by the configuration of the input data. Figure 7 shows the error plots of the prediction of ξ using deflections of the vertical only. Figure 7A shows the error plot of the prediction using the old

dataset of deflections of the vertical, Figure 7B shows the error plot of the prediction after including the simulated values of deflections of the vertical at new stations. The improvement due to the better configuration is obvious. The error plot of η shows a very similar behaviour and will not be given.

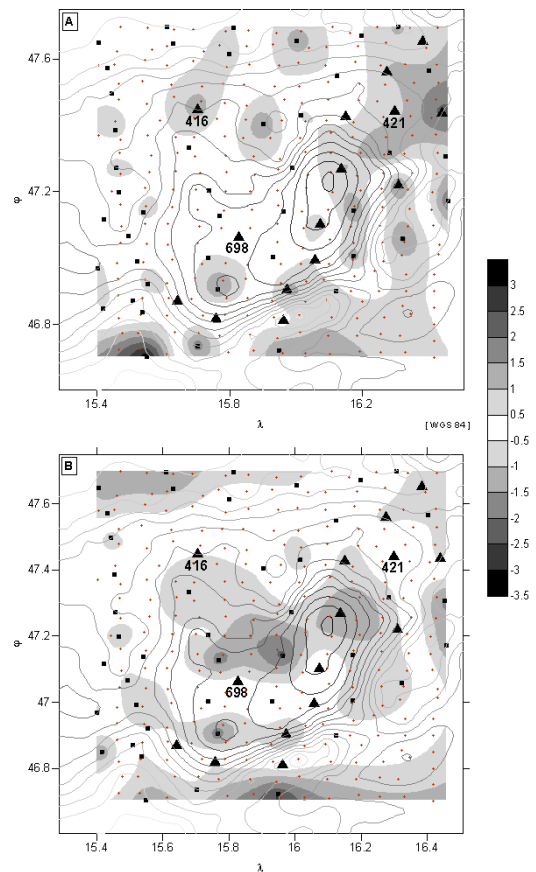


Fig. 5 Improvement by including additional points (marked with a triangle). Differences [arcsec] between the predicted and the measured values of the deflections of the vertical, prediction using deflections of the vertical only
 5A: Deflections of the vertical component ξ
 5B: Deflections of the vertical component η

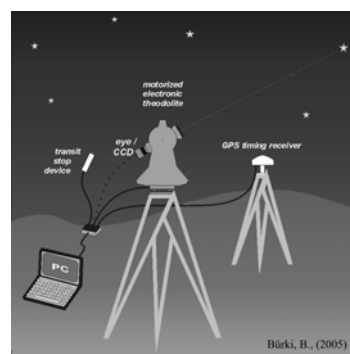


Fig. 6 Components of the measurement system ICARUS

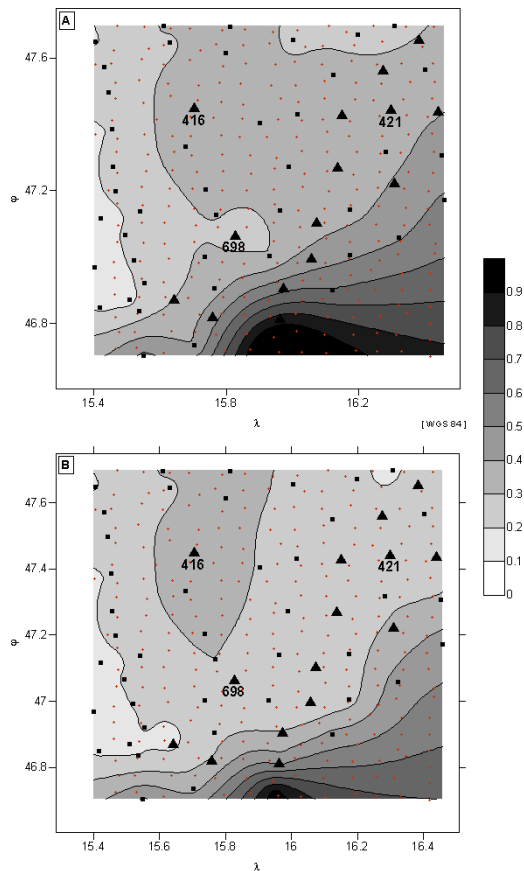


Fig. 7 Error plots of the prediction of ξ [arcsec]
 7A: Prediction using the old dataset of deflections of the vertical
 7B: Prediction including the simulated values of the deflections of the vertical

3 New Measurements

3.1 Measurement system ICARUS

The new measurements will be performed using the system ICARUS, which represents an online observation system for rapid and easy determination of the direction of the plumb line in terms of astronomical latitude and longitude as needed for the computation of deflections of the vertical. This software package has been developed at the Geodesy and Geodynamics Lab (GGL) at ETH Zurich (Bürki, 2005).

The system is based on the star catalogue FK5. A theodolite, which is driven by servo motors, is used to point towards the approximate position of the stars automatically. When the star transits through the horizontal reticle line that represents the fixed zenith angle, a measurement is manually triggered. In conjunction with the zenith angle the system measures the exact transit time which is

acquired from a GPS receiver that has been especially developed for time synchronisation and event marking. The astronomical coordinates are finally computed applying the method of reciprocal bearing together with a least squares adjustment. It proved to be useful to measure about 25 stars (each star to be measured 6 times) for each observation point. The measurement period at one station lasts about 1 to 1 ½ hours.

3 Summary

Due to the results of this investigation in the southeast of Austria it could be shown that the differences between the astrogeodetic and the gravimetric solution is mainly influenced by the distribution of the deflections of the vertical. It's expected that the planned new measurements confirm this results.

Acknowledgements

Financial support for this study comes from the Austrian Research Promotion Agency (FFG). This study is performed in co-operation with the Federal Office of Metrology and Surveying (BEV). Special thanks go to Beat Bürki, who provided the system ICARUS for these investigations.

References

- Abd-Elmotaal, H., and N. Kühtreiber (2001). Precise geoid computation employing adapted reference field, seismic moho information and variable density anomaly. *Presented at the Scientific Assembly of the International Association of Geodesy IAG 2001*, Budapest, Hungary, September 2-8, 2001.
- Bürki, B., (2005). ICARUS, Astro-geodetic on-line observation system – User manual V.05. Geodesy and Geodynamics Lab (GGL) at ETH Zurich.
- Kühtreiber, N., (2003). High Precision Geoid Determination of Austria Using Heterogeneous Data. In: *Proceedings of 3rd Meeting of the International Gravity and Geoid Commission*, Thessaloniki, Greece, August 26-30, 2002
- Tscherning, C.C., and R.H. Rapp (1974). Closed covariance expressions for gravity anomalies, geoid undulations and deflections of the vertical implied by anomaly degree-variance models. Department of Geodetic Science, the Ohio State University, Report No. 208

Realization of a Global Vertical Reference System

Johannes Ihde

Bundesamt für Kartographie und Geodäsie

Richard-Strauss-Allee 11, D-60598 Frankfurt am Main, Germany

Abstract. The basic concepts for the realization of a world height system and the unification of existing vertical reference systems will be presented. To proceed towards a unified physical height system at the centimetre accuracy level a unique global height datum, consistent parameters, models and processing procedures of the Terrestrial Reference Frame (TRF) and gravity field, a closed theory for the combination of parameters (space techniques, gravity), consideration of time depended influences, and concepts for the realization are needed.

Keywords. Global vertical reference fame, numerical conventions, tide gauges

1 Introduction

The Earth's surface may be characterized by its geometry and the potential of the Earth gravity field. The determination of heights includes both of these aspects, the geometric part and the geopotential part. Presently, space geodetic techniques allow an accuracy in geometric positioning of about 10^{-9} in global and continental scales. Gravity field parameters, including the physical height components, can at present be determined only 2 to 3 orders of magnitude less accurate than the geometric parameters. The current height reference frames around the world differ in their vertical datum and in the theoretical foundations of the height systems.

In the last 20 years several concepts for definition and realization of World Height systems were discussed (Rummel, R., Teunissen, P., 1988, Rapp, R. H., Balasubramania N., 1992, Balasubramania, N., 1994, Ihde, J., Augath, W., 2002. Rummel, R., Heck, B., 2001, Burša, et.al 2002.). However, at present here is no global height reference system defined and realized comparable the International Terrestrial Reference System (ITRS).

A considerable progress in the definition and realization of a Global Vertical Reference System (GVRS) will be attained from the data of the new satellite gravity field missions.

In 2003 IAG installed an Inter-Commission Project (ICP) of Commission 1 and Commission 2 of Vertical reference Frames. Based on the classical and modern observations, ICP1.2 on Vertical Reference Frames shall study the consistent modeling of both, geometric and gravimetric parameters to provide the fundamentals for the installation of a unified global vertical reference frame.

2 Relationship between Gravity Field, and Geometric Reference

Height determination in general and therefore the realization of a Vertical Reference System is a natural combination of space geodesy and the Earth gravity field determination.

Between the geopotential scalar field $W(X)$ and the outer Earth gravity vector field $g(X)$ the following relationship is valid:

$$\vec{g} = \text{grad} W = -g \begin{pmatrix} \cos \Phi & \cos \Lambda \\ \cos \Phi & \sin \Lambda \\ & \sin \Phi \end{pmatrix}, \quad (1)$$
$$g_P = g(X) = |\text{grad} W_P|$$

with the natural coordinates astronomical latitude Φ , astronomical longitude Λ , and the potential of Earth gravity field W .

In a very general notation the relationship can be expressed by

$$P(X, W, g) = P(X, W, -\partial W / \partial H) \quad \text{or} \quad (2)$$

$$W(X) = W_P \quad \text{collocated with}$$

$$g(X) = g_P = -\partial W_P / \partial H.$$

The two fields are functions of time in a Euclidian affine space. Therefore we have to consider the time dependence t :

$$\begin{aligned} W_p(t) &= W_p^0 + \dot{W}_p^0(t-t^0), \\ g_p(t) &= g_p^0 + \dot{g}_p^0(t-t^0), \\ X_p(t) &= X_p^0 + \dot{X}_p^0(t-t^0). \end{aligned} \quad (3)$$

Height determination is the determination of the geo-potential W_p and a combination of positioning X_p and gravity g_p .

The potential of the Earth gravity field is not directly measurable, but can be derived by integration of gravity over

- the height h with leveling

$$W_p = W_0 - c_p = W_0 - \int_0^p g dh \quad (4)$$

- or the Earth surface σ by solution of the geodetic Boundary Value Problem (BVP) in connection with precise geometrical positions (GNSS/leveling)

$$\begin{aligned} W_p &= U_p + T_p \\ &= U_p + \frac{R}{4\pi} \int_{\sigma} (\Delta g + G_1 \dots) ST(\psi) d\sigma \end{aligned} \quad (5)$$

where c_p is the geopotential number, T the disturbance potential, U the normal potential, Δg the gravity anomaly, G_1 the first term of the Molodenskij series, and ST the Stokes function.

3 General Concept for the Definition of a Global Vertical Reference System

Vertical Reference Systems (VRS) are related to the Earth gravity field on or outside the solid Earth body. A Vertical Reference System is a geopotential reference system co-rotating with the Earth in its diurnal motion in space. In such a system, positions of points attached to the solid surface of the Earth have geopotential values and corresponding coordinates in a defined Terrestrial Reference System (TRS). A Vertical Reference Frame (VRF) is a set of physical points with precisely determined geopotential values W_p or differences c_p to a geopotential reference value W_0 .

The positions P of the points are given as coordinates X in a specific spatial coordinate system attached to a Terrestrial Reference System. Such a VRF is said to be a realization of the VRS. The disturbance potential undergoes only small variations in time, due to geophysical effects (mass transports and tectonic or tidal deformations).

Ideal Vertical Reference Systems. An ideal Vertical Reference System is defined by values $W(X)$ of the geopotential scalar field of the outer Earth gravity vector field $g(X)$ in relation to a position given with coordinates X in the Euclidian space of an ideal Terrestrial Reference System co-rotating with the Earth. For the Terrestrial Reference System the Conventions of the Conventional Terrestrial Reference System and Frame (CTRS, CTRF) of the IERS Conventions 2003 are fully valid.

For practical use the geopotential values W_p in a point $P(X)$ may be related to a physical reference level represented by an equipotential surface of the Earth gravity field with a value W_0 .

The height components are differences ΔW_p between the potential W_p of the Earth gravity field through the considered point P and the potential of the VRS zero level W_0 . The potential difference $-\Delta W_p$ is also designated as geopotential number

$$c_p = -\Delta W_p = W_0 - W_p. \quad (6)$$

The geopotential numbers c_p are related to a conventional zero level W_0 , which is the vertical datum of the VRS.

We have to consider separately Vertical Reference System and Frame:

- Definition of a GVRS with conventions for datum, codes, time dependent variations, parameters
- Realization of a GVRS with conventions and specification for procedures of computations (data reductions, selections of alternative procedures), selection of data, and station distribution.

4 Definition of a Global Vertical Reference System

In alignment to the Conventions of the International Earth Rotation and Reference System Service

(IERS) 2003 (IERS, 2003) the definition of a Global Vertical Reference System (GVRs) fulfils the following four conditions:

1. The vertical datum is defined as the equipotential surface with the Earth gravity field potential:

$$W_0 = \text{const.} \quad (7)$$

The vertical datum defines the relationship of the physical heights to the Earth body. W_0 shall be conventional. The relation to the Earth body shall be reproducible.

2. The unit of length is the meter (SI). The unit of time is second (SI). This scale is consistent with the TCG time coordinate for a geocentric local frame, in agreement with IAU and IUGG (1991) resolutions. This is obtained by appropriate relativistic modelling.
3. The height components are the differences $-\Delta W_P$ between the potential W_P of the Earth gravity field through the considered points P and the potential of the GVRs conventional zero level W_0 . The potential difference $-\Delta W_P$ is also designated as geopotential number c_P :

$$-\Delta W_P = c_P = W_0 - W_P. \quad (8)$$

4. The CVRS is a zero tidal system, in agreement with the IAG Resolution No 16 adopted in Hamburg in 1983.

Not necessary is a no-net-rotation condition for the case, that $W_0 = \text{const.}$ is fixed to a conventional value and therefore time independent.

Necessary is to relate W_0 to the Earth body. The determination of W_0 is connected with the determination of the mean geoid following the Gauss/Listing definition to the mean sea surface.

For the realization of the Gauss/Listing geoid definition with geodetic measurements and models

¹ In practical use are several kind of types of heights on the basis of geopotential numbers: The normal height can be derived by $H_P^N = c_P / \bar{\gamma}$, where $\bar{\gamma}$ is the mean normal gravity between the level ellipsoid and the related point P_0 in the height H_P^N . The orthometric height can be derived by $H_P^0 = c_P / \bar{g}$, where \bar{g} is the mean gravity between geoid and Earth surface.

are different options under discussion which needs specifications e.g. the area of the free oceans and time period over which the potential values of the sea surface W_S to be averaged. Details will not be discussed here.

It is the question how to select the conventional W_0 . It makes sense to consider the selection of W_0 in connection with other fundamental parameters (Yurkina, M. I., 1996, Burša, M. et. al, 1998, Burša, M, et. al, 2002).

5 Numerical Standards

The Geodetic Reference System 1980 (GRS 80, 1980) defines major parameters for geodetic reference systems in form of a level ellipsoid. It is agreed by International Union of Geodesy and Geophysics (IUGG), International Association of Geodesy (IAG) and International Astronomical Union (IAU). The GRS80 parameters are recommended by IAG for the conversion of ITRF Cartesian coordinates in ellipsoidal coordinates. It is used worldwide for many map projections. Million of coordinates are related to it.

At the IUGG General Assembly 1991 in Vienna new values for geocentric gravitational constant GM and the semi major axis a of the level ellipsoid were recommended. Since this time these parameters were used in global gravity models e.g. EGM96. The two other defining parameters were not changed.

In the IERS 2003 conventions (IERS, 2003) in Table 1.1 numerical standards are listed. Below it are the four defining parameters of the mean a Earth ellipsoid. The value of the geocentric gravitational constant GM has not changed since 1991. The parameters in Table 1.1 have the status of standards. In parallel in chapters 4.1.4, and 4.2.5 the GRS80 is recommended for transformations.

Table 1 contains parameters of different level ellipsoids. The gravitational constant GM of GRS80 and IERS 2003 conventions differs in the metric system by about 0.9 m. The semi major axis of both standards differs by 0.4 m.

It has to be stated, that IERS 2003 conventions recommends different level ellipsoid parameters for different applications

While for geometrical applications GRS80 is recommended and mainly used, since more than 10

years for global gravity models divergent values are in the practical use.

IAG has to be remove this inconsistency for integrated geodetic applications (see e.g. Hipkin, R., 2002).

The datum parameter W_0 of a Global Vertical Reference System defines the relationship of the physical heights to the Earth body. The relation to the Earth body shall be reproducible.

The W_0 value can be defined and determined as mean value of the Earth gravity potential of the mean sea surface W_S over a defined area S of the open sea: a defined time period and related to an epoch:

$$W_{0S} = 1/S \iint_S W_S \, dS . \quad (9)$$

W_S of mean sea surface can be derived using a Global Gravity Model (GGM) expressed by a spherical function and sea surface heights h_S derived by satellite altimeter observations (ALT)

$$W_S = \frac{GM}{rS} \left[1 + \sum_{n=1}^{\infty} \left(\frac{a}{rS} \right)^n \sum_{m=0}^n [C_{nm} \cos m\lambda + S_{nm} \sin m\lambda] P_{nm}(\cos\theta) \right] + \frac{1}{2} \omega^2 r^2 \cos^2(90^\circ - \theta)$$

$$= U_0 + \partial U_0 / \partial h \cdot h_{S,ALT} + T_{S,GGM} \quad (10)$$

If the sea level is long term changing it is useful to fix W_0 of the GVRs. W_{0S} can be observed against the conventional W_0 of the GVRs.

Table 1. Level ellipsoid parameters

Ellipsoid	Semi-major axis a in m	Flattening f ⁻¹	Geocentric gravitational constant GM in 10 ⁸ m ³ s ⁻²	U ₀ /W ₀ in m ² · s ⁻²	γ _e in m · s ⁻²
Int. Ell. 1930 (Hayford)	6 378 388	297	3 986 329		
GRS 67	6 378 160	298.247	3 986 030		
GRS 80	6 378 137	298.257222101	3 986 005	6 263 6860.850	9.78032677
IUGG 91	6378136.3 0.5		3 986 004.41 0.01		
IERS 2003 Conventions (zero tide)	6378136.6 0.1	298.25642 0.00001	3986004.418 0.008	62636856.0 0.5	(9.78032666)

Angular velocity of the Earth rotation ω 10⁻¹¹ rad s⁻¹ 7 292 115

6 The Realization and Unification of Vertical Reference Systems

In general the determination of potential values or potential differences of the Earth gravity field is possible by integration of gravity over the height in form of levelling or over the Earth surface by solution of the geodetic BVP.

Most of the classical VRS were realized by levelling. The zero level of the VRS is derived by long term observations of the sea level at tide gauges. Normally the W_0 value of the zero level of the classical levelling networks is not known. The regional VRS differs in the height by the stationary sea surface topography in the tide gauges and possible for definition reasons. Globally there are differences of by the stationary sea surface topography up to 2 m.

In the past the GGM were not accurate enough to realize a global VRS or to unify regional VRS in a global level with an sub-decimetre accuracy level. The satellite gravity missions CHAMP, GRACE, and GOCE will bring a big progress in the approximation accuracy of long wave length parts of the Earth gravity field. In combination with geodetic space techniques the GGM of new generation will provide the basis for VRS realization and unification in a one-centimetre accuracy level.

Practical possibilities

There are two general possibilities for the realization and three for the unification of VRF

- i. For VRS realizations on continents the usual method is the geometric levelling. For unifications common adjustment of existing levelling networks over continents is suitable.
- ii. The general case for realization and unification is the combination of GNSS positioning or GNSS/levelling with a GGM.
- iii. For the unification of VRS a combination of tide gauge observations with sea surface topography information .

A combination of the different cases is useful.

i Levelling and common adjustments of existing levelling networks

This procedure is mainly used for the realization of VRS and unification of existing VRF. This case can not be used for the realization of a GVRF.

A classical example is the realization of the European Vertical Reference System (EVRS) (Ihde, J., Augath, W., 2001, 2002) by the United European Levelling Network (UELN, Fig. 1), which is the result of a common adjustment of 26 national European 1st order networks. Characteristic parameters are: No. of measurements: 9542, degrees of freedom: 2318, a-posteriori σ 1 km levelling distance in kgal·mm: 1.07, mean value of σ of adjusted c_p (heights), in kgal · mm: 17.19, average redundancy: 0.24.

ii General case for realization and unification: combination of GNSS and GNSS/levelling with a GGM

The VRS realization at single points P is very simple and wellknown:

$$W_P = U_0 + \partial U_0 / \partial h \cdot h_{ITRF} + T_{PGGM} \quad (11)$$

or

$$H_P = h_{ITRF} - N_{PGGM} . \quad (12)$$

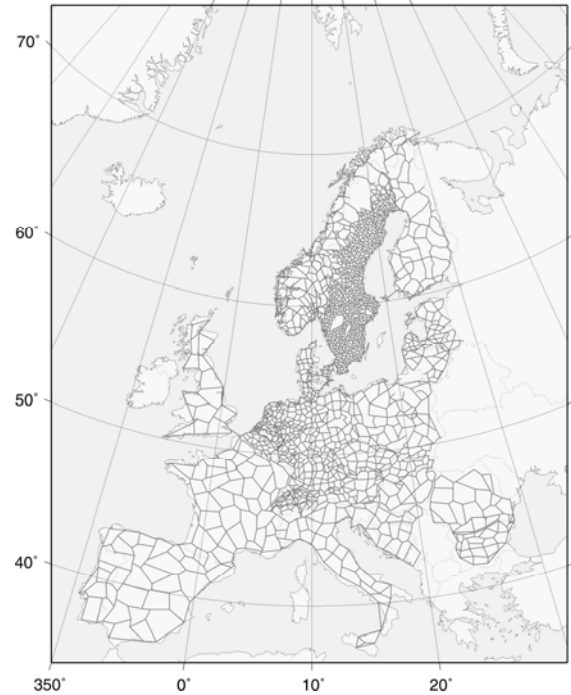


Fig. 1: United European Levelling Network (UELN), common adjustment of 1st order levelling networks of European

In many cases the geoid heights N or the disturbance potential T bases on a GGM which is improved by local gravity and related to GNSS/levelling data. With such regional geoidal solutions a unique (GVRS) can not realized.

The transformation of geopotential numbers of regional VRF in a GVRF is possible if the level W_{0k} of a regional VRF k is known:

$$W_P = W_{0k} - c_{Pk} \quad (13)$$

With a GGM and GNSS positions, the potential of levelling points can determined in a global system

$$W_P = U_P + T_{PGGM} \text{ with } U_P = U_0 + \partial U_0 / \partial h \cdot h$$

$$W_P = U_0 + \partial U_0 / \partial h \cdot h_{ITRF} + T_{PGGM} \quad (14)$$

The mean potential of the zero level of the regional VRF k and the difference to a global level W_0 can derived by:

$$\begin{aligned}
&= U_0 - \gamma_0 (h_{i,ITRF} - H_{k,i} - N_{i,GGM}) \\
W_{0k} &= \text{mean} W_{0k,i} \quad h \text{ and } N \text{ shall global} \quad (15) \\
\Delta W_{0k} &= W_{0k} - W_0
\end{aligned}$$

By combination with geopotential numbers of the regional VRF, the level of a regional VRF k can be derived in single points i

$$W_{0k,i} = U_0 + \partial U_0 / \partial h_i \cdot h_{i,ITRF} + T_{Pi,GGM} + c_{Pk,i}$$

The height of the zero level of the regional VRF can be derived for single points by

$$H_{0,VRF} = h_{i,ITRF} - H_{i,VRF} - N_{i,GGM} \quad (16)$$

To reach globally a one-centimetre accuracy level, the GGM has to be increased local or regional with gravity data. To guarantee a homogenous unification the GGM shall be conventional: CGGM. h and N shall global. (Fig. 2)

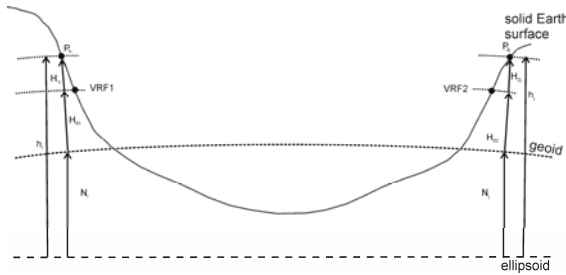


Fig. 2: Principle of GRF unification using GNSS/levelling and CGGM

iii. Unification by tide gauge observations

To use tide gauge observations for VRF unification, information about the absolute sea surface topography (SST) model and additional local modification of SST around the tide gauges are necessary. At coasts the SST is influenced by local effects and satellite altimeter observations at present can not be used with high precision. Therefore the use of offshore tide gauges should be considered. Of course a precise geoid on the basis of a CGGM is necessary to connect the offshore tide gauges with the VRF. Similar to the relationship (16) the height of the zero level of the regional VRF can be derived for single points by (Fig. 3):

$$\begin{aligned}
H_{0,VRF} &= (h_{MSS}^{TG} - N^{TG}) - H_{MSS}^{TG} + \Delta H_{TG} \quad (17) \\
&= H_{MST}^{Mod} - H_{MSS}^{TG} + \Delta H_{TG}.
\end{aligned}$$

$$(h_{MSS}^{TG} - N^{TG}) = H_{MST}^{Mod} \text{ shall global.}$$

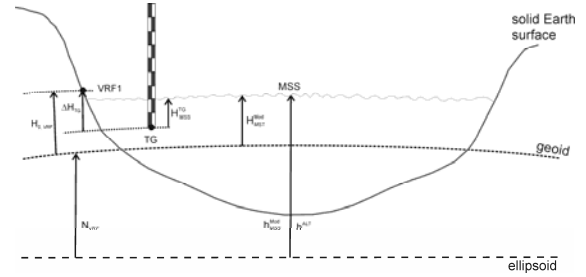


Fig. 3: Principle of GRF unification using tide gauge observations and a global model of sea surface topography

7 Role of Integrated Networks

Recently under discussion and partly in realization are integrated networks which combines at terrestrial reference stations geodetic space techniques, high precise absolute and relative gravity, levelling, and tide gauges with permanent or episodically observations and supplementary information (meteorological parameters, surrounding information of the stations e.g. eccentricities and ground water level). It is the basis to combine the geometric and height reference systems with Earth gravity field parameter estimation. These activities are in agreement with the IAG project of a Global Geodetic Observing System (GGOS, Rummel et al., 2002). In Europe the IAG project of the realization of a European Combined Network (ECGN) is in progress (Ihde et al., 2005, 2006).

The objectives of ECGN as Integrated European Reference System for Spatial Reference and Gravity are

- maintenance of long time stability of the terrestrial reference system with an accuracy 10^{-9} for Europe especially in the height component
- in-situ combination of geometric positioning (GPS) with physical heights and other Earth gravity parameters at 1 cm-accuracy level
- modelling of influences of time dependent parameters of the solid Earth of the Earth gravity field, the atmosphere, the oceans, the

hydrosphere for different applications of positioning

- contribution to the European gravity field modelling as part of a global gravity model.

It is the goal to use the available infrastructure, data bases and standards as far as possible.

Combination of various geodetic methods contributes especially to the vertical component and the determination of vertical velocities v .

In a first approximation we can assume that the disturbance potential is time independent, it means

$$v_{hi} = v_{Hi} \quad (18)$$

The velocities of the physical heights H can be derived from time series of the ITRFxx heights h :

$$H_P(t) = H_P^0 + \dot{h}_P^0(t - t^0). \quad (19)$$

An integrated GVRF network which combines the IGS TIGA Pilot Project with the network of the super conducting gravimeter of the Global Geodynamic Project (GGP) could be a begin of an GVRF. (Fig. 4)

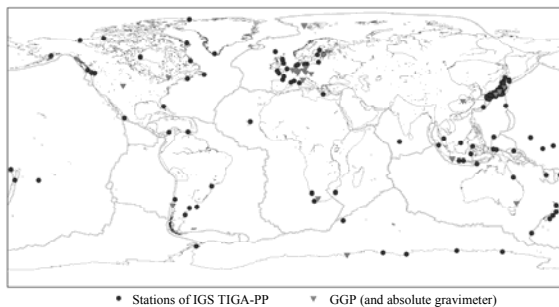


Fig. 4 GVRF an integrated network

8 Summary and Outlook

The realization of a Global Vertical Reference System bases on combinations of positioning by geodetic space techniques, levelling, gravity and tide gauge observations with a global gravity model (GGM).

The used GGM should be a satellite only solution to exclude inconsistencies from local gravity data. It should be international agreed and conventional

(CGGM). To reach a one centimetre accuracy level, the GGM has to be increased local or regional with gravity data.

To use tide gauge observations for VRF unification information about the absolute sea surface topography (SST) around the tide gauges are necessary. If the SST at coasts is influenced by local effects and satellite altimeter observations at present not can used with high precision, the use of offshore tide gauges should be considered. Of course a precise geoid on the basis of a CGGM is necessary to connect the offshore tide gauges with the VRF. For further consideration: The integration of worldwide GNSS Tsunami early warning system buoys for long term control of mean sea surface and connection to satellite altimeter observations can provide an additional progress.

The processing of contributing geodetic space techniques in ITRF solutions makes sure a global homogeneity for VRS realization and unification.

The instantaneous mean sea surface should be observed against a conventional W_0 value, which is agreed for a GVRS as zero level. A conventional W_0 value has to be consistent with other defining parameters of Earth models. IAG shall agree unique sets of parameter.

Furthermore the different processing procedures of the relevant techniques for VRS realization and unification shall to be used agreed models e.g. tidal systems.

A GVRS should realized in context with a global integrated network, which combines at terrestrial reference stations geodetic space techniques, high precise absolute and relative gravity, levelling, and tide gauges with permanent or episodically observations.

ICP1.2 Vertical Reference Frames will propose 2007 conventions for definition and realization of a IVRS.

References

- Geodetic Reference System 1980 (GRS-80) – In: Bulletin Géodésique, vol. 54, no. 3 (1980), 395-405.
- McCarthy, D. D. and Petit, G., 2004. IERS Conventions (2003). (IERS Technical Note; 32), Frankfurt am Main: Verlag des Bundesamts für Kartographie und Geodäsie, 2004. 127 pp.

- Conventions for the Definition and Realization of a Conventional Vertical Reference System (CVRS, CVRF). IAG Inter-Commission Project 1.2 Vertical Reference Frames, working draft document.
- Balasubramania, N., 1994. Definition and realization of a global vertical datum. Department of Geodetic Science and Surveying, Ohio State University, Report No. 427, Columbus, Ohio.
- Burša, M., Demianov, G. V., Yurkina, M. I., 1998. On the determination of the Earth's model – The mean equipotential surface. *Studia Geophys. et Geod.*, 42, 467-471, Prague.
- Burša, M., Groten, E., Kenyon, S., Kouba, J., Raděj, K., Vátrt, V., Vojtišková, M., 2002. Earth dimension specified by geoidal geopotential. *Studia Geophys. et Geod.*, 46, 1-8, Prague.
- Burša, M., Kenyon, S., Kouba, J., Raděj, K., Vátrt, V., Vojtišková, M., Šimek, J., 2002. World Height System specified by geopotential at tide gauge stations. Proceedings of the Symposium on Vertical Reference Systems, Cartagena, Colombia, IAG Symposia, Vol. 124, 291-296, Springer, Berlin.
- Ekman, M., 2001. On the permanent tide in the European Vertical Reference System. Veröffentlichung der Bayerischen Kommission für die Internationale Erdmessung, Nr. 61, 113-114, München.
- Hipkin, R., 2002. Is there a need for a Geodetic Datum 2000? Discussion of a "Heiskanen & Moritz" Proposition. Proceedings of the IAG 2001 Scientific Assembly, Budapest, Hungary, IAG Symposia, Vol. 125, 124-127, Springer Berlin.
- Ihde, J., Augath, W., 2001. An vertical reference system for Europe. Veröffentlichung der Bayerischen Kommission für die Internationale Erdmessung, Nr. 61, 99-110, München.
- Ihde, J., Augath, W., 2002. The European Vertical Reference System (EVRS), Its relation to a World Height System and to the ITRS. Proceedings of the IAG 2001 Scientific Assembly, Budapest, Hungary, IAG Symposia, Vol. 125, 78-83, Springer Berlin.
- Ihde, J., Augath, W., Sacher, M., 2002. The Vertical Reference System for Europe. In: International Association of Geodesy Symposia; Vol. 124, 345-350, Springer, Berlin.
- Ihde, J., Baker, T., Bruyninx, C., Francis, O., Amalvict, M., Kenyeres, A., Mäkinen, J., Shipman, S., Šimek, J., Wilmes, H., 2005. Development of a European Combined Geodetic Network (ECGN). In: *Journal of Geodynamics* 40 (2005) 450-460.
- Ihde, J., Baker, T., Bruyninx, C., Francis, O., Amalvict M., Luthardt, J., Liebsch, G., Kenyeres, A., Makinen, J., Shipman, S., Šimek, J., Wilmes, H., 2005. The Implementation of the ECGN Stations – Status of the 1st Call for Participation. In: EUREF Publication No. 14, Mitteilungen des Bundesamtes für Kartographie und Geodäsie, Band 35, 49-58
- Ihde, J., Sánchez, L., 2005. A unified global height reference system as a basis for IGGOS. In: *Journal of Geodynamics* 40 (2005) 400-413.
- Mäkinen, J., 2001. A note on the treatment of the permanent tidal effect in the European Vertical Reference System (EVRS). Veröffentlichungen der Bayerischen Kommission für die Internationale Erdmessung, Nr. 61, 111-113, München.
- Rapp, R. H., Balasubramania N., 1992. A conceptual formulation of a World Height System. Report No. 421, Department of Geodetic Science and Surveying/Ohio State University, Columbus, Ohio.
- Rummel, R., Teunissen, P., 1988. Height datum definition, height datum connection and the role of the geodetic boundary value problem. *Bulletin Géodésique*, 62, 477-498, Springer, Berlin.
- Rummel, R., Heck, B., 2001. Some critical remarks on the definition and realization of the EVRS. Veröffentlichung der Bayerischen Kommission für die Internationale Erdmessung, Nr. 61, 114-115, München.
- Rummel, R., Drewes, H., Beutler, G., 2002. Integrated Global Geodetic Observing System (IGGOS): A candidate IAG project. Proceedings of the IAG 2001 Scientific Assembly, Budapest, Hungary, IAG Symposia, Vol. 125, 609-614, Springer, Berlin.
- Yurkina, M. I., 1996. Gravity Potential at the Major Vertical Datum as Primary Geodetic Constant. *Studia Geophys. et Geod.*, 40, 9-13, Prague.

TWELVE YEARS OF DEVELOPMENTS: GEOIDAL GEOPOTENTIAL W_0 FOR THE ESTABLISHMENT OF A WORLD HEIGHT SYSTEM - PRESENT STATE AND FUTURE

M. Burša, Z. Šíma, Astronomical Institute, Academy of Sciences of the Czech Republic, Prague, CR, e-mail: bursa@ig.cas.cz, sima@ig.cas.cz

S. Kenyon, National Geospatial-Intelligence Agency, MO 63010-6238, U.S.A.; e-mail: Kenyons@nga.mil

J. Kouba, Geodetic Survey Division, Natural Resources Canada, Ottawa, Canada, e-mail: kouba@geod.nrcan.gc.ca

V. Vátrt, M. Vojtíšková Geographical Service of the Czech Armed Forces, Military Geography and Hydrometeorology Office, Dobruska, CR, e-mail: vatr@vghur.army.cz, marie.vojtiskova@vghur.army.cz

Abstract. Satellite altimetry missions, in particular the TOPEX/POSEIDON and Jason 1, have enabled a new realization of a World Height System. From altimetry data and precise global gravity models, one can determine a geopotential value W_0 , which best fits the world's oceans. W_0 specifies the geoid and it can also represent the WHS height datum. During the past 12 years, we have monitored the stability of the geopotential W_0 and proposed a rounded value of $W_0 = 62\,636\,856.0 \text{ m}^2\text{s}^{-2}$ that reflects the formal and calibration uncertainties. However, for WHS, W_0 can be chosen arbitrarily. A methodology of connecting regional vertical datums and the proposed WHS has also been developed. The proposed approach, which requires vertical datums with sufficient numbers of GPS/levelling points, covering sufficiently large areas, has been successfully used to connect vertical datums in many parts of the world. The fundamental relativistic constant, required for relativistic time transformation, adopted by IAU, is based on our value of W_0 . Since future precise clocks may be capable of "measuring" geopotential differences (heights) with respect to the fundamental relativistic constant (and W_0), it is essential that the future WHS, W_0 and the relativistic transformation are mutually consistent.

1 Introduction

Satellite altimetry missions, in particular the TOPEX/POSEIDON and Jason 1, have enabled a new realization of a World Height System (WHS). From altimetry data and precise global gravity models, one can determine a geopotential value W_0 , which best fits the world's oceans [*Gauss* (1828), *Bessel* (1837), *Listing* (1873) and *Helmert* (1884)]

$$\int_S (W - W_0)^2 dS = \text{minimum}$$

W_0 specifies the geoid and it can also represent the WHS height datum.

2 Present stay of determination of W_0 value by the SSG GGSA

In the past 12 years we monitored the geopotential value W_0 to use it in establishing the world height system.

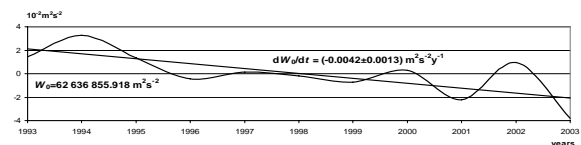


Fig. 1 Long term variation of W_0 , no IB correction applied.

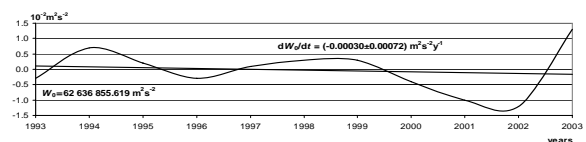


Fig. 2 Long term variation of W_0 , IB correction applied (model AVISO).

Proposed a rounded value of

$$W_0 = 62\,636\,856.0 \text{ m}^2 \text{ s}^{-2}$$

reflects the formal and calibration uncertainties. The above mentioned W_0 value has been included in the IERS Conventions. This W_0 value has been used for the determination of the defining constant

$$L_G = W_0/c^2 = 6.969\,290\,134 \times 10^{-10},$$

required for relativistic time transformations in astronomy (L_G is also included in the IERS Conventions).

3 Last improvements of W_0 value

Although the fact that W_0 could be chosen arbitrarily for WHS, we have improved its value in the last period:

- we have investigated the influence of the ice-coverage on W_0
- we have corrected the weighting of altimeter data
- we have corrected the ellipsoidal height of T/P by value -0.13 m (J. C. Ries, personal comm.).

3.1 Elimination of the influence of ice-coverage in W_0 determination by using of corrected weight of altimeter data and corrected altimeter height

From Fig. 3 it is evident that the ice-free area of the world oceans increases every year. In Fig. 3 there are depicted the ice boundary for years 1993, 2000, 2005 only.

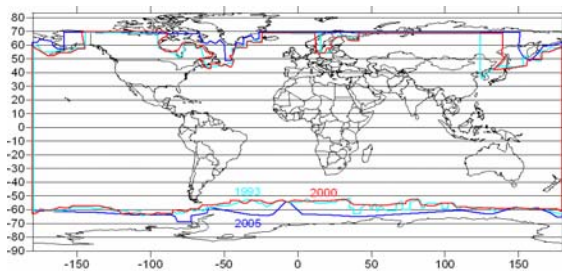


Fig. 3 The ice-free area of the world oceans in years 1993, 2000, 2005.

For determination of a “realistic” W_0 value the largest possible ice-free ocean area (the last altimetry data = 2006) should be used. Of course this ice-free area is not identical with the boundary $\phi \in \langle +60^\circ, +60^\circ \rangle$ which Laura Sanchez [2005] used for determination of W_0 value. We suggest that the conventions of ICP 1.2 ($\phi \in \langle +60^\circ, +60^\circ \rangle$, year 2000 as a reference year) for determination of W_0 value should be changed. For studies of “relative” value W_0 , ie. for studying of the long term variation of W_0

(e.g. for a finding of the rate of the increase of the ocean levels, etc.) it is necessary to use identical areas of ocean which are covered by altimeter data and which was never covered by ice. This area is depicted at Fig. 4.

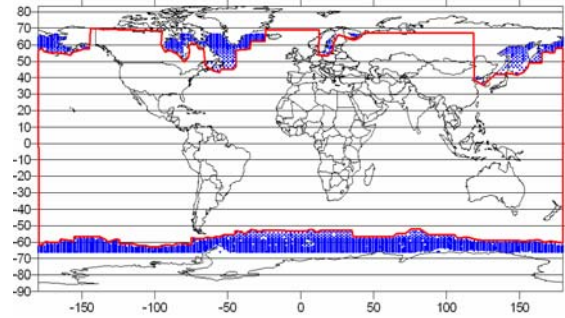


Fig. 4 Ice-free area of the world oceans from T/P data - years: 1993 – 2005.

Adopting the convention above for determination a “realistic” W_0 values (yearly ice-free area for each year used) we determined the values depicted in table 1 and at fig. 5.

Table 1 Yearly “realistic” W_0 and R_0 from ice-free T/P data

Year	Number of points (all/without ice)	W_0 [$\text{m}^2 \text{s}^{-2}$]	rms [$\text{m}^2 \text{s}^{-2}$]	R_0 [m]	rms [mm]
1993	204 909/141 148	62 636 854.720	0.013	6 363 672.6898	1.3
1994	208 022/143 740	62 636 854.687	0.013	6 363 672.6932	1.3
1995	206 794/139 146	62 636 854.590	0.012	6 363 672.7030	1.3
1996	205 004/138 786	62 636 854.636	0.013	6 363 672.6983	1.3
1997	217 888/143 682	62 636 854.624	0.012	6 363 672.6996	1.2
1998	207 850/139 235	62 636 854.592	0.012	6 363 672.7029	1.3
1999	204 868/143 407	62 636 854.720	0.013	6 363 672.6898	1.3
2000	209 991/140 796	62 636 854.556	0.012	6 363 672.7065	1.2
2001	209 053/161 009	62 636 855.000	0.013	6 363 672.6613	1.3
2002	198 543/139 804	62 636 854.764	0.013	6 363 672.6854	1.3
2003	180 380/154 505	62 636 855.064	0.013	6 363 672.6548	1.3
2004	127 752/109 256	62 636 855.215	0.016	6 363 672.6396	1.6
2005	135 937/ 116 837	62 636 855.062	0.015	6 363 672.6551	1.5
1993-2005	2 516 991/ 1 181 351	62 636 854.787	0.004	6 363 672.6830	0.4

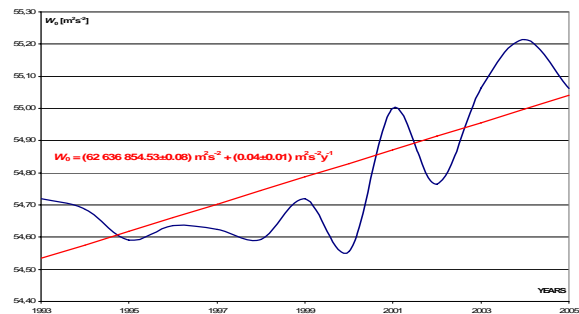


Fig. 5 Yearly “realistic” W_0 and R_0 from ice-free T/P data.

As a control of the determination of W_0 value from T/P data we used new altimetric data of Jason 1 from years 2003-2005. The result of this comparison is depicted in table 2 and at fig. 6.

Table 2 Yearly “realistic” W_0 and R_0 from ice-free Jason 1 data

Year	Number of points (all/without ice)	W_0 [$m^2 s^{-2}$]	rms [$m^2 s^{-2}$]	R_0 [m]	rms [mm]
2003	350 573/292 579	62 636 854.471	0.009	6 363 672.7158	0.9
2004	391 371/341 696	62 636 854.663	0.009	6 363 672.6963	0.9
2005	414 586/344 512	62 636 854.623	0.009	6 363 672.7003	0.9
2003-2005	1 156 530/978 787	62 636 854.586	0.005	6 363 672.7041	0.5

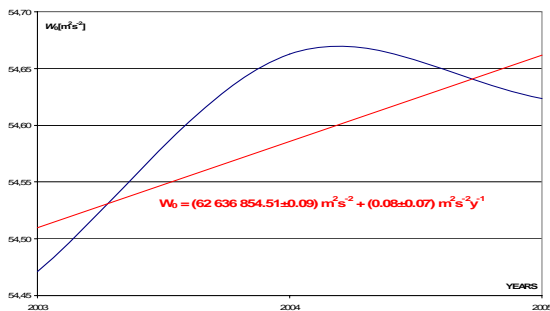


Fig. 6 Yearly “realistic” W_0 and R_0 from ice-free Jason 1 data.

4 Conclusions

Rounded value

$$W_0 = 62\,636\,855.0\,m^2\,s^{-2}$$

could be adopted because the difference between average “realistic” value $W_0 = 62\,636\,854.784\,m^2\,s^{-2}$ from ice-free T/P and average “realistic” value $W_0 = 62\,636\,854.586\,m^2\,s^{-2}$ from ice-free Jason 1 is $\approx 2\,cm\,only$.

Alternatively, to be consistent with IAU (Intern. Astron. Union) and since increase of ice-free oceans is evident, causing an increase of W_0 value from ice-free data area, then old

$$W_0 = 62\,636\,856.0\,m^2\,s^{-2}$$

could also be adopted. Such a “dateless” value will be valid for the Earth, sooner or later with a very high probability. Moreover, more complete ocean coverage causes higher value of W_0 . And it is also highly probable that such a coverage will be available in near future.

A future in the developments of W_0 and World Height System:

- adoption of a W_0

- monitoring of W_0 stability from Jason 1 data using new geopotential models like as EGM06, GOCE
- practical applications of the developed technology for connections of Local Vertical Datums to the WHS.

References

- Burša M., J. Kouba, K. Raděj, S. A. True, V. Vátrt and M. Vojtíšková (1999a). Determination of the geopotential at the tide gauge defining the North American Vertical Datum 1988 (NAVD88). *Geomatica*, 53, pp. 459-466.
- Burša M., J. Kouba, M. Kumar, A. Müller, K. Raděj, S. A. True, V. Vátrt and M. Vojtíšková (1999). Geoidal geopotential and World Height System. *Stud. Geophys. Geod.*, 43, pp. 327-337.
- Burša M., J. Kouba, A. Müller, K. Raděj, S.A. True, V. Vátrt and M. Vojtíšková (2001). Determination of geopotential differences between local vertical datums and realization of a World Height System. *Studia Geophys. Geod.*, 45, pp. 127-132.
- Burša M., S. Kenyon, J. Kouba, K. Raděj, J. Šimek, V. Vátrt and M. Vojtíšková (2002) World height system specified by Geopotential at tide gauge stations. IAG Symposium, Vertical Reference System. Cartagena, February 20-23, 2001, Colombia, Proceedings, Springer Vlg. 2002, pp. 291- 296.
- Burša M., E. Groten, S. Kenyon, J. Kouba, K. Raděj, V. Vátrt and M. Vojtíšková (2002). Earth’s dimension specified by geoidal geopotential. *Studia Geophys. Geod.*, 46, pp. 1-8.
- Burša M., S. Kenyon, J. Kouba, K. Raděj, Z. Šíma, V. Vátrt and M. Vojtíšková (2002). Dimension of the Earth’s generated ellipsoid. *Studia Geophys. Geod.*, 46, pp. 31-41.
- Burša M., S. Kenyon, J. Kouba, K. Raděj, Z. Šíma, V. Vátrt and M. Vojtíšková (2004). A Global Vertical Reference Frame based on four regional vertical datums. *Studia Geophys. Geod.*, 48, pp. 493-502.
- Burša M., S. Kenyon, J. Kouba, A. Müller, K. Raděj, V. Vátrt, V. Vitek and M. Vojtíšková (2004). Long-term stability of geoidal geopotential from Topex/Poseidon Satellite altimetry 1993-1999. *Earth, Moon and Planets*, 84, pp. 163-176.
- Sánchez, L. (2005). Definition and Realisation of the SIRGAS Vertical Reference System within a Globally Unified Height System. Dynamic Planet, Cairns, 2005, oral presentation.

EUVN_DA: Establishment of a European Continental GPS/leveling Network

A. Kenyeres

FOMI Satellite Geodetic Observatory, H-1592 Budapest, POBox 585, Hungary

M. Sacher, J. Ihde

Federal Agency for Geodesy and Cartography, Frankfurt, Germany

H. Denker

Institute für Erdmessung, Leibniz Universität Hannover, Germany

U. Marti

Federal Office of Topography, Wabern, Switzerland

Abstract EUREF, the Subcommittee for the European Reference Frame within IAG Commission 1 in cooperation with the European Geoid and Gravity Project (EGGP) is developing a homogeneous continental GPS/leveling database. EUVN_DA, the Densification Action of the EUVN (European Unified Vertical Reference Network) project is designed to support the development of the new European geoid solutions and to contribute to the realization of an accurate continental height reference surface. The cm-accuracy GPS/leveling database could also be used for future realizations of the European Vertical Reference System (EVRS) and for the analysis of the national height networks.

The establishment of the EUVN_DA network was started in 2003 and the first version of the database will be released in 2007. The database now consists of more than 1200 GPS/leveling points contributed from 20 countries. The GPS coordinates are referred to ETRS89 and the leveling data to EVRS2000. The EUVN_DA benchmarks are integrated into UELN (United European Leveling Network) to assure the long term homogeneity. Because of the large number of points, a continental coordinated GPS campaign could not be planned. The GPS database mostly relies on existing measurements, which should fulfill the quality requirements.

This paper introduces the activities within the EUVN_DA project, gives an overview on the actual status and presents the first results on the analysis of the continental geoid solutions.

Keywords. GPS/leveling, geoid, reference network, EUREF, geoid evaluation

1 Overview of EUVN

The initial aim of the EUVN project was to support the unification of the different European vertical datums at the few cm accuracy level and to prepare the realization of the European Vertical Kinematic Network. Details can be found in Ihde et. al (2000). In order to achieve this aim, a GPS campaign was organized in 1997 involving 196 points from all European countries covering the continent and the larger islands. The network incorporated selected leveling nodal points (54), permanent EUREF (66) and national (13) GPS stations and tide gauges (63). Tide gauges were included to connect the European tide gauge benchmarks for monitoring absolute sea level height variations. The GPS measurements have been processed by 10 analysis centers and a careful combination of the subnetwork solutions was prepared. The EUVN markers were connected to the nearest nodal points of the UELN 95/98 network. The results of the connection leveling were provided in geopotential numbers.

The final product of the EUVN project was an open database, where all markers were associated with cm-accuracy 3D coordinates in ETRS89 (ETRF96 epoch 1997.4) and geopotential numbers related to EVRS2000 zero level, which were used to derive normal heights.

Based on the available ellipsoidal and normal heights and the EGG97 continental geoid solution, see Denker and Torge (1997), a comparison was performed, see Ihde et al. (2000). The differences of the EGG97 and the EUVN height anomalies are plotted in Fig.1. Generally, the EGG97 and EUVN geoids agree within 2 dm and mostly the variation of their differences - within a certain limit - seems to be *random*, where several points are suspected as outliers. There are a few regions (Alps, SE-Europe,

Baltic, Central Scandinavia, Atlantic coastline), where *systematic, large scale trends and/or biases* are clearly observable. Among them, the most significant is the Alpine region, where the discrepancies go up to 40 cm. The Anatolian part of Turkey also shows significant variation of the differences, which is due to lacking gravity and terrain data in the EGG97 model.

Considering the systematic differences at that stage, it was not clear whether the long wavelength discrepancies were due to geoid errors (resulting from corresponding errors in the terrestrial gravity data or geopotential models) or due to leveling errors. One conclusion was that both EGG97 and EUVN were not sufficient to allow the determination of precise heights by the GPS technique .

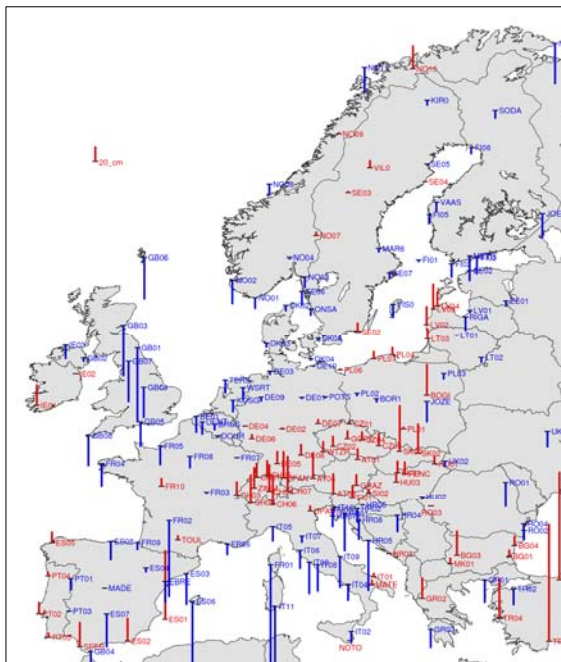


Figure 1. Differences between the EUVN GPS/leveling geoid and EGG97

2 EUVN_DA: densification of EUVN

The analysis of the EGG97 and EUVN data has clearly shown that significant inconsistencies exist between the two datasets, therefore its modeling or removal cannot be a straightforward task. In order to distinguish, identify and/or eliminate the inconsistencies, a more accurate continental geoid solution and a denser GPS/leveling network are inevitable. The denser the network is, the easier is the separation between outliers and long wave trends. However, the densification must also be

supplemented with an updated continental geoid to improve the separation of the various error components.

The difference map in Figure 1 also suggests that an improvement of the leveling networks (re-measurements or re-adjustment using homogenized standards and reductions) on national and continental scales would also be desirable. However, due to the high cost and manpower demands, this work cannot be done within a reasonable time frame. Instead of a regional activity, coordinated national actions were preferred to clarify the discrepancies observed in the current solution.

At the geoid development, a substantial improvement was expected thanks to the results of the new satellite missions (GRACE, CHAMP) and the updated marine and terrestrial gravimetric databases. In 2003 the former IAG European Subcommission IGGC (International Gravity and Geoid Commission) in cooperation with EUREF initiated the EUVN densification project. A parallel development was started targeting at the establishment of a homogeneous, cm-accuracy continental GPS/leveling database and a new improved European geoid solution.

The responsible national institutions and mapping agencies were asked to provide a set of benchmarks with high quality GPS derived coordinates and leveling data. The expected site separation is 50 – 100 km as a compromise between the spatial resolution of the global geopotential models and the data preparation costs. In order to get the one cm accuracy for the ellipsoidal heights, optimally 24 hours of GPS measurements, processed by a scientific software package (e.g. Bernese) were asked. Most of the countries could meet this requirement, if not, a denser data set was provided (e.g. Great Britain, Italy).

The reference system of the GPS coordinates is ETRS89 and for the leveling data it is EVRS2000. The submitted geopotential differences should directly refer to a UELN (United European Leveling Network) marker. Those benchmarks are integrated into UELN to assure the long term homogeneity. When a direct connection was not available, the submitted heights were transformed to EVRS2000 with existing transformation parameters. The leveling data validation and the sequential UELN adjustments are being done at the UELN/EUVN Data Centre in Leipzig. The timing of the project was perfect as several countries (Norway, Sweden, Finland, Poland, Spain) just completed the re-leveling of their networks.

In theory, the reference epoch of the ellipsoidal and leveled heights is 2000.0, but practically the data refer to the epoch of the observations. Especially the age of the leveling data is very variable, ranging from 0 – 50 years. The oldest leveling data is from Spain, but a re-leveling will be completed this year, and therefore new data will be available soon.

The weak point of the EUVN_DA database is that the validity of the height information relies on the assumption of the long term site stability. The Nordic countries are exceptional, where due to the glacial-isostatic adjustment (GIA) the heights should have been transformed to the epoch 2000.0 using the latest GIA model NKG2005LU (Agren and Svensson, 2006).

The EUVN_DA database now consists of more than 1200 GPS/leveling points contributed from 20 countries. For 5 additional countries the data preparation is in progress. The point distribution is shown in Figure 2.

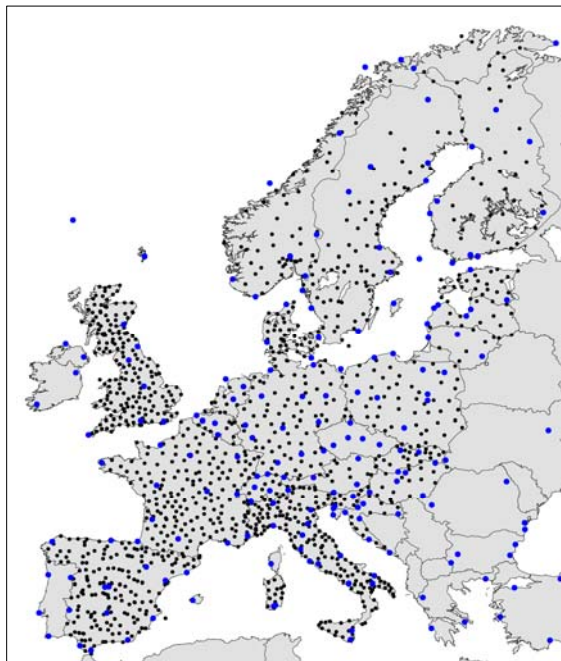


Figure 2. Distribution of the EUVN (blue dots) and EUVN_DA benchmarks (black dots) as of August 2006.

The available GPS and leveling data is being transformed to the common reference frames, then it is submitted to a detailed internal consistency check and external comparisons. The latter is being done in cooperation with EGGP. Both, EUREF and EGGP benefit from the cooperation. The European geoid may be used for identifying outliers in the

GPS/leveling data and EUVN_DA is used for the validation of the new European geoid solutions.

3 Analysis of the GPS/leveling data

The comparison of GPS/leveling derived height anomalies and independent geoid solutions is useful to check data consistency of both data sources. In this connection, leveling datum misalignments and gross errors can be easily found by geoid comparisons. This is especially important in our case, where the databases are built up from separate national contributions. In order to accommodate the comparisons, a uniform MS Excel worksheet has been developed, which includes all GPS leveling information, geoid tests and the derived statistics. The comparisons presented here are preliminary; the validation of the GPS and leveling data is not yet completed for all countries.

The 1st external test was the comparison of EUVN_DA and EGG97 height anomalies (see Fig.3).

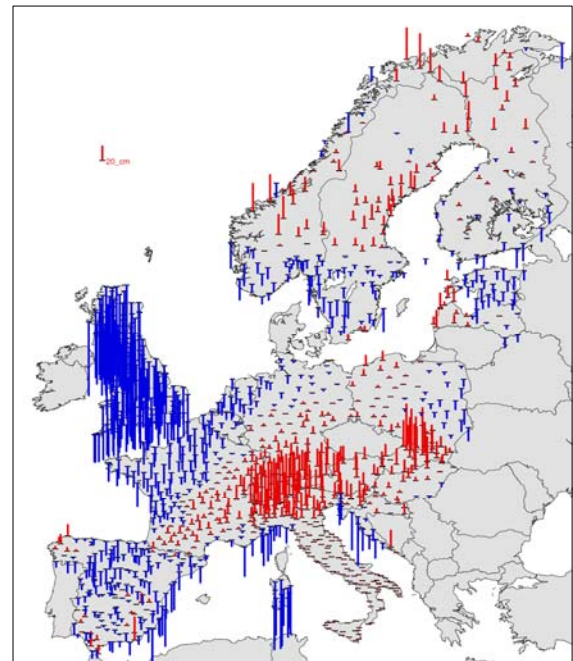


Figure 3. Height anomaly differences of EUVN_DA and EGG97.

Figure 3 shows several interesting features. Comparing with Figure 1, this is more or less the densification of the main long wavelength structures, but now they show up more clearly. The continental scale structures mainly result from the gravimetric geoid (see also below). The Spanish data shows higher scatter, because at this

comparison we could only use the old leveling dataset. In Italy only the Northern part is used, the Southern part needs further checking. The Alpine region and the High Tatra in Slovakia show higher discrepancies, which could come from EGG97 and/or EUVN_DA. The follow-on EGG solutions clarified this feature (see Fig. 4 and 5). The higher differences at the Mediterranean coastline are also remarkable.

At the British Isles, the map shows negative differences (higher EGG values with an average of -54 cm) and a clear negative trend (70 cm) against the continent, but this already starts on the territory of France. This feature is so relevant that it is present in all EGG comparisons. As the Ordnance Survey's leveling network is only connected to the continent by hydrographic leveling (the connection through the Eurotunnel is not yet finalized), a datum offset may exist. Additionally a tilt may exist in the UK network as suspected by Edge (1959) from the results of the 2nd and 3rd leveling. This topic needs further investigations.

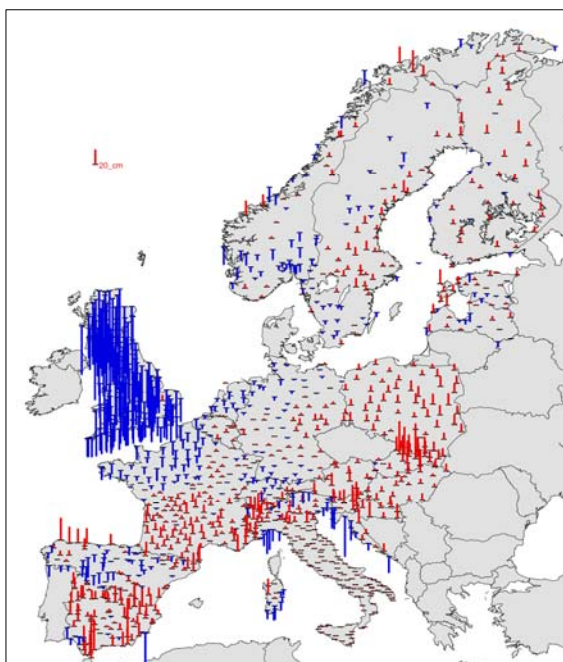


Figure 4. Height anomaly differences of EUVN_DA and EGG03C2. A bias of 35 cm was subtracted from the differences as zero undulation term.

Figure 4 shows the comparison with an updated, but not officially released test EGG solution, where the marine data was updated, the EIGEN-CG03C geopotential model was used instead of EGM96, but the terrestrial gravity data remained the same as in EGG97 (Denker et al., 2005). EGG03C2 was not

fitted to the European height reference systems; the comparison statistics suggests a zero order undulation term of around 35 cm.

According to the expectations we observe a significant improvement (see some statistics in Table 1) all over Europe; the rms of the differences dropped about 50%! The large Alpine feature disappeared, but the effect of the High Tatra remained – this clearly suggests that the data in this area is insufficient in the EGG computation. The large negative offset of Sardinia Island has also disappeared, so there was a negligible height datum offset. The Iberian part shows no improvement at all, only the mean offset changed – this may reflect the weakness of the present leveling data. The new Spanish leveling data under preparation will hopefully improve the picture. The higher offset for Poland may be caused by the fact that the new Polish leveling data is not yet integrated into UELN.

Finally, the analysis of the latest test EGG solution, EGG06 is presented in Figure 5 and Table 1. In this quasigeoid solution, the gravimetric data for Central Europe (latitude 40-60; longitude -10 – 25) has been updated completely.

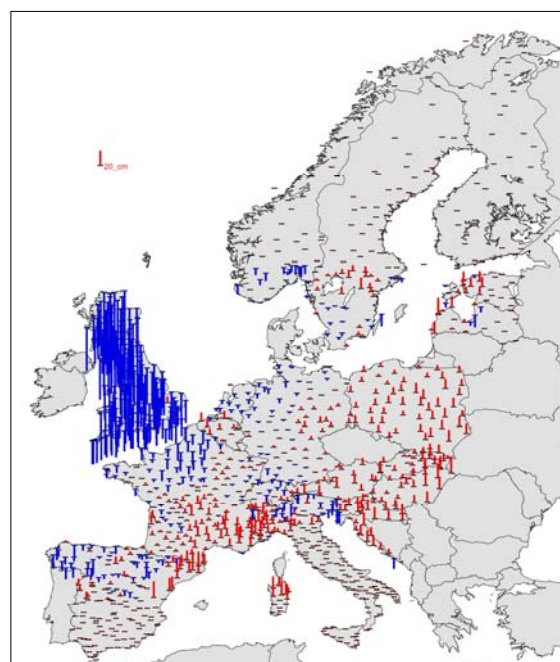


Figure 5. Height anomaly differences of EUVN_DA and EGG06. 35 cm zero undulation term was also subtracted from the differences.

We observe further improvements especially in three areas: in Spain the rms scatter decreased (but we have here less data); the High Tatra feature diminished, the cause of the discrepancy was

obviously the local gravimetric/terrain data; the Mediterranean/Adriatic coastline offsets also diminished, especially at the Croatian coastline. At some smaller regions (e.g. S-France, SE-Hungary) the differences became larger, suggesting that the database may need further improvement and with a completely revised dataset they should disappear.

Table 1. Comparison statistics of EUVN_DA and the EGG solution differences for some countries.

<i>nat. code</i>	<i>no. of pts</i>	<i>RMS [cm]</i>			<i>MAX-MIN range[cm]</i>		
		<i>EG97</i>	<i>EG03</i>	<i>EG06</i>	<i>EG97</i>	<i>EG03</i>	<i>EG06</i>
AUT	17	11	6	5	33	19	17
CRO	20	20	17	7	80	74	29
FRA	168	12	8	8	70	42	48
GER	75	10	4	4	46	15	15
GBR	189	19	13	11	74	59	56
HUN	20	9	4	5	40	20	20
SVK	28	17	13	4	57	49	16
SUI	20	10	6	5	31	23	16
SWE	84	12	5	-	54	27	-

The statistics in Table 1 well summarizes the improvement and well indicates the effect of the different data upgrades. Obviously we get better and better results, where the earlier gravimetric and terrain databases were sparse or erroneous. The RMS values indicate that the latest EGG solution already has the potential to serve as a dm-accuracy continental height reference surface in areas with a good coverage and quality of the input data. Moreover, high difference range values reflect tilts in the differences, which can be easily modeled.

4 Summary and outlook

In cooperation of EUREF and EGGP, with the support of the European mapping agencies, the creation of a regional GPS/leveling database is in progress. The current database includes some 1200 EUVN_DA points, where existing and new data, which fulfilled strict quality requirements, are collected. The submitted data is carefully tested and transformed to common reference systems (ETRS89/GRS80 for the GPS and EVRS2000/UELN for the leveling data). The uniform and homogeneous database is of great value for practical GPS-leveling applications. The first version of the database will be ready in 2007

and will be available for the data providers and for scientific, non-commercial users.

The target of these preliminary comparisons was to give a general overview of the project and demonstrate its potential for geoid testing at the cm to dm level. More detailed studies will come soon, where the potential for the analysis of the leveling networks and for the improvement of the continental geoid will be treated.

An important product could be the computation of a combined gravimetric-GPS/leveling geoid as a realization of a uniform and accurate European height reference surface. First investigations have already started to test the mathematical models (e.g. FEM, neural networks, splines) for the selection of the most feasible method.

Acknowledgments

The authors are expressing their thanks to all institutions, mapping agencies and persons who made measurements and provided GPS and leveling data to EUVN_DA. Without their extensive support, the project could not be run successfully. The corresponding author is supported by the Janos Bolyai Scholarship.

References

- Agren, J. – Svensson, R. (2006): Land Uplift Model and System Definition Used for the RH2000 Adjustment of the Baltic Levelling Ring. Pres. Paper, 15th General Meeting of the Nordic Geodetic Comm., Copenhagen, May 29 – June 2, 2006.
- Denker, H. J.-P. Barriot, R. Barzaghi, R. Forsberg, J. Ihde, A. Kenyeres, U. Marti, I.N. Tziavos (2005): Status of the European Gravity and Geoid Project EGGP. In: C. Jekeli, L. Bastos, J. Fernandes (eds.): Gravity, Geoid and Space Missions - GGSM2004, IAG Internat. Symp., Porto, Portugal, 2004, IAG Symp., Vol. 129, 125-130, Springer Verlag, Berlin, Heidelberg, New York, 2005.
- Denker, H. – Torge, W. (1997): The European Gravimetric Quasigeoid EGG97 – An IAG supported continental enterprise. In: IAG Symposium Proceedings IAG Scient. Assembly Rio de Janeiro, 1997. Springer Verlag.
- Edge, R.C.A. (1959): Some considerations arising from the results of the Second and Third Geodetic Levelings of England and Wales. Bulletin Geodesique, No.52, pp.28-36.
- Ihde, J. – Augath, W. (2000): The Vertical Reference System for Europe. Proceedings of the EUREF2000 Symposium, Tromsø, Norway, 22-24 June, 2000. Veröffentlichungen der Bayerischen Kommission für

die Internationale Erdmessung der BAW, Heft Nr. 61.,
pp.99-110.

Ihde, J.- Ádám, J. – Gurtner, W. – Harsson, B.G. –
Sacher, M. – Schlüter, W. – Wöppelman, G. (2000):
The EUVN Height Solution – Report of the EUVN
Working Group. . Proceedings of the EUREF2000
Symposium, Tromsø, Norway, 22-24 June, 2000.
Veröffentlichungen der Bayerischen Kommission für
die Internationale Erdmessung der BAW, Heft Nr. 61.,
pp.132-145.

Wessel, P. - Smith,W.H.F.: New, improved version of
Generic Mappig Tools released, EOS Trans. AGU,
Vol.79(47), pp.579, 1998.

Interrelation between the geoid and orthometric heights

A. Ellmann^{1,2}, P. Vaniček¹, M. Santos¹, R. Kingdon¹

¹Department of Geodesy and Geomatics Engineering, University of New Brunswick, Fredericton, NB, Canada

²Department of Civil Engineering, Tallinn University of Technology, Ehitajate tee 5, Tallinn, Estonia

Abstract. Height determination, like geoid modelling, is directly dependent on the gravity field. Hence it would be natural to link them for a comprehensive solution. It is known that the traditional methods for determining orthometric heights suffer from adopted approximations. In order to arrive at a more rigorous orthometric height, one must also account for the effects of the geoid-generated gravity disturbance, the shape of the topographical surface, and the density variations within topography. These effects are also considered for regional gravimetric geoid models. As a consequence, the implementation of the rigorous orthometric heights is simplified, further on, the heights become more compatible with regional geoid models. However, the two research areas have usually been discussed separately, and therefore the interrelation between them has only been vaguely considered. This contribution focuses on common features of geoid modelling and rigorous height determination. Relevant numerical results are discussed.

Keywords: mean gravity, Stokes-Helmert, upward continuation

1 Introduction

The geoid plays an essential role in the national geodetic infrastructure, as the topographic heights and the depths of water bodies are reckoned from it. Over the past years, University of New Brunswick's geodesy group has been using Stokes-Helmert's method for regional geoid determination. Nowadays, many geodetic and engineering applications require that the two essential components of the vertical positioning – the height and the corresponding reference surface (geoid), are determined precisely. They both depend on the gravity field. It is thus appealing to examine the geoid and height computation issues together. With this in mind, we are herewith revisiting the principles of height determination.

In the past, three main approximations have been applied in practice to evaluate the orthometric heights. The Helmert method, as described in Heiskanen and Moritz (1967, Chap. 4), applies the Poincaré-Prey vertical gradient of gravity in

conjunction with the measured gravity (at Earth's surface) for an estimation of the mean gravity. The Helmert height correction is simply proportional to the topographic heights. Niethammer (1932) and Mader (1954) refined the Helmert model by including the effect of the local shape of the topography. For a recent review of the three methods see Santos et al. (in press).

The simplest of the three – the Helmert orthometric height – has been adopted as the basis of the national vertical datum in many countries. Tenzer et al. (2005) showed that this commonly used method contains inadmissible approximations. Santos et al. (in press) presented the complete methodology with which to convert Helmert's heights to the rigorous orthometric heights.

It should be noted that the computation of the new rigorous heights is more involved, especially compared with the traditional Helmert approach. Indeed, as will be shown later, a number of components are needed to calculate the rigorous orthometric height. More specifically, one must account for the effect of the gravity disturbance generated by the geoid (Vaniček et al., 2004), the shape of the topographical surface, and the effects of density variations within topography.

The present contribution aims at demonstrating that the computations of the rigorous heights can be significantly simplified, if the Stokes-Helmert geoid modelling results are available. This is because several terms in this modelling are the same as those needed for computing the orthometric heights. Due to space limitations, however, the present contribution discusses only the most important causal relationships between the two research fields.

As such, this paper could also be considered as a complement to the earlier contributions by Tenzer et al. (2005), Kingdon et al. (2005) and Santos et al. (in press). Discussion on the relations between the normal heights (adopted in some countries) and the rigorous orthometric heights is considered to be outside the scope of the present contribution, but it can be found in Tenzer et al. (2005).

In Section 2 we continue with a brief recapitulation of the Stokes-Helmert geoid modelling principles. Section 3 is a review of the theory behind the rigorous orthometric heights. Section 4 deals with the assessment of components of the rigorous mean gravity. The relations between

the constituents of Stokes-Helmert's geoid modelling and those needed for the rigorous heights are spelled out as well. Section 5 presents the results of the numerical investigations along a profile in the Canadian Rockies. A brief summary concludes the paper.

2 Helmert's condensation and solution to Stokes's boundary value problem

The solution of the boundary value problem by Stokes's (1849) method requires gravity to be known on the geoid, while in reality gravity measurements are taken at the topographic surface. Thus to satisfy the boundary condition gravity anomalies need to be downward continued to the geoid level. Harmonic quantities are needed for downward continuation; thus a number of different corrections related to the existence of topographic masses need to be accounted for very carefully. [Strictly speaking, the effect of the atmospheric masses should also be considered in the geoid and rigorous orthometric height computations. Due to space limitations, however, these small effects are not discussed in this contribution]. One way of estimating the effect of topographical masses is to use Helmert's (1890) second condensation model. According to this model the Earth's topographical masses are replaced by an infinitesimally thin condensation layer on the geoid. So constructed gravity field becomes slightly different from the actual gravity field. The resulting Helmert anomalies, $\Delta g^h(r, \Omega)$, differ from the commonly used free-air anomalies, $\Delta g(r, \Omega)$. The relation between the two anomaly types can be expressed as (cf. Vaníček et al., 1999)

$$\Delta g^h(r, \Omega) = \Delta g(r, \Omega) + \frac{\partial [V^T(r, \Omega) - V^{CT}(r, \Omega)]}{\partial r} + \frac{2}{r_t(\Omega)} [V^T(r, \Omega) - V^{CT}(r, \Omega)] + e_{\text{ellips}}(r, \Omega), \quad (1)$$

where $V^T(r, \Omega)$ and $V^{CT}(r, \Omega)$ are the potentials of topographic masses and condensation layer, respectively. The geocentric position (r, Ω) is represented by the geocentric radius $r(\Omega)$ and a pair of geocentric spherical coordinates $\Omega = (f, l)$, where f and l are the latitude and longitude, respectively. All the quantities in Eq. (1) are referred to the surface of the Earth, $r_t(\Omega) = r_g(\Omega) + H^o(\Omega)$, where $r_g(\Omega)$ is the geocentric radius of the geoid surface and $H^o(\Omega)$ is the orthometric height. The

term $e_{\text{ellips}}(r, \Omega)$ represents the ellipsoidal correction needed to account for the deviation of the actual shape of the Earth from the spherical approximation employed in fundamental gravimetric equation (Vaníček et al., 1999). The topographic terms in Eq. (1) can be evaluated by using the topographic elevation/density models in numerical quadrature methods (see e.g., Martinec, 1998). For more details on estimation of the components of Eq. (1), see e.g., Vaníček and Martinec (1994), Martinec (1998), Vaníček et al. (1999) and references therein. A recent review can also be found in Ellmann and Vaníček (in press).

Importantly, the product of corresponding Helmert anomaly and geocentric radius, $\Delta g^h \times r$, is harmonic above the geoid (Vaníček et al., 1996), and therefore such a field can be continued downward to the geoid level (note that this is not the case for the free-air anomalies!). For more details the reader is referred to (Vaníček et al., 1996). Thereafter the Helmert gravity anomalies serve as an input when solving the Stokes boundary value problem. The geoidal heights, $N(\Omega)$, after the application of the Helmert condensation are expressed as follows:

$$N(\Omega) = \frac{R}{4pg_0(f)} \iint_{\Omega \in \Omega_0} S(y(\Omega, \Omega')) \Delta g^h(r_g, \Omega) d\Omega' + \frac{V^T(r_g, \Omega) - V^{CT}(r_g, \Omega)}{g_0(f)}, \quad (2)$$

where R is the mean radius of the Earth, $S(y(\Omega, \Omega'))$ is Stokes's function (Heiskanen and Moritz, 1967, Eq. 2-164), $y(\Omega, \Omega')$ is the geocentric angle between the computation Ω and integration points Ω' ; $g_0(f)$ is the normal gravity (a function of latitude) at the reference ellipsoid, $d\Omega'$ is the area of the integration element.

The geoid determination by the original Stokes formula requires the global coverage of gravity anomalies, $\Omega_0 = [f \in \langle -p/2, p/2 \rangle, l \in \langle 0, 2p \rangle]$. Nowadays it is customary to use modifications of Stokes's formula (originally proposed by Molodensky et al., 1960) in conjunction with some global geopotential model. Here we skip the aspects of our usual modification scheme, since these are not relevant in the context of the present paper. For more details the interested reader is referred to Vaníček and Sjöberg (1991).

Recall that Stokes's integral employs Helmert's gravity anomalies. Note that Eq. (2) consists of two parts. The Stokesian integration (i.e. the first term on

the right hand side of Eq. (2)) over these Helmert's anomalies results in the Helmert co-geoid. The Helmert condensation of the topographic masses yields the co-geoid which does not coincide with the actual geoid. The effect causing this change is called the primary indirect topographic effect (PITE). Accordingly, the last term in the right hand side of Eq. (2) is PITE, which transfers the Helmert co-geoid into the real geoid.

3 Theoretical background of the rigorous orthometric heights

The orthometric height $H^o(\Omega)$ of a point on the Earth's surface is defined as the length of the somewhat curved plumb-line (reckoned from the geoid!) and is given by (e.g., Heiskanen and Moritz 1967, Eq. 4-21):

$$H^o(\Omega) = \frac{C(r, \Omega)}{\bar{g}(\Omega)} \quad , \quad (3)$$

where $\bar{g}(\Omega)$ is the mean value of gravity between the geoid and the Earth's surface (along the plumb-line). $C(r, \Omega)$ is the geopotential number (see e.g. Heiskanen and Moritz, 1967, Chap. 4-2), which can be deduced from gravity measurements and spirit-leveling. Hence, the problem reduces to the determination of the mean gravity. The mean gravity is defined in an integral sense (e.g., Heiskanen and Moritz 1967, p. 166):

$$\bar{g}(\Omega) = \frac{1}{H^o(\Omega)} \int_{r_g(\Omega)}^{r_s(\Omega)} g(r, \Omega) dr \quad , \quad (4)$$

where dr is an element of the plumb-line. Note that the integral is taken in radial direction, rather than along the (curved) plumb-line. This simplification is admissible, since this has a negligible influence (< 1 mm) on the orthometric height (Tenzer et al., 2005). Because the actual values of gravity $g(r, \Omega)$ cannot be measured inside the topographic masses, the integral-mean gravity $\bar{g}(\Omega)$ has to be computed from the observed surface gravity $g(r_s, \Omega)$, using a realistic and physically meaningful model of the vertical gravity gradient. For instance, in the computations of Helmert's mean gravity, $\bar{g}^H(\Omega)$, the approximate Poincaré-Prey vertical gradient is adopted as follows (Heiskanen and Moritz, 1967, Eq. 4-25):

$$\begin{aligned} \bar{g}^H(\Omega) &= g(r_s, \Omega) - \frac{1}{2} \left(\frac{\partial g}{\partial h} + 4pGr_0 \right) H^o(\Omega) \quad , \quad (5) \\ &= g(r_s, \Omega) + 0.0424 H^o(\Omega) \end{aligned}$$

where $\partial g / \partial h$ is the linear vertical gradient of normal gravity (evaluated at the surface) and r_0 is the mean topographic density (2670 kg/m^3). The Poincaré-Prey constant (= 0.0424 mGal/m) is thus obtained as a sum of the attraction of the Bouguer plate ($+0.1119 \text{ mGal/m}$) and a half of the (negative) linear vertical gradient (-0.3086 mGal/m) of normal gravity. Consequently, the corresponding "Helmert correction to the measured surface gravity" is directly proportional to the topographic heights.

On the other hand, when computing the mean gravity rigorously one has to consider several terms. The gravity at a point $g(r, \Omega)$ can be decomposed into two terms; one comprising gravity generated by the masses inside geoid, $g^{NT}(r, \Omega)$ (in accordance with Vaníček et al. (2004) we call it *NoTopography* (NT) gravity, since the effect of the global topography has been subtracted from the "full" gravity), and another part, the gravity generated by the topography $g^T(r, \Omega)$. The geoid-generated gravity can be further decomposed into the contribution of the normal gravity and that of gravity disturbance caused by the masses inside the geoid (i.e. the *NoTopography* gravity disturbance, cf. Vaníček et al. 2004). Finally, the mean gravity is decomposed as follows (cf. Tenzer et al., 2005):

$$\bar{g}(\Omega) \approx \bar{g}^{NT}(\Omega) + \bar{g}^T(\Omega) \approx \bar{g}(\Omega) + \overline{d}g^{NT}(\Omega) + \bar{g}^T(\Omega) \quad , \quad (6)$$

where the approximate sign is due to neglecting the contribution of the atmosphere. Tenzer et al (2005, Appendix 1) have shown that this contribution is insignificant and can be neglected. To distinguish between $\bar{g}(\Omega)$ and the approximate Helmert mean gravity (Eq. (5)), the former will be referred to as 'rigorous mean gravity'.

4 Components of the rigorous mean gravity

The computation of the integral-mean (along the plumb-line) value of normal gravity, $\bar{g}(\Omega)$, in Eq.

(6) is a rather trivial task. It can be evaluated accurately enough using a second-order Taylor expansion for the analytical downward continuation of normal gravity from the Earth's surface to the geoid. The final expression for computing the mean

normal gravity can be found in Santos et al. (in press, Eq. 19).

It can be shown that the mean value of the topography-generated gravity can be evaluated (cf., Tenzer et al. 2005, Eqs. 16-18):

$$\begin{aligned} \bar{g}^T(\Omega) &= \frac{1}{H^O(\Omega)} \int_{r_g(\Omega)}^{r_t(\Omega)} g^T(r, \Omega) dr = \\ &= \frac{-1}{H^O(\Omega)} \int_{r=r_g(\Omega)}^{r_t(\Omega)} \frac{\partial}{\partial r} V^T(r, \Omega) dr = \frac{[V^T(r_t, \Omega) - V^T(r_g, \Omega)]}{H^O(\Omega)} \end{aligned} \quad (7)$$

In other words, the estimation of the $\bar{g}^T(\Omega)$ term reduces to the evaluation of the topographic potential at two points in the space: one at the surface of the earth and another one on the geoid level. Note that the terms in the numerator of Eq. (7) are already estimated during the Stokes-Helmert geoid determination, see Eqs. (1) and (2). If these terms (usually given on a grid) are made available, then evaluating Eq. (7) is quite straightforward.

Now we focus on the mean NT-gravity disturbance, the estimation of which is somewhat more involved. $\bar{d}g^{NT}(\Omega)$ is also evaluated as the integral mean in the radial direction, i.e. analogically to Eq. (4). Further on, since the geoid-generated gravity disturbance $dg^{NT}(r, \Omega)$ multiplied by r is harmonic above the geoid (because the NT-quantities by definition do not contain the contribution of the topographical masses), then $\bar{d}g^{NT}(\Omega)$ can be evaluated by making use of Poisson's integral for upward continuation (Kellogg, 1929). Applying the integration limits the definite integral can be simplified (Santos et al., in press, Eq. 37) as

$$\begin{aligned} \bar{d}g^{NT}(\Omega) &= \frac{R}{4\pi H^O(\Omega)} \\ &= \iint_{\Omega' \in \Omega_0} \bar{K}[r_t, y(\Omega, \Omega'), R] dg^{NT}(r_g, \Omega') d\Omega' \quad , \quad (8) \end{aligned}$$

where $\bar{K}[r_t, y(\Omega, \Omega'), R]$ stands for the averaged Poisson's kernel. This new kernel is a function of two inverse distances relating: (i) the computation point (on the geoid level) and the integration element; and, (ii) the surface computation point and the integration element on the geoid (see also Santos et al., in press, Eq. 38). Therefore, by no means this new kernel can be considered as an upward

continuation of $dg^{NT}(r_g, \Omega)$ to some location in the space (e.g. geometrical mean between the geoid and the earth's surface), but just an integral average of $dg^{NT}(r, \Omega)$ in radial direction. The complete derivation of Eq. (8) can be found in Santos et al. (in press, Appendix A).

Equation (8) requires that the NT gravity disturbance be known on the geoid, which it is usually not. To get it we make use of the Helmert gravity anomaly. The geoid-generated gravity disturbance $dg^{NT}(r_g, \Omega)$ for Eq. (8) is obtained (cf. Vaníček et al., 1999; Vaníček et al., 2004)

$$\begin{aligned} dg^{NT}(r_g, \Omega) &= \Delta g^h(r_g, \Omega) + \frac{2}{R} T(r_g, \Omega) + \frac{\partial V^{CT}(r_g, \Omega)}{\partial r} \\ &+ \frac{2}{R} V^{CT}(r_g, \Omega) - \frac{2}{R} V^T(r_g, \Omega) \quad . \quad (9) \end{aligned}$$

As this expression shows, the NT-disturbance can be expressed as a collection of different terms, all related to the geoid level.

Considering the well-known Bruns (1878) formula, $T(r_g, \Omega) = N(\Omega) \cdot g_0(f)$, the disturbing potential $T(r_g, \Omega)$ can be taken from a regional geoid model. By denoting the PITE (the last term in Eq. (2)) as $dN_l(\Omega)$ Eq. (9) takes the following form:

$$\begin{aligned} dg^{NT}(r_g, \Omega) &= \frac{2}{R} [N(\Omega) - dN_l(\Omega)] \cdot g_0(f) + \\ &+ \Delta g^h(r_g, \Omega) + \frac{\partial V^{CT}(r_g, \Omega)}{\partial r} \quad . \quad (10) \end{aligned}$$

Note that the three first terms on the right hand side are intermediate results of the Stokes-Helmert geoid determination. The remaining term in Eq. (10), the attraction of the condensation layer, need be evaluated on the geoid level (a suitable form of numerical expression can be deduced from Martinec, 1998). However, the latter term can also be computed as a geoid determination by-product. For this a relatively simple sub-routine can be added into the computer codes used in the Stokes-Helmert geoid modelling.

The resulting $dg^{NT}(r_g, \Omega)$ values are inserted into Eq. (8), providing the needed integral mean $\bar{d}g^{NT}(\Omega)$. This completes the methodology of linking the Stokes-Helmert geoid determination theory/results with the determination of rigorous orthometric heights. We see, that the availability of the Stokes-Helmert geoid results has important

implications in the computational aspects of the rigorous orthometric heights.

5 Numerical Investigations

Using Canadian gravity and topographic data (provided by the Geodetic Survey Division of Natural Resources Canada), we have computed the rigorous mean gravity (cf. Eq. (6)) along a profile across the Canadian Rocky Mountains. This profile coincides with the parallel 51°N and spans the longitudes between 235°E and 245°E. The topographic heights (with a spacing of 5 arc-minutes) range from 510 to 2384 m (with a mean of 1524 m). Due to high topographic elevations and very rugged landscape the mean gravity variations are expected to become significant.

Most of the terms in Eqs. (7) and (10) were ‘borrowed’ from the Stokes-Helmert geoid modelling results (Ellmann and Vaníček, in press). We discuss only a few important aspects of the numerical estimation of Eq. (8), since it is the most laborious part of approach. Note that generally, the NT-gravity disturbances are negative over mountainous regions (as a rule of thumb, the larger the average of the local topography the larger the negative NT-disturbance). The $dg^{NT}(r_g, \Omega)$ is also very smooth (for an illustration see Kingdon et al., 2005, Fig. 4, erratum). Therefore, in spite of the high elevations, the mean $\overline{dg}^{NT}(\Omega)$ values are numerically very close to the initial $dg^{NT}(r_g, \Omega)$ field. The differences $\overline{dg}^{NT}(\Omega) - dg^{NT}(r_g, \Omega)$ along the test profile do not exceed 10 mGal. At the same time the maximum upward continuation effect of $dg^{NT}(r_g, \Omega)$ from the geoid level to the earth’s surface by using the Poisson integral formula remained smaller than 15 mGal. The further discussion on the numerical evaluation of Eq. (6) is spared for a forthcoming paper.

The estimated Helmert mean gravity agrees generally well with $\overline{g}(\Omega)$. Nevertheless, in most cases $\overline{g}^H(\Omega)$ appears to be slightly weaker than the rigorous mean gravity (a few exceptions can be found inside of deep valleys). Along the selected profile the differences $\overline{g}(\Omega) - \overline{g}^H(\Omega)$ range between -21 and +30 mgal (with a mean of +6 mGal). These gravity differences can be then converted into the differences between the rigorous and Helmert orthometric heights (e.g. by using an approach in Heiskanen and Moritz, 1967, p.169). The height differences vary from -3.5 to +6.1 cm (with a mean of +1.1 cm). According to Kingdon et al. (2005) the differences at the higher elevations (>

3 km) may easily exceed a dm level. In a few extreme cases (at high elevations and very rugged areas), however, the relative height differences (due to $\overline{g}(\Omega) - \overline{g}^H(\Omega)$) disagree in about 7-8 cm for points located only some 10 km apart.

In most of the cases, especially over the mountain peaks, the Helmert orthometric heights appear to be higher than the corresponding rigorous mean heights, i.e. $H_H^o(\Omega) > H_{ng}^o(\Omega)$. This is due to the fact that the mean gravity has a ‘reverse’ effect on the height: the larger the mean gravity in the denominator the smaller the resulting height. As mentioned above, inside of some deep valleys we have $\overline{g}^H(\Omega) > \overline{g}(\Omega)$, yielding thus $H_H^o(\Omega) < H_{ng}^o(\Omega)$. Intuitively, this can be explained by the fact that in the Helmert approach the roughness of the surrounding topography is entirely neglected (cf. Eq. (5)). In other words, the contributions due the mass deficiencies and excesses (with respect to the Bouguer plate, which is embedded in the Poicaré-Prey gradient) around the computation points are not accounted for. For instance, in the case of a computation point located on a mountain top it is easy to see that due to the mass deficiency the magnitude of $\overline{g}^H(\Omega)$ becomes underestimated (in Eq. (5) note the opposite signs for the constants in the brackets). This gives an unreasonable rise to the resulting Helmert height. Conversely, the mass excess (with respect to the Bouguer plate) exists for the computation points inside of deep valleys. The magnitude of $\overline{g}^H(\Omega)$ is overestimated, the resulting Helmert height thus is lower than it should be.

Note that approaches by Mader (1954) and Niethammer (1932) attempt to improve the Helmert heights by accounting for the roughness of the topography. The resulting heights are more compatible with the rigorous orthometric height, see a numerical study by Santos et al. (in press).

6 Summary and conclusions

The aim of this paper is to demonstrate that the computations of the rigorous orthometric heights can be significantly simplified by making use of the typical by-products of the Stokes-Helmert geoid determination. More specifically, several Stokes-Helmert geoid modelling terms are exactly the same as needed for the orthometric height determination.

Accordingly, the implementation of the rigorous height system becomes a relatively simple and straightforward task. An additional bonus is that the resulting orthometric heights are more compatible

with regional gravimetric geoid models. Let us hope that these circumstances encourage those who currently use Helmert's approximate orthometric heights to upgrade them to a more rigorous height system.

The improved orthometric heights have a wide range of the practical and engineering applications. Therefore, the national agencies and organisations currently holding the Stokes-Helmert geoid determination results, should make them available to the users. For instance, both the Stokes-Helmert geoid methodology and the orthometric height system are adopted by the national agencies of the three North-American countries: Canada (Huang et al., in press), the U.S.A. (Roman et al., 2004) and Mexico (Hernandez, 2003). The existence of the needed components would allow the North-American users more easily to implement the rigorous orthometric heights, without having to recreate many of the results already calculated and held by their government agencies.

Note that the concept of the NT-gravity (as introduced in Vaniček et al., 2004) is exploited in this study. Hence, the usage of the NT-quantities, besides of its obvious value for different geophysical studies, has very promising geodetic applications as well.

Acknowledgements: The Canadian investigators have been funded by the "GEOIDE Network of Centres of Excellence" and by the National Science and Engineering Council of Canada. The prime author is supported by the European Union Structural Funds, Project # 1.0101-0335.

References

- Bruns H (1878) *Die Figur der Erde*. Veröff. Königl. Preuss. Geod. Inst., Berlin.
- Ellmann A, Vaniček (in press) UNB application of Stokes-Helmert's approach to geoid computation. Accepted by: *Journal of Geodynamics*.
- Heiskanen WH, Moritz H (1967) *Physical geodesy*. Freeman and Co, San Francisco.
- Hernandez AN (2003) Carta gravimetrica de la Republica Mexicana. *Revista cartographica*, 76/77.
- Helmert FR (1890) *Die Schwerkraft im Hochgebirge, Insbesondere in den Tyroler Alpen*. Veröff. Königl. Preuss. Geod. Inst., Berlin.
- Huang J, Fotopoulos G, Cheng MK, Véronneau M, Sideris MG (in press) On the Estimation of the Regional Geoid Error in Canada. Accepted by: *Proceedings, IAG Scientific Assembly, Cairns, Australia, 2005*.
- Kellogg OD (1929) *Foundations of Potential Theory*. Springer, Berlin.
- Kingdon R, Vaniček P, Santos M, Ellmann A, Tenzer R (2005) Toward an improved orthometric height system for Canada, *Geomatica*, **59**, 241-249. Erratum in **60**.
- Mader K (1954) Die orthometrische Schwerekorrektion des Präzisions-Nivellements in den Höhen Tauern. *Österreichische Zeitschrift für Vermessungswesen*, Sonderheft 15, Vienna
- Martinec Z (1998) *Boundary value problems for gravimetric determination of a precise geoid*. Lecture notes in Earth sciences, Vol. 73, Springer, Berlin, Heidelberg, New York.
- Molodensky MS, Yeremeev VF, Yurkina MI (1960) *Methods for Study of the External Gravitational Field and Figure of the Earth*. TRUDY TsNIIGAiK, 131, Geodezizdat, Moscow. English transl.: Israel Program for Scientific Translation, Jerusalem 1962.
- Niethammer T (1932) *Nivellement und Schwere als Mittel zur Berechnung wahrer Meereshöhen*. Schweizerische Geodätische Kommission, Berne.
- Roman DR, Wang YM, Henning W, Hamilton J (2004) Assessment of the New National Geoid Height Model - GEOID03. *Surveying and Land Information Systems*, **64**, 153-162.
- Santos MC, Vaniček P, Featherstone WE, Kingdon R, Ellmann A, Martin B-A, Kuhn M, Tenzer R (in press) Relation between the rigorous and Helmert's definitions of orthometric heights. Accepted by: *Journal of Geodesy*.
- Stokes GG (1849) On the variation of gravity at the surface of the earth. *Trans. Cambridge Philos. Soc.* VIII, 672-695.
- Tenzer R, Vaniček P, Santos M, Featherstone WE, Kuhn M (2005) Rigorous determination of the orthometric height. *Journal of Geodesy*, **79**, 82-92.
- Vaniček P, Sjöberg LE (1991) Reformulation of Stokes's Theory for Higher Than Second-Degree Reference Field and Modification of Integration Kernels. *Journal of Geophysical Research*, **96(B4)**, 6529-6339.
- Vaniček P, Martinec Z (1994) The Stokes-Helmert scheme for the evaluation of a precise geoid. *Manuscripta Geodaetica*, **19**, 119-128.
- Vaniček P, Sun W, Ong P, Martinec Z, Najafi M, Vajda P, Horst B (1996) Downward continuation of Helmert's gravity. *Journal of Geodesy*, **71**, 21-34.
- Vaniček P, Huang J, Novák P, Pagiatakis SD, Véronneau M, Martinec Z, Featherstone WE (1999) Determination of the boundary values for the Stokes-Helmert problem. *Journal of Geodesy*, **73**, 160-192.
- Vaniček P, Tenzer R, Sjöberg LE, Martinec Z, Featherstone WE (2004) New views of the spherical Bouguer gravity anomaly, *Geophysical Journal International*, **159**, 460-472.

On the problem of geoid height transformation between different geodetic reference frames

Christopher Kotsakis

Department of Geodesy and Surveying
Aristotle University of Thessaloniki
University Box 440, GR-54124, Thessaloniki, Greece
Email: kotsaki@topo.auth.gr

Abstract. Transforming geoid heights between different geodetic reference frames (GRFs) is an essential task in gravity field modeling and its proper implementation is crucial for many applications involving the use of the geoid. In this paper an attempt is made to investigate the problem of geoid height transformation between different GRFs, without considering other variations in the auxiliary geophysical or geodynamical hypotheses that may be a-priori specified for the desired geoid type (e.g. variations in the values of M and/or W_o , variations in terms of treatment of permanent tidal effects). The aim here is to present the required methodology to deal with the problem: “how should we transform geoid heights, referring to a fixed equipotential surface ($W = W_o$), from a given GRF to another GRF when we know the seven similarity transformation parameters linking the two frames?”. Special emphasis is given on the effect of GRF scale variations in coordinate transformations involving reference ellipsoids, for the particular case of geoid heights. Since every Cartesian coordinate system “gauges” an attached ellipsoid according to its own particular scale, there will exist a small contribution from the scale variation between the involved GRFs on the relative size of their adopted reference ellipsoids. Neglecting such a scale-induced indirect effect corrupts the values for the curvilinear geodetic coordinates obtained from a similarity transformation model, and significant errors can be introduced in the transformed geoid heights. The paper explains the above issues in detail and presents the necessary mathematical framework for their solution.

Keywords. Geoid, similarity transformation, reference frame, reference ellipsoid, datum scale.

1 Introduction

High-precision studies in Earth gravity field modeling require a careful treatment of several reference frame issues in order to ensure a coherent framework for data analysis and to avoid datum-related biases and artifacts in the results. Transforming

geoid heights, for example, between different geodetic reference frames is an essential and necessary component in gravity field modeling, and its proper implementation is crucial in many scientific applications involving the direct or indirect use of the geoid (e.g. consistent combination of ellipsoidal, orthometric and geoid height data for GPS-based leveling, external validation of gravimetric geoid models with GPS and leveling data, datum-consistent comparison between old and recent gravimetric, satellite-only or combined geoid models, update of existing geoid models to comply with current definitions and realizations of global geodetic reference systems, reduction of sea surface heights obtained from satellite altimetry data to a preferred geodetic reference frame, and proper utilization of geoid height information in datum transformation studies).

By definition, geoid heights refer to a specific geodetic reference system (GRS). Available geoid models (e.g. EGM96) or individually computed geoid height values (e.g. from GPS and leveling data) ought to be consistent with a particular realization of such a GRS, namely a geodetic reference frame (GRF). In this way, a gravimetric geoid determined through the generalized Stokes’ formula (Heiskanen and Moritz 1967)

$$N = \frac{G\delta M}{R\gamma} - \frac{\delta W}{\gamma} + \frac{R}{4\pi\gamma} \iint_{\sigma} \Delta g S(\psi) d\sigma \quad (1)$$

will be consistent with the geocentric GRF in which the spatial positions and the values of the gravity anomaly data Δg refer to, whereas a geoid obtained through a spherical harmonic series expansion refers to the GRF that is realized by the positions of the satellite tracking stations which were estimated at the time of the model development (Pavlis 1998, Lemoine *et al.* 1998). On the other hand, geoid heights that are computed directly from GPS and leveling data, according to $N = h - H$, refer to the same GRF implied by the GPS coordinates of the evaluation point, while the use of the orthometric height in this case fixes (in principle) the particular

equipotential surface $W = W_o$ that we should treat as “the geoid”.

Apart from the chosen spatial reference frame in which the relative position of the geoid with respect to a reference ellipsoid shall be expressed (at a particular epoch), there are additional aspects affecting the adopted GRS with respect to which a final geoid model can be delivered. Such aspects involve the treatment of the permanent tidal effects on the gravity field and the Earth’s crust (zero-frequency geoid, non-tidal geoid, mean geoid), the consideration of other loading effects on the solid and liquid parts of the Earth, the adoption of specific numerical values for fundamental GRS parameters (or “constants”) such as the Newton’s gravitational constant G , the Earth’s (including its atmosphere) mass M , the normal gravity potential value on the reference ellipsoid U_o , the gravity potential value on the geoid W_o , the semi-major axis and the flattening of the reference ellipsoid, the mean angular velocity of the Earth, etc.; see Groten (2004).

In this paper an attempt is made to highlight the essential points related to the problem of geoid height transformation between different GRFs, without considering other variations in the auxiliary geophysical or geodynamical hypotheses that may be a-priori specified for the desired geoid type (e.g. variations in the values of M and/or W_o , variations in terms of treatment of permanent tidal effects, etc.). Our objective is to present the methodology and the required formulae to deal with the following problem: “*how should we transform geoid heights, referring to a fixed equipotential surface ($W = W_o$), from a given GRF to another GRF when we know the seven similarity transformation parameters linking the two frames?*”; see Fig. 1.

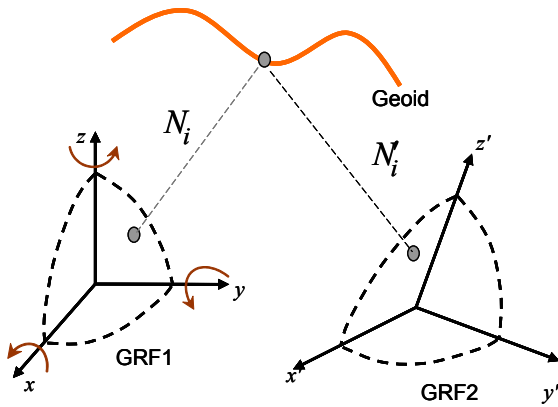


Figure 1. Geoid height transformation between different geodetic reference frames.

Special emphasis is given on the effect of GRF scale variations in coordinate transformations in-

volving reference ellipsoids, which is an important issue that has not been sufficiently stressed in the geodetic literature; see Soler and van Gelder (1987). Since every Cartesian coordinate system “gauges” an attached reference ellipsoid according to its own particular scale, there will be a small contribution from the scale variation between the involved GRFs on the relative size of their adopted reference ellipsoids. For example, if the same ellipsoid (in terms of *physical dimensions*) is attached to two different GRFs, we should generally assign different values to its semi-major axis in each case *if* the GRFs are connected through a non-zero scale change factor. Neglecting such a scale-induced indirect effect corrupts the resulting values for the curvilinear geodetic coordinates obtained from a similarity transformation model, and significant errors can be introduced in the transformed geoid heights (Soler and van Gelder 1987).

To clarify these points, an extended similarity transformation model is presented which provides a proper “de-coupling” of the geoid height variation arising from (i) the GRF scale difference and (ii) the actual change of the *physical size* of the reference ellipsoid.

2 Similarity transformation model for geoid heights

Let us consider the well known Euclidean similarity transformation model which is used to convert Cartesian coordinates between two geodetic reference frames that generally differ in terms of three translation parameters (t_x, t_y, t_z), three orientation parameters ($\varepsilon_x, \varepsilon_y, \varepsilon_z$) and a factor of uniform spatial scale change (δs)

$$\begin{bmatrix} x' - x \\ y' - y \\ z' - z \end{bmatrix} = \begin{bmatrix} t_x \\ t_y \\ t_z \end{bmatrix} + \begin{bmatrix} \delta s & \varepsilon_z & -\varepsilon_y \\ -\varepsilon_z & \delta s & \varepsilon_x \\ \varepsilon_y & -\varepsilon_x & \delta s \end{bmatrix} \begin{bmatrix} x \\ y \\ z \end{bmatrix} \quad (2)$$

Note that the above model corresponds to a first-order linear approximation of the rigorous vector transformation formula

$$\mathbf{x}'_{\text{GRF2}} = \mathbf{t} + (1 + \delta s) \mathbf{R}(\varepsilon_x, \varepsilon_y, \varepsilon_z) \mathbf{x}_{\text{GRF1}} \quad (3)$$

with \mathbf{R} being the total rotation matrix that performs three successive rotations around the axes of GRF1 so that they become parallel to the corresponding axes of GRF2, \mathbf{t} is the Cartesian coordinate vector of the origin of GRF1 with respect to GRF2, and δs is the scale difference factor between the two reference frames (see Fig. 1). The use of the approxi-

mate model (2) instead of the rigorous expression in (3) has a negligible effect on the transformed coordinates and it is justified for most geodetic applications where the rotation angles do not exceed a few arc seconds and the differential scale factor is of the order of 10^{-5} or less; for more details, see Hofmann-Wellenhof and Moritz (2005, ch. 5).

In order to derive the expression for the similarity transformation of geoid heights between the reference frames GRF1 and GRF2, we need also to consider the relationship between Cartesian and curvilinear geodetic coordinates

$$\begin{bmatrix} x \\ y \\ z \end{bmatrix} = \begin{bmatrix} (N+h) \cos \varphi \cos \lambda \\ (N+h) \cos \varphi \sin \lambda \\ (N(1-e^2)+h) \sin \varphi \end{bmatrix} \quad (4)$$

where N (to be distinguished from the symbol N that denotes the geoid height) is the prime vertical radius of curvature, given by the formula

$$N = \frac{a}{W} = \frac{a}{\sqrt{1-e^2 \sin^2 \varphi}} \quad (5)$$

The quantities a and e^2 correspond to the length of the semi-major axis and the squared eccentricity of the adopted reference ellipsoid which is used for the definition of the curvilinear geodetic coordinates φ , λ and h in (4).

By differentiation of (4), we get

$$\begin{bmatrix} dx \\ dy \\ dz \end{bmatrix} = \mathbf{J} \begin{bmatrix} d\varphi \\ d\lambda \\ dh \end{bmatrix} \quad (6)$$

where the Jacobian matrix \mathbf{J} has the following form (Soler 1976)

$$\mathbf{J} = \begin{bmatrix} -(M+h) \sin \varphi \cos \lambda & -(N+h) \cos \varphi \sin \lambda & \cos \varphi \cos \lambda \\ -(M+h) \sin \varphi \sin \lambda & (N+h) \cos \varphi \cos \lambda & \cos \varphi \sin \lambda \\ (M+h) \cos \varphi & 0 & \sin \varphi \end{bmatrix} \quad (7)$$

and $M = a(1-e^2)/W^3$ is the meridian radius of curvature.

Substituting the left hand-side in (6) according to the similarity transformation model given by (2), and then solving for dh , we obtain the following formula that corresponds to the *similarity transfor-*

mation model for ellipsoidal heights (Soler and van Gelder 1987)

$$h' - h = \delta h(t_x) + \delta h(t_y) + \delta h(t_z) + \delta h(\varepsilon_x) + \delta h(\varepsilon_y) + \delta h(\delta s) \quad (8)$$

where

$$\delta h(t_x) = t_x \cos \varphi \cos \lambda \quad (9)$$

$$\delta h(t_y) = t_y \cos \varphi \sin \lambda \quad (10)$$

$$\delta h(t_z) = t_z \sin \varphi \quad (11)$$

$$\delta h(\varepsilon_x) = -\varepsilon_x N e^2 \sin \varphi \cos \varphi \cos \lambda \quad (12)$$

$$\delta h(\varepsilon_y) = \varepsilon_y N e^2 \sin \varphi \cos \varphi \cos \lambda \quad (13)$$

$$\delta h(\delta s) = (aW + h) \delta s \quad (14)$$

Note that the rotation angle ε_z does not affect the change of the ellipsoidal height from GRF1 to GRF2 due to the rotational symmetry of the reference ellipsoid.

The above formulae perform the similarity transformation of ellipsoidal heights between two arbitrary GRFs at any point in space whose initial curvilinear coordinates (with respect to GRF1) are φ , λ and h . If we assume, in particular, that the point whose ellipsoidal height being transformed is located on the geoid (see Fig. 1), then (8) is reduced to the *similarity transformation model for geoid heights*

$$N' - N = \delta N(t_x) + \delta N(t_y) + \delta N(t_z) + \delta N(\varepsilon_x) + \delta N(\varepsilon_y) + \delta N(\delta s) \quad (15)$$

where $\delta N(t_x) = \delta h(t_x)$, $\delta N(t_y) = \delta h(t_y)$, $\delta N(t_z) = \delta h(t_z)$, $\delta N(\varepsilon_x) = \delta h(\varepsilon_x)$ and $\delta N(\varepsilon_y) = \delta h(\varepsilon_y)$.

It is important to mention that the ellipsoidal height of the evaluation point in this case is identical to the geoid height, and thus the scale-dependent term $\delta N(\delta s)$ should take the form

$$\delta N(\delta s) = (aW + N) \delta s \quad (16)$$

Remark 1. In the special case where $t_x = t_y = t_z = 0$ and $\varepsilon_x = \varepsilon_y = \varepsilon_z = 0$, the previous geoid transformation model yields

$$N' - N = \delta N(\delta s) = (aW + N) \delta s \quad (17)$$

or equivalently

$$N' = (1 + \delta s)N + aW\delta s \quad (18)$$

The interesting point in this particular case is the presence of the additional term ‘ $aW\delta s$ ’ in (18), which can be understood as the effect of an “apparent” change in the physical dimensions of the reference ellipsoid due to the scale difference between the involved GRFs. The magnitude of this term can be quite significant, reaching more than 6 m when $\delta s = 10^{-6}$ (1 ppm) and dropping to about 1 cm for $\delta s = 10^{-9}$ (1 ppb).

If the reference ellipsoid remains the same in terms of its physical dimensions in both GRFs, then the geoid height change (when $t_x = t_y = t_z = 0$ and $\varepsilon_x = \varepsilon_y = \varepsilon_z = 0$) should be given *only* by a simple re-scaling

$$N' = (1 + \delta s)N \quad (19)$$

since the same physical length (i.e. the distance between a point on the geoid and its orthogonal projection on the single reference ellipsoid) is “measured” with respect to two coinciding GRFs which differ only by a uniform scale factor δs .

In order to counter balance the effect of the term ‘ $aW\delta s$ ’ in (18), and also to properly account for an actual change in the physical size of the reference ellipsoid, the similarity transformation model for geoid heights in (15) needs to be extended as described in the following section.

3 Considering the effect of the reference ellipsoid change

Let us adopt the length of the semi-major axis (a) and the flattening (f) as the two fundamental parameters that uniquely define the geometrical size of a reference ellipsoid.

In order to account for a possible change in the physical dimensions of the reference ellipsoid in geoid height transformation problems, we need first to differentiate the vector formula in (4) as follows

$$\begin{bmatrix} dx \\ dy \\ dz \end{bmatrix} = \mathbf{J}_1 \begin{bmatrix} d\varphi \\ d\lambda \\ dh \end{bmatrix} + \mathbf{J}_2 \begin{bmatrix} da \\ df \end{bmatrix} \quad (20)$$

where the first Jacobian matrix \mathbf{J}_1 is identical to the matrix \mathbf{J} given in (7), while the analytical form of the second Jacobian matrix \mathbf{J}_2 can be found in Soler (1976); see also Soler and van Gelder (1987). Setting the left-hand side in (20) equal to zero, and

then solving for dh , we obtain the ellipsoidal height variation only from the change of the reference ellipsoid which, in conjunction with (8), leads to the following *extended similarity transformation model for ellipsoidal heights*

$$\begin{aligned} h' - h &= \delta h(t_x) + \delta h(t_y) + \delta h(t_z) \\ &+ \delta h(\varepsilon_x) + \delta h(\varepsilon_y) + \delta h(\delta s) \\ &+ \delta h(\delta a) + \delta h(\delta f) \end{aligned} \quad (21)$$

where the additional terms $\delta h(\delta a)$ and $\delta h(\delta f)$ are given by the equations (Soler and van Gelder 1987)

$$\delta h(\delta a) = -W \delta a \quad (22)$$

$$\delta h(\delta f) = \frac{a(1-f)}{W} \sin^2 \varphi \delta f \quad (23)$$

The quantities $\delta a = a' - a$ and $\delta f = f' - f$ correspond to the variation of the numerical values for the semi-major axis and the flattening of the reference ellipsoid, as these are used in the respective geodetic reference frames, GRF1 and GRF2.

With the exclusion of the terms $\delta h(\varepsilon_x)$, $\delta h(\varepsilon_y)$ and $\delta h(\delta s)$, the model in (21) is identical to the standard *Molodensky transformation formula* (Molodensky *et al.* 1962) which has often been used for transforming ellipsoidal heights between different geodetic datums (see, e.g., National Imagery and Mapping Agency 1996, pp. 7.3-7.4) and for determining the Earth’s mean equatorial radius and center of mass through the joint analysis of geometrically derived and gravimetric geoid heights (see, e.g., Grappo 1980).

Taking into account (21), the corresponding *extended similarity transformation model for geoid heights* is obtained

$$\begin{aligned} N' - N &= \delta N(t_x) + \delta N(t_y) + \delta N(t_z) \\ &+ \delta N(\varepsilon_x) + \delta N(\varepsilon_y) + \delta N(\delta s) \\ &+ \delta N(\delta a) + \delta N(\delta f) \end{aligned} \quad (24)$$

where $\delta N(\delta a) = \delta h(\delta a)$ and $\delta N(\delta f) = \delta h(\delta f)$. The translation, rotational and scale-dependent terms in (24) have already been defined and explained in the previous section.

4 What should we use for δa ?

An important issue that remains to be clarified, in the context of geoid transformation, is the proper

usage of the term $\delta N(\delta a) = -W \delta a$ which gives the geoid height variation due to the difference $\delta a = a' - a$ in the numerical values of the semi-major axis for the reference ellipsoids adopted by the frames GRF1 and GRF2.

In general, the length of the semi-major axis of the reference ellipsoid attached to GRF2 can be expressed as

$$a' = (1 + \delta s) a + \delta \bar{a} \quad (25)$$

where a is the length of the semi-major axis of the reference ellipsoid attached to GRF1, δs is the scale change factor between the two frames, and $\delta \bar{a}$ corresponds to the actual change of the *physical length* of the semi-major axis of the GRF2 ellipsoid with respect to the *physical length* of the semi-major axis of the GRF1 ellipsoid (see Fig. 2).

In this way, we have that

$$\delta a = a' - a = a \delta s + \delta \bar{a} \quad (26)$$

and thus the geoid height variation term $\delta N(\delta a)$ becomes

$$\delta N(\delta a) = -W a \delta s - W \delta \bar{a} \quad (27)$$

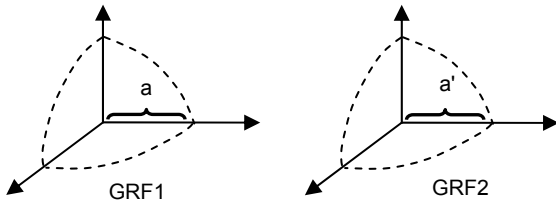


Figure 2. Each geodetic reference frame “gauges” the attached reference ellipsoid according to its own particular scale.

Remark 2. Let us consider again the special case where $t_x = t_y = t_z = 0$ and $\varepsilon_x = \varepsilon_y = \varepsilon_z = 0$, and additionally $\delta f = 0$. Based on these assumptions, the extended similarity transformation model for geoid heights in (24) yields

$$N' - N = \delta N(\delta s) + \delta N(\delta a) \quad (28)$$

Using (16) and (27), the last equation can be written in the equivalent form

$$N' = (1 + \delta s)N - W \delta \bar{a} \quad (29)$$

In contrast to the transformation formula obtained by the simple (non-extended) similarity transforma-

tion model in (18), the above result complies with geometrical intuition which dictates that the transformed geoid height should be determined by a simple re-scaling of the initial geoid height value *if* the underlying GRFs have the same origin and orientation *and* also use the same reference ellipsoid in terms of physical dimensions ($\delta f = 0$, $\delta \bar{a} = 0$). Note that the elimination of the “apparent” geoid variation term ‘ $aW\delta s$ ’ that emerged in (18) has been inherently achieved by the inclusion of the term $\delta N(\delta a)$ as given in (27).

5 Summary – Open problems

When a GRS is used in practice via an established and accessible GRF, the adopted reference ellipsoid that is required to define and quantify several important geodetic quantities does not refer to an “ideal” scale unit (e.g. the light-based meter standard) but rather to the best scale which geodesists are able to reproduce by means of their current data, measurement techniques and optimal combination procedures (Soler and van Gelder 1987). Therefore, any GRF “detects” an attached reference ellipsoid, as well as every length-type quantity that depends on it (e.g. ellipsoidal height derived from known Cartesian coordinates with respect to a given ITRF), according to its own particular scale.

Taking into account the above considerations, we have investigated the problem of geoid height conversion between different GRFs by providing a general transformation model that incorporates the contribution of GRF scale variation on the relative size of the reference ellipsoids adopted by each datum. Specifically, if we know the seven similarity transformation parameters between two given GRFs, then the conversion of the geoid height from one GRF to another can be implemented through the formula

$$\begin{aligned} N' - N &= \delta N(t_x) + \delta N(t_y) + \delta N(t_z) \\ &+ \delta N(\varepsilon_x) + \delta N(\varepsilon_y) \\ &+ \delta N(\delta f) + \delta N(\delta s, \delta a) \end{aligned} \quad (30)$$

The critical point in the above model is the treatment of the last variation term, which contains the combined effect due to the GRF scale variation and the change of the semi-major axis of the reference ellipsoid. As explained in the previous sections, the combined term $\delta N(\delta s, \delta a) = \delta N(\delta s) + \delta N(\delta a)$ can be expressed in the form

$$\delta N(\delta s, \delta a) = (aW + N) \delta s - W \delta \bar{a} \quad (31)$$

or, taking into account (26),

$$\delta N(\delta s, \delta a) = (aW + N) \delta s - W(a\delta s + \delta \bar{a}) \quad (32)$$

where $\delta \bar{a}$ is the change of the *physical length* of the semi-major axis of the reference ellipsoid.

In practice, there are two basic options for the implementation of the geoid height transformation model in (30). Both of these options relate to the evaluation of the term $\delta N(\delta s, \delta a)$ and they essentially correspond to choosing how to treat the physical size of the reference ellipsoid with respect to the underlying GRFs.

One alternative is to select $\delta \bar{a} = 0$, which implies that the *physical length* of the semi-major axis of the reference ellipsoid is invariant within the underlying GRFs. In this case, we have

$$\delta N(\delta s, \delta a) = N\delta s \quad (33)$$

which is a negligible geoid correction for all purposes (i.e. less than 1 mm even for $\delta s = 10$ ppm). Note, however, that all numerical calculations involving the semi-major axis of the reference ellipsoid *with respect to the GRF2 frame* (e.g. conversion of Cartesian coordinates to curvilinear coordinates and vice versa) should be made using the new value

$$a' = (1 + \delta s) a \quad (34)$$

and not the initial value 'a' which is used for similar calculations with respect to the GRF1 frame; see also Soler and van Gelder (1987).

The other alternative for the evaluation of the term $\delta N(\delta s, \delta a)$ is to set $\delta a = 0$, which implies that the *same numerical value* for the semi-major axis of the reference ellipsoid is used in both frames GRF1 and GRF2. In this case, the geoid height variation term $\delta N(\delta s, \delta a)$ takes the form

$$\delta N(\delta s, \delta a) = N\delta s + aW\delta s \quad (35)$$

As already mentioned, the magnitude of the above correction is quite significant and it must always be considered since the term 'aWδs' can reach more than 6 m for $\delta s = 1$ ppm. Note that this alternative carries an *inherent change in the physical dimensions of the reference ellipsoid*, since from (26) we have that

$$\delta a = 0 \Rightarrow \delta \bar{a} = -a\delta s \quad (36)$$

In closing, let us add a final remark. In contrast to $\delta N(\delta a)$ given in (27), the term $\delta N(\delta f)$ which represents the geoid height variation due to the flattening change of the reference ellipsoid, is insensitive to a uniform GRF scale difference (δs) since the ellipsoid's flattening $f=(a-b)/a$ does not depend on the scale unit of the underlying GRF.

References

- Grappo GA (1980) Determination of the earth's mean equatorial radius and center of mass from Doppler-derived and gravimetric geoid heights. *Manusc Geod*, 5: 201-216.
- Groten E (2004) Fundamental parameters and current (2004) best estimates of the parameters of common relevance to astronomy, geodesy and geodynamics. *J Geod*, 77(10-11): 724-731.
- Heiskanen W, Moritz H (1967) *Physical geodesy*. W.H. Freeman, San Francisco.
- Hofmann-Wellenhof B, Moritz H (2005) *Physical geodesy*. Springer Verlag, Wien.
- Lemoine FG, Kenyon SC, Factor JK, Trimmer RG, Pavlis NK, Chinn DS, Cox CM, Klosko SM, Luthcke SB, Torrence MH, Wang YM, Williamson RG, Pavlis EC, Rapp RH, Olson TR (1998) *The development of the Joint NASA GSFC and the National Imagery and Mapping Agency (NIMA) Geopotential Model EGM96*. NASA Technical Report 1998-206861, Goddard Space Flight Center, Greenbelt, Maryland.
- Molodensky MS, Eremeev VF, Yurkina MI (1962) Methods for study of the external gravitational field and figure of the Earth (translation from Russian). Israel program for scientific translations, Jerusalem, Israel.
- National Imagery and Mapping Agency (1996) World Geodetic System 1984: its definition and relationships with local geodetic systems. Technical Report 8350.2, Geodesy and Geophysics Department, NIMA, St. Louis, MO.
- Pavlis EC (1998) On the reference frames inherent in recent geopotential models. In: Vermeer M and Adam J (eds.) *Proceedings of the Second Continental Workshop on the Geoid in Europe*, Budapest, Hungary, March 10-14. Reports of the Finnish Geodetic Institute, Helsinki, 98:4, pp. 29-40.
- Soler T (1976) On differential transformations between Cartesian and curvilinear (geodetic) coordinates. Technical Report, No. 236, Department of Geodetic Science, Ohio State University, Columbus, Ohio.
- Soler T, van Gelder BHW (1987) On differential scale changes and the satellite Doppler system z-shift. *Geophys J R Astr Soc*, 91: 639-656.

Realization of the vertical datum and height system of Lithuania

B. Krikstaponis, E. Parseliunas, P. Petroskevicius, R. Putrimas, A. Zakarevicius
Vilnius Gediminas Technical University, Sauletekio al. 11, LT-10223 Vilnius-40, Lithuania

S. Urbanas
National Land Service, Gedimino pr. 19, LT-01103 Vilnius, Lithuania

Abstract. The vertical datum and height system adoption is crucial in development of national geodetic reference.

The gravity and height systems should be related with the geocentric geodetic coordinate system. In Lithuania such a system was adopted in 1994 as a Lithuanian Coordinate System (LKS 94). It consist with European Terrestrial Reference System 1989.

Since 1998 the main Lithuanian geodetic activities were related to the development of the Lithuanian National Geodetic Vertical Network. The network should implement unified system of heights in the territory of Lithuania and guaranty reliable connection with other European height systems. Lithuania is participating in the United European Levelling Network and European Vertical Network project, and is planning to adopt the common European Vertical System.

Keywords. Vertical datum, height system, levelling network, normal heights.

1 Introduction

The height systems adoption is crucial in development of national geodetic reference. Successful solution of this question guarantees the reliable determination of geopotential heights, usage of modern geodetic space techniques, maintenance of the navigation, geodetic and cartographic works, solution of geodynamic tasks, support the relations between the similar systems of other countries.

The Baltic Sea height system defined by Kronstadt datum is still in use in Lithuania. Therefore Lithuania is participating in the United European Levelling Network (UELN) and European Vertical Network (EUVN) project, and is planning to adopt the common European Vertical System [1–3].

Since 1998 the main Lithuanian geodetic activities were related to the development of the Lithuanian National Geodetic Vertical Network (NGVN) [4–9]. The NGVN should implement unified system of heights in the territory of Lithuania and guaranty reliable connection with

other European height systems. The NGVN should be continuously updated for the purpose of heights and their accuracy determination. Institute of Geodesy, VGTU is involved in establishment of National Networks. The main geodetic activities of Lithuania are supervised by the Department of Geodesy and Cadastre at National Land Service under Ministry of Agriculture. The development of NVGN is finished and it is planning to adopt Lithuanian vertical system in 2007.

2 Background for height systems adoption

In preparation to adopt the height system Lithuania have participated in the international projects as “United European Levelling Network” (UELN) [10–17], “European Vertical GPS Reference Network” (EUVN) [18–21] and “Baltic Sea Level” (BSL) [22–23].

The United European Levelling Network (UELN) is a continental height system, which was planned at first in 1955 as a levelling network for Western Europe with the reference point Amsterdam (NAP). The results of the first adjustment of 1960 were published as UELN-55 [10].

At present the work at the UELN was continued within the scope of the IAG Subcommission for Europe (EUREF) under the name of UELN-95. The development, results and status of UELN was well reported in each year [11–15]. In January of 1999, the results of the adjustment version UELN-95/13 were handed over to the participating countries as the UELN-95/98 solution [16, 17].

Following the Resolution of the EUREF Symposium adopted in Bad Neuenahr–Ahrweiler in 1998 requesting to extend and improve the vertical network around the Baltic Sea, Lithuanian geodesists prepared the data for connecting the state levelling network to UELN [16, 17].

The Lithuanian reference levelling network was included into UELN in 2000 (Fig. 1).

The levelling data of different epochs fit to each other at 1 mm per kilometre accuracy. The connecting lines between national networks of neighbouring countries also coincide at the same accuracy level. The accuracy of Lithuanian

levelling network is at the same level as that of the levelling networks of biggest part of other participating countries. To achieve a higher accuracy the observations of the Lithuanian fundamental network should be finished as soon as possible. Also, these data will improve the geokinematics height network and will be a basis for adoption of the European Vertical System 2000 (EVS2000).

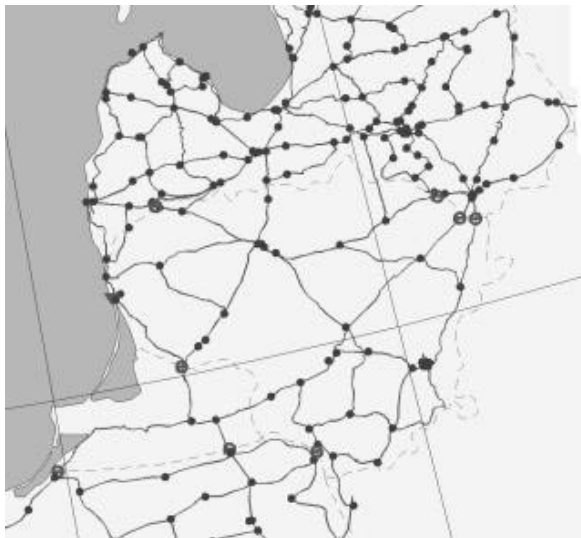


Fig. 1. UELN in Lithuania

EUVN was started to develop in 1997. It joins the European Reference Frame (EUREF) permanent GPS sites, UELN of Western Europe and United Precise Levelling Network (UPLN) of Eastern Europe points. EUVN campaign was supported by the 33 European countries. There are three points – VILNIUS, SIAULIAI and MOLAS – in EUVN.

BSL project started in 1990. Participate all countries surrounding the Baltic Sea. Lithuania joined the GPS campaign of 1993. In 1997 was organized joined BSL and EUVN GPS campaign.

As a result of EUVN the coordinates and ellipsoidal heights of the points in ETRS89 and the normal heights connected to UELN were obtained. So the points of EUVN were connected to Amsterdam datum and European Vertical Reference System.

European Combined Geodetic Network (ECGN) should combine the spatial and height reference system with Earth gravity field parameter estimation [24, 25]. So the stations of ECGN shall combine the various geodetic techniques: GPS, levelling, gravity and tide gauge observations in coastal zones.

The Lithuania proposed for the ECGN stations VILNIUS and KLAIPEDA. VILNIUS is EUREF permanent GPS station, UELN and National vertical network node, absolute gravimetric

measurements point. KLAIPEDA is European Sea Level Service observing site and International GPS service TIGA-PP project station, including tide gauge, meteorological sensors, permanent GPS station and absolute gravimetric measurements point.

The data and results of the international projects create the good conditions for the adoption of the Lithuanian height system. The points VILNIUS, SIAULIAI, MOLAS, KLAIPEDA became the most accurate fundamental geodetic points. They will be the basis for the development of the modern geodetic reference of Lithuania.

3 Existing levelling network analysis

The present reference levelling network of Lithuania is combination of levelling line of different epochs, therefore its accuracy at the same level as that of the levelling networks of biggest part of other European countries. For example, the parameters of the adjustment are the following [16]:

- Number of fixed points: 1,
- Number of unknowns: 1466,
- Number of measurements: 1490,
- Minimum length of the loop: 14.2 km
- Maximum length of the loop: 785.8 km
- Average length of the loops: 303 km
- Degrees of freedom: 24,
- Standard deviation: 0.902 kGal×mm/km
- A-posteriori standard deviation referred to a levelling distance of 1km: 0.92 kGal×mm,
- Mean value of the standard deviation of the adjusted geopotential differences: 1.41 kGal×mm,
- Mean value of the standard deviation of the adjusted geopotential heights: 8.62 kGal×mm,
- Biggest value of the standard deviation of the adjusted geopotential heights: 11.32 kGal×mm,
- Average redundancy: 0.016.

The adjustment of geopotential heights differences of enlarged UELN95/15, including levelling networks of Poland and three Baltic states, was performed as an unconstrained adjustment linked to the reference point 13600 in Amsterdam, geopotential height of which was set to 0.70259 kGal×m, and normal height to 0.71599 m. The same network was adjusted with reference point of temporal Lithuanian height system 53V12421, geopotential height of which was set to 63.76000 kGal×m, and normal height 64.963 m, and with reference point Kronstadt gauge, geopotential height and normal height of which was set to 0.000 m. Normal heights received are presented in the Table 1 (accordingly H1, H2 and H3).

Table 1. Normal heights of nodal benchmarks

UENL ID	National ID	H ₁ m	H ₂ m	H ₃ m
12001	55S-0128	141.381	141.243	141.278
12002	73S-0271	215.660	215.427	215.558
12003	25S-1322	28.284	28.147	28.186
12004	25S-1522	4.638	4.502	4.540
12005	25N-0001	6.300	6.164	6.202
12006	62N-4538	75.248	75.111	75.146
12007	52V-4302	120.562	120.428	120.460
12008	62V-2956	131.828	131.692	131.726
12009	86N-2908	122.316	122.178	122.213
12010	75N-2401	97.976	97.838	97.872
12011	73V-2338	139.257	139.121	139.155
12012	73V15007	140.556	140.420	140.454
12013	26N-6237	9.590	9.456	9.494
12014	26N-0001	7.884	7.748	7.786
12016	95N--295	140.829	140.692	140.726
12017	51V--317	133.655	133.520	133.553
12021	56N--315	47.161	47.020	47.057
12022	55N--522	131.245	131.107	131.143
12023	64V--217	68.857	68.720	68.755
12024	63V-3717	95.248	95.111	95.146
12025	75N-1390	130.742	130.604	130.639
12026	61V-0398	133.393	133.258	133.292
12027	73V-0006	164.381	164.246	164.279
12028	63V-3919	70.216	70.079	70.114
12029	53V---71	37.753	37.616	37.651
12030	53V12421	65.100	64.963	64.998
12031	43N-4216	55.568	55.430	55.466
12032	73V15100	147.169	147.033	147.066
12033	34N--371	16.009	15.870	15.909
12036	36N-1828	72.404	72.261	72.300
12037	34N52079	52.046	51.908	51.946
12038	52V-1021	131.986	131.854	131.884
12041	36N-1609	106.758	106.614	106.653
12042	36N-0553	98.622	98.478	98.517
12043	36N-1681	116.478	116.342	116.378
12044	65N-2304	58.826	58.688	58.723
12045	55N--138	126.518	126.380	126.415
12046	26N-1423	22.679	22.540	22.578
12047	55N--311	130.762	130.624	130.660
12048	44N-0020	112.382	112.244	112.281
12049	34N-4016	36.766	36.627	36.665
12050	84N---17	158.187	158.051	158.084
12051	73V-4774	186.317	186.183	186.215
12052	85N-0001	147.539	147.402	147.436
12058	51V10019	142.208	142.067	142.106
12064	73N-0705	122.287	122.154	122.185

Average difference between H1 and H2 is 14 cm, that is well-known difference between UENL and UPLN normal heights. Therefore direct computation of normal heights from Amsterdam and Kronshdat gives average difference about 10 cm [16].

Normal height differences in different epochs for single line is presented in Table 2.

The levelling line Mikytai–Klaipeda is in the south-west part of Lithuania. The normal height differences do not exceed the levelling accuracy. So, it is proofs, that the geodynamic processes in this part of Lithuania are not very significant.

Table 2. Benchmarks heights of levelling line Mikytai – Klaipeda in different epochs [16, 25–28]

ID	1888	1939	2000
25N-7379	11.325	11.343	11.333
25N-7378	12.118	12.147	12.106
25N-7376	13.805	13.831	13.803
25N-7375	20.444	20.421	20.386
25N-7372	15.452	15.482	15.455
25N-8151	16.225	16.256	16.240
25N-8148	14.932	14.971	14.943
25N-8147	13.148	13.187	13.317
25N-8146	13.036	13.058	13.018
25N-8144	14.158	14.237	14.221
25N-8142	13.418	13.421	13.269
25N-1458	16.347	16.382	16.354
25N-1459	5.635	5.659	5.625
25N-8141	4.436	4.485	4.477
25N-1463	6.961	6.991	6.955
25N-8137	9.228	9.262	9.227
25N-1466	7.221	7.259	7.225
25N-8135	11.746	11.781	11.747
25N-1469	15.579	15.614	15.579
24N-8134	15.346	15.379	15.344
24N-8132	6.704	6.750	6.728
24N-8131	9.538	9.571	9.534
24N-8130	9.186	9.217	9.182
24N-1481	9.296	9.322	9.286
24N-1482	9.590	9.621	9.587
24N-8124	15.564	15.602	15.561
24N-8123	22.340	22.349	22.307
24N-1489	16.172	16.184	16.148
24N-8119	10.347	10.414	10.386
34N-8118	8.599	8.607	8.589
34N-8116	15.591	15.596	15.560
34N-8115	12.918	12.916	12.878
34N-8114	10.811	10.777	10.730
34N-1501	9.462	9.465	9.427
34N-1502	9.657	9.659	9.623
34N-8111	10.030	10.032	9.998
34N-8109	12.589	12.590	12.559

4 Current status of Lithuanian National Geodetic Vertical Network

Activities of Lithuanian National Geodetic Vertical Network (NGVN) establishment are going on since 1998. NGVN consists of five polygons (Fig 2). Perimeter of the network is ca. 1950 km. Mean distance between ground and wall benchmarks is 1.5 km, maximum distance between benchmarks does not exceed 2.5 km. Ground benchmarks are at least each 6 km, except of urbanised territories.

Fundamental benchmarks are built at every 40–60 km of levelling line. Connections of first order vertical network with vertical networks of neighbouring countries are foreseen. All this creates good preconditions for determination of relations between height systems and for introduction of a new Lithuanian height system, as well as for geodynamic research not only on Lithuanian territory but also on wider regions.

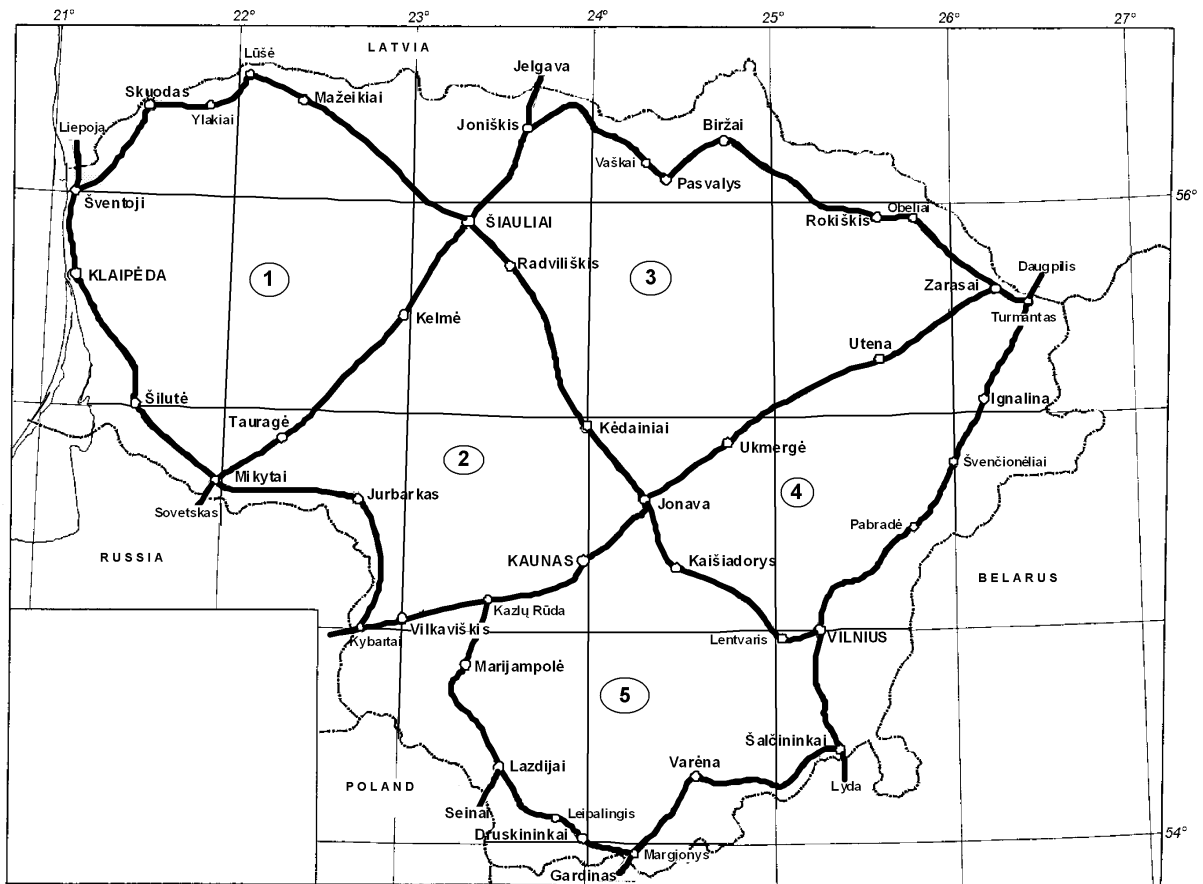


Fig. 2 Scheme of Lithuanian National Geodetic Vertical Network

Height differences between benchmarks of vertical network are determined by precise levelling. Two sets of digital levels *Wild NA3003* and precise bar coded invar staffs *GPCL3* were used for height differences determination.

Precise coded staffs *GPCL3* are calibrated every year by vertical automated laser comparator at the Finnish Geodetic Institute. Digital levelling system calibration is performed since 2004. Results of levelling system calibration, refraction and tidal effects were taken into account.

Accuracy characteristics of precise geometric levelling (standard deviations of 1 km double-run levelling) are presented in Table 2, and misclosures of loops are presented in Table 3.

Table 2. Accuracy characteristics of levelling

Year of levelling	m_{km}, mm
1998	0.48
1999	0.42
2001	0.39
2002	0.41
2003	0.43
2004	0.47
2005	0.44
2006	0.46

Table 3. Preliminary misclosures of network loops

Loop No.	Loop perimeter, km	Preliminary actual misclosure, mm	Allowable misclosure, mm
1	491.1	+4.67	33.24
2	517.8	+14.41	34.13
3	575.6	-10.83	35.99
4	451.1	+11.21	31.86
5	499.9	-10.73	33.54

Total number of points in the network is 1374. All ground benchmarks (totally 691) were observed by GPS campaigns, and ellipsoidal heights were computed.

The vertical datum and type of state heights system is not adopted in Lithuania yet. Therefore it seems that Lithuania will follow the resolution of the EUREF Symposium in 1996 in Ankara, and the normal heights system will be adopted. The normal gravity field of the Geodetic Reference System 1980 (GRS80) was adopted as part of Lithuanian Coordinate System 1994 (LKS 94).

So the way to adopt the Lithuanian national height system (LHS) could be as follows:

1. It should be realization of European Vertical Reference System based on UELN data.
2. It should utilized normal heights.
3. Apply the zero system for the permanent tide.
4. Do not implement the land uplift model. Set the reference epoch to 2000.0.
5. Obtain the geopotential number at VILNIUS (UELN ID 12002) site from a UELN adjustment relative to NAP. This is the vertical datum of LHS.
6. Adjust the Lithuanian NGVN in this datum.

5 Conclusions

1. Lithuania participates in the all main European projects related to height system development. That creates the strong premises for the Lithuanian height systems adoption.

2. The data of existing Lithuanian levelling network entered the UELN data base. It makes possible to integrate Estonian, Latvian and Lithuanian levelling networks into UELN. The accuracy of Lithuanian levelling network is at the same level as that of the levelling networks of biggest part of other participating countries.

3. Observations of Lithuanian National Geodetic Vertical Network are finished. Total number of points is 1374. The average accuracy (standard deviation of 1 km double-run levelling) of 0.44 mm was achieved. All ground benchmarks (totally 691) were observed by GPS campaigns, and ellipsoidal heights were computed.

4. Lithuanian National Geodetic Vertical Network is completed in 2006 and the country is ready to introduce the national height system, which should be the realization of European Vertical Reference System.

References

1. Augath W et al. (2000) EVS 2000 – Status and requirements. In: Veröffentlichungen der Bayerischen Kommission für die internationale Erdmessung der Bayerischen Akademie der Wissenschaften, Heft Nr. 61, München, pp 96–98
2. Ihde J, Augath W (2000) The Vertical Reference System for Europe. In: Veröffentlichungen der Bayerischen Kommission für die internationale Erdmessung der Bayerischen Akademie der Wissenschaften, Heft Nr. 61, München, pp 99–101
3. European Vertical Reference System (EVRS). In: Veröffentlichungen der Bayerischen Kommission für die internationale Erdmessung der Bayerischen Akademie der Wissenschaften, Heft Nr. 61. München, 2000, pp 101–110
4. Petroškevičius P, Paršeliūnas E (1998) Development of the European vertical network in Lithuanian territory (in Lithuanian). Geodesy and Cartography (Geodezija ir kartografija), Vol XXIV, No 3, pp 133–145
5. Parseliunas E et al. (1999) National Report of Lithuania. Mitteilungen des Bundesamtes für Kartographie und Geodäsie, Band 6, pp 187–189
6. Kazakevičius S et al. (1999) On the principles of Lithuanian Geodetic Vertical network establishment (in Lithuanian). Geodezija ir kartografija (Geodesy and Cartography), Vol XXV, No 2, pp 47–59
7. Buga A et al. (2003) Development of the Lithuanian National geodetic control. EUREF Publication No 12, Report on the Symposium of the IAG Subcommittee for Europe (EUREF) held in Ponta Delgada, 5-8 June, 2002, pp 273–281
8. Buga A et al. (2004) Main geodetic activities in Lithuania. EUREF Publication No. 14, Report on the Symposium of the IAG Subcommittee for Europe (EUREF) held in Bratislava, 2-5 June, 2004, pp 251–255
9. Petroskevicius P et al. (2005) Premises for Lithuanian gravity and height systems adoption. In: Selected papers of 6th International Conference „Environmental Engineering“, Vol 2, Vilnius: Technika, pp 985–992
10. Ernsperger W, Kok J J (1986) Status and Results of the 1986 Adjustment of the United European Levelling Network – UELN-73. Paper contributed to the Symposium on Height Determination and Recent Crustal Movements in Western Europe, Federal Republic of Germany, Sept. 15–19
11. Lang H, Sacher M (1996) Status and Results of the Adjustment and Enlargement of the United European Levelling Network 1995 (UELN-95). Report on the Symposium of the IAG Subcommittee for the European Reference Frame (EUREF) held in Kirkkonummi, Finland, May 3–6, 1995, pp 86–96
12. Lang H, Sacher M (1997) Status and Results of the Adjustment and Enlargement of the United European Levelling Network 1995 (UELN-95). Report on the Symposium of the IAG Subcommittee for the European Reference Frame (EUREF) held in Ankara, Turkey, May 22–25, 1996, pp 163–169
13. Lang H, Sacher M (1998) Status and Results of the Adjustment and Enlargement of the United European Levelling Network 1995 (UELN-95). Report on the Symposium of the IAG Subcommittee for the European Reference Frame (EUREF) held in Sofia, Bulgaria, June 4–7, 1997, pp 85–90
14. Lang H et al. (1999) Status and Results of the Adjustment and Enlargement of the United European Levelling Network 1995 (UELN-95). Report on the Symposium of the IAG Subcommittee for the European Reference Frame (EUREF) held in Bad Neuenahr-Ahrweiler, June 10–13, 1998, pp 131–141
15. Sacher M et al. (2002) Status of the UELN/EVRS Data Base – Activities between June 2000 and May 2001 and Future Plans. In: EUREF Publication No 10, Report on the Symposium of the IAG Subcommittee for Europe (EUREF) held in Dubrovnik, 16-18 May, 2001, pp 146–153
16. Paršeliūnas E et al. (2000) Preparation of Lithuanian levelling network data for United European levelling network. Geodesy and Cartography (Geodezija ir kartografija), Vol XXVI, No 4, pp 171–186
17. Sacher, M. et al. (2004) Status of the UELN/EVRS Data Base and Results of the Last UELN Adjustment. EUREF Publication No. 14, Report on the Symposium of the IAG Subcommittee for Europe (EUREF) held in Bratislava, 2-5 June, 2004, pp 172–179
18. Ihde J et al. (2000) The Height Solution of European Vertical Reference Network (EUVN). In: Veröffentlichungen der Bayerischen Kommission für die internationale Erdmessung der Bayerischen Akademie der Wissenschaften, Heft Nr. 61, pp 132–145
19. Ihde J et al. (2002) The Concept of European Vertical GPS Reference Network (EUVN). In: Mitteilungen des Bundesamtes für Kartographie und Geodäsie, Band 25, pp 11–22

20. Luthardt J et al. (2002) Report on the Preprocessing and EUVN Data center. In: Mitteilungen des Bundesamtes für Kartographie und Geodäsie, Band 25, pp 47–51
21. Wöppelmann G et al. (2002) Report on EUVN tide gauge data collection and analysis. In: Mitteilungen des Bundesamtes für Kartographie und Geodäsie, Band 25, pp 71–80
22. Petroškevičius P et al. (1995) Observations According to International Project BSL GPS-93 (in Lithuanian). Geodesy and Cartography (Geodezija ir kartografija), No 1 (21), pp 57–62
23. Final Results of the Baltic Sea Level 1997 GPS Campaign. Research Works of the SSG 8.1 of the International Association of Geodesy. Reports of the Finnish Geodetic Institute, 99:4. Helsinki, 1999, 182 p.
24. Ihde, J et al. (2004) The Implementation of the ECGN Stations – Status of the 1st Call for Participation. EUREF Publication No. 14, Report on the Symposium of the IAG Subcommittee for Europe (EUREF) held in Bratislava, 2-5 June, 2004, pp 49–58
25. Nivellements und Höhenbestimmungen der Punkte erster und zweiter Ordnung. Berlin, 1870, 172 S.
26. Nivellements der trigonometrischen Abtheilung der Landesaufnahme. Band I-VIII. Berlin, 1883.
27. Die Nivellements-Ergebnisse der Trigonometrischen Abtheilung der Königl. Preussischen Landes-Aufnahme. Heft I. Provinz Ostpreussen. Berlin, 1896, 62 S.
28. A. Krikščiūnas. Catalogue of Lithuanian precise levelling altitudes (in Lithuanian). Kaunas, 1939, 89 p.

Determination of the Mean Sea Level at Algiers Harbour From the Tidal Data Analysis

M. HADDAD, H. ABDELLAOUI, N. AMRANE

National Institute of Cartography and Remote Sensing 123, Rue de Tripoli, BP 430, Hussein-Dey 16040 - Algiers, Algeria.

Abstract. The present study aims at defining a national sea level reference in Algeria and can be integrated in other oceanographic projects for determination of the mean sea level. Whatever the principle of measure is, a tide gauge is able to provide a local information on the height of the sea referred to the chosen reference.

The main points of this study are: the calibration of the data of the electronic tidal gauge with an automatic data acquisition system installed in Algiers harbour; the comparison of these data with the data acquired from the analogical tidal gauge installed on the same site; and the determination of the mean sea level using the harmonic analysis.

The exploitation of the data recorded with the electronic tide gauge of Algiers during a period of two years provide an estimate of the mean sea level and the harmonic components which can be also used for the prediction. The estimated mean sea level differs by a few centimeters of the actual value currently used which was determined in a "arbitrary" way.

Keywords. Electronic tide gauge, analogical tide gauge, calibration, mean sea level, harmonic analysis.

1 Introduction

During the last two decades, the measurements of the height of seas using tide gauges have given acceptable results along the coastal lines. These data are used to predict a tide from harmonic components, and on the other hand, to validate the global models of tide and the observations provided by altimetric satellites.

Being aware of the interest to establish tide gauge sites, in framework of its activities, the National Institute of Cartography and Remote Sensing is currently planning a project to install new tide gauges with automatic acquisition along the Algerian coast line. A newly national altimetric referential will replace the existing reference defined from the tidal meter of La Goulette (Tunisia).

In this paper, we present the analysis of the data from the electronic tide gauges of Algiers to determine the mean sea level which will serve as the reference point for the levelling network of Algeria.

2 Description of the electronic tide gauge of Algiers

The tide gauge for automatic data acquisition installed near the analogical tide gauge is a prototype conceived by Dr. Michel van Ruymbeke of the Royal Observatory of Belgium (ORB). This prototype records every minute the height of the sea as frequencies generated by a capacitive sensor.



Fig. 1 Tidal gauge site of Algiers sheltering the two tide gauges electronic (in the left) and analogical (in the right).

3 Tidal gauge data

The electronic tide gauge with automatic data acquisition was installed in may 2003 in Algiers harbour. Due to technical problems, the store times series started in may 2004.

This electronic tide gauge is installed close to an analogical one in order to compare the observations produced from both sources.

The data of the electronic tide gauge used in this study, are those collected during the period from March 29, 2004 to February 27, 2006 with a sampling rate of one minute.

A low pass filter was applied to the electronic tidal data with a cadence of 60 readings (equivalent to one hour observation) using the software μ DAS Grapher (ORB).

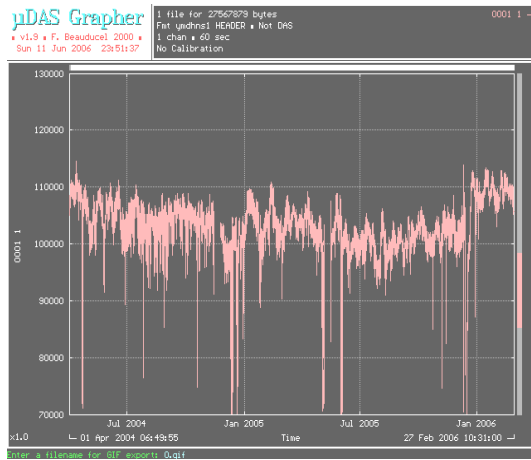


Fig. 2 Raw Recordings of the electronic tide gauge of Algiers, Period: March 29, 2004 to February 27, 2006.

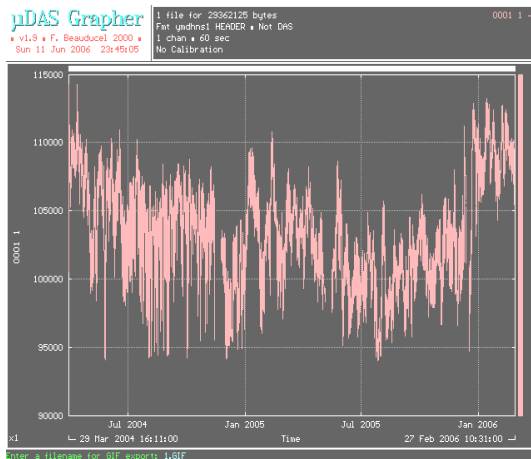


Fig. 3 Filtering of the data of the electronic tide gauge.

4 Calibration of the data automatic tide gauge

The direct measurements of the sea level using a luminous probe provided the calibration factors of the tide gauge. A linear model has been used:

$$h = a_0 + a_1 f \quad (1)$$

where a_0 and a_1 are calibration parameters, f the recorded frequency and h the height of sea observed referring to the reference of the hydrographic zero, deduced from the readings obtained by luminous probe.

The sea level referenced to the hydrographic zero is obtained by one of the following equations:

$$N_1 + N_3 - \text{height}_{\text{top of the tube - sea surface}} \quad (2)$$

$$N_2 + N_3 - \text{height}_{\text{plateforme - sea surface}} \quad (3)$$

where N_1 is the height of the top of the water stabilizer tube referring to the Algerian General Level, N_2 is the height of the plate-form referring to the Algerian General Level, N_3 is the altitude of the zero point of the AGL referring to the altitude of the

hydrographic zero which is fixed to 34 cm, and the $\text{height}_{\text{top of the tube - sea surface}}$, $\text{height}_{\text{plateforme - sea surface}}$ are the readings obtained by luminous probe.

The calibration parameters were calculated using this process for equivalent periods of one month.

5 Validation with the data of the analogical tide gauge

An external validation of the data of the electronic tide gauge measurements was carried out by comparing with the data from the analogical tide gauge measurements over the period of March 29 2004 to February 21 2005:

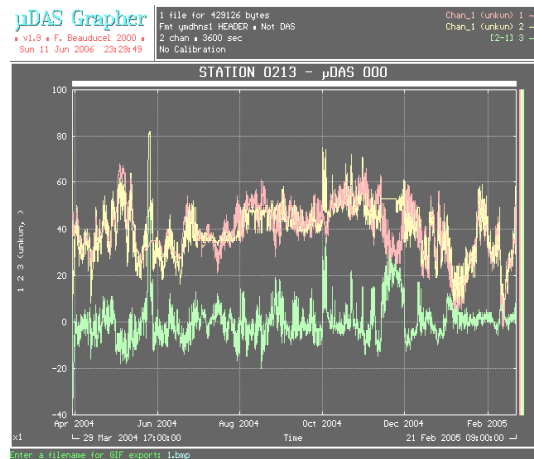


Fig. 4 Difference (in green) between the filtered and calibrated data of the electronic tide gauge (in yellow) and those stemming from the analogical tide gauge (in red). Period from March 29, 2004 till February 21, 2005.

The statistical results of this comparison are given in the following table:

Table 1. Comparison between data stemming from the electronic tide gauge and from the analogical tide gauge.

Tide gauge	Min. value (cm)	Max. value (cm)	Average (cm)	Standard deviation (cm)
Electronic	4	82	38.76	11.17
Analogical	-3	68	39.40	11.36
Difference	-37	49	0.0011	8.27

Both systems present a good agreement only where the luminous probe calibration data are available.

6 Tidal harmonic analysis

The tide can be considered as the summation of a series of periodic functions and an error (ε).

$$h(t) = Z_0 + \sum_i A_i \cos(V_i - G_i) + \varepsilon \quad (4)$$

In this expression, Z_0 is the mean level, A_i the amplitude, V_i the argument of the cosine in the harmonious development of the generative potential of the tide, and G_i the phase of the constituent i .

Z_0 , A_i and G_i are the harmonious constants in a given place.

The situation of a harmonic component of the tide represents its delay expressed in angle, regarding to the corresponding constituent of the potential (to obtain its delay expressed at time, it is enough to divide it by the angular speed dV_i/dt).

Only V_i depends on time. Its expression is generally done by astronomical elements.

7 Determination of the mean level

The preliminary determination of the mean level of the sea at Algiers harbour by the harmonic analysis is done using the T_TIDE version 1.2b package under Matlab [R. Pawlowicz, R. Beardsley, S Lentz].

Table 2. Obtained mean level and difference regarding to the current reference of Algerian General Level.

Tide gauge	Period	Mean level (cm)	Diff. / current reference (cm)
Analogical	29/03/2004 ----	39.8	5.8
	21/02/2005		
Electronic	29/03/2004 ----	39.1	5.1
	21/02/2005		
	29/03/2004 ----	38.1	4.1
	27/02/2006		

This table shows that the results of the mean level obtained from the data of the electronic and analogical tide gauges during the same period of March 29 2004 to February 21 2005 are close near (39.1 cm and 39.8 cm). This confirms the good preprocessing of electronic tide gauge measurements.

The mean level obtained from the data of the electronic tide gauge data of the period from March 29, 2004 to February 27, 2006, present an offset of 4.1 cm to the current reference.

The harmonic constants obtained from the series of the electronic tide gauge over of the period from March 29, 2004 to February 27, 2006, were also used for the prediction of the tide for the same period. The difference between the observed and predicted tides vary in an interval of ± 20 cm:

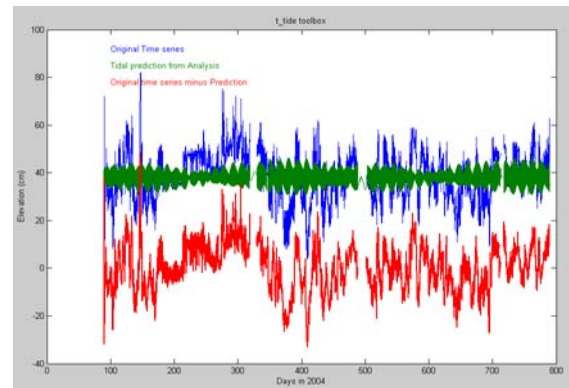


Fig. 5 Difference (in red) between the observed tide data (in blue) and the predicted tide data (in green).

9 Conclusion

The objective of this study was to determine the mean sea level at Algiers harbour using an electronic tide gauge. The calibration of data revealed the need of more frequent obtained calibration data using of the luminous probe or the ladder of tides.

The preliminary mean sea level obtained with the electronic tide gauge shows an offset of 4.1 cm compared to the mean sea level reference currently used.

Acknowledgments

We are grateful to the Hydrographic Service for the Naval Forces, to have placed at our disposal the data of the analogical tide gauge of Algiers.

References.

- G. Woppelmann, Rattachement géodésique des marégraphes dans un système de référence mondial par techniques de géodésie spatiale - Thèse de doctorat de l'Observatoire de Paris.
- Michel Van Ruymbeke, et al., Enregistrement par un marégraphe prototype, des variations de niveau de la mer à Alger durant le séisme du 21 mai 2003- Bulletin des Sciences Géographiques n°12, Octobre 2003. ISSN-1112-3745.
- M.G.G. Foreman, Manual for tidal heights- Analysis and prediction. Institute of Ocean Sciences, Patricia Bay Sidney, B.C.
- F. Beauducel, μ DAS Grapher Help File, 2000.

Airborne Scalar Gravimetry for Regional Gravity Field Mapping and Geoid Determination

A.V. Olesen, R. Forsberg

Danish National Space Center, Juliane Maries Vej 30, 2100 Copenhagen, Denmark

Abstract. Airborne gravity is capable of providing an accurate and bias-free extension of satellite gravity models and thus bridges the spectral gap between these models and the fine structure of the gravity field as mapped by the newest digital elevation models (SRTM). Airborne gravity is therefore an ideal base for regional gravity/geoid modeling. Airborne gravity may also be an efficient tool to validate existing datasets e.g. older marine surveys and is the only efficient way to cover the near coastal zone where altimetry derived gravity fails to deliver reliable data.

This paper describes some recent surveys undertaken by Danish National Space Center (DNSC) including both surveys over marine areas in the Arctic and the North Atlantic region and surveys over land covering all of Malaysia and Mongolia. The purpose has been to contribute to regional and global models (ArcGP and EGM2006), to provide geoid models for national height systems and reference surfaces for ocean current studies. The measurements were done with a LaCoste & Romberg marine/airborne gravimeter owned by the University of Bergen. This type of gravimeter has an excellent drift characteristic and can when the data are properly processed provide bias-free results also for airborne applications.

The main source for a bias in airborne data obtained with stabilized platform systems is the so-called tilt correction, which basically is a modeling of the platform orientation error. A new platform-response-modeling approach to account for this effect will be described. This approach seems to give virtual bias-free results.

1 Introduction

Today airborne gravimetry is a truly operational tool for gravity mapping and it offers a fast and economic coverage of large areas. One of the big advantages of airborne gravimetry is the uniform and seamless coverage of the near-coastal region, a region that so far is only poorly covered in many

areas of the world due to shallow water, which don't allow for marine measurements. Satellite altimetry derived models are in general not reliable near the coast (Andersen and Knudsen, 1998). This region is at the same time an area where one may want the most precise geoid due to the high population density and the economic interests related to infrastructure developments here. Also natural hazard management like flooding control and tsunami warning systems require a good coastal geoid determination in order to make use of fast and cheap GPS levelling instead of tedious and costly spirit levelling. Another advantage of airborne surveys is the ability to cover remote and otherwise inaccessible areas like mountains and jungles.

It is common practice to subject marine and airborne gravity profile data to an adjustment procedure that minimizes the misfit at the crossing points, either as a linear trend or a bias removal. It may be justified to do this to marine data, see LaFehr and Nettleton (1967) for a discussion, but for airborne data obtained with a long-term stable gravimeter like the LaCoste & Romberg meter and a proper reduction for motion induced effects there seems to be little physical justification for such an adjustment. The gravimeter is virtual drift-free during the short time span of a flight (Valliant, 1992), so bias or tilt problems in the data may indicate that the processing algorithm is less than optimal. The situation is different for systems utilizing sensors, which are known to drift, such as INS equipment (Glennie, 1999), but it doesn't make the crossover adjustment healthier. Any crossover adjustment will by nature distribute point errors at crossing points into along-track corrections, and thus provide a way for short-period random errors to leak into the longer wavelengths. Using a dense net of tie lines in the crossover adjustment will reduce this leaking, but it may be quite expensive especially for regional scale surveys.

Avoiding the need for crossover adjustment of the airborne track data therefore means that one can get away with much fewer tie lines than in a survey

that requires crossover adjustment since the tie lines now only serve as internal quality estimators (repeatability at line crossing points).

2 Tilt effect and biases. A new platform modeling approach

The effect of a tilting platform is both to make the gravimeter less sensitive in the vertical direction, and to make it sensitive to horizontal accelerations. The traditional approach to account for this effect leads to a correction term that is non-linear in the accelerations. The correction term can be found in Valliant (1992) or in Czombo (1994) and writes:

$$\delta g_{\text{tilt}} = \sqrt{f_x^2 + f_y^2 + f_z^2 - q_E^2 - q_N^2} - f_z \quad (1)$$

where f_k denotes accelerations measured by the gravimeters three accelerometers and q_k denotes horizontal kinematic accelerations derived from GPS. Valliant (1992) gives an approximate expression derived from equation (1) under the assumption that $f_z \cong g$ and $g \gg f_{x,y}$:

$$\delta g_{\text{tilt}} = \frac{f^2 - q^2}{2g} \quad (2)$$

where $f^2 = f_x^2 + f_y^2$ and $q^2 = q_E^2 + q_N^2$. The last equation is good in the sense that it highlights the problem with the tilt correction. It is basically a small difference between two potentially huge numbers. Furthermore, the two potentially huge numbers are derived by squaring discrete and very noisy measurements. In addition to that, the noise on the separate terms must be expected to have different signatures, so the noise on the squared terms is not likely to cancel out due to the subtraction. Such an approach will certainly cause problems, problems that cannot be filtered out by the final low pass filter, since the squaring will change the characteristics of the noise signal. A zero-mean noise will after the squaring have a

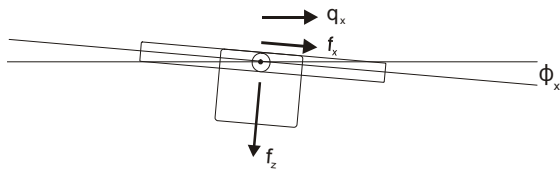


Figure 1. Tilting platform

positive mean value. In this way the tilt correction may become a way for zero-mean noise to bias the gravity estimates. Pre-filtering of the data before the tilt correction is derived may reduce the problem, but the optimal amount of filtering is somewhat ambiguous.

The tilt angles may alternatively be estimated from the combined gravimeter and GPS observations. For small tilt angles the following approximations hold for one axis, see also Figure 1:

$$f_x = q_x + \sin(\phi) \cdot f_z \approx q_x + \phi \cdot f_z \approx q_x + \phi \cdot g \quad (3)$$

or

$$\phi \approx \frac{f_x - q_x}{g} \quad (4)$$

It was shown in Olesen et al (1997) that the tilt angle has no spectral components above approximately 0.01 Hz. See also LaCoste 1967 for a thorough discussion of the spectral behavior of the LaCoste & Romberg marine gravimeter's stabilized platform. With this knowledge the tilt angles can be well modeled and filtered. High frequency noise in the tilt angle estimation can be effectively removed with a low-pass filter that matches the platform period. This leads to the computation of the tilt correction being split into two parts, (i) the modeling of a physical system with known properties (the stabilized platform) and (ii) the correction for tilt computed as a linear combination of three acceleration components:

$$\delta g_{\text{tilt}} = (1 - \cos(\phi_x) \cdot \cos(\phi_y)) \cdot f_z + \sin(\phi_x) \cdot f_x + \sin(\phi_y) \cdot \cos(\phi_x) \cdot f_y \quad (5)$$

This implies, that zero-mean noise on the acceleration estimates will propagate unbiased as zero-mean noise into the tilt correction and will therefore not induce any bias into the gravity estimates.

Table 1 shows the performance of the two different tilt correction algorithms. Two tracks from the Greenland 2001 survey are analyzed, where one track was flown under turbulent conditions and the other was flown under smooth conditions. It is seen that the two algorithms yield the same results when no filtering is applied. This should not surprise, since the two methods are identical in that case. The table shows a dramatic change in mean value when filters are applied, especially for the dynamic flight,

from 13.3 mGal to -2.1 mGal for the traditional approach, when a 1 seconds filter is applied before calculating the correction. Further filtering is seen to change the mean value several mGal, when we still look at the traditional approach. This shows that the tilt correction can add severe biases to our data, as it is unclear which amount of filtering is optimal. Moreover, the optimal filter length may change due to the dynamics of the flights. The modeling approach, on the other hand, is seen to be much less filter-sensitive for realistic filter lengths. Besides, the optimal filter length is more or less given from the platform natural period (Olesen 2003). A filter around 60 to 80 seconds should be adequate.

Table 1: Comparison of the two different tilt correction algorithms

Traditional approach				
Pre-filter	Quiet flight		Dynamic flight	
	Mean	St dv	Mean	St dv
0 sec	0.32	1.49	13.26	8.42
1 sec	-0.46	0.97	-2.09	4.29
2 sec	-0.76	0.91	-3.87	3.92
3 sec	-0.88	0.89	-3.98	3.75
5 sec	-0.92	0.86	-3.64	3.47
10 sec	-0.87	0.77	-2.82	2.81
20 sec	-0.77	0.61	-1.84	1.83

Modeling approach				
Platform filter	Quiet flight		Dynamic flight	
	Mean	St dv	Mean	St dv
0 sec	0.34	1.48	13.30	8.42
20 sec	-1.01	0.93	-5.46	4.06
40 sec	-1.02	0.93	-4.48	4.01
60 sec	-0.99	0.95	-4.26	4.18
80 sec	-0.98	0.95	-4.18	4.37
100 sec	-0.98	0.95	-4.03	4.32
120 sec	-0.97	0.95	-3.79	4.20

The standard deviation of the tilt correction in Table 1 shows somewhat the same dependency on filter length as does the mean value. But, the mean value is the main concern for us, as the data are intended for geodetic use. The modeling algorithm described in this section is a more sound way to establish the correction for platform errors, than is the traditional

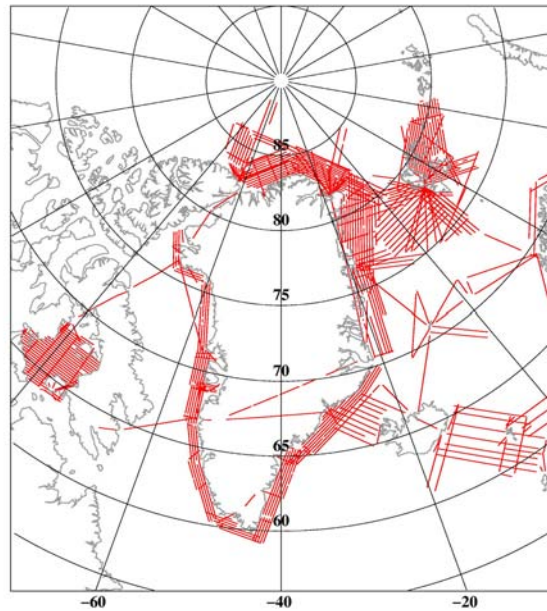


Figure 2. Arctic surveys between 1998 and 2003

algorithm. The modeling approach incorporates the known physical properties of the platform system in its algorithm in contrast to the traditional approach.

3 The Arctic surveys

Geodynamics Department at Danish National Space Center has since 1998 gathered approximately 150,000 line km of airborne gravity data in the arctic region. The surveys constitute a seawards extension of the helicopter-based conventional gravity campaigns along the Greenland coast, see Forsberg et al (1998) and Forsberg and Rubek (1998). The surveys around Greenland have mainly been funded by US National Geospatial-Intelligence Agency as part of the Arctic Gravity Project, see <http://earth-info.nga.mil/GandG/wgs84/agp/>.

To the north, in the Polar Sea, the operations were coordinated with the surveys performed by US Naval Research Laboratory (Brozena 1991, Childers et al 2001). Surveys around Svalbard were done in cooperation with and partly funded by Statens Kartverk, Norway. The survey over Foxe Basin, Canada, was done under contract to Geodetic Survey Canada.

The survey stretching from Greenland's East coast via Iceland to Scotland and Norway was done within the frame of the GOCINA project (Geoid and Ocean Circulation in the North Atlantic). The aim was to provide a Mean Dynamic Topography

model (MDT) for the area in question. The MDT would be based on a Mean Sea Surface (MSS) from satellite altimetry and a gravimetric geoid (Knudsen et al 2004). The airborne gravity data provided the constraints needed to do a healthy bias adjustment of the existing gravity data in the area before computation of the geoid. The inclusion of the airborne data had significantly effect especially along the Greenland coast where other reliable data sources are sparse.

Statistics from crossover analyses of the datasets are shown in Table 2. For all years the RMS crossover misfit was 2.5 mGal indicating a 1.8 mGal noise level on the individual tracks (2.5 mGal divided by $\sqrt{2}$ based on the assumption that the noise is uncorrelated from track to track). The results seem to be pretty constant from year to year only the year 1998 stands out with a 1.8 mGal RMS crossover error, that fits nicely with the fact that the 1998 survey was over the frozen Polar Sea with very smooth flight conditions. The 1.8 mGal misfit indicates a 1.3 mGal noise on the track data.

Table 2: Crossover error statistics for the Arctic surveys (units: mGal)

Data set	Number of cross	RMS misfit
1998	86	1.8
1999	74	2.5
2000	96	2.8
2001	66	2.6
2002	101	2.6
2003	46	2.1
All years	670	2.5

Comparison to surface data is very consistent with the noise estimates from crossover analysis, 2.5 mGal when comparing to a high quality marine data set from NUNAOIL, the national oil company of Greenland. These marine data are scattered along most of the Greenland east and west coast and are believed to be accurate at the 1 mGal level or better (Strykowski and Forsberg, 1995). The comparison to ice surface data over the Polar Sea gave a 1.3 mGal agreement, exactly the same number as the internal noise estimate from the 1998 dataset. In both cases the surface data was compared directly with the airborne free air anomalies, no upward or downward continuation was performed to the data. The airborne surveys were flown at an altitude of 80 to 200 meters so the attenuation due to upward continuation is marginal. This is especially true over the ocean where the gravity anomaly sources

are located below the surface. The good agreement between internal and external error estimates indicates that there are only little internal bias problems left in the airborne datasets. Applying a bias adjustment to the airborne dataset will of course lower the crossover misfit but the derived error estimates will be too optimistic and will no longer reflect the real noise level. Table 3 also shows that mean differences between airborne and surface data as well as global models are at the sub-mGal level suggesting that the mean value and the longer wavelengths in the airborne datasets are very precisely determined.

Table 3: Comparison to surface data within 1 km and to global models (units: mGal)

Data set	Number of points	Mean diff.	Standard deviation
NUNAOIL marine data	1178	0.1	2.5
Canadian sea ice data	12	0.4	1.3
GGM01C	NA	0.2	23.2
EIGEN-GRACE02S	NA	-0.3	24.6

4 The Malaysian and the Mongolian surveys

Geodynamics Department from National Survey and Cadastre-Denmark (now with Danish National Space Center) was asked by the Department of Surveying and Mapping Malaysia (JUPEM) to perform a nationwide airborne gravity survey. This as part of an ambitious plan to establish a modern GPS based height system integrating a precise geoid model and a real time kinematic GPS positioning system. This would allow the GPS user to get precise heights above sea level at the 'push of a button' everywhere in the country.

The airborne survey covered approximately 500,000 km² at a 5 km line spacing, see . It was flown between September 2002 and May 2003, a total of 530 hours airborne time. Tropical conditions with high temperatures and humidity causing unstable weather to build up almost every day together with a rather mountainous terrain peaking at more than 4000 meters makes it a challenging task to do airborne gravimetry here. Time constraints forcing us to fly almost every day no matter the weather conditions added to the challenge of getting quality data out of our efforts.

The crossover analysis in Table 4 should be seen in this light; 2.6 mGal RMS difference from almost 2000 line crossing points indicating a noise level around 1.8 mGal. This is to our opinion a very satisfactory result and demonstrates that airborne gravimetry is truly operational for regional gravity field mapping also under diverse and difficult conditions like in Malaysia.

Table 4: Crossover error statistics for the Malaysian and the Mongolian surveys (units: mGal)

Data set	Number of cross	RMS misfit
Malaysia	1965	2.6
Mongolia	504	3.1

Table 5: Airborne gravimetric geoid compared to global models (units: meters)

Global model	Standard dev. of difference
GGM02S to 160	1.11
EGM96 to 360	1.08
EIGEN-CG03 to 360	0.57

It was also the task of Geodynamics Department to compute a best possible geoid model based on the airborne data in combination with some terrestrial data, GRACE based geo-potentials models and the SRTM digital elevation model (Shuttle Radar Topography Mission, see <http://srtm.usgs.gov>). Table 5 shows the final geoid model compared to different global models over Sabah province in

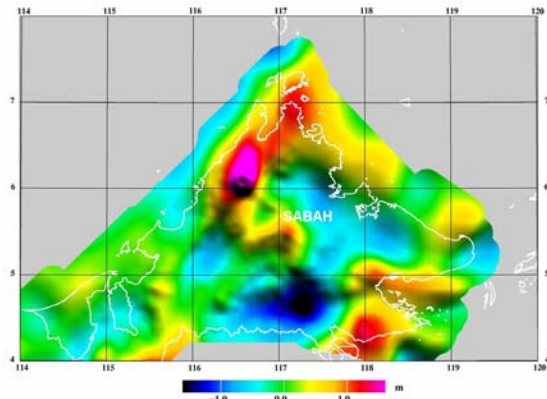


Figure 3. Difference between airborne geoid and the EIGEN-CG03 global model to degree 360

Eastern Malaysia (Malaysian part of Borneo Island). The residual is at the meter level for most models and even for the newest high-resolution model the EIGEN-CG03 to degree 360 the residual signal is 57 cm. This residual is due to shortcomings in the global models and underlines the need to collect more gravity data in many areas in order to produce geoid models of a quality suitable for GPS leveling. 5 centimeter precision or better is a typical requirement. The difference between the airborne geoid and the EIGEN-CG03 geoid is also portrayed in Figure 3 and it is seen that also in the important near coastal zone the global model has significant problems. This will be the

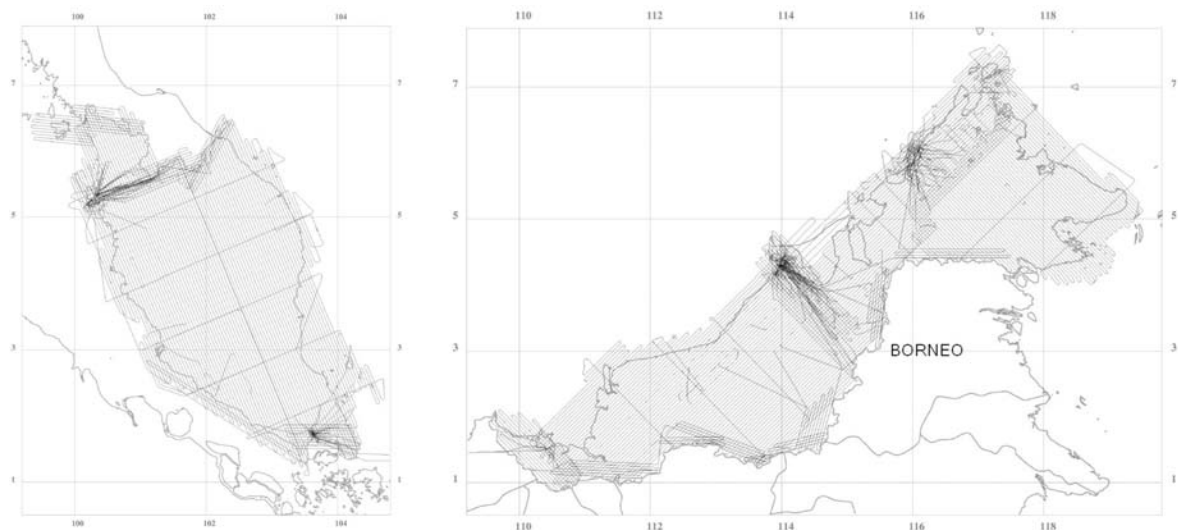


Figure 4. Ground track pattern for the Malaysia survey. The Peninsula or Western Malaysia to the left and Malaysian Borneo to the right. Flight lines could be extended over Thai and Brunei territory whereas it was not possible to get permission to enter into Indonesian or Singaporean airspace. A total of 530 hours were flown during the months of October to November 2002 and February to May 2003. Flight lines were in general planned to follow main topographic features, e.g. along a mountain ridge instead of crossing it in order to reduce the number of climbs or descents. The location of suitable airports also played a major role for the overall track layout

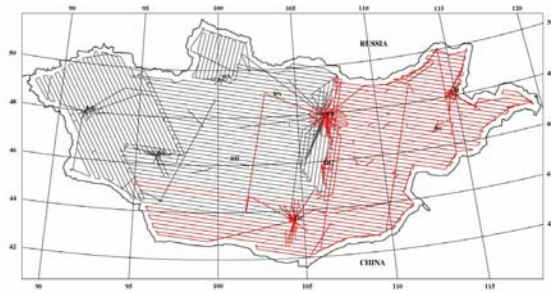


Figure 5. Ground track pattern for the Mongolian survey. The distance from east to west is approximately 2600 km. 2004 (black), 2005(red)

case in many other areas around the world and airborne gravimetry offers a fast and economic way of collecting new gravity data to supplement existing surface data and global models.

The Mongolian survey was done in the autumn months of 2004 and 2005 as this period is the most stable with mainly clear sky and not too much wind. The survey covered all of Mongolia, 1.6 million square kilometers, at a 10 nautical miles line spacing. Only a 25 km no-fly zone along the border to neighboring Russia and China was omitted. The project was a joint effort between Mongolian Administration of Land Affairs (ALaGAC), US National Geospatial-Intelligence Agency (NGA) and Danish National Space Center (DNSC). The aim was to establish a modern GPS based height system for Mongolia and to make a contribution to the soon-to-be-released geo-potential model EGM06. NGA provided the funding for the survey and DNSC was responsible for the airborne survey in cooperation with local partners. The slightly higher noise level for the Mongolian data compared to the Malaysian survey is ascribed to the different aircraft used for the two surveys and to the presence of mountain waves in Mongolia. Mountain waves are a wind generated and relatively long-wave motion of the air in mountainous areas.

Conclusion

Airborne gravimetry with a LaCoste & Romberg airborne/marine gravimeter has over the years proved to be a very reliable concept for acquiring quality gravity data for various geodetic applications. The survey in Malaysia showed that the method is also applicable under demanding conditions like in tropical and mountainous areas.

The new platform modeling approach to correct for platform off-level errors seems to yield virtual bias free data and thus eliminates the need for a bias

crossover adjustment of the data. It also means that single or coarse distributed lines can be utilized to validate existing data sets, e.g. old marine data sets.

References

- Andersen O. B. and P. Knudsen: Global Marine Gravity Field from the ERS-1 and GEOSAT Geodetic Mission Altimetry, *J. Geophys. Res.*, **103(C4)**, 8129-8137, 1998.
- Brozena, J. M.: The Greenland Aerogeophysics Project: Airborne gravity, topographic and magnetic mapping of an entire continent. In: *From Mars to Greenland: Charting Gravity With Space and Airborne Instruments*. IAG symposium series 110, pp. 203-214, Springer Verlag, 1991.
- Childers, V. A., D. C. McAdoo, J. M. Brozena, S. W. Laxon: New gravity data in the Arctic Ocean: Comparison of airborne and ERS of gravity. *Journal of Geophysical Research*, vol. 106, B5, pp 8871-8886, 2001.
- Czompo, J.: Airborne Scalar Gravimetry System Errors in the Spectral Domain. *Ph. D. Thesis, UCGE No 20067, Department of Geomatics Engineering, The University of Calgary, Canada, 1994.*
- Forsberg, R., A. V. Olesen and K. Keller: Airborne Gravity Survey of the North Greenland Shelf 1998. *Kort - og Matrikelstyrelsen Technical Report no. 10, 1999.*
- Forsberg, R. and F. Rubek: Gravity and GPS measurements in Greenland 1997. *Survey and data processing report, Office of Geodynamics, National Survey and Cadastre (KMS), Denmark, 1998.*
- Glennie, C.: An Analysis of Airborne Gravity by Strapdown INS/DGPS. *Ph.D. Thesis, UCGE Report #20, Dept. of Geomatics Engineering, The University of Calgary, 1999*
- Knudsen P., R. Forsberg, O. Andersen, D. Solheim, R. Hipkin, K. Haines, J. Johannessen & F. Hernandez. The GOCINA Project - An Overview and Status. *Proc. Second International GOCE User Workshop "GOCE, The Geoid and Oceanography"*, ESA-ESRIN, March 2004, ESA SP-569, June 2004.
- LaCoste, L. B. J.: Measurement of Gravity at Sea and in the Air. *Reviews of Geophysics*, 5, 477-526, 1967.
- LaFehr, T.R. and L.L. Nettleton: Quantitative evaluation of a stabilized platform shipboard gravity meter, *Geophysics*, 32, 110-118, 1967.
- Olesen A. V., R. Forsberg, A. Gidskehaug: Airborne gravimetry using the LaCoste & Romberg gravimeter – an error analysis. In: M.E. Cannon and G. Lachapelle (eds.). *Proc. Int. Symp. on Kinematic Systems in Geodesy, Geomatics and Navigation*, Banff, Canada, June 3-6, 1997, Publ.Univ. of Calgary, pp. 613-618, 1997
- Olesen, A.V: Improved Airborne Scalar Gravimetry for Regional Gravity Field Mapping and Geoid Determination.. *Technical Report no 24, Kort og Matrikelstyrelsen., Copenhagen 2003.*
- Strykowski, G. and R. Forsberg: Processing of marine gravity measurements off East Greenland: *Contract report for NUNAOIL A/S. Geodetic Division, National Survey and Cadastre of Denmark, 1995.*
- Valliant, H.: The LaCoste & Romberg air/sea gravimeter: an overview. In: *CRC Handbook of Geophysical Exploration at Sea*, Boca Raton Press, 1992.

LSQR based Geopotential Recovery

O. Baur

Institute of Geodesy,

Universität Stuttgart, Geschwister-Scholl-Str. 24D, 70174 Stuttgart, Germany

J. Kusche

DEOS,

Delft University of Technology, Kluyverweg 1, 2629HS Delft, The Netherlands

Abstract. In the context of present and forthcoming geoscientific satellite missions, numerical solution strategies for large and ill-conditioned linear systems of equations as occurring in geopotential recovery are of great interest. Due to the character of the inverse problem, i.e. to solve a highly overdetermined problem, least squares procedures are usually adopted. To meet the arising challenge from the computational point of view, an iterative algorithm based on bidiagonalization and QR decomposition, referred to as LSQR, is presented. Moreover, in terms of LSQR tuning, an adoption and extension of the original algorithm for its use in satellite geodesy was realized. In particular, regularization and preconditioning is addressed. The LSQR algorithm is applied to a simulated GOCE (Gravity field and Ocean Circulation Explorer) data set. Its parallel implementation on a (shared memory) supercomputing platform results in a highly effective tool for solving least squares problems.

Keywords. LSQR, Satellite Gravity Gradiometry, GOCE, High Performance Computing

1 Introduction

In satellite geodesy the estimation of the geopotential, i.e. the unknown coefficients of its harmonic series expansion, based on observation data from space is of major interest. However, solving for the unknowns in a brute force manner by normal matrix inversion requires an immense core memory, which exceeds by far the limit of most common computation platforms. Therefore, the use of LSQR as an effective and robust tool to manage this task in an iterative manner is proposed. Disregarding runtime, the method can be accomplished on an ordinary personal computer.

The LSQR algorithm itself was originally introduced by Paige and Saunders in 1973 and pu-

blished in detail at the beginning of the 1980s (Paige and Saunders, 1982a,b). The procedure is a Krylov subspace based iterative method, such as the conjugate gradients (CG) methods (Hestenes and Stiefel, 1952). Both solve linear systems of equations by means of successive approximations. Whereas the LSQR method is frequently applied in geophysics, it has found only little resonance in geodetic applications. Actually, least squares (LS) problems in geodesy are mostly treated by CG methods, leading to the CGLS procedure. Application of CGLS in terms of satellite based gravity field recovery can be found in e.g. Schuh (1996), Pail and Plank (2002) and Ditmar et al. (2003). Geodetic problems are treated with LSQR in e.g. Kusche and Mayer-Gürr (2001) and Baur and Austen (submitted). The LSQR and the CGLS method share approximately the same storage and work requirement demands. Furthermore, they generate mathematically the same sequences of approximations to the real solution. But concerning stability of the iterative progress, CGLS is shown to be outperformed by LSQR. This holds predominantly for ill-conditioned problems (Paige and Saunders, 1982a; Björck, 1996; Jacobsen et al., 2003).

The basic LSQR algorithm according to Paige and Saunders is presented in the next section. If regularization plays a role, the method is very suitable, since various regularization scenarios can be evaluated at the same time with marginal extra computational costs. This aspect is addressed in Sect. 3. Moreover, to improve the speed of convergence preconditioning is implemented as outlined in Sect. 4. Section 5 deals with the tailored parallelization of the algorithm using the OpenMP programming environment. This is done against the background of the forthcoming GOCE satellite mission as demonstrated in Sect. 6. Finally, Sect. 7 summarizes the conclusions of this contribution.

2 The LSQR Method

Figure 1 presents the principle of the iterative LSQR solver. The equation $\mathbf{Ax} = \mathbf{y} + \mathbf{e}$ constitutes an arbitrary linear (or linearized) system of equations with the vector of observations \mathbf{y} , vector of unknown parameters \mathbf{x} and the design matrix \mathbf{A} describing the functional model between them. In LS applications the number of observations n is much larger than the number of the unknown parameters u yielding an overdetermined system. Solving it by means of a standard Gauß-Markov model (L_2 -norm minimization of the residual vector \mathbf{e}) is equivalent to (Koch, 1999)

$$\min_{\mathbf{x}} \|\mathbf{e}\|^2 = \min_{\mathbf{x}} \|\mathbf{Ax} - \mathbf{y}\|_{\Sigma^{-1}}^2. \quad (1)$$

To simplify matters, decorrelated observations (white noise) with uniform level of accuracy are assumed. Thus, $D\{\mathbf{y}\} = \Sigma = \sigma^2 \mathbf{I}$ holds. Bidiagonalization (Golub and Kahan, 1965; Paige and Saunders, 1982a) transforms the original minimization problem to a much simpler one by the decomposition of the design matrix \mathbf{A} in two orthogonal matrices, \mathbf{U}_{k+1} (dimension $n \times (k+1)$) and \mathbf{V}_k ($u \times k$), and a lower bidiagonal matrix \mathbf{B}_k ($(k+1) \times k$). Thus, $\mathbf{A} \approx \mathbf{A}_k = \mathbf{U}_{k+1} \mathbf{B}_k \mathbf{V}_k^T$ holds. For each iteration step k the dimension of the matrices is enlarged by one. For $k = u$ iterations the matrix \mathbf{A} is fully decomposed ($\mathbf{A}_{k=u} = \mathbf{A}$). However, in practical applications $k \ll u$ iterations approximate the exact solution sufficiently, i.e. the iterative process can be truncated at an early stage. Both the vectors $(\mathbf{u}_1, \dots, \mathbf{u}_k)$ and $(\mathbf{v}_1, \dots, \mathbf{v}_k)$ form an orthogonal base of two Krylov subspaces, cf. e.g. Björck (1996). By a set of Givens rotations the bidiagonal matrix \mathbf{B}_k is decomposed in an orthogonal matrix \mathbf{Q}_k and an upper triangular matrix \mathbf{R}_k . The Givens transformation is a special kind of a counter clockwise rotation. Technically, it is chosen such that the successive execution per iteration equals a diagonalization process of matrix \mathbf{B}_k , i.e. the non-zero secondary diagonal elements vanish. Thus, the orthogonal matrix \mathbf{Q}_k is composed of the products of the Givens rotation matrices. Finally, this leads to

$$\hat{\mathbf{a}}_k = \mathbf{R}_k^{-1} \mathbf{Q}_k (\beta_1 \mathbf{e}_1) \quad (2)$$

for solving the bidiagonal minimization subproblem. Therein, $\beta_1 = \|\mathbf{y}\|$ denotes the norm of the observation vector \mathbf{y} and \mathbf{e}_1 is the first column of a unit matrix of appropriate size. For

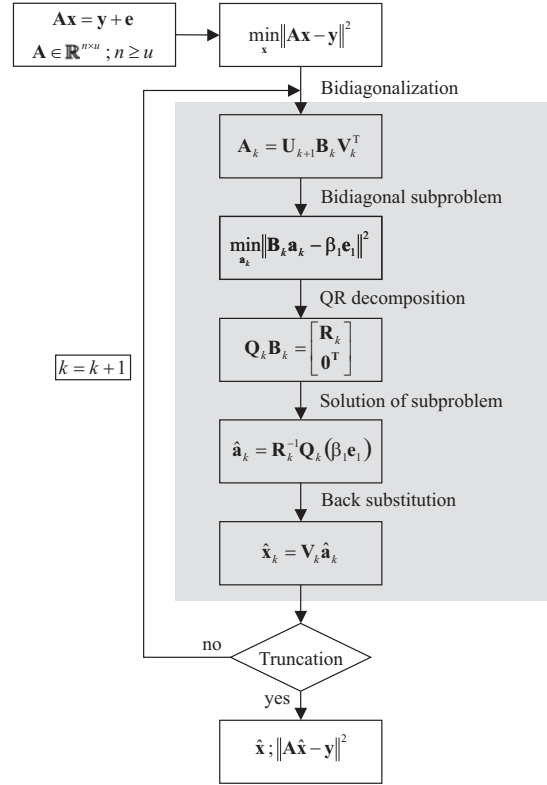


Figure 1: Flowchart of the LSQR method

the original vector of unknown parameters $\mathbf{x}_k \in \mathcal{K}_k(\mathbf{A}^T \mathbf{A}, \mathbf{A}^T \mathbf{y})$ holds, i.e. the approximate solution \mathbf{x}_k is embedded in the Krylov subspace spanned by the vectors $(\mathbf{v}_1, \dots, \mathbf{v}_k)$. Therefore, $\hat{\mathbf{x}}_k$ can be represented as a linear combination of these base vectors. The vector $\hat{\mathbf{a}}_k$ assembles the coefficients of that linear combination. The iterative process for solving the unknown parameters is terminated if the k^{th} iteration is meeting some truncation criterion. Pseudocode 1 presents a method for Givens rotation implementation. Pseudocode 2 illustrates the LSQR process step by step.

Pseudocode 1: Givens rotation

$[c, s, \rho] = \text{givrot}(\bar{\rho}, \beta)$

if $\beta = 0.0$

a. $c = 1.0, s = 0.0, \rho = \bar{\rho}$

else if $|\beta| > |\bar{\rho}|$

a. $t = \bar{\rho}/\beta, q = \sqrt{1.0 + t^2}$

b. $s = 1.0/q, c = ts, \rho = q\beta$

else

a. $t = \beta/\bar{\rho}, q = \sqrt{1.0 + t^2}$

b. $c = 1.0/q, s = tc, \rho = q\bar{\rho}$

Pseudocode 2: The LSQR method to solve $\min \|\mathbf{e}\|^2 = \min_{\mathbf{x}} \|\mathbf{A}\mathbf{x} - \mathbf{y}\|^2$

Initialization

1. $\beta_1 \mathbf{u}_1 = \mathbf{y}$
2. $\alpha_1 \mathbf{v}_1 = \mathbf{A}^T \mathbf{u}_1$
3. $\alpha_1 = \frac{\alpha_1}{\beta_1}$
4. $\bar{\phi}_1 = \beta_1$
5. $\bar{\rho}_1 = \alpha_1$

First iteration: $k = 1$

6. $\beta_2 \mathbf{u}_2 = \mathbf{A} \mathbf{v}_1 - \alpha_1 \mathbf{u}_1$
7. $\mathbf{h}_1 = \mathbf{A}^T \beta_2 \mathbf{u}_2$
8. $[c_1, s_1, \rho_1] = \text{givrot}(\bar{\rho}_1, \beta_2)$
9. $\phi_1 = c_1 \bar{\phi}_1$
10. $\bar{\phi}_2 = -s_1 \bar{\phi}_1$
11. $\mathbf{q}_1 = \frac{1}{\rho_1} \mathbf{v}_1$
12. $\mathbf{x}_1 = \phi_1 \mathbf{q}_1$
13. $\alpha_2 \mathbf{v}_2 = \mathbf{h}_1 - \beta_2^2 \mathbf{v}_1$
14. $\alpha_2 = \frac{\alpha_2}{\beta_2}$

Further iterations: for $k = 2 : u$

15. $\beta_{k+1} \mathbf{u}_{k+1} = \mathbf{A} \mathbf{v}_k - \alpha_k \mathbf{u}_k$
16. $\mathbf{h}_k = \mathbf{A}^T \beta_{k+1} \mathbf{u}_{k+1}$
17. $\theta_{k-1} = s_{k-1} \alpha_k$
18. $\bar{\rho}_k = c_{k-1} \alpha_k$
19. $[c_k, s_k, \rho_k] = \text{givrot}(\bar{\rho}_k, \beta_{k+1})$
20. $\phi_k = c_k \bar{\phi}_k$
21. $\bar{\phi}_{k+1} = -s_k \bar{\phi}_k$
22. $\mathbf{q}_k = \frac{1}{\rho_k} (\mathbf{v}_k - \theta_{k-1} \mathbf{q}_{k-1})$
23. $\mathbf{x}_k = \mathbf{x}_{k-1} + \phi_k \mathbf{q}_k$
24. $\alpha_{k+1} \mathbf{v}_{k+1} = \mathbf{h}_k - \beta_{k+1}^2 \mathbf{v}_k$
25. $\alpha_{k+1} = \frac{\alpha_{k+1}}{\beta_{k+1}}$

3 Regularization

Regularization is a commonly used tool to overcome the instability of ill-posed inversion problems. Here we exclusively focus on Tikhonov regularization (Tikhonov, 1963) which has been proven to perform very well for satellite geodetic applications, cf. e.g. Kusche and Klees (2002). Extending the original formulation in terms of the auxiliary condition of minimizing the functional $\min_{\mathbf{x}} \|\mathbf{x}\|_{\mathbf{K}}^2$ the regularized LSQR minimization problem reads

$$\min_{\mathbf{x}} \{ \|\mathbf{A}\mathbf{x} - \mathbf{y}\|^2 + \kappa \|\mathbf{x}\|_{\mathbf{K}}^2 \} \quad (3)$$

with the regularization parameter κ and the regularization matrix \mathbf{K} . For $\mathbf{K} = \mathbf{I}$, equation (3) is known as regularization in standard form (Hanke and Hansen, 1993). Since the optimal regularization parameter κ_{opt} is usually not known a priori, it is advantageous to solve the linear least squares problem (3) for multiple regularization parameters κ_i , $i = 1, \dots, i_{\text{max}}$. The optimal

one is finally chosen according to some quality criterion of the estimate $\hat{\mathbf{x}}_{\kappa_i}$, cf. e.g. Hanke and Hansen (1993), Kilmer and O’Leary (2001), Kusche and Klees (2002), Koch and Kusche (2002).

Regularization yields the subproblem matrix \mathbf{B}_{k,κ_i} to get tridiagonal structure. Thus, only the QR decomposition is affected by the additional constraint but not the bidiagonalization respectively tridiagonalization process itself. That means, the additional computational effort is manifested in i_{max} additional Givens rotation for each iteration which is marginal even for a large number of regularization parameters. This is one of the major advantages of the LSQR method compared to alternative iterative solvers.

For regularization with matrix $\mathbf{K} \neq \mathbf{I}$, called regularization in general form, it is convenient to transform the extended minimization problem (3) to standard form. This is achieved by Cholesky factorization of the symmetric and quadratic matrix \mathbf{K} with $\mathbf{K} = \mathbf{L}_{\mathbf{K}}^T \mathbf{L}_{\mathbf{K}}$ yielding

$$\min_{\mathbf{c}} \{ \|\mathbf{A}_{\mathbf{K}} \mathbf{c} - \mathbf{y}\|^2 + \kappa \|\mathbf{c}\|_{\mathbf{I}}^2 \}. \quad (4)$$

Therein, the substitutions $\mathbf{A}_{\mathbf{K}} = \mathbf{A} \mathbf{L}_{\mathbf{K}}^{-1}$ and $\mathbf{c} = \mathbf{L}_{\mathbf{K}} \mathbf{x}$ hold. The properties of (3) solving for \mathbf{x} hold for (4) when solving for \mathbf{c} . The estimate of the original parameter vector is obtained by back substitution, i.e. $\hat{\mathbf{x}}_{\kappa} = \mathbf{L}_{\mathbf{K}}^{-1} \hat{\mathbf{c}}_{\kappa}$. Note that for practical problems related to spherical harmonic analysis \mathbf{K} is diagonal. In the following, the regularized version of LSQR is denoted as R-LSQR.

According to Table 1, multiple regularization parameter treatment has no significant effect on the overall runtime. However, to find the “best” one amongst the a priori values, some quality criterion has to be evaluated for each of them (the corresponding runtime is neglected in Table 1). The increase of total wall time considering 100 regularization parameters opposite to the unregularized version is less than 1 %.

Table 1: Runtime results R-LSQR (Spectral resolution $L = 200$, $n = 518\,400$, 8 CPUs, 1 iteration).

# param.	wall time (s)	wall time (%)
no regul.	242.7	100.0
1	242.7	100.0
10	243.6	100.4
100	244.9	100.9

4 Preconditioning

The convergence behavior of an iterative solver is predominantly determined by the condition number of the normal matrix. Preconditioning is applied to improve the condition of the normal equation system and thus to increase the speed of convergence of the iterative solver. In order to outline the methodology of preconditioning on the level of the design matrix we shortly review preconditioning on the level of the normal matrix as presented in Baur and Austen (submitted).

Starting from the linear minimization model (1) the corresponding normal equation system reads $\mathbf{A}^T \mathbf{A} \mathbf{x} = \mathbf{A}^T \mathbf{y}$, respectively $\mathbf{N} \mathbf{x} = \mathbf{b}$. Inserting the identity matrix $\mathbf{I} = \mathbf{N}_{\text{bd}}^{-1} \mathbf{N}_{\text{bd}}$ in between the normal matrix \mathbf{N} and the parameter vector \mathbf{x} leads to

$$\mathbf{N} \mathbf{N}_{\text{bd}}^{-1} \mathbf{N}_{\text{bd}} \hat{\mathbf{x}} = \mathbf{b}. \quad (5)$$

Finally, the substitutions $\mathbf{N}^* = \mathbf{N} \mathbf{N}_{\text{bd}}^{-1}$ and $\hat{\mathbf{x}}^* = \mathbf{N}_{\text{bd}} \hat{\mathbf{x}}$ transform (5) into

$$\mathbf{N}^* \hat{\mathbf{x}}^* = \mathbf{b}. \quad (6)$$

Therein, \mathbf{N}_{bd} denotes the block-diagonal approximation of the true normal matrix \mathbf{N} . Setup, inversion and storage is efficiently achieved block-wise. When assuming $\mathbf{N}_{\text{bd}} \approx \mathbf{N}$, the product $\mathbf{N} \mathbf{N}_{\text{bd}}^{-1}$ is close to identity and thus the condition of the system improves considerably. However, solving (6) by means of LSQR requires design matrix assembly twice per iteration. This is a significant drawback of the method, since the setup of \mathbf{A} is the most time consuming part of the solver.

Design matrix preconditioning avoids this problem. An adequate preconditioner can be calculated by Cholesky decomposition of the block-diagonal normal matrix approximation

$$\mathbf{N}_{\text{bd}} = \mathbf{L}_{\mathbf{N}}^T \mathbf{L}_{\mathbf{N}}. \quad (7)$$

Analogously to (5), inserting $\mathbf{I} = \mathbf{L}_{\mathbf{N}}^{-1} \mathbf{L}_{\mathbf{N}}$ in the original formulation, together with the substitutions $\mathbf{A}_{\mathbf{N}} = \mathbf{A} \mathbf{L}_{\mathbf{N}}^{-1}$ and $\mathbf{z} = \mathbf{L}_{\mathbf{N}} \mathbf{x}$ finally yields

$$\mathbf{A}_{\mathbf{N}} \mathbf{z} = \mathbf{y} + \mathbf{e}. \quad (8)$$

Accordingly, $\mathbf{A}_{\mathbf{N}}$ and \mathbf{y} enter the LSQR procedure to solve the overdetermined problem (8). The initial vector of unknowns is computed from

$$\hat{\mathbf{x}} = \mathbf{L}_{\mathbf{N}}^{-1} \hat{\mathbf{z}}. \quad (9)$$

Here, the design matrix preconditioned version of LSQR is referred to as PCA-LSQR.

5 Parallel Implementation

Due to the character of the LSQR method, matrix-matrix and matrix-vector multiplications are avoided by means of repeated vector-vector operations. Since neither the design matrix nor the normal matrix must be kept in the main memory, storage requirements are by far smaller as compared to non-iterative solvers. Despite the small memory requirements of the LSQR method, runtime increases dramatically with increasing maximal resolution of the geopotential to be resolved. Thus, the efficient use of the algorithm can only be achieved by adopting high performance computing (HPC) facilities.

Fortunately, each observation, i.e. each single row of the design matrix, can be treated separately. Moreover, the major computational costs occur within the bidiagonalization process, i.e. design matrix decomposition. It is therefore reasonable to distribute the number of observations on several CPUs of a multiprocessor computation platform. Within the course of this contribution, calculations are performed on a 64 processor cc-NUMA supercomputer using OpenMP for parallelization. The platform is part of an SGI Altix 3700 system supported by the Center for Computing and Networking Services in Amsterdam (SARA). Compare Fig. 2 for the parallel programming scheme. The parallel region (black colored) embraces the successive design matrix decomposition which is split (uniformly) on the processing elements used. Moreover, in case of PCA-LSQR, the computation of the design matrix preconditioner $\mathbf{L}_{\mathbf{N}}^{-1}$ is performed in parallel.

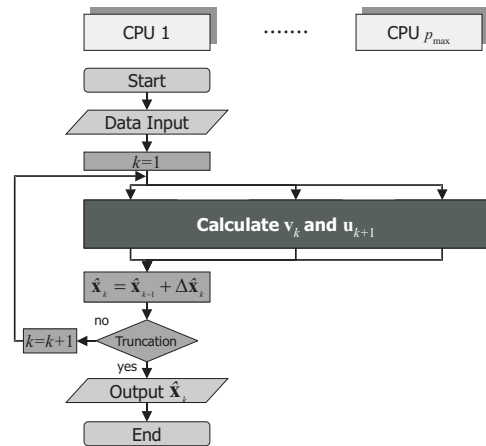


Figure 2: Parallelization of the LSQR method

6 GOCE Data Analysis

We apply the LSQR method as outlined in the sections before to a simulated GOCE data set. In particular we perform geopotential recovery based on the (quasi-)radial tensor component V_{zz} . EGM96 up to degree and order 300 is used to set up the simulation scenario (Ilk et al., 2003). The simulation covers a 30 days period with 5 s sampling. Thus, the total number of observations is $n = 518\,400$. Truncation of the iterative process is controlled by comparing the latitude-weighted RMS geoid height changes of successive approximations, denoted as ΔWRMS_h^k . If $\Delta\text{WRMS}_h^k < \delta$ holds, the iterative process stops. Within this case study, the threshold is fixed conservatively to $\delta = 0.7$ mm.

Table 2: Runtime results LSQR (8 CPUs)

spectral resolution	number of	wall time
L	iterations	(h)
100	56	1.1
200	180	13.4

Table 2 presents runtime results for the basic LSQR implementation using 8 CPUs. For V_{zz} analysis with $L = 100$, convergence is achieved after 56 iterations. However, the number of iterations increases to 180 for a spectral resolution of $L = 200$. Block-diagonal preconditioning according to Sect. 4 has been implemented and successfully parallelized. Runtime decreases significantly since the number of iterations drops dramatically compared to the basic algorithm. According to Table 3, for $L = 100$ convergence is achieved within only 8 iterations. Runtime is approximately one third compared to Table 2. Regarding $L = 200$ the number of iterations drops from 180 to 14. Runtime is reduced to 19.4%.

Table 3: Runtime results PCA-LSQR (8 CPUs)

spectral resolution	number of	wall time
L	iterations	(h)
100	8	0.4
200	14	2.6
250	19	5.1
300	32	14.4

Table 4: Runtime results PCA-LSQR (8 CPUs)

spectral resolution	wall time
L	$\mathbf{L}_{\mathbf{N}}^{-1}$ (h)
100	0.2
200	1.4
250	2.6
300	4.8

Note that the computational costs within each iteration are comparable for both LSQR and PCA-LSQR. Only the additional operations of applying $\mathbf{L}_{\mathbf{N}}^{-1}$, respectively $(\mathbf{L}_{\mathbf{N}}^{-1})^T$, on a vector occur. This has no significant runtime effect. However, the setup of the (inverse) preconditioner itself is a quite costly process. Table 4 shows the part for $\mathbf{L}_{\mathbf{N}}^{-1}$ calculation. Opposite to the total runtime in Table 3, roughly spoken half the computing time is required for $\mathbf{L}_{\mathbf{N}}^{-1}$ computation. This can be improved by approximate calculation of the block-diagonal preconditioner but is not done here. Moreover, exemplary for all scenarios, Table 5 shows runtime scaling dependent on the number of processing units. The speed-up S_p is defined as the ratio between serial runtime T_1 and the runtime achieved using p processors, denoted as T_p . Thus,

$$S_p = \frac{T_1 \text{ CPU}}{T_p \text{ CPUs}} \quad (10)$$

holds. In the optimal case the speed-up is equal to p . Needless to say that this cannot be achieved in practical applications. However, this is a quite good quality measure of the parallel implementation. Actually, according to Table 5, the speed-up is mostly close to the number of CPUs used. This demonstrates the efficient and powerful parallelization of the implementation.

Table 5: Runtime results PCA-LSQR ($L = 200$)

# CPUs	wall time (h)	speed-up
1	19.7	1
8	2.6	7.6
16	1.4	14.3
32	0.7	27.3
64	0.4	48.0

7 Conclusions

The results listed in the Table 5 demonstrate the successful application of the iterative LSQR method for solving (linear) least squares problems arising in geopotential recovery. For space geodetic applications the basic version of the iterative LS solver is not very effective with regard to both computational and methodological considerations. Preconditioning proved to be an excellent instrument to damp the number of iterations considerably and thus, to speed up the method. Additionally, Tikhonov regularization in general form has been added to the implementation without noteworthy additional effort even for a huge number of a priori regularization parameters. In the future the expansion of LSQR tuning for geopotential recovery is aimed. In particular this involves variance component estimation (VCE) for the proper weighting of different observation groups, orbital arcs respectively, and the approximate computation of error estimates.

Acknowledgment. This work was partially carried out under the HPC-EUROPA project (RII3-CT-2003-506079), with the support of the European Community - Research Infrastructure Action (under the FP6 "Structuring the European Research Area" Program). Moreover, the research was funded by the German Federal Ministry of Education and Research and the Deutsche Forschungsgemeinschaft (Geotechnologien II program, Grant No. 03F0329B).

References

- Baur, O., Austen, G. (submitted) A parallel iterative algorithm for large-scale problems of type potential field recovery from satellite data. Manuscript submitted to *Adv. Geosci.*
- Björck, A. (1996) Numerical methods for least squares problems, SIAM Philadelphia
- Ditmar, P., Klees, R., Kostenko, F. (2003) Fast and accurate computation of spherical harmonic coefficients from satellite gravity gradiometry data, *J. Geod.*, 76, pp. 690–705
- Golub, G.H., Kahan, W. (1965) Calculating the singular values and pseudoinverse of a matrix, *SIAM J. Numer. Anal.*, 2, pp. 205–224
- Hanke, M., Hansen, P.C. (1993) Regularization methods for large-scale problems, *Surv. Math. Ind.*, 3, pp. 253–315
- Hestenes, M.R., Stiefel, E. (1952) Methods of conjugate gradients for solving linear systems, *J. Res. Nat. Bur. Stand.*, 49, pp. 409–436
- Ilk, K.H., Visser, P., Kusche, J. (2003) Satellite Gravity Field Missions, Final Report Special Commission 7, *Travaux IAG*, Vol. 32, General and technical reports 1999–2003, Sapporo
- Jacobsen, M., Hansen, P.C., Saunders, M.A. (2003) Subspace preconditioned LSQR for discrete ill-posed problems, *BIT*, 43, pp. 975–989
- Kilmer, M.E., O’Leary, D.P. (2001) Choosing regularization parameters in iterative methods for ill-posed problems, *SIAM J. Matrix Anal. Appl.*, 22, No. 4, pp. 1204–1221
- Koch, K.-R. (1999) Parameter estimation and hypothesis testing in linear models, Springer Berlin Heidelberg New York
- Koch, K.-R., Kusche, J. (2002) Regularization of geopotential determination from satellite data by variance components, *J. Geod.*, 76, pp. 259–268
- Kusche, J., Mayer-Gürr, T. (2001) Iterative Solution of Ill-Conditioned Normal Equations by Lanczos Methods, in: *Proc. IAG Scientific Assembly*, Budapest, Hungary
- Kusche, J., Klees, R. (2002) Regularization of gravity field estimation from satellite gravity gradients, *J. Geod.*, 76, pp. 359–368
- Paige, C.C., Saunders, M.A. (1982) LSQR: An algorithm for sparse linear equations and sparse least squares, *ACM T. Math. Software*, 8, pp. 43–71
- Paige, C.C., Saunders, M.A. (1982) LSQR: Sparse linear equations and least squares problems, *ACM T. Math. Software*, 8, pp. 195–209
- Pail, R., Plank, G. (2002) Assessment of three numerical solution strategies for gravity field recovery from GOCE satellite gravity gradiometry implemented on a parallel platform, *J. Geod.*, 76, pp. 462–474
- Schuh, W.D. (1996) Tailored numerical solutions strategies for the global determination of the Earth’s gravity field, *Mitteilungen der geodätischen Institute der Universität Graz*, 81
- Tikhonov, A.N. (1963) Regularization of incorrectly posed problems, *Sov. Mat. Dokl.*, 4, pp. 1035–1038

A NEW APPROACH FOR DETERMINING THE POTENTIAL FIELD

WenBin Shen^{1,2}

¹ Department of Geophysics, School of Geodesy and Geomatics, Wuhan University, WUHAN, CHINA

² Key Lab. of Geospace Environment and Geodesy (MEC), Wuhan University, WUHAN, CHINA

e-mail: wbshen@sgg.whu.edu.cn

Abstract: Various methods have been put forward by geodesists to determine the Earth's external potential field based on the given boundary value or the data distributed in space. For the same purpose, a new approach is introduced in this paper. Based on the new approach (named as the fictitious compress recovery approach), once given the potential V (or any harmonic function) defined in the domain outside the Earth on the Earth's physical surface or the surface defined by the satellite altitude, the Earth's external potential field could be determined. The new approach has broad applications in geophysics (including geodesy). One example of the applications is provided: the normal gravity field generated by WGS84 reference ellipsoid is determined with the accuracy level of 0.84 mm, based on the new approach. Two simulation experimental tests are provided, which show that the new approach is valid and effective for determining the potential field, provided that the potential (or any regular harmonic function) is given on the boundary, no matter which boundary it is, the Earth's surface or the surface defined by the satellite altitude. With this new approach, the convergence problem as well as the downward continuation problem is satisfactorily solved.

Key words: fictitious compress recovery; potential field determination; normal gravity field determination; convergence and downward continuation problems; simulation experimental tests

1 Introduction

Scientists try to find laws or establish theories or methods as simple as possible, which could best fit the reality. Concerning the determination of the Earth's external gravity field, besides Stokes's method (Heiskanen and Moritz, 1967), Molodensky's method (Molodensky et al, 1962) and Bjerhammar's method (Bjerhammar, 1964), a lot of methods have been put forward. It is not the aim of this paper to judge the advantages and disadvantages of the various methods. However, it is well known that in physical geodesy the following two

problems are still open at least in theory (Moritz, 1980; Sjöberg, 1980, 2001; Rummel et al, 1993; Ågren, 2004) : i) whether the spherical harmonic expansion series expressing the Earth's potential field converges in the domain between the Earth's surface and the surface of Brillouin sphere (Arnold, 1989), simply referred to as the convergence problem; ii) theoretically, how to determine the Earth's external gravity field based only on the data (e.g., potential, gravitation or gravitational gradients) given on a simply closed surface (e.g., the surface corresponding to the satellite altitude) that completely encloses the Earth, simply referred to as the "downward continuation" problem.

In this paper, a new approach (Shen, 2004a) will be introduced, based on which the above mentioned two problems could be solved.

2 The Fictitious Compress Recovery Approach

2.1 Theoretical model

This subsection is a brief summary of the fictitious compress recovery approach, which is referred to (Shen, 2004a, 2005a). The basic idea of the method is that the "compress" and "recovery" procedures are successively executed between the given boundary (the Earth's surface $\partial\Omega$ or the surface ∂S corresponding to the satellite altitude) and the surface of an inner sphere (or Bjerhammar sphere) that lies inside Earth, and finally one gets a fictitious harmonic series solution outside the inner sphere, which coincides with the Earth's real field in the whole domain outside the Earth, no matter the given boundary is $\partial\Omega$ or ∂S (Shen and Ning, 2004), under the assumption that the above mentioned harmonic series is uniformly convergent in the domain outside the inner sphere.

Suppose there exists an unknown regular harmonic field $u(P)$ defined in the domain $\bar{\Omega}$, the

domain outside the Earth, and suppose the harmonic field $u(P)$ is uniquely determined by the given boundary value $u(P)|_{P \in \partial\Omega}$ on the Earth's surface $\partial\Omega$, which is supposed to be a "simply closed surface" ∂S (Shen, 2005b): there exists a one-to-one continuous map between ∂S and a spherical surface realized simply by ray. The problem is to find the harmonic field $u(P)$ ($P \in \bar{\Omega}$). The realization procedure could be stated as follows.

Set

$$\begin{aligned}\Theta^{(0)}(P) &\equiv u(P), \quad P \in \bar{\Omega} \\ \Theta^{(n)}(P) &= \Theta^{(n-1)}(P) - u^{*(n)}(P), \\ &P \in \bar{\Omega}, \quad n \geq 1\end{aligned}\quad (1)$$

where $\Theta^{(n-1)}(P)$ ($n \geq 1$) is called the $(n-1)^{th}$ -order residual (potential) field. Note that the $(n-1)^{th}$ -order residual field (including the 0-order residual field) is only defined in the domain $\bar{\Omega}$, and can be expressed on the Earth's boundary as follows

$$\begin{aligned}\Theta_{\partial\Omega}^{(0)} &\equiv u_{\partial\Omega} \\ \Theta_{\partial\Omega}^{(n)} &= \Theta_{\partial\Omega}^{(n-1)} - u_{\partial\Omega}^{*(n)}, \quad n \geq 1\end{aligned}\quad (2)$$

Compress the $(n-1)^{th}$ -residual boundary value $\Theta_{\partial\Omega}^{(n-1)}$ on the surface ∂K_i of an inner sphere K_i that lies inside the Earth along the radial direction, searching for the solution of the following boundary value problem

$$\begin{cases} \Delta u^{*(n)}(P) &= 0, \quad P \in \bar{K}_i \\ u^{*(n)}(P)|_{\partial K} &= \Theta_{\partial\Omega}^{(n-1)} \\ \lim_{P \rightarrow \infty} u^{*(n)}(P) &= 0, \quad n \geq 1 \end{cases}\quad (3)$$

and the solution is given by Poisson integral

$$\begin{aligned}u^{*(n)}(P) &= \frac{r^2 - R_i^2}{4\pi R_i} \int_{\partial K_i} \frac{\Theta_{\partial\Omega}^{(n-1)}}{l^3} d\sigma, \\ &P \in \bar{K}_i, \quad n \geq 1\end{aligned}\quad (4)$$

which is a regular harmonic function in the domain \bar{K}_i , the domain outside the inner sphere K_i with the radius R_i . When the above solution is constrained in the Earth's external domain $\bar{\Omega}$, it can be taken as the first approximation of the $(n-1)^{th}$ -residual field $\Theta^{(n-1)}(P)$, or $\sum_1^n u^{*(n)}(P)$ can be taken as the n^{th} approximation of the field $u(P)$.

Hence, one gets a series solution in the domain \bar{K}_i :

$$u^*(P) = \sum_{n=1}^{\infty} u^{*(n)}(P), \quad P \in \bar{K}_i\quad (5)$$

which coincides with the real field $u(P)$ in $\bar{\Omega}$ (Shen, 2004a), under the postulate that equation (5) is uniformly convergent in the domain \bar{K}_i (Cf. next subsection). On the boundary ∂K_i one has

$$u^*|_{\partial K_i} = \left(\sum_{n=0}^{\infty} \Theta^{(n)} \right) |_{\partial\Omega}\quad (6)$$

where $\Theta^{(n)}|_{\partial\Omega}$ is determined by Eq. (2).

This approach is referred to as the fictitious compress recovery approach.

2.2 The uniform convergence postulate

With intuitive reasoning and various experiments, it could be stated that (5) is uniformly convergent in the domain \bar{K}_i . Unfortunately this statement is not yet strictly proved. However, just like Einstein (Einstein, 1905), who created the special relativity theory based on two postulates (the light velocity constant postulate and the special relativity principle postulate), let us accept the following postulate (uniform convergence postulate): the series (5) is uniformly convergent in the domain \bar{K}_i .

The important thing is that, if one accepts the uniform convergence postulate, one could draw out that the series (5) coincides exactly with the real field in the domain outside the Earth (Shen, 2004a). In addition, one will find that the fictitious compress recovery approach has quite a few direct applications in geophysics, especially in physical geodesy. Whether the postulate is correct, it should be expected to be tested by various experiments and practical applications.

3 Applications

Based on the fictitious compress recovery approach, some applications could be found out directly.

3.1 Runge-Krarup theorem

Based on Runge theorem (Moritz, 1980), Krarup derived a result which could be briefly stated as follows (Krarup, 1969): any regular harmonic function ϕ defined in the domain outside the Earth can be always uniformly and infinitely approximated by a regular harmonic function ψ defined in the domain outside an inner sphere that lies inside the Earth. This result is referred to as Runge-Krarup theorem (Bjerhammar, 1975; Moritz, 1980).

In fact, one could get a stronger result than what Runge-Krarup theorem states. Suppose the function

$u(P)$ is regular and harmonic in $\bar{\Omega}$ (e.g., the gravitational potential field), which is uniquely determined by the boundary value $u_{\partial\Omega}$, then, based on the fictitious compress recovery approach, a fictitious regular harmonic function $u^*(P)$ ($P \in \bar{K}_i$) can be found out, which coincides exactly with the original field $u(P)$ in the domain $\bar{\Omega}$. Hence, Runge-Krarup theorem is simply derived out from the fictitious compress recovery approach.

3.2 The convergence problem

Given continuous or discrete boundary values on $\partial\Omega$ or ∂S , in practical applications, the Earth's global gravity field is determined based on the spherical harmonic expansion series. However, there exists a theoretical problem: whether the considered series is convergent in the domain between the Earth's surface and the surface of Brillouin sphere?

To answer this question, one could apply for the fictitious compress recovery approach. Based on the given boundary value $V_{\partial S}$ (or $V_{\partial\Omega}$), a fictitious field $V^*(P)$ is determined, which is regular and harmonic in \bar{K}_i , and coincides with the real field $V(P)$ in $\bar{\Omega}$. Since $V^*(P)$ ($P \in \bar{K}_i$) is regular and harmonic, it could be expressed as a uniformly convergent spherical harmonic series in the domain \bar{K}_i (Kellogg, 1929). Further, since it holds

$$V(P) = V^*(P), P \in \bar{\Omega} \quad (7)$$

the following conclusion is directly drawn out: the Earth's potential field $V(P)$ could be expressed as a uniformly convergent spherical harmonic expansion series in the whole domain outside the Earth. Consequently, based on the fictitious compress recovery approach, the convergence problem is solved.

In fact, independently from the fictitious compress recovery approach, the convergence problem was solved (Shen, 2005b): the gravitational potential of the Earth could be expressed as a uniformly convergent harmonic series in the domain outside the Earth. Hence, it could be considered that the new approach is supported by (Shen, 2005b).

3.3 The downward continuation

Suppose the boundary value $V(P)|_{\partial S}$ (or gravitational $V_i(P)|_{\partial S}$ or gravitational gradients $V_{ij}(P)|_{\partial S}$) on the surface ∂S corresponding to the satellite altitude is given. It is noted that the boundary value $V|_{\partial S}$ on ∂S might be determined by using the well known energy integral approach (Bjerhammar, 1967; Visser et al, 2003). To determine the

Table 1: Parameters of the WGS 84 reference ellipsoid

Semi-major axis, a	6378137 m
Flattening, f	1/298.257223563
Normal geopotential at the ellipsoidal surface, $U_0 \equiv W_0$	62636855.80 m ² s ⁻²
Angular velocity, ω	7.292115×10^{-5} rad s ⁻¹

real field $V(P)$ in the domain $\bar{\Omega} - \bar{S}$, the domain between the Earth's physical surface $\partial\Omega$ and the surface ∂S , it occurs the "downward continuation" problem, which was not solved satisfactorily by using conventional methods, due to the "ill-posed" problem (Moritz, 1980; Sjöberg, 1980, 2001; Rumel et al, 1993).

The fictitious compress recovery approach can be applied in determining the Earth's external field $V(P)$ ($P \in \bar{\Omega}$), provided that a boundary value $V(P)|_{\partial S}$ on a "simply closed surface" ∂S is given, where the closed surface ∂S completely encloses the whole Earth. Based on the boundary value $V|_{\partial S}$ and the fictitious compress recovery approach, a fictitious field $V^*(P)$ ($P \in \bar{K}_i$) can be determined, which coincides with the real field $V(P)$ in the domain outside the surface ∂S . It was further proved (Shen and Ning, 2004; Shen, 2005a) that the determined fictitious field $V^*(P)$ ($P \in \bar{K}_i$) coincides with the real field $V(P)$ in the whole domain outside the Earth. Consequently, the "downward continuation" problem is solved. This approach is referred to as the "fictitious downward continuation" (Shen et al, 2006a,b).

3.4 The normal gravity field determination

The aim is to determine the normal gravity field generated by WGS 84 ellipsoid (Shen and Zhong, 2006), based on the fictitious compress recovery approach. The parameters of WGS 84 reference ellipsoid are listed in Table 1.

There are differences among various normal geopotential values on the surface of the WGS 84 reference ellipsoid provided by different authors (Burša et al, 1997a,b; Grafarend and Ardalan, 2000), some of which are listed in Table 2. In (Shen and Zhong, 2006), W_0 is given as 62636852.4029 m²s⁻² (30' × 30'), which is determined based on the parameters listed in Table 1. On the surface ∂E of the ellipsoid, the normal geopotential $U|_{\partial E} \equiv W_0$ holds constant, and consequently the normal gravitational potential boundary value $V|_{\partial E}$ is determined by the equation $V|_{\partial E} = U|_{\partial E} - Q|_{\partial E}$, of which $Q(P)$ denotes the centrifugal potential field.

To determine the normal field outside the ellipsoid, the discrete approach is used: dividing the

Table 2: The normal geopotential $U_0 \equiv W_0$ on WGS 84 ellipsoidal surface

Burša et al., 1997a	$62636855.72 \pm 0.5 \text{ m}^2\text{s}^{-2}$
Burša et al., 1997b	$62636855.80 \pm 0.5 \text{ m}^2\text{s}^{-2}$
Grafarend et al., 2000	$62636855.80 \pm 3.6 \text{ m}^2\text{s}^{-2}$
NIMA 2000	$62636851.7146 \text{ m}^2\text{s}^{-2}$

Table 3: Statistics information about the differences ΔU between the calculated field U^* and real field U on the ellipsoidal surface (with $30' \times 30'$ grid) [Unit: m^2s^{-2}]

$\Delta U = U^* - U$	Iterative times $N = 15$
Max(ΔU)	7.063591480255127E-002
Min(ΔU)	-1.682689785957336E-002
Mean(ΔU)	8.289705838053775E-004
RMS(ΔU)	8.436805231548323E-003

spherical surface of the inner sphere into $30' \times 30'$ grids by parallel latitude and longitude lines, and mapping these grids along radial directions on the surface of the ellipsoid. In every grid on ∂E one representative value is chosen as the average value over the grid. Generally the value at the geometric center of the grid is chosen, but it is not the best way: there are other approaches (Shen et al, 2006a,b), which will not be described here because it is not essential. As the grid becomes infinitesimal, the value at every point on the grid is equivalent to the average value over the grid. Now, there are 259200 point values on the boundary ∂E : $V_{\partial E}^{(i)}$ ($i = 1, 2, \dots, 259200$). Then, based on the fictitious compress recovery approach, the fictitious boundary values $V_{\partial K_i}^{*(i)}$ ($i = 1, 2, \dots, 259200$) are determined (which were stored for the future usage), based on which the fictitious field $V^*(P)$ ($P \in \bar{K}_i$) could be determined, i.e., the value $V^*(P)$ at any point in \bar{K}_i could be determined. In the calculations, the zero-order term GM/r is taken away. The calculated results (with the iterative procedure times $N = 15$) are compared with the real field provided by the conventional approach (Heiskanen and Moritz, 1967), and are listed in Table 3.

From Table 3 one can see that, based on the fictitious compress recovery approach, with $30' \times 30'$ grid and iterative times $N = 15$, it is determined the normal gravity field $U^*(P)$ generated by WGS 84 ellipsoid with the accuracy 0.84 mm, which is good enough for general applications.

4 Simulation Calculations

In Sec.3.4, the normal gravity field is determined based on the fictitious compress recovery approach.

This strongly support the new approach. In addition, another two simulation tests are provided in the sequel.

4.1 Simulation test I

With $10^\circ \times 10^\circ$ grid and discrete values obtained by EGM96 model, the (disturbing) potential values $V_{\partial K_1}$ (648 point values ranging from $-83.676\text{m}^2\text{s}^{-2}$ to $+64.869\text{m}^2\text{s}^{-2}$) on the boundary ∂K_1 of a smaller sphere K_1 with radius $R_1 = 6338$ km are given (Shen et al, 2006a). Then, the potential values $V_{\partial K_2}$ on the spherical surface ∂K_2 (with $R_2 = 6638$ km) corresponding to the satellite altitude were calculated by using the Poisson integral. Suppose we know only the boundary values $V_{\partial K_2}$, the problem is to determine the real field in the domain outside K_1 . Based on the fictitious compress recovery approach and the given values $V_{\partial K_2}$, the fictitious field $V^*(P)$ was determined. By comparisons it is found that the determined fictitious field $V^*(P)$ coincides with the real values $V_{\partial K_1}$ on the boundary ∂K_1 at least under the accuracy (RMS) level 0.1 cm, and the largest difference $\Delta V = V - V^*$ on the boundary ∂K_1 is 0.4 cm. Hence, this simulation test supports both the fictitious compress recovery approach and the “fictitious downward continuation”.

4.2 Simulation test II

Choose two spherical boundaries ∂K_1 and ∂K_2 of two spheres K_1 and K_2 with radii $R_1 = 55$ km and $R_2 = 80.35$ km, respectively, where K_1 is taken as the inner sphere, and choose two point masses $Gm_1 = Gm_2 = 100 \text{ m}^3\text{s}^{-2}$, which are located outside and inside the smaller sphere, respectively (Shen et al, 2006b).

In the experimental test, using discrete approach, dividing the spherical surface into $1^\circ \times 1^\circ$ grids, and consequently there are 64800 point values on the boundary ∂K_2 : $V_{\partial K_2}^{(i)}$ ($i = 1, 2, \dots, 64800$). Then, based on the fictitious compress recovery approach, the fictitious boundary values $V_{\partial K_1}^{*(i)}$ ($i = 1, 2, \dots, 64800$) were determined (which were stored for the future usage), based on which the fictitious field $V^*(P)$ ($P \in \bar{K}_1$) could be determined, i.e., the value $V^*(P)$ at any point in \bar{K}_1 could be determined. 11 test points were chosen, which are listed in Table 4. The calculated results are provided in Table 5: the second column lists the real values $V(P_j)$ at test points P_j ($j = 1, 2, \dots, 11$), the third column lists the “fictitious values” corresponding to the test points P_j with the iterative procedure times $N = 30$,

Table 4: A list of the coordinates (r, θ, λ) at test points [units of (r, θ, λ) : (km, $^\circ$, $^\circ$)]

Point No.	Radius	Co-latitude	Longitude
1	60.5	90.0	90.0
2	67.0	80.0	60.0
3	100.0	20.0	30.0
4	100.0	50.0	90.0
5	100.0	120.0	150.0
6	100.0	160.0	70.0
7	90.0	60.0	80.0
8	70.0	160.0	30.0
9	70.0	80.0	30.0
10	72.0	120.0	80.0
11	120.0	30.0	80.0

Table 5: Comparisons between the real values $V(P_j)$ and calculated values $V^*(P_j)$ at 11 test points [unit: m^2s^{-2}]

P. No. j	$V(P_j)$	$V^*(P_j) _{N=30}$	ΔV
1	68.1474983	20.3624210	47.785077276
2	4.2914681	4.2370771	0.054390962
3	2.3021512	2.3024617	-0.000310552
4	2.7086108	2.7088060	-0.000195131
5	1.9344627	1.9338306	0.000632143
6	1.7847403	1.7848045	-0.000064234
7	3.2901607	3.3028124	-0.012651715
8	2.1865713	2.1894143	-0.002842985
9	2.9000400	2.9039151	-0.003875168
10	3.7610990	3.7618779	-0.000778967
11	2.0074077	2.0069548	0.000452841

where the “fictitious values” were calculated based on Poisson integral by using the “fictitious boundary values” $V_{\partial K_1}^*$, which were determined by the fictitious compress recovery approach, and the last column lists the differences between the real values and the “fictitious values” at the test points P_j .

The first point mass $m_1 = m$ and second point mass $m_2 = m$ are located at $(r, \phi, \lambda) = (30.0, 90, 90)$ and $(r, \phi, \lambda) = (63.0, 90, 90)$, respectively. The fictitious compress recovery approach predicts that all the fictitious values $V^*(P_j)$ ($j = 1, 2, \dots, 11$) on the test points should be coinciding with the corresponding real values $V(P_j)$ ($j = 1, 2, \dots, 11$), except for the test point $P_1(60.50, 90, 90)$, because it is located at the position just directly under the point mass m_2 that is located at point $(63.0, 90, 90)$, and in this case, one can’t construct a “simply closed surface” ∂S which encloses point masses m_1 and m_2 but does not enclose the first test point P_1 so that there exists one-to-one continuous map between ∂S and ∂K_1 , referring to Fig. 1. That means, the calculated value at point P_1 is the real fictitious value, and it might be far from the real value. Just considering the fictitious field in the interior of the Earth, it might deviate far from the real field. The important

thing is that the fictitious field coincides with the real field in the domain outside the Earth. Hence, the experimental test supports the “fictitious downward continuation”.

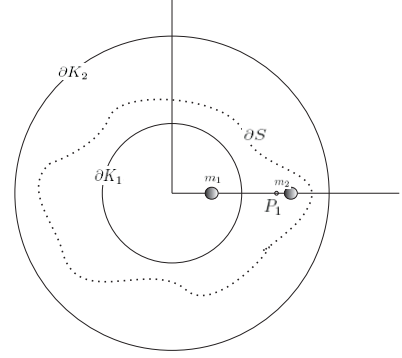


Figure 1: The smaller and larger spherical surfaces are denoted by ∂K_1 and ∂K_2 , respectively. ∂S is a simply closed surface that encloses both masses m_1 and m_2 , and it is not possible to construct the simply closed surface ∂S so that it encloses both masses m_1 and m_2 but excludes the test point P_1 . It is noted that the calculated field coincides with the real field in the domain outside ∂S (just taking ∂S as the Earth’s surface!)

The above simulation calculation is significant. The Earth could be divided into a lot of but finite “particles”. Since the potential obeys the supposition principle, the above simulation results means that the fictitious compress recovery approach as well as the “fictitious downward continuation” is valid and reliable for the potential field generated by the Earth.

5 Discussions and Conclusions

Previously, it was considered that it had been proved (Shen, 2004b) that the series (5) is uniformly convergent in the domain \bar{K}_i , the domain outside the inner sphere K_i , and consequently the fictitious field determined by the fictitious compress recovery approach coincides with the real field in the domain outside the Earth (Shen, 2004a). Later, it was found that the proof provided in (Shen, 2004b) is not rigorous. Nevertheless, various simulation experimental tests (Shen et al, 2006a,b; Shen and Zhong, 2006) support the fictitious compress recovery approach, and consequently it is reasonable to assume that the series (5) is uniformly convergent in the domain \bar{K}_i (as a postulate), the rigorous proof of which is expected to be provided in the future.

The fictitious compress recovery approach has

broad applications, based on which, e.g., the Runge-Krarp theorem can be derived out, the convergence problem as well as the downward continuation problem can be solved, and the normal gravity field can be determined, etc. Consequently, it might be suggested that the fictitious compress recovery approach could be accepted as a general approach for solving the (first kind of) boundary value problem.

Acknowledgments. This study is funded in parts by Natural Science Foundation China (No. 40574004 and No. 40174004).

References

- Ågren J (2004) The analytical continuation bias in geoid determination using potential coefficients and terrestrial gravity data. *J Geod*, DOI 10.1007/s00190-004-0395-0
- Arnold K (1989) Das gravitationspotential im außenraum der erde. *Mitteilung des Zentralinstitut für Physik der Erde Nr 1668, Vermessungstechnik* 37(3):82–86
- Bjerhammar A (1964) A new theory of geodetic gravity. Royal Institute of Technology. Geodesy Division, Stockholm
- Bjerhammar A (1967) On the energy integral for satellites. *Rep. of the R. Inst. of Techn., Stockholm, Sweden*
- Bjerhammar A (1975) Discrete approaches to the solution of the boundary value problems in physical geodesy. *Bollettino di Geodesia e Scienze Affini* 34:185–240
- Burša M, Kouba J, Raděj K, True SA, Vatrt V, Vojtišková M (1997a) Monitoring geoidal potential on the basis of topex/poseidon altimeter data and egm96. In: *Scientific Assembly of IAG, Rio de Janeiro, Brazil*
- Burša M, Raděj K, Šíma Z, True SA, Vatrt V (1997b) Determination of the geopotential scale factor from topex/poseidon satellite altimetry. *Stud Geoph et Geod* 14:203–216
- Einstein A (1905) Zur elektrodynamik bewegter körper. *Ann Phys* 17:891–921
- Grafarend EW, Ardalan AA (2000) World geodetic datum. *Journal of Geodesy* 73:611–623
- Heiskanen WA, Moritz H (1967) *Physical geodesy*. Freeman and Company, San Francisco
- Kellogg OD (1929) *Foundation of potential theory*. Frederick Ungar Publishing Company, New York
- Krarp T (1969) A contribution to the mathematical foundation of physical geodesy. *Publ. 44, Dan. Geod. Inst., Copenhagen*
- Molodensky MS, Eremeev VF, Yurkina MI (1962) *Methods for study of the external gravitation field and figure of the Earth* (transl. from Russian 1960). Israel Program for Scientific Translations, Jerusalem
- Moritz H (1980) *Advanced physical geodesy*. Wichmann, Karlsruhe
- Rummel R, Sansó F, van Gelderen M, Brovelli M, Koop P, Migliaccio F, Schrama E, Sacerdote F (1993) *Spherical harmonic analysis of satellite gradiometry*. Netherlands Geodetic Commission, Publications on Geodesy, New Series No. 39
- Shen WB (2004a) The fictitious compress recovery of the gravitational potential. *Journal of Wuhan University (Information Science)* 29:720–724 (in Chinese)
- Shen WB (2004b) The proof of the uniform convergence of the series solution about the fictitious compress recovery of the gravitational potential. *Journal of Wuhan University (Information Science)* 29:779–782 (in Chinese)
- Shen WB (2005a) *Lecture notes on satellite geodesy*. In: Royal Inst. of Techn., Stockholm, Sweden
- Shen WB (2005b) On the convergence problem. In: *IAG Meeting “Dynamic Planet 2005”, Aug. 22-26, 2005, Cairns, Australia*
- Shen WB, Ning J (2004) A proposal on the determination of the earth’s potential field. In: *18th CEOS Symposium, Beijing, China*
- Shen WB, Zhong QJ (2006) The normal gravity field determination by a new approach. *Geomatics and Information Science of Wuhan University* (submitted)
- Shen WB, Wang Z, Chao D (2006a) An approach for determining the earth’s external gravity field by using satellite gravity data and a simulation experiment test. *Geomatics and Information Science of Wuhan University* 31:189–193
- Shen WB, Yan J, Chao D (2006b) The application of the fictitious compress recovery approach in “downward continuation” and simulation experiment tests. *Journal of Geomatics* 31(3):1–4
- Sjöberg LE (1980) On the convergence problem for the spherical harmonic series of the geopotential at the surface of the earth. *Bollettino di Geodesia e Scienze Affini* 39:261–272
- Sjöberg LE (2001) The effect of downward continuation of gravity anomaly to sea level in stokes’ formula. *Journal of Geodesy* 74:796–804
- Visser PNAM, Sneeuw N, Gerlach C (2003) Energy integral method for gravity field determination from satellite orbit coordinates. *Journal of Geodesy* 77:207–216

Joint SST and SGG Gravity Field Solutions Using the Torus Approach

Chen Xu¹, Nico Sneeuw², and Michael G. Sideris¹

¹Dept. of Geomatics Engineering, University of Calgary, Calgary, Canada T2N 1N4
Tel: +1(403)220-4984, Email: {xuc, sideris}@ucalgary.ca

²Geodätisches Institut, Universität Stuttgart, Stuttgart, Germany, D-70147
Tel: +49(0)711-6858-3389, Email: sneeuw@gis.uni-stuttgart.de

Abstract. Global gravity field recovery from the dedicated gravity field satellite missions like CHAMP, GRACE and GOCE, is a computationally demanding task. This paper makes use of a torus-based “lumped coefficients” approach, which is able to deal with any geopotential functionals. Firstly, as a demonstration of its feasibility and efficiency, gravitational disturbing potentials from real CHAMP SST and simulated gravity gradient tensors from GOCE-like SGG are processed through the torus approach individually. The spherical harmonics solutions validate that SST is only sensitive to the low degrees of spherical harmonics while SGG better resolves the high degrees.

Therefore, in order to cover the whole gravity spectrum, the block-diagonal order-wise normal matrices from SST and SGG data are merged in the least-squares adjustment using proper weighting factors. The optimal weighting factors will firstly be estimated by a parametric covariance method in an iterative way. We also apply the variance components estimation as an alternative method. The joint SST and SGG solutions show better performances than either one of the stand-alone inversions in the presence of full gravity field spectrum and minimization of geoid height errors.

Keywords. gravity field recovery, torus approach, spherical harmonics, block-diagonality, SST, SGG

1 Introduction

The dedicated gravity field satellite missions, CHAMP, GRACE and GOCE provide a huge amount of homogeneous measurements in their mission life time. Thus it is a computationally demanding task to recover the Earth’s gravity field up to certain spherical harmonic degree from spaceborne gravimetry.

The torus-based semi-analytical approach has been proven a feasible and efficient tool to achieve this goal, cf. (Sneeuw, 2000a; Xu et al., 2006). In this approach, the gravitational observables derived from the position, velocity, and acceleration data are treated as the direct input in-situ observables. However, individual missions only cover certain spatial resolutions because of their implementations and prospective target goals. The CHAMP mission employs the satellite-to-satellite tracking (SST) concept and provides accurate position, velocity and acceleration data. The correspondingly derived disturbing potential data are only sensitive to the long wavelength part, while the GOCE mission makes use of the satellite gravity gradiometry (SGG) concept, and the gravity gradient tensors better resolve the signal having high gravity frequencies. As two examples, the stand-alone solutions from real CHAMP disturbing potential data and simulated GOCE gravity gradient tensor data are processed to calculate the spherical harmonics by the torus-based semi-analytical approach respectively in section 2.

In order to cover the combined gravity field spectrum, individual solutions have to be merged. The joint inversion of SST and SGG data has been studied in , e.g., Bouman (2000); Ditmar et al. (2003); Pail and Plank (2004) to list a few. The innovative point in this paper is that the block-diagonal order-wise normal matrices from both SST and SGG data are merged by proper weighting factors in the least-squares adjustment. There are two ways to optimally estimate such weighting factors, which will be addressed in section 3. One is the parametric covariance method (PC) in an iterative way. It is based on a comparison of the parameter differences between a subset solution and the joint solution, with the differences of the corresponding error estimates. The second approach is variance component estimation (VC), in which the optimal weights are introduced as reciprocal values of the iteratively estimated vari-

ances of each measurement group. In section 4, the joint solutions by two optimal weighting methods are presented with the comparison of both SST and SGG stand-alone solutions.

2 Stand-Alone Solutions from SST and SGG

As an alternative choice of traditional gravity field determination tools, i.e., the time-wise and space-wise approaches (Rummel et al., 1993), the torus approach has been proven feasible and efficient to recover gravity field from spaceborne gravimetry. In addition, the torus approach is able to deal with any geopotential functionals, cf. (Sneeuw, 2000b).

2.1 The torus representation of disturbing potentials from real CHAMP SST data

The direct output from CHAMP SST in the high-low mode are the position, velocity, as well as the acceleration data along the orbit. After applying the energy balance approach, the in situ gravitational potential V can be calculated and calibrated at the satellite height, cf. (Gerlach et al., 2003; Weigelt, 2006), which will be treated as the direct observables for the torus approach. Without any details of the rotation and transformation procedure, the potentials V can be rotated and expressed in spherical harmonics up to a maximum degree L by two orbital variables u (the argument of latitude) and Λ (the longitude of the ascending node) in an orbital frame, cf. (Sneeuw, 2000b):

$$V(r, I, u, \Lambda) = \frac{GM}{r} \sum_{l=0}^L \left(\frac{R}{r}\right)^l \sum_{m=-l}^l \sum_{k=-l}^l \bar{K}_{lm} \bar{F}_{lmk}(I) e^{j(ku+m\Lambda)}, \quad (1)$$

in which r, R, GM are the geocentric radius, the Earth's equatorial radius and gravitational constant times Earth's mass, respectively. The normalized spherical harmonic coefficients \bar{K}_{lm} with degree l and order m are in a complex-valued format. (1) introduces the normalized inclination function $\bar{F}_{lmk}(I)$ with the orbit inclination I , and the third index k due to the rotation, cf. (Kaula, 1966). Note that both orbital coordinates u and Λ attain values in the range of $[0, 2\pi)$ periodically. Topologically, the product of $[0, 2\pi) \times [0, 2\pi)$ creates a torus, which is exactly the proper domain of a two-dimensional discrete Fourier series. In order to simplify the torus-based representation, the following Fourier coefficients A_{mk} , known as "lumped coefficients", and the

transfer coefficients H_{lmk} , are introduced:

$$A_{mk}^V(r, I) = \sum_{l=\max(|m|, |k|)}^L H_{lmk}^V \bar{K}_{lm}; \quad (2a)$$

$$H_{lmk}^V(r, I) = \frac{GM}{r} \left(\frac{R}{r}\right)^l \bar{F}_{lmk}(I). \quad (2b)$$

With these quantities, (1) can be concisely re-arranged as a 2D Fourier series:

$$V(r, I, u, \Lambda) = \sum_{m=-L}^L \sum_{k=-L}^L A_{mk}^V e^{j(ku+m\Lambda)}. \quad (3)$$

The two-dimensional summation in (3) is valid to any orbits. However, a realistic orbit is always perturbed by disturbing forces, e.g., the Earth's flattening J_2 effect and air-drag perturbation. Consequently, the transfer coefficients are time-dependent due to varying heights and inclinations, i.e., $r(t)$, and $I(t)$. In order to apply the fast Fourier analysis, a nominal orbit with constant radius and constant inclination assumptions has to be introduced, under which the potential V is only the function of orbital variables $u(t)$ and $\Lambda(t)$ with constant coefficients A_{mk} and H_{lmk} . As a result, the transfer coefficients H_{lmk} in (2b) spectrally build a linear system between lumped coefficients A_{mk} in the spectral domain and spherical harmonics \bar{K}_{lm} in the spatial domain.

Under the nominal orbit assumption, the spherical harmonics \bar{K}_{lm} can accordingly be determined from the corresponding geo-functionals by three steps. Firstly, gravitational potentials are reduced from height and inclination variations and interpolated regularly onto a nominal torus. Secondly, the pseudo-observable lumped coefficients in (2a) are easily computed by a two-dimensional Fast Fourier Transform (FFT) technique. In the final step, spherical harmonics \bar{K}_{lm} for different orders m are solved individually by the least-squares adjustment based on the linear system in (2b), cf. (Xu et al., 2006). For the computational and programming purpose, the linear least-squares solution for certain order $m \in [-L, L]$ can be expressed in a matrix format like:

$$a_m = \begin{matrix} H_m & k_m \\ (2L+1) \times 1 & (2L+1) \times (L-|m|+1) \end{matrix} \begin{matrix} \\ \\ \end{matrix}; \quad (4a)$$

$$\Rightarrow k_m = (H_m^T H_m)^{-1} (H_m^T a_m), \quad (4b)$$

in which a_m and k_m stand for the order-wise vectors of coefficients A_{mk} and \bar{K}_{lm} respectively. Note that the weight matrices of observations are assumed as unit matrices and uncorrelated with respect to each other for the least-squares adjustment.

The big advantage of a semi-analytical procedure like the torus approach is that the normal matrix shows a block-diagonal structure m orderwisely with an assumption of the nominal orbit, cf. (Sneeuw, 2000b). Consequently, the normal matrix for certain order m in least-squares adjustment has the size of $(L - |m| + 1) \times (L - |m| + 1)$ for each block, which is easily inverted. However, one corresponding disadvantage of the torus approach is the correction of radius and inclination variations, which can be done by an iteration scheme, cf. (Klees et al., 2000).

For the first stand-alone example, disturbing potential data are calculated and calibrated from almost two years of real CHAMP SST data (position, velocity and acceleration), (Weigelt, 2006). These disturbing potential data V are processed to solve for the spherical harmonics up to degree $L = 90$ according to foregoing three-step computational flow. Choosing the GRACE satellite-only gravity field model GGM02S as the reference field, the root-mean-square per degree (σ_l) of CHAMP two-year overall solution is calculated by (5). The meaning of σ_l is the average standard deviation to be expected for a specific degree l :

$$\sigma_l = \sqrt{\frac{1}{2l+1} \sum_{m=-l}^l (\bar{K}_{lm}^{\text{est}} - \bar{K}_{lm}^{\text{ref}})^2}. \quad (5)$$

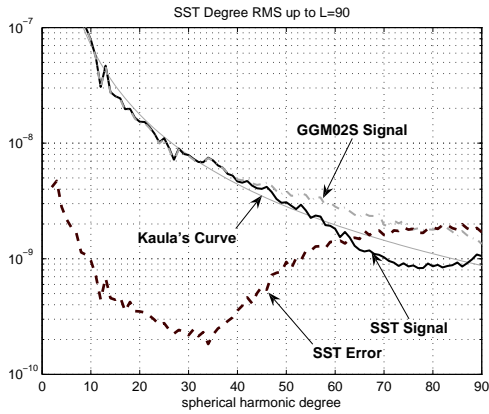


Figure 1: Degree RMS from SST gravity field recovery compared with GGM02S reference

In the above degree RMS plot, the black solid curve is the SST signal, and the black dash curve is the noise with respect to the reference field. It shows that the disturbing potentials from SST are able to recover the long wavelength part of the gravity spectrum. But the error spectrum curve goes up beyond degree 30

and intersects with the SST signal curve at degree 60, where the signal to noise ratio (SNR) is equal to one. Therefore, it can be drawn the conclusion that the disturbing potentials from CHAMP SST data are not able to recover the gravity field beyond degree 60.

2.2 The torus representation of gravity gradient tensors from GOCE SGG data

Another advantage of the torus approach is that its algorithms can be employed to not only the gravitational potential but also its functionals. The procedure of three recovering steps described before keeps same only except that the corresponding transfer coefficients have to be changed for particular functionals. For instance, transfer coefficients H_{lmk}^{zz} for gravity gradient tensor radial component V_{zz} can be derived as, cf. (Sneeuw, 2000b):

$$H_{lmk}^{V_{zz}} = \frac{GM}{r^3} \left(\frac{R}{r}\right)^l [(l+1)(l+2)] \bar{F}_{lmk}(I). \quad (6)$$

The second stand-alone example is the processing of V_{zz} simulation data, which have been simulated along a ten-day GOCE-like orbit with the altitude around 256 km and a sun-synchronous orbit with inclination $96^\circ.6$. In this close-loop simulation, disturbing forces and instrument errors have been considered in the measurement bandwidth. The spherical harmonics up to $L = 90$ are recovered by foregoing addressed three steps. The OUS91A model is selected as the reference field for this example, which is exactly the apriori input model in the close-loop simulation.

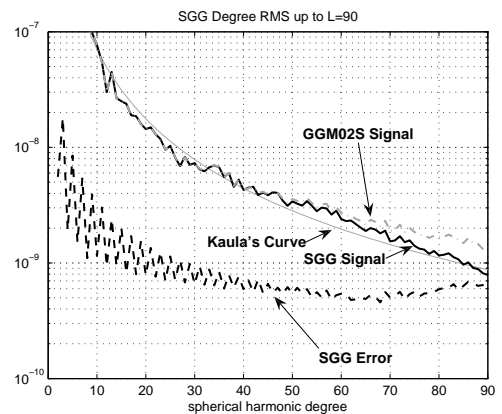


Figure 2: Degree RMS from SGG gravity field recovery compared with OUS91A reference

In the SGG degree RMS plot, again, the black solid curve is the SGG signal, the black dash curve is the

error with respect to the reference field. Compared to the previous SST RMS plot (Figure 1), Figure (2) shows that the gravity gradient tensors struggle in the low wave-number part. However, the error curve is quite flat in the higher wave-number part, which means SGG is able to recover the gravity field beyond degree 90.

3 Optimal Weighting Methods

The previous stand-alone examples from individual real SST and simulated SGG data show that SST is only sensitive to the low frequencies while SGG better resolves the high frequencies of the Earth's gravity field spectrum, the combined solution is necessary. To achieve this goal, the normal matrices from SST and SGG data are merged in the least-squares adjustment by optimal weighting factors w_i . Note that due to the block diagonality in the torus approach, the optimal weighting factors have to be consequently estimated order wise as well. The combined SST and SGG solution with assumed weighting factors w^V and w^{zz} for certain order m is given in a general formula:

$$\begin{aligned} k_m^{\text{opt}} &= \left(\sum_i w^i H_m^i \text{T} H_m^i \right)^{-1} \left(\sum_i w^i H_m^i \text{T} a_m^i \right) \\ i &= V, V_{zz} \end{aligned} \quad (7)$$

Since the optimal weight factors w^V and w^{zz} are unknown in general, they have to be estimated from the observations, i.e., the "lumped coefficients" in the linear equation (4a). Two approaches are investigated in the following section.

3.1 Parametric covariance approach

Parametric covariance approach (PC) originally was developed by Lerch (1989). It is based on a comparison of the parameter differences between the individual solutions and joint solution, leading to a calibration factor q_i :

$$q_i = \frac{(k_m^i - k_m^{\text{opt}}) \text{T} (k_m^i - k_m^{\text{opt}})}{\text{trace}[(N^{\text{opt}})^{-1} - (N^i)^{-1}]}, \quad (8)$$

in which the normal matrix from combined N^{opt} and from each stand-alone N^i are calculated as follows:

$$\begin{aligned} N^{\text{opt}} &= \sum_i w^i H_m^i \text{T} H_m^i; \\ N^i &= w^i H_m^i \text{T} H_m^i. \end{aligned} \quad (9)$$

Starting with initial values of $w_i = 1$ for both SST and SGG, the updated weights w_i^* can be obtained

iteratively by re-scaling the variances with the calibration factor q_i for each observation group:

$$w_i^* = \frac{w_i}{q_i}. \quad (10)$$

Compared with previous weighting factor w_i , under a threshold criterion, e.g., the relative accuracy between old and updated weights $\frac{|w_i^* - w_i|}{w_i} \leq 10^{-8}$, the calculation will normally converge after several iterations. After the convergence, the final weights are taken back to (7) to get the final optimal joint solution.

3.2 Variance components approach

Koch and Kusche (2002) determined the optimal weights by introducing reciprocal values of the estimated variance components (VC), i.e., $w_i = \frac{1}{\hat{\sigma}_i^2}$ in (7). Starting with initial values of $\sigma_i^2 = 1$ for each group, the posterior variance components can be iteratively estimated by:

$$\hat{\sigma}_i^{*2} = \frac{\hat{\varepsilon}_i \text{T} \hat{\varepsilon}}{\tau_i}. \quad (11)$$

Residual vector ε_i can be determined by the linear observation system with approximate values of combined \bar{K}_m and the initial weight factors $w_i = 1$ in (7) as:

$$\hat{\varepsilon}_i = H_m^i k_m - a_m. \quad (12)$$

The partial redundancies τ_i for different types of observations can be calculated from:

$$\tau_i = 2L + 1 - \text{trace} \left(\frac{N^i}{N^{\text{opt}}} \right), \quad (13)$$

where $2L + 1$ represents the number of observations a_m for each order m in (4a). The normal matrices N^i and N^{opt} can be computed in the same way as (9).

After the calculation of posterior variance components $\hat{\sigma}_i^{*2}$, the updated weighting factors are determined by:

$$w_i^* = \frac{w_i}{\hat{\sigma}_i^{*2}}. \quad (14)$$

Again, the calculating scheme works iteratively. Initially starting from one, the weighting factors for each observation group will normally converge after several iterations to fulfill the threshold criterion.

4 Joint Solutions and Discussion

In order to investigate the performances of two optimal weighting approaches, the joint solutions combining SST disturbing potentials V and SGG gravity tensor radial component V_{zz} up to $L = 90$ are

processed using the parametric covariance approach (PC) and variance components estimation (VC) respectively. Note that the corresponding optimal weights are determined order by order due to the block diagonality. After the computation in an iterative way, the final degree RMS results for PC and VC joint solutions are plotted in Figure (3).

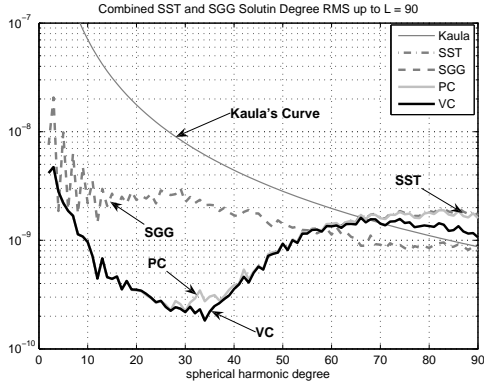


Figure 3: Joint solutions degree RMS from real SST & simulated SGG compared with GGM02S

The degree RMS plot shows that both joint SST and SGG solutions by two optimal weighting approaches are better than either one of the stand-alone solutions. Apparently, in the higher degree part, they are very close to the SST solution and the error curves are bent down towards SGG solution in the high frequency part. However, both PC and VC solutions do not totally follow the SGG curve in higher degrees because SST still takes part in the calculations.

In order to examine how much each group contributes to the optimal joint solutions, the relative weights between SST and SGG, i.e., the ratios of $w^V/w^{V_{zz}}$, for different order m are calculated and shown in Figure (4).

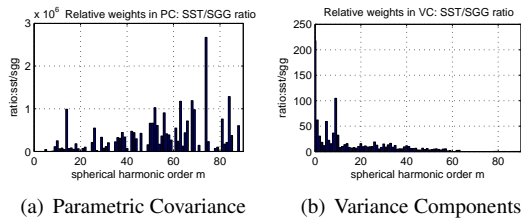


Figure 4: Relative weights for different order m : $w^V/w^{V_{zz}}$

The relative weights in parametric covariance approach are relatively arbitrary (Figure 4a). Appar-

ently, the relative weight ratios in the variance components estimation for different orders are quite reasonable, for instance, Figure (4b) shows that SST dominates the long wavelength parts, while SGG takes the lead in the high frequency part.

Another important aspect to evaluate the performance of the weighting estimation methods is the number of iterations. Although it is time consuming to calculate the partial redundancy factor τ (13) in variance components estimation, only several dozens of iterations are required compared to the parametric covariance calculation, which stops sometimes over thousand iterations. The reason why parametric covariance method needs more iterations for convergence is that the denominator $\hat{\sigma}_i^{*2}$ in (14) might be close to zero sometimes, leading the updated weight w_i^* towards infinite and hardly reaching the threshold values. As discussed thoroughly in Lemoine et al. (1998), the PC technique is not designed for calibration of distinct data types where they do not overlap in signal bandwidth. The experiment in our joint solution by PC method validates this statement. The basic idea in this experiment is for the sake of demonstrating the principle of two weighting methods. Another argument is that we are trying to reach a joint solution with two uncombinable data sets, because the SST data are derived from the “real world”, while the SGG data are generated from a “simulated world”. Thus the comparisons which are done here are only drawn this particular experiment and might not be extended for general cases.

An interesting phenomenon is that around the SST recovering limit, i.e., degree $l = 60$, VC requires larger amount of iterations compared to other degrees. It means that SST and SGG have almost equal contributions around $l = 60$ area where the leading role between SST and SGG interchanges.

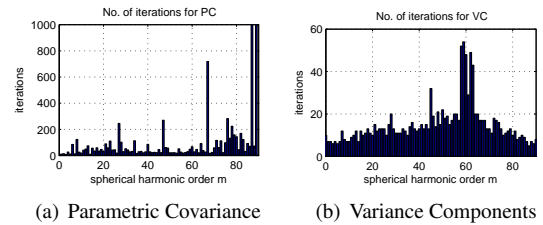


Figure 5: Number of iterations for different order m

To summarize the comparison in our specific experiment, the variance components estimation (VC) works better than the parametric covariance approach (PC) in terms of the degree RMS curve, the relative weights ratio between SST and SGG, the number of

iterations and the computational time. In addition, the variance components estimation can be applied in the regularization factor determination, cf. (Koch and Kusche, 2002).

5 Conclusion

Results from two years of real CHAMP disturbing potentials show that SST is only sensitive to the low frequency part and only able to recover the gravity field up to degree $L = 60$, while the simulated GOCE SGG radial component V_{zz} can only better resolve high frequencies of gravity spectrum beyond degree $L = 90$. In the combined SST and SGG solution, two approaches are investigated in order to calculate the optimal weighting factors for different orders m . They are parametric covariance approach and variance components estimation. m order-wise joint solutions by optimal weighting factor from each group show that the results cover the whole gravity spectrum and better than either one of the stand-alone solutions. Variance components estimation performs better than the parametric covariance method in terms of degree RMS curve, the relative weights ratio between SST and SGG, and the number of iterations. However, the conclusion only validates for this particular experiment as a tool kit. Since the two data sets may not be combinable, in general, by no means do the results imply any qualified conclusions of the PC and VC methods. Thus, the actual application of the optimal weighting approaches will be taken into consideration in the future investigation.

Acknowledgements. The authors would like to thank TU Munich for providing CHAMP orbit data. Dr. Steve Klosko and other two anonymous reviewers are highly appreciated for their valuable remarks.

References

- Bouman, J. (2000); *Quality Assessment of Satellite-Based Global Gravity Field Models*. Ph.D. thesis, Netherlands Geodetic Commission, The Netherlands.
- Ditmar, P., P. Visser, and R. Klees (2003); On the Joint Inversion of SGG and SST data from the GOCE Mission. *Advances in Geosciences*, vol. 1 (1): pp. 87–94.
- Gerlach, C., N. Sneeuw, P. Visser, and D. Švehla (2003); CHAMP Gravity Field Recovery Using the Energy Balance Approach. *Advances in Geosciences*, vol. 1: pp. 73–80.
- Kaula, W. M. (1966); *Theory of Satellite Geodesy*. Blaisdell Publishing Company, Waltham Massachusetts.
- Klees, R., R. Koop, P. Visser, and J. van den IJssel (2000); Efficient Gravity Field Recovery from GOCE Gravity Gradient Observations. *Journal of Geodesy*, vol. 74: pp. 561–571.
- Koch, K. R. and J. Kusche (2002); Regularization of Geopotential Determination from Satellite Data by Variance Components. *Journal of Geodesy*, vol. 76: pp. 259–268.
- Lemoine et al. (1998); *The Development of the Joint NASA GSFC and NIMA Geopotential Model EGM96*. Nasa/tp-1998-206861, NASA Goddard Space Flight Center, Greenbelt, USA.
- Lerch, F. J. (1989); *Optimum Data Weighting and Error Calibration for Estimation of Gravitational Parameters*. Technical Memorandum 100737, Goddard Space Flight Center, NASA, Greenbelt, Maryland.
- Pail, R. and G. Plank (2004); GOCE Gravity Field Processing Strategy. *Studia Geophysica et Geodaetica*, vol. 48 (2): pp. 289–309.
- Rummel, R., M. van Gelderen, R. Koop, E. Schrama, F. Sansò, M. Brovelli, F. Migliaccio, and F. Sacerdote (1993); *Spherical Harmonic Analysis of Satellite Gradiometry*. New Series 39, Netherlands Geodetic Commission, the Netherlands.
- Sneeuw, N. (2000a); Dynamic Satellite Geodesy on the Torus: Block-Diagonality from a Semi-Analytical Approach. *Gravity, Geoid, and Geodynamics 2000*, (edited by M. Sideris), vol. 123, pp. 137–142. IAG, Springer-Verlag.
- Sneeuw, N. (2000b); *A Semi-Analytical Approach to Gravity Field Analysis from Satellite Observations*. Dissertation, der Technischen Universität München, Deutsche Geodätische Kommission. Reihe A, Nr. 527.
- Weigelt, M. (2006); *Global and Local Gravity Field Recovery from Satellite-to-Satellite Tracking*. Ph.D. thesis, Dept. of Geomatics Engineering, University of Calgary.
- Xu, C., N. Sneeuw, and M. G. Sideris (2006); The Torus Approach in Spaceborne Gravimetry. *Challenge and Role of Modern Geodesy*, (edited by P. L. Xu), vol. 130. IAG, Springer. Accepted.

Spectral assessment of recently released CHAMP and GRACE satellite-only Earth gravity models

D. Tsoulis, K. Patlakis

Department of Geodesy and Surveying, Aristotle University of Thessaloniki, Fax: +30 2310 995948, Email: tsoulis@topo.auth.gr

Abstract. In the present study we consider some of the current satellite-only models based on the analysis of CHAMP and GRACE orbital data, computed and released mainly from Geoforschungszentrum Potsdam. In order to obtain a first quantification of their spectral characteristics, a selection of spectral quantities were computed for all of the considered models, namely correlation coefficient per degree, smoothing per degree, and percentage change by degree. Furthermore, typical geodetic measures in computing different geopotential functionals, such as RMS geoid undulation and gravity anomaly difference curves have also been evaluated for the same models, using the combined model EGM96 as reference. The comparisons quantified the level of agreement between different CHAMP-only, GRACE-only and combined models, defining the specific bandwidths where the respective correlations take place.

Keywords. CHAMP, GRACE, satellite-only models, combined models, spectral assessment

1 Introduction

Based on the detected orbit perturbations and the tracking observations the analysis of CHAMP or GRACE data gathered over finite time periods leads to the computation of new satellite-only Earth gravity models, e.g., Reigber et al. (2003), Tapley et al. (2005). Currently, Geoforschungszentrum Potsdam alone has released up to now a total of 4 different CHAMP-only models, 2 GRACE-only models and 4 combined models, the latter obtained from the merged analysis of CHAMP, GRACE, LAGEOS and surface gravity data. More precisely we examine here the CHAMP models EIGEN-1S, EIGEN-2, EIGEN-3p and EIGEN-CHAMP03S, which differ mainly as to the amount of considered CHAMP data (3 months, 10 months, 3 years and 33 months respectively), the GRACE models EIGEN-GRACE01S and EIGEN-GRACE02S

(39 and 110 days of GRACE tracking data) and the combined models EIGEN-CG01C, EIGEN-CG03C and EIGEN-GL04C (different portions of CHAMP, GRACE, LAGEOS and surface gravity data). An important aspect that has to be addressed is the level of agreement between these different new models. For example, as the aforementioned models are obtained from the same group, through an identical analysis procedure and using the same primary data types (with variable being the time span of the involved satellite observations and consequently the maximum degree and order of the evaluated harmonic coefficients), it would be useful to be able to identify any possible spectral correlations between the respective coefficient sets, and if such a correlation exists, to define the specific spectral bandwidth where it occurs.

2 Spectral assessment tools

GFZ Potsdam delivers the new gravity field solutions in terms of potential harmonic coefficients C_{lm} and S_{lm} (l and m denoting degree and order respectively), up to a specific maximum degree and order accompanied with their respective variances $\sigma_{C_{lm}}$ and $\sigma_{S_{lm}}$, as these were obtained after the completion of the adjustment process. A first spectral presentation of this information can be done by means of the degree variances (or power spectrum) and error degree variances, defined respectively as $\sigma_l^2 = \sum_0^l (C_{lm}^2 + S_{lm}^2)$ and $\hat{\sigma}_l^2 = \sum_0^l (\sigma_{C_{lm}}^2 + \sigma_{S_{lm}}^2)$. Figures 1 and 2 display the power spectrum and the respective error degree variances of all 4 CHAMP-only GFZ models. From this representation it is possible to identify an apparent relation between different models, which are assigned to a specified common methodology. It is clear, that at least in terms of signal power all models present an almost identical variation up to spherical degree 40, whereas their errors fluctuate in a different way along the whole common spectral range (0-

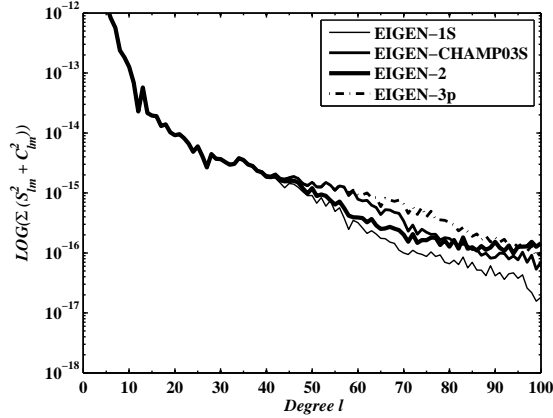


Fig. 1 Degree variances of different CHAMP-only models.

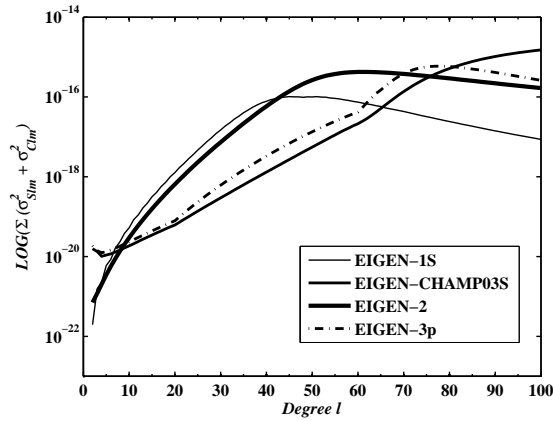


Fig. 2 Error degree variances of different CHAMP-only models.

100).

A further means of assessment that we examine here, is through the computation of so-called RMS anomaly and RMS undulation differences by degree, defined as $\delta g_l = GM/R^2(l-1)(\Delta C_{lm}^2 + \Delta S_{lm}^2)^{1/2}$ and $\delta N_l = R(\Delta C_{lm}^2 + \Delta S_{lm}^2)^{1/2}$ respectively, where $\Delta C_{lm} = (C_{lm}^A - C_{lm}^B)$ and $\Delta S_{lm} = (S_{lm}^A - S_{lm}^B)$ express the differences between corresponding coefficients of two models A and B. Figures 3 and 4 present these computations for the aforementioned CHAMP-only models, computed with respect to EGM96. We observe that the newest CHAMP models gradually tend to decrease their deviations from EGM96 in an almost consistent manner. In order to obtain a more detailed insight to the new models we will consider some

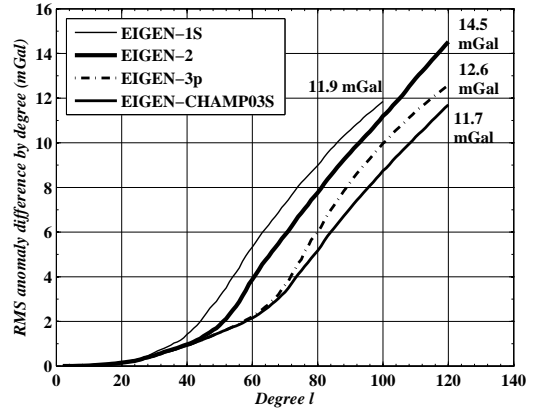


Fig. 3 RMS anomaly difference curves for CHAMP-only models with respect to EGM96.

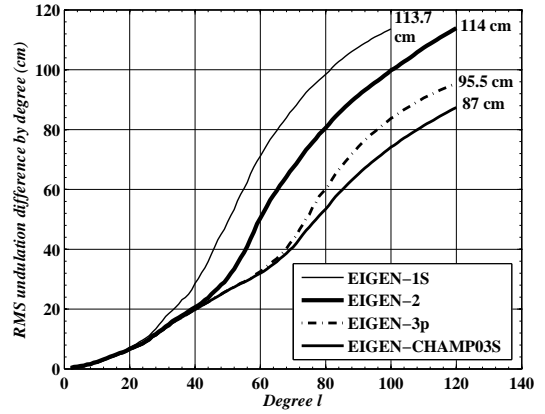


Fig. 4 RMS undulation difference curves for CHAMP-only models with respect to EGM96.

of the available tools for the spectral assessment of different global geopotential solutions (see, e.g., Tscherning 1985, Rapp 1986, Lemoine et al 1998). Thus, we evaluate the correlation by degree

$$\rho_l = \frac{\sum_{m=0}^l (C_{lm}^A C_{lm}^B + S_{lm}^A S_{lm}^B)}{\sqrt{\sigma_l^2(C_{lm}^A, S_{lm}^A) \sigma_l^2(C_{lm}^B, S_{lm}^B)}} \quad (1)$$

where (C_{lm}^A, S_{lm}^A) and (C_{lm}^B, S_{lm}^B) denote the fully normalized spherical harmonic coefficients of two expansions, symbolically expressed here as models A and B, and $\sigma_l^2(C_{lm}^A, S_{lm}^A)$, $\sigma_l^2(C_{lm}^B, S_{lm}^B)$ are the respective degree variances.

The correlation per degree provides a numerical quantification of a direct comparison between the two models, though it can not reflect entirely

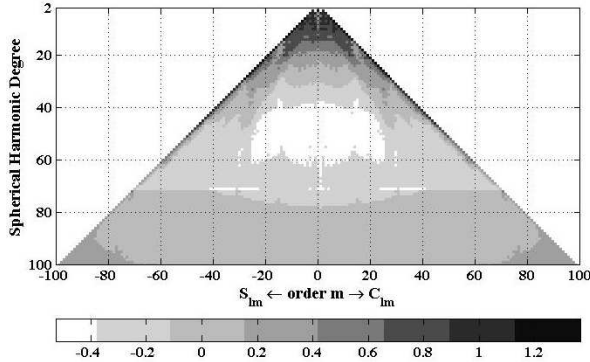


Fig. 5 Gain of CHAMP model EIGEN-1S with respect to EGM96.

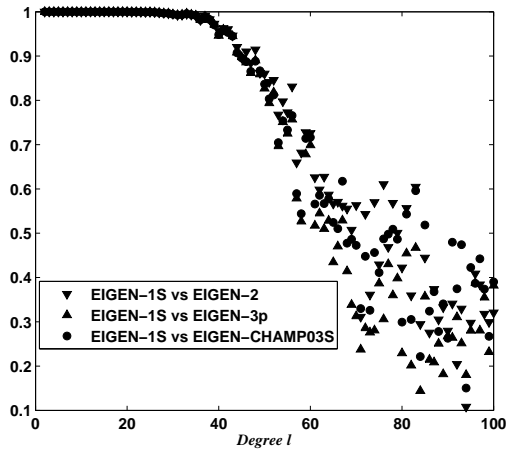


Fig. 6 Correlation by degree of the available GFZ CHAMP-only models.

the agreement or disagreement between them. For example, the computed correlation per degree may indicate a high correlation level between the two sets, even when a dominant scale factor is present in the coefficients. A better comparison measure is obtained from the so called smoothing per degree

$$S_l = \frac{\sum_{m=0}^l (\Delta C_{lm}^2 + \Delta S_{lm}^2)}{\sigma_l^2(C_{lm}^B, S_{lm}^B)} \quad (2)$$

a quantity expressing the degree of smoothing one obtains if model A is subtracted from B (Tscherning 1985). An additional quantity, of special interest for comparative analysis of two models obtained from an identical evaluation algorithm and primary observations is the percent-

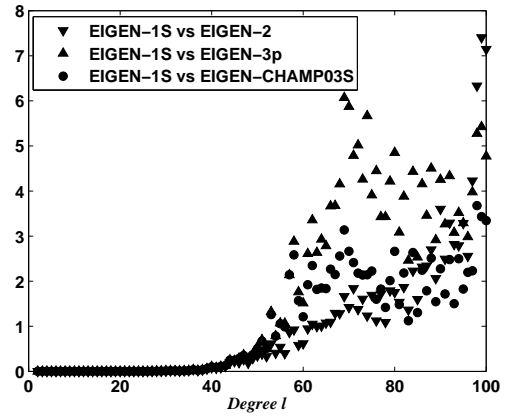


Fig. 7 Smoothing by degree of the available GFZ CHAMP-only models.

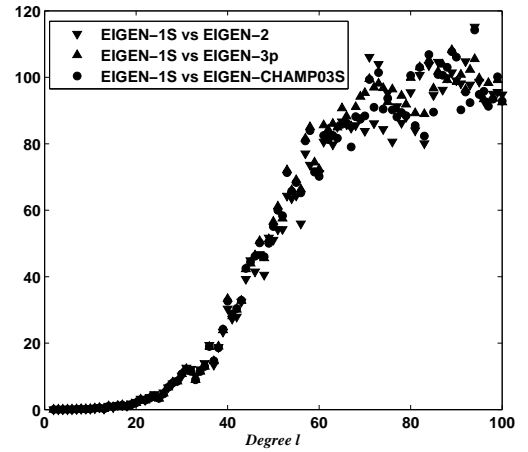


Fig. 8 Percentage difference by degree of the available GFZ CHAMP-only models with respect to model EIGEN-1S.

age difference by degree, given by

$$P_l = \frac{\left[\sum_{m=0}^l (\Delta C_{lm}^2 + \Delta S_{lm}^2) \right]^{1/2}}{\left[\sum_{m=0}^l (C_{lm}^A)^2 + (S_{lm}^A) \right]} \times 100 \quad (3)$$

Finally, we examined the so called *gain*, a relative error measure that expresses the ratio between an existing error spectrum and the error spectrum of a new model, is defined by (Sneeuw, 2000)

$$g_{lm} = \frac{\sigma_{lm}^{old}}{\sigma_{lm}^{new}} \quad (4)$$

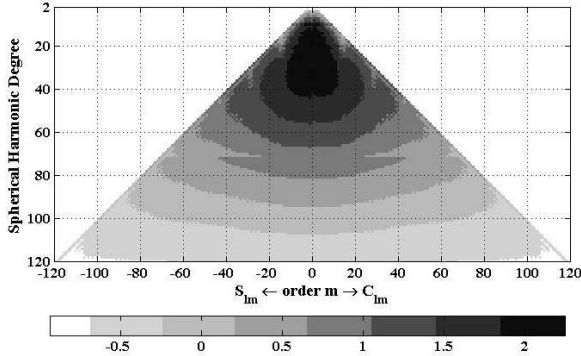


Fig. 9 Gain of GRACE model EIGEN-GRACE01S with respect to EGM96.

and merely quantifies the relation between the error estimates of the existing versus the error estimates of the new gravity model, with σ_{lm}^{old} and σ_{lm}^{new} denoting the variances of the individual coefficients $\sigma_{C_{lm}}$ and $\sigma_{S_{lm}}$. Hence, quantity g_{lm} is computed separately for the C_{lm} 's and the S_{lm} 's and its 2-D graph (e.g., Figures 5 and 9) contains the results for all coefficients.

3 CHAMP-only models

Figures 5-8 display a selection of the aforementioned spectral assessment quantities for the GFZ CHAMP-only models EIGEN-CHAMP03S, EIGEN-3p, EIGEN-2 and EIGEN-1S. The gain of one of these models (EIGEN-1S) was computed with respect to combined model EGM96. This comparison allows to describe the distribution of the change in the error estimates of the EIGEN-1S model with respect to EGM96 in the available degree range 0-100. Although not attempting to perform a one-to-one comparison it can be seen that the largest changes occur mainly over the very low degree range (0-15).

The most useful observation concerns the obtained correlation between the models. For example, we notice an almost perfect coincidence between all 4 models almost up to degree 20, as this is manifested through the combined evaluation of the correlation, smoothing and percentage difference per degree computations. Between degrees 20 and 35 this accordance loses slightly in magnitude, remains however extremely high, with the numerical values of the newer coefficients varying between 5% - 10% with respect to to the corresponding coefficients of EIGEN-1S. Beyond this limit the coefficients of the models released after EIGEN-1S, which has been

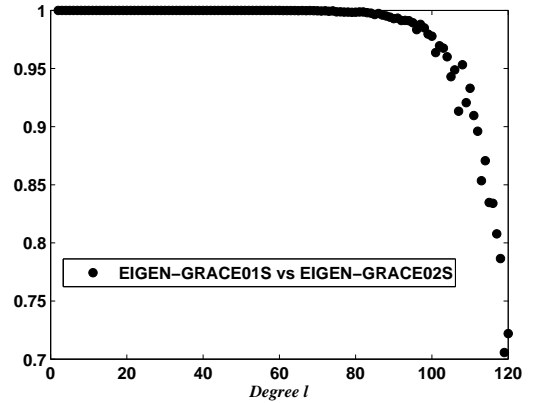


Fig. 10 Correlation by degree of the two available GFZ GRACE-only models EIGEN-GRACE01S and EIGEN-GRACE02S.

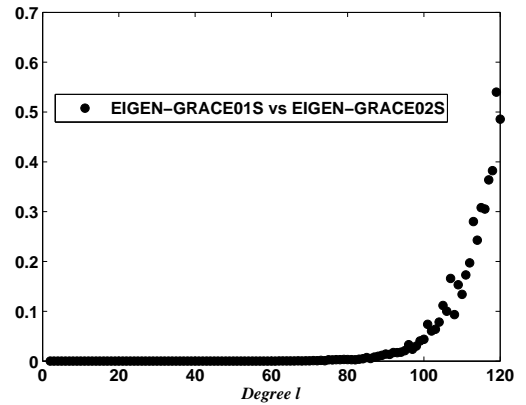


Fig. 11 Smoothing by degree computed as to the two available GFZ GRACE-only models EIGEN-GRACE01S and EIGEN-GRACE02S.

used as the reference model for all EIGEN-CHAMP models, begin to vary considerably with respect to EIGEN-1S. The discrepancy between the EIGEN models becomes more apparent at the degree range 60-100, which demonstrates a more or less expected result, if one considers the extreme variation in the portion of the used satellite data between the different solutions (from the 88 days of tracking and accelerometry data for model EIGEN-1S to the 3,5 years of mission observables for the evaluation of EIGEN-CHAMP03S).

4 GRACE-only models

Figures 9-12 present the respective computations for the only two available GFZ GRACE-

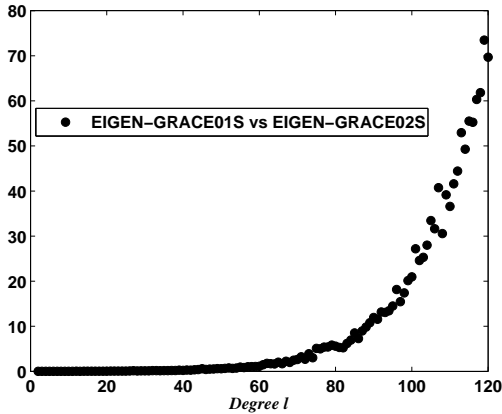


Fig. 12 Percentage difference by degree with respect to the two available GFZ GRACE-only models EIGEN-GRAGE01S and EIGEN-GRACE02S.

only models, namely EIGEN-GRAGE01S and EIGEN-GRACE02S. It is interesting to observe how differently distributed is here the gain of these models with respect to EGM96 compared with Figure 5. As Figure 9 demonstrates the region where the gain is significant is expanded uniformly over a much broader degree range of the common spectrum. The comparisons lead furthermore to the remark that the bandwidth over which the GRACE models exhibit the highest degree of correlation (up to degree 85) is much more broad than the respective degree range which was obtained for the CHAMP only models (0-35). The two models show a remarkable smoothness, while they begin to deviate quantitatively around degree 60, with the percentage difference arriving at values above 70% for degrees approaching 120.

5 Combined models

The comparison strategy for the available combined models should incorporate precedent CHAMP-only or GRACE-only models, depending on the data origin of the individual combined model. From the vast comparison possibilities Figures 13-15 present only a representative quantification of the spectral relations between selected combined models. Thus, Figures 13 and 14 display the correlation and smoothing per degree of GFZ model EIGEN-CG03C, a model complete to degree and order 360, which is obtained from the analysis of over one year of GRACE data. Since CG03C utilized CHAMP

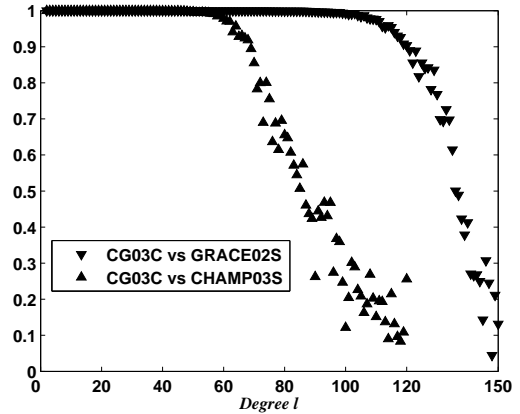


Fig. 13 Correlation per degree of model EIGEN-CG03C computed with respect to models EIGEN-GRACE02S and EIGEN-CHAMP03S.

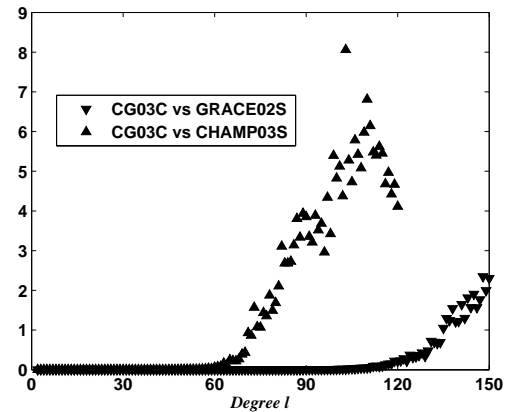


Fig. 14 Smoothing per degree of model EIGEN-CG03C with respect to models EIGEN-GRACE02S and EIGEN-CHAMP03S.

and gravity data as well, it would be plausible to attempt a direct comparison with a CHAMP only model. CHAMP03S is the almost 3 year satellite data CHAMP only model, which has been used for the construction of CG03C. The correlation of the two models up to degree 60 is demonstrated from Figures 13 and 14, however a substantial deviation is observed for the degree range 60-120.

Although referring to satellite only models Figures 15 and 16 present finally the spectral comparison between GRACE only models GGM01S (Tapley et al 2004) and EIGEN-GRACE02S. This particular comparison was selected intentionally, in order to verify whether similar level of agreement, as the one already shown for the GFZ GRACE-only models, could

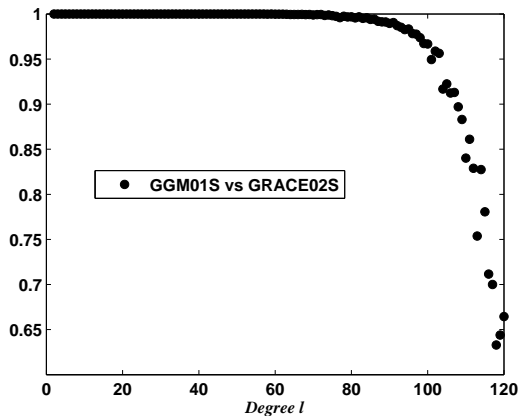


Fig. 15 Correlation by degree of model GGM01S computed with respect to EIGEN-GRACE02S.

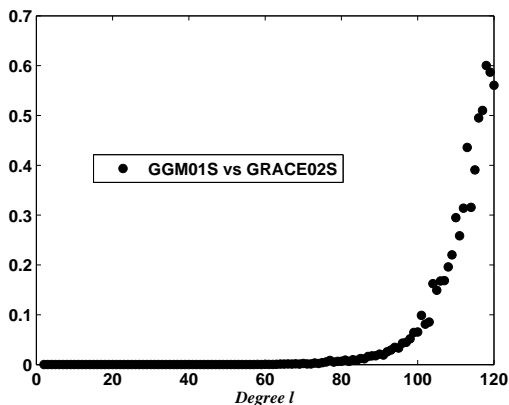


Fig. 16 Smoothing by degree of model GGM01S computed with respect to EIGEN-GRACE02S.

be obtained between GRACE models that were put out by different groups as well. Indeed, Figures 15 and 16 present almost identical characteristics with the corresponding statistics of GFZ's GRACE-only models (Figures 10 and 11).

6 Concluding remarks

Some spectral comparisons were undertaken using a selection of the most recently released satellite only and combined CHAMP and GRACE Earth gravity models. First remarks that can be drawn refer to the high correlation that exists among the GRACE only models within a degree bandwidth of roughly $l < 60$, the CHAMP models showing a significant restriction of the respective correlations to $l < 20$. The second major comment should include a reference to the

spectral behaviour of all models around their upper degree limit (100, 120 or 150). The computations revealed a significant amplification of all test statistics starting around degree 40 and 90 for the CHAMP and GRACE models respectively and obtaining maximum values as soon as the upper boundary of the respective spectral domain is approached. This observation should be directly linked to the overall characteristics of the respective satellite missions, which simply cannot recover data, or equally provide reliable gravity field information beyond a certain frequency.

References

- Lemoine FG and 14 other authors (1998) The Development of the Joint NASA GSFC and the National Imaginery and Mapping Agency (NIMA) Geopotential Model EGM96. NASA/TP-1998-206861, Goddard Space Flight Center, Greenbelt, Maryland
- Rapp RH (1986) Global geopotential solutions, In: Mathematical and Numerical Techniques in Physical Geodesy (Ed: H Stükel), Lecture Notes in Earth Sciences, No 7, 365–416
- Reigber C, Schwintzer P, Neumayer KH, Barthelmes F, König R, Förste C, Balmino G, Biancale R, Lemoine JM, Loyer S, Bruinsma S, Perosanz F, Fayard T (2003) The CHAMP-only Earth gravity field model EIGEN-2, *Advances in Space Research*, 31, 1883–1888
- Sneeuw N (2000) A semi-analytical approach to gravity field analysis from satellite observations, Deutsche Geodätische Kommission, Reihe C, Heft Nr 527, München
- Tapley B, Ries J, Bettadpur S, Chambers D, Cheng M, Condi F, Gunter B, Khang Z, Nagel P, Pastor R, Pekker T, Poole S, Wang F (2005) GGM02 - An improved Earth gravity field model from GRACE, *Journal of Geodesy*, 79, 467–478
- Tapley B, Bettadpur S, Watkins M, Reigber C (2004) The gravity recovery and climate experiment: Mission overview and early results, *Geophysical Research Letters*, 31, doi:10.1029/2004GL019920
- Tscherning CC (1985) On the long-wavelength correlation between gravity and topography, In: Proceedings of the 5th International Symposium 'Geodesy and Physics of the Earth', Magdeburg, 23-29 September 1984, Veröffentlichungen des Zentralinstituts für Physik der Erde, Nr 81, Potsdam, pp 134–142

Gravity Field Modeling on the Basis of GRACE Range-rate Combinations: current results and challenge

Pavel Ditmar, Xianglin Liu¹

DEOS, Delft University of Technology

Kluyverweg 1, P.O. box 5058, 2600 GB Delft, The Netherlands

Abstract. A new approach to gravity field modeling from GRACE KBR data is presented in detail. The functional model explicitly connects gravity field parameters with a linear combination of range-rate measurements at three successive epochs. Unlike the functional model based on inter-satellite accelerations, the new one does not require the radial component of inter-satellite velocity vectors to be determined from GPS data. Performance of the approach is tested with real GRACE data. A 176-day set and a one-month set are separately processed. The mean gravity field model computed from the 176-day data set is as accurate as the GGM01S model. The computed monthly model is 2-3 times less accurate than a model obtained by GFZ. The probable reason for a limited accuracy of the computed monthly model is noise in inter-satellite baselines, which are still determined from GPS data.

Keywords: GRACE, range-rates, Earth's gravity field

1 Introduction

The satellite mission GRACE (Tapley et al., 2004) launched in 2002 opened a new era in studying the global gravity field of the Earth. The mission consists of two satellites flying in formation at a distance of about 200 km from each other. The satellites are equipped with a K-Band Ranging (KBR) system, thanks to which changes in the inter-satellite range are continuously tracked with an accuracy of a few μm . Additionally, the on-board GPS receivers are used to determine satellites' orbits. A number of methods have been developed to model the global or regional gravity field from the KBR data (Rummel, 1979; Rowlands et al., 2002; Ilk et al., 2003; Luthcke et al., 2006; Mayer-Guerr et al., 2006). There are also methods to estimate the parameters of the global Earth's gravity field using both KBR and GPS data (Tapley et al., 2004; Reigber et al., 2005; Jekeli, 1999; Han et al., 2005). Still, the quality of the obtained gravity field models does not match original expectations. Furthermore, some of above mentioned methods, in particular the traditional

dynamic method (Tapley et al., 2004; Reigber et al., 2005), are rather time consuming. Therefore, theoretical investigations must be continued.

A new approach to GRACE KBR data processing is presented in this paper. It is based on the so-called "Range-Rate Combinations (RRC)". This approach makes use of fast spherical harmonic synthesis and co-synthesis algorithm in combination with preconditioned conjugate gradient scheme (Ditmar and van Eck van der Sluijs, 2004). Our starting point was the acceleration approach (Rummel, 1979), which connects the difference of gravitational potential gradients (\mathbf{g}) at the satellite locations with the second-order time derivatives of inter-satellite ranges ρ : $\mathbf{g} \cdot \mathbf{e} = \ddot{\rho} - \mathbf{v}_{\perp}^2 / \rho$, where \mathbf{e} is the unit vector in the Line-Of-Sight (LOS) direction, and \mathbf{v}_{\perp} is the inter-satellite velocity difference projected onto the plane orthogonal to the LOS. The satellite velocities are determined by a numerical differentiation of positions defined on the basis of GPS measurements. The magnitude of the vector \mathbf{v}_{\perp} is quite large: about 250 m/s . Therefore, the contribution of the corresponding term to the overall error budget is very significant, particularly at the low-frequencies according to our experiment [A similar conclusion was also made earlier by Visser et al. (2003) in the context of the energy integral method]. This was the reason for us to develop the RRC approach. The idea behind it is to determine the orthogonal component of inter-satellite velocities directly from KBR-data and, therefore, reduce the influence of GPS data on the overall error budget. The approach is based on a new functional model, which connects a linear combination of 3-D average inter-satellite accelerations with a linear combination of range-rate measurements at three successive epochs.

The structure of the paper is as follows. In Sect. 2, the functional model of the RRC approach is discussed in detail. In Sect. 3, we present an Earth's gravity field model computed from a 176-day data set with the RRC approach. Furthermore, we processed a 1-month data set of August 2003 using both the acceleration approach and the RRC approach. The obtained models

¹The corresponding author: x.l.liu@tudelft.nl

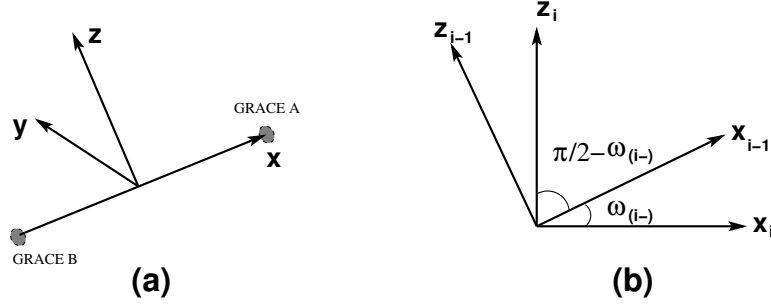


Figure 1: Definitions of the LOSRF (a), the angle $\omega_{(i-)}$ and orientation of the frame at the epoch i relatively to the axes defined for the epoch $i - 1$ (b).

are compared with a GFZ model obtained for the same month. The outcome of the comparison is discussed in the final section 4. Furthermore, this section contains overall conclusions and a discussion of further challenges we face.

2 Derivation of functional model

First of all, let us define a LOS-related Reference Frame (LOSRF) for each particular epoch (Fig.1(a)). In the frame, the x-axis is directed along the LOS, from the trailing satellite to the leading one; the z-axis is orthogonal to the x-axis in the plane formed by two satellites and the center of the Earth, and the y-axis is orthogonal to the x- and z-axis forming a right-hand frame. Thus, x-, y-, and z-axis can be understood as the along-track, cross-track, and radial axis, respectively. Three successive epochs, say $i - 1$, i and $i + 1$, are used to form one observation equation. For the sake of simplicity, assume that the satellites motion is 2-dimensional (i.e. that the inter-satellite velocity vector does not have the cross-track component). Let $\omega_{(i-)}$ be the angle between x-axes at epochs $i - 1$ and i (Fig.1(b)). Similarly, let $\omega_{(i+)}$ be the angle between x-axes at epochs i and $i + 1$. The angles $\omega_{(i-)}$ and $\omega_{(i+)}$ are assumed to be positive. The 3-D average inter-satellite accelerations between the epochs $i - 1$ and i (i.e. $\bar{\mathbf{g}}_{(i-)}$) and between the epochs i and $i + 1$ (i.e. $\bar{\mathbf{g}}_{(i+)}$) are defined as follows:

$$\bar{\mathbf{g}}_{(i-)} = \frac{\int_{t_i - \Delta t}^{t_i} \mathbf{g}(t) dt}{\Delta t}; \quad \bar{\mathbf{g}}_{(i+)} = \frac{\int_{t_i}^{t_i + \Delta t} \mathbf{g}(t) dt}{\Delta t},$$

where $\mathbf{g}(t)$ is the point-wise inter-satellite acceleration as a function of time t , and Δt is the sampling interval. From these definitions, the following equalities hold:

$$\Delta t \cdot \bar{\mathbf{g}}_{(i-)} = \mathbf{v}_i - \mathbf{v}_{i-1}, \quad (1)$$

$$\Delta t \cdot \bar{\mathbf{g}}_{(i+)} = \mathbf{v}_{i+1} - \mathbf{v}_i, \quad (2)$$

where \mathbf{v}_k ($k = i - 1, i, i + 1$) are inter-satellite velocities at three successive epochs. Consider the projections of Eqs. (1) and (2) onto the \mathbf{z}_i axis:

$$\Delta t \cdot \bar{g}_{(i-)}^\perp = v_i^\perp - v_{i-1}^\perp, \quad (3)$$

$$\Delta t \cdot \bar{g}_{(i+)}^\perp = v_{i+1}^\perp - v_i^\perp, \quad (4)$$

where v_k^\perp , $\bar{g}_{(i-)}^\perp$ and $\bar{g}_{(i+)}^\perp$ are the projections of vectors \mathbf{v}_k , $\bar{\mathbf{g}}_{(i-)}$ and $\bar{\mathbf{g}}_{(i+)}$ onto the \mathbf{z}_i axis, respectively, (thus, $v_i^z = v_i^\perp$). By adding Eqs. (3) and (4) together, we have:

$$\Delta t \cdot (\bar{g}_{(i-)}^\perp + \bar{g}_{(i+)}^\perp) = v_{i+1}^\perp - v_{i-1}^\perp. \quad (5)$$

Furthermore, v_{i-1}^\perp can be represented as a linear combination of "locally defined" x- and z-components of the vector \mathbf{v}_{i-1} , i.e. v_{i-1}^x and v_{i-1}^z (with this notation, we imply that the axes x and z correspond to the epoch of the vector under consideration, i.e. $i - 1$):

$$\begin{aligned} v_{i-1}^\perp &= v_{i-1}^x \cdot \cos\left(\frac{\pi}{2} - \omega_{(i-)}\right) + v_{i-1}^z \cdot \cos\omega_{(i-)} \\ &= d_{i-1} \cdot \sin\omega_{(i-)} + v_{i-1}^z \cdot \cos\omega_{(i-)}, \end{aligned} \quad (6)$$

where d_k is the range-rate at the epoch k , see Fig.1(b). Similarly, v_{i+1}^\perp can be represented as a linear combination of v_{i+1}^x and v_{i+1}^z :

$$v_{i+1}^\perp = -d_{i+1} \cdot \sin\omega_{(i+)} + v_{i+1}^z \cdot \cos\omega_{(i+)}. \quad (7)$$

Substitution of Eqs. (6) and (7) into (5) yields:

$$\begin{aligned} \Delta t \cdot (\bar{g}_{(i-)}^\perp + \bar{g}_{(i+)}^\perp) &= -d_{i-1} \cdot \sin\omega_{(i-)} \\ &\quad - d_{i+1} \cdot \sin\omega_{(i+)} - v_{i-1}^z \cdot \cos\omega_{(i-)} \\ &\quad + v_{i+1}^z \cdot \cos\omega_{(i+)}. \end{aligned} \quad (8)$$

Now, let us express v_{i-1}^z and v_{i+1}^z in terms of range-rates and average inter-satellite accelerations. To do

that, we can consider the projection of Eqs. (1) and (2) onto the \mathbf{x}_i axis:

$$\Delta t \cdot \bar{g}_{(i-)}^{\parallel} = v_i^{\parallel} - v_{i-1}^{\parallel} = v_i^x - v_{i-1}^x = d_i - v_{i-1}^{\parallel}; \quad (9)$$

$$\Delta t \cdot \bar{g}_{(i+)}^{\parallel} = v_{i+1}^{\parallel} - v_i^{\parallel} = v_{i+1}^x - d_i, \quad (10)$$

where v_k^{\parallel} , $\bar{g}_{(i-)}^{\parallel}$ and $\bar{g}_{(i+)}^{\parallel}$ are projections of the vectors \mathbf{v}_k , $\bar{\mathbf{g}}_{(i-)}$ and $\bar{\mathbf{g}}_{(i+)}$ onto the \mathbf{x}_i axis, respectively.

Next, v_{i-1}^{\parallel} can be represented as a linear combination of v_{i-1}^x and v_{i-1}^z :

$$v_{i-1}^{\parallel} = d_{i-1} \cdot \cos \omega_{(i-)} - v_{i-1}^z \cdot \sin \omega_{(i-)}. \quad (11)$$

Substitution of Eq. (11) into (9) yields the following expression for v_{i-1}^z .

$$v_{i-1}^z = \frac{\Delta t \cdot \bar{g}_{(i-)}^{\parallel}}{\sin \omega_{(i-)}} - \frac{d_i}{\sin \omega_{(i-)}} + d_{i-1} \cdot \cot \omega_{(i-)}. \quad (12)$$

Similarly, v_{i+1}^{\parallel} can be represented as a linear combination of v_{i+1}^x and v_{i+1}^z :

$$v_{i+1}^{\parallel} = d_{i+1} \cdot \cos \omega_{(i+)} + v_{i+1}^z \cdot \sin \omega_{(i+)}. \quad (13)$$

Then, v_{i+1}^z can be obtained by substituting Eq. (13) into (10):

$$v_{i+1}^z = \frac{\Delta t \cdot \bar{g}_{(i+)}^{\parallel}}{\sin \omega_{(i+)}} + \frac{d_i}{\sin \omega_{(i+)}} - d_{i+1} \cdot \cot \omega_{(i+)}. \quad (14)$$

Now, Eqs. (12) and (14) can be inserted into (8) with the inter-satellite accelerations being arranged in the left-hand side and the range-rates in the right-hand side:

$$\begin{aligned} & \Delta t \cdot \left(\bar{g}_{(i-)}^{\parallel} \cdot \cot \omega_{(i-)} - \bar{g}_{(i+)}^{\parallel} \cdot \cot \omega_{(i+)} \right) \\ & + \Delta t \cdot \left(\bar{g}_{(i-)}^{\perp} + \bar{g}_{(i+)}^{\perp} \right) \\ & = d_i \left(\cot \omega_{(i+)} + \cot \omega_{(i-)} \right) \\ & - \frac{d_{i-1}}{\sin \omega_{(i-)}} - \frac{d_{i+1}}{\sin \omega_{(i+)}}. \end{aligned} \quad (15)$$

After a scaling, which will be explained below, Eq. (15) can be finally written as follows:

$$\begin{aligned} & \Delta t \left[(\tau_{(i+)}) \bar{g}_{(i+)}^{\parallel} - (\tau_{(i-)}) \bar{g}_{(i-)}^{\parallel} - \nu_i (\bar{g}_{(i-)}^{\perp} + \bar{g}_{(i+)}^{\perp}) \right] \\ & = (\epsilon_{(i-)}) d_{i-1} - (\tau_{(i-)} + \tau_{(i+)}) d_i + (\epsilon_{(i+)}) d_{i+1} \end{aligned} \quad (16)$$

with $\nu_i := \frac{2}{(\Delta t)^2} / (\cot \omega_{(i-)} + \cot \omega_{(i+)})$; $\tau_{(i-)} := \nu_i \cdot \cot \omega_{(i-)}$; $\tau_{(i+)} := \nu_i \cdot \cot \omega_{(i+)}$; $\epsilon_{(i-)} := \frac{\nu_i}{\sin \omega_{(i-)}}$ and $\epsilon_{(i+)} := \frac{\nu_i}{\sin \omega_{(i+)}}$. Hereafter, the parameters ν_i ,

$\tau_{(i-)}$, $\tau_{(i+)}$, $\epsilon_{(i-)}$ and $\epsilon_{(i+)}$ are referred to as the navigation parameters.

In a special case of circular satellite orbits, we have: $\omega_{(i-)} = \omega_{(i+)} = \omega_i$; $\nu_i = \frac{\tan \omega_i}{(\Delta t)^2}$; $\tau_{(i-)} = \tau_{(i+)} = \frac{1}{(\Delta t)^2}$, and $\epsilon_{(i-)} = \epsilon_{(i+)} = \frac{1}{(\Delta t)^2 \cos \omega_i}$. If we assume further that the orbit radius approaches infinity, $\tan \omega_i \rightarrow 0$ and $\cos \omega_i \rightarrow 1$. Then, Eq. (16)

turns into: $\frac{\bar{g}_{(i+)}^{\parallel} - \bar{g}_{(i-)}^{\parallel}}{\Delta t} = \frac{d_{i-1} - 2d_i + d_{i+1}}{(\Delta t)^2}$. Thus, the computation of range-rate combinations in this special case, reduces just to the double numerical differentiation of range-rates with the 3-point scheme. In other words, the range-rate combinations become approximately equal to second time-derivatives of range-rates. This explains the scaling applied to Eq. (15).

Eq. (16) defines our functional model, which can be written as a matrix-to-vector multiplication: $\mathbf{A}\mathbf{x} = \mathbf{d}$, where \mathbf{x} is the set of gravity field parameters, \mathbf{d} is the set of range-rate combinations, and \mathbf{A} is a design matrix. The expression in the right-hand side is called hereafter the "observed RRC". For consistency, the expression in the left-hand side is referred to as the "reference RRC". The reference RRCs can be directly related to the parameters of the gravity field (e.g. spherical harmonic coefficients). Then, the set of unknown gravity field parameters can be computed from the range-rate combinations by means of a least-square adjustment.

The functional model is strictly linear, which allows a numerically efficient data processing algorithm (Ditmar and van Eck van der Sluijs, 2004) to be built on its basis. Furthermore, the GRACE KBR-data processing can be easily combined with processing of other satellite data (e.g., 3-D accelerations derived from a satellite orbit as well as satellite gravity gradiometry data).

3 Results of real data processing

The goal of real GRACE data processing was to evaluate the accuracy of a mean and a monthly gravity field model achievable by the RRC approach. Whereas some mean field models obtained with the RRC approach have been already presented (Ditmar and Liu, 2006), the computed monthly models are analysed for the first time. In both cases, the gravity field models up to spherical harmonic degree 150 are derived though we only demonstrate the solutions up to degree 120. A nearly half-year data set (176-day span, from July. 9, 2003 to Dec. 31, 2003) and a one-month data set (August 2003) have been separately processed. Each data set includes: (1) a reduced-dynamic orbit of satellite A (30-sec sampling); (2) relative baseline vectors between satellite A and B (Kroes et al. 2005) (10-sec sampling); (3) non-gravitational accelerations (1-sec

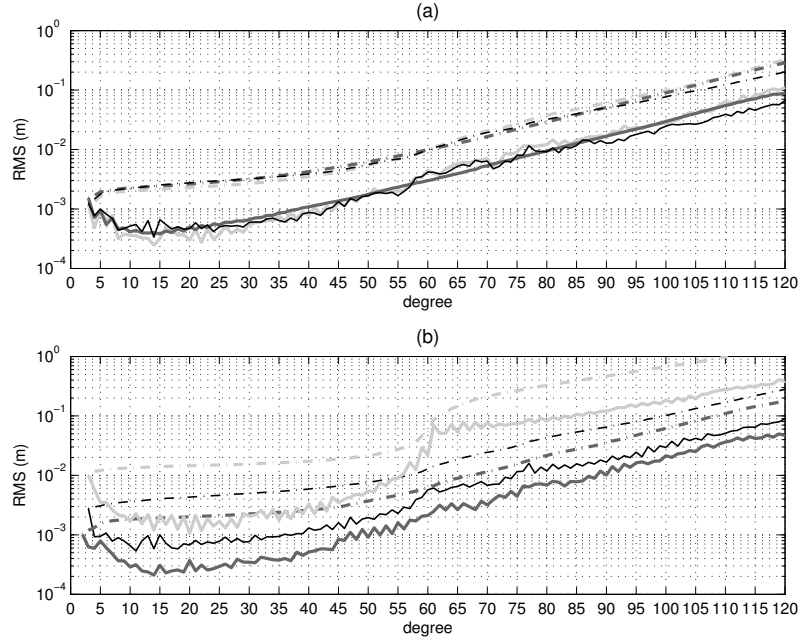


Figure 2: (a): Geoid height difference between our half-year model and EIGEN-CG03C (*thin black line*), between GGM01S and EIGEN-CG03C (*thick grey line*), formal error of GGM01S (*thick black line*). (b): Geoid height difference between our monthly model produced by the RRC approach and EIGEN-CG03C (*thin black line*), between the GFZ monthly model and EIGEN-CG03C (*thick black line*), between the monthly model produced by the acceleration approach and EIGEN-CG03C (*thick grey line*). Cumulative geoid height difference (*dash line*) and geoid height difference per degree (*solid line*) are shown, Degree 2 is excluded.

sampling); (4) quaternion data (5-sec sampling); (5) KBR range-rates (5-sec sampling). The procedure of real data processing is as follows:

- 1) Computation of the navigation parameters. The reduced-dynamic orbit of the satellite A and baseline vectors are rotated into the Celestial Reference Frame (CRF) and then interpolated onto 5-sec intervals. The orbit of the satellite B is obtained by adding baseline vectors to the orbit of satellite A. The angles $\omega_{(i-)}$ and $\omega_{(i+)}$ are computed from the baselines, and navigation parameters are therefore calculated from these angles.
- 2) Computation of the observed RRCs. The range-rates and the navigation parameters are used to calculate the observed RRCs. Furthermore, we account for minor deviations of the actual setup from the 2-D case by adding small corrections to the range-rate data. These corrections are computed on the basis of satellite orbits derived from the GPS data. Importantly, these corrections are so small that their contribution to the error budget is totally negligible.
- 3) Computation of the reference RRCs. The point-wise accelerations are firstly computed on the basis of a reference gravity field model along the orbits of two satellites. Temporal variation caused by tides, as well as by atmospheric and ocean mass changes, are also considered (Ditmar and Liu, 2006). These point-wise accelerations are then rotated into the CRF, and an averaging filter is applied (Ditmar and van Eck van der Sluijs, 2004). The averaged accelerations projected onto the corresponding \mathbf{x}_i and \mathbf{z}_i axes together with the navigation parameters are used to calculate the reference RRCs.
- 4) Computation of non-gravitational RRCs. Non-gravitational accelerations of two satellites are firstly rotated into the CRF. Then, the non-gravitational RRCs are computed similarly to step 3.
- 5) Computation of residual RRCs. The residual RRCs are obtained by subtraction of the reference and non-gravitational RRCs from the observed ones.
- 6) Least-square adjustment. Inversion of residual RRCs into corrections to the spherical harmonic coefficients of the reference model is implemented

with a frequency-dependent data weighting scheme. As described in (Ditmar et al. 2006), relatively high weights are assigned to low frequencies and low weights to high frequencies. Scale factors in non-gravitational RRCs, as well as biases, are estimated on daily intervals simultaneously. No regularization is applied in the inversion, which means that the solution is completely unconstrained, [like e.g. the GGM01S model (Tapley et al., 2004)].

The difference between the model computed from the half-year data set and the EIGEN-CG03C model (Förste et al., 2005) is shown in terms of geoid height in Fig.2(a). For comparison, the difference between GGM01S and EIGEN-CG03C models, as well as the formal error of GGM01S model are also shown (The GGM01S model is an early result produced from the data span of April to November 2002). It should be mentioned that EIGEN-CG03C and GGM01S models are computed from KBR and GPS data, while our model is produced from KBR range-rates only. As can be seen from Fig.2(a), our model and GGM01S are equally accurate at degrees 30-70. Starting from degree 70, our model is closer to EIGEN-CG03C model than GGM01S. However, our model shows a somewhat lower accuracy at low degrees (below 30). Noteworthy, it is not completely fair to compare these two models, since they are computed from different data intervals with a different amount of data. The GGM01S made use of longer data span (6-7 months) than our model (176 days). On the other hand, our model is obtained from somewhat more data (155 days) than GGM01S (111 days).

The difference between our monthly model and the EIGEN-CG03C model is also shown in terms of geoid heights, see Fig.2(b). The difference between the GFZ monthly model of August 2003 and EIGEN-CG03C is demonstrated as well. For further comparison, we have processed the same data span (August 2003) by using the acceleration approach. The data processing methodology in the acceleration approach is somewhat similar to that in the RRC approach, though the functional model is, naturally, different. As can be seen from Fig.2(b), the model produced by the RRC approach is significantly better than that computed with the acceleration approach: 2-3 times at low degrees (below 55), and 8-10 times at higher degrees (above 55). Nevertheless, the RRC approach solution is 2-3 times less accurate than the GFZ monthly model.

4 Discussion and conclusions

There might be various reasons for a limited accuracy of our solutions, particularly the monthly one. For

example, there are minor differences in using temporal geophysical phenomena models between our and GFZ's processing schemes (Flechtner, 2005). Furthermore, our choice of nuisance parameters for accelerometer data may not be optimal. We believe, however, that the dominant reason is noise in navigation parameters. In order to support this statement, we have simulated a synthetic data set similar to the one described by (Ditmar and Liu, 2006), and then added a noise with 1-mm standard deviation and the auto-correlation factor of 0.995 to the inter-satellite baseline vectors. The range-rates were assumed to be noise-free. Then, we computed a set of noise-free navigation parameters from 'true baselines' and a set of noisy navigation parameters from 'noisy baselines'. Both sets of navigation parameters together with the reference accelerations computed on the basis of the true model along the noisy orbits were used to compute the residual RRCs. For a reference, we have also computed the RRCs from the difference between the GFZ monthly model and the EIGEN-CG03C model. The latter RRCs give an indication of the expected magnitude of temporal gravity field variations (particularly, those related to the hydrological processes).

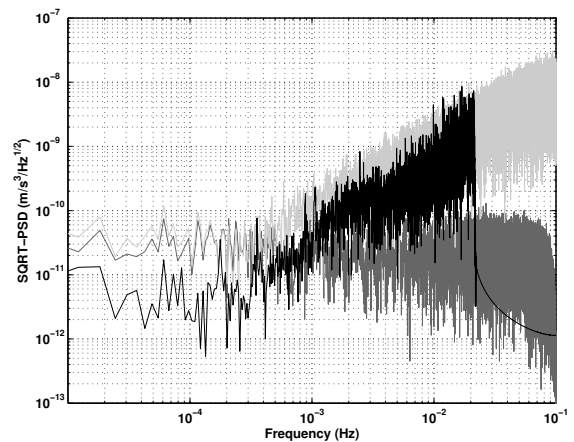


Figure 3: Square root of noise Power Spectral Density (PSD) of RRCs computed from the noise-free navigation parameters (*grey*) and the noisy navigation parameters (*light-grey*). For a reference, the square-root PSD of the residual gravity field signal of August 2002 in RRCs is shown (*black*).

From Fig. 3, it is obvious that the noise propagated from navigation parameters can be comparable to or even larger than the magnitude of temporal gravity field variations. This may explain why our monthly model is less accurate than the GFZ one. We believe there are at least two ways to reduce noise propagated

from the navigation parameters: one is to smooth the navigation parameters, and the other one is to choose a longer sampling interval. Furthermore, we consider a modification of the functional model in such a way that the navigation parameters themselves are primarily derived from KBR data. We intend to present this functional model in a forthcoming publication.

Acknowledgements

We thank Ejo Schrama for his DINGO software used for the orbit simulation. We are grateful to P. Visser, R. Kroes and T. van Helleputte for providing us with GRACE baselines. Most of the computations were done on the SGI Altix 3700 super-computer in the framework of the grant SG-027, which was provided by "Stichting Nationale Computerfaciliteiten" (NCF). The support of NCF is gratefully acknowledged.

References

- P. Ditmar, R. Klees and X. Liu. Frequency-dependent data weighting in global gravity field modeling from satellite data contaminated by non-stationary noise. *Journal of Geodesy*, on-line, 2006. doi:10.1007/s00190-006-0074-4
- P. Ditmar and A. A. van Eck van der Sluijs. A technique for Earth's gravity field modeling on the basis of satellite accelerations. *Journal of Geodesy*, 78:12-33, 2004.
- P. Ditmar and X. Liu. Gravity field modeling on the basis of GRACE range-rate combinations. *The Proceedings of the "VI Hotine-Marussi Symposium of Theoretical and Computational Geodesy: Challenge and Role of Modern Geodesy"*. May 29 - June 2, 2006, Wuhan, China, accepted.
- C. Foerste, F. Flechtner, R. Schmidt, U. Meyer, R. Stubenvoll, F. Barthelmes, R. Koenig, K.H. Neumayer, M. Rothacher, Ch. Reigber, R. Biancale, S. Bruinsma, J.-M. Lemoine, J.C. Raimondo. A New High Resolution Global Gravity Field Model Derived From Combination of GRACE and CHAMP Mission and Altimetry/Gravimetry Surface Gravity Data Poster presented at EGU General Assembly 2005, Vienna, Austria, 24-29, April 2005
- F. Flechtner. *GFZ Level-2 Processing Standards Document for Level-2 Product Release 0003*. 2005. GRACE 327-743 (GR-GFZ-STD-001) Gravity Recovery and Climate Experiment.
- S.-C. Han, C. K. Shum, C. Jekeli, and D. Alsdorf. Improved estimation of terrestrial water storage changes from GRACE. *Geophysical Research Letters*, 32, 2005. L07302, doi: 10.1029/2005GL022382.
- K. H. Ilk, M. Feuchtinger, and T. Mayer-Gürr. Gravity field recovery and validation by analysis of short arcs of a satellite-to-satellite tracking experiment as CHAMP and GRACE. In *Proceedings of the IAG Symposium G02, IUGG General Assembly 2003, Sapporo, Japan*. 2003.
- C. Jekeli. The determination of gravitational potential differences from satellite-to-satellite tracking. *Celestial Mechanics and Dynamical Astronomy*, 75:85-101, 1999.
- S. B., Luthcke, D. D. Rowlands, F. G. Lemoine, S. M. Klosko, D. S. Chinn, J.J. McCarthy. Monthly spherical harmonic gravity field solutions determined from GRACE inter-satellite range-rate data alone. *Geophysical Research Letters*, 33, L02402, doi: 10.1029/2005GL024846, 2006.
- P. Visser, N. Sneeuw, C. Gerlach. Energy integral method for gravity field determination from satellite orbit coordinates. *Journal of Geodesy*, 77: 207-216, 2003. doi:10.1007/s00190-003-0315-8.
- R. Kroes, O. Montenbruck, W. Bertiger, and P. Visser. Precise GRACE baseline determination using GPS. *GPS Solutions*, 9(1):21-31, 2005. doi:10.1007/s10291-004-0123-5.
- T. Mayer-Gürr, A. Eicker, K.H. Ilk. ITG-GRACE02s: A GRACE gravity field derived from short arcs of the satellite's orbit. *The Proceedings of the "1st international symposium of the international gravity field service (IGFS): Gravity Field of the Earth"*. Aug 28 - Sept 1, 2006, Istanbul, Turkey, submitted.
- C. Reigber, R. Schmidt, F. Flechtner, R. König, U. Meyer, K.-H. Neumayer, P. Schwintzer, and S. Y. Zhu. An earth gravity field model complete to degree and order 150 from GRACE: EIGEN-GRACE02S. *Journal of Geodynamics*, 39:1-10, 2005.
- D. D. Rowlands, R. D. Ray, D. S. Chinn and F. G. Lemoine. Short-arc analysis of intersatellite tracking data in a gravity mapping mission. *Journal of Geodesy*, 76: 307-316, 2002.
- R. Rummel. Determination of short-wavelength components of the gravity field from satellite-to-satellite tracking or satellite gradiometry - an attempt to an identification of problem areas. *Man. Geodyn.*, 4 (2):107-148, 1979.
- B. D. Tapley, S. Bettadpur, M. Watkins, and C. Reigber. The gravity recovery and climate experiment: Mission overview and early results. *Geophysical Research Letters*, 31, 2004. L09607, doi: 10.1029/2004GL019920.

High-Degree Geopotential Model Tailored to Egypt

Hussein A. Abd-Elmotaal
Civil Engineering Department, Faculty of Engineering,
Minia University, Minia 61111, Egypt
abdelmotaal@lycos.com

Abstract. The quality of the reference geopotential model used in the framework of the remove-restore technique greatly affects the accuracy of the computed geoid. None of the existing geopotential models fit the Egyptian gravity field to the desired extent. The aim of this investigation is to have a smoothed gravity field so that it is unbiased and has significantly reduced variance by using a high-degree tailored geopotential model. The window technique has been applied to get rid of the double consideration of the topographic-isostatic masses within the data window. The high-degree tailored reference model has been created by merging the available gravity anomalies in the area of investigation with the EGM96 global gravitational data set. The merged global field has been used to estimate the harmonic coefficients of the tailored reference model by FFT technique using an iteration process to enhance the accuracy of the obtained harmonic coefficients (Abd-Elmotaal, 2004). Three different tailored geopotential models have been created by maintaining the lower harmonics till degree 20, 36 and 72 to their values as of EGM96 model. The results show that the tailored geopotential models give better residual gravity anomalies. The variance has dropped to its one third.

Keywords. geopotential models, harmonic analysis, window technique, Egypt, geoid determination.

1 Introduction

The quality of the reference geopotential model used in the framework of the remove/restore technique plays a great role in estimating the accuracy of the computed geoid. In other words, if the residual field is biased and has a high RMS, then using such a biased/high variance field in the geoid computation process gives less accurate interpolated quantities, and hence worse geoid fitting to the GPS-levelling

derived geoid. Practical studies so far have proved that none of the existing reference geopotential models fit the Egyptian gravity field to the desired extent. Thus, the main aim of this investigation is to have a smoothed gravity field (in terms of gravity anomalies) so that it is, more or less, unbiased and has a significantly reduced variance by using a high-degree tailored reference geopotential model.

The used data sets are described first. The window technique (Abd-Elmotaal and Kühtreiber, 2003) within the remove/restore technique has been outlined. The local gravity anomalies for the Egyptian data window are gridded in $30' \times 30'$ grid using the remove/restore window technique. The local gridded data are merged with the global $30' \times 30'$ gravity anomalies, computed using EGM96 till $N = 360$, to establish the data set for computing the tailored geopotential models. The merged $30' \times 30'$ global field has been then used to estimate the harmonic coefficients of the tailored reference model by an FFT technique (Abd-Elmotaal, 2004). Three different tailored geopotential models have been created by restoring the low order harmonics of EGM96 till $N = 20, 36$ and 72 . A wide comparison among the developed tailored geopotential models and EGM96 geopotential model has been carried out.

It should be noted that many scholars have tried to compute tailored geopotential models to best suit their specific areas of interest. For example, Wenzel (1998) has computed a set of tailored geopotential models for Europe.

2 The Data

2.1 Local Egyptian Free-Air Gravity Anomalies

All currently available sea and land free-air gravity anomalies for Egypt and neighbouring countries have

been merged. A scheme for gross-error detection has been carried out. Figure 1 shows the distribution of the free-air gravity anomalies for Egypt used for the current investigation. The distribution of the free-air gravity anomaly stations on land is very poor, concentrated mainly along the Nile valley. Many areas are empty.

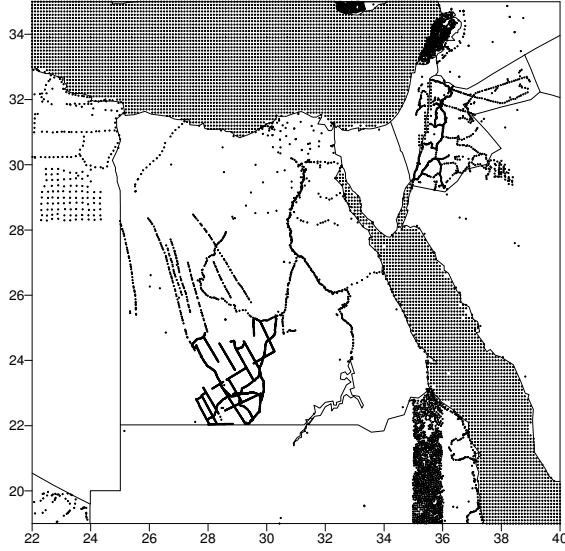


Figure 1. Distribution of the local Egyptian free-air gravity anomalies.

The values of the free-air gravity anomalies range between -190.51 mgal and 294.74 mgal with an average of -3.28 mgal and a standard deviation of about 60.36 mgal. Highest values are in sea area.

2.2 Digital Height Models

For the terrain reduction computation, a set of fine and coarse Digital Height Models DHM's is needed. The fine EGHA9930 $30'' \times 30''$ and the coarse EGHA99M3 $3' \times 3'$ DHM's (Abd-Elmotaal, 1999) are used for the current investigation. They cover the window $19^\circ \leq \phi \leq 35^\circ$, $22^\circ \leq \lambda \leq 40^\circ$. Figure 2 illustrates the EGHA9930 fine DHM.

3 The Window Technique

Within the well-known remove/restore technique, the effect of the topographic-isostatic masses is removed from the source gravitational data and then restored to the resulting geoidal heights. For example, in the case of gravity data, the reduced gravity anomalies in the framework of the remove/restore technique is

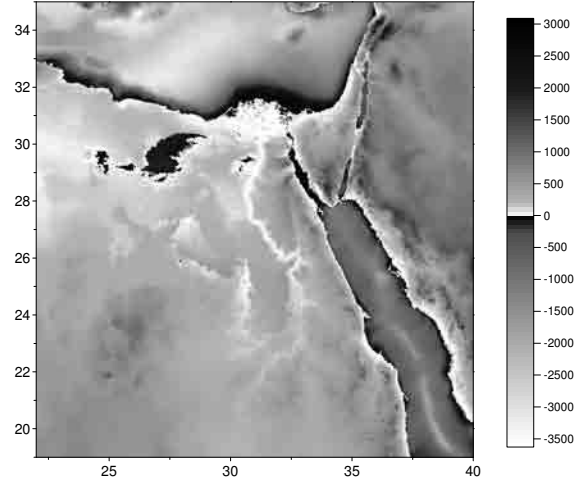


Figure 2. The $30'' \times 30''$ EGHA9930 Digital Height Model (after Abd-Elmotaal, 1999).

computed by

$$\Delta g = \Delta g_F - \Delta g_h - \Delta g_{Ref}, \quad (1)$$

where Δg_F stands for the free-air anomalies, Δg_h is the effect of topography and its compensation on the gravity anomalies, and Δg_{Ref} is the effect of the reference field on the gravity anomalies. Thus the final computed geoid N within the remove/restore technique can be expressed by:

$$N = N_{Ref} + N_{\Delta g} + N_h, \quad (2)$$

where N_{Ref} gives the contribution of the reference field, $N_{\Delta g}$ gives the contribution of the reduced gravity anomalies, and N_h gives the contribution of the topography and its compensation.

The conventional way of removing the effect of the topographic-isostatic masses faces a theoretical problem. A part of the influence of the topographic-isostatic masses is removed twice as it is already included in the global reference field. This leads to some double consideration of that part of the topographic-isostatic masses. Figure 3 shows schematically the conventional gravity reduction for the effect of the topographic-isostatic masses. The short-wavelength part depending on the topographic-isostatic masses is computed for a point P for the masses inside the circle. Removing the effect of the long-wavelength part by a global earth's gravitational potential reference field normally implies removing the influence of the global topographic-isostatic masses, shown as a rectangle in Fig. 3. The double

consideration of the topographic-isostatic masses inside the circle (double hatched) is then seen.

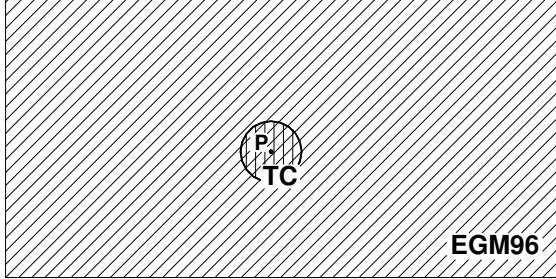


Figure 3. The traditional remove/restore technique.

A possible way to overcome this difficulty is to adapt the used reference field due to the effect of the topographic-isostatic masses for a fixed data window. Figure 4 shows the advantage of the window remove/restore technique schematically. Consider a measurement at point P , the short-wavelength part depending on the topographic-isostatic masses is now computed by using the masses of the whole data area (small rectangle). The adapted reference field is created by subtracting the effect of the topographic-isostatic masses of the data window, in terms of potential coefficients, from the reference field coefficients. Thus, removing the long-wavelength part by using this adapted reference field does not lead to a double consideration of a part of the topographic-isostatic masses (no double hatched area in Fig. 4).

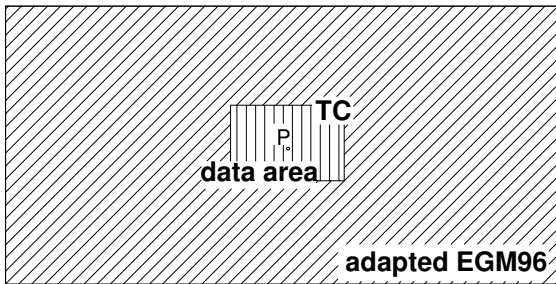


Figure 4. The window remove/restore technique.

The reader who is interested in computing the harmonic coefficients of the topographic-isostatic potential of the data window is kindly referred to (Abd-Elmotaal and Kühtreiber, 2003).

4 Gravity Anomalies

The available gravity anomalies within the local Egyptian window ($19^\circ \leq \phi \leq 35^\circ$, $22^\circ \leq \lambda \leq 40^\circ$)

Table 1. Statistics of the three gravity anomalies fields

gravity anomalies type	statistical parameters			
	min. mgal	max. mgal	average mgal	st. dev. mgal
Global (EGM96)	-329.5	403.4	-0.50	29.7
Local (Egypt)	-173.2	198.9	1.10	40.0
Merged (EGM96 + Egypt)	-329.5	403.4	-0.51	29.7

have been interpolated in $30' \times 30'$ grid using the window remove/restore technique. Figure 5 shows the local Egyptian $30' \times 30'$ interpolated anomalies.

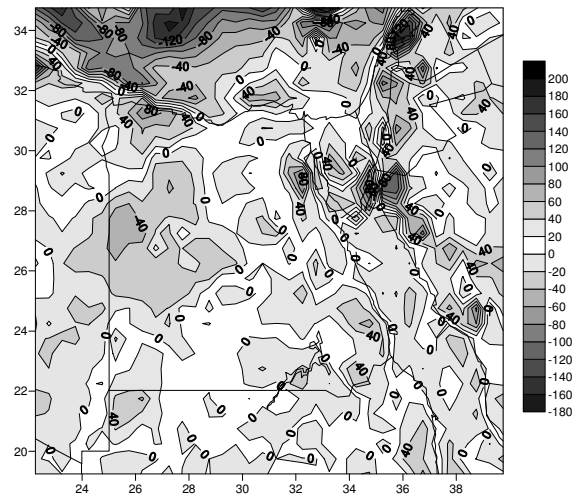


Figure 5. The local Egyptian $30' \times 30'$ interpolated gravity anomalies.

The EGM96 geopotential model till $N = 360$ has been used to create $30' \times 30'$ global gravity anomalies. The local Egyptian $30' \times 30'$ interpolated gravity anomalies using the window remove/restore technique has been merged with the created $30' \times 30'$ global gravity anomalies forming the data set for computing the tailored geopotential models. Table 1 illustrates the statistics of the three gravity anomalies fields. The statistics show that merging the Egyptian gravity anomalies data set has a minor effect on the global gravity field. Only the high-order harmonics would then change.

5 Tailored Geopotential Models for Egypt

Let us consider an analytical function $f(\theta, \lambda)$ defined on the unit sphere ($0 \leq \theta \leq \pi$ and $0 \leq \lambda \leq 2\pi$). Ex-

and $f(\theta, \lambda)$ in series of surface spherical harmonics

$$f(\theta, \lambda) = \sum_{n=0}^{\infty} \sum_{m=0}^n (\bar{C}_{nm} \cos m\lambda + \bar{S}_{nm} \sin m\lambda) \bar{P}_{nm}(\cos \theta), \quad (3)$$

where \bar{C}_{nm} and \bar{S}_{nm} are the fully normalized spherical harmonic coefficients and $\bar{P}_{nm}(\cos \theta)$ refers to the fully normalized associated Legendre function. Let us introduce the abbreviations

$$\begin{aligned} \bar{R}_{nm}(\theta, \lambda) &= \bar{P}_{nm}(\cos \theta) \cos m\lambda, \\ \bar{Q}_{nm}(\theta, \lambda) &= \bar{P}_{nm}(\cos \theta) \sin m\lambda. \end{aligned} \quad (4)$$

It is well known that the fully normalized harmonic coefficients are orthogonal, i.e., they satisfy the orthogonality relations

$$\iint_{\sigma} \bar{R}_{nm}(\theta, \lambda) \bar{R}_{n'm'}(\theta, \lambda) d\sigma = 0 \quad (5)$$

$$\iint_{\sigma} \bar{Q}_{nm}(\theta, \lambda) \bar{Q}_{n'm'}(\theta, \lambda) d\sigma = 0 \quad (6)$$

$$\iint_{\sigma} \bar{R}_{nm}(\theta, \lambda) \bar{Q}_{nm}(\theta, \lambda) d\sigma = 0, \quad (7)$$

$$\frac{1}{4\pi} \iint_{\sigma} \bar{R}_{nm}^2(\theta, \lambda) = \frac{1}{4\pi} \iint_{\sigma} \bar{Q}_{nm}^2(\theta, \lambda) = 1. \quad (8)$$

As a consequence of the orthogonality, the fully normalized harmonic coefficients \bar{C}_{nm} and \bar{S}_{nm} can be given by (Heiskanen and Moritz, 1967, p. 31)

$$\begin{aligned} \bar{C}_{nm} &= \frac{1}{4\pi} \iint_{\sigma} f(\theta, \lambda) \bar{R}_{nm}(\theta, \lambda) d\sigma, \\ \bar{S}_{nm} &= \frac{1}{4\pi} \iint_{\sigma} f(\theta, \lambda) \bar{Q}_{nm}(\theta, \lambda) d\sigma. \end{aligned} \quad (9)$$

In fact, (9) cannot be used in practice to compute the harmonic coefficients simply because the analytical function $f(\theta, \lambda)$ is generally unavailable. Only a finite set of noisy measurements $f(\theta_i, \lambda_j)$, covering the whole sphere, might be available. Discretizing (9) on an equal angular grid covering the whole sphere gives the following quadratures formula

$$\begin{aligned} \hat{C}_{nm} &= \frac{1}{4\pi} \sum_{i=0}^{N-1} \sum_{j=0}^{2N-1} f(\theta_i, \lambda_j) \bar{R}_{nm}(\theta_i, \lambda_j) \Delta_{ij}, \\ \hat{S}_{nm} &= \frac{1}{4\pi} \sum_{i=0}^{N-1} \sum_{j=0}^{2N-1} f(\theta_i, \lambda_j) \bar{Q}_{nm}(\theta_i, \lambda_j) \Delta_{ij}, \end{aligned} \quad (10)$$

where \hat{C}_{nm} and \hat{S}_{nm} are the estimate of \bar{C}_{nm} and \bar{S}_{nm} ,

respectively, Δ_{ij} indicates the segment area and N is the number of grid cells in the latitude direction. Expression (10) is used to compute the harmonic coefficients if the available data field is represented by a set of point values $f(\theta_i, \lambda_j)$. It should be noted that (10) is usually only an *approximation* due to the discretization effect of $f(\theta, \lambda)$.

If all \bar{C}_{nm} and \bar{S}_{nm} are known till degree and order N_{max} , one can compute $\tilde{f}(\theta_i, \lambda_j)$ as follows:

$$\begin{aligned} \tilde{f}(\theta_i, \lambda_j) &= \sum_{n=0}^{N_{max}} \sum_{m=0}^n (\bar{C}_{nm} \cos m\lambda_j + \\ &+ \bar{S}_{nm} \sin m\lambda_j) \bar{P}_{nm}(\cos \theta_i), \end{aligned} \quad (11)$$

which can be regarded as an *approximation* to $f(\theta, \lambda)$ at point (θ_i, λ_j) . Expression (11) defines the object of spherical harmonic synthesis: given the coefficients, it is required to estimate the function.

The double summation appearing in (10) for harmonic analysis as well as in (11) for spherical harmonic synthesis are computed using FFT. Colombo (1981) has written two subroutines for this purpose, called HARMIN and SSSYNTH. Abd-Elmotaal (2004) has written a program called HRCOFITR, which uses Colombo's subroutines, after great modifications, in an iteration process to obtain the best coefficients accuracy and minimum residual filed either the given filed is on sphere or on ellipsoid.

The merged $30' \times 30'$ global field has been used to estimate the harmonic coefficients of the tailored reference model by HRCOFITR Program (Abd-Elmotaal, 2004). Since the low order harmonics of the anomalous gravitational potential are to a great extent due to the density disturbances in the upper mantle and even deeper sources, the lower harmonics till a certain degree have been fixed to their values as of EGM96 geopotential model. Three different tailored geopotential models have been created by restoring the low order harmonics of EGM96 till $N = 20, 36$ and 72 .

Figure 6 shows the EGGM06A tailored geopotential model, in which the lower coefficients till $N = 20$ are preserved to EGM96. Figure 7 shows the EGGM06B tailored geopotential model, in which the lower coefficients till $N = 36$ are preserved to EGM96. Figure 8 shows the EGGM06C tailored geopotential model, in which the lower coefficients till $N = 72$ are preserved to EGM96. All the three figures illustrate that only minor changes to EGM96

have been made. Notice the change in the very low harmonics preserved to those of EGM96 in each of the three Figures.

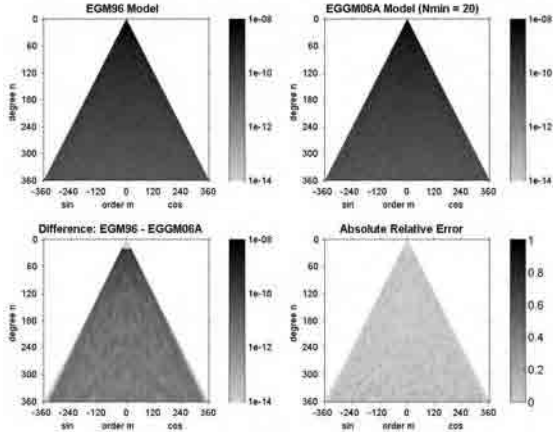


Figure 6. The EGM06A tailored geopotential model (till $N = 20$ preserved to EGM96).

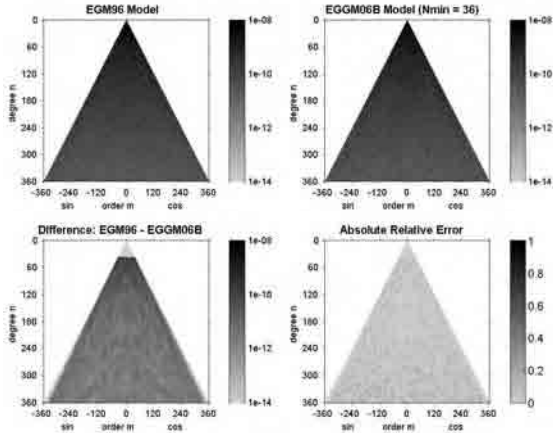


Figure 7. The EGM06B tailored geopotential model (till $N = 36$ preserved to EGM96).

Figure 9 shows the differences at the grid points between the Egyptian $30' \times 30'$ interpolated gravity anomalies and the computed gravity anomalies using the EGM06A tailored geopotential model. Figures 10 and 11 show the same differences using EGM06B and EGM06C models, respectively. The white areas indicate differences less than 5 mgal in magnitude. All three figures shows good matching especially in the data areas. From the three figures, one may conclude that the EGM06A is the better one in view of the minimum difference to the interpolated gravity anomalies.

For the sake of a more detailed comparison and

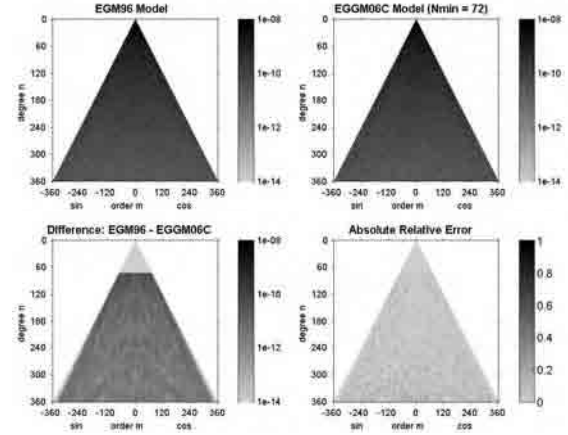


Figure 8. The EGM06C tailored geopotential model (till $N = 72$ preserved to EGM96).

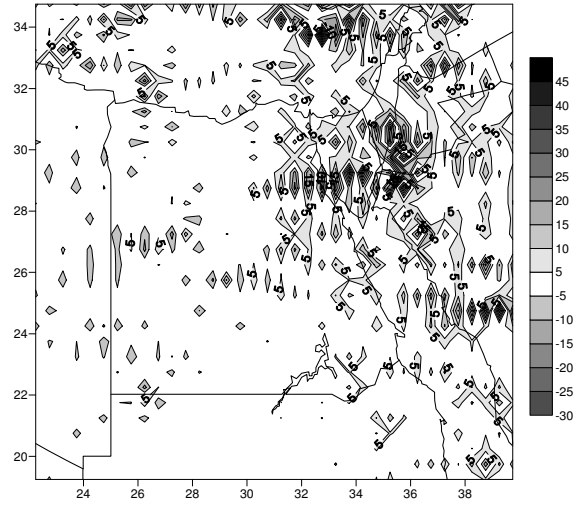


Figure 9. Differences between Egyptian $30' \times 30'$ interpolated gravity anomalies and the computed gravity anomalies using the EGM06A tailored geopotential model.

examining the computed tailored geopotential models, they have been used to compute the gravity anomalies at the data points (13566 points). Table 2 illustrates the statistics of the differences between the Egyptian gravity anomalies data and those computed by the tailored geopotential models created within this investigation. Table 2 shows that all the three developed geopotential models give practically the same results. The tailored geopotential models created in this investigation give better residual gravity anomalies (unbiased and have much less RMS than that of EGM96). The variance has dropped to its one third. The range has dropped to its one half.

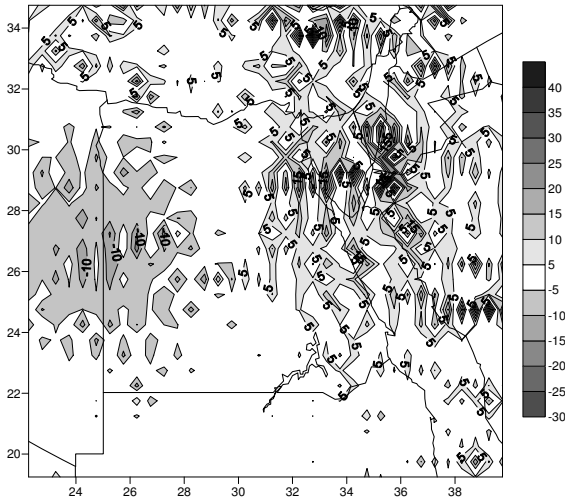


Figure 10. Differences between Egyptian $30' \times 30'$ interpolated gravity anomalies and the computed gravity anomalies using the EGGM06B tailored geopotential model.

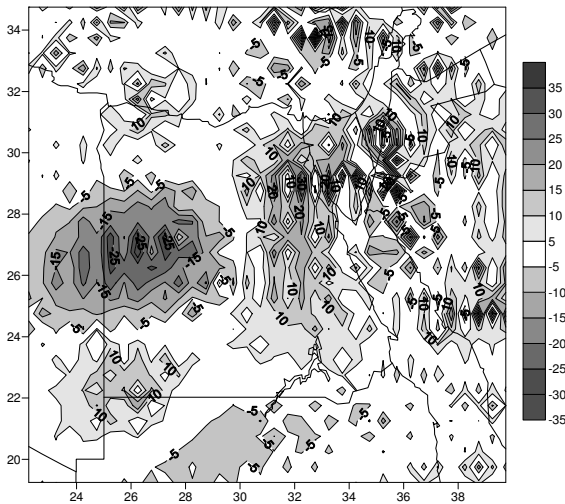


Figure 11. Differences between Egyptian $30' \times 30'$ interpolated gravity anomalies and the computed gravity anomalies using the EGGM06C tailored geopotential model.

6 Conclusions

Three high-degree tailored reference geopotential models for Egypt have been developed in this investigation. The window remove/restore technique has been applied to get rid of the double consideration of the topographic-isostatic masses within the data window. An FFT technique using an iteration process has been used to recover the harmonic coefficients to enhance the accuracy of the obtained harmonic coefficients and to minimize the residual field. The

Table 2. Statistics of the differences between the gravity anomalies at the data points (13566 points) and those computed by the tailored geopotential models

anomalies difference	statistical parameters				
	min.	max.	range	average	st. dev.
	mgal	mgal	mgal	mgal	mgal
Data - EGM96	-190.5	294.7	485.2	-3.3	60.4
Data - EGGM06A	-162.4	96.5	258.9	-1.5	21.3
Data - EGGM06B	-163.8	98.5	262.3	-1.3	21.4
Data - EGGM06C	-164.8	95.2	260.0	-1.8	21.5

lower harmonic coefficients (till $N = 20, 36$ and 72) have been fixed to their values of EGM96 as they are to a great extent due to the density disturbances in the upper mantle and even deeper sources. The tailored geopotential models created in this investigation give better residual gravity anomalies (unbiased and have much less RMS). The variance has dropped to its one third. The range has dropped to its one half. All three tailored geopotential models developed within the current investigation give practically the same results.

References

- Abd-Elmotaal, H. (2004) An Efficient Technique for Harmonic Analysis on a Spheroid (Ellipsoid and Sphere), *Österreichische Zeitschrift für Vermessung & Geoinformation*, **3+4**, 126–135.
- Abd-Elmotaal, H. (1999) The EGHA99 Digital Height Models for Egypt, *Proceedings of the 1st Minia International Conference for Advanced Trends in Engineering, Minia, Egypt, March 14–16, 1999*, **1**, 205–211.
- Abd-Elmotaal, H. and Kühtreiber, N. (2003) Geoid Determination Using Adapted Reference Field, Seismic Moho Depths and Variable Density Contrast, *Journal of Geodesy*, **77**, 77–85.
- Colombo, O. (1981) Numerical Methods for Harmonic Analysis on the Sphere, *Department of Geodetic Science, The Ohio State University, Columbus, Ohio*, **310**.
- Heiskanen, W.A., and Moritz, H. (1967) *Physical Geodesy*. Freeman, San Francisco.
- Wenzel, H.G. (1998) Ultra High Degree Geopotential Models GPM98A, B and C to Degree 1800, URL: <http://www.gik.uni-karlsruhe.de/~wenzel/gpm98abc/gpm98abc.htm>

ITG-Grace02s: a GRACE gravity field derived from range measurements of short arcs

T. Mayer-Gürr, A. Eicker, K.H. Ilk
Institute of Theoretical Geodesy,
University of Bonn, Nussallee 17, D-53115 Bonn, Germany

Abstract. Three years of GRACE data have been used to simultaneously determine the static gravity field model ITG-Grace02s up to a maximum spherical harmonic degree of $n=160$ as well as monthly variations in the long wavelength part in one recovery step. The physical model of the gravity field recovery technique is based on Newton's equation of motion, formulated as a boundary value problem in the form of a Fredholm type integral equation. The principal characteristic of this method is the use of short arcs of the satellite's orbit in order to avoid the accumulation of modelling errors and a rigorous consideration of correlations between the range observations in the subsequent adjustment procedure. Only the results of the static gravity field model are presented here. The validation of the gravity field model is performed by comparisons with existing GRACE satellite-only and combined gravity field models as well as by external validation based on different data sets. The results reveal the excellent quality of the presented gravity field model.

Keywords. GRACE, satellite-to-satellite tracking, twin-satellite mission, Fredholm integral equation, short arc, gravity field recovery

1 Introduction

As a result of the dedicated space-borne gravity field mission GRACE (Gravity Recovery And Climate Experiment – Tapley et al. 2004), a breakthrough in terms of the accuracy and the resolution of the gravity field determination has been achieved. The innovative character of this mission lies in the highly precise line-of-sight range and range-rate K-band measurements between the twin satellites. In addition, the surface forces acting on the satellites are measured and can be removed properly during the recovery procedure. As a result of this mission, various global gravity field models, satellite-only and combined ones, have been derived, such as the recent combined model EIGEN-GL04C (Förste et al. 2006) and the satellite-only model EIGEN-

GL04S1. Other GRACE gravity field models are GGM02C and the satellite-only model GGM02S (Tapley et al. 2005).

The gravity field recovery procedure to derive these models is based on the classical approach of satellite geodesy. It consists basically in deriving the spherical harmonic coefficients representing the gravitational potential from an analysis of accumulated orbit perturbations of the satellites. It is an indispensable requirement to analyse medium or long satellite arcs covering at least one day or more in order to cover the characteristic periodic and secular disturbances caused by the small corrections to the approximate force function.

It has been demonstrated that these requirements are not necessary anymore for the new generation of dedicated gravity satellites. They can be characterized by a modelling concept which acts more in-situ than by analyzing accumulated orbit perturbations (Ilk et al. 2006). Very precise results can be achieved with these new in-situ techniques and are able to compete with the results of the classical analysis procedures (e.g., Mayer-Gürr et al. 2004). In Sect. 2 of this article the computation procedure for processing the observations of the GRACE mission is sketched. In Sect. 3 results are presented and validated by different alternative data sets. Sect. 4 concludes this article with a summary and some perspectives for future work.

2 The mathematical model for low-low satellite-to-satellite tracking

2.1 Setup of the physical model

The mathematical-physical model for a single satellite is based on the formulation of Newton's equation of motion,

$$\ddot{\mathbf{r}}(t) = \mathbf{a}(t, \mathbf{r}, \dot{\mathbf{r}}; \mathbf{x}), \quad (1)$$

as a boundary value problem,

$$\mathbf{r}(t) = (1-t)\mathbf{r}_A + t\mathbf{r}_B - \int_{t'=0}^1 K(t, t') \mathbf{a}(t, \mathbf{r}, \dot{\mathbf{r}}; \mathbf{x}) dt', \quad (2)$$

with the integral kernel,

$$K(\mathbf{t}, \mathbf{t}') = \begin{cases} \mathbf{t}(1-\mathbf{t}'), & \mathbf{t} \leq \mathbf{t}', \\ \mathbf{t}'(1-\mathbf{t}), & \mathbf{t}' \leq \mathbf{t}, \end{cases} \quad (3)$$

the normalized time variable,

$$\mathbf{t} = \frac{t-t_A}{T} \text{ with } T = t_B - t_A, \quad t \in [t_A, t_B] \quad (4)$$

and the boundary values

$$\mathbf{r}_A := \mathbf{r}(t_A), \quad \mathbf{r}_B := \mathbf{r}(t_B), \quad t_A < t_B. \quad (5)$$

The specific force function in Eq. (1) with the unknown parameters \mathbf{x} can be separated as follows,

$$\begin{aligned} \mathbf{a}(t; \mathbf{r}, \dot{\mathbf{r}}; \mathbf{x}) &= \mathbf{a}_d(t; \mathbf{r}, \dot{\mathbf{r}}) + \\ &+ \nabla V(t; \mathbf{r}; \mathbf{x}_0) + \nabla T(t; \mathbf{r}; \Delta \mathbf{x}). \end{aligned} \quad (6)$$

The quantity \mathbf{a}_d is a disturbance part, which represents the non-conservative disturbing forces, ∇V is a reference part, representing the long wavelength gravity field features \mathbf{x}_0 and ∇T is an anomalous part, modeling the high frequent refinements $\Delta \mathbf{x}$ to the low frequent gravity field parameters \mathbf{x}_0 of the global model.

If precise intersatellite functionals as line-of-sight measurements are available, as in case of the GRACE mission, the mathematical model for range observations can be derived by projecting the relative vector to the line-of-sight connection,

$$\mathbf{r}(\mathbf{t}) = \mathbf{e}_{12}(\mathbf{t}) \cdot (\mathbf{r}_2(\mathbf{t}) - \mathbf{r}_1(\mathbf{t})). \quad (7)$$

Analog formulae can be derived for range-rates and range accelerations, but for the determination of ITG-Grace02s only ranges have been used. The quantity \mathbf{e}_{12} is the unit vector of the line-of-sight direction of the two GRACE satellites with the positions $\mathbf{r}_1(\mathbf{t})$ and $\mathbf{r}_2(\mathbf{t})$. This vector is known within a few *mas*, assuming that the satellite positions are measured with an accuracy of a few *cm* and taking into account the distance of approximately 200km between the two satellites. Nevertheless, the accuracy is not adequate to the high accuracy of the range measurements in the size of some *mm*. Therefore, a model refinement is necessary which improves implicitly also the relative orbit. We will not show the details here because of space and refer to Mayer-Gürr (2006). Further details to the physical model of the gravity field recovery technique based on GRACE low-low SST data can also be found in Mayer-Gürr et al. (2006).

2.2 Gravity field representation

The anomalous potential $T(\mathbf{r}, \Delta \mathbf{x})$ can be formulated as follows,

$$\begin{aligned} T &= \frac{GM_E}{r} \sum_{n=2}^{n_{\max}} \sum_{m=0}^n \left(\frac{R_E}{r} \right)^n \\ &\cdot (\Delta c_{nm} C_{nm}(\mathbf{J}, \mathbf{I}) + \Delta s_{nm} S_{nm}(\mathbf{J}, \mathbf{I})), \end{aligned} \quad (8)$$

with the corrections $\Delta c_{nm}, \Delta s_{nm} \in \Delta \mathbf{x}$ to the reference potential coefficients $c_{nm}, s_{nm} \in \mathbf{x}_0$ and with the surface spherical harmonics,

$$\begin{aligned} C_{nm}(\mathbf{J}, \mathbf{I}) &= P_n^m(\cos \mathbf{J}) \cos m \mathbf{I}, \\ S_{nm}(\mathbf{J}, \mathbf{I}) &= P_n^m(\cos \mathbf{J}) \sin m \mathbf{I}. \end{aligned} \quad (9)$$

In case of a regional recovery the anomalous potential $T(\mathbf{r})$ can be modeled by parameters of space localizing base functions as well as shown e.g., in Mayer-Gürr et al. (2006) and Schmidt et al. (2006).

2.3 The linearized deterministic model

The functional model describes the dependency of the observables on the gravity field parameters. If we write Eq. (7) as

$$\mathbf{r} = \mathbf{e}_{12}(\mathbf{t}) \cdot (\mathbf{r}_2(\mathbf{t}) - \mathbf{r}_1(\mathbf{t})) = f(\mathbf{x}), \quad (10)$$

then we can write after linearization,

$$\mathbf{r} = \mathbf{r}_0 + \frac{\partial \mathbf{r}}{\partial \mathbf{x}} \Big|_{\mathbf{x}_0} \cdot \Delta \mathbf{x} + \dots, \quad (11)$$

with

$$\frac{\partial \mathbf{r}}{\partial \mathbf{x}} = \frac{\partial \mathbf{r}}{\partial \mathbf{r}} \cdot \frac{\partial \mathbf{r}}{\partial \mathbf{a}} \cdot \frac{\partial \mathbf{a}}{\partial \mathbf{x}}. \quad (12)$$

The first term at the right hand side can be derived from Eq. (10), the second term from Eq. (2), and the third term from Eq. (6) and Eq. (8). If all linearized observation equations are collected for one short arc then we arrive at the following matrix equation,

$$\mathbf{l} = \mathbf{A} \Delta \mathbf{x} + \mathbf{e}, \quad (13)$$

with the observations \mathbf{l} and the unknowns $\Delta \mathbf{x}$,

$$\mathbf{l} = \begin{pmatrix} \mathbf{r}(\mathbf{t}_1) - \mathbf{r}_0(\mathbf{t}_1) \\ \mathbf{r}(\mathbf{t}_2) - \mathbf{r}_0(\mathbf{t}_2) \\ \vdots \\ \mathbf{r}(\mathbf{t}_N) - \mathbf{r}_0(\mathbf{t}_N) \end{pmatrix}, \quad \Delta \mathbf{x} = \begin{pmatrix} \Delta c_{2,0} \\ \Delta c_{2,1} \\ \vdots \\ \Delta s_{n_{\max}, m} \end{pmatrix}, \quad (14)$$

where the terms $\mathbf{r}_0(\mathbf{t}_i)$ contain the reference parameters; \mathbf{e} is the error and the design matrix \mathbf{A} is composed of the partial differentials as shown in Eq. (12).

2.4 The stochastic model

The ranges between the twin satellites are strongly correlated; the same holds for the range-rates and the range accelerations. Therefore, an appropriate selected stochastic model has to be introduced by a variance-covariance matrix $\mathbf{C}(\mathbf{l}) = \mathbf{s}^2 \mathbf{P}^{-1}$ for each

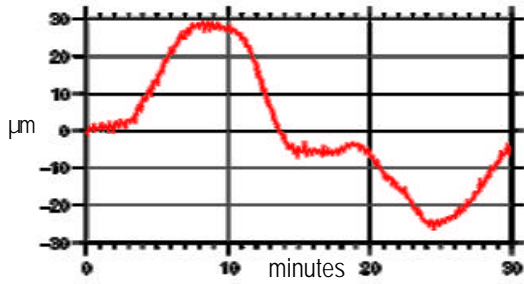


Fig. 1: Range residuals after least squares adjustment without decorrelation for a 30-minutes arc.

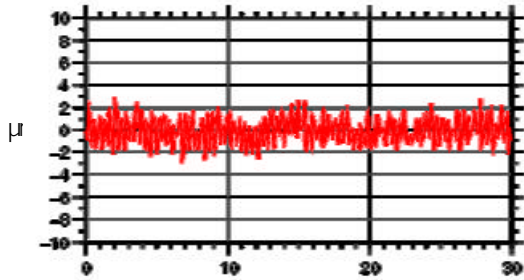


Fig. 2: Range residuals after least squares adjustment with decorrelation for a 30-minutes arc.

short arc. The consideration of this variance-covariance matrix acts as a decorrelation of the observations and the decorrelated adjusted residuals should show white noise.

The derivation of a realistic variance-covariance matrix is very important: in case of a correct decorrelation one can claim that the solution is optimal in the statistical sense, and it is not necessary to introduce calibration parameters for the K-band measurements. The formal errors of the adjustment results do not need any calibration. If the adjustment is performed without decorrelation then we get typical residual features as shown in Fig. 1 for a 30-minutes arc.

The variance-covariance matrix is composed of two parts: the first part describes the noise of the K-band measurements, $\mathbf{s}_p^2 \mathbf{F} \mathbf{C}(\mathbf{p}) \mathbf{F}^T$, and the second one the noise of the accelerometer measurements, $\mathbf{s}_a^2 \mathbf{B} \mathbf{C}(\mathbf{a}) \mathbf{B}^T$, so that it holds for the variance covariance matrix,

$$\mathbf{C}(\mathbf{l}) = \mathbf{s}_p^2 \mathbf{F} \mathbf{C}(\mathbf{p}) \mathbf{F}^T + \mathbf{s}_a^2 \mathbf{B} \mathbf{C}(\mathbf{a}) \mathbf{B}^T. \quad (15)$$

The matrix \mathbf{F} describes the filtering of the phase observations and \mathbf{B} a corresponding filtering matrix for the accelerometer measurements (cf. Mayer-Gürr 2006; Thomas 1999, Wu et al. 2004). Fig. 2 shows the residuals after least squares adjustment of the same arc as shown in Fig. 1 in case of decorrelated observations.

2.5 Combination of the normal equations

The arc-related parameters are eliminated before the arcs are merged to the complete system in order to reduce the dimension of the adjustment problem. Every short arc builds a (reduced) partial system of observation equations. Separate variance factors for each arc have been determined to combine the design matrices and to consider the variable precision. The variance factors are computed by means of a variance component estimation procedure described in Koch and Kusche (2003). The details of the iterative combination scheme combined with a variance component estimation and the computation of the regularization factor as well as the procedure to solve the complete system without establishing the normal matrices are described in Mayer-Gürr (2006).

3 Gravity field solution ITG-Grace02s

3.1 Data set and choice of parameters

For the determination of the gravity field model ITG-Grace02s K-band range measurements of the GRACE twin satellite mission have been used for the period February 2002 until December 2005 covering approximately three years. The approximately 18 million ranges are corrected for the tides caused by Sun, the Moon and the planets. The ephemerides are taken from the JPL405 data set. Effects originating from the deformation of the Earth caused by these tides are modelled according to the IERS 2003 conventions. Ocean tides are computed using the FES2004 model. Effects of high frequency atmosphere and ocean mass redistributions are removed prior to the processing by the GFZ AOD de-aliasing products. Only the K-band range measurements have been used as observations, the Level 1B orbits have only served as approximation values for the linearized observation equations. As already mentioned the three years data have been split into short arcs of approximately 30 minutes arc length. A global spherical harmonic solution up to degree $n=160$ beginning from degree $n=2$ has been determined simultaneously with monthly temporal variations of the potential coefficients from degree $n=2$ to degree $n=40$. It shall be pointed out that no regularisation has been used for this solution. The temporal variations have been modelled by linear spline functions with monthly resolution. This will be context of a later publication. In addition to the gravity field parameters for each arc a K-band range bias

and an accelerometer bias have been estimated as well.

3.2 Comparisons with alternative solutions

The model ITG-Grace02s is compared to gravity field models derived by other institutions, which are also based on GRACE data. We performed comparisons with the recent satellite-only model GGM02S (data from 2002 April – 2003 Dec) and a combined solution GGM02C of CSR, Austin (Tapley, 2006).

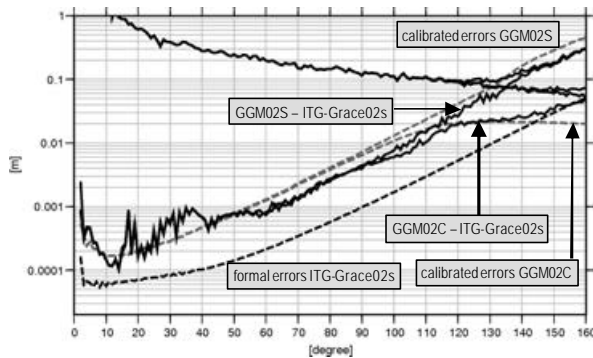


Fig. 3: Comparisons of ITG-Grace02s with GGM02 of the Center of Space Research (CSR).

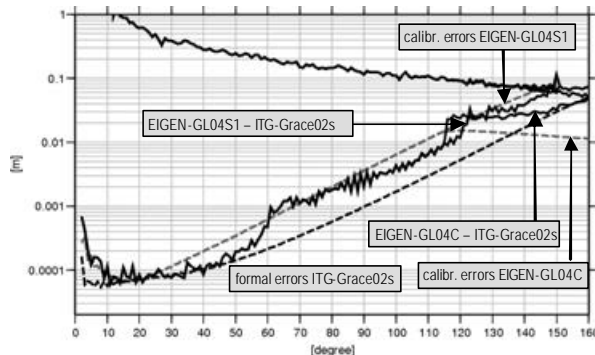


Fig. 4: Comparisons of ITG-Grace02s with EIGEN-GL04 of the GeoForschungsZentrum Potsdam.

Fig. 3 shows the results in the spectral domain: The difference degree amplitudes w.r.t. to the models GGM02S and GGM02C are approximately identical up to degree $n=90$, but are smaller from degree $n=90$ upwards for the combined solution than those for the satellite-only solution. This is since the terrestrial data in GGM02C supports the higher degrees and, obviously, these are better resolved in our satellite-only solution than in the satellite-only solution GGM02S. A similar performance can be observed if

our model is compared with the recent satellite-only solution EIGEN-GL04S1 (data from 2003 Feb – 2005 July) and the combined solution EIGEN-GL04C (Fig. 4). There is a strange jump in the difference degree amplitudes at degree $n=115$; this is the cut-off point of the GRACE data while the degrees above are dominated by terrestrial data. Obviously, the fit of the terrestrial data to the GRACE data was not smooth enough within the combination procedure in deriving the combined solution EIGEN-GL04C.

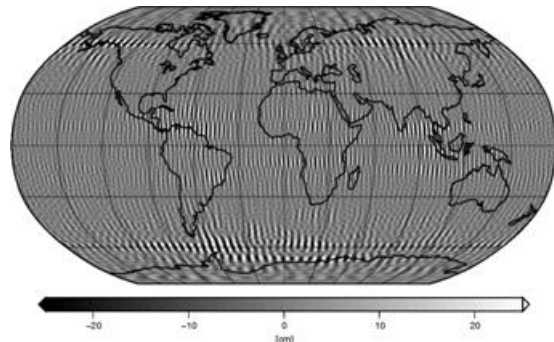


Fig. 5: Differences of ITG-Grace02s and EIGEN-GL04S1 in terms of geoid undulations (degree range 2..130, RMS=10.2cm, avg=7.3cm, max=79.4cm).

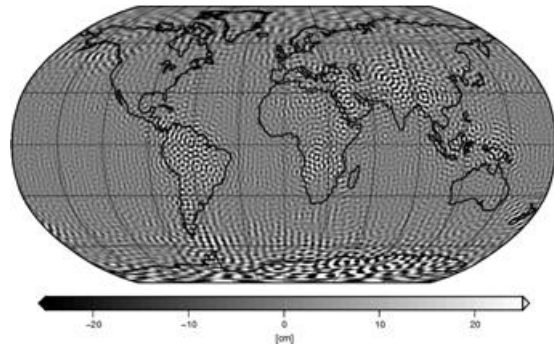


Fig. 6: Differences of ITG-Grace02s and EIGEN-GL04C in terms of geoid undulations (degree range 2..130, RMS=11.7cm, avg=7.9cm, max=141.8cm).

This can also be observed in the differences of ITG-Grace02s and the models EIGEN-GL04C and EIGEN-GL04S1 in the space domain for the degrees $n=2..130$. While the differences to EIGEN-GL04S1 show the typical stripes in various parts of the geoid there are no specific differences over the continents (Fig. 5). This is different in the difference plot with EIGEN-GL04C: here the stripes vanished to a large extent but there are clearly pronounced error effects over South America and Antarctica (Fig. 6).

3.3 External validation

ITG-Grace02s is a satellite-only solution without applying any regularization. An external validation by completely different data sets could give a hint to its precision. One possibility is the comparison with the EGM96 which is primarily derived from altimetric data over the oceans. Fig. 7 to Fig. 9 show the differences only over the oceans between ITG-Grace02s and EGM96 (Lemoine et al. 1996) in terms of geoid undulations. For comparison the differences of the models EIGEN-GL04S1 and GGM02S to the EGM96 are displayed as well. The degree range of the spherical harmonics expansion is limited to an upper degree 130.

Our model ITG-Grace02s shows the smallest global RMS values and average differences compared to the other two satellite-only models. The improvement can be demonstrated better if the differences are visualized in the space domain: the error stripes of the ITG-solution are significantly less pronounced than in case of the other models. Especially in the oceanographic important areas of the Atlantic Ocean and the region of the southern circum polar current, smaller errors can be observed.

Another external validation is the comparison with terrestrial data, in most cases the comparison with geoid undulations derived as differences of ellipsoidal heights determined by GPS and orthometric heights (or corresponding normal heights). Table 1 shows comparisons with gravity anomalies and geoid undulations, derived from GPS and levelling measurements at various benchmark locations. The values for the USA were provided by the US National Geodetic Survey, (<http://www.ngs.noaa.gov/GEOID/GPSonBM99/gpsbmdoc99.html>),

Table 1: External validation of ITG-Grace02s and other recent models with various external data sources (RMS, compared up to degree $n=130$, filled up with EGM96).

model	NIMA Altimeter	NIMA terrestrial	GPS USA	GPS Canada
ITG-Grace02s	6.6 mgal	11.2 mgal	43.6 cm	31.2 cm
EIGEN-GL04S1	6.8 mgal	11.4 mgal	43.7 cm	32.6 cm
GGM02S	7.5 mgal	11.6 mgal	45.8 cm	36.1 cm
EIGEN-GRACE02S	7.7 mgal	12.0 mgal	48.6 cm	36.7 cm

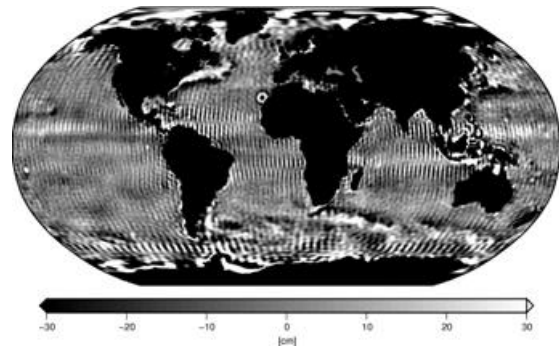


Fig. 7: Differences of EIGEN-GL04S1 and EGM96 in terms of geoid undulations for the degrees 2..130 (only oceanic areas: RMS=26.2cm, avg=14.8cm, max=512.3cm).

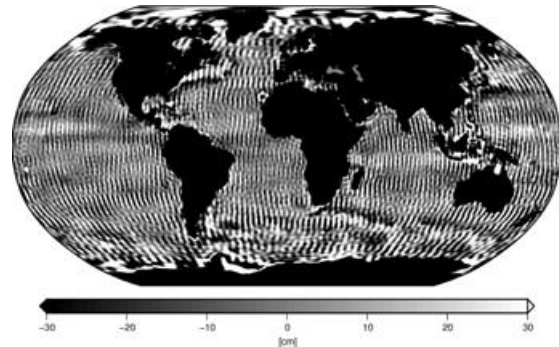


Fig. 8: Differences of GGM02S and EGM96 in terms of geoid undulations for the degrees 2..130 (only oceanic areas: RMS=30.9cm, avg=20.8cm, max=489.7cm).

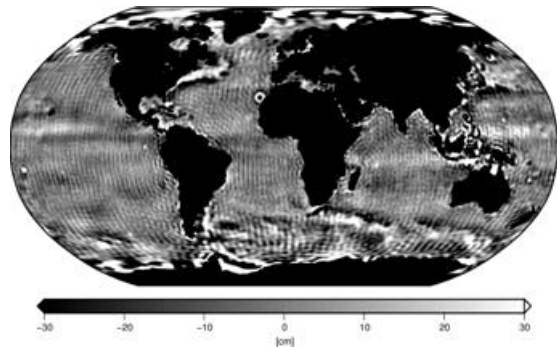


Fig. 9: Differences of ITG-Grace02s and EGM96 in terms of geoid undulations for the degrees 2..130 (only oceanic areas: RMS=24.8cm, avg=13.0cm, max=516.2cm).

the data sets for Canada by the National Resources of Canada (http://www2.geod.nrcan.gc.ca/~marc/Html/GPS_e.html). Again, over the continents the ITG-Grace02s model shows slightly smaller RMS values than the other satellite-only gravity field models.

4 Conclusions

In this paper the static GRACE-only gravity field model ITG-Grace02s, covering the degrees ranging from $n=2$ to $n=160$, has been presented. Comparisons with other recent satellite-only models and combined gravity field models demonstrate the high quality of this model. All tests show better results for our model than for the other satellite-only models. Also the comparisons with combined models confirm the high quality of ITG-Grace02s. Therefore, this model reconfirms the gravity field recovery strategy developed at the Institute of Theoretical Geodesy of the University Bonn. It is an adequate recovery procedure for the analysis of precisely determined kinematical orbits, which lead to the CHAMP models ITG-CHAMP01 and 02 (cf. Mayer-Gürr et al. 2004), and it demonstrates impressively the suitability for the processing of SST observations of the low-low type. The characteristics of our alternative in-situ gravity field recovery strategy can be sketched as follows: use of short arcs for gravity field recovery, derivation of a rigorous stochastic model for the observations based on the filtering procedure of the original observations and a physical model, based on the solution of Newton's equation of relative motion, formulated as a boundary value problem of Fredholm type.

The next steps concentrate on the improvements related to the determination of combined gravity field models and the determination of time variable regional gravity field models represented by space localizing base functions. The gravity field recovery strategy of the ITG as part of a unitized Gravity Recovery Object-Oriented Programming System (GROOPS), which is tailored to the in-situ observables of the new generation of gravity satellite missions, has to be improved and extended for various additional tasks.

References

Förste C, Flechtner F, Schmidt R, König R, Meyer U, Stubenvoll R, Rothacher M, Barthelmes F, Neumayer H, Biancale R, Bruinsma S, Lemoine J-M, Loyer S (2006) A mean global gravity field model from the combination of satellite mission and altim-

etry/gravimetry surface data EIGEN-GL04C, *Geophysical Research Abstracts*, Vol. 8, 03462

Ilk KH, Löcher A, Mayer-Gürr T (2006) Do we need new gravity field recovery techniques for the new gravity field satellites? Proceedings of the VI Hotine-Marussi Symposium of Theoretical and Computational Geodesy: Challenge and Role of Modern Geodesy, May 29 - June 2, 2006, Wuhan, China

Koch KR, Kusche J (2003) Regularization of geopotential determination from satellite data by variance components, *Journal of Geodesy* 76 :259-268,

Lemoine FG, Kenyon SC, Factor JK, Trimmer RG, Pavlis NK, Chinn DS, Cox CM, Klosko SM, Luthcke SB, Torrence MH, Wang YM, Williamson RG, Pavlis EC, Rapp RH, Olson TR (1998) The development of the joint NASA GSFC and the National Imagery and Mapping Agency (NIMA) geopotential model EGM96, NASA/TP-1998-206861, Goddard Space Flight Center, Greenbelt, MD

Mayer-Gürr T, Ilk KH, Eicker A, Feuchtinger M (2005) ITG-CHAMP01: A CHAMP Gravity Field Model from Short Kinematical Arcs of a One-Year Observation Period, *Journal of Geodesy* (2005) 78:462-480

Mayer-Gürr T, Eicker A, Ilk KH (2006) Gravity field recovery from GRACE-SST data of short arcs, in: J. Flury, et al. (eds): *Observation of the Earth System from Space*, pp. 131-148, Springer

Mayer-Gürr T (2006) Gravitationsfeldbestimmung aus der Analyse kurzer Bahnbögen am Beispiel der Satellitenmissionen CHAMP und GRACE, Dissertation at the Institute of Theoretical Geodesy, University Bonn

Reigber C, Schmidt R, Flechtner F, König R, Meyer U, Neumayer K-H, Schwintzer P, Zhu SY (2004) An Earth gravity field model complete to degree and order 150 from GRACE: EIGEN-GRACE02S, *Journal of Geodynamics*, 39(1):1-10

Schmidt, M., S.-C. Han, J. Kusche, L. Sanchez, and C. K. Shum (2006), Regional high-resolution spatiotemporal gravity modeling from GRACE data using spherical wavelets, *Geophys. Res. Lett.*, 33, L08403, doi:10.1029/2005GL025509.

Tapley BD, Bettadpur S, Watkins M, Reigber Ch (2004) The gravity recovery and climate experiment: mission overview and early results. *Geophys Res Lett* 31, L09607: doi 10.1029/2004GL019920

Tapley B, Ries J, Bettadpur S, Chambers D, Cheng M, Condi F, Gunter B, Kang Z, Nagel P, Pastor R, Pekker T, Poole S, Wang F (2005) GGM02 - An improved Earth gravity field model from GRACE, *Journal of Geodesy*, doi 10.1007/s00190-005-0480-z

Thomas JB (1999) An analysis of Gravity-Field Estimation Based on Intersatellite Dual-1-Way Biased Ranging, Number 98-15 in JPL Publication, Jet Propulsion Laboratory, Pasadena, California

Wu SC, Kruizinga G, Bertiger W (2004) Algorithm Theoretical Basis Documents for GRACE Level-1B Data Processing V1.1. Technical Report GRACE 327-741, Jet Propulsion Laboratory, Pasadena, California

Towards a characterization of temporal gravity field variations in GRACE observations and global hydrology models

S. Petrovic, R. Schmidt, J. Wunsch, F. Barthelmes, A. Güntner and M. Rothacher
GeoForschungsZentrum Potsdam, Germany

Abstract. In order to exploit the GRACE-based time-variable gravity signals e.g. in hydrological modeling of the global water cycle appropriate techniques to separate the relevant hydrological signal from the integral satellite gravity data will be needed. Recent investigations focus on comparisons on the basis of time variations of the Earth gravity field reconstructed from monthly GRACE-only gravity field solutions and global hydrological models. This shows both pronounced similarities and considerable differences. On the other hand, since the same holds for comparisons between various state-of-the-art hydrology models, a more general view on the morphology of time-variable gravity signals due to hydrological mass redistributions will be needed. In a preparatory study to this end we have investigated time-variable signals derived from three different state-of-the-art global hydrology models and from recent time series of monthly GRACE-only gravity models. In order to infer common characteristic features from the distinct data sources we use spectral coherence analysis and Empirical Orthogonal Functions analysis in the space domain. The contribution presents current results.

Keywords. time-variable gravity, GRACE satellite mission, global hydrological models, coherence, degree correlations, empirical orthogonal functions.

1 Introduction and motivation

The twin GRACE satellites were launched on March 17, 2002 (GRACE = Gravity Recovery and Climate Experiment). Their primary purpose is to monitor the gravity field of the Earth (Tapley et al. 2004a), both the static field (Reigber 2005) and the time-variable part of it (Dickey

et al. 1997, Wahr et al. 1998, Peters 2001, Tapley et al. 2004b, Wahr et al. 2004, Schmidt et al. 2006a) with unprecedented accuracy.

At GFZ Potsdam a time series of monthly GRACE-only gravity field models (labeled GFZ-RL03) covering the period 02/2003 to 06/2006 has been processed (altogether 39 models). The models are based on the most recent background models and processing standards. In order to derive the outer accuracy of these models and derived satellite-based mass anomalies to be used in applications, an accuracy assessment of these models has been performed by means of a GRACE internal calibration approach. Based on the basic assumption that residual variability in the GRACE models after removing dominant seasonal signals mainly represents errors of the models, we derived individual accuracy estimates in the space domain in order to scale the formal variance-covariance information from the adjustment. For verification we then intercompared the model accuracies, computed from error propagation of the scaled covariance matrices with the residual variability of the models in the space domain, cf. (Schmidt et al. 2006b)

The main unmodeled component in the GRACE gravity recovery processing are hydrological mass redistributions and are clearly traceable in the monthly gravity field models. However, the errors of GRACE observations and the physical models used, as well as the influences of unmodeled mass redistributions (like changes in ice shields) are still contained as well. Therefore, comparing the variations of water stocks deduced from GRACE with different state-of-the-art global hydrology models shows both a good agreement (in some regions for some time intervals) and considerable differences. On the other hand, the disagreement between existing global hydrology models (see e.g. Abrikosov et al. 2006) is also considerable and it is not possible to de-

cide what corresponds best to the real variations of water stocks. In this way a direct exploitation of GRACE-based mass signals as true observations of global water stocks as a constraint for the evaluation and calibration of a global hydrological model is not indicated. Instead, it is necessary to characterize different dynamic processes and to separate the relevant hydrological signal from the integral satellite gravity data.

2 Characteristic features of dynamic processes

In order to characterize the morphology of hydrological mass redistributions we investigated three state-of-the-art global hydrology models, H96 (Huang et al. 1996, Fan and van den Dool 2004), LaD (Milly and Shmakin 2002) and WGHM (Döll, Kaspar and Lehner 2003), as well as water storage variations deduced from GRACE to find common features that are contained in both types of information sources.

These models are compared in space and in the spectral regions. The data sets can be transformed between the gridded form and the spectral form (expressed as Stokes coefficients C_{nm} , S_{nm}), based on fully normalized spherical harmonic functions Y_n^m (Heiskanen and Moritz 1967).

Among the possible methods which we investigate are correlations in the spectral domain (degree correlations, coherence) and Empirical Orthogonal Functions (EOF/PCA = Principal Component Analysis).

3 Spectral correlations (coherence)

Different sorts of spectral correlations were computed: the usual degree correlations between two models for individual epochs, correlation between time variabilities of individual coefficients and the degree correlations between time variabilities of all coefficients belonging to the same degree. Since the reference level of the global hydrology models is relative and the scale uncertain, all correlation computations are centered and normed (corresponding to the usual statistical definition of the Pearson linear correlation coefficient).

As an example we show the spectral correlations between 156 months (1992-2004) of the hydrology models WGHM and H96 up to Legendre degree $n=100$.

Figure 1 presents the degree correlation $r(n)$ as a function of time and of degree n . The plot shows that every twelfth month has a poor correlation between WGHM and H96 (nearly white); there is also some semi-annual structure. Inter-annual variations are present, too.

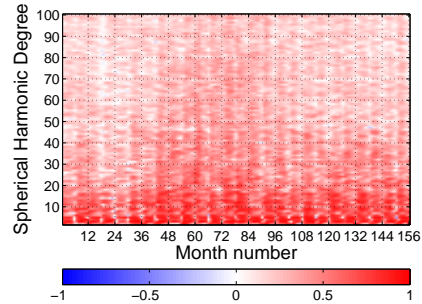


Figure 1. Degree correlations between spherical harmonic coefficients of global hydrology models WGHM and H96.

Figure 2 depicts the correlation per spherical harmonic coefficient (SHC) coded in color as a function of degree n and order m . Common features of hydrology models are indicated by high correlations, which seem to dominate the pattern. However, there are also fields of low correlations (light red) and even negative correlations (blue) spread over almost all regions. Taking into account that this approach might be too optimistic, since every computed correlation is based on a different regression, this confirms the fact already established in earlier studies performed in space domain that the differences between various global hydrological models are considerable.

Comparing 35 GRACE monthly mean fields with the WGHM model, we obtain Fig. 3 (correlation per SHC, in analogy to Fig. 2) The pattern shows high positive correlations between the temporal variability of spherical harmonic coefficients deduced from GRACE and from the global hydrology model WGHM mainly in the low degrees and orders. In this way it indicates the current sensitivity of GRACE models. The pattern may give some insight for designing GRACE-related filters.

Integral correlations in spectral domain between global hydrology models and GRACE are illustrated in Fig. 4 (degree correlations for two

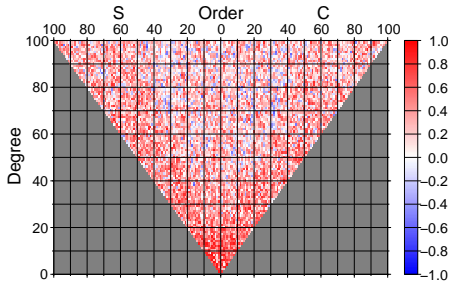


Figure 2. Correlations between time variations of individual spherical harmonic coefficients of global hydrology models WGHM and H96.

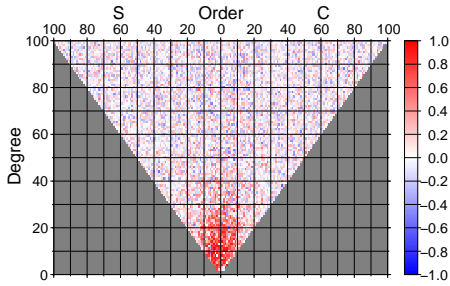


Figure 3. Correlations between time variations of individual spherical harmonic coefficients between WGHM and GRACE.

time series of vectors). The degree correlations are significant only for $n \leq 20$ which was already visible in Fig. 3.

Temporal averaging of monthly degree correlations (computed between WGHM and GRACE in the same way as those presented in Fig. 1) over the 35 months used results in curves which agree well with Fig. 4.

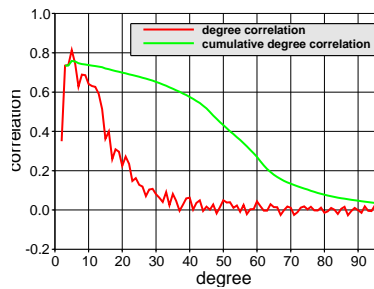


Figure 4. Degree correlations between time variabilities in WGHM and GRACE.

Concluding this section, we remark that although the results are somewhat too optimistic, several interesting features can be observed. In the future, the investigation of spectral correlations presented will be extended to individual water catchment areas.

4 Empirical Orthogonal Functions

The second method we used is EOF (Empirical Orthogonal Functions), see e.g. (Preisendorfer 1988, Wilks 1995, Bosch 2001), where a review of the history and of this method itself can be found. In its common form, the use of SVD (Singular Value Decomposition) is involved.

In order to detect systematic parts of mass redistributions from GRACE and hydrology models we apply Empirical Orthogonal Functions to time series of global grids of mass anomalies derived from the distinct data sources.

4.1 Application to global hydrology models and GRACE-derived mass variations

Figure 5 shows the eigenvectors of the first three modes for three global hydrological models: H96, LaD and WGHM. We used a FORTRAN package from D. Pierce (Scripps Institution, La Jolla), available on his internet home page. The computations were performed using covariance matrix. The corresponding principal components as functions of time are given in Fig. 6.

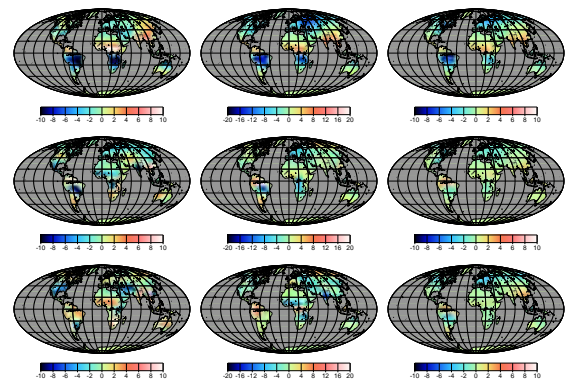


Figure 5. Patterns of eigenvectors for the first three modes (rows) of H96 (left), LaD (center) and WGHM (right).

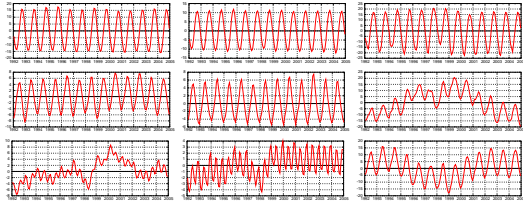


Figure 6. Curves of principal components for the first three modes (rows) of H96 (left), LaD (center) and WGHM (right).

The first modes mainly show an annual sine wave. In higher modes, also a semi-annual oscillation appears as well as long-period variations. The three models differ in their higher principal components. Mode 2 of LaD has a somewhat ‘spiky’ annual wave, revealing the presence of higher harmonics of the annual cycle.

For comparison, the pattern of eigenvectors and the curve of principal components (mode 1) for the GRACE-deduced time variations of water stocks are presented in Fig. 7.

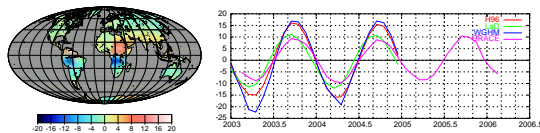


Figure 7. GRACE mode 1: pattern of eigenvectors (left) and the curve of principal components compared with H96, LaD and WGHM (right).

Tables 1 and 2 list the percentage of signal (variance resp. cumulative variance) explained by the first 10 modes. WGHM is slightly different from other hydrology models, the variances for GRACE are similar to those for WGHM.

In all four cases the first mode explains a considerable part (35-60%) of entire variations. Since the patterns of eigenvectors conform well, it makes sense to analyze the behavior of principal components.

4.2 Analysis of principal components

The application of Empirical Orthogonal Functions analysis transforms the considered models (hydrological and based on GRACE) in such a form which makes it possible to detect periodic

Table 1. Variances (in %) for the first ten modes

Mode	H96	LaD	WGHM	GRACE
1	59.46	59.16	36.07	35.60
2	8.02	11.08	13.05	11.56
3	4.05	3.74	10.22	7.10
4	3.29	3.34	6.68	4.07
5	2.45	2.06	5.10	3.41
6	2.30	1.57	4.09	3.09
7	2.09	1.48	2.55	2.89
8	1.66	1.13	2.30	2.62
9	1.41	1.11	1.66	2.48
10	1.33	0.87	1.60	2.10

Table 2. Cumulative variances (in %) for the first ten modes

Mode	H96	LaD	WGHM	GRACE
1	59.46	59.16	36.07	35.60
2	67.48	70.24	49.12	47.16
3	71.53	73.98	59.34	54.26
4	74.82	77.32	66.02	58.32
5	77.27	79.37	71.12	61.73
6	79.57	80.95	75.22	64.83
7	81.66	82.43	77.77	67.72
8	83.33	83.56	80.07	70.34
9	84.74	84.67	81.73	72.81
10	86.07	85.54	83.33	74.91

and other systematic parts of the signal. Comparison of periodic parts found in different models was performed using classical Fourier analysis, wavelets and detection of individual periods contained in the models. The last mentioned approach makes it possible to compare not only the periods, but the phases as well.

Since the time interval of the available GRACE data is much more limited than the common time interval of the global hydrological models, a comparison of the two is only conditionally possible.

The search for arbitrary periods can be performed efficiently using the methodology described in (Mautz and Petrovic 2005). In the present case (maximally 156 epochs), a systematic search with a small step also performs well.

Table 3 contains the ten most significant periods found in the first principal component of the three considered hydrological models. The phase refers to the model $\sin(\omega * t - \varphi)$ with the time coordinate origin situated in the middle of the

Table 3. Analysis of periodic features in principal components: ten most significant periods of mode 1 (periods P in years, phases φ in degrees).

period no.	H96		LaD		WGHM	
	P	φ	P	φ	P	φ
1	1.00	-86	1.00	-71	1.00	-88
2	3.98	-74	0.50	-64	7.61	33
3	0.50	-145	1.16	128	1.97	63
4	1.29	-41	7.64	14	3.93	28
5	15.25	117	1.99	79	0.50	-41
6	0.81	135	0.81	165	1.53	65
7	0.73	-83	0.33	21	0.81	146
8	0.90	-19	1.32	-23	0.66	150
9	0.33	26	1.61	53	0.61	169
10	3.08	-55	3.87	-47	1.41	-42

considered time interval.

The first (most significant) period (annual) explains 93% (H96 and LaD) resp. 82% of the principal component of the first mode. This annual period shows rather similar phase angles in the three hydrology models. The semi-annual period is also visible in all three models; however, the phase angles do not agree so well as for the annual period. Some further periods may be present, like 3.9 and 7.6 years.

Figure 8 presents the nine most significant periods for mode 1 after subtraction of an annual wave as well as the results obtained by Fourier integral. Additionally, a wavelet analysis of principal components (not shown here) was performed.

The first period (annual) explains 89% of the principal component of the first mode for GRACE, the pattern of eigenvectors for this mode is similar to respective patterns of the considered global hydrology models (cf. Fig. 5 and 7). Hence, it makes sense to compare phases of annual periods as well. A good agreement is already visible from Fig. 7 (right). Defining the origin of the time-axis in the middle of the time interval common to the three considered hydrological models and GRACE monthly solutions shows that all four phases lie inside an interval of 20 degree width. Taking into account that one month corresponds to 30 degrees and that monthly solutions for all four models were used, the agreement can be regarded as very good.

Figure 8 includes also the nine most significant periods for mode 1 after subtraction of an annual wave as well as the results obtained by Fourier integral for GRACE.

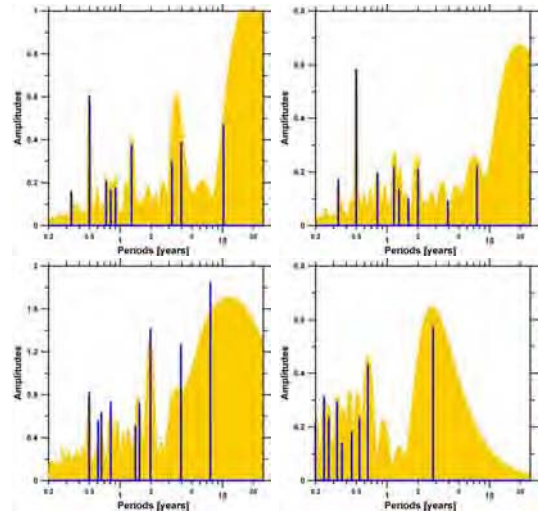


Figure 8. Fourier-spectrum and the nine most significant periods for mode 1 (annual wave subtracted): H96 and LaD (upper row), WGHM and GRACE (bottom row).

5 Conclusions

Different kinds of global spectral correlations have been investigated. They reveal interesting common spectral features.

EOF/PCA make it possible to find periodic features in principal components and to search for additional systematic behaviors. The strongest global component is annual, the phases found in the three considered global hydrology models and GRACE conform well.

It turns out that all the three models contain an almost perfect annual oscillation with almost identical phases. This means that about 30-60% of the total signal can be explained by the same annual oscillation which can be regarded as a common characteristic of all the three hydrology models considered and likely of the real hydrological variations. Comparing this with the result of the EOF analysis of GRACE-deduced water stocks variations strengthens this conclusion.

The patterns of eigenvectors compare well for the dominant modes of different global hydrology models and somewhat less well with GRACE (the problem of striped features in GRACE monthly solutions).

Acknowledgments. The German Ministry of Education and Research (BMBF) supports these investigations within the geoscientific R+D pro-

gramme GEOTECHNOLOGIEN “Erfassung des Systems Erde aus dem Weltraum” under grant 03F0424A. We thank P.C.D. Milly, Y. Fan and H. van den Dool as well as P. Döll for providing the LaD, H96 and WGHM model data, respectively. Thanks also go to D.W. Pierce for his Empirical Orthogonal Functions (EOF) software. The authors are grateful for discussions with J. Stuck and F. Flechtner.

References

- Abrikosov, O., F. Jarecki, J. Müller, S. Petrovic and P. Schwintzer (2006). The Impact of Temporal Gravity Variations on GOCE Gravity Field Recovery. In: Flury, J., Rummel, R., Reigber, C., Rothacher, M., Boedecker, G., Schreiber, U. (Eds.) *Observation of the Earth System from Space*, 494 p., Springer Berlin Heidelberg New York, ISBN: 3-540-29520-8, pp. 255-269 and 304.
- Bosch, W. (2001). EOF-Analysen der Meeresspiegel-Schwankungen im Pazifik. *ZfV (Zeitschrift für Geodäsie, Geoinformation und Landmanagement)*, 126 (2), pp. 74–81.
- Dickey, J. and National Research Council Commission (NRC) (1997). Satellite gravity and the geosphere. National Academy Press, Washington DC, pp. 112.
- Döll, P., F. Kaspar and B. Lehner (2003). A global hydrological model for deriving water availability indicators: model tuning and validation. *Journal of Hydrology*, 270, pp. 105–134.
- Fan, Y. and H. van den Dool (2004). Climate Prediction Center global monthly soil moisture data set at 0.5° resolution for 1948 to present. *J. Geophys. Res.*, 109, D10102, doi:10.1029/2003JD004345.
- Heiskanen, W. A. and H. Moritz (1967). Physical Geodesy. W. H. Freeman, San Francisco, CA.
- Huang, J., H. M. van den Dool and K. P. Georgakakos (1996). Analysis of model-calculated soil moisture over the United States (1931–1993) and applications to long-range temperature forecasts. *J. Climate*, 9, pp. 1350–1362.
- Mautz, R. and S. Petrovic (2005). Erkennung von physikalisch vorhandenen Periodizitäten in Zeitreihen. *ZfV (Zeitschrift für Geodäsie, Geoinformation und Landmanagement)*, 130 (3), pp. 156–165.
- Milly, P. C. D. and A. B. Shmakin (2002). Global Modeling of Land Water and Energy Balances. Part I: The Land Dynamics (LaD) Model. *Journal of Hydrometeorology*, 3, pp. 283–299.
- Peters, T. (2001). Zeitliche Variationen des Gravitationsfeldes der Erde. diploma thesis, TU München, IAPG/FESG No. 12.
- Preisendorfer, R. W. (1988). Principal component analysis in meteorology and oceanography. edited by: Mobley, C. D., Elsevier Science Publishers, Amsterdam.
- Reigber, C., R. Schmidt, F. Flechtner, R. König, U. Meyer, H.-K. Neumayer, P. Schwintzer and S. Y. Zhu (2005). An Earth Gravity Field Model Complete to Degree and Order 150 from GRACE: EIGEN-GRACE02S. *J. of Geodynamics*, 39, pp. 1–10.
- Schmidt, R., P. Schwintzer, F. Flechtner, C. Reigber, A. Güntner, P. Döll, G. Ramillien, A. Cazenave, S. Petrovic, H. Jochmann and J. Wunsch (2006a). GRACE Observations of Changes in Continental Water Storage. *Global and Planetary Change*, 50, pp. 112–126.
- Schmidt, R., F. Flechtner, A. Güntner, R. König, U. Meyer, K.-H. Neumayer, C. Reigber, M. Rothacher, S. Petrovic and S.-Y. Zhu (2006b). GRACE time-variable gravity accuracy assessment. *IAG/IAPSO/IABO Joint Assembly ‘Dynamic Planet 2005’*, IAG session G2, Cairns, Australia, August 22-26, 2005 (proceedings in print).
- Tapley, B. D., S. Bettadpur, M. Watkins and C. Reigber (2004a). The gravity recovery and climate experiment: Mission overview and early results. *Geophys. Res. Lett.*, 31, L09607, doi:10.1029/2004GL019920.
- Tapley, B. D., S. Bettadpur, J. C. Ries, P. F. Thompson and W. M. Watkins (2004b). GRACE measurements of mass variability in the Earth system. *Science*, 305, pp. 503–505, with electronic supplementary material.
- Wahr, J. M., M. Molenaar and F. Bryan (1998). Time variability of the Earth’s gravity field: Hydrological and oceanic effects and their possible detection using GRACE. *J. Geophys. Res.*, 103 (B12), pp. 30205–30229.
- Wahr, J., S. Swenson, V. Zlotnicki and I. Velicogna (2004). Time-variable gravity from GRACE: First results. *Geophys. Res. Lett.*, 31, L11501, doi:10.1029/2004GL019779.
- Wilks, D. S. (1995). Statistical methods in the atmospheric sciences: an introduction, Academic Press, San Diego.

Satellite-to-Satellite Laser Tracking Mission for Gravity Field Measurement

Stefano Cesare, Gianfranco Sechi, Luciana Bonino
Alcatel Alenia Space Italia, Strada Antica di Collegno 253, 10146 Turin, Italy

Roberto Sabadini, Anna Maria Marotta
Department of Earth Sciences, University of Milano, Via L. Cicognata 7, 20129 Milan, Italy

Federica Migliaccio, Mirko Reguzzoni, Fernando Sansò
DIIAR, Surveying Section, Polytechnic of Milano, Piazza Leonardo da Vinci 32, 20133 Milan, Italy

Andrea Milani
Department of Mathematics, University of Pisa, Via Buonarroti 2, 56127 Pisa, Italy

Marco Pisani
Istituto Nazionale di Ricerca Metrologica, Strada delle Cacce 73, 10135 Turin, Italy

Bruno Leone, Pierluigi Silvestrin
ESA-ESTEC, Keplerlaan 1, 2201 AZ Noordwijk ZH, The Netherlands

Abstract. A mission for monitoring the variations of Earth's gravity field at high resolution (up to harmonic degree 200) over a long time period (>5 years) has been defined within the "Laser Doppler Interferometry Mission for Determination of the Earth's Gravity Field" study for the European Space Agency. The mission exploits the use of a heterodyne laser interferometer for the high-resolution measurement of the displacement between two satellites flying at low altitude (325 km). Starting from the geophysical phenomena to be investigated, a detailed derivation of the mission requirements (orbit, satellites and measurement instruments: laser interferometer, accelerometer) was performed using analytical models and numerical simulations. A precision of about 1 nm rms is needed in the inter-satellite distance measurement, while the non gravitational accelerations must be measured with a precision of about 10^{-10} m/s² rms.

The overall metrology system designed for this mission includes, beside the heterodyne laser interferometer for the measurement of the inter-satellite distance, devices for the measurement of the lateral displacement and of the relative orientation of the two satellites (also contributing to the mission performance). Laboratory prototypes of the novel lateral displacement and angle metrology have been submitted to first proof-of-concept tests, achieving promising results.

Keywords. Space gravimetry, satellite-to-satellite tracking, laser metrology, Michelson interferometer.

1 Introduction

The last decade has been characterised by an increasing, worldwide concern about our planet and its environment. It is now commonly recognised that, in order to pursue a sustainable development, it is first necessary to monitor and to understand the ongoing evolution of the Earth's climate and environment. To address these issues in the appropriate way, it is of paramount importance to understand the geophysical processes that characterise the various sub-systems of the complex, time evolving Earth's system, namely those affecting the Geosphere, the Atmosphere, the Hydrosphere, the Cryosphere and the Biosphere.

In order to understand and to build the appropriate forward models of the geophysical processes, targeted towards the prediction of the ongoing global changes, the provision of globally distributed gravity data is of fundamental importance, since they provide information on the mass exchanges characterising the dynamic processes which interlink the various sub-systems of the evolving Earth.

Effort in space geodesy missions, from the first ones based on Satellite Laser Ranging (SLR), like LAGEOS, to the latest CHAMP, GRACE and

GOCE, belongs to this scenario. The purpose of these space missions is to detect the gravity field and its time variations at ever-increasing accuracy and spatial resolution (see Table 1). But these missions suffer a complementary limitation: CHAMP and GRACE have a lifetime long enough to allow observing time variation of the gravity field, but not at high resolution; GOCE enables to achieve a significantly larger resolution, but its lifetime is sufficient to make only a snapshot of the geopotential.

In 2004 the European Space Agency (ESA) awarded to Alcatel Alenia Space Italia a contract for studying a new space gravimetry mission, named Satellite-to-Satellite Interferometry (SSI), having the objective of monitoring the temporal variations of the Earth's gravity field at high resolution, up to harmonic degree 180-240 (as provided by GOCE, but extended also to longer wavelengths), over a long period of time of 5 to 10 years (as for CHAMP, GRACE).

Table 1. Objectives and performances of CHAMP, GRACE and GOCE

	CHAMP [1]	GRACE [2]	GOCE [3]
Launch date	July 2000	March 2002	2007
Orbit altitude, (initial value)	$h = 454$ km	$h = 494$ km	$h = 250 \div 260$ km
inclination	$i = 87^\circ$	$i = 89^\circ$	$i = 96.5^\circ$
Lifetime	>6 years	>8 years	20-30 months
Main payloads	Accelerometer, GPS receiver	K-band ranging system, Accelerometer, GPS receiver	3-axis Gradiometer, GPS receiver
Primary gravimetric measured quantities	Satellite position	Inter-satellite range rate	Diagonal components of the gravity gradient tensor
Measurement accuracy	<30 cm (range measurement), <0.2 cm (phase measurement)	$1 \mu\text{m/s}$	From ~ 50 to ~ 7 mE/Hz ^{1/2} between 5 mHz and 100 mHz
Gravity field measurement objectives	Global mapping of Earth gravity field (constant and time-variable part) with a cumulative Geoid height error of ~ 1 cm at the harmonic degree ~ 30	Global mapping of Earth gravity field (constant and time-variable part) with a cumulative Geoid height error of 1 cm at harmonic degree ~ 120	Global mapping of Earth gravity field (constant part) with a cumulative Geoid height error of 1 cm at the harmonic degree 200

To achieve its objectives, the SSI mission shall make use of the so called Low-Low Satellite-to-Satellite Tracking technique, similar to that adopted on GRACE, but where the inter-satellite distance variation produced by the geopotential is measured by a laser interferometer rather than a radio-frequency ranging system (Figure 1). A similar concept was considered also for the mission EX-5, proposed to NASA as successor to GRACE. The intrinsically higher resolution of the laser interferometry allows in principle to reconstruct the Earth gravity field with a significantly higher spatial resolution, if the other relevant mission parameters are sized to match the interferometer performance [5].

The objectives of the SSI mission assessment study, whose main results are presented here, were:

1. To review a set of geophysical phenomena involving mass redistribution (potential objectives of the SSI mission) and to derive their impact on the temporal variations of the Earth gravity field.
2. To analyze the geopotential measurement by Satellite-to-Satellite Tracking and to derive requirements on the SSI mission parameters and on the performance of its scientific instruments.
3. To establish an appropriate design for the SSI laser metrology and for its control system.
4. To outline the satellite configuration.
5. To define an R&D programme leading to the realisation of the laser metrology system.
6. To implement laboratory prototypes of some key elements of the laser metrology system and to subject them to first proof-of-concept tests.

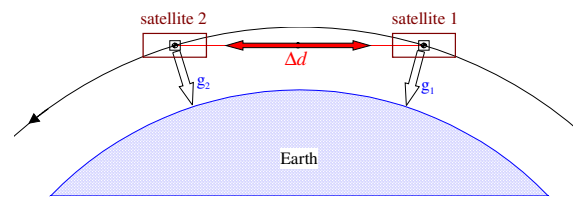


Fig. 1 Principle of the SSI technique: the inter-satellite distance variation Δd produced by the gravity accelerations g_1 , g_2 is measured by a laser metrology system

2 Geophysical Phenomena with Impacts on Earth's Gravity Field

Basically all the medium and large-scale geophysical phenomena involve significant mass redistribution in the Atmosphere (global and small-scale circulation), the Cryosphere (ice mass unbalance, mountain glaciers melting), the Hydrosphere (sea

level changes, ocean dynamics) and the Lithosphere (post glacial rebound, tectonics subduction). Therefore they can be potentially investigated and monitored by measuring the variations they induce in the Earth geopotential and in the related quantities: the height anomaly and the free air gravity anomaly (cfr. Heiskanen and Moritz, 1967 for definitions). Since these quantities will be computed at the surface level, we shall refer to them (somehow improperly) as geoid height and gravity anomaly. For understanding the long-term climatic variations, it is particularly important to identify the trends produced by these phenomena on the gravity field parameters. A summary of some geophysical phenomena reviewed during the study and of their signature on the gravity field is provided in Table 2.

Table 2. Geophysical phenomena and gravity field signature

Geophysical Phenomenon	Gravitational signature (drift rate or amplitude) ^a	Geopotential Degree ^b	Temporal Evolution
Post Glacial Rebound	1 mm/year (geoid: cumulative error)	Summed from $\ell=2$ to 200	Secular
Ice mass unbalance in Antarctica and Greenland	0.05÷0.7 mm/year (geoid: harmonic degree variance)	$\ell=200$	Secular
Tectonics – subduction	25 ÷ 100 mGal 2 ÷ 9·10 ⁻⁶ mGal/yr (gravity anomaly)	$\ell=200$ ÷ 700	10 Myr (typical period)
Mountain glaciers	0.02÷0.07 mm/yr (geoid: harmonic degree variance)	$\ell=200$	Annual to secular
Hydrology: global hydrological cycle and land water storage	0.02÷0.07 mm/yr (geoid: harmonic degree variance, Po plain basin)	$\ell=200$	Months (typical period)
Sea level changes	1 mm/yr (geoid: cumulative error)	Summed from $\ell=2$ to 200	Secular
Ocean basin-scale dynamics	1 cm (geoid: cumulative error)	Summed from $\ell=4$ to 20	Several years period
Atmosphere global circulation	0.5 mm/yr (geoid: harmonic degree variance)	$\ell=4$	Annual to secular

^a Required measurement accuracy of geoid undulation drift rate or gravity anomaly amplitude or drift rate needed to detect the phenomenon.

^b Degree ℓ of the geopotential spherical harmonic corresponding to the typical spatial resolution of the phenomenon ($\ell=20000$ km/spatial resolution km).

3 Model of the Gravity Field Measurement by Satellite-to-Satellite Tracking

An analytical model has been developed in order to express the geopotential measurement error as function of the main parameters of the SSI mission, in which the information about the Earth gravity are obtained from tracking the distance variation between two satellites flying on the same orbital path at low altitude. The gravitational potential has been split into two parts: a model potential V and the residual part U (anomalous potential) which is what we want to retrieve. By representing the anomalous gravitational potential of degree ℓ (U_ℓ) in terms of a Fourier series, the variance of the estimation error of the Fourier coefficients (A_k, B_k) is obtained as [5]

$$\sigma^2(\hat{A}_k) = \sigma^2(\hat{B}_k) = \frac{\omega^2(k^2 - J^2)^2}{a_\ell^2(k^2 - (2\ell - 1)J^2 + (\ell - 1)^2)k^2} \frac{J^2}{k^2} \left\{ \frac{4}{M} S_{v_{i,k}}^2 + \frac{(8 + 2\varepsilon^2)J^2}{M\omega^2 k^2 (k^2 - J^2)^2} (k^4 + 10k^2 J^2 + 9J^4) S_{v_{a,k}}^2 \right\} \quad (1)$$

where:

- $a_\ell = d \frac{\mu}{R^3} \left(\frac{R}{R+h} \right)^{\ell+3}$, h = orbit altitude
- J, M = number of orbits and number of measurements in the observation period respectively.
- ε = angular separation between the two satellites.
- ω = orbit mean motion.
- R, μ = Earth radius and gravitational parameter.
- $S_{v_{i,k}}, S_{v_{a,k}}$ = spectral density of the inter-satellite distance and of the non-gravitational acceleration measurement noise, respectively.

From the above expression, the errors on the determination of the geoid undulation (N) and of the gravity anomaly (Δg) can be obtained as follows

$$\sigma^2(\hat{N}) = R^2 \sum_{\ell} \sigma_{\ell}^2$$

$$\sigma^2(\Delta \hat{g}) = \left(\frac{\mu}{R^2} \right)^2 \sum_{\ell} (\ell - 1)^2 \sigma_{\ell}^2 \quad (2)$$

with:

- $\sigma_{\ell}^2 = \sigma^2(\hat{C}_{\ell 0}) + 2 \sum_{m=1}^{\ell} \sigma^2(\hat{C}_{\ell m})$ (error degree variance)
- $\sigma^2(\hat{C}_{\ell m}) = \frac{1}{\sum_{p=0}^{\ell} \frac{F_{\ell m, \ell-2p}^2}{\sigma^2(\hat{A}_{k(\ell, m, p)})}}$ (estimation error variance of the spherical harmonic coefficient $C_{\ell m}$)
- $F_{\ell m, \ell-2p}$: inclination functions.

4 Satellite-to-Satellite Interferometry Mission Sizing

4.1 Mission Reference Parameters

A high resolution measurement of the Earth gravity field calls for the lowest possible altitude. In fact, the anomalous gravitation potential of degree ℓ decreases with the orbit radius r as: $U_\ell \propto r^{-(\ell+1)}$. Conversely, a long mission lifetime (required to improve the monitoring of the gravity field temporal variations) cannot be achieved at very low altitude because of the excessive amount of propellant needed for the aerodynamic drag compensation. The orbit inclination must be as close as possible to 90° to ensure a gravity field sampling at all latitudes, compatible with the design constraints of the satellites and of the metrology system.

For any established set of values for the orbit altitude, inclination, observations duration, a suitable combination of inter-satellite distance and measurement error of the inter-satellite distance variation and of the non-gravitational accelerations acting on the satellites was determined using the expressions given in Chap. 3. At the end of an extensive analysis of the orbital perturbation and control and of the scientific performance, the following reference mission parameters have been established:

- Circular orbit spherical altitude $h = 325$ km.
- Orbit inclination $i = 96.78^\circ$ (sun-synchronous).
- In-flight measurement phase duration = 6 years.
- Inter-satellite distance $d = 10$ km.
- Spectral density of the inter-satellite distance and of the non-gravitational acceleration measurement noise: see Figure 2.

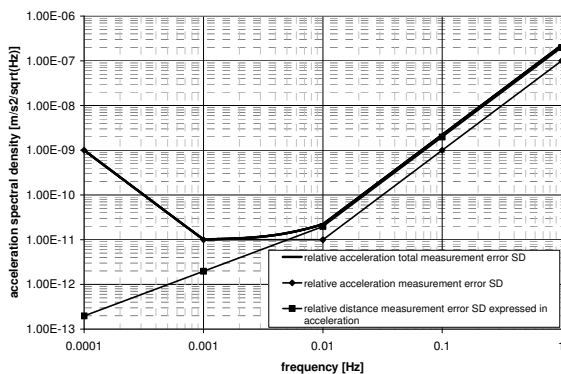


Fig. 2 Spectral densities of the measurement error of the non-gravitational relative acceleration between the two satellites and of the inter-satellite distance (converted in acceleration) suitable to fulfil the SSI mission objectives.

4.2 Scientific Performance Prediction

Using the reference SSI mission parameters of Sect. 4.1, the error made in the determination of the geoid height and gravity anomaly variation has been estimated from the error variances of the solutions computed over 1-year periods along the mission using the equation (2). The geoid height variation error is plotted in Figure 3 as function of the geopotential harmonic degree. This error is compared to the signal (geoid height variation per degree) generated by two of the smaller secular geophysical phenomena of Table 2, namely the melting of the glaciers of the Italian Alps and the ice loss over Greenland. The plot shows that the potential performance of the SSI mission is suitable to detect the signature produced by these small geophysical phenomena on the geoid height up to $\ell \cong 200$. Moreover, it has been verified that, with the established design parameters, the SSI mission would be capable of detecting the geoid modification caused by the Sumatra earthquake occurred in December 2004 [4]. The predicted performance of the SSI mission obtained with the analytical measurement model (Chap. 3) has been validated in some specific cases through high-fidelity numerical simulations of the gravity field measurement process [5], using methods described in [6].

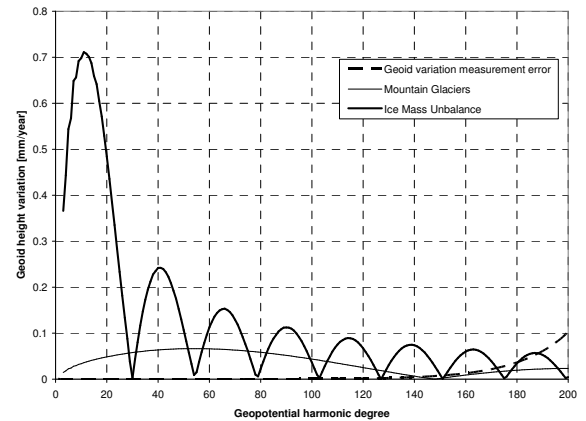


Fig. 3 Geoid height variation measurement error per harmonic degree (dashed line) compared to the signal generated by two of the secular geophysical phenomena of smaller entity (solid lines)

4.3 Measurement and Control Systems

The main measurement and control systems of the SSI mission are schematically shown in Figure 4. The instrument utilized to measure the inter-satellite

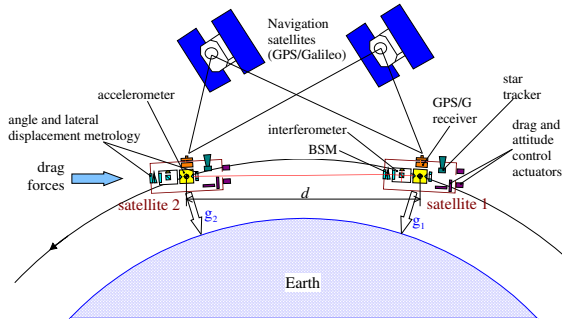


Fig. 4 Main elements of the measurement and control systems of the SSI mission

distance variation is the laser interferometer. On a low Earth orbit, this distance is modified by the action of the gravity field (let's call Δd_G the variation induced by the gravitational accelerations) and by the aerodynamic drag (let's call Δd_D the variation induced by the non-gravitational accelerations). The measure of the laser interferometer gives therefore an inter-satellite distance variation (Δd) which includes both the gravitational and the non-gravitational contribution:

$$\Delta d = \Delta d_G + \Delta d_D \quad (3)$$

In order to separate Δd_G from Δd_D , the latter must be measured using an accelerometer (similar to the GOCE one) installed on each satellite and nominally located in the position of its centre of mass (COM).

The laser metrology must provide a measurement of Δd with the error spectral density limit plotted in Figure 5, while the accelerometers must provide a measurement of the non-gravitational accelerations between the two satellites with the error spectral density limit plotted in Figure 2 (similar in shape to the intrinsic noise spectral density of the GOCE accelerometer, but shifted to lower frequencies by half a decade).

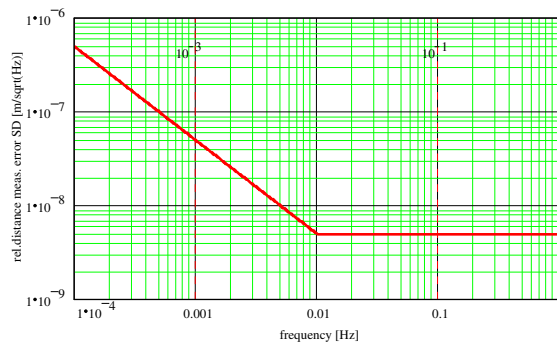


Fig. 5 Δd measurement error spectral density specification

A proper operation of the accelerometer requires a drag control system to reduce the level of the non-gravitational accelerations and of the angular accelerations and rates of each satellite. The sensors utilized by this system are the accelerometer itself (linear and angular accelerations measurement) and a set of star trackers (attitude measurement, to be combined with those of the angular accelerations). The actuators are four ion thrusters (which can be derived from the GOCE ones), for linear acceleration and orbit control, and four low-noise reaction wheels (under development) for attitude, angular rate and angular acceleration control.

The attitude control is driven by the laser beam pointing between the satellites. For this purpose a Beam Steering Mechanism (BSM) has been introduced to avoid imposing too stringent requirements on the attitude control of the whole satellite. The BSM on the satellite 1 is driven by the measurement of the satellite 2 offsets relative to the laser beam provided by a specific lateral displacement metrology (required measurement error $\leq 0.37 \text{ mm } 1\sigma$).

The non-gravitational acceleration measurement process requires the precise knowledge of the accelerometer sensitive axis orientation relative to the line joining the COMs of the two satellites. The inter-satellite distance measurement process requires the precise knowledge of the satellites orientation relative to the laser beam. These quantities are both provided by a specific angle metrology (required measurement error $\leq 0.014 \text{ arcsec } 1\sigma$).

A navigation receiver (GPS or GPS + GALILEO) placed on each satellite provides the information utilized for reconstructing the inertial position of the two satellites (required measurement error $\leq 3 \text{ cm}$).

5 Laser Metrology System Design

The selected metrology system for measuring the variation of the satellite-satellite relative distance is a heterodyne Michelson interferometer. The functional configuration of this interferometer, suitably adapted to the SSI mission, is described in Figure 6. At a relative distance $d = 10 \text{ km}$, a frequency-stabilized laser source emitting 1 W on the satellite 1, a retro-reflector with 3.14 cm^2 cross section on the satellite 2 (embedded in the accelerometer proof mass), and a receiving telescope with 8 cm diameter on satellite 1 are sufficient to achieve the measurement of Δd with an error spectral density below the limit plotted in Figure 5. The relative frequency stabilization required for the laser source is $\delta v/v \leq 1.4 \cdot 10^{-13} 1/\text{Hz}^{1/2}$ above $f = 0.01 \text{ Hz}$, with $1/f$ increase

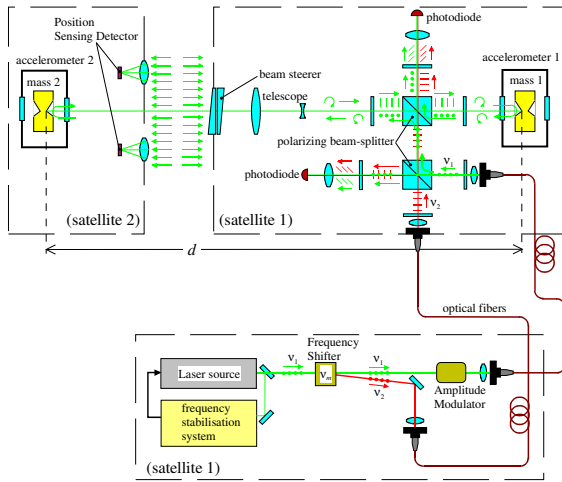


Fig. 6 Functional configuration of the laser metrology

allowed below that frequency. Such stabilization is achievable by locking the laser frequency to a resonant mode of a dimensionally stable optical cavity, a technique planned to be used in the LISA mission [7] as well as the laser source, a Nd:YAG emitting a continuous wave at the wavelength of 1064 nm, selected for the SSI mission.

The lateral displacement and angle metrology are realized by means of three Position Sensing Detectors (PSDs) endowed with focusing optics. Each PSD measures the position and the energy of the laser beam spot focused by the optics on the detector plane. The orientation and the lateral shift of the satellite 2 relative to the laser beam are derived from the spot position and from the energy measured by the three PSDs respectively.

The configuration of the metrology optical bench and that of the SSI satellites are shown in Figure 7.

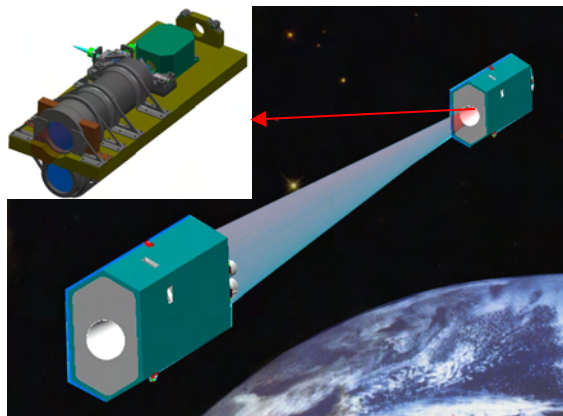


Fig. 7 Satellites and metrology optical bench configuration

6 Metrology Proof of Concept

Laboratory prototypes of the novel lateral displacement and angle metrology concept have been implemented using commercial off-the-shelf components and submitted to first proof-of-concept tests. The achieved measurement error of the orientation angles relative to the laser beam was found to be a factor 5 larger than the SSI mission requirement. The performance limit is probably due to the dark current noise of the PSD (not the best available in commerce) used in the test. The achieved measurement error of the lateral displacement relative to the laser beam was instead found well below the SSI mission requirement (see Figure 8).

The concept of the heterodyne Michelson interferometer for the measurement of Δd instead is not new, so it does not need to be demonstrated. What remains to be experimentally verified is the specific implementation of such interferometer and of its Beam Steering Mechanism for the SSI mission case.

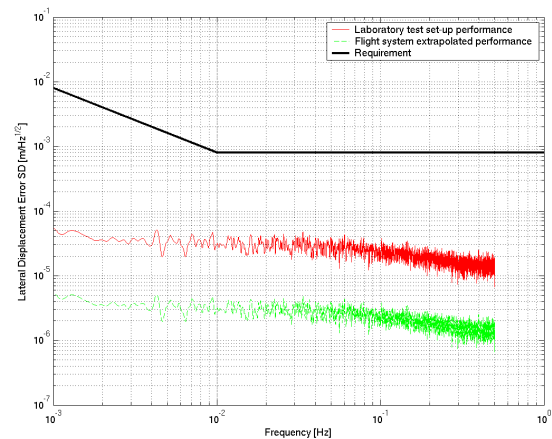


Fig. 8 Lateral displacement measurement test result

References

- [1] http://op.gfz-potsdam.de/champ/index_CHAMP.html
- [2] http://op.gfz-potsdam.de/grace/index_GRACE.html
- [3] <http://www.esa.int/export/esaLP/goce.html>
- [4] Sabadini, R., G. Dalla Via, M. Hoogland and A. Aoudia. A splash in the Earth Gravity from the 2004 Sumatra earthquake. *EOS Transactions*, American Geophysical Union, 86, No. 15, 12 April 2005, pp. 149-153.
- [5] Laser Doppler Interferometry Mission: Final Report. Alcatel Alenia Space Italia report No. SD-RP-AI-0445. 19 December 2005, pp. 33-66.
- [6] Milani, A., A. Rossi and D. Villani. A timewise kinematic method for satellite gradiometry: GOCE simulations. *Earth Moon Planets*, Vol. 97, pp. 37-68.
- [7] Tröbs, M., et al. Laser development for LISA. *Classical and Quantum Gravity*, 23 (8), 21 April 2006, pp. 151-158

Gravity recovery capability of four generic satellite formations

M.A. Sharifi, N. Sneeuw, W. Keller

Institute of Geodesy, Universität Stuttgart, Geschwister-Scholl-Str. 24D, D-70174 Stuttgart, Germany

Abstract. Of all potential satellite formations a GRACE-type in-plane leader-follower configuration is one of the weakest choices in terms of gravitational signal in the satellite-to-satellite tracking (SST) observable. In this paper we simulate four basic types of formation flying (FF) missions and analyse them in terms of sampling geometry (baseline orientation), gravitational signal content and gravity field recovery capability. The four FF types are, respectively a GRACE-type SST mission, a SWARM-like pendulum configuration, a Cartwheel formation on a 2:1 relative ellipse and a LISA-type formation. All formations have comparable orbit characteristics: near polar, near eccentric, and short baselines of typically 10–20 km length.

The baseline orientations in the latter three FF-types contain additional cross-track and/or radial information. They cover a larger azimuth-elevation sampling space. As a result, compared to the GRACE-type formation, all three other formations are superior in terms of more gravitational signal content, though not equally.

The qualitative difference in the respective FF-SST observable is reflected in the recovered gravity fields. Comparison between the input and output fields demonstrates that the recovery process using an observable with radial and/or cross-track information results in drastically improved accuracy and isotropy. The recovered solutions from the latter three formation types possess a lower error spectrum with a more homogeneous structure.

Keywords. Observation equation, formation flight, gravity field recovery, satellite-to-satellite tracking

1 Introduction

The key GRACE-type SST observables are the intersatellite distance and scalar relative velocity in a leader-follower configuration at near-polar inclination. This type of observable inherently suffers from the weakness that it is mainly sensitive along the line-of-sight, i.e. in North-South direction. Consequently, typical streaks emerge along the meridians in the monthly GRACE solutions (e.g. Tapley et al., 2004).

Sneeuw et al. (2006) have shown that the weakness can be overcome if the SST observation contains radial and/or cross-track gravitational signal. To that end, a next generation gravity mission should preferably be a FF with a rotating baseline in the satellites' local frame.

To support and quantify this assertion a gravity recovery experiment is set up that makes use of the concept of formation flying. Four generic types of Low-Earth Formations (LEF) are simulated:

- a GRACE-type leader-follower configuration, with along-track orientation;
- a pendulum scenario, which adds a cross-track component, but stays in the local horizon;
- a Cartwheel formation that performs 2:1-relative elliptical motion in the orbital plane, i.e. stays in the local vertical plane;
- and a LISA-type formation that performs circular relative motion including out-of-plane and radial relative motion.

All four LEF will have a typical baseline length of around 10–20 km. The names GRACE, Pendulum, Cartwheel and LISA will be used in this paper as generic for these basic formation types and should not be mistaken for actual missions.

The dynamics of such formations are easily understood in the framework of homogeneous Hill equations. Thus, the first part of the paper is concerned with initial conditions and modelling the relative motion of the configurations in the local Hill frame.

To show the differences in the signal content of the configurations, the second part of the paper is dedicated to their comparative analysis at the observation level. It shows how the projection of the additional components into the observable amplify the signal.

Eventually, the recovered solutions are compared from different perspectives both in the time and frequency domains.

2 Equations of relative motion

Let us adopt the following formation flying convention. All formations consist of a chief satellite and one or more deputy satellites. We assume a local orbital reference frame (or Hill frame) with its origin

in this chief satellite and oriented in along-track (x), cross-track (y) and radial (z) direction. The relative motion of the deputy in the local orbital reference frame is described in general by Schaub and Junkins (2003):

$$\ddot{x} + z\ddot{\theta} + 2z\dot{\theta} - x\left(\dot{\theta}^2 - \frac{\mu}{r_c^3}\right) = a_x \quad (1a)$$

$$\ddot{y} + \frac{\mu}{r_c^3}y = a_y \quad (1b)$$

$$\ddot{z} - z\left(\dot{\theta}^2 + 2\frac{\mu}{r_c^3}\right) - x\ddot{\theta} - 2\dot{x}\dot{\theta} = a_z \quad (1c)$$

where μ is the gravitational constant and (a_x, a_y, a_z) are non-Keplerian forces acting on the deputy satellite. They could be due to atmospheric drag, Earth oblateness effects or control thrusters.

Here we consider only formations where the chief motion is essentially circular. In this case the chief rate $\dot{\theta}$ is constant and equal to the mean orbit rate $n = \sqrt{\mu/r_c^3}$. The equations of motion simplify to the well-known linearized Hill equations (Hill, 1878), see also (Clohessy and Wiltshire, 1960):

$$\ddot{x} + 2n\dot{z} = a_x \quad (2a)$$

$$\ddot{y} + n^2y = a_y \quad (2b)$$

$$\ddot{z} - 2n\dot{x} - 3n^2z = a_z \quad (2c)$$

We will refer to them as HE in the sequel. Equation (2) has been used extensively in spacecraft formation flying mission analysis and control research. They are reasonable as long as (x, y, z) are small compared to the chief orbital radius.

Since they are linear, the HE can be solved analytically. Assuming no perturbations or thrusting is present ($a_x = a_y = a_z = 0$), all possible deputy relative motions can be expressed in closed form (Schaub and Junkins, 2003):

$$x(t) = -2A_0 \sin(nt + \alpha) - \frac{3}{2}ntz_{\text{off}} + x_{\text{off}} \quad (3a)$$

$$y(t) = B_0 \cos(nt + \beta) \quad (3b)$$

$$z(t) = A_0 \cos(nt + \alpha) + z_{\text{off}} \quad (3c)$$

Note that the out-of-plane motion is decoupled from the in-plane motion. The integration constants can be expressed in terms of initial conditions through:

$$A_0 = \frac{1}{n} \sqrt{\dot{z}_0^2 + (2\dot{x}_0 + 3nz_0)^2} \quad (4a)$$

$$B_0 = \frac{1}{n} \sqrt{\dot{y}_0^2 + (ny_0)^2} \quad (4b)$$

$$\alpha = \arctan\left(\frac{\dot{z}_0}{3nz_0 + 2\dot{x}_0}\right) \quad (4c)$$

$$\beta = \arctan\left(\frac{-\dot{y}_0}{ny_0}\right) \quad (4d)$$

$$z_{\text{off}} = \frac{2}{n}(\dot{x}_0 + 2nz_0) \quad (4e)$$

$$x_{\text{off}} = x_0 - \frac{2\dot{z}_0}{n} \quad (4f)$$

The solution of the homogeneous HE allows to analyze the motion of the aforementioned four basic formation types in terms of the parameters in (4). For the relative motion to be bounded, we must require the drift term to vanish, i.e. $z_{\text{off}} = 0$ for all missions. The four generic FF types are now characterized by:

- GRACE is purely along-track. All periodic terms are zero and the variable x_{off} determines the baseline length.
- The pendulum scenario also has a constant along-track term x_{off} , but additionally a non-zero cross-track amplitude B_0 . The relative motion takes place in the xy -plane, i.e. the local horizontal plane. The intersatellite baseline is variable. Only its component in along-track direction is constant.
- The Cartwheel configuration has a non-zero A_0 value. Without cross-track motion ($B_0 = 0$) this results in an in-plane elliptical relative motion (Massonnet, 2001). The maximum along-track separation is twice as large as the maximum radial separation. Hence a 2:1 relative ellipse.
- The LISA-type mission achieves a relative circular motion by setting $B_0 = \sqrt{3}A_0$ and matching the phases α and β . Within the approximation of the HE, the baseline is constant.

The necessary condition for achieving these configurations and the corresponding differential elements in the Hill frame are summarized in table 1. These differential elements can be converted to inertial orbital elements for integration purposes (Alfriend et al., 2000).

In table 1, relative position and velocity vectors are expressed in terms of the chief satellite's Kepler elements (a, e, u) and the baseline length ρ . The latter two configurations are defined by setting the free parameter (z_0).

The homogeneous HE are a helpful tool for first order formation design. However, the solution in (3) is no longer valid if the chief motion is not circular. Even small amounts of eccentricity can produce modelling errors comparable to those produced by J_2 gravitational perturbations or atmospheric drag.

Alternatively, the formations can be designed directly using differential Kepler elements. This ap-

Table 1. Initial conditions and state vectors of different formation types

formation	initial conditions	initial position (ρ_0)	initial velocity ($\dot{\rho}_0$)
GRACE	$A_0 = B_0 = z_{\text{off}} = 0$	$(\rho, 0, 0)$	$(0, 0, 0)$
Pendulum	$A_0 = z_{\text{off}} = 0$	$(\rho_x, \rho_y \cos u, 0)$	$(0, -n\rho_y \sin u, 0)$
Cartwheel	$B_0 = x_{\text{off}} = z_{\text{off}} = 0$	$(\pm 2\sqrt{4a^2e^2 - z_0^2}, 0, z_0 \leq 2ae)$	$(-2nz_0, 0, \pm n\sqrt{4a^2e^2 - z_0^2})$
LISA	$x_{\text{off}} = z_{\text{off}} = 0; \alpha = \beta$ $B_0 = \sqrt{3}A_0 = \sqrt{3}\rho/2$	$(\pm\sqrt{\rho^2 - 4z_0^2}, \pm\sqrt{3}z_0, z_0 \leq \rho/2)$	$(-2nz_0, \pm\sqrt{3}n\sqrt{\rho^2/4 - z_0^2}, \pm n\sqrt{\rho^2/4 - z_0^2})$

proach, in contrast, can be used for designing a configuration even with an elliptical chief motion in J_2 gravitational field (Sneeuw et al., 2006).

3 Observation equation of FF LL-SST

As for the GRACE mission, let us assume range-rate as the basic observable of a future LEF mission. The range rate $\dot{\rho}$ between two satellites is the projection of the relative vectorial velocity $\dot{\rho}$ on the line-of-sight unit vector e , e.g. (Keller and Sharifi, 2005). The scalar range acceleration is derived by time differentiation and involves additional centrifugal terms:

$$\dot{\rho} = \dot{\rho} \cdot e \quad (5a)$$

$$\Rightarrow \ddot{\rho} = \ddot{\rho} \cdot e + \frac{1}{\rho} (\dot{\rho} \cdot \dot{\rho} - \dot{\rho}^2) \quad (5b)$$

Using Newton's equations, the vectorial acceleration difference $\ddot{\rho}$ equals the difference in gravitational attraction $\nabla V_{1,2}$ between the two satellites 1 and 2.

For practical applications, the scalar range acceleration $\ddot{\rho}$ can be obtained from the observed range rate by numerical differentiation. To extract the gravitational information, one should further correct for the relative velocity terms at the right of (5b).

In the absence of the nuisance forces, the vectorial gradient difference $\nabla V_{1,2}^{\text{LOS}}$ is parameterized in terms of the unknown spherical harmonic coefficients. To set up the mathematical model for the recovery of the field, Newton's equation is employed and (5b) is recast into

$$\nabla V_{1,2}^{\text{LOS}} = \ddot{\rho} + \frac{\dot{\rho}^2}{\rho} - \frac{\|\dot{\rho}\|^2}{\rho} \quad (6)$$

The left-hand side represents the gravitational attraction difference between the two satellites projected along the Line Of Sight (LOS). As such, it is justified to speak of *spaceborne gravimetry*, though in a differential sense. The right-hand side consists of the HL- and LL-SST measurements. Depending on the formation type, each term on the observation side has different magnitude and pattern and consequently different contribution to the total observable. Furthermore, the recovered solution's quality explicitly

depends on the gravity signal captured by the formation type. Therefore, the accuracy and the resolution of the recovered field is a configuration specific aspect.

To underline this point, the signal decomposition according to (6) is visualized in 1 both for GRACE and LISA. The top row represents the quantity at the left-hand side of (6), i.e. the quantity that is used to extract gravity field information. The left column is a visualization of one orbital revolution in the time domain, whereas the right column shows the power spectral density of the signal in the measurement bandwidth.

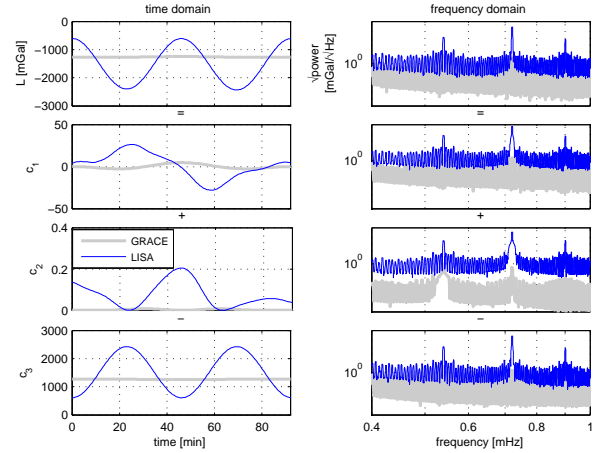


Figure 1. Observation decomposition in time and space domains ($L = \ddot{\rho} \cdot e$, $c_1 = \ddot{\rho}$, $c_2 = \dot{\rho}^2/\rho$ and $c_3 = \|\dot{\rho}\|^2/\rho$)

As can be clearly seen in the time domain representation, the total gravitational signal of LISA and its individual components are significantly larger than those of GRACE.

Comparing the missions' spectra shows that LISA captures more information than GRACE. This richer gravitational signal content is due to the radial and cross-track components in the relative motion. The GRACE mission, in contrast, only contains the along-track component which is a—from a gravity gradiometry viewpoint—a relatively weak observ-

able (Sneeuw and Schaub, 2005). Apparently the common mode motion of the satellites in a GRACE-type mission cancels a large part of the signal.

It should also be noted here that the LISA's spectrum is at least one order of magnitude higher than that of the GRACE. Moreover, more peaks are clearly visible in the LISA's spectrum. Further numerical analysis (not shown here) would demonstrate that the LISA mission has the richest signal, followed by Cartwheel and Pendulum.

4 Simulation setup

For a comparative study of the four mission types closed-loop simulations have been performed. All configurations have comparable orbit characteristics: near polar, near eccentric, and short baselines of typically 10–20 km length. In order to achieve a nearly stable and bounded motion, the necessary conditions, listed in table 1, were imposed on the initial values. The relative state vectors can then be transformed to the corresponding initial differential Kepler elements (Alfriend et al., 2000).

Alternatively, the formations can be designed directly in terms of differential Kepler elements (Sneeuw et al., 2006). We have used the latter approach and the obtained initial differential Kepler elements have been listed in table 2. The differential

Table 2. Differential mean orbital elements

	Grace	pendul.	cartwh.	LISA
Δa	0	0	0	0
Δe	0	0	0	0.001
ΔI [°]	0	0	0	0
$\Delta \Omega$ [°]	0	0.1389	0	0.15
$\Delta \omega$ [°]	0	0	180	-180
ΔM [°]	0.08	0.08	180	180

elements of the GRACE and Pendulum missions are the same, except for the ascending node definition. In the latter mission a non-zero value for $\Delta \Omega$ is required to introduce cross-track baseline component.

In a next step, for all missions observations of differential gravimetry type (6) were simulated. The mission duration and the sampling frequency are one month and 0.2 Hz, respectively. To generate these SST observations EGM96 was used up to degree and order 60 as input model. All kinematic quantities like intersatellite range, range-rate and range-acceleration vectors are derived from the orbit integration process.

As shown in (6), the observable consists of the

LL-mode observations ($\dot{\rho}$, $\ddot{\rho}$) and the HL-mode measurements $\dot{\rho}$. Noise-free simulated range-rate is contaminated with a *white noise* with $\sigma_{\dot{\rho}} = 1 \mu\text{m/s}$, comparable to the nominal noise RMS of the real GRACE mission (Reigber et al., 2005). The range-acceleration $\ddot{\rho}$ is then numerically derived from the noisy range-rate observations using *spline* differentiation.

Furthermore, noise-free simulated relative velocity vectors are contaminated with a correlated noise sequence, that reflects the GPS-derived LEO orbit coordinates. We assumed a standard deviation of 6 mm in each coordinate direction with a correlation length of about 3 minutes.

An identical noise pattern but independently simulated sequences were used for each individual component of the relative velocity vector. These noise sequences were used for all the formations.

5 Gravity field recovery

To close the simulation loop gravity fields were recovered from the noisy observations for all four scenarios. Spherical harmonic coefficients and their covariance matrix were estimated using brute-force least squares inversion.

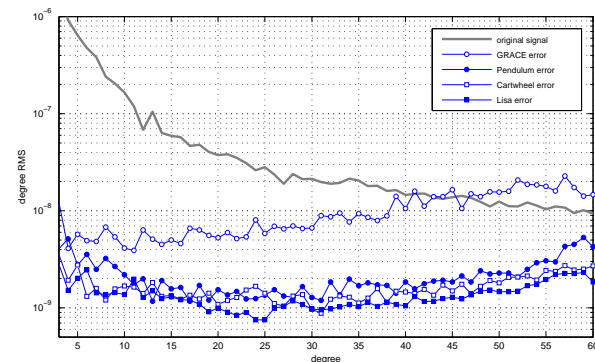


Figure 2. Dimensionless degree RMS of the recovered solutions.

The achieved results are evaluated from different perspectives. A first spectral comparison in terms of error degree RMS curves shows that the introduction of cross-track and/or radial information into the observable greatly improves the quality of the solution by nearly an order of magnitude, see figure 2. As expected, the GRACE mission, with along-track information alone, yields the poorest solution whereas the LISA mission gives the best due to the contribution of all three components. It is followed by Cartwheel mission which moves only in satellites' orbital plane. Compared to LISA, the Cartwheel ob-

servable does not carry cross-track information. Nevertheless the Cartwheel solution is just marginally worse than LISA's.

In contrast, the Pendulum observable contains only along-track and cross-track, i.e. horizontal information. Therefore, it does not achieve the performance level of the Cartwheel mission. These effects, in which the radial component is the dominant source of gravity field information, is known from satellite gravity gradiometry as well, e.g. (Sneeuw, 2000). Still, the Pendulum configuration outperforms a GRACE-type LEF.

By lumping over the order m , the degree RMS curves are not representative of non-isotropic error spectra. Therefore we visualize the full error spectra in 3, both in terms of input-minus-output coefficient differences ΔC_{lm} and ΔS_{lm} and in terms of formal standard deviations.

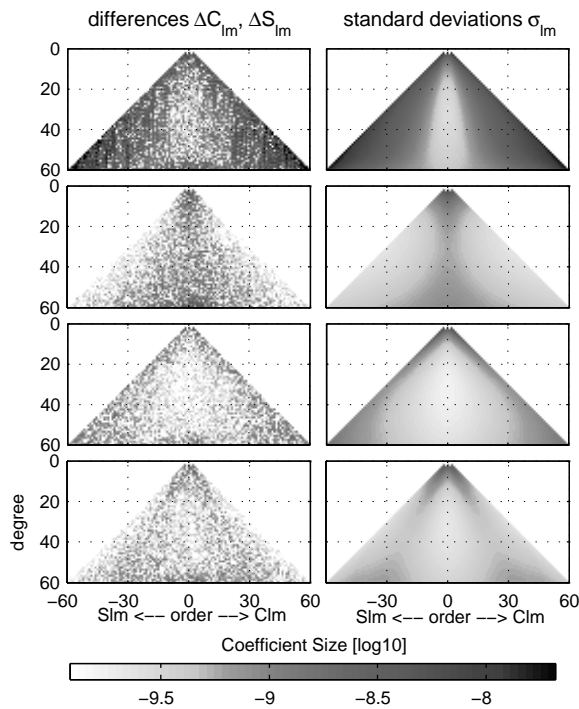


Figure 3. Spherical harmonic error spectra (from top: GRACE, Pendulum, Cartwheel and LISA). Left: actual input-minus-output coefficient differences. Right: formal standard deviations.

Indeed, these full error spectra reveal the non-isotropic behaviour of some of the mission types. A GRACE-type mission performs best in the low order range. Its error spectrum resembles that of along-track gradiometry (V_{xx}). The reverse is true for the Pendulum mission, whose error spectrum resembles that of cross-track (V_{yy}) gradiometry. Except of

sectorial harmonics, the recovered spectrum from a Cartwheel-type mission is relatively homogeneous. It's error spectrum resembles a cross between V_{xz} and V_{zz} gradiometry. A LISA-type mission also appears to provide a homogeneous error spectrum, although the error structure resembles that of the observable ($V_{xx} - V_{yy}$), a term that is obtained by rotating gradiometers.

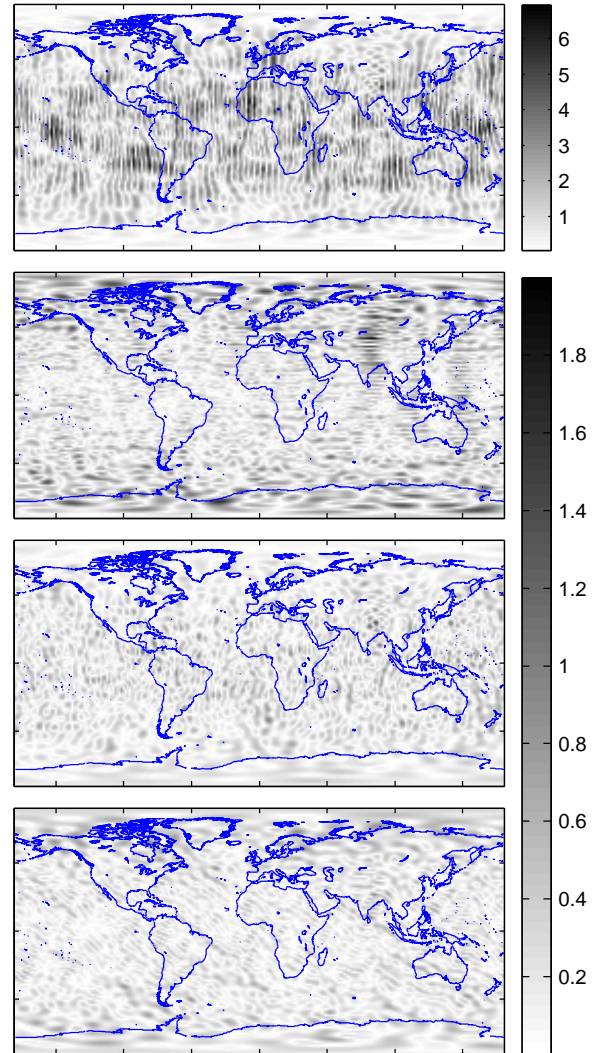


Figure 4. The geoid height residuals in meter (from top: GRACE, Pendulum, Cartwheel and LISA). Note the different gray scale for GRACE.

These spectral results are also reflected in the spatial domain. Differences between the geoid height of the input and recovered models show the spatial distribution of the errors. Due to preference for low orders, the familiar North-South streaks are clearly visible in GRACE geoid errors. In contrast, they ap-

pear in East-West direction in the Pendulum configuration. The last two solutions are almost homogeneous although a very weak diagonal pattern is observed in the LISA solution.

6 Conclusion

When designing future gravity field missions, formations that involve a cross-track or radial component outperform a GRACE-type leader-follower configuration. The observable in such formations are significantly richer in gravitational content, leading to a higher S/N ratio. Observing at least one of these components, preferably the radial one, improves the results both in terms of error level and of isotropy.

Employing the Pendulum mission involves the gravity gradient component in East-West direction whereas the Cartwheel scenario projects the radial gravity gradient V_{zz} onto the SST observable. The observable in a LISA-type mission combines all the components. Thus, the inherent weakness and the non-isotropic behaviour of the conventional low-low SST observable can be solved by formation flying.

If the relative orbits comprise a cross-track motion, the corresponding observables gain sensitivity in East-West direction. This may be helpful in dealiasing signals. Moreover, including the radial component's contribution leads to a nearly homogeneous results in the LISA configuration. Consequently, a LEF with sufficiently many satellites linked together in a strategic way, can observe full-tensor gravity gradiometry.

References

- Alfriend, K.T., H. Schaub, D.W. Gim (2000). Gravitational Perturbations, Nonlinearity and Circular Orbit Assumption Effects on Formation Flying Control Strategies. Proceedings of the Annual AAS Rocky Mountain Conference, Breckenridge, CO, Feb. 26, pp. 139158.
- Clohesy W.H., R.S. Wiltshire (1960). Terminal guidance system for satellite rendezvous. *Journal of the Aerospace Sciences*, 27:653–658.
- Hill, G.W. (1878). Researches in the lunar theory. *Am. Journal of Math.*, 1:5–26,129–147,245–260.
- Massonnet, D. (2001). The interferometric Cartwheel: a constellation of passive satellite to produce radar images to be coherently combined. *Int. J. Remote Sensing* 22:2413–2430
- Reigber, C., R. Schmidt, F. Flechtner, R. König, U. Meyer, K.H. Neumayer, P. Schwintzer, S.Y. Zhu (2005). An Earth gravity field model complete to degree and order 150 from GRACE: EIGEN-GRACE02S. *Journal of Geodynamics* 39:1–10
- Keller, W., M.A. Sharifi (2005) Gradiometry using a satellite pair. *Journal of Geodesy* 78:544–557
- Schaub, H., J.L. Junkins (2003). *Analytical mechanics of space systems*. AIAA education series Reston VA
- Sneeuw, N. (2000). *A semi-analytical approach to gravity field analysis from satellite observations*. Deutsche Geodätische Kommission, Series C, Nr. 527.
- Sneeuw, N., H. Schaub (2005). Satellite Cluster for future gravity field missions. In: Proc of IAG symposia 'Gravity, Geoid and space missions' Jekeli C Bastos L Fernandes J (eds) Vol. 129, pp 12–17, Springer
- Sneeuw, N., M.A. Sharifi W. Keller (2006). Gravity Recovery from Formation Flight Missions. In: Proc of IAG symposia *Hotine-Marussi Symposium of Theoretical and Computational Geodesy: Challenge and Role of Modern Geodesy*, Wuhan, 29 May to 2 June 2006
- Tapley B.D., S. Bettadpur, J.C. Ries, P.F. Thompson, M.M. Watkins (2004) GRACE measurements of mass variability in the Earth system. *Science* 305: 503–505

How to properly scale GRACE estimates of the continental water storage variations?

R. Klees, E.A. Zapreeva, H.C. Winsemius, H.H.G. Savenije
DEOS, Delft University of Technology,
Kluyverweg 1, PO box 5058, 2600 GB Delft, The Netherlands

Abstract. The estimation of terrestrial water storage variations at river basin scale is one of the most important applications of GRACE (Gravity and Climate Experiment) so far. Today, mature techniques are available to transform monthly GRACE gravity field models into mean water storage variations over a target area. Spatial filtering of GRACE is routinely used, and several isotropic or non-isotropic filters have been proposed in literature. Recently, more attention is paid to the problem of the bias, which is introduced by spatial filtering.

The subject of this study is the amplitude and time behaviour of the bias for several target areas in Southern Africa. The regional hydrological model LEW is used to provide a time series of water storage variations inside and outside the target areas. This information is used to compute the bias. Correspondingly, GRACE estimates of water storage variations are corrected for the bias and compared with the LEW model output.

The main conclusion of the study is that the bias caused by spatial smoothing results in monthly and annual amplitudes of mean water storage variations, which are too small. The bias-to-signal ratio is mainly determined by the filter correlation length. For the target areas in Southern Africa, a 1000 km correlation length for a Gaussian filter seems to be an appropriate choice. Then, the bias-to-signal ratio reaches values up to 50%; the monthly bias-to-signal ratio can even be larger. After bias correction, the differences in terms of annual amplitudes between GRACE and LEW take up values between 0 and 30 mm. The RMS difference of monthly amplitudes are reduced significantly and attain values up to 30 mm.

The main conclusion of the study is that GRACE annual and monthly amplitudes of mean water storage variations over a target area have to be bias-corrected before GRACE is used to calibrate hydrological models.

Keywords. GRACE, spatial smoothing, bias, time-

varying gravity field, continental hydrology, regional hydrological model LEW, water storage variation

1 Introduction

The Gravity Recovery and Climate Experiment (GRACE) monthly models are publicly available since March 2002. Commonly monthly solutions consist of a set of spherical harmonic coefficients complete to degree and order 120. Prior to gravity field estimation, GRACE measurements have already been corrected for the major contribution of ocean and atmospheric mass variations. Therefore, differences between two monthly solutions mainly reflect changes in continental water storage.

GRACE is designed to provide new hydrological information in the form of estimates of monthly mean water storage variations over river basins. However, measurement noise and aliasing of unmodelled high-frequency mass variations reduce significantly the quality of monthly GRACE gravity field solutions (Swenson and Wahr, 2002; Wahr et al., 1998, 2006; Swenson and Wahr, 2006). Therefore, spatial smoothing has become a routine operation prior to transform GRACE monthly gravity field variations into water storage variations.

Spatial smoothing reduces noise, but at the same time introduces a bias in the estimated monthly mean water storage variation. In almost all practically relevant applications, the bias is negative, i.e. GRACE underestimates the amplitude of the water storage variations.

Different studies have compared terrestrial monthly mean water storage variations at river basin scale derived from GRACE and hydrological models. It is found that GRACE estimates filtered with a 600 – 800 km Gaussian filter are in good agreement with unfiltered output of global hydrological models. This can be explained by the fact that the contribution to the bias of mass variations inside

and outside the target area partially compensate each other, if the mass variations have similar amplitude and are in phase.

It is rather difficult to make any conclusions about the quality of such estimates without any additional investigation concerned the amplitudes of the bias and its dependency on the filter parameters and target areas.

The subject of this study is to analyze the bias in GRACE estimates and investigate to what extent the bias in GRACE estimates can be corrected for by using a priori information about mass variations provided by a hydrological model.

The outline of the paper is the following: in section 2 the research methodology is outlined. Section 3 contains the approach followed in this study. The LEW regional hydrological model used in this study for bias computation and as a benchmark for GRACE estimates is the subject of section 4. The results of the analysis of the time behaviour of the bias and bias-corrected GRACE are presented in section 5. Section 6 contains the main conclusions of this study.

2 Methodology

To estimate the water storage from GRACE, we basically, follow the standard approach proposed by Swenson and Wahr (2002). We suppose the function f describes the monthly mean water storage variations on Earth. The water storage estimate averaged over the target area can be computed from:

$$\bar{f}_0 = \frac{1}{\sigma_0} \int_{\sigma_0} f d\sigma_R, \quad (1)$$

where σ_0 is the target area (e.g. a river basin) and σ_R the mean surface of the Earth, approximated by a sphere with radius R . The true monthly mean mass variation function f is of course unknown; from GRACE monthly gravity field solutions, we can obtain an estimate \hat{f} . Thus, we may write

$$f = \hat{f} + \varepsilon_f,$$

where ε_f is the error in GRACE monthly gravity field models propagated into the mean mass variation over the target area. Therefore, the mean water storage over the target area can be written as

$$\bar{f}_0 = \frac{1}{\sigma_0} \int_{\sigma_0} \hat{f} d\sigma_R + \frac{1}{\sigma_0} \int_{\sigma_0} \varepsilon_f d\sigma_R. \quad (2)$$

The second term on the right-hand side of Eq. (2) describes the error ($\bar{\varepsilon}_f$) of the GRACE estimate of

the monthly mean mass variation averaged over the target area. In reality, this term is very large, and the standard procedure to reduce it is to apply spatial smoothing with a filter function W_s ,

$$\hat{f}_s = \int_{\sigma_R} \hat{f} W_s d\sigma_R.$$

After spatial smoothing, we obtain a smoothed estimate of the mean water storage variation over the target area:

$$\bar{f}_s = \frac{1}{\sigma_0} \int_{\sigma_0} \hat{f}_s d\sigma_0 + \bar{\varepsilon}_f. \quad (3)$$

In the standard procedure by Swenson and Wahr (2002), the spatial filter function W_s is an isotropic function on the sphere (e.g. a Gaussian). Alternatively, non-isotropic functions have been developed, e.g. (Han et al, 2006). Smoothing reduces the effect of noise, but at the same time introduces a bias in the monthly mean water storage variation estimate, because the smoothed function \hat{f}_s is used in Eq. (2) instead of the function \hat{f} .

To estimate the bias, the water storage variation function f must be known within the significant support of the filter W , which is the spherical convolution of the characteristic function of the target area with the filter W_s . Given any a priori information about f , we can compute an estimate of the bias. The better the quality of the a priori information, the more accurate the bias estimate. It can be shown easily, that the equation of the bias is

$$\bar{\varepsilon}_0 = \bar{f}_0 - \bar{f}_s = \frac{1}{\sigma_0} \int_{\sigma_0} (\hat{f}_0 - \hat{f}_s) d\sigma_0. \quad (4)$$

Once the bias has been computed, the GRACE estimate of monthly mean water storage variations can be corrected for, which should result in a better estimate.

3 Approach

- To quantify the time-variable bias, we use the LEW regional hydrological model water storage estimates for the GRACE periods in four target areas located in Southern Africa. The Eq. (4) is used for the computation. We use areas of different sizes ranging from $4.7 \cdot 10^5$ km² to $5.2 \cdot 10^6$ km² in order to investigate the relation between bias and size of the target area.
- 34 monthly GRACE gravity field models, covering the period between January 2003 and

March 2006, are used to compute the water storage variation over the target areas by using Eq. (3). We use release RL03 models, provided by GFZ (GeoForschungsZentrum Potsdam). The models have been smoothed with a Gaussian filter with correlation length 600, 800, and 1000 km. This allows to investigate the relation between the correlation length and the bias.

- Estimates of the time-variable bias are used to correct the GRACE monthly mean water storage variation. Consequently, the biased and the bias-corrected GRACE monthly mean water storage variations are compared with the output of the LEW model and the fit between LEW model output and GRACE estimates is assessed.
- Some statistical information about the differences between the annual sine fitted amplitudes of the monthly mean water storage from GRACE (biased and bias-corrected) and LEW is given.

4 LEW hydrological model

For the purpose of this study, we use monthly mean water storage variations from LEW regional hydrological model for four target areas in Southern Africa (cf. Figure 1): upper Zambezi (UZ, $4.7 \cdot 10^5 \text{ km}^2$), Zambezi (Z, $1.3 \cdot 10^6 \text{ km}^2$), upper Zambezi + Okavango (UZO, $1.2 \cdot 10^6 \text{ km}^2$), Zambezi + Congo (ZC, $5.2 \cdot 10^6 \text{ km}^2$). The Lumped Elementary Watershed (LEW) approach has some advantages in comparison to any global hydrological model since it enables the implicit incorporation of redistribution of surface runoff in downstream located model units, called LEWs, that represent e.g. a wetland, lake or man-made reservoir.

For this study, the model presented in Winsemius et al. (2006) has been extended, by taking into account all river basins below the equator, in particular Shebelle, Southern part of the Nile, Congo, Zambezi, Okavango, Limpopo, and Orange.

Within the major basins, many model units or ‘LEWs’ have been delineated. Most LEWs represent not only the sub-catchments but also the major lakes and reservoirs (Lake Kariba, Lake Cahora-Bassa and Lake Nyasa) in our target area, the Zambezi, which have also been separately delineated.

For the calibration, the model has been forced by data from the Climate Research Unit (CRU) (New et al., 2002). These data consist of fields of global monthly precipitation, wind speed, relative humidity,

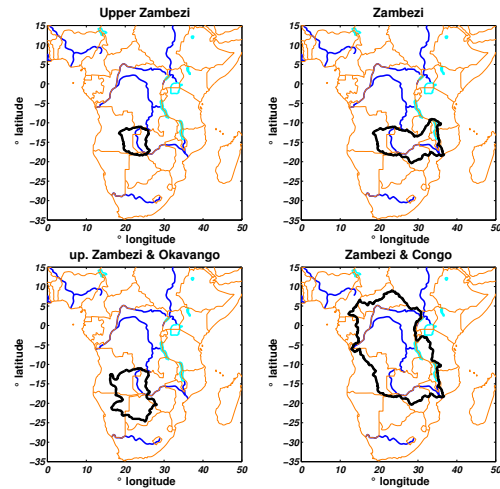


Fig 1. The four target areas being used in this study (from left to right, from top to bottom): upper Zambezi, Zambezi, upper Zambezi + Okavango, and Zambezi + Congo.

and 2 meter air temperature (minimum, maximum and mean).

The LEW water storage estimates have been generated using rainfall estimates from the Famine Early Warning System (FEWS) (Herman et al., 1997). The first 2 years of simulation are taken as warming-up time to stabilize the state variables of the LEW model structures.

5 Results

According to the approach given in section 3, we have computed the time-variable bias from the LEW hydrological model output using Eq. (4) for each target area and choice of the Gaussian filter correlation length. Figure 2 shows the bias time series for the four target areas and 1000 km Gaussian smoothing.

From the time series of monthly bias val-

ues, the amplitude of the annual bias have been computed. The same has been done for the un-smoothed monthly mean water storage from LEW. Then, the annual amplitudes of the bias and annual water storage from LEW have been compared. Finally, the bias-to-signal ratio is computed as ratio of the bias and the LEW water storage amplitudes.

The estimated bias has been used to correct GRACE monthly mean water storage variations. We used 34 release 03 monthly GRACE gravity field models between January 2003 and March 2006 provided by GFZ. The degree 2 zonal coefficient has

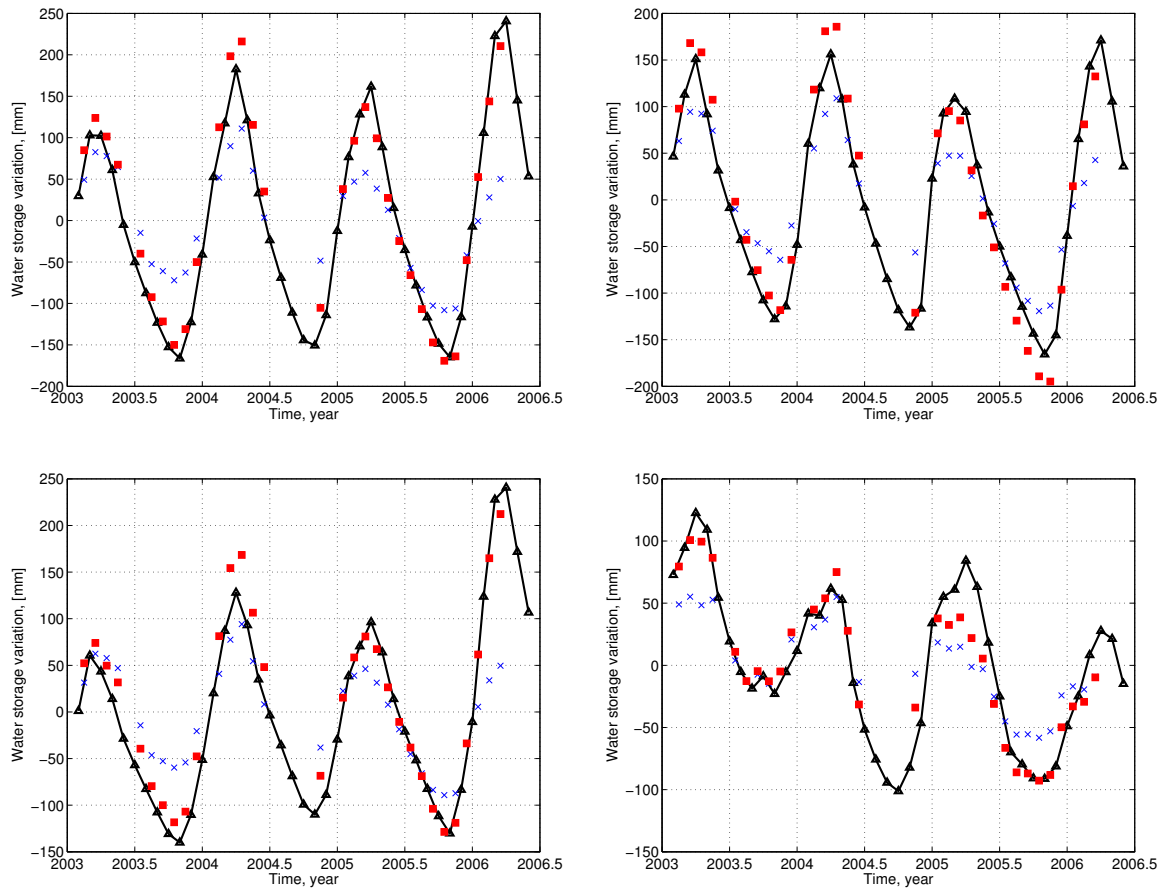


Fig 3. Time series of monthly mean water storage variations over the target areas: From left to right and top to bottom: upper Zambezi, Zambezi, upper Zambezi+Okavango, and Zambezi+Congo. A 1000 km Gaussian filter has been used. Black triangles: unfiltered LEW; blue x-marks: biased GRACE; red boxes: bias-corrected GRACE.

been excluded from the analysis. The monthly water storage variations have been inferred following the methodology and approach given in sections 2 and 3. To correct the smoothed GRACE estimates, the time-variable bias, computed from the LEW model output, is spline interpolated to the time epochs of the monthly GRACE models. The GRACE estimates smoothed by 1000 km Gaussian and corrected for the bias for all target areas are shown in Figure 3.

Finally, the annual water storage variation is computed for the biased and bias-corrected GRACE estimates and compared with the annual water storage from LEW. All results for each target area and the three Gaussian filters are summarized in table 1. As we see from the results given in table 1 the bias strongly depends on the correlation length of the filter: the smaller the correlation length, the smaller the bias. We observe a significant reduction of the bias from 73 till 36 mm, when the correlation length is

reduced from 1000 km to 600 km. However, as discussed below, there is some evidence that a 1000 km Gaussian filter has to be preferred for the selected target areas.

The bias and the bias-to-ratio-signal depend on the size of the target area: the smaller the target area, the larger their values. This is clear from the comparison of the bias-to-signal ratio for the smallest upper Zambezi area - 47% and the much larger Zambezi+Congo area - 31%.

The most remarkable result is that biased-corrected GRACE estimates of the *annual* and the *monthly* mean water storage variations fit significantly better with LEW estimates than biased GRACE estimates. For a 1000 km Gaussian filter, we observe a significant improvement of the fit between monthly GRACE and LEW amplitudes after bias correction between 44% and 63% for all target areas. The largest differences between LEW model out-

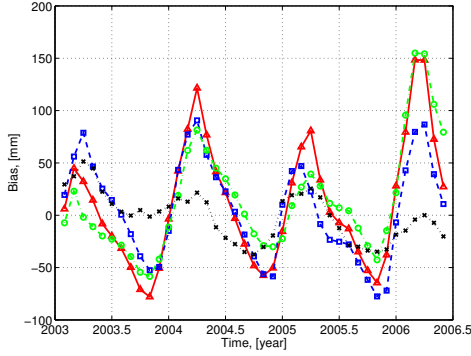


Fig 2. Bias as a function of time between January 2003 and March 2006 for four target areas: upper Zambezi (red triangles), Zambezi (blue squares), upper Zambezi+Okavango (green circles) and Zambezi+Congo (black x-marks). 1000 km Gaussian smoothing has been used.

Table 1. Amplitude of the annual water storage variation signal. [1]: GRACE estimate, mm; [2]: annual bias, [3]: bias-corrected GRACE, mm; [4]: LEW model output, mm; [5]: relative bias, %; [6]: difference between bias-corrected GRACE and LEW model output, mm.

target area	[1]	[2]	[3]	[4]	[5]	[6]
Gauss filter, 1000 km						
UPZ	82	73	155	155	47	0
Z	83	61	144	133	46	11
UPZO	68	50	118	120	42	-2
ZC	33	22	55	71	31	-16
Gauss filter, 800 km						
UPZ	102	55	157	155	35	2
Z	100	46	146	133	35	13
UPZO	80	39	119	120	33	-1
ZC	40	15	55	71	21	-16
Gauss filter, 600 km						
UPZ	124	36	160	155	23	5
Z	117	30	147	133	23	14
UPZO	91	28	119	120	23	-1
ZC	47	8	55	71	11	-16

put and bias-corrected GRACE is attained in spring 2004, whereas the differences for the other months are significantly smaller. The exceptionally large differences in spring 2004 could be attributed to either LEW model errors (e.g. poor quality of rainfall data) or to GRACE errors (e.g. poor capture of the water storage variation signal due to orbit geometry).

Table 2 gives some statistical information about the differences between the amplitudes of *monthly* mean water storage variations from GRACE and

Table 2. Statistics of the differences between GRACE monthly estimates and LEW model output before and after bias correction.

area	GRACE - LEW			$GRACE_{corr}$ - LEW		
	min	max	RMS	min	max	RMS
Gauss filter, 1000 km						
UPZ	0.4	198.0	68.0	0.3	52.0	25.0
Z	1.4	125.0	48.0	1.5	49.0	27.0
UPZO	1.6	197.0	59.0	1.5	50.0	24.0
ZC	1.5	81.0	35.0	0.0	57.0	20.0
Gauss filter, 800 km						
UPZ	0.8	174.0	56.0	0.3	61.0	28.0
Z	3.0	106.0	38.0	2.0	58.0	32.0
UPZO	0.0	177.0	52.0	0.3	56.0	26.0
ZC	0.4	80.0	31.0	0.2	66.0	22.0
Gauss filter, 600 km						
UPZ	0.2	135.0	45.0	7.0	69.0	33.0
Z	1.1	82.0	31.0	1.3	67.0	37.0
UPZO	2.8	147.0	46.0	0.4	59.0	28.0
ZC	1.1	80.0	29.0	1.0	75.0	24.0

LEW model output.

It is remarkable that the fit with LEW is the best for a filter correlation length of 1000 km; smaller filter correlation lengths lead to larger RMS differences between bias-corrected GRACE and LEW. This can be explained by the fact that filter correlation lengths smaller than 1000 km do not sufficiently suppress the noise in GRACE monthly gravity fields; after bias correction, the noise is still dominant and causes a larger misfit between GRACE and LEW. An extreme situation is the Zambezi target area for a 600 km Gaussian filter. After bias correction, the RMS difference between GRACE and LEW *increases* from 31 mm to 37 mm!

The maximum difference between bias-corrected GRACE and LEW monthly amplitudes is observed in the Zambezi+Congo area, which is the largest target area (57 mm for 1000 km Gaussian smoothing). We explain this with the poorer performance of the LEW model caused by the lack of high-quality rainfall data in the Northern part of the target area and just outside but North to the target area (Figure 1).

6 Conclusions

Spatial smoothing of GRACE monthly gravity field models introduces a significant bias in GRACE-estimated monthly mean water storage variations. For the four target areas considered in this study,

the annual bias attains values up to 50% of the total water storage variation; the monthly bias may even take up values of 75%. For most target areas in the world, GRACE always underestimates the amplitudes of monthly mean water storage variations (e.g. Chen et al., 2006).

The bias strongly depends on the amplitude of the water storage variation inside and outside the target areas and on the size of the target area. Generally, the larger the signal amplitude, the larger the bias and the larger the target area, the smaller the bias. The bias is largest if mass variations outside the target area are negligible or even out-of-phase with the mass variations inside the target area.

To compute the bias, a priori information about the mass variations inside and outside the target area is needed. This information can be provided for instance by hydrological models. In this study, the LEW regional hydrological model is successfully used to estimate the bias.

After bias correction, the annual amplitude differences of GRACE and regional hydrological model reduce significantly. The maximum difference between monthly mean water storage variations from GRACE (1000 km Gaussian smoothing applied) and LEW for the upper Zambezi area reduces from 198 mm before bias correction to only 52 mm after bias correction.

We do not observe significant phase differences between GRACE and LEW. The maximum phase difference is 0.25 month (i.e. 7.5 deg) for the upper Zambezi+Okavango area; the phase differences for the other target areas are below 0.1 month (i.e. 3 deg).

Without bias correction, it is hardly possible to calibrate hydrological models using GRACE.

Acknowledgements. *The support of the project by the Dutch Organization for Scientific Research (NWO) and the Water Research Center Delft (WRCD) is greatly acknowledged. We are thankful for the GRACE data provided by GeoForschungsZentrum Potsdam (GFZ). We greatly appreciate our collaboration with Mr. Chris Chileshe from the Department of Water Affairs (Lusaka, Zambia) and Global Runoff Data Centre for the discharge data records provided for the study, and the Netherlands Organisation for Scientific Research for their contribution to our research.*

References

Chen, J. L., R. Wilson, C., Famigletti, J. S., and Rodell, M. (2006). Attenuation effect on seasonal

basin-scale water storage change from grace time-variable gravity. *Accepted for Journal of Geodesy.*

Herman, A., Kumar, V. B., Arkin, P. A., and Kousky, J. V. (1997). Objectively determined 10-day African rainfall estimates created for Famine Early Warning Systems. *Int. J. Remote Sensing*, 18(10):2147–2159.

New, M., Lister, D., Hulme, M., and Makin, I. (2002). A high-resolution data set of surface climate over global land areas. *Climate research*, 21:1–25.

Swenson, S. and Wahr, J. (2002). Methods for inferring regional surface-mass anomalies from Gravity Recovery and Climate Experiment (GRACE) measurements of time-variable gravity. *J. Geophys. Res.*, 107(B9):2193.

Swenson, S. and Wahr, J. (2006). Post-processing removal of correlated errors in grace data. *Geophys. Res. Lett.*, 33:L08402.

Wahr, J., Molenaar, M., and Bryan, F. (1998). Time variability of the earth's gravity field: Hydrological and oceanic effects and their possible detection using GRACE. *J. Geophys. Res.*, 103(B12):30205–30230.

Wahr, J., Swenson, S., and Velicogna, I. (2006). Accuracy of GRACE mass estimates. *Geophys. Res. Lett.*, 33:L06401.

Winsemius, H. C., Savenije, H. H. G., Gerrits, A. M. J., Zapreeva, E. A., and Klees, R. (2006). Comparison of two model approaches in the Zambezi river basin with regard to model confidence and identifiability. *Hydrol. Earth Syst. Sci.*, 10:339–352.

GOCE Gradiometer Validation in Satellite Track Cross-Overs

F. Jarecki, J. Müller

Institut für Erdmessung, Leibniz Universität Hannover, Schneiderberg 50, D-30167 Hannover, Germany

Abstract. Besides external validation methods using auxiliary data, internal integrity checks will be an important technique to assure the full functionality of the GOCE gravity gradiometer.

In this paper, cross-over validation is presented to verify and to supplement other validation procedures such as interpolation methods along the orbit. The prospects of cross-over validation are discussed. Cross-over validation, as a relative approach, is capable to detect gross errors, data gaps and long term drift parameters to some extent, whereas geographically fixed error phenomena and constant biases remain undiscovered. Adequate reduction procedures to deal with altitude and attitude differences have been developed and applied. Simulated gravity gradiometry data sets with different artificial errors are processed. Combining data from different epochs, drift behaviour and short-term biases are very well identified through cross-over validation. Single gross errors and jumps might better be detected by continuous interpolation methods, depending on their temporal extent.

Cross-over validation offers a fast approach to assess the quality of space gradiometry independently with almost global coverage.

Keywords. gravity satellite mission, GOCE, gravity gradiometry, calibration, validation, cross-over

1 Motivation and Introduction

GOCE is a challenging project from the instrumental and conceptual point of view. To achieve the planned accuracy of the gravitational gradients $V_{ij} = \frac{\partial^2 V}{\partial i \partial j}$ ($i, j = X, Y, Z$) at the mEötvös (mE) level, several calibration steps (in orbit and in post-processing) are required. In addition, independent validation procedures are needed to assure the accuracy standards of the resulting gravity field quantities (e.g., gradients, spherical harmonic coefficients or geoid heights). In this paper, the use of cross-overs for in-orbit validation is addressed as one possible validation strategy and its performance is compared to other applicable strategies like interpolation along the track.

Validation understood as monitoring the temporal behaviour of the gradiometer should be performed in near real-time. Therefore, it can not be based upon a GOCE-derived geopotential model (GPM) which would not be available before some time of data assimilation and processing. Here, in contradiction to the validation of data products defined by Koop et al. (2001), an in-orbit method is needed. Such a method is provided by the analysis of the gradiometer measurements in the same geographical position, which is known as cross-over validation from satellite altimetry, see, e.g., (Shum et al., 1990), and was recommended for GOCE, too, e.g., by Albertella et al. (2000). Those studies show the concept of cross-over or repeat orbit validation for satellite gravity gradiometry (SGG) data in principle. In addition to those investigations, which used simplified assumptions on the orbit geometry, in this study a “more realistic” GOCE test data set is applied, which was derived within the GOCE-GRAND project of the GEOTECHNOLOGIEN research programme. This data set is based on an artificial GOCE-like orbit, given in a simplified inertial frame, and gravity gradients, noise-free synthesised from a geopotential model in the orbit sample points and oriented along the appropriate local orbit frame. For this GOCE-GRAND test data set, as well the simulated gravity gradients (from EGM96 up to degree and order 360) as the attitude and position information is provided with 1 Hz sampling rate in agreement with the mission design. The main orbit characteristics are semi-major axis 6628 km, inclination 96.6° and eccentricity 0.001 as initial values for the integration. The 30 days orbit of this test data set, however, shows an increase of the orbit eccentricity and a rotation of the orbital ellipse. This leads to different satellite altitudes at the same geographical position reached after different time intervals and inhibits the formulation of constant conditions for the data processing. Therefore, on one hand, a concept for the determination of ground-track cross-overs on a well defined projection surface has been developed. In contradiction to satellite altimetry, where short-term repeat orbits are realised leading to repeated cross-overs, in this scenario, every single cross-over is unique and, there-

fore, has to be processed individually. On the other hand, reductions have been calculated to consider the measurement differences caused by the different altitudes and orientations of the satellite.

2 Concept of Cross-Over Validation

The first step of the cross-over determination is the conversion of the orbit positions, given in a cartesian inertial system, to geographical coordinates by well known formulas, according to the test data definitions. Here, a spherical earth model was used for the determination of the projection direction and for the determination of the ground-track cross-over positions. The cross-overs are found by the intersection of the difference vectors between each two pairs of consecutive sample positions at the projected ascending and descending track, respectively.

An appropriate interpolation algorithm has been developed for the computation of the exact position of the ground-track cross-over (φ, λ) as well as for the interpolation of the satellite altitude (radii r_1, r_2 on the ascending and descending track, respectively), the orientation of the gradiometer ($\vartheta_{XYZ1}, \vartheta_{XYZ2}$) and the measured gradients (to be validated). The use of polynomials in the projected sample point positions, cubic ones for the positions and bivariate quadratic ones for the interpolation of the observed gradients, provides sufficient position and gradient accuracy (better than 1 m resp. 1 mE except for a small number of outliers). For a detailed description, see Jarecki et al. (2006). Obviously, the simple concept “same position, same measurement” suffers from the orbit characteristics not allowing repeated measurements and from the strongly orientation-dependent character of the gradiometer data. The measurements are aligned with the satellite, which is oriented completely different on ascending and descending tracks intersecting (at least) as ground track cross-overs. The most sensitive gradient, V_{ZZ} , differs up to 24 E in the test data sets’ ground track cross-overs. Even when filtered to the aspired measurement bandwidth between 5 mHz and 100 mHz those direct cross-over differences can reach 1.2 E. To check the data against possible errors in the mE range, those differences are completely inappropriate. Therefore, dedicated reductions have to be applied to reduce the gradients to a common altitude and attitude.

Dealing with complete, unfiltered measurements V_{ij} , the differences in the gradients in two satellite positions on crossing tracks can be calculated from an existing geopotential model:

$$\Delta V_{ij}(\varphi, \lambda) = \quad (1)$$

$$V_{ij}(\varphi, \lambda, r_1, \vartheta_{xyz1}) - V_{ij}(\varphi, \lambda, r_2, \vartheta_{xyz2}),$$

where the V_{ij} are gradients in the local orbital frame ($i, j \in \{X, Y, Z\}$), which is used as reference system for the gradiometer here. Applying this differences as reductions obviously accounts for all parameterised altitude (r_k) and attitude ($\vartheta_{XYZk}, k \in \{1, 2\}$) differences of the measurements, regardless of which origin. Gradiometer reference frames deviating from the local orbit frame would therefore be considered in this reduction step and, consequently, the concept holds as well for updated GOCE scenarios, as long as the gradiometer orientation is known with sufficient accuracy.

The accuracy of the reductions derived from (1) depends strongly on the errors of the utilised geopotential model, which can be split into three error parts, see e.g. Wenzel (1985): 1) The omission error representing those high frequency parts of the gravity field which are not covered by the maximum degree of the spherical harmonic expansion, 2) the commission error reflecting the uncertainties of the coefficients itself, and 3) the errors caused by the inaccurate input values, in this case the cross-over positions and orientations.

All three error parts have been checked with respect to the height reduction calculation. The omission error for the reductions will not exceed 0.02 mE utilising EGM96, which is a negligible order of magnitude. This estimate is obtained, applying the Tscherning-Rapp degree variance model (Tscherning and Rapp, 1974) for radial gradients in GOCE altitude. The commission error from the EGM96 coefficient variances for the reduction value applied on cross-over gradients at $\lambda, \vartheta = 90^\circ - \varphi$ with satellite altitudes h_1 and h_2 (resulting in the height difference $\Delta h = h_2 - h_1$) can be computed from

$$\sigma_{\Delta V_{ZZ}}^2 = \left(\frac{GM}{r^3} \right)^2 \cdot \quad (2)$$

$$\sum_{l=0}^{l_{max}} \left(\left(\frac{\Delta h}{r_1^2 + r_1 \Delta h} \right)^{l+3} (l+1)(l+2) \right)^2 \cdot \sigma_{Y_l}^2$$

introducing Laplace’s surface harmonics

$$Y_l(\vartheta, \lambda) = \sum_{m=0}^l c_{lm} P_{lm}(\cos\vartheta) \cos(m\lambda) + s_{lm} P_{lm}(\cos\vartheta) \sin(m\lambda) \quad (3)$$

with (commission) errors

$$\sigma_{Y_l}^2 = \sum_{m=0}^l \sigma_{c_{lm}}^2 P_{lm}(\cos\vartheta)^2 \cos^2(m\lambda) + \sigma_{s_{lm}}^2 P_{lm}(\cos\vartheta)^2 \sin^2(m\lambda). \quad (4)$$

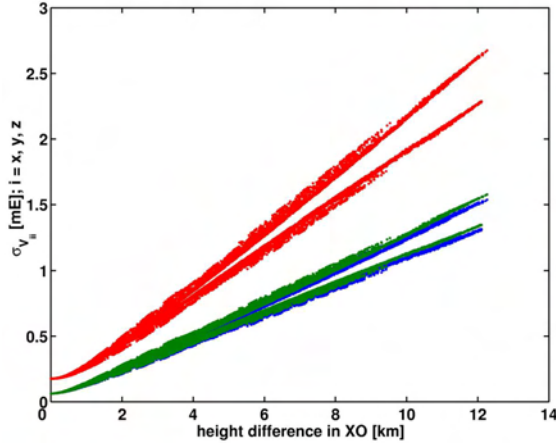


Fig. 1. Accuracy of reduction for main gradients (lower pairs of curves: V_{XX}, V_{YY} ; upper pair: V_{ZZ}) of the test data set shown with respect to the height difference in the XO.

Due to the positive correlation, introduced by evaluating the GPM in the same geographical position φ, λ , the commission error is strongly down-weighted by the factor $\left(\frac{\Delta h}{r_1^2 + r_1 \Delta h}\right)^{l+3}$, resulting in much smaller variances compared to complete gravity field functionals. Hence, the commission error for the reductions in the test data set (again from EGM96) reaches only an amount of about 3 mE. Obviously, it is strongly correlated with the satellite height difference in the cross-overs and, as most of the cross-overs show relatively small height differences, a huge amount of validation points with adequate accuracy ($> 80\%$ of the tested cross-overs are better than 1.5 mE) can be selected. Nevertheless, one has to keep in mind that correlations between the GPM coefficients are not considered here, so the estimated commission errors might be too optimistic. The contribution of the coordinate errors as third error part has to be analysed in the φ, λ and the height components separately. As discussed in (Jarecki et al., 2006) the geographical position does not play an important role: even hundreds of meters only cause some mE of error, so orbit accuracies in the range of one to some meters should be accurate enough. The height component is much more sensitive: even height reductions for small (< 1 km) height differences turn out to be as inaccurate as 1.8 mE for a height error of 1 m. Hence one has to take care of the altitude determination accuracy in both, the orbit determination itself and the cross-over interpolation to achieve a value less than 1 m. Keeping this margin, the height reduction derived from EGM96 is accurate enough for a huge amount of validation points, which can easily be selected with a condition

depending on the height differences. Fig. 1 displays the complete error budget for the reductions applied to the V_{XX}, V_{YY} and V_{ZZ} gradients in the cross-overs of the test data set, where an altitude determination accuracy of 1 dm was assumed. The accuracy is dominated by the commission error. Depending on the accuracy level aimed for, a huge amount of the tested cross-over differences can be reduced with high accuracy; over 80% of the cross-overs are suitable from the accuracy point of view.

3 Error Models in Cross-Over

3.1 Standard Cal/Val Parameters

Koop et al. (2002) introduced the parameter model (5) for the external calibration of the gradiometer. This establishes a function for the observed gradients V_{ij}^G , summing up real gradients V_{ij}^R , a constant bias V_{ij}^* , a linear trend V_{ij}' and Fourier-type periodic disturbances with coefficients a_k, b_k , finally multiplied by an overall constant scale λ :

$$V_{ij}^G(t) = \lambda[V_{ij}^R(t) + V_{ij}^* + V_{ij}'t + \sum_{k=1}^n a_k \cos(k\omega(t)) + b_k \sin(k\omega(t))]. \quad (5)$$

The relative approach applying cross-over gradient differences is not able to recover all those parameters: a constant bias cancels out and the scale parameter remains unrecovered, reappearing only in the magnitude of the errors. The complete set of parameters projects into the cross-over differences as follows:

$$\begin{aligned} \frac{\Delta V_{ij}^G}{\lambda} &= \frac{V_{ij}^G(t_2) - V_{ij}^G(t_1)}{\lambda} \\ &= V_{ij}^R - V_{ij}^R + V_{ij}^* - V_{ij}^* + V_{ij}'t_1 - V_{ij}'t_2 + \\ &\quad \sum_{k=1}^n a_k \cos(k\omega t_1) + b_k \sin(k\omega t_1) - \\ &\quad \sum_{k=1}^n a_k \cos(k\omega t_2) + b_k \sin(k\omega t_2) \\ &= V_{ij}'(t_1 - t_2) + \\ &\quad \sum_{k=1}^n a_k (\cos(k\omega t_1) - \cos(k\omega t_2)) + \\ &\quad b_k (\sin(k\omega t_1) - \sin(k\omega t_2)). \end{aligned} \quad (6)$$

Equation (6) shows, that the linear trend projects directly into the cross-over differences (associated with the time difference $\Delta t = t_1 - t_2$), whereas the periodic parameters do not appear directly. For that reason, linear trend and Fourier coefficients are addressed separately now.

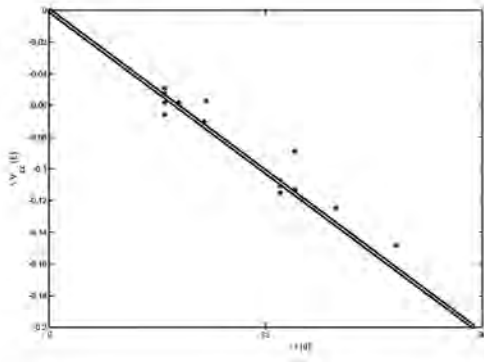


Fig. 2. Artificial trend on 30 d test data set cross-overs (black asterisks) and estimated trend (grey line) versus time differences in the cross-overs.

3.2 Linear Trend

Focussing on the linear trend and neglecting the other effects mentioned in Section 3.1, the cross-over gradient differences according to (6) are

$$\begin{aligned} \Delta V_{ij}^G &= V_{ij}^G(t_2) - V_{ij}^G(t_1) \\ &= V_{ij}^R - V_{ij}^R + V_{ij}^* - V_{ij}^* + V_{ij}'t_1 - V_{ij}'t_2 \\ &= V_{ij}'(t_1 - t_2) = V_{ij}'(\Delta t), \end{aligned} \quad (7)$$

thus being independent from the actual measurement times t_1, t_2 . Consequently, the trend parameter V_{ij}' can be estimated directly from the cross-over differences. Fig. 2 shows the effect of an artificial trend superposed to the test data set on the cross-over differences. According to (7), the trend parameter V_{ZZ}' (in this case -6.7974 mE/d, growing to 200 mE for the 30 d data set) is directly visible in the cross-over plot and can easily be estimated by least-squares adjustment. Especially a large number of sample points and a long time base result in a perfect estimation of the trend parameter. Applied as parameter for a linear calibration function, this estimated trend is depicted in Fig. 2 as well. Discrepancies of the original cross-over differences from the estimated trend are due to cross-over interpolation errors, as discussed in Sect. 2. To assess the effect of those interpolation errors on the trend estimation, smaller intervals of the cross-over data set have been analysed. The results are summarised in Table 1. A trend parameter can be obtained for each revolution, applying cross-over differences of 1 d (resulting in about 30 cross-overs) correctly and with sufficient accuracy. The formal accuracy of the adjustment degrades for shorter time base comparisons. For a single arc, the result is not sufficient any more, but the trend parameter itself is estimated correctly. Thus the method is well suited to estimate daily trends or to check the stability of a trend parameter over long time spans.

Table 1. Estimation of an artificial superposed linear trend (-6.7974 mE/d) from different intervals of the 30 d test data set.

track section investigated	cross-overs with tracks from	estimated trend std [mE/d]	relative error # samples
1 arc	30 d	-6.79675 0.03347	0.01% ca. 500
1 arc	10 d	-6.80794 0.12976	0.15% ca. 170
1 arc	5 d	-6.79388 0.12742	0.05% ca. 80
1 arc	1 d	-6.79586 2.15051	0.02% 16
1 revolution	10 d	-6.7969 0.0847	< 0.01% ca. 330
1 revolution	1 d	-6.7969 0.0847	0.12% ca. 30

3.3 Periodic Parameters

A simplified version of the complete error model (5) is given by

$$V_{ij}^G(t) = V_{ij}^R(t) + a \sin(\omega t) \quad (8)$$

for a single disturbing oscillation with 1 cpr frequency. In the cross-over differences, corresponding to (6) and (7), this simplified error will show up as

$$\begin{aligned} \Delta V_{ij}^G &= V_{ij}^G(t_2) - V_{ij}^G(t_1) \\ &= V_{ij}^R - V_{ij}^R + a \sin(\omega t_1) - a \sin(\omega t_2) \\ &= a \cdot (\sin(\omega t_1) - (\sin(\omega t_1) \cos(\omega \Delta t) + \cos(\omega t_1) \sin(\omega \Delta t))). \end{aligned} \quad (9)$$

Like all periodic errors, the effect of this simple sinusoidal variation in the cross-overs does not only depend on the cross-over time difference Δt , but also on an absolute measurement time t_k . Plotted versus the cross-over time difference, as shown in Fig. 3, a typical aliasing feature with a main period of about 8 d appears. Nevertheless, periodic parameters might be estimated from cross-over differences as well, introducing two time parameters. To sample the complete disturbing function, a sufficiently long time base has to be chosen for the investigation. Table 2 shows formal standard deviations and estimation errors rising to inadequate values for sparse sampling scenarios, i.e. when applying only cross-overs from one day. Longer time spans lead to reasonable amplitude estimations, whereas the formal accuracies are by far not as good as for the trend estimation. Resampling an 1 cpr period just from 1 arc of satellite data obviously lacks some redundancy, so main focus is put on longer test tracks here. The overall performance is not good enough to propose regu-

Table 2. Estimation of an artificial superposed sine ($f=1$ cpr, $A=1$ mE) from different intervals of the 30 d test data set.

track section investigated	cross-overs with tracks from	estd. amplitude std [mE]	relative error # samples
1 arc	10 d	0.99780	0.22%
		0.58384	ca. 170
1 arc	1 d	1.03185	3.18%
		13.9607	16
1 revolution	30 d	0.99044	0.96%
		0.21956	ca. 1000
1 revolution	10 d	1.0010	0.01%
		0.37795	ca. 330
1 revolution	5 d	0.99786	0.21%
		0.22285	ca. 170
1 revolution	1 d	1.08250	8.25%
		13.4741	ca. 30

lar, daily or weekly checks for changed periodic parameters, but the method holds for estimating global parameters for the whole time series. Moreover, sampling problems should diminish for disturbances with higher frequencies.

4 Signal Disturbances in Cross-Overs

4.1 Gross Error Detection in Cross-Overs

Possibly, the GOCE gradiometer might suffer from malfunctions, which are not modelled in the time dependent error model (5), such as single and continuous gross errors, data gaps and jumps in the gradiometric time series. In this section, we investigate the recoverability of single and continuous constant gross errors, denominated as “short term biases”, with cross-over methods and compare it with a standard interpolation approach below.

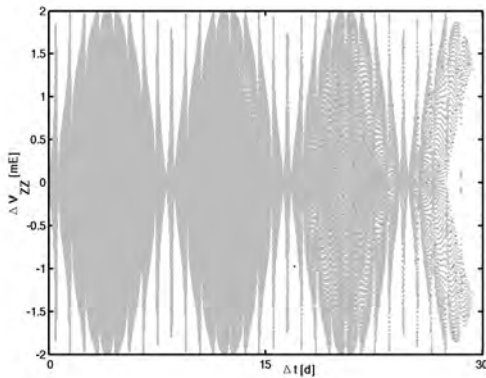


Fig. 3. Artificial 1cpr-sine signal on the test data set cross-overs (black asterisks) versus Δt , note the aliasing feature, and estimated sine (grey dots).

Table 3. Performance of cross-over detection of single gross errors and “short term biases”. The 30 d input data set has been superposed by 4400 single gross errors, affecting 1633 cross-overs theoretically detectable, and by constant gross errors of 15 mE and 25 mE, resp., affecting 6045 cross-overs theoretically detectable.

threshold	# of alarms		errors	
	total	correct	type 1	type 2
single gross errors				
1.5 mE	1773	1399	14.3%	22.9%
2 mE	1508	1152	29.5%	21.8%
”short term biases”				
1.5 mE	6018	6001	0.72%	0.28%
2 mE	6007	6001	0.72%	0.09%

The 30 d 1 Hz data set has been superposed by an equally distributed set of roughly 10000 gross errors (10 mE outliers). 3731 of those are affecting sample points used in the procedure of cross-over determination and interpolation. First disadvantages of the cross-over procedures show up here: In case of the 30 d data set, about 30% of the data are covered. Cross-over methods do not assure the check of every single measurement. Vice versa, the identification of a suspicious cross-over difference does not indicate a single erroneous measurement, but affects all sample points applied in the calculation.

For a more detailed investigation, a subset of 4400 gross errors had been chosen. Those outliers affect 1633 cross-overs in total. Table 3 shows the performance of gross error detection in cross-overs with respect to the alarm threshold applied in terms of correctly and incorrectly suspected cross-overs. The amount of cross-overs affected by a gross error, but not identified in the procedure, is indicated as type 1 error and marks the performance of the procedure. Vice versa, the type 2 error indicates the amount of false alerts. A careful choice of an adequate threshold is necessary: while the number of incorrectly highlighted cross-overs remains in the same range, the type 1 error is reduced by 50% by changing the threshold from 2 mE to 1.5 mE. Unfortunately, the outstanding high rate of false alarms, together with the missing completeness of the check, decreases the applicability of the method in terms of detecting single gross errors.

Dealing with longer erroneous intervals, the cross-over method works much more effectively. To illustrate this, three “short term biases” (several revolutions) with an artificial bias of 15 mE or 25 mE, resp., are superposed to the test data set and affect 32403 measurements or 6045 cross-overs. Due to the structure of the errors, the cross-over differences are

affected severely. The interpolation process reproduces the error in the erroneous arc. Therefore, the choice of the threshold is not as critical as with single gross errors. Table 3 shows the good performance of the cross-over approach in this error scenario.

4.2 Interpolation Approach

A standard method for searching gross errors and outliers in measurement time series is just to interpolate each measurements from the neighbours in the time series. For SGG data, this approach has been proposed and tested e.g. by (Albertella et al., 2000). Here, just a simple cubic spline along-track interpolation scheme is applied to compare the benefits of interpolation techniques with the cross-over approach. With this approach, the V_{ZZ} gradients of the 30 d 1 Hz test data set can be interpolated from their four neighbouring samples (in the time series) with an accuracy at the sub-mE level.

Applying this spline interpolation to the complete gross error data set introduced in section 4.1 and choosing an alarm threshold of 7 mE for the difference of measured and interpolated gradients at each sample point, 9890 of the 9986 gross errors are found correctly, alarming 9928 times. That means an type 1 error of just 0.96% and a false alarm rate of 0.38% is caused, therefore the interpolation approach is a very valuable method for the detection of single gross errors, exceeding the performance of the cross-over approach by far.

Dealing with the “short term biases” data set, the result is quite different: only 24 of the 32403 affected measurements from section 4.1 appear suspicious to the simple interpolation approach. As a matter of principle, this approach is only able to detect jumps in the time series. Consequently, the measurements suspicious to the interpolation approach just mark the begin and end points of the biased intervals. A more sophisticated interpolation approach would definitely be able to classify the jump as one-way change and careful analysis of this changes might lead to a safe identification of the biased measurements, too, but the cross-over approach identifies the erroneous intervals directly.

5 Summary and Conclusions

The comparison of satellite gravity gradients in ground track cross-overs is proposed as an approach for validation. A determination and reduction concept was introduced, which works with sufficient accuracy for GOCE data validation: closed-loop tests show errors in the range of only 1 mE for the full

gradients V_{ij} . Consequently, cross-over differences obtained from the tested procedure are used to estimate parameters from the standard calibration model. The differences are well suited for the estimation of linear trends and it is possible to determine Fourier-coefficients. Constant biases and scales can basically not be recovered by the cross-over approach. Furthermore, the cross-over differences are utilised to recover single and multiple gross errors by comparison with certain thresholds. The differences are well suited to detect gross errors, which are present over a certain time span, here called “short term biases”, whereas single gross errors might better and easier be detected by simple along-track interpolation. The results lead to the conclusion, that the cross-over method adds a valuable test parameter to SGG validation, although it is not suited to detect every type of error. On the other hand it offers unique features, e.g. being the only method for trend estimation without applying reference data or models.

Acknowledgments. GOCE test data was kindly provided by K.-H. Ilk, Bonn, within the framework of the GOCE-GRAND project. The German Ministry of Education and Research (BMBF) supports the GOCE-GRAND project, in whose context this study was carried out, within the GEOTECHNOLOGIEN geoscientific programme under grant 03F0421D. This is publication no. GEOTECH-xxx of that programme.

References

- Albertella A, Migliaccio F, Sansó F, Tscherning C C (2000) The space-wise approach - Overall scientific data strategy, and Scientific Data Production Quality Assessment Using Local Space-Wise Approach In: Sünkel H, From Eötvös to Milligal Final Report, pp. 267-298 and 313-330. Graz
- Jarecki F, Wolf K I, Denker H and Müller J (2006) Quality Assessment of GOCE Gradients. In Flury J, Rummel R, Reigber C, Rothacher M, Boedecker G, Schreiber U (eds.), Observation of the Earth System from Space. Berlin Heidelberg New York
- Koop R, Visser P and Tscherning C C (2001) Aspects of GOCE Calibration. In Drinkwater M R (ed.), Proc. 1st International GOCE User Workshop, pp. 51–56. Noordwijk
- Koop R, Bouman J, Schrama E J O, Visser P (2002) Calibration and Error Assessment of GOCE Data In Adam J and Schwarz K P (eds.), Vistas for Geodesy in the New Millennium, IAG Symp 125, pp.167–174. Berlin Heidelberg New York
- Shum C K, Zhang B H, Schutz B E, Tapley B D (1990) Altimeter Crossover Methods for Precision Orbit Determination and the Mapping of Geophysical Parameters, J Astronaut Sc, Vol. 38, pp. 355-368
- Tscherning C C and Rapp R H (1974) Closed Covariance Expressions for Gravity Anomalies, Geoid Undulations, and Deflections of the Vertical Implied by Anomaly Degree Variance Models. OSU Rep 208, Columbus
- Wenzel H-G (1985) Hochoauflösende Kugelfunktionsmodelle für das Gravitationspotential der Erde, Wiss. Arb. Verm. 137, Hannover

Inverting the Stokes and Vening Meinesz integrals using the Wavelet Transform

M. El-Habiby, M. G. Sideris

Department of Geomatics Engineering,

The University of Calgary, 2500 University Drive N.W., Calgary, Alberta, Canada, T2N 1N4

Abstract. A wavelet transform algorithm is used for inverting Stokes's integral and evaluating the inverse Vening Meinesz integral. Orthogonal wavelet base functions are used. For inverting the Stokes integral, a set of equations is formed and solved using a preconditioned conjugate gradient method. The full solution with all equations requires a large computer memory; therefore, multiresolution properties of the wavelet transform are used to divide the full solution into parts. High compression levels are achieved by using global wavelet thresholding. The singularity level of the kernel is studied and the compression levels depend on the singularity properties of the kernels. Global thresholding achieved a 85% compression level in the case of the Stokes kernel and 97% in the case of the Vening Meinesz kernel without a loss in accuracy. These compression levels lead to large savings in computer memory and the ability to work with sparse matrices, which increases the computations' speed. Hard thresholding is used in the compression of the matrices; however, soft thresholding is used for denoising of the data because of its smoothing properties. Conclusions and recommendations are given with respect to the suitability, accuracy, and efficiency of this method.

Keywords. Wavelet multiresolution analysis, hard thresholding, inverse Stokes, inverse Vening Meinesz.

1 Introduction

For many years, the classical approach used for the efficient evaluation of geodetic integrals has been based on the Fast Fourier Transform (FFT). This approach is well established and is now a standard tool in the geodetic arsenal. In this paper, a wavelet approach is used as an alternative to the FFT to evaluate inverse geodetic integrals.

The wavelet transform is a very efficient algorithm for decomposing and reconstructing signals

[Keinert, 2004; Debnath, 2003]. It is a very powerful tool for evaluating singular geodetic integrals because of its localization and compression properties [Gilbert and Keller, 2000]. Kernels with singularity decay from the singular point rapidly and smoothly [Vanicek and Christou, 1994]. The wavelet transform of such kernels leads to a significant number of small value coefficients. Thus, high compression levels of the kernels can be achieved.

Rauhut (1992) tested different regularization methods for the solution of the inverse Stokes problem using simulated and observed data. Hwang (1998) utilized the inverse Vening Meinesz formula, which convert the deflections of the vertical to gravity anomalies. The formula was evaluated by a 2D FFT method. Sandwell and Smith (1997) computed gravity anomalies from a dense network of satellite altimetry profiles of geoid heights and a grid of the two components of the deflection of the vertical also by using 2D FFT.

The previously mentioned approaches rely on stationary noise assumptions. The main advantage of the wavelet approach is its ability to deal with non-stationary noise. In this paper, two inverse geodetic problems are evaluated. The first is the inverse Stokes problem, which is solved using a combination of orthogonal wavelet transform by Mallat's algorithm [Mallat, 1997], hard and soft thresholding, and a preconditioned conjugate gradient algorithm. In the second problem, the inverse Vening Meinesz is treated as a direct convolution problem and is evaluated in the wavelet frequency domain.

The main objectives of this study are as follows:

- Verify the wavelet approach as a regularization tool in solving the inverse Stokes geodetic problem under non-stationary noise conditions.
- Test the wavelet approach as an alternative to the FFT approach in the solution of the inverse Vening Meinesz integral.

- Examine the efficiency of the combined global and level direction-wise thresholding compression wavelet approach in solving inverse geodetic problems.

2 Wavelets as a Filtering Tool

The wavelet theoretical background and the thresholding techniques used in this paper are briefly described in the other paper presented at the IGFS 2006 conference, by El-Habiby and Sideris (2006). The geodetic integrals evaluated using the wavelet technique are the Stokes integral and the inverse Vening Meinesz integral.

2.1 Wavelet as a regularization tool

Wavelet soft thresholding technique is used for denoising signals hidden in background noise. The main objective is to attenuate the noise while amplifying the signal. In the current case study, soft thresholding is used

$$\hat{\omega}_{j,k} = \begin{cases} \omega_{j,k} - \delta_f & \text{if } |\omega_{j,k}| \geq \delta_f \\ \omega_{j,k} + \delta_f & \text{if } |\omega_{j,k}| < -\delta_f \\ 0 & \text{otherwise} \end{cases} \quad (1)$$

The determination of the thresholding value is

$$\delta_f = \delta \sqrt{2 \log(n \times m)} / 0.6745 \quad (2)$$

where δ is computed from the following two equations:

$$\delta = \text{median}(|\text{detail wav. coef. at level } l|) \quad (3)$$

If it is equal to zero, then

$$\delta = 0.05 * \max(|\text{detail wav. coef. at level } l|) \quad (4)$$

, n and m are the dimensions of the matrix, and 0.6745 is a value obtained from Gaussian calibration and with an assumption that the wavelet coefficients are normally distributed [Keller, 2004; Donoho and Johnstone, 1994].

2.2 Inversion of Stokes integral in the wavelet frame

The equation for the Stokes integral in planar approximation is [Heiskanen and Mortiz, 1967]:

$$N(x_2, y_2) = \frac{1}{2\pi\gamma} \iint \Delta g(x_1, y_1) K_N dx_1 dy_1 \quad (5)$$

where

$$K_N = \frac{1}{[(x_2 - x_1)^2 + (y_2 - y_1)^2]^{1/2}} \quad (6)$$

(x_1, y_1, x_2, y_2) are local Cartesian coordinates of the data points (x_1, y_1) and the computational points (x_2, y_2) , Δg is the gravity anomalies and γ is the normal gravity.

The Stokes kernel produces the matrices used for determining the wavelet coefficients. These coefficients are used to build the design matrix needed for the inversion of the Stokes formula. For gridded data with equal spacing, which is the case in this study, the elements of the matrix in the spatial domain are as follows:

$$\left[\frac{\Delta x_1 \Delta y_1}{2\pi\gamma} \frac{1}{[(x_2 - x_1)^2 + (y_2 - y_1)^2]^{1/2}} \right] \quad (7)$$

for $(x_2 \neq x_1)$ or $(y_2 \neq y_1)$

and

$$\left[\frac{1}{\gamma} \sqrt{\frac{\Delta x_1 \Delta y_1}{\pi}} \right] \quad (8)$$

for $(x_2 = x_1)$ and $(y_2 = y_1)$

Equation (8) accounts for the singularity at the computational point. The procedure for inverting the Stokes integral in the wavelet frame is described in the following steps.

The first step is the wavelet representation of the of the gravity anomalies, which are unknown in the case of Stokes integral [Chui et al., 1994]:

$$\begin{aligned} \alpha^{app} &= \iint \Delta g \varphi(x) \varphi(y) dx dy \\ \alpha^H &= \iint \Delta g \varphi(x) \psi(y) dx dy \\ \alpha^V &= \iint \Delta g \psi(x) \varphi(y) dx dy \\ \alpha^D &= \iint \Delta g \psi(x) \psi(y) dx dy \end{aligned} \quad (9)$$

These coefficients are arranged in a column vector u_j .

The second step is the two-dimensional wavelet transform of the kernel:

$$\begin{aligned} \beta^{app} &= \iint K_N \varphi(x) \varphi(y) dx dy \\ \beta^H &= \iint K_N \varphi(x) \psi(y) dx dy \\ \beta^V &= \iint K_N \psi(x) \varphi(y) dx dy \\ \beta^D &= \iint K_N \psi(x) \psi(y) dx dy \end{aligned} \quad (10)$$

These four sets of coefficients are computed for each kernel corresponding to every computational point and represented by a row vector.

Using Belykin's [1993] algorithm, and Daubechies wavelets with four vanishing moments [Daubechies, 1992], the kernel (equation 10) and the gravity anomalies (equation 9) are represented

on a wavelet basis using the wavelet decomposition coefficients, h for the approximation decomposition and g for the detailing coefficients, as follows:

$$K = \sum_q \sum_s \beta^{qpp} h_q(x) h_s(x) + \sum_q \sum_s \beta^H h_q(x) g_s(x) + \sum_q \sum_s \beta^V g_q(x) h_s(x) + \sum_q \sum_s \beta^D g_q(x) g_s(x) \quad (11)$$

The summation is over dyadic intervals to avoid redundancy and decrease the computational effort. This reconstructed kernel formula (11) is substituted in the Stokes integral equation (5) to have the following equation [Salamonowicz, 2000]:

$$N(x_2, y_2) = \frac{1}{2\pi\gamma} \left[\sum_q \sum_s \beta^{app} h_q(x) h_s(y) + \sum_q \sum_s \beta^H h_q(x) g_s(y) + \sum_q \sum_s \beta^V g_q(x) h_s(y) + \sum_q \sum_s \beta^D g_q(x) g_s(y) \right] Ag(x_1, y_1) dx_1 dy_1 \quad (12)$$

Then the unknown two-dimensional wavelet transform coefficients of the gravity anomalies are substituted in equation (12). By interchanging the order of integration and summation and subsequently integrating, the equation will be as follows:

$$N(x_2, y_2) = \sum \alpha^{approx} \beta^{approx} + \sum \alpha^H \beta^H + \sum \alpha^V \beta^V + \sum \alpha^D \beta^D \quad (13)$$

This equation can be described as the element-by-element multiplication of wavelet transform coefficients of the kernel and the gravity anomalies. Then, the product output matrix is summed up to have the geoid undulation directly at the computational point. It should be mentioned that the inverse wavelet transform step is done implicitly. Consequently, using this algorithm decreases the computational effort in comparison to standard algorithms.

As mentioned before, four sets of coefficients are computed for each kernel corresponding to every computational point (equation 10) and are represented by a row vector. These row vectors are arranged in a one matrix $A_{i \times j}$. Consequently, the number of row vectors is equal to the number of computational points. The known geoid undulations are arranged in a row vector r_i . The problem is formulated in the form of the equation below:

$$A_{i \times j}^{KN} u_j^{\Delta g} = r_i^N \quad (14)$$

where

- $A_{i \times j}^{KN}$ is the design matrix containing the wavelet coefficients of the wavelet transform of the kernels; each line corresponds to one kernel.
- $u_j^{\Delta g}$ is a vector containing the wavelet coefficients of the unknown solution (gravity anomalies in the case of Stokes's integral).
- r_i^N is a vector containing the known data (geoid undulations in the case of Stokes's integral).
- i number of computation points
- j number of wavelet coefficients

Equation (14) is solved using preconditioned conjugate gradient least-squares algorithm for the unknown wavelet coefficients u_j [Barrett et al., 1994].

2.3 Inverse Vening Meinesz in the Wavelet Frame

The inverse Vening Meinesz integral is

$$Ag(x_2, y_2) = \frac{-\gamma}{2\pi} \left\{ \iint K_\xi \xi_1 dx_1 dy_1 + \iint K\eta \eta_1 dx_1 dy_1 \right\} \quad (15)$$

where

$$K_\xi = \frac{y_2 - y_1}{\left[(x_2 - x_1)^2 + (y_2 - y_1)^2 \right]^{\frac{3}{2}}},$$

$$K\eta = \frac{x_2 - x_1}{\left[(x_2 - x_1)^2 + (y_2 - y_1)^2 \right]^{\frac{3}{2}}},$$

ξ and η are the two components of the deflection of the vertical.

As shown in equation (15) there are two integrations. The first integral is taken as an example for describing the implementation procedure of these integrals in the wavelet frame. The procedure is described in the following steps: The first step is the wavelet representation of the vertical component of the deflection of the vertical [Chui et al., 1994]:

$$\begin{aligned} \alpha_\xi^{app} &= \iint \xi \varphi(x) \varphi(y) dx dy \\ \alpha_\xi^H &= \iint \xi \varphi(x) \psi(y) dx dy \\ \alpha_\xi^V &= \iint \xi \psi(x) \varphi(y) dx dy \\ \alpha_\xi^D &= \iint \xi \psi(x) \psi(y) dx dy \end{aligned} \quad (16)$$

The second step is the wavelet transform of the kernel:

$$\begin{aligned}
\beta_{\xi}^{app.} &= \iint K_{\xi} \varphi(x) \varphi(y) dx dy \\
\beta_{\xi}^H &= \iint K_{\xi} \varphi(x) \psi(y) dx dy \\
\beta_{\xi}^V &= \iint K_{\xi} \psi(x) \varphi(y) dx dy \\
\beta_{\xi}^D &= \iint K_{\xi} \psi(x) \psi(y) dx dy
\end{aligned} \tag{17}$$

The wavelet coefficients of the vertical component of the deflection of the vertical (equation 16) and the kernel (equation 17) are implemented in the first integral of equation (15) using the same procedure introduced in equations (11) and (12). The same algorithm is repeated to obtain the wavelet coefficients of the horizontal component of the deflection of the vertical to solve the second integral in equation (15), which leads to the solution of the inverse Vening Meinesz integral.

$$\begin{aligned}
\Delta g(x_2, y_2) &= \sum \sum \alpha_{\xi}^{app.} \beta_{\xi}^{app.} + \\
&\sum \sum \alpha_{\xi}^H \beta_{\xi}^H + \sum \sum \alpha_{\xi}^V \beta_{\xi}^V + \\
&\sum \sum \alpha_{\xi}^D \beta_{\xi}^D + \sum \sum \alpha_{\eta}^{app.} \beta_{\eta}^{app.} + \\
&\sum \sum \alpha_{\eta}^H \beta_{\eta}^H + \sum \sum \alpha_{\eta}^V \beta_{\eta}^V + \\
&\sum \sum \alpha_{\eta}^D \beta_{\eta}^D
\end{aligned} \tag{18}$$

This solution can be summarized as the element-by-element multiplication of wavelet transform coefficients of the kernel and the data. Then, the product output matrix is summed up to have the solution directly at the computational point. The problem is formulated as shown in the following equation.

$$r_i^{\Delta g} = A_{i \times j}^{K_{\xi}} u_j^{\xi} + A_{i \times j}^{K_{\eta}} u_j^{\eta} \tag{19}$$

where

$A_{i \times j}^{K_{\xi}}$, $A_{i \times j}^{K_{\eta}}$ are the design matrices of the wavelet coefficients of the wavelet transform of the kernels of the two components of the deflection of the vertical; each line corresponds to the kernel at each computational point

u_j^{ξ} , u_j^{η} are the vectors of the wavelet coefficients of the two components of the deflection of the vertical.

$r_i^{\Delta g}$ is the solution vector (gravity anomalies)

3 Data used and Results

3.1 Data Used

The data used are 3' × 3' grids of geoid undulations, the deflections of the vertical, and gravity anomalies in the area (18E-21.2E, 38.8N-42N) [Featherstone, 2006].

3.2 Gravity anomalies from geoid undulations

The inversion of Stokes's integral is done using equation (14). First, no compression is applied to the A matrix and the corresponding gravity anomalies are obtained with an accuracy of RMSE around 4 mGal of the differences between the solution and the reference data. Then, the solution is repeated with 78% compression level using global hard thresholding, which leads to RMSE 0.02 mGal from the first solution done with no compression (Figure 2). Higher compression levels are achieved with higher thresholding values. Table 1 shows that there is no loss of accuracy until the 94% compression level. The 94% compression level decreased the memory required for allocating the matrix from 182 MB to 15.2 MB.

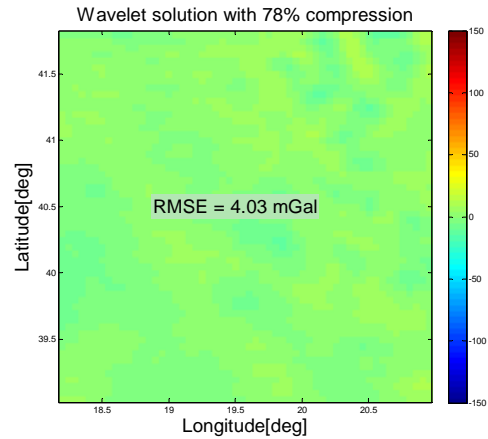


Fig. 1 Wavelet solution difference from reference data

Table 1 Wavelet solutions at different compression levels when inverting Stokes's integral

Comp %	0%	78%	85%	94%	96%	98%
Storage (MB)	182	49.7	35.1	15.2	7.24	5.58
RMSE (mGal)	4.03	4.03	4.03	4.15	11.71	24.72
ref.						

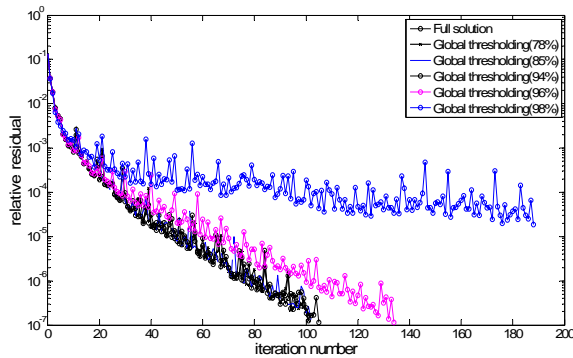


Fig. 2 Precondition conjugate gradient iterations versus relative residuals of full solution, 78%, 85%, 94%, 96%, and 98% compression levels for the inverse Stokes integral

3.3 Inverse Vening Meinesz

The solution of the inverse Vening Meinesz integral gives almost identical results to the numerical integration solution. The A matrix is built for each term of the integral shown in (19) and then multiplied with the wavelet coefficients of each component of the deflections of the vertical. The same thresholding procedure is applied to the Inverse Vening Meinesz integral. A 97% compression level is achieved with no loss in accuracy (RMSE of 0.03). The computational time is less than half a second. The comparison between equations (11) and (8) shows that the Vening Meinesz kernels drop faster than the Stokes kernel, thus leading to higher compression levels as shown in Table 2.

Table 2 Differences among wavelet thresholding solutions and numerical integration solution

Comp %	0%	85%	94%	96%	97%	99%
Storage (MB)	364	55	21.84	14.56	10.92	3.64
RMSE (mGal)	0.00	0.00	0.001	0.01	0.03	9.80

With 99% compression level a sudden degradation in accuracy can be seen. This is because wavelet coefficients representing the main energy of the kernel are removed.

3.4 Wavelet as a regularization tool

The inversion of the Stokes's integral is repeated after adding non-stationary noise to the geoid undulations. Figure 4 shows the simulated non-stationary noise.

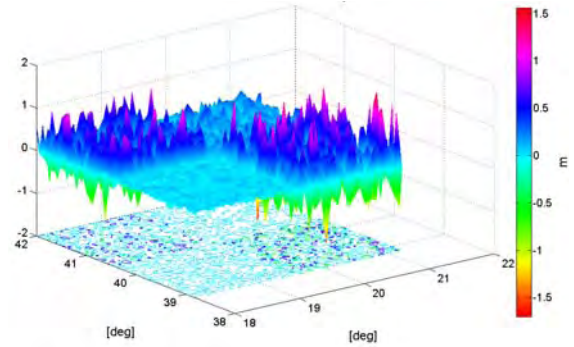


Fig. 3 Non-stationary simulated noise in metres with four different noise levels.

The non-stationary noise is simulated using four different noise levels (± 5 cm, ± 15 cm, ± 35 cm, and ± 55 cm). Each noise level is used for one quarter of the undulations matrix. A bias of 10 cm is added to the first noise level and a bias of 5 cm is added to the second. The solution using the gravity anomalies contaminated with the non-stationary noise has a large degradation in the accuracy to 221 mGal, as shown in Figure 4. After applying the wavelet de-noising algorithm introduced by equations 15, 16, 18, and 19, the recovered undulations had an RMSE equal to 12 cm, and the solution improved to RMSE equal to 20 mGal, as shown in Figure 5.

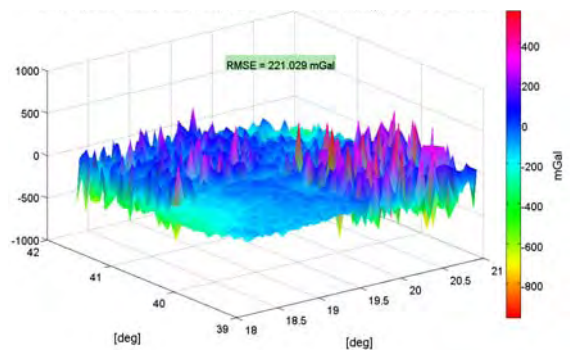


Fig. 4 Difference between reference gravity anomalies and gravity anomalies obtained using noisy geoid undulations

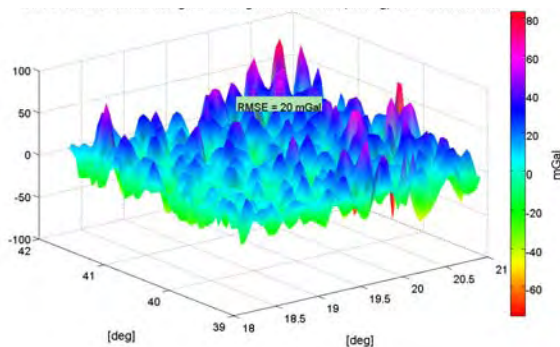


Fig. 5 Difference between reference gravity anomalies and de-noised gravity anomalies obtained using de-noised wavelet algorithm

4 Conclusions

The Wavelet representation of inverse geodetic integrals is promising. Orthogonal wavelets are essential for the use of this algorithm. Through the wavelet hard thresholding technique, the number of multiplications and the required matrix storage are significantly reduced. The compression of the Stokes kernel can reach 80% of the matrices' elements with less than a 0.05 mGal loss in accuracy. The preconditioned conjugate gradient algorithm is used for the solution of the linear equation problem. The iterations of the preconditioned conjugate gradient solution converged at 96% compression level with RMSE of 11.71 mGal in comparison to the reference data and 7.02 mGal in comparison to the full matrix solution with no compression. The solution diverged and didn't reach a solution at 98%. The compression levels achieved are mainly dependent on how fast the kernel drops to zero. Since the Vening Meinesz kernel decreases with power of -3 while Stokes's kernel decreases with power of $-1/2$, higher compression levels are achieved in the former case. Wavelet filtering is a powerful regularization tool using soft thresholding. The filtering algorithm introduced in this paper is efficient for dealing with non-stationary noise. A 90% improvement in the solution accuracy of the inversion of the Stokes integral is achieved, when wavelet filtering is used to de-noise non-stationary noise.

The compression of the Vening Meinesz kernel can reach 97% of the matrices' elements with less than 0.1 mGal RMSE in comparison to the numerical integration solution.

References

- Barrett, R., M. Berry, T. F. Chan (1994). *Templates for the Solution of Linear Systems: Building Blocks for Iterative Methods*, SIAM.
- Beylkin G. (1993), *Wavelets and Fast Numerical Algorithms*, Lecture Notes for short course, AMS-93, Proceedings of Symposia in Applied Mathematics, Vol. 47, pp. 89-117, 1993.
- Chui, C. K., L. Monefusco, and L. Puccio (1994). *Wavelets: theory, algorithms, and applications. Wavelet analysis and its applications*, Vol. 5, Academic Press, Inc.
- Daubechies, I. (1992). *Ten lectures on wavelets*. Society for Industrial and Applied Mathematics.
- Donoho, D. L., and I. M. Johnstone (1994). *Ideal Spatial Adaptation via Wavelet Shrinkage. Biometrika* 81: pp. 425-455.
- El Habiby, M.; and M. G. Sideris (2006). *Wavelet Evaluation of the Terrain Correction Integral. Session 2, regional geoid projects, IGFS 2006, Istanbul, Turkey*.
- Featherstone, W. (2006). *Self-consistent synthetic gravity anomalies, geoid heights and vertical deflections (at the geoid) over Greece. precomputed synthetic fields, IAG SSG3.177, special study group*.
- Gilbert A., and W. Keller (2000), *Deconvolution with wavelets and vaguelettes*, *J Geod* 74: 306-320.
- Heiskanen, W. A., and H. Mortiz (1967). *Physical Geodesy*. W. H. Freeman and Company, San Francisco.
- Hwang C. (1998). *Inverse Vening Meinesz formula and deflection-geoid formula: application to prediction of gravity and geoid determination over South China Sea. J Geod* 72:113-130.
- Mallat, S. G. (1997), *A wavelet tour of signal processing*, Academic Press, San Diego.
- Rauhut, A.C. (1992). *Regularization methods for the solution of the inverse Stokes problem. UCGE reports, No. 20045, Department of Geomatics Engineering, University of Calgary*.
- Salamonowicz R. H. (2000). *A wavelet based gravity model with an application to the evaluation of stokes' integral. Gravity, Geoid and Geodynamics 2000 (M. G. Sideris, ed.), IAG Symposium, Vol. 123, Springer, Berlin etc., pp. 85-90*
- Sandwell, D.T. and W.H.F., Smith (1997). *Marine gravity anomaly from Geosat and ERS 1 satellite altimetry. J of Geop R*, 102: B5, 10,039-10,054.

Determination of the quasi-stationary sea surface topography from a common adjustment of a geodetic and an oceanographic model

G.S. Vergos✉ and I.N. Tziavos

Department of Geodesy and Surveying, Aristotle University of Thessaloniki, University Box 440, 541 24, Thessaloniki, Greece, Fax: +30 31 0995948, E-mail: vergos@topo.auth.gr

Abstract. The determination of accurate marine geoid models from satellite altimetry data usually suffers from the absence and/or in-accuracy of appropriate models of the quasi-stationary sea surface topography (QSST). This is the case for the Mediterranean Sea and especially for its eastern part, where global models are inadequate since: a) The differences between the various solutions exceed the magnitude of the QSST itself and b) they are most commonly in the form of a low-degree spherical harmonics expansion of the QSST, which resolves wavelengths much longer than the extension of the area under study. From that rationale, the present study focuses on the determination of a QSST model in the eastern part of the Mediterranean Sea, from a geodetic point of view. This geodetically oriented QSST determination stands upon the simple principle that the quantity under determination can be derived as the difference between a purely altimetric and a purely gravimetric geoid model. From that initial solution an adjusted model is determined from its common adjustment with an oceanographic QSST model computed from in-situ oceanographic data. Finally, the circulation in the area under study is determined by estimating the velocities and the direction of the sea currents.

Keywords. Quasi-stationary sea surface topography, circulation, currents, velocities, adjustment.

1 Introduction

Since the early missions of GEOS-3 and SeaSat, altimeters onboard satellites have offered a tremendous amount of measurements of the sea surface resulting in the improved knowledge of the Earth's gravity field over oceanic regions. A direct consequence of that is the continuous development of Mean Sea Surface (MSS) models of the oceans, which are usually combined with satellite-only Earth Gravity Models (EGMs) to estimate models of the Quasi-Stationary Sea Surface Topography (QSST). The QSST is defined as the semi-constant over large periods of time deviation of the mean sea surface from the geoid. It reaches a maximum of +2.2 m and in closed sea areas has very small variations over large regions. This is why most QSST models developed during the last two decades are usually provided in terms of a spherical harmonics expansion of the QSST to low

degrees, e.g., 20 (which corresponds to about 2000 km full wavelength). It can be easily concluded that when the area under study is rather small or is characterised as closed, e.g., the Mediterranean Sea, then such global models are insufficient. Moreover, in areas like the aforementioned the differences between the presently available global QSST models largely exceed the magnitude of the signal under consideration itself. This signals both a significant uncertainty in the available models and a need for the development of reliable and accurate local estimates of the QSST for use in geodetic and oceanographic studies.

From a geodetic point of view, the QSST is needed for the reduction of the altimetric measurements from the sea surface to the geoid. This is so because the basic measurements of satellite altimeters, the sea surface heights (SSHs), refer to the sea surface and not the geoid itself. Therefore, the reduction of these observations to the geoid is necessary to determine a geoid and not a MSS model. Additionally, shipborne gravity measurements refer to the sea surface as well and need to be free-air reduced to the geoid to be used for the determination of a gravimetric geoid in the well-known Helmert scheme. The quantity needed for this reduction is the QSST, which is the "marine" counterpart of orthometric heights on land. It can be easily concluded that the QSST is significant for the precise and accurate determination of gravity-field related quantities, while local models are highly necessary as well to serve local to regional geoid modelling.

These form the basis for the present work, i.e., to investigate whether a determination of the QSST from a geodetic point of view, i.e., using traditional geodetic methods and quantities, is possible. Furthermore, from this initial solution an adjusted model is determined through a combination with a local oceanographic model of the QSST. Studies on a *geodetic determination* of the QSST have begun since the work by Angelis (1983) who presented in a very elegant way their feasibility (OSU83 QSST model). Consequently, there have been more works on a global determination of the QSST in terms of surface spherical harmonics (SH) (Angelis 1984, 1985, 1987), while Knudsen (1992) presented a local model for the North Sea. Lemoine et al. (1997) estimated a QSST model complete to degree and order 20 during the development of the EGM96, while Pavlis et al. (1998) used Proudman functions and data from the POCM-4 model to estimate the QSST to degree and

order 20. Finally, Andritsanos (2000) and Andritsanos et al. (2001) estimated QSST models and current velocities from an analysis of altimetric exact repeat mission data using the Multiple-Input Multiple-Output System Theory (MIMOST) method.

The area of the present study is the Eastern part of the Mediterranean Sea bounded between $33^\circ \leq \varphi \leq 38^\circ$ and $20^\circ \leq \lambda \leq 28^\circ$. This region was selected due to a) the fact that it is a closed sea, thus global models are insufficient due to both their low degree of expansion and range of differences and b) some well-known currents are present so they can provide a reasonable validation of the proposed method. The determination is based on well-known geodetic algorithms and uses purely “geodetic” data, i.e. satellite altimetry geoid heights and shipborne gravity anomalies. For the estimation of the QSST, the simple formula connecting altimetric and gravimetric geoid heights, i.e., that their difference gives the QSST, was employed. With this as a starting point, the use of low pass filtering (LPF) with a Wiener-type of filter and a blunder detection test is proposed to filter the resulting QSST field and lead to a better approximation of the SST. This filtering operation is necessary to reduce high-frequency oceanic effects contaminating geodetic mission (GM) altimetry, while the blunder removal is needed to smooth the differences between the altimetric and shipborne gravity data, due to blunders in the latter. After this initial model is developed, an adjusted one is estimated through a combination with a local oceanographic one. This adjustment procedure is based on the well known least squares principle, where the vector of the observation equations is formed by the differences of the geodetic and oceanographic QSST models. Various deterministic parametric models are tested in order to describe the differences of the observations and finally construct a corrector surface for the adjustment of the geodetic QSST model. As a final step, the direction and velocities of the ocean currents in the area are determined based on the principle of geostrophic flow.

2 Sea Surface Topography Modeling

For the determination of the QSST an altimetric and a gravimetric geoid model for the area were used. These models have been developed by Vergos (2006) and Vergos et al. (2005a, b) and by combining all available altimetric data in the area under study for the former and a recently constructed high-resolution and high-accuracy gravity database for the latter. The development of these models will be briefly discussed since the models themselves and the methodology followed are well documented in Vergos (2006), Vergos and Sideris (2003) and Vergos et al. (2005a, b).

The altimetric geoid was estimated from a combination of ERS1 and GEOSAT GM data for the area under study. The well-known remove-compute-restore method was employed, while the EGM96 (Lemoine et al. 1998) global geopotential model was used as a reference sur-

face. Finally, an altimetric geoid of 1'×1' resolution in both latitude and longitude was determined for the area under study.

For the determination of the gravimetric geoid model, an effort was made to collect all available marine, land and airborne gravity data for the area under study. Then, an editing and blunder detection and removal process, using least squares collocation, took place to construct a homogeneous and accurate gravity database. Finally, a gravimetric geoid model was estimated using EGM96 as a reference surface and the 1D FFT spherical Stokes convolution to evaluate Stokes' function (Vergos 2006; Vergos et al. 2005a, b). The statistics of the altimetric and gravimetric geoid models are summarized in Table 1.

Table 1. Statistics of the altimetric and gravimetric geoid models. Unit: [m].

MODEL	max	min	mean	σ
$N^{\text{gravimetric}}$	39.913	0.780	21.185	± 10.352
$N^{\text{altimetric}}$	40.206	1.057	21.376	± 10.484

Employing the so-derived geoid models for the area under study, a preliminary quasi-stationary sea surface topography model for the area was estimated as

$$QSST = N^{\text{alt}} - N^{\text{grav}} \quad (1)$$

where N^{alt} and N^{grav} are the altimetric and gravimetric geoid heights respectively. It should be noted that the gravity anomalies used to determine the gravimetric geoid are free-air reduced, i.e., reduced from the sea surface to the geoid. The statistical characteristics of this preliminary QSST are given in Table 2, while the model itself is depicted in Fig. 1. From Fig. 1 (see solid circle) and Table 1 it is evident that the QSST estimated presents some unreasonably large variations within the area (3.3 m) and reaches a maximum of 2.2 m. Therefore it is clear that blunders are present in the estimated field. Finally, from Fig. 1 some noisy features are evident (see the dotted circle), thus low-pass filtering (LPF) is needed to reduce these effects.

Table 2. Statistics of the preliminary QSST model before and after the 3rms test. Unit: [m].

	max	min	mean	σ
before	2.177	-1.112	0.224	± 0.326
after	0.977	-0.958	0.190	± 0.269

For the detection and removal of blunders, a simple 3σ test was performed, i.e., points with a QSST value larger than 3 times the standard deviation of the preliminary field were removed. The statistics of the QSST model after this test are given in Table 2 as well. To low-pass filter the preliminary QSST model, a collocation-type of filter (Wiener filtering) was used, assuming the presence of white noise in the QSST field that needs to be filtered (Schwarz et al. 1990). Furthermore, it is assumed that Kaula's rule for the decay of the geoid

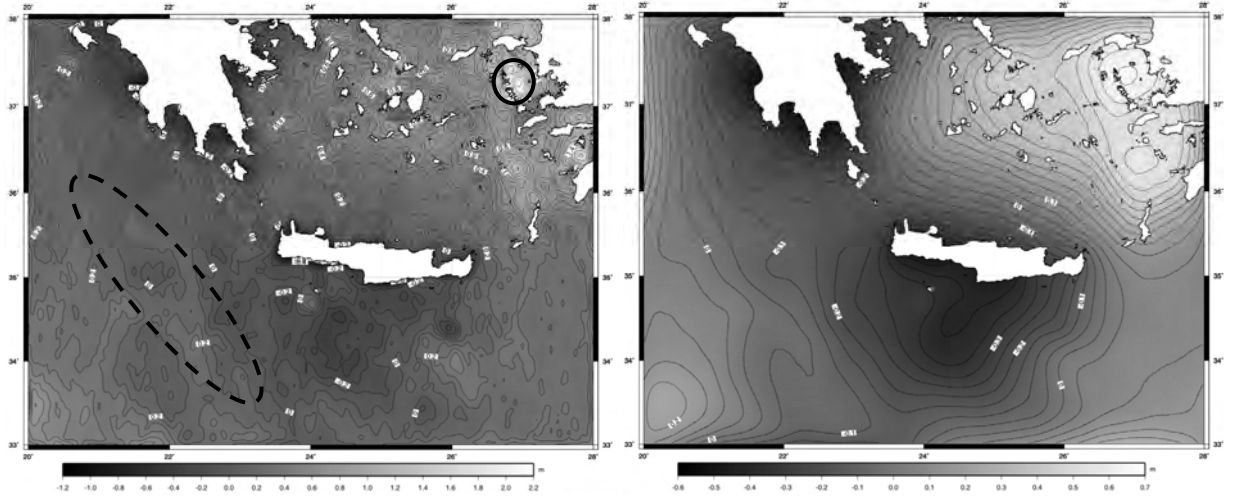


Fig. 1: The preliminary and final geodetic Q SST models.

power spectrum holds, i.e., that the geoid heights PSD decays like k^{-4} where k is the radial wavenumber. Finally, we arrive at the filtering function shown in Eq. 2, where ω_c is the cut-off frequency.

$$F(\omega) = \frac{\omega_c^4}{\omega^4 + \omega_c^4} \quad (2)$$

To filter the wanted field, the desired cut-off frequency needs to be selected. The latter relates to the final resolution of the filtered field and the reduction of the noise in the data. Thus, a trade-off is necessary, since higher resolution means more noise will pass the filter, while higher noise reduction means lower resolution of the final model. A high resolution is vital in the determination of regional to local Q SST models, since if a high value cannot be achieved then a so-derived local model has little to offer compared to a global solution. It can be clearly seen, that the disadvantage of Wiener filtering is that the selection of the cut-off frequency is based on the spectral characteristics of the field only, while its spatial characteristics are not taken into account. Furthermore, the selection of the cut-off frequency is based on solely objective criteria (noise reduction). Thus, a trial and error process, based on maximum noise reduction with minimum signal loss, is needed to determine the desired cut-off frequency.

Various cut-off frequencies have been tested corresponding to wavelengths of 5, 10, 20, 40, 60, 100 and 120 km and finally we selected a wavelength of 100 km (about 1° or harmonic degree 180) since it offered the minimum signal loss with maximum noise reduction. Wavelengths shorter than 100 km left too much noise in the field, while those larger than 100 km were reducing not only the noise but the characteristics of the field as well. If we would select a longer wavelength, then, and if the area was significantly larger (e.g. the entire Mediterranean Sea) it would have been possible to identify larger in scale Q SST features and distinguish them from smaller ones. The problem in this case is that shipborne

gravity data in such high resolutions are not available for large regions.

The final geodetic Q SST field after the filtering is shown in Fig. 1, while the statistics are given in Table 3. From Fig. 1 it can be seen that the noise present in the preliminary model is reduced significantly, while blunders cannot be identified. The Q SST model estimated has been compared with a Mean Dynamic Topography model computed for the entire Mediterranean Sea from an analysis of satellite altimetry and oceanographic data (Rio 2004). The latter is given as a grid of mean Q SST values of $3.75' \times 3.75'$ resolution in both latitude and longitude. The statistics of the differences between the MDT and the estimated Q SST model is given in Table 3 (last row). From the comparison it can be concluded that the two models agree reasonably well to each other (standard deviation at the ± 20 cm level). The maximum and minimum values of the differences are found close to land areas only, where both models are inadequate, while in purely marine regions range between -0.2 to 0.2 m. This comparison gives evidence that the estimated geodetic Q SST model is at least in good agreement with existing regional oceanographic MDT models. Nevertheless, the magnitude of the Q SST that the geodetic model provides, and the velocities of the ocean currents resulting from that, is quite large for the area under study. The presence of the oceanographic model provides the opportunity to *adjust* the geodetic one, i.e., minimize their differences in a least squares sense and thus provide a better estimate of the Q SST for the area. The corrector surface resulting from this adjustment scheme can then serve for the transformation/adjustment of future geodetic Q SST models available for the entire Mediterranean Sea.

Table 3. Statistics of the final geodetic Q SST model. Unit: [m].

	max	min	mean	σ
Q SST	0.675	-0.510	0.014	± 0.238
MDT	0.096	-0.177	-0.047	± 0.052
MDT-Q SST	-0.635	0.478	-0.058	± 0.200

3 Common Adjustment

In the common adjustment scheme of the QSST models the observation vector is of the form:

$$b_i = (N_i^{\text{alt}} - N_i^{\text{grav}}) - \zeta_i^{\text{c ocean}} = \zeta_i^{\text{c geod}} - \zeta_i^{\text{c ocean}} \quad (3)$$

where, $\zeta_i^{\text{c geod}}$ and $\zeta_i^{\text{c ocean}}$ denote the geodetic and oceanographic QSST models respectively. The observation vector entering the system of linear equations can then be describe as

$$b_i = \mathbf{a}_i^T \mathbf{x}_i + v_i \quad (4)$$

where, x is the vector of the unknown parameters of the model selected and \mathbf{a} is the vector of the known coefficients of the parametric model selected to describe and minimize the errors in the observations and estimate values in new points as well. The parametric models used in the present study are the well-known four- and five-parameter similarity transformation ones (see Eqs. 5a, b) as well as polynomial models of degrees zero to three (see Eq. 5c).

$$\mathbf{a}_i^T \mathbf{x} = x_0 + x_1 \cos \varphi_i \cos \lambda_i + x_2 \cos \varphi_i \sin \lambda_i + x_3 \sin \varphi_i \quad (5a)$$

$$\mathbf{a}_i^T \mathbf{x} = x_0 + x_1 \cos \varphi_i \cos \lambda_i + x_2 \cos \varphi_i \sin \lambda_i + x_3 \sin \varphi_i + x_4 \sin^2 \varphi_i \quad (5b)$$

$$\mathbf{a}_i^T \mathbf{x} = \sum_{m=0}^M \sum_{n=0}^N x_q (\varphi_i - \varphi_o)^n (\lambda_i - \lambda_o)^m \cos^m \varphi_i \quad (5c)$$

In Eqs. 5a-c φ_i, λ_i denote the geodetic latitude and longitude of the point under consideration, φ_o, λ_o denote the mean latitude and longitude of the area under study. In Eq. 5c vector x_q contains the q unknown coefficients, while q varies up to a maximum of $q=(M+1)(N+1)$. Depending on the choice of the parametric model 5a-c the design matrix \mathbf{A} of the system of normal equations ($\mathbf{b}=\mathbf{A}\mathbf{x}+\mathbf{v}$) is formed, so that the adjusted vector of unknown parameters $\hat{\mathbf{x}}$ is estimated as:

$$\hat{\mathbf{x}} = (\mathbf{A}^T \mathbf{P} \mathbf{A})^{-1} \mathbf{A}^T \mathbf{P} \mathbf{b} \quad (6)$$

based on the minimization principle

$$\mathbf{v}^T \mathbf{P} \mathbf{v} = \mathbf{v}_{\zeta_i^{\text{c geod}}}^T \mathbf{C}_{\zeta_i^{\text{c geod}}}^{-1} \mathbf{v}_{\zeta_i^{\text{c geod}}} + \mathbf{v}_{\zeta_i^{\text{c ocean}}}^T \mathbf{C}_{\zeta_i^{\text{c ocean}}}^{-1} \mathbf{v}_{\zeta_i^{\text{c ocean}}} = \min \quad (7)$$

In Eqs. 6 and 7 \mathbf{P} and \mathbf{C} are the weight and covariance matrices of observations, and \mathbf{v} the vector matrix of errors. The adjusted geodetic QSST $\zeta_{\text{c geod}}^{\text{adj}}$ is then estimated as:

$$\zeta_{\text{c geod}}^{\text{adj}} = \zeta_{\text{c geod}} + \mathbf{a}_i^T \hat{\mathbf{x}} \quad (8)$$

All aforementioned parametric models have been tested in order to select the most appropriate one, according to

(a) the final differences between the adjusted geodetic QSST model with the oceanographic one, (b) the goodness of fit through the coefficient of determination and the adjusted coefficient of determination (see Eqs. 9a and 9b), and (c) parameter significance (Fotopoulos 2003; Fotopoulos et al. 2004; Kotsakis and Sideris 1999).

$$R^2 = 1 - \frac{\left[\sum_{i=1}^n (b_i - \hat{b}_i)^2 \right]}{\left[\sum_{i=1}^n (b_i - \bar{b})^2 \right]} \quad (9a)$$

$$R_a^2 = 1 - \frac{\left[\sum_{i=1}^n (b_i - \hat{b}_i)^2 \right] / (n-m)}{\left[\sum_{i=1}^n (b_i - \bar{b})^2 \right] / (n-1)} \quad (9b)$$

where, \bar{b} is the mean value of the observations, \hat{b}_i are the adjusted observations, and n the number of observations. Both the adjusted and simple coefficients of determination range between 0 and 1 and the closer they are to 1 the smaller the better the fit of the parametric model is. The adjusted coefficient of determination is superior to the simple one, since the latter is influenced significantly by the degrees of freedom of the system of linear equations, i.e, the smaller the degrees of freedom, (more parameters in the model) the closer R^2 is to 1 (see Fotopoulos 2003; Sen and Srivastava 1990).

Another criterion used to assess the parametric model performance and computed the adjusted geodetic QSST model was the condition number determined as the ratio between the larger and smaller eigenvalues of the matrix $\mathbf{A}^T \mathbf{A}$, that is:

$$\text{con} = \frac{\lambda_{\max}}{\lambda_{\min}} \quad (10)$$

Larger condition numbers translate into more unstable parametric models therefore the results of the prediction tend to vary more with new observations.

Finally, the significance of each model's parameters has been tested according to Dermanis and Rossikopoulos (1991). The entire procedure is based on first fitting to the data the highest order of the selected model and then eliminating the insignificant ones by testing a null hypothesis (backward elimination).

Following this methodology the parameters of the two similarity transformation models and the polynomial ones for degrees zero to three have been computed. The differences between the adjusted geodetic QSST models and the oceanographic one are summarized in Table 4 below. In that Table, A though D denote the zero, first, second and third order polynomial models, while E and F the four and five parameter similarity transformation ones. Characters in italics show the val-

ues of the corrector surface computed and regular ones the differences after the fit. From that table it is evident that the overall best fit is provided by the third order polynomial model, with a standard deviation (1σ) of the differences after the fit at the ± 9 cm level and a range of 60 cm. These large values refer to areas across the sea-land boundary where both models suffer. Neglecting these regions, the range of the differences is at the 25 cm level with a 1σ of ± 3.5 cm.

Table 4. Differences between the adjusted geodetic QSST models and the oceanographic one and statistics of each corrector model. Unit: [m].

	max	min	mean	std
A (trend)			-0.058	
$\zeta^c_{\text{geod}} - \zeta^c$	0.596	-0.577	0.000	± 0.201
B (trend)	0.184	-0.298	-0.065	± 0.130
$\zeta^c_{\text{geod}} - \zeta^c$	0.571	-0.369	0.000	± 0.167
C (trend)	0.130	-0.755	-0.076	± 0.210
$\zeta^c_{\text{geod}} - \zeta^c$	0.499	-0.245	0.000	± 0.105
D (trend)	0.191	-0.737	-0.075	± 0.211
$\zeta^c_{\text{geod}} - \zeta^c$	0.481	-0.233	0.000	± 0.092
E (trend)	0.133	-0.532	-0.071	± 0.179
$\zeta^c_{\text{geod}} - \zeta^c$	0.553	-0.278	0.000	± 0.130
F (trend)	0.136	-0.614	-0.072	± 0.186
$\zeta^c_{\text{geod}} - \zeta^c$	0.558	-0.283	0.000	± 0.131

From that analysis it can be concluded that the model of preference is the 3rd order polynomial one, since it provides the smallest differences after the fit. During the adjustment for all models, the aforementioned statistical measures have been computed in order to test the goodness of fit of each one and the parameter significance. Table 5 summarizes the results acquired, from which it can be concluded that the 3rd order polynomial model provides the closest to one simple and adjusted coefficient of determination (0.68 and 0.74 respectively). This is much better compared to the second best four-parameter similarity transformation model (0.63 and 0.66 respectively). The results from the computation of the condition numbers are equivalent, strengthening the selection of the 3rd order polynomial model as the proper one. From the parameter significance test, all parameters were deemed as significant, while in the case of the five-parameter similarity transformation model it was concluded that the extra parameter compared to the four-parameter model is not significant. Taking these into account, the 3rd order polynomial model was selected to provide the corrector surface (see Fig. 2) with the characteristics presented in Table 4. The resulting adjusted geodetic QSST model is depicted in Fig. 2 and its statistics are presented in Table 6.

Table 5. Coefficient of determination, adjusted coefficient of determination and condition numbers for the various parametric models.

	A	B	C	D	E	F
R_a^2	0.44	0.51	0.56	0.68	0.63	0.59
R^2	0.46	0.54	0.62	0.74	0.66	0.60
co	1.6:10	4.4:10	6.7:10	2.6:10	1.2:10	7.3:10
n	2	3	4	3	7	7

4 Geostrophic Velocity Estimation

From estimation of the final adjusted geodetic QSST models for the area under study, the direction and velocities of the ocean currents can be determined. That was achieved by following the theory of geostrophic flow, i.e., that the Coriolis force and the pressure gradient acting on the currents are in balance. This method is more related to oceanographic studies and products, but its main advantage is that it can quickly provide velocity estimates and takes into account the properties of the ocean as a fluid. One of its disadvantages is that it diverges close to coastal areas, thus making the current estimates in such regions unreliable. The equations of geostrophic flow in spherical approximation, are given as (Pond and Pickard, 2000)

$$u_s = -\frac{g}{fR} \frac{\partial H}{\partial \phi} \quad (11a)$$

$$v_s = \frac{g}{fR \cos \phi} \frac{\partial H}{\partial \lambda} \quad (11b)$$

where u_s and v_s are the horizontal constituents of geostrophic flow, R is a mean earth radius (6371 km), ϕ and λ denote geographic latitude and longitude respectively, f is the Coriolis force and H the QSST previously estimated. Using Eqs. 11a and b, the north-south (u_s) and west-east (v_s) components of the currents' geostrophic velocities have been estimated for the area under study. Table 6 summarizes the statistics of the estimated velocities and the total velocity field (last row), while Fig. 2 depicts the direction and magnitude of the current velocities. From Fig. 2 we can clearly distinguish some well-known jets in the area like the Mid-Ionian (MIJ) and Mid-Mediterranean ones (Mid-MED Jet), the Western Cretan Gyre (WCG), the Ierapetra Anticyclone (IAC), Rhodes Gyre (RG) and the Cyclades Anticyclone (CAC). Furthermore, South of the island of Crete we can identify a small (in terms of magnitude) jet (dotted lines), which can be either a branch of the Mid-Mediterranean one or a jet by its own. Finally, there is a clear flow from the Aegean Sea (jets J1 and J2) which merge into the Western Cretan Anticyclone and probable "feed" the MIJ. On the other hand they can be part of the Eastern Cretan Anticyclone which is closer to mainland Crete and thus not depicted very well due to the problems of geostrophic theory close to coastal areas. The same currents are identified in the studies by Mazella et al. (2001) and Rio (2004) with the exception of the IAC which is only depicted in Mazella et al. (2001) as *known* to exist in the area under study. The fact that the small IAC and CAC can be clearly identified from the proposed methodology, gives good evidence that this "geodetic" estimation of the QSST can provide accurate and reliable estimates of the ocean circulation. From the geodetic part, the QSST can be used to reduce altimetric and marine-gravity measurements from the sea surface to the geoid.

Table 6. The final adjusted geodetic QSST model and the geostrophic velocities for the area under study. Unit: [m/s].

	max	min	mean	σ
QSST ^{adj geod}	0.332	-0.420	-0.040	± 0.133
u_s	1.416	-1.239	-0.013	± 0.283
v_s	1.440	-1.185	-0.012	± 0.245
total field	1.445	0.000	0.313	± 0.206

5 Conclusions

A method to determine the quasi-stationary sea surface topography from a purely geodetic point of view and using geodetic data has been presented. It is based on the simple relationship connecting altimetric and gravimetric geoid heights, a blunder removal and noise

filtering procedure and finally an adjustment with an oceanographic model. From the results obtained it can be concluded that the proposed methodology provides accurate and reliable results, since it gives small differences w.r.t. a MDT model derived from altimetry and oceanographic data. Furthermore, from the current velocities estimated, it was possible to identify all known features of the circulation in the area under study like the Mid-Ionian and Mid-Mediterranean Jets, the Western Cretan Anticyclone, the Ierapetra and Cyclades Anticyclones and Rhodes Gyre, which were clearly identified and outlined in the final field.

Such a local QSST model is invaluable to geodetic studies for the reduction of altimetric sea surface heights from the sea surface to the geoid. Furthermore, it provides a reference surface for oceanographic studies,

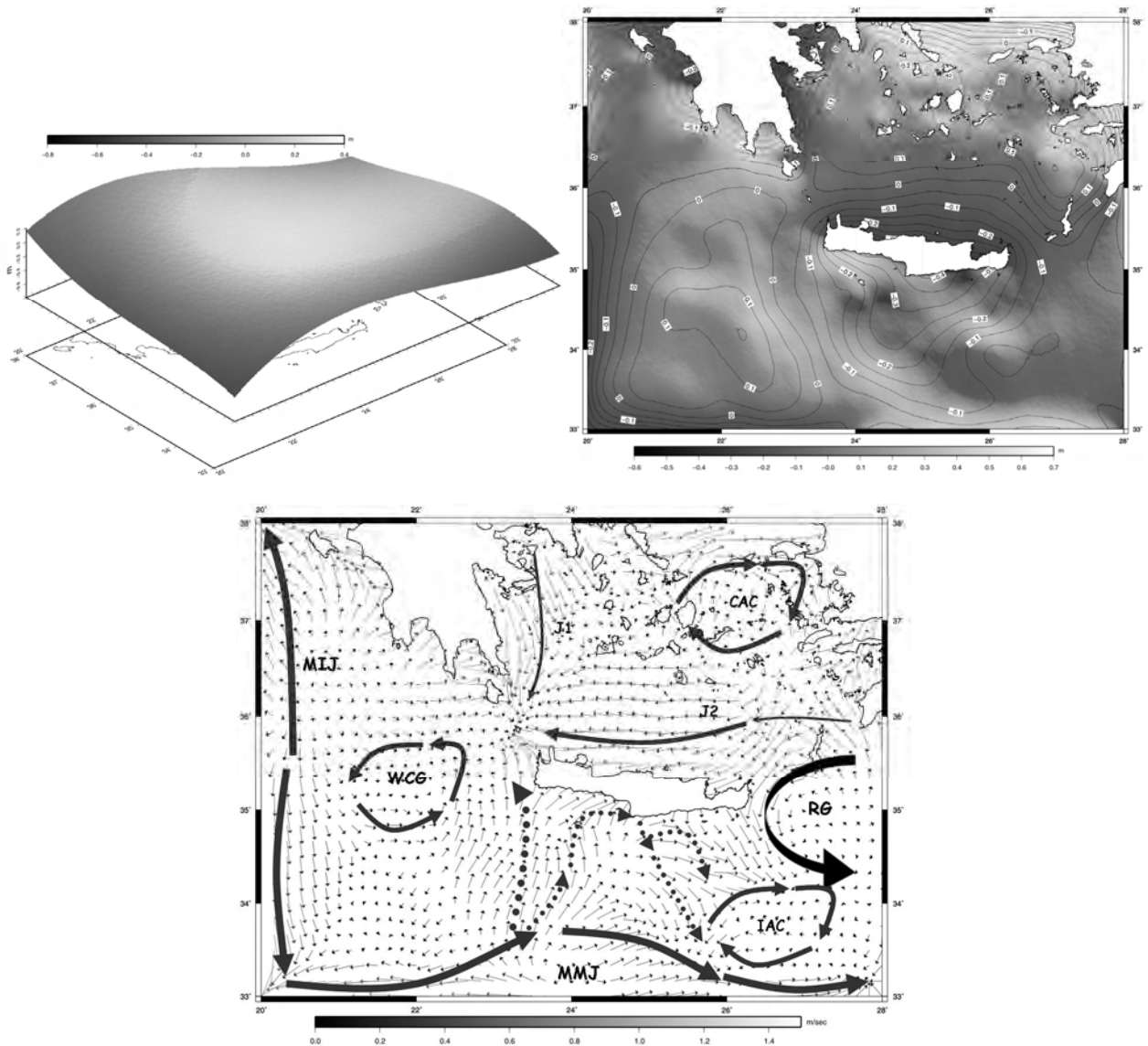


Fig. 2: The corrector surface (top left), the final adjusted geodetic QSST model (top right) and the direction and magnitude of the geostrophic currents (bottom).

where other measurements can be referred. The results of the present study offer an encouraging prospect for the synergy between geodesy and oceanography with respect to sea level monitoring, sea surface topography determination and marine geoid modeling.

From the preliminary geodetic QSST model developed, it is evident that the initial estimate contains many errors since it gives very large values for both the QSST and the current velocities. This is clearly attributed to the errors in both the altimetric and gravimetric data and the differences in the vertical reference used for each data set. Therefore, the adjustment that followed is necessary not only to adjust the geodetic model to an oceanographic one, but to minimize the aforementioned errors as well. Given that the QSST signal has a long-wavelength nature and does not vary significantly especially in closed sea areas like the Mediterranean Sea, the corrector surface estimated can be used to adjust geodetic QSST models elsewhere in the Aegean Sea and the Mediterranean in general.

Acknowledgement

Funding for this research was provided from the Greek Ministry of Education in the frame of the EPEAEK II program «Pythagoras II – Support to Research Teams in the Universities».

References

- Andritsanos VD (2000) Optimum combination of terrestrial and satellite data with the use of spectral methods for applications in geodesy and oceanography. PhD Dissertation, School of Rural and Surveying Engineering, Faculty of Engineering, The Aristotle University of Thessaloniki, Department of Geodesy and Surveying.
- Andritsanos VD, Sideris MG, Tziavos IN (2001) Quasi-stationery Sea Surface topography estimation by the multiple Input-Output method. *J Geodesy* 75: 216-226.
- Dermanis A, Rossikopoulos D (1991) Statistical inference in integrated geodesy. Presented at the IUGG XXth General Assembly, Vienna, August 11 – 21.
- Engelis T (1983) Analysis of sea surface topography determination using Seasat altimeter data. Report No. 343, Department of Geodetic Science and Surveying, The Ohio State University, Columbus, Ohio.
- Engelis T (1984) Radial orbit error reduction and sea surface topography determination using satellite altimetry. Report No. 377, Department of Geodetic Science and Surveying, The Ohio State University, Columbus, Ohio.
- Engelis T (1985) Global circulation from Seasat altimeter data. *Marine Geodesy*, Vol. 9, No. 1.
- Engelis T (1987) Spherical harmonics expansion of the Levitus sea surface topography. Report No. 385, Department of Geodetic Science and Surveying, The Ohio State University, Columbus, Ohio.
- Fotopoulos G (2003) An analysis on the optimal combination of geoid, orthometric and ellipsoidal height data. UCGE Rep Nr 20185, Calgary AB, Canada.
- Fotopoulos G, Tziavos IN, Sideris MS (2004) On the incorporation of sea surface topography in establishing vertical control. Presented at the Gravity Geoid and Space Missions 2004 Conference, Porto, Portugal, Aug. 30 – Sept. 3, 2004.
- Knudsen (1992) Estimation of sea surface topography in the Norwegian sea using gravimetry and Geosat altimetry. *Bulletin Géodésique* 66:27-40.
- Kotsakis C and Sideris MG (1999): On the adjustment of combined GPS/levelling/geoid networks. *J of Geod*, 73(8): 412-421.
- Lemoine FG, Kenyon SC, Factor JK, Trimmer RG, Pavlis NK, Chinn DS, Cox C, Klosko SM, Luthcke SB, Torrence MH, Wang YM, Williamson RG, Pavlis EC, Rapp RH, Olson TR (1998) The development of the join NASA GSFC and NIMA geopotential model EGM96, NASA Technical Paper, 1998 – 206861.
- Manzella GMR, Cardin V, Cruzado A, Fusco G, Gacic N, Galli C, Gasparini GP, Gervais T, Kovacevic C, Millot C, Petit DeLa-Villeon L, Spaggiari G, Tonani M, Tziavos C, Velasquez V, Walne A, Zervakis V, Zodiatis G (2001) EU-sponsored Effort Improves Monitoring of Circulation Variability in the Mediterranean. *EOS-Transactions American Geophysical Union*, Vol. 82(43), 497-504, October 23, 2001.
- Pavlis NK, Cox CM, Wang YM, Lemoine FG (1998) Further analysis towards the introduction of ocean circulation model information into geopotential solutions. Presented at the 2nd joint meeting of the International Gravity Commission and the International Geoid Commission, Trieste, Italy.
- Pond S, Pickard G (2000) *Introductory dynamical oceanography*. 2nd edition, Butterworth – Heinemann.
- Rio M.-H. (2004) A Mean Dynamic Topography of the Mediterranean Sea Estimated from the Combined use of Altimetry, In-Situ Measurements and a General Circulation Model. *Geoph Res Let* Vol. 6, 03626.
- Schwarz KP, Sideris MG, Forsberg R (1990) The use of FFT techniques in physical geodesy. *Geophys J Int* 100: 485-514.
- Sen A and Srivastava M (1990): *Regression Analysis: Theory, Methods and Applications*. Springer Texts in Statistics, Springer, New York.
- Vergos (2006) Study of the Earth's Gravity Field and Sea Surface Topography in Greece by combining surface data and data from the new satellite missions of CHAMP and GRACE. PhD Dissertation, Department of Geodesy and Surveying, School of Rural and Surveying Engineering, Faculty of Engineering, Aristotle University of Thessaloniki.
- Vergos GS, Sideris MG (2003) Estimation of High-Precision Marine Geoid Models Off-shore Newfoundland, Eastern Canada. In: Tziavos IN (ed) Proc of the 3rd Meeting of the Gravity and Geoid Commission “Gravity and Geoid 2002”, pp 126-131.
- Vergos GS, Tziavos IN, Andritsanos VD (2005a) On the Determination of Marine Geoid Models by Least-Squares Collocation and Spectral Methods Using Heterogeneous Data. *International Association of Geodesy Symposia*, Vol. 128, F. Sansó (ed.), A Window on the Future of Geodesy, Springer – Verlag Berlin Heidelberg, pp. 332-337.
- Vergos GS, Tziavos IN, Andritsanos VD (2005b) Gravity Data Base Generation and Geoid Model Estimation Using Heterogeneous Data. *International Association of Geodesy Symposia*, Vol. 129, Jekeli C, Bastos L, Fernandes J (eds.), Gravity Geoid and Space Missions 2004, Springer – Verlag Berlin Heidelberg, pp. 155-160.

Gravity Anomalies and Sea Ice Thickness in the Arctic Ocean from ICESat

H. Skourup, R. Forsberg
Department of Geodynamics,
Danish National Space Center, Juliane Maries Vej 30, DK-2100 Copenhagen Oe, Denmark

A. Braun
Department of Geomatics Engineering,
The University of Calgary, 2500 University Drive N.W., Calgary, Alberta, Canada, T2N 1N4

Abstract

The ICESat laser altimetry mission has since January 2003 provided satellite altimetry over the ice-covered Arctic Ocean up to 86°N. The laser altimetry surface elevation data is the sum of geoid, sea ice freeboard and ocean mean dynamic topography, but by a combination of lowest level filtering and GRACE-based geoid models the signals may be separated, and sea ice thickness and gravity field information be recovered. In the paper we derive an improved gravity anomaly field for the Arctic Ocean using FFT Wiener filtering methods. The composite ICESat gravity grid shows all the major tectonic features of the Arctic Ocean at high resolution. The results are compared to the recently revised Arctic Gravity Project anomaly grid and airborne gravity. The results show that the laser altimetry data may provide excellent gravity results comparable to open ocean altimetry even over the most heavy ice conditions.

1 Introduction

Satellite altimetry missions have in the past decade improved the knowledge of the gravity field in vast, remote regions such as the oceans. Over the oceans altimeters map the mean sea surface (MSS), after correction for tides. The MSS represent the marine geoid if the mean dynamic topography (MDT) is neglected. The marine geoid can be inverted to gravity anomalies, e.g. by use of Fast Fourier Transforms.

If we consider even more remote and hostile regions like the Arctic Ocean, access to satellite data are limited in coverage due to the inclination of the satellite orbits, leaving a gap around the pole. Since the launch in January 2003 NASA's laser altimeter onboard the Ice, Cloud and land Elevation Satellite

(ICESat) have for the first time collected data up to 86°N. This is an improvement compared to the ESA missions ERS-1/2 and ENVISAT, which covers up to 81.5°N. Another important factor in the Arctic Ocean is the presence of sea ice. To estimate the Arctic MSS it is necessary to remove the sea ice freeboard height (the part of the sea ice above sea level) from the altimetry measurements. The MSS can be expressed as

$$MSS = h - F = N + MDT \quad (1)$$

where h is the ellipsoidal height of the altimetry measurements corrected for tides, F the freeboards, N the geoid, and MDT the mean dynamic topography.

The sea ice freeboards can be obtained directly from altimetry data. Methods to determine sea ice freeboards from radar altimetry were originally developed for ERS by Laxon et al (2003). Here we apply a lowest level filtering algorithm developed for airborne lidar flights, Hvidegaard and Forsberg (2002), to estimate sea ice freeboards from ICESat data.

The studies in this paper are part of an ongoing ESA study ArcGICE, which have as a main objective to make an improved Arctic Ocean MSS, to be used as reference for future CryoSat measurements of the sea ice freeboard. In order to improve the MSS the aim is to improve the existing geoid and MDT models by combining surface, airborne and satellite measurements. Here we investigate ICESat altimetry observations to derive gravity anomalies and sea ice freeboards in the Arctic Ocean.

A preliminary gravity field based on two ICESat epochs from 2003 was published by Forsberg and Skourup (2005). In this paper we investigate how the gravity field is influenced by including seven epochs of ICESat data covering the period 2003-2005, which

Table 1. Used ICESat epochs 2003-2005

LASER	Period	Year
1	February 20 – March 29	2003
2A	September 25 – November 18	2003
2B	February 17 – March 21	2004
2C	May 18 – June 21	2004
3A	October 3 – November 8	2004
3B	February 17 – March 24	2005
3C	May 20 – June 23	2005

we have gained access to within the ArcGICE project. The ICESat epochs to be included here are listed in Table 1. We also estimate an Arctic Ocean wide sea ice freeboard map for each of the ICESat periods, and compare the gravity anomalies derived from the MSS not corrected for sea ice freeboard heights (the raw altimeter measurements) to a field corrected for sea ice. This is done to investigate whether or not the resulting field is improved by removal of the sea ice from the altimeter data. In order to validate the three gravity fields, they are compared to the Arctic Gravity Project and airborne gravity campaigns carried out during the 1990's.

The results of the ICESat derived gravity anomalies can be used to improve existing gravity models in regions with sparse or poor data. The improved gravity field or geoid can then also be used to estimate better sea ice freeboards.

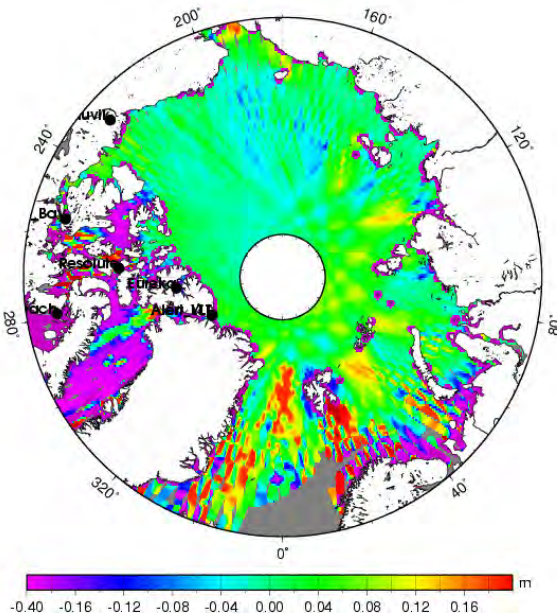


Fig. 1 Differences between GOT99.2 and the Padman tide models applied to ICESat epoch February-March, 2003.

2 Method

In order to compute the gravity anomalies from ICESat observation data have to be corrected for tidal and atmospheric effects, and the sea ice freeboards need to be removed.

2.1 Tide Corrections and Inverse Barometer Effects

ICESat altimeter data have been corrected for tides using the global tide model GOT99.2 (GOT = Goddard/Grenoble Ocean Tide) [Ray, 1999]. This tide model is primarily based on TOPEX/Poseidon altimetry data available south of 66°N. We apply here the Arctic Ocean regional tide model by Padman and Erofeeva (2004), which uses a combination of TOPEX/Poseidon and ERS altimetry, and assimilates coastal and benthic tide gauges. Accordingly, the Padman model is expected to perform better in the Arctic regions.

The tide corrections from the two models have been computed and applied to all the ICESat epochs. The differences between the two tide models are shown in Figure 1 for ICESat epoch February-March 2003. Differences between the two fields are primarily seen in the coastal regions; the Canadian Arctic Archipelago, Nares Strait, the Baffin Bay and Labrador Sea. The regional as well as the seasonal variability obtained are on the order of a few centimeters.

The inverse barometer (IB) effect removes some of the “trackiness” present in the altimeter data. The correction originating from inverse barometer (IB) effect can be calculated from the sea level pressure (SLP):

$$IB = \alpha (SLP - 1013.3) \quad (2)$$

where the constant 1013.3 mbar represent the global mean sea level pressure calculated over the oceans, and the proportionality constant α is taken to be -11.2 mm/mbar based on work done by repeated ICESat tracks in the Arctic by Kwok et al. (2006). The sea level pressure (SLP) fields used here to obtain the IB correction for each ICESat sample is linearly interpolated from 6-hourly NCEP/NCAR reanalysis products provided by the NOAA-ESRL PSD Climate Diagnostics Center Branch, Boulder Colorado. Spatial and temporal differences due to the IB effects are on the order of a few decimeters.

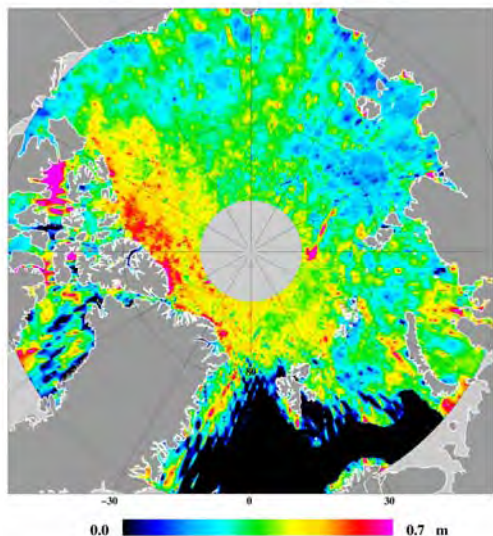


Fig. 2 Map of sea ice freeboard height in the Arctic Ocean derived from ICESat data epoch February-March, 2003.

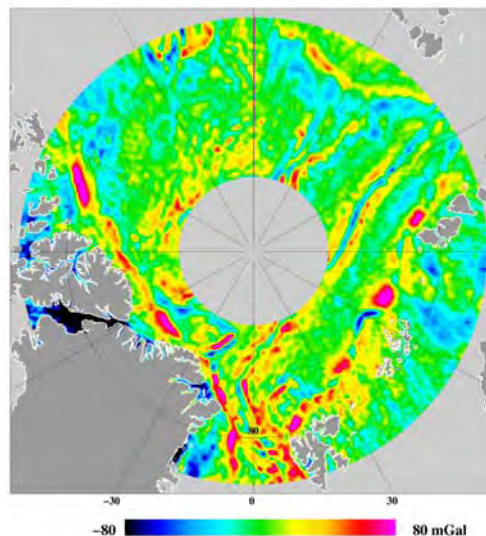


Fig. 3 Gravity anomalies in the Arctic Ocean with all seven epochs merged into one field. Corrected for sea ice.

2.2 ICESat Sea Ice Freeboard Heights

To estimate the sea ice freeboards from ICESat we are using a modified method developed for airborne lidar campaigns, Hvidegaard and Forsberg (2002). From equation (1) the freeboard (F), including snow cover, is given by

$$F = h - N - MDT - e \quad (3)$$

where h is the ellipsoidal height of the altimeter measurements after removal of tides, N is the geoid, MDT the mean dynamic topography, and e measurement errors. The first step is to remove the geoid from the altimeter data. We are here using the geoid representation from the Arctic Gravity Project (ArcGP) see Kenyon and Forsberg (2001).

We apply a lowest-level filtering scheme to the height ($h-N$) by taking the average of the three lowest values of an along-track interval of 20 km. The lowest values are believed to represent open leads or thin ice in between the floes. A smooth curve determined by least-squares collocation is computed between the lowest levels, which we assume represent the sea surface height. Subsequently the freeboard heights are estimated by subtracting the smooth curve from the data.

To remove false freeboard heights over open ocean, originating from the lowest-level algorithm favoring the trough of the waves, an open water mask

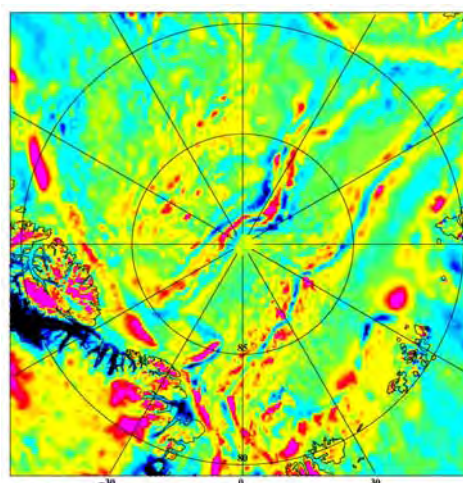


Fig. 4 The Arctic Gravity Project (ArcGP) gravity anomalies, version February 2006. Same colour scaling as in Figure 3.

is applied. The mask is obtained from SeaWinds scatterometer mission QuikSCAT, and combines backscatter and brightness temperatures to define a 40% sea ice concentration.

Figure 2 displays an example of an ICESat derived Arctic Ocean sea ice freeboard map from the period February-March, 2003. The typical winter ice situation shows thicker sea ice North of Greenland forced against the coast by the Beaufort Gyre, and thinner ice in the Russian Arctic. Some residual track noise, e.g. north of Russia, is also apparent.

2.3 ICESat-derived Gravity Anomalies

Each of the mean sea surfaces computed from ICESat is cross-over adjusted, and the seven fields (listed in Table 1) are merged and draped into one combined MSS. This MSS is approximated to be the geoid by neglecting the MDT. The geoid is then inverted into gravity anomalies by techniques equivalent to the derivation of marine gravity anomalies from satellite radar altimetry over the open ocean. Here we have used Fast Fourier Transform (FFT).

In the computations we take into account only the longer wavelengths of the freeboards, and use a Wiener filtering method to suppress short-wavelength noise. In the Fourier domain it is expressed as

$$F(\Delta g) = G \frac{k}{1 + ck^4} F(N) \quad (5)$$

where F is the two-dimensional Fourier transform, k is the wave number, and c is a resolution constant described by Forsberg and Solheim (1988), and also by Andersen and Knudsen (1998). The above technique is used in combination with a remove-restore technique, to keep longer wavelengths from the global GRACE model GGM02S.

The resulting gravity anomalies corrected for sea ice freeboards can be seen in Figure 3. The gravity anomalies based on the ICESat data alone, compares qualitatively well to the Arctic Gravity Project's (ArcGP) gravity anomalies, cf. Figure 4, and maps nicely the major tectonic features, such as the Gakkel and Lomonosov Ridges, the deeper Canadian Basin, and the continental shelves. A similar procedure has been applied to compute the gravity anomalies with no sea ice corrections applied to the ICESat altimeter observations. The differences between these fields are outlined in the next chapter.

3 Evaluation of Results

3.1 Comparison to Airborne Campaigns

For a more quantitative comparison of the ICESat derived gravity anomalies, the two fields derived above (one not corrected for sea ice freeboards, and the other corrected for sea ice), together with the fields based on only two ICESat epochs from 2003 by Forsberg and Skourup (2004), are compared to high-resolution airborne gravity campaigns.

The airborne campaigns were carried out by the US Naval Research Laboratory (NRL) in the Arctic Ocean during the years 1992-99, and by the Danish National Space Center (DNSC) in the period 1998-2003. Four sub-regions have been selected for comparison, shown in Figure 5 by different colours. The NRL survey 1998-99 north of Svalbard, marked by red, are limited by latitudes 83-86°N, the DNSC survey north of Greenland (blue) are limited by 84-86°N, and the NRL surveys of 1995 (yellow) and 1994 (green) in the Canadian Arctic, are limited to a the latitude band 79-81°N. Biases between the 1994 and 1995 survey from NRL data are found, and therefore the data are divided into two regions.

Table 2 lists the mean and standard deviation of the differences between the ICESat gravity fields and the airborne gravimetry. It is seen that more data included to determine the gravity anomalies improves the estimated gravity field. In all but one case north of Greenland, the field is improved by taking the sea ice freeboard heights into account. For this particular area north of Greenland, with very compact ice, an airborne underflight of ICESat with high-resolution laser scanning (Forsberg, and Skourup, 2005), indicates that the freeboards based on ICESat are underestimated by approximately 35 cm, mainly due to imperfect lowest level filtering. The ICESat derived gravity anomalies, including data from 2003-05 and sea ice correction, are comparable to gravity anomalies based on 7 years of ERS data (S. Laxon, pers.comm.).

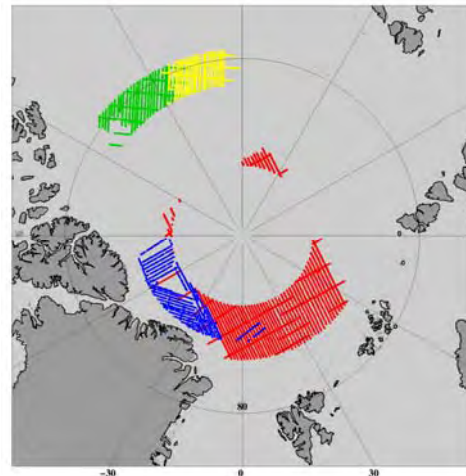


Fig. 5 Flight Lines from airborne gravity surveys used for evaluation of the ICESat gravity. NRL 98/99 survey (red), NRL 95 (yellow), NRL 94 (green), and DNSC survey 1998-2003 (blue).

Table 2 Comparison of gravity anomalies derived from ICESat and ERS to airborne gravity campaigns. NRL and DNSC are airborne campaigns carried out by the Naval Research Laboratory and the Danish National Space Center, respectively, each with an estimated accuracy around 2 mGal. The four airborne comparison regions are displayed the different colours in Fig. 5.

Gravity Field	NRL 98/99 (red)		DNSC 98-03 (blue)		NRL 95 (yellow)		NRL 94 (green)	
	mean	std.dev	mean	std.dev	mean	std.dev	mean	std.dev
ICESat 2003	-1.3	6.4	0.3	7.5	2.4	7.2	-11.5	10.9
ICESat 2003-5	-0.6	5.2	0.5	6.6	3.4	4.2	-10.8	9.4
ICESat 2003-5, ice corrected	-0.7	4.9	3.5	7.5	3.5	3.8	-10.8	9.3
ERS (Laxon)	-	-	-	-	-0.2	3.5	-14.3	9.1

4 Conclusions and Outlook

ICESat based gravity anomalies for the Arctic Ocean has been derived based on seven epochs of ICESat data (2003-05). By neglecting mean dynamic topography and sea ice freeboards the mean sea surface (MSS) for each ICESat epoch were merged and draped into a combined MSS, and inverted into gravity anomalies by FFT Wiener filtering methods. When validated to airborne gravity surveys it is concluded that the gravity field estimated from seven ICESat epochs is improved compared to gravity anomaly fields based on the hitherto only two available ICESat epochs from 2003. Thus, the more ICESat data available, the better gravity fields can be obtained, as expected.

A technique to estimate Arctic Ocean sea ice freeboard heights from ICESat data based on an along-track lowest level filtering was described and applied to the ICESat observations. The technique assumes the lowest levels to represent open water or thin ice in between the floes. The ICESat derived sea ice freeboards provides realistic Arctic Ocean freeboard heights with thicker ice north of Greenland, and thinner ice in the Russian Arctic.

The sea ice derived freeboards are used to see whether or not the gravity anomalies are improved by removing the sea ice from the observed ICESat altimeter data (h-F). By including freeboard corrections the gravity field improves in all regions except for the area north of Greenland, which are believed to be due to a combination of very compact ice conditions with few sufficiently large open leads or thin ice to allow reliable lowest-level filtering.

Overall the ICESat derived gravity anomalies compare qualitatively very well to the Arctic Gravity Project (ArcGP) gravity anomalies, and map in details the major tectonic features, such as the Gakkell and Lomonosov Ridges, the deeper Canadian Basin and the continental shelves. The ICESat gravity

results will be used to improve the existing ArcGP gravity field models for the Arctic Ocean, especially for sectors north of Russia where some of the underlying data in ArcGP has a relatively poor resolution.

Future work for improved the ICESat gravity field should include corrections to the observed ICESat heights due to e.g. laser saturation, and the influence of the mean dynamic topography on the gravity fields should be investigated.

Acknowledgements

This work was done as part of the ArcGICE project, sponsored by the European Space Agency (ESTEC, contract officer M. Drinkwater). Thanks to John Brozena, NRL, for providing original airborne gravity data, and to S. Laxon, UCL, for providing the ERS 97W gravity grid based on ERS-1.

References

- Andersen, O.B., and P. Knudsen (1998). Global marine gravity field from the ERS-1 and GEOSAT geodetic mission altimetry. *J. Geophys. Research*, 103, 8129-8137.
- Dalå, N.S., R. Forsberg, K. Keller, H. Skourup, L. Stenseng, and S. M. Hvidegaard (2005). Airborne lidar measurements of sea ice north of Greenland and Ellesmere Island 2004. GreenICE/SITHOS/CryoGreen/A76 projects. *Final Report. Technical Report, Danish National Space Center.*
- Forsberg, R., and H. Skourup (2005). Arctic Ocean Gravity, Geoid and Sea-ice Freeboard Heights from ICESat and GRACE. *Geophysical Research Letters*, vol. 32, L21502.
- Forsberg, R., and D. Solheim (1988). Performance of FFT methods in local gravity field modeling. *Proceedings, Chapman Conference on Progress in the Determination of the Earths Gravity Field, AGU, Ft. Lauderdale.*
- Hvidegaard, S.M., and R. Forsberg (2002). Sea ice thickness from airborne laser altimetry over the Arctic Ocean north of Greenland. *Geophysical Research Letters*, vol. 29, no. 20, pp.1952-1955.
- Kenyon, S., and R. Forsberg (2001). Arctic Gravity Project – A status. *In Gravity, Geoid and Geodynamics 2000,*

- International Association of Geodesy Symposia, Vol. 123, edited by M.G. Sideris, pp. 391-395, Springer, New York.*
- Kwok, R., G.F. Cunningham, H.J. Zwally, and D. Yi (2006). ICESat over Arctic sea ice: Interpretation of altimetric and reflectivity profiles. *Journal of Geophysical Research*, vol. 111, C06006, doi: 10.1029/2005JC003175.
- Laxon, S., N. Peacock, and D. Smith (2003). High interannual variability of sea ice thickness in the Arctic Region, *Nature* 425, 947-950.
- Padman, L., and S. Erofeeva (2004). A barotropic inverse tidal model for the Arctic Ocean. *Geophysical Research Letters*, vol. 31, L02303, doi:10.1029/2003GL019003.
- Ray, R.D. (1999). A global ocean tide model from TOPEX/Poseidon altimetry: GOT99.2. *NASA Tech. Memo.*, 209478, 58 pp.

Determination of Evolution of the Altimetric Mean Level of the Western Mediterranean from the Jason-1 Data: Comparison with Analysis of Tidal Gauge Measurements

M. HADDAD, H. ABDELLAOUI, N. AMRANE

National Institute of Cartography and Remote Sensing 123, Rue de Tripoli, BP 430, Hussein-Dey 16040 - Algiers, Algeria.

Prf. M.F. BELBACHIR

University of Sciences and Technology of Oran, Signals and Systems Laboratory, Institute of Electronics. BP 1505, Oran El M'naouer, Algeria.

Abstract. The sea surface topography, which is directly linked to the shape of the geoid and to oceanic effects, is only measurable thanks to the spatial and temporal resolution of satellite altimetry. The contributions of satellite altimetry study in the Mediterranean have been considerable. The first maps of the marine geoid, with relative accuracy of one to two decimetres depending on the methods used, have contributed greatly to the understanding of geophysical phenomena.

Subsequently, thanks to reductions in orbital errors, improvements in gravitational models, and to the development of pseudo-geometrical orbit computations, the accuracy of determination of the absolute mean sea level has improved from several meters to a few centimetres.

The study presented here aims to determine seasonal variations in mean sea level in the Western Mediterranean basin by analysis of Jason-1 data corrected of different perturbations like the geophysical phenomena, the ocean wave influence, the inverse barometer effect, and the orbit error.

The analysis of altimetric data Jason-1 allowed us to observe a strong amplitude of variations of the average level in the Western Mediterranean basin, of the order of 20 cm, with a characteristic period of one year.

The comparison of the variation of the average height sea level at the harbour of Algiers obtained from analysis of altimetric data Jason-1 and from the harmonic analysis of tidal gauge measurements, showed almost identical results.

Keywords. Jason-1, tide gauge, sea level, seasonal variations, Western Mediterranean sea.

1. Introduction

The United States were the first to have put in orbit an altimeter aboard satellites, on Skylab and Geos-c, then on Seasat in 1978 and Geosat in 1985. Since the 90s, new altimetric missions were launched, ERS-1 (1991-1996), Topex/Poseidon

(since 1992), ERS-2 (since 1995), Jason-1 (since 2001) and Envisat (since 2003).

This paper presents the methodology of processing and analyzing of Jason-1 altimetric data to determinate the seasonal variation of sea level of the Western Mediterranean sea.

2 Jason-1 mission

JASON-1 is a follow-on mission to the highly successful TOPEX/POSEIDON (T/P) mission. The main goal of this mission is to measure the height of sea surface at least at the same performance level of T/P.

Launched on December 7, 2001, the Jason-1 satellite measures the precise height of the sea surface using the POSEIDON-2 altimeter operating at 13.575 GHz (Ku band) and 5.3 GHz (C band), a system of positioning Doris (Doppler Orbitography and Radiopositioning by Satellite) in complement to the GPS receiver and Laser reflector and a Microwave Radiometer which provide the total water vapor content in the troposphere along the altimeter beam.

3 Principle of computation of the level of the sea

The radar altimeter embarked aboard a satellite gives out a signal to very high frequency to the vertical of this one in direction of soil, and receives in return the echo reflected by the surface of the sea.

The analysis of the echo permits to extract a very precise measure of time of round-trip journey between the satellite and the surface of the sea. This time is transformed then in distance by simple multiplication by the speed of light, speed to which propagates electromagnetic waves.

The height of the sea is therefore equal to the difference between the distance satellite-surface and the position of the satellite above the ellipsoidal reference.

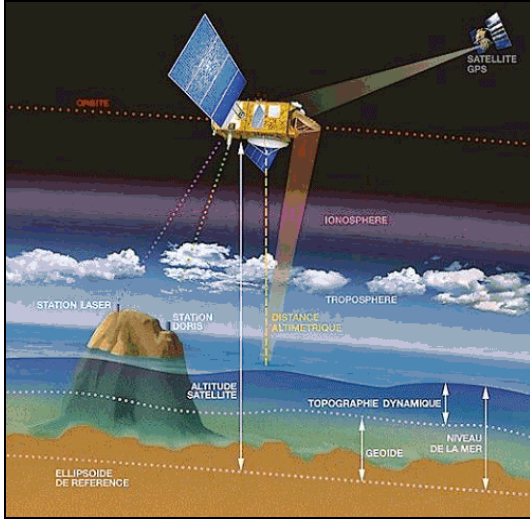


Fig. 2 Geometric principle of altimetry.

4 Sources of errors

Altimetric measurements have many sources of errors. For instance, they need to be corrected for environmental perturbations like the geophysical corrections (wet troposphere, dry troposphere and ionosphere), the ocean wave influence (sea state or electromagnetic bias). Also, the tide influence (ocean tide, earth tide and pole tide) and inverse barometer effect have to be accounted for.

4.1 Troposphere and ionosphere influence

The atmosphere slow down the velocity of radio pulses at a rate proportional to the total mass of the atmosphere (dry troposphere influence), the mass of water vapor in the atmosphere (wet troposphere influence), and the number of free electrons in the ionosphere (ionosphere influence).

- The dry meteorological tropospheric range correction is principally equal to the surface pressure multiplied by -2.277mm/mbar , with a small adjustment also necessary to reflect a small latitude dependence (Rummel, 1993):

$$Dry_Corr = 2.227 (1 + 0.0026 \cos(2\varphi)) P_s \quad (1)$$

where P_s is surface atmospheric pressure in mbar, φ is latitude, Dry_Corr is the dry troposphere correction in mm.

- The wet troposphere correction expression is (Rummel, 1993):

$$Wet_Corr = 2.227 \left(\frac{1255}{T_s} + 0.05 \right) E_s \quad (2)$$

where P_s is surface atmospheric pressure in Pascal, φ is latitude, E_s is the partial pressure of the water steam and T_s is the temperature in Kelvin.

- The ionosphere correction for an altimeter bi-frequency is given by (Rummel, 1993) :

$$Iono_Corr = \frac{f_1^2}{f_1^2 - f_2^2} \frac{40.2 E}{f_2^2} - \frac{f_2^2}{f_1^2 - f_2^2} \frac{40.2 E}{f_1^2} \quad (3)$$

where E represent the total content in electron (TEC) and f_1 and f_2 the frequencies.

4.2. Sea state bias

Due to the large footprint radar measurements, the sea surface scattering elements do not contribute equally to the radar return: troughs of waves tend to reflect altimeter pulses better than do crests. Thus the centroid of the mean reflecting surface is shifted away from mean sea level towards the troughs of the waves. The shift causes the altimeter to over-estimate the height of the satellite above the sea surface. The Sea State Bias (SSB) is the difference between the apparent sea level as measured by an altimeter and the true mean sea level.

The nature of the sea state bias has been investigated using airborne radars and lasers capable of determining for various sea states the strength of the vertically reflected signal as a function of the displacement of the reflecting area from mean sea level. It is given as a function of wind speed and the skewness and kurtosis of the probability distribution of sea surface elevation due to the waves on the sea surface.

4.3. Ocean tide

It represents the response of the ocean to motion of the moon, the sun and the other planets. It translates itself by a transport of water masses.

This correction is calculated from global models of tide : an empirical model GOT99.2 of the Goddard Space Flight Center or the FES 95.2 finite-element hydrodynamic model of the university of Grenoble.

4.4 Solid Earth Tide

The solid Earth responds to external gravitational forces similarly to the oceans. The Earth responds fast enough for it to be considered to be in equilibrium with the tide generating forces.

Then, the surface is parallel with the equipotential surface, and the tide height is proportional to the potential. The proportionality is the so-called Love number. It should be noted that, although the Love number is largely frequency independent, an exception occurs near a frequency corresponding to the K1 tide constituents due to a resonance in the liquid core (Wahr 1985). Such a tide is computed as described by Cartwright and Tayler (1971) and Cartwright and Edden (1973).

4.5 Pole tide

The Earth's rotational axis oscillates around its nominal direction with apparent periods of 12 and 14 months. This result in an additional centrifugal force which displaces the surface. The effect is thus indistinguishable from tides, and it is called the pole tide. The period is long enough to be considered in equilibrium for both the ocean and the solid Earth. The complete pole tide (in mm) expression is (Wahr, 1985):

$$H_{Pole} = -69.435 \sin(2Lat_{Tra}) \times \left(\begin{array}{l} (x_{pole} - x_{pole-avg}) \cos Lon_{Tra} \\ + (y_{pole} - y_{pole-avg}) \sin Lon_{Tra} \end{array} \right) \quad (4)$$

where: Lon_{Tra} , Lat_{Tra} are longitude and latitude of measurement point, x_{pole} , y_{pole} is axis in the direction of the IERS reference meridian and axis in the direction 90° west longitude, $x_{pole-avg} = 0.042$ arc sec and $y_{pole-avg} = 0.293$ arc sec.

4.6 Inverse barometer effect

As atmospheric pressure increases and decreases, the sea surface tends to respond hydrostatically. The ocean rises and falls, that is, a one mbar increase in atmospheric pressure depresses the sea surface by about 1 cm.

The instantaneous correction is computed using as input the surface atmospheric pressure (P_{atm} , in mbar) which is available indirectly via the dry tropospheric correction obtained from meteorology (Dry_Corr , in mm):

$$P_{atm} = \frac{Dry_Corr}{[(-2.277) (1 + (0.0026 \cos(2Lat_{Tra} 1.10^\circ \pi / 1800)))]} \quad (5)$$

The inverse barometer correction (Inv_Bar , in mm) is then:

$$Inv_Bar = -9.948(P_{atm} - 1013.3) \quad (6)$$

4.7 Orbital errors

The effect of the orbital errors is directly visible to the height in intersections between ascending and descending altimetric tracks (crossover point). The correction of this effect is based on the principle of polynomial interpolation of residues on height at the crossover points.

5 Processing and analysis

The assessment of seasonal variations in mean sea level from the Jason-1 data made on a zone covering the Western Mediterranean sea: zone understood between $35.5^\circ \leq \varphi \leq 44.5^\circ$ and $0^\circ \leq \lambda \leq 10^\circ$.

5.1 Jason-1 data used

The used Jason-1 data are supplied by AVISO (Archivage, Validation et Interprétation des données des Satellites Océanographiques) under GDR Products DVD, containing the cycles from 079 to 132 which correspond to dates from February 27, 2004 to august 16, 2005.

The pass numbers used for this application are illustrated in the following figure:

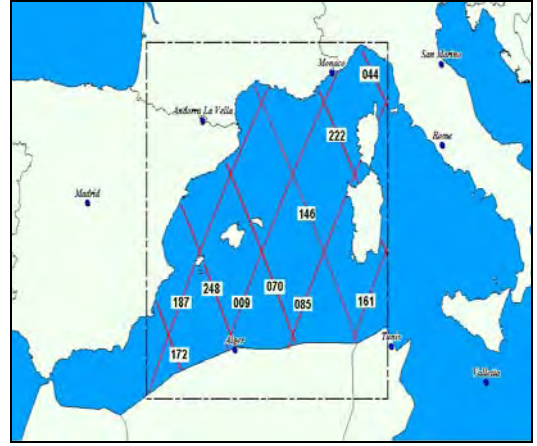


Fig.3 Jason-1 tracks over Western Mediterranean sea.

GDR (Geophysical Data Records) files contain ten-day repeat cycles data. It contains all relevant data and corrections needed to calculate the sea surface height: location, altimeter range, troposphere and ionosphere corrections, Solid Earth, ocean and polar tide corrections, inverse barometer correction ...

5.2 Model of computing sea height

The formulation of the model of computing sea surface height (SSH) is given as follows:

$$SSH = Hp_{Sat} - (H_{Alt} + \Sigma) \quad (7)$$

where Hp_{Sat} is the DORIS altitude of satellite center of mass above the GRS 80 reference ellipsoid, H_{Alt} is the altimeter range in Ku band and Σ is the sum of corrections to be added to the altimeter range:

$$\Sigma = Dry_Corr + Wet_Corr + Iono_Corr_{ku} + INV_Bar + H_Eot_FES + H_Set + H_Pol \quad (8)$$

where: Dry_Corr is the dry meteorological tropospheric correction, Wet_Corr is the wet meteorological tropospheric correction, $Iono_Corr_{ku}$ is the altimeter ionospheric correction on ku band, SSB_Corr_{k1} sea state bias correction in Ku-band, INV_Bar is the

inverted barometer height correction, H_{Eot_FES} is the geocentric ocean tide height computed from FES 95.2 model, H_{Set} is the solid earth tide height and H_{Pol} is the pole tide height.

5. 3 Processing and results

For this application, each of Jason-1 cycle is treated independently of the others to obtain a sea surface height.

Afterward and in case if crossover points exist with a significant difference of sea surface height between an ascending and descending altimetric arcs, an adjustment of the height of the sea along altimetric arcs is done.

Next, the sea surface height is compared point by point to the EGM 96 global geoid model that is closely associated with the location of the mean sea surface.

The average differences obtained by cycle between sea heights stemming from Jason-1's instantaneous profiles and the EGM 96 geoid surface is represented in the following figure:

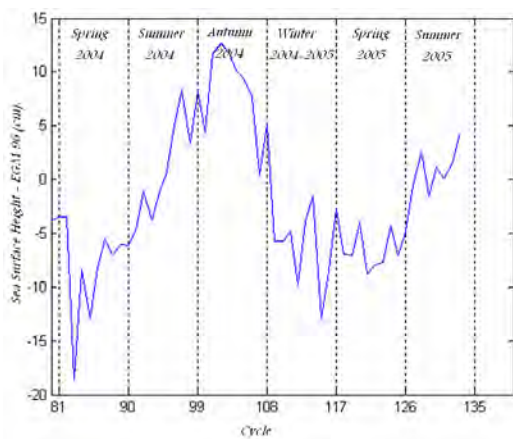


Fig.4 Average differences between the altimetric sea heights and the EGM 96 geoid surface.

The temporal variations in the Western Mediterranean basin between the instantaneous height of the sea and the EGM96's geoid have amplitude about 20 cm, with a maximum and a minimum respectively in autumn and in winter: this phenomenon is due mostly to the thermic expansion/contraction of the water under the influence of temperature variations.

The combination of Jason-1 cycles from 079 to 132 has provided an altimetric mean level surface over the Western Mediterranean sea. The comparison of this surface with the EGM 96 geoid stands out differences between -50 cm and 50 cm with a average of 2 cm :

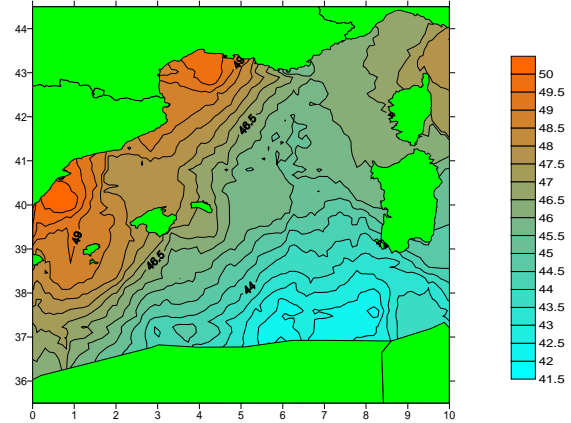


Fig.5 Altimetric mean level over the Western Mediterranean sea (in meter).

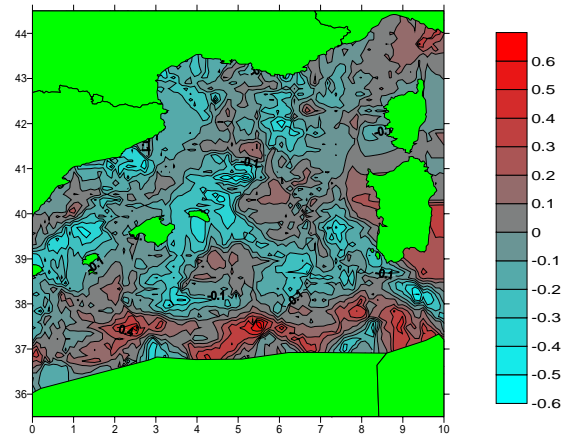


Fig.6 Differences in meters between the altimetric mean level solution and the EGM 96 geoid (in meter).

6 Comparison with tidal gauge measurements

The average Jason-1 altimetric height by cycle interpolated at the Algiers harbour is compared to the mean sea level obtained by the harmonic analysis of tidal gauge measures, obtained from analogical and automatic tide gauge installed at the same site of Algiers harbour. The periods of tidal gauge measurements analyzed are obviously equivalents to altimetric cycles.

These differences results of variation of the mean sea level at the Algiers harbour are very similar:

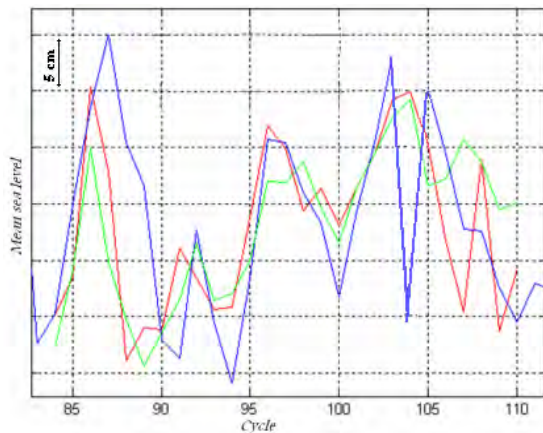


Fig.7 Comparison between the mean altimetric level Jason-1 (in blue) and the mean level obtained by harmonic analysis of the tidal data of the analogical tide gauge (in red) and the automatic tide gauge (in green).

7 Conclusion

The analysis of altimetric data Jason-1 allowed us to observe strong amplitude of variations of the average level in the Western Mediterranean basin, of the order of 20 cm, with a characteristic period of one year.

The comparison of the variation of the average height sea level at the harbour of Algiers obtained from analysis of altimetric data Jason-1 and from the harmonic analysis of tidal gauge measurements agrees well.

In terms of perspectives, the combination, on a bigger scale of time, of the data of Jason-1 with the data of the other missions of spatial altimetry such as Topex, Envisat, will allow certainly to observe with a good precision the main characteristics of the circulation in the Western Mediterranean basin and notably the seasonal swings.

References

- Aviso user handbook (1996): Merged Topex/Poseidon products (GDR-Ms). AVI-NT-02-101-CN, edition 3.3-1996.
- Aviso and Podaac - User Handbook IGDR and GDR : Jason Products. SMM-MU-M5-OP-13184-CN (AVISO), edition 2.0
- Gaspard, P., F. Ogor, Le Traon, O. Z. Zanif (1994). Estimating the sea state bias of the TOPEX/POSEIDON altimeters from crossover difference. Topex/Poseidon special issue.
- M. Haddad (2004). Détermination du géoïde en Algérie du Nord par intégration des données gravimétriques et altimétriques. Mémoire de Magister en Techniques Spatiales et Applications – CNTS (en préparation juin 2004).
- M. Haddad, S. Kahlouche, A. Rami (2004). Détermination du Géoïde Altimétrique à Partir des Données Topex/Poseidon (Cycles 365 et 366)

sur le Bassin Méditerranéen - Journées d'Études sur les Technologies Navales, 14-15 Juin 2004.

S. Kahlouche, M.I. Kariche, Benahmed S.A. Dahou (1998). Comparison between altimetric and gravimetric geoid in the south - west Mediterranean basin – in 'Geodesy on the move' - International Association of Geodesy Symposia Vol 119 [pp 281-287] – ISBN 3-540-64605- Springer Verlag Editor, 1998.

Lettre du CNES N°139 (1992). Lancement de TOPEX/POSEIDON.

R. Rummel (1993). . Satellite altimetry in geodesy and oceanography. Lecture Notes in Earth Sciences, 50, Springer-Verlag, [pp 453-466].

H. Stewart Robert (1985). Methods of satellite oceanography University of California Press. ISBN 0-520-04226-3.

Sea Surface Topography by Airborne Laser Altimetry and Offshore GPS Buoys in the Eastern Mediterranean: Comparison with JASON-1 Radar Altimeter Data and GRACE Gravity Field

Limpach, P., Geiger, A., Kahle, H.-G.

Geodesy and Geodynamics Laboratory, Institute of Geodesy and Photogrammetry, ETH Zurich, Switzerland

Abstract. Satellite radar altimetry is the basic means for global-scale sea surface height (SSH) monitoring, constituting a major source for gravity field improvements. In order to contribute to the improvement of sea level monitoring and to provide local-scale information on the short-wave structure of the marine gravity field, enhanced ground-based methods for precise SSH measurements have been developed, consisting in airborne laser altimetry, shipborne multi-antenna GPS measurements and GPS-equipped buoys. Two local survey areas were chosen in the vicinity of JASON-1 ground-tracks in the Eastern Mediterranean. The gathered SSH data could ultimately allow to contribute to the validation and calibration of radar altimeter missions.

Preliminary SSH results from airborne laser altimetry and offshore GPS surveys are presented. Furthermore comparisons with JASON-1 radar altimeter data and geoid heights from both EGM96 and GRACE-based GGM02 models are made.

Keywords. Marine geodesy, airborne laser altimetry, GPS buoys, shipborne GPS, sea surface height

1 Introduction

Enhanced ground-based methods have been developed for precise ground-truth determination of sea surface heights (SSHs), consisting in airborne laser altimetry, shipborne multi-antenna GPS measurements and GPS buoys. The SSH data provide local-scale information on the short-wave structure of the gravity field and can be used to improve local marine geoid solutions. They also contain information on local dynamic ocean topography, tides and waves, and can be used for the validation and calibration of radar altimeter missions. In addition, they provide a link between offshore radar altimeter data and tide-gauge stations.

The key area for our SSH investigations is the Eastern Mediterranean Sea, where two survey areas

were chosen around Crete and in the North Aegean Sea, respectively (Fig. 1). Differences between preliminary SSH solutions and both EGM96 (to degree/order 360) and GRACE-based GGM02 geoid models have been computed for these areas. The GGM02 model used in the comparisons is GGM02C extended to degree/order 360 using EGM96 coefficients above degree 200 (Tapley et al. 2005). The most striking feature revealed in this area by the geoid model are the extreme gradients between the central Aegean Sea and the Hellenic Trench area, which amount to 40 m along a distance of only 400 km (Fig. 1). In the Eastern Mediterranean, the differences between GGM02 and EGM96 geoid heights reveal no systematic offset, although they locally exceed 0.5 m (Fig. 2). The differences in our survey areas are around 0.3 m near Crete and 0.6 m in the North Aegean Sea.

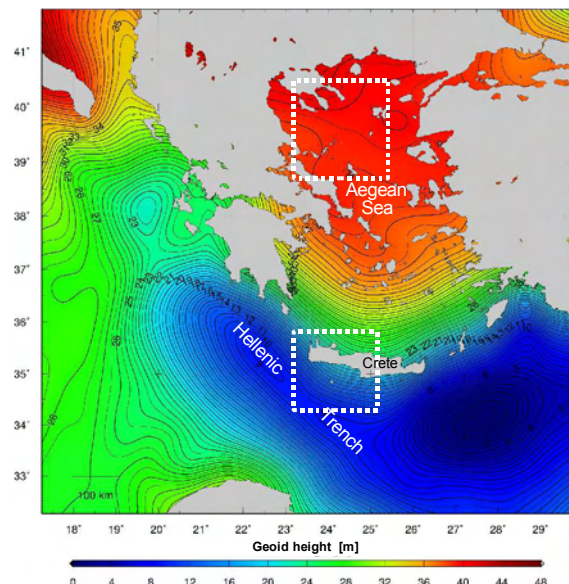


Fig. 1. Geoid heights in the Eastern Mediterranean Sea from GRACE-based GGM02 model extended to degree/order 360 using EGM96 coefficients. White rectangles: survey areas around Crete (airborne laser altimetry) and in the North Aegean Sea (shipborne/buoy GPS).

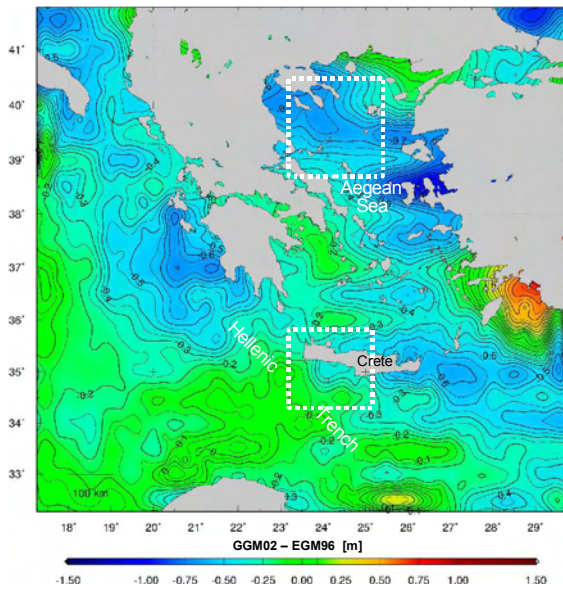


Fig. 2. Difference between GGM02 and EGM96 geoid heights in the Eastern Mediterranean Sea.

2 Airborne Laser Altimetry

2.1 Technique

Airborne laser altimetry is based on georeferencing a laser beam carried by an aircraft, yielding a 3D vector between the aircraft and the ground surface. The key elements are highly precise position and attitude of the aircraft. For this purpose, the latter was equipped with an array of four GPS antennas. One antenna is used for trajectory recovery and as a reference for moving baseline processing, where the other three antennas are the remote receivers, yielding three moving vectors used in attitude determination. As the attitude estimation is based on GPS vectors, its accuracy is dependent on the geometry of the antenna configuration. With a baseline accuracy on the order of 0.01 m and baseline lengths of about 10 m, the expected angular accuracy is 0.05° , which is sufficient for most applications.

2.2 Preliminary Field Measurement Results

A detailed airborne laser altimetry campaign was carried out around the island of Crete in the framework of the EU project GAVDOS in 2003 (Fig. 3). The aim of the latter was the establishment of a European sea-level monitoring and radar altimeter calibration site for JASON-1, ENVISAT and EURO-GLOSS (Pavlis et al. 2004). The calibration site is located on the isle of Gavdos, at a crossover of two JASON-1 ground-tracks. During the airborne campaign an area of 200x200 km adjacent to the

Hellenic Trench was covered by 24 flight lines performed at an altitude of 700 ft (210 m) with a laser profiler operated at an observation rate of 1 kHz.

In order to derive a time-independent sea surface topography from instantaneous SSHs obtained by altimetry, several corrections have to be applied, especially for tides and atmospheric effects (inverse barometer effect). In a first computation, tide corrections based on the GOT00.2 tide model have been applied. Inverse barometer corrections have been computed over the entire Mediterranean Sea using ECMWF atmospheric pressure data.

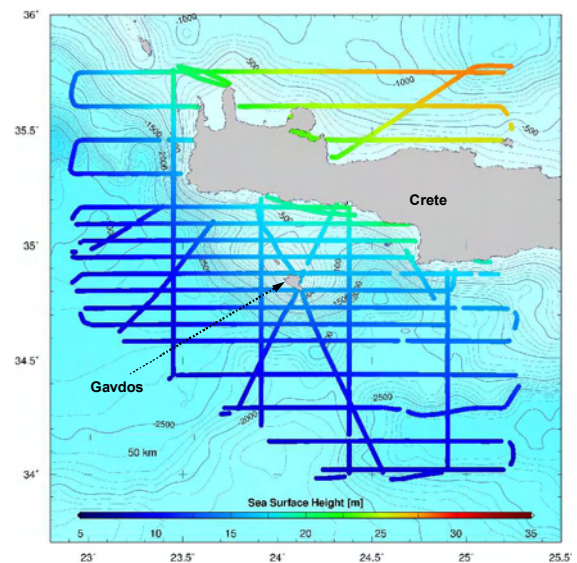


Fig. 3. Flight-tracks with color-coded SSH profiles from airborne laser altimetry around Crete.

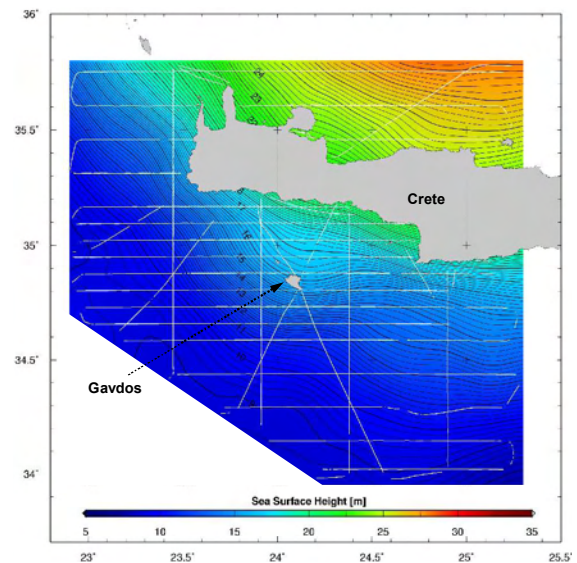


Fig. 4. Sea surface topography obtained from airborne laser altimetry SSH profiles of Fig. 3 (white lines).

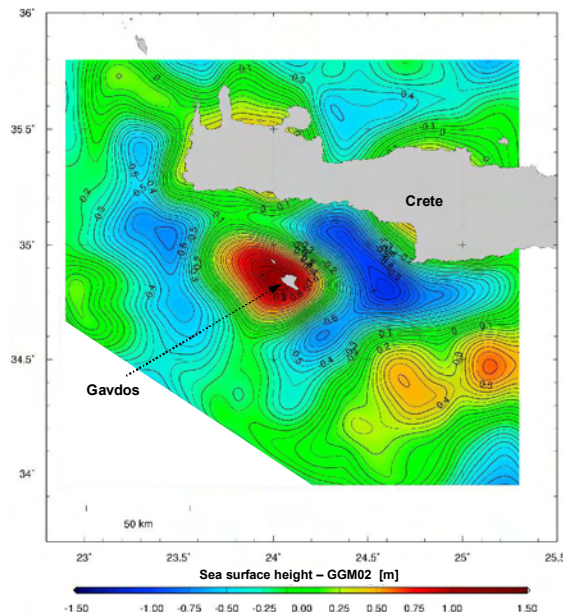
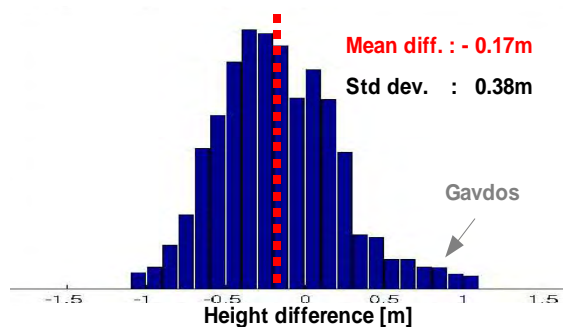
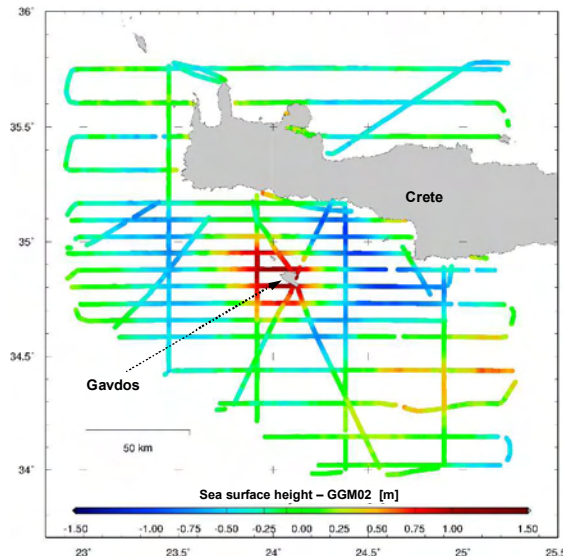
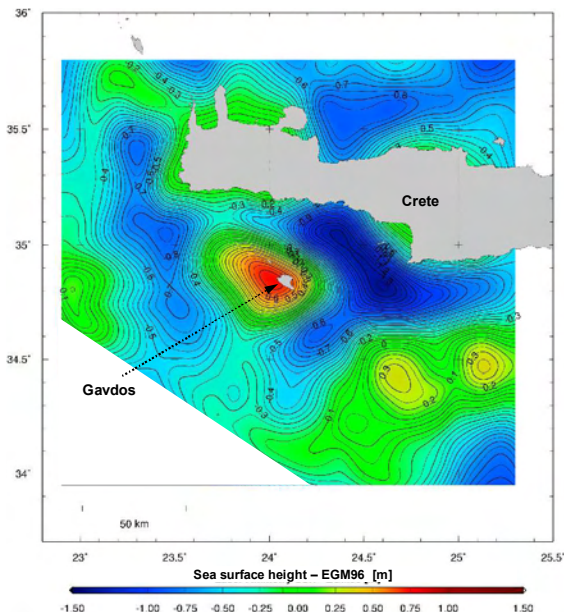
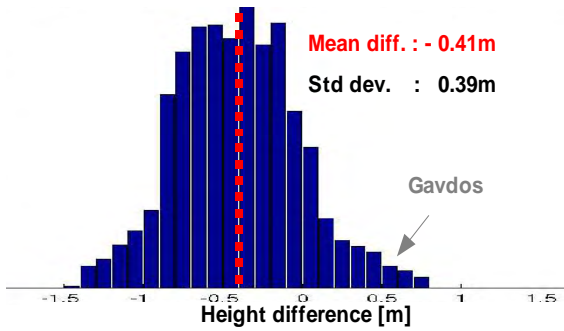
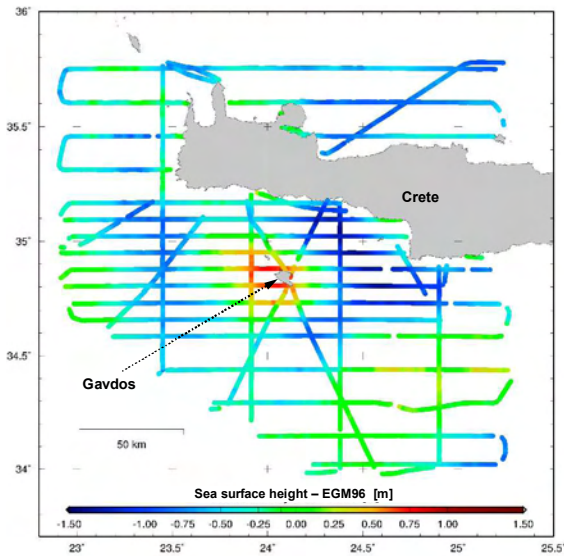


Fig. 5. Top: Height differences between SSH profiles from airborne laser altimetry and EGM96 geoid heights around Crete. **Center:** Distribution of the height differences. **Bottom:** Height differences shown as surfaces.

Fig. 6. Top: Height differences between SSH profiles from airborne laser altimetry and GRACE-based GGM02 geoid heights around Crete. **Center:** Distribution of the height differences. **Bottom:** Height differences shown as surfaces.

The SSH results shown in Fig. 3 and Fig. 4 reveal very strong gradients, with SSH decreasing from nearly 30 m in the North-East to 5 m towards the Hellenic Trench in the southern part, along a distance of 200 km only.

2.3 Comparisons Between Local SSH and Global Geoid Models

Height differences between the SSHs obtained by airborne laser altimetry and both the EGM96 (Fig. 5) and the GRACE-based GGM02 (Fig. 6) geoid heights have been computed for the survey area around Crete. The distributions of the height residuals have similar standard deviation of about 0.40 m for both geoid models. In this survey area, EGM96 is systematically higher than the sea surface (mean difference -0.41 m). The offset between the SSH and GGM02 is less pronounced (mean difference -0.17 m), meaning that the long- and mid-wave structure of the GGM02 geoid model fits the SSH better than does the EGM96. A striking anomaly is the large positive difference around the isle of Gavdos, where the sea surface is about 0.75 m above the EGM96 and 1 m above the GGM02 geoid. The highs and lows of the height residuals are too pronounced to be explained only by dynamic ocean topography effects and, therefore, seem to be related to local short-wave gravity anomalies that are not seen in both global geoid models.

3 Sea Surface Heights by GPS Buoys and Shipborne Multi-Antenna GPS

3.1 Technique

The GPS-equipped buoys deployed for ground-truth measurements of the SSH are lightweight buoys, carrying high-frequency L1/L2 GPS receivers (Fig. 7). The shell of the buoys is fabricated from microwave-transparent polycarbonate, so they can be waterproof-sealed containing the receiver, antenna and power supply.

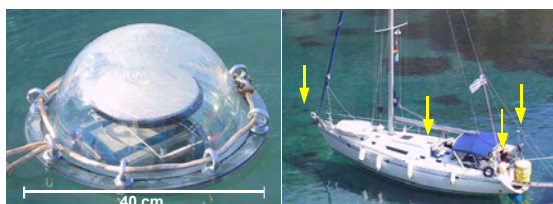


Fig. 7. **Left:** GPS-equipped buoy containing receiver, antenna and battery. **Right:** sailing boat equipped with an array of four GPS antennas (arrows) for precise position and attitude determination.

Highly-precise GPS positioning of the buoys and the boat is achieved by simultaneously operating the buoy receivers, the receivers aboard the boat (Fig. 7) and several permanent terrestrial GPS reference stations with coordinates known in the ITRF reference frame. All receivers are measuring at a sampling rate of 1 Hz. The kinematic positions of the buoys and the boat are computed through differential carrier phase processing with respect to the reference stations. In addition the multi-antenna configuration aboard the boat allows for precise attitude determination, which is of great importance for precise SSH retrieval.

3.2 Preliminary Field Measurement Results

Two campaigns for shipborne/buoy GPS SSH surveys have been carried out in the North Aegean Sea in 2004/2005, totaling more than 1000 nm of ship tracks (Fig. 8). The survey area was chosen in the vicinity of the North Aegean Trough (NAT), which is a tectonic graben-like feature characterized by a zone of deep water reaching 1500 m and trending from north-east to south-west in the North Aegean Sea. The NAT is considered to form the western continuation of the seismically active North Anatolian Fault Zone (McNeill et al. 2004).

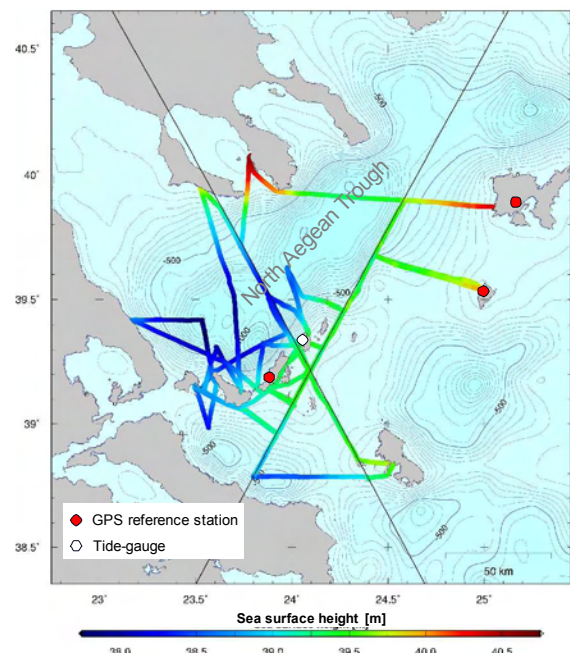


Fig. 8. GPS surveys in the North Aegean Sea. Boat-tracks with color-coded SSH profiles from combined shipborne/buoy GPS observations. Black lines: JASON-1 ground-tracks. Background: bathymetry with deep-water zone of the NAT.

In order to derive the sea surface topography from the instantaneous SSHs, the same procedure as described in Chap. 2.2 has been applied. In addition, the local tidal effects have been determined by using own tide gauges installed in the survey area.

The SSH results (Fig. 8) reveal that the bathymetric low of the NAT is associated with a distinct depression of the SSH which reaches a minimum of 37.5 m above the WGS84 ellipsoid, while the SSH in the surrounding area is more than 39 m and reaches even more than 40.5 m towards the north of the survey area.

3.3 Comparisons Between Local SSH and Global Geoid Models

Height differences between the SSHs obtained by shipborne/buoy GPS measurements and both the

EGM96 (Fig. 9) and the GRACE-based GGM02 (Fig. 10) geoid heights have been computed for the survey area in the North Aegean Sea.

While EGM96 is systematically higher than the sea surface (mean difference -0.75 m), the offset between the SSH and GGM02 is less pronounced (mean difference -0.19 m), which means that the long-wave structure of GGM02 better fits the sea surface. A striking anomaly is the large negative difference over the North Aegean Trough, where the sea surface is more than 1.5 m below EGM96 and 1 m below GGM02. This distinct low of the height residuals can be considered as being too pronounced to be explicable only by dynamic ocean topography effects and seems, therefore, to be related to a local short-wave gravity anomaly that is not detected by both global geoid models.

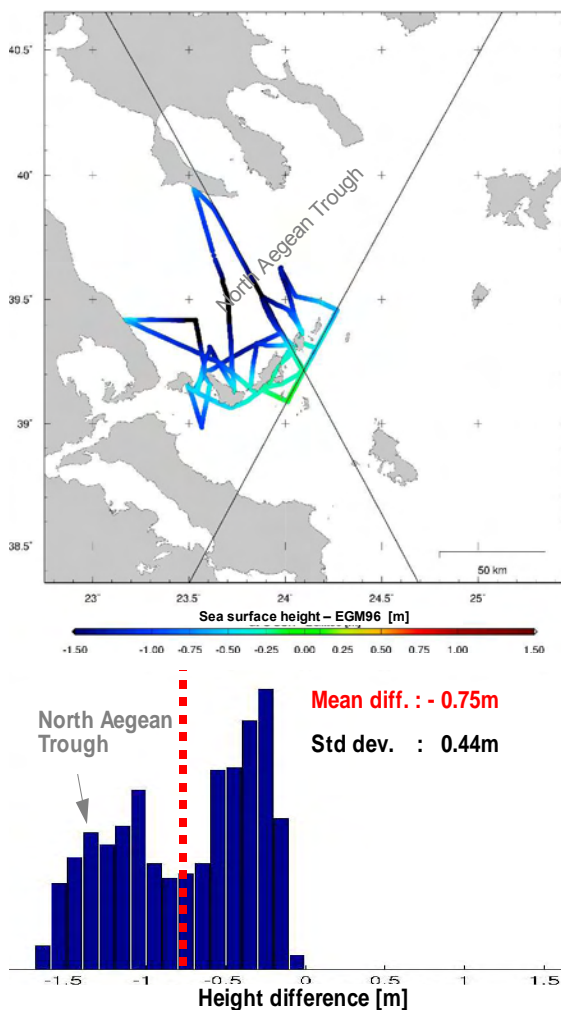


Fig. 9. Top: Height differences between SSH profiles from shipborne/buoy GPS data and EGM96 geoid heights. **Bottom:** Distribution of the height residuals.

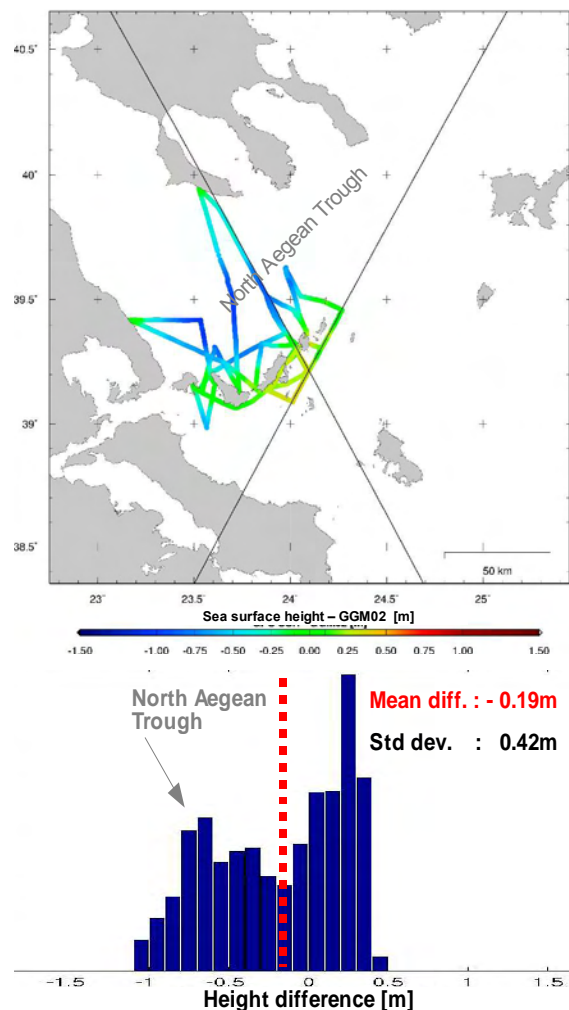


Fig. 10. Top: Height differences between SSH profiles from shipborne/buoy GPS data and GGM02 geoid heights. **Bottom:** Distribution of the height residuals.

3.4 Comparison Between JASON-1 and Ground-Truth GPS Data

For calibration and validation purposes of radar altimeter missions, the survey area has been chosen in the vicinity of JASON-1 ground-tracks. Dedicated buoy measurements were performed along these tracks, including deployments with direct JASON-1 cross-overs, which provide precise ground-truth SSH information during the overflight.

First comparisons between JASON-1 radar altimeter SSH data and the preliminary results of combined in situ shipborne and buoy GPS data have been successfully performed. Similar tide corrections have been previously applied to both datasets, as well as a cross-track correction to account for the horizontal offset between the radar altimeter ground-points and the GPS profiles. The observed height differences between the GPS buoy data and JASON-1 data varied between 0.10 and 0.12 m on six overflights. These values are in accordance with NASA/CNES results obtained at calibration sites.

An example of an encounter situated directly above the NAT is shown in Fig. 11. The mean height difference along this profile is 0.142 ± 0.042 m standard deviation, whereas the maximum and minimum height difference reached 0.224 m and 0.085 m, respectively. This significant variation of the height differences along the profile seems to be geographically-correlated and is most likely due to the effect of the different spatial resolutions of the two methods amplified in regions with strong sea surface height gradients and strong gradient variations.

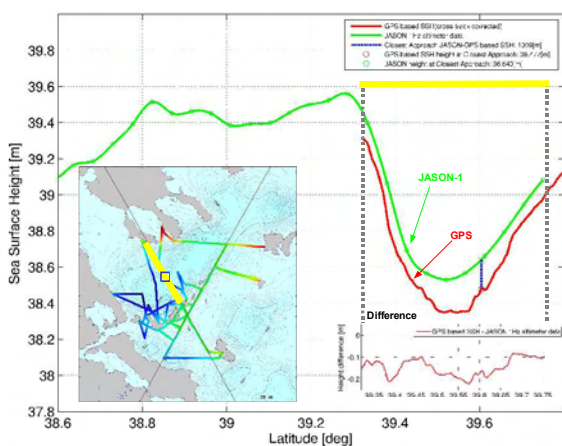


Fig. 11. Comparison between a JASON-1 SSH profile (green line) and the results of combined in situ shipborne/buoy GPS data (red line). The encounter (closest approach) is marked by the dashed blue line on the graph and the blue square on the map.

4 Conclusions

The airborne laser altimetry and shipborne/buoy GPS methods for precise SSH determination in local areas have been successfully developed. First SSH results are extremely promising in terms of accuracy and repeatability, leading to a local high resolution sea surface topography solution at cm level.

Comparisons with JASON-1 radar altimeter data along dedicated profiles showed encouraging results but revealed geographically correlated variations of the height difference between 0.1 and 0.2 m in areas with strong sea surface height gradients.

Comparisons between EGM96 and GGM02 global geoid models showed considerable local differences of up to 0.7 m in the Eastern Mediterranean. When comparing the SSHs to the EGM96 and GGM02 geoid heights, a significant improvement of the GRACE-based GGM02 model in the long- and mid-wave structure was observed, leading to a reduction of the mean difference. Comparison with the SSH's also revealed local anomalies in the vicinity of the Hellenic Trench and the North Aegean Trough, reaching more than 1 m in these regions of high geodynamic activity. These features can be considered as being too pronounced to be explicable only by dynamic ocean topography effects. Therefore they can be considered as indications for distinct mass anomalies causing local gravity anomalies in the high frequency domain that are not detected by the global geoid models.

References

- McNeill LC, Mille A, Minshull TA, Bull JM, Kenyon NH, Ivanov M (2004) Extension of the North Anatolian Fault into the North Aegean Trough: Evidence for transtension, strain partitioning and analogues for Sea of Marmara basin models. *Tectonics*, Vol. 23, TC2016, 2004
- Pavlis EC, Mertikas SP and the GAVDOS-Team (2004) The GAVDOS Mean Sea Level and Altimeter Calibration Facility: Results for Jason1", 3rd Jason special issue, *Marine Geodesy*, Vol. 27, No. 3-4, pp. 631-655
- Rio MH (2004) A Mean Dynamic Topography of the Mediterranean Sea Estimated from the Combined use of Altimetry, In-Situ Measurements and a General Circulation Model. *Geophysical Research Letter* Vol. 6, 03626.
- Tapley B, Ries J, Bettadpur S, Chambers D, Cheng M, Condi F, Gunter B, Kang Z, Nagel P, Pastor R, Pekker T, Poole S, Wang F (2005) GGM02 – An Improved Earth Gravity Field Model from GRACE. *J Geod* DOI 10.1007/s00190-005-0480-z
- Tziavos IN, Andritsanos VD (1999). Recent Geoid Computations for the Hellenic Area. *Phys. Chem. Earth (A)*, Vol-24, No. 1, pp. 91-96.
- Tziavos IN, Vergos GS, Kotzev V, Pashova L (2005) Mean sea level and sea surface topography studies in the Black Sea and the Aegean. *International Association of Geodesy Symposia*, Vol. 129, Jekeli C, Bastos L, Fernandes J (eds.), Gravity Geoid and Space Missions 2004, Springer-Verlag Berlin Heidelberg, pp. 254-259

Downward continuation and geoid determination in Mongolia from airborne and surface gravimetry and SRTM topography

Rene Forsberg, A. Olesen

Danish National Space Center, Juliane Maries Vej 30, DK-2100 Copenhagen Ø, Denmark, rf@dpsc.dk

D. Munkhtsetseg, A. Amarzaya

Administration for Land Affairs, Geodesy and Cartography, Ulaanbaatar, Mongolia.

Abstract. In this paper we outline the principles of downward continuation and geoid determination in Mongolia, based on the 2004-5 airborne gravity surveys, surface gravimetry from various sources, and detailed digital terrain models from satellite radar interferometry (SRTM). A remove-restore method is used for terrain and global spherical harmonic reference models, with the residual gravity field signal downward continued by least-squares collocation, and the geoid and quasi-geoid computed by spherical Fourier methods. For reference field a GRACE and EGM96 combination field is used, and the geoid assessed using a subset of available GPS-leveling data, indicating that recent GRACE fields still have detectable problems in the harmonic wavelength band 50-100. The gravimetric geoid model computed refers to a global vertical datum; the Kronstadt Baltic Sea level data used in Mongolia shows a difference of more than one meter to the global datum, and therefore it is essential to fit the gravimetric geoid to local height data to obtain an operational geoid model for GPS use.

Keywords. Airborne gravimetry, geoid, Mongolia

1 Introduction

The Danish National Space Center, in cooperation with the Mongolian Administration of Land Affairs, Geodesy and Cartography (ALAGaC), MonMap (a private Mongolian survey company), US National Geospatial-Intelligence Agency (NGA) and the University of Bergen, Norway, carried out a complete airborne survey of Mongolia in 2004-5.

The primary purpose of the airborne survey was to provide data for global earth gravity models (EGM07). An additional purpose was to provide data for a new geoid of Mongolia, as part of the ongoing GPS modernization of the geodetic infrastructure; training of Mongolian scientists in geoid processing was part of this process.

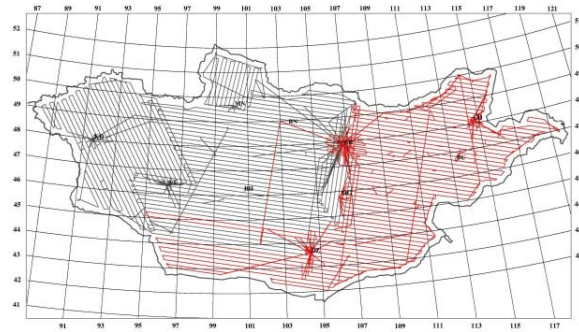


Fig. 1. Flight tracks of the airborne gravity survey: Western Mongolia fall 2004 (black), and Eastern Mongolia fall 2005 (red).



Fig. 2. Cessna Caravan aircraft used for the 2005 survey. The land gravimeter seen is used to tie to the Mongolian national gravity net, based on Russian absolute gravity measurements.

The airborne gravity surveys (Fig. 1) were carried out using an Air Greenland Twin Otter in 2004 and a Cessna Caravan aircraft in 2005 (Fig. 2). A total of 420 flight-hours were flown at a track spacing of 10 nautical miles. Because of the rough topography of Mongolia (Fig. 4), flight elevations of individual flight lines varied between 2100 m and 4800 m, necessitating a formal downward continuation.

All gravity measurements were made using a Lacoste and Romberg S-type gravimeter running the Ultrasys control system, with a number of GPS receivers onboard the aircraft and on ground providing the necessary kinematic positioning. More

details of the airborne gravity survey method are given in Olesen and Forsberg (this volume).

The estimated r.m.s. accuracy of the airborne gravity free-air anomaly data, as judged from cross-over adjustments (cf. Table 1), is 2.2 and 2.4 mGal for 2004 and 2005, respectively. This indicates a slightly better performance over the mountains with the Twin Otter aircraft compared to the Cessna Caravan. No cross-over adjustment is performed in the final data set, as such process may be a source of aliasing, and is not necessary due to excellent stability of the used LCR gravimeter (Olesen, 2003).

Taking account the harmonic continuation effect, continuing the airborne data to a common level of 3000 m, as outlined below, the r.m.s. error estimate from the cross-over analysis decreases to an average value of 2.2 mGal for the entire survey. With the inherent filtering applied in the airborne gravity processing, the along-track resolution is around 6 km, depending on the track (ground speeds varied significantly on tracks as a function of wind).

Figure 3 shows the airborne gravity anomalies, and Figure 4 a digital elevation model of Mongolia from SRTM data. The correlation of free-air anomalies to topography is evident.

Table 1. Statistics of the cross-over errors of the airborne gravity survey of Mongolia, without downw. cont. Unit mGal.

Year	No of x-ings	Max diff.	RMS diff.	RMS error
2004	201	9.5	3.1	2.2
2005	206	10.0	3.4	2.4

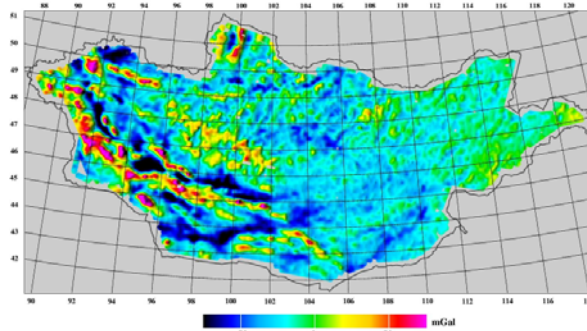


Fig. 3. Free-air anomalies at flight altitude from airborne gravity survey. Colour scale is from -75 to 75 mGal.

2 Downward continuation of airborne data and merging with surface data

The harmonic downward continuation of airborne gravity data is a classical unstable operation, making the collocation approach or stabilized Fourier methods the method of choice for treating this problem (Forsberg, 2002).

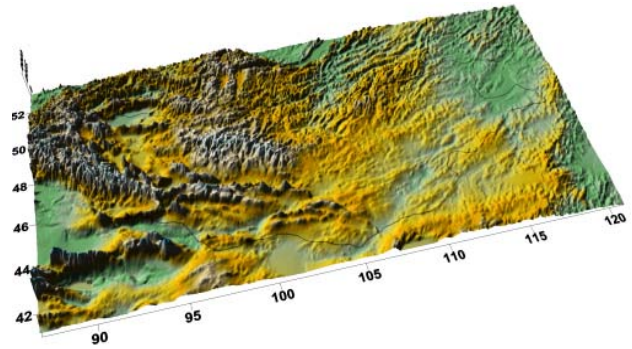


Fig. 4. Topography of Mongolia from SRTM data. The elevations range from 4500 m in Western Mongolia to 600 m in the easternmost plains.

Downward continuation is essentially a high-pass filtering operation, which will amplify short-wavelength noise in the airborne data. For geoid determination, this is offset by the gravity to geoid low-pass filtering operation; therefore, airborne gravity data are well-suited for geoid determination. Formulations for use of airborne gravity in geoid boundary value problems have been formulated by Li (2000); for more general studies on the downward continuation problem see e.g. Keller and Hirsch (1992).

In the case of Mongolia, a relatively dense surface gravity data set exists, albeit of unknown accuracy and uncertain reference system. This data set, provided by GETECH for use in the geoid determination, was given as 5' gridded values of Bouguer and free-air anomalies, together with a file of positions of the points used for generating the grid.

To utilise the GETECH data, the grid values were interpolated back to the given positions, a process which adds noise to the data. The location of the surface data is shown in Figure 5, together with a sparse ALAGaC gravity reference network data set. The surface data are especially useful for augmenting the airborne gravity data along the borders, because no flights were allowed within 25 km of the borders,

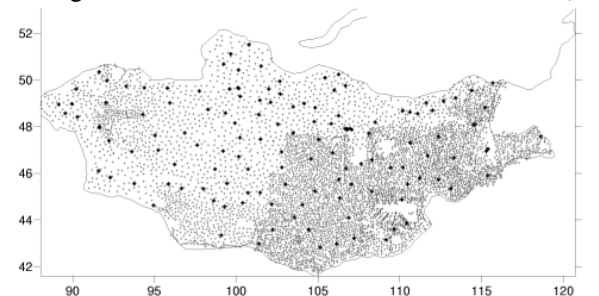


Fig. 5. Location of surface gravimetry data in Mongolia. The thicker markings are the ALAGaC reference network points.

Because of the mix of airborne and surface data, and the varying flight altitudes, we use the method of least squares collocation for the downward continuation. We thus generate a 3' surface free-air gravity grid from a combination of all data, prior to the geoid computation.

In least squares-collocation the gravity anomaly signal “s” at a ground grid point is estimated from a vector “x” containing all available surface and airborne data by

$$\hat{s} = C_{sx}[C_{xx} + D]^{-1} \quad (1)$$

Covariances C_{xx} and C_{sx} are taken from a full, self-consistent spatial covariance model, and D is the (diagonal) noise matrix. Because the gravity field of the earth is known to follow Kaulas rule, it is important to select covariance models which have an implied power spectral density decay in accordance with this. An example of such a self-consistent covariance model is the spherical earth Tscherning-Rapp model (Tscherning and Rapp, 1974), and the analogous (and simpler) planar logarithmic covariance model (Forsberg, 1987). In the latter model, the gravity covariance between gravity anomalies at two altitudes is of form

$$C(\Delta g^{h_1}, \Delta g^{h_2}) = - \sum_k \alpha_k \log(D_k + \sqrt{s^2 + (D_k + h_1 + h_2)^2}) \quad (2)$$

where α_k are weight factors combining terms relating to depth value terms ($D_k = D + kT$), with the “free parameters” D and T taking the role analogous to the Bjerhammar sphere depth of spherical collocation and a “compensating depth” attenuation factor. The attenuation of long wavelengths in the model are necessary when a spherical harmonic reference model is used.

All processing has been done using the remove-restore method, where the gravity anomalies have been split into three terms

$$\Delta g = \Delta g_1 + \Delta g_2 + \Delta g_3 \quad (3)$$

where the first term is a spherical harmonic reference field, the second term the terrain effects, and the third part the residual gravity.

For the spherical harmonic reference field, a composite model of the GGM02S satellite-only field from GRACE (Tapley et al., 2004) and EGM96 (Lemoine et al., 1996) has been used. The GGM02S and EGM96 have been merged, so that GRACE data are used for harmonic degrees below 90, and EGM96

for harmonic degrees above 100, with a linear transition in between.

The composite model, complete to harmonic degree $N = 360$, gives the geopotential V as a three-dimensional expansion

$$V(r, \phi, \lambda) = \frac{GM}{R} \sum_{n=2}^N \left(\frac{R}{r}\right)^n \times \sum_{m=0}^n (C_{nm} \cos m\lambda + S_{nm} \sin m\lambda) P_{nm}(\sin \phi) \quad (4)$$

To properly take into account the height dependency of the spherical harmonics, a “sandwich grid” grid has been used. Here gravity anomalies Δg_1 (and height anomalies ζ_1) are evaluated at grids at two elevations (0 and 4 km), from which both airborne and surface data are interpolated linearly with respect to both latitude, longitude and height. This ensures a rapid and consistent evaluation of the reference field effects.

The use of gravity terrain effects in the downward continuation process has significant advantages: It will – if properly applied – reduce the short-wavelength information in the gravity data, and thus make the problem more stable; it will also diminish the topographic aliasing, especially important for surface gravity data, which typically do not have a random distribution relative to the topography (usually there is a relative abundance of gravity data collected in valleys).

In Mongolia SRTM elevation data, averaged to 15” resolution, have been used to compute RTM terrain effects Δg_2 on all surface and airborne data. The RTM terrain effects (Forsberg, 1984) takes into account topography relative to a mean height surface. This surface is produced from the SRTM data by low-pass filtering (Fig. 6). We have selected a resolution of 0.8° for the mean height surface, representing a trade-off between the smaller residuals of a more smooth reference topography, and the errors in the higher degrees of EGM96 (a too smooth mean surface implies in principle that terrain effects, already part of EGM96, are removed twice).

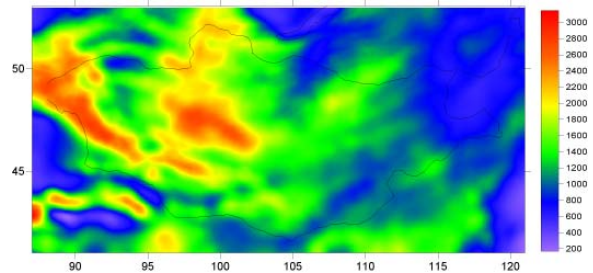


Fig. 6. Mean height surface of Mongolia used for RTM terrain reduction. Colour scale ranges from 200 to 3100 m.

The RTM terrain effects are computed by prism integration using the TC program (Forsberg, 1984), assuming a constant density of 2.67 g/cm³ for all topography. For airborne gravity data one important aspect must be taken into account: because airborne gravity data are inherently along-track *filtered*, the terrain effects computed at altitude must be filtered by the same filter algorithm as used in the airborne processing.

Table 2 shows the results for the reduction of the airborne and surface data for the GRACE/EGM96 reference field and the RTM terrain effects. It is seen that the airborne data are nicely smoothed by the composite GRACE reference field and the terrain reduction. The resulting bias of only 0.1 mGal shows the essentially bias-free nature of the airborne data.

For the GETECH surface data, biases are evident in the data, likely coming from an unknown reference system. Assuming data to be given in the conventional Russian Potsdam/Bessel ellipsoid normal gravity system do not explain the bias seen. The GETECH data have therefore been fitted to the airborne data (and GRACE) by simply adding a constant to the data.

Table 2. Statistics of the gravity data reductions. Unit mGal.

Data	Mean	Std.dev.
Airborne gravity data	-17.1	25.9
Airborne minus ref. field	0.2	19.5
Airborne minus ref. and RTM	0.1	11.9
GETECH interpolated surface gravimetry data	9.0	19.0
Surface minus ref. and RTM	12.9	11.4

For the final collocation run with the planar logarithmic model (2), D and T values were fitted to the airborne data, and the downward continuation run blockwise in 1° x 1° blocks expanded with a 0.6° x 0.8° border around the block, securing data overlap between blocks. Standard errors were assigned to data as follows: airborne gravity 2 mGal, GETECH surface data 3 mgal, and 1 mGal for ALAGaC data.

Two basic collocation 3' reduced free-air anomaly grids at the topographic surface were produced: one using all data, and a second using airborne data only, to study the effect of adding the surface data to the geoid. In addition, the airborne gravity alone were continued to a common height level grid (3 km), in order to allow a consistent cross-over error analysis.

3 Gravimetric geoid computation

Using the reduced gravity data, gravimetric geoid models were computed by spherical FFT methods.

In the used multi-band FFT method (Forsberg and Sideris, 1993), the fundamental Stokes' formula is transformed into a spherical convolution in latitude and longitude (φ, λ) for a given reference parallel φ_{ref} , and by utilization of a number of bands a virtually exact convolution expression may be obtained by a suitable linear combination of the bands. For each band the convolution expressions are evaluated by

$$\begin{aligned} \zeta_3 &= S_{\text{ref}}(\Delta\varphi, \Delta\lambda) * [\Delta g_3(\varphi, \lambda) \sin\varphi] \\ &= F^{-1}[F(S_{\text{ref}})F(\Delta g_3 \sin\varphi)] \end{aligned} \quad (5)$$

where S_{ref} is a (modified) Stokes' kernel function, and * and F are the two-dimensional convolution and Fourier transform, respectively.

In the actual implementation of the method, the data are gridded by least-squares collocation, and a 100% zero padding is used to limit the periodicity errors of FFT.

A modified Wong-Gore Stokes kernel is used, where only spherical harmonics above degree 50 are allowed to modify the underlying GRACE reference field. To avoid edge effects, the Wong-Gore kernel modification is linearly blended from degree 40 to 50, for details see Forsberg and Featherstone (1998). The use of the degree 50 modification is based on test runs, looking for the lowest residual error in GPS-leveling comparisons, and is consistent with results from other regions (Scandinavia) showing that the GRACE fields might have relatively large systematic (striping?) errors above degree 50.

After the FFT transformation to the (residual) quasigeoid, the geoid terrain effects and the spherical harmonic terrain effects, computed at the level of the topography, are restored to give the final geoid. The terrain effects on the geoid were computed by a separate FFT computation, and are shown in Fig. 7.

The final gravimetric geoid model, referring to an implicit global vertical datum, is shown in Fig. 8.

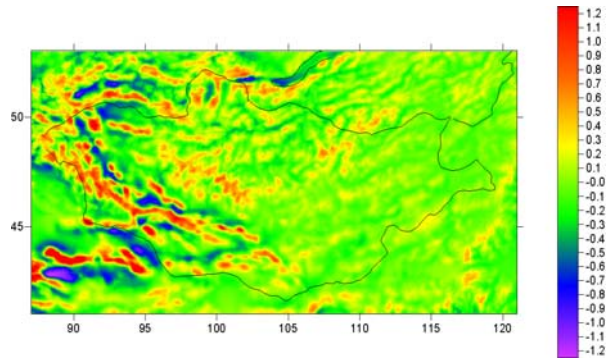


Fig. 7. Terrain restore effects on the geoid. Colour scale ranges from -1.2 to 1.2 meter.

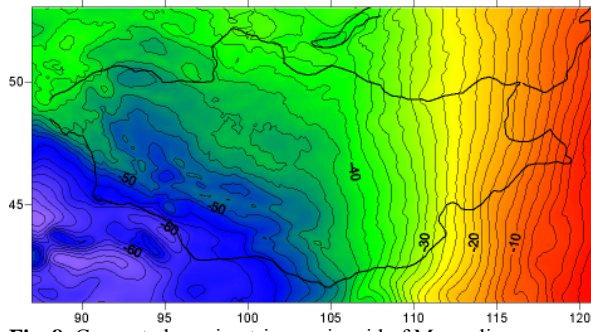


Fig. 8. Computed gravimetric quasigeoid of Mongolia.

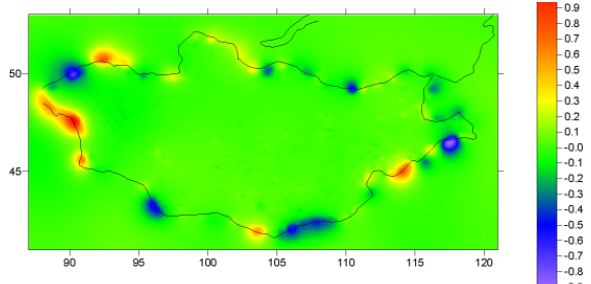


Fig. 9. Difference between geoids computed with and without the surface data. Colour scale ranges from -0.9 to 0.9 m.

The geoid models are, as earlier mentioned, computed both with and without the surface data. Figure 9 shows the difference between the two runs. As it can be seen, the impact of the surface data in the inner of Mongolia is small, but it makes a big difference to include the surface data in the border zone.

4 Geoid fit to GPS and levelling

Gravimetric geoid models need to be fitted to local GPS-leveling data for operational GPS height determination use, in order to account for datum differences, residual long-wavelength geoid errors, as well as systematic errors in the leveling.

In Mongolia the basic height system is the Kronstadt datum, i.e. tied to the Baltic Sea level through the Russian leveling network. The first order leveling network is shown in Fig. 10. Recently a new national fundamental GPS net (MONREF97), tied to ITRF and processed by Bernese software, has been established in a Swedish-Mongolian cooperation.

The MONREF97 network has been used to tie in leveling points by GPS. Quasi-geoid heights can be derived at these leveled GPS points by

$$\zeta_{\text{GPS}} = h - H^* \quad (6)$$

where h is the ellipsoidal height and H^* the normal height.

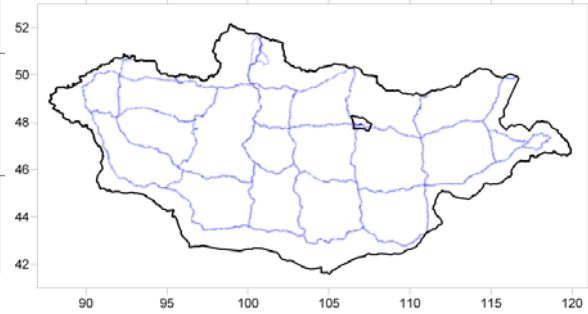


Fig. 10. First order Mongolian levelling network.

To obtain a GPS-fitted geoid model, the difference between the gravimetric geoid ζ and the quasigeoid heights from GPS-leveling is modeled by a trend surface and a stochastic signal ε '

$$\varepsilon = \zeta - \zeta_{\text{GPS}} =$$

$$\cos\phi \cos\lambda a_1 + \cos\phi \sin\lambda a_2 + \sin\phi a_3 + R a_4 + \varepsilon' \quad (7)$$

and then subtracted from the gravimetric quasigeoid, to obtain the final GPS-leveling consistent “geoid surface” in the Kronstadt system.

In eq. (7) a_1 to a_4 are empirical parameters, R the earth radius, and ε' is the residual error, modeled by least-squares collocation. A second-order Markov covariance function is used with 80 km correlation length and 5 cm apriori noise, to secure some smoothing of the leveling corrections to the geoid. A total of 58 points have been used for the fit, and results are shown in Table 3 and in Figure 11.

Table 3. Statistics of the quasigeoid comparison to GPS (before fit). Unit meter.

58 GPS levelling points	Mean	Std.dev.
GPS quasigeoid ($h - H$)	-39.57	8.50
Quasigeoid difference $\zeta - \zeta_{\text{GPS}}$	1.14	0.20

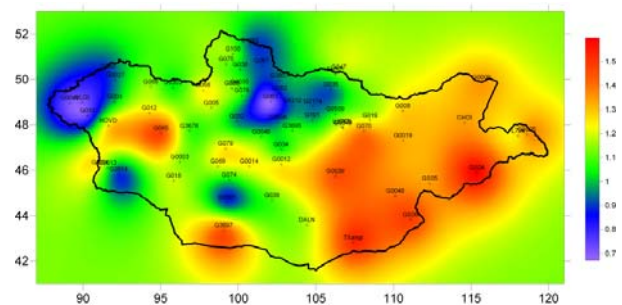


Fig. 11. Geoid fit residuals ε' , with location of GPS points. Colour scale is from -0.7 to 1.5 meter.

It is seen from Table 3 that the Kronstadt system in Mongolia is apparently offset from the implicit

global vertical system of the gravimetric geoid computation by 1.14 m. This difference is likely due to offsets in the Kronstadt W_0 -value from the global average, as well as accumulated leveling errors and quasi-geoid errors.

It is seen that a fairly large standard deviation of 20 cm exists in the r.m.s. GPS-leveling comparison. This is likely mostly due to errors in the leveling, where some loops are known to have large misclosures.

The overall r.m.s. of the fitted geoid at the control points is 6.8 cm, and comparisons to local, independent GPS data indicate that the new GPS-fitted quasigeoid is accurate to 10 cm over much of Mongolia. The accuracy estimates of the gravimetric quasigeoid, computed by a formal least squares estimation on a manageable subset of the available data, have similarly indicated formal geoid errors in the interior of Mongolia at the 10 cm level.

5 Conclusions

A major airborne gravity survey has 2004-5 covered Mongolia at 10 n.m. spacing. The overall survey accuracy, without using any internal cross-over adjustment are estimated at 2.2 mGal. The airborne gravity results have essentially no bias relative to GRACE gravity, confirming the bias-free performance of aerogravity even in the rugged topography across western Mongolia (Fig. 12).

We have in the paper outlined the procedure of downward continuation by least-squares collocation and geoid computation by spherical FFT and GRACE. This method yields a geoid model with a likely accuracy of 10 cm in the inner parts of Mongolia. The subsequent fitting of the geoid to GPS/leveling are done at the 5 cm level, with some residual errors likely due to levelling and GPS errors. The resulting geoid – MonGeoid2006 – will be used as a reference for the future modernization of the Mongolian geodetic infrastructure, and updated as new levelling and GPS data becomes available.



Fig. 12. Flight over mountains of northern Mongolia, 2004.

Acknowledgements

We thank M. Saandar, MonMap Engineering, for participation in the airborne gravity survey operations and the provision of the GETECH surface gravity data for the geoid computation. Economic support for the Mongolian airborne gravity project was proved by NGA, USA.

References

- Forsberg, R.: A Study of Terrain Reductions, Density Anomalies and Geophysical Inversion Methods in Gravity Field Modelling. *Reports of the Department of Geodetic Science and Surveying, No. 355*, The Ohio State University, Columbus, Ohio, 1984.
- Forsberg, R.: Downward continuation of airborne gravity – an Arctic case story. *Proceedings of the International Gravity and Geoid Commission Meeting, Thessaloniki*, 2002.
- Forsberg, R.: A new covariance model for inertial gravimetry and gradiometry. *Journal of Geophysical Research*, vol. 92, pp. 1305-1310, 1987.
- Forsberg, R., W Featherstone: Geoids and Cap Sizes. In: *Geodesy on the Move - gravity, geoid, geodynamics and Antarctica, Proceedings IAG scientific assembly, Rio de Janeiro, sept 3-9 1997, Forsberg, Feissel and Dietrich (eds.), IAG symposia 119, pp. 194-200*, Springer Verlag, Berlin, 1998.
- Forsberg, R., M. G. Sideris: Geoid computations by the multi-band spherical FFT approach. *Manuscripta Geodaetica*, 18, pp. 82-90, 1993.
- Olesen, A.V., R. Forsberg: Airborne Scalar Gravimetry for Regional Gravity Field Mapping and Geoid Determination. *This volume*.
- Keller, W and M. Hirsch: Downward continuation versus free-air reduction in airborne gravimetry. In: *Geodesy and Physics of the Earth, IAG proceedings 112*, 260-266, Springer Verlag, 1992.
- Lemoine, F.G., D.Smith, R.Smith, L.Kunz, E.Pavlis, N.Pavlis, S.Klosko, D.Chinn, M.Torrence, R.Williamson, C.Cox, K.Rachlin, Y.Wang, S.Kenyon, R.Salman, R.Trimmer, R.Rapp and S.Nerem: The development of the NASA GSFC and DMA joint geopotential model. *Proc. Symp. on Gravity, Geoid and Marine Geodesy*, Tokyo, pp. 461-469, 1996.
- Li, Y.: Airborne Gravimetry for Geoid Determination. *Ph.d. thesis*, 161 pp., Department of Geomatics Engineering, University of Calgary, 2000.
- Olesen, A.V: Improved Airborne Scalar Gravimetry for Regional Gravity Field Mapping and Geoid Determination.. *Technical Report no 24, Kort og MatrikelsStyrelsen*, Copenhagen 2003.
- Tapley, B D, S Bettadpur, M Watkins, C Reigber: The gravity recovery and climate experiment: Mission overview and early results. *Geoph. Res. Lett.*, 31, L09607, doi:10.1029/2004GL019920, 2004.
- Tscherning, C. C. and R. H. Rapp: Closed covariance expressions for gravity anomalies, geoid undulations and deflections of the vertical implied by degree-variance models. *Rep. 208, Department of Geodetic Science, Ohio State University*, Columbus, 1974.

Airborne Gravity Gradiometry For Exploration Geophysics – The First 5 Years

K. Zuidweg, G.R. Mumaw

Bell Geospace Ltd, Unit 5A Crombie Lodge, ASTP Bridge of Don, AB22 8GU Aberdeen, United Kingdom.

Abstract. Gravity Gradiometry for exploration geophysics became reality after declassification of the Bell Aerospace Full Tensor Gradiometer system in the mid 1990's. Initially the system was deployed seaborne for hydrocarbon exploration. Airborne applications ensued after improvements in acquisition procedures and data processing.

Airborne surveys are typically flown with a Cessna Grand Caravan. - Post processing accuracy levels are in the order of 3 E over wavelengths of 400 meters.

Data processing is a five stage process. These include: high rate software to remove self gradient effects, terrain correction, a stage with redundancies and correlation to filter out obvious spikes and shifts, manual levelling to take out drift effects and "Full Tensor Processing" to remove uncorrelated noise in the tensor components.

Slowing down the platform improves spatial resolution. This is currently observed with an instrument operating on a Zeppelin NT airship for De Beers exploration in Botswana. The results of this method are comparable to high resolution ground gravity offering less than 2 E over 100 meter wavelengths detectability.

Keywords. Airborne Gravity Gradiometry, Airship Gravity Gradiometry, Exploration Geophysics.

1 Introduction

The Full Tensor Gravity Gradiometer (FTG) system was developed in the 70's by Bell Aerospace (now Lockheed Martin) to aid navigation in stealth mode for US submarines. Bell Geospace commercialized the technology for offshore hydrocarbon exploration post military declassification in the mid 1990's. In 2001 the system was successfully tested on a single engine aircraft. This new Airborne FTG system was quickly adopted by the minerals industry as a much anticipated novel exploration tool. This paper describes the current state of the art after five years of experience and gives a with few notes

of what is expected as further developments in the near future.

2 Technology

The 3D FTG system contains three Gravity Gradiometry Instruments (GGI's), each consisting of two opposing pairs of accelerometers arranged on a spinning disc with measurement direction in the spin direction. Following logic cf. Rummel (1986) pp. 324-339, subtracting opposing accelerometer readings cancels out disc acceleration and in first-order approximation the following relation remains:

$$da_i = V_{ij} dx_j \quad (1)$$

where da_i is the acceleration difference vector, V_{ij} the gravity gradient tensor and dx_j the coordinate difference between the two accelerometers. In case of an horizontal disk, defining a local triad with the z direction vertical we can set

$$dx = D \cos \alpha \quad (2a)$$

$$dy = D \sin \alpha \quad (2b)$$

$$dz = 0 \quad (2c)$$

where α is the angle of x axis with the line connecting the two accelerometers and D is the distance between the accelerometers. It then follows that for the accelerometer difference da on an horizontal disc, rotating with angular speed ω at time t that

$$da = \frac{1}{2}D(V_{yy}-V_{xx})\sin 2\omega t + V_{xy} \cos 2\omega t. \quad (3)$$

Similarly for a vertical disk in the yz-plane it can be shown that

$$da = \frac{1}{2}D(V_{zz}-V_{yy})\sin 2\omega t + V_{yz} \cos 2\omega t. \quad (4)$$

And a similar relation holds for a third perpendicular vertical disk in the xz-plane, so that three disks resolve all six tensor components.

In reality the three GGI's in the FTG instrument are arranged such that their axes are mutually perpen-

dicular, aligned 35 degrees with the vertical and are 120 degrees apart. The assembly of GGI's, called caroussel, is rotated at a rate of 0.5 Herz. It can be shown that this configuration resolves the six tensor components in a similar way. The configuration in fact measures V_{xx} , V_{yy} and V_{zz} independently and the consistency check offered by the Laplace Equation is one of the advantages of the Full Tensor system.

3 Operation

For fixed wing airborne surveys the FTG instrument is mounted in a Cessna Grand Caravan, a single engine aircraft with sufficient size and power. The single engine minimises vibration noise levels compared to multi-engine aircraft. Surveys are typically flown VFR at 80 meters AGL (drape) which is the lowest altitude deemed safe. Speeds average 120 kph or 70 m/s. Surveys are flown with line spacings from 50 m. to 2000 m., depending on the expected signal, aliasing and the resolution required for the geologic target.

Since 2005, Bell Geospace together with Zeppelin GmbH, funded and co-ordinated by De Beers have run airborne surveys from a Zeppelin NT. This is a rigid frame airship with an overall length of 75 m. and a diameter of 14 m. The stability of such an airship and the ability to travel at slow speeds makes this a perfect platform for the high resolution surveys that are required to detect small targets such as Kimberlite pipes as will be shown in the Case Studies Section.

4 Processing

Processing is a five stage process. The first stage, called High-Rate Processing, is designed to limit effects from external forces such as centripetal forces on the disks and self gradients relating to e.g. aircraft motion and fuel movement. After this step the tensor components can be constructed in the external Cartesian co-ordinate frame. Terrain effects are removed at this early stage by subtracting a forward model derived from a digital elevation model (DEM). Proper terrain correction is essential for gradiometry since terrain accounts for the largest gradients in the data due to the proximity to the instrument. A next processing pass uses the Laplace equation and correlation between multiple survey lines to filter out obvious drift, spikes and shifts. The data can then be levelled taking out more subtle drift effects and remaining shifts. Levelling is still largely done manually as a network adjustment.

The final step called Full Tensor Processing aims to reduce the uncorrelated noise by exploiting the relationships and integrity of the full tensor.

Continuing developments in processing software concentrate on three areas.

- Maintaining the integrity of the full tensor. In particular it is being investigated how levelling can be done on the tensor as a whole rather than on individual tensor components.
- Quality Control Statistics; Several strategies are investigated that exploit tensor integrity for quality assurance, such as methods proposed by FitzGerald (2006) that make use of Mohr diagrams, tensor eigenvector and invariant statistics. Also of interest is spectral analysis summarized e.g. by While et al (2006).
- Optimising terrain correction routines. As gradiometry data resolution increases the DEM's have to be more detailed and terrain correction needs to be more precise.

5 Applications

The advent of airborne Full Tensor Gradiometry has opened up the technology to land applications, and in particular to minerals exploration. Compared to hydrocarbon exploration, minerals exploration typically investigates relatively shallow but small sized geological features which are highly suitable targets for gradiometry. Table 1 gives a non-exhaustive overview of geological target density contrasts of commercial interest causing gradient anomalies that are in the range of the FTG system sensitivity and resolution.

Table 1 Economically interesting geological density contrasts.

Geological Structure	Commercial Interest
Salt domes	Oil and Gas Traps
Kimberlite Pipes	Diamonds
Paleo Channels	Placer Minerals (Diamonds, Gold)
Hematite Ore	IronOxide, Copper, Gold
Chromite Ore	Chromium
Lithological Contacts	Various Metals
Igneous Intrusions	Porphyry Copper
Basin Edges	Oil and Gas Plays
Inclined Sheets of Massive Sulphides	Gold, Massive Sulphides

In general gravity gradiometry is not stand alone but rather an enabling technology, even though

Kimberlite pipe detection, salt dome and paleochannel mapping are examples where the technology is often used as a primary integrative geophysical data exploration tool.

In addition to the particular applications in Table 1, airborne gravity gradiometry is also employed for more general geological mapping where primary methods like seismic surveys are not economically viable or are technically inadequate. Examples include sub-salt, sub-basalt or sub-carbonate imaging and general mapping in inhospitable land areas.

6 Case Studies

6.1 Tracing and Quantifying Paleochannels

Airborne Full Tensor Gravity Gradient data was acquired 2003 by Bell Geospace over an area of 2150 km² around Ventersdorp, South Africa, to identify and map the occurrence of buried paleochannels for Etruscan Resources Inc. The diamondiferous paleochannel gravels occur as long narrow snake-like bodies, locally termed "runs". These gravels vary from 20m to over 500m wide.



Fig. 1 Outcropping Paleochannel near Ventersdorp, South Africa.

The initial evaluation survey was carried out with a line spacing of 200 meter and tie lines every 1 km. Figure 2 shows the vertical gradient, Tzz of a part of this early survey.

Over this area there was previously acquired ground gravity available with line spacing of 100 m and station spacing of 50 m. This was used to assess quality levels of the airborne data.

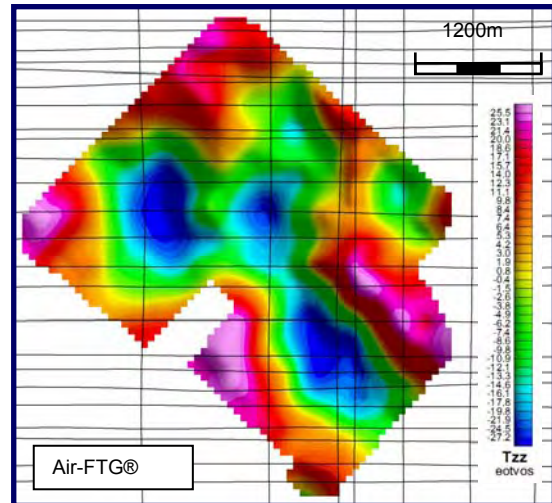


Fig. 2 Tzz Results of the Test Area near Ventersdorp.

Comparison with the gradient of upward continued ground gravity by taking the standard deviation of the difference map in Figure 3, suggests accuracy levels in the order of 5 to 6 E at a resolution of less than 400 m half wavelengths.

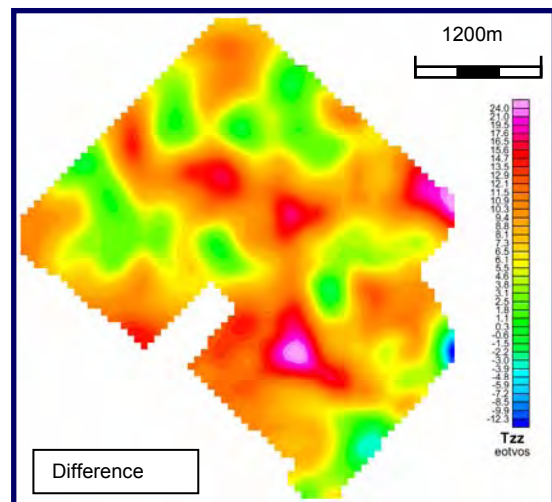


Fig. 3 Difference Map Measured Air-FTG® Tzz Minus Upward Continued Ground Gravity.

Similar accuracy levels were reported on other survey work e.g. by Hatch (2004). On larger surveys where Full Tensor Processing can now be applied, accuracies improve slightly further and levels of 3 to 4 E over less than 400 meter wavelengths are now routinely reported, e.g. Murphy (2006).

This level of quality enables detailed quantitative analysis of the bedrock potholes, by comparing observed gradients with forward models. A 2D example is shown in Figure 4. The size, shape and overburden predicted was subsequently confirmed to be within a couple of meters accurate by drilling.

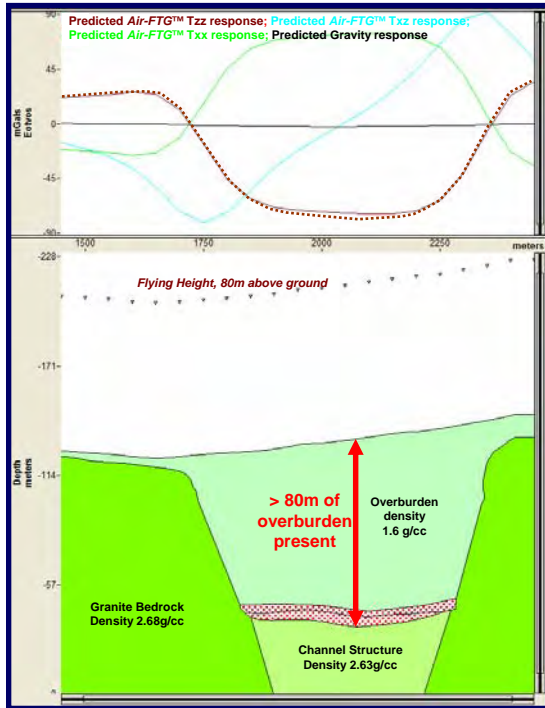


Fig. 4 Forward Modeling Paleo Channels.

6.2 Detection of Kimberlites from an Air-ship

Kimberlite bodies are usually downward-tapering cylinders (pipes) that are the main source of diamonds. The pipes are generated by the melting of small amounts of the Earth's upper mantle containing water and carbonate. The liquid moves upward, gathering crystals and rock fragments along the way in an explosive volcanic event. Where they reach the surface they display a carrot-like shape. The crater comprises debris material with much lower density than the country rock. For this reason gravity is considered a primary tool for Kimberlite pipe detection. Magnetic susceptibility and conductivity contrasts tend to be more inconsistent.

Sizes at the shallowest point can vary from a diameter of over 1000 m to less than 200 m. The resolution of fixed wing airborne gravity gradiometry as described above is sufficient to detect larger pipes

but may miss smaller ones. Also, system noise has a significant component in the bandwidth of the smaller Kimberlites, which could create false anomalies.

Slowing down and stabilising the measurement platform would be the obvious way to improve the data. A lighter-than-air platform has been suggested in the past. De Beers organised a cooperation with Bell Geospace and Zeppelin Luftschifftechnik GmbH to put the idea into practise.



Fig. 5 The Zeppelin NT Gravity Gradiometry Survey Platform Operating for De Beers.

Figure 5 shows the platform of choice, a Zeppelin NT. The rigid structure allows engines to be mounted away from the gondola. This reduces engine noise and vibrations as compared to the more common blimps. Due to the large dimensions gusts and turbulence have less effect than on fixed wing aircraft. A three-degree of freedom accelerometer demonstrated that acceleration noise is between 10 and 100 times less than that in a Cessna Grand Caravan (Hatch, 2006).

The airship surveys at airspeeds of 60 km/h and at altitudes of 80m. AGL. Figure 6 compares some results from an early survey in Southern Africa. The comparison with ground gravity data gives a standard deviation of the difference of 3 E before Full Tensor Processing and about 2.5 E after. The major gain however is in resolution. Data from a test survey flown with 100 m linespacing compared to a DTM showed very strong correlation with DTM peaks as small as 100 m. This confirms the intuitive figure of 100 meter resolution, given that the survey speed of the Zeppelin is about a third of that of the Grand Caravan.

A system capable of detecting 2.5 E anomalies of 100 meter width can safely be called the ultimate Kimberlite detection tool. The Zeppelin equipped with the Bell Geospace Full Tensor Gravity gradi-

ometer is therefore contracted on a long term exploration campaign for De Beers in Southern Africa.

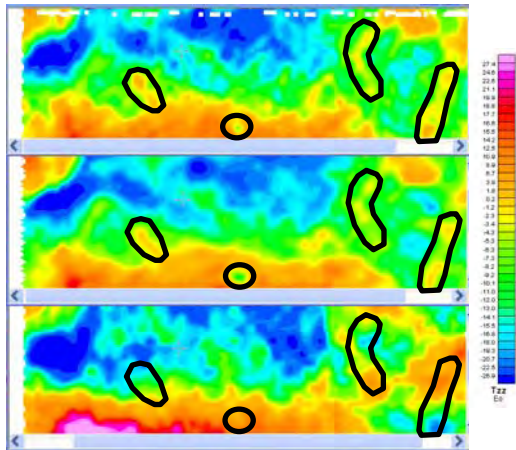


Fig. 6 Gravity Gradient Tzz from Airship (top), Ground Gravity (middle) and Cessna (bottom). The area is about 10 by 3 km.

7 Discussions

7.1 Terrain Correction

It can be shown that a 40 centimeter rise in terrain of 300 meter diameter will result in an anomaly of 3 E at 80 meter height. As shown above this is detectable by Air-FTG[®] from a Zeppelin. This gives an idea of the quality level required of a DEM for terrain correction.

A detailed and accurate DEM is important for data quality and to aid geological interpretation. Jekeli (2006) gives an excellent comparison of methods to compute the terrain correction.

At the accuracy levels mentioned density differences in the weathered layer really cannot be ignored. Taking the density of the weathered layer into account is not routinely done yet but this needs to be addressed in future software. One problem that is foreseen is that density information is generally discontinuous. The sharp density contrasts found in geological maps will create false anomalies unless this contrast corresponds exactly to the real situation also in location and in size, which is unlikely since it is hard to measure directly and accurately.

7.2 Quality Control

Quality of airborne gravity gradiometry is affected by environmental factors at the time of measurement, particularly turbulence. Continuous Quality Assurance is therefore necessary.

To assess the quality one needs to have some form of redundant data. There are several options.

- High resolution gravity from another source. This will only be available in a test scenario, e.g as described above and will overestimate noise since it compares two signals with noise.
- Terrain data. But comparison with terrain data will give an incomplete picture of the quality since there of course are other signal sources.
- Multiple passes or repeat line. This is an expensive option and hence can only be applied to a limited portion of any survey. It is not routinely done.
- Analysis of crosspoints between inlines and tie-lines. Crossover points however can be quite sparse and for airborne surveys applicability is reduced because the signal is “smeared” due to speed of the Grand Caravan.
- Spectral relations and Laplace equation in the full tensor. This is an area of continuous investigation. Tensor integrity characteristics are successfully used as a filter tool, but meaningful QA measures have not been adopted yet.
- Autocorrelation of the gravity signal. Application of Wiener filtering or Collocation techniques are not fully exploited and should be investigated further. Better understanding of the Autocorrelation behaviour of shorter wavelengths is necessary. Flury (2006) shows that local generalisation of the autocorrelation is possible but the analysis should be extended to even shorter wavelengths.

8 Summary & Conclusions

Airborne gravity gradiometry has come of age and is now a recognized geophysical tool. The installation of the FTG system on a Zeppelin airship pioneered by De Beers is capable of very detailed density contrast investigation and direct kimberlite detection.

Future gradiometry techniques may yield better accuracies but at some point interpretation will be limited by geologic noise. Indeed, detailed knowl-

edge of topography and surface density to correct for terrain is an increasing challenge.

Acknowledgements

Acknowledgements go out to Etruscan Resources Inc for permission to publish the Ventersdorp data and De Beers Group for all data relating to the Zepelin surveys.

References

- FitzGerald, D. J. (2006). Innovative Data Processing Methods for Gradient Airborne Geophysical Datasets. *The Leading Edge, Volume 25*, 1, pp. 87-94
- Flury, J. (2006). Short-Wavelength Spectral Properties of the Gravity Field from a Range of Regional Data Sets. *Journal of Geodesy*, 79, pp.624-640
- Hatch, D.M. (2004). Evaluation of a Full Tensor Gravity Gradiometer for Kimberlite Exploration. In: *Abstracts from the ASEG-PESA Airborne Gravity 2004 Workshop – Geoscience Australia Record 2004/18*, pp. 125-134
- Hatch, D.M., Kuna, S., Fecher, J. (2006). Evaluation of an Airship Platform for Airborne Gravity Gradiometry. In: *Abstracts from the AESC 2006, Melbourne Australia*.
- Hatch, D.M., Murphy, C.A., Mumaw, G.R., Brewster, J. (2006). Performance of the Air-FTG® System Aboard an Airship Platform. In: *Abstracts from the AESC 2006, Melbourne Australia*.
- Jekeli, C. (1993). A Review of Gravity Gradiometer Survey System Data Analyses. *Geophysics*, 58, pp. 508 - 514.
- Jekeli, C., Zhu, L. (2006). Comparison of Methods to Model the Gravitational Gradients from Topographic Data Bases. *Geophysical Journal International*, 166, pp. 999 - 1014.
- Murphy, C.A. (2004). The Air-FTG Airborne Gravity Gradiometry System. In: *Abstracts from the ASEG-PESA Airborne Gravity 2004 Workshop Geoscience Australia Record 2004/18*.
- Murphy, C.A., Brewster, J., Robinson, J. (2006). Evaluating Air-FTG® Survey Data: Bringing Value to the Full Picture. In: *Abstracts from the AESC 2006, Melbourne Australia*.
- Rummel, R. (1986) Satellite Gradiometry. In: *Mathematical and Numerical Techniques in Physical Geodesy*, Springer Verlag, pp. 317 – 363.
- While, J., Jackson, A., Smit, D., Biegert, E. (2006) Spectral Analysis of Gravity Gradiometry Profiles. *Geophysics*, 71, pp. J11-J22

System Functions Estimates for Airborne Gravimetry

G. Boedecker

Kommission für die Internationale Erdmessung, Bavarian Academy of Sciences and Humanities
Alfons-Goppel-Str. 11, 80539 München, Germany

Abstract. One major challenge in airborne gravimetry is increasing not only accuracy but also spatial resolution of both necessary observations for gravity $g=a-b$, total acceleration (a) and kinematic acceleration (b). To this end, it is necessary to study system characteristics of all components involved. This enables to avoid subsystems mismatch resulting in information loss and to tune hardware and model parameters.

The main observation subsystems in our approach are GPS (L1 or L1L2 50/s) receivers (Javad & Novatel) and QFlex_QA3000 accelerometers which are mass/spring systems indicating the specific force; but also ancillary components such as dampers, the aircrafts body itself etc. play a major role. The investigations are based on data from flights as also from experiments such as stroke tests and observations on a kinematic test stand for aircraft-like kinematic height variations.

The system characteristics of various components were determined and represented by means of transfer functions or parametric models. Some of these were in agreement with prior information, others were not. This shows that such own tests can make a significant contribution to the improvement of airborne gravimetry. Also, the various test approaches proved to be useful and complementary.

Keywords. Airborne gravimetry, system function, ARMA modelling, kinematic GPS

1 Motivation

The basic equation of airborne gravimetry is

$$\vec{g} = \vec{a} - \vec{b} \quad , \quad (1-1)$$

where these vector quantities represent \vec{g} - gravity, \vec{a} - total observed acceleration onboard a moving carrier, and \vec{b} - kinematic acceleration. In order to fully exploit the above equation, all quantities have to refer to the identical reference frame including identical location in space and time. For data fusion,

also the system functions of the contributing subsystems have to be known.

This paper will focus on the latter requirement.

System function studies will enable

- to pinpoint component deficiencies and initiate improvements
- to equalise signal contributions from different sensors
- to identify system characteristics if specifications of components are unknown.

1.1 State of the art of airborne gravimetry

The majority of existing airborne gravimeters for the observation of the *total acceleration* \vec{a} is still dominated by scalar platform gravimeters for the vertical component only. Part of them evolved from ship-borne gravimetry such as the US LaCoste Romberg 'Air-Sea Gravity System' or the Russian Elektropribor 'CHEKAN' or they are directly developed for airborne gravimetry such as the Canadian SGL company 'AirGrav' or the 'GT-1A' of Russian origin. Also because of long sensor response times and considerable filter lengths being typically in the range of 1-2 minutes, the spatial resolution is of the order of a few km. Vector strapdown gravimetry is a big desire since decades, starting from off the shelf SINS (Strapdown Inertial Navigation System) of various brands or composing the components, see Boedecker G, Stürze A (2005). The components typically have very short response times and sampling rates of e.g. 100 /s or more.

In contrast to marine gravimetry, where the vertical kinematic acceleration was simply averaged out, the *kinematic acceleration* \vec{b} of the aircraft has to be observed with a compatible accuracy, typically using GNSS. The sampling rate is typically 10 /s, but may be as high as 100 /s.

This means, the observation sampling rate would allow a much higher spatial resolution¹, provided the observation noise is sufficiently low and the subsystem functions are known. This will be studied in this paper, focussing on the system characteristics of the participating sensors.

2 Methodology

We shall make use of different types of system modelling and system description in the time domain or spectral domain e.g. by nonparametric transfer / system functions or by using parametric modelling such as ARMA (Auto Regressive Moving Average) models. The basic formulae will be given further down in this section. Then we shall focus on the application of these approaches to the real physical system comprising various subsystems of our prototype airborne gravimetry system SAGS4² such as GNSS receivers, accelerometers, mechanical components, various signal processing modules etc. As pointed out above, an important aim is to analyse the relation of the **a** signals of the accelerometers and the **b** signals deduced from GNSS receivers. This could be achieved by directly relating these two types of sensor signals. This approach would allow us to study the *relative* transfer function between these two sensors. We could use data from test flights where both sensors participated. However, we could not conclude as to which of the sensors and other components has any specific characteristics that could be improved.

Therefore, besides other approaches, we chose to aim at an (quasi) *absolute* transfer functions, i.e. to compare both signals to a reference signal of superior quality. One straightforward approach would be to track the aircrafts trajectory by means of an earthbound (e.g. laser-) tracking system. However, in view of the aimed at accuracy of 1 mm or better and the introduction of yet another ancillary reference point at the hull of the aircraft, this seems to be very ambitious and costly. For this reason, we chose to create a lift device to be used on the ground. More technical details are given in the section 'Experiments'. All sensor readings, i.e. GNSS positioning, accelerometer and lift vertical scale readings, are independently referred to GPS time at the microsecond level. Hence, we can independently study the

absolute transfer functions of the **a** and the **b** sensors.

Looking at the orders of magnitude of the participating signals, we recognize that in the aircraft the variation of **a** and **b** will be of the order of 10 ms^{-2} while the variation of **g** will be marginal. This means, for system behaviour, we may neglect the variation of **g**.

For this study, we have carried out three types of experiments:

1. Impulse experiments
2. Aircraft experiments
3. Lift experiments

This investigation does not take into account e.g. the rotation sensors that are also necessary for (strapdown) airborne gravimetry. Rather, we restrict our view to the linear acceleration in one direction.

In the said lift experiments, we can be sure that the sensors refer to the identical reference location, i.e. the cage of the lift. This is different from the real scenario in the aircraft, where we have the GNSS antenna at the upper fuselage of the aircraft and the accelerometers inside the hull. This means, we have to take into account the relative deformations of the reference points of the participating sensors.

As we shall see below, the total 'airborne gravimetry' system consists of several subsystems, these again of subsystems etc. The depth of this fragmentation is arbitrary. However, it does not make sense to breakdown the system into the tiniest subsystems if there is no chance to acquire information about their characteristics either from own observations or from else information. Therefore, we stay at a medium breakdown level. Some of these partial systems are accessible, many are not.

In principle, we could find out about the overall system characteristics by a composition of the system functions of all subsystems. However, from own experience, this sometimes may be successful, in other cases it is not, because the available information is quite inhomogeneous.

*For the above reasons, we decided to carry out real observations of **a** and **b** on a test bed, refer these observations to a common quasi absolute reference and to infer on some major system component characteristics from the analysis of these observations. This main approach is complemented by other experiments. The analysis will make use of some tools of system analysis and signal processing.*

3 Basics

3.1 System representation

¹ Given typical values for an aircraft speed of 200 km/h and a sampling rate of 100 /s, we have 1 observation every 0.55 m.

² SAGS4: Strapdown Airborne Gravimetry System, prototype #4, c.f. Boedecker G, Stürze A (2004)

The real physical system is a composition of sensor and signal processing components and ancillary components. The conceptional mathematical 'system model' may be found by 'system identification'. However, we shall not dig into theory of modelling and system identification, nor shall we carefully observe peculiarities of continuous time vs. discrete time observations etc. Comprehensive presentations of the matter can be found e.g. in Kiencke U, Jäkel H (2002), Kronmüller H (1991), Lahti BP (2005); for similar applications see Eissfeller B (1997) . Rather, we shall focus on the insights provided by these concepts for our work. See some system structures in fig. 1:

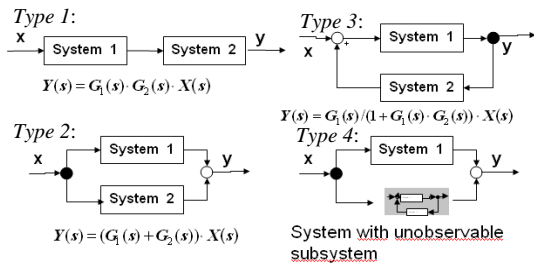


Fig. 1: System structures

The graphs also include formulae for the composite system function to be explained in the next section.

3.2 Spectral domain system description

A systems behaviour may be characterised by its impulse response, e.g. input and output can be related by the time domain convolution

$$y(t) = g(t) * x(t), \quad (3-1)$$

$x(t)$ Input
 $y(t)$ Output
 $g(t)$ Impulse response

Using the Fourier transform,

$$X(f) = F\{x(t)\} = \int_{-\infty}^{\infty} x(t)e^{-j2\pi ft} dt, \quad (3-2)$$

we get the frequency response $G(f)$ in the spectral domain

$$Y(f) = G(f) \cdot X(f) \quad (3-3)$$

Similarly, we can make use of the power spectra and cross-spectra:

$$P_{xy}(f) = T_{xy}(f) \cdot P_{xx}(f) \quad (3-4)$$

Using the Laplace Transform

$$X(s) = L\{x(t)\} = \int_0^{\infty} x(t)e^{-st} dt, \quad s = \sigma + j\omega \quad (3-5)$$

we get the transfer function or system function being the Laplace transform of the impulse response, viz. the transfer function $G(s)$:

$$Y(s) = G(s) \cdot X(s) \quad (3-6)$$

In this paper, we shall make use of the frequency response and time domain system descriptions.

3.3 Time domain ARMA modeling

If we relate the current system output y_n on a discrete time scale $n=1, 2, \dots$ to the original observations x_{n-k} , (3-1) may specialize to

$$y_n = \sum_{k=1}^{na} a_k \cdot y_{n-k} + \sum_{k=0}^{nb} b_k \cdot x_{n-k} \quad (3-7)$$

where it is obvious that the first term on right hand side refers to past system output (AR, autoregressive) and hence is the recursive part, whereas the second term refers to the past original system input and performs a weighted averaging (MA). Because a system also may be considered a filter, the a and b coefficients are also called filter coefficients.

4 Lay-out of experiments

Physical system

The system model scheme outlined in section 3.1 will be applied to the real hardware and software we are using. An impression of the hardware is provided by fig.2:

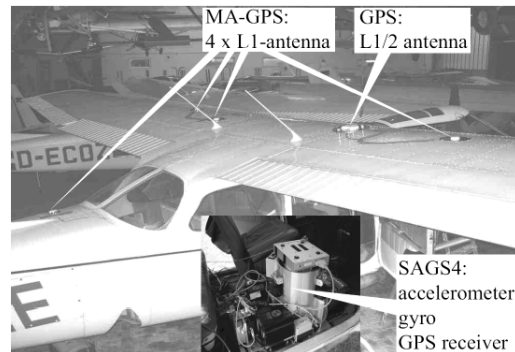


Fig. 2: SAGS4 in aircraft (here: montage for better visibility)

The photograph in Fig. 2 shows the two main sensors in their real setting, c.f. Boedecker G, Stürze A (2004):

- **a** is observed by the high precision QFlex QA3000 spring / mass accelerometers inside 'SAGS4', typically sampled at 100/s, attached to the co-pilots seat rails.

- **b** is observed by GPS receivers Javad JNS100 and NovAtel OEM4G2 at 20 to 50 /s, represented by the L1L2 antenna on the fuselage of the aircraft.

Besides these two main sensor systems, we have to take into account also other subsystems such as the vibratory spring-mass system of the aircraft itself, the shockmounts etc. and the subsystems of the sensor systems such as filters etc. An initial idea shall be provided by fig. 3. For the fusion of the two respective data streams, we have to relate these to an identical location.

There were several experiments carried out. Sections 4 and 5 present a selection.

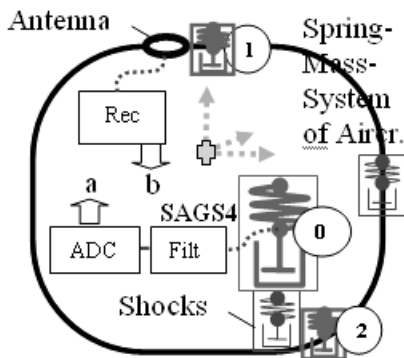


Fig. 3: System of Sensors and Aircraft
0: SAGS4, 1: test accelerometer near antenna,
2: test accelerometer near seat rails

4.1 Stroke experiments

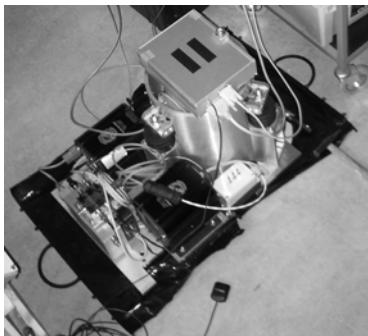


Fig. 4: SAGS4 on its base plate ready for stroke experiment

SAGS4 on its standard baseplate was put on loose sand in order not to introduce any more vibratory subsystems. An impulse was generated by a stroke with a hammer on the baseplate. One accelerometer was mounted to the base plate recording at 500 /s the immediate input signal. The acceleration signal passes through the SAGS4-shockmounts, is converted to an electrical signal by QFlex, analogue filtered with Bessel characteristics, A/D converted and subsequently digitised, c.f. fig. 3. The partial system to be studied in this experiment comprises a series of subsystems, particularly the damper and the analogue filter, c.f. system type 1 of fig. 1

4.2 Aircraft experiments

Test accelerometers were mounted at different places of the aircraft, e.g. directly at the GNSS L1L2 antenna, fig. 3 (1), in order to find out about the vibratory dynamical load that may affect the GPS receiver control loops, or at the base plate of SAGS4, fig. 3 (2).

4.3 Lift experiments

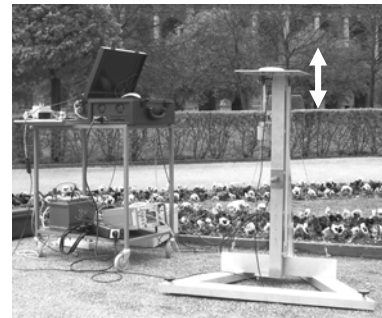


Fig. 5: Lift

Most importantly, we have been using a lift, c.f. fig 5, in order to relate the observed signals for **a** and **b** to a quasi-absolute standard.

The lift cage can be moved up and down over 0.60 m height amplitude and at dynamics similar to the aircraft. The cage can carry the GNSS antenna and the accelerometer. An electronic vertical scale is capable of vertical positioning sampling at rates > 100 /s at a resolution of <0.001 mm. This way, the lift provides a superior height positioning quality and time resolution for ground truth kinematic acceleration and thus enables the determination of quasi absolute system functions.

Note that no dampers and no analogue filters were used, i.e. we focus on the QFlex itself.

5 Results

5.1 Stroke experiment

The impulse response Laplace transformation provides immediately the transfer function, the periodogram provides the spectral domain PSD frequency response. The shockmounts and the electrical analogue filter subsystems will have the biggest effects on the signal transfer. The electrical analogue filter was of Bessel type, the filter characteristics of the shockmounts were provided by a curve.

In fig. 6, the resulting periodogram of the immediate impulse response (up) shows near zero frequency a slight dislocation and further an even spectrum – as it should be. The SAGS4-response, (down) shows the overlay damping of shockmounts and analogue filter, as was designed, and confirms the sampling rate of 100, because this is about three times the highest frequency contribution seen in the data. However, the frequency response in the very low frequency range is much less than expected. This calls for improvement of the shockmounts. This statement, however, is based on low amplitude signals and in view of the nonlinear behaviour of the shockmounts it has to be confirmed by other experiments with higher amplitudes in the lower frequency range.

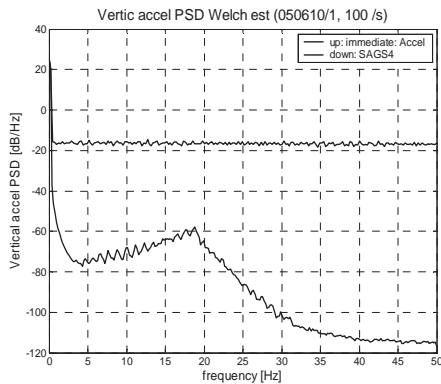


Fig. 6: Stroke frequency response of SAGS4

5.2 Aircraft experiment

The vertical accelerations of a normal flight with acceleration observed as described in sec. 4.2 were used to estimate the transfer function according to (3-4). We recognize from fig. 7 that it is similar to the above stroke experiment, as it should be, with plausible differences because of higher motion amplitudes and a different setting. It is confirmed that the damping in the range about 3 ...8 Hz is higher than to be expected from the given information about the shockmount filter curve. This has to be

remedied either by means of more appropriate shockmounts or by a proper post filter that corrects for the undesired effect on the signal.

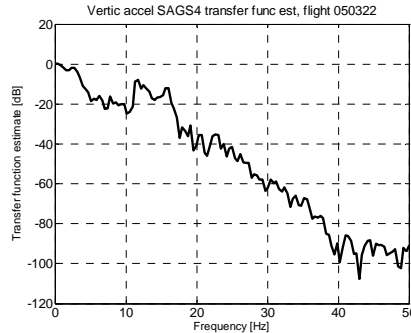


Fig. 7: Transfer function estimate of SAGS4 mounted in aircraft

5.3 Lift experiments

From a first look at fig 9 (for details see further down) at a sampling rate of 100, we are confirmed by the unfiltered vertical accelerations that

- the raw data, viz. the immediate unfiltered second derivative of the vertical scale position provides superior ground truth accelerations over amplitudes of ± 1 g and over a similar motion spectrum as our aircraft
- the delay and other characteristics of the accelerometer control loop become visible

This will be analysed further:

Nonparametric transfer function estimate:

The frequency domain transfer function estimate has been used to (pre) calibrate the accelerometer and it exhibits a rather linear phase. However, we shall focus on the parametric system modelling.

Parametric (ARMA) modelling:

We have applied two different approaches to determine coefficients a, b for (3-7):

- Steiglitz-McBride
- In an own procedure, we computed an LS-approximation without iteration.

The aim is to find an appropriate time domain system model for the real accelerometer system described by autoregressive (AR) coefficients a_k and moving average (MA) coefficients b_k to map the real acceleration input signal x_k taken from the second derivative lift heights and the output signal y_k taken from the accelerometer. Because both signals – the second derivative with time of the lift

heightings and QFlex output - are strictly referred to GPS time within microseconds, and because the accelerometer output and the scale are calibrated independently, we need not introduce any more parameters.

As to the number of coefficients n_a , n_b , we tested several variants by their r.m.s. residuals, see fig. 8, and selected $n_a=4$, $n_b=3$ at the noise floor. The computation time for our own procedure was much shorter and the r.m.s. residuals were about 10...20% smaller than using Steiglitz-McBride.

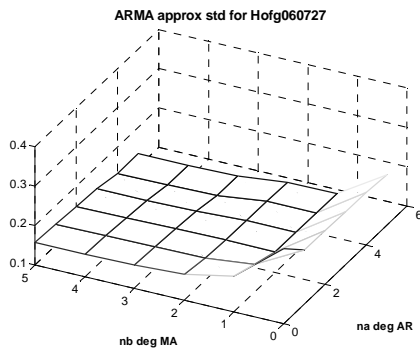


Fig 8: ARMA modeling rms error for different orders

A look at fig. 9 confirms the usability of our procedure: The QFlex accelerometer output is well explained by the ground truth acceleration input and the linear model identified. Particularly, we see that the spikes in 'acc out' curve are not noise or outliers and hence are not to be filtered out by a physically blind low pass filter.

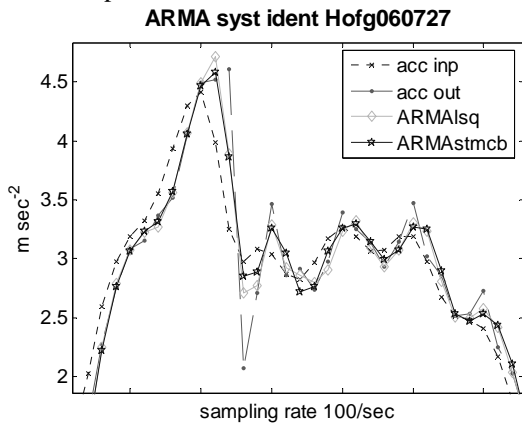


Fig 9: ARMA modeling rms error for different orders

Lift experiments for GNSS:

Similar investigations have been carried out for the GPS receivers and this way optimum receiver parameters for PLL (Phase Locked Loop) order and

bandwidth were found, see Stürze A, Boedecker G (2004), Boedecker G, Stürze A (2005).

6 Conclusions / Summary

Recognizing the necessary improvement in resolution of airborne gravimetry, it is necessary to have good system models for all components as a prerequisite for data fusion, see e.g. Bendat JS, Piersol AG (2000).

- Time domain ARMA models and spectral domain transfer functions studies have been applied
- Different experiments provided complementary information
- The kinematic lift provides ground truth values and hence permits absolute modelling in an environment similar to aircraft dynamics.
- A procedure for the inverse problem, i.e. to compute optimum acceleration values from accelerometer output, will be published in a forthcoming paper.

7 References

Bendat JS, Piersol AG (2000) Random Data Analysis and Measurement Procedures. 3rd ed., John Wiley, NY etc.,
 Boedecker G, Stürze A (2004) Acceleration Sensors Development for SAGS4 (StrapDown Airborne Gravimetry System). GGSM Koll. 30.8.-3.9.2004, Porto. Presentation, Paper, Proceedings
 Boedecker G, Stürze A (2005) SAGS4 - StrapDown Airborne Gravimetry System Analysis. In: Rummel, R., Reigber, C., Rothacher, M., Boedecker, G., Schreiber, U., Flury J. (Ed.): Observation of the Earth System from Space, Springer
 Eissfeller B (1997) Ein dynamisches Fehlermodell für GPS Autokorrelationsempfänger. Doctoral Thesis, Institute of Geodesy and Navigation, University FAF, Munich
 Kiencke U, Jäkel H (2002) Signale und Systeme. Oldenbourg
 Kronmüller H (1991) Digitale Signalverarbeitung. Springer, Berlin Heidelberg
 Lathi B P (2005) Linear Systems and Signals. 2nd ed, Oxford University Press, Oxford New York
 Ljung L (1999) System Identification, 2nd ed, Prentice Hall, Upper Saddle River, NJ
 Stürze A, Boedecker G (2004) High Precision Kinematic GNSS Observations Up to 50 S/s for Airborne Gravimetry. Proc of the ION GNSS 2004, Long Beach

Airborne Scalar Gravimetry for Regional Gravity Field Mapping and Geoid Determination

A.V. Olesen, R. Forsberg

Danish National Space Center, Juliane Maries Vej 30, 2100 Copenhagen, Denmark

Abstract. Airborne gravity is capable of providing an accurate and bias-free extension of satellite gravity models and thus bridges the spectral gap between these models and the fine structure of the gravity field as mapped by the newest digital elevation models (SRTM). Airborne gravity is therefore an ideal base for regional gravity/geoid modeling. Airborne gravity may also be an efficient tool to validate existing datasets e.g. older marine surveys and is the only efficient way to cover the near coastal zone where altimetry derived gravity fails to deliver reliable data.

This paper describes some recent surveys undertaken by Danish National Space Center (DNSC) including both surveys over marine areas in the Arctic and the North Atlantic region and surveys over land covering all of Malaysia and Mongolia. The purpose has been to contribute to regional and global models (ArcGP and EGM2006), to provide geoid models for national height systems and reference surfaces for ocean current studies. The measurements were done with a LaCoste & Romberg marine/airborne gravimeter owned by the University of Bergen. This type of gravimeter has an excellent drift characteristic and can when the data are properly processed provide bias-free results also for airborne applications.

The main source for a bias in airborne data obtained with stabilized platform systems is the so-called tilt correction, which basically is a modeling of the platform orientation error. A new platform-response-modeling approach to account for this effect will be described. This approach seems to give virtual bias-free results.

1 Introduction

Today airborne gravimetry is a truly operational tool for gravity mapping and it offers a fast and economic coverage of large areas. One of the big advantages of airborne gravimetry is the uniform and seamless coverage of the near-coastal region, a region that so far is only poorly covered in many

areas of the world due to shallow water, which don't allow for marine measurements. Satellite altimetry derived models are in general not reliable near the coast (Andersen and Knudsen, 1998). This region is at the same time an area where one may want the most precise geoid due to the high population density and the economic interests related to infrastructure developments here. Also natural hazard management like flooding control and tsunami warning systems require a good coastal geoid determination in order to make use of fast and cheap GPS levelling instead of tedious and costly spirit levelling. Another advantage of airborne surveys is the ability to cover remote and otherwise inaccessible areas like mountains and jungles.

It is common practice to subject marine and airborne gravity profile data to an adjustment procedure that minimizes the misfit at the crossing points, either as a linear trend or a bias removal. It may be justified to do this to marine data, see LaFehr and Nettleton (1967) for a discussion, but for airborne data obtained with a long-term stable gravimeter like the LaCoste & Romberg meter and a proper reduction for motion induced effects there seems to be little physical justification for such an adjustment. The gravimeter is virtual drift-free during the short time span of a flight (Valliant, 1992), so bias or tilt problems in the data may indicate that the processing algorithm is less than optimal. The situation is different for systems utilizing sensors, which are known to drift, such as INS equipment (Glennie, 1999), but it doesn't make the crossover adjustment healthier. Any crossover adjustment will by nature distribute point errors at crossing points into along-track corrections, and thus provide a way for short-period random errors to leak into the longer wavelengths. Using a dense net of tie lines in the crossover adjustment will reduce this leaking, but it may be quite expensive especially for regional scale surveys.

Avoiding the need for crossover adjustment of the airborne track data therefore means that one can get away with much fewer tie lines than in a survey

that requires crossover adjustment since the tie lines now only serve as internal quality estimators (repeatability at line crossing points).

2 Tilt effect and biases. A new platform modeling approach

The effect of a tilting platform is both to make the gravimeter less sensitive in the vertical direction, and to make it sensitive to horizontal accelerations. The traditional approach to account for this effect leads to a correction term that is non-linear in the accelerations. The correction term can be found in Valliant (1992) or in Czombo (1994) and writes:

$$\delta g_{\text{tilt}} = \sqrt{f_x^2 + f_y^2 + f_z^2 - q_E^2 - q_N^2} - f_z \quad (1)$$

where f_k denotes accelerations measured by the gravimeters three accelerometers and q_k denotes horizontal kinematic accelerations derived from GPS. Valliant (1992) gives an approximate expression derived from equation (1) under the assumption that $f_z \cong g$ and $g \gg f_{x,y}$:

$$\delta g_{\text{tilt}} = \frac{f^2 - q^2}{2g} \quad (2)$$

where $f^2 = f_x^2 + f_y^2$ and $q^2 = q_E^2 + q_N^2$. The last equation is good in the sense that it highlights the problem with the tilt correction. It is basically a small difference between two potentially huge numbers. Furthermore, the two potentially huge numbers are derived by squaring discrete and very noisy measurements. In addition to that, the noise on the separate terms must be expected to have different signatures, so the noise on the squared terms is not likely to cancel out due to the subtraction. Such an approach will certainly cause problems, problems that cannot be filtered out by the final low pass filter, since the squaring will change the characteristics of the noise signal. A zero-mean noise will after the squaring have a

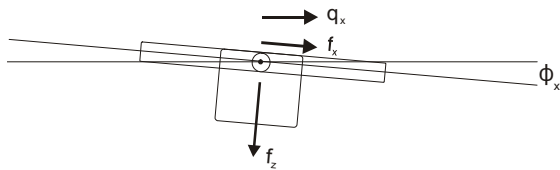


Figure 1. Tilting platform

positive mean value. In this way the tilt correction may become a way for zero-mean noise to bias the gravity estimates. Pre-filtering of the data before the tilt correction is derived may reduce the problem, but the optimal amount of filtering is somewhat ambiguous.

The tilt angles may alternatively be estimated from the combined gravimeter and GPS observations. For small tilt angles the following approximations hold for one axis, see also Figure 1:

$$f_x = q_x + \sin(\phi) \cdot f_z \approx q_x + \phi \cdot f_z \approx q_x + \phi \cdot g \quad (3)$$

or

$$\phi \approx \frac{f_x - q_x}{g} \quad (4)$$

It was shown in Olesen et al (1997) that the tilt angle has no spectral components above approximately 0.01 Hz. See also LaCoste 1967 for a thorough discussion of the spectral behavior of the LaCoste & Romberg marine gravimeter's stabilized platform. With this knowledge the tilt angles can be well modeled and filtered. High frequency noise in the tilt angle estimation can be effectively removed with a low-pass filter that matches the platform period. This leads to the computation of the tilt correction being split into two parts, (i) the modeling of a physical system with known properties (the stabilized platform) and (ii) the correction for tilt computed as a linear combination of three acceleration components:

$$\delta g_{\text{tilt}} = (1 - \cos(\phi_x) \cdot \cos(\phi_y)) \cdot f_z + \sin(\phi_x) \cdot f_x + \sin(\phi_y) \cdot \cos(\phi_x) \cdot f_y \quad (5)$$

This implies, that zero-mean noise on the acceleration estimates will propagate unbiased as zero-mean noise into the tilt correction and will therefore not induce any bias into the gravity estimates.

Table 1 shows the performance of the two different tilt correction algorithms. Two tracks from the Greenland 2001 survey are analyzed, where one track was flown under turbulent conditions and the other was flown under smooth conditions. It is seen that the two algorithms yield the same results when no filtering is applied. This should not surprise, since the two methods are identical in that case. The table shows a dramatic change in mean value when filters are applied, especially for the dynamic flight,

from 13.3 mGal to -2.1 mGal for the traditional approach, when a 1 seconds filter is applied before calculating the correction. Further filtering is seen to change the mean value several mGal, when we still look at the traditional approach. This shows that the tilt correction can add severe biases to our data, as it is unclear which amount of filtering is optimal. Moreover, the optimal filter length may change due to the dynamics of the flights. The modeling approach, on the other hand, is seen to be much less filter-sensitive for realistic filter lengths. Besides, the optimal filter length is more or less given from the platform natural period (Olesen 2003). A filter around 60 to 80 seconds should be adequate.

Table 1: Comparison of the two different tilt correction algorithms

Traditional approach				
Pre-filter	Quiet flight		Dynamic flight	
	Mean	St dv	Mean	St dv
0 sec	0.32	1.49	13.26	8.42
1 sec	-0.46	0.97	-2.09	4.29
2 sec	-0.76	0.91	-3.87	3.92
3 sec	-0.88	0.89	-3.98	3.75
5 sec	-0.92	0.86	-3.64	3.47
10 sec	-0.87	0.77	-2.82	2.81
20 sec	-0.77	0.61	-1.84	1.83

Modeling approach				
Platform filter	Quiet flight		Dynamic flight	
	Mean	St dv	Mean	St dv
0 sec	0.34	1.48	13.30	8.42
20 sec	-1.01	0.93	-5.46	4.06
40 sec	-1.02	0.93	-4.48	4.01
60 sec	-0.99	0.95	-4.26	4.18
80 sec	-0.98	0.95	-4.18	4.37
100 sec	-0.98	0.95	-4.03	4.32
120 sec	-0.97	0.95	-3.79	4.20

The standard deviation of the tilt correction in Table 1 shows somewhat the same dependency on filter length as does the mean value. But, the mean value is the main concern for us, as the data are intended for geodetic use. The modeling algorithm described in this section is a more sound way to establish the correction for platform errors, than is the traditional

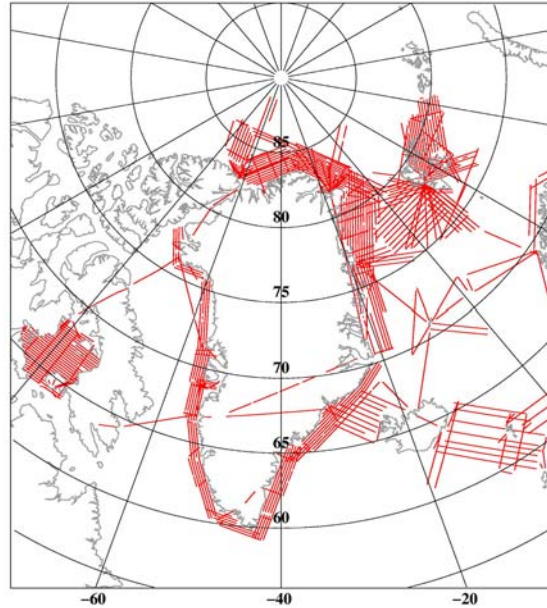


Figure 2. Arctic surveys between 1998 and 2003

algorithm. The modeling approach incorporates the known physical properties of the platform system in its algorithm in contrast to the traditional approach.

3 The Arctic surveys

Geodynamics Department at Danish National Space Center has since 1998 gathered approximately 150,000 line km of airborne gravity data in the arctic region. The surveys constitute a seawards extension of the helicopter-based conventional gravity campaigns along the Greenland coast, see Forsberg et al (1998) and Forsberg and Rubek (1998). The surveys around Greenland have mainly been funded by US National Geospatial-Intelligence Agency as part of the Arctic Gravity Project, see <http://earth-info.nga.mil/GandG/wgs84/agp/>.

To the north, in the Polar Sea, the operations were coordinated with the surveys performed by US Naval Research Laboratory (Brozena 1991, Childers et al 2001). Surveys around Svalbard were done in cooperation with and partly funded by Statens Kartverk, Norway. The survey over Foxe Basin, Canada, was done under contract to Geodetic Survey Canada.

The survey stretching from Greenland's East coast via Iceland to Scotland and Norway was done within the frame of the GOCINA project (Geoid and Ocean Circulation in the North Atlantic). The aim was to provide a Mean Dynamic Topography

model (MDT) for the area in question. The MDT would be based on a Mean Sea Surface (MSS) from satellite altimetry and a gravimetric geoid (Knudsen et al 2004). The airborne gravity data provided the constraints needed to do a healthy bias adjustment of the existing gravity data in the area before computation of the geoid. The inclusion of the airborne data had significantly effect especially along the Greenland coast where other reliable data sources are sparse.

Statistics from crossover analyses of the datasets are shown in Table 2. For all years the RMS crossover misfit was 2.5 mGal indicating a 1.8 mGal noise level on the individual tracks (2.5 mGal divided by $\sqrt{2}$ based on the assumption that the noise is uncorrelated from track to track). The results seem to be pretty constant from year to year only the year 1998 stands out with a 1.8 mGal RMS crossover error, that fits nicely with the fact that the 1998 survey was over the frozen Polar Sea with very smooth flight conditions. The 1.8 mGal misfit indicates a 1.3 mGal noise on the track data.

Table 2: Crossover error statistics for the Arctic surveys (units: mGal)

Data set	Number of cross	RMS misfit
1998	86	1.8
1999	74	2.5
2000	96	2.8
2001	66	2.6
2002	101	2.6
2003	46	2.1
All years	670	2.5

Comparison to surface data is very consistent with the noise estimates from crossover analysis, 2.5 mGal when comparing to a high quality marine data set from NUNAOIL, the national oil company of Greenland. These marine data are scattered along most of the Greenland east and west coast and are believed to be accurate at the 1 mGal level or better (Strykowski and Forsberg, 1995). The comparison to ice surface data over the Polar Sea gave a 1.3 mGal agreement, exactly the same number as the internal noise estimate from the 1998 dataset. In both cases the surface data was compared directly with the airborne free air anomalies, no upward or downward continuation was performed to the data. The airborne surveys were flown at an altitude of 80 to 200 meters so the attenuation due to upward continuation is marginal. This is especially true over the ocean where the gravity anomaly sources

are located below the surface. The good agreement between internal and external error estimates indicates that there are only little internal bias problems left in the airborne datasets. Applying a bias adjustment to the airborne dataset will of course lower the crossover misfit but the derived error estimates will be too optimistic and will no longer reflect the real noise level. Table 3 also shows that mean differences between airborne and surface data as well as global models are at the sub-mGal level suggesting that the mean value and the longer wavelengths in the airborne datasets are very precisely determined.

Table 3: Comparison to surface data within 1 km and to global models (units: mGal)

Data set	Number of points	Mean diff.	Standard deviation
NUNAOIL marine data	1178	0.1	2.5
Canadian sea ice data	12	0.4	1.3
GGM01C	NA	0.2	23.2
EIGEN-GRACE02S	NA	-0.3	24.6

4 The Malaysian and the Mongolian surveys

Geodynamics Department from National Survey and Cadastre-Denmark (now with Danish National Space Center) was asked by the Department of Surveying and Mapping Malaysia (JUPEM) to perform a nationwide airborne gravity survey. This as part of an ambitious plan to establish a modern GPS based height system integrating a precise geoid model and a real time kinematic GPS positioning system. This would allow the GPS user to get precise heights above sea level at the 'push of a button' everywhere in the country.

The airborne survey covered approximately 500,000 km² at a 5 km line spacing, see . It was flown between September 2002 and May 2003, a total of 530 hours airborne time. Tropical conditions with high temperatures and humidity causing unstable weather to build up almost every day together with a rather mountainous terrain peaking at more than 4000 meters makes it a challenging task to do airborne gravimetry here. Time constraints forcing us to fly almost every day no matter the weather conditions added to the challenge of getting quality data out of our efforts.

The crossover analysis in Table 4 should be seen in this light; 2.6 mGal RMS difference from almost 2000 line crossing points indicating a noise level around 1.8 mGal. This is to our opinion a very satisfactory result and demonstrates that airborne gravimetry is truly operational for regional gravity field mapping also under diverse and difficult conditions like in Malaysia.

Table 4: Crossover error statistics for the Malaysian and the Mongolian surveys (units: mGal)

Data set	Number of cross	RMS misfit
Malaysia	1965	2.6
Mongolia	504	3.1

Table 5: Airborne gravimetric geoid compared to global models (units: meters)

Global model	Standard dev. of difference
GGM02S to 160	1.11
EGM96 to 360	1.08
EIGEN-CG03 to 360	0.57

It was also the task of Geodynamics Department to compute a best possible geoid model based on the airborne data in combination with some terrestrial data, GRACE based geo-potentials models and the SRTM digital elevation model (Shuttle Radar Topography Mission, see <http://srtm.usgs.gov>). Table 5 shows the final geoid model compared to different global models over Sabah province in

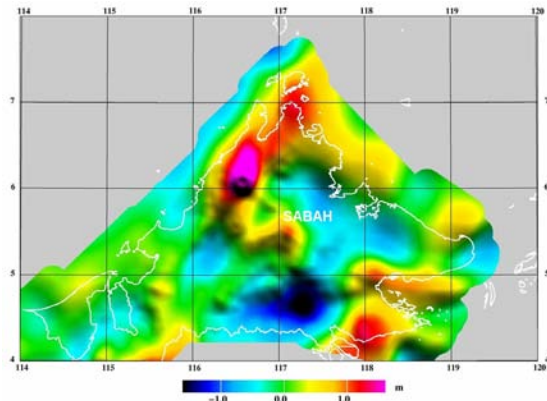


Figure 3. Difference between airborne geoid and the EIGEN-CG03 global model to degree 360

Eastern Malaysia (Malaysian part of Borneo Island). The residual is at the meter level for most models and even for the newest high-resolution model the EIGEN-CG03 to degree 360 the residual signal is 57 cm. This residual is due to shortcomings in the global models and underlines the need to collect more gravity data in many areas in order to produce geoid models of a quality suitable for GPS leveling. 5 centimeter precision or better is a typical requirement. The difference between the airborne geoid and the EIGEN-CG03 geoid is also portrayed in Figure 3 and it is seen that also in the important near coastal zone the global model has significant problems. This will be the

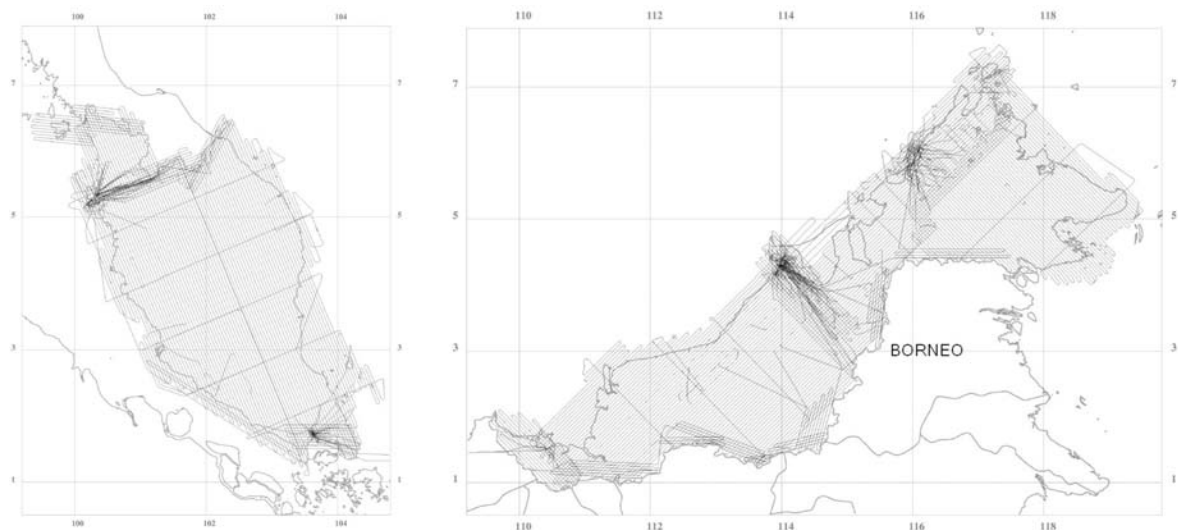


Figure 4. Ground track pattern for the Malaysia survey. The Peninsula or Western Malaysia to the left and Malaysian Borneo to the right. Flight lines could be extended over Thai and Brunei territory whereas it was not possible to get permission to enter into Indonesian or Singaporean airspace. A total of 530 hours were flown during the months of October to November 2002 and February to May 2003. Flight lines were in general planned to follow main topographic features, e.g. along a mountain ridge instead of crossing it in order to reduce the number of climbs or descents. The location of suitable airports also played a major role for the overall track layout

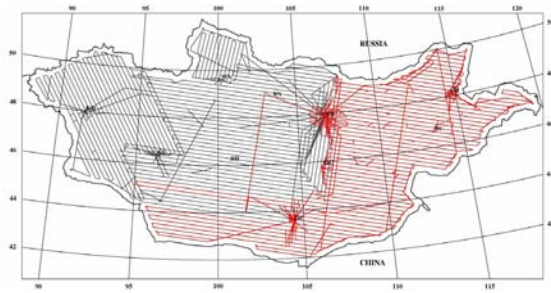


Figure 5. Ground track pattern for the Mongolian survey. The distance from east to west is approximately 2600 km. 2004 (black), 2005(red)

case in many other areas around the world and airborne gravimetry offers a fast and economic way of collecting new gravity data to supplement existing surface data and global models.

The Mongolian survey was done in the autumn months of 2004 and 2005 as this period is the most stable with mainly clear sky and not too much wind. The survey covered all of Mongolia, 1.6 million square kilometers, at a 10 nautical miles line spacing. Only a 25 km no-fly zone along the border to neighboring Russia and China was omitted. The project was a joint effort between Mongolian Administration of Land Affairs (ALaGAC), US National Geospatial-Intelligence Agency (NGA) and Danish National Space Center (DNSC). The aim was to establish a modern GPS based height system for Mongolia and to make a contribution to the soon-to-be-released geo-potential model EGM06. NGA provided the funding for the survey and DNSC was responsible for the airborne survey in cooperation with local partners. The slightly higher noise level for the Mongolian data compared to the Malaysian survey is ascribed to the different aircraft used for the two surveys and to the presence of mountain waves in Mongolia. Mountain waves are a wind generated and relatively long-wave motion of the air in mountainous areas.

Conclusion

Airborne gravimetry with a LaCoste & Romberg airborne/marine gravimeter has over the years proved to be a very reliable concept for acquiring quality gravity data for various geodetic applications. The survey in Malaysia showed that the method is also applicable under demanding conditions like in tropical and mountainous areas.

The new platform modeling approach to correct for platform off-level errors seems to yield virtual bias free data and thus eliminates the need for a bias

crossover adjustment of the data. It also means that single or coarse distributed lines can be utilized to validate existing data sets, e.g. old marine data sets.

References

- Andersen O. B. and P. Knudsen: Global Marine Gravity Field from the ERS-1 and GEOSAT Geodetic Mission Altimetry, *J. Geophys. Res.*, **103(C4)**, 8129-8137, 1998.
- Brozena, J. M.: The Greenland Aerogeophysics Project: Airborne gravity, topographic and magnetic mapping of an entire continent. In: *From Mars to Greenland: Charting Gravity With Space and Airborne Instruments*. IAG symposium series 110, pp. 203-214, Springer Verlag, 1991.
- Childers, V. A., D. C. McAdoo, J. M. Brozena, S. W. Laxon: New gravity data in the Arctic Ocean: Comparison of airborne and ERS of gravity. *Journal of Geophysical Research*, vol. 106, B5, pp 8871-8886, 2001.
- Czompo, J.: Airborne Scalar Gravimetry System Errors in the Spectral Domain. *Ph. D. Thesis, UCGE No 20067, Department of Geomatics Engineering, The University of Calgary, Canada, 1994.*
- Forsberg, R., A. V. Olesen and K. Keller: Airborne Gravity Survey of the North Greenland Shelf 1998. *Kort - og Matrikelstyrelsen Technical Report no. 10, 1999.*
- Forsberg, R. and F. Rubek: Gravity and GPS measurements in Greenland 1997. *Survey and data processing report, Office of Geodynamics, National Survey and Cadastre (KMS), Denmark, 1998.*
- Glennie, C.: An Analysis of Airborne Gravity by Strapdown INS/DGPS. *Ph.D. Thesis, UCGE Report #20, Dept. of Geomatics Engineering, The University of Calgary, 1999*
- Knudsen P., R. Forsberg, O. Andersen, D. Solheim, R. Hipkin, K. Haines, J. Johannessen & F. Hernandez. The GOCINA Project - An Overview and Status. *Proc. Second International GOCE User Workshop "GOCE, The Geoid and Oceanography"*, ESA-ESRIN, March 2004, ESA SP-569, June 2004.
- LaCoste, L. B. J.: Measurement of Gravity at Sea and in the Air. *Reviews of Geophysics*, 5, 477-526, 1967.
- LaFehr, T.R. and L.L. Nettleton: Quantitative evaluation of a stabilized platform shipboard gravity meter, *Geophysics*, 32, 110-118, 1967.
- Olesen A. V., R. Forsberg, A. Gidskehaug: Airborne gravimetry using the LaCoste & Romberg gravimeter – an error analysis. In: M.E. Cannon and G. Lachapelle (eds.). *Proc. Int. Symp. on Kinematic Systems in Geodesy, Geomatics and Navigation*, Banff, Canada, June 3-6, 1997, Publ.Univ. of Calgary, pp. 613-618, 1997
- Olesen, A.V: Improved Airborne Scalar Gravimetry for Regional Gravity Field Mapping and Geoid Determination.. *Technical Report no 24, Kort og Matrikelstyrelsen., Copenhagen 2003.*
- Strykowski, G. and R. Forsberg: Processing of marine gravity measurements off East Greenland: *Contract report for NUNAOIL A/S. Geodetic Division, National Survey and Cadastre of Denmark, 1995.*
- Valliant, H.: The LaCoste & Romberg air/sea gravimeter: an overview. In: *CRC Handbook of Geophysical Exploration at Sea*, Boca Raton Press, 1992.

Gravity field modelling from airborne gravimetry using fundamental solutions of Laplace's equation in Cartesian coordinates

B.A. Alberts, R. Klees and P. Ditmar

Delft Institute of Earth Observation and Space Systems (DEOS),

Delft University of Technology, Kluyverweg 1, PO box 5058, 2600 GB Delft, The Netherlands.

Abstract. We present a new approach to reduce edge effects in regional gravity field modelling, which occur when fundamental solutions of Laplace's equation in Cartesian coordinates are used to parameterize the disturbing potential. The base functions implicitly assume periodicity of the gravity signal, which results in highly oscillating distortions in the adjusted gravity disturbances near the boundaries of the area. These distortions cause long-wavelength errors in the geoid solution over the whole area. A new method to solve this problem is introduced, which performs better than those tried earlier, such as zero-padding or data tapering. We demonstrate the performance of the developed methodology using airborne gravity data acquired during the CHICAGO survey performed by GFZ Potsdam, offshore the coast of Chile. To improve the results, we estimate nuisance parameters, such as scaling factors and biases, simultaneously with the gravity field parameters.

Keywords: Airborne gravimetry, regional gravity field modelling, edge effects, gravimeter scaling factors

1 Introduction

One of the most suitable techniques to determine the regional gravity field with high accuracy is airborne gravimetry, since it can provide accurate gravity data in a fast and efficient way. To improve the accuracy and resolution of regional gravity field solutions, we are developing a new approach for the processing of airborne gravity data. The approach combines several individual pre-processing steps, such as band-pass filtering, gridding, and bias and trend removal, with the estimation of the gravity field parameters. The methodology was described in detail by Alberts et al. (2005); a short summary is given in section 2. The performance of this approach in terms of RMS errors is similar to more traditional

methods such as least-squares collocation (see Klees et al., 2005), but the solution may be affected by strong artifacts near the boundaries of the area. In Alberts et al. (2006) several approaches to reduce these edge effects were investigated. Among these methods were zero-padding and data-tapering. The best results, however, were obtained when least-squares (LS) prediction was used to estimate gravity disturbances outside the data area. Nevertheless, the solution still suffered from long-wavelength geoid errors. Therefore, a new method to reduce edge effects is proposed, which is described in section 3. Furthermore, the results are compared with previously investigated approaches as described in (Alberts et al., 2006).

The developed approach is used to process airborne gravity data, acquired during the CHICAGO survey (Meyer and Pflug, 2003), which was performed in 2002 near the coast of Chile. Gravity disturbances are directly computed on a grid at ground level from the data along the tracks at flight level. A proper choice of scaling factors of the airborne gravimeter plays an important role in the pre-processing. Instead of using the initial laboratory values, these parameters are estimated per profile, together with bias and gravity field parameters. The data processing strategy and the results are discussed in section 4. The paper concludes with a short summary and an outlook to future work.

2 Representation of the gravity field

For the representation of the disturbing potential we use a linear combination of harmonic functions, that are fundamental solutions of Laplace equation in Cartesian coordinates (Alberts et al., 2005):

$$T(x, y, z) = \sum_{l=-L}^L \sum_{m=-M}^M C_{lm} \varphi_l(x) \varphi_m(y) e^{-\gamma_{lm}z}, \quad (1)$$

where C_{lm} are the unknown coefficients. The base functions are given as

$$\varphi_l(x) = \begin{cases} \cos \frac{2\pi lx}{D_x}, & l \geq 0 \\ \sin \frac{2\pi |l|x}{D_x}, & l < 0 \end{cases}$$

$$\varphi_m(y) = \begin{cases} \cos \frac{2\pi my}{D_y}, & m \geq 0 \\ \sin \frac{2\pi |m|y}{D_y}, & m < 0 \end{cases}$$

and

$$\gamma_{lm} := 2\pi \sqrt{(l/D_x)^2 + (m/D_y)^2},$$

where D_x and D_y are the lengths of the computation area in the x and y directions. By applying the z -derivative to Eq. (1), a linear relationship is obtained between observed gravity disturbances T_z and the coefficients C_{lm} , where a small difference between the radial direction and the z -direction is neglected, i.e. $\partial T/\partial z \approx \partial T/\partial r$. The functional model for this linear relation may be written as a standard Gauss-Markov model

$$\mathbf{y} = \mathbf{A}\mathbf{x} + \mathbf{e}; \quad E\{\mathbf{e}\} = 0; \quad D\{\mathbf{e}\} = \mathbf{Q}_y, \quad (2)$$

where \mathbf{y} is the $n \times 1$ observation vector containing the gravity disturbances, \mathbf{e} is the vector of random observation noise, \mathbf{Q}_y is the noise covariance matrix and \mathbf{x} is the $r \times 1$ vector of unknown coefficients. These coefficients can be solved for using least-squares techniques.

3 Edge effect reduction

3.1 Controlled area extension

The base functions used in the representation of the gravity potential, Eq. (1), are periodic in the horizontal directions, whereas the gravity signal is not. Inequality of gravity at the opposite boundaries of the computation area result in strong oscillations, that propagate into the area. In Alberts et al. (2006) five approaches to reduce the edge effects were investigated. Among these methods, the best results were obtained when least-squares (LS) prediction was used to estimate gravity disturbances outside the data area. Due to the nature of LS prediction, the signal gradually approaches zero for distances larger than the correlation length. Unfortunately, the resulting gravity disturbances at ground level still showed some artifacts near the boundaries of the original area. Furthermore, the geoid heights were distorted

by long-wavelength errors which affected the whole area. Therefore a new approach to reduce edge effects, called 'controlled area extension', will be discussed here. As mentioned in section 2, the area size is determined by the parameters D_t (with t being either x or y). Increasing the parameter D_t by Δ_t , makes the estimated signal periodic on the interval $D_t + \Delta_t$, whereas data are only available on the interval D_t . This simple modification reduces edge effects significantly, especially for larger Δ_t . However, an increase of Δ_t also results in an increase of the condition number, i.e. the system of normal equations becomes unstable. Thus, the optimal value of the parameter Δ_t has to be found. Testing showed that an extension of the area by at least twice the smallest wavelength to be estimated, which is set by L and M , already provides a sufficient reduction of the edge effects, when the system of normal equations is stabilized using regularization.

3.2 Simulation study

To assess the performance of the controlled area extension, we used the same test setup as in Alberts et al. (2006). Gravity disturbances were generated from GPM98b (Wenzel, 1998) at an altitude of 4000 meters for an area of 400 km \times 400 km, with a grid spacing of 5 km. The frequency content was limited to the spherical harmonic degrees 360 to 1800. Using these noise-free data, coefficients C_{lm} were estimated, and then used to compute disturbing potential values and gravity disturbances at ground level. The results of the new approach are compared with the case when no action is taken to reduce edge effects and with the method that previously provided the best results: extension by LS prediction. For the controlled area extension, the parameter Δ_t was set equal to 25 km, which equals twice the smallest wavelength to be estimated. To stabilize the solution, Tikhonov regularization was applied with variance component estimation to determine the regularization parameter (e.g. Koch and Kusche, 2002). The errors are shown in figures 1 and 2, and statistics are given in tables 1 and 2 for the computed gravity disturbances and geoid heights, respectively. Both figures and statistics show a large improvement with respect to the previous results. Especially the geoid height errors at ground level show that the results are no longer affected by long-wavelength errors in the whole area. Only near the boundaries of the area some errors of a few centimeters remain.

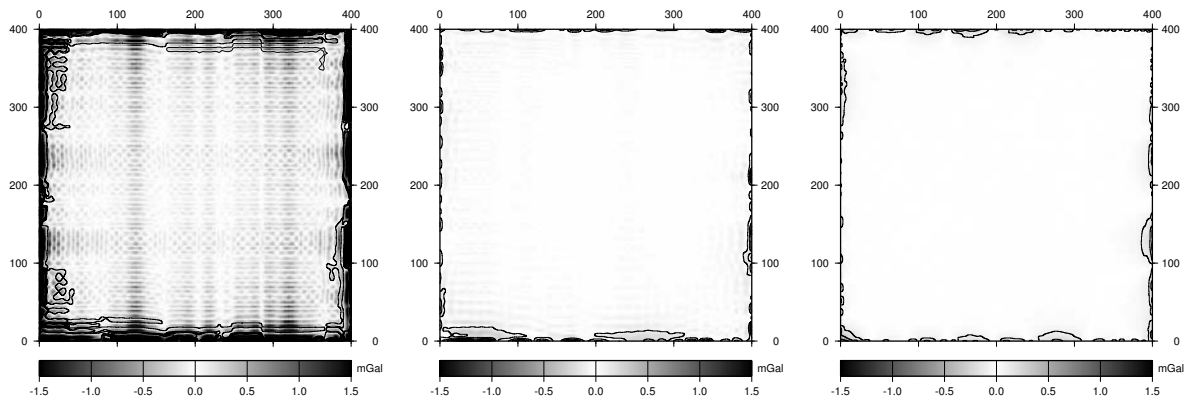


Figure 1. Gravity disturbance errors at ground level. From left to right: no reduction of edge effects, extension by LS prediction and controlled area extension [1 mGal contour lines].

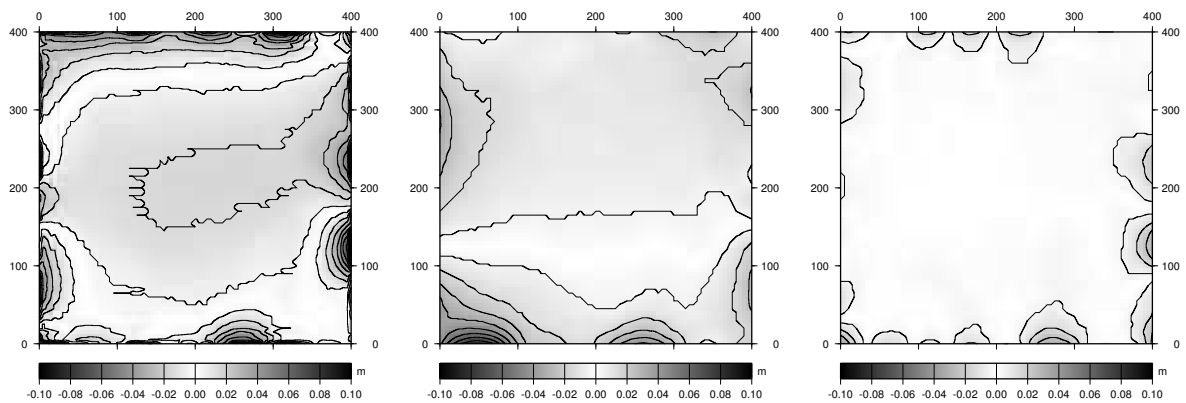


Figure 2. Geoid height errors at ground level. From left to right: no reduction of edge effects, extension by LS prediction and controlled area extension [1 cm contour lines].

Table 1. Statistics of gravity disturbance errors [mGal] at ground level.

Method	Min	Max	RMS
no edge effect reduction	-10.24	15.94	1.12
extension by LS prediction	-1.23	1.95	0.11
controlled area extension	-0.85	0.75	0.07

Table 2. Statistics of geoid height errors [m] at ground level.

Method	Min	Max	RMS
no edge effect reduction	-0.119	0.115	0.017
extension by LS prediction	-0.085	0.036	0.011
controlled area extension	-0.035	0.045	0.005

4 Airborne gravity processing

4.1 Data description

The data for which the performance of the developed methodology is tested was acquired in 2002 by GeoForschungsZentrum Potsdam (GFZ) during the CHICAGO campaign in Chile (Meyer and Pflug, 2003). The area is of particular interest due to the Peru-Chile trench; a subduction zone west of the South American continent. As a result, strong gravity gradients are observed. The survey consisted of 13 off-shore flights near the coast of Chile and 4 flights above the Chilean mainland, resulting in 27 off-shore profiles (of which 24 were used in the computations) and 12 on-shore profiles. All off-shore flights, except one because of an island, were performed at about 300 meters altitude, whereas the flights above the

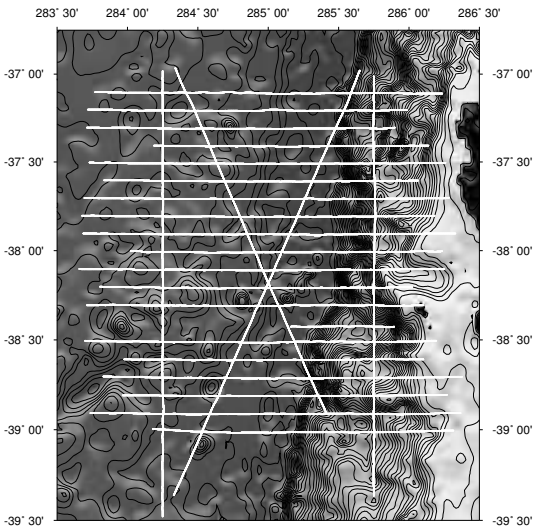


Figure 3. The off-shore flights tracks and the main bathymetric features in the investigation area.

mainland were flown at an altitude of 2100 - 3000 meters. To minimize the effect of downward continuation, we only use the data from the off-shore profiles for this study. The flight tracks and the main bathymetric features of the area are shown in figure 3.

4.2 Estimation of nuisance parameters

The gravimeter used during the survey was a LaCoste & Romberg air/sea gravity meter, which consists of a highly damped, spring-type gravity sensor mounted on a gyro-stabilized platform. Because of the high damping, the motion of the gravity meter beam can be described by the following differential equation (Valliant, 1992)

$$g + \ddot{z} + k\dot{B} - cS = 0, \quad (3)$$

where g denotes gravity, \ddot{z} the vertical acceleration, \dot{B} the beam velocity, S the spring tension, and k and s are scaling factors. This equation is just an approximation and correction terms, known as cross-coupling, are applied as well. The scaling factor k , which is usually called k-factor, and the scaling factor c (or spring tension calibration factor) may be determined by laboratory calibration. An alternative method to determine the k-factor is given in Olesen et al. (1997). Here we propose to estimate the scaling factors simultaneously with the gravity parameters, by incorporating beam velocities and/or spring tension values in the functional model. The functional model for estimating one k-factor for the whole data

set can be written as

$$\mathbf{y} = \mathbf{A}\mathbf{x} + \mathbf{B}\delta k + \mathbf{e}; \quad D\{\mathbf{e}\} = \mathbf{Q}_y, \quad (4)$$

where $\mathbf{B} = (\dot{B}_1 \dot{B}_2 \dots \dot{B}_n)^T$ and δk is the correction to the k-factor k_p that was initially used in the pre-processing, i.e. the estimated k-factor \hat{k} is obtained as $\hat{k} = k_p + \delta k$. The model can easily be extended for the estimation of one k-factor per profile. The same holds for including the calibration factor or bias and tilt parameters (see also Alberts et al., 2005).

4.3 Results

Gravity disturbances were computed on a grid at ground level from 85000 pre-processed observations along the tracks at flight level. For the parametrization of the potential 624 base functions were estimated. In the first test the initial values of the k-factor ($k = 39.0$) and calibration factor ($c = 1.014$) were used. The result is shown in figure 4. Next we estimated one k-factor and one calibration factor for the whole data set. This yielded values of $\hat{k} = 39.121 \pm 5 \cdot 10^{-3}$ and $\hat{c} = 1.01531 \pm 1 \cdot 10^{-5}$. The estimated k-factor deviates only slightly from the original value and this difference has little effect on the gravity solution: the maximum effect is around 3 mGal. The difference in c is also small, but because spring tension values are between 9000 and 12000 cu, a non-negligible bias is introduced. When we estimate one k-factor and one calibration factor per profile the differences with respect to the initial values are larger, which is demonstrated in figures 6 and 7. For some profiles, the variation of the k-factors results in a change in gravity with respect to the original solution of about ± 15 mGal, whereas the variation of the calibration factor has an effect on the solution of -10 to +40 mGal. The resulting gravity disturbances are shown in figure 5. When compared to the results obtained with the initial values (cf. figure 4), it is clear that the solution of figure 5 is much smoother. Note that the obtained values of the calibration factors should not be interpreted as new instrument values, but as corrections that result from inconsistencies in the spring tension data.

When the estimation of calibration factors is combined with the estimation of bias parameters, we found that these parameters are highly correlated (almost equal to -1), i.e. they cannot be estimated simultaneously. When bias parameters are estimated instead of spring tension calibration factors, nearly the same results are obtained. Differences between both solutions were below 1 mGal for the whole area. The estimated bias parameters (cf. figure 8)

show the same pattern as the calibration factors in figure 7. Correlations computed between k -factors and bias parameters, and between k -factors and calibration factors are much smaller (below 0.5).

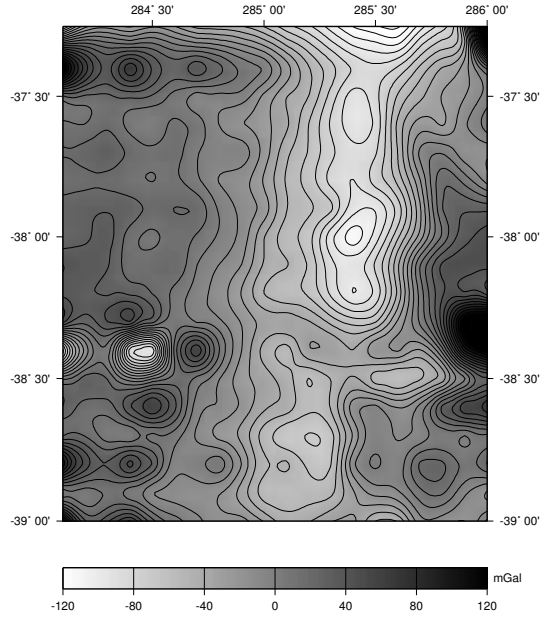


Figure 4. Gravity disturbances at ground level using the initial scaling factors.

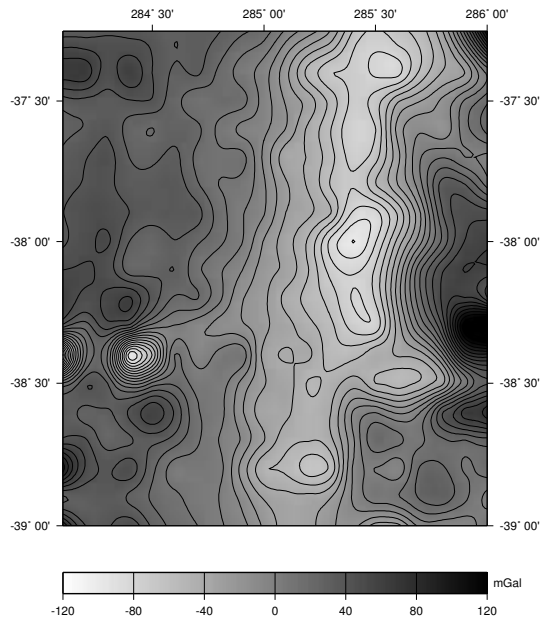


Figure 5. Gravity disturbances at ground level. Scaling factors k and s were estimated per profile.

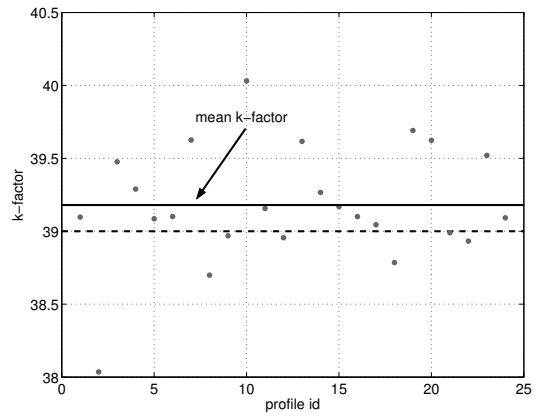


Figure 6. Estimated k -factors per profile. The dashed line shows the initial value.

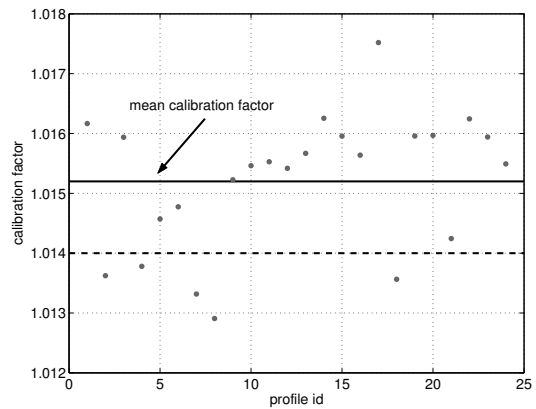


Figure 7. Estimated spring tension scaling factors per profile. The dashed line shows the initial value.

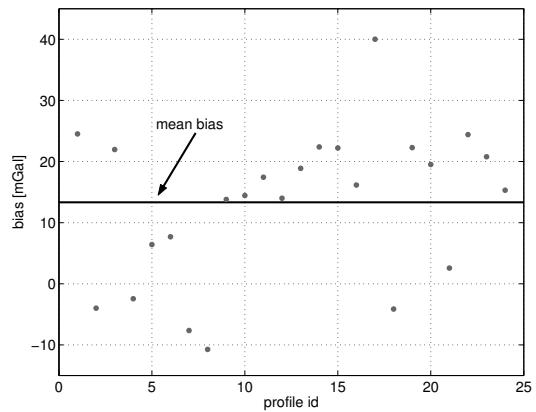


Figure 8. Estimated biases per profile, multiplied by -1 to show the similarity to figure 7.

5 Summary and outlook

In this paper we introduced a new method to reduce edge effects and compared the results with solutions obtained in a previous study. This new method, which uses a controlled extension of the computation area, reduces edge effects much more efficient, especially in terms of geoid heights. The developed methodology for airborne gravity data processing was used to process data acquired during the CHICAGO campaign, performed by GFZ Potsdam. Nuisance parameters, such as scaling factors and bias parameters, were estimated simultaneously with gravity field parameters. The estimated scaling factors show significant changes with respect to the preset values, leading to a smoother gravity field solution. In future work we will validate the results using ground truth data and make a comparison with other approaches such as least-squares collocation.

Acknowledgements. We are grateful to GFZ Potsdam for providing the airborne gravity data. We thank J. Neumayer (GFZ) and U. Meyer (BGR) for their help on the gravity data pre-processing and G. Xu (GFZ) for the GPS data processing.

References

- Alberts BA, Klees R, Ditmar P (2005) *A new strategy for processing airborne gravity data*. In: Jekeli C, Bastos L, Fernandes J (Eds.) Proc. IAG International Symposium on Gravity, Geoid and Space Missions 2004 (GGSM2004), Porto, Portugal, pp. 161-166.
- Alberts BA, Ditmar P, Klees R (2006) *A new methodology to process airborne gravimetry data: advances and problems*. In: Tregoning P, Rizos C (Eds.) Proc. Dynamic Planet 2005 - Monitoring and Understanding a Dynamic Planet with Geodetic and Oceanographic Tools, Cairns, Australia, pp. 251-258.
- Klees R, Marchenko AN, Alberts BA, Wittwer T, Ditmar P (2005) *Comparison of various methods for the inversion of airborne gravimetry data*. Submitted to the Proc. Dynamic Planet 2005 - Monitoring and Understanding a Dynamic Planet with Geodetic and Oceanographic Tools, Cairns, Australia.
- Koch KR, Kusche J (2002) *Regularization of geopotential determination from satellite data by variance components*. J Geodesy 76, pp. 259-268.
- Meyer U, Pflug H (2003) *CHICAGO - Chilean Aerogeophysical Observations - Survey Report*. Scientific Technical Report STR03/12, GeoForschungsZentrum Potsdam.
- Olesen AV, Forsberg R, Gidskehaug A (1997) *Airborne gravimetry using the LaCoste & Romberg gravimeter - an error analysis*. In: Cannon ME and Lachapelle G (Eds.) Proc. International Symposium on Kinematic System in Geodesy, Geomatics and Navigation, Banff, Canada, June 3-6, 1997, pp. 613-618.
- Valliant HD (1992) *The LaCoste & Romberg air/sea gravimeter: an overview*. In: CRC Handbook of Geophysical Exploration at Sea, 2nd edition, Hydrocarbons. CRC Press.
- Wenzel G (1998) *Ultra high degree geopotential models GPM98A, B and C to degree 1800*. Proc Joint Meeting International Gravity Commission and International Geoid Commission, 7-12 September 1998, Trieste, Italy

Gravity-Lidar Study for 2006: Refined Gravity Field For the North-Central Gulf of Mexico

D.R. Roman and Y.M. Wang
National Geodetic Survey, NOAA, Silver Spring MD 20910 USA

J.M. Brozena and V.A. Childers
Marine Physics Branch, NRL, Washington DC 20375 USA

D.L. Rabine, S.B. Lutcke and J.B. Blair
Laser Remote Sensing Branch, NASA GSFC, Greenbelt MD 20771 USA

S.A. Martinka and M.A. Hofton
University of Maryland - University Campus, College Park MD 20742 USA

Abstract. To determine a more accurate geoid model for North America, several refinements must occur in theory and data holdings. This paper focuses on the improvements to the data to provide a consistent, seamless gravity field for such a geoid model, particularly in the poorly covered littoral regions. A LaCoste-Romberg Air-Sea Gravimeter II from the Naval Research Laboratory was loaded onto the NOAA Citation II aircraft to collect data in the northern Gulf of Mexico region in January 2006. An Applanix IMU was mounted onto the gravimeter to provide information about aircraft movement in addition to the dual GPS receivers and antennas. NASA's Laser Vegetation Imaging Sensor was also mounted to collect lidar profiles nadir to the aircraft flight lines. Data were collected in 41 north-south lines spaced at 10 km and at 10.5 km altitude. Each was 500 km long; hence, the covered region is 400 km by 500 km. Individual flights were processed for all corrections, and a 420 second filter was applied to dampen out most of the noise. The resulting profiles agree at crossovers at about 4 mgal RMS, which indicates 3 mgal accuracy along the profiles. The resulting grid of gravity compares very favorably with upward-continued surface gravity. The differences appear to be related to either geophysical or oceanographic sources and represent a potential improvement in resolving ambiguities between mean sea surface and geoid models. Further refinements will be made when GPS/IMU data are processed and a comparison is made with the LVIS data and an available dynamic topography model.

Keywords. Gravimetric geoid, airborne gravimetry, lidar, ocean dynamic topography, datums.

1 Introduction

Coastal regions of the northern Gulf of Mexico remain a priority for understanding the complex interactions between sea and land. A study area encompassing the coastal regions of the states of Florida, Alabama, Mississippi, and Louisiana was selected to coincide with a VDatum (NOAA 2006) model being developed for the same region. VDatum enables the user to transform between various oceanographic and terrestrial datums. It has a geoid model built in as the primary mechanism for transforming between ellipsoidal and orthometric heights. The Gravity-Lidar Study for 2006 (GLS06) complemented this VDatum study by refining the gravimetric geoid model and obtaining lidar profiles of the instantaneous sea surface for later comparison.

In addition to the VDatum tool, a model of the Mean Dynamic Topography (MDT) is also available (Patchen 2006) to account for the expected differences between Mean Sea Surface Heights (MSSH) and the geoid. The combination of geoid heights, MDT, and VDatum-derived tidal surfaces would be compared to the lidar-observed sea surface at the time of the gravity observations. The expected level of agreement is about decimeter as a result of a number of factors. One of these is the longer baselines associated with the kinematic GPS solutions for the aircraft's position. Another relates to ambiguities in resolving the off-level correction for the gravimeter. The desire is to make the aerogravity as error-free and internally consistent as possible, particularly at longer wavelengths that more directly impact geoid height models. Then, they can be used to evaluate other sets of data.

The aerogravity from these flights will be used to ensure a seamless transition of the gravity field from onshore through far offshore regions. Such a consistent gravity field would reduce artifacts in the existing gravity data and fill in coverage gaps in the near shore environment where shipborne and altimetric anomalies are lacking. A gravimetric geoid height model developed from such data would be more consistent in testing available datum transformations and observed heights.

In turn, the geoid height model can be compared at Tidal Bench Marks (TBM's) where the height above the North American Vertical Datum of 1988 (NAVD 88) is known (Zilkoski *et al.* 1992). Such an analysis would enable the estimation of the absolute errors in NAVD 88 for the first time. This would directly benefit Height Modernization (Daley *et al.* 1998) efforts in that region intended to better define the vertical reference system in the United States. This should result in better estimates of flooding potential due to storm surge, tsunamis, etc.

2 Observation Campaign

Forty-One (41) north-south profiles were flown that were designed to begin 50-100 km inland to ensure coverage in relatively stable interior regions (Figure 1). These profiles were to extend several hundred kilometers offshore to reach oceanic regions where altimetric anomalies from GSFC00.1 (Wang 2001) are fairly reliable (generally with depths greater than 500 m). In the generation of gravimetric geoid models for the U.S., altimetric anomalies are usually excluded inside the 500 m depth curve (Smith and Milbert 1999, Smith and Roman 2001, Roman *et al.* 2004). Hence, these aerogravity profiles represent the only other source of data in that region aside from shipborne tracks. Eight east-west tracks were flown to provide sufficient crossover analysis.

The aircraft utilized for this study was a Cessna Citation II made available by the National Oceanic and Atmospheric Administration (NOAA) Airborne Operations Center.

Airborne Tracks and NGS Database Gravity Anomalies Over the Gulf of Mexico

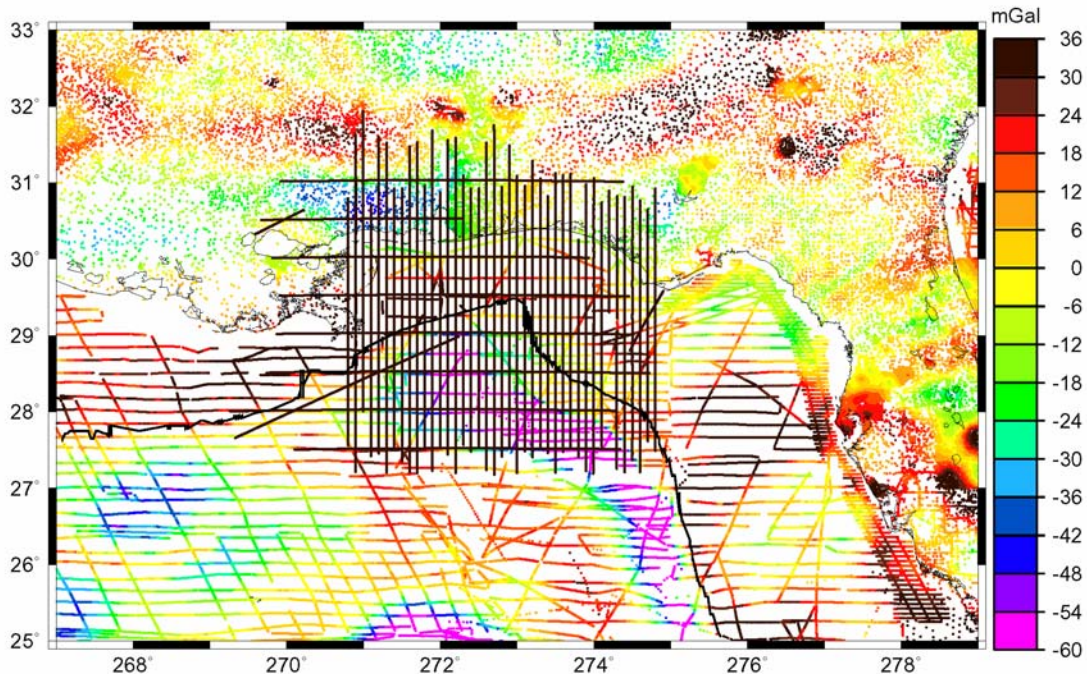


Figure 1. Available terrestrial and shiptrack point gravity data are shown in colored dots. Overlain are the 500 m depth contour (parallel to the shoreline) and the actual flight legs where aerogravity and lidar data were collected. Note the gaps in coverage near shore.

The aircraft is equipped with two GPS antennas and receivers. A Universal Avionics Flight Management System (FMS) and Applanix AV-410 Inertial Measurement Unit (IMS) resolved aircraft accelerations for the gravity observations. The Naval Research Laboratory (NRL) placed their gravimeter in the rear of the aircraft and mounted the IMU directly to its frame. Loading the gravimeter and IMU in the baggage compartment, located nearly between the engines provided for more stability, while keeping a reasonable lever arm to the GPS receivers. Sea surface heights were measured by the Laser Vegetation Imaging Sensor (LVIS) from NASA GSFC's Laser Remote Sensing Branch (Blair *et al.* 1999) for later comparison.

For flight stability, the profiles were flown at 500 km/h at an elevation of 35,000 feet (approximately 10.5 km). The profiles were spaced 10 km apart to minimize aliasing and to provide a consistent signal across track as well as along track. The main north-south profiles were flown in pairs (one heading south and another heading back north). As the profiles were 500 km long, this kept total flight times below 3.5 hours, the aircraft's endurance limit. Several of the east-west profiles were flown individually due to transit times. All profiles were collected in about a month's time from about mid-January to mid-February to minimize the impact of adverse weather during the more tropical times of the year.

3 Data Processing

The NRL team reduced the aerogravity data following standard methodology (Childers *et al.*, 1999). A filter using a frequency-domain cosine-taper with half-amplitude point at 420s was selected. It best retained the expected signal content while providing sufficient short-wavelength noise attenuation to reduce crossover RMS to 4 mgals and, therefore, the along track signal to 3 mgals. This is more filtering than has been required with previous surveys and the cause of that is still under investigation.

Figure 2 shows the free-air anomaly gravity field created from the filtered profiles. Four of the profiles were adjusted for bias problems based on crossover analysis. However, most profiles remain unadjusted. This signal compares very favorably with a similar set of aerogravity data previously collected by NRL at very low altitudes for this same study region. The commonality of the two different sets of data support the approach used here to collect high altitude data as a means of rapidly collecting a gravity field sufficient for geodetic analysis.

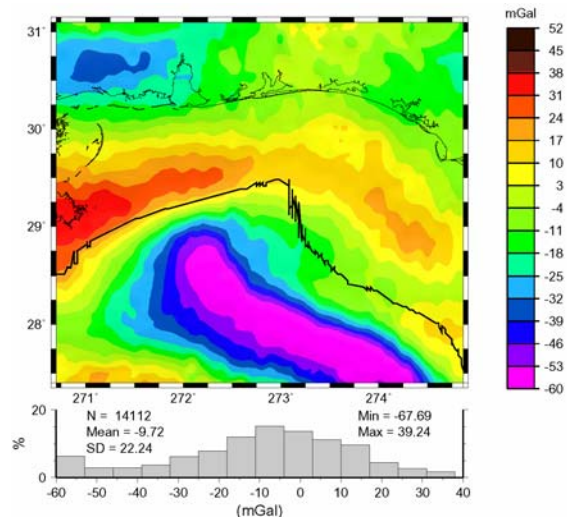


Figure 2 Grid at two arc-minutes of aerogravity profiles collected at 10.5 km height in the North-Central Gulf of Mexico region. Created using 41 N-S and 8 E-W profiles filtered at 420 seconds with 4 profiles adjusted for bias.

The aerogravity provide a consistent reference from which to determine if NGS surface gravity (Figure 1) may have potential errors of omission or commission. Assuming uniform data collection and processing, the aerogravity will ensure consistency in the gravity field from onshore to offshore.

Figure 3 shows the difference from that in Figure 2 with a grid of the analytically upward-continued (Eq. 6-75 in Heiskanen and Moritz 1967) surface data. There are still some track-related features, however, significant features with lateral extents across multiple survey lines can be observed.

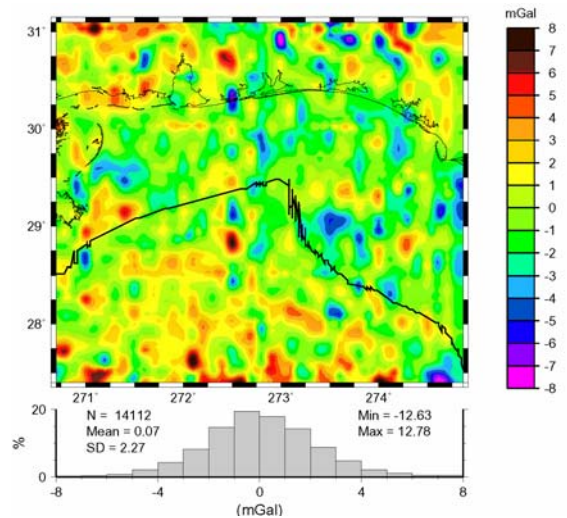


Figure 3 Grid of residual gravity anomalies produced from the total signal in Figure 2 less an upward continued NGS surface gravity data. Note the prominent positive and negative features on either side of the 500 m curve.

Some sinusoidal signal remains along the profiles, but significant large scale features can still be seen across the tracklines. In particular, note the large region of positive anomalies south of the 500 meter depth curve. North of that curve (i.e., in water shallower than 500 m), a region of negative anomalies is observed. There is a mixture of features in the onshore portions as well.

The grid shown in Figure 3 was processed using a 1D FFT with 100% padding on each side to reduce errors. The resulting pseudo-geoid grid is shown in Figure 4.

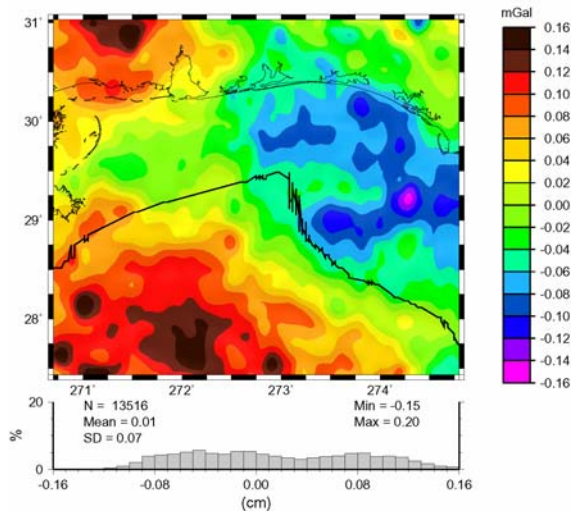


Figure 4 Residual pseudo-geoid signal derived from the data shown in Figure 3 using a 1D FFT of the Stokes function. Significant offshore features follow the 500 meter depth curve. Other features are seen over land.

As used here, the term pseudo-geoid implies the difference between the geopotential and ellipsoidal potential surfaces at 10.5 km elevation instead of on the ellipsoid where geoid heights are normally given. Since the residual gravity field implies the difference between aerogravity and existing surface gravity from the NGS database, the residual pseudo-geoid implies the change in geoid heights expected to result from use of this new data. The magnitude of the features seen in the pseudo-geoid is expected to be similar but greater at the surface than at elevation.

4 Residual Pseudo-Geoid Model Analysis

Several significant features can be observed in Figure 4. The most obvious are the decimeter magnitude offshore features near the 500 meter depth contour. These features derive from several possible sources. A first possibility is that they represent

erroneous signal in and between the altimetric and shipborne data.

The gravity data used to make the reference field derive in part from altimetric anomalies derived from the GSFC00.1 data. These data become unreliable inshore and are generally rejected in the near shore environment at depths less than 500 m. The significant contrast in signal seen around the 500 meter curve may represent the unmodeled MDT signal present in the GSFC00.1 data used to make the reference field. Comparisons with other MDT models being developed as a part of the VDatum study will be needed to refine this.

Another possible source for these differences would be errors of omission. The near shore data are much sparser in some regions. The observed differences may derive from signal lacking in the surface data and present in the airborne data. Other possibilities will also be investigated as well.

The signal seen in the northwest corner is more problematic in that it describes a difference between the airborne and terrestrial data. The consistency of the airborne data between profiles and at crossovers argues that the difference may lie in the terrestrial data. The region represents the easternmost portions of the Louisiana subsidence region (Shinkle and Dokka 2004) where the terrestrial data were collected several decades ago. Over time, most of this region has subsided but some areas may have undergone uplift. Hence, a real change in gravity field over time may have occurred. However, this is in the corner of the collection area and is not sufficiently constrained to offer a firm answer. Additional aerogravity profiles to the west and north of the region may help resolve the question.

The signal observed in the northeast corner appears more a function of the lack of coverage and the filtering algorithms. The signal there can vary based on the filtering applied. Weather and other factors (air traffic control, etc.) affected collections here and reduced crossovers and available data. Only further collection here will resolve this region.

Probably the most useful outcome for this study relates to the signal seen along the shoreline. Decimeter sized undulations can be seen along the shoreline from +0.12 m in the west to -0.10 cm in the middle and then back to zero near the east. These features represent the possible uncertainty in the geoid in the coastal regions. Given the desire for a cm-level accurate geoid to go with cm-level accurate GPS, this is unacceptable.

5 Conclusions and Future Work

Aerogravity profiles collected from onshore to off-shore have helped to identify possible problems in existing surface data coverage. The profiles were filtered in such a way as to reduce short wavelength signal likely associated with collection but still not create artificial effects at longer wavelengths. The optimal filter length was determined to be at 420s for these purposes. However, the filtering process will remain an area for further refinement in future work.

All other available data held by the National Geodetic Survey were combined and the resulting grid upward continued to flight elevation. This grid was removed from the processed aerogravity grid to create residual gravity anomalies at altitude. These data were then processed to create a residual pseudo-geoid, which was examined for features that might indicate areas of disagreement between the aerogravity data and the various forms of surface gravity data (terrestrial, shipborne, and altimetric). These features may represent previously unmodeled signal or represent an error in the existing data coverage related either to the gravity data or mean dynamic topography (MDT) models that affect altimetric anomalies.

The analysis of the gravity data will be made in conjunction with several other analyses. MDT and other tidal surface models are being developed as a part of the VDatum study. These datums can be combined with the geoid height models developed from these airborne gravity data to compare with the lidar-observed sea surface heights at the time of the gravity collections. The LVIS lidar data are being processed to develop profiles nadir to the aircraft. A direct comparison of the models to the profiles will provide decimeter-level accurate absolute error estimates of the entire system.

In turn, the geoid heights can then be compared to heights above the NAVD 88 datum at tidal bench marks to obtain NAVD 88 errors with respect to actual MSL at the same level of accuracy. This would provide the basis for further evaluating the utility of the NAVD 88 datum in coastal regions prone to storm surge and tsunamis.

Additional comparisons will also be made with gravity derived from GPS/INS. The GPS and IMU information collected during the flights will eventually be processed to generate an equivalent gravity field. Similarly developed data are also being acquired from Intermap Technologies, Inc. The intent of such comparisons would be to determine if the GPS-IMU-derived data sufficiently model the grav-

ity field for the purposes of determining a geoid height model. These data may not be as useful in the dynamic coastal regions but may prove beneficial in stable interior regions.

Lastly, the region covered by this study is approximately 400 km by 500 km. This is sufficient to compare directly with newer EGM's derived using GRACE (Tapley *et al.* 2004) data. Such comparisons will help to decide to move forward from using EGM96 (Lemoine *et al.* 1998) as a reference gravimetric model. Reduced long wavelength differences between independent data such as were collected here and from GRACE data would point to improved global and regional geoid height models.

As a final note, this study highlights the need for continued research into littoral aerogravity to supplement existing terrestrial coverage. The improvements that will likely result to geoid height models in and near the shorelines will enable the use of GPS-derived orthometric heights and a better understanding of the land-ocean interface.

Acknowledgements. This study was made possible in part by the Remote Sensing Division at NGS, which provided more than 100 hours of R&D flight hours (equivalent to about \$300,000). Additionally, funding for NRL and NASA collection and processing was covered by the NOAA Ocean Service Storm Surge Partnership Project.

References

- Blair, J. B., D. L. Rabine, and M. A. Hofton (1999). The Laser Vegetation Imaging Sensor (LVIS): A medium-altitude, digitization-only, airborne laser altimeter for mapping vegetation and topography. *ISPRS Journal of Photogrammetry and Remote Sensing*, 54, pp. 115-122.
- Childers, V.A., R.E. Bell, and J.M. Brozena (1999). Airborne gravimetry: an investigation of filtering, *Geophysics*, 64(1), 61-69.
- Daley, W.M., D.J. Baker, T.D. Garcia, N. Foster, and C.W. Challstrom (1998). National Height Modernization Study: Report to Congress, NOAA.
- Heiskanen, W.A. and H. Moritz (1967). *Physical Geodesy*. W.H. Freeman, San Francisco.
- Lemoine F.G., S.C. Kenyon, J.K. Factor, R.G. Trimmer, N.K. Pavlis, D.S. Chinn, C.M. Cox, S.M. Klosko, S.B. Luthcke, M.H. Torrence, Y.M. Wang, R.G. Williamson, E.C. Pavlis, R.H. Rapp and T.R. Olson (1998). The Development of the Joint NASA GSFC and NIMA Geopoten-

- tial Model EGM96. *NASA/TP-1998-206861*, NASA Goddard Space Flight Center, Greenbelt, Maryland, 20771 USA.
- NOAA (2006). VDatum Transformation Tool, <http://nauticalcharts.noaa.gov/csdl/vdatum.htm>
- Patchen, R. (2006). Personal communication.
- Roman, D.R., Y.M. Wang, W. Henning, and J. Hamilton (2004). Assessment of the New National Geoid Height Model, GEOID03. *Surveying and Land Information Systems*, 64 (3), 153-162.
- Shinkle, K.D. and R.K. Dokka (2004). Rates of Vertical Displacement at Benchmarks in the Lower Mississippi Valley and Northern Gulf Coast, NOAA Technical Report NOS/NGS 50, NOAA, Silver Spring, Maryland, 20910 USA.
- Smith, D.A. and D.G. Milbert (1999). The GEOID96 high resolution geoid height model for the United States, *Journal of Geodesy*, 73, pp. 219-236.
- Smith, D.A., and D.R. Roman (2001). GEOID99 and G99SSS: One arc-minute models for the United States. *Journal of Geodesy*, 75, pp. 469-490.
- Tapley, B.D., S. Bettadpur, M.M. Watkins, and Ch. Reigber, (2004). The gravity recovery and climate experiment: Mission overview and early results. *Geophysical Research Letters*, 31, L09607, doi: 10.1029/2004GL019920.
- Wang, Y.M. (2001). GSFC00 mean sea surface, gravity anomaly, and vertical gravity gradient from satellite altimeter data, *Journal of Geophysical Research*, 106, pp. 31167-31174.
- Zilkoski, D.B., J.H. Richards, and G.M. Young (1992). Results of the General Adjustment of the North American Vertical Datum of 1988, *Surveying and Land Information Systems*, 52 (3), 133-149.

Outline of a New Space-Domain Method of Forward Modelling

G. Strykowski

Department of Geodynamics

Danish National Space Center, Juliane Maries Vej 30, DK-2100 Copenhagen Ø, Denmark, Email: gs@spacecenter.dk

Abstract

The present paper outlines the main aspects of a new method of forward space-domain modeling of the gravitational attraction from known sources. Compared to the methods known from the literature—the presented method has a potential to improve decisively. Complicated mass density models (reflecting the real geology) will not increase the computational task, because, unlike in the existing methods, the field point computations are not done by integrating the source attraction for each field point, but from the pre-computed and stored mass density information. This is done only once and completely independent of the field point. A very large class of functions approximating the mass density distributions and interfaces between geological layers can be used. Expressions for higher order derivatives of the gravitational potential are automatically obtained and make use of the same stored mass density information. The mathematical formulation, based on power series expansion of the reciprocal distance function, uses a setup with local Cartesian coordinates, but is able to handle the ellipsoidal Earth's models (for positioning and for reference gravity) automatically. The quality of approximation for all derivatives of the gravitational potential is pre-defined and controlled.

The paper outlines the mathematical structure of the method and shows clearly that 'it can be done'. However, to be fully operational a good strategy for storing the integrated mass density information must be invented. The brute-force implementation of the method will not work because the dimensionality of the problem is too big.

1 Introduction

To date, the forward modelling in space-domain of the gravity and magnetic signals generated by known sources in 3D (potential fields) is based on two main

techniques: the *elementary bodies* and the *Gauss' integral formula*; see the general overview of methods in e.g. (Torge, 1989) or (Blakely, 1996).

The *elementary bodies*. The source volume Ω is approximated by a finite set of disjoint three-dimensional bodies of simple geometrical shape; *the elementary bodies*. Commonly, for each elementary body Ω_i , a constant source strength (the density ρ_i) is assumed. Furthermore, for an arbitrary field point P the potential field quantity $\Delta\chi_i$ generated by each elementary body can be described by a closed functional expression. Thus, for a given type of potential field quantity χ (e.g. the gravitational potential, the gravity disturbance, the gravity gradients ... etc.) the following is valid:

$$\chi(P) = \sum_i \rho_i \Delta\chi_i(P) \quad (1)$$

The elementary bodies are e.g. homogenous rectangular prisms (Nagy, 1966), a stack of infinitely thin laminas with a polygonal shape (Talwani and Ewing, 1960) or a polyhedron (Paul, 1974; Barnett, 1976). A number of authors have also been looking into elementary bodies with varying source strength; the exponential (Cordell, 1973; Chai & Hinze, 1988), linear (Genzwill, 1970; Holstein, 2003) or quadratic (Rao, 1990).

The Gauss' integral formula or *Gauss' divergence theorem* (Heiskanen & Moritz, 1967, sec. 1-5; Sigl, 1985, sec 6.1). This general theorem is applied twice so that the attraction of 3D-bodies bounded by planar, triangular facets is computed efficiently. The volume integration is replaced by a surface integration, which is replaced by a line integration (Petrović, 1996; Götze & Schmidt, 2002). In the present paper, this technique is viewed as a speed-up of the elementary body method for homogenous polyhedrons.

Some important common features of the existing techniques in relation to the present paper are:

- The gravitational attraction is computed from 'scratch' by source integration for each

field point.

- Limited class of mass density functions.
- Finite number of volumetric ‘building blocks’ to approximate the source. Complex models (reflecting real geology) require more elementary bodies and the increased computational task.

2 The Power Series Expansion of the Reciprocal Distance Function

Following Sigl (1985), we will start with the power series expansion of the reciprocal distance function. The derivations here are more general and involve both *the field point-domain* and *the source point-domain* (only one domain is considered by Sigl).

The basic setup is as shown on Fig. 1. We have two fixed points, P for the field point-domain Ω_P , and Q for the source point-domain Ω_Q . For simplicity, we choose the domains to be cubic and centered at the fixed points, so that the domains are characterized by one parameter; the side lengths L_P and L_Q .

Within each of the two domains we have variable points $P^*, P^* \in \Omega_P$, and $Q^*, Q^* \in \Omega_Q$. The idea is to express the reciprocal distance between the two variable points, $(r_{Q^*P^*})^{-1}$, as a power series expansion with respect to the reciprocal distance between the two fixed points, $(r_{QP})^{-1}$.

The elementary vector algebra gives $r_{QP} = |\mathbf{r}_{QP}|$:

$$\begin{aligned} r_{Q^*P^*} &= |\mathbf{r}_{Q^*Q} + \mathbf{r}_{QP} + \mathbf{r}_{PP^*}| = \sqrt{(\mathbf{r}_{Q^*Q} + \mathbf{r}_{QP} + \mathbf{r}_{PP^*})^2} = \\ &= \sqrt{(\mathbf{r}_{QP})^2 + 2\mathbf{r}_{QP}(\mathbf{r}_{Q^*Q} + \mathbf{r}_{PP^*}) + (\mathbf{r}_{Q^*Q} + \mathbf{r}_{PP^*})^2} = \\ &= |\mathbf{r}_{QP}| \sqrt{1 + \left[2 \frac{\mathbf{r}_{QP}(\mathbf{r}_{Q^*Q} + \mathbf{r}_{PP^*})}{(\mathbf{r}_{QP})^2} + \frac{(\mathbf{r}_{Q^*Q} + \mathbf{r}_{PP^*})^2}{(\mathbf{r}_{QP})^2} \right]} = \\ &= r_{QP} \sqrt{1 + q_{Q^*P^*}} \end{aligned} \quad (2)$$

where

$$\begin{aligned} q_{Q^*P^*} &\equiv 2 \frac{\mathbf{r}_{QP}(\mathbf{r}_{Q^*Q} + \mathbf{r}_{PP^*})}{(\mathbf{r}_{QP})^2} + \frac{(\mathbf{r}_{Q^*Q} + \mathbf{r}_{PP^*})^2}{(\mathbf{r}_{QP})^2} = \\ &= 2 \frac{\mathbf{r}_{QP}}{r_{QP}} \frac{(\mathbf{r}_{Q^*Q} + \mathbf{r}_{PP^*})}{r_{QP}} + \frac{(\mathbf{r}_{Q^*Q} + \mathbf{r}_{PP^*})^2}{r_{QP}^2} = \\ &= 2\mathbf{e}_{QP}(\mathbf{f}_{QQ^*} + \mathbf{f}_{PP^*}) + (\mathbf{f}_{QQ^*} + \mathbf{f}_{PP^*})^2 \end{aligned} \quad (3)$$

where $\mathbf{e}_{QP} \equiv \frac{\mathbf{r}_{QP}}{r_{QP}}$, $\mathbf{f}_{QQ^*} \equiv \frac{\mathbf{r}_{Q^*Q}}{r_{QP}}$, $\mathbf{f}_{PP^*} \equiv \frac{\mathbf{r}_{PP^*}}{r_{QP}}$

where

Thus, from eqs. (2)-(3) the reciprocal distance is:

$$\begin{aligned} \frac{1}{r_{Q^*P^*}} &= \frac{1}{r_{QP} \sqrt{1 + q_{Q^*P^*}}} = \\ &= \frac{1}{r_{QP}} \left(1 - \frac{1}{2} q_{Q^*P^*} + \frac{1 \cdot 3}{2 \cdot 4} q_{Q^*P^*}^2 - \frac{1 \cdot 3 \cdot 5}{2 \cdot 4 \cdot 6} q_{Q^*P^*}^3 + \dots \right) \\ &\approx \frac{1}{r_{QP}} \left(1 + b_1 q_{Q^*P^*} + b_2 q_{Q^*P^*}^2 + \dots + b_N q_{Q^*P^*}^N \right) \end{aligned} \quad (4)$$

i.e. approximated by a truncated (N is the truncation degree) binomial series. The convergence criterion for the binomial series is: $-1 < q_{Q^*P^*} \leq 1$

Few important general comments. Firstly, the role of the field point-domain and the source point domain is to ensure a pre-defined quality of approximation for a given truncation degree N in the approximation of the reciprocal distance function by the truncated series. Thus, the domains are not the elementary bodies.

The second comment concerns the last part of eq. (3). Introducing the unit-length vector \mathbf{e}_{QP} and the two ‘local vectors’ \mathbf{f}_{Q^*Q} and \mathbf{f}_{PP^*} (one in the source point-domain through \mathbf{r}_{Q^*Q} and scaled by the fixed distance r_{QP} , and one in the field point-domain through \mathbf{r}_{PP^*} , scaled by the fixed distance r_{QP}). Identical quantities were obtained in eq. (3) had we chosen \mathbf{r}_{Q^*Q} to be given in a local Cartesian frame of reference, LCFR, with the origo in Q and obtained from the original Cartesian frame of reference by a simple translation, and similarly for \mathbf{r}_{PP^*} which can be expressed in a local Cartesian frame of reference for the field point-domain. This splitting into the LCFRs is quite important for the method. Conversely, by introducing the LCFRs we can integrate locally the gravitational effect of possibly very detailed and local mass density information and compute its attraction locally for any point in a field point-domain.

The final comment is on the convergence. From eq. (3), the convergence criterion of eq. (4), and after some simple considerations it is valid ($|\mathbf{e}_{QP}|=1$):

$$0 \leq |q_{Q^*P^*}| \leq 2 \left(|\mathbf{f}_{QQ^*}| + |\mathbf{f}_{PP^*}| \right) + \left(|\mathbf{f}_{QQ^*}| + |\mathbf{f}_{PP^*}| \right)^2$$

which is equivalent to

$$0 \leq |q_{Q^*P^*}| \leq \left(1 + |\mathbf{f}_{QQ^*}| + |\mathbf{f}_{PP^*}| \right)^2 - 1$$

Thus, a simple and rough criterion for convergence of the binomial series is:

$$0 \leq \left(|\mathbf{f}_{QQ^*}| + |\mathbf{f}_{PP^*}| \right) \leq \sqrt{2} - 1 \quad (5)$$

By comparing with the definitions in eq. (3) the general convergence criterion of eq. (5) limits the absolute size of the cubical domains by limiting L_P and L_Q . Formally, the following is valid:

$$0 \leq |\mathbf{f}_{QQ^*}| \leq \sqrt{\frac{3}{4}} \frac{L_Q}{r_{PQ}} \quad 0 \leq |\mathbf{f}_{PP^*}| \leq \sqrt{\frac{3}{4}} \frac{L_P}{r_{PQ}} \quad (6)$$

which in combination with eq. (5) can be used to find the maximal domain size for a given r_{PQ} .

3 Relation to Physical Geodesy

In this section we will relate the mathematical formalism introduced in sec. 2 to the practical forward modelling problems in physical geodesy (Heiskanen and Moritz, 1967; Moritz, 1980). The reciprocal distance function is the fundamental kernel function for the Newtonian gravitational potential (Heiskanen and Moritz, 1967). The observable quantities of the gravitational attraction are obtained by means of linear- or linearized functionals applied to the gravitational potential (Moritz, 1980).

Unlike the method of elementary bodies (see Introduction), where finite set of volumetric building blocks is used, the proposed method addresses the source as infinitesimal mass elements. In sec 4 we will demonstrate that the class of possible mass density distributions that can be included is larger than in standard methods, see Introduction

The standard methods (the elementary bodies and the Gauss' integral formula) compute the attraction of the known sources by source integration for each field point individually. Thus, even if the new field point is in the vicinity of the old one, the computations start from scratch as if nothing was known. Conversely, the present day methods are 'memory less'. In contrast, the main idea behind the proposed method is to pre-compute and to store the information about the sources in the fixed field points P and use this information for high-quality field recovery in the associated field-point domain.

To be of practical use, the proposed technique should address the relation to the ellipsoidal Earth's model used globally both for positioning (GPS) and for the reference gravity field (GRS80). The two LCFRs, one for the field point domain, and one for the source point-domain, and associated with the fix points P and Q should be the standard local North-East-Zenith frames of reference. Thus, there is no need to switch to e.g. the ellipsoidal coordinates to relate to the ellipsoidal Earth model.

In this context, the notion of LCFR follows a standard in satellite geodesy (Seeber, 1993) relating the global body-fixed Cartesian frame of reference (GCFR, the origo in the CM of the Earth, the xy-plane in the equatorial plane, x-axis pointing towards the Greenwich meridian and the z-axis pointing to the North along the axis of rotation) and the local Cartesian frames of reference (LCFR). Forward and inverse transformations from GCFR to LCFR involve a translation, rotation and there is a change from a right-handed frame of reference to the left-handed North-East-Zenith frame of reference.

Consequently, the two LCFR are related to each other by a simple translation and rotation through GCFR. The expression for the relative rotation matrix \mathbf{R}_{QP} (from LCFR for the source point-domain to the LCFR for the field point-domain) is lengthy, but straightforward. It involves the ellipsoidal geographic coordinates and height (φ, λ, h) of both P and Q in a sequence of inverse- and forward transformations between GCFR and the two LCFR. The net result is (in the LCFR for the field point domain):

$$q_{Q^*P^*} \equiv 2 \frac{\mathbf{r}_{QP}(\mathbf{R}_{QP}\mathbf{r}_{Q^*Q} + \mathbf{r}_{PP^*})}{(r_{QP})^2} + \frac{(\mathbf{R}_{QP}\mathbf{r}_{Q^*Q} + \mathbf{r}_{PP^*})^2}{(r_{QP})^2} \quad (7)$$

and where \mathbf{r}_{Q^*Q} and \mathbf{r}_{PP^*} are in the respective LCFR.

Concerning the convergence properties of the binomial series, in sec. 2 the developed formalism was for the two LCFR that were aligned, i.e. related by a simple translation. Fig. 2 shows the setup where the two LCFR are rotated with respect to each other. For simplicity, the corresponding cubic domains are also rotated. The convergence properties for the rotated domain are the same, but it is smaller in size.

Another remark concerns the arbitrary field point P^* within the domain Ω_P associated with P . For reasons explained below, we want \mathbf{r}_{PP^*} in eq. (7) to be expressed as \mathbf{r}'_{PP^*} in a LCFR associated with P^* . This new LCFR has still the origo in P , but it is rotated with respect to P -LCFR. If \mathbf{R}_{P^*P} is a rotation matrix from P^* -LCFR to P -LCFR, eq. (7) becomes:

$$q_{Q^*P^*} \equiv 2 \frac{\mathbf{r}_{QP}(\mathbf{R}_{QP}\mathbf{r}_{Q^*Q} + \mathbf{R}_{P^*P}\mathbf{r}'_{PP^*})}{(r_{QP})^2} + \frac{(\mathbf{R}_{QP}\mathbf{r}_{Q^*Q} + \mathbf{R}_{P^*P}\mathbf{r}'_{PP^*})^2}{(r_{QP})^2} \quad (8)$$

Conceptually, after source integration (see sec. 4) the information is stored in the LCFR associated with P . Subsequently, when using the stored information it is convenient to express it in the LCFR associated with P^* , because the general structure of the scalar $q_{Q^*P^*}$ is a 2nd order polynomial of six variables:

$$q_{Q^*P^*} = \sum_{i_1, i_2, i_3, i_4, i_5, i_6=0}^2 a_{i_1, i_2, i_3, i_4, i_5, i_6} \left[(x_{Q^*})^{i_1} (y_{Q^*})^{i_2} (z_{Q^*})^{i_3} \right] \left[(x_{P^*})^{i_4} (y_{P^*})^{i_5} (z_{P^*})^{i_6} \right] \quad (9)$$

where $a_{i_1, i_2, i_3, i_4, i_5, i_6}$ is a constant [only 29 out of the possible 729 ($=3^6$) constants are non-zero] and where $\mathbf{r}_{Q^*Q} \equiv [x_{Q^*}, y_{Q^*}, z_{Q^*}]$ and $\mathbf{r}_{P^*P^*} \equiv [x_{P^*}, y_{P^*}, z_{P^*}]$. This general structure is preserved for the powers of $q_{Q^*P^*}$, see eq. (4), but for a higher maximal degree (which is twice the power of $q_{Q^*P^*}$ because eq. (9) yields a 2nd order polynomial).

The structure of eq. (9) has two important consequences (which are also valid for the powers of $q_{Q^*P^*}$ and, thus, for the truncated series in eq.(4)):

1. The source point coordinates and the field point coordinates are separated. Thus, source integration can be done independently of the field point, sec. 4.

2. Higher order derivatives of the gravitational potential, which affect only the coordinates of the field point, and which in physical geodesy are used to model any observable quantity of the gravitational attraction (Moritz, 1980), can be approximated by differentiating the truncated binomial series, eq.(4):

$$\frac{\partial^{i+j+k}}{\partial x_{P^*}^i \partial y_{P^*}^j \partial z_{P^*}^k} \left(\frac{1}{r_{Q^*P^*}} \right) \approx \frac{1}{r_{QP}} \sum_{n=0}^N b_n \frac{\partial^{i+j+k}}{\partial x_{P^*}^i \partial y_{P^*}^j \partial z_{P^*}^k} \left(q_{Q^*P^*}^n \right) \quad (10)$$

Subsequently, each power of $q_{Q^*P^*}$ which according to the above discussion has exactly the same structure as shown in eq.(9), can be differentiated. For example,

$$\frac{\partial \left[(q_{Q^*P^*})^n \right]}{\partial x_{P^*}^i} = \sum_{i_1, i_2, i_3, i_4, i_5, i_6=0}^2 b_{i_1, i_2, i_3, i_4, i_5, i_6} \left[x_{Q^*}^{i_1} y_{Q^*}^{i_2} z_{Q^*}^{i_3} \right] \left[(i_4 x_{P^*}^{i_4-1}) y_{P^*}^{i_5} z_{P^*}^{i_6} \right] \quad (11)$$

where $b_{i_1, i_2, i_3, i_4, i_5, i_6}$ is a constant for a similar expression to eq. (9) but for $(q_{Q^*P^*})^n$.

Thus, the differentiation is again independent of the source integration. Furthermore, the fact that the coordinates of P^* are expressed in a P^* -LCFR (see above) has as a consequence that the directional derivatives are aligned with the ellipsoidal normal and the North- and East component. Thus, for the ellipsoidal Earth's models it is possible to make use of the simplicity of the local Cartesian coordinates without the need to go into spherical- or ellipsoidal geometry.

4 Source Integration – storing the information

Using the formalism introduced in the previous section, we will now address the problem of integrating the contributions from all sources. We start with the contribution to the gravitational potential ΔV_k from the source point-domain Ω_k associated with a fixed point Q_k (see eq. (4))

$$\Delta V_k = \int_{\Omega_k} \frac{G \cdot \rho(Q^*)}{r_{Q^*P^*}} d\Omega_Q = \iiint_{\Omega_k} \frac{G \cdot \rho(Q^*)}{r_{Q^*P^*}} dx_Q dy_Q dz_Q \approx \frac{G}{r_{Q_k P^*}} \sum_{i=0}^N b_i \int_{\Omega_k} (q_{Q^*P^*})^i \rho(Q^*) d\Omega_Q = \frac{G}{r_{Q_k P^*}} \sum_{i=0}^N b_i I_k^{(i)} \quad (11)$$

where G is the gravitational constant, $\rho(Q^*)$ is the density distribution within the domain and where:

$$I_k^{(n)} \equiv \sum_{i_1, i_2, i_3, i_4, i_5, i_6=0}^2 c_{i_1, i_2, i_3, i_4, i_5, i_6} \times \left\{ \iiint_{\Omega_k} \left[x_{Q^*}^{i_1} y_{Q^*}^{i_2} z_{Q^*}^{i_3} \right] \rho(Q^*) dx_Q dy_Q dz_Q \right\} \left[x_{P^*}^{i_4} y_{P^*}^{i_5} z_{P^*}^{i_6} \right] \quad (12)$$

The definition given by eq. (12) shows, in principle, how this can be done. One detail is that the formula makes use of eq. (7) rather than eq. (8), i.e. it involves coordinates $\mathbf{r}_{P^*P^*} \equiv [x_{P^*}, y_{P^*}, z_{P^*}]$ in P^* -LCFR. This is the LCFR that we use for storing the information. As explained above, the recovery of the field quantity for an arbitrary point P^* within the field point domain requires additional rotation, which is only known once the field point is known.

In sec. 3 we showed that the source integration is independent of the field point and that it is unchanged for other derivatives of the gravitational potential. This is an interesting property, which at least in principle, makes it possible to pre-compute and to store the source information. The same integrals can be used for all the derivatives of the gravitational potential. Consequently, it is not necessary to store the information individually for all the derivatives.

Another important issue is the class of functions for the source approximation that can be integrated. It is larger than those known in the literature for the elementary-body techniques (see Introduction). For example, the piecewise polynomial functions of the type:

$$\rho(Q^*) = \sum_{j_1, j_2, j_3=0}^M r_{j_1, j_2, j_3} x_{Q^*}^{j_1} y_{Q^*}^{j_2} z_{Q^*}^{j_3} \quad (13)$$

can easily be integrated. Also, the interfaces between geological layers approximated by surfaces like:

$$z(x_{Q^*}, y_{Q^*}) = \sum_{k_1, k_2=0}^K s_{j_1, j_2, j_3} x_{Q^*}^{k_1} y_{Q^*}^{k_2} \quad (14)$$

can also easily be included. This opens a possibility of computing the attraction from very complicated (i.e. realistic) structures.

At the present, we do not as yet have a good strategy for storing the source information. The dimensionality of the brute-force approach is simply too big (there is a trade-off between the truncation degree and the size of the field point domain which we want to have as big as possible). Looking at eqs. (3)-(4), i.e. for the problem prior to the integration, we can see the analogy to how it could work. Once the arbitrary point P^* within the field point domain is known we have the value of $q_{Q^*P^*}$ for this point. We can then take powers of this value and insert them into the truncated binomial series, see eq. (4). This relationship is no longer valid for after the integration. Conversely, and looking at eq. (11)

$$I_k^{(n)} \neq \left(I_k^{(1)} \right)^n \quad (15)$$

To the author's opinion, there is no doubt that there must be a way. The reason is that the field away from the physical sources is smooth. Conversely, it only requires few low-degree polynomials to describe the field. It should be noted that the present paper does not address the problems of optimizing the technique by only adding the most significant contributions. One reason is, that we want to use the same mathematical formalism (and the same stored information) for all derivatives of the gravitational potential. This requires that the truncation degree of the binomial series is higher than what is strictly necessary for e.g. a high-accuracy approximation of the gravitational potential. Another reason is that we, at this stage, want to investigate the problem in its full scale and see if we can come up with some good strategy. Looking at eq. (12) we also understand how the density information translates into gravitational attraction and for all the derivatives – which is useful for techniques of geophysical inversion.

At the present we investigate the possible recursive structure of the integrals $I_k^{(i)}$. This would be analogous to the above example. Another point, not discussed here, but which is the integral part of the present investigations, is how to store and, subsequently, how to add the information from different source point-domains.

5 Accuracy of approximation

The considerations in sec. 2 about the domain sizes (L_P and L_Q) in relation to the convergence of the binomial series of eq. (4) are, in fact, more refined. We have tried to design techniques for assessing the maximal possible truncation error for a given truncation degree and for a given size of the domains – both for the gravitational potential and for higher order derivatives. This would allow us to assess the maximal error for the forward model computed by truncated series as compared to the ‘true model’ computed by means of infinite series (‘exact’).

We found, that it is convenient to study these issues on the truncated binomial series prior to the integration of sources (see eq.(4)). The reason is, that we can use for comparison simple point-mass formulas for the gravitational potential and its derivatives as a ‘true’ absolute value. Thus, for all points Q^* , $Q^* \in \Omega_Q$ and for all points P^* , $P^* \in \Omega_P$ in a field point domain, we study the maximal error of ‘approximated’ (eq. (4) or its derivatives) versus the ‘exact’ (point-mass attraction for Q^* and P^*). Only if this maximal approximation error is 100% correlated for all Q^* in the source point domain the error after integration would be the same. Otherwise, it must be less. Thus, the truncation error in relation to the problem after mass integration is less than what is found.

We can show that, for a set of parameters L_P , L_Q and N and for the setup shown on fig. 1, there is a set of characteristic points (Q^* , P^*) within both domains so that the truncation error becomes maximal. This is valid for the gravitational potential (and probably also for other derivatives). We are still working on formal proofs of that.

Finally, we will illustrate what can be expected in practice. Consider a problem of detecting the land uplift in Scandinavia studied from GRACE (altitude 300 km – 500 km) by tracing point-by-point, and along the satellite orbit, the signal coherent with the attraction of the topography. Regional DEMs used for the computation of the Scandinavian geoid have a spacing of $0.01^\circ \times 0.02^\circ$ (approx. 1.1 km \times 1.0 km). The maximal heights in the area [52°N - 72°N, 4°E - 32°E (approx. 2224 km \times 1462 km)] are 2366 m. Thus, it is possible to design source point domain with fixed points in height 1200 m and $L_Q=2400$ m (corresponding approximately to 2 \times 2 grid points of the DEM). For the field point-domain we could place the fixed points with a spacing of $1^\circ \times 2^\circ$ at the

'mid'-altitude of GRACE of 400 km and $L_P=200$ km. For $N = 30$ the following maximal relative [(‘approximated’-‘true’)/‘true’] misfit errors ε were found for different orders of the derivative:

0-order (gravitational potential)	$ \varepsilon < 6.01 \times 10^{-12}$
1-order (gravity vector)	$ \varepsilon < 1.12 \times 10^{-9}$
2-order (gravity gradient)	$ \varepsilon < 6.38 \times 10^{-7}$
3-order	$ \varepsilon < 5.99 \times 10^{-5}$

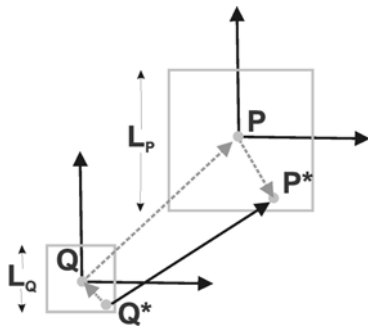


Fig. 1 The setup, see sec 2. The cubical field point-domain (P -fixed point in the center, P^* arbitrary point, L_P -side length of the cube, LCFR with origo in P); The cubical source point-domain (Q -fixed point in the center, Q^* arbitrary point, L_Q -side length of the cube, LCFR with origo in Q)

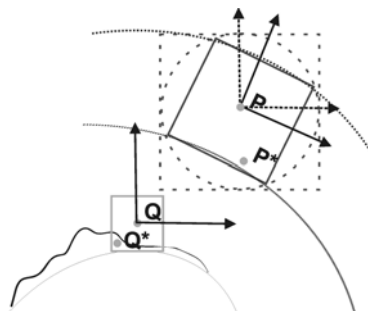


Fig. 2 Ensuring the quality of approximation when the domains are not-aligned, see sec. 3. The rotated domain is smaller than the original one.

6 Conclusions

In this paper we have outlined a new space-domain method of forward modelling for computation of the gravitational attraction from known sources. Compared to the existing methods known in the literature the proposed method has the following advantages:

- The source integration is done once, independently of the field point, and stored. The same stored information can be used for all derivatives of the gravitational potential.

- It is possible to accommodate, a large class of mass density distributions (including the geologically realistic density models in 3D)
- Controlled accuracy of approximation.
- Local Cartesian Frames of reference are used. All the important aspects of the ellipsoidal Earth's models can be included.

One serious outstanding issue is, that there is no good strategy for storing the integrated source information. However, there is reason to believe that this must be possible.

Smaller outstanding issues are the mathematical proofs ensuring bounds on the maximal errors of truncation for the higher order derivatives of the gravitational potential.

References

- Blakely, R.J. (1996). Potential Theory in Gravity and Magnetic Applications. Cambridge University Press
- Barnett C.T. (1976) Theoretical Modelling of the Magnetic and Gravitational Fields of an Arbitrarily Shaped Three-dimensional Body. *Geophysics*, 41, 1353-1364.
- Chai, Y and W. J. Hinze (1988) Gravity Inversion of an Interface above which the Density Contrast Varies Exponentially with Depth. *Geophysics*, 53, 837-845.
- Cordell L. (1973) Gravity Analysis Using an Exponential Density-Depth Function-San Jacinto Graben, California. *Geophysics*, 38, 684-690.
- Gendzwil, D.J. (1970) The Gradational Density Contrast as a Gravity Interpretation Model. *Geophysics*, 55, 270-278.
- Götze, H.J., S. Schmidt (2002) Geophysical 3D Modelling using GIS-functions. In 8th Annual conference of the International Association of Mathematical Geology. ISSN 0946-8978, Terra Nostra, 04/2002, 87-92
- Heiskanen W. A. and H. Moritz (1967) *Physical Geodesy*. W.H. Freeman & Co. San Francisco.
- Holstein H. (2003) Gravimagnetic Anomaly Formulas for Polyhedra of Spatially Linear Media, *Geophysics*, 64, 157-167
- Moritz H. (1980) *Advanced Physical Geodesy*. Abacus Press.
- Nagy, D. (1966) The Gravitational Attraction of Right Rectangular Prism, *Geophysics*, 31, 362-371
- Paul, M.K. (1974) The Gravity Effect of a Homogenous Polyhedron for Three Dimensional Interpretation. *Pure and Applied Geophysics*, 112, 553-561
- Petrović, S. (1996) Determination of the Potential of Homogenous Polyhedral Bodies Using Line Integrals. *Journal of Geodesy*, 71, 44-52
- Rao D.B. (1990) Analysis of Gravity Anomalies of Sedimentary Basins by an Asymmetrical Trapezoidal Model with Quadratic Density Function. *Geophysics*, 55, 226-231
- Seeber G. (1993) *Satellite Geodesy*. deGruyter.
- Sigl. R. (1985) *Introduction to Potential Theory*. Abacus Press
- Talwani and Ewing (1960) Rapid Computation of Gravitational Attraction of Three-Dimensional Bodies of Arbitrary Shape. *Geophysics*, 25, 203-225.
- Torge, W. (1989). *Gravimetry*. Walter de Gruyter

Residual Terrain Correction on the Sphere by an FFT Algorithm

D. Sampietro, G. Sona, G. Venuti

Politecnico di Milano, Polo regionale di Como, via Valleggio 11, 22100 Como, Italy;

Abstract. The computation of the vertical attraction due to masses above the mean topography (Residual Terrain Correction, RTC) is still a matter of study in the high precision geoid estimation by remove-restore technique. This topographical effect can be evaluated from the knowledge of a Digital Terrain Model (DTM) in two different ways: numerical integration by prisms or Fast Fourier Transform (FFT) technique. Both these methods can't be used when wide areas are considered, the first approach, more rigorous, requires an excessive computation time, while the second one, faster, implies restrictive hypotheses like planar approximation of the topographical surface. For these reasons a new algorithm, based on a convenient transformation of the starting DTM, has been studied and implemented. This new method enables the use of planar formulas also with the spherical approximation of the area. The new algorithm is presented both from a theoretical and practical point of view, particular attention is paid to neglected terms that are of the order of about $10^{-5}Gal$. The method has been studied in order to compute the RTC in a large area like that implied by the new European geoid project. Some tests have been performed for proving the goodness of the model.

Keywords. Residual Terrain Correction, FFT

1 Introduction

Modeling of local details of the gravity field via Newton integral with accuracies that can meet modern demands requires the use of high resolution digital terrain models (DTM) and application of the Newton Integral in terms of geodetic coordinates over a large amount of data (Ardalan and Safari, 2004 [1]). The first problem can be solved by means of photogrammetric and remote sensing techniques, that made it possible to develop high resolution DTMs, the second problem

is still a matter of study: the Fast Fourier Transform techniques (FFT) in fact make it possible to compute Newton integral in a fast way, but only in planar approximation (see for details Sideris, 1984 [8] or Forsberg, 1985 [4]), while the integral in terms of geodetic coordinates can be evaluated only using numerical methods, but this approach is very time consuming (see for example Tsoulis, 1998 [10]). With the aim to overcome the limits of classical models, advanced algorithms, like the one implemented in TcLight, have been developed.

In this work we analyse an improvement that allows the use of TcLight planar formulae also considering spherical approximation. In order to prove the goodness of this new method numerical results for a synthetic and a real DTMs are presented. This study is a continuation of the efforts of *IGeS* to develop a tool for computing RTC over a wide area in a fast and rigorous way.

1.1 TcLight, an Overview.

In planar approximation, with the geometry shown in Fig. 1 and with a constant density distribution ($\sigma(P) = \sigma = cost$), the potential generated at a point $P(n, e, h)$ by the masses of a body of base B is (Heiskanen and Moritz, 1967 [5]):

$$V(P) = G \sigma \iint_B dx dy \int_0^z \frac{d\zeta}{\sqrt{(n-x)^2 + (e-y)^2 + (h-\zeta)^2}}. \quad (1)$$

Reminding that $\delta g = -\partial V / \partial h$ and assuming the Newtonian operator to be evaluated only inside a disk of assigned radius D , and that outside D the terrain can be supposed to have zero heights, the following Eq. 2 was proved (Sansò et al., 1998 [7]):

$$\begin{aligned} \delta g(n, e, h) &= k_G \iint_B \left[\frac{dx dy}{\sqrt{l^2 + (h-H)^2}} - \right. \\ &\quad \left. - \frac{dx dy}{\sqrt{l^2 + (h-\tilde{H})^2}} \right] = \\ &= k_G (\Gamma_1 - \Gamma_2 - \Gamma_3 + \Gamma_4) \end{aligned} \quad (2)$$

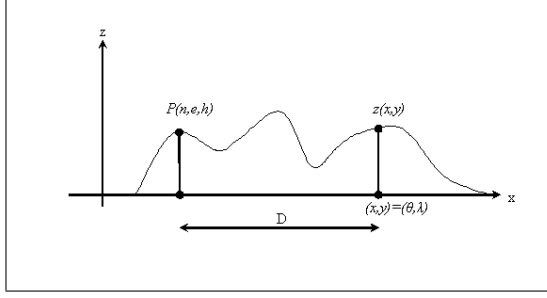


Figure 1: Geometry used in TcLight.

where:

$$k_G = G\sigma; \quad \Gamma_1 = 2\pi h; \quad \Gamma_2 = \pi h^2 (D^2 + h^2)^{-\frac{1}{2}};$$

$$\Gamma_3 = \frac{1}{2} \int_0^{2\pi} d\theta \int_0^D dl \frac{x(\theta, l)^2}{[1+x(\theta, l)^2]^{\frac{3}{2}}};$$

$$\Gamma_4 = \frac{1}{2} \int_0^{2\pi} d\theta \int_0^D dl \frac{x(\theta, l)^3 z'(\theta, l)}{[1+x(\theta, l)^2]^{\frac{3}{2}}};$$

$$x(\theta, l) = \frac{h-z(\theta, l)}{l}; \quad z'(\theta, l) = \frac{\partial z}{\partial l}(\theta, l);$$

and (θ, l) are polar coordinates in the plane with respect to P, (x, y) .

To numerically compute these integrals TcLight adopts different approaches according to the characteristics of the integrand functions: particularly the domain is divided into two parts, the first defined as a square near the computational point P (called inner domain) and the remaining part of the DTM called outer domain. In the inner domain Eq. 2 is solved by describing the topography inside every DTM cell as a bilinear surface and applying numerical integration. In the outer domain Γ_3 and Γ_4 are reduced to convolution integrals, which can be solved by FFT technique. In this way we are able to obtain results, comparable with that of numerical integration, practically as fast as classical FFT computations also in rough topography. For a more detailed description of TcLight see Biagi and Sansò 2001 [3].

2 Spherical Approximation

2.1 Theoretical Approach.

In general, considering again the hypothesis of a constant density of the topographical masses ($\sigma = \sigma(Q) = \text{cost}$) and with geometry shown in Fig. 2, the gravity effects of an extended mass body Ω is given by:

$$\delta g(P) = -\vec{\nu}_P \cdot \vec{\nabla}_P \iiint_{\Omega} \frac{\sigma G d\Omega_Q}{l_{PQ}} \quad (3)$$

where Ω are topographical masses between the actual and the mean topographical surface.

If we call $\sigma G = \mu$, Eq. 3 can be written as:

$$\delta g(P) = \mu \vec{\nu}_P \cdot \iiint_{\Omega} -\vec{\nabla}_P \frac{d\Omega_Q}{l_{PQ}}. \quad (4)$$

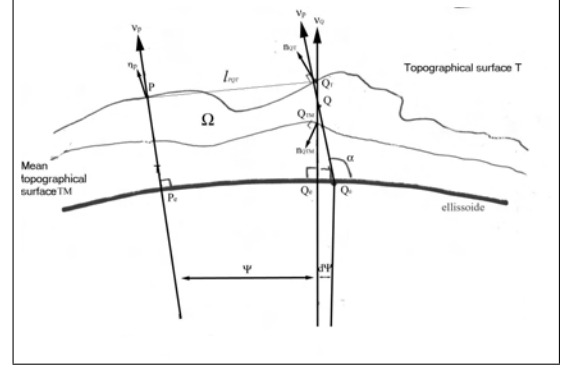


Figure 2: Geometry used for modeling at the observation point P the gravity effect due to the point Q in ellipsoidal approximation.

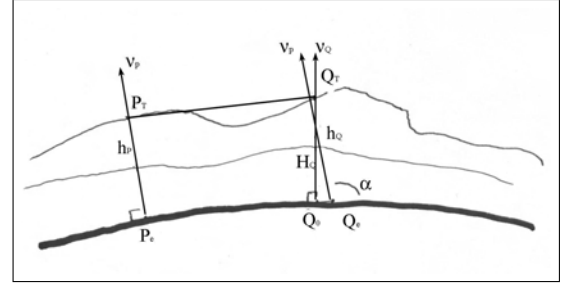


Figure 3: Geometry used for computing $|\vec{l}_{PQT}|$

The domain of the integral in Eq. 4 can be split into two parts, the first referred to points near P (at a maximum distance of about 4° as we shall explain in the sequel of the paragraph) and the second one referred to all other points. Concentrating on the first part all we have to do is just to rewrite Eq. 4 simplifying some irrelevant terms and to compute the integral over a conformal projection of the DTM.

First of all, applying Gauss theorem to Eq. 4 and considering \vec{n} the direction of the normal to the topographical surface pointing up, we get:

$$\delta g(P) = \mu \left[\iint_T \frac{\vec{\nu}_P \cdot \vec{n}_{QT} dT}{l_{PQT}} - \iint_{TM} \frac{\vec{\nu}_P \cdot \vec{n}_{QTM} dTM}{l_{PQTM}} \right] \quad (5)$$

where T refers to actual surface, while TM refer to the mean topographic surface. We can observe that numerators in the two integrands of Eq. 5 are merely the projections of dT and dTM on a plane perpendicular to $\vec{\nu}_P$. Just to simplify the notation we shall consider then: $\vec{\nu}_P \cdot \vec{n}_{QT} dT = dS$; and $\vec{\nu}_P \cdot \vec{n}_{QTM} dTM = dS'$. Let us consider for the moment only $|\vec{l}_{PQT}|$. From Fig. 3 we can note that: $h_P \vec{\nu}_P + \vec{l}_{PQT} = \vec{l}_{P_e Q_0} + H_Q \vec{\nu}_P$ so \vec{l}_{PQT} is :

$\vec{l}_{PQT} = \vec{l}_{P_eQ_0} + (H_Q - h_P) \vec{\nu}_P$ and with a plainly algebraic step we find:

$$|\vec{l}_{PQT}|^2 = |\vec{l}_{P_eQ_0}|^2 + (H_Q - h_P)^2 - 2|\vec{l}_{P_eQ_0}|(H_Q - h_P) \cos \alpha \quad (6)$$

where $\alpha = \frac{1}{2}(\psi + \delta\psi) + \frac{\pi}{2}$. From the geometry of the problem we notice that $\delta\psi$ is negligible in comparison with ψ , in fact: $\psi = \frac{|\vec{l}_{P_eQ_e}|}{R} \cong \frac{60km}{6000km} = 10^{-2}rad$ while $d\psi = \frac{|\vec{l}_{P_eQ_0}|}{R} = \frac{H_Q \sin \psi}{R} \cong \frac{10^{-2}}{10^3} = 10^{-5}rad$. With this simplification, assuming $\cos \psi \cong 1$ and $\sin \psi \cong \psi$ and recalling that $\cos(\frac{\pi}{2} + \theta) = -\sin \theta$ Eq. 6 becomes:

$$|\vec{l}_{PQT}| \cong \sqrt{l^2 + (H_Q - h_P)^2 - l(H_Q - h_P) \psi} \quad (7)$$

As ψ is so small and $h_Q = H_Q \cos \psi$, we can consider $h_Q \cong H_Q$. This simplification implies an error of about $5H_Q \cdot 10^{-5}$. With this remark we find that, with good approximation, the following expression holds:

$$\begin{aligned} \|\vec{l}_{PQT}\| &\cong \sqrt{l^2 + (h_Q - h_P)^2 - l(h_Q - h_P) \psi} \\ &= \sqrt{l^2 + \Delta h^2 - l\Delta h \frac{l}{R}} \end{aligned} \quad (8)$$

where $l = |\vec{l}_{P_eQ_e}| \cong |\vec{l}_{P_eQ_0}|$. We can note that the last term in Eq. 8 is 10 time smaller than the second one and 1000 time smaller than the first one. In fact if we suppose: $l \cong 60km$; $R \cong 6300km$; $\Delta h \cong 5km$ we obtain: $|\vec{l}_{PQT}| \cong 60km\sqrt{1 + 0.007 - 0.0008} = 60.19km$ so we can assume $|\vec{l}_{PQT}| \cong \sqrt{l^2 + \Delta h^2}$ with an approximation in the worst hypothesis of about $0.024km$. We can proceed in an analogous way for $|\vec{l}_{PQTM}|$ considering that in this case $\Delta \tilde{h}$ (where $\Delta \tilde{h}$ is just the same as Δh but referred to TM) will be even smaller. What we have to do now is to reduce infinitesimal areas dS and dS' over the reference sphere. This can be simply done by observing from Fig. 4 that:

$$\frac{dS'}{dS_e} \cong \frac{dS}{dS_e} \cong \cos \delta\psi \cong 1 \quad (9)$$

and therefore $dS' \cong dS \cong dS_e$. At last we can write:

$$\begin{aligned} \delta g(P) &= \mu \left[\iint_T \frac{dS_{eQ_0}}{\sqrt{l^2 + \Delta h^2}} - \right. \\ &\quad \left. - \iint_{TM} \frac{dS_{eQ_0}}{\sqrt{l^2 + \Delta \tilde{h}^2}} \right]. \end{aligned} \quad (10)$$

At this point, in order to compute integrals in Eq. 10, we can pass to a conformal projection.

Considering now a generic infinitesimal surface on the ellipsoid dS_e , in the conformal projection this area will be the product of the square of linear deformation index m and the infinitesimal surface dS .

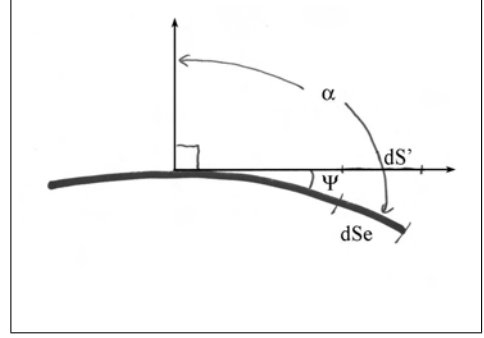


Figure 4: Relation between infinitesimal surfaces dS_e and dS' .

Considering that the distance l referred to the ellipsoid becomes $D_{PQ} \cong \frac{l}{m}$ on the map, we have:

$$\begin{aligned} \delta g(P) &= \mu \left[\iint_T \frac{m^2 dS}{\sqrt{D_{PQ}^2 + \Delta h^2}} - \right. \\ &\quad \left. - \iint_{TM} \frac{m^2 dS}{\sqrt{D_{PQ}^2 + \Delta \tilde{h}^2}} \right]. \end{aligned} \quad (11)$$

In Eq. 11, using a conformal projection, m is the same in all directions, moreover the two integrals are not significant if the distance is bigger than 2° or 3° , so for these distances we can suppose, at every point P , m to be constant (in a Lambert conformal projection, e. g., we have $\Delta m \cong 0.005$ if the two points are 4° far away). With this agreement we find that Eq. 11 can be written with a suitable approximation as:

$$\begin{aligned} \delta g(P) &= \mu \frac{m^2}{m} \left[\iint_T \frac{dxdy}{\sqrt{D_{PQ}^2 + \left(\frac{h_P}{m_P} - \frac{h_Q}{m_Q}\right)^2}} - \right. \\ &\quad \left. - \iint_{TM} \frac{dxdy}{\sqrt{D_{PQ}^2 + \left(\frac{h_P}{m_P} - \frac{\tilde{h}_Q}{m_Q}\right)^2}} \right]. \end{aligned} \quad (12)$$

If we denote reduced altitudes with $\bar{h} = \frac{h}{m}$ and we compare Eq. 12 with Eq. 2 we can note that the following relation holds:

$$\delta g_{sphere}(P) = m(P) \delta g_{plane}(P)|_{\bar{h}}, \quad (13)$$

i.e. if we consider an interval around P , $\delta g_{sphere}(P)$ can be computed with TcLight formulae in spherical approximation by applying to the DTM a conformal projection, dividing heights h by m and then multiplying the resulting RTC by m .

Taking into account now the contribution of the remaining part of the sphere, external to the area considered, we will prove that integrals in Eq. 10 can be neglected when computing RTC at point P. In fact, also in this case Eq. 10 must holds. In the first integral we can split the difference between h_P and h_Q as $h_P - \tilde{h}_Q - \Delta h$. Inserting this last expression in Eq. 10 we obtain:

$$\delta g(P) = \mu \iint_{out} \frac{2(h_P - \tilde{h}_Q)}{\sqrt{l^2 + (h_P - \tilde{h}_Q - \Delta h_Q)^2}} dS_{eQ0} \quad (14)$$

the modulus of which, for the triangular inequality, must satisfy:

$$|\delta g(P)| \leq \mu \sqrt{\iint_{out} \frac{2|h_P - \tilde{h}_Q|}{\sqrt{l^2 + (h_P - \tilde{h}_Q - \Delta h_Q)^2}} dS_{eQ0}} \quad (15)$$

$$\sqrt{\iint_{out} \frac{2|h_Q - \tilde{h}_Q|}{\sqrt{l^2 + (h_P - \tilde{h}_Q - \Delta h_Q)^2}} dS_{eQ0}}.$$

From the geometry of the problem we can note that $\sqrt{l^2 + (h_P - \tilde{h}_Q - \Delta h_Q)^2} \cong 2R \sin \frac{\psi}{2}$, while the infinitesimal surface is: $dS_{eQ0} = R^2 \sin \psi d\alpha$. Substituting these relations in Eq. 15 and with opportune algebraic steps we obtain:

$$|\delta g(P)| \leq \mu \sqrt{\frac{1}{R} \int_0^{2\pi} \int_{\psi_0}^{\pi} \frac{\cos \frac{\psi}{2} (h_P - \tilde{h}_Q)^2 d\psi d\alpha}{4 (\sin \frac{\psi}{2})^2}} \quad (16)$$

$$\sqrt{\frac{1}{R} \int_0^{2\pi} \int_{\psi_0}^{\pi} \frac{\cos \frac{\psi}{2} (h_Q - \tilde{h}_Q)^2 d\psi d\alpha}{(4 \sin \frac{\psi}{2})^2}}$$

It is easy to observe that quantities in Eq. 16 can be neglected, in fact, supposing $E[(h_P - \tilde{h}_Q)^2] = \Delta h_{PQ}^2 \cong 4km^2$ and $E[(h_Q - \tilde{h}_Q)^2] = \Delta h_{Q\tilde{Q}}^2 \cong 0.25km^2$, with a course valuation we find that: $|\delta g(P)| \leq 0.16mGal$

2.2 Algorithm Implementation

Usually to compute RTC we have DTM on a regular grid in geodetic coordinates (ϕ, λ) . Taking into account the spherical approximation what we should do is to obtain a DTM on a regular grid in planar cartesian coordinates (x, y) by applying a conformal Lambert projection. For this purpose a 4 steps procedure has been developed:

1. First of all we just consider the extremes of the DTM boundaries in (ϕ, λ) and apply to these 4 points the Lambert projection. With this simple operation we find the limits of the new grid in cartesian coordinates.

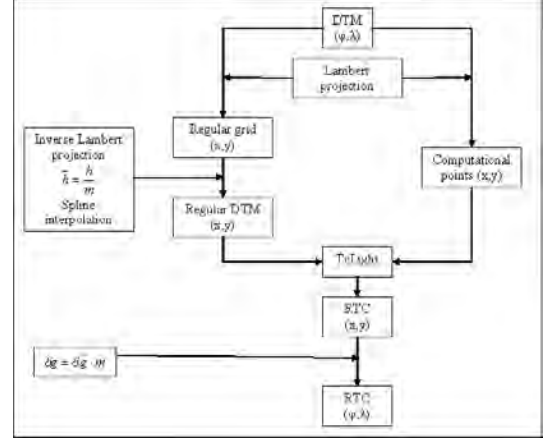


Figure 5: Practical algorithm for computing RTC with TcLight in spherical approximation.

2. The next step consists in creating a regular planar grid in (x, y) inside the 4 points found in point 1.
3. In step three we apply an inverse Lambert projection to the regular grid nodes in (x, y) producing a set of sparse points in (ϕ, λ) .
4. By interpolating with bilinear spline the original DTM on the points found in step 3 we get the height values on the regular grid at x, y . In order to prepare the DTM for computing RTC with TcLight we have also to divide heights by linear deformation m .
5. This point consists in preparing the computational points (where RTC will be estimates) simply using Lambert projection over the regular grid in (ϕ, λ)

The result of these operations are two set of points, the first one containing DTM over a regular grid in cartesian coordinates, and the second one containing an amount of sparse points in cartesian coordinates corresponding to the nodes of a regular grid in (ϕ, λ) . Finally we can compute RTC over the points in the second set, using the DTM of the first set. Applying at the result of this last operation a simple reordering procedure we finally get RTC over a regular grid in (ϕ, λ) .

The whole process is summarized in Fig. 5.

3 Numerical Tests

In this section we will present numerical tests performed in order to check the accuracy of the new method. It is worth remarking that the RTC is simply the difference between a classical TC computed on true topography and a TC on the mean topography, so in numerical testing we performed only

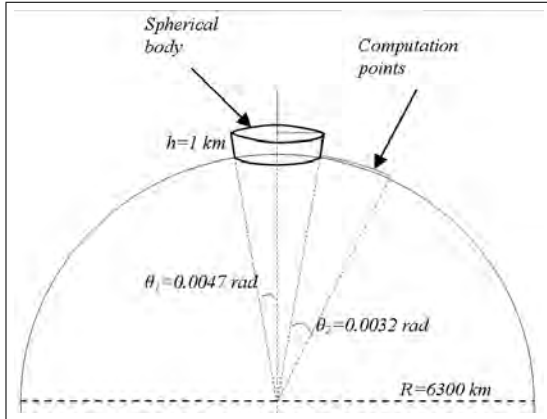


Figure 6: Geometry of the body used for numerical tests.

classical TC. First of all we performed a test over a small patch of real DTM ($\phi_{min} = 45.5$; $\phi_{max} = 46.5$; $\lambda_{min} = 8.5$; $\lambda_{max} = 9.5$; $\delta\phi = \delta\lambda = 3arcsec$). This test gave results quite similar to that obtained with classical numerical integration and planar TcLight and proved the correctness of the software developed (differences are of the order of $0.2mGal$).

For the purpose of algorithm testing the availability of the exact potential of bodies is essential; unfortunately a closed solution for the Newton integral in geodetic coordinates doesn't exist. So we tried to compute it over a simple synthetic DTM with different methods. We considered a simple body with a cylindrical symmetry around the polar axis, built on the pole of a sphere (see Fig. 6). In this case the exact potential of the gravity field can be analytically evaluated using spherical harmonics:

$$\nu(P) = 2\pi\mu \sum_{n=0}^{+\infty} b_n(R, H, \Delta) r_P^n P_n(\cos \theta_P). \quad (17)$$

From Eq. 17 we have computed the radial attraction of the body i. e. the topographic correction. The problem of this method is that the series converges in a very slow way (see Fig. 9) and it is quite difficult to reach the required precision. A new test was developed using numerical integration by Gauss-Legendre quadrature. In the quadrature method the gravity components of the spherical prism can be computed accurately by summing up at each observation point the effects of a number of equivalent point poles opportunely weighted (M. F. Asgharzadeh et al., 1998 [2]); for details on this method see for example Swarztrauber 2002 [9] or Press, Vetterling and Flanners, 1994 [6]. For the purpose to have a TC as accurate as possible we divided the body in $(800 \times 800 \times 800)$ cells.

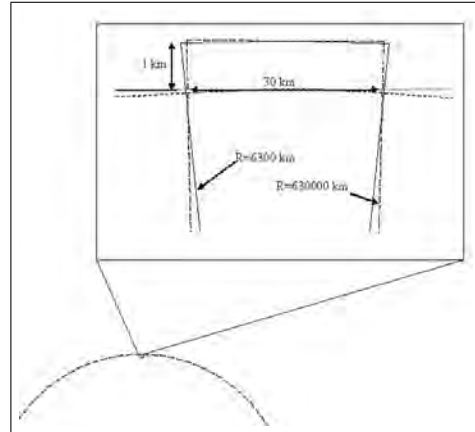


Figure 7: Geometry used to model spherical and planar approximation with numerical integration.

To try to estimate differences between planar and spherical approximation, TC was evaluated over 2 different bodies, the first one built over a sphere of radius $6300km$ while in the second case we consider a sphere of $63000km$ of radius (geometry used in this test is shown in Fig. 7). Empirically we can consider the TC computed over the second sphere a good model for planar approximation. The next step was just to compute TC with TcLight in planar approximation and applying the new algorithm. Since the synthetic DTM in exam has a cylindrical symmetry, RTC has been computed along a single profile; in order to have an idea of the results obtained, RTC evaluated with spherical harmonics and the new methods over the whole profile are shown in Fig. 8. In Fig. 9 the results obtained with all the methods, over an interval of about $10km$, are presented. We can notice that RTC computed with the new algorithm are similar to the one obtained with numerical integration over the small sphere, while RTC computed with simple TcLight is more similar to results obtained over the big one, as it was to be expected. Finally in Fig. 10 is presented the difference between spherical and planar approximation computed both with TcLight and numerical integration.

4 Conclusion

In this paper we have presented a new algorithm for computing TC using FFT also in a spherical domain and some tests to prove the goodness of the model. From Fig. 8, Fig. 9, Fig. 10 we can see that, if we consider points distant more than $3km$ from the large DTM discontinuity ($1000m$), the new method approximates the correct RTC in a good way (less than $0.1mGal$ for the test developed). From Fig. 10 we can note that differences between planar and spher-

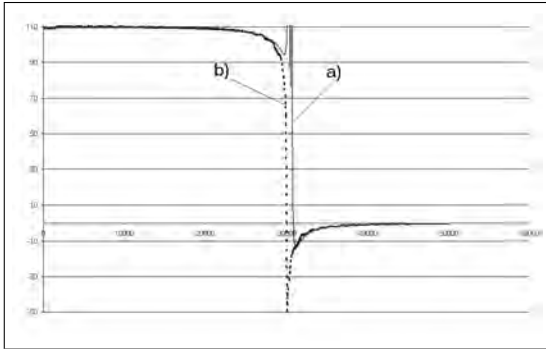


Figure 8: TC evaluated over the whole profile with TcLight case *a)* and spherical harmonics case *b)* [distances in *m*. TC in *mGal*].

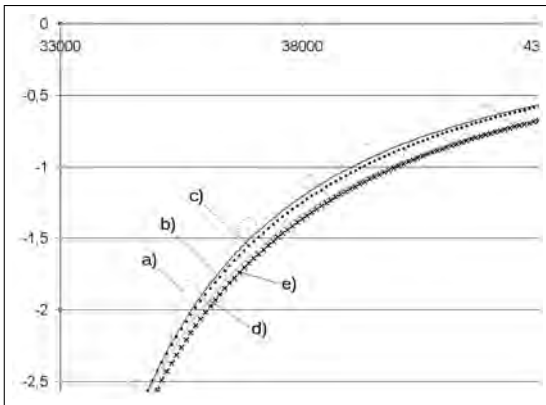


Figure 9: TC evaluated over a 10km interval with spherical harmonics case *a)*, TcLight and new algorithm case *b)*, numerical integration in spherical approximation case *c)*, simple TcLight case *d)* and numerical integration in planar approximation case *e)* [distances in *m*. TC in *mGal*].

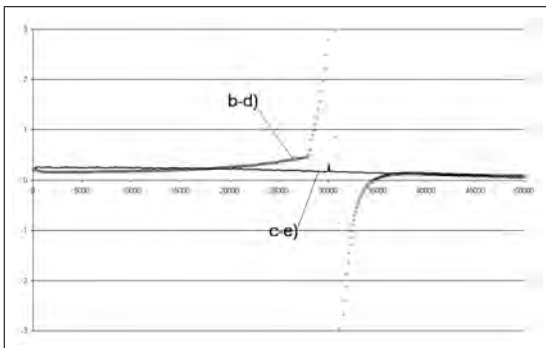


Figure 10: Spherical effect estimated with TcLight (*b – d*) and with numerical integration (*c – e*) [distances in *m*. TC in *mGal*].

ical coordinates are of the order of about $0.2mGal$ for this simple synthetic example. Tests with more realistic data over larger areas (e. g. $2^\circ \times 2^\circ$ in the mont Blanc area) perform much more significant differences ($5.7mGal$ r.m.s.) even if we can't say directly that one is better than the other. We should keep in mind the fact that even if the differences between planar and spherical model are not so relevant, this new algorithm permits to treat topographical masses in a correct way from a teoretical point of view and in a very fast way. Tests conducted over a $3arcsec \times 3arcsec$ DTM over an area of $1^\circ \times 1^\circ$ was performed in less then 10min: 8 minutes and 22 seconds for the effective terrain correction computation and about 1 minute for preparing the DTM and rearranging the result(SO: Microsoft Windows XP; PC: Pentium(R) 1.70GHz, 1.50GB RAM. Test performed over 1442401 points).

References

- [1] A. A. Ardalan and A. Safari. Ellipsoidal terrain correction based on multi-cylindrical equal-area map projection of the reference ellipsoid. *J Geod*, 78:114–123, 2004.
- [2] M. F. Asgharzadeh, R. R. B. von Frese, H. R. Kim, T. E. Leftwich, and J.W. Kim. Spherical prism gravity effects by gauss-legendre quadrature integration. *Geophysical Journal International*, research paper, 2005.
- [3] L. Biagi and F. Sansó. TcLight: a new technique for fast rtc computation. *IAG Symposia*, 123:61–66, 2001.
- [4] R. Forsberg. Gravity field terrain effect computation by fft. *Bull. Geod.*, 59:342–360, 1985.
- [5] W. A. Heiskanen and H. Moritz. *Physical Geodesy*. Freeman and Company, S. Francisco, 1967.
- [6] W. H. Press, W. T. Vetterling, and B. P. Flannery. *Numerical recipes in fortran, second edition*. Cambridge University PRESS, New York, 1994.
- [7] F. Sansó, C. Sciarretta, and F. Vespe. New iges formulas for the terrain correction. *IGeS Bulletin*, 7:68–83, 1998.
- [8] G. Sideris. Geoid determination by fft technique. *International School for the Determination and Use of the Geoid*, Lecture Notes:IV1–IV64, 2005.
- [9] P. N. Swarztrauber. On computing the points and weights for gauss-legendre quadrature. *J. Sci Comput*, 24:945–954, 2002.
- [10] D. Tsoulis. A combination method for computing terrain correction. *Phys Chem. Earth*, 23:53–58, 1998.

Comparison of the modelling of topographic and isostatic masses in the space and the frequency domain for use in satellite gravity gradiometry

F. Wild-Pfeiffer, B. Heck

Geodetic Institute, University of Karlsruhe, Englerstr 7, D-76128 Karlsruhe, Germany

e-mail: wild@gik.uni-karlsruhe.de; Fax: +49-721-608-6808

Abstract. In terrestrial and airborne gravity field determination the formulae for the gravitational potential and its first order derivatives have been evaluated, while second order derivatives are related to the analysis of upcoming satellite gravity gradiometry missions of GOCE type. Especially there, the reduction of topographic and isostatic effects within the remove-restore concept is important to produce a smooth gravity field suitable for downward continuation. Another application of topographic and isostatic reductions consists in the external calibration of the GOCE gravity gradiometer. Based on two different isostatic models (Airy-Heiskanen, condensation models of Helmert) the topographic-isostatic effects of the second radial derivative of the potential are calculated for a GOCE-like satellite orbit. In the space domain tesserooids modelled by Gauß-Legendre cubature (3D) are used. In this paper, the focus is put on the comparison between the modelling of masses in the space and frequency domain.

Keywords. Satellite gravity gradiometry, topographic reduction, isostatic reduction (Airy-Heiskanen model, Helmert's condensation models), space domain, frequency domain

1 Introduction

The effects of the topographic and isostatic masses are visible in the gravitational signals, e.g. in the satellite gravity gradiometry (SGG) observations of the GOCE mission. Because of the rough gravity field the downward continuation is rather complex and challenging. The smoothing of the data using a topographic-isostatic reduction would make the downward continuation more easy.

In this paper, the modelling in the space domain (see chap. 2) is compared with the modelling in the frequency domain (see chap 3). In the space domain the gravitational effects of volumetric mass elements can be approximated by prisms, point masses, mass lines, mass layers and tesserooids. The volume integrals are analytically solvable for all mentioned mass elements, except the tesseroid. Approximate solutions of the elliptic integrals related to the tesseroid can be produced by semi-analytical or purely numerical methods as described

in chap 2.3. The comparison between the computation methods in the space and frequency domain is made in chapter 4 by the aid of a simulation.

2 Modelling of the masses in the space domain

2.1 Modelling of the topographic masses

To describe the effect of the topographic masses between the geoid and the Earth's surface S , the geoid is approximated by a sphere Σ_g of radius R . The computation point is denoted by Q and has the geocentric radius $r = R + h$; $r' = R + h'$ is the radius of the running surface point P' . ψ is the spherical distance between the radius vectors of Q and P' (see Fig. 1).

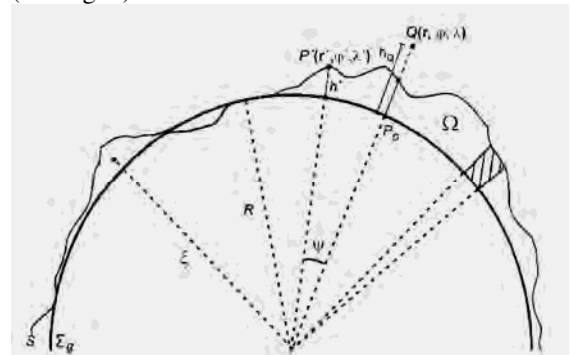


Fig. 1 Geometry of the topography in spherical approximation

The potential of the topographic masses can be described by the Newton integral in spherical coordinates

$$V_i(Q) = G \cdot \iiint_{\Omega} \frac{\rho}{\ell} d\Omega, \quad (1)$$

$$\begin{aligned} \ell &= \sqrt{r^2 + \xi^2 - 2r\xi \cdot \cos \psi}, \\ \cos \psi &= \sin \varphi \sin \varphi' + \cos \varphi \cos \varphi' \cos(\lambda - \lambda'), \end{aligned} \quad (2)$$

where (r, φ, λ) and $(\xi, \varphi', \lambda')$ denote the spherical coordinates of the computation point and the variable integration point, respectively, related to a terrestrial reference frame. G is the gravitational constant, ρ the local mass density and $d\Omega = \xi^2 d\xi d\sigma$ the volume element ($d\sigma$: surface element of the unit sphere).

2.2 Modelling of the isostatic masses

In this paper the focus is on two isostatic models, the Airy-Heiskanen model and the generalized condensation model of Helmert (see Wild and Heck 2005).

2.2.1 Isostatic model of Airy-Heiskanen

The compensation in the model of G.B. Airy and W.A. Heiskanen (Heiskanen and Vening Meinesz 1958) occurs in local, vertical columns. The standard column ($h' = 0$) has the constant density ρ_0 and the thickness T . Continental columns generate “roots” ($t' > 0$), whereas oceanic columns create “anti-roots” ($t' < 0$) (see Fig. 2). The density difference between the mantle and the crust is $\Delta\rho = \rho_m - \rho_0$; the crustal thickness is $T + h' + t'$.

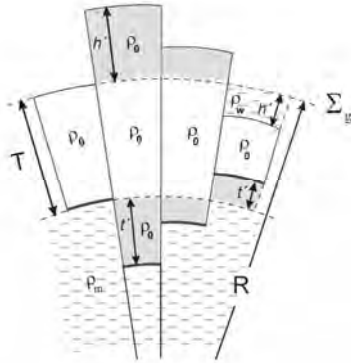


Fig. 2 Isostatic model of Airy-Heiskanen in spherical approximation

The boundary between the (anti-)roots and the mantle is practically equivalent to the Mohorovičić discontinuity (“Moho discontinuity”). In general, the normal thickness T is assumed to be 25 or 30 km (see e.g. Heiskanen and Moritz 1967; Kuhn 2000; Tsoulis 2001).

The formula of the isostatic potential of Airy-Heiskanen in spherical approximation is

$$V_{A-H} = G \cdot \Delta\rho \cdot \iint_{\sigma} \left[\int_{R-T-t'}^{R-T} \frac{\xi^2}{\ell} \cdot d\xi \right] \cdot d\sigma, \quad (3)$$

where

$$t'_{h'>0} = R - T - \sqrt{(R - T)^3 - \frac{\rho_0}{\Delta\rho} \cdot [(R + h')^3 - R^3]}, \quad (4)$$

$$t'_{h'<0} = R - T - \sqrt{(R - T)^3 - \frac{\Delta\rho_w}{\Delta\rho} \cdot [(R + h')^3 - R^3]}.$$

$\Delta\rho_w = \rho_0 - \rho_w$ is the density difference between the crust and the water. No distinction between the cases $h' \geq 0$ and $h' < 0$ has to be made if a “rock-equivalent” digital terrain model (e.g. JGP95E) is applied.

2.2.2 Generalized condensation model of Helmert

In the compensation models of F.R. Helmert (see Helmert 1884) the masses are condensed either on a spherical layer Σ_c with the radius R_c parallel to the geoid Σ_g at a fixed depth $d = 21$ km (first Helmert model) or on the geoid itself (second Helmert model). A generalized condensation model is achieved by attributing an arbitrary, but constant value to $d \geq 0$ (see Heck and Wild 2005). The compensation in both cases is local in terms of the condensation of the topographical column on the condensation layer (see Fig. 3).

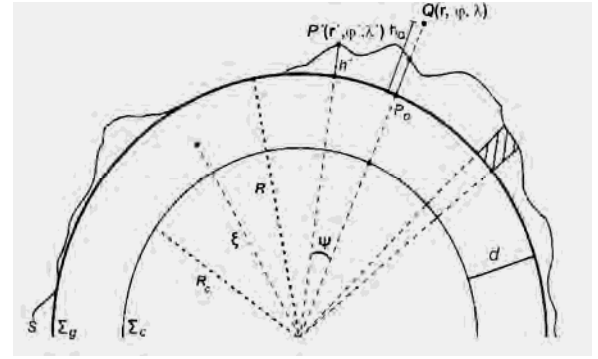


Fig. 3 Isostatic model of Helmert in spherical approximation

The potential of the condensed masses on a spherical layer Σ_c beneath the geoid is

$$V_c = G \cdot \iint_{\sigma} \frac{\kappa'}{\ell_c} \cdot R_c^2 \cdot d\sigma, \quad R_c = R - d \quad (5)$$

$$\ell_c = \sqrt{r^2 + R_c^2 - 2rR_c \cdot \cos\psi},$$

where κ' denotes the surface density. By means of the mass conservation principle the formula for the surface density is (see Martinec 1998; Heck 2003)

$$\kappa' = \rho_0 \cdot \frac{r^3 - R^3}{3R_c^2}, \quad r' = R + h'. \quad (6)$$

2.3 Gravitational effect of massive bodies

To model the topographic and isostatic masses a segmentation into volume elements Ω_i is made where the density ρ_i is assumed to be constant:

$$V(Q) = G \cdot \sum_i \rho_i \iiint_{\Omega_i} \frac{d\Omega}{\ell} \quad (7)$$

The coordinates of the Marussi tensor with respect to the local (North/East/Up) triad at the computation point Q , composed of the second derivatives of the potential, are given by Tscherning (1976). The triple integral of each volume element is analytically solvable for the prism and its approximation by the point mass, the mass line and

the mass layer. In case of the tesseroid – bounded by geographical grid lines and planes of constant height (see Heck and Seitz 2006) – no analytical solution exists in general; one variant to solve the triple integral is the evaluation by purely numerical methods, e.g. the Gauß-Legendre cubature (3D), see Wild (2006). A second alternative is provided by a Taylor series expansion of the integrand, where the term of zero order is equivalent to the point mass expression. Another possibility to compute the volume integral is the decomposition into a one-dimensional integral over the radial parameter ξ for which an analytical solution exists, and a two-dimensional spherical integral which is solved by quadrature methods, especially the Gauß-Legendre cubature (2D). In case of the second radial derivative, the respective formulae can be found in Heck and Wild (2005). The approximation of the tesseroids by prisms, postulating mass conservation, also provides an option for the solution of the triple integral; this procedure requires a transformation of the coordinate system of the prism into the local coordinate system at the computation point. The mass element approximation and computation methods as well as the comparison between these mass elements and computation methods concerning accuracy and computation time are described in detail in Wild (2006).

3 Modelling of the masses in the frequency domain

In chapter 2 the gravity field of the topographic and isostatic masses has been described in the space domain. The transformation in the frequency domain provides a better insight in the spectral behaviour of each model (see e.g. Rummel et al. 1988, Sünel 1985). In the case of satellite gravity gradiometry, the computation points are situated outside the Brillouin sphere. Therefore there exist no problems with respect to the divergence of spherical harmonic series expansions. Engels et al. (1995) describe the situation for terrestrial gravimetry where the effects of masses below and above the level of the computation point have to be discriminated.

3.1 Modelling of the topographic masses

The potential of the topographic masses in the frequency domain can be derived from Eq. (1) by series expansion of the inverse distance

$$\frac{1}{\ell} = \frac{1}{r} \sum_{n=0}^{\infty} \left(\frac{\xi}{r} \right)^n \cdot P_n(\cos \psi) \quad (8)$$

(P_n Legendre polynomial of degree n). Inserting Eq. (8) into Eq. (1) and interchanging integration and summation, the topographic potential yields

$$V_t(Q) = G\rho_0 \cdot \sum_{n=0}^{\infty} \frac{1}{r^{n+1}} \iint_{\sigma} \left[\int_{\xi=R}^{\xi=R+h'} \xi^{n+2} d\xi \right] \cdot P_n(\cos \psi) d\sigma, \quad (9)$$

where

$$P_n(\cos \psi) = \frac{1}{2n+1} \cdot \sum_{m=-n}^n Y_{nm}(\varphi, \lambda) \cdot Y_{nm}(\varphi', \lambda') \quad \text{and} \quad (10)$$

$$Y_{nm}(\varphi, \lambda) = \begin{cases} \bar{P}_{nm}(\sin \varphi) \cdot \cos m\lambda & m \geq 0 \\ \bar{P}_{n|m|}(\sin \varphi) \cdot \sin |m|\lambda & m < 0 \end{cases}$$

are the fully normalized surface spherical harmonics. Integration over the variable ξ results in

$$\int_{\xi=R}^{\xi=R+h'} \xi^{n+2} d\xi = \frac{1}{n+3} \cdot \left((R+h')^{n+3} - R^{n+3} \right) \\ = \frac{R^{n+3}}{n+3} \cdot \left(\left(1 + \frac{h'}{R} \right)^{n+3} - 1 \right) \\ = \frac{R^{n+3}}{n+3} \cdot \left(\sum_{k=0}^{n+3} \binom{n+3}{k} \cdot \left(\frac{h'}{R} \right)^k - 1 \right). \quad (11)$$

Because of the small order of magnitude of $lh'/R \leq 1.5 \cdot 10^{-3}$ the binomial series converges very fast. Using

$$H_{nm}^k = \frac{1}{4\pi} \cdot \iint_{\sigma} \left(\frac{h'}{R} \right)^k \cdot Y_{nm}(\varphi', \lambda') d\sigma, \quad (12)$$

$$H_{nm} = \frac{1}{n+3} \cdot \sum_{k=1}^{n+3} \binom{n+3}{k} \cdot H_{nm}^k$$

the final expression for the potential of the topographic masses is

$$V_t(Q) = 4\pi G\rho_0 \cdot R^2 \\ \cdot \sum_{n=0}^{\infty} \frac{1}{2n+1} \cdot \left(\frac{R}{r} \right)^{n+1} \cdot \sum_{m=-n}^n H_{nm} \cdot Y_{nm}(\varphi, \lambda) \\ = 4\pi G\rho_0 \cdot R^2 \cdot \sum_{n=0}^{\infty} \frac{1}{2n+1} \cdot \left(\frac{R}{r} \right)^{n+1} \cdot \sum_{m=-n}^n \left[H_{nm}^1 \right. \\ \left. + \frac{n+2}{2} \cdot H_{nm}^2 + \frac{(n+1) \cdot (n+2)}{6} \cdot H_{nm}^3 \right. \\ \left. + \frac{1}{n+3} \sum_{k=4}^{n+3} \binom{n+3}{k} \cdot H_{nm}^k \right] \cdot Y_{nm}(\varphi, \lambda). \quad (13)$$

Similar expressions have been presented by Rummel et al. (1988) and Tsoulis (1999).

3.2 Modelling of the isostatic masses

3.2.1 Isostatic Model of Airy-Heiskanen

Based on the series expansion (Eq. (8)) of the reciprocal distance $1/\ell$ the potential of the isostatic masses can be transformed from the space domain, Eq. (3), to the frequency domain. The radial integration results in

$$\begin{aligned}
\int_{\xi=R-T-t'}^{\xi=R-T} \xi^{n+2} d\xi &= \frac{1}{n+3} \cdot \left((R-T)^{n+3} - (R-T-t')^{n+3} \right) \\
&= \frac{(R-T)^{n+3}}{n+3} \cdot \left(1 - \left(1 - \frac{t'}{R-T} \right)^{n+3} \right) \\
&= \frac{(R-T)^{n+3}}{n+3} \\
&\quad \cdot \left(1 - \sum_{k=0}^{n+3} (-1)^k \cdot \binom{n+3}{k} \cdot \left(\frac{t'}{R-T} \right)^k \right).
\end{aligned} \tag{14}$$

Using

$$\begin{aligned}
T_{nm}^k &= \frac{1}{4\pi} \cdot \iint_{\sigma} \left(\frac{t'}{R-T} \right)^k \cdot Y_{nm}(\varphi', \lambda') d\sigma, \\
T_{nm} &= \frac{1}{n+3} \cdot \sum_{k=1}^{n+3} (-1)^k \cdot \binom{n+3}{k} \cdot T_{nm}^k
\end{aligned} \tag{15}$$

the isostatic potential of Airy-Heiskanen is

$$\begin{aligned}
V_{A-H}(Q) &= 4\pi G \rho_0 \cdot R^2 \cdot \sum_{n=0}^{\infty} \frac{1}{2n+1} \cdot \left(\frac{R}{r} \right)^{n+1} \\
&\quad \cdot \sum_{m=-n}^n \left(-\frac{\Delta\rho}{\rho_0} \right) \cdot \left(\frac{R-T}{R} \right)^{n+3} \cdot T_{nm} \cdot Y_{nm}(\varphi, \lambda) \\
&= 4\pi G \rho_0 \cdot R^2 \cdot \sum_{n=0}^{\infty} \frac{1}{2n+1} \cdot \left(\frac{R}{r} \right)^{n+1} \\
&\quad \cdot \sum_{m=-n}^n \frac{\Delta\rho}{\rho_0} \cdot \left(\frac{R-T}{R} \right)^{n+3} \cdot \left[T_{nm}^1 - \frac{n+2}{2} \cdot T_{nm}^2 \right. \\
&\quad \left. + \frac{(n+1) \cdot (n+2)}{6} \cdot T_{nm}^3 \right. \\
&\quad \left. - \frac{1}{n+3} \sum_{k=4}^{n+3} (-1)^k \cdot \binom{n+3}{k} \cdot T_{nm}^k \right] \cdot Y_{nm}(\varphi, \lambda).
\end{aligned} \tag{16}$$

The (anti-)root depth t' is described in Eq. (4) resp. by the series expansion in (h'/R)

$$\begin{aligned}
t' &= \left(\frac{R}{R-T} \right)^2 \cdot \frac{\rho_0}{\Delta\rho} \cdot R \cdot \left\{ C_1 \cdot \left(\frac{h'}{R} \right) + C_2 \cdot \left(\frac{h'}{R} \right)^2 \right. \\
&\quad \left. + C_3 \cdot \left(\frac{h'}{R} \right)^3 + o\left(\left(\frac{h'}{R} \right)^4 \right) \right\}
\end{aligned} \tag{17}$$

where

$$\begin{aligned}
C_1 &= 1 \\
C_2 &= 1 + \frac{\rho_0}{\Delta\rho} \cdot \left(\frac{R}{R-T} \right)^3 \\
C_3 &= \frac{1}{3} + 2 \frac{\rho_0}{\Delta\rho} \cdot \left(\frac{R}{R-T} \right)^3 + \frac{5}{3} \left(\frac{\rho_0}{\Delta\rho} \right)^2 \cdot \left(\frac{R}{R-T} \right)^6
\end{aligned} \tag{18}$$

The term of first order equals the approximation of Rummel et al (1988) and Tsoulis (1999).

3.2.2 Helmert's condensation model

Helmert's condensation potential is described in Eq. (5). The expansion of the reciprocal distance ℓ_c in a series of Legendre polynomials (see Heck 2003, Eq. (C10)) and the description of the surface density as binomial series

$$\begin{aligned}
\frac{1}{3} \cdot (t'^3 - R^3) &= \frac{R^3}{3} \cdot \left(\left(1 + \frac{h'}{R} \right)^3 - 1 \right) \\
&= \frac{R^3}{3} \cdot \left(\sum_{k=0}^3 \binom{3}{k} \cdot \left(\frac{h'}{R} \right)^k - 1 \right)
\end{aligned} \tag{19}$$

yields

$$\begin{aligned}
V_c &= G \rho_0 \cdot \frac{R^3}{r} \cdot \sum_{n=0}^{\infty} \left(\frac{R_c}{r} \right)^n \\
&\quad \cdot \iint_{\sigma} \left(\frac{1}{3} \cdot \sum_{k=1}^3 \binom{3}{k} \cdot \left(\frac{h'}{R} \right)^k \right) \cdot P_n(\cos \psi).
\end{aligned} \tag{20}$$

Using Eq. (10) and Eq. (12) resp.

$$C_{nm} = \frac{1}{3} \cdot \sum_{k=1}^3 \binom{3}{k} \cdot H_{nm}^k \tag{21}$$

the final formula for the condensation potential is

$$\begin{aligned}
V_c &= 4\pi G \rho_0 \cdot R^2 \\
&\quad \cdot \sum_{n=0}^{\infty} \frac{1}{2n+1} \cdot \left(\frac{R}{r} \right)^{n+1} \cdot \sum_{m=-n}^n \left(\frac{R_c}{R} \right)^n \cdot C_{nm} \cdot Y_{nm}(\varphi, \lambda) \\
&= 4\pi G \rho_0 \cdot R^2 \cdot \sum_{n=0}^{\infty} \frac{1}{2n+1} \cdot \left(\frac{R}{r} \right)^{n+1} \cdot \sum_{m=-n}^n \left(\frac{R_c}{R} \right)^n \\
&\quad \cdot \left[H_{nm}^1 + H_{nm}^2 + \frac{1}{3} \cdot H_{nm}^3 \right] \cdot Y_{nm}(\varphi, \lambda).
\end{aligned} \tag{22}$$

4 Results

The modelling in the space and the frequency domain is compared for the second radial derivative of the potential. In the space domain modelling the tesseroïd approach using numerical integration has been applied, involving 3D Gauß-Legendre cubature with $2 \times 2 \times 2 = 8$ nodes per tesseroïd for the calculation of the topographic and the Airy-Heiskanen isostatic components. In Wild (2006) it is shown that this method is precise and needs low computation time. In case of Helmert's models, the surface integral is evaluated by the 2D Gauß-Legendre product formula with $2 \times 2 = 4$ nodes per element.

For the simulation the following standard numerical values of the respective parameters have been used: $R = 6378137$ m, $G = 6.673 \cdot 10^{-11}$ m³kg s⁻², $h_Q = r - R = 260$ km (satellite height), $\rho_0 = 2670$ kg m⁻³, $\Delta\rho = 600$ kg m⁻³, $T = 25$ km (Airy-Heiskanen), $d = 21$ km (Helmert I) or $d = 0$ (Helmert II). Furthermore, the digital „rock-equivalent” terrain model JGP95E with a resolution of $1^\circ \times 1^\circ$ has been used. For the second radial derivative of the potential the formulae (13), (16) and (22) have to be expanded by the factor $(n+1) \cdot (n+2) / r^2$ in the frequency domain. The root depth t' of Airy-Heiskanen is evaluated via Eq. (4).

Fig. 4 displays the different contributions of H_{nm}^k resp. T_{nm}^k until $k = 3$ to the second radial derivative

of the topographic potential resp. the isostatic potential of Airy-Heiskanen at the satellite height $h_Q = 260$ km. The coefficients H_{nm} (see Eq. (12)) and T_{nm} (see Eq. (15)) are multiplied by the factors of Eq. (13) in case of the topographic potential and the factors of Eq. (16) in case of the isostatic potential of Airy-Heiskanen. The dimension of the degree variances is therefore $(1/s^2)^2$. For the topographic potential the maximum value of the degree variances of H_{nm}^1 is about 10^{-18} , the order of magnitude of the degree variances of H_{nm}^2 and H_{nm}^3 are less by a factor of 10^{-5} and 10^{-10} , respectively. The maximum value of the coefficients T_{nm} is 10^{-19} for T_{nm}^1 resp. 10^{-23} and 10^{-26} for T_{nm}^2 and T_{nm}^3 in the case of the Airy-Heiskanen model. In Fig. 4 a convergence is visible which also holds for Helmert's models. In Fig. 5 the power spectra of the different isostatic models for the second radial potential derivative are compared up to maximum degree 180. Here the power spectra result from the difference of the respective spherical harmonic coefficients. It is obvious that the Airy-Heiskanen and the Helmert I models are practically equivalent, while the degree variances for the topographic-isostatic potential related to the Helmert II model are smaller by a factor of 10^{-4} . In Tab. 1 the statistics of the different contributions to the second radial derivative of the topographic potential are listed. Comparing the terms of various orders in $(h/R)^k$ it becomes clear that third order terms ($k = 3$) can be neglected. The rms value is about 10^{-5} smaller than the total value. In Tab. 2 the statistics of the difference between the modelling in the space and frequency domains is displayed. For this investigation the second radial derivative of the topographic and isostatic potentials has been evaluated on an equiangular grid of $1^\circ \times 1^\circ$ resolution on a sphere with radius $r_Q = R + h_Q$, where $h_Q = 260$ km, on the one hand by summing up the contributions of the tesseroids in space domain, on the other hand by spherical harmonic synthesis involving the coefficients H_{nm} , T_{nm} and C_{nm} . The rms of each difference is at the level of $2 \cdot 10^{-2}$ E.U..

5 Conclusions

The numerical results show that the spectral behaviour of the Airy-Heiskanen model is practically equivalent to the Helmert I model. Therefore the Helmert I model – calculated with a simpler integral kernel – is an efficient alternative to the classical Airy-Heiskanen model (see Wild and Heck 2005). The degree variances of the topographic-isostatic effect of the Helmert II model are 5 orders of magnitude smaller; due to this

underestimation the residual field is (after removing the effect of the topographic-isostatic masses from the observed gravity gradients) not as smoothed as in the case of the Helmert I model. The investigations in the frequency domain confirm the results of the space domain evaluations (see Heck and Wild 2005). It has also been shown that third order contributions of the coefficients H_{nm}^3 and T_{nm}^3 can be neglected.

Acknowledgements: The authors thank Dr. Kurt Seitz for making available his software for harmonic analysis.

References

- Engels J, Grafarend EW, Sorcik P (1995) The gravitational field of topographic-isostatic masses and the hypothesis of mass condensation – Part I and II. Schriftenreihe der Institute des Fachbereichs Vermessungswesen. Tech rep 1995.1, Department of Geodesy, Stuttgart
- Heck B (2003) On Helmert's methods of condensation. *J Geod* 77: 155-170 DOI: 10.1007/s00190-003-0318-5
- Heck B, Seitz K (2006) A comparison of the tesseroid, prism, and point mass approaches for mass reductions in gravity modelling. Accepted for publication in *J Geod*
- Heck B, Wild F (2005) Topographic reductions in satellite gravity gradiometry based on a generalized condensation model. In: Sansò F (ed) *A Window on the Future of Geodesy*. Springer, Berlin Heidelberg New York, pp 294-299
- Heiskanen WA, Moritz H (1967) *Physical Geodesy*. Freeman and Company, San Francisco
- Heiskanen WA, Vening-Meinesz FA (1958) *The Earth and its Gravity Field*. In McGraw-Hill Series in the Geological Sciences
- Helmert FR. (1884) *Die mathematischen und physikalischen Theorien der Höheren Geodäsie*. II. Teil: Die physikalischen Theorien, B.G. Teubner, Leipzig (Neuaufgabe 1962)
- Kuhn M (2000) *Geoidbestimmung unter Verwendung verschiedener Dichtehypothesen*. Reihe C, Heft Nr. 520, Deutsche Geodätische Kommission, München
- Martinez Z (1998) *Boundary-value problems for gravimetric determination of a precise geoid*. Lecture notes in Earth Sciences 73. Springer Berlin Heidelberg New York
- Mooney WD, Laske G, Masters TG (1998) CRUST 5.1: a global crustal model at $5^\circ \times 5^\circ$. *J. Geophys. Res.* 103: 727-747
- Rummel R et al. (1988) Comparisons of global topographic/isostatic models to the Earth's observed gravity field. Department of Geodetic Science and Surveying, Rep. No 388, The Ohio State University, Columbus, Ohio
- Sünel H (1985) *An isostatic Earth model*. Department of Geodetic Science and Surveying, Rep. No 367, The Ohio State University, Columbus, Ohio
- Tsouliis D (1999) *Spherical harmonic computations with topographic/isostatic coefficients*, Schriftenreihe des Instituts für Astronomische und Physikalische Geodäsie und der Forschungseinrichtung Satellitengeodäsie der TU München, Nr. 3
- Tsouliis D (2001) A comparison between the Airy/Heiskanen and the Pratt/Hayford isostatic models for the computation of potential harmonic coefficients. *J Geod* 74: 637-643 DOI: 10.1007/s001900000124
- Tscherning CC (1976) *Computation of the Second-Order Derivatives of the Normal Potential Based on the Representation by a Legendre Series*. *manuscripta geodaetica* 1: 71-92
- Wild F, Heck B (2005) A comparison of different isostatic models applied to satellite gravity gradiometry. In: Jekeli C, Bastos L, Fernandes J (eds.) *Gravity, Geoid and Space Missions*, Springer, Berlin Heidelberg New York, pp 230-235
- Wild F (2006) A comparison of different mass elements for use in gravity gradiometry, Submitted to *J Geod*

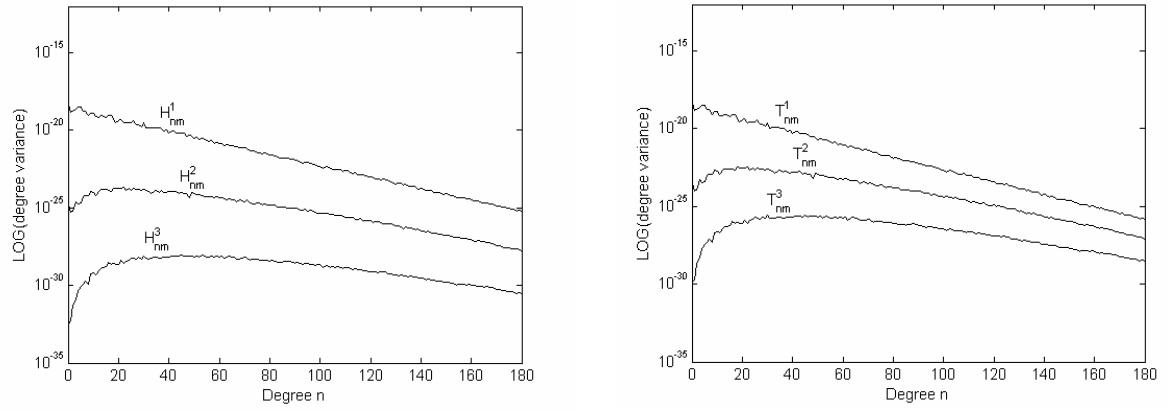


Fig. 4 Degree variances of the different contributions H_{nm}^k / T_{nm}^k of the second radial derivative of the topographic potential/isostatic potential of Airy-Heiskanen

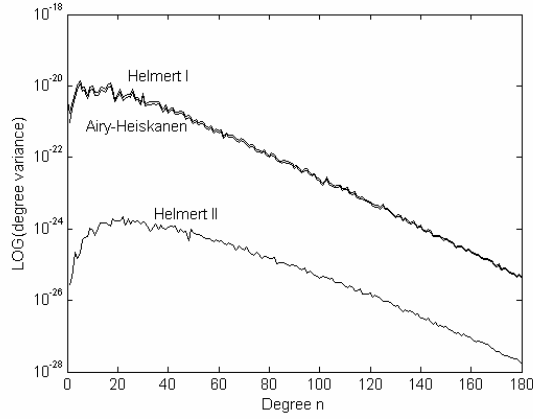


Fig. 5 Degree variances of the second radial derivative of the topographic-isostatic potential at satellite altitude

Tab. 1 Statistics of the different contributions to the second radial derivative of the topographic potential at satellite altitude

	min [E.U.]	max [E.U.]	rms [E.U.]
H1nm	-4.47616	6.67277	2.19989
H2nm	-4.27182e-002	7.36917e-002	8.98439e-003
H3nm	-7.54736e-004	9.97737e-004	7.01472e-005
Total	-4.44416	6.72857	2.19964

Tab. 2 Statistics of the differences in the second radial derivative between the modelling in the space and frequency domain

	min [E.U.]	max [E.U.]	rms [E.U.]
Topographic potential	-1.98811e-001	3.36186e-001	2.52421e-002
Isostatic potential of Airy-Heiskanen	-1.77375e-001	2.75949e-001	2.18956e-002
Isostatic potential of Helmert I	-1.66461e-001	2.87043e-001	2.26816e-002
Isostatic potential of Helmert II	-1.96958e-001	3.34318e-001	2.57458e-002

Terrain-Related Gravimetric Quantities Computed for the Next EGM

Nikolaos K. Pavlis¹, John K. Factor², and Simon A. Holmes¹

¹ SGT, Inc., 7701 Greenbelt Road, Suite 400, Greenbelt, Maryland 20770, USA, npavlis@sgt-inc.com

² National Geospatial-Intelligence Agency, Arnold, Missouri 63010, USA

Abstract. The development of a new Earth Gravitational Model (EGM) to degree 2160 is underway within the National Geospatial-Intelligence Agency (NGA) of the USA and its supporting group at SGT, Inc.. Among other things this endeavor requires the compilation of a very high-resolution global topographic database, to be used consistently in the computation of all terrain-related quantities necessary for the pre-processing of gravity data and for the development and subsequent use of the new EGM. Such quantities include Residual Terrain Model (RTM) effects, analytical continuation terms (g_1), Topographic/Isostatic gravitational models, and models necessary to convert height anomalies to geoid undulations. Given the very high degree of the new EGM, all these quantities and models have to be computed at a sufficiently high resolution. Towards this goal, we have compiled a global 30"×30" Digital Topographic Model (DTM2006.0), relying heavily on elevation information made available from the Shuttle Radar Topography Mission (SRTM). We have computed, over all land areas, RTM effects and g_1 analytical continuation terms using the DTM2006.0 30"×30" data. We have also used 5'×5' and 2'×2' versions of DTM2006.0 to compute models of the Topographic/Isostatic gravitational potential complete to degree 2160. In this paper we present these results and discuss their possible use for the development of the new EGM.

Keywords. Digital Terrain Model, Earth Gravitational Model, Residual Terrain Model, Forward Modeling, Analytical Continuation

1 Introduction

The pre-processing and analysis of the detailed surface gravity data necessary to support the development of an Earth Gravitational Model (EGM) complete to harmonic degree and order 2160, depends critically on the availability of accurate topographic data, at a resolution sufficiently higher than the

resolution of the area-mean gravity anomalies, which will be used eventually for the development of the EGM. In *Lemoine et al.* (1998, Section 2.1) *Factor* discusses some of the uses of such topographic data within the context of the development and the subsequent use of a high-resolution EGM. These include the computation of Residual Terrain Model (RTM) effects, the computation of analytical continuation terms (g_1), the computation of Topographic/Isostatic gravitational models that may be used to “fill-in” areas void of other data, and the computation of models necessary to convert height anomalies to geoid undulations. For these computations to be made consistently, it is necessary to compile first a high-resolution global Digital Topographic Model (DTM), whose data will support the computation of all these terrain-related quantities.

2 The DTM2006.0 Database

For EGM96 (*Lemoine et al.*, 1998), which was complete to degree and order 360, a global digital topographic database (JGP95E) at 5'×5' resolution was considered sufficient. JGP95E was formed by merging data from 29 individual sources, and, as acknowledged by its developers, left a lot to be desired in terms of accuracy and global consistency. Since that time, thanks primarily to the Shuttle Radar Topography Mission (SRTM) (*Werner*, 2001), significant progress has been made on the topographic mapping of the Earth from space. During approximately 11 days in 2000 (February 11-22), the SRTM collected data within latitudes 60°N and 56°S, thus covering approximately 80% of the total landmass of the Earth with elevation data of high, and fairly uniform, accuracy. *Rodriguez et al.* (2005) discuss in detail the accuracy characteristics of the SRTM elevations. Comparisons with ground control points whose elevations were determined independently using kinematic GPS positioning, indicate that the 90% absolute error of the SRTM elevations ranges from ± 6 to ± 10 meters, depend-

ing on the geographic area (*ibid.*, Table 2.1). Additional information regarding the SRTM can be obtained from the web site of the United States' Geological Survey (USGS) (<http://srtm.usgs.gov/>), and from the web site of NASA's Jet Propulsion Laboratory (<http://www2.jpl.nasa.gov/srtm>). Unfortunately no error estimates associated with the SRTM data were made available to us.

We compiled DTM2006.0 by overlying the SRTM data over the data of DTM2002 (*Saleh and Pavlis, 2003*). In addition to the SRTM data, DTM2006.0 contains ice elevations derived from ICESat laser altimeter data over Greenland (*Ekholm, personal communication, 2005*) and over Antarctica (*DiMarzio, personal communication, 2005*). Over Antarctica, we have also used data from the "BEDMAP" project (<http://www.antarctica.ac.uk/aedc/bedmap/>) to define ice and water column thickness. Over the ocean, DTM2006.0 contains essentially the same information as DTM2002, which originates in the estimates of bathymetry from altimetry data and ship depth soundings of *Smith and Sandwell (1997)*. DTM2006.0 was compiled in 30"×30" resolution (providing height and depth information only), and in 2'×2' and 5'×5' resolutions, where lake depth and ice thickness data are also included. DTM2006.0 is identical to DTM2002 in terms of database structure and information content.

3 Harmonic Models of Elevation-related Quantities

3.1 Topography

We define the spherical harmonic expansion of mean values of an elevation-related quantity \bar{H}_{ij} as:

$$\bar{H}_{ij} = \bar{H}(\theta_i, \lambda_j) = \frac{1}{\Delta\sigma_i} \sum_{n=0}^N \sum_{m=-n}^n \bar{H}_{nm} \cdot \bar{Y}_{nm}^{ij} , \quad (1)$$

with the area element:

$$\Delta\sigma_i = \Delta\lambda \int_{\theta_i}^{\theta_{i+1}} \sin\theta d\theta = \Delta\lambda \cdot (\cos\theta_i - \cos\theta_{i+1}) , \quad (2)$$

and the integrated surface spherical harmonic:

$$\begin{aligned} \bar{Y}_{nm}^{ij} &= \int_{\theta_i}^{\theta_{i+1}} \bar{P}_{n|m|}(\cos\theta) \sin\theta d\theta \times \\ &\int_{\lambda_j}^{\lambda_{j+1}} \begin{cases} \cos m\lambda & \text{if } m \geq 0 \\ \sin|m|\lambda & \text{if } m < 0 \end{cases} d\lambda \quad . \quad (3) \end{aligned}$$

θ_i is the co-latitude and λ_j the longitude associated with a cell on the i -th "row" and j -th "column" of a global equiangular grid. N is the maximum degree and order of the expansion, and \bar{H}_{nm} are the fully normalized spherical harmonic coefficients associ-

ated with the data \bar{H}_{ij} . $\bar{P}_{n|m|}$ are fully-normalized Associated Legendre functions. We define the degree variance \bar{H}_n at degree n to be:

$$\bar{H}_n = \sum_{m=-n}^n (\bar{H}_{nm})^2 . \quad (4)$$

Starting from the 2'×2' DTM2006.0 mean elevations we computed two separate sets of \bar{H}_{nm} coefficients, both complete to degree and order 2700. For the first expansion, the \bar{H}_{ij} values represented both heights and depths, while for the second, \bar{H}_{ij} were set to zero over all oceanic cells. In both expansions the \bar{H}_{nm} coefficients were estimated using a "Type 1" block diagonal least squares adjustment (see *Pavlis in Lemoine et al., 1998, Sect. 8.2.2* for details). The use of 2'×2' area-mean values implies a sampling Nyquist degree of 5400; hence the expansions to degree and order 2700 are only marginally affected by aliasing errors (see also *Colombo, 1981*). Furthermore, for the applications related to the EGM under development (computation of RTM effects, computation of models necessary to convert height anomalies to geoid undulations), it is sufficient to use these expansions up to degree and order 2160, or 2190 at the most. Figure 1 shows the degree variances of these two expansions. As expected, the expansion representing heights only, possesses significantly less power than the one representing both heights and depths.

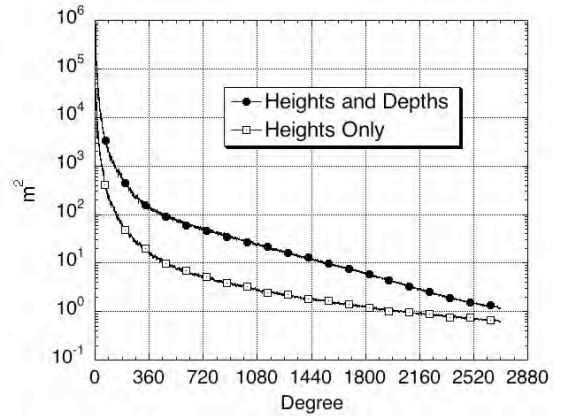


Fig. 1 Elevation-related degree variances from two expansions to $N=2700$, based on 2'×2' DTM2006.0 data.

3.2 Topographic/Isostatic Potential

We have used the formulation described by *Pavlis and Rapp (1990)* to determine spherical harmonic coefficients of the Topographic/Isostatic (T/I) potential implied by the Airy/Heiskanen isostatic hy-

pothesis, with a constant 30 km depth of compensation. We evaluated these coefficients up to degree and order 2160, using the DTM2006.0 data, in two ways: (a) using 5'x5' data, and, (b) using 2'x2' data. Figure 2 shows the gravity anomaly degree variances implied by these coefficients and by their differences.

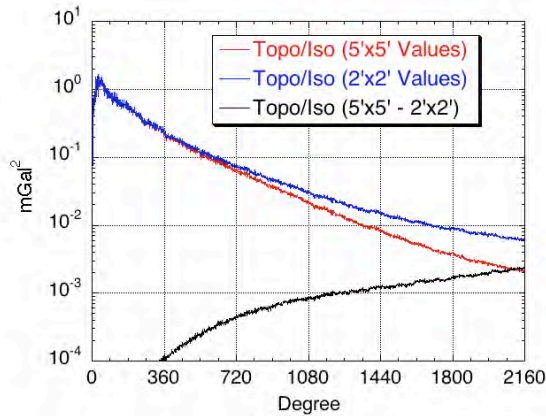


Fig. 2 Gravity anomaly degree variances implied by two estimates of the Topographic/Isostatic coefficients and by their difference (see text for details).

As expected, coefficients estimated from 2'x2' values imply higher power than those estimated from 5'x5' values, the difference being increasingly more significant after degree 720 or so. This suggests that in order to obtain a T/I spectrum that possesses full power (especially as this pertains to the Topographic potential), one may have to use a very high-resolution DTM (e.g., 30''x30''). Figure 3 shows the gravity anomaly spectra of the Topography only, its Isostatic compensation, and their combination (T/I), from the estimation using the 2'x2' values.

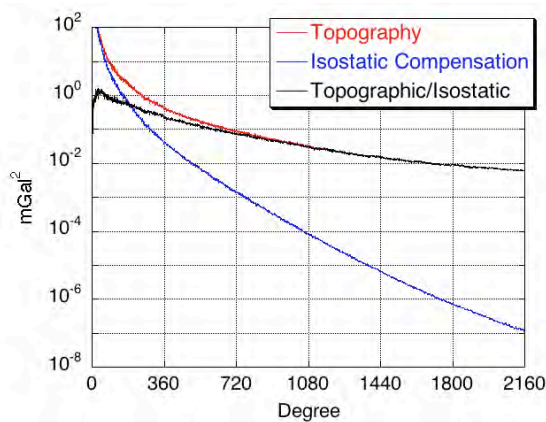


Fig. 3 Gravity anomaly degree variances of the potential of the Topography, its Isostatic compensation, and their combination (T/I).

As expected, isostatic compensation, being of regional character, has limited effect on the T/I spectrum beyond degree 720 or so.

As in the case of several global gravitational models developed previously (e.g., OSU89A/B *Rapp and Pavlis*, 1990; EGM96 *Lemoine et al.*, 1998), within the development of the new EGM, the T/I model is intended to aid the creation of synthetic gravity anomaly values. These will be used to “fill-in” areas where actual gravity data are unavailable, or their spectral content beyond some degree n where ($360 \leq n \leq 720$), cannot be used due to proprietary data issues. In the past, some geophysicists have criticized this practice, since it forces into the geopotential solution the isostatic hypothesis that underlies the T/I model’s development. This renders the geopotential model useless for some geophysical applications, at least over the regions filled-in with the T/I gravity anomalies, and over the wavelengths implied by the degree range of the T/I coefficients used. With these considerations in mind, and in view of the implications of Figures 2 and 3, we decided to test also an alternative approach for the creation of the synthetic “fill-in” gravity anomalies that is free of any isostatic hypothesis. This approach is discussed next.

4 Forward Modeling Using RTM Gravity Anomaly Spectra

We used the 30''x30'' data of the DTM2006.0 database to compute over *all* of the Earth’s landmass (including a margin extending into the ocean), a 30''x30'' grid of the gravity anomalies (Δg) implied by a Residual Terrain Model (RTM). This RTM was referenced to a topographic surface, created from the elevation harmonic coefficients described in Section 3.1, to degree and order 360. We computed the RTM Δg as described in detail by *Forsberg* (1984). We then formed 2'x2' area-mean values of these RTM Δg , and supplemented this (primarily) land dataset with zero values for the 2'x2' cells that are located over ocean areas (excluding the margin mentioned above). In this fashion we created a *global* 2'x2' RTM Δg dataset. We then analyzed harmonically this dataset, and computed the ellipsoidal harmonic coefficients of the RTM Δg up to degree and order 2700. For degrees ($n < 360$) these coefficients are small (and of no further use to us) due to the use of a reference topographic surface to degree 360. Figure 4 shows the anomaly degree variances of these RTM Δg .

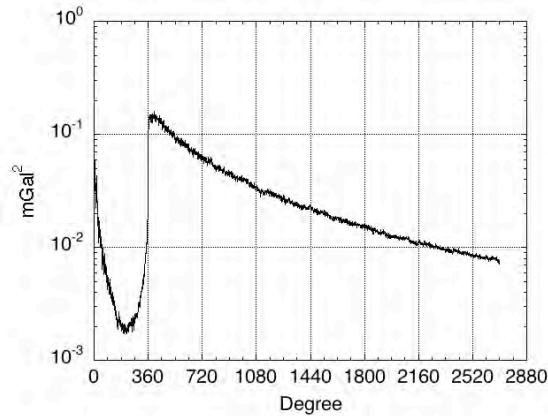


Fig. 4 Residual Terrain Model (RTM) gravity anomaly degree variances.

Availability of these ellipsoidal harmonic coefficients of the RTM Δg allowed us to synthesize “fill-in” values as follows:

- A global $5' \times 5'$ Δg file that includes proprietary data was created (and kept) within NGA. Over areas void of *any* gravity anomaly data, proprietary or not, (e.g., Antarctica and some areas in South America and Africa), the $5' \times 5'$ Δg were synthesized from GGM02S (Tapley *et al.*, 2005) ($n \leq 60$), augmented with EGM96 (Lemoine *et al.*, 1998) ($61 \leq n \leq 360$), and further augmented with the RTM Δg coefficients for ($361 \leq n \leq 2160$).
- NGA personnel analyzed harmonically this dataset, and computed the ellipsoidal harmonic coefficients of these Δg values. NGA provided to us *only* the anomaly degree variances from this expansion, to degree 2160.
- Lower degree coefficients of the above expansion (up to some maximum degree commensurate with the minimum cell size that the use of the proprietary data is unrestricted) were then augmented with higher degree coefficients of the RTM Δg expansion. In this fashion, NGA created synthetic “cut-and-paste” model(s), all extending to degree and order 2160.
- Using such “cut-and-paste” model(s), synthetic “fill-in” $5' \times 5'$ Δg values were created for all the areas occupied by proprietary data (as well as for the areas void of *any* gravity anomaly values).
- The collection of all these “fill-in” $5' \times 5'$ Δg values, along with the unrestricted $5' \times 5'$ data, constitutes the *global* $5' \times 5'$ Δg file that NGA made available to us for further analysis.

This approach allowed NGA to provide us a global $5' \times 5'$ Δg database that does not include proprietary information.

We tested the effectiveness of this approach *globally*, by comparing the anomaly degree variances obtained from step (b), to the anomaly degree variances that we obtained from the harmonic analysis of the unrestricted $5' \times 5'$ Δg database that we received from NGA. Figure 5 shows these spectra.

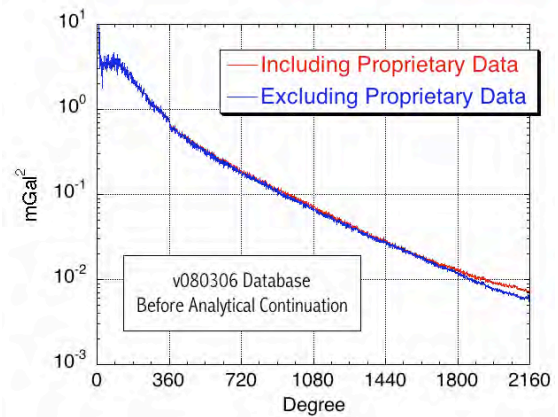


Fig. 5 Gravity anomaly degree variances implied by the analysis of two global $5' \times 5'$ gravity anomaly databases (one including and one excluding proprietary data).

As can be seen from Figure 5, the degree variances obtained from the analysis of the unrestricted data are in excellent agreement with those obtained from the proprietary data. Only after degree ~ 1650 does the unrestricted data analysis provide a systematically underpowered spectrum. Figure 5 indicates that the forward modeling approach using the RTM anomaly spectra, which we have devised and implemented, circumvents the proprietary data issues without degrading the gravitational solution significantly (at least in terms of the recovered power spectrum).

We also tested the effectiveness of the approach *locally*, as follows. Over areas with high quality, unrestricted $5' \times 5'$ gravity anomalies, (e.g., USA, Australia) we compared the actual data to synthetic values created from pairs of harmonic coefficient sets. Each pair contains: (a) a gravitational expansion truncated to some maximum degree N_{max} (denoted by $G_{N_{max}}$), and, (b) a corresponding expansion that is augmented beyond degree N_{max} and up $n=2160$, with the coefficients implied by the RTM Δg (denoted by $G+RTM_{N_{max}}$). Figure 6 shows the discrepancies between the actual $5' \times 5'$ data and the synthetic values over the USA, for $N_{max}=360$ and $N_{max}=720$.

It is clear from Figure 6, that augmenting the lower degree gravitational expansion with the higher degree coefficients of the RTM Δg expansion, improves significantly the agreement with the actual $5' \times 5'$ data. As expected, this is especially true over mountainous regions like the Rocky Mountains. An obvious shortcoming of our RTM-based forward modeling approach is that it can only improve the modeling of short wavelength gravitational signals, if these signals are correlated with the topography. Table 1 summarizes the results from comparisons over the USA.

Table 1. Statistics of differences between actual $5'$ gravity anomalies and synthetic values over the USA (mGal).

Model	Min.	Max.	Mean	S. Dev.
G_360	-144	150	0.2	16.3
G-540	-123	140	0.2	13.4
G_720	-137	125	0.2	11.5
G+RTM_360	-57	107	0.3	8.7
G+RTM_540	-51	84	0.3	6.5
G+RTM_720	-51	61	0.3	5.4

Table 1 shows that over the USA, augmenting the gravitational model with the RTM coefficients, reduces the standard deviation of the differences between actual and synthetic $5' \times 5'$ gravity anomalies by about a factor of two. Corresponding comparisons over Australia showed considerably less improvement obtained by augmenting the gravitational expansion with the RTM coefficients, compared to Table 1. This is because the terrain in Australia is generally less mountainous than over the USA.

5 Computation of g_1 Terms

We used the $30'' \times 30''$ data of DTM2006.0 to compute analytical continuation terms, according to:

$$(g_1)_P = -G\rho R^2 H_P \cdot \iint_{\sigma} \frac{H - H_P}{l_0^3} d\sigma, \quad (5)$$

(see Wang, 1987) over all land areas. These terms may be used to analytically continue surface gravity anomalies to the ellipsoid. These g_1 terms represent an approximation to the *linear* gravity anomaly gradient, *assuming* linear correlation between free-air anomaly and elevation. We are currently investigating if this approximation is adequate for the expansions to degree 2160, or if a better continuation procedure can be implemented based on the iterative computation of a Taylor series employing considerably higher order gradients, computed from the harmonic coefficients themselves. This work is still in progress. We have also formed $2' \times 2'$ and $5' \times 5'$

averages of the g_1 terms, and we have analyzed harmonically the $2' \times 2'$ averages to estimate harmonic coefficients to degree and order 2700.

6 Summary and Future Work

In preparation for a new EGM complete to degree 2160, we have compiled a new $30'' \times 30''$ global DTM (DTM2006.0). We have used its data to evaluate various terrain-related quantities, including RTM-implied Δg , Topographic/Isostatic potential coefficients, and g_1 analytical continuation terms. We have also analyzed harmonically topographic elevations, RTM-implied gravity anomalies, and the g_1 terms. We have devised and implemented successfully a forward modeling technique using the RTM anomaly spectrum, to circumvent proprietary data issues. Improvements to the analytical continuation procedure are still under study.

References

- Colombo, O. (1981). Numerical methods for harmonic analysis on the sphere. *Report 310*, Dept. of Geod. Sci. and Surv., Ohio State University, Columbus, USA.
- Forsberg, R. (1984). A study of terrain reductions, density anomalies and geophysical inversion methods in gravity field modelling. *Report 355*, Dept. of Geod. Sci. and Surv., Ohio State University, Columbus, USA.
- Lemoine, F.G. and 14 co-authors (1998). The development of the joint NASA GSFC and the National Imagery and Mapping Agency (NIMA) geopotential model EGM96. *NASA Tech. Pub.* 1998-206861, Goddard Space Flight Center, Greenbelt, Maryland, USA.
- Pavlis, N.K. and R.H. Rapp (1990). The development of an isostatic gravitational model to degree 360 and its use in global gravity modelling. *Geophys. J. Int.*, 100, 369-378.
- Rapp, R.H. and N.K. Pavlis (1990). The development and analysis of geopotential coefficient models to spherical harmonic degree 360. *J. Geophys. Res.*, 95, 21885-21911.
- Rodriguez, E., C.S. Morris, J.E. Belz, E.C. Chapin, J.M. Martin, W. Daffer, S. Hensley (2005). An assessment of the SRTM topographic products. *Tech. Rep.* D-31639, Jet Propulsion Laboratory, Pasadena, California, 143 pp.
- Saleh, J. and N.K. Pavlis (2003). The development and evaluation of the global digital terrain model DTM2002. *Gravity and Geoid 2002*, Proc. of the 3rd Meeting of the IGGC, Tzavos, I.N. (Ed.), Ziti, Thessaloniki, Greece.
- Smith, W.H.F. and D.T. Sandwell (1997). Global sea floor topography from satellite altimetry and ship depth soundings. *Science*, 277, pp. 1956-1962.
- Tapley, B., and 12 co-authors (2005). GGM02 – An Improved Earth Gravity Field Model from GRACE, *J. Geod.*, DOI 10.1007/s00190-005-0480-z.
- Wang, Y.M. (1987). Numerical aspects of the solution of Molodensky's problem by analytical continuation. *Manusc. Geod.*, 12, pp. 290-295.
- Werner, M. (2001). Shuttle Radar Topography Mission (SRTM), Mission overview. *J. Telecom.*, 55, pp. 75-79.

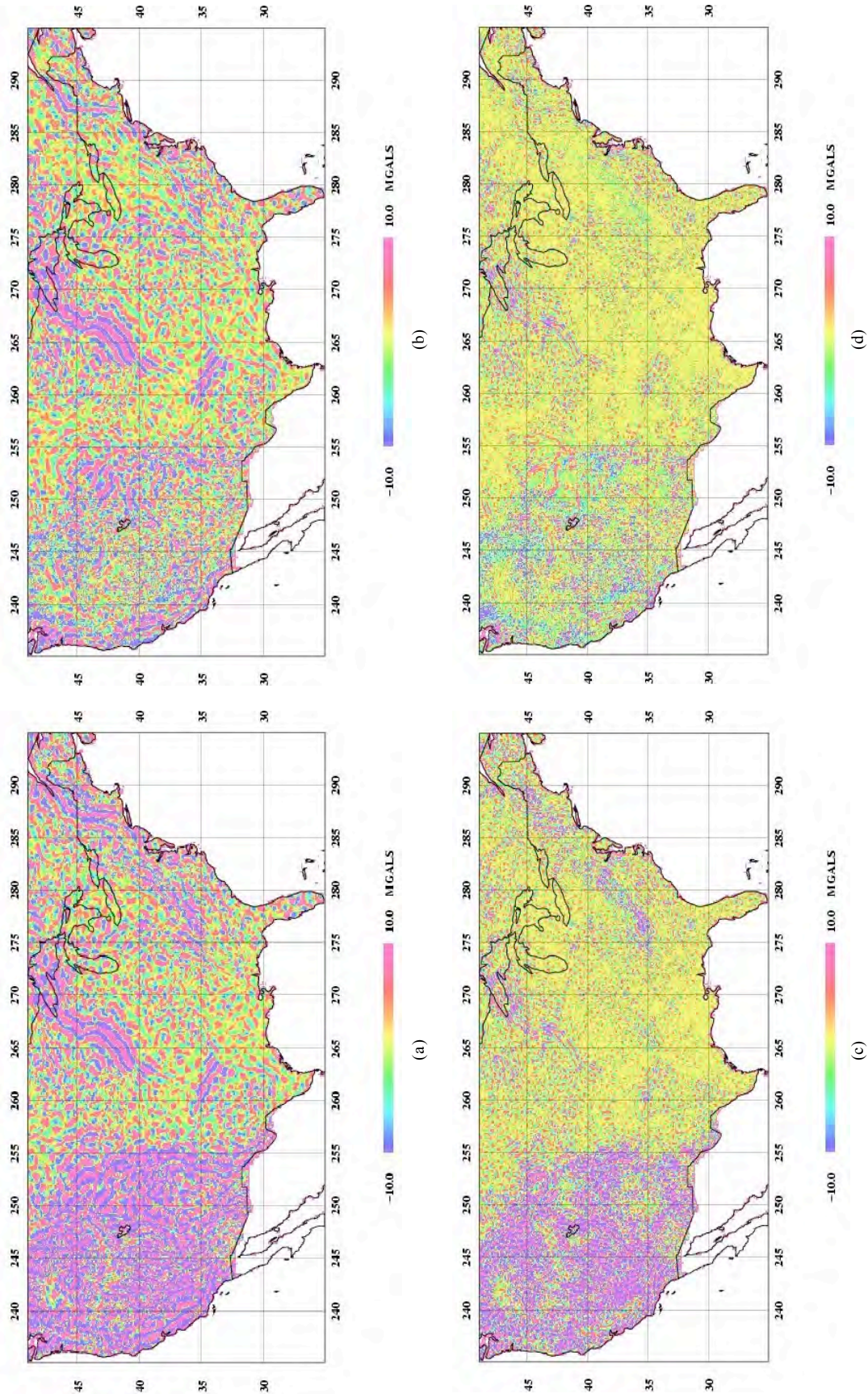


Fig. 6 Discrepancies between $5' \times 5'$ NGA gravity anomalies and synthetic values over the continental United States, with synthetic values constructed from synthesis using: (a) gravity ($0 \leq sn \leq 360$); (b) gravity ($0 \leq sn \leq 360$) and RTM ($361 \leq sn \leq 720$); (c) gravity ($0 \leq sn \leq 720$); (d) gravity ($721 \leq sn \leq 160$).

Evaluation of the SRTM data over Argentina and its Implications to gravity field and geoid modelling

C. Tocho

Facultad de Ciencias Astronómicas y Geofísicas, La Plata, Argentina, e-mail: ctocho@fcaglp.unlp.edu.ar

G. S. Vergos

Aristotle University of Thessaloniki, Department of Geodesy and Surveying, Thessaloniki, Greece

M.G. Sideris

Department of Geomatics Engineering,

University of Calgary, 2500 University Drive N.W., Calgary, Alberta, Canada, T2N 1N4

Abstract. With the realization of the Shuttle Radar Topographic Mission (SRTM) and the distribution of the 3 arc-seconds (90 m) data over South America, a high-resolution digital elevation model (DEM) became available for Argentina. DEMs are an important source of data for gravimetric geoid computation since they provide the high-frequency content of the gravity field spectrum. Gravimetric geoid undulations are usually calculated using the remove-compute-restore technique. This technique combines a global geopotential model, local gravity anomalies, and the topography, represented by a DEM. There are two main objectives in this paper. The first objective is to validate and assess the accuracy of the SRTM 90 m DEM over Argentina. This is performed through comparisons with existing global elevation models, like GLOBE, GTOPO30 and SRTM30. The second objective is to investigate the terrain aliasing effects on geoid determination for different gravimetric reductions. All available DEMs are used to compute terrain effects on both gravity anomalies and geoid heights at variable spatial resolutions. The following terrain reduction techniques are investigated in this study: Helmert's second condensation method, the Airy-Heiskanen topographic-isostatic reduction, the residual terrain model method and the Ruzdki inversion method. Numerical tests are carried out in the most rugged area of Argentina, one of the most mountainous areas in the world. From the results acquired, the performance of the SRTM model is evaluated and conclusions are drawn on the effect of the DEM resolution on the accuracy of the gravimetric geoid.

Keywords. SRTM, gravity reductions, Argentina, DEMs.

1 Introduction

The gravimetric geoid models for Argentina have been computed using the remove-restore technique, which uses a high-resolution digital elevation model to supply the short wavelengths geoid information and also to take care of the mathematical demands to solve the boundary-value problem of physical geodesy. The global digital elevation model GTOPO30 with a resolution of 30" x 30" (LP DAAC, 2006) has been used for the determination of the current gravimetric geoid due to the lack of a national DEM available for Argentina.

The recently available SRTM3 DEM, with a resolution of 3" x 3" (JPL, 2006), and SRTM30 DEM, with a resolution of 30" x 30" (JPL, 2006), must be evaluated and validated in Argentina.

Another objective in this paper is to investigate the use of different DEM grid resolutions for the computation of various gravimetric terrain reductions within the context of gravimetric geoid determination.

The terrain aliasing is investigated for the Ruzdki inversion method, the Airy-Heiskanen topographic-isostatic reduction, the residual terrain model reduction (RTM), and also for the classical terrain corrections.

2 Area and Digital Terrain Models

The numerical tests presented in this paper are carried out in an area near the Andes bounded by latitude 29° S and 32° S and longitude between 70° W and 67° W.

Four DEMs were investigated in the area under study: SRTM3, GTOPO30, GLOBE and SRTM30.

The SRTM data was acquired during the 11 day mission of the Space Shuttle Endeavour, launched in February 11, 2000. The data covers landmasses

between 56° south to 60° north latitude, which comprises almost exactly 80% of Earth's total landmass. All elevations are in metres and referenced to the WGS84/EGM96 geoid. The absolute horizontal accuracy is 20 m and the absolute vertical accuracy is specified as 16 m (Bamler, 1999; JPL, 2006; and Farr and Kobrick, 2000).

In the area under study, SRTM3 consisted of a total of 12949757 elevations and contained a total of 17444 voids caused by shadowing, phase, unwrapping anomalies or other radar-specific causes so a first step consisted of making a regular grid to fill in the existing voids. The nearest neighbour gridding method, which assigns the value of the nearest point to each grid node, was used. This method is useful when data are already evenly spaced, or in cases where the data are nearly on a grid with only a few missing values for filling in the holes in the data. From here on, we will refer to the SRTM3 after the gridding as SRTM3ARG06 (SRTM3 Argentina 2006). Figure 1 shows the original SRTM3, where black dots represent undefined elevations, and Figure 2 depicts the corrected SRTM3ARG06. Table 1 presents the statistics for both models.

GTOPO30 is a global DEM developed by the U.S. Geological Survey's EROS Data Center and it was completed in 1996. Elevations in GTOPO30 are regularly spaced at 30 arc-seconds (approximately 1 kilometer). GTOPO30 is a global data set covering the full extent of latitude from 90 degrees south to 90 degrees north, and the full extent of longitude from 180 degrees west to 180 degrees east. The horizontal grid spacing is 30 arc-seconds. The horizontal coordinate system is decimal degrees of latitude and longitude referenced to the WGS84. The vertical units represent elevation in meters above mean sea level. A subgrid was extracted over the study area and the elevation values can also be seen in Table 1.

SRTM30 is a near-global digital elevation model comprising a combination of data from the Shuttle Radar Topography Mission and the GTOPO30 data set. It can be considered to be either an SRTM data set enhanced with GTOPO30 or as an upgrade to GTOPO30 (JPL, 2006).

The Global Land One-Kilometer Base Elevation (GLOBE) DEM was released by NOAA's National Geophysical Data Center (NGDC). GLOBE is a global data set covering 180 degrees west to 180 degrees east longitude and 90 degrees north to 90 degrees south latitude. The horizontal grid spacing is 30 arc-seconds in latitude and longitude. The

horizontal coordinates are referenced to WGS84. The vertical units represent elevation in metres above mean sea level. The statistics of SRTM30 and GLOBE are also listed in Table 1.

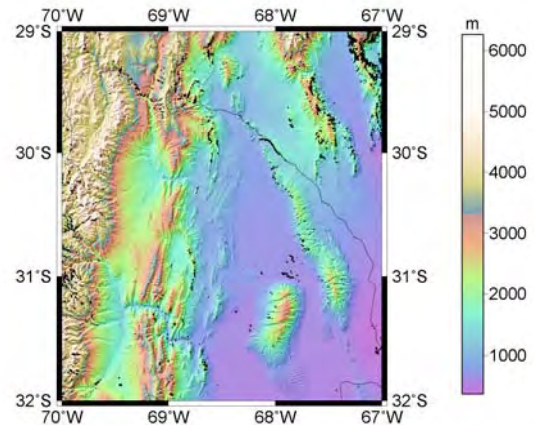


Figure 1: The original SRTM3 in the area under study

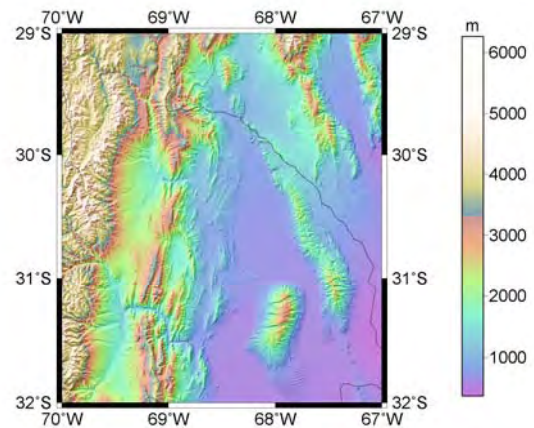


Figure 2: The corrected SRTM3ARG06 (SRTM3 Argentina 2006)

3 Numerical Tests

3.1 Evaluation of Digital Elevation Models

Digital elevation models play an important role in the accuracy of the precise gravimetric geoid; they are used to compute terrain corrections, direct topographical effects on gravity and indirect effects on geoid, and also to generate mean gravity anomalies (Featherstone and Kirby, 2000).

The four models available in the area under study are first evaluated making comparisons between them.

Even though SRTM30 can be considered as an upgrade to GTOPO30 the differences between both models are over 1000 m. The main differences are correlated with the rough topography in the west part of the area under study, between longitudes 69° W and 70° W as shown in Figure 3. The statistics of the differences are presented in Table 1. The differences between SRTM30 and GLOBE are of the same order of magnitude and again the largest values are located west the meridian 69° W. It is difficult to say that the differences are only a problem of longitude shifting as it was reported by Denker (2004) for Germany.

SRTM3ARG06 was evaluated by comparisons with GTOPO30, SRTM30 and GLOBE DEMs. Table 1 presents the statistics of the differences between SRTM3ARG06 and SRTM30, which have a mean value of 0.6 m and a standard deviation (STD) of 26 metres with maximum differences up to about 240 metres. The differences between SRTM3ARG06 and GTOPO30 and GLOBE are over the 1000 m and the largest differences are located again west the meridian of 69° W over the Andes mountain range

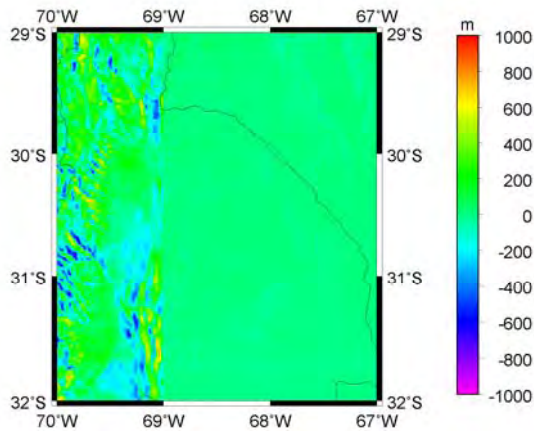


Figure 3: Differences between SRTM30 and GTOPO30 data. Unit: [m]

Table 1: Statistical of DEMs and their differences. Unit: [m]

DEM	min	max	mean	STD
SRTM3	370	6253	1927.1	1255.7
SRTM3ARG06	370	6263	1927.8	1255.6
GTOPO30	391	6253	1918.5	1240.4
SRTM30	393	6123	1927.0	1254.2
GLOBE	390	6253	1923.8	1240.6
SRTM30 - GTOPO30	-1168	1062	8.6	138.6
SRTM3ARG06-SRTM30	-234	238	0.6	26.7
SRTM3ARG06-GTOPO30	-1165	1157	9.1	143.1
SRTM3ARG06-GLOBE	-1165	1157	3.8	154.6

3.2 Terrain aliasing effects on geoid determination

The term aliasing means, in this contribution, the loss of detail information as terrain reductions are evaluated from a high resolution DEM to a coarse one (Bajracharya, 2003). The original grid resolution available in the area under study is 3 arc-seconds (SRTM3ARG06). Grids of 6", 15", 30", 1' and 2' were generated by simply picking point elevation values from the 3" grid.

The direct topographic effects on gravity calculated were: full topographic effects of all masses above sea level, assuming constant density, topographic-isostatic effects according to Airy-Heiskanen model, gravimetric terrain corrections, RTM effects (effect of the topographic irregularities with respect to a mean surface) and the direct topographical effect on gravity using Rudzki inversion gravimetric reduction scheme (constant density). These effects were computed using the TC program (Forsberg, 1984; Forsberg, 1997) and with a modified version made by Bajracharya (2003) to compute the direct topographical effect on gravity using Rudzki's inversion method.

The results from the densest DEM were taken as control values and the differences between these results and the results obtained from the lower resolution DEMs were considered as aliasing effects.

Table 2 summarizes the statistics of the differences between terrain corrections (TC) using different DEMs resolutions with the 3" original grid and different DEMs.

Table 2: Statistics of the differences of the classical terrain corrections between the 3" grid and different grid resolutions and different DEMs. Unit: [mGal]

Grid resolution	min	max	mean	STD
3" - 6"	-2.37	3.36	0.01	0.13
3" - 15"	-3.50	6.88	0.11	0.46
3" - 30"	-4.72	12.94	0.33	1.02
3" - 1'	-7.65	18.50	0.68	1.77
3" - 2'	-68.98	29.05	-0.82	6.98
3" - GTOPO30	-75.07	23.38	-2.00	8.22
3" - SRTM30	-23.06	23.86	1.24	2.42
3" - GLOBE	-75.07	23.38	-2.17	8.27

The differences in TC using different DEMs resolutions are correlated with the topography as we can see in Figure 4. TC varies from ± 6.6 mGal to ± 9.7 mGal in terms of standard deviation and from 55 mGal to 101 mGal in maximum, using a grid of resolution of 3" and 2', respectively. The differences between the TC effects on gravity are almost four

times bigger in magnitude when comparing them computed from GTOPO30 and GLOBE with those computed from SRTM30.

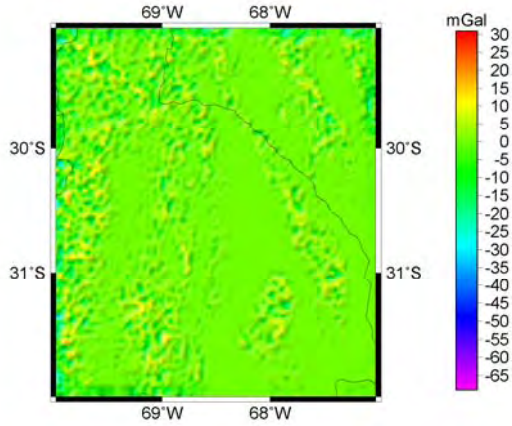


Figure 4: Differences in TC using 3'' and 2' grid resolution [mGal]

Tables 3 and Table 4 show the maximum value and the standard deviation, respectively of the differences between the estimated full topographic effect, isostatic effects using an Airy model, RTM, and Ruzzki on gravity between the 3'' grid and different DEMs.

Table 3: The differences in maximum value. Unit: [mGal]

Grid resolution	FTE	AH	RTM	Rudzki
3'' - GTOPO30	82.63	82.39	97.97	75.89
3'' - SRTM30	37.32	37.39	53.93	41.62
3'' - GLOBE	82.63	82.39	97.97	75.89

Table 4: The differences in standard deviation Unit: [mGal]

Grid resolution	FTE	AH	RTM	Rudzki
3'' - GTOPO30	12.18	12.15	14.14	12.19
3'' - SRTM30	3.09	3.09	3.79	3.46
3'' - GLOBE	12.64	12.60	14.60	12.59

The differences between the full topographic effect and the isostatic effects on gravity computed from SRTM30 and SRTM3ARG06 are at ± 3.1 mGal in terms of STD and for the RTM and the Ruzzki direct topographical effect on gravity ± 3.8 and ± 3.5 mGal, respectively. The differences are approximately four times larger when they are computed with GTOPO30 and GLOBE, the STD reach ± 14 mGal, and the range of the differences increase from near 80 to 200 mGal. The results obtained from GTOPO30 and GLOBE seems disappointed compared to the SRTM30 and SRTM3.

Comparing the different topographic effects from the generated resolutions grids (6'', 15'', 30'', 1', and 2') to the original grid resolution of 3'' of the

SRTM3ARG06 some aliasing effects are clear. The maximum and STD values increase for all the terrain effects computed. Figures 5 and 6 show the differences in maximum value and standard deviation, respectively, between control values (3'') and coarser grid resolutions (6'', 15'', 30'', 1', and 2'):

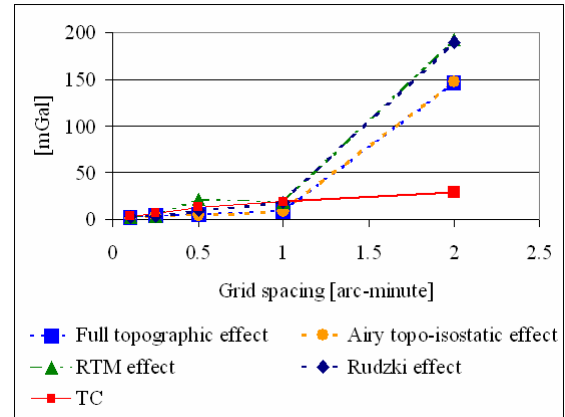


Figure 5: The differences in maximum value between control terrain effects on gravity and terrain effects on gravity obtained using different DEM resolutions

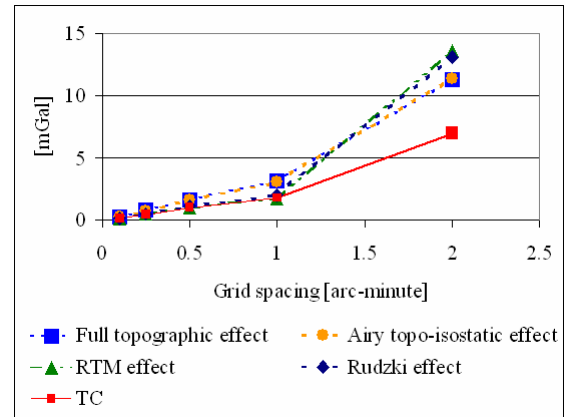


Figure 6: The differences in standard deviation between control terrain effects on gravity and terrain effects on gravity obtained using different DEM resolutions

From Figures 5 and 6, we can see that the maximum value and the standard deviation increase as moving from the dense DEM to the coarser DEM resolutions for all terrain effects computed

The gravimetric geoids are usually computed with the remove-compute-restore technique. The indirect effect on the geoid, which depends on the mass reduction scheme used in the remove step, must be restored in the restore step.

The same topographic effects were computed for geoid heights. Table 5 shows the standard deviation of the differences between TC, full topographic, AH

isostatic, and RTM effects on geoid heights computed from the 3" grid and different DEMs. There is no indirect effect on geoid using the Rudzki inversion scheme.

Table 5: The differences in standard deviation between effects on geoid heights from 3" grid and different DEMs. Unit: [m]

Grid resolution	TC	FTE	AH	RTM
3" - GTOPO30	0.10	0.08	0.07	0.07
3" - SRTM30	0.04	0.07	0.01	0.01
3" - GLOBE	0.11	0.08	0.07	0.07

The differences between SRTM3ARG06 and SRTM30 are the smallest for all terrain effects on geoid. The differences between SRTM3ARG063 and GTOPO30 or GLOBE are larger in magnitude and similar between them. For RTM effects (see Figures 7 to 9), the big differences are present in the west part.

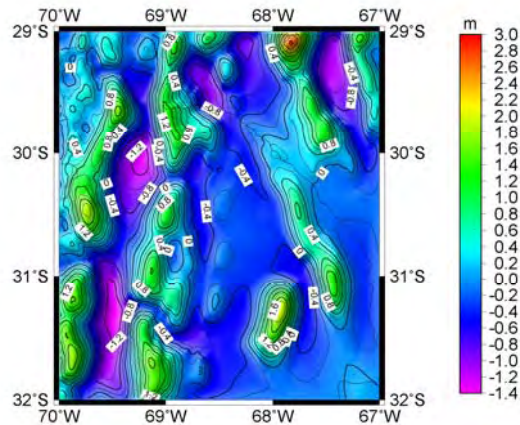


Figure 7: RTM effects on geoid computed with SRTM3ARG06

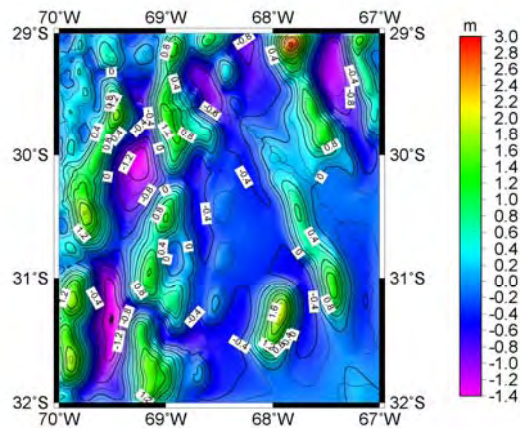


Figure 8: RTM effects on geoid computed with GTOPO30

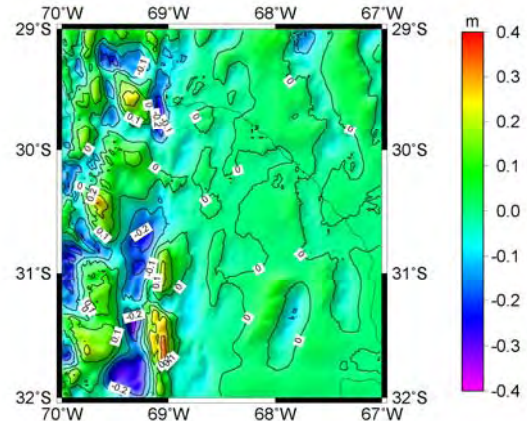


Figure 9: Differences of RTM effects on geoid between SRTM3ARG06 and GTOPO30

Figures 10 and 11 show the differences in maximum value and standard deviation, respectively, between control values (3") and terrain effects on geoid obtained using different DEM resolutions.

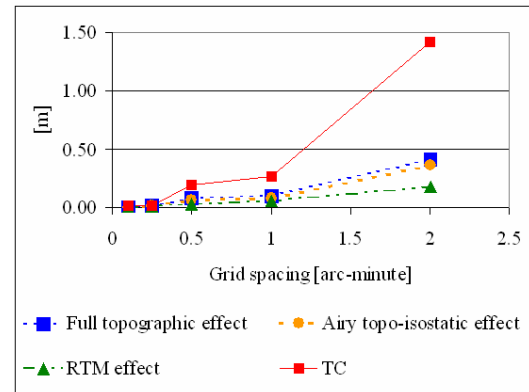


Figure 10: The differences in maximum value between control terrain effects on geoid and terrain effects on geoid obtained using different DEM resolutions

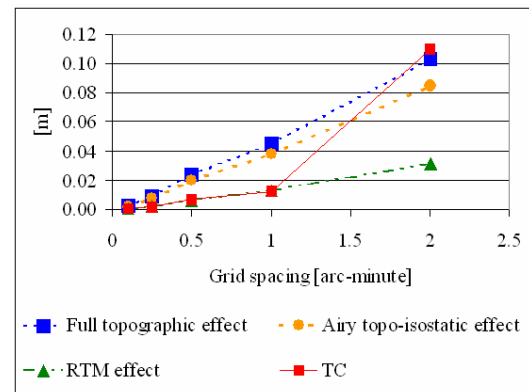


Figure 11: The differences in standard deviation between control terrain effects on geoid and terrain effects on geoid obtained using different DEM resolutions

From Figures 10 and 11, we conclude that aliasing effects are present when we use a coarse grid. The largest error will be introduced using a grid of 2'.

4 Conclusions

Various DEMs were evaluated in a rough area of Argentina, near the Andes. SRTM3, GTOPO30, SRTM30 and GLOBE global digital elevation models. GTOPO30 has been used until now to compute the gravimetric geoid models for Argentina.

SRTM3ARG06 is the result of the original SRTM3 DEM after the grid was converted into a regular grid by interpolation with elevations from the neighbouring data.

The differences between SRTM30 and GTOPO30 have a mean value of 9 m and a standard deviation of ± 139 m. Even though, SRTM30 can be considered as an upgrade to GTOPO30, there is no doubt that the combination of the GTOPO30 data set and the data from the Shuttle Radar Topography Mission has modified the GTOPO30 original DEM.

This paper investigated the terrain aliasing effects introduced on both gravity anomalies and geoid heights by using various DEM resolutions. The differences from the results computed from the densest grid (3") and the results from the sparser grids were considered as aliasing effects. First, the terrain effects were computed for terrain corrections, full topographic effects, RTM, Rudzki and AH isostatic effects on gravity at the generated grid resolutions and then, the same effects were computed for geoid heights. The results show that a high resolution DEM of 15" or finer should be used in mountainous areas like the Andes. If a 15" or finer DEM is used, the error introduced in the geoid heights does not exceed ± 1 cm but if a lower resolution DEM is used the error in geoid heights will exceed ± 11 cm. So a DEM not coarser than 15" is recommended for high-accuracy geoid determination.

As future work, a comparison of the SRTM data with the heights of gravity station from the gravity database and with the heights of GPS/levelling points must be evaluated. The height of gravity stations must be carefully revised. Also the geoid of Argentina should be recomputed by using the SRTM3ARG06 DEM for the topographic reductions. This DEM may also produce better

gridded gravity anomalies, especially in the Andes area.

References

- Bajracharya S (2003): Terrain effects on geoid determination, MSc. Thesis, University of Calgary, Department of Geomatics Engineering, UCGE Reports Number 20181.
- Bamler R (1999): The RTM Mission. A World Wide 30 m Resolution DEM from SAR Interferometry in 11 Days. www.ifp.uni-stuttgart.de/publications/phowo99/bamler.pdf
- Denker H (2004): Evaluation of SRTM3 and GTOPO30 Terrain Data in Germany. Presented in the Gravity Geoid and Space Missions 2004 (GGSM2004) conference, August 30-September 3, Porto, Portugal.
- Farr TG and Kobrick M (2000): Shuttle Radar Topography Mission produces a wealth of data, Amer. Geophys. Union Eos, v. 81, pp. 583-585.
- Featherstone WE and Kirby JF (2000): The reduction of aliasing in gravity anomalies and geoid heights using digital terrain data, Geophys. J. Int., vol. 141, pp. 204-214.
- Forsberg R (1984): A study of terrain corrections density anomalies and geophysical inversion methods in gravity field modeling, Report of the Department of Geodetic Science and Surveying no. 355, The Ohio State University, Columbus, Ohio.
- Forsberg R (1997): Terrain effects in geoid computations, in Lectures Notes for the IAG's International Geoid School, Rio de Janeiro, Brazil.
- GLOBE Task Team and others (Hastings, David A, Paula K Dunbar, Gerald M Elphinstone, Mark Bootz, Hiroshi Murakami, Hiroshi Maruyama, Hiroshi Masaharu, Peter Holland, John Payne, Nevin A Bryant, Thomas L Logan, J-P Muller, Gunter Schreier, and John S MacDonald), Eds., (1999): The Global Land One-kilometer Base Elevation (GLOBE) Digital Elevation Model, Version 1.0, National Oceanic and Atmospheric Administration, National Geophysical Data Center, 325 Broadway, Boulder, Colorado 80303, U.S.A. Digital data base on the World Wide Web: (<http://www.ngdc.noaa.gov/mgg/topo/globe.html>)
- LP DAAC (2006): <http://edc.usgs.gov/products/elevation/gtopo30/gtopo30.html>
- JPL (2006): SRTM. The Mission to Map the World. Jet Propulsion Laboratory, California Inst. of Techn. <http://www2.jpl.nasa.gov/srtm/index.html>
- Tscherning CC, Forsberg R, Knudsen P, (1992): The GRAVSOFIT package for geoid determination, in Holota P, Vermeer M (Eds), 1st Continental Workshop for the Geoid in Europe: Towards a precise European geoid in the nineties, Prague, June 7-9, pp. 327-334.
- Wessel P and Smith WHF (1998): New improved version of The Generic Mapping Tools released. EOS Trans 79(47): 579.

AN APPROACH FOR DETERMINING THE PRECISE GLOBAL GEOID

WenBin Shen^{1,2}

¹ Department of Geophysics, School of Geodesy and Geomatics, Wuhan University, Wuhan, CHINA

² Key Lab. of Geospace Environment and Geodesy, MEC, Wuhan University, Wuhan, CHINA

e-mail: wbshen@sgg.whu.edu.cn

Abstract: The task is to precisely determine the global geoid, which attracts a lot of geodesists' attention. Without precise knowledge of the density distribution in the domain between the geoid ∂G and the Earth's surface $\partial\Omega$, it is almost impossible to complete the task. Under the assumption that the density distribution of the shallow mass layer bounded by $\partial\Omega$ and a closed reference surface $\partial\Gamma$ that lies under the geoid ∂G is precisely given, an approach for completing the task is proposed. After the launch of the GOCE satellite system, it might be determined a precise global potential field V defined in the domain outside the Earth, and V is a regular harmonic field. The potential field V_1 generated by the shallow mass layer above $\partial\Gamma$ and defined in the domain outside $\partial\Gamma$ could be also determined, once the mass density distribution of the Earth's shallow mass layer is given. Then, with a technical procedure, it is theoretically determined the potential field (consequently the geopotential field W) generated by the Earth and defined in the domain outside $\partial\Gamma$. Finally, the geoid ∂G is determined based on the basic equation $W = W_0$, where the constant W_0 is the value of the geopotential on the geoid, given by e.g. GRS 80 system.

Key words: geopotential field; geoid; $1^\circ \times 1^\circ$ global geoid determination with centimeter level

1 Introduction

The determination of the global geoid with centimeter level is one main task in physical geodesy in this century. The gravity field model EGM 96 (Lemoine et al, 1998) provided a global $30' \times 30'$ gravity reference frame with the accuracy level of several tens of centimeters. Will-be launched GOCE satellite system might provide a global $1^\circ \times 1^\circ$ gravity reference frame with the accuracy level of one centimeter (Visser et al, 2001; Bouman et al, 2004). This will establish a good foundation for realizing the global $1^\circ \times 1^\circ$ geoid with centimeter level.

By general definitions (Listing, 1872; Moritz, 1980; Grafarend, 1994), the geoid is the equipotential surface that is nearest to the non-tide

mean sea level. To determine the geoid as well as external gravity field, an average ellipsoid (or reference ellipsoid) is introduced, e.g., GRS 80 reference ellipsoid (GRS80, 2005). If the geoidal height or geoid undulation N (the distance between the geoid and the ellipsoidal surface) is determined, then the geoid is determined. The datum of the geoid could be chosen arbitrarily under international convention, as well as under the requirement that the determined geoid should be as near as possible to the non-tide mean sea level. Taking the geoid as the boundary, using gravity anomalies on the geoid, based on Stokes approach (Heiskanen and Moritz, 1967) one could determine the disturbing potential T , and by Bruns formula the geoid undulation N could be determined as follows

$$N = \frac{T}{\gamma} \quad (1)$$

where γ is the normal gravity.

In Stokes approach, to calculate disturbing potential T , it is required the global gravity anomaly Δg covered the whole geoid. Hence, the gravity observations on the Earth's surface should be reduced on the geoid, which requires two conditions: (i) the orthometric height H (the height above the mean sea level or the distance between the Earth's surface and the geoid) should be known; (ii) the mass distribution between the Earth's surface and the geoid should be known. The condition (i) could be realized by gravimetry and leveling. Condition (ii) is completed by using an average density value 2.67 gcm^{-3} . In practice, there are many areas, where there are no gravity observations. In these areas, the estimated gravity data are applied, based on terrain data and possible geophysical data, and consequently the determined geoid has poor accuracy in these areas, around tens of centimeters or several meters.

The errors in geoid determination caused by (ii) depend on the accuracy of the given density distribution. If given the accurate enough density distribution outside the geoid, the influences stemmed

from the density errors might be reduced to centimeter level. However, the errors in geoid determination caused by (i) depend largely on the height errors. In the mountain areas or at the positions where a series of long distance leveling transportation is needed, there exist obvious additive errors. This is a great obstacle, and consequently it is difficult to achieve the accuracy with centimeter level. This is also the reason why it is difficult to determine the centimeter-level geoid by using Stokes approach.

Taking the Earth's surface as the boundary, using gravity anomaly Δg on the Earth's surface, based on Molodensky approach (Molodensky et al, 1962) the disturbing potential T could be determined, and using Bruns formula one could determine the height anomaly

$$\zeta = \frac{T}{\gamma} \quad (2)$$

which is the distance between the Earth's surface and the telluroid.

With Molodensky approach, the mass adjustment problem (or gravity reduction problem) is avoidable, and consequently the mass density distribution between the Earth's surface and the geoid is not required (Moritz, 1980). In applying Molodensky approach, generally a spherical approximation is used, which causes errors about several tens of centimeters. In addition, to transfer height anomaly ζ to geoid undulation N , the following equation can be used (Heiskanen and Moritz, 1967)

$$N = \zeta + (H^* - H) \quad (3)$$

where H^* is the normal height, the distance between the Earth's surface and the quasi-geoid (or the distance between the surface of the reference ellipsoid and the telluroid), which could be determined by the following formula (Heiskanen and Moritz, 1967):

$$H^* = \frac{C}{\bar{\gamma}} \quad (4)$$

where C is the geopotential number, $\bar{\gamma}$ is the average normal gravity along the plumb line between the Earth's surface and the quasi-geoid.

To determine N based on (3), it is still needed to determine the orthometric height H , the errors contained in which are generally much larger than centimeters in mountain areas. The purpose of determining the geoid undulation is to determine the position of the geoid, which is an equi-geopotential surface and has important applications. The quasi-geoid defined based on the height anomaly ζ is not

an equi-geopotential surface, and consequently it could not be properly and effectively used in practice. The quasi-geoid is such a kind of surface so that the distance between it and the surface of the reference ellipsoid is just the height anomaly ζ . Taking into account of the following equation (Heiskanen and Moritz, 1967)

$$H = \frac{C}{\bar{g}} \quad (5)$$

where \bar{g} is the average gravity along the plumb line between the Earth's surface and the geoid, and combining equations (3)–(5), one gets (Heiskanen and Moritz, 1967)

$$N = \zeta + \frac{\bar{g} - \bar{\gamma}}{\bar{\gamma}} h \approx \zeta + 10^{-3} \Delta g_B H \quad (6)$$

where Δg_B is the Bouguer anomaly, with the unit Gal, and the unit of the orthometric height H as well as the geoid undulation N is meter.

Based on the above reasoning, due to the limitation of the leveling itself, no matter which approach, Stokes approach or Molodensky approach, is used, it is almost impossible to achieve the centimeter-level accuracy in determining the global geoid.

2 The challenging problem in determining the global geoid

The developments of space technique (especially the GPS and gravimetric satellite technique) make it possible to precisely determine the Earth's external gravity field. Based on the designment of the will-be launched GOCE satellite system, a gravity field model with degree and order about 180/180 could be provided, which can achieve the accuracy of 1 centimeter or better. Hence, in the present paper it is assumed that a global $1^\circ \times 1^\circ$ external gravity field with the accuracy 1 centimeter has been determined. In another aspect, GPS and satellite altimetry technique can provide the position of the Earth's surface, with accuracy of one-centimeter in the land areas, and several centimeters in the ocean areas.

Now the problem is stated as follows: given the Earth's surface with the accuracy of centimeter level, and given a global $1^\circ \times 1^\circ$ gravity field model with degree and order 180/180 with the accuracy of 1 centimeter, how to determine the global $1^\circ \times 1^\circ$ geoid with the accuracy of centimeter level? The difficulty of solving this problem comes from the fact that the geoid lies in many cases inside the Earth and it could not be directly observed.

Concerning about the determination of the geoid, if Stokes approach is applied, then, in the procedure of gravity reduction, the orthometric height of measurement point on the Earth's surface is required, which is realized by leveling and gravimetry. Generally, in the ocean areas, the gravity reduction procedure is neglected. This problem will be discussed in a separated paper. However, if the orthometric height of measurement point on the Earth's surface is known, one need not to solve the Stokes problem any more, because the geodetic height h could be determined by GPS or satellite altimetry technique.

Suppose there does not exist problem in determining the geoid in ocean areas. Concerning only the geoid determination problem in land areas, the geodetic height h could be determined by GPS technique with high accuracy (at least in the level of one centimeter), and the orthometric height H can be determined by leveling and gravimetry, the accuracy of which depends on the areas and the length of the measurement line. Hence, the geoid undulation is determined as

$$N = h - H \quad (7)$$

The accuracy of which depends mainly on that of the geoid undulation. As discussed above, concerning the determination of the global geoid, based on conventional approach (Stokes approach or Molodensky approach), it is almost impossible to achieve the centimeter-level accuracy.

3 An approach for determining the global $1^\circ \times 1^\circ$ geoid with centimeter level

3.1 Basic assumptions

It is assumed that a global $1^\circ \times 1^\circ$ external gravity field model with the accuracy of 1 centimeter is given (e.g., provided by GOCE satellite system), which is defined in the external domain $\bar{\Omega}$, the domain outside the Earth. Ω denotes the domain occupied by the Earth.

The geopotential is expressed as

$$W(P) = V(P) + Q(P), \quad P \in \bar{\Omega} \quad (8)$$

where $Q(P)$ is the centrifugal force potential, $V(P)$ is the gravitational potential, P the field point. Since $Q(P)$ is known, given the geopotential field $W(P)$, the gravitational potential field $V(P)$ is determined, and vice versa.

It is further assumed that the Earth's surface is determined with the accuracy of centimeter level. Hence, once the geoid is determined with the accuracy of the centimeter level, then, the orthometric height of the Earth's surface could be determined with the accuracy of the centimeter-level.

Now, it is assumed that the density distribution ρ_1 of the shallow layer of the Earth is known very well. The shallow layer is defined as follows: it is the mass layer between the Earth's surface $\partial\Omega$ and a closed surface $\partial\Gamma$ that lies inside the geoid, where $\partial\Gamma$ is relatively near or very near to the geoid, referred to Fig.1. Since the variation range of the geoid undulation N is around magnitude of 100 meters, generally the depth D of the shallow layer does not exceed 10 km; in ocean areas D is around the magnitude of 1 to 10 meters; in land D is generally around 10 to 100 meters; and in mountain areas D is around 1000 meters (e.g., near Everest in Himalaya Mountains D is around 8000 meters).

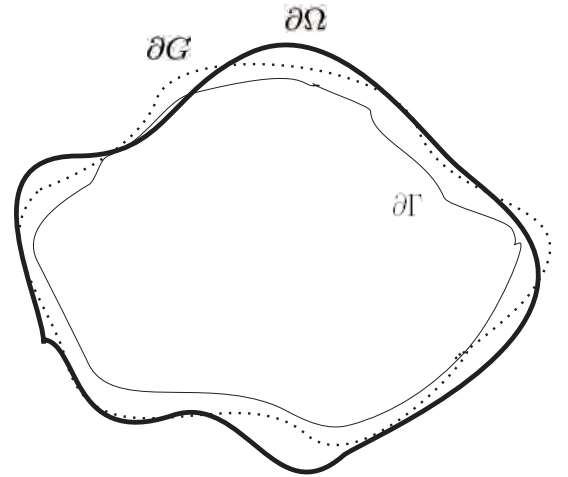


Figure 1: The bold line denotes the Earth's surface $\partial\Omega$, the imagine line denotes the geoid ∂G , the closed thin line denotes a closed surface $\partial\Gamma$ that lies inside the geoid and near to geoid. The mass layer bounded by $\partial\Omega$ and $\partial\Gamma$ is referred to as the shallow layer

Geology investigations (including drilling holes) and seismic detection technique can provide more and more precise information about the shallow layer. In 1980s, PREM (Dziewonski and Anderson, 1981) provided a spherical symmetric density distribution of the Earth, with poor accuracy and without the transverse variation. Recently, there appeared successively more precise density distribution models, CRUST 5.1 with resolution $5^\circ \times 5^\circ$ (Mooney et al, 1998) and CRUST 2.0 with resolution $2^\circ \times 2^\circ$

(Bassin et al, 2000; Tsoulis, 2004). Hence, it is expected that in the near future, there will be appeared a precise enough density distribution ρ_1 of the shallow layer.

3.2 Theoretical model

The gravitational potential generated by the shallow mass layer is denoted as $V_1(P)$, which could be determined based on the Newtonian potential formula

$$V_1(P) = G \int_{\bar{\Gamma}-\bar{\Omega}} \frac{\rho_1}{l} d\tau, \quad P \in \bar{\Gamma} \quad (9)$$

where ρ_1 is the density distribution of the shallow layer, G the gravitational constant; $\bar{\Gamma}$ denotes the domain outside $\partial\Gamma$, which includes the Earth's external domain $\bar{\Omega}$ as well as the domain $\bar{\Gamma}-\bar{\Omega}$, and it is noted that $\bar{\Gamma}-\bar{\Omega}$ denotes the domain occupied by the shallow mass layer (i.e., the domain bounded by $\partial\Gamma$ and $\partial\Omega$, Cf. Fig.1); l is the distance between the field point P and the volume integration element $d\tau$. Consequently, the external gravitational field $V_0(P)$ in the domain $\bar{\Omega}$ generated by the mass enclosed by $\partial\Gamma$ can be determined

$$V_0(P) = V(P) - V_1(P), \quad P \in \bar{\Omega} \quad (10)$$

It is noted that the above equation is defined only in the Earth's external domain $\bar{\Omega}$, because it is not previously given the gravitational potential field $V(P)$ in the domain $\bar{\Gamma}-\bar{\Omega}$ (the given potential field is defined only in the domain $\bar{\Omega}$).

Since the potential field $V_0(P)$ generated by the mass enclosed by $\partial\Gamma$ is regular and harmonic in the domain $\bar{\Gamma}$, and since $V_0(P)$ is known in the domain $\bar{\Omega}$, based on the fictitious compress recovery approach (Shen, 2004) or spherical harmonic approach (Heiskanen and Moritz, 1967) one could determine the gravitational potential field in the domain $\bar{\Gamma}$ generated by the mass enclosed by $\partial\Gamma$

$$V_0(P) = V_0^*(P), \quad P \in \bar{\Gamma} \quad (11)$$

where $V_0^*(P)$ denotes the fictitious solution, which is in fact the natural downward continuation of the field $V_0(P)$ ($P \in \bar{\Omega}$) toward the boundary $\partial\Gamma$: the boundary could be chosen as a spherical surface ∂K which includes the Earth (e.g., Brillouin sphere, Cf. Arnold 1989), the boundary value $V_0|_{\partial K}$ is given by equation (10), and the theoretical foundation is guaranteed by (Shen and Ning, 2004; Shen, 2005a,b). Concerning the spherical harmonic approach, the harmonic coefficients could be determined based on the boundary value $V_0|_{\partial K}$ given on

the spherical surface ∂K , and consequently it is determined the potential field in the domain \bar{K} generated by the mass enclosed by $\partial\Gamma$. This solution is also the real solution in the domain $\bar{\Gamma}-\bar{\Omega}$ generated by the mass enclosed by $\partial\Gamma$ (Shen, 2005b). If the fictitious compress recovery approach (Shen, 2004) is applied, based on the boundary value $V_0|_{\partial K}$, with a series of procedure of (downward identity) "compress" and (upward Poisson integration) "recovery" between the surface ∂K and the surface ∂K_i of an inner sphere K_i which lies inside Γ , the domain bounded by $\partial\Gamma$, one obtains a fictitious field $V_0^*(P)$ ($P \in \bar{K}_i$), where \bar{K}_i denotes the domain outside the inner sphere. After the solution $V_0^*(P)$ ($P \in \bar{K}_i$) is constrained in the domain $\bar{\Gamma}$, it coincides with the real field $V_0(P)$ ($P \in \bar{\Gamma}$) (Shen, 2004, 2005b).

Hence, the real field generated by the Earth defined in the domain $\bar{\Gamma}$ could be determined

$$V(P) = V_0^*(P) + V_1(P), \quad P \in \bar{\Gamma} \quad (12)$$

where $V_0(P)$ is determined by equation (11), $V_1(P)$ is given by the Newtonian potential formula (9). It is noted that now both $V_0^*(P)$ and $V_1(P)$ are defined in the domain $\bar{\Gamma}$. In $\bar{\Gamma}$, the geopotential is expressed as

$$W(P) = V(P) + Q(P), \quad P \in \bar{\Gamma} \quad (13)$$

The difference between equation (8) and equation (13) rests with that the former is defined in the domain $\bar{\Omega}$ and the latter in the domain $\bar{\Gamma}$. That is to say, equation (8), which is known, holds only in the domain outside the Earth, while equation (13) holds in the domain $\bar{\Gamma}$ which includes the geoid ∂G , and it is also known now.

Now, the problem of precisely determining the position of the geoid is the problem of solving the following equation

$$V(P) + Q(P) = W_0 \quad (14)$$

where W_0 is the geopotential on the geoid, which might be chosen as $W_0 = 62636860.850 \text{ m}^2\text{s}^{-2}$, provided by GRS 80 system. In practical applications, W_0 should be chosen in such a way that the determined geoid is nearest to the (non-tide) mean sea level. In determination of the geoid based on equation (14), "test approach" and iterative technique might be used. Exactly saying, the following procedures could be applied.

1) It is referred to Fig.2. Introducing a ray l along an arbitrary direction (θ, λ) from the coordinate origin o which coincides with the mass center of the

Earth, it intersects a point P_0 on the surface $\partial\Gamma$. Starting from P_0 , along the ray l moving slowly toward a distant, there must exist one and only one point P_G so that equation (14) holds, because different equi-geopotential surfaces never intersect with each other. In fact, defining

$$f(P) = V(P) + Q(P) \quad (15)$$

and fixing P on the ray l , since the direction (θ, λ) is fixed, $f(P)$ is a monotonous descending function of P (the discussions are constrained in the near-Earth space).

2) First, it might be chosen P_0 and let it enter equation (14). If P_0 is just located on the geoid (i.e., $P_0 = P_G$), equation (14) holds; otherwise, it must hold

$$f(P) > W_0 \quad (16)$$

That means the point P_G should be searched at a further distance from the origin. In fact, one can use Bruns formula to speed up the procedure. Defining the step length

$$l_i = \frac{f(P_{i-1}) - W_0}{\gamma}, \quad i = 1, 2, \dots, \quad (17)$$

then, along the ray l , starting from point P_{i-1} a further point P_i could be detected according to the step length l_i .

3) As the N -th step is tested, if

$$\left| \frac{f(P_N) - W_0}{\gamma} \right| < \delta \quad (18)$$

holds, then stop; otherwise, continue the above procedure. In equation (18), δ is the accuracy standard. Choosing $\delta = 5$ cm, the global geoid ∂G with the accuracy of centimeter level could be determined.

In non-mountain areas, one can also determine the geoid directly based on the Bruns formula:

$$N = - \frac{T(P)|_{P \in \partial E}}{g(P)|_{P \in \partial E}} \quad (19)$$

where both $T(P)|_{P \in \partial E}$ and $g(P)|_{P \in \partial E}$ are known, ∂E is the surface of the reference ellipsoid, $T(P) = W(P) - U(P)$ is the disturbing potential field, $U(P)$ is the normal potential field generated by the reference ellipsoid. Equation (19) could be directly derived out from equation (14), based on Taylor expansion, and noting that $U(P)|_{P \in \partial E} \equiv W_0$.

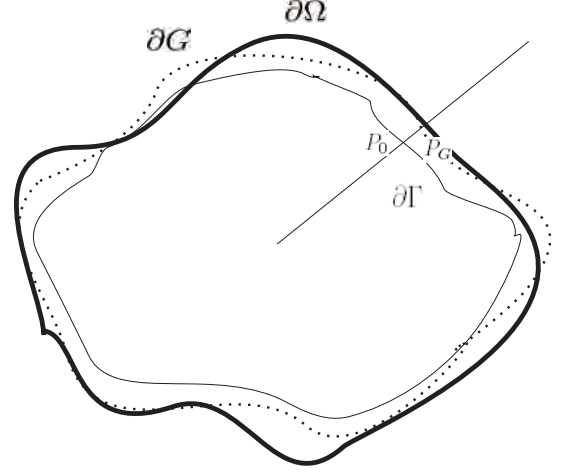


Figure 2: The notations of the surfaces have the same meaning as stated in Fig.1. The ray l intersects at points P_0 and P_G on the surfaces $\partial\Gamma$ and ∂G , respectively

4 Conclusion

Even if the density distribution outside the geoid is known very well, it is hardly to precisely determine the global geoid (in the centimeter level) by using the conventional approaches (e.g., Stokes approach or Molodensky approach), due to the fact that the orthometric height (height above sea level) of the Earth's surface is always needed. The orthometric height of the Earth's surface is determined by leveling and gravimetry. Since the measurement errors increase with the length of the surveying line, it can not be guaranteed that the orthometric height could achieve the centimeter-level accuracy globally, especially in the mountain areas.

Theoretically, using the approach proposed in this paper it could be determined the global $1^\circ \times 1^\circ$ geoid with the centimeter-level accuracy. The advantage of this approach lies in that the leveling is not needed (the orthometric height is not required previously). However, the following conditions (pre-requirements) should be satisfied: a) given the Earth's surface with centimeter-level accuracy; b) given the density distribution of the shallow layer with good enough accuracy; c) given the Earth's external $1^\circ \times 1^\circ$ gravitational potential field model with the accuracy of one centimeter level.

Acknowledgment: Comments given by Professor Dingbo Chao on the original manuscript are highly appreciated. This study is funded in parts by Natural Science Foundation China (No.40574004 and

No.40174004).

References

- Arnold K (1989) Das gravitationspotential im außenraum der erde. Mitteilung des Zentralinstitut für Physik der Erde Nr 1668, Vermessungstechnik 37(3):82–86
- Bassin C, Laske G, Masters TG (2000) The current limits of resolution for surface wave tomography in north america. EOS Trans AGU 81:F897
- Bouman J, Koop R, Tscherning CC, Visser P (2004) Calibration of goce sgg data using high-low sst, terrestrial gravity data and global gravity field models. J Geod DOI 10.1007/s00190-004-0382-5
- Dziewonski AM, Anderson DL (1981) Preliminary reference earth model. Phys Earth Planet Inter 25:297–356
- Grafarend EW (1994) What is a geoid? In: P Vaniček, NT Christou (eds), Geoid and Its Geophysical Interpretations, CRC Press, London
- GRS80 (2005) online <http://dgfi2.dgfi.badw-muenchen.de/geodis/REFS/grs80.html>
- Heiskanen WA, Moritz H (1967) Physical geodesy. Freeman and Company, San Francisco
- Lemoine FG, Kenyon SC, Factor JK, Trimmer RG, Pavlis NK, Chinn DS, Cox CM, Klosko SM, Luthcke SB, Torrence MH, Wang YM, Williamson RG, Palvis EC, Rapp RH, Olson TR (1998) The development of the joint nasa gsfc and the national imagery and mapping agency (nima) geopotential model egm96. Tech. Rep. NASA Technical Paper NASA/TP-1998-206861, Goddard Space Flight Center, Greenbelt
- Listing JB (1872) Regarding our present knowledge of the figure and size of the earth. Rep Roy Soc Sci Gottingen66
- Molodensky MS, Eremeev VF, Yurkina MI (1962) Methods for study of the external gravitation field and figure of the Earth (transl. from Russian 1960). Israel Program for Scientific Translations, Jerusalem
- Mooney WD, Laske G, Masters TG (1998) Crust 5.1: a global crustal model at $5^\circ \times 5^\circ$. J Geophys Res 103:727–747
- Moritz H (1980) Advanced physical geodesy. Wichmann, Karlsruhe
- Shen WB (2004) The fictitious compress recovery of the gravitational potential. Journal of Wuhan University (Information Science) 29:720–724 (in Chinese)
- Shen WB (2005a) Lecture notes on satellite geodesy. In: Royal Inst. of Techn., Stockholm, Sweden
- Shen WB (2005b) On the convergence problem. In: IAG Meeting “Dynamic Planet 2005”, Aug. 22–26, 2005, Cairns, Australia
- Shen WB, Ning J (2004) A proposal on the determination of the earth’s potential field. In: 18th CEOS Symposium, Beijing, China
- Tsouliis D (2004) Short note spherical harmonic analysis of the crust 2.0 global crustal model. Journal of Geodesy 78:7–11
- Visser P, Van Den Ijssel J, Koop R, Klees R (2001) Exploring gravity field determination from orbit perturbations of the european gravity mission goce. J Geod 75(2/3):89–98

Geophysical Inversion of On Board Satellite Gradiometer Data: A Feasibility Study in the ALPACA Region, Central Europe

Judit Benedek

West-Hungarian University, Department of Statistics, H-9401 Sopron, POB 132, Hungary

Gábor Papp

Geodetic and Geophysical Research Institute of the Hungarian Academy of Sciences, H-9401 Sopron, POB 5, Hungary

Abstract. The structure of the lithosphere of the ALPACA (Alpine-Pannonian-Carpathian) region is described by a model containing about 200000 rectangular volume elements (prisms) of variable dimensions defined in the mapping system of Hungary. Forward computations show that the contribution of the structural units (topography and upper mantle) of the lithosphere to the disturbing potential T of the Earth may reach several tenth of E unit at 400 km elevation. The contribution from the sediments is less by a factor of ten but even its magnitude exceeds the planned sensitivity of the satellite on board measurements. It is expected that some regional information about the horizontal density variation of the crust can be deduced from the GOCE data, especially for the density contrast between the lower crust and upper mantle. Since the density distribution of either the topographical masses or the sedimentary complex is much better known than the density jump on the Moho, therefore their effect on the second derivatives of T can be removed from the measurements. The residuals can be interpreted by inversion using the closed analytical formulae available for rectangular volume elements. The modelling approach based on the local planar coordinate frame was compared to the polyhedron representation of the same crustal model defined in a global rectangular coordinate system. In this comparison no significant effect of the Earth's curvature could be indicated.

Keywords. Gravity modelling, prism, polyhedron inversion, GOCE, ALPACA

1 Introduction

The ALPACA (Alps – Pannonian basin – Carpathians) region is located in Central Europe, in the collision zone between the African and the

Eurasian plates. It is characterised by variable crustal thickness. On the perimeter of the area the depth of the Moho discontinuity may reach the value of 60 - 67 km beneath the arcs of the Alps and the Carpathians (Fig. 1). Its central part (the Pannonian basin) is a so called back-arc basin having a thin crust (Royden and Horváth, 1988). Here the upper mantle is elevated up to 22 km - 24 km depth producing high heat flow values (Lenkey et al, 2002). The basin is covered by thick Neogene-Quaternary sediments and fragmented into smaller sub basins (Fig. 2). The depth of the basement in the sub basins may reach 7-8 km and its average is about 2 km.

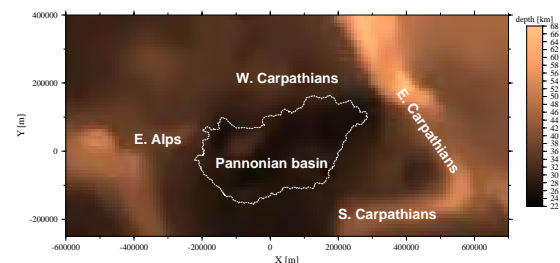


Fig. 1. Color coded map of the Mohorovičić discontinuity in the ALPACA region. The white dashed line shows the state border of Hungary

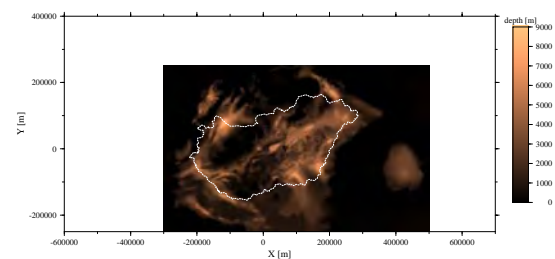


Fig. 2. Color coded map of the pre-Tertiary basement in the Pannonian basin. The white dashed line shows the state border of Hungary

This “rugged” crustal structure represents significant horizontal density variation which certainly dominates the regional picture of the gravity field near to the surface of the Earth. Its significant contribution to the disturbing potential at the altitude of the GOCE gradiometer satellite is also demonstrated.

Gravity modelling studies in the ALPACA region indicate that the mass balance/density distribution of the main structural units of the crust is not known with a satisfactory accuracy. The application of the generally assumed/accepted density contrasts both on the Moho discontinuity (e.g. $\Delta\rho=+500 \text{ kg/m}^3$) and in the sediments ($M\{\Delta\rho(\text{depth})\} \cong -350 \text{ kg/m}^3$ related to the crystalline basement rocks) provides high residual values of gravity field parameters (e.g. Bouguer gravity anomalies). After removing the gravitational effect of these “known” structural units from the observations the amplitude of the residuals is often larger than that of the observations themselves (Bielik et al, 2004). The residuals can be diminished significantly if the applied density contrasts are also decreased (Papp, 2001). In this context one should remember that the density distribution can only be derived indirectly from seismic tomography for the depth range of the Moho discontinuity. For the sediments the big number of borehole samples available in the basin (~10000) gives a relatively good control on the density distribution (Bielik, 2004, Szabó and Páncsics, 1999), however there are only a few data from the bottom regions (depth > 3 km). Therefore it is hoped that the GOCE on board measurements will give a possibility to clear up the regional mass distribution of the area.

2. Discrete models of the crust in the ALPACA region

Two versions of the crustal model of the ALPACA region exist. These can be derived from each other using the map projection system of Hungary. One of the models is built up from *rectangular parallelepipeds (prisms)* representing a local rectangular/planar mapping system (Fig. 3), whereas the elementary building blocks of the other are *polyhedrons*. These are defined in a global Cartesian coordinate system connected to the IUGG67 ellipsoid through the relative Hungarian Datum (HD72). There is a one-to-one geometrical correspondence between the corner points of prisms and polyhedrons, because each prism was split into two polyhedrons (Fig. 4). Obviously, the model in global Cartesian coordinates gives a possibility to

“follow” the curvature of the ellipsoid therefore it can also be used to investigate the effect of the Earth’s curvature neglected in the planar approximation. Both models contain three sub models: the surface topography, the Neogene-Quaternary sediments and the upper mantle.

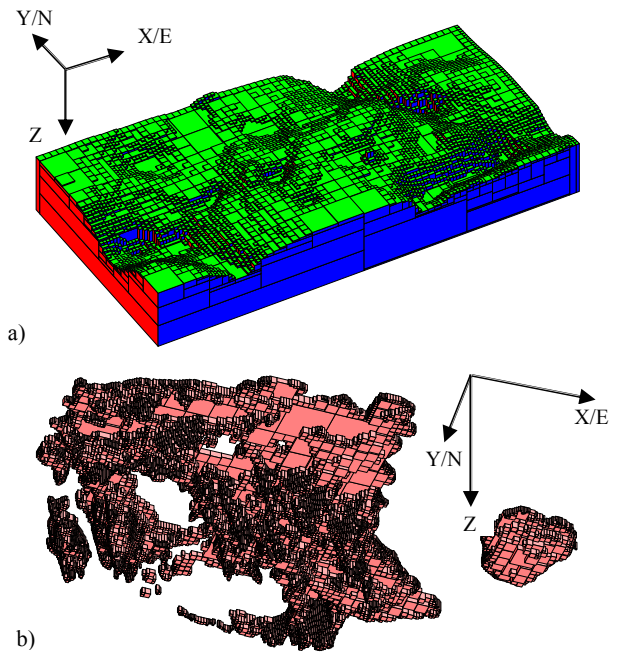


Fig. 3. Rectangular volume element models of a) the upper mantle bounded by the Moho discontinuity and b) the Neogene-Quaternary sediments viewed from above and below, respectively. The horizontal extensions of the models can be obtained from Fig. 1 and Fig. 2

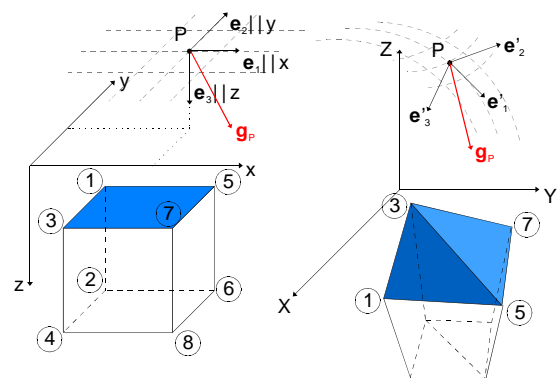


Fig. 4. The relation between the geometry of a prism and a corresponding polyhedron volume element defined in local $\{x,y,z\}$ and global $\{X,Y,Z\}$ rectangular coordinate systems, respectively. e'_1, e'_2, e'_3 are the unit vectors of the local tangential coordinate system fixed to the computation point P

The total numbers of prisms and polyhedrons are 198946 and 397892, respectively. The spatial resolution of the models depends on the local variability of the surfaces representing the dominant interfaces (topographical surface, pre-Tertiary basement and the Moho discontinuity) of the lithosphere. An adaptive algorithm (Kalmár et al. 1995) is used to obtain a minimum number of prisms according to some generalization parameters.

3. Forward computation of the second derivatives of the disturbing potential

All the structural units of the Earth's crust have a certain contribution to the disturbing potential T of the Earth's gravity field. The models introduced in Sec. 3 give a local contribution to it what can be determined by forward gravitational computations. For both type of discretization the closed analytical formulae are available also for the 2nd order derivatives of the gravitational potential ($U_{ij}=G \cdot \rho \cdot u_{ij}$) generated by the *prism* (Nagy et al, 2000):

$$\text{e.g. } u_{xx}(P) = \left\| \left\| -\tan^{-1} \frac{yz}{xr} \right\|_{x_1}^{x_2} \right\|_{y_1}^{y_2} \Big|_{z_1}^{z_2}, \quad (i=j=x) \quad (1)$$

where $P(0,0,0)$ is the computation points, ρ is the constant volume density of the prism or polyhedron, G is the gravitational constant, r is the distance and $\langle x_1, x_2 \rangle, \langle y_1, y_2 \rangle, \langle z_1, z_2 \rangle$ define the boundaries of the prism relative to $P(0,0,0)$; or by the *polyhedron*:

$$u_{ij} = -\sum_{k=1}^K n_k \cdot e_i \left[\sum_{l=1}^{L_k} \theta_1(u_{k,l}, v_{k,l}, w_{k,l}, z_k, \varepsilon) \cdot v_{k,l} \cdot e_j \right] - \sum_{k=1}^K n_k \cdot e_i \left[\sum_{l=1}^{L_k} \theta_2(u_{k,l}, v_{k,l}, w_{k,l}, z_k, \varepsilon) \cdot \text{sign}(z_k) \cdot n_k \cdot e_j \right] \quad (2)$$

where K is the number of the bounding planes (faces) of the polyhedron and L_k is the number of the corners of the k^{th} face of the polyhedron, $\text{sign}(z_k)$ is -1 when \mathbf{n}_k points to the half-space (bordered by the L_k plane) containing the point P , and +1 when it points to the other half-space.

$$d_{k,l} = |\mathbf{a}_{k,l+1} - \mathbf{a}_{k,l}|$$

$$\boldsymbol{\mu}_{k,l} = \frac{\mathbf{a}_{k,l+1} - \mathbf{a}_{k,l}}{d_{k,l}}, \quad \mathbf{n}_k = \frac{\boldsymbol{\mu}_{k,l-1} \times \boldsymbol{\mu}_{k,l}}{|\boldsymbol{\mu}_{k,l-1} \times \boldsymbol{\mu}_{k,l}|}, \quad \mathbf{v}_{k,l} = \boldsymbol{\mu}_{k,l} \times \mathbf{n}_k$$

$$u_{k,l} = \boldsymbol{\mu}_{k,l} \cdot \mathbf{a}_{k,l}, \quad w_{k,l} = \mathbf{v}_{k,l} \cdot \mathbf{a}_{k,l}, \quad z_k = \mathbf{n}_k \cdot \mathbf{a}_{k,l},$$

$$v_{k,l} = u_{k,l} + d_{k,l}, \quad \theta_1(u, v, w, z, \varepsilon) =$$

$$= \text{sign}(v) \cdot \ln \left(\frac{V_\varepsilon + |v|}{W_\varepsilon} \right) - \text{sign}(u) \cdot \ln \left(\frac{U_\varepsilon + |u|}{W_\varepsilon} \right)$$

$$\theta_2(u, v, w, z, \varepsilon) = 2 \tan^{-1} \frac{2wd}{(T_\varepsilon + d) \cdot |T_\varepsilon - d| + 2T_\varepsilon z_\varepsilon}$$

$$z_\varepsilon = z + \varepsilon, \quad W_\varepsilon = w^2 + z_\varepsilon^2,$$

$$U_\varepsilon = \sqrt{u^2 + W_\varepsilon^2}, \quad V_\varepsilon = \sqrt{v^2 + W_\varepsilon^2}, \quad T_\varepsilon = U_\varepsilon + V_\varepsilon$$

The detailed explanation of (2) and its parameters is given by e.g. Benedek (2004).

Applying a suitable reference model generating U^{ref} potential the local contribution of the density model to T_{ij} , containing n prisms/polyhedrons, can be defined (Papp, 1996):

$$T_{ij}^{\text{local}} = -U_{ij}^{\text{ref}} + \sum_{k=1}^n U_{ij}$$

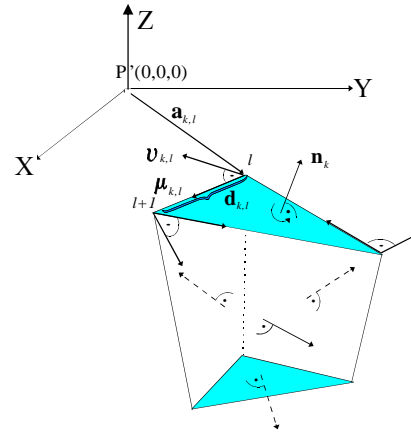


Fig. 5. The geometrical explanation of some variables of Eq.2

4. Simulation of the local contributions to T_{xx} , T_{yy} and T_{zz} from the crustal models at 400 km altitude

The analytical formulae (1) and (2) give an evident way to compute the gravitational effects of the models at satellite altitude. The results of this computation provide information about the expectable magnitude of the local contributions to the second derivatives of T in both coordinate systems. The effect of the Earth's curvature can also be investigated numerically if the parameters (e.g. $T_{xx}^{\text{local}}, T_{yy}^{\text{local}}, T_{zz}^{\text{local}}$) computed in the local $\{x, y, z\}$

and the global $\{X,Y,Z\}$ frames are compared. The 2nd derivatives computed from the *polyhedron model* ($u_{ij}^{\{X,Y,Z\}}$) contain the effect of the curvature. These quantities are transformed into the local system represented by a local tangential frame fixed to the actual computation point (Fig. 4):

$$\begin{bmatrix} u_{11} & u_{12} & u_{13} \\ u_{21} & u_{22} & u_{23} \\ u_{31} & u_{32} & u_{33} \end{bmatrix}^{\{x,y,z\}} = \mathbf{R}^T \begin{bmatrix} u_{11} & u_{12} & u_{13} \\ u_{21} & u_{22} & u_{23} \\ u_{31} & u_{32} & u_{33} \end{bmatrix}^{\{X,Y,Z\}} \quad \mathbf{R} \quad (3)$$

$$\text{where } \mathbf{R} = \langle \mathbf{e}'_1 \quad \mathbf{e}'_2 \quad \mathbf{e}'_3 \rangle = \begin{bmatrix} e'_{1X} & e'_{2X} & e'_{3X} \\ e'_{1Y} & e'_{2Y} & e'_{3Y} \\ e'_{1Z} & e'_{2Z} & e'_{3Z} \end{bmatrix}$$

defines the local tangential frame (Fig. 4). Then the results are compared with the corresponding quantities ($u_{ij}^{\{x,y,z\}}$) in the local/planar system computed directly from the *prism model*.

In the case of the upper mantle a constant density contrast value ($\Delta\rho=+250 \text{ kg/m}^3$) was used to obtain some 2nd derivatives of T (Fig. 6 and Fig. 7), whereas a depth dependent density contrast function (Szabó and Páncsics, 1999) was applied for the sediments (Fig. 8). For the central part of the surface topography model a variable density distribution was introduced which is based on geological information (Fig. 9). The outer zone of the ALPACA region was characterized by the usual constant 2670 kg/m^3 density value. The results of the forward simulations can be seen in Fig. 10.

The differences between the T_{zz} parameters calculated in the local and the global frames can be seen in Fig. 11 whereas the statistics are listed in Table 1. The extensions of the computation grids in the local/planar system were $[-640 \text{ km}, 630 \text{ km}] \times [-640 \text{ km}, 630 \text{ km}]$ and $[-1280 \text{ km}, 1270 \text{ km}] \times [-1280 \text{ km}, 1270 \text{ km}]$ for the surface topography and the upper mantle/e sediments, respectively. The grid spacing was $10 \text{ km} \times 10 \text{ km}$.

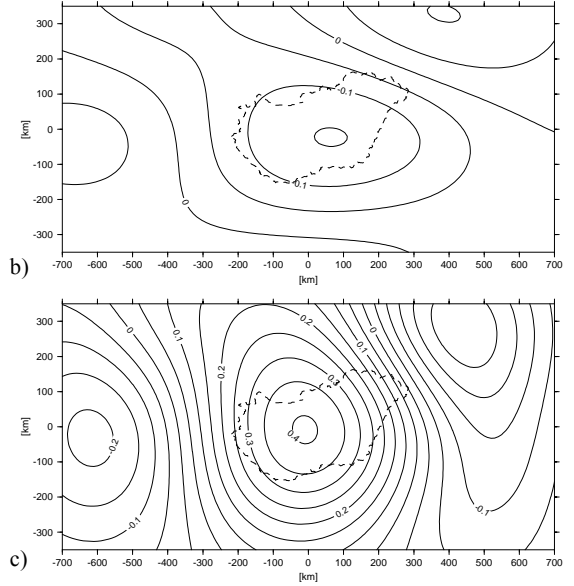
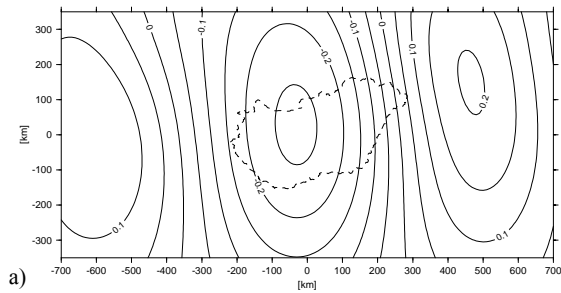


Fig. 6. Local contribution to a) T_{xx} , b) T_{yy} and c) T_{zz} simulated from the prismatic model of the upper mantle at $H=400 \text{ km}$ with $\Delta\rho=+250 \text{ kg/m}^3$. The contour interval is 0.05 Eötvös unit

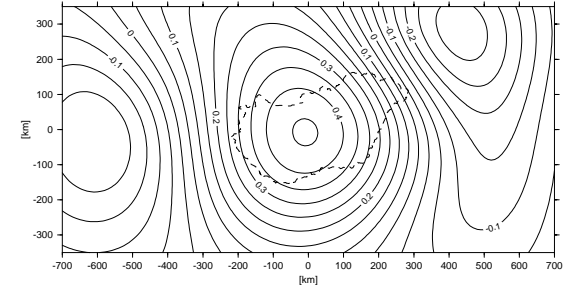
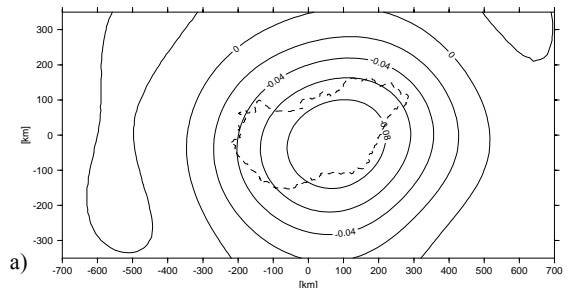


Fig. 7. Local contribution to T_{zz} simulated from the polyhedron model of the upper mantle at $H=400 \text{ km}$. The contour interval is 0.05 Eötvös unit



a)

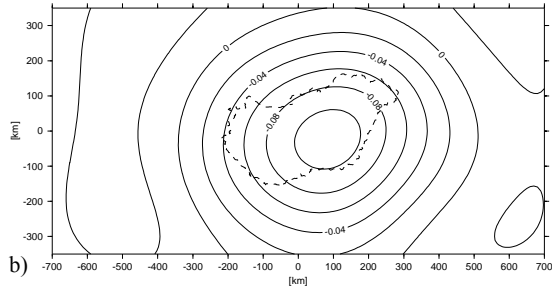


Fig. 8. T_{zz} values estimated from a) the prism and b) the polyhedron models of the Neogene-Quaternary sediments in the Pannonian basin at $H=400$ km. The contour interval is $0.02 E$

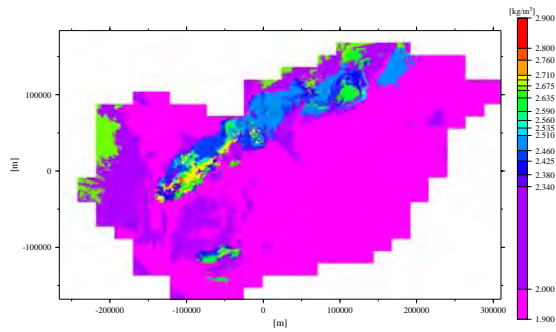


Fig. 9. Density model for the inner zone of the topography of the ALPACA region

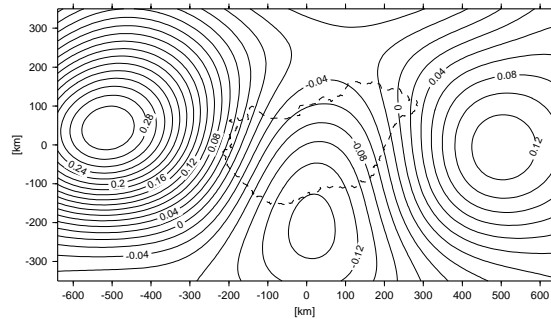
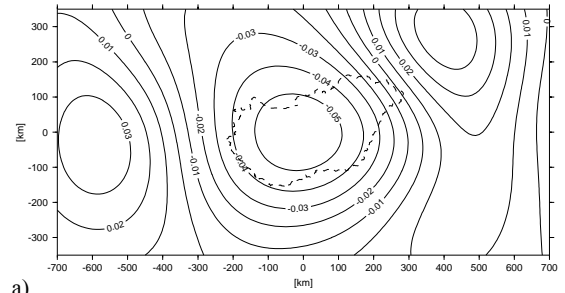


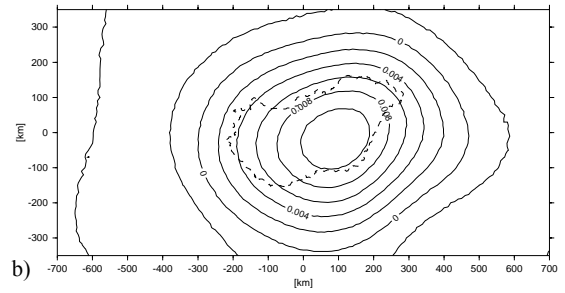
Fig. 10. T_{zz} values estimated from the prism model of the topography in the ALPACA region at $H=400$ km. The contour interval is $0.02 E$

Table 1. Statistical parameters of the differences of some second derivatives of T^{local} determined from the prism (local) and polyhedron (global) models of the upper mantle at two altitudes and the Neogene-Quaternary sediments

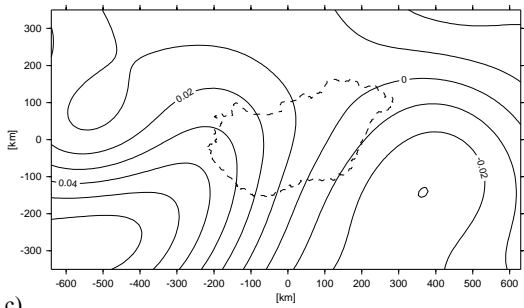
		parameters	min	max	mean	σ
		$\Delta T_{ii} = (T_{ii})^{\text{prism model}} - (T_{ii})^{\text{polyhedron model}}$	[E]	[E]	[E]	[E]
H=400km	Upper mantle	ΔT_{xx}	-0.034	0.032	0.0000	± 0.0088
		ΔT_{yy}	-0.015	0.023	0.0002	± 0.0047
		ΔT_{zz}	0.051	0.041	-0.0001	± 0.0096
	Neogene-Quaternary sediments	ΔT_{xx}	-0.006	0.005	0.0001	± 0.0012
		ΔT_{yy}	-0.006	0.005	0.0000	± 0.0012
		ΔT_{zz}	-0.004	0.011	-0.0001	± 0.0016



a)



b)



c)

Fig. 11. The difference of T_{zz} values simulated from the prismatic/local and polyhedron/global volume element models of a) the upper mantle (contour interval: 0.01) b) the sediments (contour interval: $0.002 E$) and c) the topography (contour interval: $0.01 E$)

5. Spectral analysis of the second derivatives

The forward computation of the 2nd derivatives of T indicates very smooth variation of the parameters at satellite altitude. In order to get a quantitative estimation about the attenuation of the spectral components the so called radial power spectra are determined and compared at different altitudes. In the FFT based computation of the spectra a cosine tapering window was used to diminish the spectral leakage. The attenuation of some individual spectral components generated by the model of the upper mantle can be seen in Fig. 12. It clearly shows that probably there will be no chance to resolve the part of the spectrum below 300 km wavelength. Around this point ($\lambda \approx 300$ km) the amplitude of spectral components hardly reaches the value of one μE .

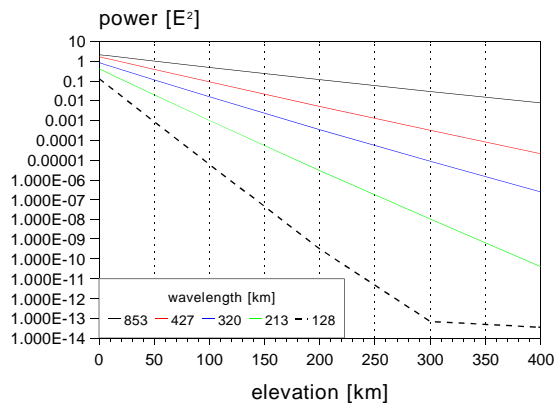


Fig. 12. The altitude dependence of the power of some spectral components generated by the model of upper mantle

6. The analysis of the computation results in the local and the global coordinate systems

Fig. 9 and Fig. 10 clearly show some systematic difference between the simulated 2nd derivatives of T^{local} . Although the ranges of deviations may reach a few hundredths of E unit, their standard deviations remains below ± 0.01 E (Table 1). It is a bit more than the expected accuracy (a few μE) of the GOCE measurements. A part of the differences certainly caused by the Earth's curvature neglected in the local frame. However, it is not obvious from the maps because no "edge effects" (increasing deviations near/on the borders of the area) are indicated. The differences are correlated well with the signals generated by the models, so probably those are partly due to local mass differences between the two types of mass discretization. The polyhedron model always gives a bit larger absolute contribution (max. $\sim 10\%$) than the prism model.

7. Conclusions

The contribution of the lower crust – upper mantle density interface (Moho discontinuity) to T can reach several tenth of the Eötvös unit at the satellite altitude even if the density contrast on the Moho is only half of what is generally assumed. The GOCE gradiometers, however, will sense the integrated effect of all the structural units of the crustal anomalies, so a source separation (isostatic decompensation, basin effects) will be necessary to prepare the on board data for inversion.

The pure effect of the Earth's curvature cannot be bigger than a few hundredths of E unit on the area of investigation. Therefore, as a first approximation, the planar frame is feasible for the

inversion of satellite gradiometer data in the ALPACA region. If more accurate density estimation is needed then the inversion must be performed in the global $\{X,Y,Z\}$ frame, using the polyhedron volume elements.

The gravitational contribution of the crustal density anomalies to the 2nd derivatives of T having a wavelength less than 300 km probably cannot be indicated by the gradient measurements carried out in the altitude range of the GOCE satellite.

Acknowledgements. The research was supported by the Hungarian National Research Fund (project number: OTKA T043413).

References

- Benedek J (2004): The application of polyhedron volume elements in the calculation of gravity related quantities. in: *Meurers B and Pail R (eds), Proceedings of the 1st Workshop on International Gravity Field Research, Graz 2003, Special Issue of Österreichische Beiträge zu Meteorologie und Geophysik, Heft 31., pp. 99-106.*
- Bielik M, Makarenko I, Legostaeva O, Starostenko V, Dérerová J, and Šefara J (2004): Stripped gravity map of the Carpathian-Pannonian region. in: *Meurers B and Pail R (eds), Proceedings of the 1st Workshop on International Gravity Field Research, Graz 2003, Special Issue of Österreichische Beiträge zu Meteorologie und Geophysik, Heft 31., pp. 107-114.*
- Kalmár J, Papp G, Szabó T (1995): DTM-based surface and volume approximation. *Geophysical applications. Comp. and Geosci.*, 21, pp. 245-257.
- Lenkey L, Dövényi P, Horváth F and Cloething SAPL (2002): *Geothermics of the Pannonian basin and its bearing on the neotectonics.* EGU Stephan Mueller Special Publication Series, 3, pp. 29-40
- Nagy D., Papp G., Benedek J. (2000): The gravitational potential and its derivatives for the prism. *Journal of Geodesy*, 74. pp. 552-560.
- Papp, G. (1996): On the application of physical filtering in 3-D forward gravity field modelling. In: *Meurers, B. (ed.), Proceedings of the 7th International Meeting on Alpine Gravimetry, Special Issue of Österreichische Beiträge zu Meteorologie und Geophysik, Heft 14, pp. 145-154.*
- Papp G (2001): On some error sources of geoid determination. In: *Meurers, B. (ed.), Proceedings of the 8th International Meeting on Alpine Gravimetry, Leoben 2000, Special Issue of Österreichische Beiträge zu Meteorologie und Geophysik, Heft 26., pp. 167-179.*
- Royden L, Horváth F (editors) (1988): The Pannonian basin. A study in basin evolution. *Am. Assoc. Pet. Geol. Mem.* 45.
- Szabó Z and Páncsics Z (1999): Rock densities in the Pannonian basin – Hungary. *Geophysical Transactions of ELGI*, 42, pp. 5-27.

A Study of High Frequency Terrain Effects in Gravity Field Modelling

Christian Voigt, Heiner Denker
Institut für Erdmessung, Leibniz Universität Hannover,
Schneiderberg 50, D-30167 Hannover, Germany
E-Mail: voigt@ife.uni-hannover.de

Abstract. Within the framework of the GOCE-GRAND II project and in cooperation with the Bundesamt für Kartographie und Geodäsie (BKG), it is planned to validate the GOCE gravity field models by independent terrestrial data sets. Besides GPS and levelling data, gravity and terrain data shall be combined with a global spherical harmonic model to provide an independent gravimetric (quasi)geoid model, and, in addition, deflections of the vertical shall be observed with the Hannover digital zenith camera TZK2-D in a 500 km long profile to provide another completely independent data set for the GOCE validation.

For this purpose, it is necessary to study the high frequency gravity field components related to the terrain, as all effects not included in the GOCE models have to be filtered out before the actual validation step. In this contribution, a digital terrain model for Germany with a grid spacing of 1" x 1" (approx. 30 m) is used to study the high frequency effects of the terrain on gravity anomalies, deflections of the vertical and geoid heights. Besides an investigation of different DTM resolutions, a covariance and spectral analysis is performed. The aim of the study is to find the optimal resolution of the terrain data for given accuracy levels.

Keywords. Terrain effects, digital terrain models, covariance and spectral analysis, gravity field

1 Introduction

Digital Terrain models (DTM) play an important role in gravity field modelling, as local gravity field effects are strongly correlated with the topography. For gravimetric geoid determinations, high-resolution DTMs are usually employed to model short-wavelength effects.

The aim of this study is to find adequate DTM resolutions for given accuracy requirements, which is also important to optimize the costly terrain effect computations without any significant accuracy loss.

In this contribution, a very high resolution DTM with a grid spacing of 1" x 1" (approx. 30 m) is employed to determine the high frequency terrain effects for different gravity field parameters. Several similar studies were published (see, for example, Forsberg 1984a; Vassiliou and Schwarz 1987; Kotsakis and Sideris 1999), but all of them are based on much coarser data grids.

In this study, terrain effects for various gravity field functionals are analyzed up to spherical harmonic degree $n_{\max} = 648000$, which corresponds to a spatial resolution of 1". Both space domain and frequency domain methods are employed in three test areas in Germany.

This investigation is carried out in the context of a regional validation and combination experiment in Germany within the framework of the GOCE GRAND II project. In this project, GPS and levelling data, gravity and terrain data as well as deflections of the vertical, observed in profiles with the Hannover digital zenith camera TZK2-D, shall be used as independent data sets for the validation of the GOCE products. For this purpose, it is important to study the high frequency gravity field components related to the terrain, as all effects not included in the GOCE models have to be filtered out before the actual validation step. Besides the validation aspect, the second major issue within the project is the combination of the terrestrial data with the global models from the GOCE mission in order to provide the complete geoid spectrum over all wavelengths with accuracy at the centimetre level.

Within this context, a remove-restore procedure and residual terrain model (RTM) reductions, suitable for modelling only short-wavelength terrain effects, are applied. In the first part of this contribution, RTM effects on gravity, vertical deflections and geoid are computed in the space domain using different DTM resolutions. Besides the statistics of the computed gravity field parameters, the differences between the values from the 1" x 1" DTM and coarser grids are analysed. Secondly, DTM resolution requirements are investigated through covariance and spectral analyses of the

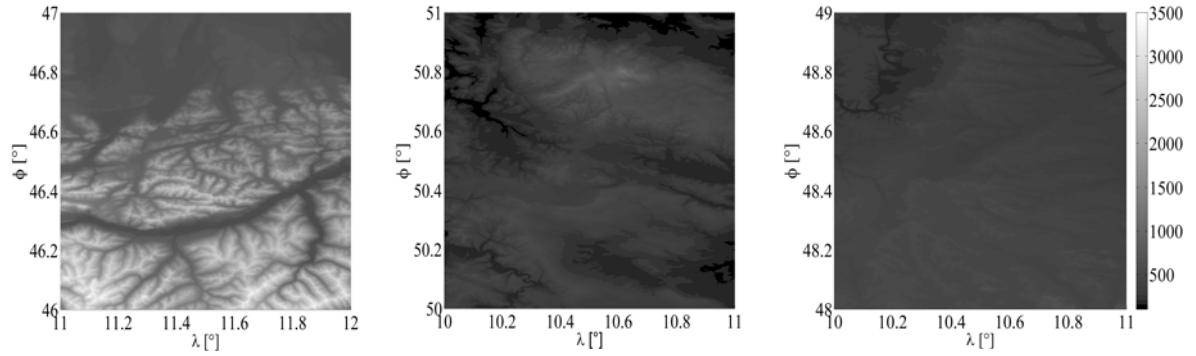


Fig. 1: Topographic heights [m] in the German Alps (left), Harz (middle) and Franconia (right)

RTM gravity effects in 1" x 1" grids. Basic covariance parameters are estimated along with the geoid RMS power in various spectral bands. The aim of both parts of the study is to find appropriate DTM resolutions for given accuracy levels. Finally, all results are inter-compared and discussed.

2 Data Sets

Three test areas with hilly to alpine terrain type were chosen in different parts of Germany. Three 1° x 1° bins were extracted from the Digital Terrain Model DGM50 M745 by the Bundesamt für Kartographie und Geodäsie (BKG) with a grid spacing of 1" x 1" (approx. 30 m) and an accuracy of about ±1 – 8 m. Graphical displays and the statistics of the topographic heights are provided in Fig. 1 and Table 1 for the three selected test areas, respectively.

Table 1. Statistics of the topographic heights in the three selected 1° x 1° test bins [m]

Test area	Number	Mean	Std.dev.	RMS	Min	Max
German Alps	3600 x 3600	1236	629	1387	475	3479
Harz	3600 x 3600	315	135	343	97	1140
Franconia	3600 x 3600	370	83	379	170	688

3 Methodology

3.1 RTM effects in the space domain

For the practical evaluation of gravitational effects of a topographic mass model, integrals of the type

$$L(T) = G\rho \iiint_V L(1/r) dV \quad (1)$$

have to be computed under the assumption of a constant topographic density ρ , where $L(T)$ are the gravity field functionals, G is the Newton's gravitational constant, $L(1/r)$ are functionals of the reciprocal distance between the volume element dV and the computation point, which is used as the origin of the coordinate system. The integrals were evaluated in the space domain by numerical integration using rectangular prisms. Effects for gravity anomalies, vertical deflections und geoid undulations were computed by exact prism formulas when the computation point was near the prism, while at larger distances, the MacMillan series expansions and finally point mass approximations were chosen for all three functionals.

For the innermost topography surrounding the computation point, a bicubic spline interpolation of the DTM elevations was carried out in order to densify the data grid and to reduce discontinuity effects between adjacent prisms. Furthermore, the curvature of the earth was taken into account to the second order. All computations were done with the program tc; for further details and formulas see Forsberg (1984a).

For the computation of RTM effects in the space domain, the 1° x 1° test areas were extended to 3° x 3° in order to avoid edge effects. The RTM computations were based on a fixed area reduction with 3° x 3°, constant density value of 2.67 g/cm³, 15' x 21' reference topography, and DTM grid spacings of 1" x 1", 3" x 3", 6" x 6", 12" x 12" and 30" x 30", where the coarser grids are derived from the 1" x 1" grid by moving averages.

In order to save computation time, the calculations were only carried out for stations in a 1' x 1' grid within the 1° x 1° bins, yielding 3600 stations in total for each of the test areas.

3.2 Covariance and spectral analysis

In this section, covariance and spectral analyses of gridded RTM gravity effects are performed. The RTM gravity effects were computed by the classical terrain correction and a Bouguer reduction to the level of the reference topography h_{ref} :

$$\Delta g = 2\pi G\rho(h - h_{ref}) - tc. \quad (2)$$

Here h is the topography level in the computation point, G is again the Newton's gravitational constant, ρ is the constant topographic density and tc the terrain correction term.

The terrain correction was expanded into a Taylor series using a linear approximation:

$$tc = \frac{1}{2}G\rho \iint_F \frac{(h - h_p)^2}{r_0^3} dF + \dots \quad (3)$$

In the above equation, r_0 is the planar distance between the surface element dF and the computation point P and h_p is the (constant) elevation of the computation point. This integral can be treated as a convolution of h and h^2 with $1/r_0^3$, and it can thus be computed in the frequency domain by Fast Fourier Transform (FFT). For further details and formulas see Forsberg (1984a, 1985).

The RTM reduction parameters are identical to ones used in the previous section; the terrain correction radius was 50 km. The RTM gravity effects were again computed for $1^\circ \times 1^\circ$ bins; in order to reduce edge effects, the data areas were extended to $2^\circ \times 2^\circ$.

Covariance and spectral analyses of the RTM gravity effects were performed in $1'' \times 1''$ data grids for each of the three test areas described above. The 2D power spectral densities (PSD) were estimated directly using FFT algorithms. The 2D planar covariance functions (CV) were computed indirectly by taking the inverse Fourier transform of the PSD. For formulas see, for example, Vassiliou and Schwarz (1999).

No windowing was carried out as tests with and without windowing gave only insignificant differences. In accordance with the isotropy assumptions, the 2D CVs and PSDs were radially averaged into 1D isotropic functions. Furthermore, the gravity and geoid degree variances were estimated from the 1D isotropic PSDs, where the extent and grid spacing of the test areas define the recoverable spectral band, in this case the degree range is $360 \leq n \leq 648000$. The gravity degree variances at the harmonic degrees n were estimated by

$$\sigma_{\Delta g, n}^2 = \frac{n + 0.5}{2\pi R^2} \cdot PSD(\omega), \quad (4)$$

where $PSD(\omega)$ is the 1D isotropic planar PSD at the radial wave number ω and R is the mean radius of the Earth.

The geoid degree variances were computed using

$$\sigma_{\zeta, n}^2 = \frac{R^2}{\gamma^2(n-1)^2} \cdot \sigma_{\Delta g, n}^2, \quad (5)$$

where γ is the normal gravity. For details see Heiskanen and Moritz (1967), Forsberg (1984b) and Kotsakis and Sideris (1999).

4 Analysis of the results

4.1 RTM effects in the space domain

In Tables 1 and 2, the RTM gravity and geoid effects based on the DTM with a grid spacing of $1'' \times 1''$ are displayed for each of the three test areas. The RTM reductions alone create a geoid signal between 2 cm (Franconia) and 12 cm RMS (German Alps), which confirms the well-known fact that topographic effects should always be taken into account to obtain a geoid with an accuracy of one centimetre.

Table 2: Statistics of RTM gravity effects [mGal] based on the DTM $_{1'' \times 1''}$

Test Area	RMS	Min	Max
Bayern	40.9	-173.7	90.3
Harz	8.7	-20.0	61.1
Franken	4.1	-13.3	19.1

Table 3: Statistics of RTM geoid effects [cm] based on the DTM $_{1'' \times 1''}$

Test Area	RMS	Min	Max
Bayern	12.3	-35.6	34.5
Harz	4.3	-5.7	19.9
Franken	1.8	-4.8	4.8

Moreover, RTM effects on gravity, deflections of the vertical and geoid were computed for different DTM resolutions. In Table 4, the statistics of the differences with regard to the DTM with a grid spacing of $1'' \times 1''$ are displayed.

Table 4: Statistics of the RTM reduction differences with regard to the DTM_{1" x 1"}

DGM 1" x 1" -	German Alps			Harz			Franconia		
	RMS	Min	Max	RMS	Min	Max	RMS	Min	Max
Gravity anomalies [mGal]									
DGM 3" x 3"	0.45	-5.58	3.56	0.15	-1.86	1.01	0.10	-0.80	0.62
DGM 6" x 6"	1.08	-7.70	7.16	0.41	-4.44	2.38	0.28	-3.33	1.43
DGM 12" x 12"	2.45	-16.58	10.48	0.93	-6.82	5.38	0.63	-5.67	3.28
DGM 30" x 30"	6.94	-52.81	26.35	2.03	-15.68	8.56	1.27	-10.37	7.76
Deflections of the vertical ["]									
Components in north-south direction ξ									
DGM 3" x 3"	0.04	-0.28	0.26	0.02	-0.09	0.09	0.01	-0.07	0.06
DGM 6" x 6"	0.11	-0.61	0.48	0.04	-0.23	0.21	0.03	-0.20	0.15
DGM 12" x 12"	0.24	-1.65	0.94	0.10	-0.66	0.56	0.07	-0.51	0.38
DGM 30" x 30"	0.66	-2.53	2.61	0.23	-1.40	1.20	0.16	-0.89	0.89
Components in east-west direction η									
DGM 3" x 3"	0.03	-0.20	0.25	0.01	-0.08	0.08	0.01	-0.04	0.04
DGM 6" x 6"	0.09	-0.71	0.58	0.04	-0.24	0.24	0.02	-0.16	0.18
DGM 12" x 12"	0.21	-1.36	1.24	0.10	-0.73	0.65	0.06	-0.33	0.45
DGM 30" x 30"	0.61	-2.68	2.46	0.23	-1.21	1.27	0.13	-0.78	0.85
Geoid [cm]									
DGM 3" x 3"	0.0	-0.3	0.4	0.0	-0.1	0.1	0.0	-0.1	0.1
DGM 6" x 6"	0.1	-0.4	0.4	0.0	-0.1	0.0	0.0	-0.1	0.0
DGM 12" x 12"	0.1	-0.8	1.1	0.0	-0.1	0.1	0.0	-0.1	0.1
DGM 30" x 30"	0.2	-1.4	1.8	0.1	-0.3	0.2	0.0	-0.2	0.2

In the German Alps, the use of 3" x 3" and 6" x 6" grids already causes maximum differences in the RTM geoid effects of 4 mm. Coarser grids cause differences of more than 1 cm. In the Harz and Franconia regions, however, the terrain effects are much smaller. The differences of RTM geoid effects are less than or equal to 3 mm with grid spacings up to 30" x 30".

Although the RTM reductions for gravity anomalies vary by several mGal when using denser grids, the effects on geoid signals barely reach a maximum of 1 mm and are thus negligible.

With regard to the analysis of high-precision vertical deflections observed with digital zenith cameras with an accuracy level of approx. 0.1" (see Hirt 2004), a DTM with a resolution of 1" x 1" should be used in alpine regions and 3" x 3" in other areas.

4.2 Covariance and spectral analysis

The results for the basic parameters that describe the behaviour of the covariance functions for the

RTM gravity effects are displayed in Table 5 for each of the three test areas. Large differences appear in the variance of the RTM gravity effect C_0 . The correlation lengths $\chi_{1/2}$ and the anisotropy indices are very similar in spite of the different relief types of the test areas. The correlation lengths are much smaller than in other previous studies (see, for example, Forsberg 1984a; Kotsakis and Sideris 1999). The results for the anisotropy index show that the isotropy assumptions can be justified.

Table 5: Local covariance function parameters for RTM reductions

Test area	C_0 [mGal ²]	$\sqrt{C_0}$ [mGal]	$\chi_{1/2}$ [arcmin]	Anisotropy index
German Alps	1558.88	39.5	1.3	1.3
Harz	74.20	8.6	1.8	1.5
Franconia	15.85	4.0	1.2	1.4

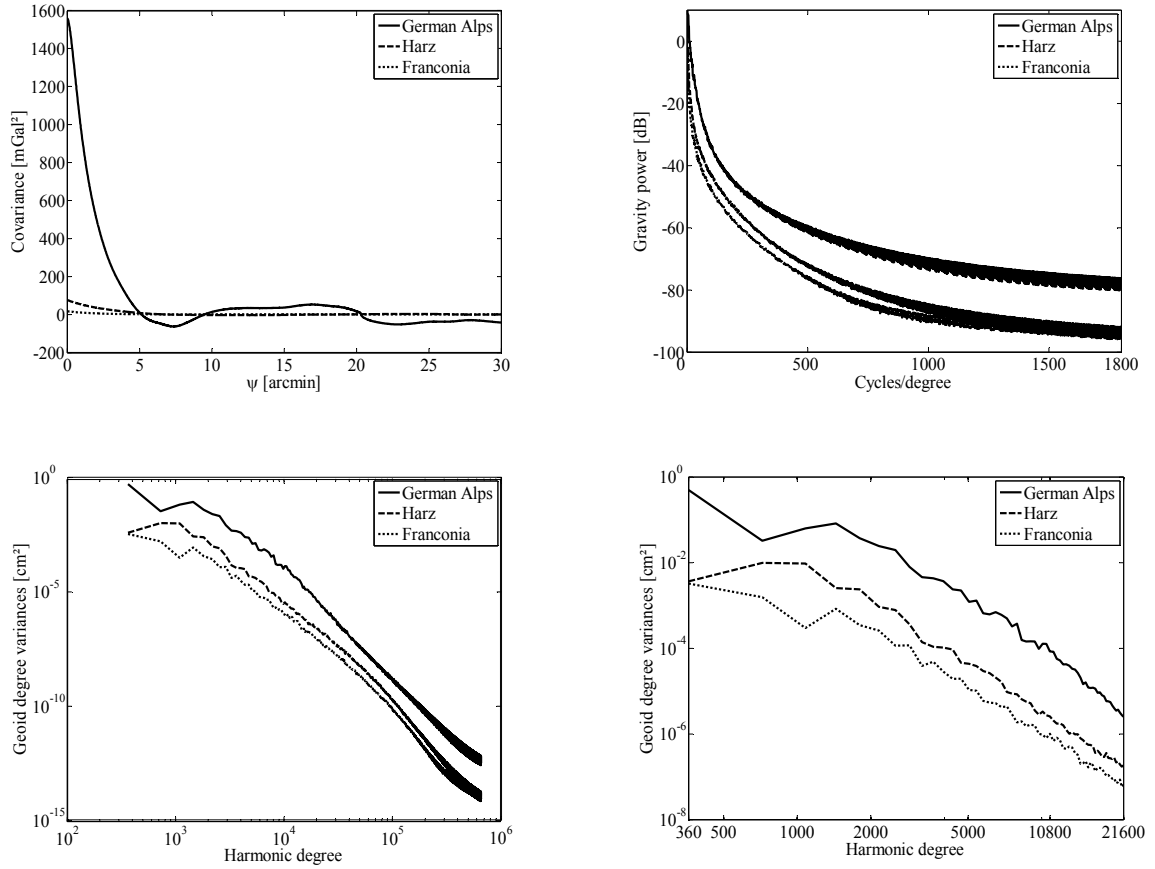


Fig. 2: Empirical covariance functions (top left) and power spectra (top right) for RTM reductions; geoid degree variances from RTM reductions for the entire recoverable spectral band (bottom left) and for the spectral band with a degree range of $360 \leq n \leq 21600$ (bottom right)

In Fig. 2, the 1D covariance functions and power spectral densities are displayed as well as the geoid degree variances for the entire recoverable spectral band of $360 \leq n \leq 648000$ (bottom left) and for the spectral band with a degree range of $360 \leq n \leq 21600$ (bottom right). In addition, the geoid RMS power was computed from the estimated geoid degree variances in different spectral bands (see Table 6).

It can be seen that the RTM gravity effects alone create a geoid signal between 2 cm (Franconia) and 17 cm RMS (German Alps). In each of the three test areas, the spectral band with the degree range of $360 \leq n \leq 10800$ contains approx. 99.90 % of the geoid variance. In the spectral band with a degree range of $10800 < n \leq 21600$, merely 0.09 % and for $n > 21600$ only 0.01 % of the geoid variance can be found. Based on these results, degrees up to $n=21600$ should be taken into account for alpine regions and up to $n=10800$ for other regions, which

corresponds to spatial resolutions of $30'' \times 30''$ and $1' \times 1'$, respectively. However, it has to be noted that these results are based on RMS values and thus represent the average situation. This also means that significantly higher maximum effects may exist in some points or even areas.

Table 6: Geoid RMS power [cm] in various recoverable spectral bands

Spectral band	German Alps	Harz	Franconia
$360 \leq n \leq 648000$	16.9	3.3	1.6
$360 \leq n \leq 10800$	16.9	3.3	1.6
$10800 < n \leq 21600$	0.5	0.1	0.1
$21600 < n \leq 648000$	0.1	0.0	0.0

5 Summary and conclusions

In the present paper, high frequency terrain effects (RTM) are analysed in various parts of Germany. Both space domain and frequency domain methods are applied based on a DTM with a grid spacing of 1" x 1" (approx. 30 m).

In the space domain, differences between RTM effects on gravity, deflections of the vertical and geoid were analysed with respect to different DTM resolutions. The major aim was to find the appropriate DTM resolution for different relief types and accuracy requirements. From covariance and spectral analyses in the frequency domain, basic parameters of the covariance functions were estimated, and gravity and geoid degree variances for RTM gravity effects were computed, allowing an investigation of the geoid power at different spectral bands.

Both methods gave similar RMS values of the RTM effects, creating a geoid signal between 2 cm (Franconia) and approx. 15 cm (German Alps). Regarding the different DTM resolutions and considering also the maximum values, a DTM resolution of at least 6" x 6" is recommended in the German Alps, while in the Harz and Franconia regions a resolution of 30" x 30" may be sufficient for a one centimetre geoid.

Acknowledgements. GOCE-GRAND II is supported under grant 03F0422A BMBF/DFG Research and Development Programme "Geotechnologien".

References

- Forsberg, R. (1984a). A Study of Terrain Reductions, Density Anomalies and Geophysical Inversion Methods in Gravity Field Modelling. Report No. 355, Department of Geodetic Science and Surveying, The Ohio State University, Columbus, Ohio.
- Forsberg, R. (1984b). Local Covariance Functions and Density Distributions. Report No. 356, Department of Geodetic Science and Surveying, The Ohio State University, Columbus, Ohio.
- Forsberg, R. (1985). Gravity Field Terrain Effect Computations by FFT. Bulletin Géodésique, Volume 59, N° 4, pp. 342-360.
- Heiskanen, W.A., and H. Moritz (1967). Physical Geodesy. W.H. Freeman and Company, San Francisco.
- Hirt, C. (2004). Entwicklung und Erprobung eines digitalen Zenitkamarasystems für die hochpräzise Lotabweichungsbestimmung. Wissenschaftliche Arbeiten der Fachrichtung Vermessungswesen der Universität Hannover Nr. 253.
- Kotsakis, C., and M.G. Sideris (1999). Study of the gravity field spectrum in Canada in view of cm-geoid determination. Bollettino Di Geofisica teoretica ed applicata. Vol. 40, N. 3-4, pp. 179-188.
- Vassiliou, A.A., and K.P. Schwarz (1985). Study of the High Frequency Spectrum of the Anomalous Gravity Potential. Paper presented at the 13th Moving Base Gravity Gradiometer Review, U.S. Air Force Academy, Colorado Springs1, February 12-13, 1985.

The utilization of global digital crustal databases in regional applications of forward gravity field modelling

D. Tsoulis, V.N. Grigoriadis, I.N. Tziavos

Department of Geodesy and Surveying, Aristotle University of Thessaloniki, Fax: +30 2310 995948, Email: tsoulis@topo.auth.gr

Abstract. The release of model CRUST 2.0 offers an advanced and efficient means of modelling crust-induced potential contributions both globally and regionally. Providing rigorous geometric as well as physical information concerning the structure and consistency of distinct crustal layers from the Earth's topography down to the crust-mantle boundary, the information contained in model CRUST 2.0 is of special interest to studies related to gravity field modelling and interpretation. The present paper investigates the possibilities of utilizing the CRUST 2.0 data in the frame of local and regional forward gravity field modelling applications. For this reason a thorough numerical analysis of the model has been carried out for the area surrounding Greece. In terms of geoid modelling and local gravity field investigations the CRUST 2.0 information can be used mainly in the frame of isostatic anomalies. Thus, isostatic effects on gravity have been computed for this region and are compared with the corresponding computations resulting from two other independent sources of determining the Moho interface, namely the Airy isostatic mechanism and the application of deconvolution methods to surface gravity data.

Keywords. global digital databases, forward modelling, CRUST 2.0, Moho interface

1 Introduction

The publication of CRUST 2.0, a global digital crustal database at a $2^\circ \times 2^\circ$ resolution (Bassin et al. 2000), produced a significant impulse over the last years to research activities related with the Earth's structure and gravity field. Among the topics that profited substantially from the release of the new crustal data were for example regional lithosphere investigations (Danesi and Morelli 2001, Schmid et al 2004, Koulakov and

Sobolev 2006), seismic studies (Obayashi et al 2004) or the derivation and analysis of isostatic Earth gravity models (Kaban et al 2004, Tsoulis 2004).

CRUST 2.0, which has been compiled and is now administered by the U.S. Geological Survey and the Institute for Geophysics and Planetary Physics at the University of California, is the descendant of CRUST 5.1, a global crustal model at $5^\circ \times 5^\circ$ (Mooney et al 1998). Both models are based on seismic refraction data published up to 1995 and a detailed compilation of ice and sediment thickness. CRUST 2.0 offers density, geometry and seismic information for a total of seven crustal layers, from ice and water to lower crust, the boundary surface between crust and mantle, otherwise known as the Mohorovicic discontinuity. The data consist of density values (the detailed density structure includes the additional layer of the uppermost mantle), layer boundary values in terms of depths with respect to mean sea level and values for compressional and shear wave velocities, all of which are given globally and explicitly for each of the 16200 grid elements that define each layer at the $2^\circ \times 2^\circ$ resolution. Thus, the model consists ultimately of a total of 29 matrices, each of dimensions 180×90 , where global bathymetry and surface topography data were adopted from the 5 arc minute resolution data set ETOPO-5 (NGDC, 1988).

The availability of recent Digital Terrain Models on the other hand, especially over continental areas, offers a new prospective of unprecedented resolution in calculations of local and regional gravity field modelling (Vergos et al 2005). In the frame of these new terrain data one could also incorporate the crustal information of databases, such as CRUST 2.0, and devise computational strategies where both of these data sources could be combined, for example for the computation of isostatic anomalies. The present paper investigates the possibilities of utilizing the CRUST

2.0 data to local or regional gravity field related computations. It turns out, that two are the key issues connected with the CRUST 2.0 database, that can be exploited for regional investigations. The geometry of the final crustal layer, which represents the Moho boundary over the specific region and will occupy the calculations presented in this paper and the detailed stratification of the database that could be employed in studies of gravity field interpretation.

2 Local assets of CRUST 2.0 database

The window selected for the local assessment of the CRUST 2.0 database was defined between $14^\circ < \lambda < 34^\circ$ and $28^\circ < \varphi < 48^\circ$, an area stretching over the southeast Mediterranean with Greece at its center. The area is characterized by the absence of hard sediments, thus a total of only four layers exist in the database for this region, namely soft sediments, upper, middle and lower crust. Table 1 presents the statistics regarding the layer depth information for the area under consideration. Examining the soft sediments layer we observe a direct correlation of the variations of the lower bound of this layer with the variations of the surface topography. The largest numerical values for the depths (3 – 5 km) occur, as one would expect, under the Mediterranean part of the region, while the smallest values are observed at the continental parts. The largest depth values of the next crustal layer (upper crust) are obtained over East Turkey (20 km), with large values of the order of 17 km occurring at the marine region south of Greece. The continental part of Greece exhibits smaller values for this layer of the order of 12 km with respect to marine areas. In overall larger numerical values for the depths of the upper crust layer occur at continental rather than marine regions. Moving towards the deeper crustal layers one begins to verify numerically the connection of the surface topography variations with the underlying crustal thickness according to the Airy/Heiskanen isostatic theory. Thus, in overall greater crustal depths are observed at continental regions compared to marine regions. The middle crust layer in particular shows a maximum depth value of 40 km at the eastern part of Turkey, with the minima appearing at the marine area stretching over the Ionian trench. The continental part of Greece

Table 1: Layer thickness information obtained from CRUST 2.0 for the test area. Unit is km.

Layer	Min	Max	Mean	SD
Soft Sediments	0.50	1.50	1.13	0.35
Upper Crust	1.70	20.00	9.70	4.01
Middle Crust	2.30	20.00	9.79	3.56
Lower Crust	2.50	13.50	8.74	2.50

has an almost constant depth value around 23 km. The overall variation of the boundary surface between middle and lower crust assimilates roughly with the basic scheme of mass compensation after Airy. Finally, the lower crust layer, which expresses also the Mohorovicic discontinuity, appears to have a mean value of 32.89 km for the whole test area. Especially over Greece, for which another independent dataset of Moho depths is available, the largest values are of the order of 40 km and occur underneath the continental part of the state, whereas the smallest Moho depths according to CRUST 2.0 appear again at the marine area of the Ionian trench.

The layer thickness information provides an additional source of information, which is mainly of interest to potential field determination studies. The information of Table 1 indicates the position of the density contrast between two subsequent layer. Table 2 on the other hand offers a measure of the quantity of the crustal masses defined by the respective layer. From the overall assessment of this information it follows that the values of the soft sediments thickness (0.5 – 1.5 km) are distributed uniformly over the test region, with small values appearing at continental regions and larger values at lower elevation areas or at sea. The thickness data for the rest of the crustal layers (upper, middle and lower crust) appear with similar characteristics. Thus, all layers show a variation in their vertical size that complies in general with the Airy/Heiskanen hypothesis. Smaller layer thickness values appear for all three crustal layers at marine regions, while larger values occur below continental parts. Furthermore, all three layers obtain mean thickness values of the order of 12 km over continental regions, while they all reveal the same mean of almost 7 km at marine areas.

Figure 1 presents the Moho data obtained from CRUST 2.0 for the area under consideration and their comparison with Airy-derived crustal

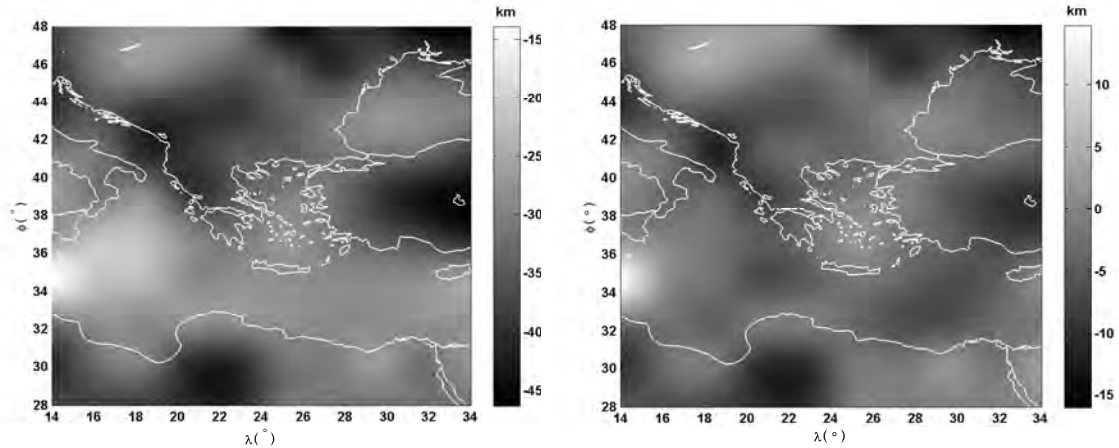


Fig. 1 Moho depth values with respect to mean sea level obtained from CRUST 2.0 database (left panel) and differences with respect to Airy-derived Moho depths for the same region (right panel). Unit is km.

thickness T , according to the standard scheme $T_{land} = D + t$ and $T_{sea} = D - t'$ defined respectively below continental and marine regions. In the frame of the Airy hypothesis the root and anti-root quantities are calculated according to the expressions $t = (\rho_{crust}/(\rho_m - \rho_{crust}))h$ and $t' = ((\rho_{crust} - \rho_w)/(\rho_m - \rho_{crust}))h'$ respectively (Lambeck 1988). These quantities express some crude estimates of the mean crustal, mantle and water density, for which the numerical values $\rho_{crust} = 2.67 \text{ g cm}^{-3}$, $\rho_m = 3.27 \text{ g cm}^{-3}$ and $\rho_w = 1.03 \text{ g cm}^{-3}$ where used here, h and h' denote the height of the topography and the depth of the bathymetry in absolute values with respect to mean sea level and D describes the depth where the actual compensation takes place, taken here equal to 30 km. The discrepancies between the CRUST 2.0 provided Moho information with the theoretically derived Moho structure after Airy are significant for the test area, having a mean value of about 4 km and a standard deviation of roughly 3 km, these values expressing the discrepancies between the two sets in absolute sense. The larger differences (maximum: 16.02 km) are located at the areas with the large Moho depths according to the CRUST 2.0 values. The right panel of Figure 1 indicates in more detail the relative relation between the two databases, as negative values express regions where the CRUST 2.0 data represent larger Moho estimations than the theoretical Airy values and vice-versa for the regions where positive differences are reported. The overall performance is fairly poor and indicates a large discrepancy between the two datasets, which could

only be properly assessed if a further independent Moho information for the same area was utilized.

3 Assessment of Moho information

Among the different interface estimation methods that exist in the literature, deconvolution methods appear to be of special interest when local surface gravity data are available. Tsokas and Hansen (1997) applied such an analytical signal analysis technique (Multiple Source Werner Deconvolution, MSWD) for the estimation of the Moho interface for the area surrounding Greece ($19^\circ < \lambda < 27^\circ$, $34.5^\circ < \varphi < 42^\circ$), based on gravity measurements that were available over this area. Their computations provide a means of independent assessment for the Moho information given by CRUST 2.0 and the aforementioned Airy-based calculations. The original resolution of the available Moho depths based on the MSWD method for the area surrounding Greece stretching over the above geographical limitations was approximately $5' \times 5'$. In order to enable the comparisons between the different Moho databases for this region (CRUST 2.0, Airy and MSWD) we selected the resolution of the MSWD Moho dataset as our reference and densified the other two databases to this analysis. In this stage special care has been taken, so that no undesired numerical artifacts would enter into the data due to this upgrade. Thus, the resolution of the original database has been stepwise increased, by artificially assigning the original Moho values to a gradually increasing number

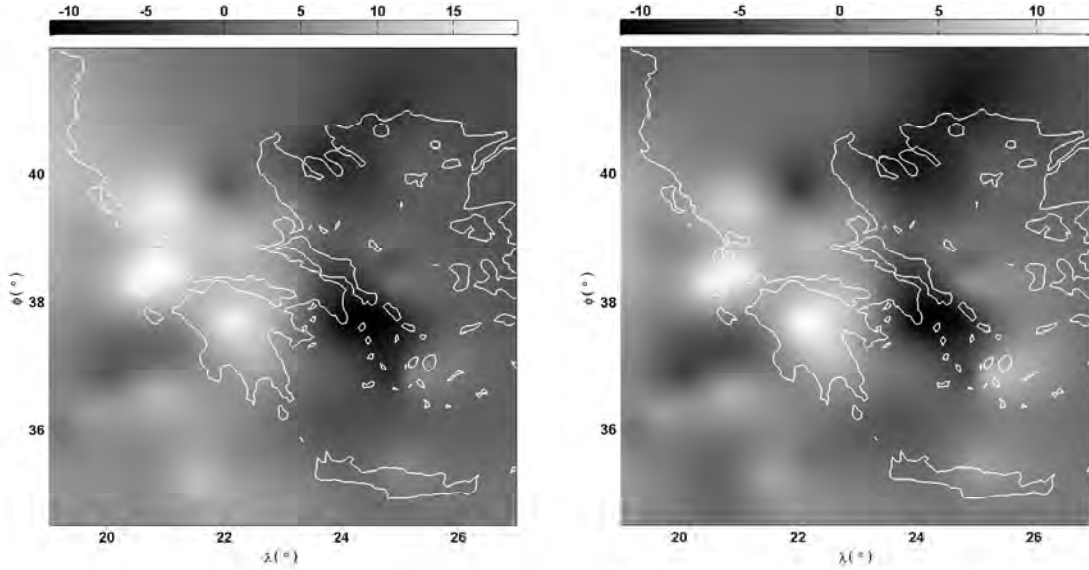


Fig. 2 Differences between estimated Moho depth values according to the MSWD-method and (a) computed Moho depths applying Airy hypothesis (left panel), (b) CRUST 2.0 Moho data (right panel). Unit is km.

Table 2: Available Moho data for the area surrounding Greece ($19^\circ < \lambda < 27^\circ$ and $34.5^\circ < \varphi < 42^\circ$) and their comparisons. Unit is km.

Data	Min	Max	Mean	SD
MSWD	-48.97	-18.16	-31.56	5.56
Airy	-34.32	-20.06	-28.33	3.33
CRUST 2.0	-42.31	-22.74	-31.74	4.15
MSWD - Airy	-11.35	19.15	3.23	5.17
MSWD - CRUST 2.0	-11.11	12.75	-0.19	3.69

of geographical sub-cells and by ultimately applying a biharmonic spline interpolation method in order to reach the desired resolution. This final step of the grid densification has been implemented through MATLAB's `griddata` command, using as option the method described in Sanwell (1987). Table 4 provides an overview of the available Moho data and Figure 2 presents the distribution of the obtained differences when comparing MSWD with Airy and CRUST 2.0 Moho depths. The Airy and CRUST 2.0 Moho values show in overall a poor agreement with the locally computed MSWD Moho depths. The computed differences between the two surfaces with respect to the MSWD estimated Moho interface obtain maximum values (in absolute sense) of 19.15 km and 12.75 km respectively. In overall, CRUST 2.0 database appears to perform better compared with the Airy-computed depths, although the numerical discrepancy with respect

to the MSWD values remains here significant as well. In order to quantify the effect of this geometrical variation (of the order of several kilometers) in the Moho interface between the different available procedures we proceed to the computation of the corresponding isostatic effects.

4 Isostatic effects on gravity

The utilization of the crustal layer geometry given by CRUST 2.0 for geodetic applications of local or regional scale involves an efficient means of modelling the respective disturbing masses. Common motivation for the analysis is the evaluation in terms of forward modelling techniques of the gravitational signal of the crustal mass distributions for selected computation points situated on or above the surface topography. The areas of application could include the computation of isostatic effects on gravity or the evalua-

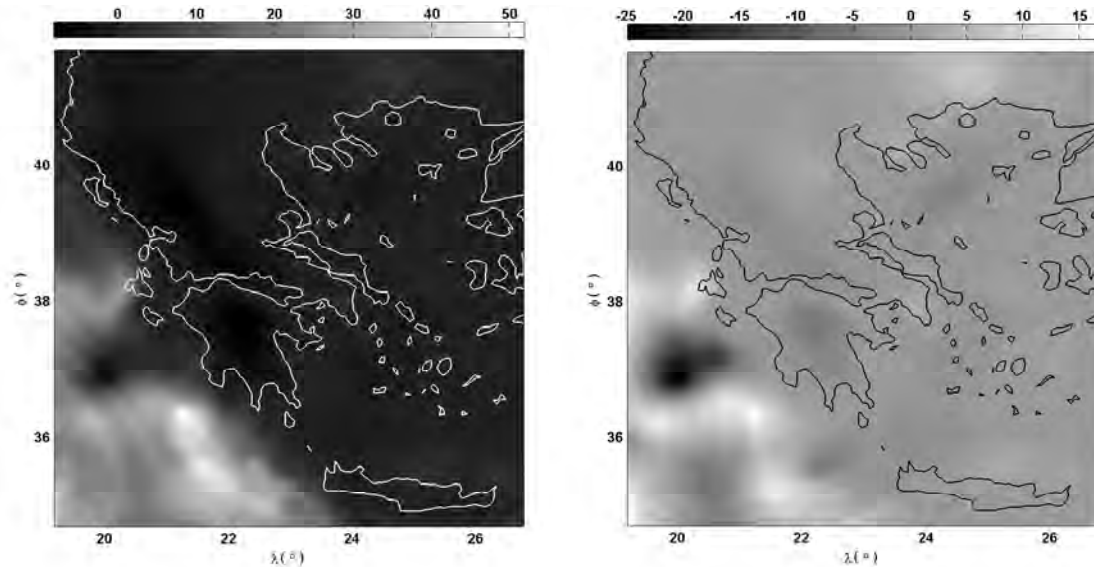


Fig. 3 Differences in isostatic effects on gravity between the MSWD estimated Moho surface and (a) the effects that are induced by a Moho interface according to Airy hypothesis (left panel), (b) isostatic effects obtained when using CRUST 2.0 Moho data (right panel). Values express differences in mGal.

Table 3: Isostatic effects on gravity induced from the different available Moho data for the area surrounding Greece ($19^\circ < \lambda < 27^\circ$ and $34.5^\circ < \varphi < 42^\circ$) and their comparisons. Unit is mGal.

Data	Min	Max	Mean	SD
MSWD (A)	-191.873	197.076	-17.55	74.011
Airy (B)	-145.119	194.219	-13.283	65.889
CRUST 2.0 (C)	-176.83	197.608	-17.056	73.308
(B) - (C)	-5.044	40.689	3.772	8.946
(B) - (A)	-8.102	51.801	4.266	10.38
(C) - (A)	-25.038	16.747	0.494	3.329

tion of second order derivatives. The former incorporates the information provided only by the last CRUST 2.0 layer while the computation of second order derivatives due to the mass distributions described by the database can refer to all the individual crustal layers and defines an application with special interest to assessment studies of GOCE gradiometry data. The question of modelling the given crustal distributions is similar to the problem of terrain modelling for surface gravity studies. An efficient way of performing this step could be by invoking the flexible general polyhedral modelling. If the topology information of the three dimensional mass distributions defined in a layer-wise manner by CRUST 2.0 is available, then the closed analytical expressions for the gravity field of a generally shaped polyhedron of constant density could be

applied to compute directly the distinct CRUST 2.0 layers induced gravity field signal (potential and derivatives up to second order). An intermediate computation step that is necessary for the correct application of the respective working formulae is the one transforming the original (ϕ, λ, h) CRUST 2.0 data to (x, y, z) values at an appropriately defined local coordinate system. Although all the aforementioned computations are straightforward they have proven to be tedious and time consuming in the implementation process. An alternative (and for the purposes of the present investigation equally efficient) modelling method would be by means of the rectangular prism. If the crustal masses defined through the two boundary surfaces, i.e. the surface topography and the Moho interface, are modelled through a finite decomposition into regular rect-

angular prisms, then the gravitational attraction of these masses at any given surface point can be computed by simply adding the individual contribution of each of these columns to the point in question, a quantity which will represent the vertical gradient of the gravitational potential of the specific prismatic body. Choosing a regular grid of computation points situated at the nodes of the respective surface terrain model we obtain these potential contributions for all points of the grid, forming thus a regular grid of isostatic effects on gravity, as the resulting potential quantities express exactly the attraction of the crustal masses to gravity measurements obtained at the surface.

Table 5 presents the results of the aforementioned computations carried out for the same area and for all available Moho data. Figure 3 displays the differences between the isostatic effects induced by the MSWD Moho surface and the Moho interfaces according to Airy and CRUST 2.0. As the upper boundary surface of the visible topography and bathymetry remained unchanged, the question was to what extent the observed discrepancies between the different estimated Moho structures would affect the isostatic contributions obtained at surface points. The presented calculations demonstrate that the respective differences are significant. In overall they fluctuate between several mGal, however they obtain differences of up to 50 mGal at the marine region across the Ionian trench.

5 Concluding remarks

The availability of global crustal databases enhances typical gravity field modelling studies in local and regional scales significantly. The present study demonstrated how one can combine the inherent information of CRUST 2.0 database with standard forward modelling tools and obtain a completely new source of information, that can be used both as an assessment tool for other available databases as well as an independent source for gravity field modelling and interpretation. The numerical handling of the different resolutions of the heterogeneous databases is one of the matters that has to be addressed further, as it represents the basic handicap of utilizing and merging present and future databases for the purposes of gravity field modelling.

Acknowledgements. Financial support from the Greek Ministry of Education under the O.P. Edu-

cation II program “Pythagoras II – Support to Research Teams in the Universities” is gratefully acknowledged.

References

- Bassin C, Laske G, Masters G (2000) The Current Limits of Resolution for Surface Wave Tomography in North America, *EOS Trans AGU*, 81, F897
- Danesi S, Morelli A (2001) Structure of the upper mantle under the Antarctic Plate from surface wave tomography, *Geophysical Research Letters*, 28 (23), 4395–4398
- Kahan MK, Schwintzer P, Reigber C (2004) A new isostatic model of the lithosphere and gravity field, *Journal of Geodesy*, 78 (6), 368–385
- Koulakov I, Sobolev SV (2006) A tomographic image of Indian lithosphere break-off beneath the Pamir-Hindukush region, *Geophysical Journal International*, 164 (2), 425–440
- Lambeck K (1988) *Geophysical geodesy; the slow deformations of the Earth*. Clarendon Press, Oxford
- Mooney WD, Laske G, Masters TG (1998) CRUST 5.1: A global crustal model at $5^\circ \times 5^\circ$, *Journal of Geophysical Research*, 103, 727–747
- National Geophysical Data Center (1988) ETOPO-5, bathymetry/topography data, Data Announc 88-MGG-02, National Oceanic and Atmospheric Administration, US Department of Commerce, Washington, DC
- Obayashi M, Suetsugu D, Fukao Y (2004) PP-P differential travelttime measurement with crustal correction, *Geophysical Journal International*, 157 (3), 1152–1162
- Sandwell DT (1987) Biharmonic Spline Interpolation of GEOS-3 and SEASAT Altimeter Data, *Geophysical Research Letters*, 2, 139–142
- Schmid C, van der Lee S, Giardini D (2004) Delay times and shear wave splitting in the Mediterranean region, *Geophysical Journal International*, 159 (1), 275–290
- Tsokas G, Hansen RO (1997) Study of the crustal thickness and the subducting lithosphere in Greece from gravity data, *Journal of Geophysical Research*, 102 (B9), 20,585–20,597
- Tsoulis D (2004) Spherical harmonic analysis of the CRUST 2.0 global crustal model, *Journal of Geodesy*, 78 (1/2), 7–11
- Vergos GS, Grigoriadis VN, Kalampoukas G, Tziavos IN (2005) Accuracy assessment of the SRTM 90m DTM over Greece and its implications to geoid modelling. Presented at the Dynamic Planet 2005 Symposium, Cairns, accepted for publication in the Proceedings

The utilization of global digital crustal databases in regional applications of forward gravity field modelling

D. Tsoulis, V.N. Grigoriadis, I.N. Tziavos

Department of Geodesy and Surveying, Aristotle University of Thessaloniki, Fax: +30 2310 995948, Email: tsoulis@topo.auth.gr

Abstract. The release of model CRUST 2.0 offers an advanced and efficient means of modelling crust-induced potential contributions both globally and regionally. Providing rigorous geometric as well as physical information concerning the structure and consistency of distinct crustal layers from the Earth's topography down to the crust-mantle boundary, the information contained in model CRUST 2.0 is of special interest to studies related to gravity field modelling and interpretation. The present paper investigates the possibilities of utilizing the CRUST 2.0 data in the frame of local and regional forward gravity field modelling applications. For this reason a thorough numerical analysis of the model has been carried out for the area surrounding Greece. In terms of geoid modelling and local gravity field investigations the CRUST 2.0 information can be used mainly in the frame of isostatic anomalies. Thus, isostatic effects on gravity have been computed for this region and are compared with the corresponding computations resulting from two other independent sources of determining the Moho interface, namely the Airy isostatic mechanism and the application of deconvolution methods to surface gravity data.

Keywords. global digital databases, forward modelling, CRUST 2.0, Moho interface

1 Introduction

The publication of CRUST 2.0, a global digital crustal database at a $2^\circ \times 2^\circ$ resolution (Bassin et al. 2000), produced a significant impulse over the last years to research activities related with the Earth's structure and gravity field. Among the topics that profited substantially from the release of the new crustal data were for example regional lithosphere investigations (Danesi and Morelli 2001, Schmid et al 2004, Koulakov and

Sobolev 2006), seismic studies (Obayashi et al 2004) or the derivation and analysis of isostatic Earth gravity models (Kaban et al 2004, Tsoulis 2004).

CRUST 2.0, which has been compiled and is now administered by the U.S. Geological Survey and the Institute for Geophysics and Planetary Physics at the University of California, is the descendant of CRUST 5.1, a global crustal model at $5^\circ \times 5^\circ$ (Mooney et al 1998). Both models are based on seismic refraction data published up to 1995 and a detailed compilation of ice and sediment thickness. CRUST 2.0 offers density, geometry and seismic information for a total of seven crustal layers, from ice and water to lower crust, the boundary surface between crust and mantle, otherwise known as the Mohorovicic discontinuity. The data consist of density values (the detailed density structure includes the additional layer of the uppermost mantle), layer boundary values in terms of depths with respect to mean sea level and values for compressional and shear wave velocities, all of which are given globally and explicitly for each of the 16200 grid elements that define each layer at the $2^\circ \times 2^\circ$ resolution. Thus, the model consists ultimately of a total of 29 matrices, each of dimensions 180×90 , where global bathymetry and surface topography data were adopted from the 5 arc minute resolution data set ETOPO-5 (NGDC, 1988).

The availability of recent Digital Terrain Models on the other hand, especially over continental areas, offers a new prospective of unprecedented resolution in calculations of local and regional gravity field modelling (Vergos et al 2005). In the frame of these new terrain data one could also incorporate the crustal information of databases, such as CRUST 2.0, and devise computational strategies where both of these data sources could be combined, for example for the computation of isostatic anomalies. The present paper investigates the possibilities of utilizing the CRUST

2.0 data to local or regional gravity field related computations. It turns out, that two are the key issues connected with the CRUST 2.0 database, that can be exploited for regional investigations. The geometry of the final crustal layer, which represents the Moho boundary over the specific region and will occupy the calculations presented in this paper and the detailed stratification of the database that could be employed in studies of gravity field interpretation.

2 Local assets of CRUST 2.0 database

The window selected for the local assessment of the CRUST 2.0 database was defined between $14^\circ < \lambda < 34^\circ$ and $28^\circ < \varphi < 48^\circ$, an area stretching over the southeast Mediterranean with Greece at its center. The area is characterized by the absence of hard sediments, thus a total of only four layers exist in the database for this region, namely soft sediments, upper, middle and lower crust. Table 1 presents the statistics regarding the layer depth information for the area under consideration. Examining the soft sediments layer we observe a direct correlation of the variations of the lower bound of this layer with the variations of the surface topography. The largest numerical values for the depths (3 – 5 km) occur, as one would expect, under the Mediterranean part of the region, while the smallest values are observed at the continental parts. The largest depth values of the next crustal layer (upper crust) are obtained over East Turkey (20 km), with large values of the order of 17 km occurring at the marine region south of Greece. The continental part of Greece exhibits smaller values for this layer of the order of 12 km with respect to marine areas. In overall larger numerical values for the depths of the upper crust layer occur at continental rather than marine regions. Moving towards the deeper crustal layers one begins to verify numerically the connection of the surface topography variations with the underlying crustal thickness according to the Airy/Heiskanen isostatic theory. Thus, in overall greater crustal depths are observed at continental regions compared to marine regions. The middle crust layer in particular shows a maximum depth value of 40 km at the eastern part of Turkey, with the minima appearing at the marine area stretching over the Ionian trench. The continental part of Greece

Table 1: Layer thickness information obtained from CRUST 2.0 for the test area. Unit is km.

Layer	Min	Max	Mean	SD
Soft Sediments	0.50	1.50	1.13	0.35
Upper Crust	1.70	20.00	9.70	4.01
Middle Crust	2.30	20.00	9.79	3.56
Lower Crust	2.50	13.50	8.74	2.50

has an almost constant depth value around 23 km. The overall variation of the boundary surface between middle and lower crust assimilates roughly with the basic scheme of mass compensation after Airy. Finally, the lower crust layer, which expresses also the Mohorovicic discontinuity, appears to have a mean value of 32.89 km for the whole test area. Especially over Greece, for which another independent dataset of Moho depths is available, the largest values are of the order of 40 km and occur underneath the continental part of the state, whereas the smallest Moho depths according to CRUST 2.0 appear again at the marine area of the Ionian trench.

The layer thickness information provides an additional source of information, which is mainly of interest to potential field determination studies. The information of Table 1 indicates the position of the density contrast between two subsequent layer. Table 2 on the other hand offers a measure of the quantity of the crustal masses defined by the respective layer. From the overall assessment of this information it follows that the values of the soft sediments thickness (0.5 – 1.5 km) are distributed uniformly over the test region, with small values appearing at continental regions and larger values at lower elevation areas or at sea. The thickness data for the rest of the crustal layers (upper, middle and lower crust) appear with similar characteristics. Thus, all layers show a variation in their vertical size that complies in general with the Airy/Heiskanen hypothesis. Smaller layer thickness values appear for all three crustal layers at marine regions, while larger values occur below continental parts. Furthermore, all three layers obtain mean thickness values of the order of 12 km over continental regions, while they all reveal the same mean of almost 7 km at marine areas.

Figure 1 presents the Moho data obtained from CRUST 2.0 for the area under consideration and their comparison with Airy-derived crustal

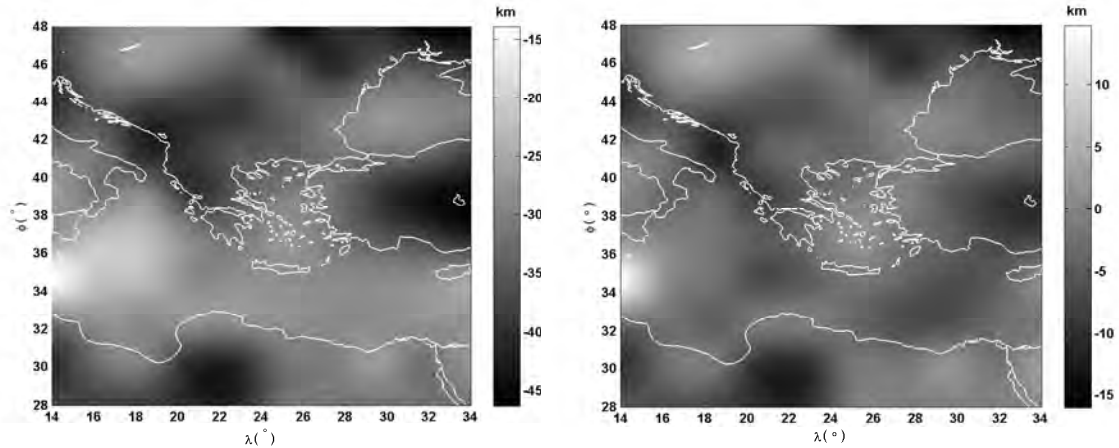


Fig. 1 Moho depth values with respect to mean sea level obtained from CRUST 2.0 database (left panel) and differences with respect to Airy-derived Moho depths for the same region (right panel). Unit is km.

thickness T , according to the standard scheme $T_{land} = D + t$ and $T_{sea} = D - t'$ defined respectively below continental and marine regions. In the frame of the Airy hypothesis the root and anti-root quantities are calculated according to the expressions $t = (\rho_{crust}/(\rho_m - \rho_{crust}))h$ and $t' = ((\rho_{crust} - \rho_w)/(\rho_m - \rho_{crust}))h'$ respectively (Lambeck 1988). These quantities express some crude estimates of the mean crustal, mantle and water density, for which the numerical values $\rho_{crust} = 2.67 \text{ g cm}^{-3}$, $\rho_m = 3.27 \text{ g cm}^{-3}$ and $\rho_w = 1.03 \text{ g cm}^{-3}$ where used here, h and h' denote the height of the topography and the depth of the bathymetry in absolute values with respect to mean sea level and D describes the depth where the actual compensation takes place, taken here equal to 30 km. The discrepancies between the CRUST 2.0 provided Moho information with the theoretically derived Moho structure after Airy are significant for the test area, having a mean value of about 4 km and a standard deviation of roughly 3 km, these values expressing the discrepancies between the two sets in absolute sense. The larger differences (maximum: 16.02 km) are located at the areas with the large Moho depths according to the CRUST 2.0 values. The right panel of Figure 1 indicates in more detail the relative relation between the two databases, as negative values express regions where the CRUST 2.0 data represent larger Moho estimations than the theoretical Airy values and vice-versa for the regions where positive differences are reported. The overall performance is fairly poor and indicates a large discrepancy between the two datasets, which could

only be properly assessed if a further independent Moho information for the same area was utilized.

3 Assessment of Moho information

Among the different interface estimation methods that exist in the literature, deconvolution methods appear to be of special interest when local surface gravity data are available. Tsokas and Hansen (1997) applied such an analytical signal analysis technique (Multiple Source Werner Deconvolution, MSWD) for the estimation of the Moho interface for the area surrounding Greece ($19^\circ < \lambda < 27^\circ$, $34.5^\circ < \varphi < 42^\circ$), based on gravity measurements that were available over this area. Their computations provide a means of independent assessment for the Moho information given by CRUST 2.0 and the aforementioned Airy-based calculations. The original resolution of the available Moho depths based on the MSWD method for the area surrounding Greece stretching over the above geographical limitations was approximately $5' \times 5'$. In order to enable the comparisons between the different Moho databases for this region (CRUST 2.0, Airy and MSWD) we selected the resolution of the MSWD Moho dataset as our reference and densified the other two databases to this analysis. In this stage special care has been taken, so that no undesired numerical artifacts would enter into the data due to this upgrade. Thus, the resolution of the original database has been stepwise increased, by artificially assigning the original Moho values to a gradually increasing number

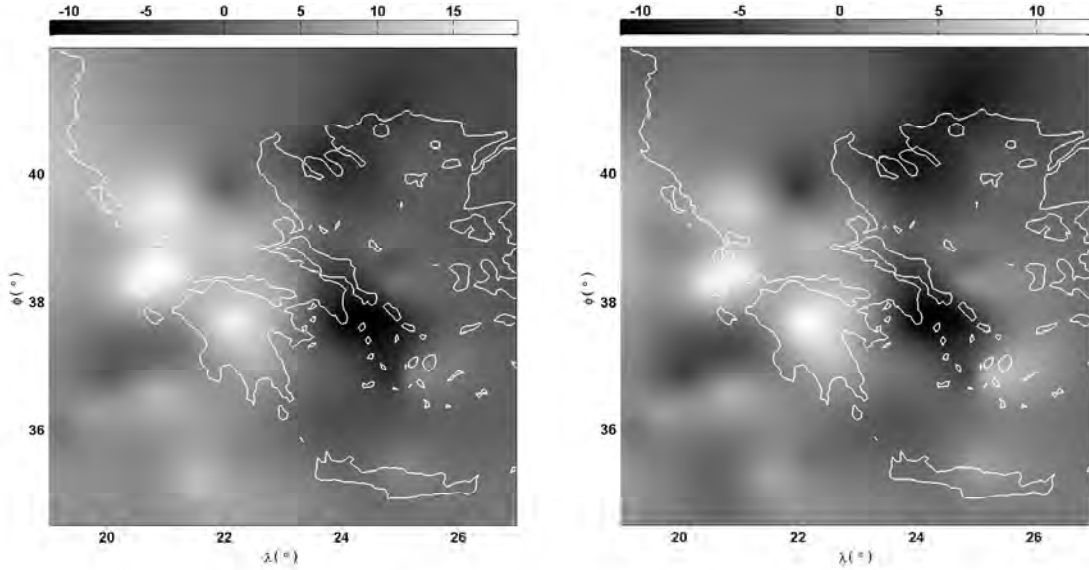


Fig. 2 Differences between estimated Moho depth values according to the MSWD-method and (a) computed Moho depths applying Airy hypothesis (left panel), (b) CRUST 2.0 Moho data (right panel). Unit is km.

Table 2: Available Moho data for the area surrounding Greece ($19^\circ < \lambda < 27^\circ$ and $34.5^\circ < \varphi < 42^\circ$) and their comparisons. Unit is km.

Data	Min	Max	Mean	SD
MSWD	-48.97	-18.16	-31.56	5.56
Airy	-34.32	-20.06	-28.33	3.33
CRUST 2.0	-42.31	-22.74	-31.74	4.15
MSWD - Airy	-11.35	19.15	3.23	5.17
MSWD - CRUST 2.0	-11.11	12.75	-0.19	3.69

of geographical sub-cells and by ultimately applying a biharmonic spline interpolation method in order to reach the desired resolution. This final step of the grid densification has been implemented through MATLAB's `griddata` command, using as option the method described in Sanwell (1987). Table 4 provides an overview of the available Moho data and Figure 2 presents the distribution of the obtained differences when comparing MSWD with Airy and CRUST 2.0 Moho depths. The Airy and CRUST 2.0 Moho values show in overall a poor agreement with the locally computed MSWD Moho depths. The computed differences between the two surfaces with respect to the MSWD estimated Moho interface obtain maximum values (in absolute sense) of 19.15 km and 12.75 km respectively. In overall, CRUST 2.0 database appears to perform better compared with the Airy-computed depths, although the numerical discrepancy with respect

to the MSWD values remains here significant as well. In order to quantify the effect of this geometrical variation (of the order of several kilometers) in the Moho interface between the different available procedures we proceed to the computation of the corresponding isostatic effects.

4 Isostatic effects on gravity

The utilization of the crustal layer geometry given by CRUST 2.0 for geodetic applications of local or regional scale involves an efficient means of modelling the respective disturbing masses. Common motivation for the analysis is the evaluation in terms of forward modelling techniques of the gravitational signal of the crustal mass distributions for selected computation points situated on or above the surface topography. The areas of application could include the computation of isostatic effects on gravity or the evalua-

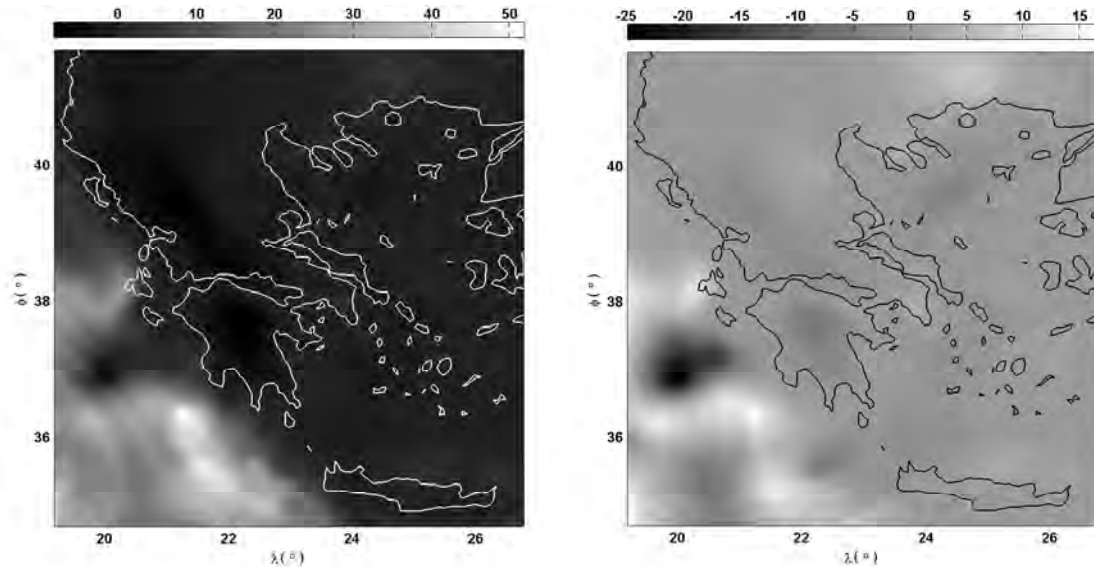


Fig. 3 Differences in isostatic effects on gravity between the MSWD estimated Moho surface and (a) the effects that are induced by a Moho interface according to Airy hypothesis (left panel), (b) isostatic effects obtained when using CRUST 2.0 Moho data (right panel). Values express differences in mGal.

Table 3: Isostatic effects on gravity induced from the different available Moho data for the area surrounding Greece ($19^\circ < \lambda < 27^\circ$ and $34.5^\circ < \varphi < 42^\circ$) and their comparisons. Unit is mGal.

Data	Min	Max	Mean	SD
MSWD (A)	-191.873	197.076	-17.55	74.011
Airy (B)	-145.119	194.219	-13.283	65.889
CRUST 2.0 (C)	-176.83	197.608	-17.056	73.308
(B) - (C)	-5.044	40.689	3.772	8.946
(B) - (A)	-8.102	51.801	4.266	10.38
(C) - (A)	-25.038	16.747	0.494	3.329

tion of second order derivatives. The former incorporates the information provided only by the last CRUST 2.0 layer while the computation of second order derivatives due to the mass distributions described by the database can refer to all the individual crustal layers and defines an application with special interest to assessment studies of GOCE gradiometry data. The question of modelling the given crustal distributions is similar to the problem of terrain modelling for surface gravity studies. An efficient way of performing this step could be by invoking the flexible general polyhedral modelling. If the topology information of the three dimensional mass distributions defined in a layer-wise manner by CRUST 2.0 is available, then the closed analytical expressions for the gravity field of a generally shaped polyhedron of constant density could be

applied to compute directly the distinct CRUST 2.0 layers induced gravity field signal (potential and derivatives up to second order). An intermediate computation step that is necessary for the correct application of the respective working formulae is the one transforming the original (ϕ, λ, h) CRUST 2.0 data to (x, y, z) values at an appropriately defined local coordinate system. Although all the aforementioned computations are straightforward they have proven to be tedious and time consuming in the implementation process. An alternative (and for the purposes of the present investigation equally efficient) modelling method would be by means of the rectangular prism. If the crustal masses defined through the two boundary surfaces, i.e. the surface topography and the Moho interface, are modelled through a finite decomposition into regular rect-

angular prisms, then the gravitational attraction of these masses at any given surface point can be computed by simply adding the individual contribution of each of these columns to the point in question, a quantity which will represent the vertical gradient of the gravitational potential of the specific prismatic body. Choosing a regular grid of computation points situated at the nodes of the respective surface terrain model we obtain these potential contributions for all points of the grid, forming thus a regular grid of isostatic effects on gravity, as the resulting potential quantities express exactly the attraction of the crustal masses to gravity measurements obtained at the surface.

Table 5 presents the results of the aforementioned computations carried out for the same area and for all available Moho data. Figure 3 displays the differences between the isostatic effects induced by the MSWD Moho surface and the Moho interfaces according to Airy and CRUST 2.0. As the upper boundary surface of the visible topography and bathymetry remained unchanged, the question was to what extent the observed discrepancies between the different estimated Moho structures would affect the isostatic contributions obtained at surface points. The presented calculations demonstrate that the respective differences are significant. In overall they fluctuate between several mGal, however they obtain differences of up to 50 mGal at the marine region across the Ionian trench.

5 Concluding remarks

The availability of global crustal databases enhances typical gravity field modelling studies in local and regional scales significantly. The present study demonstrated how one can combine the inherent information of CRUST 2.0 database with standard forward modelling tools and obtain a completely new source of information, that can be used both as an assessment tool for other available databases as well as an independent source for gravity field modelling and interpretation. The numerical handling of the different resolutions of the heterogeneous databases is one of the matters that has to be addressed further, as it represents the basic handicap of utilizing and merging present and future databases for the purposes of gravity field modelling.

Acknowledgements. Financial support from the Greek Ministry of Education under the O.P. Edu-

cation II program “Pythagoras II – Support to Research Teams in the Universities” is gratefully acknowledged.

References

- Bassin C, Laske G, Masters G (2000) The Current Limits of Resolution for Surface Wave Tomography in North America, *EOS Trans AGU*, 81, F897
- Danesi S, Morelli A (2001) Structure of the upper mantle under the Antarctic Plate from surface wave tomography, *Geophysical Research Letters*, 28 (23), 4395–4398
- Kahan MK, Schwintzer P, Reigber C (2004) A new isostatic model of the lithosphere and gravity field, *Journal of Geodesy*, 78 (6), 368–385
- Koulakov I, Sobolev SV (2006) A tomographic image of Indian lithosphere break-off beneath the Pamir-Hindukush region, *Geophysical Journal International*, 164 (2), 425–440
- Lambeck K (1988) *Geophysical geodesy; the slow deformations of the Earth*. Clarendon Press, Oxford
- Mooney WD, Laske G, Masters TG (1998) CRUST 5.1: A global crustal model at $5^\circ \times 5^\circ$, *Journal of Geophysical Research*, 103, 727–747
- National Geophysical Data Center (1988) ETOPO-5, bathymetry/topography data, Data Announc 88-MGG-02, National Oceanic and Atmospheric Administration, US Department of Commerce, Washington, DC
- Obayashi M, Suetsugu D, Fukao Y (2004) PP-P differential traveltimes measurement with crustal correction, *Geophysical Journal International*, 157 (3), 1152–1162
- Sandwell DT (1987) Biharmonic Spline Interpolation of GEOS-3 and SEASAT Altimeter Data, *Geophysical Research Letters*, 2, 139–142
- Schmid C, van der Lee S, Giardini D (2004) Delay times and shear wave splitting in the Mediterranean region, *Geophysical Journal International*, 159 (1), 275–290
- Tsokas G, Hansen RO (1997) Study of the crustal thickness and the subducting lithosphere in Greece from gravity data, *Journal of Geophysical Research*, 102 (B9), 20,585–20,597
- Tsoulis D (2004) Spherical harmonic analysis of the CRUST 2.0 global crustal model, *Journal of Geodesy*, 78 (1/2), 7–11
- Vergos GS, Grigoriadis VN, Kalampoukas G, Tziavos IN (2005) Accuracy assessment of the SRTM 90m DTM over Greece and its implications to geoid modelling. Presented at the Dynamic Planet 2005 Symposium, Cairns, accepted for publication in the Proceedings

Recent developments in synthetic Earth gravity models in view of the availability of digital terrain and crustal databases of global coverage and increased resolution

D. Tsoulis¹, M. Kuhn²

1. Department of Geodesy and Surveying, Aristotle University of Thessaloniki, Fax: +30 2310 995948, Email: tsoulis@topo.auth.gr

2. Western Australia Centre for Geodesy, Curtin University of Technology, Perth, WA 6845, Australia

Abstract. The basic idea of a synthetic or simulated Earth gravity model (SEGM) is to validate theories and algorithms used in gravity field modelling. However, if a SEGM represents the Earth's gravity field reasonably well it can also be used to identify and interpret local, regional and global interactions between the Earth's interior and its gravity field. This paper presents an overview of the most recent developments in the construction of SEGMs and their possible use in gravity field recovery including the use of forward gravity field modelling techniques and the application of topographic/isostatic compensation models. Characteristic results of recent global as well as regional computations over Australia are included.

Keywords. Synthetic earth gravity models, forward modelling, global digital databases, topographic/isostatic models

1 Introduction

The construction of SEGMs is gaining more and more interest in the geodetic research community. This is partly due to the availability of new satellite only gravity models (e.g. from CHAMP, GRACE and in future GOCE). While most current studies on the Earth's gravity field and its temporal variation focus on the results of the new geodetic satellite missions CHAMP, GRACE and in future GOCE, the full potential of these missions can only be obtained through a combination with information on the Earth's geophysical properties and their change with time. The latter can be obtained from different databases with ever increasing resolution, such as the current release of SRTM-derived terrain models. This permits the construction of synthetic models that

can record, identify and interpret interactions between the Earth's geophysical properties and the gravity field observed in the high-frequency spectrum.

To some extent the availability of an increasing number of databases has also provoked recent research activities in this area. For example new high-resolution databases available allow the inclusion of higher frequency information obtained by the application of different forward modelling techniques. More recent contributions on this field of research include the so-called source and effect modeling technique (Kuhn and Featherstone 2003, 2005; Baran et al. 2006), the so-called direct integration and spherical harmonic approaches (Kuhn and Featherstone 2005), or the analytical approaches in geopotential modeling (Petrovskaya et al. 2001). The analysis of the structure and the variable density information of a distinct number of crustal layers, which is provided by global crustal models such as CRUST 2.0 (Bassin et al. 2000; Mooney et al. 1998), leads on the other hand to the computation of so-called topographic/isostatic Earth gravity models, utilizing forward gravity field modelling techniques as well (see e.g. Tsoulis 2004).

2 Topographic/isostatic Earth gravity models

A significant contribution in the construction of synthetic Earth gravity models is expressed by the analysis and interpretation of available global topographic/isostatic gravity models, which can be obtained from the straightforward analysis of a global terrain database, applying some theory of isostatic compensation of the crustal masses over the denser underlying mantle. This analysis leads to the computation of gravity models which reflect the gravity signal information con-

tent present in the topographic masses (i.e. the high frequency part of the geopotential). The application of denser topographic data in a global sense, has lead recently to the derivation of such topographic/isostatic models (t/i in the sequel) of very high maximum degree and order (see e.g. Tsoulis 2005). This permits the correlation of such a model with the local high frequency gravity field characteristics, which may be primarily modelled using the detailed terrain and crustal information provided for a restricted study area by the aforementioned databases.

The fundamental parameter that underlines the evaluation of a topographic/isostatic model is the spatial resolution of the respective terrain or crustal database. The denser a global digital terrain or crustal database is, the higher the maximum degree and order of the computed t/i gravity model will be. Thus, the analysis of global crustal database CRUST 2.0, which is defined on a $2^\circ \times 2^\circ$ global resolution produces a t/i gravity model that is restricted only up to degree and order 90 (Tsoulis 2004), whereas the utilization of denser global terrain models, such as ETOPO5, and the application of standard Airy and Pratt isostatic theories leads to the computation of respective t/i models up to degree 1082 (Tsoulis, 2005). The most recent t/i gravity model is available up to degree 2160 (Pavlis et al. 2005) and is based on the analysis of the global digital terrain model DTM2002, a global DTM provided in a 2' and a 5' global resolution.

Neglecting here the theoretical background of t/i model computation, which can be found in Claessens (2003), we focus on the spectral assessment of the available t/i models with respect to the combined reference gravity model EGM96 (Lemoine et al. 1998). From the different means of numerical evaluation of some available sets of potential coefficients, we compute here four distinct quantities, namely (a) the RMS geoid undulation difference by degree and (b) the RMS gravity anomaly difference by degree, which provide a measure of a direct comparison between two different models expressed in geoid height (length) and gravity anomalies (mGal) respectively and (c) the correlation by degree and (d) smoothing by degree, which offer a means of direct spectral comparison between two arbitrary models.

Figures 1 to 4 depict the RMS geoid height and gravity anomaly difference curves of three different t/i models, the uncompensated topog-

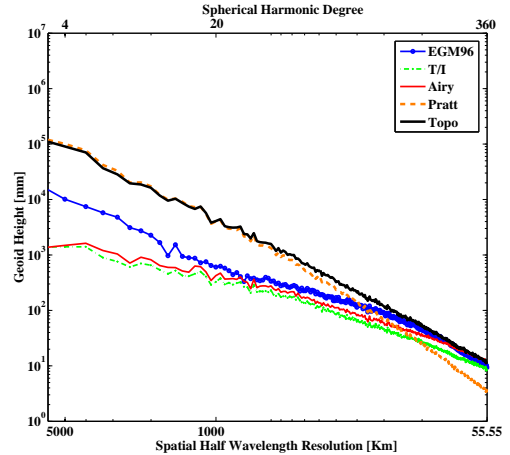


Fig. 1 RMS geoid height difference by degree up to degree 360 including EGM96. Unit is mm.

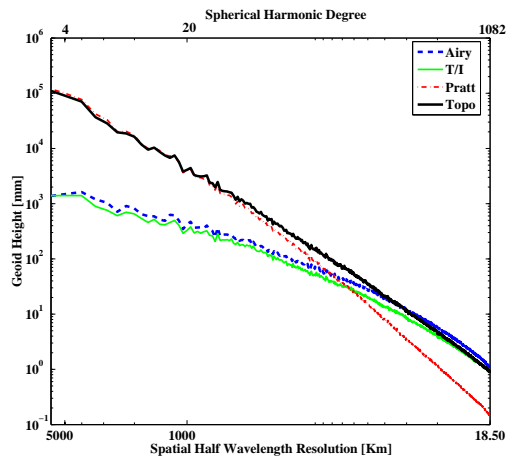


Fig. 2 RMS geoid height difference by degree up to degree 1082. Unit is mm.

raphy and EGM96. Models 'Airy' and 'Pratt' are obtained from the analysis of ETOPO5 data and are available up to degree 1082, while model 'T/I' expresses the t/i model obtained by Pavlis et al. (2005) up to degree and order 2160. Figures 1 and 3 are of course truncated up to degree 360 in order to provide a direct comparison to EGM96, while Figures 2 and 4 present the whole common range of the available coefficients, i.e. up to degree 1082. The figures' axes also indicate the respective spatial resolution, which is helpful for the interpretation of the presented information. An interesting remark from these computations can be made regarding the Pratt-based t/i model. Thus, while all t/i models, includ-

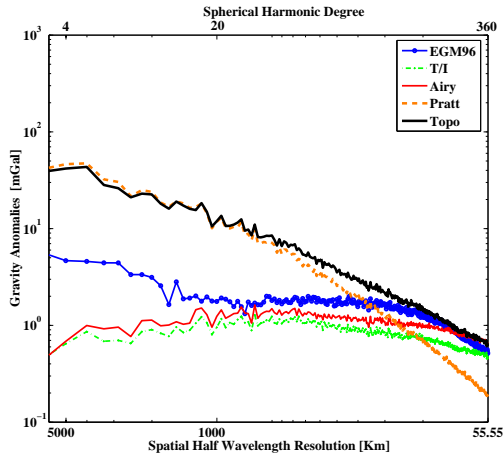


Fig. 3 RMS gravity anomaly difference by degree up to degree 360 including EGM96. Unit is mGal.

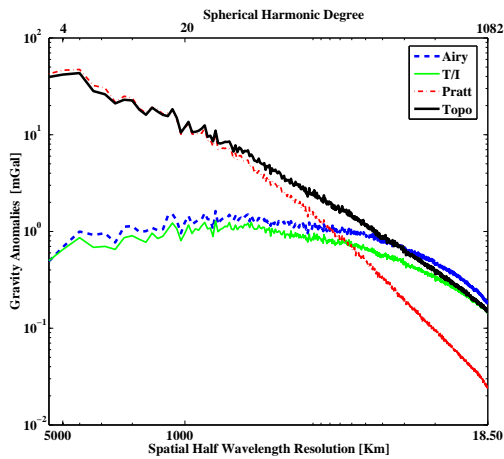


Fig. 4 RMS gravity anomaly difference by degree up to degree 1082. Unit is mGal.

ing EGM96, tend to converge to the power of the uncompensated topography, after a significant 'compensation' in the power spectrum over the lower to medium degree range is performed, the Pratt model, begins to contribute isostatically to the observed gravity signal only for the high and very high frequencies, performing at the same time badly for the low and medium wavelengths. A similar observation concerning the high frequencies can be made for the Airy model as well (this almost coincides with the T/I model over the available common degree range where also Airy is applied, the small discrepancies expressing merely the different DTM data), which exhibits a notable reduction to the uncompen-

sated topography spectrum at least up to degree 360.

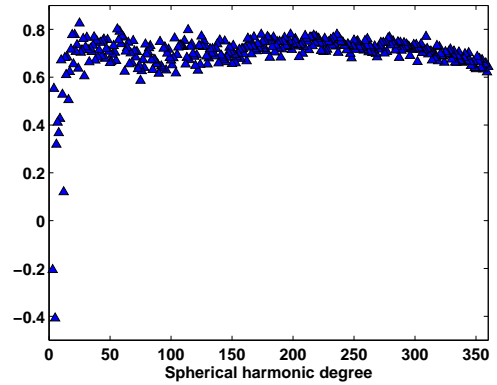


Fig. 5 Correlation by degree between EGM96 and truncated T/I model up to degree 360.

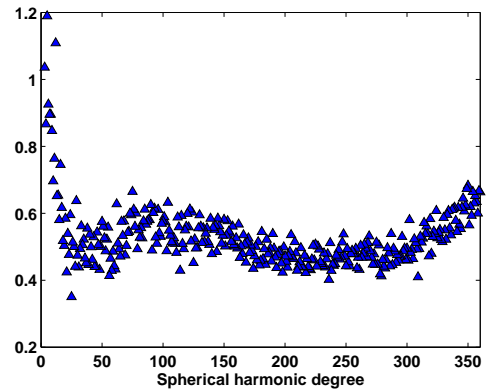


Fig. 6 Smoothing by degree of T/I model (truncated up to degree 360) with respect to EGM96.

Figures 5 and 6 present the correlation and smoothing coefficients per degree of truncated model T/I with respect to EGM96. Although a detailed analysis of all individual t/i models has been carried out, these representative results manifest the overall spectral content of the computed t/i coefficients. It becomes evident that the two coefficient sets are characterized by a relative high degree of correlation (of the order of 70%), which by itself cannot imply an agreement or disagreement of the two sets, as they may also differ by a scale factor. The computation of the degree of smoothing, which we obtain if we subtract one model from the other, is a more interesting assessment measure of the t/i model. As

Figure 6 indicates there exists a rough agreement between the two models. The non-linear trend of the smoothing coefficient per degree, leaves however no space for the formulation of an apparent coincidence of the two models. On the contrary, the apparent discrepancies between them indicate the differences in the respective spectral information.

3 Synthetic Earth gravity models

In this section the construction and results of two different SEGMs, which have been proposed recently, are outlined. A global forward gravity model (e.g. Kuhn and Featherstone 2005) and a regional model over Australia (e.g. Baran et al. 2006). Both models are good examples on what can be achieved in the construction of SEGMs with currently available databases.

3.1 A Global Forward Gravity Model

A global gravity model based solely on forward gravity modelling has been constructed at the Western Australian Centre for Geodesy (WACG) at Curtin University of Technology (Kuhn and Featherstone 2005). The gravity field of Curtin Synthetic Earth Gravity Model (CurtinSEGM) is based on mass-density information of topography, bathymetry, crust and mantle. Both topography and bathymetry are taken from the global $5' \times 5'$ Digital Elevation Model (DEM) JGP95E (Lemoine et al. 1998) expressed here in terms of equivalent rock heights. The use of equivalent rock heights allows for simple modelling of different terrain types but changes the geometry of the mass distribution if the mass-density is largely different from the adopted constant density value (here $\rho = 2,670 \text{ kg/m}^3$). Information on the Earth's crust are taken from the global $2^\circ \times 2^\circ$ CRUST2.0 model describing the crust by five different layers with bottom of the lowest layer representing the Moho-discontinuity. Density heterogeneities throughout the whole mantle (between 25 km and 2891 km depth) have been derived from the 3-D seismic shear-wave velocity heterogeneity model S12WM13 (Su et al. 1994), which is expanded to spherical harmonic degree and order 12 and to order 13 in Chebyshev polynomials to describe the horizontal and vertical variations, respectively. The outer and inner core are assumed to be composed of homogeneous spherical mass layers with a total mass chosen in the way that CurtinSEGM conserves the total

mass of the Earth (here $M = 5.973710^{24} \text{ kg}$).

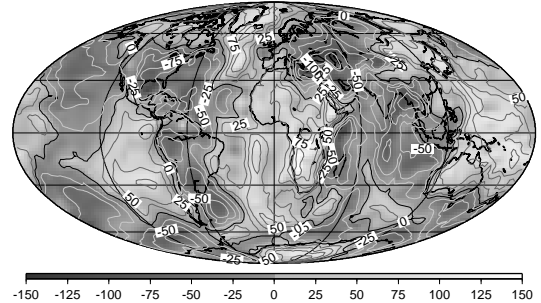


Fig. 7 CurtinSEGM: Combined effect in terms of geoid height of all mass-density anomalies. Contour interval: 25 m, Min.: -133.8 m, Max.: +141.4 m

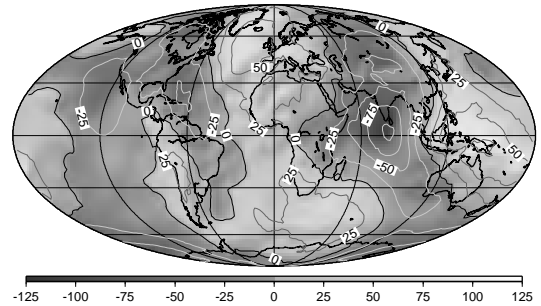


Fig. 8 EGM96: Geoid height used here as reference for the observed gravity field. Contour interval: 25 m, Min.: -105.8 m, Max.: +85.2 m

Based on the given mass distributions only mass-anomalies taken with respect to a reference density model have been considered here, which compose the anomalous gravity field. The reference density model assumes a constant mass-density of $2,670 \text{ kg/m}^3$ and $2,861 \text{ kg/m}^3$ for the topography (masses above the geoid) and crust (masses between Moho and geoid) respectively. Below the Moho-Discontinuity the density distribution given by the preliminary reference Earth model (PREM, Dziewonski and Anderson 1981) has been adopted.

All mass-density anomalies have been converted into potential anomalies using Newton's integral expressed in spherical harmonics, where the regarded mass-density anomalies have been expressed by the spherical harmonic coefficients of surface density functions (Kuhn and Featherstone 2004). In this approach a set of Love-numbers (constant with a specific mass layer) has been introduced so that CurtinSEGM has

similar amplitudes than EGM96 (see Kuhn and Featherstone 2005 for more details).

The spatial pattern of the CurtinSEGM geoid height is displayed in Figure 7. Comparison with the geoid height obtained by EGM96 (Figure 8) shows that it reproduces the general features of the observed gravity field. All major geoid highs and lows are clearly identified. Therefore, CurtinSEGM is suited for studies of the global Earth gravity models. Most of the considerable large differences (in some places about the same order of magnitude than the signal itself) can be associated with geophysical active zones where modelling becomes difficult. Furthermore, remaining differences can be (loosely) associated to a spectral range of degree 7 to 100, presumably caused by mantle mass anomalies situated in the depth range 1,000 km to 60 km.

3.2 A Regional SEGM over Australia

Also at the WACG a high-resolution $1' \times 1'$ regional source/effects SEGM over the Australian continent has been constructed (Australian Synthetic Earth Gravity Model, AusSEGM) for validating regional gravimetric geoid determination theories, techniques and computer software (Baran et al. 2006). AusSEGM provides synthetic [simulated] gravity field functionals (gravity, gravity anomaly and geoid height) on a regular $1' \times 1'$ as well as arbitrary points with similar distribution as observed gravity points (e.g. in valleys rather than on mountain tops).

The long-wavelength effect part (up to and including spherical harmonic degree and order 360) is taken from an assumed errorless EGM96 global geopotential model. The latter is a reasonable assumption in the context of the construction of a SEGM and ensures it replicates reasonably well the actual Earth's gravity field. Here EGM96 has been evaluated to obtain gravity values on the (synthetic) Earth's surface and geoid heights. A high-resolution ($3'' \times 3''$) synthetic digital elevation model (SEDM), which is essentially a fractal surface based on the GLOBE v1 DEM (Hastings and Dunbar 1998) has been constructed over Australia in order to model the short-wavelength source part of AusSEGM. Furthermore, the global topography outside Australia has been taken from JGP95E. Numerical (discretised) Newton integration based on spherical volume elements (tesseroids) approximated by mass-equal prisms (e.g. Kuhn 2003) has been used to evaluate the effect on gravity and geoid

height (gravitational potential divided by gravity) from the high-resolution topography. These effects have been developed in spherical harmonics so to remove any long-wavelength constituent present but already included by that obtained from EGM96, thus has to be removed from the source part to include solely spectral constituents beyond degree and order 360.

Both long- and short wavelength parts form the final gravity and geoid height values of AusSEGM. Therefore, their spatial structure is similar to EGM96 with additional high-frequency constituents. This can be seen in the final geoid height illustrated in Figure 9 demonstrating the general trend from south-west to north-east with high frequency information e.g. in the region of the highest elevation (south-east). Amazingly a comparison of AusSEGM gravity values with about 300,000 measured gravity values over Australia shows a very good agreement with most (99.3 % of all values) of differences below 20 mGal and no evident systematic effect visible (see Figure 10 in Baran et al. 2006). Furthermore, the behavior of the spectral power of the geoid heights (degree variances) does not show any major discontinuity (it is rather seamless) between the long- and short-wavelength contribution at spherical harmonic degree 360 (see Figure 10). Therefore, despite being a synthetic model AusSEGM reproduces the Earth's gravity field rather realistically. This leads to the conclusion that AusSEGM can also be used for the interpretation of the gravity field over Australia e.g. providing evidence of distortions present in the Australian Height Datum.

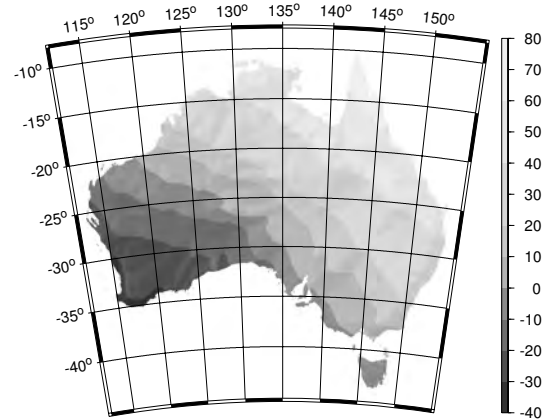


Fig. 9 Geoid height over Australia obtained from AusSEGM. Min.: -34.9 m, Max.: +72.0 m

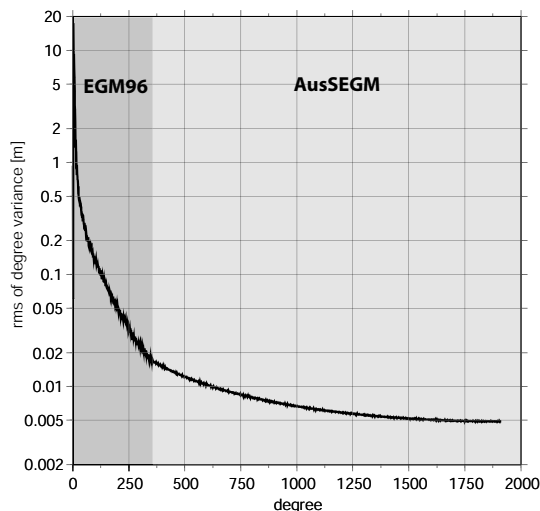


Fig. 10 Comparison of the AusSEGM gravity values with 333,929 measured gravity values over Australia. Min.: -244.2 mGal, Max.: +70.4 mGal, Mean: -1.0 mGal, Stdv.: 12.0 mGal.

4 Concluding remarks

The increased resolution of currently available digital terrain and crustal databases, enables the investigation of the high and very high frequency part of the observed geopotential spectrum. Although at the time being the crustal structure is given globally at a fairly rough analysis, the very dense resolution of satellite-based terrain models over continental parts of the globe is expected to play a very crucial role in the development of future Synthetic Earth Gravity Models and assist the interpretation of the gravity field in local and regional scales.

Acknowledgements. Michael Kuhn would like to acknowledge funds to this research partly by the Australian Research Council (ARC) through Discovery Project DP0345583 (awarded to M Kuhn, WE Featherstone and W Keller) and Large Grant A00001127 (awarded to WE Featherstone and P Vanicek).

References

- Baran I, Kuhn M, Claessens SJ, Featherstone WE, Holmes SA, Vanicek P (2006) A synthetic Earth gravity model designed specifically for testing regional gravimetric geoid determination algorithms, *J Geod*, 80:1–16
- Bassin C, Laske G, Masters G (2000) The Current Limits of Resolution for Surface Wave Tomography in North America, *EOS Trans AGU*, 81, F897
- Claessens SJ (2003) A Synthetic Earth Model; analysis, implementation, validation and application. Delft University Press, Delft, 61 pp
- Dziewonski AM, Anderson (1981) Preliminary reference Earth model. *Phys Earth Planetary Inter* 25(4):297-356
- Hastings DA, Dunbar PK (1998) Development and assessment of the global land one-km base elevation digital model (GLOBE). *ISPRS Arch* 32(4):218-221.
- Kuhn M (2003) Geoid determination with density hypothesis from isostatic models and geological information. *J Geod* 77(1-2):50-65.
- Kuhn M, Featherstone WE (2003) On the construction of a Synthetic Earth Gravity Model (SEGM), In: Tziavos, IN (ed.) Gravity and Geoid 2002, Proc. 3rd Meeting of the Int. Gravity and Geoid Commission, Thessaloniki, Greece, pp. 189–194
- Kuhn M, Featherstone WE (2005) Construction of a synthetic Earth gravity model by forward gravity modelling. In: Sansò, F (ed.) A Window on the Future of Geodesy, IAG Symposia, Vol. 128, pp. 350–355
- Lemoine FG and 14 other authors (1998) The Development of the Joint NASA GSFC and the National Imaginery and Mapping Agency (NIMA) Geopotential Model EGM96. NASA/TP-1998-206861, Goddard Space Flight Center, Maryland
- Mooney WD, Laske G, Masters TG (1998) CRUST 5.1: A global crustal model at $5^\circ \times 5^\circ$, *J Geophys Res*, 103:727–747
- Petrovskaya MS, Vershkov AN, Pavlis NK (2001) New analytical and numerical approaches for geopotential modeling, *J Geod*, 74:661–672
- Pavlis NK, Holmes SA, Kenyon SC, Schmidt D, Trimmer R (2005) A preliminary gravitational model to degree 2160, In: Jekeli, C, Bastos, L, Fernandes, J (eds.) Gravity, Geoid and Space Missions, IAG Symposia, Vol. 129, pp. 18–23
- Sue W-J, Woodward RL, Dziewonski AM (1994) Degree 12 model of shear velocity heterogeneity in the mantle. *J Geophys Res* 99(B4):6945–6980
- Tsoulis D (2004) Spherical harmonic analysis of the CRUST 2.0 global crustal model, *J Geod*, 78(1/2):7–11
- Tsoulis D (2005) The derivation and analysis of topographic/isostatic gravity models up to degree and order 1082, *Bollettino di Geodesia e Scienze Affini*, No 4, 211–225

Simultaneous Determination of Terrain Correction and Local Average Topographic Density

Gábor Papp

Geodetic and Geophysical Research Institute of the Hungarian Academy of Sciences, H-9401 Sopron, POB 5, Hungary

Abstract Nettleton's method is based on the elevation dependence of the surface free-air gravity anomalies and widely used to obtain an optimal average density value by applying e.g. L2 norm model inversion. Its accuracy, however, strongly depends on how efficiently the regional trends and very local (terrain) effects are removed from the gravity anomalies processed. If the geometry of the topography is fixed then the terrain correction term at the evaluation point P is a linear function of the unknown average topographical density. Therefore it can also be included in the equation system to be solved by inversion and an estimation of the density can be obtained in one step, without iteration. The results of this simple refinement of Nettleton's method as well as the distorting effect of the regional trend are demonstrated by a local example. It reviews the gravity survey of a loess bluff and its surrounding on the bank of the river Danube. The derived density values increase from $\rho_t=1163\pm543$ kg/m³ to $\rho_t=1764\pm113$ kg/m³ as the gravity anomalies are gradually reduced by regional and local (terrain) effects during data processing. The lab determination of surface loess samples from the area having only 3.5% water content gives 1610 ± 100 kg/m³.

Keywords Nettleton's method, average density, terrain correction, L2 norm solution

1. Introduction

Neglecting the atmospheric mass distribution, the free-air gravity anomalies defined at the surface point P (Fig. 1) reflects all the gravitational effects of the density inhomogeneities of the Earth's body:

$$\Delta g_{\text{free-air}} = g_P - \gamma_{P'}, \quad (1)$$

where g_P is the gravity acceleration value at P and $\gamma_{P'}$ is the normal value of the gravity acceleration of the reference ellipsoid at P'.

Usually the most dominant local mass density anomaly relative to a reference ellipsoid is the topography itself in the close vicinity of the gravimetric surveying points. This is the reason

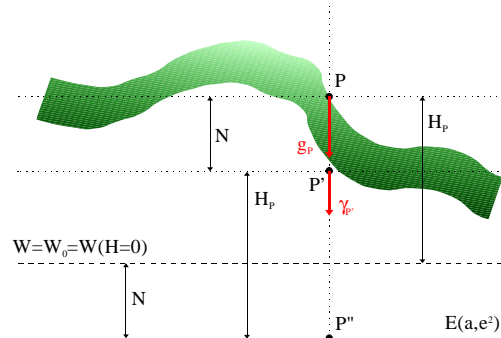


Fig. 1. Simplified interpretation of the surface free-air gravity anomaly assuming parallelism of the real W and reference $E(a, e^2)$ potential surfaces. H_P is the elevation of point P, P'' is its projection on $E(a, e^2)$ and N is the geoid undulation

why $\Delta g_{\text{free-air}}$ correlates well with the station elevation of gravimetric points. The correlation is simply approximated by a linear form the height dependent term of which is the gravitational effect of a Bouguer slab:

$$\Delta g_{\text{free-air}} \cong 2\pi G \rho_t H_P + a, \quad (2)$$

where G is the universal gravitational constant, ρ_t is the local average density of topographical masses, H_P is the elevation of P above the height datum and a is the area mean of the Bouguer gravity anomalies.

2. The conditions of the application of Nettleton's method

Nettleton's method (Nettleton, 1939) is based on an iterative parameter determination of (2) and frequently used to obtain a suitable value of ρ_t for the Bouguer correction. Originally it was invented to eliminate/remove the "disturbing" gravitational effect of topographical masses from the gravity observations (e.g. Camacho et al., 2001). In this context the *primary disturbing source* (Fig. 2) is the topographical surface itself representing a significant density interface between the atmospheric masses and the Earth's body. The density jump on this interface varies between ~ 1000

kg/m^3 and $\sim 2800 \text{ kg/m}^3$ from point to point on the physical surface of the Earth. The *secondary disturbing source* (Fig. 2) is the density variation inside the Earth. The range of variation is usually much smaller ($< 1000 \text{ kg/m}^3$) in the subsurface region than at the boundary surface. However, the total volume of these density anomalies can be much bigger than that of the topography. Therefore many times the gravitational effect of the primary and secondary disturbing sources has the same magnitude.

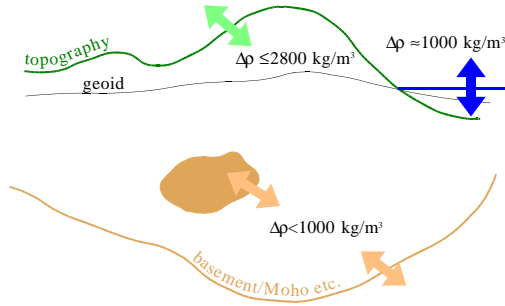


Fig. 2. Sketch of common density anomalies located near the surface of the Earth. $\Delta\rho$ means the absolute value of the density variation

In this context the validity of (2) is strongly influenced by two factors: 1) the variability of the topographical surface and 2) the variability of subsurface density distribution (Rao and Murty, 1973).

The *variability of the topographical surface* is taken into account as the terrain correction (TC). It represents the gravitational effect of mass surplus and deficiency above and below the point level H_p , respectively, relative to a Bouguer slab of thickness H_p . If TC is included in the computations then (2) gets the following form:

$$\Delta g_{\text{free-air}} \cong a + 2\pi G \rho_t H_p + TC(\rho_t). \quad (3)$$

Obviously, once the geometry of the topography is fixed, then TC is only a function of ρ_t . Although in the original solution of Nettleton's problem an iterative process may lead to the final value of both ρ_t and TC , a one step least squares solution is also possible using the observation equation

$$\begin{aligned} \Delta g_{\text{free-air}} &= a + (2\pi G H_p + TC_{\rho=1}) \rho_t + \delta g_{\text{CB}} = \\ &= \Delta g_{\text{CB}} + (2\pi G H_p + TC_{\rho=1}) \rho_t, \end{aligned} \quad (4)$$

where $\Delta g_{\text{CB}} = a + \delta g_{\text{CB}}$ is the so called complete Bouguer anomaly for which

$$(M\{\delta g_{\text{CB}}\}=0)$$

holds, and $TC_{\rho=1}$ is the value of TC computed with unit density. In the terminology of the adjustment theory δg_{CB} is a correction of observation $\Delta g_{\text{free-air}}$

and it represents the misfit between the linear model (4) and the measurement.

The *variability of the subsurface density distribution* may influence significantly the correctness of Nettleton's method. If the density variation on a given area shows dominant systematic (trend like) features, then it biases the estimated surface density ρ_t . The constant term a in (2) - that is the mean Bouguer anomaly of the area under investigation - can represent only stationary features of the density distribution. It indicates the local state of average mass balance between the real Earth and its ellipsoidal model generating γ in (1). The two terms in (2) assumes that the sub-topographical (crustal) density variation has only "random" or short wavelength characteristics and also a stationary part. Obviously the terms "random" and "short wavelength" are subject to the horizontal extension of the area because what is a systematic feature on a small area, can be just an insignificant local detail on a larger scale.

Nevertheless, $\Delta g_{\text{free-air}}$ superimposes all the characteristics of the crustal density distribution. Consequently before the application of the Nettleton's method the trend-like, non-stationary components independent from the topography must be removed from the observation.

3. The description of the topography of the test area

The test area $\sim (1.5 \text{ km} \times 1.2 \text{ km})$ is situated in a small town called Dunaföldvár, Hungary on the bank of the Danube (Fig. 3). The loess wall parallel to the river divides the area into a plateau with an average elevation of 107 m and the embankment with an average elevation of 97 m. The height of the wall may reach the maximum of 30 m. The sediments composing the ground are layered horizontally and contain mainly loess, sand and clay.

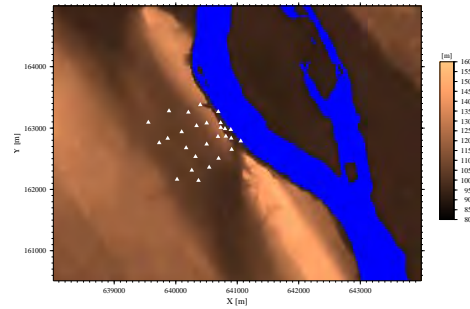


Fig. 3. Topographical map of the test area. White triangles show the location of gravimetric points. Blue color indicate the surface of the water

4. Gravity data and gravity reductions

27 gravimetric points were measured by the LCR G949 instrument (Papp et al, 2004). The distribution of the points was adjusted to the local variation of topography therefore the points were densified near the edge of the loess wall (Fig. 3). The accuracy of the g values at the gravimetric points is estimated below $\pm 20 \mu\text{Gal}$ ($1 \mu\text{Gal} = 10^{-8} \text{m/s}^2$).

The free-air gravity anomalies

$$\Delta g_{\text{free-air}} = g_p - \gamma_p + 0.3086H_p \quad (5)$$

were derived by the application of the normal gravity formula of GRS80 and the normal value (-0.3086 mGal/m) of the vertical gradient of gravity. Fig. 4 shows some correlation with the topography, as it is expected. A local maximum of $+13.2 \text{ mGal}$ having elongated shape in NW-SE direction is located near the edge of the bank. A smooth general trend dipping toward NW ($\sim -2 \text{ mGal/km}$) can also be recognised but it is not related to the topography which is rather flat except in the close vicinity of the loess wall. This feature is certainly neither stationary nor random, so it has to be removed prior to the estimation of the average topographical density of the area. The physical reason of the trend of $\Delta g_{\text{free-air}}$ can be the geometry of the pre-tertiary basement dipping also in NW direction (Fig. 5). It starts from 1000 m and reaches a depth of 2000 m in about 5 km distance. The gravitational effect of the sediments representing a significant mass deficiency can be approximated by a simple first order polynomial surface (actually a plane)

$$\Delta g_{\text{free-air}}^{\text{trend}} = \sum_{i=0}^1 \sum_{j=0}^1 a_{ij} x^i y^j, \quad (2)$$

where a_{ij} are the coefficients of the polynomial and x and y are the horizontal coordinates of the gravity points. It was fitted to the data by applying L2 norm (Fig. 6). The trend plane obtained tilts toward West and North, at a rate of $\partial(\Delta g)/\partial x = 1.07 \text{ mGal/km}$ and $\partial(\Delta g)/\partial y = -1.27 \text{ mGal/km}$, respectively. The dominant non-stationary component (Fig. 6) of the anomalous gravity field obtained from (2) was subtracted from all the free-air gravity data available on the test area:

$$\Delta g_{\text{free-air}}^{\text{res}} = \Delta g_{\text{free-air}} - \Delta g_{\text{free-air}}^{\text{trend}}, \quad (4)$$

where $\Delta g_{\text{free-air}}^{\text{res}}$ is the residual free-air gravity anomaly (Fig. 6).

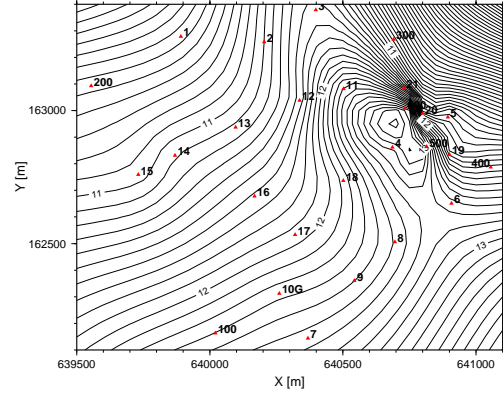


Fig. 4. Free-air gravity anomalies on the test area. The red triangles show the location of gravimetric points. The contour interval is 0.1 mGal

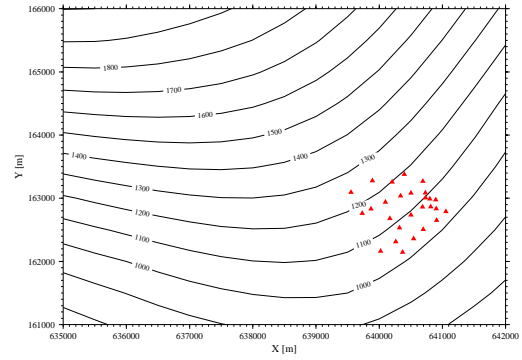


Fig. 5. Contour map of the pre-tertiary basement depth obtained from borehole and seismic measurements. The red triangles show the location of gravimetric points. The contour interval is 100 m

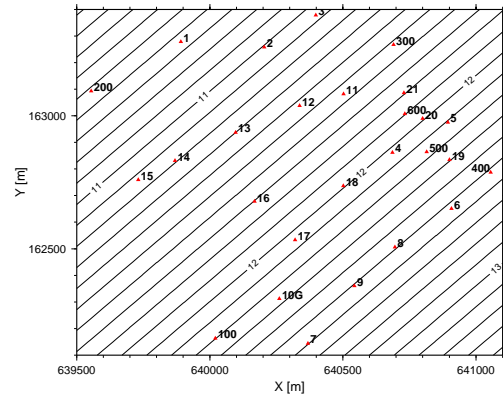


Fig. 6. The first order trend surface of the free-air gravity anomalies on the test area. The red triangles show the location of gravimetric points. The contour interval is 0.1 mGal

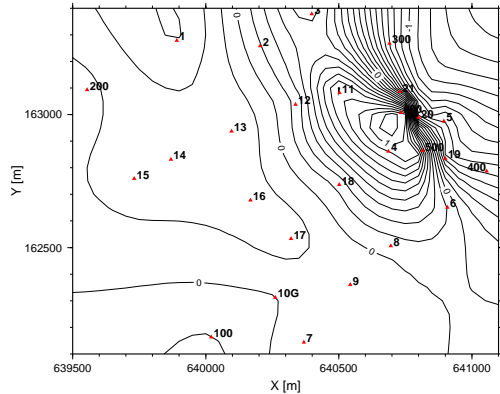


Fig. 7. Residual free-air gravity anomalies on the test area obtained by (7). The red triangles show the location of gravimetric points. The contour interval is 0.1 mGal

For the computation of the terrain correction in a planar approximation a $20 \text{ m} \times 20 \text{ m}$ digital elevation model (DEM) of the surrounding area was used (Fig. 8). This detailed model was merged with the 3D rectangular prism model of the topography representing the distant terrain effects up to the usual distance of 167 km. The regional model is a generalisation of the initial $500 \text{ m} \times 500 \text{ m}$ DEM of Hungary in the sense of the volume of topographic masses (Kalmár et al., 1995).

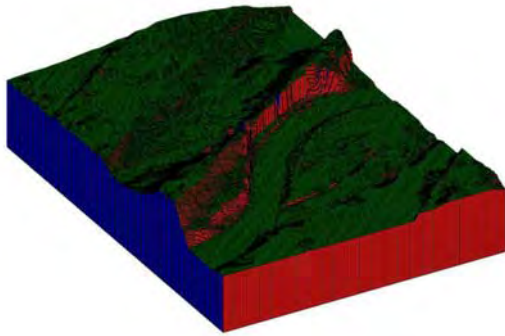


Fig. 8. The volume element representation of the topographical masses on the test area. The horizontal extension of the model is $6 \text{ km} \times 4.5 \text{ km}$. The elevation of the mass columns varies between 90 m and 152 m

5. Least squares estimation of the average topographic density

Three variants of the observation equation were used to estimate ρ_t and TC_p in L2 norm:

$$\Delta g_{\text{free-air}} = a + (2\pi G H_p + TC_{\rho=1})\rho_t + \delta g_{\text{CB}}, \quad (8)$$

$$\Delta g_{\text{free-air}}^{\text{res}} = a + 2\pi G H_p \rho_t + \delta g_{\text{CB}}, \quad (9)$$

$$\Delta g_{\text{free-air}}^{\text{res}} = a + (2\pi G H_p + TC_{\rho=1})\rho_t + \delta g_{\text{CB}}, \quad (10)$$

In (8) free-air anomalies were used as observations and TC was included, in (9) residual anomalies obtained by (7) were applied without TC correction and in (10) also residual anomalies were evaluated and the terrain correction term was included.

The elevation dependence of the three types of observables can be seen in Fig. 9. The details of the least squares adjustment of the parameters of an elevation dependent, linear model are listed in Table 1.

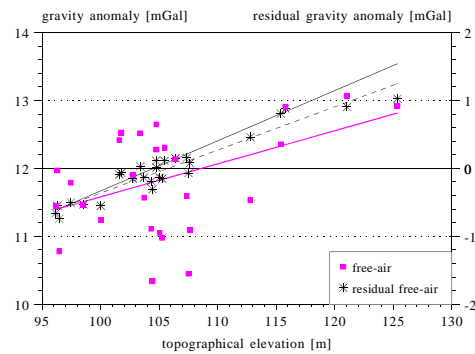


Fig. 9. Elevation dependence of free-air and residual free-air gravity anomalies. The thick magenta line, black dashed line and the black solid line represents solutions (8), (9) and (10), respectively

Table. 1. The statistics of the least squares density estimation. μ_0 and μ_p are the standard deviations of the observation having unit weight and of the estimated density ρ_t , respectively

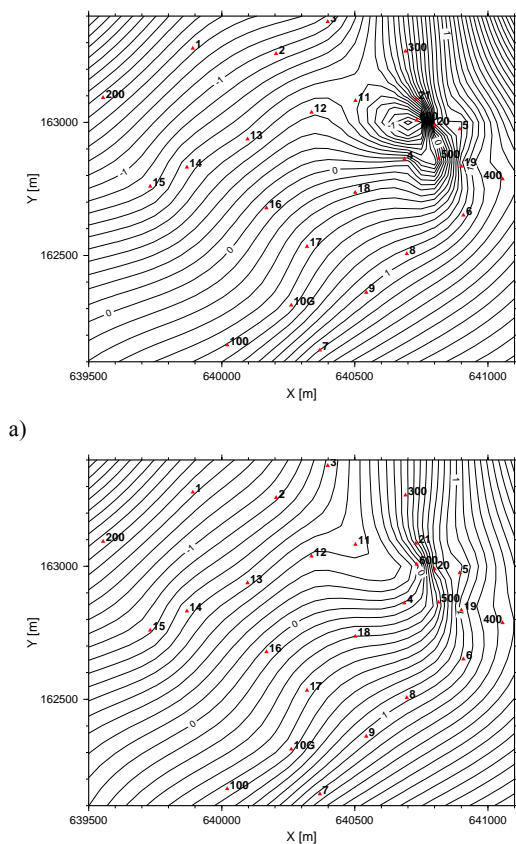
parameters	μ_0	$\rho_t \pm \mu_p$	a	number
observables	[mGal]	[kg/m ³]	[mGal]	of equations
Eq. 8	± 0.72	1163 ± 543	6.71	27
Eq. 9	± 0.14	1517 ± 92	-6.72	27
Eq. 10	± 0.15	1764 ± 113	-7.72	27

6. Computation of simple and complete Bouguer anomalies

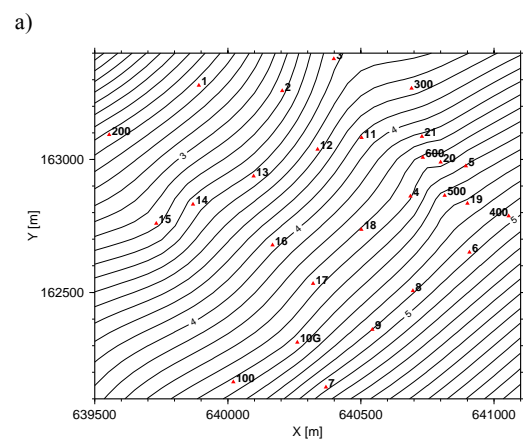
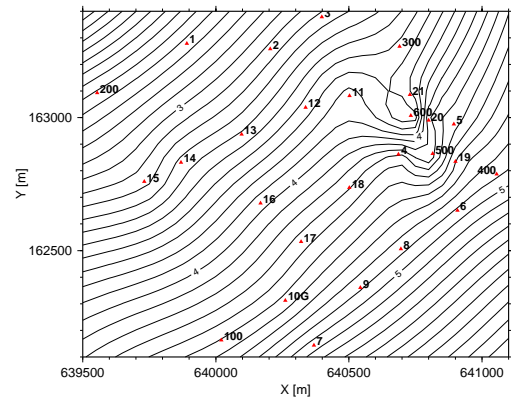
The two types of Bouguer anomalies were calculated using two different average topographic densities ρ_t . Figure 10. shows, that the computations with the most frequently used density value of the topographic masses ($\rho_t = 2670 \text{ kg/m}^3$) results in so called “ghost” gravity anomalies even if the terrain correction is applied. The anomalies obtained are still strongly correlated with the topography. The contour lines virtually indicate a disturbing body/structure located exactly below the loess bluff.

Undoubtedly, the normal density value is too high for this area since the topography is formed by thick loess layers/deposits.

Decreasing the density to its most probable value ($\rho_l = 1764 \text{ kg/m}^3$) it became clear that no small-scale (local) geological/tectonic structures representing horizontal density variation are covered by the topographical masses, because the local “anomaly” disappeared (Fig. 11.). This computation, however, also demonstrates that the proper terrain correction must be taken into account and only the complete Bouguer anomalies can be used for the correct interpretation.



b) **Fig. 10.** Simple (a) and complete (b) Bouguer gravity anomalies computed with $\rho_l = 2670 \text{ kg/m}^3$ density value. Note the “ghost” anomaly indicated near the edge of the loess wall (points: 4,11,500,600). The red triangles show the location of gravimetric points. The contour interval is 0.1 mGal



b) **Fig. 11.** Simple (a) and complete (b) Bouguer gravity anomalies computed with $\rho_l = 1764 \text{ kg/m}^3$ density value. The red triangles show the location of gravimetric points. The contour interval is 0.1 mGal

7. Comparison of density values obtained from gravity data and sample analysis

Four undisturbed surface samples of loess were collected from the test area and analyzed in order to determine their volume density values in laboratory. The lab measurements resulted in an average value of $1610 \pm 100 \text{ kg/m}^3$ density at 3.7% actual water content. The porosity of the samples varied between 32% and 47% which is in a good agreement with other estimations (Borsy, 1993). It indicates that the groundwater or the soil moisture may influence significantly the in situ volume density of the topographical masses of the test area. According to the parameters measured the mass of one m^3 of waterlogged loess may reach more than 2000 kg. The results of density estimations are summarized in Fig. 12.

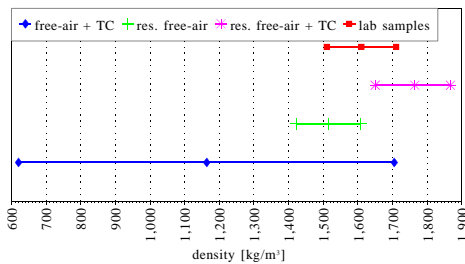


Fig. 12. Comparison of density estimations obtained from Nettleton's method (Table 1) and lab samples. The horizontal bars show $\pm 66\%$ (one-sigma) probability intervals

It seems that the most probable value of the average density is somewhat higher ($\Delta\rho \approx +150 \text{ kg/m}^3$) than the mean density value of lab samples. The significant difference between the water contents of the actual (in situ) topographical masses and of the lab samples can be a possible reason of that. The area itself is in the close vicinity of the river Danube, which certainly increases the soil moisture and the water table level in the surrounding. Based on the hydrological map of the area (Boczán, 1965) it is supposed that the volume density below the depth of the average water table surface ($\sim 10 \text{ m}$) is higher than on the surface, where the samples were collected from.

6. Conclusions

Nettleton's method implemented in a usual L2 norm inversion scheme and combined with the simultaneous determination of terrain corrections may lead to realistic density estimations of the topographical masses. The condition of its successful application is rigorous. The non-stationary components (regional/local trends) not connected to the topography have to be removed from the gravity data before processing them by any methods related to Nettleton's original idea. Otherwise the result is strongly biased. In this context some gravity independent (e.g. seismic) information about the subsurface geology is very useful.

Acknowledgement. The research was supported by the Hungarian National Research Fund (project number: OTKA T043413) and EU5 EVG1-2001-00061 OASYS project.

References

Papp G, Benedek J and Kalmár J (2004): Gravity investigations in Dunaföldvár test area. in: Mentés Gy and Eperné I (eds): Landslide monitoring of loess structures in Dunaföldvár,

Hungary, Geodetic and Geophysical Res. Inst. Hung. Acad. Sci., pp. 39-46.

Boczán B ed. (1965): Water table level beneath the topographical surface. L-34-VII-Székesfehérvár. Series of 1:200000 scale maps of the Geological Institute of Hungary

Borsy Z ed. (1993): Physical geography (in Hungarian). Nemzeti Tankönyvkiadó, Budapest

Camacho AG, Montesinos FG, Vieira R and Arnosó J (2001): Modelling of crustal anomalies of Lanzarote (Canary Islands) in light of gravity data. *Geophys. J. Int.* 147, pp. 403-414

Kalmár J, Papp G, Szabó T (1995): DTM-based surface and volume approximation. *Geophysical applications. Comp. and Geosci.*, 21, pp. 245-257.

Nettleton LL (1939): Determination of density for reduction of elevation factor. *Geophysics*, 4, pp. 176

Rao VB, Murty BVS (1973): Note on Parasnis' method for surface rock densities. *Pure and Applied Geophysics*, Vol. 110. pp. 1927-1931.

Absolute Gravity Measurements at Ulusal Metroloji Enstitüsü

B. Karaböce, E. Sadıkoğlu, E. Bilgiç, C. Kırbaş, A.İ. Turan, A. Çolak
Tübitak Ulusal Metroloji Enstitüsü (UME)
Gebze - Kocaeli /Turkey

Abstract. Acceleration of gravity, g value is widely used for research purposes in many areas such as geology and geography. Absolute determination of g plays an important role in metrology in calibrations of mechanical force standards, pressure transducers and load cells. An also current trend in mass metrology demonstrates that new mass standards based on electrical references for re-definition of kilogram are under development. This device would balance the force of a current (as determined by the quantum Hall effect and the Josephson junction effect) against the weight of a test mass. This application requires knowledge of the absolute value of g at parts in 10^9 . The gravity datum and the gravity scale in a given geographical area play the role of a metrological standard for geodetic and geophysical applications. For those reasons an absolute gravimeter system was bought at UME from Micro-g Lacoste/USA. It is a portable device so that it can also be used outdoor measurements. Uncertainty in g measurements is at the level $10 \mu\text{Gal}$. Acceleration of gravity g , value was measured in force, pressure, torque, mass and vibration laboratories in order to have more accurate measurements at UME. The reproducibility and repeatability measurements have been carried out at Vibration Laboratory. A brief summary about absolute gravimeter and performed gravimetry measurements are presented in this paper.

Keywords. Acceleration of gravity, g , absolute gravimeter, metrology

1 Introduction

Absolute gravity measurements have been carried out by using an absolute gravimeter (called as A-

10) which is a high accurate and transportable instrument. It operates on a 12V DC power supply, and is optimized to facilitate fast field operation. A retroreflector corner cube is dropped vertically by 7cm with a mechanical device inside a vacuum chamber. The A-10 uses a He-Ne laser, Michelson interferometer, long period inertial isolation device, and a rubidium atomic clock to determine accurately the position of the free-falling test mass. The acceleration of the test body is calculated directly from the measured trajectory. Stabilized laser and atomic clock are used to provide traceability to standard of length and time unit correspondingly. Both of these units have been specified to very high precision in UME laboratories. This direct link to metrological standards ensures the necessary condition for measuring absolute gravity.

2 Theory of Operation

The most common way to determine g is to directly measure the free-fall acceleration of a test body. The laser interferometer generates optical interference fringes as the test mass falls as shown in Figure 1. The fringes are counted and timed with an atomic clock to obtain time and displacement pairs. These data are fit to a parabolic trajectory to give a measured value of g . Expression for determination of g value is given in equation 1.

$$\begin{aligned} x &= x_0 + v_0 \tilde{t}_i + \frac{g_0 \tilde{t}_i^2}{2} + \frac{\gamma x_0 \tilde{t}_i^2}{2} \\ &+ \frac{1}{6} \gamma v_0 \tilde{t}_i^3 + \frac{1}{24} \gamma g_0 \tilde{t}_i^4 \\ \tilde{t} &= t_i - \frac{(x_i - x_0)}{c} \end{aligned} \quad (1)$$

where γ is the vertical gravity gradient ($\sim 3 \mu\text{Gal}/\text{cm}$), c the speed of light, x_0 the initial position, v_0 the initial velocity, g_0 the initial acceleration.

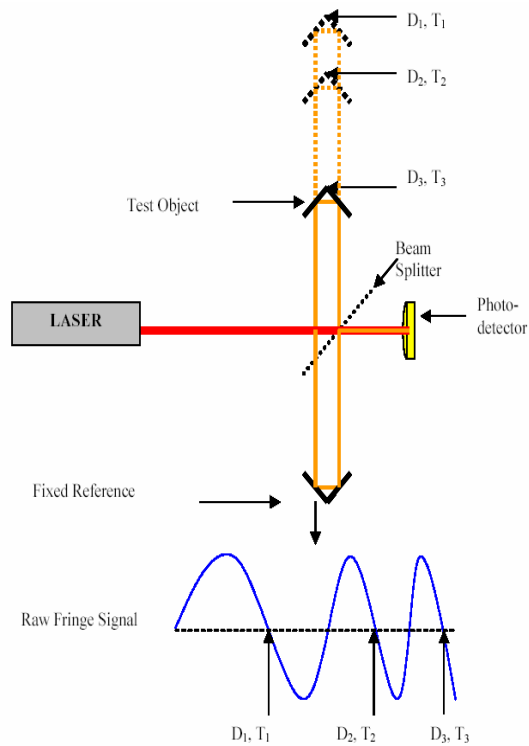


Fig. 1 Absolute g measurement

Figure 2 shows the general scheme of A-10 absolute gravity measurement device. It consists of upper unit, lower unit and electronics console.

The Dropping Chamber (in Figure 3) is a vacuumed volume at 10^{-6} mbar (10^{-4} Pa) in two processes as turbo pump first and second ion pump. The dropping test mass contains a retro-reflective corner-cube surrounded by a support structure which is balanced at the optical center of the corner-cube. At the beginning of a drop, the carrier carrying the test mass accelerates downwards with an acceleration greater than g . Then carrier and test mass drops together down. Finally, at the bottom of the drop, the carrier gently catches the test mass. Laser light passes through a window in the bottom of the Dropping Chamber to the corner cube (inside the test mass), and is then reflected back down through the window to the interferometer.

When in contact with the carrier, the corner-cube is supported by three spherical or balls that fit and

orient it to “vees” in the carrier. The carrier mechanism is a DC servo motor transfers the motion with shaft via ferrofluidic feedthrough and located outside the chamber.

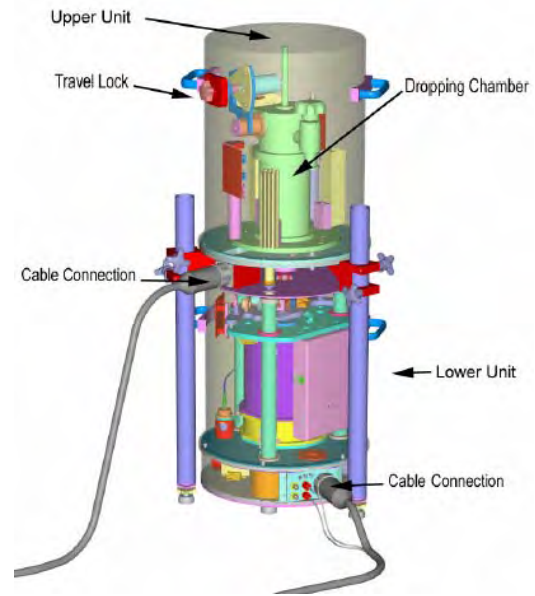


Fig. 2 A-10 Absolute gravimeter

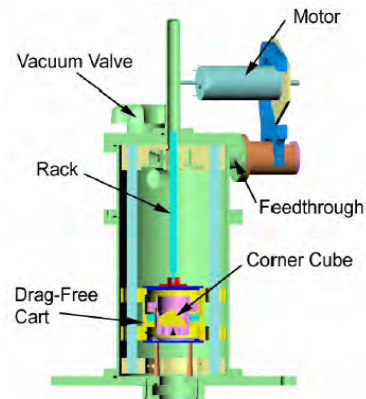


Fig. 3 Dropping chamber

Reference mirror of interferometer that is retroreflector corner cube was placed on the superspring system in order to have stable reference mirror. Details of system can be seen in schematic in Figure 4. An inner support assembly hangs from the superspring base structure on three short springs. This mainspring is approximately 10 cm in length and has a natural frequency of about 2 Hz. The inner support assembly is actively servo-controlled to track the vertical location of the superspring mass. By keeping the length of the

mainspring as constant as possible, the resulting system has a period of approximately 30 seconds.

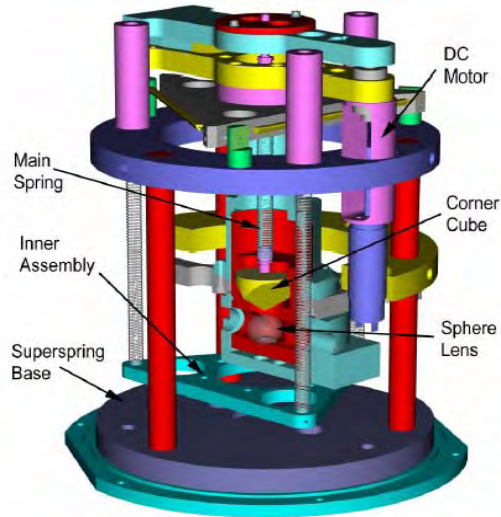


Fig. 4 Reference mirror (retroreflector corner cube) placed on superspring system

3 Description of Measurement Station at UME Vibration Laboratory

Absolute gravity measurements have been carried out at UME Vibration Laboratory. The Laboratory building is located in Gebze where is 40 km's away from İstanbul as seen in figure 5 and 6.



Fig. 5 Location of UME

The Laboratory has been located at the basement floor where is 12 meters (or 3 floor) below the ground level. There are three sismic masses in the laboratory. Sismic masses are isolated from the main building with micron level silisium sand. Sismic mass floor is covered with a hard plastic. The laboratory is temperature and humidity controlled at $23^{\circ}\text{C}\pm 1^{\circ}\text{C}$ and $\%45\pm 10$ RH.



Fig. 6 UME (National Metrology Institute of Turkey) Building

Detailed description of measurement station is given in Table 1.

Table 1. Description of absolute gravity measurement station

State	Kocaeli
City	Gebze
Country	Turkey
Location	UME Vibration Laboratory
Situation	Isolated sismic mass
Latitude, +N	40,7986111 degrees
Longitude, +E	29,6405556 degrees
Elevation	129 m
Gradient	-2,06 $\mu\text{Gal}/\text{cm}$

4 Absolute Gravity Measurements performed at UME Vibration Laboratory

Absolute gravity measurements were carried out by using an A-10 (Serial No.: 005) Portable Absolute gravimeter as seen in figure 7. Preliminary adjustments were performed before g measurement. Dropping chamber, interferometer and laser temperature must be switched on and reach to declared temperatures for half a day. Lower part that includes laser, reference mirror, interferometer and inclinometers was placed on measurement surface. Laser light verticality must be aligned in

two steps. First is automatic alignment with inclinometers. Second alignment is with an external interferometer which is called as beam checker located on top of laser beam exit manually.



Fig 7. A-10 Absolute gravimeter during measurement.

The travel lock disengaged and placed the dropper part on top of the lower part allowing the feet to fit neatly into the three wells on the top of lower part. At this point the two parts are in mechanical contact with each another. The legs of dropper units were lowered to ground manually by taking care to be as vertical as possible and tightened. Mechanical contact was disengaged by lowering the legs of lower part.

After mechanical arrangements were completed, software was prepared. Input parameters, site specification, latitude, longitude, elevation, gradient and polar motion were set. Data acquisition parameters, number of drops/set, number of sets, interval between drops and start time of data acquisition were adjusted. Earth tides, ocean loading, barometer, polar motion, gradient and speed of light corrections were applied.

Absolute gravity measurements have been carried out for three years in order to observe fluctuations of g value. Measurements results can be seen from figures 8 and 9.

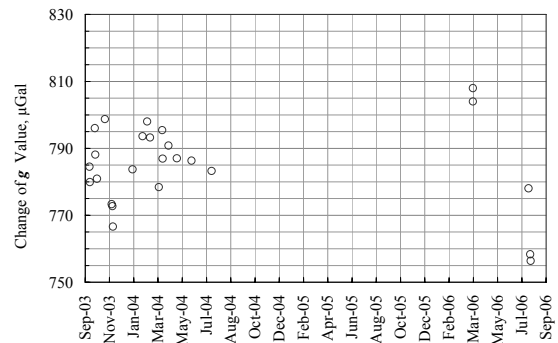


Fig. 8. Absolute gravity measurement results for three years.

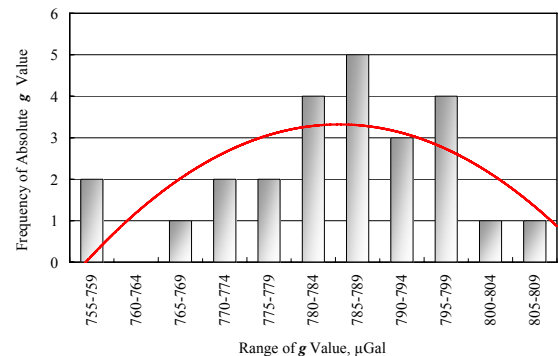


Fig. 9. Frequency of absolute gravity measurement values for three years.

References

- Niebauer, T., G. Sasagawa, J. Faller, R. Hilt, F. Klocking (1995). A new generation of absolute gravimeters, *Metrologia*, 32, 159-180.
- Zumberge, M., R. Rinker, J. Faller (1982). A portable apparatus for absolute measurements of the Earth's gravity, *Metrologia*, 18, 145-152.
- Francis, O., van Dam T. (2006). International Comparison of Absolute Gravimeters in Walferdange (Luxembourg) of November 2003.
- A-10 Portable Absolute Gravimeter User's Manual (2006). Micro-g LaCoste, 2006

Liard, J., Gagnon, C. (2002). The New A-10 Absolute Gravimeter at the 2001 International Comparison of Absolute Gravimeters.

Metrologia, 39, 477-483.

Vitushkin L., Becker M., Jiang Z., Francis O., van Dam T.M., Faller J., Chartier J.-M., Amalvict M., Bonvalot S., Debeglia N., Desogus S., Diament M., Dupont F., Falk R., Gabalda G., Gagnon C. G. L., Gattacceca T., Germak A., Hinderer J., Jamet O., Jeffries G., Kärer R., Kopaev A., Miard J., Lindau A., Longuevergne L., Luck B., Maderal E.N., Mäkinen J., Meurers B., Mizushima S., Mrlina J., Newell D., Origlia C., Pujol E.R., Reinhold A., Richard Ph., Robinson I.A., Ruess D., Thies S., Van Camp M., Van Ruymbeke M., de Villalta Compagni M.F., Williams S. (2002). Results of the Sixth International Comparison of Absolute Gravimeters, ICAG-2001. *Metrologia*, 39, 407-424.

Relative campaign during the International Comparison of Absolute Gravimeters ICAG-2005 and the strategy of data treatment combined with the absolute results

Zhiheng Jiang¹, Leonid Vitushkin¹, Matthias Becker², Olivier Francis³, Philippe Jousset⁴
and

Matthieu Ferry³, François Dupont⁴, Sébastien Deroussi⁵, Laurent Métivier⁵, Gwendaline Pajot⁵, Chiungwu Lee⁶, Chin-Lung Tsai⁶, Reinhard Falk⁷, Herbert Wilmes⁷, Alexander Kopaev⁸, Diethard Ruess⁹, Christian Ullrich⁹, Bruno Meurers¹⁰, Jan Mrlina¹¹, Vojtech Palinkas¹², Jakub Kostecky¹², Franck Pereira¹³, Michel van Ruymbeke¹⁴, Sébastien Naslin¹⁴

1 Bureau International des Poids et Mesures (BIPM)

2 Institute of Physical Geodesy, Darmstadt University of Technology (IPGD), Germany

3 University of Luxembourg and Centre Européen de Géodynamique et de Séismologie (ECGS), Luxembourg

4 Bureau de Recherches Géologiques et Minières (BRGM), France

5 Institut de Physique du Globe de Paris (IPGP), France

6 Industrial Technology Research Institute (CMS/TRI), Chinese Taipei

7 Federal Agency of Cartography and Geodesy (BKG), Germany

8 Sternberg Astronomical Institute of Moscow State University, Russia

9 Federal Office of Metrology and Surveying (BEV), Austria

10 Institute of Meteorology and Geophysics (IMG), University of Vienna, Austria

11 Geophysical Institute Prague (GI), Czech Republic

12 Geodetic Observatory Pecny (GOP), Research Institute of Geodesy, Topography and Cartography, Czech Republic

13 Laboratoires Nationaux de Métrologie (LNE-SYRTE), France

14 Royal Observatory of Belgium (ROB), Belgium

Abstract

As a tradition following the first International Comparison of Absolute Gravimeters in 1981 (Becker and Groten, 1983), during the 7th International Comparison of Absolute Gravimeters (ICAG-2005) at the BIPM (Bureau International des Poids et Mesures), high precision relative gravity ties and vertical gradients were measured over the BIPM ICAG-network which includes sites with a gravity difference up to 9 mGal^{*}. 12 institutes of 10 countries with 15 gravimeters of 6 different types were employed.

We report in this paper the organisation of the relative campaign, the raw data analysis, the relative-only measurement adjustment and the combined adjustment of the relative and absolute data. Related problems issued during the measurements and data processing are introduced.

When preparing the final version of this paper, the absolute g-values of the ICAG 2005 are not yet available (Vitushkin et al., IGFS2006). In consequence, results presented here are preliminary. The detailed analysis of adjusted g-values and gravimeter calibration etc. will be discussed in a forthcoming paper.

The relative gravimetry raw data analysis, the comparison between the relative-only adjustment

and the absolute-only adjustment shows that the uncertainty of an adjusted gravity difference given by the relative campaign is of the order of 1~2 μ Gal, probably $\pm 1.3 \mu$ Gal, and that of the gradient is of the order of 1~2 μ Gal/m.

Keywords. Gravity values, gravimetry, absolute gravimeter, relative gravimeter

* 1 Gal = 1 cm s⁻²

1 Introduction

Since 1981, the comparisons of absolute gravimeters have been carried out every four years at the BIPM, Sèvres France. The 7th ICAG was held in 2005 at the BIPM, organised by the IAG Study Group 2.1.1 “Comparisons of Absolute Gravimeters” (SGCAG 2.1.1), the Working Group on Gravimetry of Consultative Committee on Mass (CCM WGG) and the BIPM. The steering committee of the ICAG-2005 consisted of L. Vitushkin (BIPM), M. Becker (IPGD, Germany), O. Francis (ECGS Luxembourg), A. Germak (INRIM Italy), Z. Jiang (BIPM), Wangxi Ji (NIM China). Totally 19 absolute gravimeters from 14 countries took part in the comparison. There were 7 types of absolute gravimeters made by different manufactures. As it is well known, different

absolute gravimeters have different reference heights where the g -values are determined and at present the vertical gradient can not be derived from their observations with sufficient accuracy. In the recent comparisons absolute measurements are performed on multiple points to allow the determination of instrumental biases. The comparison is possible only when the gravity differences are well known. In consequence, the relative campaign is organised to measure the vertical gradients over every point and the gravity differences between the points. Traditionally, people take this change to make some special studies in relative gravimetry. This is changed since the 7th ICAG. During the 1st Joint Meeting of the CCM WGG and SGAG 2.1.1 of the IAG on 25-26 May 2004, it was decided that the role of the relative campaign is as a service, in the sense of metrology, to the absolute gravimeter comparison. For this purpose, one of the investigations made during the ICAG2005 was the reachable uncertainty of relative measurements under the 'laboratory' conditions at BIPM (see below). 12 institutes of 10 countries with 15 gravimeters of 6 different types were participating in the campaign.

The organisation and the data analysis of the absolute measurements are reported by a parallel paper (Vitushkin et al., IGFS2006). We report in this paper only the relative campaign activities and the strategy of the data processing of the relative-only adjustment, the absolute-only adjustment and the combined absolute-relative adjustment. However, when preparing this paper, the absolute g -values of the ICAG 2005 have not been officially released. All results here are therefore preliminary. In consequence, a detailed analysis of the adjusted g -values and the gravimeter calibration etc. will be discussed in a forthcoming paper.

2 Optimal design of the BIPM network

The purpose of the optimal design is to look for the best reachable uncertainty of the gravity difference determination. Experiences based on the error sources' analysis (Jiang et al. 2005) shows that the main disturbances of the relative measurement accuracy are due to calibration and the apparent zero-drift caused by: temperature change, transport vibration as well as operating errors and blunder or typing errors in gravimeter readings or instrument height measurements. The latter happens often and can be evaded by following a fixed and traceable schedule using the BIPM level-fixed tripods (Fig. 1). The first two error sources, calibration and zero-drift, can be greatly reduced with the so called

quasi-zero technique, that is, small gravity difference, small distance, short, symmetric and equal time intervals with triangle-closing sequence of observations.

The BIPM ICAG-network is comprised of 12 points over 4 sites of A, B, C1 and C2 (Fig. 2). All points are precision levelling measured, absolute gravity determined and air-conditioned with maximal temperature variation of 0.5 °C. Having the gravity difference of 8.7 mGal, the new outdoor sites C1 and C2 were built in spring 2005 mainly for the relative meter calibration. The 10 indoor points, 3 over site A and 7 over site B, are used for the absolute meter comparison. Obviously, most of the comparisons are made separately within the site A or B but few between A and B. The gravity difference ties within a site (between A, A1, A2 and between B, B1 to B6) are the most favourable quantities in view of the optimal design. Most of the gravity differences are less than 10 μ Gal with a maximum of 23 μ Gal. The inter-point distances are 3 m at maximum. The average occupation takes about 3~4 minutes. All relative observations following the same scheme, over A site: A, A1, A2, A, A1, A2, A, A1, A2, and A; over B site: B, B1, B2, B, B2, B6, B, B6, B3, B, B3, B4, B, B4, B5, B, B5, B1, B, B2, B1, B, B3, B6, B, B5, B4, ended at B. Each point has at least three occupations. The meters were always set up to be oriented to north. One of the advantages of the triangle-closed scheme is to better monitor the zero-drift behaviour of meter. A special program is developed to determine and reduce it. A normal drift is approximated by a polynomial while an abnormal drift (jumps for example) will be cut off into several drift periods. The outdoor ties are designed for mainly the relative meter calibration following the schedule: C1, C2, C1, B, A, B, C2, A, C1, C2 and C1.

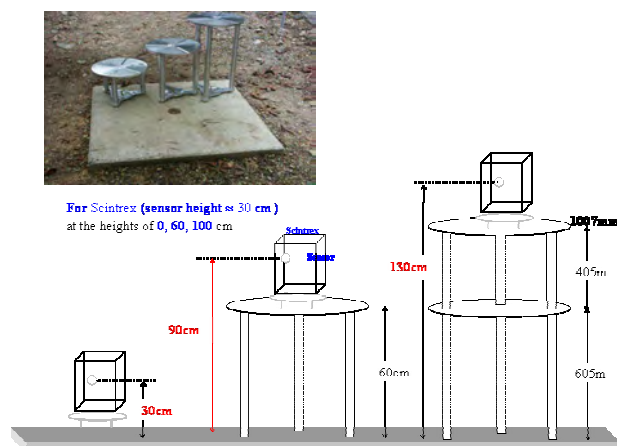


Fig. 1 The BIPM level-fixed tripods and its setting up for the gradient measurement by Scintrex CG gravimeter

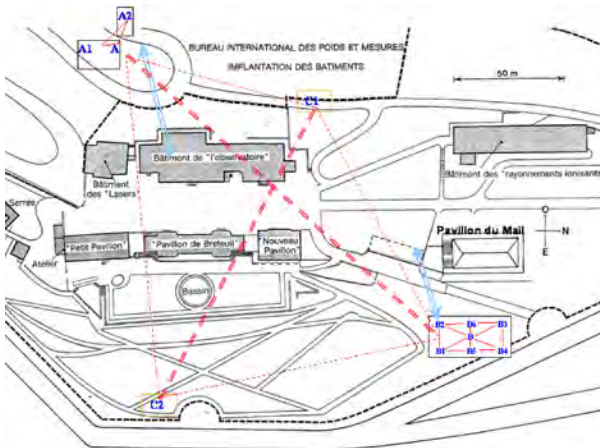


Fig.2 The BIPM ICAG horizontal network with 12 points over 4 sites: A and B indoor site, C1 and C2 outdoor

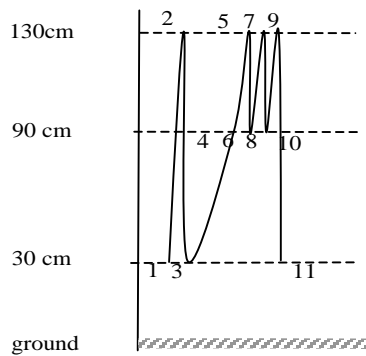


Fig. 3 The gradient measuring positions and the schedule with 11 occupations

The BIPM ICAG-network is consisting of the horizontal part and the vertical part. The comparison network is horizontally defined at 90 cm above the ground, about the average reference height of the different existing absolute gravimeter models. The vertical part serves for the gradient determination. Fig. 3 shows the gradient measuring schedule and the positions at 30, 90 and 130 cm above ground, knowing that the reference heights of all absolute gravimeters are between 30 and 130 cm. The gradient between 90 and 130 cm is strengthened due to the fact that the reference height of the most frequent absolute meter (FG5) is close to 130 cm. The BIPM level fixed tripod is designed (Fig. 1) to allow the instrument sensors of the LCR and Scintrex relative meters to be located within 1~2 cm w.r.t. the 30, 90 and 130 cm height levels above ground by different combination of the tripod towers. Slight eccentricities of the instrument sensor to the defined point (up to a few cm) are corrected by using the vertical and horizontal gradients obtained in an iteration procedure (cf. Fig. 9 and 10). The horizontal and vertical parts of the

network are adjusted as a whole hence their accuracy is globally homogeneous. Over C1 and C2, only the gradient between 90 and 130 cm is measured. The gradient is approximated by a polynomial.

3 The relative gravity campaign and precision levelling measurements

The relative campaign was carried out during the 4th ~ 8th, the 24th ~ 28th July and on the 12th Sept. 2005. Totally 14 relative gravimeters from 12 institutes of 10 countries took part in it. Among them, there are 8 Scintrex (model CG-3 and CG-5) and 6 LaCoste-Romberg (model G, D and EG) as well as a ZLS model B, of which 11 meters performed the complete (or almost) measurement schedules that take about 15 to 18 hours for an experienced operator.

Tab. 1 Participants of ICAG relative campaign

Main Observers	Institute	Gravimeters
J. MRLINA	GI	LCR D188
M.RUYMBEKE, S.NASLIN	ORB	LCR G336
O. FRANCIS, M.FERRY	ECGS	CG-5 008
C.W. LEE, C.L. TSAI	ITRI	LCR EG184
P. JOUSSET		CG-3 245
F. DUPONT	BRGM	CG-5 028
M. BECKER	IPGD	LCR D038
B. MEURERS	IMG	LCR D009
F. PEREIRA	SYRTE	CG-3 105
S. DEROUSSI		CG-3 193
L. METIVIER	IPGP	CG-3 323
G. PAJOT		CG-3 424
V. PALINKAS		
J. KOSTELECKY	GOP	ZLS B020
H. WILMES, R. FALK	BKG	CG-3 202
D. RUESS, M.C. ULLRICH	DMG	LCR D051



Fig. 4 The IGN69 precision levelling point served as the starting point of the height measurement

The height of the benchmarks of all the points are monitored by the repeated precision levelling

carried out by BRGM of France. The reference point is the French IGN 69 levelling station located at the BIPM Observatory building (Fig. 4). The ICAG levelling measurement was performed the 6~7 July, 2005. For C1 and C2, it was the first time they were levelled. No detectable height change has been observed over the points on the sites A and B since ICAG 2001.

4 Strategy of data processing

The goal of the relative campaign is:

- Determination of gradients and *reachable* uncertainty: $dg/dh \pm U_d$: (14 relative meters)
- Determination of gravity values and *reachable* uncertainty $g \pm U_g$: (12 points with totally 34 positions at 30, 90 and 130 cm)
- Estimation of the offsets of absolute meters and their uncertainties: $d_k \pm U_d$: (N=19 absolute meters)
- Investigation of the detailed structures of the BIPM local gravity and gradient fields

Principally three different adjustments are made depending on the data introduced: the absolute-only, the relative-only and absolute-relative combined adjustment. The first two methods give the independent analysis of each data type and comparisons of them. The last gives the best estimations of the gravity values, gradient values at each point, relative meter calibration and absolute meters' offsets and their uncertainties.

The observation equations of the adjustments are described in brief as follows:

4.1 Absolute-only observation equation for meter k over point i :

$$V_i = g_{ki} - G_i + d_k$$

Offset condition: $\sum d_k = 0$, ($k = 1, N$), with

- V_i - adjustment residual
- g_{ki} - measured g value of meter k at point i
- G_i - adjusted g value at point i
- d_k - Offset of the meter k (*against the adjusted G*)
- N - Number of absolute gravimeters involved

4.2 Relative only observation equation for meter q between points i and j :

$$V_{qij} = s_q \times (R_{qi} - R_{qj}) - (G_i - G_j)$$

It is an unconstrained network adjustment with the absolute value of g fixed at the point B:

$$G_B = G_{B-absolute}$$

with

$$V_{ij} - \text{adjustment residual}$$

- R_{qi}, R_{qj} - measurement reading of meter q at point i and j
- G_i, G_j - adjusted g value at points i and j
- s_q - Scale of a relative meter q w.r.t. a defined reference scale.

4.3 Combined Absolute and Relative observation equation with the adjusted gravity value G as common unknowns:

$$\begin{aligned} V_{qij} &= s_q \times (R_{qi} - R_{qj}) - (G_i - G_j) \\ V_i &= g_{ki} - G_i + d_k \end{aligned}$$

with the Offset condition: $\sum d_k = 0$, ($k = 1, N$)

4.4 Weights in principle

Absolute observation equation (point i of meter k):

$$W_{i,k} = \mu^2_0 / (m^2_{i,k} + M^2_k)$$

Relative observation equation (the tie j of meter q):

$$w_{j,q} = \mu^2_0 / m^2_{j,q}$$

with:

- μ_0 - unit weight mean square error
- m - measurement error
- M - systematic error

4.5 The gradients

Suppose the adjusted gravity value G at a point can be approximated by a polynomial as function of the height H :

$$G(H) = a + bH + cH^2$$

Because the three positions of 30, 90 and 130 cm are measured, the coefficients a , b , c can be uniquely determined. The gravity difference and average gradient between H_1 and H_2 ($H_1 > H_2$) can be written:

$$\begin{aligned} dG &= G(H_2) - G(H_1) = b(H_2 - H_1) + c(H_2^2 - H_1^2) \\ dG/(H_2 - H_1) &= b + c(H_2 + H_1) \end{aligned}$$

The gradient at height H : $dG/dH = b + 2cH$

5 Preliminary results

The results here are preliminary and may be subject to minor changes.

Fig. 5 is the histogram of the adjustment residuals of all the measured ties for the CG-5 008. The completed schedule gives 157 measured relative ties. The RMS (root of mean square) of the 157 residuals is $\pm 1.5 \mu\text{Gal}$. This implies the most probable error of a measured gravity difference of this meter is $\pm 1.5 \mu\text{Gal}$. For other meters, the RMS varies between $1.5 \sim 2.5 \mu\text{Gal}$. Table 2 lists the

adjusted gravity differences of the combined adjustment between any two ICAG points.

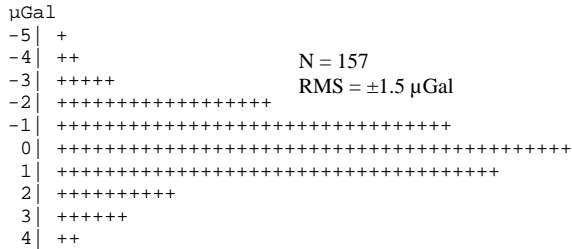


Fig. 5 Histogram of the adjustment residuals for Scintrex CG-5 8 with observation number N=157, RMS=1.5 µGal

Fig. 6 presents the discrepancies of the two completely independent solutions. The relative solution is that of the unconstrained network adjustment with the gravity value at B fixed to the mean of the measured absolute g values and the scale is fixed to that of the CG-5 008. The maximum difference is 2 µGal at A2 with the RMS of the total differences being +/-1.3 µgal. Further investigation is required to explain the discrepancy at each point. Generally speaking, the discrepancy is within the uncertainties of the absolute and relative determinations. Here 14 absolute gravimeters out of the total 19 meters were used in this preliminary analysis. Further investigation should be made for using the results of other 5 meters.

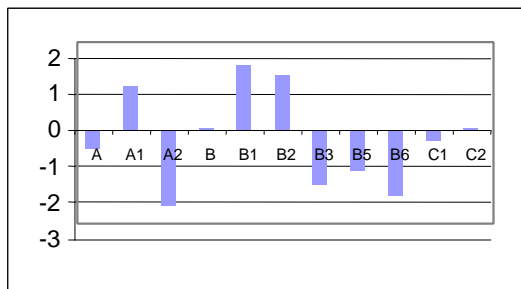


Fig. 6 Differences between the adjusted absolute-only (14 meters) and relative-only (14 meters) g values: RMS= +/-1.3 µgal (µGal, preliminary)

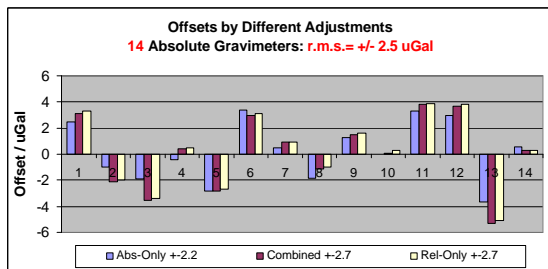


Fig. 7 Offsets of the 14 absolute meters computed by different adjustment methods (µGal, preliminary)

Fig. 7 shows the offsets of the 14 absolute gravimeters determined by the three different adjustment methods, they are close to each other and within the uncertainties. Fig. 8 gives the daily-variation of the offset of the FG5-108 belonging to BIPM. The FG5-108 followed a special schedule to occupy 6 points and 29 continuous one day-determinations (average of each full day measurements) were made in total. Further investigation is required to explain the offset determined at B point, of which the variation seems too big.

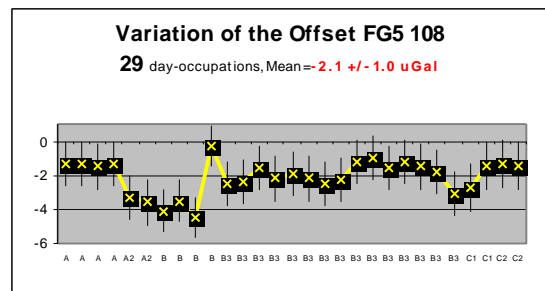


Fig. 8 Offsets of the daily-averaged gravity value by FG5-108 (µGal, preliminary)

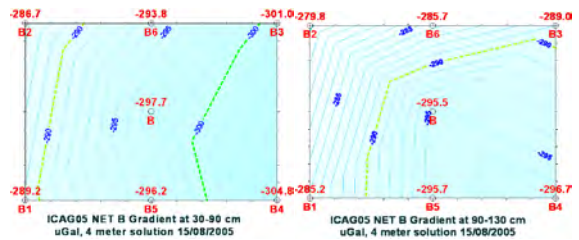


Fig. 9 B site vertical gradient between 30-90-130 cm (µGal/m, preliminary)

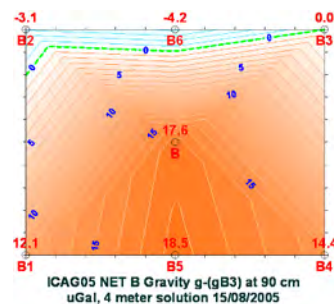


Fig. 10 Horizontal gravity variation over the B site at 90 cm w.r.t. B3 (µGal, preliminary)

Fig. 9 shows the non-linearity of the gradients between 30-90-130 cm at the 7 points over the site B, especially the points B2, B3, B4 and B6. Table 3 lists the polynomial coefficients of the gradients at the 12 points. Fig. 10 gives the horizontal gravity

changes over the site B. Fig. 9 and 10 were plotted using a 4-meter solution which is slightly different to the 14-meter solution (Table 2).

Tab. 2 Gravity differences between the ICAG points at 90 cm (μGal , preliminary)

Point	A	A1	A2	B	B1	B2	B3	B4	B5	B6	C1	C2
A	0	11	-5	-2317-2311-2296-2299-2313-2318-2295	2420-6338							
A1	-11	0	-16	-2327-2322-2306-2310-2324-2329-2306	2410-6349							
A2	5	16	0	-2311-2306-2290-2294-2308-2313-2290	2426-6333							
B	2317	2327	2311	0	5	21	17	3	-1	21	4737-4022	
B1	2311	2322	2306	-5	0	16	12	-2	-7	16	4732-4027	
B2	2296	2306	2290	-21	-16	0	-4	-18	-22	0	4716-4043	
B3	2299	2310	2294	-17	-12	4	0	-14	-19	4	4720-4039	
B4	2313	2324	2308	-3	2	18	14	0	-5	18	4734-4025	
B5	2318	2329	2313	1	7	22	19	5	0	23	4739-4020	
B6	2295	2306	2290	-21	-16	0	-4	-18	-23	0	4716-4043	
C1	-2420	-2410	-2426	-4737	-4732	-4716	-4720	-4734	-4739	-4716	0	-8759
C2	6338	6349	6333	4022	4027	4043	4039	4025	4020	4043	8759	0

Tab. 3 Polynomial gradient coefficients and dG(gravity differences) between 90 and 130 cm ($\mu\text{Gal}/\text{m}$, preliminary)

Point	a	b	c	dG/ μGal
A	25983	-318	7.6	-120
A1	25975	-328	14.9	-118
A2	25989	-321	9.3	-120
B	28290	-305	4.4	-118
B1	28276	-295	3.4	-115
B2	28256	-293	6.0	-112
B3	28274	-309	7.3	-117
B4	28292	-312	6.2	-119
B5	28289	-299	1.4	-118
B6	28261	-295	3.6	-115
C1	23282	-315	-	-126
C2	32041	-287	-	-115

6. Conclusion

During the ICAG 2005, relative gravity difference and precision levelling measurements were carried out in addition to the absolute gravity determinations. An optimal design was developed for the relative campaign for the network and the scheme of observations. The uncertainty of the adjusted g-difference is of the order of 1~2 μGal , probably $\pm 1.3 \mu\text{Gal}$ in the average. Consequently the uncertainty of the adjusted gravity gradient is about $\pm 1.3 \mu\text{Gal}/\text{m}$. The agreement of relative-only and absolute-only g values is about $\pm 1.3 \mu\text{Gal}$ if the relative differences are referred to the mean absolute g-value; uncertainty of the g-values of the combined adjustment is about $\pm 1 \mu\text{Gal}$; the combined adjustment gives also the offset of the absolute meters with an uncertainty of about 1 μGal ; the absolute g difference of ICAG 2005 to the previous comparison ICAG2001 is about $\pm 1 \mu\text{Gal}$.

Further investigation in the behaviour of each individual relative gravimeter will be discussed in a

forthcoming paper after the ICAG 2005 absolute gravity values will be officially released. Only then a final statement on the benefits of a combined adjustment of absolute and relative gravity observations and the impact on offset determination, e.g. at points with few absolute occupations can be made. This will allow an assessment of the necessity of the huge efforts associated with the relative network observation scheme.

Acknowledgement

We thank the BIPM staff for their administration and material supports during the ICAG relative campaign.

References

- Becker, M. and E. Groten: Relative Gravimeter Measurements at the 1981 Absolute Gravimeter Campaign in Paris Sèvres. BGI, Bulletin d'Information No. 52, 86-96, Toulouse 1983.
- Becker, M., Zhiheng Jiang, L. Vitushkin: Adjustment of Gravity Measurement at the Sixth International Comparison of Absolute Gravimeters ICAG-2001. Proceedings of the workshop IMG-2002, Instrumentation and Metrology in Gravimetry, IMG-2002, Institut d'Europe, Münsbach Castel, Luxemburg, 28-30 Oct., 2002, Cahiers of ECGS, Luxemburg, ISBN 2.-9599804-7-6, Vol. 22, pp. 49-56, 2003
- Vitushkin, L., M. Becker, Z. Jiang, O. Francis, T. M. van Dam, J. Faller, J.-M. Chartier, M. Amalvict, S. Bonvalot, N. Debeglia, S. Desogus, M. Diament, F. Dupont, R. Falk, G. Gabalda, C. G. L. Gagnon, T. Gattacceca, A. Germak, J. Hinderer, O. Jamet, G. Jeffries, R. Käker, A. Kopaev, J. Liard, A. Lindau, L. Longuevergne, B. Luck, E. N. Maderal, J. Mäkinen, B. Meurers, S. Mizushima, J. Mrlina, D. Newell, C. Origlia, E. R. Pujol, A. Reinhold, Ph. Richard, I. A. Robinson, D. Ruess, S. Thies, M. van Camp, M. van Ruymbeke, M. F. de Villalta Compagni, S. Williams: Results of the Sixth International Comparison of Absolute Gravimeters ICAG-2001, Metrologia, 39 (5), pp 407-424, 2002
- Jiang, Z. L. Vitushkin, M. Becker, O. Francis, P. Jousset, Matthiew Ferry, J. Mrlina, M. V. Ruymbeke, S. Naslin, Lee C., Tsai C. L., F. Dupont, B. Meurers, A. Kopaev, F. Pereira, H. Wilmes, R. Falk, D. Ruess, C. Ullrich, S. Deroussi, L. Metivier, G. Pajot, V. Palinkas, J. Kostelecky: ICAG05 Relative Measurement and Raw Data Analysis, ICAG 2005 workshop, BIPM, 12 Sept. 2005
- Vitushkin L., Z. Jiang, M. Becker, O. Francis, A. Germak, The Seventh International Comparison of Absolute Gravimeters ICAG-2005 at the BIPM, this Proceedings.

Modelling the vertical gravity gradient for gravity measurements reduction

H. Duquenne

Laboratoire de Recherche en Géodésie, Institut Géographique National, 6-8 avenue Blaise Pascal, F-77455 Marne la Vallée CEDEX, France

Abstract.

When establishing the gravity network, precise values of the vertical gravity gradient are needed to reduce measurements at the level of benchmarks. As the determination of the gradient is time-consuming and expensive, this article presents the first effort of modelling it within the scope of the new French gravity network. Some existing mathematical models based upon derivation of geoid undulation or gravity anomalies integration are listed and commented. Variants using terrain information are also tested. Gradients measured and modelled by several methods are compared, leading to a standard deviation of the differences of $14.5 \times 10^{-8} \text{ s}^{-2}$ (145 E) with the best method.

Keywords. Vertical gravity gradient.

1 Motivations and objectives

Since 2000, the Institut Géographique National has been measuring gravity on the points of the French geodetic GPS network. At the same time, the Ecole et Observatoire des Sciences de la Terre has created or re-measured 12 fundamental stations with an FG5 gravity meter. This work aims at:

- renovating the old gravity network, which dates

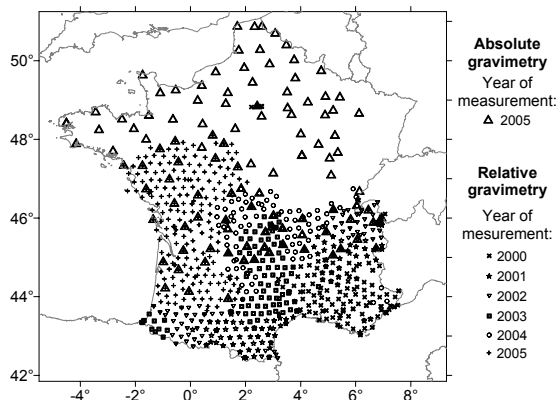


Fig. 1. Gravity measurements made by the IGN on the French geodetic network – progress state at the end of 2005.

- from 1983 and which has been partly destroyed,
- setting up an integrated geodetic and gravimetric network in accordance with the recommendations of the EUREF,
- verifying and improving the old gravity coverage in view of a more accurate geoid model.

An accuracy of $10 \times 10^{-8} \text{ m s}^{-2}$ ($10 \mu\text{Gal}$) is expected. It is planned to measure 200 points by absolute and relative gravimetry and 900 points by relative gravimetry. Figure 1 shows the state of the observations at the end of 2005. Presently the regions of Alsace and the Vosges are being observed by IGN. Observations should be completed by the end of 2008.

The gravity values are recorded with 3 kinds of instruments:

- Absolute Mico-g FG5 and A10 gravity meters,
- Relative Scintrex CG3M gravity meters.

Of course the vertical gravity gradient is needed to account for the various instruments heights and to reduce the measurements at the level of the benchmarks. Instruments height varies from about 9.5 cm with the Scintrex put directly on a benchmark, to 1.31 metres with the FG5. In some cases, the instrument height can be larger.

When using the FG5, the gravity gradient is always measured. In other cases, measurement of the gradient on the field is problematic because time consuming. For instance, a measurement with the A10 takes half an hour, this time would be increased by a factor of 3, if the gradient had to be measured.

So, the objective of this study is to determine if the vertical gravity gradient can be modelled from available data. The required accuracy is about some 10^{-8} s^{-2} (some $\mu\text{Gal/m}$ or 10 E).

2 Mathematical models

2.1 Expression of the vertical gradient in terms of geoid undulation

A first method to compute the vertical gravity gra-

dient has been offered in (Heiskanen and Moritz, 1967, p. 116). Starting from Laplace's equation applied to the anomalous potential and the fundamental equation of physical geodesy in the spherical approximation, they propose an expression for the radial derivative of the gravity anomaly Δg as a function of the geoid undulation and its derivative toward north and east. It can easily be shown that, *with the same approximation*, the geoid undulation can be replaced by the height anomaly ζ which is more commonly used in France. R stands for the mean radius of the Earth, r the radius vector, φ and λ the geographic latitude and longitude respectively, γ the normal gravity:

$$\begin{aligned} \frac{\partial \Delta g}{\partial r} = & \frac{2\gamma}{R^2} \zeta - \frac{\gamma}{R^2} \tan \varphi \frac{\partial \zeta}{\partial \varphi} \\ & + \frac{\gamma}{R^2} \frac{\partial^2 \zeta}{\partial \varphi^2} + \frac{\gamma}{R^2 \cos^2 \varphi} \frac{\partial^2 \zeta}{\partial \lambda^2} \end{aligned} \quad (1)$$

The vertical gravity gradient is then obtained by adding the normal gravity gradient, with g the gravity and h the height above the reference ellipsoid:

$$\frac{\partial g}{\partial h} \approx \frac{\partial \Delta g}{\partial r} + \frac{\partial \gamma}{\partial h} \quad (2)$$

This first method is only valid given the hypotheses of harmonicity of potential and spherical approximation. Furthermore the accuracy of the results is very sensitive to the resolution of the geoid or quasigeoid model and to truncation errors. As suggested in (Heiskanen and Moritz, 1967), it is convenient to approximate geoid undulation locally by a polynomial to compute its derivatives, choosing the degree to reach the best compromise between loss of resolution and gain in accuracy.

2.2 Integral methods

An integral method is presented in (Heiskanen and Moritz, 1967, pp. 115-116). From Poisson's integral and the development of gravity anomalies in spherical harmonics, they derived the formula:

$$\frac{\partial \Delta g}{\partial r} = \frac{1}{16\pi R} \iint_{\sigma} \frac{\Delta g - \Delta g_P}{\sin^3 \frac{\psi}{2}} d\sigma - \frac{2}{R} \Delta g_P \quad (3)$$

where P refer to the computation point, ψ is the spherical angle between the computation point and the integration point, σ the domain of integration (a

portion of the unit sphere). Then, the vertical gravity gradient can be obtained in the spherical approximation by equation (2). The computation point P and the running point are assumed to be on the same sphere of radius R surrounding the Earth to ensure harmonicity. As explained in the cited book, the indetermination $0/0$ which seems to affect the integrand when the integration point tends toward the computation point is easily overcome if the gravity anomaly is twice derivable northward and eastward. In that case the innermost element of integral (3) can be computed for a small circle of radius s_0 on the surface of the sphere:

$$\left(\frac{\partial \Delta g}{\partial h} \right)_i = \frac{s_0}{4R^2} \left(\frac{\partial^2 \Delta g}{\cos^2 \varphi \partial \lambda^2} + \frac{\partial^2 \Delta g}{\partial \varphi^2} \right) \quad (4)$$

Another integral approach is given in (Rózsa and Tóth, 2005). The radial derivative of the gravity anomaly is expressed as:

$$\frac{\partial \Delta g}{\partial r} = \frac{1}{4\pi R} \iint_{\sigma} \Delta g K(r, \psi) d\sigma \quad (5)$$

where K is a kernel function which depends not only upon the spherical distance ψ , but also on the vector radius of the computation point r :

$$K(r, \psi) = \sum_{l=2}^{\infty} \left(\frac{R}{r} \right)^{l+3} \frac{(l+1)(l+2)(2l+1)}{(l-1)} P_l(\cos \psi) \quad (6)$$

P_l is the Legendre polynomial of degree l . Formulas (5) and (6) can be derived from relations between the coefficients of the developments of Δg and its radial derivative in spherical harmonics, implying harmonicity and the spherical approximation. With equation (5), the computation point can be at a different level from the points where gravity anomalies are known (which should lie on the sphere of radius R). The drawback of (5) in its present form is that the integrand tends to infinity in the vicinity of the computation point. Although promising, this method has not been numerically tested in this study.

2.3 The use of terrain information

With the integration methods, terrain information can be used in a well known remove-compute-restore process. This has the advantage of smoothing the gravity anomalies and to ensure harmonic-

ity. For instance, refined Bouguer anomalies can be computed. Then, after integration by (3) or (5), the terrain effect on the vertical gradient of gravity is restored. Nevertheless, difficulties may occur with inconsistencies between point heights and the digital terrain model. Furthermore, the terrain effect on the gravity gradient is very sensitive to the distribution of neighbouring masses. Very high resolution DTM and sophisticated software are needed. When using the prism method, it is suitable to keep in mind the discontinuity of the vertical gradient on that face (Nagy et al., 2000). The inclination of the top face of the prism should be taken into account.

Terrain data are also useful to improve the interpolation of gravity anomalies before integration. In that case and as it will be viewed later, even medium-resolution digital terrain models and standard method bring appreciable gain in accuracy.

3 Data description

Gravity gradients

Measurements of vertical gravity gradients have been provided by four institutions: the Ecole et Observatoire des Sciences de la Terre, the Bureau de Recherches Géologiques et Minières, the Service Hydrographique et Océanographique de la Marine and the Institut Géographique National. They followed roughly the same procedure: at least two sets of gravity values were measured at three levels with a Scintrex CGM3 gravity meter. The gradient has been derived by linear regression. An accuracy of $3 \times 10^{-8} \text{ s}^{-2}$ to $7 \times 10^{-8} \text{ s}^{-2}$ ($3 \times 10^{-8} \mu\text{Gal}$ to $7 \times 10^{-8} \mu\text{Gal}$) has been reported. 31 measurements on 29 points have been made in all, 22 on the topo-

graphic surface and 7 inside buildings or in cellars (Figure 2). Two points were measured twice in different seasons and climatic conditions: the first one in the town of Clermont-Ferrand, the second one at the top of the old “Puy de Dôme” volcano. Variations reached 13×10^{-8} and $27 \times 10^{-8} \text{ s}^{-2}$, respectively. At the top of the Puy de Dôme, gravity gradients were measured at 2 places, one outside and one inside a garage. A difference of $50 \times 10^{-8} \text{ s}^{-2}$ was recorded. These remarks illustrate once again how difficult the measurement and modelling of the gravity gradient can be.

Quasigeoid model

In order to compute the vertical gravity gradient from height anomalies by the method described in section 2.1, the EGG97 quasigeoid model (Denker and Torge, 1998) has been used. This model has the advantages of a high resolution in grid spacing ($1' \times 1.5'$, i.e. 1.9 km) and a great accuracy.

Gravity data

The Bureau de Recherches Géologiques et Minières and the Bureau Gravimétrique International provided gravity data covering France, the neighbouring countries and marine areas (Figure 3). Their mean density is 0.59 points per square kilometer with significant variations: data are particularly sparse in some mountainous areas like the Alps and the center part of the Massif Central and in the Atlantic Ocean along the coastline. The accuracy of terrestrial gravity values has been evaluated to 0.25–0.75 mGal by the BRGM. These figures may worsen up to 1 or 2 mGal when computing Bouguer

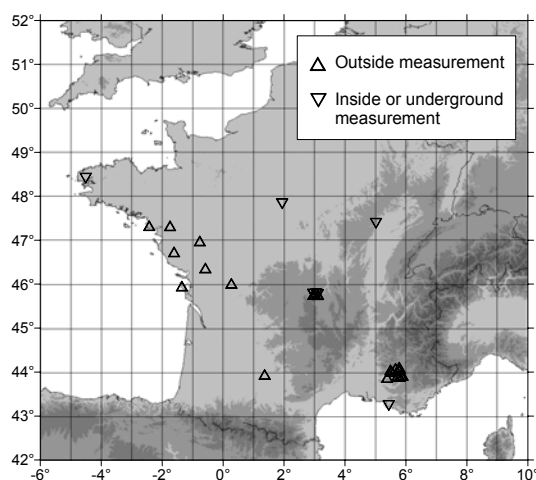


Fig. 2. Location of vertical gradient measurements.

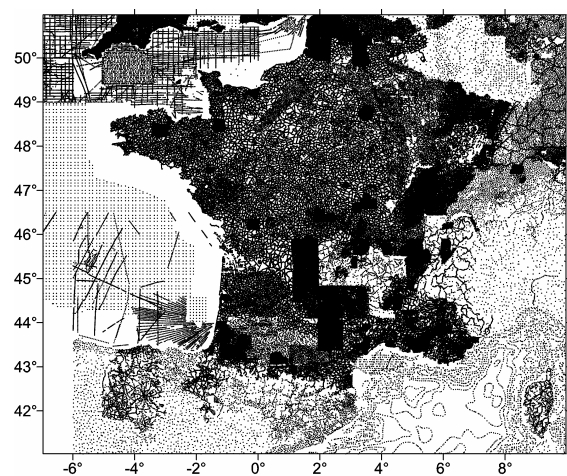


Fig. 3. Distribution of gravity data.

or residual anomalies due to errors in position or inconsistencies with the digital terrain model.

Digital terrain model

The digital terrain model has been extracted from the IGN data base. It covers the whole of France and surrounding countries with a resolution of 4.5" in latitude and 6" in longitude (about 140 m). Its accuracy has been evaluated to 5 metres (up to 15–20 m in rough terrain) in a comparison with 753 geodetic benchmarks.

4 Numerical tests

4.1 Comparisons between modelled and measured gradients

Five sets of vertical gravity gradients have been compared to values determined in the field. Only 22 points outside any building and located on the topographic surface were considered. Table 1 summarizes the results.

For the first test, the EGG97 height anomalies in addition to Eqs. (1) and (2) were used. For each point, the quasigeoid was locally approximated by a polynomial of degree 2 using 9 nodes of the grid. The height anomaly and its derivatives were computed from the polynomial.

For the 2nd test, point free-air gravity anomalies were gridded by collocation with a resolution of 0.0015°×0.002° (about 165 metres), then Eqs. (3) and (2) were applied. No terrain information was used.

In the 3rd test, point Bouguer anomalies were first computed then gridded with the same resolution as above. Residual gradients were obtained through Eq. (3). Terrain effects were restored with standard prism method and TC software (Forsberg, 1994). For this step, the point heights were assigned the

value interpolated in the digital terrain model augmented by 1 metre, in order to avoid two kinds of problems: singularities which occur if points lie just on the topographic surface and inconsistencies between the point heights and the DTM. Finally the normal gradient was added.

In the 4th test, Bouguer anomalies were first computed then gridded with a medium resolution of 0.01°×0.015°. Terrain effects were restored, leading to a grid of free-air anomalies made denser by up to 0.0015°×0.002°. Eq. (3) and (2) were used to compute gradients.

The 5th row of Table 1 appears as a reference: only the normal gravity gradient was computed and compared to measurements.

Comparison of tests 1 and 5 shows that the introduction of height anomalies and their derivatives improves the normal gradient only slightly. The spectral content of the quasigeoid is probably insufficient. Test number 2 proves that interpolating gravity anomalies carelessly, leads to an inaccurate solution. The remove-integrate-restore method employed in test number 3 does not give as good a result as the integration of high quality free-air anomalies, as in test number 4, which produces the best results. This is probably due to the poor resolution of the DTM (about 140 m) and inaccuracies in terrain effects: they were computed by splitting up the terrain into right rectangular prisms, neglecting the slope of the topographic surface. This has more serious consequences on the gradients than on the accelerations.

4.2 The influence of the radius of integration

In order to find an optimal radius of integration, vertical gravity gradients were computed with the same method as in the 4th test above, using a radius of integration increasing from 0° to 0.5°. The results

Table 1. Comparison of measured and modelled vertical gravity gradients.

Test #	Input data	Method	Measured – computed (10 ⁻⁸ s ⁻²)			
			Mean	Min	Max	Std Dev
1	Height anomalies	Combination of height anomalies and their derivative	-1.5	-53.1	29.6	18.0
2	Gravity anomalies	Integration of free-air anomalies (no terrain information used)	5.3	-55.9	86.9	27.0
3	Gravity anomalies	Removing terrain, interpolation, integration, restoration	-1.1	-49.1	36.6	17.6
4	Gravity anomalies	Removing terrain, interpolation, restoration, densification, integration	-1.5	-35.9	41.4	14.5
5	Just φ, h	Normal gradient	-2.2	-65.8	26.3	20.5

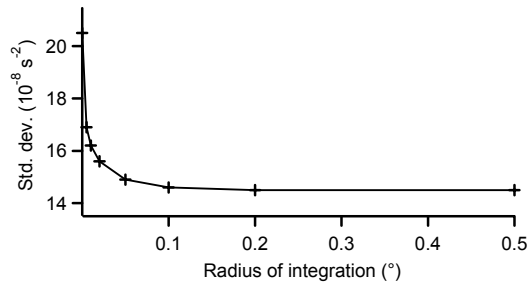


Fig. 4. Influence of the radius of integration on the accuracy of gradient prediction.

were compared with measured gradients. The graph in Figure 4 represents the standard deviation of the differences as a function of the radius. Points inside buildings were not considered. From this we can conclude that an optimal radius would be between 0.1° and 0.2°, that is 10 to 20 kilometres. Obviously this value would have to be adapted to the accuracy of the method of computation. Furthermore, this value confirms that the spectral contents of gradients are concentrated in the short wavelengths, and that global geopotential models are of little use for gradient modelling, as long as their resolution exceeds ten kilometres or so.

4.3 Gradients inside buildings

In this section, the accuracies of gradient prediction for two sets of points are compared: points outside buildings, on the topographic surface and points inside buildings or in cellars. As shown in Table 2, the precision of prediction is about 2.5 times worse for the latter set. This confirms that gradient modelling is somewhat adventurous inside buildings. Accurate local mass models are needed and direct measurement could be the best solution.

Table 2. Comparison of the quality of gradient prediction of points outside and inside buildings.

Points	Point number	Measured – computed		(10 ⁻⁸ s ⁻²) Std Dev
		Min	Max	
Outside	22	-35.9	41.4	14.5
Inside	7	-54.2	48.2	36.7

5 Conclusions and perspectives

With a view to reducing field operations when the new French gravimetric network is established, several methods to predict vertical gravity gradient have been compared to a set of 22 measured gradients. Using height anomalies and their derivatives issued from the EGG97 quasigeoid model, the accuracy of $20.5 \times 10^{-8} \text{ s}^{-2}$ (205 E) of the normal gradient was slightly improved at the level of $18.0 \times 10^{-8} \text{ s}^{-2}$. Better results were obtained by integrating free-air gravity anomalies carefully interpolated with the help of a medium-resolution digital terrain model: a standard deviation of $14.5 \times 10^{-8} \text{ s}^{-2}$ was reached with a radius of integration of 10~20 km. This accuracy is not sufficient to ensure a proper reduction of measurements in a modern high-precision gravity network. The use of high-resolution terrain models and more accurate algorithms to compute terrain effects on gravity gradients seems to be the key issues in view of reaching a precision of some 10^{-8} s^{-2} .

References

- Denker, H. and Torge, W. (1998). The European gravimetric quasigeoid EGG97 – An IAG supported continental enterprise. In: IAG Symposia 119:249-254, Springer Verlag.
- Heiskanen, W.A. and Moritz, H. (1967). Physical Geodesy. Institute of Physical Geodesy, T.U. Graz, Austria. Reprint 1999.
- Forsberg, R. (1994). Terrain effects in Geoid Computations. Lectures Notes. In: International School for the Determination and Use of the Geoid. International Geoid Service. DIAR, Milan, Italy.
- Nagy, D., Papp, G. and Benedek, J. (2000). The gravitational potential and its derivatives for the prism. *J Geod* 74:7-8, pp 552-560.
- Rozsa, S. and Toth, G. (2005). Prediction of Vertical Gravity Gradients Using Gravity and Elevation Data. In: A Window on the Future of Geodesy, IAG Symposia 128:344-349, Springer Verlag.

The Seventh International Comparison of Absolute Gravimeters ICAG-2005 at the BIPM. Organization and preliminary results

Leonid Vitushkin¹, Zhiheng Jiang¹, Matthias Becker², Olivier Francis³, Alessandro Germak⁴
and
Martine Amalvict⁵, Roger Bayer⁶, Mirjam Bilker-Koivula⁷, Giancarlo D'Agostino⁴, Sergio Desogus⁴,
James Faller⁸, Reinhard Falk⁹, Jacques Hinderer⁵, Carey Gagnon¹⁰, Thomas Jakob⁶, Evgeny Kalish¹¹,
Jakub Kostelecky¹², Chiungwu Lee¹³, Jacques Liard¹⁰, Yuriy Lokshyn¹⁴, Bernard Luck⁵, Jaakko Mäkinen⁷,
Shigeki Mizushima¹⁵, Nicolas Le Moigne⁶, Vladimir Nalivaev¹, Claudio Origlia⁴, Vojtech Palinkas¹²,
Enrique Rodriguez Pujol¹⁶, Philippe Richard¹⁷, Lennart Robertsson¹, Diethard Ruess¹⁸, David Schmerge¹⁹,
Yury Stus¹¹, Sergiy Svitlov¹⁴, Simon Thies^{17,*}, Christian Ullrich¹⁸, Michel Van Camp²⁰,
Artyom Vitushkin²¹, Herbert Wilmes⁹

1 Bureau International des Poids et Mesures (BIPM), Sèvres, France

2 Institute of Physical Geodesy, Darmstadt University of Technology (IPGD), Darmstadt, Germany

3 University of Luxembourg and Centre Européen de Géodynamique et de Séismologie (ECGS), Luxembourg

4 National Institute of Metrological Research, Torino, Italy

5 École et Observatoire des Sciences de la Terre (EOST), Strasbourg, France

6 Dynamics of the Lithosphere Laboratory CNRS/Montpellier University, Montpellier, France

7 Finnish Geodetic Institute (FGI), Masala, Finland

8 JILA, University of Colorado – National Institute of Standards and Technology (NIST), Boulder, Colorado, USA

9 Federal Agency of Cartography and Geodesy (BKG), Frankfurt/Main, Germany

10 Natural Resources Canada (NRCan), Ottawa, Canada

11 Institute for Automation and Electronics, Russian Academy of Sciences, Novosibirsk, Russian Federation

12 Geodetic Observatory Pecny (GOP), Research Institute of Geodesy, Topography and Cartography, Czech Republic

13 Center for Measurement Standards, Industrial Technology Research Institute (CMS/ITRI), Chinese Taipei

14 National Scientific Centre “Institute of Metrology”, Kharkov, Ukraine

15 National Metrology Institute of Japan, National Institute for Advanced Industrial Sciences and Technology (NMIJ/AIST), Tsukuba, Japan

16 Instituto Geográfico Nacional (IGN), Madrid, Spain

17 Swiss Federal Office of Metrology and Accreditation (METAS), Bern-Wabern, Switzerland

18 Federal Office of Metrology and Surveying (BEV), Vienna, Austria

19 United States Geological Survey, Longmont, Colorado, USA

20 Royal Observatory of Belgium (ROB), Brussels, Belgium

21 Minex-Engineering Corp., Antioch, California, USA

***Abstract.** ICAG-2005, an international comparison of absolute gravimeters, was held in September 2005 at the Bureau International des Poids et Mesures (BIPM), Sèvres, France. Nineteen absolute gravimeters performed measurements of free-fall acceleration g at eleven sites of the BIPM gravity network. Fifteen relative gravimeters were used to measure the vertical gravity gradients and to provide gravity ties between the sites. The

maximum g -difference was about 9 mGal. The status of a pilot study was agreed for this comparison by the Consultative Committee for Mass and Related Quantities. For the first time in the ICAG series, a technical protocol specifying the organization, measurement strategy, data processing, calculation of the uncertainties and presentation of the results, was developed for the ICAG 2005. The unweighted mean value of the results of absolute measurements referred to the site A is presented and compared with the similar values obtained in ICAG-1997 and ICAG-2001.

* deceased, April 2006

Corresponding author : Leonid Vitushkin, BIPM,
LVitushkin@bipm.org

Keywords. gravimetry, absolute gravimetry, international comparison

1 Introduction

The seventh in the series of International Comparisons of Absolute Gravimeters begun in 1980, ICAG 2005 was carried out at the BIPM (Sèvres, France). This comparison was organized by the Working Group on Gravimetry of the Consultative Committee for Mass and Related Quantities (CCM) of the International Committee of Weights and Measures (CIPM), Study Group 2.1.1 of the International Association of Geodesy (IAG) and the BIPM.

Comparing the measurement results of absolute gravimeters of the highest metrological quality is the best, and perhaps the only, way to test the uncertainty in absolute measurements of free-fall acceleration.

In a worldwide metrology system all the measuring instruments in any measurement field should be traceable to a primary measurement standard in the corresponding field (often, but not necessarily, the national standard). A primary standard is designated or widely acknowledged as having the highest metrological qualities and whose value is accepted without reference to other standards of the same quantity [1].

According to the CIPM Mutual Recognition Arrangement (CIPM MRA) between more than sixty national metrology institutes (NMIs) worldwide (see the information on the CIPM MRA on the website of the BIPM [2]), the equivalence of national measurement standards should be established in key comparisons (KCs). The participants of the KC are the NMIs or other laboratories designated by a NMI as holding the national measurement standards. In the field of gravimetry very often absolute gravimeters are not recognized as the national metrology standards. Such absolute gravimeters can also participate in the KC and their designation can be obtained during the course of the KC. According to the CIPM MRA rules, the results of laboratories which are not NMIs or designated by NMIs cannot appear on the Key Comparison Data Base (KCDB), neither can their results be used in calculation of the Key Comparison Reference Value (KCRV). The KCDB also contains lists of calibration and measurement capabilities (CMCs) offered by NMIs and designated laboratories to the general public. Whenever possible, CMC claims must be supported by KC results.

Ideally, the determination of the KCRV in the ICAGs is a natural way to obtain the shifts of the results of the individual gravimeters from the KCRV and to use them as a correction in the measurement of free-fall acceleration. The realization of such a programme is possible if the reproducibility in the measurement of individual gravimeters is confirmed.

Considering that choosing KC status would limit the participation in ICAG-2005, the BIPM and the steering committee (L. Vitushkin, M. Becker, O. Francis, A. Germak, Z. Jiang) suggested that this comparison be organized as a pilot study. The status of a pilot study made it possible to be more flexible in the invitation of the participants which could be not only the NMIs but also other organizations, for instance the geophysical institutes.

Except for a more inclusive participation, the ICAG-2005 was organized according the rules for KCs. In particular, a technical protocol specifying the organization, measurement strategy, data processing, calculation of the uncertainties and presentation of the results, was developed.

2 Organization of absolute measurements.

To prepare for the ICAG-2005, the BIPM constructed two new outdoor sites having a difference of free-fall acceleration g of about 9 mGal to make it possible to calibrate relative gravimeters. Prior to the absolute measurements, the vertical gravity gradients at all the sites and the ties (differences of g between the sites) of the BIPM gravity network were measured using seventeen relative gravimeters [3].

The gravity network of the BIPM consists of four sites: A, A0, A1 and A2 in the Observatory building, seven sites: B, B1 – B6 in the Pavillon du Mail and two outdoor sites: C1 and C2.

The FG5-108 absolute gravimeter belonging to the BIPM occupied the B3 site from 3 to 24 September 2005, during the absolute measurements. This gravimeter has performed regular (almost daily) measurements to monitor the stability of the gravity field of the BIPM. With the same goal, the FG5-202 absolute gravimeter (Royal Observatory of Belgium) was used to check the stability of the gravity field at the A2 site from 6 to 21 September. Nineteen absolute gravimeters from seventeen countries and the BIPM have participated in the comparison (Table 1).

As seen in Table 1, some of gravimeters have already participated in two or even three ICAGs at

the BIPM. It is interesting to analyze, in particular, the reproducibility of their results.

The gravimeters IMGC-2 [4] and TBG are that with the symmetric (up-down) trajectory of free moving test body. All other gravimeters are of a free-fall type. The FGC-1 gravimeter [5] has an original cam-driven dropper mechanics different from that of FG5 gravimeters.

In the GABL-G gravimeter an iodine-stabilized diode-pumped solid-state Nd:YAG laser at 532 nm is used as a coherent light source in the laser displacement interferometer. All other gravimeters used the iodine-stabilized He-Ne lasers at 633 nm.

Table 1. Participation of institutes and gravimeters participated in ICAG-1997, ICAG-2001 and ICAG-2005

	Country, institute	Gravimeter		
		1997	2001	2005
1	Germany, BKG	FG5-101	FG5-101	FG5-101
2	BIPM	FG5-108	FG5-108	FG5-108
3	Belgium, ORB	FG5-202	FG5-202	FG5-202
4	France, EOST	FG5-206	FG5-206	FG5-206
5	Switzerland, METAS		FG5-209	FG5-209
6	Spain, IGN		FG5-211	FG5-211
7	Japan, AIST/NMIJ		FG5-213	FG5-213
8	Czech Republic, GOP			FG5-215
9	Luxemburg, UL/ECGS			FG5-216
10	Finland, FGI	JILAg-5	JILAg-5	FG5-221
11	Chinese Taipei, CMS/ITRI			FG5-224
12	France, DLL CNRS/MU			FG5-228
13	USA/USGS			A10-008
14	USA/JILA CU/NIST			FGC-1
15	Russia/ IAE RAS	GABL-E		GABL-G
16	Italy/INRIM	IMGC	IMGC	IMGC-2
17	Austria/BEV	JILAg-6	JILAg-6	JILAg-6
18	Canada/NRCan	JILA-2	JILA-2	JILA-2
19	Ukraine/NSC IM			TBG

The BIPM calibrated the frequencies of all the lasers and verified the frequency of Rb-clocks and GPS receivers of the absolute gravimeters. The atmospheric pressure was measured continuously during the comparison using a calibrated digital barometer and these data were provided to the participants.

In addition, for the first time the laser beam shapes were determined using the CMOS camera for those gravimeters, whose construction allows this measurement.

During the comparison up to nine absolute gravimeters occupied simultaneously the sites of the BIPM gravity network. The absolute gravimeters usually were installed on the sites and adjusted in

the day-time and the measurements were performed in the night (during at least 12 hours).

3 Results of absolute measurements.

97 absolute measurements at eleven sites of the BIPM were performed in the period from 3 to 25 September 2005.

The results of the measurements of FG5-108 at B3 and FG-202 at A2 were stable with the standard deviation of the mean results within 1 μ Gal. This confirms the appropriate stability of gravity field at the BIPM during the comparison.

According to the Technical Protocol two forms of the presentation of the results of the absolute measurements were used.

For the gravimeters JILA, FG5 and A10 the raw data (pairs of time and length intervals in the format used in the software developed by “Micro-g Solutions, Inc.”, now “Micro-g La Coste, Inc.”) were presented. Then, as in ICAG-1997 and ICAG-2001, the raw data were re-processed using, when possible, the same software. This, in principle, should allow better understanding of the sources of the uncertainties.

For the gravimeters IMGC-2, TBG and GABL-G the presentation of raw data is not possible because data formats different from that used in the gravimeters JILA, FG5 and A10.

Taking in consideration that 1) in the future, wider participation of the gravimeters of different types is possible, including instruments based on atom interferometry, and 2) the participating laboratory is responsible for the presentation of the final results of the measurements obtained during the comparison, the Technical Protocol of ICAG-2005 requires that the final results of the absolute measurements be calculated and presented by the participants.

Finally, the pilot laboratory (BIPM) obtained the raw data from the operators of JILA, FG5 and A10 gravimeters and the final results from all the gravimeters, as calculated and presented by the participants.

It is worth noting, that for the most part, the differences between the results re-processed in the unified manner and those presented by the operators were within 1 μ Gal.

The CIPM MRA “Guidelines for CIPM key comparisons” (see on BIPM website [2]) define the rules that we followed for the preparation of the report. The first draft, draft A, includes the results transmitted by the participants. It is confidential to the participants. The second draft, draft B, is no

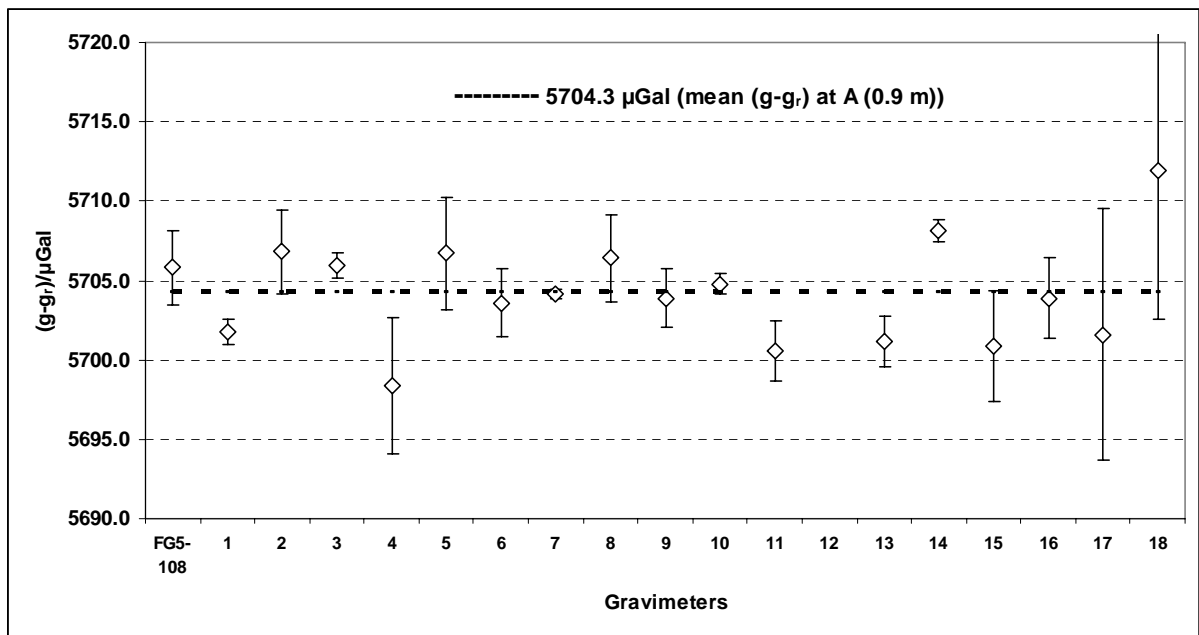


Fig.1. Results of the measurements of the absolute gravimeters during ICAG-2005 transferred to the site A (height of 0.9 m).

longer confidential and may be the subject of a publication. It must include uncertainty estimates for all results. For Key Comparisons, draft B is published as a final report on the KCDB, upon approval of the Consultative Committee.

At the time of preparation of this paper not all the uncertainty budgets were presented and it was decided to present the results of the comparison without the names of the absolute gravimeters.

The results of the absolute measurements of individual gravimeters in ICAG-2005 are presented in Fig. 1 with their standard deviations. The unweighted means of the results of each gravimeter at each site are transferred to site A at a height of 0.9 m above the pillar. The ties between the sites are calculated as the g -differences of the means of all the results of gravimeters measured at that site. Such g -differences (ties) were used to transfer the g -value from each site to site A.

The unweighted mean of all the results transferred to A (at 0.9 m) is $(g - g_r)_A = 5704.3 \mu\text{Gal}$ with the standard deviation of $3.2 \mu\text{Gal}$. The reference value is $g_r = 980920000 \mu\text{Gal}$.

In Fig. 2 the unweighted mean values $(g - g_r)$, obtained at the site A (height of 0.9 m) in three consecutive comparisons at the BIPM in 1997 ([6], Table 7), 2001 ([7], Table 5a) and 2005, are compared.

These values are $(5707.8 \pm 2.8) \mu\text{Gal}$, $(5698.5 \pm 2.2) \mu\text{Gal}$ and $(5704.3 \pm 3.2) \mu\text{Gal}$ in 1997, 2001 and 2005, respectively.

The results the absolute gravimeter FG5-108 belonging to the BIPM (transferred to A at the height of 0.90 m), obtained in the comparisons in 1997, 2001 and 2005 are also shown in Fig. 2. All these results are within $1 \mu\text{Gal}$.

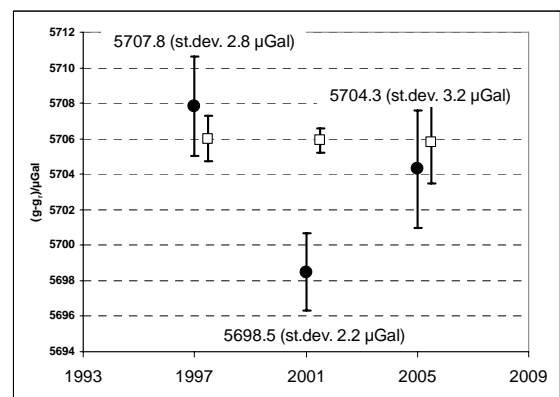


Fig. 2. The unweighted means (\bullet) of the results of all the absolute gravimeters transferred to A (at 0.9 m) obtained in the ICAGs in 1997, 2001 and 2005, and that of FG5-108 (\square).

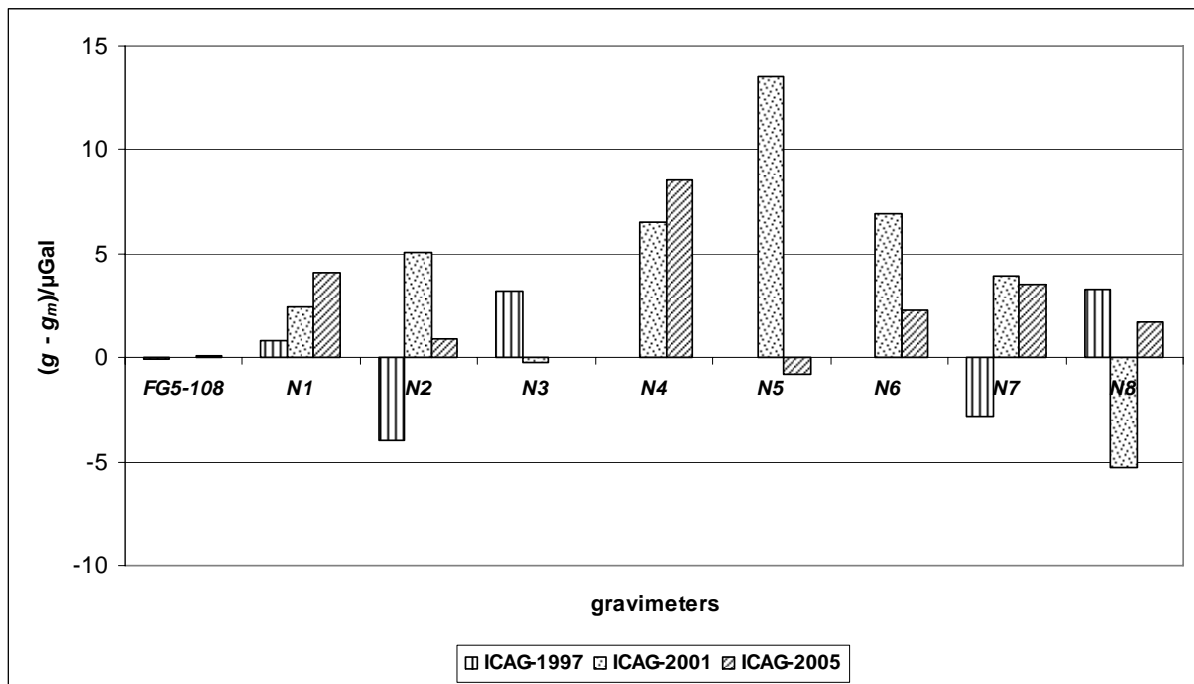


Fig. 3. The results of the measurements of the individual absolute gravimeters, obtained in the ICAGs at the BIPM in 1997, 2001 and 2005 and transferred to site A at the height of 0.9 m. $g_m = 980925705.9 \mu\text{Gal}$ is the mean of g -values of the FG5-108, obtained in 1997, 2001 and 2005.

The availability of the results of from two or even three consecutive comparisons for some absolute gravimeters allows the analysis of the reproducibility of the results of their measurements on condition that the gravity field at the BIPM is stable. One can come to some conclusions on such reproducibility from the Fig. 3. This figure plots the deviations of the results of individual absolute gravimeters, obtained in the comparisons from 1997 to 2005, with respect to the mean value $980925705.9 \mu\text{Gal}$ of the results of FG5-108 at A (0.90 m) over these three comparisons..

As seen in Fig. 3, the deviations of the results of the measurements of individual gravimeters from the reference value vary in sign and magnitude. The changes in the results of the measurements by the same gravimeters in three ICAGs can reach about $10 \mu\text{Gal}$. However, the changes in measured values do not imply changes of gravity field of the BIPM for, in this case, all the changes would be of the same sign and of almost the same magnitude. This demonstrates the level of the reproducibility of the measurements of absolute gravimeters.

One of the reasons for such low reproducibility could be the change of the shape of the laser beam

in the interferometer [8-10]. It was possible to measure the beam shape of majority of absolute gravimeters that participated in ICAG-2005. Results showed that the diameters of the output beams from the beam splitter of the interferometer, measured by CMOS camera were between 3.2 mm and 6.2 mm (at an intensity level $1/e^2$ relative to the maximum) for the different gravimeters at the same position of the cross section where the beam was measured. If the laser beam diameter is smaller than a certain cut-off value, which depends on the wavelength, the diffraction correction should be calculated. This correction depends on the optical layout of the interferometer (for example, on the difference of the lengths of the measuring and reference arms of the interferometer). In ICAG-2005 the diffraction correction was applied only for the gravimeter GABL-G, which uses a 532 nm laser.

When all the uncertainty budgets for all the absolute gravimeters are completed, a global adjustment of absolute and relative data obtained at all the sites of the BIPM gravity network will be performed to obtain the final weighted results at the sites A and B.

4 Conclusions

The number of the absolute gravimeters participating in the ICAGs at the BIPM continues to increase.

The development of the Technical Protocol brings the ICAG closer to a CIPM key comparison. One aim of CIPM key comparisons is to determine the degree of equivalence among national standards. ICAG-2005 paves the way for including national standards of gravimetry in this programme.

The work on the evaluation of uncertainty budgets for measurement using the absolute gravimeters should be continued.

The analysis of the results of three consecutive ICAGs at the BIPM in 1997, 2001 and 2005 shows that the level of irreproducibility of the results of absolute gravimeters cannot be attributed to long-term instability in the gravity field at the BIPM.

Further investigations of the sources of the uncertainties in absolute measurements should be continued and the methods of adjusting the gravimeters should be improved to make them less operator dependent and better controlled, as, for example, control of the laser beam-shape and evaluation of the diffraction correction, if necessary.

The organization of regional multilateral comparisons of the absolute gravimeters with the appropriate technical protocol is of importance for the further study of their metrological characteristics and of the establishment of the link between the ICAG at the BIPM and regional comparisons and for better understanding of the role of the Key Comparison Reference Values in absolute measurement of free-fall acceleration.

As was concluded after all the previous comparisons, we continue to emphasize the importance of participation in future comparisons of various types of absolute gravimeters based on different basic principles and different designs.

It is important to develop a unified format for the presentation of the final results of the measurements of absolute gravimeters, which will contain the information necessary for the comparison of their results and for the application of the data of the measurements of gravity field.

Regular monitoring of the gravity field at the BIPM between the comparisons as well as continuous monitoring during the comparison should be continued to control the possible changes of gravity field at the BIPM.

The experience in the organization of the pilot study ICAG-2005 according to the rules of CIPM

key comparisons is invaluable for the improvement of the technical protocol for the next ICAG at the BIPM in 2009 and for the organization of regional comparisons of absolute gravimeters.

Acknowledgments

The authors wish to thank Mr J.Labot, Mrs Yimei Lee and all staff members of the BIPM for their help in the preparation and execution of the ICAG-2005. We thank Dr R.Davis for helpful discussions on the preparation of the technical protocol and organization of comparison.

References

1. International Vocabulary of Basic and General Terms in Metrology, ISO, 1993
2. Mutual recognition of national measurement standards and of calibration and measurement certificates issued by national metrology institutes, International Committee for Weights and Measures, 1999, available from <http://www.bipm.org>
3. Z.Jiang, et al. (2006), Relative campaign during the International Comparisons of Absolute Gravimeters ICAG-2005 and the strategy of data treatment combined with the absolute results, in this Proceedings.
4. A.Germak, S.Desogus, C.Origlia (2002), Interferometer for the IMGC rise-and-fall absolute gravimeter, *Metrologia*, vol 39, pp. 471-475.
5. A.L.Vitouchkine, J.E.Faller (2002), Measurement results with a small cam-driven absolute gravimeter, *Metrologia*, vol. 39, pp. 465-469.
6. L.Robertsson et al. (2001), Results from the Fifth International Comparison of Absolute Gravimeters, ICAG-97, *Metrologia*, vol. 38, pp. 71-78.
7. L.Vitushkin et al. (2002), Results of the Sixth International Comparison of Absolute Gravimeters, ICAG-2001, *Metrologia*, vol. 39, pp. 407-424.
8. V.V.Lyubimov, V.L.Shur, I.Sh.Etsin (1978), Diffraction phenomena in a two-beam laser interferometer, *Opt.Spectrosc.* (USSR), vol. 45, No. 2, pp. 204-207.
9. G. Mana (1989), Diffraction effects in optical interferometers illuminated by laser sources, *Metrologia*, vol. 26, pp.87-93.
10. D. van Westrum, T.M.Niebauer (2003), The diffraction correction for absolute gravimeters, *Metrologia*, vol.40, pp. 258-263.

Quality of Lithuanian National Gravimetric Network

E. Parseliunas, P. Petroskevicius

Vilnius Gediminas Technical University, Sauletekio al. 11, LT-10223 Vilnius, Lithuania

Abstract. In 1994 the absolute gravity measurements were carried out by J. Mäkinen (Finish Geodetic Institute) at three stations of Lithuania. Measurements were performed by ballistic gravimeter JILAg-5. Absolute gravity measurements were repeated in 2002. The 5 μGal precision of the gravity acceleration was derived. The differences between the gravity acceleration values, obtained in 1994 and 2002 fall into the limits of the accuracy of measurements.

These three stations form the National zero order gravimetric network – the basis of the new gravity system and further densification of the gravimetric network.

From 1998 to 2001 the National first order gravimetric network was observed. There are 51 gravimetric points in the National first order gravimetric network, evenly distributed in the territory of country. Measurements were carried out by *LaCoster & Romberg* gravimeters. Each gravity difference of the network was measured at least three times with 3 or even 6 gravimeters. Accuracy of adjusted gravity acceleration values of 3–4 μGal was received, and the standard deviation of the single gravity difference observation of 14 μGal was derived.

In July of 2006 some points were re-observed by 2 pairs of SCINTREX CG-5 gravimeters. Accuracy of adjusted gravity acceleration values of 3–7 μGal was received, and the standard deviation of the single gravity difference observation of 17 μGal was derived. Comparison of computed gravity acceleration values shows, that differences are bigger, than it was expected. It can be concluded that further studies of the stability of the gravimeters performance and the uncertainties in relative measurements is still required.

Keywords. Gravimetric network, gravimeter, gravity measurements

1 Introduction

Analysis of the gravimetric networks of the neighbour countries [1–6] show, that existing gravimetric control of Lithuania do not fit to the modern requirements. Lithuanian National Gravimetric Network was established and gravimetric reference was evaluated by support of

Finnish, Danish, Polish and USA specialists in 1994–2001.

National Lithuanian Gravity Network is built on three absolute gravity stations measured by dr. Jaakko Mäkinen (Finnish Geodetic Institute) in 1994 and 2002 [7–9]. Network consists of 51 gravimetric points. Observations were performed by 3 – 6 *LaCoster & Romberg* gravimeters. Calibration of gravimeters was performed between absolute gravimetric points in Lithuania and Poland. Errors of gravity accelerations changes determined between points are less than 5 μGal .

By creating the National gravimetric Network the IGSN71 datum was transferred over the territory of the country. Network is a precise gravimetric reference for detailed research of gravity field and other activities.

2 Absolute gravity stations

National Lithuanian Gravity Network is built on three absolute gravity stations measured by dr. Jaakko Mäkinen (Finnish Geodetic Institute) in 1994 and 2002 (Figure 1). These stations form the zero order gravimetric network.

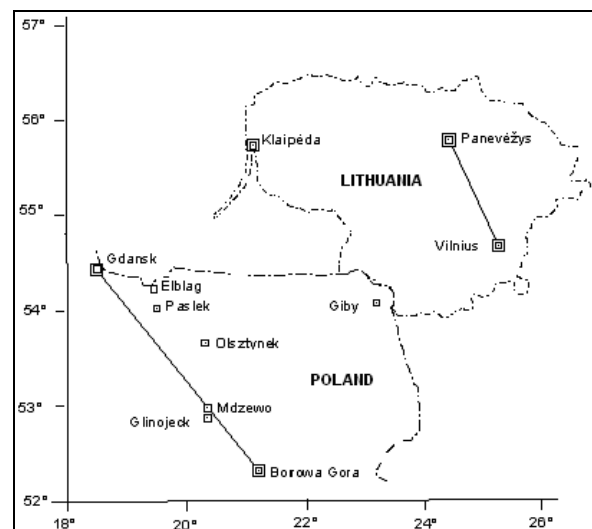


Fig. 1. Scheme of absolute gravity stations and calibration lines

The ballistic gravimeter JILAg-5 was used. Sites for gravimetric points were selected in calm and geologically stable locations. Station VILNIUS –

cellar, PANEVEŽYS – basement and KLAIPEDA – ground floor. Monuments for the points are – reinforced concrete poles, 2 m in depth. There are brass marks fixed into monuments. Elevation of marks was determined by precise levelling.

Absolute gravity measurements were organized by series of 25 falls. Time period of each series was 5 minutes, and time between series – 10 minutes. Total number of measurements in 1994 and 2002 is presented in Table 1 and 2 respectively.

Table 1. Absolute gravity measurements in 1994

Station	Period	Height, mm	Number of series	Number of falls
VILNIUS	07 15–17	826	168	4200
KLAIPĒDA	07 22–23	835	140	3500
PANEVĒŽYS	07 28–29	832	110	2750

Table 2. Absolute gravity measurements in 2002

Station	Period	Height, mm	Number of series	Number of falls
VILNIUS	08 04–05	832	102	2550
KLAIPĒDA	08 07–09	842	142	3550
PANEVĒŽYS	08 11–13	843	144	3600

Differences between gravity values at marker height Δg_0^{02-94} determined in 1994 and 2002 are presented in Table 3. These are not large, and do not exceed 10,8 μGal , that is within an observation accuracy. Mean values of gravity g_0^v at the markers level were used for the new adjustment of National Lithuanian Gravity Network.

Table 3. Absolute gravity stations

Station name	Δg_0^{02-94} , μGal	g_0^v , μGal
VILNIUS	-10,7	981459083,6
KLAIPĒDA	-4,4	981547766,6
PANEVĒŽYS	-4,2	981527060,0

Satellite points have been established at the close neighbourhood of absolute gravimetric points. Gravity value at the satellite points was determined by relative observations from absolute points using *LaCoste & Romberg* gravimeters. A precise levelling and soil moisture measurement of the points is performed periodically. Ground water level is observed continuously.

Lithuanian National Gravimetric Network was related to absolute stations in Poland BOROWA GORA and GDANSK and to gravimetric point GIBY. In these points the calibration of *LaCoste & Romberg* gravimeters *G-1012*, *G-1036*, *G-1078*, *G-1084* was performed.

3 Relative gravity measurements

The relative gravity measurements have started in 1998. Two *LaCoste & Romberg* gravimeters *G-618* and *G-867* were used. Initially the gravimetric network consists of 64 points [9]. Gravimeters were calibrated at absolute gravity stations in Denmark, Estonia, Latvia and Lithuania. The measurement campaign was organized in “loops” of 8 to 12 points, and the initial and final point was the same (more often – absolute gravity station). Totally the 16 loops were performed.

There are the 51 gravity point in the final scheme of the Lithuanian National Gravimetric Network (including 3 absolute gravity stations) (Figure 2) [10–12].

Points are located at the solid public buildings (mostly – churches), either on the stable fundaments of the buildings.

Relative gravity measurements were performed by *LaCoste & Romberg* gravimeters in 1999, 2000 and 2001. Scale factors of the gravimeters *G-191*, *G-192*, *G-193* were detected by intensive measurements on the calibration line VILNIUS–PANEVEŽYS. Linear scale factors k and its standard deviations m of *LaCoste & Romberg* gravimeters are presented in Table 4.

Totally were observed 117 gravity differences. Every difference was measured three times by 3 or even 6 *LaCoste & Romberg* gravimeters: *G-1012*, *G-1036*, *G-1078*, *G-1084* by Polish Institute of Geodesy and Cartography and *G-191*, *G-192*, *G-193* by NIMA. There are 62 closed figures (48 triangles and 14 quadrangles) in the gravimetric network (Figure 2). Maximal closing error 27 μGal . 60% of closing errors are below 10 μGal .

4 Network adjustment and quality analysis

Several adjustments of the gravimetric network following different strategies were made [11]. In Table 5 some data on relative gravity measurements is presented: k – number of observed points, n – number of measurements, m – standard deviations of single measurement in μGal . Total number of measurements is 6200.

Lithuanian National Gravimetric Network was adjusted in six variants:

1. Six initial points – absolute gravity stations (VILNIUS, KLAIPĒDA, PANEVĒŽYS, BOROWA GORA and GDANSK) and station GIBY – and their standard deviations were used. All relative gravity measurements were put in the adjustment procedure.

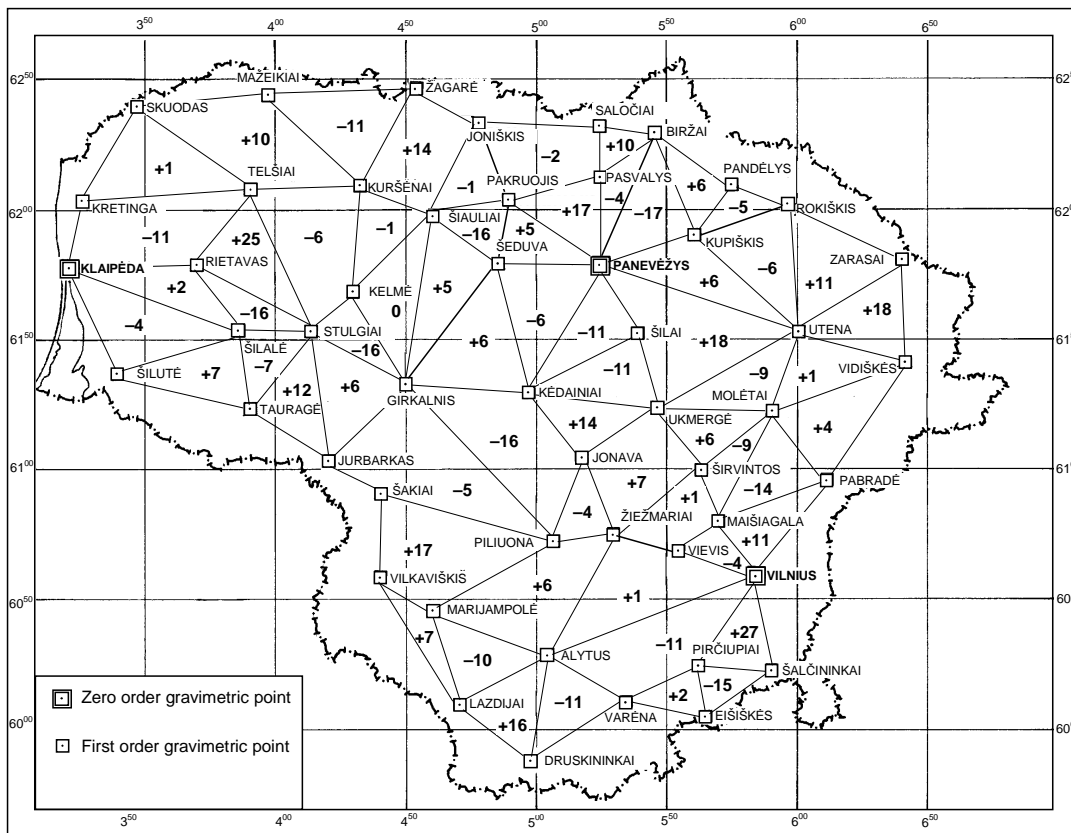


Fig 2. Scheme of Lithuanian National Gravity Network and misclosures

2. Three initial points – absolute gravity stations (VILNIUS, KLAIPĖDA, PANEVĖŽYS) and their standard deviations were used. Relative gravity measurements of 1998 was not used.
3. Three initial points – absolute gravity stations (VILNIUS, KLAIPĖDA, PANEVĖŽYS), but their standard deviations were not used. All relative gravity measurements were put in the adjustment procedure.
4. As (3), but standard deviations of initial points were used as well.
5. Only one initial point – absolute gravity station VILNIUS – was used.
6. Two initial points – absolute gravity stations VILNIUS and PANEVĖŽYS – were used.

Differences of gravity acceleration values, computed in six variants, do not exceed 8 μGal .

Corrections to absolute gravity stations after adjustment are presented in Table 6. It is seen, that in all adjustments corrections are slightly bigger to station KLAIPĖDA. It is systematic effect, which probably was called due the station was not included into detection of gravimeters scale factors.

Table 4. Linear scale factors of *LaCoste & Romberg* gravimeters

Gravimeter	1998		1999		2000		2001	
	<i>k</i>	<i>m</i>	<i>k</i>	<i>m</i>	<i>k</i>	<i>m</i>	<i>k</i>	<i>m</i>
<i>G-618</i>	1,00083	0,00020						
<i>G-867</i>	1,00066	0,00020						
<i>G-191</i>					0,999330	0,00022	0,999563	0,00003
<i>G-192</i>					1,000152	0,00022	1,000220	0,00021
<i>G-193</i>					1,001703	0,00022	1,002053	0,00021
<i>G-1012</i>			1,001682	0,00011	1,001531	0,00015	1,001487	0,00013
<i>G-1036</i>			1,003940	0,00015				
<i>G-1078</i>			1,000533	0,00009	1,000542	0,00015	1,000097	0,00010
<i>G-1084</i>					1,000771	0,00015		

Table 5. Information about relative gravity measurements

Gravimeter	1998			1999			2000			2001			Totally
	<i>k</i>	<i>n</i>	<i>m</i>	<i>k</i>	<i>n</i>	<i>m</i>	<i>k</i>	<i>n</i>	<i>m</i>	<i>k</i>	<i>n</i>	<i>m</i>	<i>n</i>
<i>G-618</i>	53	180	16	–	–	–	–	–	–	–	–	–	180
<i>G-867</i>	53	180	14	–	–	–	–	–	–	–	–	–	180
<i>G-191</i>	–	–	–	–	–	–	20	279	16	29	566	12	845
<i>G-192</i>	–	–	–	–	–	–	20	290	14	32	654	14	944
<i>G-193</i>	–	–	–	–	–	–	20	289	16	33	666	15	955
<i>G-1012</i>	4	62	8	30	532	17	24	304	16	24	235	11	1000
<i>G-1036</i>	4	62	9	30	530	20	–	–	–	–	–	–	592
<i>G-1078</i>	4	62	10	30	532	16	24	302	13	24	235	19	1000
<i>G-1084</i>	–	–	–	–	–	–	24	294	15	–	–	–	294

Table 6. Corrections to absolute gravity stations after adjustments, μGal

Station/Variant	1	2	4	5	6
VILNIUS	–1	–4	–2	0	+1
PANEVĖŽYS	–4	–6	–4	–2	–1
KLAIPĖDA	+4	+10	+6	+9	+10

5 Relative gravity measurements in 2006

In July of 2006 some points were re-observed by 2 pairs of SCINTREX CG-5 gravimeters. Gravimeters were calibrated at absolute gravity stations VILNIUS and PANEVĖŽYS (Table 7).

Table 7. Linear scale factors of CG-5 gravimeters

No	2006 07 13		2006 07 28	
	<i>k</i>	<i>m</i>	<i>k</i>	<i>m</i>
182	1.008788	0.000117	1.008285	0.000120
183	0.999935	0.000024	0.999884	0.000035
184	1.000931	0.000113	1.000393	0.000105
185	1.000001	0.000029	0.999876	0.000021

The measurement campaign was organized in “loops” of 8 to 12 points, and the initial and final point was the absolute gravity station. Totally the 8 loops were performed and 27 points of the National Gravimetric Network were observed. At each point 10 cycles of 55 seconds read time by two gravimeters were done.

Accuracy of adjusted gravity acceleration values of 3–7 μGal was received, and the standard deviation of the single observation of 17 μGal was derived. Differences of gravity acceleration values against the officials (adopted from the first variant of adjustment) are presented in Table 8 and 9.

Comparison of computed gravity acceleration values shows, that differences are bigger, than it was expected. Especially contradictory results were received by pair of gravimeters 182 and 184. It can be concluded that further studies of the stability of the gravimeters performance and the uncertainties in relative measurements is still required.

Table 8. Differences of gravity acceleration values, derived in 2006 by CG-5 gravimeters No 182 and 184, μGal

No.	Point	182	184
1	ALYTUS	0	+1
4	EIŠIŠKĖS	+10	–24
6	JONAVA	–16	–41
9	KĖDAINIAI	–7	–34
16	MARIJAMPOLĖ	–1	–41
25	RIETAVAS	+6	+9
30	ŠAKIAI	–12	–48
31	ŠALČININKAI	+23	–16
34	ŠILAI	–5	+14
36	ŠILUTĖ	–28	–21
38	TAURAGĖ	–23	–15
40	UKMERGĖ	–14	–13
42	VARĖNA	+34	–7
44	VIEVIS	–28	+1

Table 9. Differences of gravity acceleration values, derived in 2006 by CG-5 gravimeters No 183 and 185, μGal

No.	Point	183	185
2	BIRŽAI	0	–1
7	JONIŠKIS	–3	+38
10	KELMĖ	–1	–14
11	KRETINGA	–29	–28
13	KURŠĖNAI	–6	–
17	MAŽEIKIAI	–9	–
26	ROKIŠKIS	0	–4
29	STULGIAI	–19	–20
33	ŠIAULIAI	–14	–6
34	ŠILAI	+15	+6
39	TELŠIAI	–12	–
40	UKMERGĖ	+7	+10
41	UTENA	+11	+16
43	VIDIŠKĖS	+19	+1
46	ZARASAI	0	+13

6 Conclusions

1. The IGSN71 datum instead of Potsdam system was introduced in Lithuania. The absolute gravity datum is now accurate to 5 μGal . Measurements were performed in 1994 and 2002 by ballistic gravimeter JILAg-5 at three stations: VILNIUS, KLAIPĖDA and PANEVĖŽYS.

2. From 1998 to 2001 the National first order gravimetric network was observed. There are 51

gravimetric points in the National first order gravimetric network. Each gravity difference of the network was measured at least three times with 3 or even 6 *LaCoster&Romberg* gravimeters. Accuracy of adjusted gravity acceleration values of 3–4 μGal was received, and the standard deviation of the single gravity difference observation of 14 μGal was derived.

3. In July of 2006 some points were re-observed by 2 pairs of SCINTREX CG-5 gravimeters. Accuracy of adjusted gravity acceleration values of 3–7 μGal was received, and the standard deviation of the single observation of 17 μGal was derived. Therefore comparison of computed gravity acceleration values shows, that differences are too big, and the quality of the Lithuanian National Gravimetric Network should be studied deeper.

References

1. Torge W (1998) The changing role of gravity reference networks. In: Geodesy on the move. Gravity, Geoid, Geodynamics and Antarctica. IAG Scientific Assembly, Rio de Janeiro, Brasil, Sept 3–9, 1997, Springer, pp 1–10
2. Richter B et al. (1998) The German gravity base net 1994 (DSGN 1994). In: Geodesy on the move. Gravity, Geoid, Geodynamics and Antarctica. IAG Scientific Assembly, Rio de Janeiro, Brasil, Sept 3–9, 1997, Springer, pp 37–44
3. Andersen OB, Forsberg R (1996) Danish precision gravity reference network. Publ. 4.4, National Survey and Cadastre – Denmark
4. Sas-Uhrynowski A et al. (1999) Modern state gravimetric control – POGK 97 (in Polish). Prace IGiK, Vol XLVI, No 98, pp 41–49
5. Sas-Uhrynowski A, Cisak M. (2000) Absolute gravity measurements in Poland (in Polish). Prace IgiK, Vol XLVIII, No 103, pp 193–215
6. Sas-Uhrynowski A (2002) Absolute gravity measurements in Poland. Prace IGiK, Monographic series No 3, pp 7–65
7. Mäkinen J et al. (1995) Establishment of Lithuanian national zero-order gravity (in Lithuanian). Geodesy and Cartography (Geodezija ir kartografija), No 2 (22), pp 3–21
8. Mäkinen J et al. (1996) Absolute-gravity measurements in Lithuania, Estonia and Latvia in 1994–1995. European Geophysical Society, Annales Geophysicae, Supplement I to Vol 14, pp 231
9. Petroskevičius P, Parseliūnas E (1999) Investigation and improvement of the Lithuanian gravity control (in Lithuanian). Geodesy and Cartography (Geodezija ir kartografija), Vol XXV, No 2, pp 73–82
10. Sas-Uhrynowski A et al. (2002) Establishment of Lithuanian Gravimetric First Order Network.. Geodesy and Cartography (Geodezija ir kartografija), Vol XXVII, No 3, pp 75–82
11. Petroškevičius P, Paršeliūnas E (2003) Statistics of the Lithuanian reference gravity network (in Lithuanian). Geodesy and Cartography (Geodezija ir kartografija), Vol XXIX, No 2, pp 31–39
12. Petroskevičius P (2004) Gravitation field effect on geodetic observations (in Lithuanian). Technika, Vilnius

Methods of Periodical Errors Analysis for Relative Gravimeters

P. Lukavec

Center of Earth Dynamic Research, Department of Advanced Geodesy, Faculty of Civil Engineering, Czech Technical University in Prague, Thakurova 7, Prague 6, Czech Republic
Department of Gravimetry, Czech Land Survey Office in Prague, Pod Sidlistem 9, Prague 8, Czech Republic

M. Lederer, O. Nesvadba

Department of Gravimetry, Czech Land Survey Office in Prague, Pod Sidlistem 9, Prague 8, Czech Republic

Abstract. The aim of the article is the confrontation of the methods of periodical errors analysis for the relative gravimeters LaCoste&Romberg G No.1068 (LCR1068) and No.176 (LCR176). Two methods were used, the harmonic analysis (HA) using least-squares method and the spectral analysis (SA) using Fourier transformation (FFT).

Imperfections of gearwheels in the measuring mechanical system cause systematic periodical errors in reading. The periodical errors are being determined at the special gravimetric baselines. The analysis is based on the comparison of gravimeter readings in a counter unit (CU), supposedly affected by periodical errors, with the fixed values of the gravity acceleration (based on many measurements of various gravimeters). Both methods were applied to the same data files and the results were compared.

The significant equalities for some periods were found in results. The amplitude magnitudes (almost $0.12 \mu\text{ms}^{-2}$) can significantly affect the results of the gravity measurements. However, some discrepancies were found in the results of both methods that limiting usability of these methods.

Keywords. Relative gravimetry, gravimetric baseline, spectral analysis

1 Introduction

Gravimeter LaCoste & Romberg (LCR) is a relative static gravimeter (Simon (1995)). Its measuring system is metallic. The beam is using a „zero length“ spring, which is a patent of LaCoste & Romberg. The movement of spring is realized with the assistance of gearing system, which connected it with the nulling dial (reading screw). The principle is based on adjustment of the beam (represented by

movement of the mass) to the nulling (equilibrium) setting with the assistance of the nulling dial. The simply rotary motion of toothed wheel could produce systematic errors by its imperfect shape. Next source of errors could be irregularity in division of nulling dial scale and irregularity in the height of the micrometer screw thread. Expected periodical errors are combination of number of teeth on toothed wheel in the gear box (Tab.1). The parameters of periodical errors are being determined at special gravimetric baselines (Lederer (2002)). Gravimetric baselines consist of gravimetric points with high accuracy of gravity acceleration. It means baseline where were done many accurate relative or absolute measurements. The baseline must be gauged not only with the same type of many various gravimeters but also with the various type of gravimeters, in order to eliminate influence of periodical and other systematic errors for each individual gravimeter. The concept of periodical errors analysis is based on comparison between gravimeter reading (affected by periodical errors) and adjusted values of gravity acceleration on baseline points (Kostecky (1998)). Conditions for acquisition of objective results is carrying out in the whole range of measuring system.

Period [CU]	
Up to No.485	From No.485
1.00	1.00
3.94	3.67
7.89	7.33
35.47	36.67
70.94	73.33
603.00	110.00
1206.00	220.00

Table.1 Expected periodical errors for gravimeters LaCoste & Romberg.

2 Source data

As an input data in our analyses was used all data from the measurements of gravimeters LCR 176 and LCR 1068 at the baselines till the year 2005 (see Figure 1).

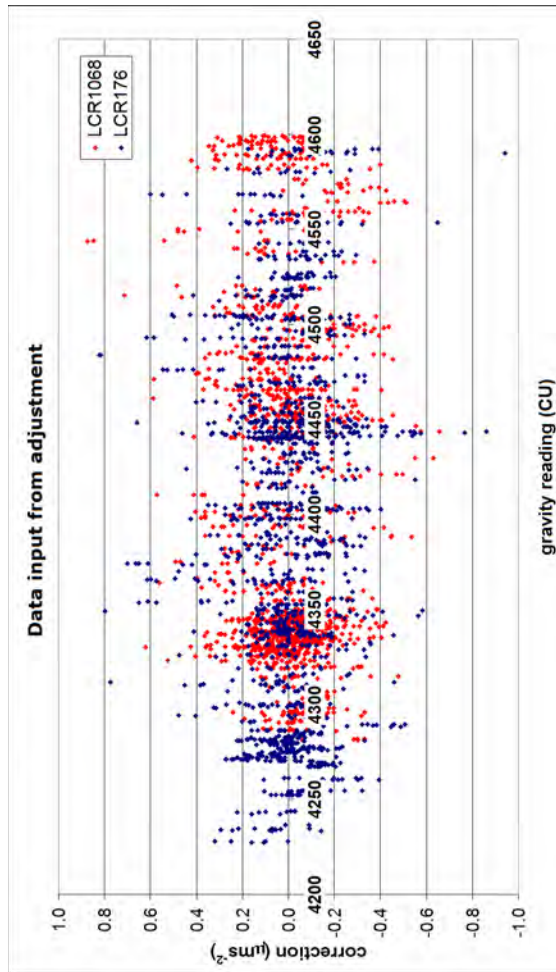


Fig.1 Input data for the harmonic and spectral analysis acquired from the adjustment (both gravimeters, all baselines).

2.1 Microbaseline Pecny-Chocerady (Pec.)

Microbaseline Pecny-Chocerady was established in the neighborhood of the Geodetic Observatory Pecny (GOPE). Gravity difference of the points is approximately $492 \mu\text{m/s}^2$ and the baseline consists of 19 points, which have a typical gravity difference $2.5 \mu\text{m/s}^2$ (the tower), $25 \mu\text{m/s}^2$ (area of GO Pecny) and $90 \mu\text{m/s}^2$ (Ondrejov-Chocerady).

Baseline Pecny-Chocerady is suitable for determination of periodical errors in the range 1-40

CU for G meter. Upper part of the baseline is applicable for computation of errors with smaller periods, but the number of measurements does not allow us to determine small periods with the sufficient accuracy.

2.2 Baseline Modra-Piesok (Mod.)

Baseline Modra-Piesok (Slovakia) was built in the calm area at the Small Carpathians foothill at the beginning of nineties of the last century. The baseline consists of 21 (originally 17) points stabilized in high quality with forced centering. The total gravity difference between final points is $199 \mu\text{m/s}^2$, gravity difference between consecutive points is nearly regular, little bit less than $10 \mu\text{m/s}^2$ in average.

2.3 Main Gravimetric Baseline (MGB)

Main Gravimetric Baseline (see Figure 2) (Lederer (2002)) was built in the year 1959. Nowadays it is being measured from Litomerice to Horni Dvoriste in total amount of 25 points with variable gravity difference.

The total gravity difference between final points is approximately $3000 \mu\text{m/s}^2$. This huge gravity range can be exploited for long-periodical errors determination. As a adjusted values of gravity acceleration we can use more than 40 years of measurements with many different gravimeters.

3 Methods comparison

Our input data may be understood as a signal function $f \in L^2(R)$. We can suppose, the signal is band-limited, i.e. the spectrum $\hat{f} \in L^2(R)^\#$ has a compact support. The signal is represented by a set of samples $f_n = f(x_n), n \in Z$.

Our task is to find (reconstruct) an original signal $f(x)$ from its samples f_n . The problem is narrowly connected with famous **Shannon-Whittaker sampling theorem** (Mallat (1999)): supposing \hat{f} has a support in $\langle \frac{-\pi}{T}, \frac{\pi}{T} \rangle$, we can write

$$f(x) = \sum_{k \in Z} f(nT) \frac{\sin(x\frac{\pi}{T} - m)}{x\frac{\pi}{T} - m} \quad (1)$$

Here we use a "regular sampling" $x_n = nT$ of a frequency $1/T$.

In practice we have only a finite number N of samples f_n , $n = 0, \dots, N-1$. Moreover, in our case we have a non-uniformly sampled data, so in general $x_n < x_{n+1}$ but $x_n \neq nT$. Remind also, that the condition for support in $\langle \frac{-\pi}{T}, \frac{\pi}{T} \rangle$ might not be entirely valid in practice! For that reasons Shannon-Whittaker theorem can not be used directly, but we can follow its principle to find a signal approximation.

In our case (periodical errors of relative gravimeters) exists a good reason to suppose, the signal consists of a bunch of sine waves with known periods (sourced by the instrument) and some additional random noise (unknown spectral properties, we can say nearly-white noise). There can be other functions in signal (i.e. polynomials) in some situations, but in our case there was not reason for this presumption.

The reconstructed signal approximation will be element of finite-dimensional space of dimension M , spanned by the set of basis functions $\varphi_k \in L^2(\mathcal{R})$, $k = 0, \dots, M-1$. We will use a linear algebra approach for the signal reconstruction.

$$f_n = f(x_n) = \sum_{k=0}^{M-1} c_k \varphi_k(x_n) \quad (2),$$

here we are looking for the set of unknown coefficients $c_k \in \mathcal{C}$.

Following the principles of Shannon-Whittaker theorem and from reasons treated before, we put $\varphi_k(x) = \cos\left(\frac{x}{P_k}\right) + i \sin\left(\frac{x}{P_k}\right)$, where $P_k > 0$ are some periods. The periods should correspond to the Shannon-Whittaker theorem; especially we cannot choose frequency equal to or higher than *Nyquist*

critical frequency $\frac{1}{2T}$ (Mallat (1999)). Note that

$$\varphi_k(x) = e^{i\frac{x}{P_k}}, \text{ taking into account formula } e^{i\theta} = \cos \theta + i \sin \theta.$$

Two different approaches were used in our paper.

3.1 Harmonic analysis

With a knowledge of sources of the signal (i.e. knowledge of periods of sine waves in the signal), we take only limited set of M basis functions with given periods P_k . In this case $M < N$, so the problem is *overdetermined*. We should apply some

regularization method like LSM. This would also efficiently suppress the influence of noise included in samples f_n . On the other hand, there can remain some undetermined waves in the signal. Helpfully, the signal-samples residua can be statistically checked (Divis et al. (1992)) for randomness of the noise.

3.2 Spectral analysis

In the preceding case we could not be sure if there remain some frequencies in the signal. For that reason we can attempt to find most of possible (allowable/available) frequencies. We are limited to N frequencies, so the problem will be uniquely solvable. The common idea is to choose the periods equidistantly, $P_k = \frac{2\pi}{NT} k$. Note the basis φ_k is orthogonal in $L^2(\mathcal{R})$ (with standard inner product). The linear system

$$f_n = f(x_n) = \sum_{k=0}^{N-1} c_k \varphi_k(x_n) = \sum_{k=0}^{N-1} c_k e^{i\frac{2\pi k}{N} x_n} \quad (3)$$

can be solved uniquely for $c_k \in \mathcal{C}$. In the case of regular sampling, i.e. $x_n = nT$ the solution can be understood as a discrete Fourier transform (Mallat (1999)), where $c_k = \frac{\hat{f}_k}{T}$. So, the advantage of the FFT algorithm can be exploited. Because our sampling is non-uniform, we use interpolation methods to resample the signal regularly. Note that this process adds “interpolating” noise to the set of new samples. This noise might significantly (it depends on original sampling characteristics, maximal gap, ...) affect the original signal, so the “spectrum coefficients” c_k would be strongly inaccurate.

The future research will be aimed to finding and applying of an efficient method for determining spectrum from non-uniformly sampled data. The method should be also connected with some robust statistic method to determine relevancy of an acquired waves.

4 Proceeding

4.1 Spectral analysis

Because of the significantly irregular (non-uniform) data sampling (Fig.1) and gaps between baselines, it is better to proceed spectral analysis for every baseline separately. From this reason each baseline fits for different periods. The microbaseline

Pecny-Chocerady is completely unsuitable for spectral analysis because of the significant irregularity of the data sampling and a very small amount of data.

Because of the non-uniform sampling, the interpolation between the data samples was processed. Three interpolation methods were used to check and moderate an impact of the “interpolation” noise.

4.2 Harmonic analysis

The calculated amplitudes were checked by the 2.5 multiple of the standard deviation. The resultant amplitudes are not possible to consider as independent. As it is clear from analysis, the amplitudes are little bit different in the case of common or separated computing.

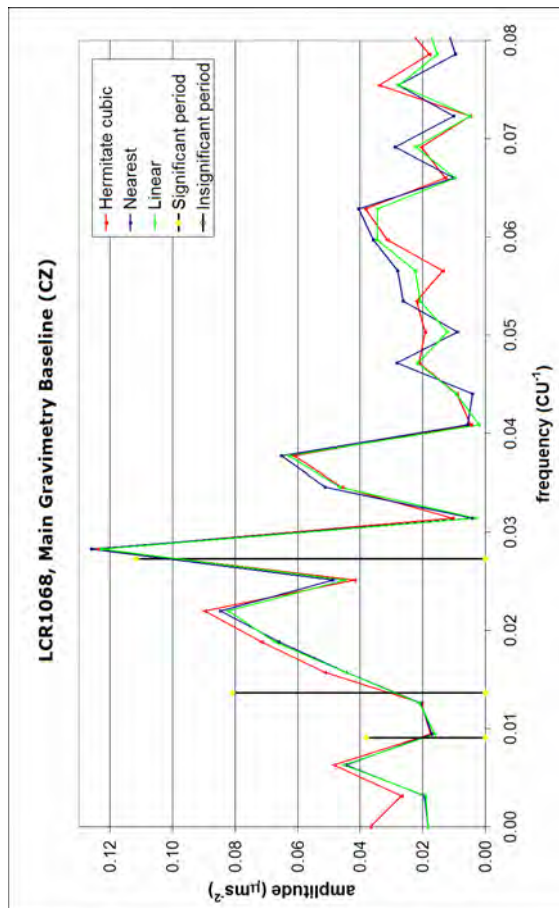


Fig.2 Resultant FFT spectra from SA (different data interpolation methods) and harmonic amplitudes (checked by 2.5 multiple of their standard deviation) for the gravimeter LCR1068 and the Main Gravimetry Baseline (CZ).

As the conclusive results, only the amplitudes which corresponds significantly in both the harmonic analysis and the spectral analysis results were taken (see Table 2a, Table 2b).

5 Conclusions

5.1 LCR1068 results

We have found the systematic error of period **36.67CU** with amplitude **12µGal** and the systematic error of period **7.33CU** with amplitude **7µGal**. The appearances of other frequencies were not proved (see Table 2a).

The results of harmonic analysis have found some periods, which can be considered as significant due to the standard deviation, but these periods have not been detected in the FFT spectra (see Figure 2). This non-existence of some systematic periods in the FFT spectra is not possible to explain as the result of the data spacing. There is also necessary to consider, the result of harmonic analysis is affected by an interference of close significant noise frequencies.

LCR1068			
baseline	period (CU)	amplitude P/SA (µms ⁻²)	amplitude FFT (µms ⁻²)
Mod.	1.00	-	-
	3.67	-	0.034
	7.33	0.066	0.073
Pec.	7.33	-	-
	36.67	0.016	-
MGB	36.67	0.112	0.124
	73.33	0.081	-
	110.00	0.038	-
	all data	1.00	-
	3.67	-	-
	7.33	0.050	-
	36.67	0.061	0.113
	73.33	0.050	-
	110.00	0.045	-
	220.00	-	-

Table.2a Results LCR1068 summary

5.2 LCR176 results

As the result we found the systematic error of period **7.89CU** and amplitude **4.5µGal**. The appearance of other systematic frequencies is arguable (see Table 2b).

The future research will be aimed to finding and applying of an efficient method for determining spectrum from non-uniformly sampled data. The method should be also connected with some robust

statistic method to determine relevancy of an acquired waves.

The issue of the comparison of the results of both methods is the possibility of separation of the true systematic frequencies and the noise frequencies in the cases, when the results of harmonic analysis might be affected by the noise interference (Fig.2).

LCR176

baseline	period (CU)	amplitude P/SA (μms^{-2})	amplitude FFT (μms^{-2})
Mod.	1.00	-	-
	3.94	0.041	0.017 ??
	7.89	0.080	0.044
Pec.	7.89	-	-
	35.47	-	-
MGB	35.47	-	-
	70.94	0.041	-
all data	1.00	0.027	-
	3.94	0.074	0.035
	7.89	0.044	0.037
	35.47	-	-
	70.94	-	-
	603.00	-	-
	1206.00	-	-

Table.2b Results LCR176 summary

6 Acknowledgment

Authors are gratefully appreciated to Ministry of Education, Youth and Sport of the Czech Republic for support of this work in the frame of projects LC506 “Recent Dynamics of the Earth”.

References

- Lederer, M.: Periodical errors of gravimeters LaCoste & Romberg (in Czech). Geodeticky a kartograficky obzor 51 (93), 2005, No. 1, p. 1-8.
- Divis, K. and Kostelecky, J.: Determination of the periodical errors of the gravimeters (in Czech). Geodeticky a kartograficky obzor 38(80), 1992, No. 3, p.47-50.
- Kostelecky, J.: Software for the analysis of the periodical errors of the gravimeters measuring system (in Czech). Research report, Research Institute of Geodesy, Topography and Cartography, No.983/98, Zdiby 1998.
- Mallat, S.: A wavelet tour of signal processing. 2nd ed. Academic Press, New York 1999.
- Lederer, M.: Main Gravimetric Baseline (in Czech). Geodeticky a kartograficky obzor 48 (90), 2002, No. 3, p. 45-52.
- Simon, Z.: Gravimeters LaCoste & Romberg (in Czech). Geodeticky a kartograficky obzor 41 (83), 1995, No. 3, p. 52-54.

Fringe Signal Effect on the Absolute Gravimeter FG5 No. 215

V. Pálinkáš, J. Kostelecký (jr.)

Research Institute of Geodesy, Topography and Cartography, Geodetic Observatory Pecný,
25165 Ondřejov 244, Czech Republic

Abstract. For highly accurate absolute gravity measurements (on the level of 1-2 μGal) using FG5 gravimeters it is necessary to ensure a correct adjustment of the meter and to guarantee many optimal conditions at the observing site. Effects of the interference fringe size on the FG5 No. 215 results were experimentally studied by absolute gravity measurements repeated under different conditions. The fringe signal size was changed for first by rotation of the Faraday isolator and for second with the help of additional polarization filter. The relation between the gravity and fringe signal size within the range of 180-430 mV was approximated by a regression line with the regression coefficient of $0.015 \pm 0.002 \mu\text{Gal/mV}$ and $0.011 \pm 0.002 \mu\text{Gal/mV}$, respectively. Although the fringe signal effect is not dramatic for FG5 No. 215, the correction of FG5 results to the same fringe signal level improve the accuracy of absolute measurements.

Keywords. Absolute gravity, FG5, fringe signal

1 Introduction

Absolute gravity measurements belong to the progressive methods of which results are important for monitoring geodynamic phenomena. At present the most precise absolute gravimeters are the FG5 gravimeters (Niebauer et al. 1995). For achieve the accuracy on the level of 1-2 μGal it is necessary to ensure a correct adjustment of the meter and to guarantee many optimal conditions at the observing site.

The FG5 uses a laser interferometer to determine the position of the free-falling test mass accelerated due to gravity. The laser interferometer generates interference fringes as the test mass falls. The fringes are counted and timed with an atomic clock to obtain precise time and distance pairs (FG5 Operator's Manual). These pairs are necessary for determination of free-fall acceleration.



Fig. 1 Absolute gravimeter FG5 No. 215 at the GOP.

This study was motivated by the emerged problem with the dependence of FG5 results on the fringe amplitude, caused by frequency dependent time delay of the ultra fast comparator (Niebauer et al. 1995) placed on the APD (Avalanche Photo Diode) circuit board. The comparator converts the sinusoidal fringe signal (frequency up to about 6 MHz) to a TTL square wave suitable for timing measurements.

The effect of the fringe signal on the FG5 No. 215 (see, Figure 1) results were observed in spite of the fact that the fringe problem described above was basically solved in 1995 by interchange of the problematic comparator (AMD686) for a much faster comparator (AD9696). The comparator AMD686 caused a “gravity” change of about

12 μGal for the fringe signal in the range of 200–400 mV.

2 Experiments

Repeated absolute gravity measurement with FG5 No. 215 for different fringe signal were used for investigation of the fringe effect. The APD circuit board was equipped by two different ultra fast comparators (AD9696 and newer AD8561) during experiments. Both comparators should be resistant for the fringe problem described above (Niebauer et al. 1995).

The fringe signal size was changed first by rotation of the Faraday isolator and second with the help of additional polarization filter placed to the interferometer base (see, Figure 2). The size of the fringe signal (peak to peak) was changed within the range of 180–430 mV. The nominal fringe signal is 280–360 mV (see, FG5 Operator’s Manual).

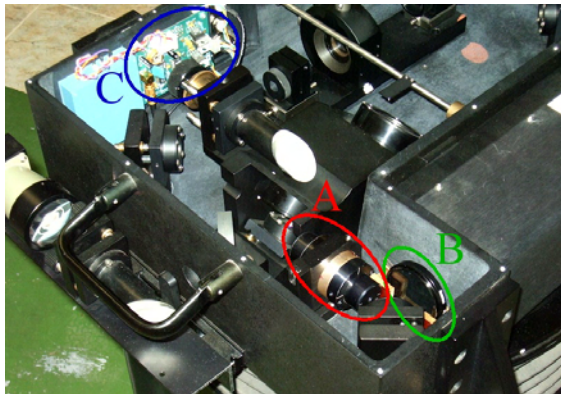


Fig. 2 Interferometer base of the FG5 No. 215. Faraday isolator (A), polarization filter (B) and APD circuit board (C).

At least 600 drops during 4 hours were measured for each fringe signal setting. The results of free-fall acceleration were converted to the gravity with the help of correction for:

- synthetic earth tides,
- air pressure variations using the coefficient $-0.3 \mu\text{Gal}/\text{hPa}$,
- polar motion using IERS (International Earth Rotation Service) data.

3.1 Experiment with Rotation of the Faraday Isolator

Fringe signal change by rotation of the Faraday isolator is the usual procedure for setting of the fringe size. The experiment was carried out for two

different ultra fast comparators on APD circuit board (AD9696 and newer AD8561), see Figure 3.

The measurement has been carried out during three 3-day periods. The interferometer was repeatedly aligned after each rotation of the Faraday isolator and 6 sets (900 drops during 6 hours) were measured with FG5 No. 215 after this alignments.

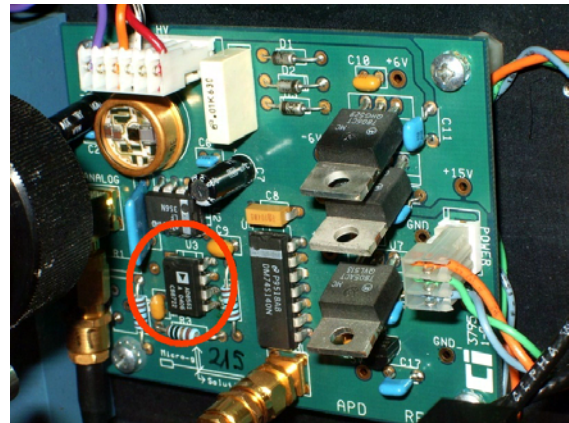


Fig. 3 Ultra fast comparator on APD circuit board.

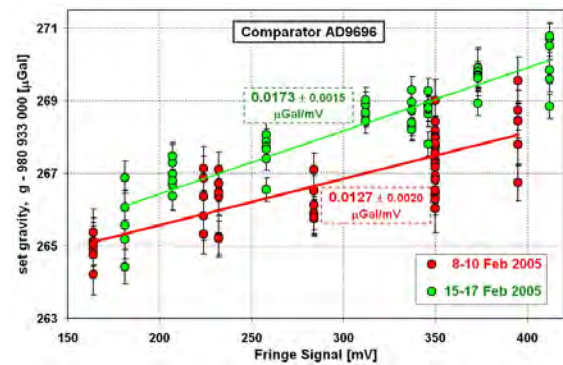


Fig. 4 Relation between set gravity of the FG5 No. 215 and fringe signal for ultra fast comparator AD9696.

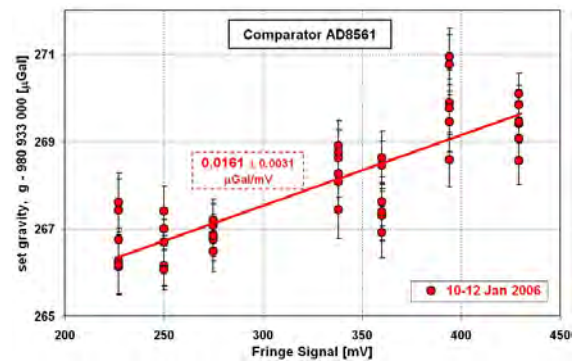


Fig. 5 Relation between set gravity of the FG5 No. 215 and fringe signal for ultra fast comparator AD8561.

The relation between the fringe signal and the measured gravity was approximated by a regression line (see, Figure 4 and 5). The regression coefficients for both type of comparators indicate comparable results. The change of the fringe signal size by the rotation of the Faraday isolator induced the “gravity” change characterized by the regression coefficient of $0.0152 \pm 0.0014 \mu\text{Gal/mV}$.

3.2 Experiment with Polarization Filter

A polarization filter was added to the interferometer base of the FG5 No. 215. It was placed directly next to the output of the laser beam from the laser baseplate. The fringe signal was changed by the rotation of the polarization filter after 4 measured sets (600 drops during 4 hours). The newest type of ultra fast comparator (AD8561) was installed on the APD circuit board.

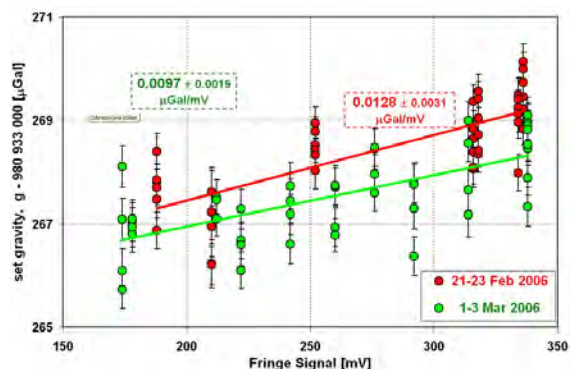


Fig. 6 Relation between set gravity of the FG5 No. 215 and fringe signal changed by polarization filter.

The relation between the fringe signal and the measured gravity was once again approximated by a regression line (see, Figure 6). The regression coefficient of $0.0110 \pm 0.0016 \mu\text{Gal/mV}$ was estimated from two epochs of measurements (21-23 February 2006 and 1-3 March 2006).

4 Conclusions

The experiments carried out at the Geodetic Observatory Pecný detected an effect of the interference fringe signal on the results of the FG5 No. 215. This effect was confirmed for the change of the fringe size first by rotation of the Faraday isolator and second by rotation of the additional polarization filter placed to the interferometer. The relation between the gravity and the fringe signal within the range of 180–430 mV was approximated by a regression line with the regression coefficient

of $0.015 \pm 0.002 \mu\text{Gal/mV}$ and $0.011 \pm 0.002 \mu\text{Gal/mV}$, respectively. It means a correction of about $1.3 \mu\text{Gal}$ for 100 mV . Both methods are technically same. Advantage of the method with the additional polarization filter is the simplicity - the interferometer needn't be aligned after rotation of the filter.

The source of the fringe effect is not known. The experiments were carried out for two different types of ultra fast comparators (AD9696 and newer AD8561) with the same results.

The changeable fringe signal causes a systematic error which size is on the level of FG5 accuracy. The correction of FG5 results to the same fringe signal improves the accuracy of absolute measurements.

It would be useful to carry out a similar experiment also for new type of FG5 interferometer with fiber optics. Technically, same results should be reached like for FG5 No. 215 equipped with bulk type of interferometer.

Acknowledgement

This presentation is based on the research carried out within the project „Recent Dynamic of the Earth“ No. LC506 supported by the Ministry of Education, Youth and Sports of the Czech Republic. This support is gratefully acknowledged.

References

- Niebauer, T., G. S. Sasagawa, J.E. Faller, R. Hilt, F. Klopping (1995). A New Generation of Absolute Gravimeters. *Metrologia*, 32, pp. 159-180.
- FG5 Operator's Manual. Colorado, Erie, Micro-g Solutions Inc. 1999.

Precision Gravimetry in the New Zugspitze Gravity Meter Calibration System

J. Flury, T. Peters, M. Schmeer

Institute for Astronomical and Physical Geodesy (IAPG), Technische Universität München, 80290 München, Germany, flury@bv.tum.de

L. Timmen

Institut für Erdmessung (IFE), University of Hannover, Schneiderberg 50, 30167 Hannover, Germany

H. Wilmes, R. Falk

Bundesamt für Kartographie und Geodäsie (BKG), Richard-Strauss-Allee 11, 60598 Frankfurt/M., Germany

Abstract. The precise calibration of relative gravity meters is essential for the accuracy of gravimetric surveys. We show that in the new Zugspitze calibration system established in 2004 – 2005 excellent accuracies of the linear calibration factor of relative gravity meters in the range of $1-2 \cdot 10^{-5}$ can be obtained. The calibration system is particularly useful for the precise calibration of Scintrex linear quartz gravity meters. The key advantages of the new calibration system are (a) the large gravity range of up to 528 mGal and (b) the short transport time of instruments by cable cars between the absolute gravity reference stations. This allows improving the accuracy of the Scintrex relative gravimetric observations by carrying out numerous ties over large gravity differences in a day or less. We study the accuracy and repeatability of Scintrex CG3 and CG5 calibration observations and the influence of seasonal effects due to environmental mass changes based on a time series of 57 calibration experiments over a period of 22 months. We show that variable attraction of snow can cause considerable effects up to $40 \mu\text{Gal}$, in particular on stations in the summit zone. This is confirmed by forward modelling using a hydrological snow model with a 1km grid. We conclude that gravity meter calibration should be preferably carried out between July and December when the snow effect is small and repeatability of calibration experiments is within $\pm 10 \mu\text{Gal}$.

Keywords. Gravity meter calibration, Scintrex Autograv gravity meter, gravity change

1 Introduction: The Zugspitze Gravity Meter Calibration System

The precise determination of gravity differences with the widely used mechanical (e.g., LaCoste-

Romberg) and electrostatic (e.g., Scintrex CG3 and CG5) spring gravity meters requires a best possible calibration. The excellent suitability of the Zugspitze summit (2962 m) for gravity meter calibration has already been recognized in 1937, when reference gravity stations have been established by pendulum observations (Weiken 1950). The stations have been used for gravity meter calibration, e.g., by Morelli (1951).

Today, with high precision free fall absolute gravity meters reference gravity values improved by 2 - 3 orders of magnitude in accuracy can be obtained. Therefore, in 2004 - 2005 a new calibration system has been established by repeated observations at 6 stations using the free fall absolute gravity meters FG5-220 (IFE) and A10-002 (BKG), cf. Figs. 1 and 2.

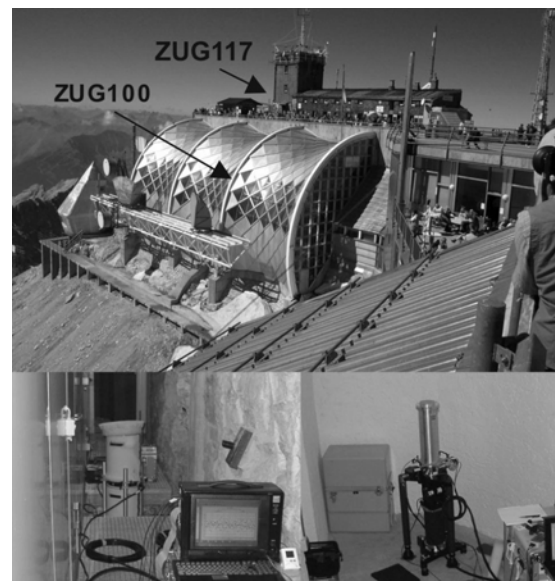


Fig. 1 Absolute gravity stations on Zugspitze summit; gravity meters A10 (BKG, lower left) and FG5 (IFE, lower right)

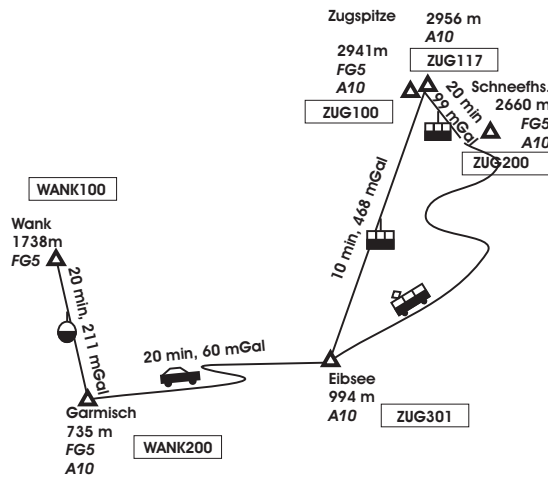


Fig. 2 Gravity stations, gravity differences and transportation in the Zugspitze calibration system

The calibration system is designed in particular for the best possible calibration of Scintrex Autograv CG3 and CG5 gravity meters for which only a linear calibration factor or at most a very small quadratic term have to be determined. The key advantages of the Zugspitze calibration system are large gravity differences of up to 528 mGal and – at the same time – transport times of only 10 – 20 minutes between the absolute stations. The short transport time allows carrying out a number of station ties within a day which considerably increases redundancy and accuracy of the relative gravimetric observation.

Table 1 Results of absolute gravimetry in the Zugspitze calibration system. For FG5 results cf. Timmen et al. (2006). A10 results are preliminary.

Station (Height), Vertical Grav. Gradient	Epoch	Instrum.	Dur. (h)	Gravity (μ Gal)	Gravity (μ Gal)	Gravity (μ Gal)
				Scintr. ref. level 0.26 m	A10 ref. level 0.705 m	FG5 ref. level 1.20 m
ZUG117 (2956m) -522.0 μ Gal/m	2005 02 17	A10-002	1	980056179	980055946	980055688
	2005 09 28	A10-002	0	980056146	980055914	980055656
ZUG100 (2941m) -465.3 μ Gal/m	2004 09 18	FG5-220	24	980062587	980062380	980062149
	2005 02 17	A10-002	1	980062613	980062406	980062176
	2005 09 28	A10-002	0.3	980062586	980062379	980062149
ZUG200 (2660m) -350.5 μ Gal/m	2004 09 09	FG5-220	24	980155017	980154861	980154687
	2005 02 17	A10-002	5	980155016	980154860	980154687
ZUG301 (994m) -282.0 μ Gal/m	2005 07 20	A10-002	0.5	980524498	980524373	980524233
	2005 09 28	A10-002	0.3	980524504	980524379	980524239
WANK100 (1738m) -387.7 μ Gal/m	2004 12 01	FG5-220	24	980373710	980373537	980373346
WANK200 (735m) -284.7 μ Gal/m	2004 12 03	FG5-220	24	980584700	980584573	980584432
	2005 02 19	A10-002	1	980584694	980584568	980584427
	2005 07 20	A10-002	0.3	980584702	980584575	980584435
	2005 09 27	A10-002	0.3	980584701	980584574	980584433

Table 1 shows the absolute gravimetry results for all epochs and reference levels. The FG5 accuracy estimate is 3 μ Gal (Timmen et al. 2006). The preliminary A10 accuracy estimate obtained from comparisons at other stations is 5 - 10 μ Gal. The reduction to another reference level is done using the precisely observed vertical gravity gradients given in Table 1. This accounts for another error of about 3 μ Gal. Note the extremely large vertical gradient in station ZUG117 at the very top of Zugspitze. At ZUG100 – only 15 m below – the gradient is already considerably smaller.

At the summit stations ZUG100 and ZUG117 significant gravity changes have been observed. The gravity result in February is larger by 26 - 33 μ Gal than in September. We show in Sect. 5 that this variation can largely be attributed to the attraction of snow masses in the summit zone. At other stations, the largest change is 8 μ Gal which is within the observation accuracy.

As the calibration system is intended to serve as a long-term calibration reference, the height differences between the gravity stations have been precisely measured. This will allow checking the long-term stability by repeated observations. Each of the stations is connected by precision levelling to benchmarks. Some of the benchmarks have been tied by static GPS observations to GPS permanent stations provided by the Institute for Meteorology and Climate Research in Garmisch as well as by the German Sapos permanent network.

The absolute gravimetry stations are easily accessible. On station ZUG117, no FG5 observations have been feasible due to the restricted space. Station ZUG200 unfortunately is no more accessible

due to construction activities.

2 Calibration of Scintrex CG3 and CG5 Gravity Meters

To obtain the maximum accuracy for the linear calibration factor, the instrument to be calibrated has to perform observations over a large gravity range with accuracy similar to that of the reference gravity differences from absolute gravimetry. Taking into account the accuracy of the reduction to the Scintrex reference level (0.26 m above ground), the reference gravity differences in the Zugspitze calibration system have an accuracy of 6 – 15 μGal . Thus, the best achievable calibration accuracy is about $1.2 \cdot 10^{-5}$. *Instrumental errors* of the Scintrex gravity meters have to be thoroughly examined, and a suitable sequence of observations has to be found. If calibration is not carried out simultaneously with absolute gravimetry, gravity changes by *environmental mass changes* have to be considered in addition. They should be modelled as far as possible and required, or mitigated, e.g., by avoiding calibration at seasons when such effects are strong.

3 CG3 and CG5 Instrumental Errors

Previous investigation on the accuracy performance of the CG3 and CG5 gravity meters led to rather inhomogeneous results. In microgravimetric surveys, often excellent accuracies of a few μGal have been obtained. Timmen and Gitlein (2004) found a relative accuracy limit of $1 \cdot 10^{-4}$. Hackney (2001) obtained rather poor accuracies in a gravimetric network in Australia. Budetta and Carbone (1997) observed a large change in the calibration factor by $1 \cdot 10^{-3}$ over one year, together with a strongly varying drift parameter. For calibration experiments in the Zugspitze calibration system, the following error sources deserve special attention:

Transport After transport, many Scintrex gravity meters exhibit a significant time-dependent change in the reading, possibly due to the relaxation of tension in the sensor which has been accumulated during transport (Hackney 2001). For the CG3 310218 instrument of IAPG, this hysteresis is often strong (up to 60 μGal) during 30 minutes after transport. Figure 3 (top) shows strong but homogeneous hysteresis most of which is cancelled out in the station difference. Figure 3 (bottom) shows inhomogeneous hysteresis which can result in large errors. Hysteresis of the instruments CG3 310218 (IAPG) and CG3 303202 (BKG) has been found to decrease for most station occupations. In contrast to

this, Hackney (2001) reported strongly increasing hysteresis of his instrument for all occupations. For the CG5 44 of BKG a considerably lower hysteresis magnitude has been found. Thus, hysteresis magnitude and direction seem to vary from instrument to instrument.

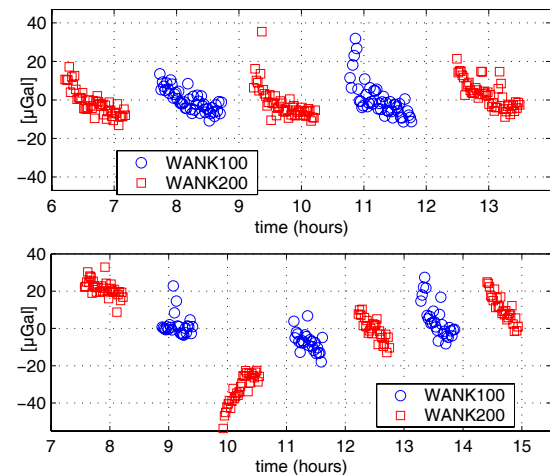


Fig. 3 CG3 hysteresis after transport. Each signature corresponds to a 60 sec observation set. Station occupation duration is 30 - 60 min (25 - 60 sets), and cable car transport between stations is about 25 min. Top: strong but homogeneous hysteresis, bottom: inhomogeneous hysteresis

Temperature effects The temperature of the gravity sensor is stabilized by heaters within 10^{-3} K. Residual temperature variations are observed with an accuracy of 10^{-5} K and corrected for. During observations in the Zugspitze calibration system, relatively strong residual variations have been observed for ties between station pairs with very different ambient temperature. Thus, an error of the temperature correction coefficient could cause significant errors. We did not find a correlation between the sensor temperature and gravity reading. However, this should be further studied.

Stability of the instrument electronics On the $1 \cdot 10^{-5}$ accuracy level, instabilities of the instrument electronics could play a role. E.g., the AD converter of the electrostatic gravity sensor is not specified to be stable to this accuracy.

Accelerations due to microseismics, wind and human noise The large number of observations (cf. Sect. 4) allow comparisons between instruments, stations and days with respect to the amplitude of these effects.

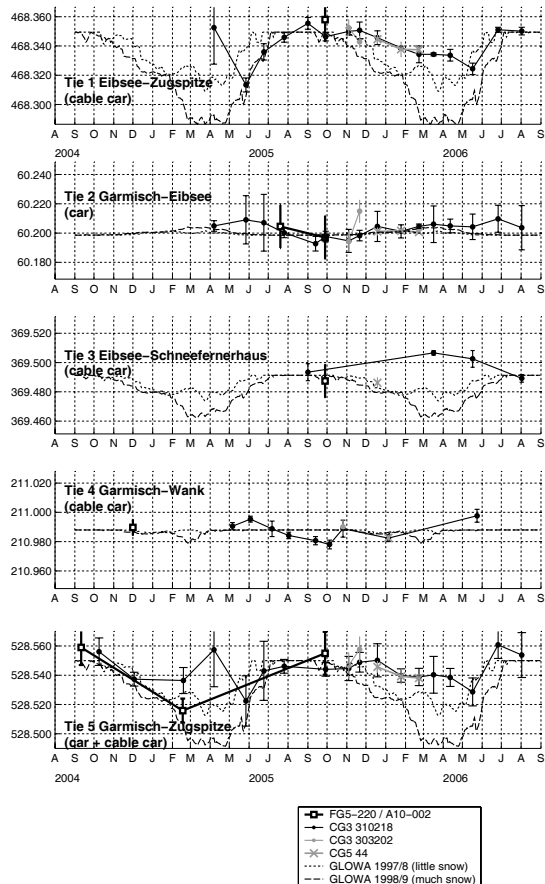


Fig. 4 Time series of gravity differences (in mGal) for 5 station ties from absolute gravimetry and calibrated Scintrex relative gravimetry, together with seasonal gravity variation obtained from the GLOWA Danube snow model

4 A Time Series of Calibration Experiments

To investigate the instrument accuracy and long-term stability as well as gravity changes due to environmental mass changes, a time series of 57 calibration experiments have been carried out during a total time span of 22 months. At each epoch, gravity differences (ties) between one or several pairs of stations have been observed with CG3 310218. For some epochs, simultaneous observations of CG3 303202 and CG5 44 of BKG have been carried out. The results are shown in Fig. 4 together with the reference gravity differences from absolute gravimetry. Each Scintrex gravity difference is derived from 3 - 9 single ties observed during one day. From least squares adjustment very good accuracies of 1 - 6 μ Gal have been obtained for most station ties (Fig. 4). For station tie no. 2

only 3 - 4 single ties have been observed at some epochs due to time limitations, resulting in poorer accuracies of up to 20 μ Gal. Results for tie no. 5 are obtained from the sum of ties no. 1 and 2, except for the first epochs which have been observed directly.

The consistency between epochs is rather poor for the first few epochs of ties no. 1 and 5, when stations were occupied during 5 min only and undetected hysteresis effects may have caused large errors. Later, the station occupation duration was gradually increased to 30 min, leading to an improved repeatability below ± 10 μ Gal for ties no. 2 - 4 which is similar to the accuracy of the reference gravity differences from absolute gravimetry. Ties no. 1 and 5 involving Zugspitze summit are constant within ± 10 μ Gal from July to December only, while showing a seasonal trend from January to June with results smaller by up to 40 μ Gal. The time variation in both absolute and relative gravimetry results is approximately consistent with differences in snow attraction obtained by forward modelling using data of the GLOWA-Danube snow module, cf. Sect. 5.

From all epochs where simultaneous absolute and relative gravimetry is available, linear calibration factors for the employed Scintrex instruments have been determined by least squares adjustment. Table 2 shows the calibration accuracies obtained.

instrument	# of ties	calibr. factor accuracy
CG3 310218	9	1.2e-5
CG3 303202	5	2.0e-5
CG5 44	7	1.4e-5

Table 2 Accuracies of calibration from repeated calibration experiments

5 Effects of Environmental Mass Changes

Snow Around Zugspitze summit, in winter maximum snow heights of up to 5 m are observed (1 - 2 m water column equivalent). In the higher regions, significant snow masses persist until June. We used a snow model from the GLOWA-Danube hydrological project (Mauser and Ludwig 2002) to compute the attraction of snow mass up to a distance of 40 km on each gravity station. The model contains snow water column equivalent in a 1 km grid and daily resolution for the years 1995 to 1999. For the computation of attraction, the snow

data have been represented by point masses on a digital terrain model grid. In the near zones around the gravity stations, the coarse GLOWA Danube snow grid has been interpolated to a 50 m high resolution digital terrain model. Thus, the proper terrain height of the snow data is used. However, the model cannot represent local (sub-grid) snow variability. Nevertheless, a point-wise comparison with observed snow height at a station of German Weather Service (DWD) near Zugspitze summit showed a fairly good agreement.

As no model data have been available for the time period of the calibration experiments, the results for a winter with little snow (1997/98) and for another with very much snow (1998/1999) have been selected for a qualitative comparison. Figure 4 includes the differences in snow attraction for all station ties. For ties no. 2 and 4, the effect of the snow model is below 9 μGal throughout the year. For ties no. 1 and 5, large variations up to 60 μGal are obtained which are largely due to the snow effect at the Zugspitze summit station ZUG117.

For these ties, both the observed gravity differences and the modelled differences in snow attraction decrease rather slowly in the period from December to May together with increasing snow mass accumulation in the summit region. The values increase again sharply in June and July together with snow melt in the summit region. The amplitudes of the modelled snow effect are, however, larger than the observed gravity variations. For calibration purposes it is important to note that in the period from July to December the snow effects are small also for the ties involving Zugspitze summit. For tie no. 3 the agreement is poor. Probably the Scintrex accuracy estimates obtained for this tie are too optimistic.

Glacier melting The melting of the small Schneeferner glacier below Zugspitze summit was estimated to cause a gravity change of about 2 $\mu\text{Gal}/\text{year}$. This effect is slightly too small to be detected in the gravity time series available so far.

Groundwater and other water storages The valleys around Garmisch contain important groundwater storages with significant temporal variations. Unfortunately, there are no hydrological observations available close to the gravity stations. The time series of gravity differences may contain effects from water storage changes, but they seem to be smaller than $\pm 10 \mu\text{Gal}$.

Atmosphere The gravity observations have been reduced for the deviation from normal air pressure using the empirical regression coefficient 0.3 $\mu\text{Gal}/\text{mbar}$. However, in the complex topography of the Zugspitze calibration system the effect of actual

air mass distribution may deviate significantly from this simple relation.

6 Conclusions

The large number of observations carried out during the calibration experiment time series allow valuable insight into the characteristics and accuracy of the Scintrex CG3 and CG5 gravity meters. The repeatability of the gravity differences in the Zugspitze calibration system observed by these instruments is within $\pm 10 \mu\text{Gal}$ for most station pairs which is similar to the accuracy of the reference gravity differences from absolute gravimetry. For ties involving Zugspitze summit, a seasonal variation of up to 40 μGal is observed. This is approximately consistent with the variation in snow attraction derived from the snow module of the GLOWA Danube hydrological model. The effects of snow are large in the months January to June, which should be avoided for precise calibration. The effects of other environmental mass changes seem to be moderate. Hysteresis after transport has been identified as a critical error source for several CG3 instruments. A preliminary recommendation is to extend station occupations to a duration of at least 30 minutes.

Taking properly into account the instrument characteristics and the seasonal effects, in the Zugspitze calibration system gravity differences of about 500 mGal can be observed with an accuracy of 5 - 10 μGal by the Scintrex CG3 and CG5 instruments, allowing a calibration with an excellent relative accuracy of $1 - 2 \cdot 10^{-5}$.

Acknowledgement

The support of the observation campaigns by the Environmental Research Station Schneefernerhaus is gratefully acknowledged. The GLOWA Danube snow data have been made available by the Commission for Glaciology of Bavarian Academy of Sciences.

References

- Budetta G, Carbone D (1997) Potential application of the Scintrex CG3M gravimeter for monitoring volcanic activity. *J Volc Geotherm Res* 76:199-214
- Hackney R (2001) A gravity-based study of the Pilbara-Yilgarn Proterozoic Continental Collision Zone. PhD Thesis Curtin Univ Perth
- Mausser W, Ludwig R (2002) GLOWA-DANUBE A research concept to develop integrative

- techniques, scenarios and strategies regarding global changes of the water cycle. In: Beniston M (ed), Climatic Change: Implications for the Hydrological Cycle and for Water Management. Advances in Global Change Research, 10. Kluwer, p. 171-188
- Morelli C (1951) Taratura di due gravimetri Worden e collegamenti europei. Annali di Geofisica IV(4). Cited after Grossmann W (1953) Deutsche Geodätische Kommission Vol. B 11
- Timmen L, Gitlein O (2004) The capacity of the Scintrex Autograv CG3M no. 4492 gravimeter for absolute scale surveys. Rev Bras Cart 56(02):89-95
- Timmen L, Flury J, Peters T, Gitlein O. (2006) A new absolute gravity base in the German Alps. Proc Internat Gravity Field Workshop Smolenice
- Weiken K (1950) Ergebnisse der Pendelmessungen der Jahre 1934 bis 1943, Publications of the Geodetic Institute Potsdam No. 3

Absolute Gravity Measurements in Terre Adélie (Antarctica) and at Canberra (Australia)

M. Amalvict, Martine.Amalvict@eost.u-strasbg.fr

Institut de Physique du Globe de Strasbourg / École et Observatoire des Sciences de la Terre (UMR 7516 CNRS-ULP), 5 rue René Descartes, 67000, Strasbourg, France

Y. Rogister, J. Hinderer, B. Luck

Institut de Physique du Globe de Strasbourg / École et Observatoire des Sciences de la Terre (UMR 7516 CNRS-ULP), 5 rue René Descartes, 67000, Strasbourg, France

H.McQueen,

RSES, ANU, Canberra ACT0200, Australia

G. Luton

Geoscience Australia, Symonston ACT 2609, Australia

Abstract.

The team of the Gravity Observatory of Strasbourg, France, took absolute gravity measurements at Dumont d'Urville (Antarctica) and Canberra (Australia) in February 2006. First we report on these measurements and then we compare with previous measurements taken by the same group at Dumont d'Urville in 2000 and by American and Japanese groups at Canberra in 2003 and 2004. The results show a very large stability of the Antarctic site demonstrated both by absolute gravity variation ($0 \pm 1.94 \mu\text{Gal}/\text{yr}$) and height variations from DORIS ($0.29 \pm 0.13 \text{ mm}/\text{yr}$) and GPS ($-0.01 \pm 0.21 \text{ mm}/\text{yr}$) observations. At Canberra an uplift is observed by GPS ($+2.39 \pm 0.06 \text{ mmyr}^{-1}$) and DORIS ($+5.49 \pm 0.49 \text{ mm}/\text{yr}$) at the Mt Stromlo sites whereas absolute gravity would show an uplift at the seismic vault ($-2.5 \pm 0.1 \mu\text{Gal}/\text{yr}$) and a subsidence at the superconducting gravimeter site ($+3.7 \pm 1.6 \mu\text{Gal}/\text{yr}$). At Tidbinbilla, absolute gravity variations ($-3.90 \pm 0.76 \mu\text{Gal}/\text{yr}$) and vertical GPS ($+2.16 \pm 0.25 \text{ mm}/\text{yr}$) both show an uplift.

Note: in the following we shall use $1 \mu\text{Gal} = 10^{-8} \text{ m}/\text{s}^2$.

Keywords. Absolute Gravity, DORIS, GPS, Antarctica, Dumont d'Urville, Canberra, Tidbinbilla

1. Introduction

During the 2005-2006 summer season of the Southern Hemisphere, the team of the Gravimetric Observatory of Strasbourg (France) using the FG5#206, completed a 5-year program of absolute gravity (AG) measurements supported by the French Polar Institute (I.P.E.V.). During the previous campaigns, AG measurements were taken at Dumont d'Urville (DdU, Antarctica) in 2000

(Amalvict et al., 2001, Hinderer et al., 2002) and in Islands of the Indian Ocean: Kerguelen in 2001 (Amalvict et al., 2001a), Kerguelen and Crozet in 2003 (Amalvict et al., 2003), Kerguelen, Crozet and Amsterdam in 2005 (Amalvict et al., 2005).

Antarctica is a very large area the behaviour of which is decisive for climatology, ice melting, study of mean sea level variations, etc... However very few AG measurements have been operated on this continent; Amalvict initiated in 2003 the listing of these measurements (Amalvict, 2003; Amalvict and de Linage, 2004) and a subsequent complete list, as for 2005, can be found in Mäkinen et al. (2006). New measurements were taken in 2006 and there are now 26 measurements at 12 stations, among them only few benefit from repeated measurements (four stations), though repetition is crucial for the determination of trends which can be interpreted in terms of constraints for the modelling of Post Glacial Rebound (PGR) or Glacial Isostatic Adjustment (GIA). There are indeed various models of deglaciation predicting gravity and height variations in Antarctica (James & Ivins, 1995, 1998; Peltier, 1995; Nakada et al., 2000), but to be better constrained, they need the input of observational data. This enhances the call for new AG values.

The ship (*Astrolabe*) goes to Terre Adélie from Hobart (Tasmania, Australia) and we took this opportunity to make AG measurements in Canberra (Mt Stromlo and Tidbinbilla) on the way back from Antarctica (Fig. 1). The Canberra Observatory, on Mt Stromlo, hosts since 1997 a superconducting gravimeter (SG) belonging to the National Astronomical Observatory (NAO) of Mizusawa, Japan. Different teams visited the site for AG measurements several times (Amalvict et al., 2001b), in order to calibrate the SG, to monitor the stability of the station and to establish a high quality reference station. Unfortunately, a severe bushfire destroyed the buildings of the Observatory, sparing nevertheless the SG room and the SG itself. Our 2006 measurements repeated the 2004

measurements taken by the Kyoto University group, one year after the bushfire. All the mentioned AG measurements are collocated with precise satellite positioning techniques (GPS, DORIS), which becomes now the standard *modus operandi* for repeated AG measurements.



Figure 1 –Location of the AG measurements sites.

2. Antarctica – Dumont d’Urville

2.1. 2006 AG measurements

A 5-year project, supported by the French Polar Institute (IPEV), started in 2000. The aim of the project was to measure for the first time AG in the French scientific stations located in Antarctica (DdU in Terre Adélie) and in South Indian Ocean Islands (Kerguelen, Crozet, Amsterdam). Measurements at DdU are repeated after 6 years. The station is located on Petrels Island at 5 km of the continent; the gravimeter, the FG5#206, was deployed in 2000 in a small shelter. It has been enlarged in 2006 with great care for saving the AG point and its access for the repetition of the precise levelling operated in 2000 by the French Oceanographic Service (SHOM). DdU is a very windy station, so it was decided to have a large number of drops per set to get the value of gravity with a set standard deviation as small as possible, by averaging a high number of single values. The adopted sequence in 2006 is 200 drops per set, 10 s between drops and 1 set per hour. Measurements took place from 5 to 8 February 2006, 82 sets were measured and the final value was obtained from 16187 drop values. The parameters of the station are presented in Table A1. We processed the raw data by mean of the ‘g6’ software from Micro-g Solutions. We applied the standard corrections to

the raw data: polar motion, vertical gradient of gravity, atmospheric pressure using the standard nominal pressure, solid Earth and oceanic tides. The final value of gravity at the ground level is $g = 982\,387\,167.0 \pm 3.5 \mu\text{Gal}$. The set standard deviation is mainly due to the remaining part of the loading tide, which is not modelled precisely enough, and to the noisy conditions of the station.

2.2. 2000 AG measurements

The first absolute measurements ever performed in Terre Adélie were operated from 26 February to 2 March 2000 with FG5#206. At that time we measured 25 drops per set with a 10s interval between drops and 4 sets per hour, averaging the final value from 11800 individual drops. The final value, after correcting according to the same regulation than for the 2006 measurements is: $g = 982\,387\,167.0 \pm 11.11 \mu\text{Gal}$. Let us note that it is not the value published in Amalvict et al., 2001 and Hinderer et al., 2002. In these two papers, the nominal pressure was calculated from the average value of the pressure observed at the station for 50 years, instead of the standard pressure. The correction that we have to apply to the 2000 result, due to the change of nominal pressure is $-7.2 \mu\text{Gal}$ (Mäkinen et al., 2006). The high value of the set sd in 2000 is mainly due to the small number of drops per set, but also to the remaining un-modelled oceanic tide and to the super-spring performances at that time that has been improved later by Micro-g.

2.3. Height changes and gravity variation

2.3.1. AG measurements

The difference between the two values of gravity ($\Delta g = g_{2006} - g_{2000}$) is null with a large set sd (set SD = $\{(set\ SD_{2006})^2 + (set\ SD_{2000})^2\}^{1/2}$) $11.65 \mu\text{Gal}$, which is dominated by the 2000 set SD. The 6-year time interval between measurements leads to a ‘trend’ of gravity $\dot{g} = 0 \pm 1.94 \mu\text{Gal/yr}$.

A negative value of \dot{g} corresponds to an uplift.

2.3.2. Precise positioning

Two techniques of precise positioning using satellites are collocated at DdU. Guy Woppelman (TIGA, SONEL) derived a trend from GPS observations between 1998.2 and 2005.7 (2006, private communication, still preliminary result)

equal to $\dot{h} = -0.01 \pm 0.21 \text{ mm/yr}$.

Pascal Willis (IGN – JPL) derived in the ITRF2005 (2006, private communication, also as a preliminary result) a trend equal to $\dot{h} = 0.29 \pm 0.13 \text{ mm/yr}$.

A positive value of \dot{h} corresponds to an uplift.

2.3.3. Comparison

The combined effect of PGR, and PDIM (present day ice melting) is supposed to be the cause of changes in the vertical position of the station. Models of prediction ((James & Ivins, 1995, 1998; Peltier, 1995; Nakada et al., 2000), which take into account several scenarios of PGR and GIA, all predict in the DdU region (Wilkes Land) a small vertical displacement, ranging from 0 to 4 mm/yr.

Model	AG	DORIS	GPS
\dot{h}	\dot{g}	\dot{h}	\dot{h}
mm/yr	$\mu\text{Gal/yr}$	mm/yr	mm/yr
0 to 4	0 ± 1.94	0.29 ± 0.13	-0.01 ± 0.21

Table 1 – Changes in gravity and in height, at DdU (Antarctica).

Summarising the results in Table 1, we are facing a very good agreement between predictions, AG changes and vertical position changes. All the results are in favour of a large stability of the station.

3. Australian sites

A SG is installed at the Canberra Observatory since 1997, which belongs to the National Astronomical Observatory of Mizusawa, Japan. The site has been visited several times by AG meters from different teams (Japan, Australia and France), in order to calibrate the SG (Amalvict et al., 2001b) and to determine the absolute value of gravity and establish a high quality reference point (Murakami et al., 1997). Unfortunately, a severe bushfire destroyed the Observatory building in 2003, including the AG reference station. Luckily, the SG itself remained untouched by the fire. It has been recalibrated for the first time in 2004 by a Japanese team (Fukuda et al., 2005). The FG5#210 was deployed in a room close to the SG, establishing the first AG measurement at this temporary site, prior to the establishment of the future permanent AG reference site at Mt Stromlo. In addition, measurement was taken at the nearby Seismic Vault (SV) which shelters instruments of the GEOSCOPE network; the site will remain a secondary reference site in the future. Moreover, we measured the AG at Tidbinbilla where the NASA deploys the Canberra Deep Space Communication Complex as the only Australian tracking station. We decided to re-measure all these sites on the way back from Antarctica

3.1. Mount Stromlo

3.1.1. 2006 measurements – FG5#206

SG site -

The measurements took place from February 18 to 22 2006. The adopted sequence is 100 drops per set, 10 s between drops and 1 set per hour. The total experiment led to 10314 accepted drops; the series is long in order to calibrate the SG, which requires several days of parallel recording. The coordinates of the station and the parameters for corrections are given in Table A1 of the Appendix. The solid Earth tides and loading tides are corrected by using the tidal parameters (amplitude and phase) derived from a tidal analysis of SG recording. The final value at the ground level is $g = 979\,549\,878.0 \pm 0.9 \mu\text{Gal}$. Let us notice that the use of the observed tidal parameters leads to a strong reduction of the set sd.

Seismic Vault

The site located at the GEOSCOPE station was occupied on 25 and 26 February 2006, with the same sequence of 100 drops per set and hour and 10 s between drops. The station information is given in Table A1. As the station is only 5 km from the SG site, we correct for the tides with the observed tidal parameters. Due to a technical problem, the pressure sensor was out of use during the measurements. We correct for the atmospheric pressure, in post-processing the data, by taking into account the pressure observed at the SG site. The final value of gravity, at ground level, is: $g = 979\,569\,851.5 \pm 0.8 \mu\text{Gal}$. The set sd is even smaller than at the SG site, showing the high quality of the GEOSCOPE station.

3.1.2. Previous measurements

SG site -

The site was occupied for the first time, by the FG5#210 from Kyoto University from March 29 to April 4 2004. They processed the 2004 raw data with vertical gradient of gravity and nominal pressures values identical to the ones we used in 2006 to compare both results. Nevertheless, their tidal corrections were calculated using the nominal tidal models from the ‘*g-software*’ of Micro-g Solutions. The final value at the ground level is $g = 979\,549\,870.7 \pm 3.0 \mu\text{Gal}$ (Fukuda et al., 2005). The set sd is higher than in 2006, mainly because of the imperfect modelling of the tides.

Seismic Vault

The site was, as well, occupied for the first time by the FG5#210 operated by the Kyoto University group. The SG site being a temporary one, it seemed useful to measure at a perennial place for a future link to the future reference AG point. Measurements took place from 23 to 26 March 2004 and the raw data were corrected in a similar way than at the SG site. The final value at the

ground level was: $g = 979\,569\,856.6 \pm 1.7 \mu\text{Gal}$ (Fukuda et al., 2005). Again, the set sd, though small, is higher than in 2006.

3.1.3. Changes in gravity and height of the station

AG variation

The change of gravity at the SG site is $\Delta g = g_{2006} - g_{2004} = +7.3 \pm 3.1 \mu\text{Gal}$ with a time span $\Delta t = 2$ years. The consequent trend is $\dot{g} = +3.7 \pm 1.6 \mu\text{Gal/yr}$. In the same way, we derive at the seismic vault $\Delta g = g_{2006} - g_{2004} = -5.1 \pm 1.9 \mu\text{Gal}$ over 2 years leading to the trend $\dot{g} = -2.5 \pm 0.1 \mu\text{Gal/yr}$.

The two sites are separated by 5 kilometres and we would expect a similar behaviour of gravity changes at the two locations. We could think of several explanations to explain the difference: tectonics and hydrology do not seem to be good candidates, we can also dismiss a possible annual cycle since the two series of measurements took place at the same period of the year (February and March). Of course, a very local hydrological effect could be the source of the difference. One could also consider an instrumental offset between the instruments but it does not seem to be likely for it would appear at the 2 sites; moreover the two FG5s were controlled at their respective home sites, both of which controlled by SGs.

Precise positioning techniques

Mt Stromlo is equipped with both GPS and DORIS facilities. Zuheir Altamimi (IERS) provided us with a trend over the 1999.2 – 2005 period equal to $\dot{h} = +4.42 \pm 0.23 \text{ mm/yr}$ (private communication). The 2000.2 – 2005 GPS data have been processed by Paul Tregoning (RSES, ANU – Canberra) leading to the trend: $\dot{h} = +2.39 \pm 0.06 \text{ mm/yr}$ (Fig. 2, private communication). The data gap in 2003 is due to the outrage caused by the bushfire. The clear difference between 2000 – 2002.75 and 2004 – 2006 is responsible for the apparent positive uplift. We do not include the data before 2000 because of the radial change in the nature of global tracking data during 1999/2000 when the Rogue / Turborogue GPS receivers had their firmware upgrades (Tregoning et al.). The analysis of DORIS data is provided by Pascal Willis (IGN, JPL) over 7.3 years and the trend is $\dot{h} = +5.49 \pm 0.49 \text{ mm/yr}$.

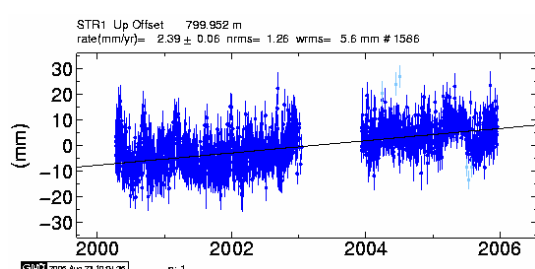


Figure 2 – Time series of GPS observations at the Mt Stromlo station, courtesy P. Tregoning, 2006.

The above analyses of data for precise positioning by satellite observations agree for uplift, though its rate may vary by a factor 2.

Comparison

Table 2 summarises the above results:

AG \dot{g} $\mu\text{Gal/yr}$	DORIS \dot{h} mm/yr	GPS \dot{h} mm/yr
Seismic Vault -2.55 ± 0.96	$+5.49 \pm 0.47$	$+2.39 \pm 0.06$
SG site $+3.71 \pm 1.56$		

Table 2 – Changes in gravity and height at Mt Stromlo sites (Australia).

The change of gravity at the seismic vault is in agreement with the uplift observed by both GPS and DORIS, but the positive change of gravity at the SG site is still to be explained.

3.2. Tidbinbilla

The Canberra Deep Space Communication Complex is located at Tidbinbilla, roughly distant of 25 kilometres from the Mt Stromlo sites. A garage hosted, in the past, several absolute gravity measurements.

3.2.1. 2006 measurements – FG5#206

Measurements took place on 24-25 February 2006 with a sequence similar to Mount Stromlo one: 100 drops per set and per hour, 10 s between drops. The total number of accepted drops is 2382 for 24 sets. The coordinates and parameters of the site are in Table A1. As the station is near to Mount Stromlo, we used the observed tidal parameters to correct the raw gravity data for the tides (solid Earth and oceanic). The final value of gravity at the ground level is then: $g = 979\,576\,105.0 \pm 0.7 \mu\text{Gal}$.

The small number of rejected drops and the small set sd demonstrate the high quality of the station.

3.2.2. Previous measurements

This site has been visited twice in the recent past. In June 2003 Micro-g Solutions measured with the FG5#111 and Kyoto University measured with the FG5#210 on 14-16 April 2004. Using both the same corrections, parameters and modelled tides for tidal correction, the respective results are: $g_{2003} = 979\,576\,114.4 \pm 2.3 \mu\text{Gal}$ and $g_{2004} = 979\,576\,114.3 \pm 2.4 \mu\text{Gal}$.

3.2.3. Changes in gravity and height of the station

There is no DORIS beacon at Tidbinbilla, but there is a permanent GPS receiver. Its trend from IGS00 is $\dot{h} = +2.16 \pm 0.25$ mm/yr whereas the linear fit of the 3 AG measurements (2003, 2004 and 2006) lead to $\dot{g} = -3.90 \pm 0.76$ μ Gal/yr. These results both suggest an uplift

The point SV / DORIS is the only one whose error bars include the free-air gradient. A second comment is that the solutions at Tidbinbilla and at the SV / GPS_PT agree within the error bars. This could reflect a common behaviour, which is consistent with the proximity of the stations. The cause to explain gravity/height ratios larger than the free air one is still under investigation. A possible reason is hydrology as shown in Hinderer et al. (2006).

3.3. Comparing Mt Stromlo and Tidbinbilla

Figure 3 shows the change in gravity (Δg) with respect to the change of height (Δh).

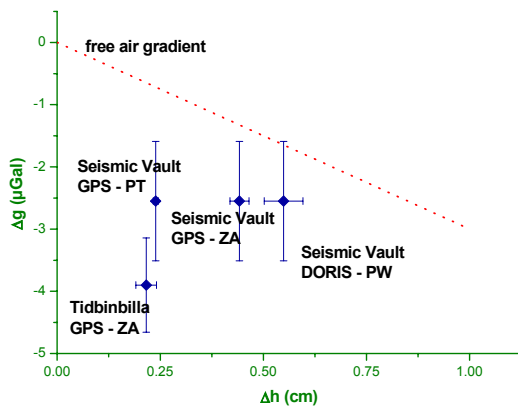


Figure 3 – Change of height vs gravity change at Tidbinbilla; PT = Paul Tregoning, ZA = Zuheir Altamimi, PW = Pascal Willis.

For the Mt Stromlo we choose the change of gravity at the seismic vault that is in agreement with the observations of positioning techniques and plotted the 3 points corresponding to the solutions we have there. We also plotted the straight line corresponding to the free air gradient (- 0.3 μ Gal/mm).

The first comment is that all the points are below this line whereas the points are usually below it.

Appendix

Table A1 shows the parameters and final g-value at each station measured in 2006 with the FG5#206 of Strasbourg (France). The value of gravity is given at the ground level, after all reductions. Table A1 provides altogether the coordinates of the stations, the nominal pressure calculated according to IAGBN standards (Boedecker, 1988), the vertical gradient of gravity at the reference point, the number of measured drops and the date of measurements.

Station	Latitude Longitude Height m	Nominal pressure hPa	Vertical gradient of gravity μ Gal/cm	Number of drops	Date 2006	g value μ Gal
---------	--------------------------------------	----------------------------	--	--------------------	--------------	----------------------

4. Conclusions

We have repeated AG measurements in Antarctica at DdU, six years after the first measurement. The lack of change in the gravity value agrees with the small trend of vertical displacement observed by the collocated GPS and DORIS stations. Vertical stability is also the prediction of the various existing modelling for that part of the Antarctic continent. A new measurement is planned at DdU in 2008 during the International Polar Year, with additional measurements at Dome C (Concordia station) which will be the first measurement performed on ice, repetition of measurements after approximately ten years at Terra Nova Bay and Mc Murdo and first measurements at Casey. We have repeated AG measurements at three sites near Canberra, Australia. Two of them give good agreement between AG and height changes observed by GPS and DORIS at the Mt Stromlo Seismic Vault ($\dot{g} = -2.5 \pm 0.1$ μ Gal/yr and $\dot{h} = +2.39 \pm 0.06$ mm/yr, $\dot{h} = +5.49 \pm 0.49$ mm/yr) and Tidbinbilla, Canberra Deep Space Complex, ($\dot{g} = -3.90 \pm 0.76$ μ Gal/yr and $\dot{h} = +2.16 \pm 0.25$ mm/yr). On the contrary the variation of gravity and the vertical displacement disagree at the Mt Stromlo SG site ($\dot{g} = +3.7 \pm 1.6$ μ Gal/yr).

These measurements should also be repeated in 2008 on the way back from Antarctica.

DdU Antarctica	66.67° S 140.17° E 35	996.5441	-3.82 ± 0.03	16187	5-8 February	982 387 167.0 ± 3.5
SG site Mt Stromlo Australia	35.3206° S 149.0075° E 762.51	924.94	-2.78	10314	18-22 February	979 549 878.01 ± 0.91
Seismic Vault Mt Stromlo Australia	35.3188° S 148.9963° E 685	933.62	-2.65	3474	25-26 February	979 569 851.50 ± 0.80
Tidbinbilla Canberra DSCC Australia	35.4010° S 148.9821° E 640.81	938.60	-2.604	2382	24-25 February	979 576 105.0 ± 0.70

Table A1 – AG measurements in 2006 with the FG5#206 - Station parameters and gravity value, at the ground level.

Table A2 shows the parameters and final g-value at the same stations, measured in 2003 and 2004 with the FG5s#111 & 210. The value of gravity is given at the ground level, after all reductions.

Station	Operator gravimeter	Instrument	Number of drops	Date	g value (μ Gal)
SG site Mt Stromlo	Kyoto University	FG5#210	9224	29 March – 4 April 2004	979 549 870.7 ± 3.0
Seismic Vault Mt Stromlo	Kyoto University	FG5#210	3581	23-26 March 2004	979 569 856.6 ± 1.8
Tidbinbilla Canberra DSCC	Micro-g Solutions	FG5#111		June 2003	979 576 114.4 ± 2.3
Tidbinbilla Canberra DSCC	Kyoto University	FG5#210	7060	31 March – 3 April 2004	979 576 114.3 ± 2.4

Table A2 – AG measurements at Australian sites in 2003 and 2004 with the FG5s#210 and 111 - Station parameters and gravity value, at the ground level, after Fukuda et al., 2004

Acknowledgments. We thank all the people from IPEV, TAAF, and *Astrolabe* for their support and help in Antarctica and RSES and R. Tracey for their support and help in Australia, M.N. Bouin, Z. Altamimi, P. Tregoning, G. Woppelman, P. Willis for providing their respective solutions.

References

- Amalvict M., Hinderer J. & Luck B. 2001, First absolute gravity measurements at the French station Dumont d'Urville (Antarctica), IAG Symposia, vol. **123**, M. Sideris (ed.), Gravity, Geoid and Geodynamics 2000, Springer Heidelberg, 373-377.
- Amalvict M., Hinderer J., Boy J.P. and Luck B., 2001a, Gravity at Kerguelen (Indian Ocean): Absolute Gravity Measurements and Tidal Analysis from a relative gravimeter data, IAG General Scientific Assembly, Budapest, September 2001, proceedings on CD-Rom.
- Amalvict, M., McQueen H. & Govind R., 2001b, Absolute Gravity Measurements and Calibration of SG CT #31 at Canberra, 1999-2000, Journal of Geodetic Society of Japan, 47, 410-416.
- Amalvict M., Bouin M-N., Hinderer J. and Luck B., 2003, Results of the first absolute gravity measurements at Crozet Island, and repetition at Kerguelen and La Réunion Islands, 9th Symposium on Antarctic Earth Sciences, Potsdam, Germany, September 2003.
- Amalvict M., 2003., Gravity measurements in Antarctica: a review, 9th Symposium on Antarctic Earth Sciences, Potsdam, Germany, September 2003
- Amalvict M. and de Linage C., 2004, Vertical displacement and variation of gravity predicted and observed in Antarctica, SCAR Open Science, Bremen, Germany, July 2004

- Amalvict M., Rogister Y., Luck B. and Hinderer J., 2005, Absolute Gravity Measurements in the Southern Indian Ocean, Cairns IAG meeting, accepted.
- Boedecker, G. 1988. International Absolute Gravity Basestation Network (IAGBN). Absolute gravity observations data processing standards & station documentation. BGI Bull. Inf. 63, 51–57.
- Fukuda Y., Higashi T., Takemoto S., Iwano S., Doi K., Shibuya K., Hiraoka Y., Kimura I., Mc Queen H. and Govind R., 2005, Absolute gravity measurements in Australia and Syowa station, Antarctica, IAG proceedings Porto meeting.
- Hinderer J., Amalvict M. & Luck B., 2002, Premières mesures françaises de gravimétrie absolue dans les régions polaires Antarctique (Terre Adélie) et Arctique (Spitzberg), C.R. Geoscience **334**, 819-826
- Hinderer, J., O. Andersen, F. Lemoine, D. Crossley & J.-P. Boy, 2006. Seasonal changes in the European gravity field from GRACE: A comparison with superconducting gravimeters and hydrology model predictions, Journal of Geodynamics, 41, 59-68.
- James T.S. and Ivins E.R., 1995, Present-day Antarctic ice mass changes and crustal motion, Geophysical Research Letters, **22**, n°8, 973-976.
- James T.S. and Ivins E.R., 1998, Predictions of Antarctic crustal motion driven by present-day ice sheet evolution and by isostatic memory of the last glacial maximum, JGR B, 103, n°3, 4993-5017.
- Mäkinen J., Amalvict M., Shibuya K. and Fukuda Y., 2006, Absolute Gravimetry in Antarctica: Status and Prospects, Journal of Geodesy, accepted.
- Murakami Msk, Murakami Mkt, Nitta K., Yamaguchi K., Yamamoto H., Karasawa M., Nakahori Y., Doi K., Murphy B., Govind R., Morse M. and Gladwin M., 1997, Absolute determination of gravity for the purpose of the establishment of precise reference frame for sea level change monitoring in the Southwestern Pacific, IAG Symposia, **117**, 32-39.
- Nakada M., Kimura R., Okuno J., Moriwaki K., Miura H. and Maemoku H., 2000, Late Pleistocene and Holocene melting history of the Antarctic ice sheet derived from sea-level variations, Marine Geology, **167**, Issues 1-2, 85-103.
- Peltier W.R., 1995, VLBI baseline variations from the ICE-4G model of postglacial rebound, Geophysical Research Letters, 22, n°4, 465-468
- Tregoning P. Morgan P.J. and Coleman R., The effect of receiver firmware upgrades on GPS vertical time series,

Gravity and positioning control for the revision of the French gravity map and network

G. Martelet¹, M. Sarrailh², N. Debeglia¹

¹ BRGM – 3 av. Claude Guillemin, 45060 Orléans Cedex 2 – France

² BGI – 18, Avenue Edouard Belin 31500 Toulouse Cedex 9 – France
g.martelet@brgm.fr - Michel.Sarrailh@cnes.fr - n.debeglia@brgm.fr

1 - INTRODUCTION

In order to improve its national geoid, and be able to address high accuracy gravity-related issues, France plans to update its national gravity network and gravity map by the end of year 2008.

In this context, a careful validation and improvement of the existing gravity data is necessary since the existing gravity stations (about 410000) and base stations (more than 1000) should be integrated in the new gravity references.

Integration of new gravity network measurements (performed by IGN since 2003) and existing ones require that both the gravity data and their position are controlled.

The controls address possible distortions :

- 1- between the new and old networks: field tie measurements are done,
- 2- between the new network and the national gravity map: gravity prediction is performed at the new network base locations using the existing gravity measurements.

For this purpose, the accuracy of both the gravity and position of the ~410000 gravity stations, must be verified.

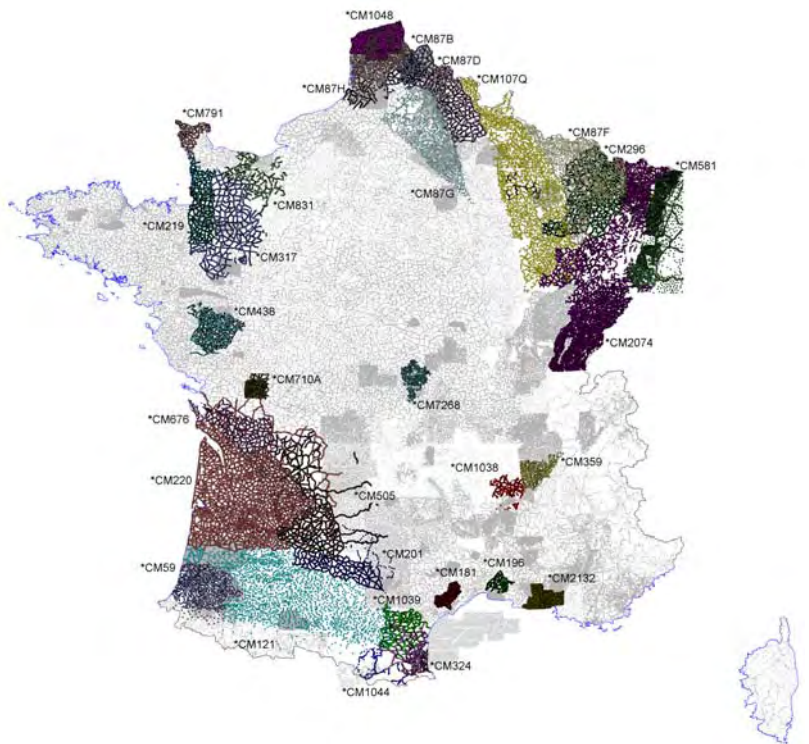


Fig.1: Location of the 414400 gravity stations of the BGF. The 30 mis-positioned surveys are highlighted.

THE FRENCH GRAVITY DATABASE All the gravity data are integrated in the « Banque Gravimétrique de la France » (BGF), under the responsibility of the BRGM, and can be accessed via the BRGM Infoterre Web portal (<http://www.brgm.fr>). A large part of the French gravity data have been measured between 1945 and 1975, by several operators. The diversity of the sources and the drastic evolution of archiving procedures since then, have required very careful management of these data.

Inevitably, while changing from one gravity or positioning system to an other, or when digitizing these data, some errors have been introduced. For example, the survey CM571, which was referred to an old german cadastral system in Elsass, has a shift of ~800 m.

In order to identify and eliminate as much as possible such erroneous data, several methods have been developed or adapted. These methods concern :

- 1- the gravity value and corrections of the data,
- 2- their positioning.

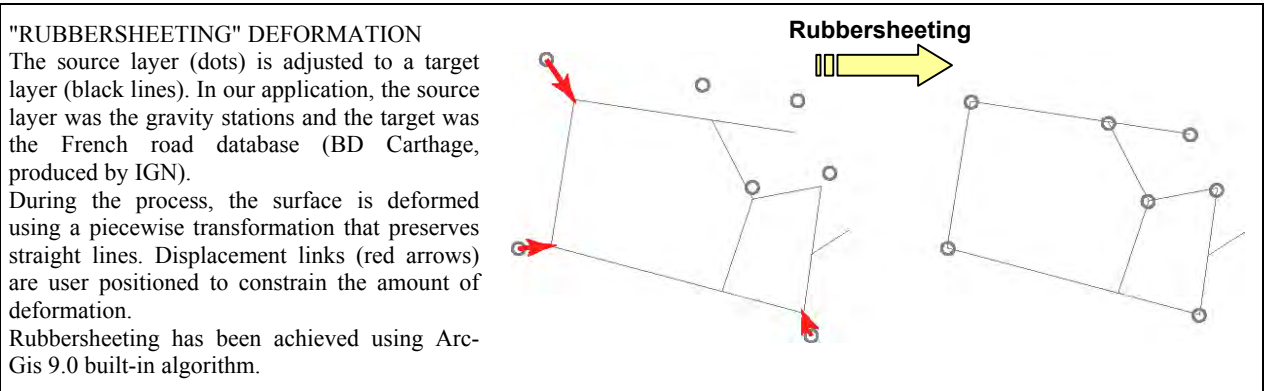
2 - REVISION OF THE POSITIONING

2.A – Methodology of re-positionning

The BGF contains more than 410000 gravity stations divided into 173 gravity surveys.

The main objective of this work was to identify and correct existing systematic shifts of the gravity stations for each survey. For each survey, two different approaches have been adopted:

- an automated approach designed to find the optimal horizontal displacement of the survey that minimises the difference of altitude between the stations and a DTM (see insert),
- a visual identification of the shifts and distortions of the positioning with respect to the roads (where most stations were measured) and *ad hoc* re-positioning of the surveys using a GIS « rubbersheet » algorithm (see insert).



2.B – Results of re-positionning

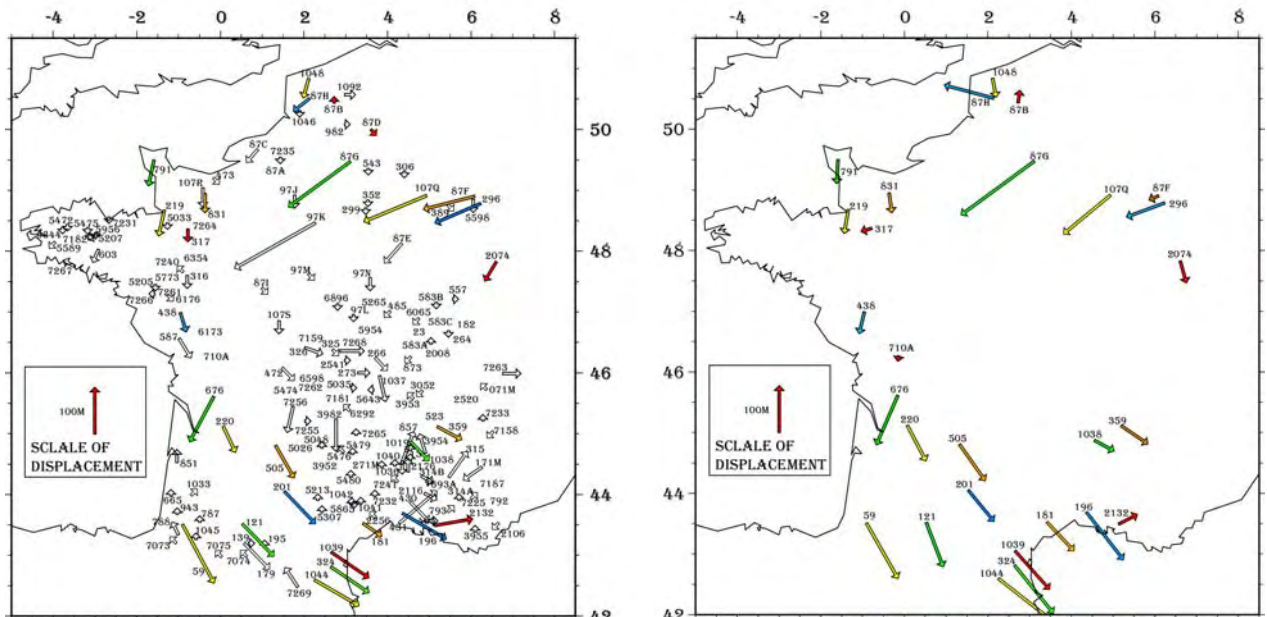


Fig. 2: X-Y shifts of the gravity surveys, obtained on the left by comparison with the DTM, on the right, with the rubbersheet method.

Average displacements of the gravity surveys obtained for each method are shown in Figure 2. In the visual approach, only 30 surveys out of the 173, were re-positioned since the others appeared properly positioned at the 1/25000^e scale (discrepancies not more than half a millimeter, *i.e.* ~15m).

Improvement of the positioning before and after the two methods were applied, has been evaluated for each method:

- comparing visually the location of the gravity stations with respect to the roads,
- computing the average and standard deviation of the difference of altitude of the gravity stations with the IGN 50x50m DTM, for each gravity survey (Fig. 3a). This indicator was also expressed as a percentage of improvement of the standard deviation (Fig. 3b).

Data used to evaluate the positioning quality of the gravity surveys (produced by IGN), are:

- DTM 140x140m, DTM 50x50m – vertical accuracy: ~1 m to +/- 20 m in the mountains
- BDCarto, digitized roads – horizontal accuracy: ~10 m
- Scan25, digital 1:25000 topo maps – horizontal accuracy: ~10 m

Fig. 3: Statistics showing the improvement of the new positioning in terms of reduction of the difference of altitude of the gravity stations with the 50x50m DTM;

a) Average difference of altitude between the gravity stations and the DTM for each re-positioned survey,
 b) Improvement (%) of the standard deviation of the difference of altitude between the DTM and stations.

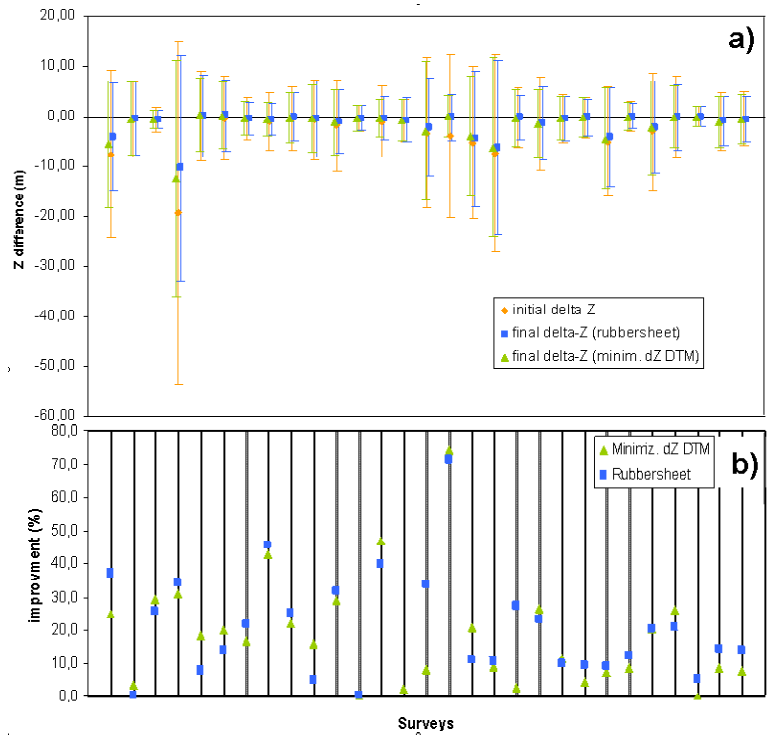
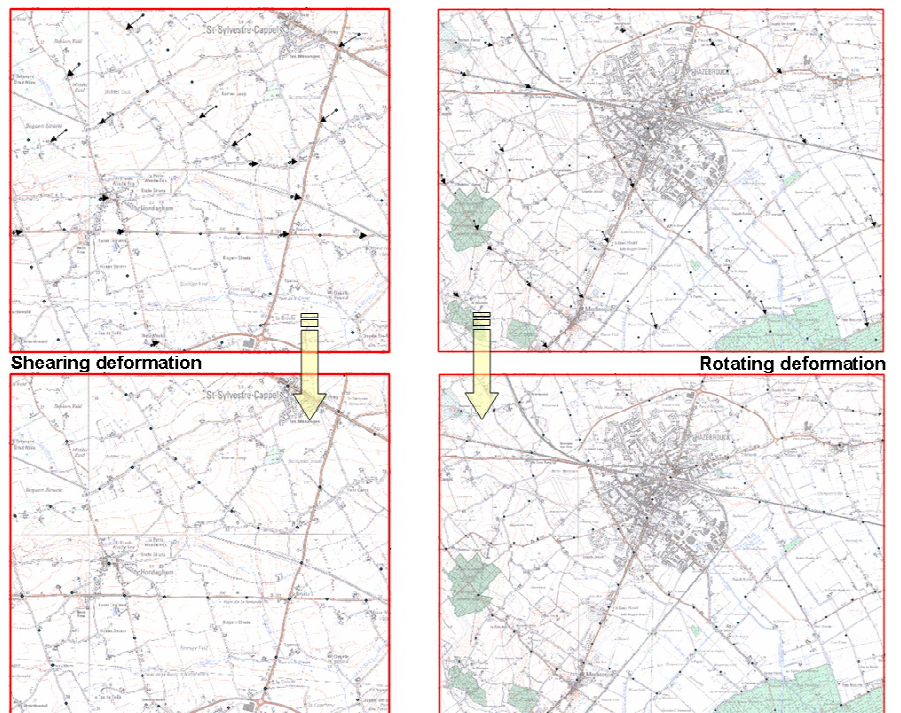


Fig. 4: Examples of rubbersheeting re-positioning showing (left): shearing deformation, (right): rotating deformation. Both deformations were probably introduced while digitizing old datasets.



For the 30 surveys re-positioned by the two methods, the difference of altitude with the DTM is always improved. The comparison of the results of the two methods of re-positioning don't show large discrepancies (Fig. 3b).

The method based on the adjustment on a DTM (see insert), has the advantage to be automated, but a graphic control is nevertheless useful.

The method based on the rubbersheeting deformation can take into account piecewise local deformations (Fig. 4) (for example due to the digitizing of old maps), but can be used only when the stations where measured mainly on the roads.

DEFORMATION BASED ON THE ADJUSTMENT ON A DTM

In this method, constant X-Y shifts of the gravity stations for each survey are assumed.

Adjustment of the location of gravity stations is achieved, searching the shifts in latitude and longitude which minimize the differences between the altitudes of the stations and a DTM.

The algorithm uses an iterative process which converges quickly.

Adjustment of the location of gravity stations by this method have been compared using 140x140m and 50x50m DTMs (Fig. 5). Both adjustments produce coherent results. Adjustment with the more detailed DTM generally produces results intermediate between the rubbersheet and 140x140m DTM.

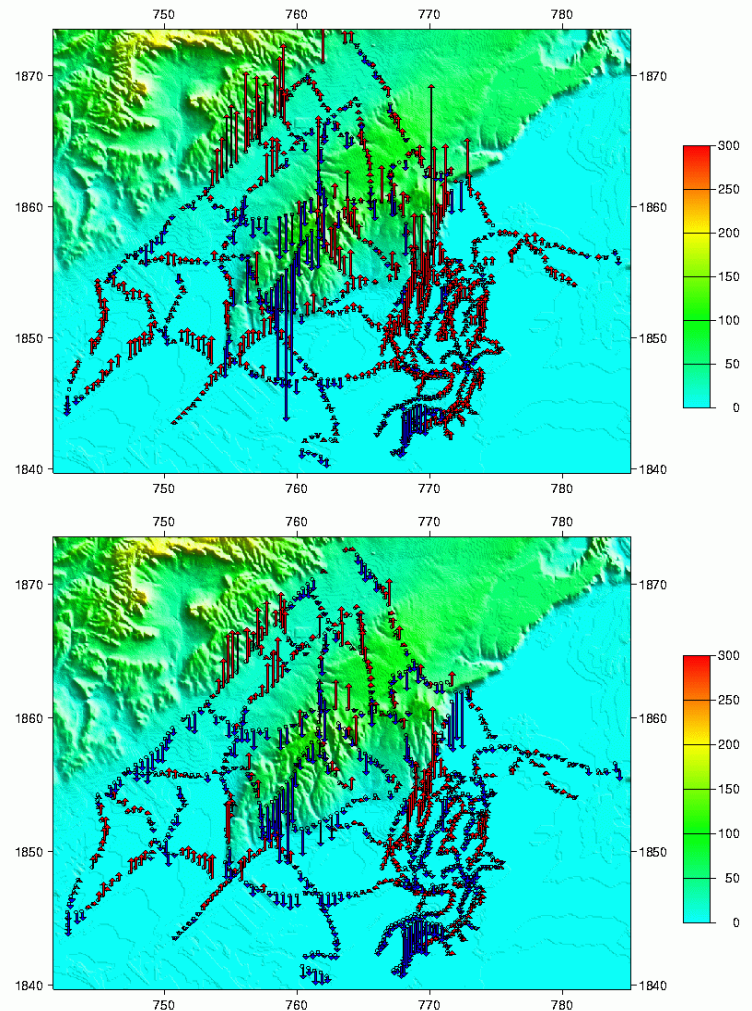


Fig. 5 : Altitude differences between DTM 50x50m and the CM196 gravity data: (up) before adjustment ($-23.2 < dz < 25.8$ m), and (down) after adjustment to the 50x50m DTM ($-12.2 < dz < 9.0$ m).

2.C – Conclusions and perspective of the re-positioning

A careful validation of the results and subsequent choice of the type of displacement that should be applied to each survey is necessary.

After the modifications of positioning will be applied:

- terrain corrections of the displaced stations will be re-computed. They might be significantly improved, since the principal source of error of the terrain effect is erroneous altitude differences between the stations and the DTM.

- precision of the control of erroneous gravity values will be more accurate (next section).

2 - CONTROL OF ERRONEOUS GRAVITY VALUES

2.A – Introduction

The objective of this work was to identify among the ~410000 stations of the BGF, existing erroneous gravity values, if possible, understand the source of the error and correct it, or remove the outliers.

The validation procedure adopted is based on an algorithm of prediction of the Bouguer anomaly for every station of the database, using the surrounding gravity measurements. When the difference between the station value and the computed prediction exceeds a determined threshold, the station is flagged.

The prediction is computed using a surface fitting triangulation procedure (DSURF module, from the IMSL library) using the following control parameters:

- *Raymax* (m): maximum search radius, - *Toldz* (m): maximum difference of altitude of the stations used for the prediction, - *Kdata*: maximum number of stations used for the prediction.

If too few stations (less than 4) are available in the search radius, the prediction cannot be achieved.

A gravity station is considered erroneous:

- if the difference between the station value and the average computed prediction exceeds a tolerance value *tol* (mGal),
- or if the difference between the station value and the average computed prediction exceeds (*ksig* x standard deviation).

2.B – Evaluation of the method

The gravity validation procedure has been evaluated on a regional 100x100 km subset dataset, extracted from the BGF (Fig. 6).

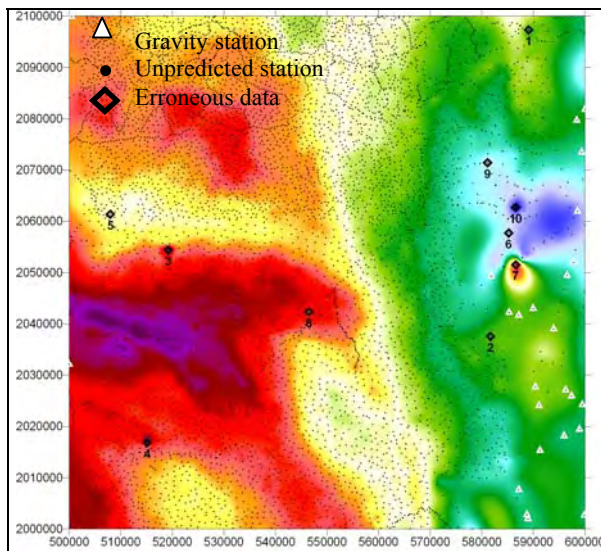


Fig. 6: Test of the validation procedure at a regional scale. Parameters used are: *Raymax* = 5000 m; *toldz* = 250 m; *kdata* = 20; *tol* = 3 mGal; *ksig* = 3.

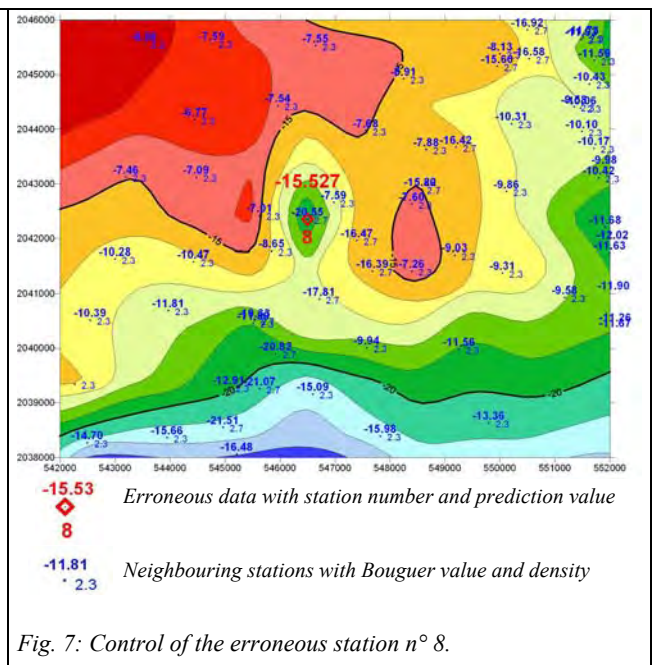


Fig. 7: Control of the erroneous station n° 8.

Careful local analysis of the results of the procedure was done (Fig. 7), which allowed to modify the algorithm, in order to obtain results as close as possible to visual estimations.

The validation procedure can be parameterized in order to identify poor quality gravity data, in a more or less restrictive manner.

It will be used:

- to identify and eliminate punctual erroneous data,
- to identify possible systematic errors and correct them, if possible,

These errors being cleared out, the overall accuracy of the dataset will be evaluated and a map will be produced, displaying levels of confidence of the gravity stations.

2.C – Preliminary determination of erroneous gravity data

The gravity validation procedure has been tested on the whole French gravity database in order to:

- present a first evaluation of the amount and repartition of poor quality gravity data,
- evaluate the computation time necessary to achieve a complete control of the stations of the French database.

These results are preliminary since neither the modifications of the positioning have been introduced yet in the database, nor the terrain corrections have been recomputed.

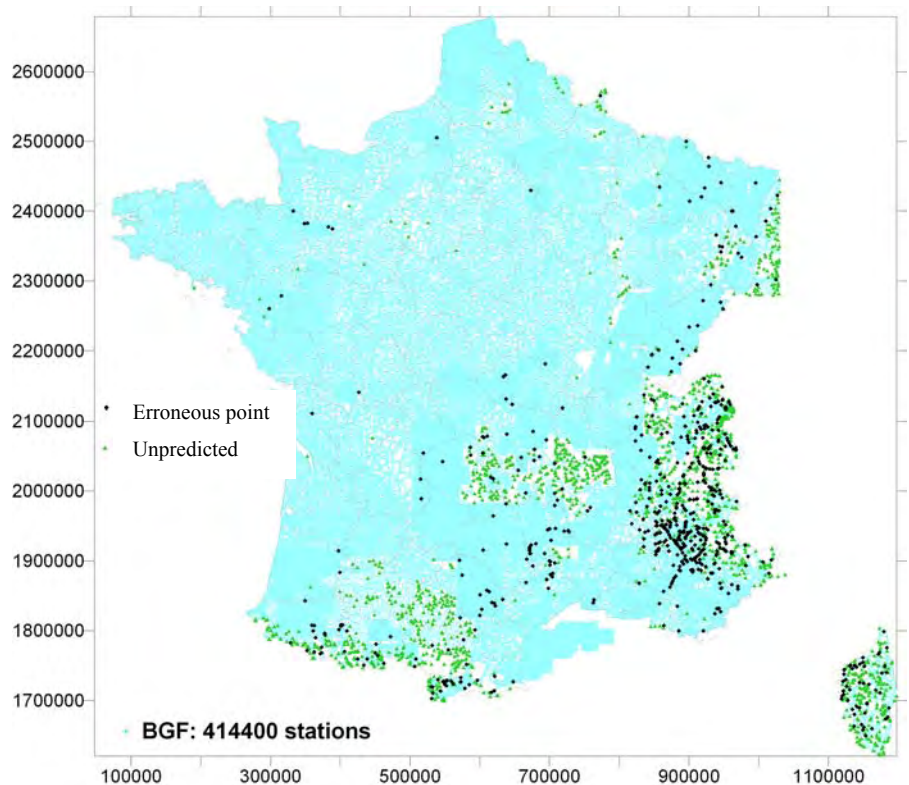
The results of the computation (Fig. 8) show that most erroneous data (black dots) are located in the mountainous areas (Alps, Pyrénées, Massif Central). This suggests a strong importance of the relief on the errors.

Possibly, the control of positioning and re-computation of terrain corrections in these areas might improve the accuracy of these data.

The computation time on a standard desktop Pentium PC, for the whole database, was about 8 hours.

This relatively short computation time is compatible with several runs with gradual thresholds of validation.

Fig. 8: Test of the validation procedure at the scale of France. Parameters used are: Raymax = 5000 m; toldz = 250 m; kdata = 20; tol = 5 mGal; ksig = 3.



2.D – Conclusions and perspectives to the gravity validation

A robust method of identification of erroneous gravity data by prediction of the Bouguer anomaly for every station of the database, using the surrounding gravity measurements has been implemented.

After correction of the positioning and re-computation of terrain corrections, use of this algorithm for the whole BGF should allow:

- the elimination of punctual erroneous data,
- the identification and possibly correction of systematic errors.

The production of a map displaying levels of confidence of the gravity stations would provide a more realistic evaluation of the accuracy of the data than the existing averaged error informations (based on instrumental characteristics of the surveys).

ACKNOWLEDGMENTS

This work was funded by BRGM research programs, as part of project « Référentiel Cartographique 3D Intégré ».

First Order Gravity Network of Republic of Moldova

V. Chiriac, V. Pantikin

Institute of Geodesy, Engineering Research and Cadastre,
Land Relations and Cadastre Agency, 49 Puskin Street, Chisinau, MD-2005, Moldova

K.W. Krauterbluth

Florida Geodetic Surveys Office, Geospatial Sciences Division,
National Geospatial-Intelligence Agency, 698 O'Malley Road, Patrick AFB, FL 32925-3329, USA

I. Ilies

Institute of Geophysics and Geology,
National Academy of Sciences, 3 Academia Street, MD-2028, Chisinau, Moldova

I. Cretu

Geodesy, Cadastre and Geotechnical Department,
Technical University of Moldova, 41 Dacia Street, MD-2062, Chisinau, Moldova

Abstract. In 2006 the Land Relations and Cadastre Agency of Republic of Moldova in cooperation with the National Geospatial-Intelligence Agency (NGA) of United States of America performed gravity campaign to establish a new fundamental gravity network MOLDGRAV06.

Gravity measurements were carried out at 20 base stations and their excentric. In order to constrain the relative gravity measurements 3 absolute gravity stations were determined using FG5 absolute gravimeter.

The absolute gravity data acquisition and processing were done by Micro-g software. The Total uncertainties of the absolute gravity measurements are about 5 μ Gal. The relative gravity stations and local vertical gradients have been measured using three LaCoste & Romberg G meters. The gravity network was designed as polygons. Each station was occupied at least twice.

The preliminary data processing was performed by GVREC, ETIDE and GVCOMP programs. The network adjustment was performed by GRAVNET program. The RMS value of the relative gravity stations is better than 10 μ Gal.

Keywords. Absolute gravity, relative gravity, gravimeter, gravity network, gravity vertical gradient.

1 Introduction

This report presents the results of the first-order gravity network survey campaign carried out by Institute of Geodesy, Engineering Research and Cadastre (INGEOCAD) subordinated to Land Relations and Cadastre Agency of Republic of

Moldova in cooperation with the National Geospatial-Intelligence Agency (NGA). The project was requested by National Army Topographic Service, Chiriac (2006).

Three absolute gravity stations were established throughout the country using a Micro-g Solutions FG5 absolute gravimeter. Excenters and several satellite stations for each absolute as well as 17 additional first-order gravity base stations were also established relative to the absolutes using three LaCoste & Romberg G gravimeters (see Fig. 1.1).

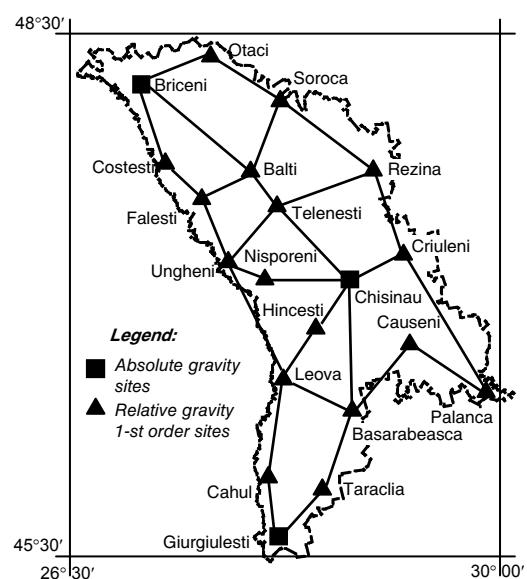


Fig. 1.1 The First order Gravity Network Diagram

The survey fieldwork was conducted during the period May–June, 2006. The value of the absolute gravity was established at the floor. The absolute gravity sites were selected by INGEOCAD and Institute of Geophysics and Geology personnel, at two existing seismic stations with stable isolated concrete piers suitable for the measurements.

The location of the absolute gravity sites follow a set of criteria developed to optimize performance of the absolute gravimeter. These criteria include permanency, stability of the underlying ground, adequate space and electricity, temperature stability and protection from the weather (see Fig 2.1). The relative sites were chosen more as an accessible and stable location to provide a high accuracy base station available for future surveys (see Figs 2.2, 2.3).

2 Survey operations

The FG5 107 absolute gravimeter was set up and placed into automatic operation at each of the three sites (see Fig 1.1). The meter ran for 24 to 36 data sets, one set of 100 drops per hour. Data was then analyzed and certain sets were rejected. All gravity data were stored on disk for post processing.



Fig. 2.1. Chisinau AA absolute gravity station on the main pillar of the Institute of Geophysics and Geology Seismic observatory.

A vertical gradient was measured at each absolute and two satellite stations using a combination of three LaCoste & Romberg model G relative gravimeters. The vertical gradient was measured directly over the station by observing at ground level and at a height of +1.00 meter.

For easier accessibility, an excenter gravity station was established out of doors close to each absolute station. This was accomplished with the same instruments used for determination of the vertical gradient.



Fig. 2.2. Palanca E relative gravity station on the pillar of EUREF site.

First-order base stations were established using three relative gravimeters in standard double ladder sequence loops with either a newly established absolute or excenter station as control. Each station was observed at least twice by each meter. In some cases stations were observed in multiple loops from the same or a different control station. A series of polygons were later combined in the data reduction to form a strong country wide first-order gravity network.



Fig. 2.3. Balti C relative gravity station on the main entrance stairs of the St. Nicolae Cathedral.

Satellite stations were observed in close proximity to each absolute station. The stations were all observed with its respective absolute or excentric station as control, in the same manner as the previously mentioned base stations. Each of these stations also meets the first-order requirements.

3 Computations and analysis

The vertical gradient, updated polar motion coordinates, and position information were entered into the Micro-g Solutions program “g” version 4.0 to compute the absolute observations. Standard input parameters, such as earth tides, speed of light correction, local barometric pressure correction, and the DC tidal term (Honkasalo correction) were set to the appropriate values as recommended by Micro-g Solutions and the International Gravity Commission.

The data from the relative gravimeters were recorded and field checked at each site using NGA programs GVREC and GVCOMP. Later it was combined by site and reduced using the NGA program GRAVNET which performs a least squares adjustment on the data, automatically setting the internal weight codes. The preliminary absolute gravity value from the field observations was used as initial control to determine the vertical gradient. The corrected absolute gravity value was held fixed in the final adjustment of the relative gravity data, for each site. A combined network adjustment was performed on all network base stations, holding all three absolute stations fixed. Satellite stations were adjusted separately holding only each respective absolute station fixed.

The final mean gravity value is set within the FG5 gravimeter at a reference height above the ground. The gravity gradient is then mathematically applied to the value in order to obtain a gravity value at the ground surface where the actual station exists. This ground surface value is the absolute station value reflected in this publication from which all relative measurements are based.

4 Survey results

The accuracy of the absolute stations is based on the FG5 manufacturer’s estimated uncertainties for many different components (see Table 4.1). These components include uncertainties in the modelling, system and set up. Default values as recommended by Micro-g were used for each set up. Total uncertainties for each setup are approximately

± 0.005 mGal, see NGA (2006).

The measurement precision and set scatter for each station is the standard deviation of all drop sets at each site, each set being approximately 100 drops. This value is a good indication of site stability and should be included when determining the overall accuracy of the gravity station.

Table 4.1. Gravity value of the absolute stations.

Station name	Gravity Value (mgal)	Total uncertainty (mGal)
CHISINAU AA	980767.445	0.00444
GIURGIULESTI AA	980628.643	0.00507
BRICENI AA	980867.919	0.00453

The Root Mean Square (RMS) of the remaining relative stations (see Table 4.2) based on the least squares adjustment of the relative gravity observations is better than 0.010 mGal, see NGA (2006).

Table 4.2. Gravity value of the relative stations.

Station name	Gravity Value (mGal)	RMS (mGal)
HINCESTI D	980762.084	0.007
LEOVA B	980751.437	0.007
BASARABEASCA D	980739.426	0.007
CAUSENI D	980762.251	0.009
PALANCA E	980727.001	0.009
CAHUL B	980670.650	0.008
TARACLIA C	980670.489	0.007
NISPORENI D	980798.552	0.008
UNGHENI C	980801.701	0.007
CRULENI D	980802.994	0.007
COSTESTI D	980860.949	0.008
FALESTI D	980822.745	0.008
BALTI C	980846.797	0.007
OTACI E	980867.847	0.008
SOROCA B	980887.697	0.008
REZINA D	980849.917	0.008
TELENESTI C	980837.674	0.007

The final precision of the remaining relative stations is based on the least squares adjustment of the relative gravity observations with respect to the absolute station. It is obtained by calculating the Root Sum Square (RSS) of the precision of the absolute measurements along with the adjusted precision value of the relative measurements.

5 Comparison with the previous network

In 2000 a preliminary national gravity reference network of Republic Moldova which consist of 7 stations, have been measured using one LaCoste & Romberg D-214 gravity meter owned by the Geological Institute of Romania. Two base stations of the national gravity reference network of Romania were used to transfer the gravity value into the cross-border area, Besutiu et al. (2004).

Five stations are common to both networks. The difference of absolute gravity values between the previous preliminary network and the new one vary from +19 μ Gal to +85 μ Gal.

6 Conclusions

Have been measured 53 ties with 3 different instruments which linking the 20 base stations and their satellite stations. The solution is perfectly stable everywhere on the territory of the country with accuracy better than 10 μ Gal.

The new first order gravity network over Republic of Moldova is well constrained by the 3 absolute gravity stations with the accuracy around 5 μ Gal.

We recommend in the future to densify the relative gravity network about 1 point per 15-20 square kilometres for geophysical applications and modelling of the high resolution national quasigeoid.

Acknowledgement

The work was accomplished through a collective effort from NGA (Keith W. Krauterbluth), INGEOCAD (Dr. Vasile Chiriac, Vladimir Pantikin, Uliana Danila), Institute of Geophysics and Geology of the National Academy of Sciences of Moldova (Dr. Vasile Alcaz, Ion Ilies and Ion Borodatii) and Technical University of Moldova (Ion Cretu).

We are very grateful to Alexandr Cebanu and Tamara Grec from National Army Topographic Service who negotiates with NGA in order to start this project.

The Land Relations and Cadastre Agency of Republic of Moldova provided a full support to the field operations.

We would like to gratitude especially the NGA who provided gravimeters and an experienced surveyor.

References

- Besutiu L., Neaga V., Nicolescu A., Lorinczi J., Ilies I., Besutiu G. (2003): Preliminary results in the achievement of the new gravity system of Republic of Moldova. *Newton's Bulletin* - n°1, Dec. pp. 28-40.
- Chiriac V. (2006) National Report of Republic of Moldova. EUREF Symposium, June14-17, Riga. *EUREF Publication*, in print.
- NGA (National Geospatial - Intelligence Agency) 2006. Gravity Network Survey Moldova. *Geodetic Survey Report*. Publication 06-4018, August, 48 p.

Determination of Mass Variations in Northern Europe From GRACE Data

J. Müller, M. Neumann-Redlin, H. Denker

Institut für Erdmessung, Leibniz University of Hannover, Schneiderberg 50, 30167 Hannover, Germany
mueller@ife.uni-hannover.de

Abstract. In Northern Europe the region of Fennoscandia is characterised by present-day uplift caused by glacial isostatic adjustment (GIA). The uplift effect reaches up to 11 mm/year at the Earth's surface. This effect can be observed geometrically, e.g. by GPS or spirit levelling, and gravitationally by absolute gravimetry. A new challenge is the determination of the GIA-induced gravity changes by the satellite mission GRACE. During the mission duration of GRACE (more than five years), a temporal gravity change of about 100 nm/s^2 is expected in the centre of the Fennoscandian land uplift area (the Bothnian Bay). The configuration of GRACE is basically suited to determine this magnitude of variation. But the GRACE observations contain the integral signal of various geophysical processes such as atmospheric, oceanic and hydrological effects which may conceal the uplift signal.

In this study, we determine secular and periodic gravity changes in Fennoscandia from the GRACE monthly solutions as provided by CSR, University of Texas, and Geoforschungszentrum Potsdam (GFZ) for the first 4 years of the GRACE mission. We compare the resulting variations with hydrological models and match the GRACE derived signals with those obtained from a simple uplift model based on geophysical predictions.

Keywords. glacial isostatic adjustment, land uplift, GRACE, gravity changes, hydrological models, pattern recognition

1 Motivation

Gravity field variations as derived from the monthly GRACE solutions result from the integral effect of mass variations in the atmosphere, hydrosphere and geosphere. These effects include oceanic, atmospheric and hydrological mass movements and those caused by dynamics in the Earth's interior. In addition, residual signals from insufficient pre-processing may be present. The main objective of this study is to extract mass variations in Northern Europe from the

GRACE data, especially those which are related to the Fennoscandian land uplift resp. glacial isostatic adjustment (GIA). One key issue is the separation of the various signal parts and the reduction of the observed (or derived) quantities by applying dedicated filter (e.g. Gaussian) and analysis techniques (e.g. pattern recognition). Besides filtering of the various signal parts, the quality assessment of the individual measurements and the reduction models are of special relevance, in order to determine the interrelations and the corresponding accuracies.

Up to now mainly terrestrial data sets (like tide gauges, GPS measurements, levelling or terrestrial gravimetry) were used to determine the present-day land uplift in Fennoscandia (e.g. Ekman 1996, Ekman and Mäkinen 1996, Johannsson et al. 2002, Kuo et al. 2004, Milne et al. 2001, Scherneck et al. 2003, Wilmes et al. 2005). According to Ekman (1996), these observations reveal a maximum orthometric height change of 10.2 mm/year over the Bothnian Bay and show symmetry around the maximum. The height change in the centre is associated with a maximum gravity variation of 20 nm/s^2 per year. Based on these numbers, a geoid change of 0.6 mm/year has been derived for the central area (e.g. Ekman and Mäkinen 1996).

The detection and recovery of temporal gravity variations (e.g. caused by hydrological or oceanic effects) from GRACE data was shown in several investigations, cf. Chen et al. (2006), Famiglietti et al. (2005), Frappart et al. (2006), Han et al. (2005), Rodell et al. (2004), Rowlands et al. (2005), Schmidt et al. (2006), Swenson et al. (2006), Tapley et al. (2004), Thompson et al. (2004) and Wahr et al. (2004). Further references are given in the report of Ilk et al. (2005). According to sensitivity studies (e.g. Velicogna and Wahr 2004, NRC 1997) the recovery of GIA-induced uplift signals might be possible from gravity variations observed by GRACE.

During the mission duration of GRACE (about five years), a temporal geoid change of 3 mm is expected in the centre of the Fennoscandian land uplift area, corresponding to a gravity change of about 100 nm/s^2 . As the geoid derived from GRACE data

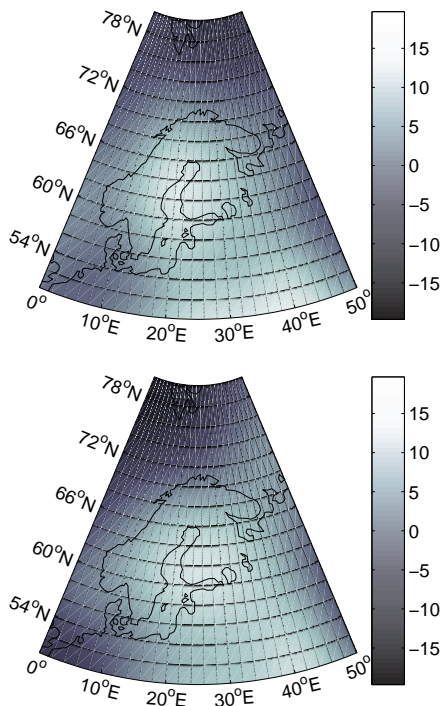


Fig. 1. Secular variation in Fennoscandia determined from GRACE monthly solutions as provided by GFZ (top) and CSR (bottom), units: $\text{nm/s}^2/\text{year}$. Here a Gaussian filter with radius 500 km has been applied.

can be determined on a monthly basis with an accuracy of about 1 mm at a spatial resolution of 800 km (see also Tapley et al. 2004), the land uplift causes a measurable signal in the observations (NRC 1997, Wahr and Velicogna 2002). The separation of this effect from other time-variable gravity changes is a big challenge.

2 Processing of GRACE Solutions

The primary objective of the GRACE mission is to provide global models of the Earth's gravity field with high accuracy. The mission allows to determine the mean gravity field as well as temporal gravity changes on a monthly basis. Dedicated processing even allows a higher temporal resolution up to 10 days. The duration of the mission was originally planned for 5 years starting in 2002, but operations might be possible for a considerably longer time span until 2009 (Flechtner, priv. comm. 2006).

Besides mean global gravity field models from GRACE, for example EIGEN-GRACE02S (Reigber et al. 2005), various investigations have been made on the temporal gravity changes in the past years. They have shown the ability of GRACE to detect

seasonal water or ice-mass changes in large regions, such as river basins and in polar regions, where various processing and filtering techniques as well as reduction models were applied (e.g. Chen et al. 2006, see also section 1). With an increasing time span of GRACE data, these computations became more reliable and also studies of secular gravity variations came into touch. We have been following the development of GRACE processing since the start of the mission in 2002 and performed analyses of the GRACE solutions for the Fennoscandian uplift area (e.g. Müller et al. 2006). For our computations we have used the monthly solutions provided by the Centre of Space Research (CSR) at the University of Texas and Geoforschungszentrum Potsdam, Germany (GFZ). CSR has provided 47 solutions, from April 2002 until June 2006 with gaps in May to July 2002 and June 2003. Due to processing instabilities in August to November 2004, we used the constrained solutions of R01 provided by CSR. GFZ has so far released 34 monthly gravity field solutions, starting in February 2003 to June 2006, with gaps in June 2003, July to October 2004 and December 2004. We used Release 03 of the GFZ solutions. In addition also the JPL GRACE solutions have been compared, but they are not further discussed in this paper.

All analysis centres have reduced the atmospheric and oceanic contributions as well as the tidal effects during the standard GRACE processing by applying corresponding global models. In Release 03, GFZ has used the non-mass-conserving OMCT model, where spurious slopes over land occurred. These interfere with the investigation of hydrological variations over land, therefore the GAB product was re-added to the GFZ gravity solutions (Bettadpur et al. 2006).

Each monthly GRACE gravity field solution consists of a set of Stokes coefficients C_{lm} and S_{lm} up to degree and order 120 with corresponding "best guess" calibrated errors (GRACE 2006). Due to the higher errors at shorter wavelengths, the spherical coefficients were only considered up to degree and order 50, followed by Gaussian filtering with a radius of 500 km. Former investigations (Müller et al. 2005, 2006) were made with larger radii (800 and 1000 km). But considering the present accuracy of the spherical harmonic models and the longer time span of the monthly solutions, 500 km seemed to be appropriate for continental areas. This was confirmed by the investigations of King et al. (2005) comparing GRACE and GPS data.

For each monthly solution gravity values were

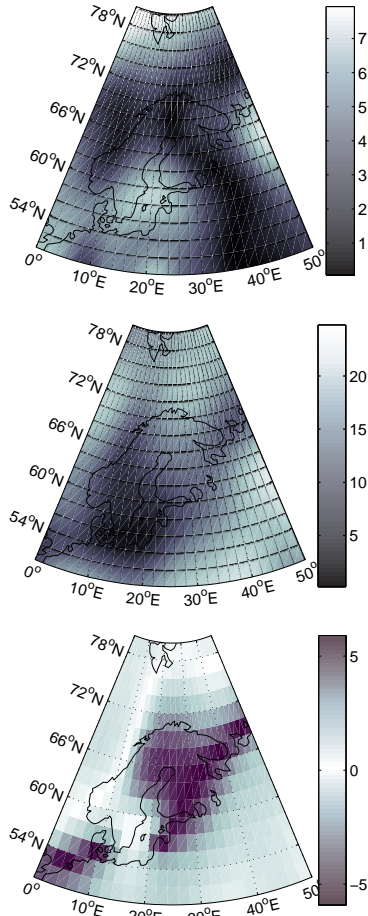


Fig. 2. Periodic gravity changes in Fennoscandia derived from the GFZ solutions. Amplitudes of semi-annual variations (top) and annual variations (middle), and the annual phase in months obtained with respect to January 2003 (bottom). Units are nm/s^2 for the amplitudes.

computed on a $2^\circ \times 2^\circ$ grid. In each grid point the data were used to determine secular (B) and periodic (amplitudes C_i and D_i of typical periods ω_i) gravity variations over the corresponding time span:

$$dg(\varphi, \lambda, t) = A + B\Delta t + \sum_{i=1}^{i=2} C_i \cos(\omega_i \Delta t) + D_i \sin(\omega_i \Delta t). \quad (1)$$

Δt is the time difference relative to January 2003. Index $i = 1$ indicates the semi-annual and $i = 2$ the annual period. The accuracy of the derived gravity values in the grid points is about 20 nm/s^2 , the accuracy of the determined parameters is about $3\text{--}4 \text{ nm/s}^2$ for the annual and $5\text{--}6 \text{ nm/s}^2$ for the semi-annual amplitudes and about $3 \text{ nm/s}^2/\text{year}$ for the secular trend, when applying a Gaussian filter with 500 km radius.

Fig. 1 (top) shows the secular gravity changes as

determined from the GFZ GRACE solutions. A clear signal in the order of $13 \text{ nm/s}^2/\text{year}$ is visible for the central area. The magnitude of the CSR trend (Fig. 1, bottom) corresponds to the GFZ one, but both signals show slightly different spatial extension and also differ from the expected Fennoscandian uplift area (Lambeck et al. 1998). However, in comparison to previous studies (Müller et al. 2006), the centre of the secular signal has moved in north-western direction towards the expected location of the uplift signal. Besides different processing techniques, the varying results may also be caused by the different time spans of the input data, changed processing and filtering strategies as well as by the use of refined reduction models during the standard GRACE processing. Further investigations of the secular signal are discussed in the following sections. Besides the secular gravity change, large periodic variations in the GRACE data are present, which might be mainly caused by hydrological processes. Fig. 2 shows annual and semi-annual amplitudes of these periodic variations. Annual gravity changes of up to 20 nm/s^2 (Fig. 2, middle) can be detected. Small semi-annual changes of max. 7 nm/s^2 are also present (Fig. 2, top), but may not be significant as the maximum signal is just a little bit larger than the corresponding error. When interpreting the results, one has to consider, that the overall time series of 4 years is still relatively short and therefore may be corrupted to some extent by more episodic events like the very dry summers 2003 and 2006.

3 Comparison with Hydrological Models

Numerous studies have proved that GRACE data is able to detect continental water storage changes (e.g. Swenson et al. 2006). For our investigations we compared the results of GRACE data with results of the hydrological model LaDWorld. LaDWorld is a series of retrospective simulations of global continental water and energy balances, created by forcing the Land Dynamics (LaD) model (Milly et al. 2002). For our research we used the sum of simulated variables for snow water equivalent, soil water and shallow ground water. Data is provided in monthly solutions from January 1980 until May 2005 in a $1^\circ \times 1^\circ$ grid, in units of water column. We used the time span of April 2002 until May 2005. When comparing this data with GRACE data, one has to consider that GRACE monthly solutions do not agree to calendar months, as hydrological monthly solutions do. Further errors may be caused by the applied filters as well as the

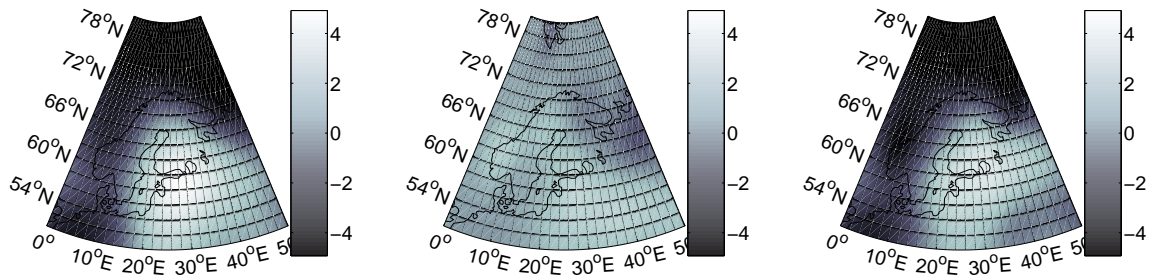


Fig. 3. Secular gravity variations in Fennoscandia as derived from the CSR solutions (left), LaDWorld (middle) and CSR minus LaDWorld (right), units: change in equivalent water column cm/year. Here, the considered time span covered three years only.

uncertainties from the hydrological input variables. Comparisons of LaDWorld with the WaterGapHydrologicalModel (Döll et al. 2003) show significant discrepancies between the two models.

In order to compare the hydrological data with the GRACE data, the grid was resampled to a $2^\circ \times 2^\circ$ grid followed by Gaussian smoothing, comparable to the GRACE smoothing. Only data of the corresponding time span of the CSR solutions was used. The gravity values of GRACE data were converted into columns of equivalent water thickness using the equations given in Wahr et al. (1998).

Fig. 3 (left) shows the GRACE trend for the corresponding time span with a maximum of almost 5 cm/year (equivalent water column). Fig. 3 (middle) shows the secular variation of the hydrological model LaDWorld. A significantly smaller signal of about 2 cm/year is present in that region, but no clear centre can be identified. We then reduced the GRACE signal by the hydrological secular signal, a smaller secular trend of about 3.5 cm/year remained (Fig. 3, right). This reduced GRACE signal still shows differences in amplitude and location to the expected GIA-induced present-day uplift signal, which indicates the presence of further signals not considered so far. These signals may be caused by errors in the GRACE data, filtering of the data sets, mismodelling in the reductions, hydrological effects not contained in the models as well as surges in the Baltic Sea. For a reliable interpretation these regional effects as well as the processing strategy have to be considered in more detail. Our present understanding of the gravity changes in Fennoscandia is, that the periodic and episodic variations might be of hydrological origin, whereas the major part of the secular changes can not significantly be attributed to hydrological processes.

4 Pattern Recognition of the Uplift Signal

As mentioned above, the Fennoscandian uplift has already been observed and modelled within the BIFROST project, where mainly GPS measurements were analysed. In addition geophysical models were, e.g., determined by Lambeck et al. (1998). Based on this information, we modelled the uplift signal assuming an ellipsoidal shape with the parameters $a = 1070$ km and $b = 690$ km, and a certain distribution of the gravity variation. The maximum gravity change in the centre has been selected with $20 \text{ nm/s}^2/\text{year}$. Then, we constructed a 2-dimensional cosine-surface with the maximum gravity change in the centre and decreasing gravity change values to the edges (Fig. 4, middle). The modelled cosine-surface was fitted to the results of the GRACE trend signal, which still includes possible hydrological or further signals. (Fig. 4, right). In this matching process, we only allowed the simple model to be shifted and rotated. In that way of pattern recognition, the centre of the uplift area was determined at the latitude 62° and the longitude 22° . The direction of the semi-major axis of the uplift model was found to be oriented from North-West to South-East, where the expected signal should be oriented from South-West to North-East. Note, that this fit was just a first rough approach and may be improved by better uplift modelling (e.g. based on Thoma 2004) as well as by using more and better GRACE solutions and refined reduction models for the other phenomena like hydrology. In further tests we will construct more complex models based on the various constraints from geophysics and will allow the amplitudes to vary. At that level, we will also investigate how different land uplift models will fit to the GRACE results.

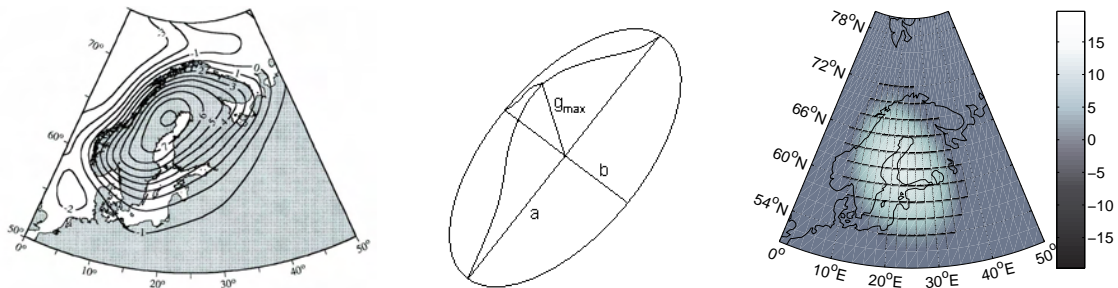


Fig. 4. Pattern recognition of the Fennoscandian uplift: Geophysical uplift model of Lambeck et al. (1998) (left), parameters of a simple model based on the geophysical model (middle), and best fit of the simple uplift model to the GFZ-based solution (right); units: changes in equivalent water column cm/year

5 Summary and Outlook

In this study we investigated temporal gravity variations in Northern Europe based upon the monthly gravity field solutions from GRACE. The GRACE data clearly show temporal gravity variations in Scandinavia. These variations have secular and periodic signatures. Especially the periodic amplitudes, caused by seasonal effects, show good correlation to the hydrological model used. In contrast the secular variations are not in good agreement with other PGR studies, but are getting closer to the expected signal and distribution when longer time series are considered. First results show, that hydrological effects can be reduced partly by considering corresponding hydrological models. More GRACE data and a better modelling of regional effects, like hydrological signals not contained in the models and surges in the Baltic Sea, are required. Also, the separation of the individual signal parts is still a challenging task, where different reductions, models and auxiliary measurements have to be applied to the terrestrial and the satellite data respectively. In addition, the processing and filtering (e.g. isotropic – non-isotropic) of the various data sets have to be considered more extensively. In a first approach, we determined a simple model of the land uplift effect based on the parameters of the expected uplift signal from other models. We then compared this simple model to the GRACE secular variation using a best-fit algorithm. The location and orientation of the model did not agree with the expected PGR-signal, but the amplitude of the GRACE-based result from GFZ looks similar. In the future, more refined uplift models shall be developed and compared to the GRACE solutions, which may help to improve the estimation of the land uplift signal from GRACE data and to discriminate between the different assumptions and parameters used in the geophysical uplift models.

Acknowledgments. We would like to thank the GRACE science team for overall support, CSR, University of Texas, and GFZ Potsdam for providing the monthly GRACE solutions, and Prof. Döll and her group for making the WGHM data available.

References

- Bettadpur, S., F. and R. Schmidt (2006): GRACE Technical Note No. 4. Usage Guidelines for GFZ RL03 and JPL RL02 GRACE Gravity Fields and Atmosphere/Ocean Background Models, Version 1.1.
- Chen, J., C. Wilson, D. Blankenship, and B. Tapley (2006). Antarctic mass rates from GRACE. *Geophysical Research Letters*, Vol. 33, L11502.
- Döll, P., Kaspar, F., Lehner, B. (2003): A global hydrological model for deriving water availability indicators: model tuning and validation. *Journal of Hydrology* 270, 105-134.
- Ekman, M. (1996): A consistent map of the postglacial uplift of Fennoscandia. *Terra Nova* 8, 158-165.
- Ekman, M. (1996b): Extreme annual means in the Baltic Sea level during 200 years. *Small Publications in Historical Geophysics*, No. 1-12, Summer Institute for Historical Geophysics, Åland Islands, 1995-2003.
- Ekman, M. and Mäkinen, J. (1996): Recent postglacial rebound, gravity change and mantle flow in Fennoscandia. *Geophysical Journal International* 126, 229-234.
- Famiglietti, J. S., J. L. Chen, M. Rodell, and C. R. Wilson (2005): Terrestrial Water Storage Variations From GRACE, in *New Satellite Mission Results for the Geopotential Fields and Their Variations*, edited by C. Reigber and B. Tapley, Special Issue of *Advances in Geosciences*, in press.
- Frappart F., G. Ramillien, S. Biancamaria, N.M. Mognard, A. Cazenave (2006): Evolution of high-latitude snow mass derived from the GRACE gravimetry mission (2002-2004). *Geophysical Research Letters*, Vol. 33, No. 2.
- GRACE (2006), web pages: <http://www.csr.utexas.edu/grace/> or <http://www.gfz-potsdam.de/pb1/op/grace/>.

- Han, S.-C., C. K. Shum, C. Jekeli, and D. Alsdorf (2005): Improved estimation of terrestrial water storage changes from GRACE, *Geophys. Res. Lett.*, 32, L07302, 2005.
- Ilk, K. H., Flury, J., Rummel, R., Schwintzer, P., Bosch, W., Haas, C., Schröter, J., Stammer, D., Zahel, W., Miller, H., Dietrich, R., Huybrechts, P., Schmeling, H., Wolf, D., Götze, H.J., Riegger, J., Bardossy, A., Güntner, A., Gruber, T. (2005): Mass Transport and Mass Distribution in the Earth System. Contribution of the New Generation of Satellite Gravity and Altimetry Missions to Geosciences, 2nd edition, GOCE-Projektbüro Deutschland, TU München, GFZ Potsdam.
- Johansson, J.M., Davis, J.L., Scherneck, H.-G., Milne, G.A., Vermeer, M., Mitrovica, J.X., Bennett, R.A., Jonsson, B., Elgered, G., Elseguí, P., Koivula, H., Poutanen, M., Rönnäng, B.O., Shapiro, I.I. (2002): Continuous GPS measurements of postglacial adjustment in Fennoscandia, 1. geodetic results. *J. Geophys. Res.* 107, B8, ETG 3, 1-27.
- King, M.A., Nigel T. Penna, and Peter J. Clarke (2005): Validation of ocean tide models around Antarctica using on-shore GPS and gravity data. *Journal of Geophysical Research* 1003, Vol. 110, B08401.
- Kuo, C. Y., C. K. Shum, A. Braun, and J. X. Mitrovica (2004), Vertical crustal motion determined by satellite altimetry and tide gauge data in Fennoscandia, *Geophys. Res. Lett.*, 31, L01608, doi:10.1029/2003GL019106.
- Lambeck, K., C. Smither, M. Ekman (1998): Tests of glacial rebound models for Fennoscandia based on instrumented sea- and lake-level records. *Geophys. J. Int.* (1998) 135, 375-387.
- Milly, P. C. D., Shmakin, A. B. and Dunne, K. A. (2002). Global Modeling of Land Water and Energy Balances. The Land Dynamics (LaD) Model. *Journal of Hydrometeorology*, Vol. 3, S. 283-299.
- Milne, G.A., Davis, J.L., Mitrovica, J.X., Scherneck, H.-G., Johannson, J.M., Vermeer, M., Koivula, H. (2001): Space-geodetic constraints on glacial isostatic adjustment in Fennoscandia. *Science* 291, 23, 2381-2385.
- Müller, J., Timmen, L., Gitlein, O., Denker, H. (2005): Gravity Changes in the Fennoscandian Uplift Area to be Observed by GRACE and Absolute Gravimetry. In *Gravity, Geoid and Space Missions*. C. Jekeli, L. Bastos, J. Fernandes (eds.), Springer, IAG Symposia 129, 304-309.
- Müller, J., Neumann-Redlin, M., Jarecki, F., Denker, H., Gitlein, O. (2006): Gravity Changes in Northern Europe as Observed by GRACE. Reviewed Proceedings of the IAG General Assembly, held in Cairns, Australia, 22-26 August 2005, accepted, in print.
- NRC (1997): *Satellite gravity and the geosphere*. National Research Council, National Academic Press, Washington.
- Reigber, Ch., Schmidt, R., Flechtner, F., König, R., Meyer, U., Neumayer, K.-H., Schwintzer, P., Zhu, S.-Y. (2005): An earth gravity model complete to degree and order 150 from GRACE: EIGEN-GRACE02S, *Journal of Geodynamics*, 39(1), 1-10.
- Rodell, M., J. S. Famiglietti, J. Chen, S. Seneviratne, P. Viterbo, S. Holl, and C. R. Wilson (2004): Basin scale estimates of evapotranspiration using GRACE and other observations, *Geophysical Research Letters*, 31, L20504.
- Rowlands, D. D., S. B. Luthcke, S. M. Klosko, F. G. R. Lemoine, D. S. Chinn, J. J. McCarthy, C. M. Cox, and O. B. Anderson (2005): Resolving mass flux at high spatial and temporal resolution using GRACE intersatellite measurements, *Geophys. Res. Lett.*, 32, L04310.
- Scherneck, H.-G., Johannson, J.M., Koivula, H., van Dam, T., Davis, J.L. (2003): Vertical crustal motion observed in the BIFROST project. *Journal of Geodynamics* 35, 425-441.
- Schmidt, R., Schwintzer, P., Flechtner, F., Reigber, Ch., Güntner, A., Döll, P., Ramilien, G., Cazenave, A., Petrovic, S., Jochmann, H., Wunsch, J. (2006): GRACE observations of changes in continental water storage, *Journal of Global and Planetary Change*, 50, 112-126.
- Swenson, S. C., Milly, P. C. (2006): Climate model biases in seasonality of continental water storage revealed by satellite gravimetry, *Water Sources Research*, Vol. 42.
- Tapley, B., Bettadpur, S., Ries, J., Thompson, P., Watkins, M. (2004): GRACE measurements of mass variability in the Earth System. *Science* 305, 503-505.
- Thoma, M. (2004): *Materiell und lokal inkompressible Erdmodelle: Theorie und Anwendungen in der glazialen Isostasie*. Scientific Technical Report STR04/13, Geoforschungszentrum Potsdam.
- Thompson, P. F., S. V. Bettadpur, and B. D. Tapley: Impact of short period, non-tidal, temporal mass variability on GRACE gravity estimates, *Geophys. Res. Lett.*, 31, L06619.
- Wahr, J., Molenaar, M., Bryan, F., (1998): Time variability of Earth's gravity field: Hydrological and oceanic effects and their possible detection using GRACE. *Journal of Geophysical Research* 1003, (B12) 30,205-30,230.
- Wahr, J. and Velicogna, I. (2002): What might GRACE contribute to studies of postglacial rebound? *Space Sciences Series of ISSI* 18, Kluwer Academic Publishers, Dordrecht.
- Wahr, J., S. Swenson, I. Velicogna, V. Zlotnicki (2004): Time-variable gravity from GRACE: First results, *Geophysical Research Letters* paper 10, 1029/2004GL019779.
- Wilmes, H., Falk, R., Roland, E., Lothhammer, A., Reinhold, A., Richter, B., Plag, H.-P., Mäkinen, J. (2005): Long-term gravity variations in Scandinavia from repeated absolute gravity measurements in the period 1991 to 2003. *Proceedings (CD publ.) of IAG Symposium GGSM2004, Porto*.

GPS and Gravity Measurements Along the Western Part of the North Anatolian Fault and Their Relation to Crustal Deformations

U. Doğan, H. Demirel, C. Aydın

Department of Geodesy and Photogrammetry Engineering, Yildiz Technical University, 34349, Besiktas, Istanbul

S. Ergintav, R. Çakmak, A. Belgen

TUBITAK MRC Earth and Marine Sciences Institute, Gebze, Kocaeli, Turkey

C. Gerstenecker

Darmstadt University of Technology, Institute of Physical Geodesy, Petersenstr. 13, Darmstadt, Germany

Abstract. The post seismic time dependent motions of 1999 Izmit and Düzce earthquake sequences in Marmara region, Turkey, provide the opportunity to improve significantly our understanding of the mechanical behaviour of the western part of North Anatolian Fault. Therefore, an international cooperative project have been started to determine the long-term potential post seismic crustal deformations along the tectonic fault using GPS and gravity data sets in this region.

We focus into the first results of joint gravity and GPS studies to understand 3-dimensions post seismic deformations of 1999 earthquakes along the North Anatolian Fault between the 2003 and 2005 years in the Marmara Region. The GPS data set following the 1999 earthquakes and the gravity observations were analyzed to detect of the accurate 3-dimension post seismic deformations and to determine gravity changes in time and space dependent on vertical crustal movements. The first results indicate that the gravity changes and some of the GPS time series show, strongly, seasonal unmodeled behaviours, and vertical motion from GPS field and gravity results shows good correlation. Furthermore, they show that height, gravity and potential changes between the western and eastern part of the network are very different. The western part shows significant strain loading, which is documented by horizontal displacements and potential increases.

Keywords. GPS, Gravity, Marmara Region, Crustal Deformation

1 Introduction

A high magnitude potential earthquake in the Marmara region making up to great deal of population and economical sources of Turkey would be a significant threat to the region. Therefore, it has been very important to identify the seismic risk in the Marmara region by monitoring it with today's techniques. GPS campaigns in the region have been started since 1988 (Reilinger et al. (1997), Barka and Reilinger (1997)). After the 17 August 1999 Izmit earthquake, numerous studies were carried out to identify the scientific details about the region with the help of these studies. (Özalaybey et al. (2002); Ergintav et al. (2002)). Despite of these studies, it is still not clear the relation between NAF and the secular faults around this region, especially in the vertical component, which shows important earthquake activity in the region.

The aim of the observations is to determine the geometric and elastic parameters of the active faults by inversion of post seismic deformations. Due to the accuracy limitation of GPS up to now only horizontal deformations are analyzed. Vertical deformations are neglected as well as possible gravity changes. The common use of both parameters however can help to improve the error situation significantly (Gerstenecker et al. (2006)).

In 2003, an international cooperative project was started by The Scientific and Technical Research Council of Turkey Marmara Research Center (TUBITAK-MAM), Earth & Marine Sciences

Research Institute, along with Yıldız Technical University, Department of Geodesy and Photogrammetry Engineering in Turkey and Darmstadt University of Technology, Institute of Physical Geodesy in Germany. The goal of this project is to detect horizontal and vertical crustal motions using GPS and gravimetric methods. In this project, it has been aimed to understand about the vertical component that was not studied before in this region and to monitor the time-dependent tectonically induced gravity changes along the NAF.

The first precise gravimetric survey covering in the Marmara region was carried out on October 2003 to determine the mass and or density changes inside the earth crust related to pre seismic and post seismic deformations of the region. GPS stations which are subset of the Marmara Continuous GPS Network (MAGNET), and survey sites constituted as two GPS profiles perpendicular to the main branch of NAFZ were studied to monitor the crustal deformations in long term (Ergintav et al. (2005)). With GPS and gravity data, the fault geometry and the seismic risk around the region can be tried to identify, relative to the stress regime of NAF. Moreover, interpretation about physical features of these crustal movements occurred before and after the earthquakes in the Marmara region will be able to estimate future seismic risk.

The measurement of vertical time dependent deformations are very important to understand the mechanics of post seismic deformation and the accelerated slip as well as stress transfer between particular fault branches because of the dynamic long term response of the viscoelastic layer. Hence, better estimates of vertical post seismic motions are a key factor in seismic hazard analyses (Ergintav et al. (2006)).

In this study, we describe the first results of joint gravity and GPS studies to understand 3-dimensions post seismic deformations of 1999 earthquakes along the North Anatolian Fault between the 2003 and 2005 years in the Marmara Region.

2 GPS&Gravity Network and Data Processing

Before the 1999 earthquakes, the Marmara Continuous GPS network (MAGNET) (Fig. 1) was established to measure the deformations associated

with strain accumulation along the western NAF system. We realized 2 GPS profiles perpendicular to the main branch of the North Anatolian Fault (NAF) in the Marmara Region to determine the temporal and spatial deformation variations from which we estimate processes at depth. The first GPS profile crosses the Ganos fault in the Western Marmara Region and the second one in the Eastern Marmara traverses the western part of the 1999 Izmit earthquake rupture (Fig. 1). In addition, these profiles are supplemented by additional stations of the so called Tuzla GPS Network “TUGANET” to observe deformations at the western part of the rupture of the Izmit earthquake (Fig. 1). We observe the GPS stations twice a year in June and October. During each campaign at each station, two sessions of 10 hours are observed. In order to reduce the antenna phase pattern problems and the errors on the computation of the vertical components, we used same receivers and antennas at all campaign sites (Trimble 4000 and 5700 with choke-ring and Zephyr antennas) (Ergintav, et al. (2006)).

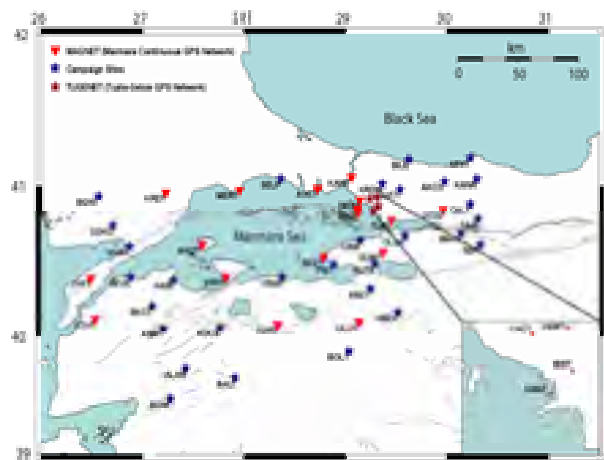


Fig. 1 GPS stations around the Marmara Sea. Gray lines show the active faults according to Saroglu et al. (1992), Le Pichon et al. (2003) and Armijo et al. (2005). Ganos fault is shown on the European side of the Dardanelles. Black lines show the break of the 1999 earthquakes (Bürgmann et al. (2002a-b)).

GPS data were analyzed with the GAMIT/GLOBK GPS processing software (Herring, 2000; King and Bock (1998)). The reference frame was constrained on each day using a reliable set of global IGS stations. Positions of the fiducial IGS stations were constrained to ITRF2000

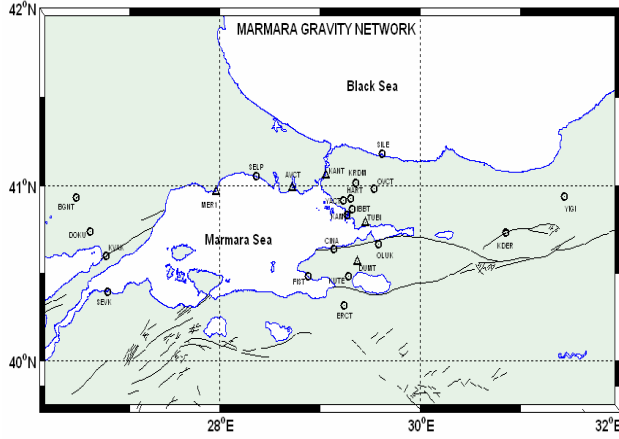


Fig. 2 Marmara Gravity Network (MAGRANET), and triangle points are permanent GPS stations belonging to MAGNET.

coordinates. Details about the processing method are described in McClusky et al. (2000).

The Marmara Gravity Network (MAGRANET) is a precise gravimetric control network for monitoring gravity changes along the NAF due to geodynamic processes. The network whose points belong to MAGNET was established and consists of 25 stations (Fig. 2). The MAGRANET was re-observed five times in October and June of each year between 2003 and 2005, simultaneously with the GPS campaigns. The effect of seasonal variations on both observation sets should therefore be similar. We have used the relative spring gravimeters LaCoste Romberg LCR-G 85 and LCR-G 858 at all campaigns. The Scintrex CGS5 10076 and 10079 gravimeters have been also used since October 2004. The characteristics of the five surveys are given in Table 1.

Table 1 Summary of the gravity observation campaigns

Epoch	Number of Ins.	Number of Obs.	Mean point errors (μgal)
10-2003	2	434	5.93
06-2004	2	543	4.26
10-2004	2	477	4.04
06-2005	2	450	4.19
10-2005	2	466	4.53

We computed for each epoch stational point gravity values (\mathbf{g}_p) from the following a least squares

adjustment model (Drewes et al. (1991); Torge (1989)):

$$\mathbf{l}_k + \mathbf{v}_k = \mathbf{g}_p - \mathbf{n}_d - \mathbf{y}_i \mathbf{l}_k - \mathbf{d}_i \Delta t_k, \text{ weight } \mathbf{P}_k \quad (1)$$

where, \mathbf{l}_k is the vector of the reduced gravimeter observation due to the earth tide, air pressure and instrument height effects, \mathbf{v}_k is the residual vector, \mathbf{n}_d is the unknown gravimeter reading level vector at a day, \mathbf{y}_i is the scale correction vector for gravimeter (i), \mathbf{d}_i is the unknown drift polynomial coefficient vector for gravimeter (i), and Δt is the time of observation referring to an initial time at a day.

The adjustment was carried out with the software package “GRAV” developed for adjustment of absolute gravity measurements and estimation of gravity values as well as gravimeter parameters using different adjustment models at the Institute of Physical Geodesy, Darmstadt University of Technology. A priori as unit weight standard deviation $\sigma_0 = \pm 10 \mu\text{gal}$ for a particular observation is introduced.

3 Results and Evaluation

Fig. 3 indicates an example of the GPS time series from MAGNET. It starts following the 1999 earthquake sequence and is fit well by a function of the form

$$\mathbf{x}(t_i) = \mathbf{x}(t_0) + \mathbf{a} \ln(\Delta t) + \mathbf{v} \Delta t + \text{Annual} + \text{Semi-annual} \quad (2)$$

where, $\mathbf{x}(t_i)$ and $\mathbf{x}(t_0)$ are the observed site positions at epoch t_i and t_0 , respectively, \mathbf{a} is the amplitude of the post-seismic response, \mathbf{v} is the steady state velocity, and $(t-t_0)$ is the time elapsed since the earthquake. The “Annual” and “Semi-annual” terms account for the unmodeled seasonal systematic effects. After the onset of the 1999 Izmit earthquake, the steady state site velocities can be predicted by this functional form, and they are equal within uncertainties to the observed site velocity prior to the earthquake (Ergintav et al. (2002); Ergintav et al. (2004)). The offsets of the 1999 Düzce earthquake were removed from the time series using the detailed coseismic deformations

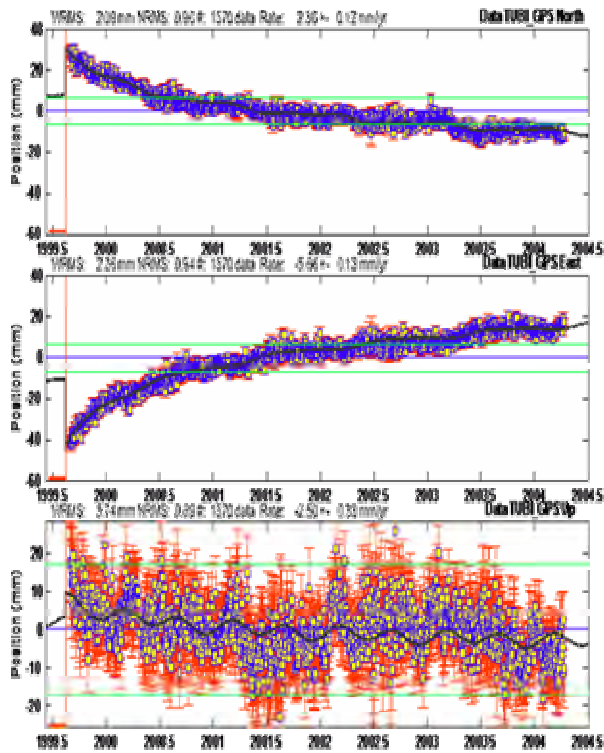


Fig. 3 GPS time series of TUBI site in MAGNET.

determined from a geodetic model of the earthquake (Ayhan et al. (2001)).

In Fig. 3, the vertical line shows the time of the Izmit earthquake. The thick black line indicates the long term behavior of the time series in (2). The green lines show the 1-sigma limits of the uncertainties. The height component has larger scatter and uncertainties than the horizontal components. As can be seen in Fig.3, the sinusoidal fluctuations of the seasonal effects can be identified easily for the continuous GPS sites. The seasonal effects were also identified on the campaign data by the six-month re-occupation frequency. While one of the campaigns was made in October, the other was carried out in June for each year.

To obtain a reliable long-term velocity for the GPS sites, we calculated the velocities from the nearly steady-state part of the data between the 2003 and 2005. Fig. 4 shows the up-to-date horizontal velocity field of the Marmara Region in a Eurasian fixed frame for the period 2003 - 2005.

The general characteristics of the velocity field shown in Fig. 4 reflect two different properties for the northern and southern parts of NAF. In the

southern part of NAF, the velocities are approximately equal to the pre-earthquake velocities (McClusky et al. (2000); Meade et al., (2002)), except a rotation component to the southwest. In contrast to this area, the velocities in the northern part of NAF are larger than pre-earthquake velocities, and indicate a high correlation with the co-seismic deformation and early post seismic motions (Ergintav et al. (2002)). The logarithmic behaviour of the time series and the spatial character of the observed post seismic deformation suggest that early phase of post seismic deformation, is due to afterslip extending through the crust and perhaps into the upper mantle (Ergintav et al. (2002)).

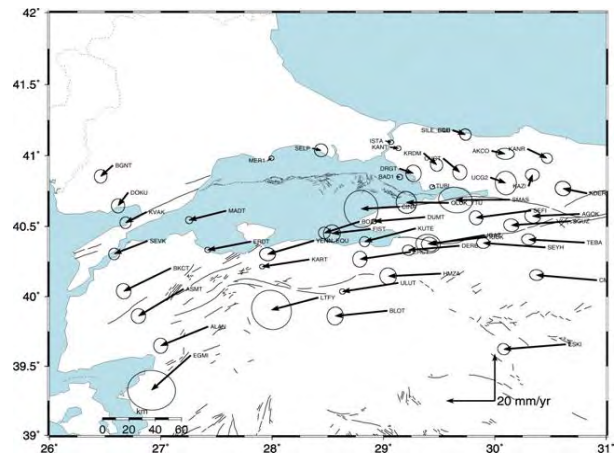


Fig. 4 Horizontal velocity field of the Marmara Region in a Eurasian fixed frame. Thin lines show the active fault traces (Saroglu et al. (1992); Le Pichon et al. (2003); Armijo et al. (2005)).

Moreover, we study here temporal variations of the gravity field. When the effect of external phenomena such as tides or environmental parameters (e.g atmospheric pressure) are removed, the residual change in the gravity field at a location is sensitive to the measurement position mainly the elevation, since gravity gradients are stronger vertically than horizontally, and to the mass movement and density change beneath and around the measurement point (Ballu et al. (2003)).

From the individual point gravity values per epoch with respect to TUBI station, we computed a linear fit to the gravity variation (single point linear gravity change). In addition to the point gravity values at a zero-epoch (t_0), we introduced the linear

temporal change (dg/dt) per station. The point gravity values per epoch are expressed as a function of linear variation as follows:

$$g(t_i) = g(t_0) + (dg/dt)(t_i - t_0) \quad (4)$$

where $g(t_i)$ is the observed gravity value at epoch t_i . The resulting data (dg/dt) are showed in Fig. 5. The linear temporal gravity changes indicate significant offsets depended anomalies. While the northern part of fault zone shows negative, the southern part shows positive changes in time. This is further evidence that the gravity changes reflect subsurface changes and not only vertical surface motions (Ergintav et al. (2006)).

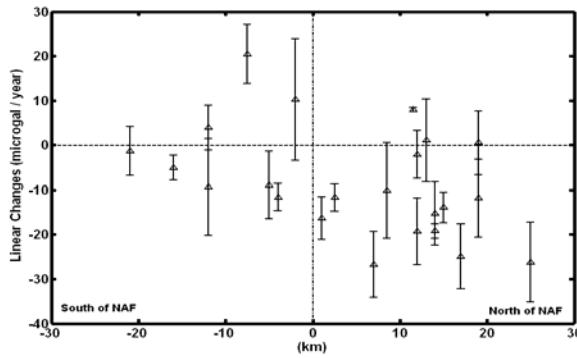


Fig. 5 Linear changes as functions of distance from NAF with respect to TUBI station

Gravity and height changes in time dg and dh are interpreted as potential changes dW according to (Gerstenecker, et al. (2006)):

$$dW = dg dh \text{ [Nm]}. \quad (5)$$

We computed for the interpretation the changes of the potential dW/year . The results in Fig. 6 for the stations at NAFZ and Ganos fault. Applying the law of error propagation for the potential changes, we obtain statistically significant results. Obviously potential changes along NAFZ and Ganos fault are quite different. We observe generally a potential decrease at NAFZ, whereas at all stations near Ganos fault potential increase exists. The regimes of both fault zones are quite different (Gerstenecker et al. (2006)).

Fig. 7 indicates the plots of the linear temporal gravity changes and the vertical displacements for the stations at NAFZ for October 2004-October

2003 with respect to TUBI site. As can be seen from Fig. 7, while many sites show the expected negative correlation, and only DUMT site shows the positive correlation in the south of the Marmara Region. However, the linear temporal gravity changes indicate significant offsets depended anomalies. While the northern part of fault zone shows negative, the southern part shows positive changes in time. This is further evidence that the gravity changes reflect subsurface changes and not only vertical surface motions (Ergintav et al. (2006)).

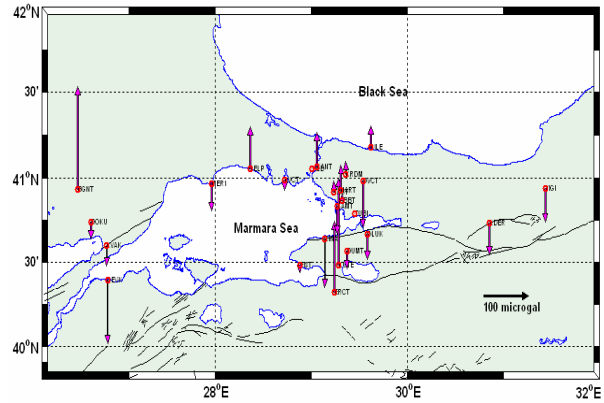


Fig. 6 Time dependent potential regression coefficients

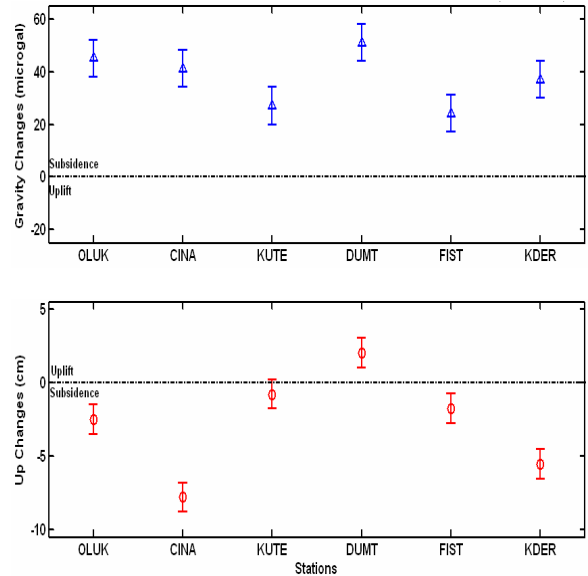


Fig. 7 Gravity changes and the vertical displacements for the stations in the south of the Marmara Region

In Fig. 8, the GPS height variations and gravity changes at site OLUK with respect to the TUBI site are given as an example. In Fig. 8, each measurement of the GPS and gravity changes has a negative correlation as expected. The long term trend also shows the negative correlation.

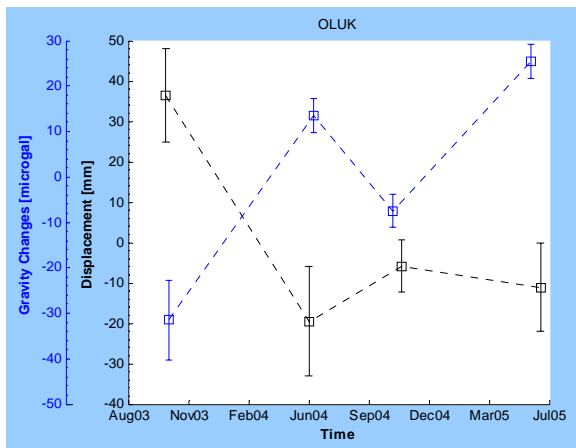


Fig. 8 The gravity changes and the vertical displacements by GPS with respect to the TUBI site for the OLUK site.

4 Conclusion

We report the first results of joint gravity and GPS studies to understand 3-dimensions post-seismic deformations of 1999 earthquakes along the North Anatolian Fault between the 2003 and 2005 years in the Marmara Region. The horizontal and vertical deformation changes were obtained by GPS studies and the studies for vertical deformation changes were augmented by the gravity changes in the Marmara region. The MAGRANET was re-observed five times in October and June of each year between 2003 and 2005, at the same time with the GPS campaigns.

The results indicate the different present-day character of strain accumulation in the western and eastern part of the Marmara Region. The post seismic motions still influence the seismic hazard in the eastern part of the region; the western part needs further studies to understand the rheology of the fault zone and seismic hazard. The velocity field reflects two different properties for the northern and southern parts of NAF. While the velocities are approximately equal to the pre-earthquake velocities except a rotation component to the

southwest in the southern part of NAF, the velocities in the northern part of NAF are larger than pre-earthquake velocities, and indicate a high correlation with the co-seismic deformation and early post seismic motions.

The potential changes along NAFZ and Ganos fault are quite different. The potential decreases at NAFZ, whereas at all stations near Ganos fault potential increase exists. The linear temporal gravity changes indicate significant offsets depended anomalies and the gravity changes reflect subsurface changes, not only vertical surface motions.

The accuracy of the relative gravity measurements can be significantly increased by establishing an absolute calibration line in the region and by adding absolute gravity measurements in our gravity network.

Acknowledgments

This study supported by TUBITAK CAYADAG Project No: 103Y100 and EU 6. Frame FORESIGHT Project (Contract no: 511139).

References

- Ayhan, E., R. Bürgmann, S. McClusky, O. Lenk, B. Aktug, E. Herece, R.E. Reilinger (2001). Kinematics of the $M_w = 7.2$, 12 November, 1999, Duzce, Turkey earthquake. *Geophys. Res. Lett.*, 28, 367-370.
- Armijo, R., N. Pondard, B. Meyer, B. Mercier de Lepinay, G. Uçarkus, J. Malavieille, S. Dominguez, M. Gustcher, A. Beck, N. Çagatay, Z. Kadir, C. Imren, E. Kadir and Natalin and MARMARASCARPS cruise party (2005). Submarine Fault Scarps in the Sea of Marmara Pull-Apart (North Anatolian Fault): Implications for Seismic Hazard in Istanbul. *Geochem., Geophys., Geosyst.*, 6, 1-29.
- Ballu, V., M. Diament, P. Briole and J.C. Ruegg (2003). 1985-1999 Gravity Field Variations across the Asal Rift: Insights on Vertical Movements and Mass Transfer. *Earth and Planetary Science Letters*, 208, 41-49.
- Barka, A. and R. Reilinger (1997). Active Tectonics of the Eastern Mediterranean region: Deduced from GPS, Neotectonic, and Seismicity Data. *Ann. Geofis.*, 40, 587-610.
- Bürgmann, R., S. Ergintav, S. Segall, E.H. Hearn, S. McClusky, R.E. Reilinger, H. Woith and J. Zschau (2002a). Time-Space Variable Afterslip on and Deep below the Izmit Earthquake Rupture. *Bull. Seism. Soc. Am.*, 92, 126-137.
- Bürgmann, R., M.E. Ayhan, E. Fielding, T.J. Wright, S. McClusky, B. Aktug, C. Demir, O. Lenk and A. Türkerzer (2002b). Deformation during the 12

- November 1999 Düzce, Turkey, Earthquake, from GPS and InSAR Data. *Bull. Seism. Soc. Am.*, 92, 161-171.
- Drewes, H., W. Torge, R.H. Röder, C. Badell, D. Bravo and O. Chourio (1991). Absolute and Relative Gravimetric Surveys of National and Geodynamic Networks in Venezuela. *J. of South American Earth Sciences*, 4, 273-286.
- Ergintav, S., U. Doğan, C. Gerstenecker, R. Cakmak, A. Belgen, H. Demirel, C. Aydın and R. Reilinger (2006). A Snapshot of the 3D Postseismic Deformations in the Marmara Region, Turkey by First results of Joint Gravity and GPS Monitoring. *submitted in Journal of Geodynamic*.
- Ergintav, S., U. Doğan, C. Gerstenecker, H. Demirel, R. Çakmak, C. Aydın, A. Belgen, C. Tiede and C. Erenoğlu (2005). Monitoring of Recent Crustal Movements in the Marmara Region, Turkey, Using GPS and Gravity Observations. *European Geosciences Union General Assembly, Geophysical Research Abstracts*, Vol. 7, 07298, 24-29 April, Vienna, Austria.
- Ergintav, S., R. E. Reilinger, R. Cakmak, S. McClusky, E. H. Hearn, B. Meade, O. Lenk and H. Ozener (2004). Geodetic Constraints on the Earthquake Deformation Cycle Along the Western North Anatolian Fault: Implications for Earthquake Mechanics and Seismic, *EGU*, Nice.
- Ergintav, S., R. Bürgmann, S. McClusky, R. Cakmak, R.E. Reilinger, O. Lenk, A. Barka and O. Gurban (2002) Postseismic Deformation Near the Izmit Earthquake 17 August, 1999. *Bull. Seism. Soc. Am.*, 92, 194-207.
- Gerstenecker, C., U. Doğan and S. Ergintav (2006). Analysis of Gravity Changes and Deformations, observed between 2003 and 2005 along the Western Part of the North Anatolian Fault. *Fifth Turkish-German Joint Geodetic Days*, March 28-31, Berlin, Germany.
- Herring, T.A. (2000). GLOBK: Global Kalman Filter VLBI and GPS Analysis Program Version 10.0. *MIT*, Cambridge.
- King, R.W. and Y. Bock (1998). Documentation for the GAMIT Analysis Software, Release 9.7. *MIT*, Cambridge.
- Le Pichon, X., N. Chamot-Rooke, C. Rangin and A.M.C. Şengör (2003). The North Anatolian Fault in the Sea of Marmara. *J. Geophys. Res.*, 108, 2170-2179.
- McClusky, S., et al. (2000). Global Positioning System Constraints on Plate Kinematics and Dynamics in the Eastern Mediterranean and Caucasus. *J. Geophys. Res.*, 105, 5695-5719.
- Meade, B., B. Hager, S. McClusky, R. E. Reilinger, S. Ergintav, O. Lenk, A. Barka and H. Ozener (2002). Estimates of Seismic Potential in the Marmara Sea Region from Block Models of Secular Deformation Constrained by GPS Measurements. *Bull. Seism. Soc. Am.*, 92, 208-215.
- Özalaybey, S., N. Ergin, M. Aktar, C. Tapırdamaz, F. Biçmen and A. Yörük (2002). The 1999 Izmit Earthquake Sequence in Turkey: Seismological and Tectonic Aspects. *Bull. Seism. Soc. Am.*, 92, 376-386.
- Saroglu, F., Ö. Emre and İ. Kuşçu (1992). Türkiye Diri Fay Haritası. *MTA, Turkey*.
- Torge, W. (1989). Gravimetry. de Gruyter, Berlin, New York, 465 pp

Combination of GRACE, gravity and GPS data for determination of long-term geoid changes in North America

E. Rangelova and M. G. Sideris, Department of Geomatics Engineering,
University of Calgary, 2500 University Drive NW, Calgary, Alberta, Canada, T2N 1N4

Abstract. Two independent solutions for the rate of change of geoid in North America, assumed to be due to PGR, are presented. The first solution is based on principal component analysis of a GRACE time series of geoid change. The second solution is derived via least-squares collocation using absolute gravity rates and GPS vertical velocities available in Canada. The GRACE geoid rate shows good agreement with postglacial rebound models based on the ICE5G de-glaciation history, in contrast with the geoid rate derived from gravity and GPS data, which agrees better with the ICE3G and ICE4G models. In view of the still short time span of the GRACE time series, and acknowledging the fact that the errors of the geopotential coefficients have not been taken into account, it is found that the GRACE geoid rate should be down-weighted when the two geoid rates are combined.

Keywords. GRACE, postglacial rebound, rate of change of geoid.

1 Introduction

Temporal variations of the geoid comprise an area of growing scientific interests since the start of the NASA/DLR Gravity Recovery and Climate Experiment (GRACE) satellite mission in March 2002; see Tapley *et al.*, 2004. With a temporal sampling of one month, GRACE data provide a unique opportunity to study seasonal, interannual and long-term geopotential changes due to mass redistributions at the surface of the Earth and its interior. One of the expected outcomes of the GRACE mission involves constraints on postglacial rebound (PGR) models; see Peltier (2004). The estimated secular rate, which will be referred to long-term rate in view of the satellite mission lifetime, will help to decrease uncertainties in the mantle viscosity and de-glaciation histories currently used in PGR simulations.

In Canada, the geoid rate is necessary for realization of the new vertical datum, which will be

based on a precise model of the regional geoid; see Véronneau *et al.* (2006). The availability of absolute rates of change of gravity, see Pagiatakis and Salib (2003), and GPS vertical velocities allows the geoid rate to be modeled independently of GRACE. The relatively good gravity data coverage permits sampling of the characteristic wavelengths of the PGR signal, but also other local processes, such as subsidence due to fluid extraction, erosion, tectonics, etc., are present which may or may not be accompanied by mass changes and are hardly seen by GRACE. However, a comparison of independently derived geoid rates is useful and might be indicative for the data quality and achievable accuracy of the geoid rate at present.

The purpose of this paper is to model the geoid rate using the distributed GRACE Level 2 data and to compare it with the geoid rate from gravity rates and vertical velocities. For the sake of brevity, the first model will be called the GRACE geoid rate and the second model will be called the Gdot/GPS geoid rate. Furthermore, the two solutions are combined via least-squares adjustment, and variance component estimation is performed in order to assess the relative errors of both models.

The estimation of geoid rate from the GRACE data is based on principal component analysis (PCA) of GRACE time series. On the other hand, the combination of gravity rates and GPS velocities is, in essence, a two dimensional approximation problem using known relationships between gravity field components. The approximation problem is solved via least-squares collocation (LSC). Below the modeling approaches used are described followed by a description of the combination procedure and discussion of the results obtained.

2 Methodology

2.1 Principal Component Analysis of GRACE Time Series

Principal component analysis provides estimates of empirical orthogonal functions (EOF) loading patterns of single scalar fields and their variation in

time described by the principal component (PC) time series. Data are organized in a $(n \times p)$ matrix \mathbf{D} , where n is the number of observations, i.e., the monthly values of the geoid change with respect to the long-term mean, and p is the number of variables, i.e., the grid cells. The data matrix \mathbf{D} is decomposed by singular value decomposition according to *Jolliffe (2002)* as follows:

$$\mathbf{D} = \mathbf{U}\mathbf{S}\mathbf{V}', \quad (1)$$

where \mathbf{U} and \mathbf{V} are $(n \times n)$ and $(p \times p)$ matrices, respectively, for which $\mathbf{U}\mathbf{U}' = \mathbf{I}$ and $\mathbf{V}\mathbf{V}' = \mathbf{I}$ hold. The main diagonal of the matrix \mathbf{S} contains the square roots of the eigenvalues of the spatial covariance matrix $\mathbf{D}\mathbf{D}'$, and the column vectors of \mathbf{V} give the EOF loading patterns. The PC time series are obtained from the column vectors of the matrix \mathbf{P} determined as follows:

$$\mathbf{P} = \mathbf{U}\mathbf{S}. \quad (2)$$

The data are approximated by means of m principal components according to:

$${}_m\hat{\mathbf{D}} = {}_m(\mathbf{U}\mathbf{S}\mathbf{V}'), \quad (3)$$

where ${}_m\hat{\mathbf{D}}$ is the best rank m approximation of the data matrix.

To represent accurately physical relations in the data, rotated PCA is applied by means of different schemes to find a new basis in the m -dimensional space which simplifies the interpretation of the principal components. A ‘‘varimax’’ rotation on the PC time series, as given by *Preisendorfer (1988, pp. 273-283)*, is used herein. In order to select the principal components that will undergo rotation, the PC time series are tested for being random samples of a white noise process by means of the Kolmogorov-Smirnov rule (*ibid*). The PC is accepted to represent a signal mode if the null hypothesis (white noise process) is rejected at 95% confidence level.

2.2 Least-squares Prediction of Geoid Rates Using Absolute Gravity Rates and GPS Velocities

As a generalized approximator/interpolator, least-squares collocation is an appropriate method for predicting geoid rates using available heterogeneous data that can include absolute and relative gravity rates, point vertical velocities (GPS and tide gauges), velocity gradients (repeat precise leveling) and rates

of change of the geoid (GRACE). Alternatively, geodetic integrals (Stokes and Hotine) can be applied using absolute or relative rates of gravity and vertical velocities. However, this approach does not allow incorporation of new data when available, which can be considered as a substantial shortcoming in view of improving the time span of, for example, the GPS and GRACE time series. This, in addition to the error propagation, clarifies why LSC is the approach adopted in this study.

The observation equation of the general least-squares collocation model is given by *Moritz (1980, p. 144)* as follows:

$$\mathbf{l} = \mathbf{A}\mathbf{X} + \mathbf{t} + \mathbf{n}, \quad (4)$$

where \mathbf{l} is the data vector, \mathbf{t} is the signal vector component of the data, \mathbf{n} comprises the vector of observational errors, and $\mathbf{A}\mathbf{X}$ describes the systematic component of the data. In this study, it is assumed that the trend in the data is solely due to postglacial rebound and, therefore, it is modeled using relationships between the rates of gravity and vertical velocities on the one hand and the rate of geoid and vertical velocities (rate of vertical displacement) on the other hand. The first relationship is given in terms of gravity-to-height ratio, based on a-priori knowledge about the ongoing process. The second relationship is given by the mass flow model, see *Sjöberg (1982)*, which is adopted in this study. The relationships between signal components of gravity rates, vertical velocities and geoid rates are defined in terms of cross-covariance matrices as given by *Heck (1984)*. The applied computational procedure is described in detail in *Rangelova et al. (2005)*.

2.3 Combination of Geoid Rates

The GRACE and Gdot/GPS geoid rates can be combined via least-squares adjustment using a Gauss-Markov model, with the observation equation given as follows:

$$\mathbf{A}_i\mathbf{X} = \mathbf{l}_i + \mathbf{e}_i, \quad D(\mathbf{l}_i) = \sigma_i^2\mathbf{Q}_i, \quad i = 1,2, \quad (5)$$

where i denotes the two data sets. \mathbf{A}_i are the $(n \times u)$ coefficient matrices (assumed of full column rank) for the two data sets, \mathbf{X} is the $(u \times 1)$ vector of the unknown parameters, and \mathbf{l}_i and \mathbf{e}_i denote the data and error vectors, respectively; σ_i^2 are the variance factors for the two sets of data, known from the a-priori modeling, and \mathbf{Q}_i are the positive definite

cofactor matrices of the data. The unknowns are estimated as follows:

$$\begin{aligned} (\sigma_1^{-2} \mathbf{A}'_1 \mathbf{Q}_1^{-1} \mathbf{A}_1 + \sigma_2^{-2} \mathbf{A}'_2 \mathbf{Q}_2^{-1} \mathbf{A}_2) \hat{\mathbf{X}} = \\ \sigma_1^{-2} \mathbf{A}'_1 \mathbf{Q}_1^{-1} \mathbf{I}_1 + \sigma_2^{-2} \mathbf{A}'_2 \mathbf{Q}_2^{-1} \mathbf{I}_2. \end{aligned} \quad (6)$$

One possible way to define the unknown parameters is to transform both data sets in a spherical cap centered at Hudson Bay. This approach is useful when a global GRACE geoid rate and a regionally estimated Gdot/GPS geoid rate are combined. The so-called adjusted spherical cap harmonic analysis, introduced by De Santis (1992), is applied herein. The adjusted spherical cap harmonics comprise two sets of base functions that are not orthogonal to each other. If only one set is used, the orthogonality is preserved, and this offers flexibility to test the significance of the estimated parameters (harmonic coefficients) and to keep necessary redundancy by deleting the insignificant ones.

The variance component estimation is performed using the iterated BIQUÉ method according to Koch (1999).

3 Description of Data Sets

3.1 GRACE Time Series

The constrained gravity field solutions from August 2002 to February 2006 from Release 1 of the CSR GRACE Level 2 products in terms of coefficients of geopotential are used to construct a time series by removing a long-term mean field. The GRACE data was corrected for the ocean pole tide (IERS conventions 2003). Because of its large variability, the C_{20} coefficient in each solution was replaced by the values obtained via satellite laser ranging and distributed with the GRACE data. The solution for June 2003 is not available and was predicted via least-squares fit of the mean, trend, annual cosine and sine components to coefficients. The geoid changes at each epoch t were calculated from the residual (with respect to the three-year mean) coefficients $\Delta \bar{C}_{lm}(t)$ and $\Delta \bar{S}_{lm}(t)$ as follows:

$$\begin{aligned} \Delta N(\theta, \lambda, t) = a \sum_{l=2}^N \sum_{m=0}^l W_l \bar{P}_{lm}(\cos \theta) \\ [\Delta \bar{C}_{lm}(t) \cos(m\lambda) + \Delta \bar{S}_{lm}(t) \sin(m\lambda)] \end{aligned} \quad (7)$$

where a is the Earth's radius, θ and λ are the co-latitude and longitude, respectively, and $\bar{P}_{lm}(\cos \theta)$ are the normalized associated Legendre functions. W_l are the weighting coefficients of the isotropic Gaussian filter applied to smooth the random errors present in the geopotential coefficients; see Wahr *et al.* (1989). The smoothing radius of the filter applied is 600 km; see, for example, Chen *et al.* (2005).

3.2 Absolute Gravity Rates and GPS Vertical Velocities

Absolute gravity rates are obtained from the re-adjustment of the historic relative gravity measurements in the Canadian Gravity Standardization Network (CGSN) with reference epoch 2000.0 and constraints provided by absolute gravity stations; see Pagiatakis and Salib (2003). The CGSN is not designed for geodynamic studies and the stations are not observed on a regular basis in time. However, gravity measurements span over 40 years, which allows gravity rates to be estimated at the 64 “primary gravity control” sites from the network.

The GPS vertical velocities are provided by Natural Resources Canada. They are obtained through combining 36 individual Canadian Base Network (CNB) campaigns from 1994 to 2004 using single station minimum constraints (Joe Henton, personal communication).

The CBN sites are not co-located with the CGSN sites. This precludes the derivation of a reliable gravity-to-height ratio. However, from the weighted least-squares adjustment of gravity-to-height ratios at 13 GPS and gravity sites (located within 100 km radius), a value of $-0.18 \pm 0.02 \mu\text{Gal}/\text{mm}$ was obtained, which matches the result of Lambert *et al.* (2006) derived with the North American mid-continent tilt profile data. This value is (within the standard error) close to the theoretical value for PGR, i.e., $-0.16 \mu\text{Gal}/\text{mm}$; see, e.g., Fang and Hager (2001). This indicates that CBN and CGSN data can be combined to model the PGR signal in Canada.

4 Analysis of Results

In the applied PCA of the GRACE time series, the first four principal components comprise physical modes. The first PC, which explains more than 50% of the data variability, represents the long-term geoid changes. The second PC represents the hydrologic mass variability in the region; see Figure 1. The estimated trend in the first PC time series was used to scale the corresponding EOF loading pattern

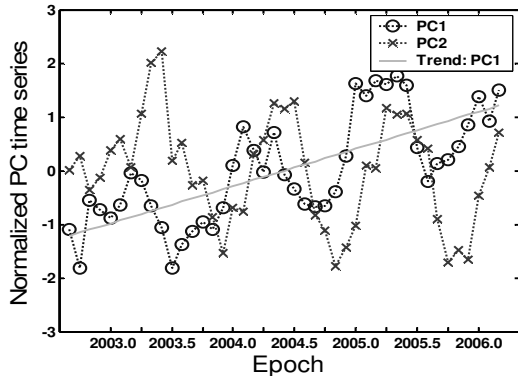


Fig.1 The first two principal component time series normalized with the standard deviations. Also, trend is fitted to the first PC time series.

and to derive the geoid rate according to eq. (3); see Figure 2. The peak values observed west of Hudson Bay correspond, as a location, to the thick Keewatin Dome of ice present in the ICE5G model of Peltier (2004). In contrast, the Gdot/GPS geoid rate exhibits a maximum in the eastern part of Hudson Bay) see Figure 3), thus showing better agreement with the PGR models based on ICE3G and ICE4G deglaciation histories. In fact, the maximum values in the eastern part of Hudson Bay are due to the large gravity rate observed there. A detailed comparison with the ICE3G model can be found in Rangelova *et al.* (2005). Note, however, that the geoid rate in Figure 3 was smoothed so it has the same spectral content as the GRACE geoid rate. The Gdot/GPS geoid rate has more high frequencies (in the spectral band between degrees 15 and 20) as a result of the least-squares collocation procedure that accounts for the local signal in the data.

It is worth mentioning also that when a three-year time series was analyzed, the first two principal components reversed their order. This simply demonstrates that the hydrologic signal dominates the short geoid change time series.

The GRACE geoid rate was derived from homogeneous observations in space and time. This is a ultimate advantage compared to the geoid rate estimated from gravity and GPS data, and, therefore, the GRACE geoid rate is more suitable for PGR studies. On the other hand, GRACE measures integral mass changes and the long-term geoid rate, assumed to be due to PGR, may be corrupted with an interannual hydrologic signal. The latter is difficult to be verified if it is not present in the continental water storage models.

The Gdot/GPS geoid rate may contain systematic distortions inherited from the data sets used. In

addition, the assumption for gravity-to-height ratio may be invalid. Although the a-priori value is close to the theoretical one, the gravity-to-height ratio should be estimated rigorously in the least-squares collocation procedure.

Despite the uncertainties involved in the modelling, a combination of geoid rates via least-squares adjustment together with the estimation of variance components (VCE) can provide an assessment of relative errors and weights in the GRACE and Gdot/GPS geoid rates. This is important in view of the fact that the pronounced PGR signal in the Laurentide is clearly observed after four years of GRACE measurements. In the following, the results of the combination procedure are discussed.

A spherical cap (see Sec. 2.3) with an angular radius of 30° was centered at the west part of Hudson Bay. The original geoid rate grids of $1^\circ \times 1^\circ$ were transformed into the spherical cap using standard coordinate transformation procedures. To decrease the computational load in the least-squares adjustment, only those values that account for virtually all data variability (more than 99%) were selected via a modified Gram-Schmidt orthogonalization of the coefficients matrices, see Chen *et al.* (1989). Thus, the total number of data is 106, while the number of unknown parameters is 21 if the maximum degree of the spherical cap harmonics is 5. Figure 4 shows the combined geoid rate. The peak is centered over Hudson Bay and the maximum rate is 1.5 mm/yr.

Two different cases are investigated via variance component estimation. In the first case, the cofactor matrix is a unit matrix, i.e., no weights are introduced for both data sets. In the second case, the covariance matrix for Gdot/GPS geoid rate is available from the least-squares collocation procedure. The a-priori variance factor for VCE is $0.78 \text{ mm}^2/\text{yr}^2$. Since no errors of the geopotential coefficients are provided for the GRACE constrained solutions, the accuracy of the geoid rate was estimated via propagating the error of the estimated trend of the first PC. Thus obtained, the maximum errors are between 0.8 and 1 mm/yr over Hudson Bay.

Table 1 contains the estimated variance factors. For the case of equal weights, the variance factors are unrealistically small. In fact, although convergence is achieved at the sixth iteration, the standard deviations of the variance factors are quite large. When proper weighting of the data sets is introduced, the estimated variance components are $0.72 \pm 0.28 \text{ mm}^2/\text{yr}^2$ and $0.50 \pm 0.19 \text{ mm}^2/\text{yr}^2$ for the GRACE and Gdot/GPS geoid rates, respectively.

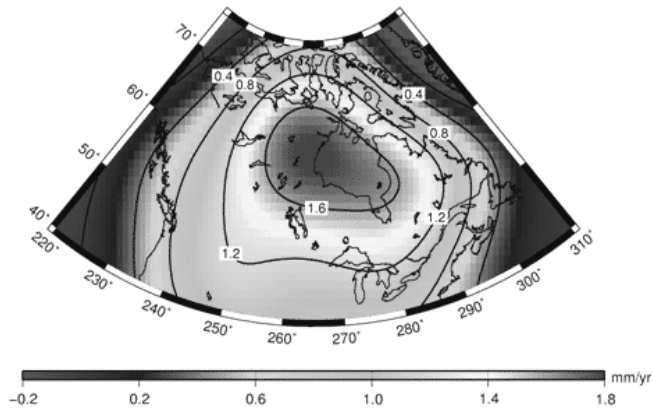


Fig. 2 Rate of change of geoid estimated via principal component analysis of the GRACE time series.

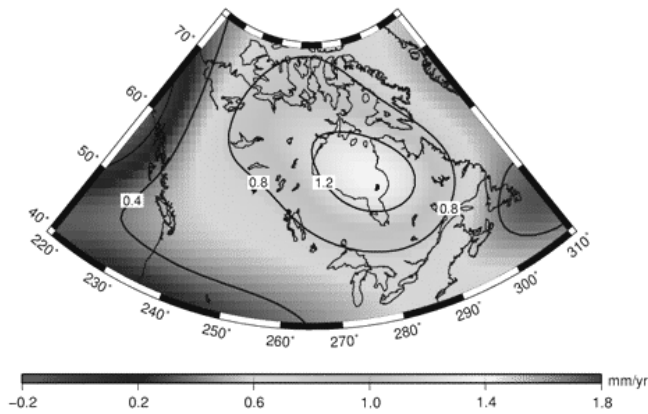


Fig. 3 Rate of change of geoid estimated via least-squares collocation. The data used are absolute rates of gravity and GPS.

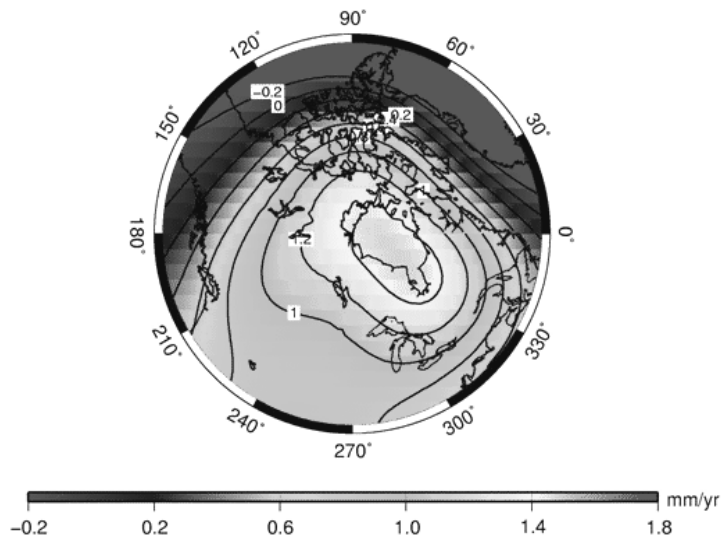


Fig. 4 Combined solution with GRACE and Gdot/GPS geoid rate.

These estimates depend on the selected subset of data through the coefficient matrix in the least-squares adjustment, and it is expected that they will vary if the locations of data points change. For a harmonic expansion of degree 5, the estimated variance factors indicate that the GRACE geoid rate should be down-weighted by a factor of 1.4 relatively to the Gdot/GPS geoid rate. With longer GRACE time series available, it is expected that this ratio will decrease.

Table 1 A priori and estimated variance factors.

geoid rate	weights	σ^2 , mm ² /yr ²	$\hat{\sigma}^2$, mm ² /yr ²
GRACE	no	1.00	0.25
Gdot/GPS	no	1.00	0.13
GRACE	yes	1.00	0.72
Gdot/GPS	yes	0.78	0.50

Conclusions

Two independent solutions for the geoid rate in North America were combined via least-squares adjustment. The first solution was obtained via spatio-temporal analysis of GRACE time series with almost four years time span. The second solution is based on least-squares collocation using as input absolute gravity rates and GPS velocities. Both solutions differ in terms of magnitude and location of peak values. While GRACE geoid rate is close to ICE5G(VM2) model, the geoid rate estimated solely from surface measurements agrees better with postglacial rebound models based on ICE3G and ICE4G de-glaciation histories.

The estimated variance factors of the two solutions indicate that the covariance matrix for the GRACE geoid rate should be up scaled compared to the covariance matrix for the geoid rate from gravity and GPS data. More realistic results can be expected if errors of the geopotential coefficients are taken into consideration and longer time series are analyzed. It is planned to repeat this study as soon as new information becomes available.

Acknowledgments

We thank the GRACE project for the GRACE Level 2 data. Also, Natural Resources Canada is gratefully acknowledged for providing the GPS data.

References

- Chen, S., S. A. Billings, W. Luo (1989). Orthogonal least squares methods and their application to non-linear system identification. *Int. J. Control*, Vol. 50, No. 5, pp.1873-1896.
- Chen, J. L., C. R. Wilson, J. S. Famiglietti, M. Rodell (2005). Spatial sensitivity of the Gravity Recovery and Climate Experiment (GRACE) time-variable gravity observations. *J. Geophys. Res.*, 110, B08408, doi:10.1029/2004JB00353.
- De Santis, A. (1992). Conventional spherical harmonic analysis for regional modelling of the geomagnetic field. *Geophys. Res. Lett.*, Vol. 19, No.10, pp. 1065-1067.
- Fang, M. and B.H. Hager (2001). Vertical deformation and absolute gravity. *Geophys. J. Int.*, Vol.146, pp. 539-548.
- Heck, B. (1984). Zur Bestimmung vertikaler rezenter Erdkrustenbewegungen und zeitlicher Änderungen des Schwerefeldes aus wiederholten Schweremessungen und Nivellements. *Deutsche geodätische commission*, Reihe C, Nr.302, München.
- Jolliffe, I. T. (2002). Principal Component Analysis, Springer Series in Statistics, Springer, New York.
- Koch, K.-R. (1999). Parameter estimation and hypothesis testing in linear models, 2nd edn., Springer-Verlag.
- Lambert A., N. Courtier and T. S. James (2006). Long-term monitoring by absolute gravimetry: Tides to postglacial rebound. *J. Geodynamics*, 41, pp. 307-317.
- Moritz, H., (1980). Advanced Physical Geodesy. H.Wichmann, Karlsruhe, Germany.
- Pagiatakis, S. D., P. Salib (2003). Historical relative gravity observations and the time rate of change of gravity due to postglacial rebound and other tectonic movements in Canada. *J. Geophys. Res.*, Vol. 108, No B9, 2406, doi:10.1029/2001JB001676.
- Peltier, W. R. (2004). Global Glacial Isostasy and the Surface of the ICE-Age Earth: The ICE-5G (VM2) Model and GRACE. *Annu. Rev. Earth Planet Sci.*, 32, 111-149, doi: 10.1146/annurev.earth.32.082503.144359.
- Preisendorfer, R. W. (1988). Principal Component Analysis in Meteorology and Oceanography, *Developments in Atmospheric Science*, vol. 17, Elsevier.
- Rangelova E., W. van der Wal, M. G. Sideris, P.Wu (2005). Numerical models of the rates of change of the geoid and orthometric heights over Canada. In : *Proc. of Dynamic Planet 2005, Joint Assembly of IAG, IAPSO and IABO*, Cairns, Australia, August 22- 26, 2006.
- Sjöberg, L.E. (1982). Studies on the land uplift and its implications on the geoid in Fennoscandia. University of Uppsala, Institute of Geophysics, Department of Geodesy, *Report No 14*.
- Tapley, B. D., S. Bettadpur, M. Watkins, and C. Reigber (2004a). The gravity recovery and climate experiment: Mission overview and early results. *Geophys. Res. Lett.*, 31, L09607, doi:10.1029/2004GL019920.
- Véronneau, M., R. Duval, and J. Huang (2006). A gravimetric geoid model as a vertical datum in Canada, *Geomatics*, Vol. 60, pp. 165-172.
- Wahr, J., M. Molenaar, F. Bryan (1998). Time variability of the Earth's gravity field: Hydrologic and oceanic effects and their possible detection using GRACE, *J. Geophys. Res.*, 103(B12), 30,205-30,229.

Low-degree load harmonic coefficients from combining GRACE, GPS time series and a-priori dynamics

M.J.F. Jansen, J. Kusche, E.J.O. Schrama
Delft Institute of Earth Observation and Space Systems (DEOS),
TU Delft, Kluyverweg 1, PO box 5058, 2600 GB Delft, The Netherlands

Abstract. One of the primary aims of the Gravity Recovery and Climate Experiment (GRACE) mission is to monitor large-scale surface mass changes by measuring their associated variations in gravity. We proposed in earlier work to combine the GRACE measurements with GPS time series provided by e.g. the International GNSS service (IGS) to strengthen the long wavelengths of the solution. This appears necessary because GRACE monthly gravity solutions not yet match the targeted baseline accuracies at the lower degrees, and they do not provide degree-1 coefficients. The method of GPS inversion has been proposed by Blewitt et al. (2001), and sensitivity studies based on formal error propagation have indicated that GPS could contribute up to 60% to degrees 2-4, and up to 30% for selected higher degrees in a combination. Characteristic in our approach is a) the combination of GRACE and GPS in a weighted least-squares sense, and b) the introduction of a dynamic constraint on the mass change in time. Degree-1 load coefficients, derived from GPS through loading inversion, benefit indirectly from the combined determination of higher-order coefficients from GRACE and GPS. We find geocenter estimates which are consistent with previous studies. Selected degree-2 coefficients are provided in this paper.

Keywords. Surface mass redistribution, GPS, GRACE, inversion, hydrology

1 Introduction

One of the main objectives of the GRACE mission is to monitor hydrological and ocean mass redistribution through its gravitational effect (Tapley et al., 2004). Monthly gravity fields have been released to the public, covering a time span from April 2002 onwards. It has been proposed by Blewitt et al. (2001); Wu et al. (2003), and others, that at larger spatial scales surface load changes may be derived

independently by geometrically measuring the elastic response of the Earth. We have used the International GNSS Service combination solutions for this purpose. This is particularly interesting as long as GRACE monthly gravity solutions not yet match the targeted baseline accuracy at the lower degrees. Furthermore GRACE does not provide estimates on degree-1, which corresponds to the geocenter motion of the Earth. Fig. 1, modified from Blewitt and Clarke (2003), is an illustration of the dynamic model behind the methods of GPS and GRACE inversion for surface loads. Load Love number (LLN) theory relates load distribution, geoid change and Earth deformation. In this approach, the estimated degree-1 surface mass redistribution, obtained from 3D network deformation by consistent choice of degree-1 load Love numbers, consequently yields geocenter estimates. This method is called the “deformation” approach considered in Lavallée et al. (2006). It is important to note that these estimates are not derived within the GPS orbit determination process, but rather follow from the conservation of momentum in the Earth-load system. (In theory, a purely geometrical technique like VLBI would be capable to provide geocenter estimates through a loading inversion; assuming there would be a sufficient number of homogeneously distributed observation sites). In principle,

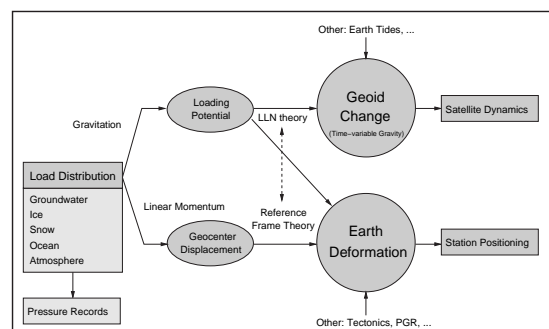


Fig 1. The dynamic model used in this study.

gravity field changes sensed by GRACE and surface loading observed by GPS networks include the combined direct and indirect effect of all mass redistributions within the Earth and its atmospheric and fluid envelope. It is well-known that one cannot uniquely solve for 3D density distributions from gravity data; however, the majority of the mass transports important on time scales from daily to inter-annual occur at or near the Earth's surface. Under this hypothesis, gravity changes on these time scales can be uniquely inverted into mass redistribution within a spherical shell at the surface (Chao, 2005). Because the atmospheric contribution to the surface density change can be reasonably modelled using atmospheric pressure data, GRACE gravity and GPS displacements allow to detect changes in the Earth's hydrological storage systems.

One is forced to constrain solved-for mass configurations either by low-degree truncation, by spatial averaging, or by regularisation operations employing mathematically or physically motivated constraints. This is because the errors in GRACE or GPS-derived spherical harmonic coefficients are not "white" over the spectral domain but increase with higher resolution, because elastic load Love numbers quickly loose their power and so the spectral sensitivity decreases, and, in the case of GPS inversion, the Earth's coverage with observations is far from homogeneous. Combining satellite gravity and geometrical displacements in a joint inversion, proposed by Kusche and Schrama (2005), is expected to relieve these constraints and improve the reliability of estimates. In this paper, we combined GRACE time-variable gravity fields with global weekly GPS time series provided by the International GNSS Service (IGS), in a weighted least-squares sense, for the period February 2003 - July 2006. A-priori dynamics derived from hydrological, ocean and atmosphere models are used within the combination, to avoid unrealistic changes and jumps in the solution. We find that geocenter estimates from this combination fit quite well to earlier estimates, including our own in Kusche and Schrama (2005) obtained using a regularised GPS-only inversion. Moreover, changes in the Earth's flattening from the combination were found fitting remarkably well to those from SLR (Kusche et al., 2006).

2 Loading Model

As usual, we parameterise the surface mass density change $\Delta\sigma$, i.e. the anomaly with respect to a long-

term eference average, in spherical harmonics

$$\Delta\sigma(\lambda, \theta) = a\rho_w \times \sum_{l=0}^{\infty} \sum_{m=0}^l (\Delta C_{lm}^{\sigma} \cos m\lambda + \Delta S_{lm}^{\sigma} \sin m\lambda) P_{lm}(\cos \theta). \quad (1)$$

Here a is Earth's mean radius, ρ_w seawater density, P_{lm} are the fully normalised associated Legendre polynomials, and ΔC_{lm}^{σ} , ΔS_{lm}^{σ} are the spherical harmonic coefficients of the surface density anomaly. Using Farrell's (1972) loading theory, they can be related to the spherical harmonic coefficients of geoid change (ΔC_{lm}^g , ΔS_{lm}^g), height deformation (ΔC_{lm}^h , ΔS_{lm}^h), and lateral deformation (ΔC_{lm}^{ψ} , ΔS_{lm}^{ψ}), through the elastic load Love numbers k_l' , h_l' , l_l'

$$\Delta C_{lm}^g = \frac{3\rho_w}{\rho_e} \frac{(1+k_l')}{2l+1} \Delta C_{lm}^{\sigma} \quad (2)$$

$$\Delta C_{lm}^h = \frac{3\rho_w}{\rho_e} \frac{h_l'}{2l+1} \Delta C_{lm}^{\sigma} \quad (3)$$

$$\Delta C_{lm}^{\psi} = \frac{3\rho_w}{\rho_e} \frac{l_l'}{2l+1} \Delta C_{lm}^{\sigma}. \quad (4)$$

Degree-1 Love numbers deserve special attention. Starting with h_1' , l_1' values from Farrell (1972), referring to the centre of mass of the solid Earth (CE), Blewitt (2003) derived h_1' , l_1' for the centre of figure (CF) frame as follows

$$[l_1']_{CF} = -\frac{1}{3}([h_1']_{CE} - [l_1']_{CE}) = 0.134 \quad (5)$$

$$[h_1']_{CF} = \frac{2}{3}([h_1']_{CE} - [l_1']_{CE}) = -0.269. \quad (6)$$

We implemented these numbers, which implies that our estimates for ΔC_{11}^{σ} , ΔS_{11}^{σ} , ΔC_{10}^{σ} and the geocenter refer to the motion of the CF origin as defined in Blewitt (2003) with respect to the centre of mass of the Earth-load system (CM system). (The origin of the CF frame is by definition such that the integral of the moment of the vector displacement field, taken over the solid Earth surface, is zero). The ITRF is a realisation of the CF reference system. From the conservation of momentum \mathbf{m} in the Earth-load system, it follows that the geocenter estimates relate to the surface mass change as:

$$X = \frac{1}{M} \mathbf{m}_x = \frac{1}{M} \frac{4\pi a^4 \rho_w}{3} \Delta C_{11}^{\sigma} \quad (7)$$

$$Y = \frac{1}{M} \mathbf{m}_y = \frac{1}{M} \frac{4\pi a^4 \rho_w}{3} \Delta S_{11}^{\sigma} \quad (8)$$

$$Z = \frac{1}{M} \mathbf{m}_z = \frac{1}{M} \frac{4\pi a^4 \rho_w}{3} \Delta C_{10}^{\sigma}. \quad (9)$$

Here M is the total mass of the Earth, and the factor in eqs. (7-9) amounts to ~ 0.32 . In the method of

GPS inversion, 3D displacement vectors are used to infer for the load distribution. With height Δh , East Δx and North Δy components, the relations to be employed are

$$\Delta h = a \quad (10)$$

$$\times \sum_{l=0}^{\infty} \sum_{m=0}^l (\Delta C_{lm}^h \cos m\lambda + \Delta S_{lm}^h \sin m\lambda) P_{lm}(\cos \theta)$$

$$\Delta x = \frac{a}{\sin \theta} \quad (11)$$

$$\times \sum_{l=1}^{\infty} \sum_{m=0}^l m (-\Delta C_{lm}^{\psi} \sin m\lambda + \Delta S_{lm}^{\psi} \cos m\lambda)$$

$$\times P_{lm}(\cos \theta)$$

$$\Delta y = -a \quad (12)$$

$$\times \sum_{l=1}^{\infty} \sum_{m=0}^l (\Delta C_{lm}^{\psi} \cos m\lambda + \Delta S_{lm}^{\psi} \sin m\lambda)$$

$$\times \frac{\partial}{\partial \theta} P_{lm}(\cos \theta).$$

GRACE observes changes in the Stokes coefficients of the Earth's gravity field, typically averaged over one month. (For the IGS station positions the displacements are cumulated over typically a week). This results in observation equations

$$\Delta C_{lm}^g = \frac{1}{\Delta t} \int_t^{t+\Delta t} \frac{3\rho_w}{\rho_e} \frac{(1+k'_l)}{2l+1} \Delta C_{lm}^{\sigma}(\tau) d\tau, \quad (13)$$

where the Δt for GRACE is one month and for GPS it will be one week; this difference in time span has to be taken into account when combining the different solutions.

3 Inversion

Previous studies (Wu et al., 2002; Blewitt and Clarke, 2003; Kusche and Schrama, 2005; Mendes Cerveira et al., 2006) have shown that the design of the inversion strategy is a serious issue. It is very likely that differing results in the literature may be partly due to different parameterisation, truncation or regularisation approaches. In these previous studies, as well as in all GRACE analysis and evident in geophysical models, the seasonal signal was clearly present, but not taken as a a-priori information in the estimation. Our inversion strategy which takes advantage of the a-priori dynamics will be briefly described here.

3.1 Parameterisation

In a least-squares model, after truncation of the spherical harmonic series eq. (1) at degree L , the

unknowns of the inverse problem described in the previous chapter may be collected in the finite-sized vectors $\mathbf{x}_1 = (X, Y, Z)^T$ and $\mathbf{x}_2 = (\Delta C_{20}^{\sigma}, \dots, \Delta S_{LL}^{\sigma})^T$. For the IGS GPS solution time series it was found that augmenting the vector with residual Helmert parameters $\boldsymbol{\delta}$ may improve the solution (Kusche and Schrama, 2005), although this strategy to some extent weakens the normal equation (Wu et al., 2002), (Lavallée et al., 2006). For the GRACE observation only vector \mathbf{x}_2 is given. We will treat this situation in the well-known concept of local and global parameters. Hence, \mathbf{x}_2 are the global parameters and \mathbf{x}_1 and $\boldsymbol{\delta}$ are local parameters for GPS. Even GRACE coefficients of degree $> L$ could be improved in such a combination scheme, but for that a full variance covariance matrix is needed to carry the correlation information. This leaves us for a single data set with a parameter vector which can be split into a local \mathbf{x}_l and a global \mathbf{x}_g part

$$\mathbf{x} = \begin{bmatrix} \boldsymbol{\delta} \\ \mathbf{x}_1 \\ \mathbf{x}_2 \end{bmatrix} = \begin{bmatrix} \mathbf{x}_l \\ \mathbf{x}_g \end{bmatrix}. \quad (14)$$

Using both GPS and GRACE observations a Gauss-Markov model (Koch, 1999) for weighted data sets can be formulated. For a single data set the Gauss-Markov model looks like

$$\mathbf{y} + \mathbf{e} = \mathbf{A}\mathbf{x}, \quad E\{\mathbf{e}\} = \mathbf{0}, \quad D\{\mathbf{e}\} = \mathbf{C} \quad (15)$$

with observations collected in \mathbf{y} , stochastic residuals \mathbf{e} , and variance covariance matrix \mathbf{C} . Note this interpretation requires that spatial non-stochastic aliasing effects are small; meaning that the truncation degree L must be sufficiently high. The data covariance matrix is extracted from the SINEX files in case of GPS. For GRACE, we have used either a diagonal matrix containing calibrated standard deviations, or a full covariance matrix that has been kindly provided to us by S. Bettadpur (CSR) from the analysis of August 2003. Combining subsequent GPS solutions with a GRACE gravity field there will be one set of global parameters \mathbf{x}_g and every data set will have their own local parameters $\mathbf{x}_{l,i}$. With this assumption the design matrix \mathbf{A} and solution vector \mathbf{x} in eq. (15) for p data sets will become

$$\mathbf{A} = \begin{bmatrix} \mathbf{A}_{l,1} & \mathbf{0} & \dots & \mathbf{0} & \mathbf{A}_{g,1} \\ \mathbf{0} & \mathbf{A}_{l,2} & \dots & \mathbf{0} & \mathbf{A}_{g,2} \\ \vdots & \vdots & \ddots & \vdots & \vdots \\ \mathbf{0} & \mathbf{0} & \dots & \mathbf{A}_{l,p} & \mathbf{A}_{g,p} \end{bmatrix}, \quad \mathbf{x} = \begin{bmatrix} \mathbf{x}_{l,1} \\ \mathbf{x}_{l,2} \\ \vdots \\ \mathbf{x}_{l,p} \\ \mathbf{x}_g \end{bmatrix},$$

where $\mathbf{A}_{l,i}$ is the design matrix for the local parameters of data set i and $\mathbf{A}_{g,i}$ is the design matrix of

the global parameters for data set i . The variance covariance matrix in this model will consist of a block diagonal matrix holding \mathbf{C}_i . In the case discussed in Chap. 4, typically $p = 5$.

3.2 Dynamics model

Constraining the estimated surface mass distribution with respect to time evolution is one of our goals in our approach. The motivation here is to strengthen the solution and to avoid unrealistic jumps. For the time evolution we have to define representative time stamps; for this we use the centre t_k of a data interval. Within a Kalman filter scheme only the global parameters are propagated in time, as they already carry the information of the local parameters. Propagating the global parameters from t_k to t_{k+1} will be done by

$$\mathbf{x}_g(t_{k+1}) = \Phi_{k,k+1} \mathbf{x}_g(t_k) \quad (16)$$

$$\mathbf{P}_g(t_{k+1}) = \Phi_{k,k+1} \mathbf{P}_g(t_k) \Phi_{k,k+1}^T + \mathbf{R}_{k,k+1} \quad (17)$$

with \mathbf{P}_g the covariance matrix of the estimated load SH coefficients, $\Phi_{k,k+1}$ the transition matrix from time t_k to t_{k+1} and $\mathbf{R}_{k,k+1}$ the propagation noise matrix which accounts for the uncertainty when propagating from time t_k to t_{k+1} using an a-priori model. The matrix $\mathbf{R}_{k,k+1}$ is empirically estimated from a combination of a hydrological model, a ocean model and a atmospheric model, by fitting the a-priori dynamics through the combined model and evaluating the residuals.

3.3 Combined inversion

After propagating the load coefficients in time they will be combined with the data. The measurement update step of our estimation scheme combines the new data with the estimated load coefficients on the normal equation level. Using the reduced system of normal equations (Reigber, 1989) for local and global parameters the observations can be combined with the global parameters in a Kalman filter. When the time span of a data set does not completely fit into the time epoch of interest, the covariance matrix is scaled with the inverse of the percentage of the overlap. After the new load coefficients are estimated from the new data the local parameters (geocenter and nuisance parameter) are derived.

4 Results

Statistics of the analysed combination of IGS station position time series and GRACE monthly grav-

ity field models from Geoforschungszentrum Potsdam are shown in Fig. 2. GPS and GRACE products have been preprocessed (cleaned, edited, referred to a common reference in time) as described in (Kusche et al., 2006). Our results for annual geo-

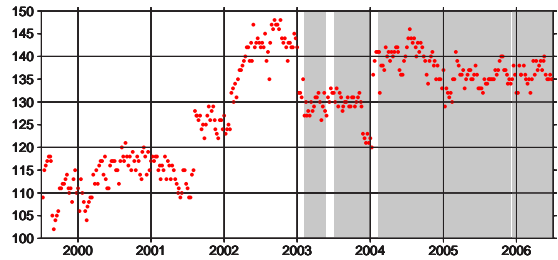


Fig 2. Data used for this study: Dots give the number of GPS sites used per week. Grey-shaded time intervals are where GRACE solutions have been used.

center estimates, estimated in a 6-parameter post-analysis model (bias, trend, semi-/annual term) and valid for the time span 2003.0-2006.5, are summarised in Table 1. They do not contradict those of others, e.g. Wu et al. (2003) who used JPL GPS solutions of an earlier time frame and a different solution strategy, or Mendes Cerveira et al. (2006) who used SOPAC GPS solutions and a different technique of regularisation. The influence of the constraint in time applied here (Markov process of first order) is generally little but can amount to a few mm in some epochs; a slight phase shift is observed which is a consequence of the modelled dynamics. Using a full GRACE covariance in the inversion alters the results only slightly. Fig. 3 shows the estimation of the geo-

Table 1. Geocenter results, annual term (amplitude [mm]/phase [day of year, since 1 January]), for period 2003.0-2006.5. Diagonal (std) or full (cov) covariance matrix for GRACE.

model	X	Y	Z
No dynamics (std)	2.1/21	2.6/334	3.6/24
No dynamics (cov)	2.3/26	2.7/331	3.6/18
Markov (std)	2.1/23	2.7/330	4.0/18
Markov (cov)	2.3/24	2.8/328	4.1/14

center motion as time series and after an additional monthly smoothing. The 1σ error bars are almost identical for all four solutions; we show only those for the solution without a-priori dynamics and diagonal GRACE covariance. For the GRACE fields, here the atmospheric and oceanographic background

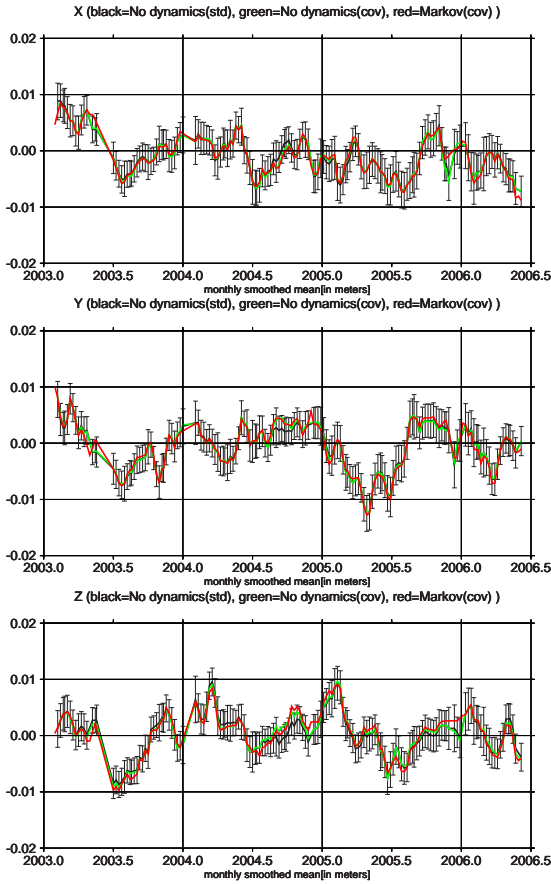


Fig 3. Geocenter motion for GPS/GRACE combination, with no a-priori dynamics and standard deviations for GRACE(black), with no a-priori dynamics and full covariance matrix from GRACE(green), with Markov dynamics and full covariance matrix from GRACE(red)

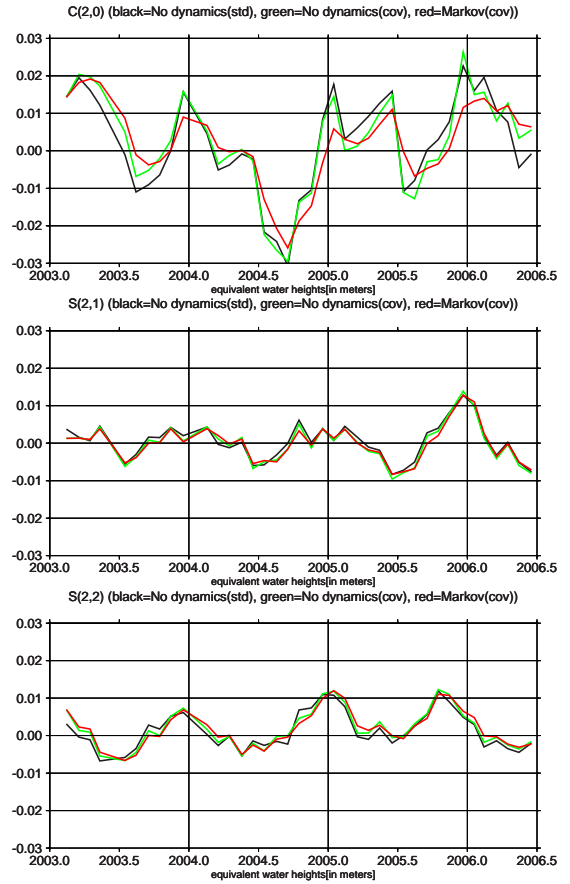


Fig 4. Degree two coefficients for GPS/GRACE combination, with no a-priori dynamics and standard deviations for GRACE(black), with no a-priori dynamics and full covariance matrix from GRACE(green), with Markov dynamics and full covariance matrix from GRACE(red)

fields were reinstated, for the combination fields they were not subtracted again after the combination with GPS. Both should thus represent the total of atmospheric, hydro-logic and oceanic mass variability. Selected degree-2 load coefficients are provided in Fig. 4. For C_{20} , the seasonal cycle is clearly visible; but significantly damped through the inclusion of a priori dynamics in case of the “Markov” solution.

5 Discussion

Several authors have discussed the possibility that geophysical station displacements may be masked by other periodic or episodic effects: multi-path, snow coverage, ocean-tidal or Earth-tidal mismodelling, other site-specific or antenna-specific effects. Indeed it appears likely that these non-geophysical effects are partly responsible for the difference of GPS-derived mass distribution fields and GRACE-derived

ones that can be observed for some regions. On the other hand, on the global scale there is a clear correspondence between geophysical models, GRACE, and GPS-derived solutions. It is not likely that all potential distortions pass uncontrolled into GPS inversion or GPS+GRACE combination estimates. First, apparent 3D displacements due to non-geophysical effects are not necessarily consistent with the loading theory – in mathematical terms they are not within the range of the forward operator described in section 2 of this paper – which means there is a reasonable chance that they get caught in an outlier rejection procedure, regardless the spherical harmonic resolution. Second, if they are consistent with the loading theory, they act like local geophysical loading effects. Then, dependent on the network density and homogeneity, it is not necessarily the case that they will distort low-degree spherical harmonic es-

timates – of course for isolated stations it may happen. What is harmful for this kind of analysis are non-geophysical signals that appear either on a scale comparable to the spherical harmonic resolution of eq. (1) or that correlate with lower-degree harmonics due to spatial inhomogeneous site distribution. A histogram of the geometric vulnerability of the solution due to isolated location of stations had been provided in Fig. 5 of Kusche et al. (2006). The combination methodology discussed in this contribution will serve as a starting point for carrying out more elaborate parameterisation schemes.

It should be further mentioned that any direct comparison of GRACE-predicted vertical or horizontal deformation signals with GPS time series has to circumvent the missing degree-1 terms in the GRACE analysis. Two solutions exist for this problem: employing geophysical models or SLR results for geocenter motion, or estimating and removing the degree-1 terms from the GPS data themselves through loading inversion. In the latter case we are back with the problem discussed here, as one of the most promising ways to prevent spatial aliasing of higher-degree loading signals into the degree-1 estimation is just the use of GRACE.

We have implemented a scheme for the joint inversion of global 3D GPS time series, GRACE gravity fields, and a-priori dynamics into low-degree surface mass redistribution fields. We arrive at reasonable geocenter estimates through an elastic loading theory. The choice of the combination scheme is an issue of investigation, but for the cases discussed here solutions are largely consistent.

Acknowledgements. *We acknowledge the use of IGS GPS station coordinate SINEX files made publicly available through ftp. Thanks go also to the GRACE project for using their level 2 products, and to S. Bettadpur for providing a GRACE covariance.*

References

- Blewitt, G (2003). Self-consistency in reference frames, geocenter definition, and surface loading of the solid Earth. *J. Geophys. Res.*, 108(B2).
- Blewitt, G and Clarke, P (2003). Inversion of Earth's changing shape to weigh sea level in static equilibrium with surface mass redistribution. *J. Geophys. Res.*, 108(B6).
- Blewitt, G, Lavallée, D, Clarke, P, and Nurutdinov, K (2001). A new Global mode of Earth Deformation: Seasonal Cycle Detected. *Science*, 294:2342–2345.
- Chao, BF (2005). On inversion for mass distribution from global (time-variable) gravity field. *J. Geodynamics*, 39:223–230. doi:10.1016/j.jog.2004.11.001.
- Farrell, W (1972). Deformation of the Earth by surface loads. *Rev. Geophys. Space Phys.*, 10(3):761–797.
- Koch, KR (1999). Parameter estimation and hypothesis testing in linear models. *Springer*. Berlin.
- Kusche, J and Schrama, EJO (2005). Surface mass redistribution inversion from global GPS deformation and GRACE gravity data. *J. Geophys. Res.*, 110(B9). doi:10.1029/2004JB003556.
- Kusche, J, Schrama, EJO, and Jansen, MJF (2006). Continental hydrology retrieval from GPS time series and GRACE gravity solutions. In *Proceedings of the IAG, Dynamic Planet, Cairns, in print*, Proceedings of the IAG, Dynamic Planet, Cairns.
- Lavallée, D, van Dam, T, Blewitt, G, and Clarke, P (2006). Geocenter motion from GPS: A unified observation model. *J. Geophys. Res.*, 111.
- Mendes Cerveira, PJ, Hobiger, T, Weber, R, and Schuh, H (2006). Spatial spectral inversion of the changing geometry of the Earth from GPS data. In *Proceedings of the IAG, Dynamic Planet, Cairns, in print*, Proceedings of the IAG, Dynamic Planet, Cairns.
- Reigber, C (1989). Gravity field recovery from satellite data. In Sansò, F and Rummel, R, editors, *Theory of satellite geodesy and gravity field determination*, volume 25 of *Lecture Notes in Earth Sciences*. Springer.
- Tapley, BD, Bettadpur, S, Ries, JC, Thompson, PF, and Watkins, MM (2004). GRACE Measurements of Mass Variability in the Earth System. *Science*, 305:503–505.
- Wu, X, Argus, DF, Helfin, MB, Ivins, ER, and Webb, FH (2002). Site distribution and aliasing effects in the inversion for load coefficients and geocenter motion from GPS data. *Geophys. Res. Lett.*, 29(24). doi:10.1029/2002GL016324.
- Wu, X, Helfin, MB, Ivins, ER, Argus, DF, and Webb, FH (2003). Large-scale global surface mass variations inferred from GPS measurements of load-induced deformation. *Geophys. Res. Letters*, 30(14). doi:10.1029/2003GL017546.

A comparison of different methods for determining the topographic-condensation mass effects at airborne altitude

A.A. Makhloof, F. Müller, K.H. Ilk

Institute of Theoretical Geodesy,

University of Bonn, Nussallee 17, D-53115 Bonn, Germany, email: atef@geod.uni-bonn.de

Abstract. Airborne gravimetry is a fast and sufficiently accurate gravity measurement technique to derive high resolution geoids in not easily accessible regions. Under optimal conditions the measurement accuracy varies around 1 to 2 mGal for a spatial resolution of approximately 2 km. The downward continuation of these observations requires data filtering to reduce the intrinsic instabilities. To ease the downward continuation procedure it is helpful to additionally apply a remove-restore technique based on gravity field information provided by digital elevation models, available nowadays for most parts of the world. This paper discusses three different methods for determining the effects of topographic masses at aircraft altitude. In the first method, the topographic condensation masses are expanded into a spherical harmonic expansion up to a maximum degree of approximately 360, which corresponds to a resolution of approximately 30 arc minutes block size. In addition, the residual fine structure of the topography is modeled by a spherical spline representation. A second method is based again on the spherical harmonic expansion of the topography, but the fine structure is modeled by the integral over the residual topography, numerically evaluated by a quadrature method based on digital elevation blocks with a resolution of 2.5 arcmin side length. The third method consists in the integration over the complete topographic masses, again numerically evaluated by an elevation block quadrature formula. The integration area is restricted to a specific region and the far zone effect is estimated based on a technique proposed by Molodenskii. These three methods are compared by a numerical example of the Canadian Rocky Mountains. The results are validated by evaluating the integral of topography over the whole earth.

Keywords. Helmert's condensation method, far-zone terrain effect, space localizing base function, direct topographical effect.

1 Introduction

The effects of the topographic-condensed masses on the geoid heights from airborne gravity are evaluated as two separate contributions: the direct topographical effect on the gravity and the indirect topographical effect on the geoid (Novák et al. 2001). Since this investigation puts the emphasis on modeling aspects of the topography, we would like to show this on the basis of the direct effect of topography only. Questions regarding the geoid calculations itself, which include the indirect effect as well as a downward continuation step are not part of this study. For further interest see (Müller, Mayer-Gürr 2003 and Makhloof, Ilk 2006).

The Helmert disturbing gravity potential T^h at flight level $R + D$ is related to the disturbing gravity potential T of the Earth's gravity field as follows (Martinec 1993, Eq. (8)),

$$T^h(r, \varphi, \lambda) = T(r, \varphi, \lambda) - \delta V(r, \varphi, \lambda) . \quad (1)$$

where $\delta V(r, \varphi, \lambda)$ is the difference between the gravitational potential of the topography V^t and the gravitational potential of the condensed topography V^c at a surface inside the Earth or at the geoid,

$$\delta V(r, \varphi, \lambda) = V^t(r, \varphi, \lambda) - V^c(r, \varphi, \lambda) . \quad (2)$$

The spherical coordinates r, φ, λ of the computation point at airborne altitude refer to a geocentric coordinate system. By applying the partial radial derivative to Eq. (2), the direct topographical effect on gravity can be determined as:

$$\left. \frac{\partial \delta V(r, \varphi, \lambda)}{\partial r} \right|_{r=R+D} = \frac{\partial V^t}{\partial r} - \frac{\partial V^c}{\partial r} \quad (3)$$
$$:= DTE(R + D, \varphi, \lambda)$$

2 Helmert's condensation methods

In the following, the geoid is approximated by a geocentric reference sphere of a radius R (6378 km). The geocentric radii of the computation and the integration points are given by adding the orthometric heights of these points to the radius of the geocentric sphere. The density of the topographic masses is considered to be constant throughout this investigation.

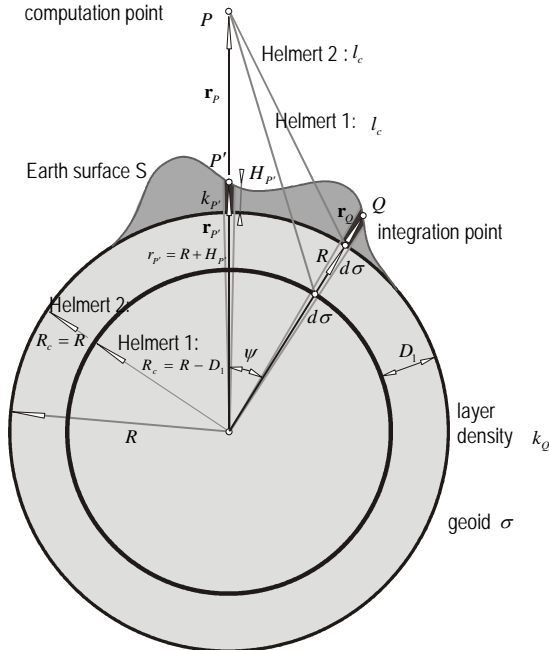


Fig. 1 Helmert's condensation model

The potential of the topographic masses according to Newton's law of gravitation is given by (see Fig. 1):

$$V^t = G\rho \iiint_v \frac{1}{l(R+D, \lambda, \phi)} dv \quad (4)$$

$$= G\rho \iint_{\sigma} \left[\int_R^{R+H} \frac{\xi^2}{l(R+D, \psi, \xi)} d\xi \right] d\sigma$$

where G denote the gravitational constant, ρ the density of the topographic masses, l the distance between the computation point and the integration point and ξ the geocentric radius of the mass element.

In this investigation the Helmert's methods of condensation are used. In this case the topographic masses are shifted along the local vertical and condensed at a parallel surface below the geoid. In the present application the condensation layer is 32km

below the geoid (*first condensation method of Helmert*). In case of the *second condensation method of Helmert* the masses are condensed onto the geoid directly.

Then the potential of the condensation masses is given by:

$$V^c = G \cdot R^2 \iint_{\sigma} \frac{\kappa_Q}{l_c(R+D, \psi, R_c)} d\sigma, \quad (5)$$

where κ_Q is the single layer density, the quantity R_c is the radius of the (approximate) condensation sphere. In case of Helmert's first condensation method it holds $R_c = R - D_1$ and in case of Helmert's second method $R_c = R$ where D_1 is the Helmert condensation depth.

3 Computation methods for the effects of the topographic masses at airborne altitude

It is known that the total topographic-condensation masses must be calculated globally which is very expensive in terms of computation time. To overcome this problem, three methods are investigated in this paper which will be discussed in the following.

In the *first method*, the topographic-condensation masses are expanded into a spherical harmonic expansion up to a maximum degree of approximately 360, which corresponds to a resolution of approximately 30 arc minutes block size. Then the residual fine structure of the topography is modeled by a spherical spline representation.

In general, the direct effect of topography can be derived by transforming the inverse distance $1/l(R+D, \psi, \xi)$ in Eqs. (4) and (5) into a spherical harmonic expansion (Heiskanen and Moritz, 1967):

$$l^{-1} = \frac{1}{R+D} \sum_{n=0}^{\infty} \left(\frac{\xi}{R+D} \right)^n P_n(\cos \psi_{PQ}). \quad (6)$$

where $P_n(\cos \psi_{PQ})$ are the Legendre polynomials of degree n . A separation of Eq. (6) into terms related to the coordinates of the computation point P from those related to the integration point Q can be made by means of the addition theorem of the spherical harmonic functions. Therefore the inverse distance can be written in the following form (Rummel et al., 1988):

$$l^{-1} = \frac{1}{(R+D)} \sum_{n,m,\alpha} \left(r_Q / (R+D) \right)^n \frac{1}{2n+1} Y_{nm}^{\alpha} Y_{nm}^{\alpha'} \quad (7)$$

and with $Y_{nm}^\alpha = Y_{nm}^\alpha(P), Y_{nm}^{\alpha'} = Y_{nm}^{\alpha'}(Q)$ the surface spherical harmonics, e.g.,

$$\begin{aligned} Y_{nm}^{\alpha=0} &= P_n^m(\cos \vartheta) \cos m\lambda, \\ Y_{nm}^{\alpha=1} &= P_n^m(\cos \vartheta) \sin m\lambda. \end{aligned} \quad (8)$$

Inserting Eq. (7) into Eq. (4), interchanging the summation and subsequent integration results in:

$$\begin{aligned} V_i &= G\rho R^2 \left[\sum_{n=0}^{\infty} \left(\frac{R}{R+D} \right)^{n+1} \sum_{k=1}^{n+3} \frac{1}{k} \binom{n+2}{k-1} \right. \\ &\quad \left. \cdot \iint_{\sigma} P_n(\cos \psi_{PQ}) \left(\frac{H_Q}{R} \right)^k d\sigma \right]. \end{aligned} \quad (9)$$

The same procedure is applied to the potential of the condensation masses V^c .

In case of the potential of the condensation masses eq. (5), the single layer density κ_Q can be determined based on the mass condensation condition (Martinec, 1998) as:

$$\kappa_Q = \rho R \left[\frac{H_Q}{R} + \left(\frac{H_Q}{R} \right)^2 + \frac{1}{3} \left(\frac{H_Q}{R} \right)^3 \right] \quad (10)$$

Then the direct effect of topography DTE^{res} for the residual fine structure can be given according to eq. (3) as:

$$\begin{aligned} DTE^{res}(R+D, \varphi, \lambda) &= -G\rho R \sum_{n=0}^{\infty} \left(\frac{R}{R+D} \right)^{n+2} (n+1) \\ &\quad \cdot \left\{ \left[1 - \left(\frac{R-D_1}{R} \right)^n \right] \frac{1}{R} \iint_{\sigma} H_Q P_n(\cos \psi_{PQ}) d\sigma \right. \\ &\quad + \left[\frac{n+2}{2} - \left(\frac{R-D_1}{R} \right)^n \right] \frac{1}{R^2} \iint_{\sigma} H_Q^2 P_n(\cos \psi_{PQ}) d\sigma \\ &\quad \left. + \left[\frac{(n+2)(n+1)}{6} - \frac{1}{3} \left(\frac{R-D_1}{R} \right)^n \right] \frac{1}{R^2} \iint_{\sigma} H_Q^3 P_n(\cos \psi_{PQ}) d\sigma \right\}. \end{aligned} \quad (11)$$

The topographic heights will be represented by the following approximation approach:

$$H_Q^k = \sum_{i=1}^I a_i^k \Phi^k(r_Q, r_{S_i}), \quad (12)$$

where a_i^k ($k=1, \dots, 3$) are the unknown spline parameters, r_Q represents the field point and the I nodal points r_{S_i} indicate the location of the spline functions $\Phi^k(r_Q, r_{S_i})$. A general form of the spline function can be given as:

$$\Phi^k(r_Q, r_{S_i}) = \sum_{n=0}^{N_{\max}} C_n^k P_n(\cos \psi_{QS_i}). \quad (13)$$

The coefficients C_n^k define the shape of the spline function. In this particular case degree variances of the heights are used to scale the spline functions. The quadratic and cubic heights will also be mod-

eled by spline functions. With this definition, the base functions can be interpreted as isotropic and homogeneous harmonic spline functions (Freedeen et al. 1998). The nodal points can be generated on a geographical grid, on a grid by a uniform subdivision of icosahedrons or on Gauss-Legendre grids. Substituting Equation (13) into Equation (12) results in:

$$H_Q^k = \sum_{i=1}^I a_i^k \sum_{n=0}^{N_{\max}} C_n^k P_n(\cos \psi_{QS_i}). \quad (14)$$

Applying the addition theorem of spherical harmonics:

$$P_n(P, Q) = \frac{1}{2n+1} \sum_{m=-n}^n Y_{nm}(P) Y_{nm}(Q), \quad (15)$$

and taking the orthogonality conditions,

$$\iint_{\sigma} Y_{\bar{m}}(Q) Y_{m}(Q) d\sigma(Q) = 4\pi \delta_{\bar{m}m}, \quad (16)$$

into account, then the double integral (exemplarily for $k=1$) in Eq. (11) can be expressed as:

$$\begin{aligned} \sum_{n=0}^{\infty} \left(\frac{R}{R+D} \right)^{n+2} (n+1) \left\{ \left[1 - \left(\frac{R-D_1}{R} \right)^n \right] \frac{1}{R} \iint_{\sigma} H_Q^1 P_n(\cos \psi_{PQ}) d\sigma = \right. \\ \left. \sum_{n=0}^{\infty} \left(\frac{R}{R+D} \right)^{n+2} (n+1) C_n^1 \frac{4\pi}{2n+1} \left[1 - \left(\frac{R-D_1}{R} \right)^n \right] \sum_{i=1}^I a_i^1 P_n(\cos \psi_{PS_i}) \right\} \end{aligned} \quad (17)$$

By substituting Eq. (17) (for $k=1, \dots, 3$) into Eq. (11), the direct topographical effect of the residual terrain in terms of spherical splines as base functions is finally given by:

$$\begin{aligned} DTE^{res}(R+D, \varphi, \lambda) &= -4\pi G\rho R \sum_{n=361}^{n_{\max}} \left(\frac{R}{R+D} \right)^{n+2} \frac{(n+1)}{2n+1} \\ &\quad \cdot \left\{ \left[1 - \left(\frac{R_c}{R} \right)^n \right] \frac{1}{R} \sum_{i=1}^I a_i^1 C_n^1 P_n(\cos \psi_{PS_i}) + \left[\frac{n+2}{2} - \left(\frac{R_c}{R} \right)^n \right] \right. \\ &\quad \cdot \frac{1}{R^2} \sum_{i=1}^I a_i^2 C_n^2 P_n(\cos \psi_{PS_i}) \\ &\quad \left. + \left[\frac{(n+2)(n+1)}{6} - \frac{1}{3} \left(\frac{R_c}{R} \right)^n \right] \frac{1}{R^3} \sum_{i=1}^I a_i^3 C_n^3 P_n(\cos \psi_{PS_i}) \right\}. \end{aligned} \quad (18)$$

In the **second method**, the topography again is expanded into a spherical harmonic expansion in analogy to the first method but the fine structure is modeled by the integral over the residual topography. Then the potentials of the topographical and condensation masses are given by:

$$V_i^{residual} = G\rho \iint_{\sigma} \left[\int_{R+H_{ref}}^{R+H} \frac{\xi^2}{l(R+D, \psi, \xi)} d\xi \right] d\sigma \quad (19)$$

$$V_c^{\text{residual}} = G \cdot R^2 \iint_{\sigma} \frac{\kappa_{Q'}}{l_c(R+D, \lambda, \phi)} d\sigma \quad (20)$$

In this case the spherical density layer $\kappa_{Q'}$ is calculated only for the residual topography. The evaluation of the integral formulas in eqs. (19) and (20) as well as for the first derivatives are given in Martinec (1998).

In the *third method* the area around the computation point is divided into two parts: a spherical cap around the computation point with an appropriate radius, called near-zone (σ_0) and the rest of the Earth, called far-zone (σ_{Fz}). A fine resolution DTM must be used in the near zone while in the far-zone a coarser DTM is sufficient in most cases. Near-zone topography effects on the gravity and geoid heights can be calculated using rectangular prisms, which lead to a particularly simple formula (Nagy, 1966) or by using a Gauss-quadrature method in case of a spherical Earth approximation. In this research, the far-zone effects of the global topography on gravity and geoid heights are studied for Helmert's methods of condensation. The near-zone effect is modeled as described in method 2.

For an economic computation, the formula for the far-zone effect is calculated from the global spherical harmonic expansion of the topography. This will be performed by a Molodenskii-type spectral approach. The formula for calculating the far-zone direct terrain effect is given by:

$$\begin{aligned} DTE_{fz}^{\text{ter}} \Big|_{r=r_p} &= 2\pi G \rho \left(\sum_{n=0}^{N_{\text{max}}} t_n(\eta, \psi, \psi_0) H_n(\varphi, \lambda) \right. \\ &+ \frac{1}{R+H_p} \sum_{n=0}^{N_{\text{max}}} u_n(\eta, \psi, \psi_0) H_n^2(\varphi, \lambda) \\ &- \frac{2H_p}{R+H_p} \sum_{n=0}^{N_{\text{max}}} u_n(\eta, \psi, \psi_0) H_n(\varphi, \lambda) \\ &- \sum_{n=0}^{N_{\text{max}}} w_n(H_p, \psi, \psi_0) H_n(\varphi, \lambda) \\ &- \frac{2(H_p' - H_p)}{R+H_p} \sum_{n=0}^{N_{\text{max}}} v_n(\eta, \psi, \psi_0) H_n(\varphi, \lambda) \\ &\left. - \frac{1}{R} \sum_{n=0}^{N_{\text{max}}} w_n(H_p, \psi, \psi_0) H_n^2(\varphi, \lambda) \right) + [C_1 - C_2] \end{aligned} \quad (21)$$

The coefficients t_n, u_n, v_n, w_n are the Molodenskii truncation coefficients. A detailed description of equation (21) can be found in Makhloof and Ilk (2006).

4 Numerical tests

The computational area is bounded by the geographical coordinates $\lambda \in [-118.75^\circ, -117.25^\circ]$ and $\varphi \in [49.25^\circ, 50.75^\circ]$. The density of the topog-

raphy was assumed to be 2670 kg/m^3 . The height of the calculation points is chosen to be $D=6 \text{ km}$ above the geoid. The Helmert's condensation depth in case of Helmert's first method of condensation is assumed to be 32 km (see Makhloof and Ilk 2006). The numerical tests are based on the DEM GEBCO (<http://www.ngdc.noaa.gov/mgg/gebco>). The topography of the tested area is shown in Fig. 2.

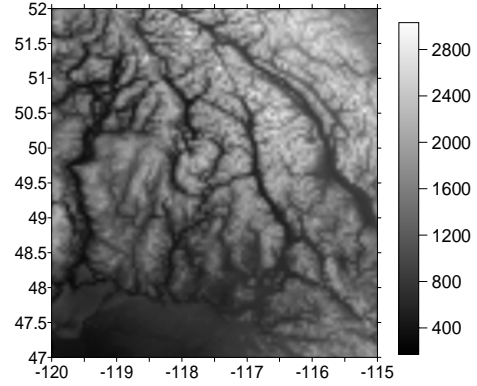


Fig. 2 topography of the tested area

4.1 Direct topographical effect

In a first step the long wavelengths contributions of the topography are calculated. This is done by developing the heights, the quadratic heights and the cubic heights into a spherical harmonic expansion up to a degree of 360. In the next step the unknown spline parameters a_i^k are determined from the residual topography.

Table. 1 Statistical behaviour of the direct topographical effect in the case of Helmert's second method of condensation (units in mGal).

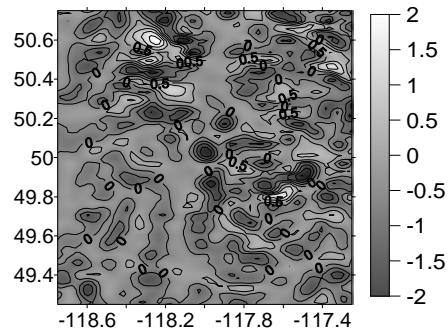
Method	Max	Min	Mean	Std
True-Method(1)	1.35	-1.89	0.02	0.42
True-Method(2)	2.550	-3.15	0.20	0.61
True-Method(3)	2.3	-2.62	0.02	0.51

Table. 2 Statistical behaviour of the direct topographical effect in the case of Helmert's first method of condensation (units in mGal).

Method	Max	Min	Mean	Std
True-Method(1)	6.60	-4.86	0.04	1.41
True-Method(2)	7.35	-6.11	0.53	1.75
True-Method(3)	4.89	-6.10	0.21	1.47

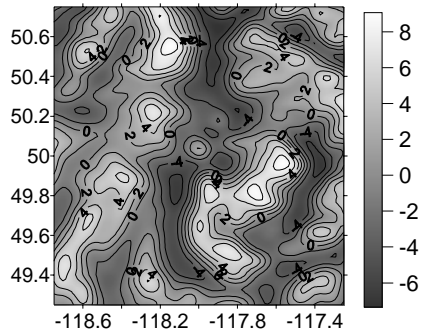
Afterwards the residual effects of the topographic and condensation masses are calculated for the two

Helmert's methods of condensation using all three described approaches. All calculations are based on a sampling of 2.5 arcmin. The results are validated by using the GEBCO DTM in a higher resolution (interpolated to a sampling rate of 15 seconds) and by a global integration. These values are considered to be the "true" values. The differences between the "true" DTE and the calculated DTE by means of the three approaches are shown in the following. Their statistical behaviour is represented in Table 1 and Table 2.

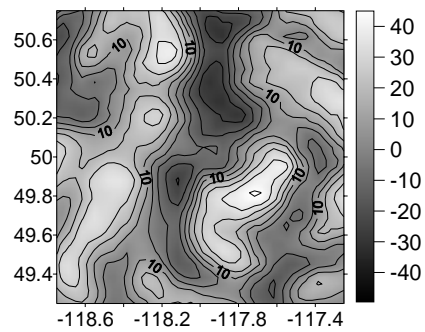


3d) Errors N/Fzone Method(3)[mGal]

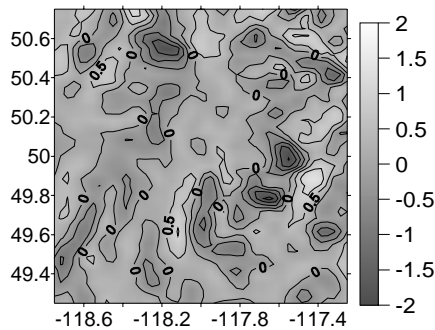
Fig. 3a-d: Results for Helmert's second method of condensation.



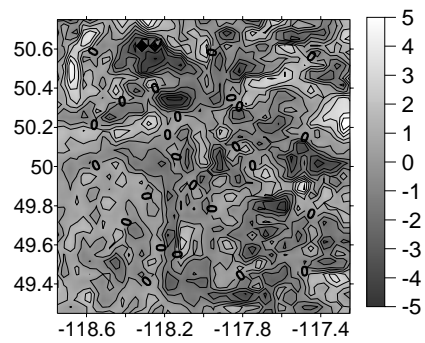
3a) True DTE [mGal]



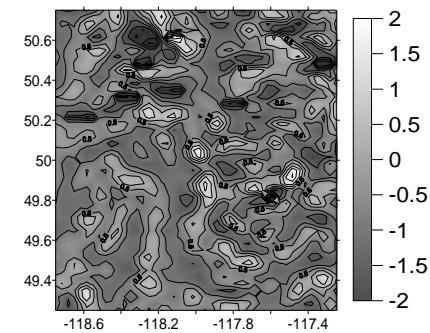
4a) True DTE [mGal]



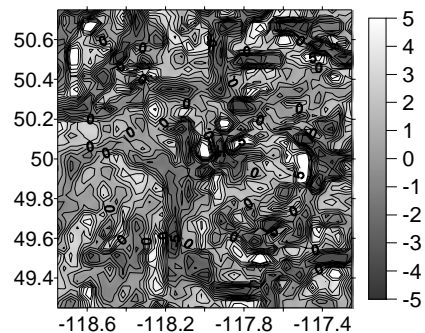
3b) Errors Spline Method (1) [mGal]



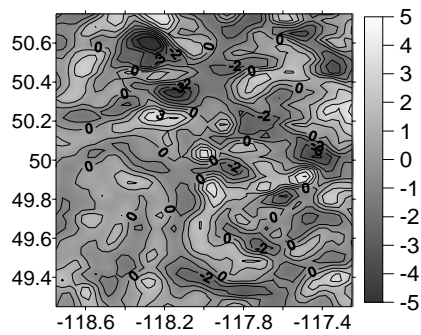
4b) Errors Spline Method (1) [mGal]



3c) Errors Integral Method (2) [mGal]



4c) Errors Integral Method (2) [mGal]



4d) Errors N/Fzone Method(3)[mGal]

Fig. 4a-d: Results for Helmert's first method of condensation.

Table 1 represents the statistical behaviour of all 3 approaches in case of Helmert's second method of condensation. Regarding the min and max values the spline approach performs slightly better than the other two approaches. The standard deviation and mean value for approaches 1 and 3 yield similar results. Looking at Fig. 3b however shows that the errors using the spline approach behave smoother than those depicted in Fig. 3c-d. In case of Helmert's first method of condensation (see Table 2) approaches 1 and 3 again yield similar results. Approach 2 seems to be less accurate in comparison to the other approaches for both condensation methods.

5. Conclusions

In this investigation, three methods for calculating the direct topographical effects at airborne altitude were studied. It has been demonstrated that the spline approach and the N/Fzone approach yield similar results. Considering Fig. 3b the spline approach seems to model the high frequencies parts better than the other approaches, in particular for Helmert's second method of condensation. Further investigations should be focused on the spectral error budget. Another important aspect regarding the accuracy is the choice of an appropriate sampling of the topography. A higher sampling rate could improve the results. For further research we also would like to investigate the demand on the sampling rate for different altitudes to achieve an accuracy level of 1-2 mGal, which corresponds to the accuracy level of present airborne gravimetry applications. In this test scenario ($D=6\text{km}$, sampling 2.5 arcmin) only Helmert's second method of condensation calculated with the spherical spline approach meets the demand regarding the min and max values.

References

- Freeden, W., Gervens, T. Schreiner, M. (1998) *Constructive Approximation on the Sphere*. Oxford University Press, Oxford.
- Heck B (2003) On Helmert's Methods of Condensation, *J Geod* 77: 155-170
- Heiskanen WA, Moritz H (1967) *Physical Geodesy*, WH Freeman and company, San Francisco
- Helmert F R (1884) *Die mathematischen und physikalischen Theorien der höheren Geodäsie*, Vol 2, Leipzig, B. G. Teubner
- Makhloof A. A., Ilk, K. H. (2006) Far-zone Effects for Different Topographic-Isostatic Models Based on a Spherical Harmonic Expansion of the Topography, submitted to *J Geod*
- Martinec Z, Matyska C, Grafarend EW, Vaniček P (1993) On Helmert's Second Condensation Method. *Manusc Geod* 18: 417-421
- Martinec Z (1998) *Boundary-Value Problems for Gravimetric Determination of a Precise Geoid*. Lecture notes in Earth sciences, 73, Springer, Berlin Heidelberg New York
- Molodenskii MS, Eremeev VF, Yurkina MI (1960) *Methods for the Study of the External Gravitational Field and Figure of the Earth* [translated from Russian by the Israel Program for the Scientific Translation], Office of Technical Services, Department of Commerce, Washington
- Müller, F., Mayer-Gürr, T. (2003) Comparison of Downward Continuation Methods of Airborne Gravimetry Data, in: F. Sansò (ed.) *A Window on the Future of Geodesy*, IUGG General Assembly 2003, Sapporo, Japan, International Association of Geodesy Symposia, Vol. 128, pp. 254-258, Springer
- Nagy D (1966) The gravitational attraction of a right rectangular prism, *Geophysics* (31): 362-371.
- Novák P, Vaniček P, Martinec Z, Veronneau M (2001) Effect of the Spherical Terrain on Gravity and the Geoid, *J Geod* 75: 491-504
- Novák, P., Kern, M., Schwarz, K.-P., Heck, B(2003) Evaluation of Band-Limited Topographical Effects in Airborne Gravimetry, *J Geod* 76: 597-604.
- Novák P, Grafarend EW (2005) The Ellipsoidal Representation of the Topographical Potential and its Vertical Gradient, *J Geod* (78): 691-706
- Rummel R, Rapp RH, Sünkel H, Tscherning CC (1988) *Comparisons of Global Topographic/Isostatic Models to the Earth's Observed Gravity Field*. Rep. 388, Department of geodetic Science and Surveying, The Ohio State University, Columbus

Multi-resolution representation of the gravity field from satellite data based on wavelet expansions with time-dependent coefficients

M. Schmidt⁽¹⁾, J. Kusche⁽²⁾, S.-C. Han⁽³⁾, C.K. Shum⁽⁴⁾, M.O. Karslioglu⁽⁵⁾

⁽¹⁾ Deutsches Geodätisches Forschungsinstitut (DGFI), Alfons-Goppel-Strasse 11, 80539 Munich, Germany

⁽²⁾ Delft Institute of Earth Observation and Space Systems (DEOS), TU Delft, The Netherlands

⁽³⁾ NASA Goddard Space Flight Center, Planetary Geodynamics Laboratory, Greenbelt, U.S.A.

⁽⁴⁾ Geodetic Science, School of Earth Sciences, The Ohio State University, Columbus, U.S.A.

⁽⁵⁾ Department of Civil Engineering, Geodesy and Photogrammetry Division, Middle East Technical University, Ankara, Turkey

Abstract. In this paper we determine a regional spatio-temporal gravity field over the northern part of South America including the Amazon region using GRACE inter-satellite range-rate measurements by application of a wavelet-based multi-resolution technique with respect to space and a Fourier series with respect to time. Since the spherical wavelet theory is based on spherical harmonics, our approach accommodates for loading computations in the spectral domain as easily as for spherical harmonics.

Keywords. Multi-resolution representation, spherical wavelets, Fourier series, gravity data, GRACE

1 Introduction

Traditionally in satellite gravity recovery problems the global gravity field of the Earth is modeled as a series expansion in terms of spherical harmonics (Reigber et al., 2005). Spatio-temporal gravity fields from the Gravity Recovery And Climate Experiment (GRACE) data are usually computed for fixed time intervals, like one month (Tapley et al., 2004). Since the Earth's gravity field shows heterogeneous structures over the globe, a multi-resolution representation (MRR) is an appropriate candidate for an alternative spatial modeling (Freedon et al., 1998 and Schmidt et al., 2007). The MRR means basically the approximation of a signal under different resolution levels applying low- and band-pass filters, here realized by spherical scaling functions and wavelets, i.e., spherical isotropic functions. Thus, the MRR is interpreted to be an assembly concept based on

modules, each related to a specific geographical region and frequency band. Whereas the modeling of coarse structures generally needs only a few observations, finer structures, however, require a considerably larger number of observations. Consequently, the computation of the individual modules depends on the distribution of the observation sites. The temporal variation of the gravity field can be considered, e.g., by estimating the modules for specific time intervals (Schmidt et al., 2006) or by introducing one-dimensional series expansions for scaling and wavelet coefficients.

In this paper we determine a regional spatio-temporal gravity model from GRACE data using the spherical wavelet technique for the spatial part. The temporal component is modeled by annual and semi-annual sine and cosine terms. Consequently, we end up with a four-dimensional (4-D) geopotential model of tensor product type. Since the spherical scaling functions and wavelets are derived from spherical harmonics, our approach accommodates for loading computations in the spectral domain as easily as for spherical harmonics. We demonstrate the 4-D model exemplarily for the Amazon basin.

2 Four-dimensional Modeling

The basic idea of the MRR is to split a given input signal $V(\mathbf{r}, t)$, here thought as the geopotential or the disturbing potential of the Earth, depending on position vector $\mathbf{r} = r \cdot \boldsymbol{\xi}$ ($r = |\mathbf{r}|$; $|\boldsymbol{\xi}| = 1$) and time t into a smoother version (approximation) and a number of detail signals (modules) by successive low-pass filtering. The latter are the spectral components of the MRR because they are related to certain

frequency bands. In order to explain this procedure in more detail we introduce the scaling function

$$\phi_i(\mathbf{r}, \mathbf{r}_k) = \sum_{n=0}^{\infty} \frac{2n+1}{4\pi R^2} \left(\frac{R}{r}\right)^{n+1} \Phi_i(n) P_n(\boldsymbol{\xi}^T \boldsymbol{\xi}_k) \quad (1)$$

of resolution level (scale) $i \in \mathbb{N}_0$ ($P_n(\cdot)$ = Legendre polynomial of degree $n \in \mathbb{N}_0$; $\mathbf{r}_k = R \cdot \boldsymbol{\xi}_k$ = position vector of a point on the sphere Ω_R with radius R , $r \geq R$). The Legendre coefficients $\Phi_i(n)$ define the low-pass filter behavior of the scaling function; cf. Eq. (9). The MMR states that the level- $(i+1)$ approximation of V , i.e.

$$V_{i+1}(\mathbf{r}, t) = (\phi_{i+1} \star V(\cdot, t))(\mathbf{r}) \quad (2)$$

(' \star ' means spherical convolution) can be decomposed into the smoother level- i approximation

$$V_i(\mathbf{r}, t) = (\phi_i \star V(\cdot, t))(\mathbf{r}) \quad (3)$$

and the detail signal

$$v_i(\mathbf{r}, t) = (\psi_i \star V(\cdot, t))(\mathbf{r}) \quad (4)$$

absorbing all the fine structures of V_{i+1} missing in V_i , i.e. $V_{i+1}(\mathbf{r}, t) = V_i(\mathbf{r}, t) + v_i(\mathbf{r}, t)$. Consequently, the MRR of an input signal $V(\mathbf{r}, t) = V_{I+1}(\mathbf{r}, t) + \Delta V(\mathbf{r}, t)$ can be written as

$$V(\mathbf{r}, t) = V_{i'}(\mathbf{r}, t) + \sum_{i=i'}^I v_i(\mathbf{r}, t) + \Delta V(\mathbf{r}, t) \quad (5)$$

with $i' \in \{0, \dots, I\}$. Since the scaling functions ϕ_{i+1} and ϕ_i act as low-pass filters, the spherical wavelet function

$$\psi_i(\mathbf{r}, \mathbf{r}_k) = \sum_{n=0}^{\infty} \frac{2n+1}{4\pi R^2} \left(\frac{R}{r}\right)^{n+1} \Psi_i(n) P_n(\boldsymbol{\xi}^T \boldsymbol{\xi}_k) \quad (6)$$

of level i means a band-pass filter defined by its Legendre coefficients

$$\Psi_i(n) = \Phi_{i+1}(n) - \Phi_i(n). \quad (7)$$

Setting $\phi_i(\mathbf{r}, \mathbf{r}_k) =: \phi_{i,k}(\mathbf{r})$ and $\psi_i(\mathbf{r}, \mathbf{r}_k) =: \psi_{i,k}(\mathbf{r})$, respectively, the two-scale relation

$$\phi_{i+1,k}(\mathbf{r}) = \phi_{i,k}(\mathbf{r}) + \psi_{i,k}(\mathbf{r}) \quad (8)$$

follows from the Eqs. (1), (6) and (7). In order to adapt the number of detail signals, i.e. levels, to the specific input signal V we use for our investigations

the modified Blackman scaling function defined by the Legendre coefficients

$$\Phi_i(n) = \begin{cases} 1 & \text{for } 0 \leq n < b^{i-1} \\ A_i(n) & \text{for } b^{i-1} \leq n < b^i \\ 0 & \text{for } n \geq b^i \end{cases} \quad (9)$$

with $A_i(n) = 0.42 - 0.50 \cos(2\pi n_i/b_i) + 0.08 \cos(4\pi n_i/b_i)$, $n_i = n + \text{int}(b^i) - 2 \cdot \text{int}(b^{i-1})$, $b_i = 2 \cdot (b^i - b^{i-1})$ and $b \in \mathbb{R}^+$ (Schmidt et al., 2007). The Blackman wavelet function defined via the Eqs. (6), (7) and (9) is strictly band-limited, i.e. only the Legendre coefficients $\Psi_i(n)$ within the frequency band $B_i := \{n | b^{i-1} \leq n < b^{i+1}\}$ are different from zero. Since this function is characterized by its localization behavior w.r.t. both space and frequency it can be applied to regional data sets in order to establish a regional MRR.

According to Eq. (2) the signal value $V_{i+1}(\mathbf{r}, t)$ can be modeled as

$$V_{i+1}(\mathbf{r}, t) = \sum_{k=1}^{N_i} d_{i,k}(t) \phi_{i+1,k}(\mathbf{r}), \quad (10)$$

wherein the level- $(i+1)$ scaling functions $\phi_{i+1,k}(\mathbf{r})$ are related to N_i computation points on the sphere Ω_R with position vectors $\mathbf{r}_k^i = R \cdot \boldsymbol{\xi}_k^i$. Here we identify the computation points with the knots of a level- i Reuter grid (Freedeen et al., 1998). By introducing the $N_i \times 1$ vectors $\boldsymbol{\phi}_{i+1}(\mathbf{r}) = (\phi_{i+1,k}(\mathbf{r}))$ and $\mathbf{d}_i(t) = (d_{i,k}(t))$ of the level- $(i+1)$ scaling functions $\phi_{i+1,k}(\mathbf{r})$ and the level- i scaling coefficients $d_{i,k}(t)$ with $k = 1, \dots, N_i$, respectively, we rewrite Eq. (10) as

$$V_{i+1}(\mathbf{r}, t) = \boldsymbol{\phi}_{i+1}^T(\mathbf{r}) \mathbf{d}_i(t). \quad (11)$$

With the $N_i \times 1$ vectors $\boldsymbol{\phi}_i(\mathbf{r}) = (\phi_{i,k}(\mathbf{r}))$ and $\boldsymbol{\psi}_i(\mathbf{r}) = (\psi_{i,k}(\mathbf{r}))$ we obtain from Eq. (8)

$$\boldsymbol{\phi}_{i+1}(\mathbf{r}) = \boldsymbol{\phi}_i(\mathbf{r}) + \boldsymbol{\psi}_i(\mathbf{r}). \quad (12)$$

Considering Eq. (12) it follows from Eq. (11) $V_{i+1}(\mathbf{r}, t) = V_i(\mathbf{r}, t) + v_i(\mathbf{r}, t)$, wherein the detail signal v_i is defined as

$$v_i(\mathbf{r}, t) = \boldsymbol{\psi}_i^T(\mathbf{r}) \mathbf{d}_i(t). \quad (13)$$

Analogous to Eq. (11) the level- i approximation $V_i(\mathbf{r}, t)$ can be written as

$$V_i(\mathbf{r}, t) = \boldsymbol{\phi}_i^T(\mathbf{r}) \mathbf{d}_{i-1}(t), \quad (14)$$

wherein $\boldsymbol{\phi}_i(\mathbf{r})$ and $\mathbf{d}_{i-1}(t)$ are $N_{i-1} \times 1$ vectors of the level- i scaling functions $\phi_{i,k}(\mathbf{r})$ and the

level- $(i-1)$ scaling coefficients $d_{i-1,k}(t)$ with $k = 1, \dots, N_{i-1}$ related to $N_{i-1} \leq N_i$ computation points on the sphere Ω_R with position vectors $\mathbf{r}_k^{i-1} = R \cdot \boldsymbol{\xi}_k^{i-1}$ (level- $(i-1)$ Reuter grid). Starting with the coefficient vector $\mathbf{d}_I(t)$ of highest level I the vectors $\mathbf{d}_i(t)$ of the lower levels $i = i', \dots, I-1$ are computable via the relation

$$\mathbf{d}_{i-1}(t) = \mathbf{H}_i \mathbf{d}_i(t) \quad (15)$$

between the scaling coefficient vectors of consecutive levels. This procedure, wherein the given matrices \mathbf{H}_i operate as low-pass filters, is known as the pyramid algorithm; for details see Schmidt et al. (2007). The recursive application of the two-scale relation (12) yields finally the MRR according to Eq. (5) with detail signals v_i defined in Eq. (13).

Schmidt et al. (2006) estimated the coefficient vectors $\mathbf{d}_i(t)$ of the levels $i = i', \dots, I$ from different data sets covering level-dependent observation time intervals. Here, however, we model each element $d_{I,k}(t)$ of the unknown time-dependent scaling coefficient vector $\mathbf{d}_I(t)$ as a Fourier series, i.e.

$$\begin{aligned} d_{I,k}(t) &= \sum_{l=0}^L (a_{I,k;l} \cos(l\omega_0 t) + b_{I,k;l} \sin(l\omega_0 t)) \\ &= \sum_{l=-L}^L d_{I,k;l} \phi_l(t) \end{aligned} \quad (16)$$

with $\omega_0 = 2\pi/T_0$ being the fundamental frequency ($T_0 =$ fundamental period) and

$$\begin{aligned} d_{I,k;l} &:= \begin{cases} a_{I,k;l} & \text{for } l = 0, \dots, L \\ b_{I,k;|l|} & \text{for } l = -L, \dots, -1 \end{cases}, \\ \phi_l(t) &:= \begin{cases} \cos(l\omega_0 t) & \text{for } l = 0, \dots, L \\ \sin(|l|\omega_0 t) & \text{for } l = -L, \dots, -1 \end{cases}. \end{aligned}$$

Introducing the $(2L+1 = N_L) \times 1$ vector $\boldsymbol{\phi}_L(t) = (\phi_l(t))$ and the $N_I \times N_L$ matrix

$$\mathbf{D}_{I;L} = \begin{bmatrix} d_{I,1;-L} & d_{I,1;-L+1} & \dots & d_{I,1;L} \\ d_{I,2;-L} & d_{I,2;-L+1} & \dots & d_{I,2;L} \\ \dots & \dots & \dots & \dots \\ d_{I,N_I;-L} & d_{I,N_I;-L+1} & \dots & d_{I,N_I;L} \end{bmatrix} \quad (17)$$

of the spatio-temporal coefficients $d_{I,k;l}$ we obtain

$$\mathbf{d}_I(t) = \mathbf{D}_{I;L} \boldsymbol{\phi}_L(t) \quad (18)$$

from Eq. (16). Inserting Eq. (18) into Eq. (11) yields

$$\begin{aligned} V_{I+1}(\mathbf{r}, t) &= \boldsymbol{\phi}_{I+1}^T(\mathbf{r}) \mathbf{D}_{I;L} \boldsymbol{\phi}_L(t) \\ &= (\boldsymbol{\phi}_L^T(t) \otimes \boldsymbol{\phi}_{I+1}^T(\mathbf{r})) \text{vec} \mathbf{D}_{I;L}, \end{aligned} \quad (19)$$

wherein the symbol ' \otimes ' means the Kronecker product (Koch, 1999); in addition the vec -operator orders the columns of a matrix one below the other as a vector (Koch, 1999). Applying the two-scale relation (12) recursively we end up with the MRR

$$V_{I+1}(\mathbf{r}, t) = V_{i'}(\mathbf{r}, t) + \sum_{i=i'}^I v_i(\mathbf{r}, t) \quad (20)$$

with the level- i' approximation

$$\begin{aligned} V_{i'}(\mathbf{r}, t) &= \boldsymbol{\phi}_{i'}^T(\mathbf{r}) \mathbf{H}_{i'} \mathbf{D}_{i';L} \boldsymbol{\phi}_L(t) \\ &= \boldsymbol{\phi}_{i'}^T(\mathbf{r}) \mathbf{D}_{i'-1;L} \boldsymbol{\phi}_L(t) \end{aligned} \quad (21)$$

and the level- i detail signals

$$v_i(\mathbf{r}, t) = \boldsymbol{\psi}_i^T(\mathbf{r}) \mathbf{D}_{i;L} \boldsymbol{\phi}_L(t) \quad (22)$$

according to the Eqs. (13) to (15). It is worth to be mentioned again that the $N_{i-1} \times N_L$ matrix $\mathbf{D}_{i-1;L}$ of level- $(i-1)$ spatio-temporal scaling coefficients $d_{i-1,k;l}$ is computed from the corresponding level- i matrix $\mathbf{D}_{i;L}$ via

$$\mathbf{D}_{i-1;L} = \mathbf{H}_i \mathbf{D}_{i;L}. \quad (23)$$

If we subtract a reference signal $\bar{V}(\mathbf{r}, t)$ from the input signal $V(\mathbf{r}, t)$, we rewrite Eq. (5) as

$$\delta V(\mathbf{r}, t) = V_{i'}(\mathbf{r}, t) + \sum_{i=i'}^I v_i(\mathbf{r}, t) + \Delta V(\mathbf{r}, t). \quad (24)$$

Consequently, in Eq. (24) $V_{i'}(\mathbf{r}, t)$ means the level- i' approximation of the residual signal $\delta V(\mathbf{r}, t) = V(\mathbf{r}, t) - \bar{V}(\mathbf{r}, t)$ and $v_i(\mathbf{r}, t)$ are the corresponding level- i detail signals. If the summation limits in Eq. (24) are chosen appropriately, the subsignals $V_{i'}(\mathbf{r}, t)$ and $\Delta V(\mathbf{r}, t)$ can be omitted, i.e. we define $\delta V_{I+1}(\mathbf{r}, t) =: V_{I+1}(\mathbf{r}, t) - \bar{V}(\mathbf{r}, t)$ and obtain

$$\delta V_{I+1}(\mathbf{r}, t) = \sum_{i=i'}^I v_i(\mathbf{r}, t). \quad (25)$$

For the estimation of the unknown parameter matrix (17) we recall Eq. (19), i.e.

$$\delta V_{I+1}(\mathbf{r}, t) = (\boldsymbol{\phi}_L^T(t) \otimes \boldsymbol{\phi}_{I+1}^T(\mathbf{r})) \text{vec} \mathbf{D}_{I;L} \quad (26)$$

as will be explained in subsection 3.2.

3 Four-dimensional Gravity Field of South America

3.1 GRACE Input Data

We processed GRACE L1B data, i.e. KBR-measurements, accelerometer data and precise orbits, via the energy balance approach to produce *residual GRACE geopotential difference observations*

$$\Delta V_{1,2}(t) = \delta V_{I+1}(\mathbf{r}_1(t), t) - \delta V_{I+1}(\mathbf{r}_2(t), t) \quad (27)$$

(Han et al., 2006). Herein, $\mathbf{r}_1 = \mathbf{r}_1(t)$ and $\mathbf{r}_2 = \mathbf{r}_2(t)$ are the trajectories of the two GRACE satellites. Geographically we selected a region in South America which includes the Amazon Basin (see Fig. 3). We chose a total observation interval between February 2003 and June 2005 with a sampling rate of 5 seconds. As explained by Han et al. (2006) the observations (27) are corrected by a priori time-variable gravitational potentials w.r.t. planetary bodies, Earth rotation, Earth and ocean tides, (barotropic effect of) oceans and atmosphere (AOD1B), etc., i.e. they primarily reflect hydrology variations. We assume an a priori standard deviation of approximately $0.003 \text{ m}^2/\text{s}^2$. As can be seen from Fig. 1 the data show large gaps w.r.t. the time, in particular no data are given for June 2003 and the second half of 2004. Furthermore, as the reference potential $\bar{V}(\mathbf{r}, t) = \bar{V}(\mathbf{r})$, introduced in Eq. (24), we apply GGM01C.

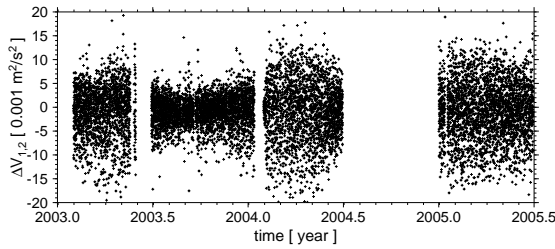


Fig. 1: Time series of the observations $\Delta V_{1,2}(t)$ within the region of interest related to the observation interval between February 2003 and June 2005.

3.2 Parameter Estimation

For the derivation of the observation equation we introduce Eq. (26) into Eq. (27) once for $\mathbf{r} = \mathbf{r}_1(t)$ and once for $\mathbf{r} = \mathbf{r}_2(t)$. Applying the computation rules for the Kronecker product the observation equation for a single observation $\Delta V_{1,2}(t_p)$ at time $t = t_p$

with $p = 1, \dots, P$ reads

$$\begin{aligned} \Delta V_{1,2}(t_p) + e_{1,2}(t_p) \\ = \left(\phi_L^T(t_p) \otimes \Delta \phi_{I+1}^T(\mathbf{r}_1, \mathbf{r}_2) \right) \text{vec} \mathbf{D}_{I;L} \end{aligned} \quad (28)$$

with $\Delta \phi_{I+1}(\mathbf{r}_1, \mathbf{r}_2) = \phi_{I+1}(\mathbf{r}_1(t)) - \phi_{I+1}(\mathbf{r}_2(t))$. Introducing the $P \times 1$ vectors $\mathbf{y} = (\Delta V_{1,2}(t_p))$ and $\mathbf{e} = (e_{1,2}(t_p))$ of the observations and the measurement errors $e_{1,2}$, respectively, the $P \times u$ coefficient matrix $\mathbf{A} = (\phi_L^T(t_p) \otimes \Delta \phi_{I+1}^T(\mathbf{r}_1, \mathbf{r}_2))$ with $u = N_L \cdot N_L$, the $u \times 1$ vector $\boldsymbol{\beta} = \text{vec} \mathbf{D}_{I;L}$ of the unknown spatio-temporal scaling coefficients $d_{I,k;l}$ and the $P \times P$ covariance matrix $D(\mathbf{y})$ of the observations, the linear model

$$\mathbf{y} + \mathbf{e} = \mathbf{A} \boldsymbol{\beta} \quad \text{with} \quad D(\mathbf{y}) = \sigma_y^2 \mathbf{P}_y^{-1} \quad (29)$$

is established. Herein σ_y^2 and \mathbf{P}_y are denoted as the variance factor and the weight matrix, respectively; see (Koch, 1999). Since the normal equation matrix $\mathbf{A}^T \mathbf{P}_y \mathbf{A}$ is usually not of full rank or at least ill-conditioned due to downward continuation, we introduce prior information for regularization. The applied procedure explained in detail by Schmidt et al. (2007), is visualized in the upper part of Fig. 2 (initial step).

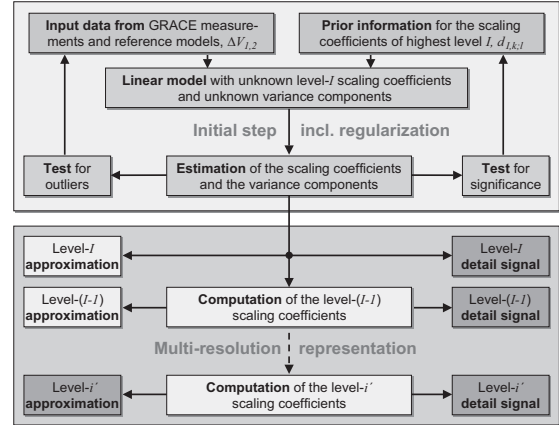


Fig. 2: Upper part: flowchart of the estimation procedure. Prior information for the unknown spatio-temporal scaling coefficients $d_{I,k;l}$ is introduced; the regularization is performed by estimation of variance components; see e.g., Koch and Kusche (2001). Lower part: flowchart of the MRR following the Eqs. (21) to (23).

3.3 Results

For the spatial part in Eq. (28) we chose the Blackman representation with base $b = 2.1$ and highest level $I + 1 = 5$, i.e. we solved for signal parts until

degree $n = 40$ according to the definition (9). Furthermore, for the temporal part we set $L = 2$ within the Fourier series (22) and, thus, determined the annual and semi-annual oscillations of the scaling coefficients $d_{4,k}(t)$. In order to interpret these results we calculated the level-4 amplitudes $A_{4,k;l}$ and phases $\varphi_{4,k;l}$, generally defined as

$$A_{I,k;l} = \sqrt{d_{I,k;l}^2 + d_{I,k;-l}^2}, \quad (30)$$

$$\varphi_{I,k;l} = \arctan(d_{I,k;-l}/d_{I,k;l}) \quad (31)$$

for $l = 1, \dots, L$ in each spatial computation point $\mathbf{r}_k^4 \in \Omega_R$ within the area of investigation. Figure 3 shows the distribution of the annual amplitudes $A_{4,k;1}$ and the semi-annual amplitudes $A_{4,k;2}$. The highest annual variability is detected along the Amazon, where also the phases change (not shown here).

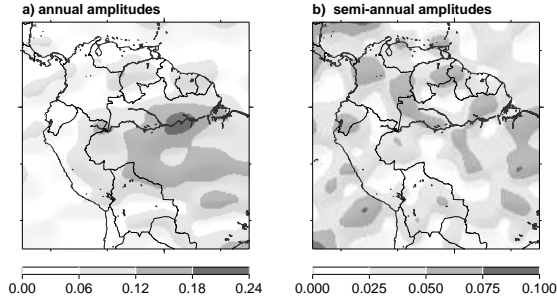


Fig. 3: Distribution of the (a) annual and (b) semi-annual amplitudes of the scaling coefficients $d_{4,k}(t)$ in the computation points \mathbf{r}_k^4 .

Following Farrell (1972) the geopotential V or the residual geopotential δV , respectively, can be transformed into level- $(I + 1)$ height deformations

$$\delta h_{I+1}(\mathbf{r}, t) = \sum_{i=i'}^I h_i(\mathbf{r}, t) \quad (32)$$

at the Earth's surface w.r.t. the reference model GGM01C by evaluating the spherical convolutions

$$h_i(\mathbf{r}, t) = (k \star v_i(\cdot, t))(\mathbf{r}) \quad (33)$$

w.r.t. the detail signals v_i introduced in Eq. (22). In Eq. (33) the kernel $k(\mathbf{r}, \mathbf{r}_k)$ is defined as

$$k(\mathbf{r}, \mathbf{r}_k) = \sum_{n=0}^{\infty} \frac{2n+1}{4\pi R^2} \frac{h'_n}{g(1+k'_n)} P_n(\boldsymbol{\xi}^T \boldsymbol{\xi}_k) \quad (34)$$

with k'_n and h'_n being the static gravitational and vertical load Love numbers of degree n , respectively; g = gravitational constant. Figure 4 shows "snap shots" of the level-5 height deformations



Fig. 4: Level-5 height deformations $\delta h_5(\mathbf{r}, t_j)$ at times $t_j = 01/02/2003 + j \cdot 10$ days with $j = 0, \dots, 35$.

$\delta h_5(\mathbf{r}, t_j)$, i.e. until degree $n = 40$, at selected times $t = t_j$ within one year, again considering annual and semi-annual oscillations for the scaling coefficients. The results reveal that the height deformations vary in the Amazon basin of about ± 10 mm. These results are in good agreement with other investigations, e.g., with Han et al. (2005).

Figure 5 shows the corresponding values of the level-4 height deformations $\delta h_4(\mathbf{r}, t_j)$ considering signal parts until degree $n = 19$. Finally, Fig. 6 depicts the level-4 detail signal $h_4(\mathbf{r}, t_j) = \delta h_5(\mathbf{r}, t_j) - \delta h_4(\mathbf{r}, t_j)$ of height deformations computed according to Eq. (33). This signal comprises signal parts related to the frequency band $B_4 = \{n | 9 < n < 40\}$ as mentioned in the context of Eq. (9), i.e. the finest structures within the level-5 height deformations $\delta h_5(\mathbf{r}, t_j)$.

4 Conclusions

We have demonstrated that a spatial multi-resolution technique can be successfully combined with an appropriate series expansion in the time domain in order to derive a spatio-temporal, i.e. 4-D gravity field. It is based on a spherical wavelet MRR, using the Blackman scaling function, w.r.t. space and a Fourier series considering annual and semi-annual terms w.r.t. time. The combination is performed by

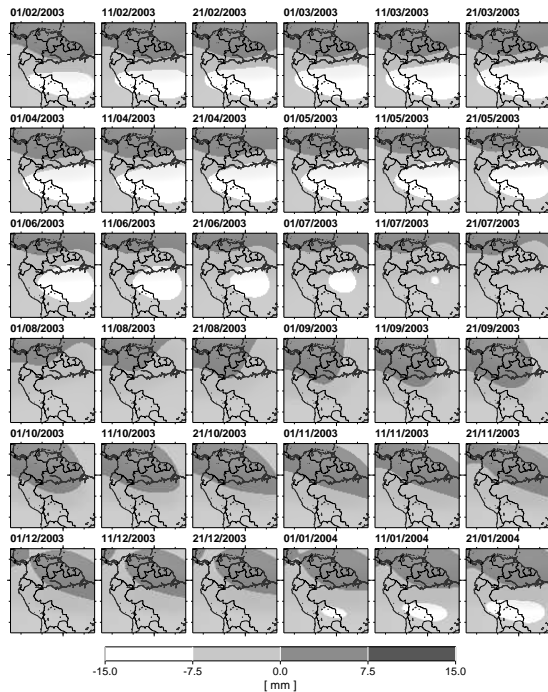


Fig. 5: Level-4 height deformations $\delta h_4(\mathbf{r}, t_j)$ at times $t_j = 01/02/2003 + j \cdot 10$ with $j = 0, \dots, 35$.



Fig. 6: Level-4 detail signal $h_4(\mathbf{r}, t_j)$ at times $t_j = 01/02/2003 + j \cdot 10$ with $j = 0, \dots, 35$.

introducing tensor-product base functions. We computed a regional geopotential model of the northern

part of South America from GRACE-derived data up to level $I+1 = 5$.

As a disadvantage of this approach we mention that a MRR w.r.t. time is not considered. This fact can be seen from Eq. (22), because each detail signal v_i is modeled by the same matrix $\phi_L(t)$. This restriction can be overcome by substituting one-dimensional scaling functions for the Fourier series expansion, e.g., B-spline functions. This procedure is a topic for future studies.

Acknowledgements

This work is partially supported by NASA (NNG04GF01G and NNG04GN19G), and by NSF's CMG Program (EAR0327633). We acknowledge the NASA/GFZ GRACE project for the GRACE data products (distributed by JPL PODAAC), and thank Srinivas Bettadpur of the University of Texas for providing precise GRACE orbits with finer temporal resolutions for our data processing.

References

Farrell, W.E. (1972). Deformation of the Earth by surface loads. *Rev. Geophys. Space Phys.*, 10, pp 761-797

Freeden, W., T. Gervens, and M. Schreiner (1998). *Constructive Approximation on the Sphere (with Applications to Geomatics)*. Clarendon Press, Oxford

Han, S.-C., C.K. Shum, C. Jekeli, and D. Alsdorf (2005). Improved estimation of terrestrial water storage changes from GRACE. *Geophys. Res. Lett.*, 32, L07302, doi: 10.1029/2005GL022382

Han, S.-C., C.K. Shum, and C. Jekeli (2006). Precise estimation of in situ geopotential differences from GRACE low satellite-to-satellite tracking and accelerometry data. *J. Geophys. Res.*, 111, B4411, doi:10.1029/2005JB003719

Koch, K.R. (1999). *Parameter Estimation and Hypothesis Testing in Linear Models*. Springer, Berlin

Koch, K.R., and J. Kusche (2001). Regularization of geopotential determination from satellite data by variance components. *J. Geod.*, 76, pp 259-268

Reigber, C., R. Schmidt, F. Flechtner, R. Koenig, U. Meyer, K.-H. Neumayer, P. Schwintzer, and S. Zhu (2005). An Earth gravity field model complete to degree and order 150 from GRACE: EIGEN-GRACE02S. *Journal of Geodynamics*, 39, pp 1-10

Schmidt, M., S.-C. Han, J. Kusche, L. Sánchez, and C.K. Shum (2006). Regional high-resolution spatiotemporal gravity modeling from GRACE data using spherical wavelets. *Geophys. Res. Lett.*, 33, L08403, doi:10.1029/2005GL025509

Schmidt, M., M. Fengler, T. Mayer-Gürr, A. Eicker, J. Kusche, L. Sánchez, and S.-C. Han (2007). Regional Gravity Modelling in Terms of Spherical Base Functions. *J. Geod.*, 81, pp 17-38, doi: 10.1007/s00190-006-0101-5

Tapley, B.D., S. Bettadpur, J. Ries, P. Thompson, and W. Watkins (2004). GRACE measurements of mass variability in the Earth system. *Science*, 305, pp 503-505